Studies of Gas Phase Electron, Ion and Atom Collision Processes

by

Peter W. Harland

B.Sc.(Hons)(Wales), Ph.D.(Edin), M.N.Z.I.P., F.N.Z.I.C.

Thesis presented for the Degree of
Doctor of Science
of the
The University of Edinburgh

March 1995

EX BIBL. UNIV. EDINBURGH

Knowledge for the sake of understanding not merely to prevail,
that is the essence of our being.
None can define its limits, or set its ultimate boundaries.

Vannevar Bush 1890 - 1974
Director Office of Scientific Research and Development (US) 1941 - 1946

Abstract

The research papers submitted in this thesis describe experimental and theoretical investigations of particle collisions in which the projectiles have been electrons, ions and atoms, and the targets have been atoms and molecules. Non-reactive and reactive collisions have been studied in order to explore the fundamental nature of the collision event, to understand the dynamics, and to facilitate the determination of thermochemical parameters and reaction properties.

The formation of positive and negative ions under single collision conditions as a function of electron impact energy has been investigated for small molecules and for molecular clusters. The measurement of accurate ionization efficiency curves and ionization thresholds has been achieved using custom designed near-monochromatic electron sources or analytical deconvolution. In many cases, detailed energy balancing has been attempted through the measurement of the recoil energies of fragment ions using retarding electric fields. Ionization mechanisms for associative and dissociative resonance electron capture and the formation of isomeric positive ions have been deduced. Thermochemical parameters, including electron affinities, ionization potentials, enthalpies of formation and bond dissociation energies, have been determined. Experiments in which the molecular targets were spatially oriented have shown, for the first time, that the mass spectrum and the ionization efficiency are orientation dependent. A theoretical model has been developed which accounts for the experimental measurements.

Investigations of ion-molecule chemistry and non-reactive ion-molecule interactions have been carried out using a custom designed drift-tube mass spectrometer. It has been shown that isomeric ions can be distinguished by their ion transport properties and that the isomeric form of an ion-molecule reaction product ion can be directly measured. A theoretical model based on a generalised ion-helium interaction potential was developed which qualitatively accounted for the relative ion mobilities of a wide range of ions according to their physical properties. The calculation of *ab initio* interaction potentials has been used with scattering theory and ion transport theory to successfully calculate ion mobilities for ground state and electronically excited ions drifting in helium over a wide range of electric field to particle density ratios. Comparison between experimental data and theoretical calculations have been used to refine the theory and interpret experimental results.

Experimental measurements and theoretical modelling of expanding supersonic jets has enabled the calculation of supersonic molecular beam properties. Cross beam experiments have been employed to investigate the effect of molecular orientation on collisions between potassium atoms and symmetric top molecules as a function of the relative collision energy. It has been shown that: i) the reaction cross-section is dependent on the orientation; ii) the reaction mechanism (scattering behaviour) depends on orientation in some cases; iii) both the exit and entrance channels exhibit orientation effects. These experiments have provided the first evidence for the dependence of electron transfer on the spatial orientation of the acceptor molecule.

Acknowledgements

There are too many colleagues and friends around the world to acknowledge individually. However, I owe a special thanks to David Smith F.R.S. for his friendship, support over the past decade, and his suggestion and encouragement to submit this application.

I am grateful to my academic colleagues in the Chemistry Department and other Departments at the University of Canterbury for their friendship and professional association, and to my graduate students and the technical staff who have contributed so much enthusiasm and hard work. I should like to express my appreciation to friend and colleague Rod Claridge and to those colleagues from the Chemistry Department who have also been co-authors over the years, Robert Maclagan, Leon Phillips, Colin Freeman, and Murray McEwan. I should like to express my gratitude to Barrie Wood and Russell Gillard from the Departmental Machineshop and to Derek Williams, Sandy Ferguson, and John Davis from the Electronics Workshop, without whose expertise and advice the instruments and machines could not have been constructed. I have been fortunate to have always had first class graduate students who have worked hard and contributed so much. The Ph.D. students from Canterbury who have contributed to the work in this thesis are Bruce McIntosh, Richard Simpson, Simon Petrie, Steven Grice, Brett Cameron, Craig Aitken, and David Blunt.

My association with Rice University and the Rice Quantum Institute has always been very important to me. It began as a Post-Doctoral Fellow in 1971 and continues today as an adjunct Professor of Chemistry. I should like to express my gratitude to the Faculty and staff of the Chemistry Department at Rice for always making me so welcome. In particular, I wish to acknowledge my good friend and co-worker Phil Brooks and Bob Curl who have been collaborators on several exciting research projects over many years, and former graduate students Howard Carman and Mike Barnes for the good times working together "at the coal face", for the humour, enthusiasm and continuing friendship.

A very special acknowledgement and appreciation to Jen, Duane, Amanda and Bruce. Without my family, their tolerance and support, I would not have been able to pursue an active career in scientific research.

1. Contents

2. Introduction

This research submitted in this dissertation covers the development and application of experimental techniques, mathematical models and theoretical methods for the investigation of particle collisions involving electron, ion and atomic projectiles on atomic and molecular targets carried out over the period from 1971 to 1995. The motivation behind the research has been a desire to advance our understanding of the collision event, to explore the dynamics and mechanisms for reactive processes at the molecular level, to make use of mathematical models as a guide for the interpretation of experimental observations and to predict the outcome of experiments to be performed.

At the molecular level, many of the parameters needed to characterise the collision event are essentially independent of the projectile and target identities. However, the experimental techniques and theoretical methods employed to probe the dynamics and deduce interaction mechanisms can differ significantly for different particle target combinations. In an ideal situation, the velocities of projectile and target would be controlled or at least measured, the quantum states would be preselected and the relative spatial orientation of particles in the collision would be prearranged. The products would then be similarly characterised and, in the case of reactive collisions, their identities (chemical formula and structural) would be established. Experiments would be repeated for a range of reagents in order to assess the effect of molecular properties such as dipole moment, molecular polarisability, electron affinity etc., on reactivity or non-reactive energy transfer processes. This is indeed a tall order, the signal level in any experiment appears to be inversely related to the degree of control exercised and you very quickly run out of anything to measure. Despite this limitation, experiments can be performed in which one or more parameters are controlled, and the collision mechanism can then be explored from different aspects. This has been the philosophy underlying the work described in this thesis.

Positive and negative ion formation by electron impact ionization of molecules and clusters has been studied as a function of electron energy. The mechanisms for ionization have been deduced through the identification of product ions by mass spectrometry and an accounting of the energy balance through the measurement of ion translational energies. A mathematical deconvolution method was used and near-monochromatic electron sources designed in order to minimise the effect of the electron energy distribution on the measurement of accurate appearance energies. A large number of previously unknown thermochemical parameters for ions and radicals have been determined in these studies. Isomeric ions formed from selected series of cyano, isocyano, and small oxygen containing ions of interstellar interest have been identified and their enthalpies of formation determined. This led to experiments in which attempts to identify isomeric ions and the isomeric form of ion-molecule product ions were carried out in a drift-tube mass spectrometer designed for the purpose. The latest papers submitted in this thesis describe new experiments in which the first investigation of electron collisions with spatially oriented molecules are reported. This work has shown that the electron ionization cross-section and the mass spectrum are dependent on the electron-molecule orientation. A new theoretical model for electron impact ionization has been developed which predicts the main features of the experimental results and can be used to calculate unknown ionization cross-sections. A mechanism for the formation of cluster ions and fragments was proposed in order to account for the measurements in an experimental study of the electron impact ionization of molecular clusters produced in supersonic expansions of small polar and non-polar molecules.

Reactive and non-reactive ion-molecule interactions have been studied in a flow tube and a drift-tube. Flow tube experiments were carried out to investigate ion-molecule mechanisms for the formation of cyano ions and neutral molecules in interstellar dust clouds. The drift-tube mass spectrometer was designed for an investigation of isomeric ions and for the measurement of ion transport properties as a function of electric field strength. The drift-tube was used to demonstrate for the first time that measurable differences between the transport properties of small isomeric ions could be determined. In addition, the first experimental identification of the isomeric form of an ion-molecule reaction product was made through a measurement of its mobility. Trends in the ion transport properties for a series of ions of different mass, structure and dipole moment, measured in the drift-tube, were successfully modelled by a theoretical analysis based on a generalised ion-molecule interaction potential. This model predicted that isomeric forms of ions should be distinguishable by their differences in ion velocity in the drift-tube, and confirmed by experiment. A series of *ab initio* quantum mechanical computations of ion-neutral interaction potentials was then initiated and used with scattering theory and ion transport theory to calculate macroscopic ion transport properties for ground state and electronically excited ions. Comparisons between the theoretical predictions and experimental measurements have led to refinements in the theoretical method and to a better understanding of non-reactive ion-atom and ion-molecule interactions. Mobilities for atomic ions in inert gas buffers can now be reliably calculated within the experimental accuracy available with the most sophisticated drift-tubes.

The flow dynamics of expanding atomic and polyatomic supersonic expansions has been theoretically modelled and used with accurate velocity distributions measured in a molecular beam machine to calculate rotational to translational energy transfer parameters, axial and radial temperatures, and other useful molecular beam characteristics. Supersonic molecular beams of symmetric top molecules have been spatially oriented in a combination of inhomogeneous and homogeneous electric fields and crossed in the scattering chamber of a molecular beam machine by thermal and accelerated beams of potassium atoms. The effect of molecular orientation, relative collision velocity and molecular identity on the reaction of potassium atoms with a wide range of methyl halides, trifluoromethyl halides, tertiary butyl halides and the haloforms have been explored. These experiments have established that the reactive cross-section is higher for collision at the end of the molecule with the leaving group, irrespective of dipole polarity. Through scattering experiments it has been demonstrated that the mechanism for the reaction of thermal energy potassium atoms with the alkyl halides depends on the molecular orientation and that reactions involving the trifluoromethyl halides proceed exclusively by the harpoon mechanism. Theoretical models developed in the course of the work and experiments with fast potassium atoms have shown that orientation effects arise in both the exit and entrance channels of reactions involving adiabatic transitions between covalent and ionic diabats. Since the entrance channel involves an electron transfer from the electropositive potassium atom to the electronegative molecule, the experiments have shown that the electron transfer step is orientation dependent.

In summary, the research outlined here has included studies of particle collisions in which the projectiles have been electrons, ions and atoms, the targets have been atoms and molecules, the physical properties of reagents have been systematically varied, the relative velocities have been controlled, the spatial orientation of molecular targets have been prearranged, and the quantum states have been taken into account. Specialised instruments have been designed and applied in the measurements and theoretical models have been developed and used to guide the interpretation of experimental results and to plan new experiments.

3. Academic Autobiography

On reflection, I am sure that we can all identify twists and turns in our careers that have led to our present position and ponder the possible outcome if decisions, often taken with some trepidation, had "gone the other way". I can readily identify a number of such occasions and I will endeavour to include reference to them in this preamble, in so much as it serves to guide the reader through my professional career, the research fields I have explored and the areas of Chemical Physics in which I have made some contribution. I cannot, in all honesty, claim that my research career has been planned in the way a military campaign or the organisation of one's superannuation fund may have been mapped out. My continuing interest in isolated collision processes as well as my addiction to the design and construction of machines permeates my research career, although there is a degree of branching, a touch of serendipity and a long term interest in chemical education.

1965 - 1968

I read for an Honours degree in Chemistry at the University of Wales, Aberystwyth from 1965 to 1968, studing maths, physics and chemistry in my first year and physics and chemistry in the second year. I carried out my final year Honours project in Chemistry working on peroxy-radical kinetics with Professor Aubrey Trotman-Dickenson (T-D). An interest in Chemical Physics was established during my High School years with extensive reading of New Scientist, Scientific American and paperbacks on Space, Relativity, the Universe and everything. These interests were subsequently reflected in my choice of Physics and Chemistry in my Honours 2 year at Aberystwyth. I remember the difficulty in making that final choice between Physics and Chemistry for the final Honours year, the enthusiasm and high quality of the lecturing in Chemistry being the deciding factor. I had been accepted into T-D's research group for Ph.D. studies on completion of my degree when I heard that he was leaving at the end of that year to take up the position of Principal of the newly established University of Wales Institute of Science and Technology, UWIST, in Cardiff. I had already completed a literature survey in the field of gas phase kinetics and made applications to Baldwin at Hull, Gowenlock at Heriot-Watt, Edinburgh and both Thynne and Knox at the University of Edinburgh. I interviewed with Brian Gowenlock at Heriot-Watt in Edinburgh one snowy morning in April 1968 and later the same day with John Thynne (JCJ) and John Knox at the University of Edinburgh. I received an offer from John Thynne a week later to work on a joint project with John Knox, "when the 1st Class Honours degree was in the bag".

1968 - 1971

When this became a reality in the June of that year I was able to confirm my acceptance of the offer and I moved to Edinburgh at the end of September 1968. Brian Gowenlock had offered me a BP graduate fellowship to work on the desalination and detoxification of sea water. Although this was attractive, my fascination with fundamental processes steered me towards the free radical kinetics project offered by JCJ and John Knox. If the choice had gone the other way, this account would read rather differently. JCJ had taken delivery of a Bendix Model 3015 time-of-flight mass spectrometer, TOFMS, about a year before I arrived in

Edinburgh. It was the first machine in Europe at that time which had been designed for both positive and negative ion detection. I was about 3 weeks into the design and construction of a glass vacuum line for free radical studies when JCJ asked if I would like to transfer to the TOFMS to work on negative ion formation in the gas phase by low energy electron impact. He already had a final year Ph.D. student, Ken MacNeil, who had worked with the instrument since its delivery and JCJ was anxious that a transfer of mechanical, electrical and chemical knowledge take place during a reasonable period of graduate student overlap. I was absolutely delighted, I had already admired the Bendix, talked with Ken about his work and expressed my interest in the project. I transferred my laboratory notebook the next day and this new turn of events became the launching pad for my subsequent excursions into particle dynamics.

I should add at this point that JCJ explained to me that the enormous investment in the Bendix and the responsibility it placed on him to produce results required that the instrument be fully utilised. This meant 24 hours a day. So, it was decided that one student work the daylight shift, from 8 a.m. to 8 p.m. and that the other work the night shift, from 8 p.m. to 8 a.m. It was left up to Ken and I to organise the roster to our mutual satisfaction. To cut a long story short, I took the night shift and worked 10 to 12 hours a day, 6 days a week for most of my first year. When Ken McNeil began writing his thesis in mid 1969 I modified my routine. I had become accustomed to the fast pace resulting from an empty building, uncluttered computer time on the University mainframe and a "clean" electrical mains supply, and I completed my post-graduate years on an 8 a.m. to 11 p.m. schedule. I married Jennifer Brown, who was working on a Ph.D. project in the Botany Department, on the 1st August 1969. JCJ left the University later that year to take up an appointment as the Scientific Advisor to the Minister of Science, Mr. Anthony Wedgewood-Benn, in London, and Ken left in October 1969 for a post-doctoral fellowship with Jean Futrell at the University of Utah in Salt Lake City. I telephoned JCJ every Friday afternoon at 4 p.m. and he visited every 4 to 6 weeks for an extended weekend. Dr. David Whan was appointed as my associate supervisor after JCJ left Edinburgh and Dr. Robert Donovan, who had arrived as a lecturer in Physical Chemistry about this time, provided additional support. I began to apply for post-doctoral positions in the United States early in 1971 and Robert advised me to apply for a Fulbright Scholarship. Although he had spotted the "invitation to apply notice" a week after the deadline an application was put together at breakneck speed and posted off, despite my conviction that it was already too late. I was therefore pleasantly surprised to receive a letter several months later informing me that my application had been successful and I had been awarded a Fulbright Travel Scholarship in support of post-doctoral studies in the United States over a two year period. Like so many other opportunities taken and decisions made, the Fulbright was to become a major factor in the future course of my career some 2 years later. I began writing my thesis, entitled "Studies of Negative Ion Formation by Low Energy Electron Impact", in June 1971 and submitted the bound copies in late August. My Ph.D. oral in October 1971 was conducted by Professor Morris Sugden, JCJ and John Knox at the Shell Thornton Research Institute near Chester where Professor Sugden was the Director of Research. He was also Professor of Physical Chemistry at Cambridge

University. Jennifer had already successfully survived her Ph.D. oral examination in Edinburgh during September, so we were able to depart a week after my oral examination to take up a post-doctoral appointment with Professor J. L. Franklin (Joe) at Rice University, Houston.

1971 - 1973

Joe picked us up at Houston Inter-Continental Airport and drove the 40 miles to his home where we stayed for the first few days. He had been Head of Research at Exxon until moving to Rice as Head of the Department of Chemistry in the mid-60's. His strength was in research and his ability to cure insomnia by lecturing was a well established fact. I remember as we drove into Houston on that first day asking Joe about the almost overwhelming smell of chemical pollution, he replied, "that, boy, is the smell of money". Unfortunately, one cannot capture in writing the rich southern drawl with which the comment was delivered. So began an association with Joe and Rice that was to continue beyond Joe's death in 1982, through to the present. Rice was a scientifically stimulating environment as well as boasting one of the most attractive campus's in the United States. The space programme was in full swing just 2 years after the first moon landing and Rice had forged close ties with NASA headquarters, 25 miles south of the campus at Clear Lake. Research projects associated with the Space Programme were in evidence everywhere. The Space Science Department was the main recipient of NASA funding with projects on modelling the magnetosphere and van Allen belts, experimental particle physics, laser development, computer software development and rocket probing of the upper atmosphere from a site in Alaska. Joe was able to arrange a post-doctoral fellowship for Jennifer within a few days of our arrival. She interviewed with Professor Ward in the Environmental Sciences Department one morning and began work the following day on the effects of simulated hypergravity on plant growth funded by the NASA Skylab Programme. At the conclusion of that project she moved to the Biology Department for the second year to work on enzyme kinetics.

My training at Edinburgh had been ideal for the projects at Rice. I had learned about high vacuum technology, electronics, computing, mass spectrometry and ion formation processes in the gas phase. I had become a devoted experimentalist, I had learned how to generate and control thermal energy electron beams, the importance of cleanliness and the materials which were both suitable and unsuitable for studies of charged particles in high vacuum conditions. I had also worked on the application of mathematical algorithms for deconvolution of electron beam energy distributions from negative ion resonance curves. When I started at Rice I was surprised to find that my knowledge and experience was not widely shared by others attempting similar experiments and I was able to contribute to several of the major programmes in the Chemistry Department. My first job was to convert a Model 3012 Bendix TOFMS to negative ion mode and to make an attempt to measure the recoil energy released in dissociative resonance electron capture by small molecules. The remodelling of the TOFMS, which involved replacement and upgrading of the vacuum pumping systems, a total redesign of the ion source and signal handling electronics and the generation of computer programmes for data manipulation, further stimulated my passion for instrumental technique and electronics. The project was very successful. Through the measurement of recoil energies we were able to advance a model for the distribution of internal energy between the available vibrational modes of the intermediate molecular negative ion during fragmentation. In some cases, we were able to reconcile specific excess energy differences between experimental measurement and thermochemical accounting with electronic states of the neutral free radical fragmentation product which had been predicted theoretically but not previously detected experimentally.

In the first few weeks at Rice I met several people who would continue to play important roles in my future career, as colleagues and as friends. These include Phil Brooks and Bob Curl, who have visited Canterbury over recent years, Ron Stebbings and Barry Dunning from Space Physics and Jim Hudson, a mass spectroscopist from the Chemistry Department, who will be spending time in my laboratory during 1995. When I joined the group meetings for Phil Brooks's molecular beams group at his home during those post-doctoral years at Rice, I had no idea that I would eventually develop a very rewarding collaborative research programme with Phil and Bob, spend two separate years and many shorter visits as a Visiting Professor at Rice and be appointed as an Adjunct Professor of Chemistry at Rice University and the Rice Quantum Institute in 1990.

All too soon the two year tenure of my Fulbright Scholarship approached an end, Joe had offered extra funding to stay on at Rice as a senior post-doctoral fellow but one of the conditions of my Fulbright was to return to Britain or a Commonwealth country within two years. After considerable debate we decided, rather reluctantly, that it would have been unethical to break the conditions accepted with the Scholarship. I began searching Nature, C&E News, New Scientist and Chemistry in Britain in April 1973 for research and academic appointments and quickly found two advertisements for Australia. One was for a Lecturer in Physical Chemistry with interests in ionization processes at La Trobe University, Melbourne with Jim Morrison and the second was for a Research Physicist or Physical Chemist to work on ion-molecule kinetics with Keith Ryan in the Division of Physics, CSIRO (Commonwealth Scientific and Industrial Research Organisation) in Sydney. I submitted applications for both positions and received a telephone offer from CSIRO, via the Australian Embassy in Washington D.C. within a month of submitting the application. Since my application had been sent in shortly after the deadline the response had been faster than I had expected. I was given one week to respond to the Australian Embassy by telephone. I sent a telex to La Trobe enquiring on the time scale for their appointment exercise, it was due to be discussed that week and an offer would go out in two to three weeks. I really wanted to teach as well as research, but I had an offer, and the opportunity to devote full time to research in ion-molecule interactions was appealing. The salary was very high by British standards and it was an opportunity to see Australia. I telephoned the Australian Embassy at the end of the week and accepted the appointment verbally. I was told that an offer in writing would appear in two to three weeks from Sydney. The secretary to the scientific attaché spent over an hour on the telephone telling me all about CSIRO and Australia. She also suggested that I might want to tour ion-molecule laboratories in the United States before leaving for Australia and suggested that I send her a list. She discussed our move to Sydney and gave us the choice of second class airfare from

Houston to Sydney or first class on a luxury liner sailing from Genoa, Italy with airfares to Italy via England and an inconvenience allowance paid in addition to my salary for the duration of the 6 week voyage. That was the least difficult decision I have ever had to make and although she offered me a week to think about it, I was able to accept the ocean voyage on the spot.

Two weeks after the telephone call from Washington D.C. I received an offer on the Lectureship at La Trobe from Professor Morrison, Head of the Chemistry Department. I had met Jim Morrison at Conferences and we had very similar interests. However, I felt obliged to turn down the offer following my earlier acceptance of the CSIRO position and a telex was sent immediately. Two weeks later and I had still not received the CSIRO offer in writing and I decided to call the Embassy. They informed me that an administrative error had occurred, I had been offered the position through the Embassy, but CSIRO headquarters in Canberra had assumed that I had already been interviewed, and I hadn't. I was lost for words, I had turned down a lectureship based on an offer that was suddenly gone? However, it was explained to me that the problem could be resolved through an interview in Washington and this was arranged for the following week.

Airline tickets arrived through the post a week later and I left Houston Intercontinental one Friday morning late in May on a 7 a.m. flight arriving at Washington National at 1:30 p.m. local time. As I entered the concourse I located the gentleman in a chauffeur's uniform holding a chalkboard with my name on it, as arranged, and I was driven to the Embassy in the back of a shiny black limousine with the Australian flag fluttering from the hood. I became a little nervous at such attention until I was directed to a second floor library where I was greeted by the scientific attaché, a short untidily dressed middle age man with a strong Yorkshire accent, who said, "ow-up lad, 'ave a cup of tea". It was 2:30 p.m. and my return flight had been booked for 4:50 p.m. so I thought there was just enough time for my carefully prepared seminar and the interview. However, the tea and general chat about Australia went on and on. It got to 3:15 p.m. and I mentioned the seminar that I had prepared, he said, "wouldn't mean a bloody thing to me lad, all I need to do is check that your hair isn't purple, if you know what I mean". I suddenly realised that this was it. There was no interview, it was my appearance that was being scrutinised and a check that I did not breach Australia's "all-white policy". He assured me that all was well and at his request I gave him the list of laboratories I wished to visit. I was back at the airport by 4:30 p.m. and at Houston Intercontinental by 10 p.m. All in all, a most interesting experience.

I spent two weeks during June 1973 visiting laboratories and giving seminars: the University of California at Berkeley to see Bruce Mahan; Hanscom Field USAF Research Laboratories, Boston, Massachusetts to visit John Paulson and Ed Murad; the USAF Wright-Patterson AeroSpace Research Laboratories at Dayton, Ohio to see Tom Tiernan; the Naval Research Laboratories in Washington D.C. to visit John DeCorpo, an old graduate student of Joe's; Johns Hopkins University, Baltimore to see John Koski and the University of Delaware at Newark to talk with Barnaby Munson and Doug Ridge. I learned more about the experimental technique involved in the study of ion-molecule collisions by cross beams from my day with Bruce

Mahan than I had gained from all the articles I had read on the subject. His enthusiasm for particle beam studies and my two year exposure to the cross beam work of Phil Brooks at Rice convinced me that this was the only way to fully appreciate the finer details of the collision event, although it was to take a further decade before I found the opportunity to acquire hands-on experience as a Visiting Professor at Rice.

1973 - 1976

We departed from Houston at the end of July 1973, sailed from Genoa, Italy at the end of August and arrived in Sydney on the 7th October. During the voyage I wrote my half of a review on negative ions in the gas phase that I was writing with Joe Franklin for the Review of Physical Chemistry. I had spent several months in the library at Rice researching the literature and the voyage provided the ideal opportunity to put it together. During the 3 years I spent as a Research Scientist in the Physics Division of CSIRO, the organisation underwent a major overhaul which included government control of the research. I began working on the ion-molecule kinetics of the ^2P spin-orbit states of Ar^+ and Kr^+ ions with CO_2 and N_2O, and on ion-molecule reactions carried out under single collision conditions in an electron beam space-charge trap. Concurrently, I was designing a drift-tube mass spectrometer for the study of negative ion clustering in perfluorocarbons. Half way through my first year the Government decided that CSIRO should carry out routine service work in support of other government agencies and Australian industry. I was instructed to allocate one-third of my time to the preparation and analysis of gas mixtures for the New South Wales Pollution Control Commission and Keith Ryan, as Group Leader, was asked to offer the expertise of the group (both of us) to the Atmospheric Pollution Research Group under Morris Mulcahy in the Materials Science Division at Chatswood (Sydney). About this time, Bert Stock, who was returning to Australia after a 2 year post-doctoral fellowship working on ion-molecule chemistry in a flowing afterglow with Norman Twiddy at the University of Wales, Aberystwyth, was appointed as an Experimental Officer with the group.

After my first year we were instructed to decrease our fundamental research activities further and I was assigned the job of designing a flow reactor for the study of free radical reactions of tropospheric interest in a joint project with Mulcahy's group. Keith Ryan decided that the drift-tube project had to be cancelled in order to devote more time to the joint programme with Materials Science Division. The drift-tube, which had just been delivered by the Mechanical Workshop, was put to one side as I began work on the design of the flow reactor, while Bert Stock was transferred to the measurement standards section to work on applications of interferometry to the calibration of industrial tape measures. When I joined CSIRO, the Physics Division was devoted exclusively to academic research with applied spin-offs taken up by the Division of Applied Physics. However, the Labour Government of Gough Whitlam decided that CSIRO research should be re-directed to serve Australian Industry with all research activities associated with identifiable economic goals. (This transition was complete by the late 1970's, three or four years after I left).

I began reading the Positions Vacant sections of the International Journals in mid-1975 and I successfully tested the flow reactor in April 1976, weeks before leaving to take up a Lectureship in Physical Chemistry at the University of Canterbury in Christchurch, New Zealand. I was offered a position as Head Scientist at the Boliver Water Analysis Laboratory in Adelaide following an interview early in 1976. I had also applied for the Lectureship at the University of Canterbury and was hoping for a communication when the offer from Adelaide arrived. They gave me one week to respond and another "bird in the hand" decision was required. This time I took a risk and decided to hold out (with fingers crossed) for a positive response from Canterbury. It came a week later with a telephone call from Leon Phillips, the Professor of Physical Chemistry at the University of Canterbury, I was to be offered the position and a verbal commitment to accept was required before the letter was posted. I accepted without hesitation. Keith Ryan, and my successor Ian Plumb, used the flow reactor from 1977 to the mid-80's and published a series of papers on the reactions of alkylperoxy radicals and other species of tropospheric interest.

1976 - present

We arrived in Christchurch at 6 p.m. on Thursday the 25th May 1976, the day before our son's 2nd birthday. I was surprised to find Brian Gowenlock in the Department when I arrived the following day. He was visiting the Department as a University of Canterbury Erskine Fellow. He remembered my visit to Heriott-Watt in April 1968 and pointed out that the New Zealand post-doctoral fellow who he had assigned to show me around was Colin Freeman, one of my new colleagues in the Department (and Head of Department from 1987-present). It also turned out that Brian was an old friend of JCJ's and we spent many hours over the following few months chatting about Edinburgh and swopping stories.

My first job was writing lectures. I also joined Murray McEwan and Colin Freeman in a joint research programme. Murray had recently returned from a Study Leave with Eldon Ferguson at NOAA (National Oceanographic and Atmospheric Administration), in Boulder, Colorado, where he had worked on a flowing afterglow studying ion-molecule kinetics. He had returned with blueprints and a flowing afterglow apparatus was close to completion. Over the next three years we worked together on ion-molecule equilibria and on charge transfer problems following on from the work I had carried out at CSIRO. During this period I synthesized all of the compounds we used in the research and designed a monochromatic electron impact ion source for the study of positive and negative ion formation processes which was fabricated in the Departmental Mechanical Workshop. I also designed a drift-tube mass spectrometer for the measurement of gas phase ion transport properties and ion-molecule interactions which could not be made in the Department. I had applied for a research grant from the UGC (University Grants Committee) in 1977 and received a grant of NZ$35,000 in late 1978. This was used to purchase vacuum equipment and a quadrupole mass filter for the monochromatic electron source and materials for the fabrication of the drift-tube. I gave a seminar on ion chemistry at the Physics and Engineering Laboratories, the Physics Division of the Department of Scientific and Industrial Research in Petone, Lower Hutt, early in 1979 and the Director offered machineshop facilities as a grant-in-aid to build the drift-tube, if I supplied the materials. The job was completed in 1980 and my first Ph.D. student, Bruce McIntosh, began work in February 1981 after completing a six month Honours project with me in 1980. I was promoted to Senior Lecturer in 1979.

I was eligible for my first Study Leave from May 1981 and I wrote to Phil Brooks at Rice University with a proposal to study the influence of molecular electron affinity on the effect of molecular orientation in the outcome of collisions with potassium atoms. He arranged for a visiting Professorship and we returned to Rice almost 8 years after leaving Houston for Australia in 1973. My first job was to redesign and rebuild a molecular beam machine, aptly named Pedro, that had suffered the ravages of a series of inexperienced summer season undergraduates. The oriented beam experiment had not operated successfully for quite a few years. Fortunately, a new graduate student, Howard Carman from Texas Christian University in Fort Worth (originally from Memphis, Tennessee) had signed up to join the group and we worked together. The machine was reconfigured and revitalised. Differences in the scattering behaviour between CF_3Br and CF_3I gave the first hint that the entrance channel for reaction, the electron transfer step in the harpoon mechanism, may exhibit orientation dependence, although we were able to qualitatively account for our results through exit channel effects exclusively.

My own research at Canterbury proceeded briskly after my return from Study Leave. The monochromatic electron source was used to study the formation and thermochemical properties of isomeric positive ions and the drift-tube was used to measure ion transport properties and ion-molecule kinetics. I was able to travel overseas to talk about the drift-tube work during 1985 on an Erskine Travel Fellowship. John Angus Erskine was a contemporary of Ernest Rutherford at Canterbury College from 1891-6. He studied mining and engineering and went on to become very wealthy and a prominent citizen in the Canterbury Province. On his death in 1960 he bequeathed a considerable sum to the University from his estate to be used for the funding of visits to the University by prominent overseas scientists and engineers and for funding overseas travel by Canterbury scientists and engineers on a competitive basis. As a result of this programme, the Chemistry Department has been fortunate to receive a constant stream of prominent overseas scientists at the rate of two to three a year since 1966. These have included a number of visitors in my general research area, several have become good friends and co-authors such as Professors David Smith FRS, H. F. Schaefer (Fritz), Bob Curl and Phil Brooks.

I returned to Rice again for Study Leave in 1988/89 with a proposal to explore the effect of orientation on the cross-sections for electron impact ionization and ion-molecule reactions. However, following the successful work with Phil Brooks and Howard Carman in 1982 we had proposed studying the entrance channel in the reaction of potassium atoms with spatially oriented alkyl halides using accelerated potassium atoms which would transfer sufficient energy in the collision to preclude ion recombination. The K^+ ions produced in the entrance channel could then be directly counted to provide direct information on the electron transfer step. A grant had been secured for this investigation but experiment efforts over the interim period had failed. So there was pressure to concentrate effort into this area first. We pursued this using beams of fast potassium atoms produced by resonance charge transfer from accelerated potassium ions in a metal vapour oven with a wide range of oriented symmetric top molecules. We successfully measured the number of potassium ions produced as a function of collision orientation for a wide range of oriented symmetric top molecules providing further evidence that the electron transfer step was orientation dependent. Experiments on CH_3Br and CF_3Br with a higher signal to noise ratio carried out by Phil Brooks, Guoqiang Xing and Toshio Kasai over the following 4 years confirmed our earlier measurements, showing a difference in the threshold for reaction at the positive and negative ends of the molecular dipole.

I was invited back to Rice again in 1989 by Phil Brooks and Bob Curl to assist in a triple beam experiment for the study of transition species spectroscopy. In 1980, this experiment had provided the first demonstration for the absorption of photons by a transition state species during the bimolecular reaction of potassium atoms with sodium chloride in a cross beam experiment although it had not produced any new results for many years. Working with graduate student Mike Barnes, who had worked on the experiment since 1984, we were able to iron out the problems and get the machine operational in a few weeks of intensive activity. We re-examined the reaction of potassium atoms with NaCl and extended the measurements to the NaBr and NaI systems, and produced the first evidence for structure in the absorption spectrum of a transition state species. I was appointed as an Adjunct Professor in Chemistry at Rice University and the Rice Quantum Institute and promoted to Reader at the University of Canterbury in 1990.

I began construction of a molecular beam machine at Canterbury for the study of electron impact ionization of spatially oriented molecules in 1987. Since there was little research funding I used vacuum equipment I had been allowed to take from Joe's old research laboratory at Rice while on Study Leave during 1982. The nozzle chamber comprised a 6" cross pumped by a 4" Edwards diffusion pump and the differentially pumped flight tube and detector chamber, housing a Vacuum Generators SXP300 quadrupole mass filter, was connected through a home-made skimmer and pumped by a VHS-4 diffusion pump. My first student on this project was Brett Cameron, who enrolled as a Ph.D. graduate student in March 1988. Since we were limited to a near zero budget and the machine characteristics had to be determined we decided to develop and refine the crude thermal conduction model for the supersonic expansion process and to explore the efficiency of rotational to translational energy transfer. This required the measurement of accurate arrival time distributions for chopped gas pulses which we generated using a Honda Civic fuel injector. We borrowed a LeCroy transient digitizer belonging to my colleague Professor Leon Phillips to collect data and the modelling was carried out using the University VAX. I received research grants totalling NZ$100,000 (£40,000) between 1989-92 and a Ministry of Research, Science and Technology grant of $250,000 (£100,000) in 1993 for the period 1994-96. Between 1991 and 1994 three extra students joined the group and the machine underwent two major transformations over a 2 year period. The first of these involved the addition of an extra chamber housing a hexapole electrostatic filter for the selective focusing of upper Stark states of symmetric top molecules into a scattering chamber housing a homogeneous field assembly for spatial orientation. A custom designed near-monochromatic electron gun mounted off a side-arm in the 8" six-way cross scattering chamber was mounted on an x-y-z vacuum translator and positioned to intersect the oriented beam. Ions produced by electron impact ionization were then collected by an on-axis shielded particle multiplier. Once it had been demonstrated that the ionization cross-section was indeed orientation dependent, the machine was totally rebuilt around a large scattering chamber fabricated in the Departmental Mechanical Workshop. The 8" six-way cross mounted on a VHS-10 diffusion pump was used as the nozzle chamber and a buffer chamber was introduced between the nozzle and hexapole chambers. The machine was built on a large frame with all chambers mounted on platforms with x-y-z adjustment. This is the situation as it currently prevails, the work on electron impact ionization of oriented molecules continues, an experiment is to be set up for the measurement of absolute ionization cross-sections and a new experiment has been designed to investigate elastic, inelastic and Stark state relaxation cross-sections.

During the first few years at Canterbury I travelled around South Island High Schools giving chemistry demonstration lectures with a fellow lecturer Alan Metcalfe, a good friend who died of a heart attack at age 45 in 1984. I continue to give "flashes and bangs" public demonstration lectures and still visit High Schools when time permits. I developed a more serious interest in Chemical Education after the Head of Department, the late Professor Jack Vaughan, nominated me for the Canterbury Regional Chemistry Syllabus Committee in 1981. I became a member in 1982 after returning from Study Leave at Rice and became Chairman in 1988. One of our functions was to scrutinise the University Entrance (called Bursary) and Scholarship Examinations. The 7th Form (final school year) chemistry syllabus involved a great deal of rote learning and very little in the way of applied or "relevant" topics. I wrote several articles for ChemNZ, a journal of the New Zealand Institute of Chemistry, on the deficiencies in the syllabus and the poor mathematical preparation of students for University chemistry. I surveyed High Schools and discovered that students had a poor opinion of the subject in relation to physics and biology, they found it to be the most difficult of the sciences and the least relevant to the world around us! I was appointed as the Chief Examiner (author and marker) for the New Zealand Entrance Scholarship examination in Chemistry in 1989 and as Moderator for the Bursary Examination in 1990. I was appointed to a Reference Group to develop a General Science Syllabus for all levels in New Zealand schools in 1991 and as an advisor to a working group of High School Chemistry Teachers in the preparation of a new draft syllabus statement for 6th and 7th Form Chemistry in 1993 which is now being used for a re-write of these syllabi.

4. Contribution to the Research Papers Submitted

All of the work described and presented in this thesis was undertaken by the author, with students under his supervision, or with collaborators. In the case of publications which have been carried out with academic colleagues, the author has contributed at least an equal share of the work. The research was carried out in the following laboratories over the periods indicated:-

Rice University and Rice Quantum Institute, Houston, Texas, U.S.A.

1971 - 1973	Fulbright Scholar and Post-Doctoral Fellow
1981 - 1982	Visiting Professor of Chemistry
1988 - 1989	Visiting Professor of Chemistry
1990	Adjunct Professor of Chemistry

CSIRO, Division of Physics, Sydney, Australia.

1973 - 1976	Research Scientist

Chemistry Department, University of Canterbury, Christchurch, New Zealand.

1976 - present	Lecturer / Senior Lecturer from 1979 / Reader from 1990

A complete list of the author's publications follow with a separate listing of the contributions submitted in this application.

5. Full List of Publications

1. The Electron Attachment Cross-Section for Hexafluoroacetone,
   P.W. Harland and J.C.J. Thynne,
   J.Phys.Chem., 1969, **73**: 2791-2.
2. Ionization and Dissociation of Pentafluorosulphur Chloride by Electron Impact,
   P.W. Harland and J.C.J. Thynne,
   J.Phys.Chem., 1969, **73**: 4031-5.
3. Positive and Negative Ion Formation in Hexafluoroacetone by Electron Impact,
   P.W. Harland and J.C.J. Thynne,
   J.Phys.Chem., 1970, **74**: 52-9.
4. Studies of Negative Ion Formation at Low Electron Energies,
   P.W. Harland, K.A.G. MacNeil and J.C.J. Thynne,
   Dynamic Mass Spectrometry, Editors: D. Price and J.E. Williams, 1970, Volume **1**: Chapter 8, 105-38.
5. Negative Ion Mass Spectra of Inorganic Compounds: Evidence for the Existence of GeF_5^-,
   S. Cradock, P.W. Harland and J.C.J. Thynne,
   Inorg.Nucl.Chem.Letters, 1970, **6**: 425-7.
6. Autodetachment of Electrons in Sulphur Tetrafluoride and Sulphur Hexafluoride,
   J.C.J. Thynne, P.W. Harland and R. MacDonald,
   Dynamic Mass Spectrometry, Editor: D. Price, 1971, Volume **2**: Chapter 6, 171-6.
7. Decomposition of the Metastable SF_4^- Ion,
   P.W. Harland and J.C.J. Thynne,
   Inorg.Nucl.Chem.Letters, 1971, **7**: 29-31.
8. Autodetachment Lifetimes, Attachment Cross-Sections and Negative Ion Formation by Sulphur Hexafluoride and Sulphur Tetrafluoride,
   P.W. Harland and J.C.J. Thynne,
   J.Phys.Chem., 1971, **75**: 3517-23.
9. Studies of Negative Ions Formed by Low Energy Electron Impact,
   P.W. Harland,
   Ph.D. Thesis, Edinburgh University, 1971, 297 pages.
10. Ionization by Electron Impact of some Inorganic Fluorides,
    P.W. Harland and J.C.J. Thynne,
    Advances in Mass Spectrometry, 1971, Volume **5**: 493-6.

11. Dissociative Electron Capture in Perfluoropropylene and Perfluoropropane,
P.W. Harland and J.C.J. Thynne,
Int.J.Mass Spectrom.Ion Phys., 1972, **9**: 253-66.

12. Negative Ion Formation and Ion-Molecule Reactions in Cyclo-pentadiene,
A. di Domenico, P.W. Harland and J.L. Franklin,
J.Chem.Phys., 1972, **56**: 5299-307.

13. Ionization of Perfluorocyclobutane by Electron Impact,
P.W. Harland and J.C.J. Thynne,
Int.J.Mass Spectrom.Ion Phys., 1972, **10**: 11-23.

14. Positive and Negative Ion Formation due to the Electron Bombardment of Germanium Tetrafluoride,
P.W. Harland, S. Cradock and J.C.J. Thynne,
Int.J.Mass Spectrom.Ion Phys., 1972, **10**: 169-95.

15. The Positive and Negative Ion Mass Spectra of some PF_2X Compounds,
D.W.H. Rankin, P.W. Harland and J.C.J. Thynne,
Inorg.Nucl.Chem.Lett., 1972, **8**: 1101-4.

16. Effects of Substituents upon Autodetachment Lifetimes of Perfluorobenzene and Nitrobenzene Anions,
P.W. Harland and J.C.J. Thynne,
J.Chem.Soc.Chem.Commun., 1972, **8**: 476-7.

17. Use of Translational Energy Measurements in the Evaluation of the Energetics of Dissociative Attachment Processes,
P.W. Harland, J.L. Franklin and D.E. Carter,
J.Chem.Phys., 1973, **58**: 1430-7.

18. High Temperature Negative Ions: Group III Fluorides,
F. Petty, J. Ling-Fai Wang, R.P. Steiger, P.W. Harland, J.L. Franklin and J.L.Margrave
High Temp.Science, 1973, **5**: 25-33.

19. Bond Dissociation Energies, Ionization Potentials and Electron Affinities of some Germanium Flouride Species,
P.W. Harland, S. Cradock and J.C.J. Thynne,
Inorg.Nucl.Chem.Letters, 1973, **9**: 53-8.

20. Comparison of Negative Ion Formation by the Hexafluorides of Sulphur, Selenium, Tellurium and Tungsten,
P.W. Harland and J.C.J. Thynne,
Inorg.Nucl.Chem.Letters, 1973, **9**: 265-9.

21. Negative Ions Containing Fluorine,
J. Ling-Fai Wang, F. Petty, P.W. Harland, R.P. Steiger, S.L.Bennett, J.L.Franklin and J.L. Margrave,
Proceedings of the Seventh International Symposium on Fluorine Chemistry, American Chemical Society., 1973.

22. Ionization and Dissociation by Electron Impact of Methanol, Tri-deuteromethanol and Methanol-D,
    J.C.J. Thynne and P.W. Harland,
    Int.J.Mass Spectrom.Ion Phys., 1973, **11**: 127-35.
23. Negative Ion Formation by Tungsten Hexafluoride,
    J.C.J. Thynne and P.W. Harland,
    Int.J.Mass Spectrom.Ion Phys., 1973, **11**: 137-47.
24. Negative Ion Formation by Perfluoro-n-butane as the Result of low Energy Electron Impact,
    P.W. Harland and J.C.J. Thynne,
    Int.J.Mass Spectrom.Ion Phys., 1973, **11**: 445-54.
25. Dissociation and Ionization of Difluorocyanophosphine,
    P.W. Harland, D.W.H. Rankin and J.C.J. Thynne,
    Inorg.Chem., 1973, **12**: 1442-3.
26. Ionization of Pentafluoroethyl Cyanide and Heptafluoro-n-propyl Cyanide by Electron Impact,
    J.C.J. Thynne and P.W. Harland,
    Int.J.Mass Spectrom.Ion Phys., 1973, **11**: 399-408.
27. Gaseous Negative Ions,
    J.L.Franklin and P.W. Harland,
    Annual Review of Physical Chemistry, 1974, Volume **25**: 485-526.
28. Partitioning of Excess Energy in Dissociative Resonance Capture Processes,
    P.W. Harland and J.L. Franklin,
    J.Chem.Phys., 1974, **61**: 1621-36.
29. Ionic Collision Processes in Mixtures of Methane with Carbon Dioxide and Nitrous Oxide,
    K.R. Ryan and P.W. Harland,
    Int.J.Mass Spectrom.Ion Phys., 1974, **15**: 197-213.
30. Electron Affinity of SF_4,
    R.J. Donovan, P.W. Harland, J.H. Knox, J.A. Makowski and J.C.J. Thynne,
    Int.J.Mass Spectrom.Ion Phys., 1974, **13**: 464-6.
31. Ionization by Electron Impact of Phosphorus Triflouride and Difluorocyanophosphine,
    P.W. Harland, D.W.H. Rankin and J.C.J. Thynne,
    Int.J.Mass Spectrom.Ion Phys., 1974, **13**: 395-410.
32. Studies of the Energies of Negative Ions at High Temperatures,
    J.L. Franklin, J.Ling-Fai Wang, S.L. Bennett, P.W. Harland and J.L. Margrave,
    Advances in Mass Spectrometry, 1974, Volume **6**: 319-25.

33. Some Low Energy Charge Transfer Processes for CO_2 and N_2O,
P.W. Harland and K.R. Ryan,
Int.J.Mass Spectrom.Ion Phys., 1975, **18**: 215-27.

34. Dissociative Electron Capture in Trifluoroacetaldehyde, Pentafluoropropionaldehyde and Heptafluorobutyraldehyde,
P.W. Harland and J.C.J. Thynne,
Int.J.Mass Spectrom.Ion Phys., 1975, **18**: 73-86.

35. A Fast Flowing Chemical Reactor for Atmospheric Pollution Studies,
K.R. Ryan, J.R. Steven, M.F.R. Mulcahy and P.W. Harland,
Proceedings of the Fourth Biennial Conference of the Australian and New Zealand Society for Mass Spectrometry, (1977).

36. Electron Attachment to the Stable Free Radical Bis-trifluoromethylnitroxide in the Gas Phase.
P.W. Harland,
Int.J.Mass Spectrom.Ion Phys., 1977, **25**: 61-70.

37. The Equilibrium $H_3S^+ + HCN = H_2CN^+ + H_2S$ and the Relative Proton Affinities of HCN and H_2S,
C.G. Freeman, P.W. Harland and M.J. McEwan,
Int.J.Mass Spectrom.Ion Phys., 1978, **27**: 77-82.

38. Some Ion-Molecule Reactions of HCN,
C.G. Freeman, P.W. Harland, J.P. Liddy and M.J. McEwan,
Aust.J.Chem., 1978, **31**: 963-6.

39. The Equilibrium Systems H_3CO^+ (HCN,HCHO) H_2CN^+, $H_3CO^+(H_2S,HCHO)$ H_3S^+ and the Relative Proton Affinities of HCHO, HCN and H_2S,
C.G. Freeman, P.W. Harland and M.J. McEwan,
Int.J.Mass Spectrom.Ion Phys., 1978, **28**: 19-25.

40. Gas Phase Proton-transfer Equilibria in Binary Mixtures of CH_3OH, CH_3NO_2 and HCOOH and the Relative Proton Affinities of CH_3OH, CH_3NO_2 and HCOOH,
C.G. Freeman, P.W. Harland and M.J. McEwan,
Int.J.Mass Spectrom.Ion Phys., 1978, **28**: 377-88.

41. Ion-Molecule Reactions of Formic Acid. Part I: Proton Transfer Reactions,
C.G. Freeman, P.W. Harland and M.J. McEwan,
Aust.J.Chem., 1978, **31**: 2157-60.

42. Ion-Molecule Reactions of Formic Acid. Part II: Rearrangement Reactions,
C.G. Freeman, P.W. Harland and M.J. McEwan,
Aust.J.Chem., 1978, **31**: 2593-9.

43. The Interstellar Synthesis of HC_3N and HC_5N,
C.G. Freeman, P.W. Harland and M.J. McEwan,
Astrophys.Lett., 1978, **19**: 133-5.

44. Laboratory Investigations of Ion-Molecule reactions of HC_3N in Dense Interstellar Clouds,
C.G. Freeman, P.W. Harland and M.J. McEwan,
Mon.Not.R.Astr.Soc., 1979, **187**: 441-4.

45. The Positive Ion Chemistry of Trifluoronitrosomethane, CF_3NO,
C.G. Freeman, P.W. Harland and M.J. McEwan,
Int.J.Mass Spectrom.Ion Phys., 1979, **30**: 285-91.

46. Thermal Energy Charge Transfer Reactions of Acetone and Biacetyl,
C.G. Freeman, P.W. Harland and M.J. McEwan,
Chem.Phys.Lett., 1979, **64**: 596-600.

47. Software Controlled Multiple Pulse Generator and its Applications to a Drift-Tube Gating System,
P.W. Harland and B.J McIntosh,
Int.J.Mass Spectrom.Ion Procs., 1983, **54**: 217-23.

48. Reactions of Orientated Molecules in Crossed Molecular Beams,
P.W. Harland,
Chem. in N.Z., 1983, **47**: 119-21.

49. Mobilities of HCN^+, H_2CN^+, C_2N^+, $C_2N_2^+$ and $C_2H_3N^+$ in Helium at 293K,
P.W. Harland and B.J. McIntosh,
Int.J.Mass Spectrom.Ion Procs., 1984, **57**: 283-97.

50. Mobility of CN^+ in Helium at 293K,
P.W. Harland and B.J. McIntosh,
J.Chem.Soc., Faraday Trans.2, 1985, **81**: 169-76.

51. Enthalpies of Formation for the Isomeric Ions H_XCCN^+ and H_XCNC^+ (x= 0 to 3) by 'Monochromatic' Electron Impact on C_2N_2, CH_3CN and CH_3NC.
P.W. Harland and B.J. McIntosh,
Int.J.Mass Spectrom.Ion Procs., 1985, **67**: 29-46.

52. The Attachment of Low Energy Electrons to Dicyanogen in the Gas Phase.
P.W. Harland and B.J. McIntosh,
Aust.J.Chem., 1985, **38**: 967-76.

53. The ESR observation of $^{14}NH_3^+$ and $^{15}NH_3^+$ trapped in an argon matrix at 14K.
A.J. McKinley, R.F.C. Claridge, and P.W. Harland,
Chem.Phys., 1986, **102**: 283-8.

54. Reaction of K atoms with orientated CF_3Br.
H. S. Carman, P.W. Harland, and P.R. Brooks,
J.Phys.Chem., 1986, **90**: 944-8.

55. Appearance Energies and Enthalpies of Formation from the Ionization of Cyanoacetylene by 'Monochromatic' Electron Impact.
P.W. Harland.
Int.J.Mass Spectrom.Ion Procs., 1986, **70**: 231-6.

56. The Effect of Ion Structure on Gas Phase Ion Transport Properties.
P.W. Harland, B.J. McIntosh, R.W. Simpson, and N.R. Thomas,
J.Chem.Soc., Faraday Trans. 2, 1986, **73**: 2039-46.

57. Ab-Initio Calculations of the Mobility of F^- in Helium,
R.G.A.R. Maclagan, P.W. Harland and R.W. Simpson,
J. Phys. B, At. Mol. Phys., 1987, **20**: 2723-31.

58. Student Preparation for Stage 1 Chemistry,
P.W. Harland,
Chem.NZ, 1987, **34**: 7-11.

59. The Structure and Energetics of the C_3N^+ Ion,
P.W. Harland and R.G.A.R. Maclagan,
J.Chem.Soc, Faraday Trans., 1987, **83**: 2133-7.

60. Interaction Potentials and Mobility Calculations for the HeO^+ System,
R.W. Simpson, R.G.A.R. Maclagan and P.W. Harland,
J.Chem.Phys., 1987, **87**: 5419-24.

61. Book: Energy in Nature. (300 pages, 200 diagrams),
P.W. Harland and G.A. Rodley,
University of Canterbury Printery, 1988. Sold through the Science Teachers Association and the University of Canterbury.

62. The Dependence of Zero-field Ion-Mobilities on Well Depth ε and Minimum Position r_m in the Ion-Neutral Interaction Potential,
P.W. Harland, R.G.A.R. Maclagan and R.W. Simpson,
Aust.J.Phys., 1988, **41**: 545-8.

63. Ab-Initio HeF^+ ($^3\Pi$, $^3\Sigma^+$) Interaction Potentials and Calculations of the Mobility of $F^+(^3P)$ and $F^-(^1S)$ in Helium,
P.W. Harland, R.G.A.R. Maclagan and R.W. Simpson,
J.Chem.Soc., Faraday Trans., 1988, **84**: 1847-53.

64. Ab Initio Calculations of the Mobilities of C^+ (^2P, ^4P) in Helium,
S.T. Grice, P.W. Harland and R.G.A.R. Maclagan,
Int.J.Mass Spectrom. Ion Procs., 1989, **87**: 181-6.

65. Kinetic and Electron Impact Studies of the HCO^+/COH^+ Isomers,
P.W. Harland, N. Kim and S.A.H. Petrie,
Aust. J. Chem., 1989, **42**: 9-15.

66. Theoretical Calculation of the HeB^+ Interaction Potential and the Mobility of B^+ in Helium,
R.W. Simpson, P.W. Harland and R.G.A.R. Maclagan, D. Smith and N.G. Adams,
Int.J.Mass Spectrom. Ion Procs., 1989, **87**: 193-6.

67. Structures and Energies of $C_2NH_2^+$ Isomers,
P.W. Harland, R.G.A.R. Maclagan and H.F. Schaefer III,
J. Chem. Soc., Faraday Trans., 1989, **85**: 187-93.

68. Effect of Molecular Orientation on Electron Transfer,
P.W. Harland, H.S. Carman, L.F. Phillips and P.R. Brooks,
J.Chem.Phys., 1989, **90**: 5201-3.

69. Electron Transfer to Oriented Molecules: K + CF_3I and K + CH_3I,
P.W. Harland, H.S. Carman, L.F. Phillips and P.R. Brooks,
J.Chem.Phys., 1990, **93**: 1089-97.

70. Experimental Measurements and Theoretical Calculations of the Mobility of the N^+ Ion in Helium,
S.T.Grice, P.W. Harland, J.A. Harrison, R.G.A.R. Maclagan and R.W. Simpson,
Int.J.Mass Spectrom.Ion Procs., 1991, **107**: 215-24.

71. Flow Dynamics of Supersonic Molecular Beams and the Measurement of Rotational-Translational Coupling Parameters for N_2 and H_2,
B.R.Cameron and P.W.Harland,
J.Chem.Soc., Faraday Trans., 1991, **87**: 1069-73.

72. Observation of Structure in Transition State Spectra of the Bimolecular Reactions K + XNa → KX + Na (X = Br, Cl),
M.D.Barnes, P.R.Brooks, R.F.Curl,Jr., and P.W.Harland,
J.Chem.Phys., 1991, **94**: 5245-7.

73. Effects of Molecular Orientation on Electron Transfer Collisions,
P.W.Harland, H.S.Carman,Jr., L.F.Phillips and P.R.Brooks,
J.Phys.Chem., 1991, **95**: 8137-42.

74. The 7th Form Chemistry Syllabus,
P.W.Harland,
Chem.N.Z., 1991, **45**: 3-12.

75. Collision Dynamics of Alkali-Metal Atoms with Oriented Symmetric-Top Molecules,
P.R.Brooks, P.W.Harland, L.F.Phillips and H.S.Carman,Jr.,
J.Phys.Chem., 1992, **96**: 1557-61.

76. Photoexcitation Spectra of Transition Region Species Formed in Reactions of Potassium with Sodium Halides,
M.D.Barnes, P.R.Brooks, R.F.Curl,Jr., P.W.Harland and B.R.Johnson,
J.Chem.Phys., 1992, **96**: 3559-68.

77. Calculation of the Potential Energy Surface of Li^++N_2,
S.T.Grice, P.W.Harland and R.G.A.R.Maclagan,
Chem.Phys., 1992, **165**: 73-87.

78. Relevance in the Teaching of Chemistry,
P.W.Harland,
Chem.N.Z., 1992, **49**: 24-8.

79. Application of the Thermal Conduction Model to Rotational Relaxation in Molecular Beams,
B.R.Cameron and P.W.Harland,
J.Chem.Soc., Faraday Trans., 1993, **89**: 1903-8.

80. Monte Carlo Calculations of Rotational Relaxation in Small Molecules,
B.R.Cameron and P.W.Harland,
J.Chem.Soc., Faraday Trans., 1993, **89**: 3517-25.

81. Book: Energy in Nature and the Material World. (250 pages, 200 diagrams),
P.W. Harland and J.E.Fergusson,
University of Canterbury Printery, 1993.

82. The Potential Energy Surface of Li^++CO,
S.T.Grice, P.W.Harland and R.G.A.R.Maclagan,
J.Chem.Phys., 1993, **99**: 7619-30.

83. Cross-sections and Transport Numbers of Li^++CO,
S.T.Grice, P.W.Harland and R.G.A.R.Maclagan,
J.Chem.Phys., 1993, **99**: 7631-37.

84. Deconvolution of Unchopped Time-of-Flight Waveforms,
B.R.Cameron and P.W.Harland,
Rev.Sci.Instrum., 1994, **65**: 108-115.

85. Appearance Energies of Small Cluster Ions and their Fragments,
B.R. Cameron, C.G. Aitken and P.W. Harland,
J.Chem.Soc., Faraday Trans., 1994, **7**: 935-9.

86. The Atmosphere of Earth,
P.W. Harland,
ChemNZ., 1994, **55**: 4-16.

87. Effect of molecular orientation on electron impact ionization and fragmentation,
C.G. Aitken, D.A. Blunt, and P.W. Harland,
J.Chem.Phys., 1994, **101**: 11074-6.

88. Ion Mass Analyzers,
P.W. Harland,
in *Atomic, Molecular, and Optical Physics, Volume 1, Charged Particles.*
Editor F. B. Dunning, Academic Press, Inc., New York, in press, 1995.

89. Effect of Spatial Orientation on Electron Transfer and Electron Impact Ionization in the Gas Phase.
P.R. Brooks, and P.W. Harland,
in *Advances in Gas Phase Ion Chemistry,*
Editors N. G. Adams and L. M. Babcock, Volume **2**, JAI Press Inc., London, in press, 1995.

6. Published Work Submitted for Application
(Chronological Order)

1. Negative Ion Formation and Ion-Molecule Reactions in Cyclo-pentadiene,
   A. di Domenico, P.W. Harland and J.L. Franklin,
   J.Chem.Phys., 1972, **56**: 5299-307.
2. Use of Translational Energy Measurements in the Evaluation of the Energetics of Dissociative Attachment Processes,
   P.W. Harland, J.L. Franklin and D.E. Carter,
   J.Chem.Phys., 1973, **58**: 1430-7.
3. High Temperature Negative Ions: Group III Fluorides,
   F. Petty, J. Ling-Fai Wang, R.P. Steiger, P.W. Harland, J.L. Franklin and J.L.Margrave
   High Temp.Science, 1973, **5**: 25-33.
4. Partitioning of Excess Energy in Dissociative Resonance Capture Processes,
   P.W. Harland and J.L. Franklin,
   J.Chem.Phys., 1974, **61**: 1621-36.
5. Studies of the Energies of Negative Ions at High Temperatures,
   J.L. Franklin, J.Ling-Fai Wang, S.L. Bennett, P.W. Harland and J.L. Margrave,
   Advances in Mass Spectrometry, 1974, Volume **6**: 319-25.
6. Gaseous Negative Ions,
   J.L.Franklin and P.W. Harland,
   Annual Review of Physical Chemistry, 1974, Volume **25**: 485-526.
7. Ionic Collision Processes in Mixtures of Methane with Carbon Dioxide and Nitrous Oxide,
   K.R. Ryan and P.W. Harland,
   Int.J.Mass Spectrom.Ion Phys., 1974, **15**: 197-213.
8. Some Low Energy Charge Transfer Processes for CO_2 and N_2O,
   P.W. Harland and K.R. Ryan,
   Int.J.Mass Spectrom.Ion Phys., 1975, **18**: 215-27.
9. Electron Attachment to the Stable Free Radical Bis-trifluoromethylnitroxide in the Gas Phase.
   P.W. Harland,
   Int.J.Mass Spectrom.Ion Phys., 1977, **25**: 61-70.
10. The Equilibrium $H_3S^+ + HCN = H_2CN^+ + H_2S$ and the Relative Proton Affinities of HCN and H_2S,
    C.G. Freeman, P.W. Harland and M.J. McEwan,
    Int.J.Mass Spectrom.Ion Phys., 1978, **27**: 77-82.

11. Some Ion-Molecule Reactions of HCN,
    C.G. Freeman, P.W. Harland, J.P. Liddy and M.J. McEwan,
    Aust.J.Chem., 1978, **31**: 963-6.

12. The Equilibrium Systems H_3CO^+ (HCN,HCHO) H_2CN^+, $H_3CO^+(H_2S,HCHO)$ H_3S^+ and the Relative Proton Affinities of HCHO, HCN and H_2S,
    C.G. Freeman, P.W. Harland and M.J. McEwan,
    Int.J.Mass Spectrom.Ion Phys., 1978, **28**: 19-25.

13. Gas Phase Proton-transfer Equilibria in Binary Mixtures of CH_3OH, CH_3NO_2 and HCOOH and the Relative Proton Affinities of CH_3OH, CH_3NO_2 and HCOOH,
    C.G. Freeman, P.W. Harland and M.J. McEwan,
    Int.J.Mass Spectrom.Ion Phys., 1978, **28**: 377-88.

14. Ion-Molecule Reactions of Formic Acid. Part I: Proton Transfer Reactions,
    C.G. Freeman, P.W. Harland and M.J. McEwan,
    Aust.J.Chem., 1978, **31**: 2157-60.

15. Ion-Molecule Reactions of Formic Acid. Part II: Rearrangement Reactions,
    C.G. Freeman, P.W. Harland and M.J. McEwan,
    Aust.J.Chem., 1978, **31**: 2593-9.

16. The Interstellar Synthesis of HC_3N and HC_5N,
    C.G. Freeman, P.W. Harland and M.J. McEwan,
    Astrophys.Lett., 1978, **19**: 133-5.

17. Laboratory Investigations of Ion-Molecule reactions of HC_3N in Dense Interstellar Clouds,
    C.G. Freeman, P.W. Harland and M.J. McEwan,
    Mon.Not.R.Astr.Soc., 1979, **187**: 441-4.

18. The Positive Ion Chemistry of Trifluoronitrosomethane, CF_3NO,
    C.G. Freeman, P.W. Harland and M.J. McEwan,
    Int.J.Mass Spectrom.Ion Phys., 1979, **30**: 285-91.

19. Thermal Energy Charge Transfer Reactions of Acetone and Biacetyl,
    C.G. Freeman, P.W. Harland and M.J. McEwan,
    Chem.Phys.Lett., 1979, **64**: 596-600.

20. Software Controlled Multiple Pulse Generator and its Applications to a Drift-Tube Gating System,
    P.W. Harland and B.J McIntosh,
    Int.J.Mass Spectrom.Ion Procs., 1983, **54**: 217-23.

21. Mobilities of HCN^+, H_2CN^+, C_2N^+, $C_2N_2^+$ and $C_2H_3N^+$ in Helium at 293K,
    P.W. Harland and B.J. McIntosh,
    Int.J.Mass Spectrom.Ion Procs., 1984, **57**: 283-97.

22. Mobility of CN^+ in Helium at 293K,
P.W. Harland and B.J. McIntosh,
J.Chem.Soc., Faraday Trans.2, 1985, **81**: 169-76.

23. Enthalpies of Formation for the Isomeric Ions H_XCCN^+ and H_XCNC^+ (x= 0 to 3) by 'Monochromatic' Electron Impact on C_2N_2, CH_3CN and CH_3NC.
P.W. Harland and B.J. McIntosh,
Int.J.Mass Spectrom.Ion Procs., 1985, **67**: 29-46.

24. The Attachment of Low Energy Electrons to Dicyanogen in the Gas Phase.
P.W. Harland and B.J. McIntosh,
Aust.J.Chem., 1985, **38**: 967-76.

25. Reaction of K atoms with orientated CF_3Br.
H. S. Carman, P.W. Harland, and P.R. Brooks,
J.Phys.Chem., 1986, **90**: 944-8.

26. Appearance Energies and Enthalpies of Formation from the Ionization of Cyanoacetylene by 'Monochromatic' Electron Impact.
P.W. Harland.
Int.J.Mass Spectrom.Ion Procs., 1986, **70**: 231-6.

27. The Effect of Ion Structure on Gas Phase Ion Transport Properties.
P.W. Harland, B.J. McIntosh, R.W. Simpson, and N.R. Thomas,
J.Chem.Soc., Faraday Trans. 2, 1986, **73**: 2039-46.

28. Ab-Initio Calculations of the Mobility of F^- in Helium,
R.G.A.R. Maclagan, P.W. Harland and R.W. Simpson,
J. Phys. B, At. Mol. Phys., 1987, **20**: 2723-31.

29. The Structure and Energetics of the C_3N^+ Ion,
P.W. Harland and R.G.A.R. Maclagan,
J.Chem.Soc, Faraday Trans., 1987, **83**: 2133-7.

30. Interaction Potentials and Mobility Calculations for the HeO^+ System,
R.W. Simpson, R.G.A.R. Maclagan and P.W. Harland,
J.Chem.Phys., 1987, **87**: 5419-24.

31. The Dependence of Zero-field Ion-Mobilities on Well Depth ε and Minimum Position r_m in the Ion-Neutral Interaction Potential,
P.W. Harland, R.G.A.R. Maclagan and R.W. Simpson,
Aust.J.Phys., 1988, **41**: 545-8.

32. Ab-Initio HeF^+ ($^3\Pi$, $^3\Sigma^+$) Interaction Potentials and Calculations of the Mobility of $F^+(^3P)$ and $F^-(^1S)$ in Helium,
P.W. Harland, R.G.A.R. Maclagan and R.W. Simpson,
J.Chem.Soc., Faraday Trans., 1988, **84**: 1847-53.

33. Ab Initio Calculations of the Mobilities of C^+ (^2P, ^4P) in Helium,
S.T. Grice, P.W. Harland and R.G.A.R. Maclagan,
Int.J.Mass Spectrom. Ion Procs., 1989, **87**: 181-6.

34. Kinetic and Electron Impact Studies of the HCO^+/COH^+ Isomers,
P.W. Harland, N. Kim and S.A.H. Petrie,
Aust. J. Chem., 1989, **42**: 9-15.

35. Theoretical Calculation of the HeB^+ Interaction Potential and the Mobility of B^+ in Helium,
R.W. Simpson, P.W. Harland and R.G.A.R. Maclagan, D. Smith and N.G. Adams,
Int.J.Mass Spectrom. Ion Procs., 1989, **87**: 193-6.

36. Structures and Energies of $C_2NH_2^+$ Isomers,
P.W. Harland, R.G.A.R. Maclagan and H.F. Schaefer III,
J.Chem.Soc., Faraday Trans., 1989, **85**: 187-93.

37. Effect of Molecular Orientation on Electron Transfer,
P.W. Harland, H.S. Carman, L.F. Phillips and P.R. Brooks,
J.Chem.Phys., 1989, **90**: 5201-3.

38. Electron Transfer to Oriented Molecules: K + CF_3I and K + CH_3I,
P.W. Harland, H.S. Carman, L.F. Phillips and P.R. Brooks,
J.Chem.Phys., 1990, **93**: 1089-97.

39. Experimental Measurements and Theoretical Calculations of the Mobility of the N^+ Ion in Helium,
S.T.Grice, P.W. Harland, J.A. Harrison, R.G.A.R. Maclagan and R.W. Simpson,
Int.J.Mass Spectrom.Ion Procs., 1991, **107**: 215-24.

40. Flow Dynamics of Supersonic Molecular Beams and the Measurement of Rotational-Translational Coupling Parameters for N_2 and H_2,
B.R.Cameron and P.W.Harland,
J.Chem.Soc., Faraday Trans., 1991, **87**: 1069-73.

41. Observation of Structure in Transition State Spectra of the Bimolecular Reactions $K + XNa \rightarrow KX + Na$ (X = Br, Cl),
M.D.Barnes, P.R.Brooks, R.F.Curl,Jr., and P.W.Harland,
J.Chem.Phys., 1991, **94**: 5245-7.

42. Effects of Molecular Orientation on Electron Transfer Collisions,
P.W.Harland, H.S.Carman,Jr., L.F.Phillips and P.R.Brooks,
J.Phys.Chem., 1991, **95**: 8137-42.

43. Collision Dynamics of Alkali-Metal Atoms with Oriented Symmetric-Top Molecules,
P.R.Brooks, P.W.Harland, L.F.Phillips and H.S.Carman,Jr.,
J.Phys.Chem., 1992, **96**: 1557-61.

44. Photoexcitation Spectra of Transition Region Species Formed in Reactions of Potassium with Sodium Halides,
M.D.Barnes, P.R.Brooks, R.F.Curl,Jr., P.W.Harland and B.R.Johnson,
J.Chem.Phys., 1992, **96**: 3559-68.

45. Calculation of the Potential Energy Surface of Li^++N_2,
S.T.Grice, P.W.Harland and R.G.A.R.Maclagan,
Chem.Phys., 1992, **165**: 73-87.

46. Application of the Thermal Conduction Model to Rotational Relaxation in Molecular Beams,
B.R.Cameron and P.W.Harland,
J.Chem.Soc., Faraday Trans., 1993, **89**: 1903-8.

47. Monte Carlo Calculations of Rotational Relaxation in Small Molecules,
B.R.Cameron and P.W.Harland,
J.Chem.Soc., Faraday Trans., 1993, **89**: 3517-25.

48. The Potential Energy Surface of Li^++CO,
S.T.Grice, P.W.Harland and R.G.A.R.Maclagan,
J.Chem.Phys., 1993, **99**: 7619-30.

49. Cross-sections and Transport Numbers of Li^++CO,
S.T.Grice, P.W.Harland and R.G.A.R.Maclagan,
J.Chem.Phys., 1993, **99**: 7631-37.

50. Deconvolution of Unchopped Time-of-Flight Waveforms,
B.R.Cameron and P.W.Harland,
Rev.Sci.Instrum., 1994, **65**: 108-115.

51. Appearance Energies of Small Cluster Ions and their Fragments,
B.R. Cameron, C.G. Aitken and P.W. Harland,
J.Chem.Soc., Faraday Trans., 1994, **7**: 935-9.

52. Effect of molecular orientation on electron impact ionization and fragmentation,
C.G. Aitken, D.A. Blunt, and P.W. Harland,
J.Chem.Phys., 1994, **101**: 11074-6.

53. Effect of Spatial Orientation on Electron Transfer and Electron Impact Ionization in the Gas Phase.
P.R. Brooks, and P.W. Harland,
in *Advances in Gas Phase Ion Chemistry,*
Editors N. G. Adams and L. M. Babcock, Volume **2**, JAI Press Inc., London, in press, 1995.

7. Commentary on Submitted Research

The experimental techniques designed by the author and the theoretical models developed in the course of the research will be briefly described with the appropriate publication numbers from the above list. This will be followed by a synopsis of the main achievements from the papers submitted under the headings: electron-molecule collisions; ion-molecule collisions; atom-molecule collisions.

A. Experimental Techniques

These have included:

i) Electron guns and ion sources

The deconvolution or unfolding of ionization efficiency curves has successfully facilitated the determination of ionization thresholds normally smeared by the effect of the electron energy distribution. However, deconvolution can only be used reliably for single resonance peaks or for multiple peaks which do not overlap extensively. There have been numerous attempts over the years to design a general purpose monochromatic electron gun with sufficient intensity for negative ion studies and for positive ion studies near threshold, with minimal success. Two successful near-monochromatic electron guns, each with novel features, have been designed in the course of the research submitted in this application. They were designed to investigate the electron impact ionization of low pressure gases under single collision conditions in single beam and cross-beam experiments. An electron gun based on a hemispherical electrostatic velocity analyzer was designed for the measurement of ionization efficiency curves and ionization mechanisms over the electron energy range 0 - 100 eV[23]. It has been employed to measure accurate positive and negative ion appearance energies, to determine thermochemical parameters for ions and free radical fragments (enthalpies of formation, bond dissociation energies, ionization potentials and electron affinities), to study the ionization mechanism through detailed energy balancing using fragment ion kinetic energy analysis and to investigate the formation and energetics of isomeric forms of ions considered to play an important role in interstellar chemistry[23,24,26,29,34,36]. A linear pencil-beam electron gun (20 - 300 eV) based on a Pierce element was designed for an investigation of the effect of spatial orientation on the ionization efficiency and fragmentation of molecules in a cross electron-oriented molecular beam experiment[52,53].

ii) Drift-tube mass spectrometer

A drift-tube mass spectrometer was designed to investigate ion transport properties and ion molecule reactions as a function of collision energy[20,21] over the operating pressure range 10^{-2} torr to 10 torr. The drift-tube was fitted with a movable electron impact ion source with the capability of operating in a pulsed or continuous mode. In pulsed mode, He^+ ions were produced by electron pulses admitted into the source by a computer controlled electronic gate[20] and the ions of interest were generated in the ion source by He^+ ion charge transfer on an appropriate trace source gas (ppm to ppt) in He buffer gas. A second electronic gate, triggered and variably delayed from the electron gate, was applied to a fine grid at the exit orifice and used to measure ion arrival time profiles using a quadrupole mass filter detector in a second differentially pumped chamber. This technique facilitated the determination of accurate ion drift velocities over a wide range of electric field strength and particle density[21,22,27,33,38]. Continuous mode operation was used to establish the mechanism for consecutive ion-molecule reactions and to measure ion-molecule rate constants[34,39].

iii) **Cross beam machines**

A machine for the study of collisions between thermal potassium atoms and spatially oriented symmetric top molecules, originally designed and constructed by Phil Brooks at Rice University in the late 1960's, was totally redesigned and rebuilt by Howard Carman (a new graduate student) and I during 1981-82[25]. It was later modified and successfully used by the author during 1988-89 to investigate collisions between spatially oriented symmetric top molecules and fast potassium atoms generated by resonance charge transfer in an effusive potassium beam source oven[37,38,42]. A cross beam machine to determine accurate arrival time profiles for chopped supersonic beams[40], to investigate the electron impact ionization of molecular clusters[51] and to study the effect of spatial orientation on electron impact ionization of molecules[52,53] was designed by the author and constructed at the University of Canterbury from 1987 - present. The detection of near-thermal energy ions produced in the electron impact ionization of molecules oriented in a homogeneous electric field presented a number of technical difficulties unique to this study and a number of new features were included in the design[52,53].

B. Mathematical Models and Theoretical Methods

These have included:-

i) **Deconvolution**

A novel approach to the elucidation of accurate supersonic beam flow velocities and effective particle temperatures from unchopped time-of-flight waveforms was developed using fast Fourier transforms to evaluate a global instrument response function[50]. During my Ph.D. studies at the University of Edinburgh, I worked with Ken MacNeil and John Thynne to develop the first application of deconvolution to the unfolding of the electron energy distribution from negative ion associative and dissociative resonance capture curves using a van Cittert iterative algorithm (Studies of Negative Ion Formation at Low Electron Energies, P.W. Harland, K.A.G. MacNeil and J.C.J. Thynne, in *Dynamic Mass Spectrometry*, Editors: D. Price and J.E. Williams, 1970, Volume 1, Chapter 8, pages 105-138). I applied this method extensively as a Post-Doctoral Fellow at Rice University in studies of energy dispersion in resonance electron capture processes[1-5]. This also involved a theoretical model for energy partitioning in metastable molecular negative ions based on statistical mechanics which was modified in accord with the experimental results[2,4].

ii) Energy transfer in supersonic expansions

The simple Thermal Conduction Model (Beijerinck, H. C. W., and Verster, N. F., *Physica C*, 1981, 111, 327.) for gas expansions was developed for the calculation of supersonic beam properties as a function of distance along the expansion axis. Collision frequency, flow velocity, particle density, mean free path, and axial and radial particle temperatures in supersonic atomic and homonuclear diatomic molecular beams were calculated for various species using realistic interaction potentials and collision cross-sections computed from scattering theory[27]. A new approach to the calculation of rotational relaxation times and collision numbers in supersonic expansions was developed and used to calculate rotational relaxation times and rotational collision numbers for H_2, N_2, O_2 and Cl_2[46]. A Monte Carlo procedure was devised for the investigation of rotational relaxation in small molecules[47] and used to calculate rotational relaxation parameters for H_2, N_2, O_2 and Cl_2, and for the polyatomic species CO_2, OCS, NH_3, CH_4, CH_3Cl and C_2H_4. Results obtained using the Monte Carlo procedure were used to investigate the breakdown of translational and rotational equilibrium in supersonic expansions of CO_2, OCS and CH_3Cl.

iii) Reaction asymmetry in collision of fast K atoms with oriented molecules

A model based on Landau-Zener Theory of avoided potential energy surface crossings was devised to account for the reaction asymmetry measured in collisions of fast K atoms on a series of spatially oriented molecules[38,53]. The model predicted relationships between measured ion signals and collision energy which provided estimates of the critical atom-molecule separation corresponding to the avoided crossing. The reactions of electropositive K and electronegative alkyl halide molecules are considered to proceed through a harpoon mechanism, in which the first step corresponds to an electron transfer from the metal atom to the molecule. The critical atom-molecule separation in the entrance channel for these reactions, estimated from the model and experimental results, corresponded to an adiabatic transition between the covalent and ionic adiabats (the electron "jump"). Similarly, the model also provided estimates for the surface crossing distance in the exit channel. The calculations provided a guide for the development of a physical picture of the reaction event.

iv) Non-reactive ion-molecule interactions - interaction potentials and ion transport properties

Ion drift theory was used with a generalised interaction potential to predict the relative effects of molecular parameters (ion mass, dipole moment, well depth and well minimum) on the ion transport properties of polyatomic ions drifting in helium. Trends in the ion transport properties for a wide range of ions of dissimilar chemical composition were found to be in accord with the qualitative predictions of the calculations, the spatial volume of the ion being the dominant factor on the momentum transfer cross-section and the ion drift velocity[27]. The calculations were extended to include *ab initio* interaction potentials, calculated at the MP4SDQ/6-311+G(3df,3dp) level of theory. The calculated interaction potentials were then used with scattering theory and the two-temperature and three-temperature theories of ion transport to calculate macroscopic ion transport properties. Where multiple ion states correlated with the separated ion and helium atom, the mobilities were deduced by summing over the statistical weights of the molecular ion states or over the interaction potentials[28,30-33,35,39,45,48,49]. The transport properties were calculated for the excited electronic states of several ions measured experimentally with a confirmation of the identity of the excited ion electronic state in one case[33] and a re-interpretation of the original assignments in another[30]. The methods developed can be applied confidently to calculate the mobilities of ground state and excited state ions which are not readily amenable to experimental determination and used as a guide to identification of the excited ion state.

v) **Electron impact ionization**

A model for electron impact ionization based on Coulomb potential considerations and the coupling of the electron wave to the molecular orbital is under development. Although the model is semi-empirical it has yielded useful expressions for the estimation of maximum ionization cross-sections and it predicts both the direction and magnitude of the orientation effects measured[53].

C. Publications Submitted

a) Electron - Molecule Collisions

i) **Negative ion formation** - fundamental processes Papers 1 - 6, 9, 24

Although studies of positive and negative ion formation in the gas phase were carried out by J. J. Thomson as early as 1912, until the mid-1960's negative ion formation had attracted only a small fraction of the attention afforded positive ion formation processes. This had been due largely to the experimental difficulties associated with the detection of negative ions, which are produced with characteristically low electron capture cross-sections, often some orders of magnitude lower than for positive ion formation. Since many negative ions are formed in the energy range below 10 eV, the influence of contact potentials, space charge effects, ground loops and stray electric and magnetic fields necessarily affect the ionization efficiency curves and the linearity of the electron energy scale.

At the time I began my Ph.D. studies on negative ion formation at the University of Edinburgh in 1968, studies of associative and dissociative resonance electron capture processes were strictly the domain of the physicist with attention focused on diatomic and triatomic molecules. Accurate determinations of the threshold energies for dissociative electron capture and the relative capture efficiencies for associative electron capture could yield important radical, ion and molecular properties such as electron affinities, bond dissociation energies, electron capture cross-sections, enthalpies of formation, the identification or confirmation of new electronic states, and autodetachment lifetimes for metastable molecular negative ions. The major obstacle to realising these goals was the inherent width of the thermionically generated electron energy distribution used in the ionization process. During the course of my Ph.D. studies we developed the first analytical deconvolution method for unfolding associative and dissociative electron capture curves thus facilitating the extraction of useful mechanistic information and molecular parameters. The major driving force in the research described in this submission has been the desire to gain a more fundamental understanding of electron capture and electron impact ionization through the development of more sophisticated instruments, new experimental techniques and theoretical modelling.

Papers 1-6 involve research carried out as a Post-Doctoral Fellow with Prof. Joe Franklin at Rice University, in some cases involving collaboration with Prof. Margrave, graduate students and other Post-Doctoral Fellows. **Paper 1** describes an investigation of negative ion formation and ion-molecule chemistry in cyclopentadiene using a time-of-flight mass spectrometer that I rebuilt for negative ion research. Deconvolution was applied in the determination of EA(C_5H_5), $\Delta H_f(C_5H_5)$, $\Delta H_f(C_5H_5^-)$, D(H-C_5H_5), and four other previously unknown thermochemical parameters. The molecular parameters determined were then used to predict which small negative ions would undergo proton transfer and proton plus hydrogen transfer reactions with cyclopentadiene. The predictions were confirmed experimentally providing additional support for the values determined by the deconvolution of resonance curves. **Paper 2** describes a study of dissociative electron capture in CO, NO, CO_2 and SO_2. The results from accurate electron capture thresholds determined using deconvolution and from the measurement of the negative ion translational energies using ion time-of-flight peak profiles, led to the proposal of a semi-empirical equation relating the fragment ion translational energy, which can be measured, the excess energy involved in the dissociative capture process, which could be determined from thermochemical considerations for the cases selected, and the number of vibrational degrees of freedom in the molecular ion intermediate. This expression can be used to obtain a complete energy balance for complex systems and, in most cases, a better interpretation of the electron capture process.

Paper 3 describes the first application of deconvolution and the excess energy distribution equation to the mechanistics and energetics of negative ion formation processes in inorganic solids. Group III Fluorides were vapourised from a Knudsen cell into the source of a time-of-flight mass spectrometer and the electron capture curves measured. Previously unknown thermochemical parameters were determined for all fluorides. In **Paper 4** the concepts were extended to a series of polyatomic molecules with 4 to 12 atoms. The results led to the discovery that the degree of vibrational activation in the metastable molecular ion state undergoing dissociation was dependent on the molecule and varied from one dissociation channel to another. These results were discussed in terms of theoretical concepts and 14 new thermochemical parameters were determined, including the first measurement for $\Delta H_f(BF_2^*(^2B_2))$. **Paper 5** compares the negative ion processes in the Group IV fluorides, from C to Pb, and in As_4, with the evaluation of previously unknown thermochemical properties in all systems.

Paper 6 was not only an extensive review of the negative ion formation and negative ion-molecule reaction literature, it also critically evaluated the methods, techniques and data interpretation. It also included new data we had not previously published. In **Paper 9**, associative and dissociative electron capture by the stable free radical $(CF_3)_2NO$ revealed a number of new and unexpected results and produced a number of negative ions not previously recorded. The molecular negative ion exhibited an unusually high capture cross-section and an exceptionally long lifetime of 650 μs with a broad associative capture curve peaking at 1.2 eV. Molecular orbital calculations were used as a guide for the interpretation of the results. The calculations, supported by the measured dissociative resonance curves, revealed the possibilty of forming a singlet of high electron affinity and a triplet state of lower electron affinity, the singlet as a nuclear excited Feshbach resonance at low energy and the triplet as an electron excited Feshbach resonance at higher energies. Electron capture over the energy range 0 - 2 eV could generate both molecular negative ion states with overlapping resonance capture curves. **Paper 24** was a study of negative ion formation in C_2N_2 using the high intensity near-monochromatic electron gun described in Section 7A(i), including fragment ion translational energy analysis. The molecular ion, $C_2N_2^-$, was detected and a mechanistic analysis of the dissociative capture curves for the CN^- ion revealed that the CN radical was being produced in both $^2\Sigma$ and $^2\Pi$ electronic states. An energy balance analysis was used to construct a potential energy diagram for CN^- formation in the C-C dimension. The methods employed in the study of C_2N_2 could be usefully applied to other systems.

ii) **Positive ion formation** - formation and thermochemistry of isomeric ions

Papers 23, 26, 29, 34, 36, 51, 52, 53

In **Paper 23**, the near-monochromatic hemispherical electron source was combined with ion kinetic energy analysis in the first such investigation of the energetics of isomeric positive ion formation from the interstellar molecules C_2N_2, CH_3CN and CH_3NC. Mechanisms for ion formation were proposed and used to evaluate enthalpies of formation for all ions of the type $H_xC_2N^+$, where x = 0 to 3. This study provided the first experimental evidence for stable non-interconverting isomeric ions of the cyanide/isocyanide series in the gas phase. Enthalpies of formation, and hence relative stabilities, were reported for all species and SCF computations were employed to predict the most stable isomeric structures. An interesting find was that the CNC^+ isomer of the C_2N^+ ion, which is lower in energy than the isomeric CCN^+ isomeric structure, was the isomer formed at the threshold for C_2N^+ ion formation in C_2N_2 (N≡C-C≡ N). The study of isomeric ions was extended to another interstellar molecule, HC_3N, in **Paper 26**. The ionization efficiency curve for the C_2N^+ ion formed from HC_3N was unusually complex with 3 breaks above the threshold. Ionization mechanisms constructed using the thermochemical data determined in Paper 23 closely reproduced the energies corresponding to the breaks, thus lending support to the experimental techniques and the enthalpy data reported.

In **Paper 29**, my colleague Robert Maclagan and I carried out *ab initio* calculations of the relative energies and electronic states of the C_3N^+ ion in order to interpret the experimental measurements reported in Paper 23. We were able to conclude that the threshold measured in the experimental ionization efficiency curve for the C_3N^+ ion corresponded to the $CCCN^+$ structure with a $^3\Sigma^-$ ground state. The $CCNC^+$ isomer was calculated to lie ~0.15 eV above the cyanide isomer and would not have been resolved in the experiments. The break at 0.9 eV above the threshold corresponded to the c-C_3N^+ isomer which was calculated to lie 1.0 eV above the ground state. So, the relative energies of the isocyanide and cyanide isomeric structures for ions of the type $H_xC_2N^+$ and C_3N^+ are reversed. **Paper 36**, written with Robert Maclagan and Fritz Schaeffer, from the Center for Computational Quantum Chemistry, at the University of Georgia, employed *ab initio* calculations at high levels of theory to explore the relative energies of isomers for $C_2NH_2^+$, one of the ions investigated in Paper 23. The calculations show three low lying ion structures, the ground state being the cyclic form followed by the CH_2NC^+ isomer and then the CH_2CN^+ isomer. The calculations showed that, in contrast to the CH_3NC case where the lowest energy cyclic isomer is formed at the threshold, the formation of this isomer from CH_3CN is precluded by the barrier height for the interconversion of the CH_2CN^+ isomer to the cyclic form. Papers 23, 26, 29 and 36 demonstrated that chemical intuition has limitations, the isomeric ions of significance to models of molecular synthesis in interstellar dust clouds cannot be reliably formulated in the absence of accurate laboratory measurements and theoretical calculations (both are required for an unambiguous picture).

Paper 34 explores the formation, thermochemistry and chemical reactions of the HCO^+/COH^+ isomeric pair, which has been detected spectroscopically in interstellar dust clouds. In **Paper 51**, the electron impact ionization of molecular clusters formed in supersonic jet expansions of CO_2, NH_3 and N_2O were studied. Appearance energies for small molecular clusters and their fragments were measured, cluster binding energies were deduced and a new mechanism for the formation of fragment ion clusters was proposed.

Paper 52 reports experimental details and results for the first study of the electron impact ionization of a spatially oriented molecule. It was shown that the ionization cross-section and the mass spectrum for 200 eV electron impact ionization of CH_3Cl were orientation dependent. The steric ratio, the ratio of ionization cross-section for electron impact ionization on the positive CH_3-end of the molecular dipole to ionization on the negative Cl-end, was found to be 2.6 for formation of the molecular ion, CH_3Cl^+. The steric ratio for formation of the CH_3^+ fragmentation product was close to 1.0, that is, independent of spatial orientation of the dipole. This was interpreted as reflecting a preference for fragmentation in broadside collisions and confirmed by an experiment in which a mass insensitive detector was used to replace the quadrupole mass filter detector. **Paper 53** is a detailed review of the effect of molecular orientation on electron transfer and electron impact ionization written with co-worker Phil Brooks from Rice University. This article includes previously unpublished data for electron impact ionization on spatially oriented CH_3Br, CF_3Br

and $CHCl_3$ and introduces a new theoretical model for electron impact ionization which accounts for all of the experimental features.

b) Ion - Molecule Collisions

i) Ion-molecule chemistry Papers 1, 7, 8, 10 - 19, 51

During an investigation of low energy electron capture by GeF_4 as a Ph.D. student, I recorded a number of complex negative ions with two Ge atoms. They were most likely negative ion clusters or the result of ion-molecule reactions in the ion source of the time-of-flight mass spectrometer. My first determined study of negative ion chemistry is described in **Paper 1**, as discussed in Section 7.C.a) i) above.

Papers 7 and 8 report research on positive ion-molecule reactions carried out as a Research Scientist in the Physics Division of CSIRO in Sydney. In **Paper 7**, positive ion-molecule reactions in CH_4 and N_2O were studied at pressures of only 10^{-5} torr while the ions were contained in a potential well generated by an electron space charge trap. Ions could be held for up to 10 ms with little degradation in density and the depth of the well could be adjusted to allow controlled ion leakage for an assessment of product ion kinetic energies. The relative importance of electron transfer and hydrogen ion abstraction for reactions of N_2O^+ and CO_2^+ with CH_4 were determined. In **Paper 8** electron transfer from the molecules N_2O and CO_2 to the ions Ar^+, Kr^+ and N_2^+ were studied for primary ions of near thermal energy in the electron space charge trap. In the reactions involving $Ar^+$and Kr^+ ions the ion attenuation curves were found to exhibit a double exponential decay which was interpreted in terms of different reactivities of the spin-orbit states of the inert gas ions. The initial relative ion intensities deduced by extrapolation of the decay curves to zero time were in the correct statistical ratio for the spin-orbit states. We were able to determine rate constants for individual spin-orbit states by mathematical modelling of the curves and to deduce that favourable Franck-Condon factors coupling the reactant molecule to the product ion states were not necessary prerequisites for fast electron (charge) transfer.

I continued investigations of energy transfer and reaction mechanism, and the evaluation of thermochemical properties of gas phase ions, with two academic colleagues, Colin Freeman and Murray McEwan, at the University of Canterbury, **Papers 10-19**. A series of ion-molecule equilibria and proton transfer reactions, **Papers 10, 12-15 and 18**, were studied using a Flowing Afterglow apparatus, based on the original design of Eldon Ferguson of NOAA, Colorado. Proton transfer reactions for which equilibrium could be established were studied from both forward and reverse directions and the equilibrium constants and free energy of reaction determined. These were used to deduce previously unknown proton affinities. Several of the ions studied were known to be present in interstellar dust clouds and we became interested in the role played by ions in the interstellar medium. This resulted in a series of studies on the ion-molecule reaction mechanisms for ion formation in interstellar dust clouds with the proposal of several new routes to observed polyatomic neutral species, **Papers 11, 16 and 17**. A mechanism for the formation of HC_3N was proposed and it was concluded that no simple gas phase ion-molecule mechanism could be found for the formation of HC_5N. The implication was that dust grain surface chemistry may play a role in the synthesis of the heavier polymeric cyanoacetylenes. Thermal electron (charge) transfer reactions were investigated in several systems and in the cases of electron transfer from acetone and biacetyl to a number of atomic and molecular ions, **Paper 19**, the rate constants were found to exceed the gas kinetic collision frequency by a factor of two or more. These rapid rates were interpreted in terms of a dissociative charge transfer process in which an electron is transferred in a non-spiralling collision from outside the Classical capture limit and the factors promoting such a mechanism were discussed.

ii) **Ion transport properties** Papers 20 - 22, 27, 28, 30 - 35, 39, 45, 48, 49

Although my research papers in particle interactions had been confined to electron-molecule and ion-molecule collisions up to the early 1980's, I had designed a drift-tube during my first year at CSIRO in 1973/74, Section 2, in order to study non-reactive, momentum transfer collisions through the measurement of ion transport properties. **Papers 20 and 21** detail the design and application of a drift-tube for the measurement of the ion transport properties of positive ions through inert gas buffers over the pressure range from 10^{-2} torr to 10 torr, see Section 7.a) ii). **Paper 20** describes a software-controlled multiple pulse generator for the gating of ions in the drift-tube which employs self modifying assembly code. The mobilities in helium of the molecular positive ions and major fragmentation products formed from the cyano-molecules HCN, CH_3CN, CH_3NC and C_2N_2 studied with the near-monochromatic electron source in Papers 23 and 26, discussed in Section 7.C.a) ii), were reported for the first time in **Papers 21 and 22**. The structural isomers characterised by the electron impact studies did not appear to exhibit drift velocities that were sufficiently different to be differentiated in the drift-tube experiments. However, in the drift-tube the ions were produced by electron transfer to helium and the possibility that the lowest energy isomer was formed could not be discounted. The study described in **Paper 27** achieved three significant objectives: i) the first demonstration that isomeric forms of small ions, $C_2H_xO^+$ ($x = 3$ to 5), can be differentiated through the measurement of ion transport properties; ii) the first identification of the isomeric form of an ion-molecule reaction product through mobility measurements (the isomeric form of the $C_2H_5O^+$ ion formed by proton transfer to CH_3CHO); iii) the application of a simple interaction potential model to predict the relative effects of structural parameters on the ion transport properties of polyatomic ions drifting in helium, Section 7.B.iv).

The generalised interaction potential used in the analysis of structural parameters on ion transport properties in Paper 27 could not be used to reliably inter-relate the momentum transfer efficiency of the ion-neutral interactions to the macroscopic ion transport properties of the system. In **Paper 28**, the two-temperature theory of ion mobility was used with an *ab initio* interaction potential, calculated using the Gaussian program at the MP4SDQ level of theory, to calculate ion mobilities for the F^- ion in helium over a wide range of field strength to particle density ratio, E/N. The fit between the computed ion transport behaviour and accurate experimental data from the literature was well within experimental uncertainties for $E/N > 20$ Td (for

MP2, MP4 and Hartree-Fock) and deviated outside the reported experimental uncertainties, according to the method and basis set used, below 20 Td. Matching of the mobility curves for the full range of E/N was achieved through a small adjustment in the well depth for the $HeF^-(^1\Sigma)$ interaction potential. The calculations were extended in **Paper 30** to O^+ in He. There were two experimental studies of O^+ in He in the recent literature claiming that a shoulder on the arrival-time peak for the O^+ ion in helium measured in a flow drift-tube corresponded to the $O^+(^2D)$ electronically excited state. Valence Bond and Molecular Orbital calculations of the interaction potentials were carried out for the three low lying states of the HeO^+ molecular ion: $^4\Sigma(^4S)$; $^2\Pi(^2D)$; $^2\Pi(^2P)$. These were used with the two temperature theory of ion transport to calculate the transport properties for the ground state and the two electronically excited states of the O^+ ion in He. These were the first calculations of excited ion state transport properties. The calculated $HeO^+(^4\Sigma)$ interaction potentials adequately described the reported mobility data for the ground state O^+ ion in He, however, the mobility calculated using the $HeO^+(^2\Pi(^2D))$ interaction potential did not match the experimental data reported as the $O^+(^2D)$ state. The interaction potential calculated for the $HeO^+(^2\Pi(^2P))$ state successfully matched the experimental results and we were able to conclude that the assumption that the shoulder in the arrival time peak corresponded to an electronically excited ion was correct, but that the state assignment had been incorrect. The calculated interaction potentials revealed a surface crossing between the $^2\Pi(^2D)$ state and the $^4\Sigma(^4S)$ ground state of HeO^+ providing an effective channel for depletion of the $^2\Pi(^2D)$ state of HeO^+ to lower lying surfaces. So, the ^2D state is quenched in the flow drift tube by He but the higher energy ^2P state is not.

Paper 31 explores the dependence of zero-field mobility, $K_0(0)$, on the well depth, ε, and minimum interparticle separation, r_m, in the ion-neutral interaction potential. For large values of r_m, $K_0(0)$ was found to be very sensitive to small changes in ε whereas at small r_m, $K_0(0)$ was found to vary only slightly from the Langevin value. This result has implications for the calculation of rate constants using flow tubes, where the diffusion correction is estimated using the Langevin equation. It also has important ramifications for the level of theory required when *ab initio* methods are used to compute interaction potentials, particularly for the attractive region of the potential greater than 0.3 nm which determines ion mobility at low E/N (as discovered in Paper 28). Taking the conclusions of Paper 31 into account, **Paper 32** reports *ab initio* calculations of interaction potentials at the MP4 level of theory for the HeF^+ system in which the two molecular states $HeF^+(^3\Sigma, {}^3\Pi)$ correlate with the separated He atom and F^+ ion. Two temperature and three temperature theories of ion mobility were used to calculate the mobility of $F^+(^3P)$ in He by summing over the appropriate statistical weights for the two molecular ion states separating to $He(^1S)$ + $F^+(^3P)$. Good agreement with reported experimental measurements was found for both mobility theories and it was concluded that the additional processor time required for the three temperature theory could not be justified by the returns.

Paper 33, reports calculations for the ^2P ground electronic state and the ^4P excited state of the C^+ ion in helium using two temperature theory and HeC^+ interaction potentials at the MP4 level of theory. The $HeC^+(^2\Pi)$ state was shown to be weakly bound by 200 - 200 cm^{-1}. A literature report of a gas phase ion of m/z 16 generated from a helium discharge between carbon electrodes has been assigned to a stable HeC^+ or $He_2C_2^{2+}$ ion. In **Paper 35** theoretical calculations and experimental mobility measurements are reported for the B^+ ion in helium and in **Paper 39** the calculations and experimental results are reported for N^+ in helium. Two limiting methods for the calculation of atomic ions in atomic gases with orbital angular momentum greater than zero were developed and discussed in Paper 39. **Papers 45, 48 and 49** introduced an extension of the method to atomic ions in diatomic buffer gases. **Paper 45** described the calculation of interaction potentials for Li^+ in the homonuclear diatomic N_2 and **Papers 48 and 49** reported interaction potential calculations and mobility calculations for Li^+ in the heteronuclear diatomic CO.

Papers described in this Section have demonstrated that the transport properties of ground state and electronically excited atomic ions, which may not be readily amenable to experimental measurement, can be reliably calculated within the experimental precision available with the most sophisticated drift-tubes. The work has also clearly demonstrated that a combination of experimental and theoretical methods is essential for a complete appreciation of particle interactions.

c) Atom - Molecule Collisions

i) Oriented molecules Papers 25, 37, 38, 42, 43, 52, 53

The first experiments involving collisions between thermal energy alkali metal atoms, K or Rb, and spatially oriented CH_3I carried out from 1966 onwards demonstrated that the reaction cross-section for collisions on the I-end of the molecule was greater than that for collisions on the CH_3-end. During the 1970's the experiments were extended to include oriented CF_3I and a harpoon mechanism was proposed in which the first step is an electron transfer from the electropositive alkali metal atom to the electronegative CF_3I molecule. **Paper 25,** see Sections 7.A.iii) and 7.B.iii), reports the first systematic investigation of the effect of spatial orientation on chemical reactivity. The effects of orientation on the outcome and mechanisms for collisions of thermal energy K atoms with oriented CF_3Br, CF_3I and CH_3I were investigated. The measurements could be rationalised qualitatively in terms of an exit channel effect, although it was noted in the paper that the significant differences found between the scattering behaviour of the CF_3Br and CF_3I systems suggested that the entrance channel, the charge transfer step, might also exhibit orientation dependence. This was the first indication that electron transfer might be influenced by molecular orientation.

Papers 37 and 38 report the first experiments involving collisions of fast K atoms and oriented CH_3I and CF_3I molecules. The fast K atom beam was generated by resonant electron transfer and accelerated to energies over the range from 5 to 30 eV. These experiments added further evidence for the dependence of the electron transfer step on molecular orientation which was confirmed in more refined experiments reported in **Paper 53**. The range of oriented molecules was extended in **Paper 42** to include most members of the CH_3X and CF_3X series, t-BuX and CHX_3 molecules, where X is the halogen leaving group. A theoretical model based on Landau-Zener potential energy curve-crossing was developed and introduced in Paper 38 and applied in Paper 42. A Classical model for the orientation effects, which reproduced the main features of the experimental measurements, was introduced in **Paper 43**. **Paper 53** reviews the experimental and theoretical evidence for the influence of molecular orientation on electron transfer and for the effect of molecular orientation of electron impact ionization.

ii) **Transition region species** Papers 41, 43

Papers 41 and 44 report the observation of Na atom emission at 589.0 nm when beams of K atoms and NaX (X = Cl, Br, I) molecules intersect inside the cavity of a cw dye laser tuned to wavelengths which are not resonant with either the isolated reagents or the reaction products. The emission was interpreted as the signature of light absorption by the systems, K---NaX, in the process of chemical reaction. The variation in emission intensity with the probe laser wavelength is an excitation spectrum of the transition region species (or activated complex) formed in the reactions. This was the first identification of spectral features for a transition region species. Mechanisms were proposed to account for the spectra in terms of the reaction dynamics.

iii) **Flow dynamics** Papers 40, 46, 47, 50

Papers 40, 46 and 47 form a series in which the flow dynamics of supersonic molecular beam sources and the efficiency of rotational to translational energy transfer were mathematically modelled and experimentally tested, see Section 7.B.ii). In **Paper 40**, the flow dynamics of supersonic atomic and molecular beams were mathematically modelled using a modification of the thermal conduction model as a framework with realistic interaction potentials and collision cross-sections calculated from Classical scattering theory. Expressions were developed for the calculation of collision frequency, flow velocity, particle density, mean free path, and axial and radial temperatures in atomic and homonuclear diatomic supersonic beams as a function of axial distance from the nozzle. A comparison between experimentally measured velocity distributions for the inert gases, N_2 and H_2 were used to calculate values for the rotational to translational coupling parameters for the diatomic gases. Good agreement between the calculated values for N_2 using this new method and the mean literature value, measured using microwave techniques, afforded some confidence in the flow parameters calculated from the theory and for the value of the rotational to translational coupling parameter calculated for H_2.

Paper 46 extended the calculations to O_2 and Cl_2 and reported an expression based on the experimental measurements which enabled the rotational relaxation time for unknown cases to be estimated with a high degree of confidence. In **Paper 47**, a direct simulation Monte Carlo procedure was used to determine flow parameters and rotational collision numbers for the diatomic molecules previously studied and, in addition, the energy dependence of the coupling parameter was investigated. This was extended to include the polyatomic molecules CO_2, OCS, NH_3, CH_4, CH_3Cl and C_2H_4. The energy dependent translational to rotational coupling parameters calculated for CO_2, OCS and CH_3Cl were used in thermal conduction model calculations to investigate the breakdown of translational and rotational equilibrium in supersonic expansions of these gases.

The experimental determination of accurate velocity distributions using chopped supersonic atomic and molecular beams, required in the studies reported in Paper 40, drew attention to the requirement for a reliable, practical deconvolution method for unfolding unchopped time-of-flight waveforms. In **Paper 50**, this was achieved using Fourier Transform and Wiener filtering methods to determine a universal instrument response function which could be subsequently applied to unfold unchopped waveforms. Chopped arrival time distributions, determined experimentally, were used to calculate the response function. The response function could then be used to deconvolute any unchopped time-of-flight waveforms measured under similar experimental conditions. The response function could also be determined by the deconvolution of an unchopped inert gas arrival-time-distribution using a calculated ideal inert gas profile and then applying this to other systems. Results were presented for beams of $CHCl_3$ and CH_3Cl with comparisons between the experimental and deconvoluted profiles.

8. Papers 1 - 53

Reprinted from:

THE JOURNAL OF CHEMICAL PHYSICS VOLUME 56, NUMBER 11 1 JUNE 1972

Negative Ion Formation and Negative Ion–Molecule Reactions in Cyclopentadiene

A. DI DOMENICO,* P. W. HARLAND, AND J. L. FRANKLIN
Department of Chemistry, Rice University, Houston, Texas 77001

(Received 25 January 1972)

The low pressure source of a Bendix time-of-flight mass spectrometer has been employed for a study of positive and negative ion formation in cyclopentadiene (C_5H_6). Six negative ions in the mass spectrum of C_5H_6 have been investigated and particular attention has been paid to the cyclopentadienyl negative ion ($C_5H_5^-$). The appearance potential data for $C_5H_5^+$ and $C_5H_5^-$ ion formation were used to estimate the following previously unknown thermochemical parameters: $\Delta H_f(C_5H_5^-) = 19 \pm 2$ kcal mole^{-1}, $\Delta H_f(C_5H_5) \leq 70 \pm 5$ kcal mole^{-1}, $\Delta H_f(C_5H_5^+) \leq 273 \pm 4$ kcal mole^{-1}, E.A.$(C_5H_5) \leq 2.2 \pm 0.3$ eV, and $D(C_5H_5\text{–}H) \leq 3.9 \pm 0.2$ eV. A high pressure source was employed to carry out negative ion–molecule proton transfer and proton plus hydrogen transfer reactions between C_5H_6 and a variety of reactant ions. An evaluation of the energetics for these processes provided a second approach for the estimation of a value for $\Delta H_f(C_5H_5^-)$ and also gave an upper limit of 58 kcal mole^{-1} for $\Delta H_f(C_5H_4^-)$.

INTRODUCTION

"Sandwich"–bonded derivatives with transition metal–carbon bonds have been known for two decades. The first compound of this class, $(\pi\text{-}C_5H_5)_2Fe$ or "ferrocene", was reported in 1951[1] and marked the beginning of extensive studies on cyclopentadienyl derivatives as well as on similar carbocyclic systems in which the organic molecule is a π-electron donor. The investigation of the chemistry of these molecules which followed was accompanied by extensive research into the structural properties of C_5H_6, cyclopentadienyl radical, cation and anion by means of conventional experimental techniques.[2–13] Following the development of semiempirical MO methods,[14–24] theoretical models were built and analyzed. However, in spite of the large amount of work, important structural and thermodynamic parameters, such as $\Delta H_f(C_5H_5)$, E.A.(C_5H_5) and $\Delta H_f(C_5H_5^-)$, are still unknown.

To our knowledge only one previous investigation of the free cyclopentadienyl anion and the negative ions formed from C_5H_6 by electron impact in the energy range 0–10 eV, has been reported.[9] In this paper, the ionization efficiency curve of SF_6^- was used to calibrate the electron energy scale and to measure the electron energy distribution. Since the use of SF_6^- as an energy scale reference may be misleading[25] and has been found to result in erroneous calibration,[26] and as no further information relating to C_5H_6 was contained therein, we thought it of interest to undertake a mass spectrometric study of negative ion formation and negative ion–molecule reactions in the energy range 0–10 eV.

In electron impact studies, when the source of electrons is a heated filament, uncertainties arise in the interpretation of the ionization efficiency data because of the energy spread of the thermionically emitted electron beam. The ionization thresholds become indeterminate or smeared out because of the high energy tail of the electron energy distribution. This source of uncertainty has been largely removed in this work using the analytical deconvolution method

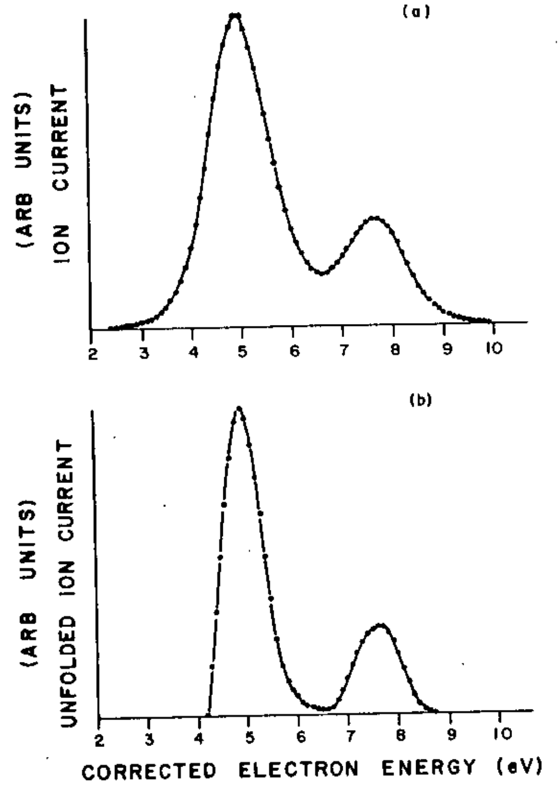

FIG. 1. Ionization efficiency curve for O⁻ ion formation from SO_2. (a) Experimental data, (b) deconvoluted results obtained using 16 smoothing and 20 unfolding iterations.

of Morrison[27] which was adapted for negative ion data by MacNeil and Thynne.[28] This technique has been previously employed in the investigation of negative ion formation by a number of molecules[29–34] and was used in this study to unfold the ionization efficiency curves of O^-/SO_2 and O^-/CO used for calibration of the electron energy scale and $C_6H_6^-/C_6H_6$ for the calculation of $\Delta H_f(C_6H_6^-)$. The experimental and unfolded ionization efficiency curves for O^-/SO_2 and O^-/CO after 16 smoothing and 20 unfolding iterations are shown in Figs. 1 and 2, respectively.

The electron energy scale was calibrated against the appearance potentials of the O⁻ ion formed from SO_2 at 4.2 and 6.6 eV[35,30] and the O⁻ ion formed from CO at 9.6 eV.[36] The formation of the O⁻ ion from CO has been studied by several workers[36–38] and it has been shown that the cross section for Reaction (1) rises vertically to a maximum value at the ionization threshold,

$$CO+e\rightarrow O^-+C(^3P). \qquad (1)$$

In Fig. 2(b) the ionization threshold was taken as the point of maximum slope on the onset edge of the unfolded ionization curve and this was set equal to 9.6 eV. The second peak, which has been partially resolved by the unfolding procedure, is found to onset at about 10.8 eV, in accord with the observations of Chantry,[36] who has suggested that this dissociative attachment process corresponds to Reaction (2), which has a calculated minimum energy requirement of 10.88 eV,

$$CO+e\rightarrow O^-+C(^1D). \qquad (2)$$

The electron energy distribution used in the unfolding procedure was controlled using an arrangement previously described[39] and measured using the SF_6^- ion formed by SF_6.[40,25] In all experiments, including the ion–molecule reactions, the width of the SF_6^- capture peak at half-height never exceeded 0.6 eV.

Further checks on the energy scale calibration were provided by the peak maxima for Cl^-/HCl at 0.8,[41] O^-/SO_2 at 4.9,[30] NH_2^-/NH_3 at 5.6,[42,43] and O^-/CO at 10.0 eV.[36,44] These independent calibrants provided consistent results over the entire energy range within ±0.1 eV using the low pressure source and ±0.2 eV when high pressure experiments were carried out.

The positive ion appearance potentials were calibrated using the spectroscopically determined appearance potential for CO^+ ion formation by CO at

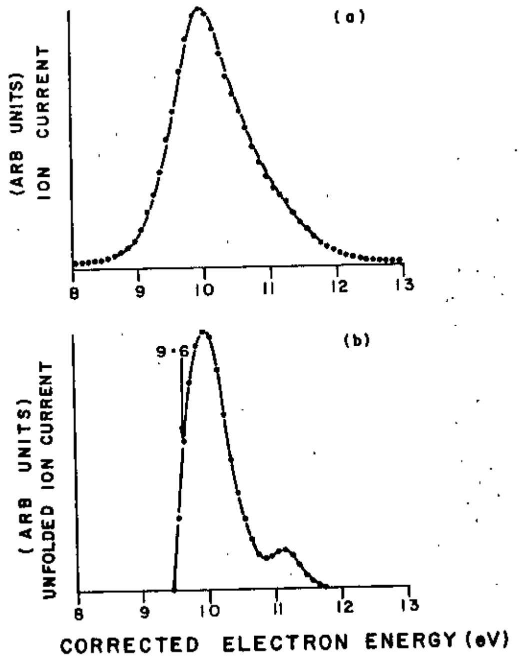

FIG. 2. Ionization efficiency curve for O⁻ ion formation from CO. (a) Experimental data, (b) deconvoluted results obtained using 16 smoothing and 20 unfolding iterations.

14.01 eV[45] and measured using the semilogarithmic plot technique.

EXPERIMENTAL

The data were obtained using a Bendix Model 12 time-of-flight mass spectrometer modified with a Model 3015 output scanner. This instrument was equipped with low and high pressure sources, the latter being operative up to 0.05 torr. For the high pressure studies an mks Type 77 Baratron pressure meter was used to monitor the pressure directly in the ionization region.

The magnitude of the ion focus pulse applied to the ion drawout grid was always carefully adjusted to be consistent with maximum resolution and symmetric ion peaks.

A Lambda power supply, Model LH 121 FM, was employed to maintain a constant current of 3.6 A dc through a 0.007-in. rhenium filament. Finally, when accurate measurements of ionization efficiency curves were carried out, the trap anode was maintained at earth potential. Further details on this instrumentation are reported in previous papers.[46–48]

Except for ion–molecule reactions, when the C_5H_6 pressure was varied from 0.001 to 0.04 torr, the C_5H_6 pressure was normally held in the range 0.01 to 0.015 torr. No attempts were made to measure accurate rate constants for the reactions investigated.

All materials employed in this research were commercial products: ammonia (99.99%), carbon dioxide 99.99%), carbon monoxide (99.5%), cyanogen (98.5%), hydrogen chloride (99.0%), hydrogen sulphide (99.6%), sulphur dioxide (99.9%), and sulphur hexafluoride (99.8%) were obtained from Matheson Gas Products and used with no additional purification. Spectroquality carbon disulphide was purchased from Matheson, Coleman, and Bell, and degassed before use. C_5H_6 was prepared from technical dicyclopentadiene supplied by Aldrich. Dicyclopentadidne was first refluxed on barium oxide for 12 h and then carefully distilled with a fractionating column.[49] The distilled product, C_5H_6, was thoroughly degassed and held on liquid nitrogen to prevent dimerization. From this reservoir, about 200 torr of gaseous C_5H_6 were taken when needed and stored at room temperature in a 3-liter vacuum flask to provide a uniform supply of sample throughout the experiments. The positive ion mass spectrum of C_5H_6 at 70 eV was recorded prior to all experiments as a check of sample purity. Normally, the C_5H_6 purity was greater than 99% with the dimer present to less than 0.1%. The only detectable trace of water originated from the background and other contaminants were present in only trace amounts.

RESULTS AND DISCUSSION

Positive Ion Data

The ionization potential of C_5H_6 was found to be 8.5±0.1 eV in reasonable agreement with values of 8.9[4] and 9.0 eV[2] reported previously. Using this value in conjunction with the heat of formation of C_5H_6[2,28] (32 kcal $mole^{-1}$), the heat of formation of the molecular ion, $C_5H_6^+$, is estimated to be 228 kcal $mole^{-1}$.

The cyclopentadienyl positive ion formed in Reaction (3),

$$C_5H_6+e\rightarrow C_5H_5^{+}+H+2e, \qquad (3)$$

was the only fragment ion studied. The appearance potential was measured to be 12.7±0.1 eV in good agreement with values reported previously, 12.6[2] and 11.9±0.5 eV.[6] The ionization potential of the cyclopentadienyl radical has been determined experimentally by Harrison *et al.*[2] to be 8.76±0.1 eV and calculated using a modified MO method by Streitwieser[16] to be 8.82 eV. Using an average value of 8.8 eV, a value of 3.9±0.2 eV is calculated as an upper limit for the C_5H_5–H bond dissociation energy and an upper limit of 273±4 kcal $mole^{-1}$ for $\Delta H_f(C_5H_5^+)$ and of 90 kcal $mole^{-1}$ for $\Delta H_f(C_5H_5)$.

Negative Ion Data

The negative ions recorded in the low and high pressure sources are listed in Table I. The low energy resonance for $C_5H_5^-$ ion formation exhibits the highest

Table I. Energy maxima of dominant negative ions from cyclopentadiene in low and high pressure sources.

Mass	Ion	Low pressure source electron energy in eV[a]		High pressure source electron energy in eV[a]				Σ[b]
65	$C_5H_5^-$	2.0±0.1	~9.3[c]	2.0±0.3	5.3±0.3[c]	7.2±0.3[c]	~9.3[c]	1
39	$C_3H_3^-$		8.7±0.1			8.7±0.1		10
25	C_2H^-		9.2±0.1				9.2±0.1	10
64	$C_5H_4^-$		9.2±0.2				9.3±0.2	20
63	$C_5H_3^-$		9.2±0.2				9.3±0.2	20
38	$C_3H_2^-$		9.2±0.2				9.2±0.1	20

[a] Corrected.

[b] Relative sensitivities: $\Sigma(C_5H_5^-)=1$ at 2.0 eV.

[c] These resonances are about 10 times less intense than that at 2.0 eV.

TABLE II. Appearance potentials (A.P.), energy maxima (EM), half-height peak width (*W*), and relative intensity (RI) of the negative ions for CPD from Ref. 9. Ions have been listed as in Table I.

Mass	Ion	A.P. (eV)	EM (eV)	*W* (eV)	RI %
65	$C_5H_5^-$	1.1	1.65	0.5	100
65	$C_5H_5^-$	...	8.85	...	3.6
39	$C_3H_3^-$	7.30	8.35	1.15	11
25	C_2H^-	7.4	8.9	1.7	20.5
64	$C_5H_4^-$	7.9	9.0	...	1.6
63	$C_5H_3^-$	...	...	...	1.2
38	$C_3H_2^-$	7.5	9.6	...	1.5

dissociative capture cross section and has been used as a reference in reporting the relative sensitivities, Σ, at which each ion had been recorded. A comparison can be made against Table II where previous experimental results[9] are shown. The discrepancies in the reported resonance peak maxima between the two sets of data may be attributed to the use of different energy scale calibrants, as pointed out above.

Since we have not carried out cross section determinations, we are unable to report any reliable data on the subject. However, from a comparison of the main resonance capture processes for Cl^-/HCl, O^-/CO, and $C_5H_5^-$ obtained at known pressures, it may be assumed that O^- and $C_5H_5^-$ have similar dissociative capture cross sections at equal multiplier response.

The following ions were also detected, but their intensities were too low to allow any kind of quantitative measurement: 16^-, 62^- and the isotopic 66^- ($C_5H_5^-$). The maximum position of 13^- and 14^-, CH^- and CH_2^-, respectively, was also approximately determined at 9.8 eV.

At mass 1 we could detect a weak ion current which had an onset at approximately 3.5 eV and was spread over the entire energy range. Because of the lack of reproducibility and well defined peaks, we cannot supply any further information, although in some experiments two maxima have been tentatively identified with the resonances at 6.5 and 8.6 eV of H^- from water.[50] While the presence and the shape of the ionization efficiency curve from mass 16 (O^-) would support the hypothesis that water may somewhat contribute to the H^- ion current, from a comparison with the literature[50] we are inclined to assume that the onset at about 3.5 eV is truly due to H^- from C_5H_6.

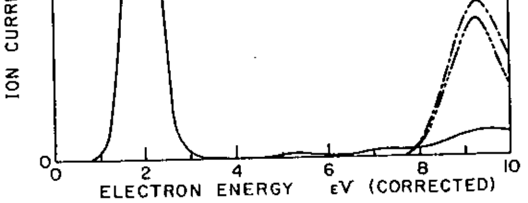

FIG. 3. Ionization efficiency curves for C_5H_6. — $C_5H_5^-$, —·— $C_5H_4^-$, —‑‑‑— $C_5H_3^-$. $\Sigma(C_5H_5^-):\Sigma(C_5H_4^-):\Sigma(C_5H_3^-)=1:20:20$. See text.

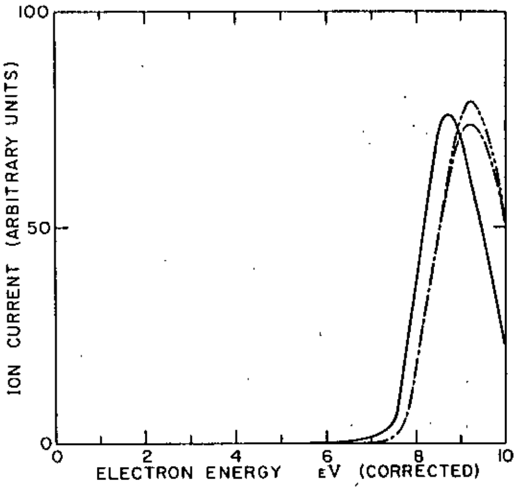

FIG. 4. Ionization efficiency curves for C_5H_6. — $C_3H_3^-$, —·— $C_3H_2^-$, —‑‑‑— C_2H^-. $\Sigma(C_3H_3^+):\Sigma(C_3H_2^-):\Sigma(C_2H^-)=10:20:10$. See text.

No negative ion-molecule reactions leading to secondary ions were observed when pure C_5H_6 was introduced into the reaction chamber. Only $C_3H_3^-$ exhibited a very faint signal at 2.0 eV when the C_5H_6 pressure was sufficiently high ($\gtrsim 0.015$ torr). A pressure study was carried out to ascertain whether $C_3H_3^-$ was a secondary ion at that electron energy, but the change in its intensity was too small to give any conclusive proof.

The list of values reported in Table I shows the excellent agreement between the low and high pressure results and needs no additional explanation. A brief discussion of individual ionic species will follow.

Experimental ionization efficiency curves are reported in Figs. 3–5 and, with the only exception of $C_5H_5^-$, they represent the ion currents at low pressure as well as at high pressure. From these figures, the half-height peak widths and the ion intensity ratios can be obtained. Table III summarizes the heats of formation, $\Delta H_{f298}{}^{\circ}$, of the various ions and neutrals employed in this study. When not mentioned, values are taken from Natl. Bur. Std. (U. S.) Note **270**, 3 (1968). D. D. Wagman, W. H. Evans, V. Parker, I. Halow, S. M. Bailey, and R. H. Schumm.

Cyclopentadienyl Anion, $C_5H_5^-$

The dissociative electron capture cross section for $C_5H_5^-$ ion formation by Reaction (4) is at least an order of magnitude greater than for any of the other negative ions detected,

$$C_5H_6+e\rightarrow C_5H_5^-+H. \quad (4)$$

If the energy at maximum cross section, 2.0±0.1 eV, is taken as the average energy, $\bar{E}$, required to produce $C_5H_5^-$ by Reaction (4), then the following expression,

$$\Delta H_f(H)+\Delta H_f(C_5H_5^-)-\Delta H_f(C_5H_6)-\bar{E}\leq 0, \quad (5)$$

may be used to estimate a value of 26 kcal $mole^{-1}$ as an upper limit for $\Delta H_f(C_5H_5^-)$. The inequality sign in Eq. (5) accounts for any excess energy involved in Reaction (4).

A comparison between the $C_5H_5^-$ capture peak and that measured for O^- formed from CO revealed that the leading edges of these resonances could be very closely matched after a −7.9 eV shift of O^- on the energy scale as shown in Fig. 6. As these two resonances are of similar cross section and exhibit similar peak widths at half height, it is concluded that the $C_5H_5^-$ ion is also formed by a process which attains maximum cross section at threshold. A comparison between the unfolded capture curves shown in Fig. 7 and the half-height widths of the two ions at their respective capture maxima serve to confirm this conclusion.

The appearance potential for $C_5H_5^-$ ion formation by Reaction (4) was determined by two methods: (i) the energy shift required for superposition of the O^-/CO curve on the $C_5H_5^-$ curve, −7.9 eV, is subtracted from the known appearance potential for Reaction (1), 9.6 eV,[36] to give 1.7 eV; (ii) from the

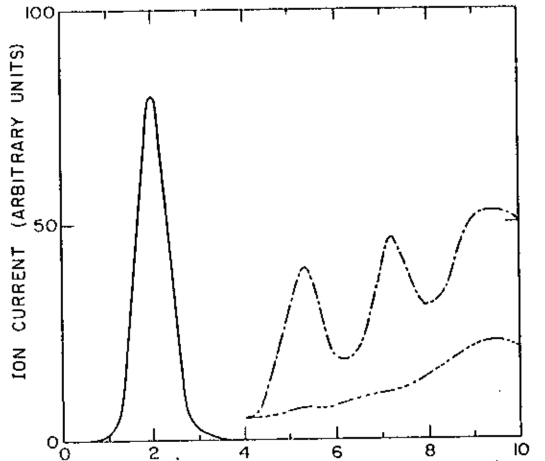

FIG. 5. Ionization efficiency curves for C_5H_6: $C_5H_5^-$. The curves are normalized at the 2.0 eV peak and magnified a factor of 10 above 4 eV. — - — $C_5H_5^-$ at high pressure, — - - - — $C_5H_5^-$ at low pressure. (— $C_5H_5^-$, at the two different pressures.) See text.

TABLE III. Heats of formation at 298°K of ions and neutrals used in this study (kilocalories per mole).

H	52.095	CN	105.5[k]
C	171.291		100[e]
NH_2	37[a]	CN^-	17.4[k]
NH_2^-	20[b]		22[l,e]
NH_3	−11.02	$(CN)_2$	73.84[e]
O	59.553	CO	−26.416
O^-	25.469[c]	CO_2	−94.051
OH	9.31	S	66.636
C_2H	117[d]	S^-	17.734[m]
C_2H	112[e]	SH	34.10
C_2H^-	26 to 69[f]	H_2S	−4.93
C_2H_2	54.19	SO	1.496
C_2H_3	64[g]	SO_2	−70.944
C_2H_4	12.49	Cl^-	−58.8
$C_3H_3^-$	≤63[h]	HCl	−22.062
	≤71[h]	CS	56
C_5H_6	31.84[i]	CS_2	28.05
	32.44[j]		
	30.16		

[a] Calculated from $D(NH_2-H)=100$ kcal $mole^{-1}$ (Ref. 43).

[b] Calculated from E.A.$(NH_2)=0.74$ eV. [K. C. Smyth, R. T. McIver, Jr., and J. I. Brauman, J. Chem. Phys. **54,** 2758 (1971).]

[c] Calculated from E.A.(O) = 1.478 eV. [R. S. Berry, J. C. Mackie, R. L. Taylor, and R. Lynch, J. Chem. Phys. **43,** 3067 (1965).]

[d] $D(C_2H-H)$ has been assumed 115 kcal $mole^{-1}$. [V. I. Vedeneyev, L. V. Gurvich, V. N. Kondrat'yev, V. A. Medvedev, and Ye. L. Frankevich, *Bond Energies, Ionization Potentials and Electron Affinities* (St. Martin's, New York, 1966).]

[e] J. L. Franklin, J. G. Dillard, H. M. Rosenstock, J. T. Herron, K. Draxl, and F. H. Field, Natl. Std. Ref. Data Ser. Natl. Bur. Std. (U.S.) **26** (1969).

[f] For the electron affinity of C_2H, the following values have been reported: 2.1 eV [R. Locht and J. Momigny, Chem. Phys. Letters **6,** 273 (1970)], 2.68 eV (Ref. 56), and 3.73 eV [D. Feldmann, Z. Naturforsch **25A**, 621 (1970)].

[g] J. A. Kerr, Chem. Rev. **66,** 465 (1966).

[h] Reference 57.

[i] Reference 2. The value of 32.00 kcal $mole^{-1}$ has been used in our calculations.

[j] Reference 23. The value of 32.00 kcal $mole^{-1}$ has been used.

[k] Reference 58.

[l] Reference 59.

[m] Calculated from E.A.(S) = 2.0772 eV [W. C. Lineberger and B. W. Woodward, Phys. Rev. Letters **25,** 424 (1970)].

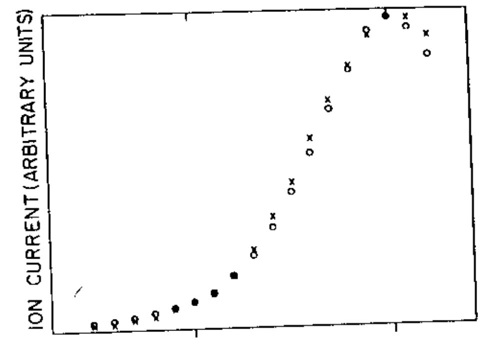

FIG. 6. Comparison of the ionization efficiency curves for O^-/CO (crosses) and $C_5H_5^-/C_5H_6$ (open circles). Energy scale for O^- shifted by −7.9 eV to allow overlap.

energy scale separation of the two unfolded peaks, taking the point of maximum slope on the onset edges as being the appearance potentials, an average value of 1.7 was determined for A.P.($C_5H_5^-$). Thus, the appearance potential for $C_5H_5^-$ ion formation is taken as 1.7±0.1 eV, where the error limit represents the maximum difference of several repeated determinations.

The intermediate molecular negative ion state involved in Reaction (4), therefore, exhibits a potential well, the dissociating limits of which intersect the Franck–Condon region. The fragments are then formed with zero kinetic energy at the threshold and since no excess energy can be found in the excited electronic states of H[51] and the same may be assumed for $C_5H_5^-$,[18,20] the following equation may be used to calculate $\Delta H_f(C_5H_5^-)$:

$$\Delta H_f(\mathrm{H})+\Delta H_f(C_5H_5^-)-\Delta H_f(C_5H_6)-\mathrm{A.P.}=0, \qquad (6)$$

from which we obtain $\Delta H_f(C_5H_5^-)=19\pm2$ kcal mole^{-1}.

If Reaction (4) does not involve excess energy at threshold, the following energy balance equation

$$D(C_5H_5-H)=\mathrm{A.P.}(C_5H_5^-)+\mathrm{E.A.}(C_5H_5) \qquad (7)$$

may be employed in conjunction with the value of $\leq3.9\pm0.2$ eV deduced for $D(C_5H_5-H)$ above to estimate a value of $\leq2.2\pm0.3$ eV for the electron affinity of the cyclopentadienyl radical. The magnitude of E.A.(C_5H_5) is in accord with that expected from the fact that $C_5H_5^-$ is a pseudoaromatic species.[20]

Since

$$\Delta H_f(C_5H_5^-)=\Delta H_f(C_5H_5)+\mathrm{E.A.}(C_5H_5), \qquad (8)$$

an upper limit of 70±5 kcal mole^{-1} may be estimated for $\Delta H_f(C_5H_5)$.

In the high pressure study, two peaks which have not been reported previously[9] were consistently reproduced at 5.3 and 7.2 eV, respectively, as Table I and Fig. 5 show. Since these peaks were not confirmed by the low pressure study, a process other than dissociative resonance capture must account for them. Chantry[52] has recently pointed out that certain peaks, which may appear to be formed by direct dissociative attachment, are actually due to an indirect mechanism in which the ionizing electron first releases discrete quantities of energy in inelastic collisions with the gas molecules, and then collides again causing ionization by dissociative resonance capture. This pattern has been tentatively applied to our case. In Reaction (9) the electron is inelastically scattered from a C_5H_6 molecule,

$$e(E^*+E_{\mathrm{res}})+C_5H_6\rightarrow C_5H_6^*+e(E_{\mathrm{res}}), \qquad (9)$$

$$e(E_{\mathrm{res}})+C_5H_6\rightarrow C_5H_6^{-*}\rightarrow C_5H_5^-+\mathrm{H}, \qquad (10)$$

losing energy E^* and thereby retaining the correct amount of energy E_{res} to produce a dissociative resonance capture Process (10). If Reaction (9) occurs to a reasonable extent and E^* is sufficiently well defined, a $C_5H_5^-$ "spurious" dissociative attachment peak should be observed at an electron energy of (E^*+E_{res}). Hence, if $E_{\mathrm{res}}=1.7$ eV, E^* will be 3.6 eV when $(E^*+E_{\mathrm{res}})=5.3$ eV, and 5.5 eV when $(E^*+E_{\mathrm{res}})=7.2$ eV. These assumptions would be supported by the following points:

(a) The low energy resonance peak exhibits a much higher relative intensity.

(b) The two medium-energy peaks occur when the high-pressure source is used.

(c) C_5H_6 is known to have an excited electronic state at about 5 eV.[5,20,43]

However, no evidence has been obtained that the medium-energy processes are quadratically dependent

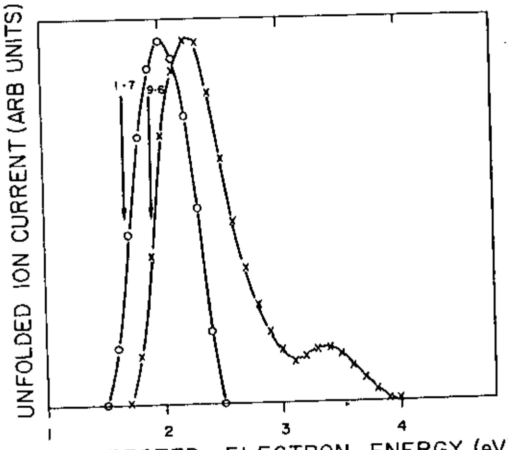

FIG. 7. Deconvoluted ionization efficiency curves for O^-/CO (crosses) and $C_5H_5^-/C_5H_6$ (open circles). Energy scale for O^- shifted by −7.7 eV.

on the pressure of C_5H_6. Even if some experimental factors could partially account for that and if a different type of mechanism, such as Reaction (11) followed by Reaction (10), could be invoked,

$$e(5.3\ \text{eV})+C_5H_6\rightarrow C_5H_5+H+e(1.7\ \text{eV}), \qquad (11)$$

to justify the energy loss of 3.5 eV, the difference between the high and low pressure study has still to be satisfactorily explained.

The production of $C_5H_5^-$ at 9.3 eV has been reported in a previous paper.[9] Several other ions also have maxima at this energy, as Figs. 3 and 4 and Table I show, suggesting the multichannel dissociation of a common electronically excited molecular negative ion state,[53]

$$C_5H_6+e_{9.3\ \text{eV}}\rightarrow[C_5H_6^{-*}]\rightarrow C_5H_5^-, C_5H_4^-, \cdots. \qquad (12)$$

The relative intensities of the dissociative capture products so formed will then reflect the relative probabilities for the various dissociation channels.[54] Assuming that Reaction (12) accounts for the $C_5H_5^-$ current detected at 9.3 eV, then the following expression[48,55] may be used to calculate the disposition of the excess energy involved in the process

$$\bar{\epsilon}_t=E^*/\alpha N, \qquad (13)$$

where $\bar{\epsilon}_t$ is the total translational energy of the fragments, E^* is the total excess energy involved in the process, N is the number of harmonic oscillators in the parent ion, and α is an empirical correction factor which is 0.42 for dissociative capture processes. Thus, as the formation of $C_5H_5^-$ by Reaction (12) involves 7.6 eV of excess energy, we find that approximately 7 eV is proportioned to internal excitation of the $C_5H_5^-$ ion. As this is unacceptable, it may be tentatively suggested that $C_5H_5^-$ ion formation at 9.3 eV occurs as the result of a further energy loss collision, Reactions (9) and (10), or, alternatively, that the empirical correction factor used in Eq. (13) does not provide an adequate analysis of this particular system. Other than these suggestions, no further explanation can be forwarded.

$C_3H_3^-$

The $C_3H_3^-$ ionization efficiency curve exhibits only one resonance with a maximum at 8.7 eV. From the thermodynamic values reported in Table III, we can calculate the energy $\bar{E}$ to produce $C_3H_3^-$ along a reaction channel which requires the smallest supply of energy (14),

$$C_5H_6+e\rightarrow C_3H_3^-+C_2H_3. \qquad (14)$$

If we take $\Delta H_f(C_3H_3^-)=63$ kcal mole^{-1}, $\bar{E}\geq 95$ kcal, where the lower limit of 95 kcal would decrease if $\Delta H_f(C_3H_3^-)<63$ kcal mole^{-1}. Hence, at least 105 kcal of excess energy would be involved in Reaction (14) at an electron energy of 8.7 eV. About 10 kcal would be found as translational energy of the fragments and the remaining 95 kcal in the vibrational modes of the fragments. If we assume that the internal energy will distribute equally amongst the harmonic oscillators of $C_3H_3^-$ and C_2H_3, $C_3H_3^-$ and C_2H_3 would have 54 and 41 kcal mole^{-1}, respectively, of excess vibrational energy. Since the electron affinity of C_3H_3 has been estimated to be 53.8 kcal mole^{-1} [56] or higher than 10 kcal mole^{-1},[57] the amount of excess energy in the charged fragment could be sufficient to cause the electron to be ejected from the ion. Since the latter is formed with a reasonably large ionization cross section, it seems likely that processes where the neutral undergoes further fragmentation, rather than Reaction (14), would lead to the formation of $C_3H_3^{-1}$. The probable processes are:

$$C_5H_6+e\rightarrow C_3H_3^-+C_2H_2+H, \qquad (15)$$

$$C_5H_6+e\rightarrow C_3H_3^-+C_2H+H_2. \qquad (16)$$

C_2H^-, $C_5H_4^-$, $C_5H_3^-$, $C_3H_2^-$

These ions seem to arise from the unstable parent ion which may also generate $C_5H_5^-$ at the same electron energy.

The heat of formation of C_2H^- is too uncertain to be of help in deciding which processes lead to its production. This ion could be formed through Reaction (17),

$$C_5H_6+e\rightarrow C_2H^-+\text{neutrals}, \qquad (17)$$

where about 175–218 kcal are available to produce several combinations of neutrals. No estimate of the excess internal energy can be carried out.

We have observed that $C_5H_5^-$ is formed at 9.3 eV with a large amount of excess energy; the latter is probably sufficient to produce $C_5H_4^-$ and $C_5H_3^-$ by loss of hydrogen from $C_5H_5^-$. Alternatively, the electron impact on C_5H_6 could originate dissociative resonance capture processes in which the ions and hydrogen radicals would be obtained through the intermediate $C_5H_6^{-*}$. However, since no thermodynamic data are available on $C_5H_4^-$ and $C_5H_3^-$, there is no basis for a more detailed treatment of the subject.

Analogously, we have no information on $C_3H_2^-$. Reaction (18),

$$C_5H_6+e\rightarrow C_3H_2^-+C_2H_4, \qquad (18)$$

may account for its production, although we think that the excess internal energy would be quite high and further fragmentation should be expected.

Ion–Molecule Reactions

The occurrence of ion–molecule reactions was usually easily identified since the secondary ion exhibits an ionization curve which is identical to that of the

TABLE IV. Collision reactions in mixtures of C_5H_6.

Proton transfer: System	Proton transfer: Reactant	Electron energy (eV)	Reactant excess energy (kcal mole^{-1})	Reaction $X^-+C_5H_6\rightarrow C_5H_5^-+XH$		$\Delta H_f(C_5H_5^-)$ (kcal mole^{-1})
HCl/C_5H_6	Cl^-	0.8	Negligible	Unreactive	(19)	≥ -5
$(CN)_2/C_5H_6$	CN^-	5.4	~ 0 (See text)	Unreactive	(20)	≥ 17
H_2S/C_5H_6	SH^-	2.6	Negligible	Unreactive	(21)	≥ 18
H_2S/C_5H_6	S^-	~2.6	2	Unreactive	(22)	≥ 19
CS_2/C_5H_6	S^-	3.5	12	Unreactive (see text)	(23)	≥ 29
CO/C_5H_6	O^-	10.0	3	$O^-+C_5H_6\rightarrow C_5H_5^-+OH$	(24)	≤ 50
CO_2/C_5H_6	O^-	4.3	3	$O^-+C_5H_6\rightarrow C_5H_5^-+OH$	(25)	≤ 50
SO_2/C_5H_6	O^-	4.9	10	$O^-+C_5H_6\rightarrow C_5H_5^-+OH$	(26)	≤ 57
NH_3/C_5H_6	NH_2^-	5.6	30	$NH_2^-+C_5H_6\rightarrow C_5H_5^-+NH_3$	(27)	≤ 93

Proton+hydrogen transfer: System	Proton+hydrogen transfer: Reactant	Electron energy (eV)	Reactant excess energy (kcal mole^{-1})	Reaction $X^-+C_5H_6\rightarrow C_5H_4^-+H_2X$		$\Delta H_f(C_5H_4^-)$ (kcal mole^{-1})
H_2S/C_5H_6	S^-	~2.6	2	$S^-+C_5H_6\rightarrow C_5H_4^-+H_2S$	(28)	≤ 58
CO_2/C_5H_6	O^-	4.3	3	$O^-+C_5H_6\rightarrow C_5H_4^-+H_2O$	(29)	≤ 118
SO_2/C_5H_6	O^-	4.9	10	$O^-+C_5H_6\rightarrow C_5H_4^-+H_2O$	(30)	≤ 125

primary ion. A pressure study was always carried out to confirm the initial findings.

In Table IV the results of an investigation of proton transfer and proton plus hydrogen transfer reactions occurring in mixtures of C_5H_6 are reported. The electron energies listed in the third column correspond to the resonance peak maxima for reactant ion formation. The amount of reactant ion kinetic energy at the resonance peak maximum, calculated using Eq. (13) and given in the fourth column, was taken into account for the calculation of $\Delta H_f(C_5H_5^-)$.

Although Table IV is self-explanatory, Reactions (20) and (23) merit further comment. Initially, Reaction (20) contradicted the behavior predicted from the value for $\Delta H_f(C_5H_5^-)=19\pm2$ kcal mole^{-1} deduced above. The resonance peak maximum for CN^- ion formation from cyanogen was found to be at 5.4±0.1 eV, and, using Chupka's[58] thermochemical data for the nitrile radical, the excess energy associated with the dissociative capture process

$$(CN)_2+e\rightarrow CN^-+CN \qquad (31)$$

is calculated to be approximately 3.3 eV. Using Eq. (13), the translational energy of the CN^- ion is calculated to be 13 kcal mole^{-1}, and, since no reaction with C_5H_6 could be detected, a value of ≥ 31 kcal mole^{-1} is deduced for $\Delta H_f(C_5H_5^-)$. The substitution of alternative thermochemical data[58,59] for the nitrile radical resulted in equivalent values for $\Delta H_f(C_5H_5^-)$. A comparison of the CN^- ion mass peak at the resonance maximum with the mass peaks of O^-/CO and $C_5H_5^-/C_5H_6$ indicated that the nitrile ion is formed with little or no translational energy and as the total excess energy involved in Reaction (31), $E^*=3.3$ eV, is very close to the $B\ \Sigma_u^+$ state of CN at 3.2 eV,[60] the following dissociative capture process is suggested to replace (31) at 5.4±0.1 eV:

$$(CN)_2+e\rightarrow CN^-+CN(B\ \Sigma_u^+). \qquad (32)$$

In this, the CN^- ion is formed with practically zero kinetic energy, and failure to detect Reaction (20) indicates that $\Delta H_f(C_5H_5^-)\geq 17$ kcal mole^{-1}, in agreement with the value of 19±2 kcal mole^{-1} deduced above.

Failure to detect Reaction (23) also results in a lower limit for $\Delta H_f(C_5H_5^-)$ which is in disagreement with the value deduced above. The value of $\Delta H_f(C_5H_5^-)\geq$ 29 kcal mole^{-1} shown in Table IV is subject to several sources of uncertainty, primarily that associated with the thermochemical data used and the unknown limitations of Expression (13). These, coupled with the possibility that the cross section for Reaction (23) may be so low as to be below the instrumental sensitivity, are forwarded to explain this anomalous result.

TABLE V. Thermochemical data evaluated.

Parameter	kcal mole^{-1}	eV
$\Delta H_f(C_5H_5^-)$	19±2	0.82±0.1
$\Delta H_f(C_5H_5)$	$\leq$70±5	$\leq$3.0±0.2
$\Delta H_f(C_5H_5^+)$	$\leq$273±4	$\leq$11.8±0.2
E.A.(C_5H_5)	$\leq -51\pm7$	$\leq$2.2±0.3
$D(C_5H_5\text{–}H)$	$\leq$90±5	$\leq$3.9±0.2
$\Delta H_f(C_5H_4^-)$	$\leq$58	2.5
$\Delta H_f(C_5H_6^+)$	228	9.9
I.P.(C_5H_6)	196±2	8.5±0.1

Thus, with the possible exception of Reaction (23), the results obtained from the ion-molecule reaction studies shown in Table IV are in agreement with the value of $\Delta H_f(C_5H_5^-) = 19 \pm 2$ kcal mole^{-1} calculated from $C_5H_6^-$ ion formation. It is apparent from Reactions (20) to (22) that $\Delta H_f(C_5H_5^-)$ is not less than 17 kcal mole^{-1}, therefore adding further support for the assignment of a vertical onset to Reaction (4). If an appearance potential of 1.5 eV (see Fig. 7) had been chosen, an upper limit of 14.6 kcal mole^{-1} would have been imposed on $\Delta H_f(C_5H_5^-)$.

The three proton plus hydrogen transfer reactions listed in Table IV were observed resulting in an upper limit of 58 kcal mole^{-1} for $\Delta H_f(C_5H_4^-)$. The lack of any further thermochemical data for C_6H_4 precludes further conclusions.

The thermochemical data derived during the course of this study are tabulated in Table V.

ACKNOWLEDGMENTS

The authors wish to express their appreciation for the support of The Robert A. Welch Foundation.

---

[*] Current address: Laboratorii di Chimica, Istituto Superiore di Sanità, V. le Regina Elena 299, 00161 Roma, Italy.

[1] F. A. Cotton and G. Wilkinson, *Advanced Inorganic Chemistry* (Interscience, New York, 1967), 2nd ed., p. 761.

[2] A. G. Harrison, L. R. Honnen, H. J. Dauben, Jr., and F. P. Lossing, J. Am. Chem. Soc. **82**, 5593 (1960).

[3] R. F. Pottie and F. P. Lossing, J. Am. Chem. Soc. **85**, 269 (1963).

[4] F. Meyer and A. G. Harrison, Can. J. Chem. **42**, 2256 (1964).

[5] N. L. Allinger and J. C. Tai, J. Am. Chem. Soc. **87**, 2081 (1965).

[6] F. H. Dorman, J. Chem. Phys. **43**, 3507 (1965).

[7] A. Sadô, R. West, H. P. Fritz, and L. Schäfer, Spectrochim. Acta **22**, 509 (1966).

[8] (a) M. J. S. Dewar and S. D. Worley, J. Chem. Phys. **49**, 2454 (1968). (b) M. J. S. Dewar and S. D. Worley, J. Chem. Phys. **50**, 654 (1969).

[9] V. I. Khvostenko, I. I. Furlei, A. N. Kost, V. A. Budylin, and L. G. Yudin, Dokl. Akad. Nauk SSSR **189**, 817 (1969).

[10] B. O. Wagner and H. F. Ebel, Tetrahedron **26**, 5155 (1970).

[11] D. A. Demeo and M. A. El-Sayed, J. Chem. Phys. **52**, 2622 (1970).

[12] K. E. Blick, J. W. DeHaan, and K. Niedenzu, Spectrochim. Acta **26A**, 2319 (1970).

[13] P. J. Derrick, L. Åsbrink, O. Edqvist, B.-Ö. Jonsson, and E. Lindholm, Intern. J. Mass Spectry. Ion Phys. 6, 203 (1971).

[14] F. Combet-Farnoux and G. Berthier, Compt. Rend. **248**, 688 (1959).

[15] A. Streitwieser, Jr., J. Am. Chem. Soc. **82**, 4123 (1960).

[16] A. Mangini and C. Zauli, J. Chem. Soc. **1960**, 2210.

[17] S. Ehrenson, J. Phys. Chem. **66**, 706 (1962).

[18] R. Hoffmann, J. Chem. Phys. **39**, 1397 (1963).

[19] F. Billeš, Acta Chim. Acad. Sci. Hung. **56**, 131 (1968).

[20] J. Del Bene and H. H. Jaffé, J. Chem. Phys. **48**, 4050 (1968).

[21] H. Preuss and R. Janoschek, J. Mol. Struct. **3**, 423 (1969).

[22] P. S. O'Sullivan and H. F. Hameka, Chem. Phys. Letters **4**, 123 (1969).

[23] N. C. Baird and M. J. S. Dewar, J. Chem. Phys. **50**, 1262 (1969).

[24] L. Schäfer and H. H. Jensen, Acta Chem. Scand. **24**, 415 (1970).

[25] G. J. Schulz, J. Appl. Phys. **31**, 1134 (1960).

[26] L. G. Christophorou, R. N. Compton, G. S. Hurst, and P. W. Reinhardt, J. Chem. Phys. **43**, 4273 (1965).

[27] J. D. Morrison, J. Chem. Phys. **39**, 200 (1963).

[28] K. A. G. MacNeil and J. C. J. Thynne, Intern. J. Mass. Spectry. Ion Phys. **3**, 35 (1969).

[29] P. W. Harland and J. C. J. Thynne, J. Phys. Chem. **73**, 4031 (1969).

[30] P. W. Harland and J. C. J. Thynne, J. Phys. Chem. **74**, 52 (1970).

[31] K. A. G. MacNeil and J. C. J. Thynne, J. Phys. Chem. **74**, 2257 (1970).

[32] K. A. G. MacNeil and J. C. J. Thynne, Intern. J. Mass Spectry. Ion Phys. **3**, 455 (1970).

[33] K. A. G. MacNeil and J. C. J. Thynne, Intern. J. Mass Spectry. Ion Phys. **5**, 329 (1970).

[34] P. W. Harland and J. C. J. Thynne, Advan. Mass Spectry. 5, 493 (1971).

[35] K. Kraus, Z. Naturforsch. **16a**, 1378 (1961).

[36] P. J. Chantry, Phys. Rev. **172**, 125 (1968).

[37] H. D. Hagstrum, Rev. Mod. Phys. **23**, 185 (1951).

[38] G. G. Cloutier and H. I. Schiff, J. Chem. Phys. **31**, 793 (1959).

[39] A. di Domenico and J. L. Franklin, "Negative Ions in the Mass Spectrum of Nitromethane," Intern. J. Mass Spectry. Ion Phys. (to be published).

[40] W. M. Hickam and R. E. Fox, J. Chem. Phys. **25**, 642 (1956).

[41] L. G. Christophorou, R. N. Compton, and H. W. Dickson, J. Chem. Phys. **48**, 1949 (1968).

[42] T. E. Sharp and J. T. Dowell, J. Chem. Phys. **50**, 3024 (1969).

[43] R. N. Compton, J. A. D. Stockdale, and P. W. Reinhardt, Phys. Rev. **180**, 111 (1969).

[44] L. G. Christophorou and J. A. D. Stockdale, J. Chem. Phys. **48**, 1956 (1968).

[45] P. H. Krupenie, Natl. Std. Ref. Data Ser. Natl. Bur. Std. (U.S.) **5** (1966).

[46] J. L. Franklin, Y. Wada, P. Natalis, and P. M. Hierl, J. Phys. Chem. **70**, 2353 (1966).

[47] J. L. Franklin, P. M. Hierl, and D. A. Whan, J. Chem. Phys. **47**, 3148 (1967).

[48] A. di Domenico, D. K. Sen Sharma, J. L. Franklin, and J. G. Dillard, J. Chem. Phys. **54**, 4460 (1971).

[49] L. F. Fieser and M. Fieser, *Reagents for Organic Synthesis* (Wiley, New York, 1967), p.181.

[50] R. N. Compton and L. G. Christophorou, Phys. Rev. **154**, 110 (1967).

[51] C. E. Moore, Natl. Bur. Std. (U.S.) Circ. **467**, (1949).

[52] P. J. Chantry, J. Chem. Phys. **55**, 1851 (1971).

[53] F. H. Dorman, J. Chem. Phys. **44**, 3856 (1966).

[54] T. F. O'Malley, Phys. Rev. **150**, 14 (1956).

[55] J. J. DeCorpo, D. A. Bafus, and J. L. Franklin, J. Chem. Phys. **54**, 1952 (1971).

[56] F. M. Page and G. C. Goode, *Negative Ions and the Magnetron* (Wiley-Interscience, New York, 1969).

[57] D. K. Bohme and L. B. Young, J. Am. Chem. Soc. **92**, 3301 (1970).

[58] J. Berkowitz, W. A. Chupka, and T. A. Walter, J. Chem. Phys. **50**, 1497 (1969).

[59] F. M. Page, J. Chem. Phys. **49**, 2466 (1968).

[60] G. Herzberg, *Spectra of Diatomic Molecules* (Van Nostrand, Princeton, N.J., 1963), 2nd ed.

Reprinted from:
THE JOURNAL OF CHEMICAL PHYSICS VOLUME 58, NUMBER 4 15 FEBRUARY 1973

Use of translational energy measurements in the evaluation of the energetics for dissociative attachment processes

P. W. Harland, J. L. Franklin, and D. E. Carter
Department of Chemistry, Rice University, Houston, Texas 77001

(Received 2 October 1972)

The translational energies of negative ions formed by dissociative resonance capture processes from CO, NO, CO_2, and SO_2 have been measured as functions of excess energy. The sums of the translational energies of O^- and the corresponding neutral from CO and NO were found to be equal to the electron energy above onset over a range of about 1 eV. At higher energies, the translational energies dropped down from the expected values because of loss of the more energetic ions to the walls. With CO_2 and SO_2 the total translational energy was always E^*/N, where E^* is excess energy and N the number of vibrational modes, 3 in each case. The measurement of translational energy has also helped in interpreting the states involved in the various processes and in computing the ground state thermochemical properties of the decomposition products.

INTRODUCTION

An evaluation of the energetics of negative ion formation by dissociative electron capture processes [Eq. (1)] can provide a wealth of thermochemical information which would otherwise be difficult to obtain:

$$AB+e\rightarrow A^-+B. \qquad (1)$$

The quality of these data, however, depend not only on the experimental accuracy with which the ionization thresholds are determined but also on the scope of the measurements.

The potential energy surfaces describing the capture of electrons by the diatomic molecule, AB, are illustrated in Fig. 1. Following electron capture in the energy range E_a to E_b, a vertical (Franck–Condon) transition from the ground state of AB to the repulsive surface representing an electronically excited state of the molecular ion AB^- takes place. The transient intermediate species AB^{-*} then dissociates along the surface shown to form the negative ion A^- and the radical B, provided it does not undergo autodetachment reverting back to the ground or an excited state of the neutral molecule AB. The dissociation fragments thus formed will have distributed between them translational energy in the range E_1 to E_2 according to the principle of conservation of momentum. From Fig. 1 the energy balance equation

$$D(A\text{–}B)=A(A^-)+E(A)-EE \qquad (2)$$

is obtained where $D(A\text{–}B)$ is the dissociation energy of AB, $A(A^-)$ is the appearance potential for the dissociative resonance process, $E(A)$ is the electron affinity of the radical A and EE is the excess energy involved in the process at the threshold and encompasses electronic excitation of the fragmentation products, if any, and the translational energy distributed between them, i.e.,

$$EE=\epsilon_e+\epsilon_t. \qquad (3)$$

Without a knowledge of EE, Eq. (2) is written with an inequality sign:

$$D(A\text{–}B)\leq A(A^-)+E(A), \qquad (4)$$

and the thermochemical data so obtained will be only limiting values and, therefore, subject to unknown inaccuracy.

The form of Eq. (2) remains the same for a polyatomic molecule but EE must now account for vibrational and rotational partitioning of excess energy, also:

$$EE=\epsilon_e+\epsilon_v+\epsilon_r+\epsilon_t. \qquad (5)$$

The form of this partitioning is the subject of much discussion[1–3] and is essential if reliable thermochemical data are to be obtained from dissociative capture processes. A rough estimation of the energetics of such processes in the 0–10 eV energy range using the thermochemical data available in the literature will often be sufficient to determine if electronic excitation of fragmentation products is occurring. However, no approximate method can be used to obtain information regarding the vibrational or rotational excitation of such products as the fraction of excess energy surviving in these modes depends upon the potential energy surfaces of the activated complex which are unknown.

Lack of knowledge of potential energy surfaces has been circumvented in gas kinetics for many years by treating a complex molecule as a collection of simple harmonic oscillators. Rosenstock *et al.*[4] used this concept with the further assumption that the transfer of energy between the oscillators in the activated state is much faster than the dissociation into products (so that the oscillators achieve energy equilibrium) to successfully predict ionic-dissociation rate constants. In the application of this model to the calculation of translational energies, rotational excitation is neglected and it is assumed that the activated complex and the products have the same ground state energies. The calculation of the total translational energy $\bar{\epsilon}_t$ is then reduced to the problem of calculating the distribution of vibrational energy among a collection of oscillators whose total

EX BIBL. UNIV. EDINBURGH

energy is E^*. The probability that the system will have ϵ_v vibrational energy and total energy E^* is

$$P(E^*, \epsilon_v) = \rho(\epsilon_v)/W(E^*), \qquad (6)$$

where $\rho(\epsilon_v)$ is the density of states at ϵ_v and $W(E^*)$ is the total number of states with energy $\leq E^*$. Since $\epsilon_v = E^* - \epsilon_t$

$$P(E^*, \epsilon_t) = \rho(E^* - \epsilon_t)/W(E^*). \qquad (7)$$

For N classical oscillators,

$$W(E) = E^N/[\Gamma(N+1)\Pi h\nu_i], \qquad (8)$$

$$\rho(E) = dW/dE = NE^{N-1}/[\Gamma(N+1)\Pi h\nu_i]. \qquad (9)$$

For N oscillators in the molecular ion, there will be $N-1$ oscillators in the activated complex, giving

$$P(E^*, \epsilon_t) = (N-1)(E^* - \epsilon_t)^{N-2}/(E^*)^{N-1}. \qquad (10)$$

The average ϵ_t is calculated using

$$\bar{\epsilon}_t = \int_0^{E^*} \epsilon_t P(E^*, \epsilon_t) d\epsilon_t, \qquad (11)$$

which gives the classical result,

$$\bar{\epsilon}_t = E^*/N. \qquad (12)$$

Thus, for the diatomic molecule AB, $N=1$ and $\bar{\epsilon}_t = E^*$ and $\bar{\epsilon}_i = E^*(m_n/M)$ where $\bar{\epsilon}_i$ is the translational energy of the ionic fragment (A^-) in the center of mass, m_n is the mass of the neutral fragment (B), and M is the weight of the transition complex (molecular weight of AB).

Using the experimental data of Taubert[5] on positive ion fragmentation, Klots[1] found that the best agreement between theory and experiment resulted from a nonclassical counting of vibrational states in the transition complex. The classical predictions resulted in low values for $\bar{\epsilon}_t$. Therefore, only a fraction of the oscillators appear to be effective for the distribution of excess energy and more than one vibrational mode is converted into translational degrees of freedom. These conclusions were borne out by the experimental work of Haney and Franklin[2] who proposed the modified expression:

$$\bar{\epsilon}_t = E^*/\alpha N. \qquad (13)$$

Their study of positive ionization of polyatomic molecules suggested a value of $\alpha = 0.44$. A theoretical analysis of these data by Spotz, Seitz, and Franklin[3] concluded that $N-3$ rather than $N-1$ vibrational degrees of freedom are transferred into translation in the activated complex.

The translational energy of a negative ion produced in a dissociative capture process should therefore increase over the resonance according to Eq. (14) which takes the thermal motion of the target gas into consideration:

$$\bar{\epsilon}_i = (E^*/\alpha N)(m_n/M) + \tfrac{3}{2}RT(m_i/M). \qquad (14)$$

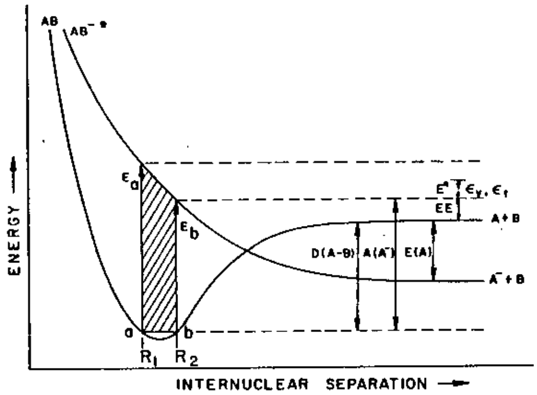

FIG. 1. Schematic representation of the energy surfaces involved in dissociative electron attachment to the diatomic molecule AB.

E^* is defined as the energy in excess of the ionization threshold and is given by

$$E^* = E_e - [D - E(A) + EE], \qquad (15)$$

where E_e is the nominal energy of the bombarding electrons, EE is the excess energy at the ionization threshold and E^* is the energy in excess of the threshold. For a diatomic molecule $\alpha = 1$ and $N = 1$ in Eq. (14) and for a polyatomic molecule α will be some value less than unity and $N = 3n - 6$.

The present study was carried out to (i) apply the method previously described by Franklin, Hierl, and Whan[6] for measuring translational energies in a time-of-flight mass spectrometer to negative ion processes previously examined by workers using specially constructed apparatus, (ii) to illustrate the importance of these measurements for the interpretation of dissociative capture processes and to find a value for α best fitting data obtained for triatomic molecules. Since in dissociative resonance capture processes the energy introduced with the electron remains in the molecular system, a study of the variation of translational energy of the fragment with internal energy before fragmentation will be of considerable interest in extending our understanding of molecular dynamics.

EXPERIMENTAL

The translational energies of the ions studied were measured using the method described by Franklin, Hierl, and Whan.[6] This method employs the effect of the translational energy distribution of the ions leaving the source chamber of a time-of-flight mass spectrometer on the width of the ion mass peak scanned at the detector. Initially, a calibration curve of mass peak full width at half maximum (FWHM) against the square root of the ionic weight (amu) is constructed. The

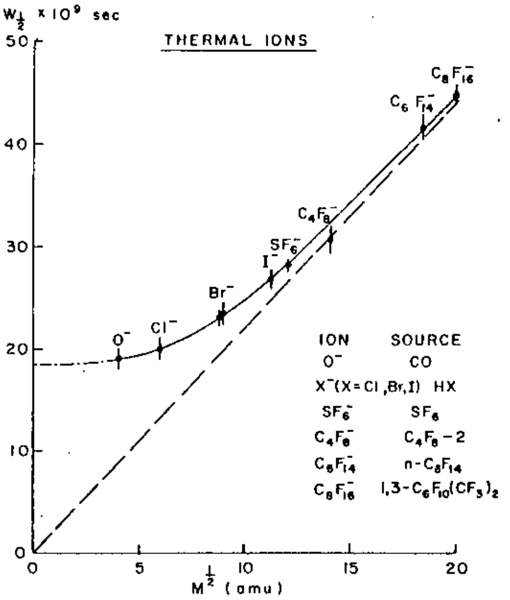

FIG. 2. Calculated and experimental peak widths (FWHM) for ions of known (i.e., thermal) energy. The dashed line represents the FWHM ($W_{1/2}$) calculated for an infinitely narrow gate pulse and an ion drawout pulse amplitude of 105 V. The intercept on the ordinate represents the effective width of the gate pulse.

FWHM of the ion mass peak under investigation is then used with the calibration curve to obtain an apparent ionic mass, m_{app}, for the translationally excited species. The translational energy of the ion in three-dimensions is then calculated from the expression[2]

$$\bar{\epsilon}_t = \tfrac{3}{2}RT[m_{app}/m_i]. \qquad (16)$$

The calibration curve obtained with a Bendix TOFMS Model 14-107 equipped with Model 3015 Output Scanners is shown in Fig. 2. This curve was taken using a low pressure source (gas pressures maintained below 1×10^{-5} torr). A separate calibration curve was constructed using a high pressure source (with gas pressures in the range 1×10^{-3} to 1×10^{-2} torr) and equivalent results were obtained with the two sources and their respective calibration curves. The ions used for these calibration curves were all formed as the result of associative (thermal) electron capture[7,8] or ions formed in dissociative capture processes which attain maximum cross section at the threshold[9,10] thereby resulting in fragments with zero, or thermal, translational energy at the threshold. Experiments performed with the ion lens switched on gave results in agreement with those obtained with the lens off within the experimental accuracy of the measurements.

Weinstein[11] has recently pointed out that the assumption of Gaussian peak shapes inherent in the Franklin, Hierl, and Whan method is valid only for thermal ions and that translational energies so measured may be in error by some 6%–24%. He further argues that these errors will be all negative. Franklin and Sen Sharma[12] have reproduced the earlier positive ion work of Haney and Franklin[2] using the deflection method of Taubert.[13] Their results qualitatively support Weinstein's conclusions but have found the agreement to be generally less than 10% in error for translational energies less than 9 kcal mole^{-1}. The translational energies so measured are therefore well within the experimental error incurred in appearance potential determinations (±0.1 eV).

The materials used in these experiments were all purchased from Matheson Gas Products and used with no additional purification.

RESULTS AND DISCUSSION

O^-/CO

Chantry[9] used a mass spectrometer equipped with a Wien filter arrangement to monitor the translational energy distribution of the O^- ions formed from CO and NO over their respective resonances. These experiments showed the O^- ion from CO to be formed with thermal energy at the ionization threshold, 9.7±0.1 eV, which corresponds to the minimum enthalpy requirement for process (17), i.e., 9.62 eV:

$$CO + e \rightarrow O^- + C(^3P). \qquad (17)$$

It was further concluded that the cross section for this process attains maximum at the threshold. This latter conclusion also follows from an examination of the unfolded ionization efficiency curve for this process when the onset edge exactly reflects the high energy part of the electron energy distribution.[13,14]

From Chantry's RPD work[9] and from the unfolded ionization efficiency curve,[13,14] it is evident that a second resonance is immersed in the tail of that corresponding to Process (17). The Wien filter was successful in resolving two peaks in the translational energy distribution at the ionization threshold for the second process, one peak corresponding to a thermal distribution due to Process (18) and the second peak corresponding to Process (17) where the excess energy above the threshold is distributed as translational energy between the products:

$$CO + e \rightarrow O^- + C^*(^1D). \qquad (18)$$

Figure 3 shows the experimental data obtained using the low pressure source in this present study. The theoretical increase in translational energy, calculated from Eq. (14), for Processes (17) and (18) are shown with arrows representing the theoretical ionization thresholds for these processes. The points shown are those averaged over several repeated determinations which show good agreement with the theoretical slope for Process (17) up to the second resonance where the experimental points break away.

Only the translational energy of the ion at the threshold is important for the calculation of thermochemical data (heats of formation, electron affinities and bond dissociation energies), although a knowledge of the translational energy over the resonance should also prove valuable in identifying processes involving the formation of neutral fragmentation products in electronically excited states. In this respect, Chantry's technique offers considerable advantage over the present method which measures average values for all the ions present.

In accord with Chantry's study, the ions are formed with thermal energy at the first ionization threshold. The falloff in the curve occurs close to the threshold for Process (18) and can be attributed to the influence of the thermal ions produced by this process on the ion peak shapes corresponding to the translationally excited ions produced by Process (17). Process (18) could thus have been inferred. It is evident from the points in Fig. 3 that the observed falloff does not accurately reflect the relative cross sections for these processes which is probably due to a combination of wall effects and the deviation of the mass peaks from a Gaussian distribution.

The major effect being observed is the collision of the energetic ions with the ionization chamber walls. Under ideal source conditions with an electron beam profile exactly reflecting the slit dimensions in the electron gun, an O^- ion formed with an average of 12 kcal mole^{-1} translational energy in three dimensions will have a velocity component in the flight tube axis of 1.25×10^5 cm/sec. An O^- ion with this energy can then travel 1.2 mm from the edge of a well-defined electron beam in the present apparatus (slitwidth 0.7 mm). Ions with energies in the high energy tail of the translational energy distribution formed in a divergent electron beam will then be capable of traveling much further. From the source dimensions of our apparatus (2.5 mm from beam center to backing plate in low pressure source and 2.0 mm in high pressure source), we consider that ions are being lost to the collision chamber walls through diffusion. Obviously, the greater the average translational energy, the greater will be the proportion lost to the walls with the result that the average translational energy will appear to rise at a slower rate and will eventually level off. Because the ions have further to travel in the low pressure source, this leveling should occur at higher energies as was found to be the case, i.e., ~11 kcal mole^{-1} for the high pressure source and ~18 kcal mole^{-1} for the low pressure source. This loss to the walls was proved by changing the ion residence time in the source when longer times resulted in broader mass peaks which attain a maximum width at lower translational energies.

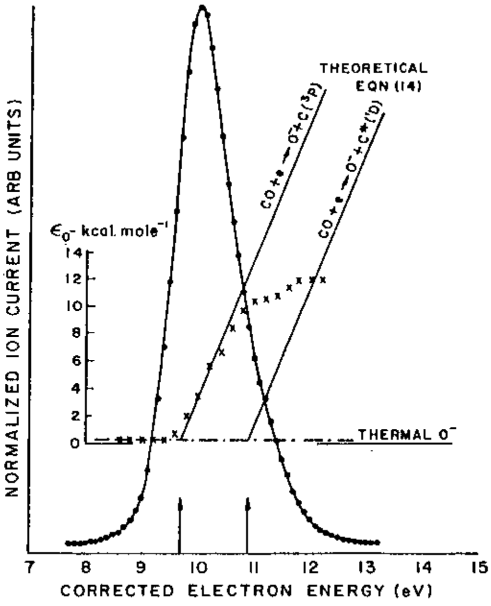

FIG. 3. Experimental ionization efficiency curve and translational energy data for O^-/CO measured using the low pressure ion source.

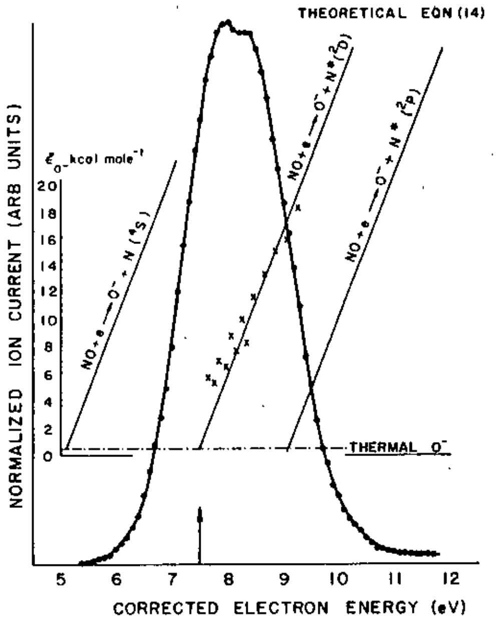

FIG. 4. Experimental ionization efficiency curve and translational energy date for O^-/NO measured using the low pressure ion source.

O^-/NO

The ionization efficiency curve and translational energy measurements for O^-/NO in the low pressure

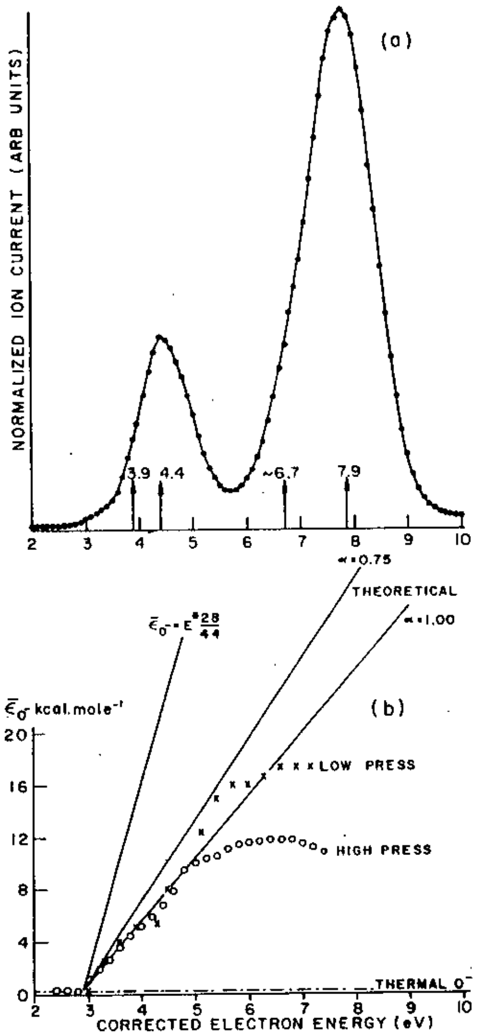

FIG. 5. Experimental data for O^-/CO_2; (a) ionization efficiency curve, (b) translational energy data.

source are shown together in Fig. 4. Again, there is good agreement between this data and that presented in Chantry's paper.[9] In this work, however, the low cross section for ion formation precluded measurements near the ionization threshold. From the theoretical slopes included in Fig. 4, only Process (19) is involved in ion formation:

$$NO+e\rightarrow O^-+N^*(^2D). \qquad (19)$$

The double resonance peak observed may thus be consistent with the occurrence of two separate states of NO^{-*} in the Franck–Condon region which both share the same dissociation limit.[9] As NO^- is isoelectronic with O_2, the electronic states may be quite similar and information available for O_2 [15,16] suggests that the intermediate molecular ion state may be $NO(B\ ^3\Sigma_u^-)$ corresponding to $O_2(B\ ^3\Sigma_u^-)$ which forms part of a band system at this energy.

There was no evidence for the occurrence of the process leading to formation of the nitrogen atom fragment in the ground state, $N(^4S)$, although this process is energetically feasible at about 5 eV. This suggests that the process would involve a forbidden transition from the intermediate NO^{-*} state at this energy. If NO^{-*} were in a singlet state, Process (20) would be forbidden and, hence, O^- would not be formed:

$$NO^-(^1\Sigma)\rightarrow O^-(^2P)+N(^4S). \qquad (20)$$

Alternatively, an appropriate triplet state might be formed at too low an energy to permit Process (20) to occur. NO^- is isoelectronic with O_2 which has a $^3\Sigma_u^+$ state at 4.5 eV and a $^3\Sigma_u^-$ state at 6.18 eV.[16] If in NO^- both of these states occurred at energies less than 5 eV, they would be incapable of decomposing by Process (20).

Noisy data in this particular series of experiments imposes extra limitations on the accuracy of the average points shown in Fig. 4. The translational energy points undoubtedly follow the path imposed by wall effects at the higher energies and the noisy peaks in this case precluded reliable measurements over the wings of the resonance. Thus, the points at the low and high energy ends in Fig. 4 are associated with large uncertainties.

O^-/CO_2

The ionization efficiency curve and translational energy measurements of O^- from CO_2 using the low (×) and high (○) pressure ion sources are shown in Figs. 5(a) and 5(b). Theoretical lines were calculated using Eq. (14) for $\alpha=1.00$ and $\alpha=0.75$. N was set equal to 3 as CO_2^{-*}, the activated complex involved in ion formation by Process (21), is bent with a bond angle of approximately 134° [17,18]:

$$CO_2+e\rightarrow[CO_2^{-*}]\rightarrow O^-(^2P)+CO(X\ ^1\Sigma^+). \qquad (21)$$

There are three pertinent features in Fig. 5(b); (i) the O^- ion is formed with thermal energy at the threshold, (ii) the data points fall along a line corresponding closely to $\alpha=1.00$ and (iii) the points deviate from the theoretical line at higher translational energies. The best straight line drawn through the data points in the linear section indicates the first ionization threshold to be at about 3.9 eV lending support to the earlier work reported by Kraus[19] and Schulz.[20] If the intermediate negative ion state involved is the $(^2\Pi_u)$ state of CO_2^- [18] then using a value of 1.465 eV for the electron affinity of the oxygen atom[21] and 5.45 eV for $D(OC\text{–}O)$,[22] the minimum enthalpy requirement for process (21) is calculated to be 3.99 eV, close to the observed peak maximum at 4.4±0.1 eV. Christophorou and Stockdale[23] have discussed the assignation of a vertical onset for this process and the calculated potential energy surfaces[18] and present experimental work lend support to this proposal. After normalization of the first O^-/CO_2 peak to that measured for O^-/CO, the onset edges are found to match perfectly (after an appropriate shift along the energy scale).

Schulz[20] also measured the translational energy of the O^- ions formed from CO_2 and found that his data points fitted a theoretical line of slope 28/44 (see Fig. 5), i.e., a line calculated without reference to vibrational energy partitioning.[1-4] A further feature observed by Schulz which was beyond the scope of this study (see section on O^-/CO) was the formation of thermal energy ions at the ionization threshold for the second resonance while the remaining points measured over the resonance followed the theoretical line calculated for the first process onsetting at ~3.9 eV. This result cannot be readily interpreted, as Process (22) has a minimum enthalpy requirement of ~12.0 eV and is therefore energetically unfavorable at these lower energies:

$$CO_2+e\rightarrow O^-+CO(a\ ^3\Pi). \qquad (22)$$

Assuming (21) is the only dissociative capture process occurring, these observations[20] necessitate that all the excess energy, ~2.8 eV, is absorbed as vibrational and rotational excitation of the CO which cannot be reconciled with the theory[1-4] discussed in the Introduction. The only explanation which can be forwarded to explain the discrepancies which exist between the theoretical lines followed by the two sets of experimental data is that the retarding method employed by Schulz yields only maximum translational energies compared to the average values reported in this work.

The data plotted in Fig. 5(b) show a best fit to the theoretical line calculated using $\alpha = 1.00$ as for diatomics. Taking consideration of Weinstein's[11] comments, however, α is possibly <1 and a future study of polyatomics may serve to deduce a more exact value for α.

Following Chantry's[9] argument for O^- ion formation from NO, the fact that the translational energy data points fall along the same line over the two separate resonances suggests the formation of two states of CO_2^{-*} in the Franck–Condon region which share the same dissociation limit. This is illustrated in Fig. 6. The difference in cross-sections reflects the stability of the activated intermediates involved, the probability for dissociative capture being smaller for the bound state associated with the first resonance. This representation is in qualitative agreement with the surfaces calculated by Claydon, Segal, and Taylor.[18]

Because of the smearing effect of the broad electron energy distribution (~1.0 eV) the translational energy appears to increase continuously across the two resonances. The inflection seen in the data points in the dip region was reproducible and undoubtedly a narrower electron energy distribution would result in far better energy resolution.

The flattening of the experimental points at high translational energies, ~11 kcal mole⁻¹ for the high pressure source and ~18 kcal mole⁻¹ for the low pressure source, has already been attributed to two experimental artifacts; (i) the theoretical analysis of the method by Weinstein[11] indicated that values lower than the real value are to be expected due to the basic assumption of Gaussian peak shapes. The ion mass peaks recorded during the course of these experiments were found to deviate from Gaussian as the translational energy increased. This anomaly, however, has been shown to result in values less than 10% in error[12] for translational energies less than about 9 kcal mole⁻¹ and (ii) the effect due to diffusion of the translationally excited species to the wall which is the major effect.

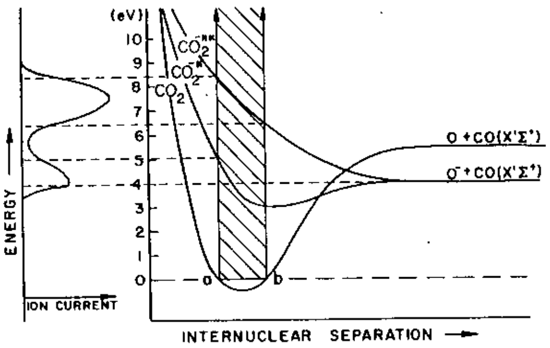

FIG. 6. Hypothetical potential energy surfaces representing O^- ion formation from CO_2 in the 0–10 eV energy range.

One further point of interest regarding Fig. 5 is that the first excited vibrational level in CO lies 6 kcal mole⁻¹ above the ground zero point and is therefore inaccessible until $E^*=9$ kcal mole⁻¹ (~0.4 eV). For thermal energy ions from CO_2 there is a population distribution of rotational states about $J=9$ and as the excitation energy is increased, with increasing E^*, a rotational quantum number of 32 is attained before vibrational excitation is possible. Rotational energy partitions cannot, therefore, be neglected in diatomic fragments where the vibrational energy span is large compared to the width of the dissociative capture resonance. A high resolution study of translational energy in this case may show an initial slope different to that predicted by Eq. (14) and determined by the competition between rotational and translational energy partitioning among the fragments.

O^-/SO_2

The ionization efficiency curve measured for O^- ion formation from SO_2 is shown in Fig. 7(a) and the translational energy data in 7(b). Following Fig. 5(b), theoretical lines with $N=3$ and $\alpha=1.00$ and 0.75 have been constructed with arrows indicating previously determined[24,25] onsets and maxima for these resonances.

The O^- ions are formed with thermal energy at the

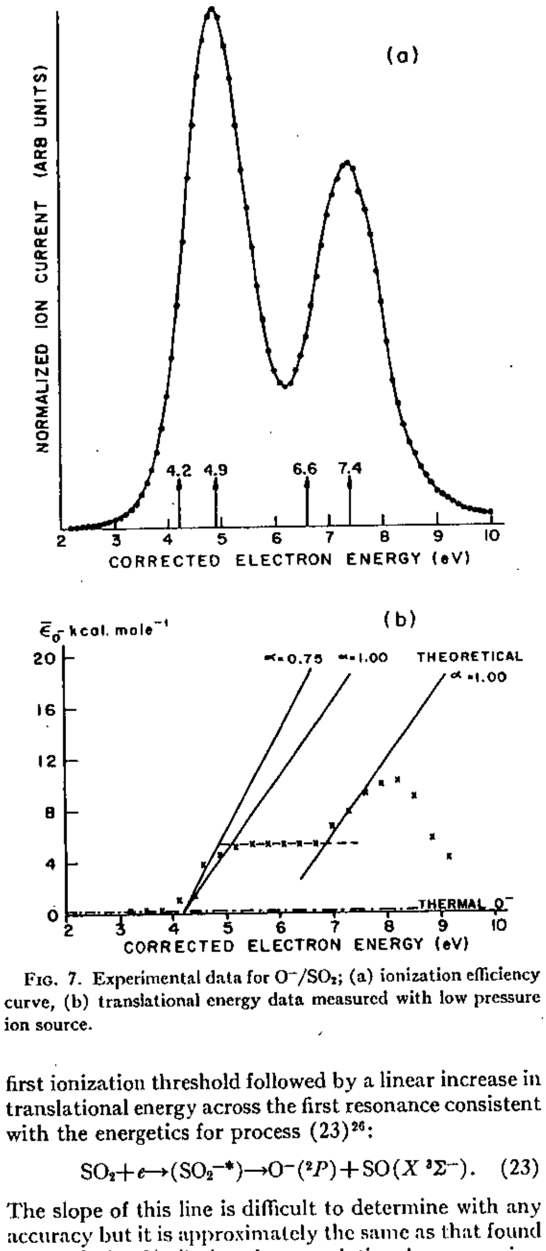

FIG. 7. Experimental data for O^-/SO_2; (a) ionization efficiency curve, (b) translational energy data measured with low pressure ion source.

first ionization threshold followed by a linear increase in translational energy across the first resonance consistent with the energetics for process (23)[26]:

$$SO_2+e\rightarrow(SO_2^{-*})\rightarrow O^-(^2P)+SO(X\,^3\Sigma^-). \quad (23)$$

The slope of this line is difficult to determine with any accuracy but it is approximately the same as that found for O^-/CO_2. Similarly, the translational energy rises linearly over the second resonance, the break in the curve indicating that the intermediate molecular negative ion states involved in the two resonances do not go to the same dissociation limit as was inferred for O^-/CO_2. Extrapolating the data points between the resonances to the theoretical line of slope 1.00 drawn through the data points measured over the second resonance results in a translational energy of 5.4 kcal mole^{-1} at the threshold. After subtracting the thermal contribution, the total translational energy shared between the O^- and SO fragments is given by $\bar{\epsilon}_t=\bar{\epsilon}_i M/m_n=6.9$ kcal mole^{-1} from which $E_{\mathrm{exptl}}^*=\bar{\epsilon}_t\cdot\alpha\cdot N=20.7$ kcal mole^{-1}. E_{calc}^*, the energy in excess of the minimum requirement for Process (23), is 2.4 eV resulting in a discrepancy of $E_{\mathrm{calc}}^*-E_{\mathrm{exptl}}^*=1.5$ eV. The following process is therefore suggested in light of this data:

$$SO_2+e\rightarrow(SO_2^{-**})\rightarrow O^-(^2P)+SO^*(a\,^1\Delta_g), \quad (24)$$

where the $(a\,^1\Delta_g)$ state of SO has not been reported previously.

The data in Table I, which are taken from Herzberg,[16] lend support to our conclusions.

Translational energy measurements over the trailing edge of the second resonance show a decrease in energy corresponding to the decay of the resonance. This falloff behavior was also observed although less intensely in the other cases discussed above.

A study of O^- from SO_2 reported recently by Rallis and Goodings[27] also included translational energy measurements. Following Schulz,[20] their data was found to fit a theoretical line of slope set equal to 48/64, although a best line drawn through their data points suggests that a line of lower gradient may be more

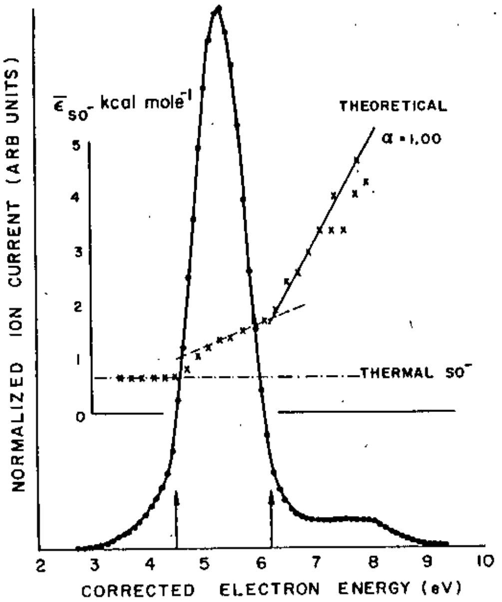

FIG. 8. Experimental ionization efficiency curve and translational energy data for SO^-/SO_2 measured using low pressure ion source.

appropriate. This still leaves a discrepancy between the magnitude of the translational energy measurements in the two studies. Consideration of Weinstein's comments[11] and assuming that the values reported by Rallis and Goodings[27] are maximum values will go only part way to explaining the differences found.

SO^-/SO_2

The ionization efficiency curve and translational energy data for SO^- ion formation from SO_2 are presented in Fig. 8. Extrapolation of the data points which are linear over the first resonance process (24) show that the SO^- ion is formed with approximately thermal energy (0.65 kcal mole^{-1}) at the threshold:

$$SO_2 + e \rightarrow SO^-(^2\Pi) + O(^3P), \qquad (25)$$

which is estimated to be 4.5 eV. This value is in agreement with the value found by MacNeil and Thynne[28] using Morrison's deconvolution procedure[29,30] to reduce the energy spread of the electron beam. Now, using Eq. (2) in conjunction with the (OS–O) bond dissociation energy (given as 5.6 eV by Herzberg[22]), a value of 1.1 eV is deduced for the electron affinity of the SO radical in good agreement with the photodetachment value of 1.09 eV reported by Feldmann.[31]

A second, low cross section, resonance on the tail of the first resonance has been reported previously by MacNeil and Thynne.[28] Figure 8 shows an inflection in the translational energy curve between the two resonances followed by a linear increase in translational energy over the second resonance. The leveling of the points over the first resonance may be due to the influence of low energy ions produced in the second process. As $E_{\mathrm{calc}}^* \simeq 6.2 - 4.5 \simeq 1.7$ eV and the ions are formed with near thermal energy at the second ionization threshold, the following process is tentatively proposed:

$$SO_2 + e \rightarrow (SO_2^{-**}) \rightarrow SO^-(^2\Pi) + O^*(^1D), \qquad (26)$$

where the (^1D) state of the oxygen atom lies 1.96 eV above the ground state.

TABLE I. Established electronic states for O_2, SO, and S_2.

Molecule	State and energy (eV)		
O_2	$(a\,^1\Delta_g)$ 0.982	$(b\,^1\Sigma_g^+)$ 1.635	$(A\,^3\Sigma_u^+)$ 4.474
SO	···	···	$(B\,^3\Sigma^+)$ 4.88
S_2	Band system 1.52–1.78		$(B\,^3\Sigma_u^-)$ 3.94

ACKNOWLEDGMENTS

The authors wish to thank Dr. J. Ling-Fai Wang for helpful suggestions and to express their appreciation for the support of the Robert A. Welch Foundation.

[1] C. E. Klots, J. Chem. Phys. **41**, 117 (1964).

[2] M. A. Haney and J. L. Franklin, J. Chem. Phys. **48**, 4093 (1968).

[3] E. L. Spotz, W. A. Seitz, and J. L. Franklin, J. Chem. Phys. **51**, 5142 (1969).

[4] H. M. Rosenstock, M. B. Wallenstein. A. L. Wahrhaftig and H. Eyring, Proc. Natl. Acad. Sci. U.S. **38**, 677 (1952); H. M. Rosenstock and M. Krauss, *Mass Spectrometry of Organic Ions*, edited by F. W. McLafferty (Academic, New York, 1963), pp. 2–64.

[5] R. Taubert, Z. Naturforschg. **19**, 911 (1964).

[6] J. L. Franklin, P. M. Hierl, and D. A. Whan, J. Chem. Phys. **47**, 3148 (1967).

[7] W. T. Naff, C. D. Cooper, and R. N. Compton, J. Chem. Phys. **49**, 2784 (1968).

[8] P. W. Harland and J. C. J. Thynne (unpublished).

[9] P. J. Chantry, Phys. Rev. **172**, 125 (1968).

[10] L. G. Christophorou, R. N. Compton, and H. W. Dickson, J. Chem. Phys. **48**, 1949 (1968).

[11] N. D. Weinstein, J. Chem. Phys. **58**, 408 (1973).

[12] J. L. Franklin and D. K. Sen Sharma, J. Chem. Phys. (to be published).

[13] K. A. G. MacNeil and J. C. J. Thynne, Int. J. Mass Spectrom. Ion Phys. **3**, 455 (1970).

[14] A. di Domenico, P. W. Harland, and J. L. Franklin, J. Chem. Phys. **56**, 5299 (1972).

[15] F. R. Gilmore, U.S. Air Force Project Rand Memo. RM-4034-1-PR, April 1966.

[16] G. Herzberg, *Spectra of Diatomic Molecules* (Van Nostrand, Princeton, N.J., 1950).

[17] M. Krauss and D. Neumann, Chem. Phys. Letters **14**, 26 (1972).

[18] C. R. Claydon, G. A. Segal, and H. S. Taylor, J. Chem. Phys. **52**, 3387 (1970).

[19] K. Kraus, Z. Naturforsch. **16**, 1378 (1961).

[20] G. J. Schulz, Phys. Rev. **128**, 178 (1962).

[21] L. M. Branscombe, D. S. Burch, S. J. Smith, and S. Geltman, Phys. Rev. **111**, 504 (1958).

[22] G. Herzberg, *Electronic Spectra of Polyatomic Molecules* (Van Nostrand, Princeton, N.J., 1966).

[23] L. G. Christophorou and J. A. D. Stockdale, J. Chem. Phys. **48**, 1959 (1968).

[24] P. W. Harland and J. C. J. Thynne, J. Phys. Chem. **74**, 52 (1970).

[25] K. Krauss, Z. Naturforsch. **16**, 1378 (1961).

[26] J. L. Franklin, J. G. Dillard, H. M. Rosenstock, J. T. Herron, K. Draxl, and F. H. Field, NSRDS NBS **26** (1969).

[27] D. A. Rallis and J. M. Goodings, Can. J. Chem. **49**, 1571 (1971).

[28] K. A. G. MacNeil, Ph.D. thesis, Edinburgh University, 1969.

[29] J. D. Morrison, J. Chem. Phys. **39**, 200 (1963).

[30] K. A. G. MacNeil and J. C. J. Thynne, Int. J. Mass Spectrom. Ion Phys. **3**, 35 (1969).

[31] D. Feldmann, Z. Naturforsch. **25**, 621 (1970).

HIGH TEMPERATURE SCIENCE 5, 25–33 (1973)

High Temperature Negative Ions: Gaseous Group III Fluorides

FREDERICK PETTY,* J. LING-FAI WANG, R. P. STEIGER, P. W. HARLAND,
J. L. FRANKLIN, AND J. L. MARGRAVE

Department of Chemistry, Rice University, Houston, Texas 77001

Received May 9, 1972

Solid AlF_3, GaF_3, InF_3 and TlF were vaporized from a Knudsen cell into the source of a time-of-flight mass spectrometer in order to study their negative ions in the gas phase. Species observed include F^- from all four compounds, and AlF_2^-, GaF_2^-, InF_2^-, TlF_4^- and TlF_5^-, respectively. Appearance potentials of these ions were determined and measurements made of the excess kinetic energy of the ions produced by dissociative electron attachment in order to estimate values for the electron affinities of the corresponding neutral species.

INTRODUCTION

Collision of a low energy (0–15 eV) electron with a neutral molecule will frequently produce negatively charged fragment ions through the process of dissociative electron attachment. This process is illustrated in Fig. 1 for the archetypal molecule AB, whose potential energy curve describes a bound state and which on electron attachment undergoes a Franck-Condon transition to the repulsive curve of AB^- which subsequently dissociates to A and B^-. Consideration of the energetics involved leads to the equation

$$\begin{aligned} EA(B) &= D(A-B) - AP(B^-) + E^* \\ &= \Delta H_f(A) + \Delta H_f(B) - \Delta H_f(AB) - AP(B^-) + E^* \qquad (1) \end{aligned}$$

where $EA(B)$ is the electron affinity of the neutral fragment B, $D(A-B)$ is the dissociation energy of the molecule AB, $AP(B^-)$ is the appearance potential of the ion B^-, E^* is the excess energy of the process at threshold, and ΔH_f is the heat of formation of the indicated species. Obviously, determination of electron affinity by electron impact methods without knowledge of this excess energy will yield only a lower limit for this parameter. Since the excess energy may be distributed among translational, vibrational, rotational, and electronic degrees of freedom of the dissociation products, its exact experimental measurement is difficult indeed.

It has been shown, however, that there is a correlation between the excess energy of dissociative electron attachment E^* and the translational energy of the product ion (*1*, *2*) the latter quantity being far more amenable to experimental measurement. By measuring the width of the ion's mass peak at half maximum at the onset for its formation, it is possible to obtain in a simple manner the ion's translational energy,

---

* Present address: Brain Research Institute, University of Tennessee, Medical Units, Memphis, Tennessee 38103.

Copyright © 1973 by Academic Press, Inc.
All rights of reproduction in any form reserved.

and using considerations of momentum conservation, to compute the total translational energy of the dissociation products, E_t. This may then be used in Eq. (2) to calculate the total excess energy E^*,

$$E^* = E_t \alpha N \tag{2}$$

where α is a constant (0.42 for dissociative resonance capture), and N is the number of vibrational degrees of freedom of the molecule.

The excess energy E^* thus obtained may then be used in Eq. (1), along with the appearance potential experimentally obtained, to determine the electron affinity, bond dissociation energy, or heat of formation of the species under consideration.

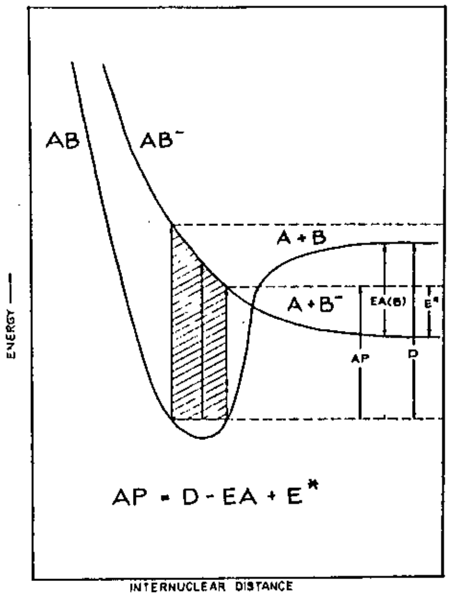

FIG. 1. Potential energy diagram illustrating a possible dissociative resonance capture process.

The fluorides of the Group III metals were chosen for investigation as likely candidates for the formation of negative ions from electron attachment to their gas phase molecules. As part of a continuing program of investigation of high temperature negative ions, it was hoped to achieve some understanding of the energetics of decomposition of such species as well as some idea of their relative efficiencies as electron scavengers.

EXPERIMENTAL

A Bendix time-of-flight mass spectrometer, Model 14-107, modified with a Bendix Model 3015 output scanner was used for these investigations (Fig. 2). Neutral molecules were generated by a Bendix Knudsen Cell Sample Inlet System, with a tantalum cell/Lucalox liner holding the solid sample for heating by a tungsten wire filament through either radiation or electron bombardment. The temperature of the cell was determined with a tungsten/tungsten–26% rhenium thermocouple inserted in the base of the cell. Appearance potentials were determined by deconvolution of the ion intensities with the MacNeil–Thynne modification (*3*) of Morrison's method (*4*). The electron energy scale was calibrated with O^-/SO_2, O^-/CO_2, O^-/CO and F^-/SF_6, and the energy distribution of ionizing electrons was determined from SF_6^-/SF_6 to be approximately 0.8 eV full width at half maximum.

For each of the systems investigated the sample was thoroughly degassed and then the temperature of the Knudsen cell was increased slowly until shutterable negative ions were first observed. The temperature was then raised until an ion intensity was achieved adequate for the determination of the appearance potentials and, where possible, the translational energies of the ions.

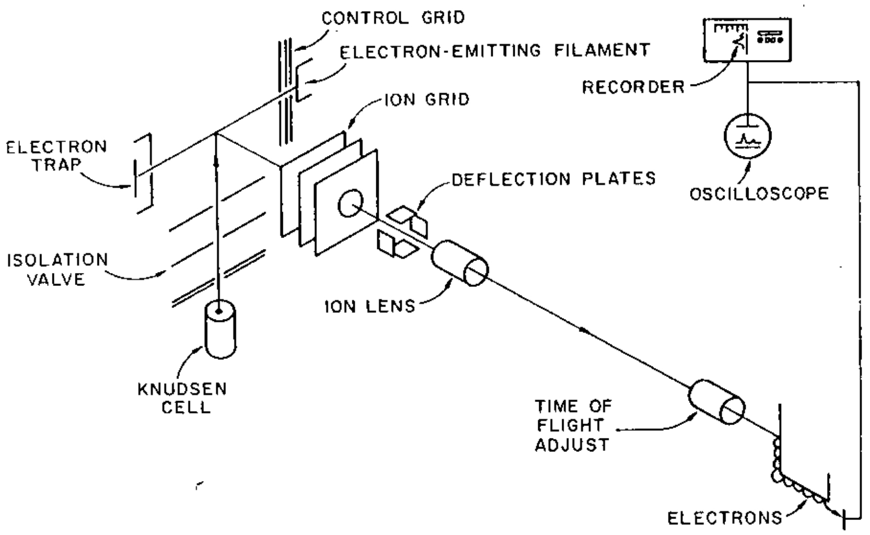

FIG. 2. Schematic diagram of a time-of-flight mass spectrometer fitted with Knudsen cell.

RESULTS AND DISCUSSION

Table 1 and Figs. 3–6 present the results of our investigations. Several features merit comment. None of the systems we studied produced F_2^-, although this ion is formed by the analogous BF_3. The fact that several of the ion peaks are so broad in energy is probably an indication that the potential energy curves in the Franck-Condon region pertinent to molecular dissociation are relatively "flat."

AlF_3, GaF_3, InF_3

Aluminum trifluoride has been shown to be monomeric in the gas phase (*5*), and it seems reasonable to assume that gallium and indium trifluoride behave in the same way since all three molecules produce similar ions by low energy electron attachment. Relative intensities of AlF_2^- were about ten times stronger than F^- from AlF_3; both GaF_3 and InF_3, however, generate about ten times as much F^- as they do the corresponding MF_2^- ion.

TABLE 1

SUMMARY OF EXPERIMENTAL RESULTS

Process	AP (eV)	Res. max. (eV)	E_t (kcal) at onset	E^* (kcal)
$AlF_3 + e^- \rightarrow F^- + AlF_2$	7.9	8.6	25.2	63.4
$T = 1268K$				
$AlF_3 + e^- \rightarrow AlF_2^- + F$	7.2	8.3	15.4	38.9
$GaF_3 + e^- \rightarrow F^- + GaF_2$	6.5	7.9	24.1	60.6
$T = 1143K$				
$GaF_3 + e^- \rightarrow GaF_2^- + F$	6.0	7.5		
$InF_3 + e^- \rightarrow F^- + InF_2$	3.7	7.4	24.4	61.6
$T = 1443K$				
$InF_3 + e^- \rightarrow InF_2^- + F$	1.9	6.0		
$TlF(s)$ $T = 843K$				
$+ e^- \rightarrow F^-$	5.6	9.6		
$+ e^- \rightarrow TlF_5^-$	0.0	1.2		
$+ e^- \rightarrow TlF_4^-$	5.4	9.0		
$Tl_2F_6 + e \rightarrow F^- + Tl_2F_5$			21.7	164
$Tl_2F_6 + e \rightarrow TlF_5^- + TlF$			0.0	0.0

Consideration of the energetics of the process of fluoride ion production (Table 2) reveals that the measured excess energies computed from translational energies are too low to balance the equation

$$\Delta H_f(MF_3) = \Delta H_f(F) + \Delta H_f(MF_2) - EA(F) + E^*_{\text{total}} - AP(F^-). \quad (3)$$

Note, for example, the values for AlF_3:

$$-288 = +19 - 165 - 84 + 63(E^*_{vt}) - 182.$$

However, if the decomposition is assumed to proceed according to the equation

$$AlF_3 + e \rightarrow AlF + F + F^- \quad (4)$$

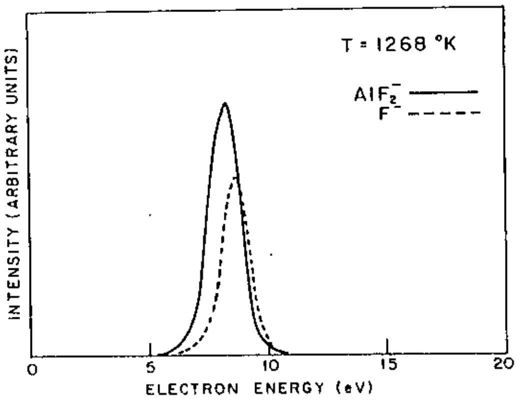

FIG. 3. Dissociative resonance capture curves for AlF_3.

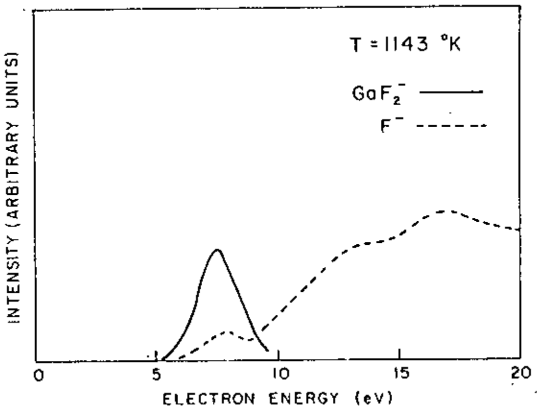

FIG. 4. Dissociative resonance capture curves for GaF_3.

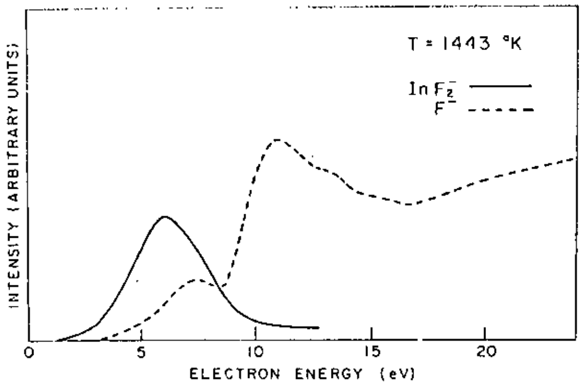

FIG. 5. Dissociative resonance capture curves for InF_3.

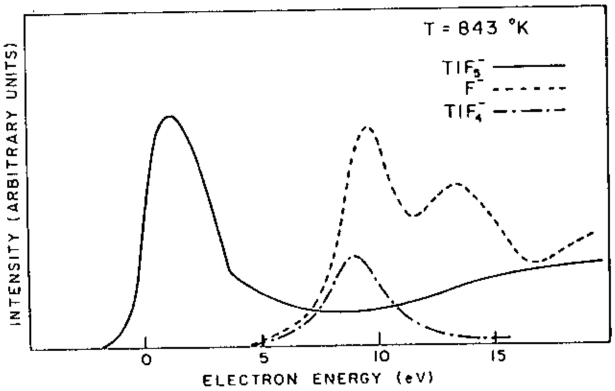

FIG. 6. Resonance capture curves for thallium fluoride.

the appearance potential is found to be just sufficient to provide the heat of reaction without any excess energy. But, the translational energy of the F^- ion alone was found to be 19 kcal/mole and, hence, fragmentation according to Eq. (4) is not possible. Fragmentation to give either $Al + F_2$ or $Al + 2\,F$ as the neutral species would be quite endothermic and, hence, would not occur at the measured appearance potential. If we assume then that the total excess energy is correctly given by Eq. (2), we must conclude that the neutral AlF_2 contains excess energy other than vibrational. It is reasonable to infer that this additional excess energy (61 kcal/mole for AlF_2) is electronic. A similar conclusion was reached by DeCorpo *et al.* (*1*) in considering the formation of F^- from BF_3 by dissociative resonance capture. Although the results are somewhat less definite, similar conclusions are obtained with the F^- ion from GaF_2 and, making reasonable assumptions as to its thermochemical properties, with InF_3. It thus appears to be a general property of the fluorides of boron, aluminum, gallium and indium that F^- formed from them by dissociative electron capture occurs with simultaneous formation of MF_2 that is excited both electronically and vibrationally.

TABLE 2

$MF_3 \rightarrow F^- + MF_2^*$ (all energies in kcal/mole)

M	AP	E^*_{vt}	E^*_{el}	$\Delta H_f(MF_2)$
B	243	47	115	−131
Al	182	63	61	−165
Ga	150	61	65	-130^a
In	85	62	50	-112^a

[a] Estimated—see text.

The results obtained from this process for the various Group III fluorides are given in Table 2. In order to make these calculations for the gallium and indium fluorides, certain approximations have been necessary since several key thermochemical values have not been determined. In the case of gallium fluoride, values for $\Delta H_f(GaF_3)$ and $\Delta H_f(GaF)$ are known (see Table 4). From these and the known heat of formation of F, we compute the energy required to remove two F atoms from GaF_3. Assuming the strength of the two first and second bonds to be proportional to the comparable bonds in AlF_3, we compute the approximate value of $\Delta H_f(GaF_2)$ to be −130 kcal/mole. Since the heats of formation of only InF and In have been determined, it has been

TABLE 3

$MF_3 \rightarrow MF_2^- + F$ (all energies in kcal/mole)

M	AP	E^*	$\Delta H_f(MF_2^-)$	$EA(MF_2)$
B	175^a	30^b	−146	15
Al	166	39	−180	15
Ga	138	39^c	−139	9
In	44	0	−125	13

[a] Ref. 7.

[b] Estimated.

[c] Assumed to be same as for AlF_2^- from AlF_3.

necessary to make considerably more tenuous estimations of thermochemical properties of InF_3 and InF_2. By plotting known heats of formation of Group III fluorides and chlorides, $\Delta H_f(InF_3)_g$ was estimated to be -150 kcal/mole. From this, $D(InF_2\text{–}F)$ was estimated to be 88 kcal/mole from heats of atomization. This leads to an estimated $\Delta H_f(InF_2)$ of -112 kcal/mole. From these values we can then estimate the electronic excitation energy in the formation of GaF_2 and InF_2. The results are given in Table 2.

TABLE 4

THERMOCHEMICAL VALUES EMPLOYED

	ΔH_f, kcal/mole	Ref.
AlF_3	-287.9	*8*
AlF_2	-159	*9*
	-165 ± 30	*10*
	-180	*11*
AlF	-61.7	*8*
Al	78	*8*
GaF_3	-278^a	*8*
	$-219.2^{b,c}$	*12*
GaF	-60.2	*8*
Ga	66.2	*8*
InF	-48.6	*8*
In	58.15	*8*
TlF	-43.6	*8*
Tl	43.55	*8*
F	18.88	*8*
F^-	-64.7	*8*

[a] The enthalpy of formation of solid GaF_3.

[b] The enthalpy of sublimation of monomeric GaF_3 at 298K is 58.8 Kcal/mole.

[c] Calculated enthalpy of formation of gaseous GaF_3 from (*a*) and (*b*).

Processes leading to the formation of the ion MF_2^- are summarized in Table 3, along with the data of MacNeil and Thynne (*3*) on BF_2^-. Unfortunately, the intensities of the ions GaF_2^- and InF_2^- were so low as to preclude determination of their translational energy. However, since the translational energy of F^- from both AlF_3 and GaF_3 is practically identical, it seems reasonable to estimate a translational energy of 31 kcal/mole for the GaF_2^- ion. When the appropriate values for appearance potential and excess energy are substituted into Eq. (1), we obtain the listed values for the heats of formation of the negative ions and, thus, their electron affinities. These electron affinities are all relatively and consistently low (0.4–0.6 eV).

TlF

TlF produces negative ions quite different in nature from those of the other Group III fluorides, namely, TlF_5^-, TlF_4^-, and the ubiquitous F^- (Fig. 6). Positive ion mass spectrometry has established the existence of dimeric neutral species in the gas phase produced by vaporization of TlF(s) (*6*). Keneshea and Cubiciotti (*6*) reported observing intense $Tl_2F_2^+$ and Tl_2F^+ peaks and very weak peaks for $Tl_2F_3^+$ and $Tl_2F_4^+$. We were able to observe $Tl_2F_2^+$ and Tl_2F^+ peaks of moderate intensity with an appearance potential around 10 eV. It thus seems reasonable to assume that certain of the negative ions we observed were produced from a gas phase dimer, probably Tl_2F_6. An exception is TlF_5^- which is discussed below. The appearance potentials we obtained were 0.0 eV (TlF_5^-), 5.4 eV (TlF_4^-), and 5.6 eV (F^-), with peak maxima at 1.2 eV, 9.0 eV, and 9.6 eV, respectively. The relative intensities of these ions is interesting: $TlF_5^- : TlF_4^- : F^- = 1000:6:26$.

The appearance potential of 0 eV for TlF_5^- suggests a dissociative resonance capture process, possibly

$$Tl_2F_6 + e \rightarrow TlF_5^- + TlF \tag{5}$$

However, the fact that TlF_5^- is formed with only thermal energy requires that the heats of formation of the two products exactly balance that of the reactants. While this would no doubt be possible, it would involve a surprising coincidence. Alternatively, the observed appearance potential and translational energy are just what would be expected of simple electron attachment. Quite similar behavior is observed, for example, in the attachment of electrons to SF_6. However, if TlF_5^- occurs by electron attachment, we must accept the existence of TlF_5 neutral, which would have to be present in large amounts to account for the large ion intensities observed. TlF_5 would be a quite surprising molecule and could only be considered as demonstrated if independent confirming evidence were available. We are thus unable to account for the origin of TlF_5^-. The precursor of TlF_4^- is even more uncertain. If TlF_5 exists, TlF_4^- might be formed from it, as indeed, F^- might be also. On the other hand, since Tl_2F_6 is known to occur in considerable abundance, it is not unreasonable to assume that TlF_4^- and F^- come from it. In any event, the near coincidence of the onset and resonance maxima for these two ions strongly suggests that they arise from the same excited state of a common precursor. Taking this to be Tl_2F_6, we compute for the reaction

$$Tl_2F_6 \rightarrow F^- + Tl_2F_5 \tag{6}$$

a bond dissociation energy of 45 kcal/mole, using the appearance potential and translational energy given in Table 1. The result is, of course, speculative. The intensity of TlF_4^- was too small to permit the measurement of translational energy. Since the reaction involves considerable rearrangement if the precursor is Tl_2F_6, we can draw no reasonable conclusions as to its heat of formation.

CONCLUSION

Our work has shown electron impact dissociative ionization to be a novel and useful technique, when combined with measurement of translational energies of product ions, for the measurement of electron affinities that might otherwise be difficult to obtain. The method is not suited to determination of electron affinities if one of the products is electronically excited, unless the electronic excitation energy is known. The need for further work on the TlF system has been shown.

ACKNOWLEDGMENT

The authors are pleased to acknowledge the support of this work by the Office of Naval Research, U.S. Navy, under Contract No. 67-A-0145-0002.

REFERENCES

1. DeCorpo, J. J., Bafus, D. A., and Franklin, J. L., *J. Chem. Phys.* **54**, 1592 (1971).
2. DeCorpo, J. J. and Franklin, J. L., *J. Chem. Phys.* **54**, 1885 (1971).
3. MacNeil, K. A. G. and Thynne, J. C. J., *Int. J. Mass Spectrom. Ion Phys.* **3**, 35 (1969).
4. Morrison, J. D., *J. Chem. Phys.* **39**, 200 (1963).
5. Porter, R. N. and Zeller, E. E., *J. Chem. Phys.* **33**, 858 (1960).
6. Keneshea, F. J. and Cubicciotti, D., *J. Phys. Chem.* **69**, 3910 (1965).
7. MacNeil, K. A. G. and Thynne, J. C. J., *J. Phys. Chem.* **74**, 2257 (1970).
8. Wagman, D. D., Evans, W. H., Parker, V. B., Halow, J., Bailey, S. M., and Schum, R. H., "Selected Values of Chemical Thermodynamic Properties," NBS 270-3 (1969).
9. Hildebrand, D. L., *Adv. High Temp. Chem.* **1**, 193 (1967).
10. JANAF Tables.
11. Farber, M. and Harris, S. P., *High Temp. Sci.* **3**, 231 (1971).
12. Feather, D. H., Büchler, A., and Searcy, A. W., *High Temp. Sci.* **4**, 290 (1972).

Partitioning of excess energy in dissociative resonance capture processes

P. W. Harland* and J. L. Franklin

Department of Chemistry, Rice University, Houston, Texas 77001

(Received 9 July 1973)

The translational energies of selected negative ions formed by dissociative resonance capture processes from the polyatomic systems NF_3, BF_3, CF_4, C_2F_6, C_3F_8, and c-C_4F_8 have been measured as functions of excess energy over the resonances. The excess energy in the molecular negative ion intermediate prior to dissociation has been calculated and partitioned into translational, vibrational, and, in some cases, electronic excitation of the dissociation products. The degree of vibrational activation in the intermediate state before dissociation is found to depend on the particular molecule under investigation and to vary from one dissociation channel to another. These observations are discussed in relation to theoretical concepts of dissociative resonance capture and given a qualitative explanation. The measurement of translational energy has led to a more complete interpretation of the states involved in the various processes and in computing ground state thermochemical properties of the decomposition products.

INTRODUCTION

When an electron is captured by a molecule the excess kinetic energy of the electron is distributed among the internal degrees of freedom of the transient molecular negative ion species produced which then decomposes by competitive autodetachment and various allowed dissociative capture channels. This study is concerned with the distribution of the excess energy in the intermediate molecular negative ion state and how it is partitioned among the dissociative capture fragments.

This study follows an earlier investigation[1] of the diatomic systems CO and NO in which the sums of the translational energies of the ions and the corresponding neutrals were found to be equal to the excess energy above threshold and the triatomic systems CO_2 and SO_2 for which this was not the case. At higher energies, the measurement of translational energies was impaired because of ion loss to the ionization chamber walls. This complementary study of the polyatomic systems NF_3, BF_3, CF_4, C_2F_6, C_3F_8, and c-C_4F_8 has been carried out using an enlarged ionization chamber which precluded the effects of ion loss to the walls. A discussion of the limiting instrumental and analytical factors inherent in the techniques employed will be presented in the Conclusion.

If it is assumed that energy is rapidly distributed among vibrational modes and if the average energy in the reaction coordinate is taken as the translational energy, a classical counting of vibrational states in the molecular negative ion intermediate results in the expression[1]

$$\bar{\epsilon}_t = E^*/N, \tag{1}$$

where $\bar{\epsilon}_t$ is the sum of the translational energies of the fragmentation products, E^* is the energy in excess of the heat of reaction in the molecular negative ion intermediate prior to dissociation, and N is the number of oscillators in the intermediate. An experimental investigation of translational energy for a number of positive ionization processes by Haney and Franklin[2] showed that N in Eq. (1) had to be replaced by αN where α is an empirically determined constant and has the dimensions of the fraction needed to reduce N to an "effective" or "active" number of vibrational modes in the intermediate compound ion state,

$$\bar{\epsilon}_t = E^*/\alpha N. \tag{2}$$

It therefore appears that only a fraction of the available vibrational modes capable of absorbing excess energy in the compound ion state are utilized, a conclusion which was also reached by Klots[3] and Franklin *et al.*[4] who found that the best agreement between theory and available experimental results came from a nonclassical counting of vibrational states in the transition complex. An average value of 0.44 was determined[2] for α although the spread found over the 16 positive ion processes investigated was in the range 0.36–0.56 and in the range 0.35–0.57 in a similar study of negative ion formation at onset.[5] These values for α were determined from the minimum heat of reaction calculated from literature heats of formation, $\Delta H_{\min}$calc, in conjunction with the experimentally determined appearance potentials, AP, and translational energies in Eq. (3),

$$\Delta H_{\min}\text{calc} = \text{AP} - E^*, \tag{3}$$

where E^* is given by Eq. (2). The value for α so determined is therefore subjected to any uncertainties in the determination of the appearance potential or associated with the literature thermochemical data. In this study the value of α has been determined experimentally from a measurement of the negative ion translational energy over the resonance as a function of excess energy above threshold. The translational energy of the fragment ion at the measured appearance potential, $\bar{\epsilon}_i$, is then used to calculate the total translational energy of the fragmentation products $\bar{\epsilon}_t$ which, after correction for the thermal motion of the target gas, is used to evaluate E^* and $\Delta H_{\min}$exptl. $\Delta H_{\min}$exptl is used in conjunction with the energy balance equation shown below for the dissociative capture process $AB + e \rightarrow A^- + B$ to calculate any unknown thermochemical parameters,

$$\Delta H_{\min}\text{exptl} = \Delta H_f(A^-) + \Delta H_f(B) - \Delta H_f(AB) = \text{AP} - E^*. \tag{4}$$

The experimental data have shown that the number of vibrational modes "activated" in the transition state

Copyright © 1974 American Institute of Physics

(AB^{-*}) varies from one molecule to another and is different for the various dissociative capture channels in any one system,

$$ABC + e_{(1)} \rightarrow (ABC^{-*})_{\alpha_1} \rightarrow A^- + BC,$$
$$ABC + e_{(2)} \rightarrow (ABC^{-*})_{\alpha_2} \rightarrow C^- + AB. \tag{5}$$

This parameter may also vary for the various dissociation channels from a single transition state in which different ions are formed over the same energy range,

$$ABC + e_{(1)} \rightarrow ABC^{-*}_{\alpha 1} \rightarrow A^- + BC,$$
$$ABC^{-*}_{\alpha 1'} \rightarrow C^- + AB. \tag{5'}$$

Distinct sets of vibrational modes in the intermediate state can therefore be "activated," each set corresponding to a particular dissociation channel which is then characterized by its own value for α. This physical picture of the process involved in energy transfer is not intended to be complete as it neglects the nonclassical nature of the oscillators involved and takes no account of Jahn–Teller and similar perturbations of the transition complex. However, until a theoretical model for energy partitioning in such processes evolves, this picture suffices to explain the experimental results along the same lines as the quasiequilibrium theory of mass spectra.

Several authors[5a,6b,7a,7b] have presented theoretical treatments of dissociative resonance capture. The capture cross section σ_{da} is given by Holstein[6a] (and more explicitly in a later paper by O'Malley[6b]) by this expression,

$$\sigma_{da} = \sigma_a e^{-T_s/T_a}, \tag{6}$$

where σ_a is the capture cross section at the resonance energy, T_s is the time required for the nuclei to move apart sufficiently far that autoionization can no longer occur, and T_a is the autodetachment lifetime. The exponential term in (6) is sometime called the survival probability. For the case depicted in Eq. (5), where the electron energy is a constant, σ_a is also constant and σ_{da} is dependent on the survival probability for each particular dissociative capture channel. Each channel is therefore characterized by the rate of dissociation (competition between autodetachment and dissociative capture) which is manifest in the dissociative resonance capture cross section, σ_{da}. Each channel is also characterized by its own value for α which may then represent different configurational isomers of the intermediate state.

EXPERIMENTAL

The experiments were performed using a Bendix TOFMS Model 14-107 equipped with two Model 3015 output scanners. The ionization chamber was enlarged by removal of the backing plate and the insertion of larger spacers between the block and the first ion drawout plate (ionization chamber depth, 7 mm). With the exception of one part of the study of NF_3, all measurements were made at source pressures less than 10^{-5} torr and residence times of 3×10^{-7} sec. Within this pressure range, ion intensities were linear with pressure. The electron energy scale was calibrated against the O^- ion formed from CO_2[1,8–10] and CO.[11] The smearing effect of the electron energy distribution on the experimental resonance data was partially removed by an iterative deconvolution procedure.[1,12,13]

The dissociative capture cross sections for ion formation, σ_{A^-}, at their resonance maxima were estimated using mixtures of CO_2 with the experimental gas where the capture cross section for the formation of O^- at the second resonance maximum, σ_{O^-}, was taken to be 4.5×10^{-19} cm^2.[9] This was then used in

$$\sigma_{A^-} = \sigma_{O^-}[I(A^-)/I(O^-)](P_{CO_2}/P_{AB}), \tag{7}$$

where $I(A^-)$ and $I(O^-)$ are the ion intensities at their respective resonance maxima and P_{AB} and P_{CO_2} are the partial pressures of AB, the parent molecule for A^-, and CO_2, respectively. This method for estimating dissociative capture cross sections is subject to the assumptions of equal detector sensitivity to ions over the experimental mass range 16–69 amu and translational energy range thermal to about 40 kcal mole. These values are therefore expected to be approximations only, but do serve to provide a useful indication of the negative ion intensities to be anticipated in these systems.

The experimental procedure used for the measurement of translational energies has been described previously.[1] Further points on the thermal ion calibration curve were provided by the perfluorocyclohexene ion $C_6F_{10}^-$ at m/e 262, the perfluoromethylcyclohexane ion $C_6F_{11}\cdot CF_3^-$ at m/e 350, and the perfluoroheptene-1 ion C_7F_{14}-1^- also at m/e 350.

The average translational energy for an ion in three dimensions, $\bar{\epsilon}_i$, was calculated from the experimental mass peak width (arrival time distribution) using the expression[1]

$$\bar{\epsilon}_i = \tfrac{3}{2}RT\,(m_{app}/m_i), \tag{8}$$

where m_{app} is the apparent mass of the translationally excited ion taken from the calibration curve and m_i is the real ionic mass. The principle of conservation of linear momentum is then invoked to calculate $\bar{\epsilon}_t$, the total translational energy imparted to the fragmentation products, $A^- + B$, from Eq. (9), which also corrects the experimental value for the thermal energy of the target gas at the ionization chamber temperature (300 °K),

$$\bar{\epsilon}_t = (\bar{\epsilon}_i - \tfrac{3}{2}RT\,m_i/M)\,M/m_n. \tag{9}$$

In this m_n and M are the masses of the neutral fragment and the parent molecule, respectively. $\bar{\epsilon}_t$ is then used in Eq. (2) with the value of α calculated from the rate of change of $\bar{\epsilon}_t$ with excess energy over the resonance, to calculate E^* and, hence, to find ΔH_{min}exptl from Eq. (3). A comparison between this experimental value for the minimum heat of reaction and that calculated from available thermochemical data is then made or, in the cases where such data are unavailable or quoted with large uncertainties, ΔH_{min}exptl is used to calculate the missing thermochemical parameters (heats of formation, electron affinities, or bond dissociation energies).

The excess energy derived from the measured translational energy is vibrational energy in the excited parent ion, in whatever electronic state it occurs, before it dissociates. It is thus energy in excess of that of the fragments in their ground translational, vibrational, and rotational states. It sometimes occurs that the state in which the parent ion is formed yields one fragment in an electronically excited state. Several such dissociations to electronically excited neutrals have previously been reported (1). If, when the excess vibrational energy is removed, the reaction clearly has required far more energy than is necessary to produce fragments in their ground state, it is necessary to ascertain the cause. If the neutral fragment is polyatomic, there is the possibility that it might in fact consist of two or more fragments. We consider that such a fragmentation probably occurs in steps. The over-all process must then yield the ionic fragment with the observed translational energy. If no reasonable sequence of reactions gives this result, we conclude that one of the fragments (usually the neutral) is electronically excited and that the remaining excess energy is electronic. Where electronic states of the fragment are known, we have usually obtained quite good agreement.

NF_3 was purchased from Air Products; BF_3, SF_6, CO, and CO_2 from Matheson Gas Products, CF_4 and C_2F_6 from PCR Incorporated, and C_3F_8 and c-C_4F_8 from Pierce Chemical Company. Except for freeze–thaw cycles, these materials were used without further purification.

RESULTS AND DISCUSSION

NF_3

Under single collision conditions in the ion source (1×10^{-5} torr), the ions F^-, NF^-, F_2^-, and NF_2^- were formed in the ratio 1000.0:0.2:3.0:0.5 at 70 eV and 1000.0:0.0:5.0:1.2 at their respective capture maxima. Using mixtures of NF_3 and CO_2 the dissociative electron capture cross section for F^- ion formation at the resonance maximum (1.7 eV) was estimated to be 6×10^{-17} cm^2.

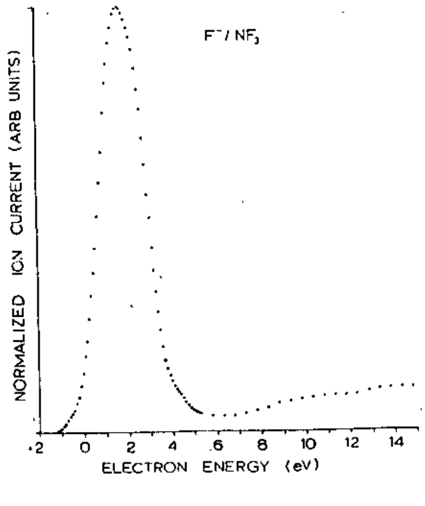

FIG. 1. Experimental resonance data for F^-/NF_3.

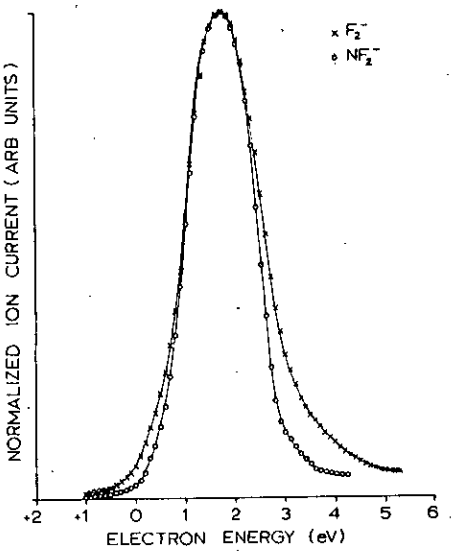

FIG. 2. Experimental resonance data for F_2^-(x) and NF_2^-(o)/NF_3.

The experimental resonance data for F^- ion formation over the energy range −2 to +15 eV are shown in Fig. 1 and for F_2^- and NF_2^- ion formation over the energy range −2 to +6 eV in Fig. 2. The unfolded data for all ions are shown together in Fig. 3. Table I is a list of all the experimental measurements made in the NF_3 system and includes ionization efficiency and translational energy

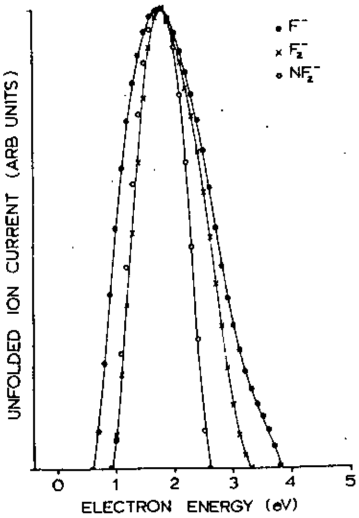

FIG. 3. Deconvoluted resonance curves for F^-(o), F_2^-(x), and NF_2^-(o)/NF_3.

TABLE I. Experimental data for NF_3.

Ion	AP (eV)	Res max (eV)	σ_{max} (cm^2)	$\bar{\epsilon}_t$ at AP (kcal $mole^{-1}$)	α (slope)
F^-	0.6 ± 0.2	1.7 ± 0.1	6×10^{-17}	9.3 ± 0.9	0.43
F_2^-	0.9 ± 0.1	1.8 ± 0.1	3×10^{-19}	thermal	...
NF_2^-	0.9 ± 0.1	1.8 ± 0.1	3×10^{-20}	thermal	...

data. The low capture cross sections for F_2^- and NF_2^- ion formation precluded detailed measurements of translational energies, although an examination of the ion mass peaks at their resonance maxima indicated that both ions are formed with close to thermal energy at onset.

The translational energy of the F^- ion measured over the resolved resonance maximizing at 1.7 eV is shown in Fig. 4. The translational energy data points shown in these figures are from a single experiment, whereas the value determined from a repeated number of experiments and used in the calculations is indicated by an arrow protruding from the appropriate point on the energy ordinate. The appearance potential or resonance threshold as determined by the deconvolution procedure is similarly indicated by an arrow protruding from the electron energy abscissa. The slope of the best straight line drawn through the data points is used to calculate α, which is also given in the figure.

The F^- ion exhibited a significant background signal over the entire energy range and this, together with the large resonance width, 2.6 eV at half-maximum, resulted in an uncertainty of 0.2 eV in the unfolded threshold. Using the available thermochemical data (Table XVI) for

$$NF_3 + e \rightarrow F^- + NF_2, \tag{10}$$

ΔH_{min}calc is found to be -0.83 ± 0.12 eV. For an appearance potential of 0.6 eV for this process, the translational energy of the F^- ion at the threshold is then predicted to be 9.7 ± 2.1 kcal $mole^{-1}$ in good agreement with our experimental value of 9.3 ± 0.9 kcal $mole^{-1}$. The results of calculations for the NF_3 system are presented in Table II where a value of ~8.8 kcal $mole^{-1}$ is shown for $\Delta H_f(NF_2)$ calculated from the experimental $\bar{\epsilon}_{F^-}$ at AP. The agreement between this and the thermochemically determined value of 8.9 ± 2.5 kcal $mole^{-1}$ by Kennedey and Colburn[14] illustrates the potential of this method for the determination of thermochemical parameters.

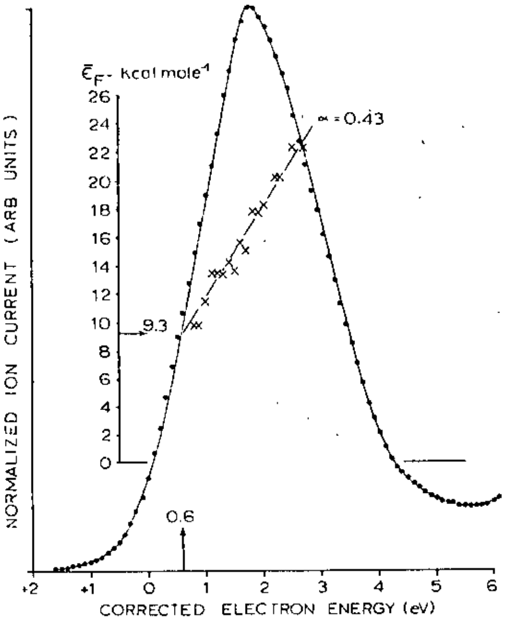

FIG. 4. Experimental resonance data and translational energy data for F^-/NF_3.

The value of 0.43 determined for α corresponds approximately to half of the vibrational degrees of freedom in the molecular negative ion state. One could speculate on a classical basis that certain of the vibrational modes have a higher probability of being active than others; however, the effects of Jahn–Teller distortion in the ion could not be predicted and the difficulties associated with such an analysis would increase dramatically with N. For this reason, we have not attempted to speculate on the identity of active modes in the transition complex.

The width of the F^- resonance, 2.6 eV at half-maximum, suggests the possibility of further unresolved capture processes in the energy range above the first resonance. No deviation of the translational energy was observed in this energy region, although evidence for the occurrence of another channel was obtained from a study of NF_3 in a high pressure source. Above 50 μHg, a

TABLE II. Processes deduced and thermochemical parameters calculated for negative ion formation from NF_3.

Ion	AP (eV)	Reaction	E^* calc (eV)	ΔH_{min} (eV) Exptl	ΔH_{min} (eV) Calc	Parameter deduced
F^-	0.6 ± 0.2	$NF_3 + e \rightarrow F^- + NF_2$	1.48 ± 0.10	-0.88	-0.83 ± 0.12	$\Delta H_f(NF_2) \simeq 8.8$ kcal · $mole^{-1}$
	~2.5	$NF_3 + e \rightarrow F^- + NF_2^*(^2B_1)$ or/		~2.5	2.57	
		$NF_3 + e \rightarrow F^- + F + NF$		~2.5	2.1	
F_2^-	0.9 ± 0.1	$NF_3 + e \rightarrow F_2^- + NF$	0	0.9		E. A. $(F_2) = 2.94 \pm 0.10$ eV
NF_2^-	0.9 ± 0.1	$NF_3 + e \rightarrow NF_2^- + F$	0	0.9		E.A. $(NF_2) = 1.68 \pm 0.21$ eV $\Delta H_f(NF_2^-) = -29.5 \pm 7.5$ kcal $mole^{-1}$

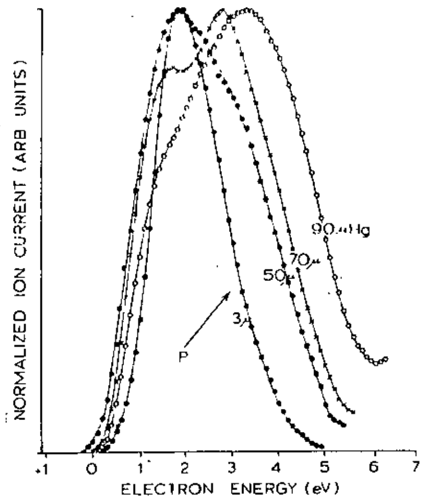

FIG. 5. Experimental resonance data for F$^-$/NF$_3$ taken over the pressure range 3–90 μHg. NF$_3$ source pressure: 3 μ (o), 50 μ (o), 70 μ(×), and 90 μHg(o).

weak NF_3^- signal was detected over the energy range encompassing the F$^-$ resonance and a shoulder appeared on the trailing edge of the F$^-$ resonance at 2.5–3.5 eV which, at 100 μHg NF$_3$ pressure, was the dominant peak in the resonance, Fig. 5. We do not understand this behavior, but we suggest that it might be due to collisional deactivation in a fashion that increases T_a more than T_s [Eq. (6)] and thus increases σ_{da}. A more complete study of the effect of pressure upon the formation of F$^-$ and NF_3^- is beyond the scope of this paper but will be attempted later.

Reaction (10) has a minimum enthalpy requirement of about −0.85 eV and, assuming the second resonance to be in the range 2.5–3.5 eV, there is an energy difference of >3.35 eV. This value is very close to that of 3.4 eV for the NF_2^* ($^2B_1 - {}^2A_2$) electronic transition[15] which suggests Reaction (15) as a further capture channel for F$^-$ formation:

$$NF_3 + e \rightarrow F^- + NF_2^* (^2B_1), \qquad (11)$$

$$NF_3 + e \rightarrow F^- + F + NF. \qquad (12)$$

Reaction (12), with a minimum enthalpy requirement of 2.1 eV, is also possible in the energy range under discussion and cannot be excluded from analysis of our experimental data. We can thus conclude only that either Reaction (11) or (12) is responsible for F$^-$ ion formation in the 2.5–3.5 eV energy range.

The occurrence of F$^-$ signal in the range above the resonances already discussed may, in part, be due to Reactions (13)–(16), which have calculated minimum enthalpy requirements of 3.7, 5.3, 6.2, and 7.8 eV, respectively,

$$NF_3 + e \rightarrow F^- + F_2 + N(^4S), \qquad (13)$$

$$NF_3 + e \rightarrow F^- + 2F + N(^4S), \qquad (14)$$

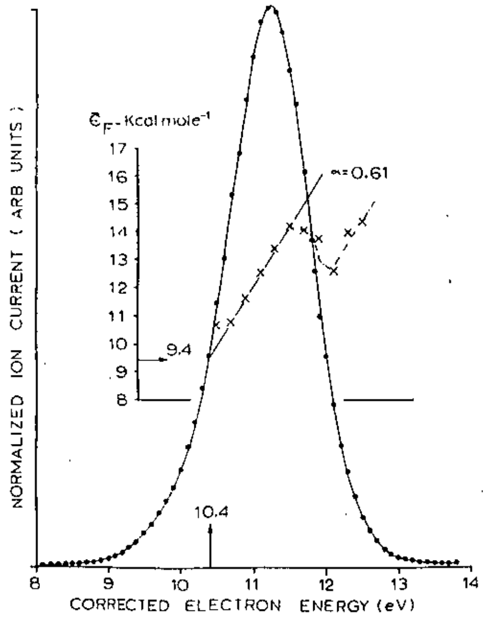

FIG. 6. Experimental resonance data and translational energy data for F$^-$/BF$_3$.

$$NF_3 + e \rightarrow F^- + F_2 + N^*(^1D), \qquad (15)$$

$$NF_3 + e \rightarrow F^- + 2F + N^*(^1D). \qquad (16)$$

The experimental data for F_2^- ion formation are given in Table I and the processes deduced in Table II,

$$NF_3 + e \rightarrow F_2^- + NF. \qquad (17)$$

The value of 2.94±0.10 eV for the electron affinity of the fluorine molecule deduced from Reaction (17) is in good agreement with previously determined values; 3.08 ±0.10,[16] ~2.8,[13] and ~3.0 eV.[17]

From a consideration of the energetics for NF_2^- ion formation according to

TABLE III. Comparison of electron affinities for hydrogenated and corresponding fluorinated radicals.

Hydrogenated radical	Radical electron affinities (eV)	Fluorinated radical	Radical electron affinities (eV)
CH_3[a]	1.08	CF_3[d]	2.0
CH_3O[a]	0.38	CF_3O[a]	1.35
CH_3S[a]	1.36	CF_3S[a]	1.80
NH_2[b]	0.74	NF_2[e]	1.68
PH_2[c]	1.25	PF_2	···

[a] F. M. Page and G. C. Goode, *Negative Ions and the Magnetron* (Wiley-Interscience, New York, 1969).

[b] K. C. Smyth and J. I. Brauman, J. Chem. Phys. 56, 4620 (1972).

[c] K. C. Smyth and J. I. Brauman, J. Chem. Phys. 56, 1132 (1972).

[d] Average literature value.

[e] This study.

$$NF_3 + e \rightarrow NF_2^- + F, \qquad (18)$$

the electron affinity of the difluoroamino radical is calculated to be 1.68 ± 0.21 eV, i.e., 1.7 eV. This radical is known to be very reactive and has been used extensively in gas-phase kinetics experiments. Investigations of positive ion formation in NF_3[18] and N_2F_4[19] have resulted in values of 11.0 and 11.75 ± 0.1 eV for the ionization potential of this radical, although to our knowledge there have been no reliable values reported for the electron affinity. A comparison of this value with those reported for various hydrogenated and their corresponding fluorinated radicals is made in Table III. When combined with Kennedey and Colburn's[14] value of 8.9 ± 2.5 kcal mole^{-1} for $\Delta H_f(NF_2)$, our value for E.A.(NF_2) results in $\Delta H_f(NF_2^-) = -29.5 \pm 7.5$ kcal mole^{-1}.

BF_3

Negative ion formation in boron trifluoride has been examined previously by MacNeil and Thynne.[20] The negative ions observed in the present study were F^-, F_2^-, and BF_2^- with relative intensities in the ratio 1000 : 20 : < 1 at their respective capture maxima. This is in good agreement with the earlier study, although we did not detect BF_4^- under our operating conditions (source pressures maintained below 1×10^{-5} torr).

The dissociative capture cross sections measured for the F^- and F_2^- ions at their maxima are given in Table IV and the experimental resonance curves and translational energy measurements in Figs. 6 and 7. Figure 8 shows the unfolded resonance curves for the F^- and F_2^- ions.

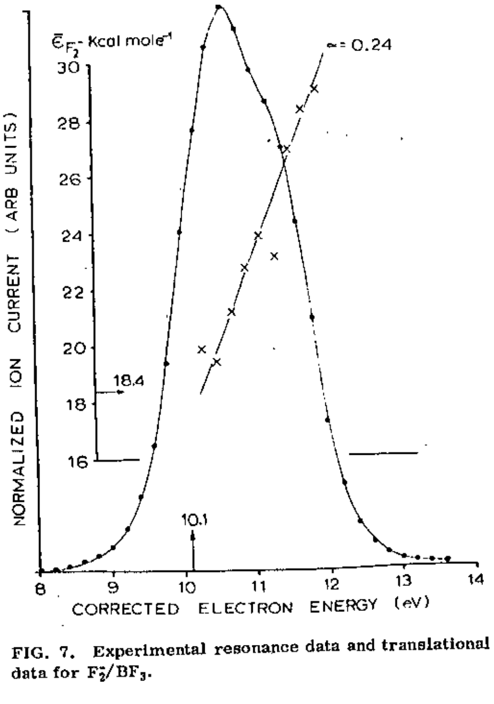

FIG. 7. Experimental resonance data and translational energy data for F_2^-/BF_3.

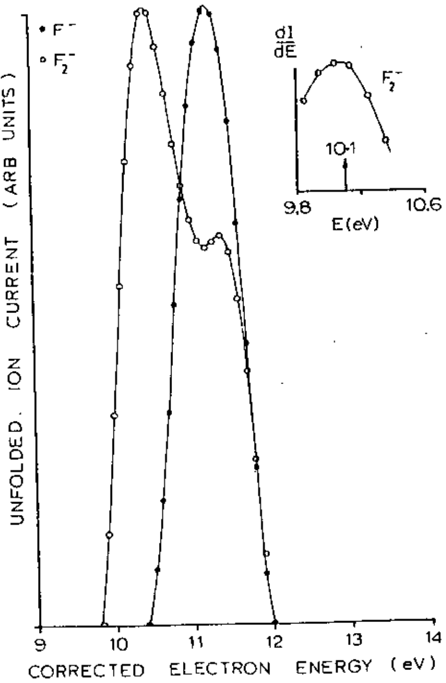

FIG. 8. Deconvoluted resonance curves for F^-(∘) and F_2^-(∘)/BF_3.

The shoulder on the trailing edge of the F_2^- resonance was reproducible and is partially resolved after deconvolution. These observations were also reported by MacNeil and Thynne[20] and by Stockdale *et al.*[21] Within our energy resolution, the leading edge of the F_2^- resonance exhibits the same profile as the high energy side of the electron energy distribution and matches exactly the leading edge of the O^-/CO resonance used for energy scale calibration. As the O^-/CO is known to occur with a vertical onset,[11,22] it may be inferred[20] that F_2^-/BF_3 formation is similarly vertical. Then, assuming a delta function for the leading edge, the onset is found by differentiation as shown in Fig. 8. However, in a diatomic system an ion exhibiting a resonance with a vertical onset is also formed with zero translational energy at onset as the dissociation limit of the molecular negative ion intermediate intersects the repulsive part of the surface in the Franck–Condon region. Only those electrons with an energy in excess of the intersection energy will result in dissociative capture, the less energetic electrons in the Franck–Condon band undergoing associative

TABLE IV. Experimental data for BF_3.

Ion	AP (eV)	Res max (eV)	σ_{max} (cm^2)	$\bar{\epsilon}_t$ at AP (kcal mole^{-1})	α (slope)
F^-	10.4 ± 0.1	11.2 ± 0.1	1×10^{-18}	9.4 ± 1.0	0.61
	~12.1	···	···	~13	···
F_2^-	10.1 ± 0.1	10.6 ± 0.1	2×10^{-20}	18.4 ± 0.9	0.24

capture to form a short-lived vibrationally excited molecular ion which rapidly undergoes autodetachment. In this case, the F_2^- ion is formed with considerable translational energy at the onset (18.4 ± 0.9 kcal mole^{-1}). This may be evidence for a nonvertical resonance, although it is evident from our unfolded data that the rise from onset to maximum is at least as sharp as the effective electron energy distribution, 0.4 eV. Stockdale *et al.*,[21] using an RPD source delivering an electron energy distribution with a width of 0.1 eV at half-maximum, also report the leading edge of the F_2^- resonance to mirror their distribution. This behavior is consistent with the existence of an activation energy for recombination with a maximum in the Franck–Condon energy range. Sharp and Dowell[22a] have interpreted the behavior of NH_2^- from NH_3 in a similar way. The appearance potential determined from differentiation of the leading edge should not therefore be much in error whichever is the true resonance type.

The F_2^- ion may be formed in

$$BF_3 + e \rightarrow F_2^- + BF \qquad (19)$$

or

$$BF_3 + e \rightarrow F_2^- + B + F. \qquad (20)$$

Reaction (20), which has a minimum enthalpy requirement of 15.4 eV, can be neglected on energetic grounds. Reaction (19) must then be responsible for the observed resonance, Fig. 7. A value of 2.86 ± 0.22 eV deduced for the electron affinity of the fluorine molecule using the measured appearance potential and translational energy results for Reaction (19) compare favorably with the value of 2.94 ± 0.10 eV deduced from the F_2^- ion formation in NF_3. The partially resolved resonance appearing as a shoulder on the trailing edge of the unfolded curve is coincident with the F^- resonance and suggests a common origin, i.e., same BF_3^{-*} state. The formation of F_2^- by Reaction (19) over this shoulder is inferred from the translational energies which are continuous over both resonances (see section on nitric oxide, Ref. 1).

The F^- resonance, Figs. 6 and 8, does not appear to exhibit a vertical onset and the deconvoluted onset at 10.4 ± 0.1 eV was employed in the calculations. The translational energy at the appearance potential is measured to be 9.4 ± 1.0 kcal mole^{-1} and corresponds to translationally excited ions produced by Reaction (22) or (23).

$$BF_3 + e \rightarrow F^- + BF_2(^2A_2), \qquad (21)$$

$$BF_3 + e \rightarrow F^- + BF_2^*(^2B_2), \qquad (22)$$

$$BF_3 + e \rightarrow F^- + F + BF. \qquad (23)$$

Reaction (21), which involves formation of ground electronic state products, has a minimum enthalpy requirement of only 3.1 ± 0.1 eV. E^* would then be 7.3 ± 0.2 eV compared to our experimental value of 2.02 ± 0.16 eV. The 5.3 eV discrepancy could then be assigned to the $BF_2^*(^2B_2 - {}^2A_2)$ electronic transition. The only spectroscopic reference to this transition is the tentative assignment of a band system in the range 2100–3700 Å (5.9–3.3 eV) detected in the uv emission spectrum of BF_3 excited with 200 eV electrons.[22] The electronic transitions for the isoelectronic molecule NO_2 are accurately known,[23] however, and several states in the 5–8 eV range are recorded. The $\tilde{B}^2B_2$ state lies 4.97 eV above the ground state and the $\tilde{C}$, $\tilde{D}$, and $\tilde{E}\,^2\Sigma_u^+$ states at 5.27, 6.20, and 7.225 eV, respectively. It is unlikely that our experimental energy resolution could differentiate between closely spaced states such as the $NO_2(\tilde{B}^2B_2)$ and $\tilde{C}$ states of NO_2. The value of 5.3 eV estimated for the $(^2B_2)$ transition in BF_2 from our data may be an average value for equivalent closely spaced states in this radical.

The alternative process, (23), has a calculated enthalpy requirement of 8.7 ± 0.1 eV and would involve a value of 1.7 eV for E^* at the appearance potential. If Reaction (23) occurs in a single step, we are unable to relate the measured translational energy to the total excess energy. It seems highly improbable, however, that three fragments would separate simultaneously and, if the fragmentation is stepwise, a reasonable analysis of the energy distribution is possible. Two such mechanisms may be expected to form F^-,

$$BF_3^- \rightarrow F_2^- + BF, \qquad (24a)$$

$$F_2^- \rightarrow F^- + F, \qquad (24b)$$

or

$$BF_3^- \rightarrow BF_2^- + F, \qquad (25a)$$

$$BF_2^- \rightarrow F^- + BF. \qquad (25b)$$

At the appearance potential (10.4 eV) of F^-, E^* for (24a) is 68 kcal/mole which, using $\alpha = 0.24$ determined for this process, gives $\bar{\epsilon}_t(24a) = 47$ kcal/mole. The remaining 21 kcal/mole would be distributed as vibrational (or rotational) energy between F_2^- and BF. However, even if all 21 kcal/mole reside in the F_2^-, reaction (24b) would be endothermic by 10 kcal/mole and would not occur.

The reaction sequence (25a) and (25b) is less readily analyzed because $\Delta H_f(BF_2^-)$ is not known. From AP(F^-) and thermochemical values from Table XVI, we compute $\Delta H_f(BF_2^-) + E_i^*$ to be -51 kcal/mole. BF_2^- is known to exist and so it must have a positive electron affinity. Since $\Delta H_f(BF_2)$ is -139 kcal/mole, $\Delta H_f(BF_2^-)$ must be less than this. If we assume $\Delta H_f(BF_2^-)$ to be -141 kcal/mole, $E^*(25a) = 90$ kcal/mole, $\bar{\epsilon}_t(25a) = 24.6^*$ kcal/mole, (taking α as 0.61 kcal/mole), and $\bar{\epsilon}(BF_2^-) = 6.9$ kcal/mole. The excess vibrational energy of BF_2^- is then 65.4 kcal/mole. When this is combined with the thermochemical values for (25b), we find $E^*(25b)$ to be 12 and $\bar{\epsilon}_t(25b)$ to be 4 kcal/mole, taking α as 1 as we have found to be true for triatomic ions. From these results $\bar{\epsilon}_{F^-} = 5$ kcal/mole. This is only about half the measured translational energy of F^- at onset.

If we assume $\Delta H_f(BF_2^-)$ to be -190 kcal/mole, corresponding to an electron affinity of BF_2 of 2.2 eV, and carry out a similar series of calculations, we find $E^*(25a)$ to be approximately 0 and $\bar{\epsilon}(F^-)$ to be 4 kcal/mole (assuming BF_2^- is able to fragment with essentially zero excess energy). Several calculations at intermediate assumed values of $\Delta H_f(BF_2^-)$ all gave $\bar{\epsilon}(F^-)$ between 4 and

TABLE V. Processes deduced and thermochemical parameters calculated for negative ion formation from BF_3.

Ion	AP (eV)	Reaction	E^* calc (eV)	ΔH_{min} (eV) Exptl	Calc	Parameter deduced
F^-	10.4 ± 0.1	$BF_3 + e \rightarrow F^- + BF_2^*(^2B_2)$	2.02 ± 0.16	8.4 ± 0.5	3.1 $BF_2(^2A_1)$	$BF_2^*(^2B_2) = 5.3$ eV
	~12.1	$BF_3 + e \rightarrow F^- + BF_2^*(\tilde{D})$	~2.8	~9.3	···	$BF_2^*(\tilde{D}) = 6.2$ eV
		or/				
		$BF_3 + e \rightarrow F^- + F + BF$ use	3.4	···	8.7 ± 0.1	
F_2^-	10.1 ± 0.1	$BF_3 + e \rightarrow F_2^- + BF$	2.53 ± 0.12	7.6 ± 0.2	7.5	E. A. $(F_2) = 2.86 \pm 0.22$ eV

5 kcal/mole. Further, if we assume a negative electron affinity of BF_2 of 2.1 eV [$\Delta H_f(BF_2^-) = -91$ kcal/mole], the computed translational energy of F^- is only 6.5 kcal/mole. Thus, we find that no reasonable value of $\Delta H_f(BF_2^-)$ results in a translational energy of F^- that agrees with the experimental value.

Thus, neither fragmentation mechanism (24a), (24b) or (25a), (25b) accounts for the translational energy of F^-. The possibility of simultaneous separation of three fragments cannot be completely eliminated, but it seems improbable. Consequently, the most probable mechanism for the formation of F^- is Reaction (22) in the resonance region onsetting at 10.4 eV. The 5.3 eV electronic transition for BF_2 probably corresponds to the $^2B_2$ electronic state of the radical.

The break in the translational energy data at 12 eV, shown in Fig. 6, may correspond to another electronic state of the BF_2 radical. Assuming this to be the case and taking the translational energy to be 13 kcal mole^{-1} at 12.1 eV, an electronic transition of 6.2 eV is required to satisfy the reaction energetics. A continuum in the NO_2 uv absorption spectrum with a maximum at 1700 Å is assigned to the $\tilde{D}$ state of NO_2 at 6.20 eV. The equivalent transition may thus be suggested to explain our electron impact data. However, if one carried out computations of the translational energy for mechanism (25a), (25b) but for this higher state leading to F^-, fair agreement with the measured values is obtained. Thus, it is quite possible that in the higher energy range F^- is formed by Reaction (25a), (25b). Our data do not permit a decision.

A summary of the capture processes deduced and thermochemical parameters estimated is presented in Table V.

CF_4

The experimental data for CF_4 are shown in Table VI. The appearance potentials and resonance maxima are in good agreement with the values reported by MacNeil and Thynne[24] in an earlier study of CF_4. These authors reported the $F^-:CF_3^-$ ratio at their respective capture maxima to be 1000 : 570 compared to the ratio of 1000 : 660 in this study where $\sigma_{da}(F^-) = 6 \times 10^{-19}$ cm^2 at the maximum.

TABLE VI. Experimental data for CF_4.

Ion	AP (eV)	Res max (eV)	σ_{max} (cm^2)	$\bar{\epsilon}_t$ at AP (kcal mole^{-1})	α (slope)
F^-	4.65 ± 0.1	6.15 ± 0.1	6×10^{-19}	16.8 ± 0.6	0.40
	6.2 – 6.5	~7.5	4×10^{-19}	thermal	0.46
CF_3^-	5.4 ± 0.1	6.9 ± 0.1	4×10^{-19}	4.0 ± 0.2	0.33

The experimental resonance curve and translational energy data for CF_3^- ion formation are shown in Fig. 9 and the unfolded resonance data are shown in Fig. 10. Using the experimentally determined value of 0.33 for α in conjunction with the translational energy of 4.0 ± 0.2 kcal mole^{-1} at the onset, 5.4 ± 0.1 eV for Reaction (26), the electron affinity of

$$CF_4 + e \rightarrow CF_3^- + F \qquad (26)$$

the trifluoromethyl radical is deduced to be 2.2 ± 0.3 eV. Values reported in the literature lie in the range 1.8[25]–2.6 eV.[26]

The F^- resonance, shown in Fig. 11, is broad, width at half-maximum 2.9 eV, and exhibits a shoulder on the high energy side of the maximum. Ion mass peak shapes or arrival-time distributions at various points over the

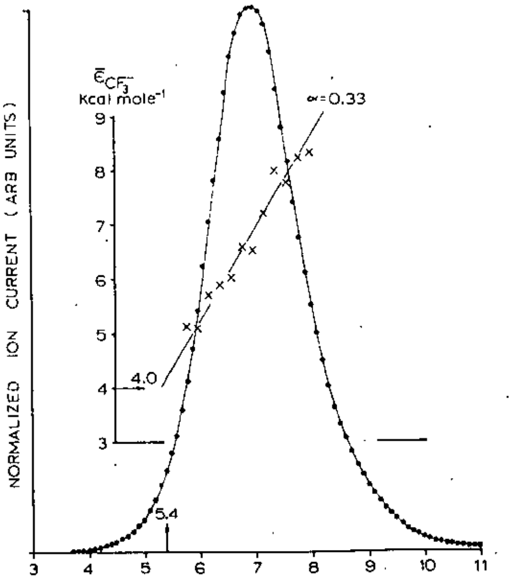

FIG. 9. Experimental resonance data and translational energy data for CF_3^-/CF_4.

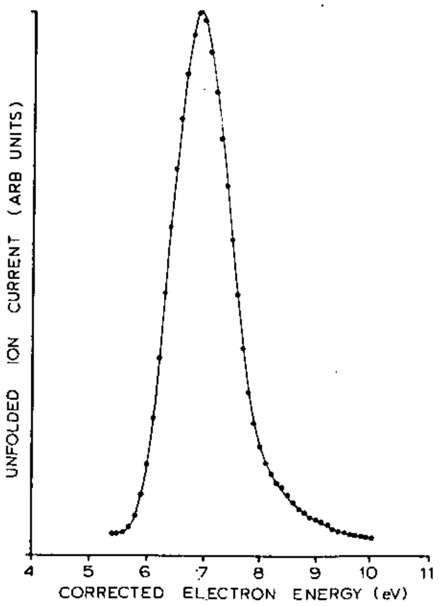

FIG. 10. Deconvoluted resonance curve for CF_3^-/CF_4.

resonance are illustrated in Fig. 11. The broad "doublet" distributions associated with the leading edge of the F^- resonance are the result of highly excited ions moving away from the ionization region prior to application of the ion drawout pulse. The quasithermal peak, representing low energy F^- ions, which appears near the resonance maximum is the dominant feature in the arrival-time distributions towards the tail of the resonance. This peak represents the contribution of a second capture process to the observed resonance. The unfolded resonance is shown in Fig. 12 together with the arrival-time distributions. The second resonance, which has been partially resolved, is that associated with the quasithermal translational energy distributions shown in Figs. 11 and 12.

A plot of the quasithermal peak amplitude divided by the energetic ion peak amplitude (to the base line) has been extrapolated to zero to provide an estimated value for the second onset. The average value of several repeated determinations is 6.2 eV, which is in reasonable agreement with the value of 6.5 eV determined by extrapolation of the translational energy measurements (from the quasithermal ion peaks) to thermal energy, Fig. 13. A reconstruction of the second resonance from the quasithermal mass peak amplitudes resulted in a value of 7.5 eV for the resonance maximum.

Reaction (27) is considered responsible for the energetic F^- ions formed at 4.65 eV and Reaction (28) or (29) as responsible for the formation of thermal F^- ions at 6.2 eV,

$$CF_4 + e \rightarrow F^- + CF_3(X^2A), \tag{27}$$

$$CF_4 + e \rightarrow F^- + CF_3^*, \tag{28}$$

$$CF_4 + e \rightarrow F^- + F + CF_2. \tag{29}$$

The discrepancy between $\Delta H_{\min}$exptl $\Delta H_{\min}$calc (Table VII) for Reaction (27) undoubtedly reflects the uncertainty involved in our analysis of the broad mass peaks. The translational energy at the threshold is measured to be 16.8 ± 0.6 kcal mole^{-1} compared to the predicted value of 12.3 kcal mole^{-1}. The 4.5 kcal mole^{-1} difference, 0.2 eV, has to be multiplied by αN, the number of active modes in the CF_4^{-*} intermediate. This multiplication of a small uncertainty by a large number can result in misleading discrepancies in E^* which imposes limits on the translational energy which can be accurately analyzed and the complexity of the molecule which can be studied.

Reaction (27), which results in ground electronic state products, has a calculated minimum enthalpy requirement of 2.2 ± 0.1 eV. For Reaction (28), the discrepancy between the calculated minimum and the experimentally observed appearance potentials could be assigned to a CF_3 electronic transition, i.e., 4.0–4.3 eV. Hastie and Margrave[27] employed an extended Hückel method utilizing single-exponent one-electron Slater orbitals to calculate structural and thermochemical parameters for many of the Group I, IIa, IIIa, and IVa halides, including CF_3. A value of 5.9 eV was suggested for the $CF_3^*(^2B - X^2A)$ electronic transition, and Wang and Franklin[28] have proposed that the inflection observed at 8 eV on the trailing edge of the deconvoluted F^- resonance by MacNeil and Thynne[24] (see Fig. 12) is consistent with Reaction (28) where CF_3^* represents the ^2B electronic state at 5.9 eV above the ground state. The

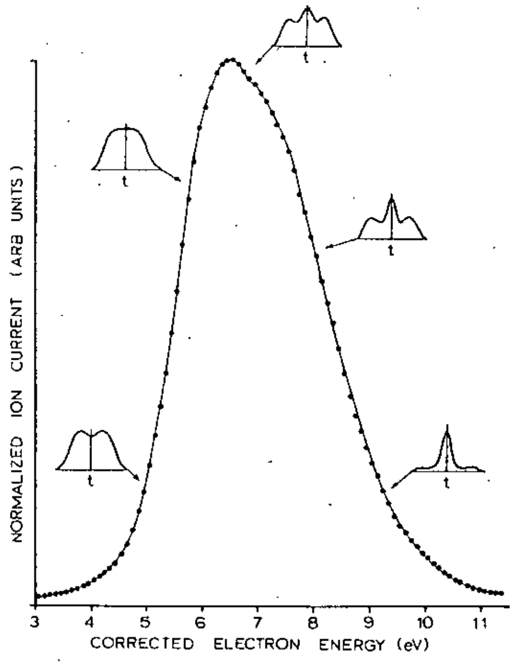

FIG. 11. Experimental resonance data and ion arrival-time-distributions for F^-/CF_4.

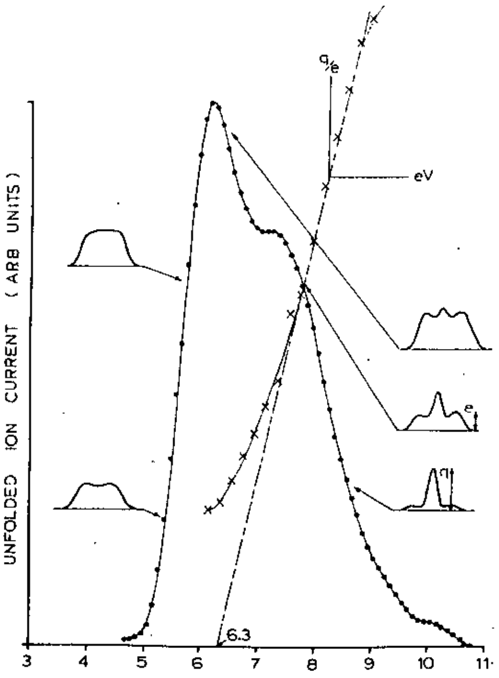

FIG. 12. Deconvoluted resonance curve and experimental ion arrival-time distributions for F^-/CF_4.

formation of thermal F^- ions in the range 6.2–6.5 eV may not be associated with $CF_3^*(^2B)$, although the formation of a low lying CF_3^* quartet state is also a possibility for Reaction (28) at this energy. Since Reaction (29) has a minimum enthalpy requirement of 6.1 ± 0.1 eV to give products in their ground states at onset and since $\epsilon_t(F^-)$ at onset is thermal, this reaction appears to be a reasonable mechanism for the formation of F^-. However, we consider it probable that the reaction occurs in two steps by one of the following mechanisms:

$$CF_4 \rightarrow CF_3^- + F, \tag{30a}$$

$$CF_3^- \rightarrow F^- + CF_2, \tag{30b}$$

or

$$CF_4 \rightarrow F_2^- + CF_2, \tag{31a}$$

$$F_2^- \rightarrow F^- + F. \tag{31b}$$

If the reaction occurs through mechanism (30), the first step will involve 64 kcal/mole excess energy of which 21 kcal/mole is in translation and 43 in internal energy of CF_3^-. This is not sufficient energy to permit (30b) to occur, this step being about 63 kcal/mole endothermic. Similar considerations applied to the second mechanism result in a total internal energy of F_2^- and CF_2 in (31a) of 23 kcal/mole. Even if all of this energy is given to F_2^-, its decomposition by (31b) would be endothermic by about 8 kcal/mole and so would not occur. Thus, unless we assume decomposition to occur in a single step, we must conclude that reaction to form F and CF_2 along with F^- does not occur and that F^- is formed in the second resonance region by Reaction (28). We are not, however, able to identify the electronic state of CF_3.

A summary of the processes deduced and thermochemical data estimated for CF_4 are presented in Table VII.

C_2F_6

There has been no previous investigation of negative ion formation in hexafluoroethane employing a technique for reducing the effect of the electron energy distribution on the resonance capture peaks.[28,29] The ions detected in the present study were F^-, CF_3^-, and $C_2F_5^-$ in the ratio 100 : 21 : 1 at their respective capture maxima. The low cross section for negative ion formation from C_2F_6 precluded a detailed examination of the $C_2F_5^-$ ion, although data for F^- and CF_3^- are presented in Table VIII and the experimental and unfolded resonance peaks are shown in Fig. 14(a) and 14(b), respectively.

The formation of thermal F^- ions at 2.1 ± 0.2 eV (Fig. 15) is attributed to Reaction (32), which has a calculated minimum enthalpy requirement of 2.0 ± 0.4 eV,

$$C_2F_6 + e \rightarrow F^- + C_2F_5. \tag{32}$$

Invoking the energy balance equation for this process,

$$D(C_2F_5-F) = AP(F^-) + E.A.(F) - E^*, \tag{33}$$

where $E^* = 0$ and E. A. (F) is taken to be 3.40 eV,[30] the (C_2F_5-F) bond dissociation energy is estimated to be 5.5 ± 0.2 eV. A value of 5.61 ± 0.09 eV has been measured for the (CF_3-F) bond dissociation energy by Coomber and Whittle.[31]

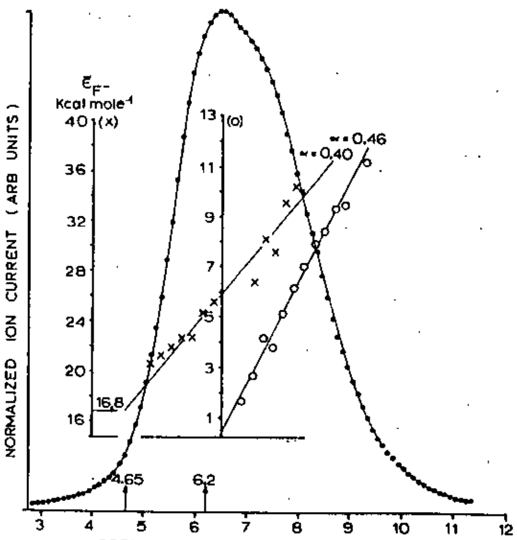

FIG. 13. Experimental resonance data and translational energy data for F^-/CF_4. The left side translational energy ordinate, 16–40 kcal mole⁻¹ range, corresponds to the broad ion distributions (x) and the ordinate, 0–13 kcal mole⁻¹ range, corresponds to the quasithermal ion distribution (o) shown in Fig. 11 or 12.

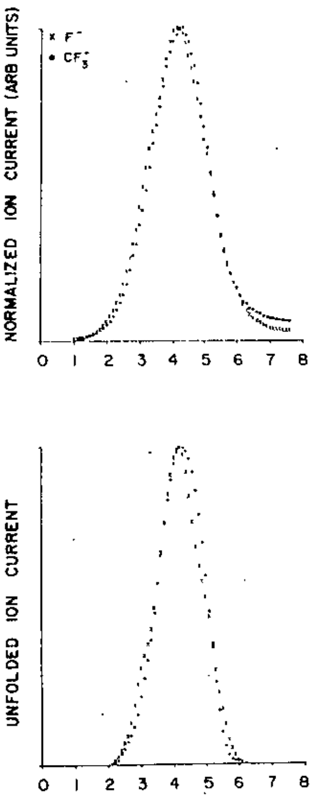

FIG. 14. Experimental (upper half of figure) and deconvoluted resonance data for F^-(x) and CF_3^-(o)/C_2F_6.

The break observed in the translational energy curve shown in Fig. 15 is interpreted as resulting from the formation of F^- ions from a different capture process, the points over the first resonance being attenuated by lower values associated with the second resonance. Extrapolation of the second set of points to thermal energy indicates an onset at ~4.9 eV. Reactions (34)–(36) may be considered as possible reactions leading to thermal F^- ions at 4.9 eV,

$$C_2F_6 + e \rightarrow F^- + C_2F_5^*, \qquad (34)$$

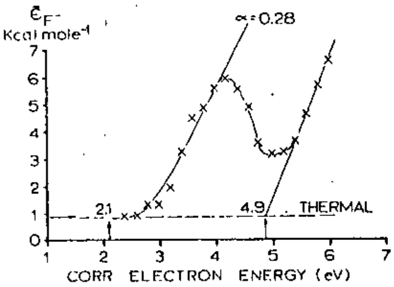

FIG. 15. Translational energy data for F^-/C_2F_6.

$$C_2F_6 + e \rightarrow F^- + CF_2 + CF_3, \qquad (35)$$

$$C_2F_6 + e \rightarrow F^- + F + C_2F_4. \qquad (36)$$

There is no information on the electronic states of the pentafluoroethyl radical, hence the value of 2.9 eV deduced for a possible electronic transition from the energetics in this case cannot be verified. The minimum enthalpy requirements of Reactions (35) and (36) are 4.5±0.2 and 5.3±0.3 eV, respectively. The uncertainties involved in these estimates from the use of the thermochemical data in Table XVI make it difficult to draw any firm conclusions from the available information and none will be attempted.

The CF_3^- ion is formed with 1.35±0.2 kcal mole^{-1} translational energy at the onset, 2.2±0.2 eV, and corresponds to

$$C_2F_6 + e \rightarrow CF_3^- + CF_3. \qquad (37)$$

E^* for this process is calculated to be 0.66±0.10 eV from which a value of 2.4±0.5 eV is deduced for the electron affinity of the trifluoromethyl radical. Within their respective experimental uncertainties this value and that deduced from CF_3^- ion formation in CF_4 are in agreement. The (CF_3–CF_3) bond dissociation energy is calculated to be 4.6±0.6 eV which, within the error limits, is in accord with the value of 4.19±0.05 eV reported by Coomber and Whittle.[31] The uncertainties quoted with these parameters are conservative estimates determined by summing the error limits of all the experimental parameters measured and must be considered as upper limits.

A summary of the processes deduced and the thermochemical parameters estimated is presented in Table IX.

TABLE VII. Processes deduced and thermochemical parameters calculated for negative ion formation from CF_4.

Ion	AP (eV)	Reaction	E^* calc (eV)	ΔH_{min} (eV)		Parameter deduced
				Expt.	Calc	
F^-	4.65±0.1	$CF_4 + e \rightarrow F^- + CF_3$	3.26±0.12	1.4±0.2	2.2±0.1	
	~6.2	$CF_4 + e \rightarrow F^- + CF_3^*$	0	~6.2	···	CF_3^* 4.0–4.3 eV
		or/				
		$CF_4 + e \rightarrow F^- + F + CF_2$	0	~6.2	6.1±0.1	
CF_3^-	5.4±0.1	$CF_4 + e \rightarrow CF_3^- + F$	2.0±0.1	3.4±0.2	3.7±0.2	E. A. (CF_3)=2.2±0.3 eV

TABLE VIII. Experimental data for C_2F_6.

Ion	AP (eV)	Res max (eV)	σ_{max} (cm^2)	$\bar{\epsilon}_t$ at AP (kcal mole^{-1})	α (slope)
F^-	2.1 ± 0.2	4.3 ± 0.1	5×10^{-18}	thermal	0.28
	4.9 ± 0.2			thermal	0.26
CF_3^-	2.2 ± 0.2	4.4 ± 0.1	1×10^{-18}	1.35 ± 0.2	0.47

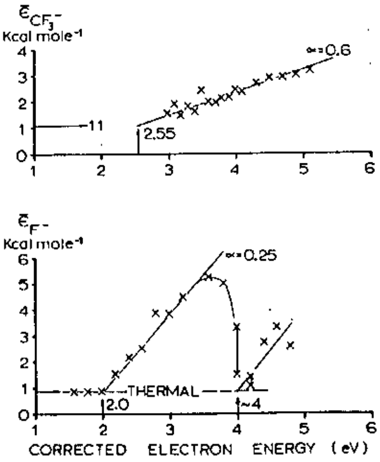

FIG. 16. Translational energy data for CF_3^- (upper half of figure) and F^-/C_3F_8.

C_3F_8

Negative ion formation in perfluoropropane has been the subject of several investigations,[29,32-34] the most recent being that by Harland and Thynne[34] using deconvolution to reduce the effect of the electron energy distribution on the resonance curves.

The ions investigated in this study were F^- and CF_3^- and the experimental data are presented in Table X. The resonance curves have not been reproduced here as they are in agreement with those reported by Harland and Thynne.[34] The only discrepancy found was in the F^- appearance potential which was given as 1.8 ± 0.1 eV[34] and was found to be 2.0 ± 0.1 eV in this study. However, both values are equivalent within their respective experimental uncertainties.

The experimental translational energy data are shown in Fig. 16. The thermal F^- ions formed at 2.0 ± 0.1 eV correspond to Reaction (38) or (39), which have minimum enthalpy requirements of 1.4 and 1.9 eV, respectively,

$$C_3F_8+e\rightarrow F^-+i\text{-}C_3F_7, \tag{38}$$

$$C_3F_8+e\rightarrow F^-+n\text{-}C_3F_7. \tag{39}$$

From thermodynamic considerations Reaction (38) would be chosen as the most probable mechanism leading to F^- ion formation at low energy, although from the measured appearance potential and translational energy this does not appear to be the case. ΔH_{min}exptl is found to be 2.0 ± 0.1 eV in good accord with the ΔH_{min}calc for Reaction (39). The heats of formation used in the calculations were those calculated by Bryant,[35] and although these values may be subject to some uncertainties, a discrepancy of 0.5 eV in the calculated values is highly unlikely. Assuming Reaction (39) to be that responsible for the observed data, the heat of formation of the n-C_3F_7 radical is deduced to be -305.4 ± 7.0 kcal mole^{-1} (Table XI) in good agreement with Bryant's[35] number, -306.5 kcal mole^{-1}.

The break observed in the translational energy data at 4 eV may be attributed to the formation of F^- ions by one of the reactions (40)–(42). Reactions (41) and (42) have calculated minimum enthalpy requirements of 3.7 and 4.2 eV, respectively,

$$C_3F_8+e\rightarrow F^-+C_3F_7^*, \tag{40}$$

$$C_3F_8+e\rightarrow F^-+CF_3+C_2F_4, \tag{41}$$

$$C_3F_8+e\rightarrow F^-+CF_2+C_2F_5. \tag{42}$$

The absence of information on the electronic states of the heptafluoropropyl radical precludes an assessment of the viability of Reaction (40) although, if such an electronic transition were to occur, its magnitude would be in the range 2.6–2.1 eV depending on the configuration of the ground state radical. Reactions (41) and (42) are also energetically acceptable and following the discussion on C_2F_6 no distinction can be made between these alternatives.

The experimental data for CF_3^- ion formation by Reaction (43) are given in Table X and Fig. 16(a),

$$C_3F_8+e\rightarrow CF_3^-+C_2F_5. \tag{43}$$

TABLE IX. Processes deduced and thermochemical parameters calculated for negative ion formation in C_2F_6.

Ion	AP (eV)	Reaction	E^* calc (eV)	ΔH_{min} (eV) Exptl	ΔH_{min} (eV) Calc	Parameter deduced
F^-	2.1 ± 0.2	$C_2F_6+e\rightarrow F^-+C_2F_5$	0	2.1 ± 0.2	2.0 ± 0.4	$D(F-C_2F_5)=5.5\pm0.2$ eV
	4.9 ± 0.2	$C_2F_6+e\rightarrow F^-+C_2F_5^*$	0	4.9 ± 0.2	···	$C_2F_5^*$ ~2.9 eV
		or				
		$\rightarrow F^-+CF_2+CF_3$	0	4.9 ± 0.2	4.5 ± 0.2	
		or				
		$\rightarrow F^-+F+C_2F_4$	0	4.9 ± 0.2	5.3 ± 0.3	
CF_3^-	2.2 ± 0.2	$C_2F_6+e\rightarrow CF_3^-+CF_3$	0.66 ± 0.10	1.54 ± 0.3	2.0 ± 0.4	E. A.(CF_3) = 2.4 ± 0.5 $D(F_3C-CF_3)=4.6\pm0.6$ eV

TABLE X. Experimental data for C_3F_8.

Ion	AP (eV)	Res max (eV)	σ_{max} (cm^2)	ϵ_t at AP (kcal mole^{-1})	α (slope)
F^-	2.0±0.1	3.15±0.1	5×10^{-18}	thermal	0.25
	4.0			thermal	
CF_3^-	2.55±0.1	3.65±0.1	5×10^{-19}	1.1±0.2	0.60

Values of 2.05±0.2 eV for the electron affinity of the trifluoromethyl radical and 4.6±0.3 eV for the (CF_3–C_2F_5) bond dissociation energy are calculated from these data (Table XI).

The second, low cross-section resonance observed on the tail of the initial resonance[34] was also reproduced in this study, although the ion current was insufficient to permit translational energy measurements.

c-C_4F_8

Perfluorocyclobutane was chosen for a translational energy study because negative ion fragmentation occurs about 2 eV higher than predicted from thermochemical calculations.[36] The rearrangement ions CF_3^- and $C_3F_5^-$ are also formed in the same energy range as the F^- ion suggesting a common intermediate state which may rearrange on decomposition.[36] The appearance potential data shown in Table XII are taken from Harland and Thynne[35] although the resonance curves were reproduced in this study for energy scale calibration of the translational energy data. Low cross-section resonances for F^- and $C_3F_5^-$ in the 1 eV region reported by Lifshitz and Grajower[37] were not detected under the operating conditions employed in this study.

The F^- resonance curve is very complex, at least four different resonances being identified.[36] The translational energy data shown in Fig. 17 reflect the complexity of the resonance data and are consequently difficult to analyze with any confidence. It is, however, interesting to note that the translational energy data increase in a steplike manner, the steps corresponding closely to the four resonances onsetting at 3.7, 6.6, 7.5, and 10.0 eV. Extrapolation of the first portion of the curve suggests that the ions formed at the first onset are thermal, thus excluding the occurrence of Reaction (44), which has a minimum enthalpy requirement of 1.8 eV,[36]

$$c\text{-}C_4F_8+e\rightarrow F^-+c\text{-}C_4F_7, \qquad (44)$$

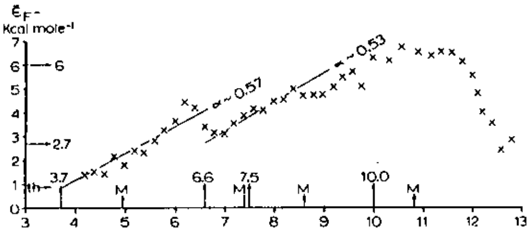

FIG. 17. Translational energy data for F^-/c-C_4F_8. Resonance onsets and their corresponding maxima (M) as determined in Ref. 35 are indicated by arrows protruding from the electron energy abscissa at the appropriate points.

$$c\text{-}C_4F_8+e\rightarrow F^-+F+c\text{-}C_4F_6, \qquad (45)$$

$$c\text{-}C_4F_8+e\rightarrow F^-+c\text{-}C_4F_7^{*}. \qquad (46)$$

Reaction (45) which has a minimum enthalpy requirement of 3.8 eV may be responsible for ion formation at 3.7 ±0.1 eV but this does not exclude the possibility of Reaction (46) involving an electronic transition of 1.9 eV for the C_4F_7 species, whether it be the heptafluorocyclobutyl radical or an isomer of it. This is also true for the higher energy onsets given in Tables XII and XIII. However, for the sake of completeness the various energetically acceptable reactions will be briefly mentioned. Taking the translational energy of the F^- ions formed at 6.6 eV as 2.7 kcal mole^{-1} and $\alpha=0.53$, E^* is calculated to be 2 eV. This assumes only two fragmentation products and would result in an electronic transition of 2.8 eV for process (46) but is also consistent with the energetics for Reaction (47) (Table XIII) and no distinction can be made;

$$c\text{-}C_4F_8+e\rightarrow F^-+CF_2CF+C_2F_4, \qquad (47)$$

$$c\text{-}C_4F_8+e\rightarrow F^-+CF_2+C_3F_5. \qquad (48)$$

The same arguments apply to the appearance potential at 10 eV where E^* is determined to be 4.6 eV from the data. Reaction (46), involving an electronic transition of 3.8 eV, or Reaction (48) which has a calculated minimum enthalpy requirement of 6.3 eV may be invoked to satisfy the reaction energetics and, again, no conclusion can be made as to which is responsible for the observed resonance data.

TABLE XI. Processes deduced and thermochemical parameters calculated for negative ion formation from C_3F_8.

Ion	AP (eV)	Reaction	E^* calc (eV)	ΔH_{min} (eV) Exptl	ΔH_{min} (eV) Calc	Parameter deduced
F^-	2.0±0.1	$C_3F_8+e\rightarrow F^-+n\text{-}C_3F_7$	0	2.0±0.1	1.9	$\Delta H_f(n\text{-}C_3F_7)=$ −305.4±7.0 kcal mole^{-1}
	~4.0	$C_3F_8+e\rightarrow F^-+C_3F_7^{*}$	0	~4.0	...	$C_3F_7^{*}$ 2.1→2.6 eV
		or $\rightarrow F^-+CF_3+C_2F_4$	0	~4.0	3.7	
		or $\rightarrow F^-+CF_2+C_2F_5$	0	~4.0	4.2	
CF_3^-	2.55±0.1	$C_3F_8+e\rightarrow CF_3^-+C_2F_5$	0.85±0.08	1.7±0.2	1.75	E.A. $(CF_3)=2.05\pm0.2$ eV $D(F_3C\text{–}C_2F_5)=4.6\pm0.3$ eV

TABLE XII. Experimental data for c-C_4F_8.

Ion	AP[a] (eV)	Res max[a] (eV)	σ_{max} (cm^2)	ε_t at AP (kcal mole^{-1})	α (slope)
F^-	3.7 ± 0.1	4.95 ± 0.1	9×10^{-19}	thermal	0.57
	6.6 ± 0.2	7.4 ± 0.2	2×10^{-19}	2.7	0.53
	7.5 ± 0.2	8.6 ± 0.2	4×10^{-19}	···	
	10.0 ± 0.2	10.8 ± 0.2	5×10^{-19}	6.0	
CF_3^-	3.85 ± 0.1	4.95 ± 0.1	10^{-21}	2.0 ± 0.2	0.78

[a]Taken from Ref. 34.

The CF_3^- ion is formed with 2.0 ± 0.2 kcal mole^{-1} translational energy at the resonance onset. Using this in conjunction with the experimental value of 0.78 for α, E^* is calculated to be 2.6 ± 0.3 eV for Reaction (49),

$$c\text{-}C_4F_8 + e \rightarrow CF_3^- + C_3F_5 . \tag{49}$$

The heat of formation of the C_3F_5 radical is estimated to be − 174 ± 10 kcal mole^{-1} from this data and may be compared to the *JANAF* estimate of − 159 kcal mole^{-1}.

CF_3^- ion formation must involve a rearrangement of the c-$C_4F_8^{-*}$ intermediate into a linear species prior to dissociation. The high value of α, consistent with a high degree of vibrational activation in the intermediate molecular negative ion state, is therefore not surprising in this case.

A summary of the c-C_4F_8 processes is given in Table XIII together with the thermochemical data deduced.

TABLE XIV. Values for α determined in this study.

Molecule	Ion	α	α Average
NF_3	F^-	0.43	0.44
BF_3	F^-	0.61	
	F_2^-	0.24	
CF_4	F^-	0.40	
		0.46	
	CF_3^-	0.33	
C_2F_6	F^-	0.28	
		0.26	
	CF_3^-	0.47	
C_3F_8	F^-	0.25	
	CF_3^-	0.60	
c-C_4F_8	F^-	0.57	
		0.53	
	CF_3^-	0.78	

CONCLUSION

The distribution and partitioning of excess energy in fragmentation processes is still not fully understood although such processes play a basic role in the chemistry of our atmosphere and numerous terrestrial phenomena. The intrinsic value of translational energy measurements as a prerequisite to accurate thermochemical data evaluation from positive and negative ionization efficiency data has been emphasized in the Introduction and is evident from the Results and Discussion section. A rigorous treatment of the reaction energetics is still beyond present theoretical models although the semiempirical approach used in this study is sufficiently reliable to provide valuable thermochemical data from the experimentally determined parameters. The unambiguous assignment of many dissociative capture reactions to measured appearance potentials has been possible and in many cases the formation of electronically excited neutral fragmentation products has been demonstrated or inferred. The formation of electronically excited neutrals may be a common occurrence in electron impact experiments. Besides the evidence presented here to support this suggestion, Wang and Franklin[28,38] have discussed electron impact and spectroscopic evidence for the formation of the electronically excited radicals SiF_3^* and GeF_3^* from SiF_4 and GeF_4, respectively.

Table XIV lists the values determined for α and the value averaged over the 14 capture processes investigated. The agreement between the average value 0.44 and those obtained previously from positive ion studies, 0.44,[2] and negative ion studies, 0.42,[5] leads us to the conclusion that use of such an average value for analysis of a large polyatomic molecule would not be much in error. However, α is not a constant and depends on the system studied. In these studies, the average translational energy increased linearly over the greater part of the resonance. This behavior has been observed for a large number of systems[1,28,38] including diatomic, triatomic, and more complex ones. It is of course possible that other systems will not behave in this way, but our

TABLE XIII. Processes deduced and thermochemical parameters calculated for negative ion formation from c-C_4F_8.

Ion	AP (eV)	Reaction	E^* calc (eV)	ΔH_{min} (eV) Exptl	ΔH_{min} (eV) Calc	Parameter deduced	
F^-	3.7 ± 0.1	c-$C_4F_8 + e \rightarrow F^- + C_4F_7^*$	0	3.7 ± 0.1	···	$C_4F_7^*$	~1.9
		or $\rightarrow F^- + F + c$-C_4F_6	0	3.7 ± 0.1	3.8		
	6.6 ± 0.2	c-$C_4F_8 + e \rightarrow F^- + C_4F_7^*$	2.0	4.6	···	$C_4F_7^*$	~2.8
		or $\rightarrow F^- + CF_2CF + C_2F_4$	2.0	4.6	4.5		
	7.5 ± 0.2						
	10.0 ± 0.2	c-$C_4F_8 + e \rightarrow F^- + C_4F_7^*$	4.6	5.6	···	$C_4F_7^*$	~3.8
		or $\rightarrow F^- + CF_2 + C_3F_5$	4.6	5.6	6.3		
CF_3^-	3.85 ± 0.1	c-$C_4F_8 + e \rightarrow CF_3^- + C_3F_5$	2.6 ± 0.3	1.25 ± 0.4	···	$\Delta H_f(C_3F_5) = -174$ kcal mole^{-1}	

studies have not thus far encountered one. These experimental conclusions provide considerable evidence to support the validity of Eq. (2). The classical expression, Eq. (1), provides a poor approximation to E^* which reflects the inadequacy of the assumptions inherent in its derivation. In this respect, the assumption of energy equilibration in the transition state prior to dissociation merits further comment. The experimental evidence indicates that the "effective" number of vibrational degrees of freedom in the transition state involved in dissociation is somewhat less than the total number available for absorption of the excess energy. The transition states involved in dissociative attachment processes can be described by a repulsive surface in the Franck–Condon region and the time available for complete energy equilibration may not be available. The transition state may attain the necessary geometrical configuration and the energy find itself in the reaction coordinate before equilibration is achieved, a picture consistent with our experimental observations. In this respect, our data for the triatomics CO_2 and SO_2 were consistent with the predictions of the classical equation within our experimental uncertainty.

A list of the thermochemical data deduced during this study is presented in Table XV. The heats of formation of the negative ions in this table have been determined from our experimental electron affinities and literature heats of formation for the neutral species involved; Table XVI lists such literature data used.

Finally, the reader must be aware of the limitations which restrict the usefulness of the time-of-flight method[39] for translational energy measurements. The assumption of Gaussian peak shapes inherent in the analysis limit the magnitude of the translational energy which can be accurately assessed. The broad peaks observed for the F^- ions formed from CF_4 are a clear example of this limitation which restricts the discussion of such energetic ions to a qualitative nature only. The complexity of the molecular system presents another limitation on this technique. When N is greater than about 25, the rate of increase of translational energy of an atomic negative ion with excess energy above onset is so small that the differences in the ion mass peak widths approach the experimental uncertainty involved in the measurements and considerable scatter results. If these limitations are respected, the use of this technique in conjunction with accurate appearance potential data and heats of formation provides a powerful tool for the investigation of the energetics of fragmentation processes.

TABLE XV. Thermochemical data evaluated in this study.

Parameter			Source
$\Delta H_f(NF_2^-)$	≃	8.8 kcal mole^{-1}	F^-/NF_3
E. A. (NF_2)	=	1.68 ± 0.21 eV	NF_2^-/NF_3
$\Delta H_f(NF_2^-)$[a]	=	−29.5 ± 7.5 kcal mole^{-1}	
E. A. (F_2)	=	2.94 ± 0.10 eV	F_2^-/NF_3
	=	2.86 ± 0.22 eV	F_2^-/BF_3
$\Delta H_f(F_2^-)$[b]	=	−68.0 ± 2.3 kcal mole^{-1}	
E. A. (CF_3)	=	2.2 ± 0.3 eV	CF_3^-/CF_4
	=	2.4 ± 0.5 eV	CF_3^-/C_2F_6
	=	2.05 ± 0.2 eV	CF_3^-/C_3F_8
$\Delta H_f(CF_3^-)$[c]	=	−163.4 ± 5.8 kcal mole^{-1}	
$BF_2^*(^2B_2)$	$\leftarrow BF_2(^2A_2)$	= 5.3 eV	F^-/BF_3
$\Delta H_f[(BF_2^*(^2B_2)]$	≃	−16.5 kcal mole^{-1}	
$D(F-C_2F_5)$	=	5.5 ± 0.2 eV	F^-/C_2F_6
$D(F_3C-CF_3)$	=	4.6 ± 0.6 eV	CF_3^-/C_2F_6
$D(F_3C-C_2F_5)$	=	4.6 ± 0.3 eV	CF_3^-/C_3F_8
$\Delta H_f(n\text{-}C_3F_7)$	=	−305.4 ± 7.0 kcal mole^{-1}	F^-/C_3F_8
$\Delta H_f(C_3F_5)$	=	−174 ± 10 kcal mole^{-1}	$CF_3^-/c\text{-}C_4F_8$

[a] Deduced using $\Delta H_f(NF_2) = 8.9 \pm$ kcal mole^{-1}, Table XVI.

[b] Value for E. A. (F_2) deduced from NF_3 data used because the thermochemical data are known more accurately for the NF_3 system.

[c] Used average value of E. A. $(CF_3) = 2.2 \pm 0.2$ eV in conjunction with value of -112.6 ± 1.2 kcal mole^{-1} for $\Delta H_f(CF_3)$, Table XVI.

TABLE XVI. Heats of formation in kilocalories per mole at 298 °K used in this study.

F	18.8	a	CF	58 ± 1	f
F^-	−59.48	a, Ref. 30	CF_2	−41.7 ± 0.4	f
F_2	0.0	b	CF_3	−112.6 ± 1.2	Ref. 30
N	112.98	a	CF_4	−222.87 ± 0.38	g
NF	57	a	C_2F_4	−154.5 ± 2.3	h
NF_2	8.9 ± 2.5	c	C_2F_5	−212	Ref. 35
NF_3	−31.6 ± 0.3	d	C_2F_6	−317.5 ± 3.5	i
BF	−29.2	a	C_3F_5	−159	j
BF_2	−138.9 ± 2.5	e	C_3F_6	−258.75	Ref. 35, k
BF_3	−271.75	a	$n\text{-}C_3F_7$	−306.5	Ref. 35
			$i\text{-}C_3F_7$	−319.9	Ref. 35
			C_3F_8	−411.0	Ref. 35
			C_4F_6	−224	l
			$c\text{-}C_4F_6$	−233	l
			$c\text{-}C_4F_8$	−362	m

[a] J. L. Franklin, J. G. Dillard, H. M. Rosenstock, J. T. Herron, K. Draxl, and F. H. Field, Natl. Std. Ref. Data Ser. 26 (1969).

[b] *JANAF Thermochemical Tables*, edited by D. R. Stull (Dow Chemical, Midland, MI 1965).

[c] A. Kennedey and C. B. Colburn, J. Chem. Phys. 35, 1892 (1961).

[d] $\Delta H_f(NF_3) = -31.6 \pm 0.3$ is the average of the following reported values: (i) -31.95 ± 1.3; J. R. Ludwig and W. J. Cooper, J. Chem. Eng. Data 18, 76 (1963). (ii) -31.75 ± 0.2; P. A. G. O'Hare, J. L. Settle, and W. H. Hubbard, Trans. Faraday Soc. 62, 558 (1966). (iii) -31.44 ± 0.3; G. C. Sinke, J. Phys. Chem. 70, 1326 (1966).

[e] R. D. Srivastava and M. Farber, Trans. Faraday Soc. 67, 2298 (1971).

[f] M. Farber, M. A. Frisch, and H. C. Ko, Trans. Faraday Soc. 65, 3202 (1969).

[g] E. S. Armstrong and G. T. Domalski, J. Res. Natl. Bur. Stand. U.S. A 71, 105 (1967); also, J. D. Cox, H. A. Gundry, and A. J. Head, Trans. Faraday Soc. 61, 1594 (1965).

[h] *JANAF* (see b); Ref. 35 gives −151.9; a gives −155.5.

[i] $\Delta H_f(C_2F_6) = -317.5 \pm 3.5$ is the average of the following reported values: (i) −316.5; Ref. 35. (ii) −318; G. C. Sinke, J. Phys. Chem. 70, 1326 (1966). (iii) −321; J. W. Coomber and E. Whittle, Trans. Faraday Soc. 63, 1398 (1967).

[j] *JANAF* (see b).

[k] *JANAF* gives −260 (see b).

[l] S. W. Benson and H. E. O'Neal, Natl. Std. Ref. Data Ser. XX (1970).

[m] *JANAF* (see b).

ACKNOWLEDGMENTS

The authors would like to express their appreciation for the support of The Robert A. Welch Foundation and one of us (P. W. H.) would like to acknowledge the Fulbright–Hays Fellowship Program and the United States–United Kingdom Educational Commission for the provision of a Traveling Scholarship.

*Present address: CSIRO, National Standards Laboratory, Division of Physics, University Grounds, City Road, Chippendale, NSW 2008; Australia.

[1] P. W. Harland, J. L. Franklin, and D. E. Carter, J. Chem. Phys. 58, 1430 (1973).

[2] M. A. Haney and J. L. Franklin, J. Chem. Phys., 48, 4093 (1968).

[3] C. E. Klots, J. Chem. Phys. 41, 117 (1964).

[4] E. L. Spotz, W. A. Seitz, and J. L. Franklin, J. Chem. Phys. 51, 5142 (1969).

[5] J. J. DeCorpo, D. A. Bafus, and J. L. Franklin, J. Chem. Phys. 54, 1592 (1971).

[6] (a) T. Holstein, Phys. Rev. 84, 1073 (1951). (b) T. F. O'Malley, Phys. Rev. 155, 59 (1967).

[7] (a) J. N. Bardsley, A. Herzenberg, and F. Mandl, *in Atomic Collision Processes*, edited by M. R. C. McDowell (North-Holland, Amsterdam, 1964), p. 417 (b) J. C. Y. Chen and J. L. Peacher, Phys. Rev. 163, 103 (1967).

[8] K. Kraus, Z. Naturforsch. 16, 1378 (1961).

[9] G. J. Schulz, Phys. Rev. 128, 178 (1962).

[10] L. G. Christophorou and J. A. D. Stockdale, J. Chem. Phys. 48, 1959 (1968).

[11] P. J. Chantry, Phys. Rev. 172, 125 (1968).

[12] J. D. Morrison, J. Chem. Phys. 39, 200 (1963).

[13] K. A. G. MacNeil and J. C. J. Thynne, Int. J. Mass Spectrom. Ion Phys. 3, 35 (1969).

[14] A. Kennedey and C. B. Colburn, J. Chem. Phys. 35, 1892 (1961).

[15] J. P. Simons, J. Chem. Soc. 1965, 5406.

[16] W. A. Chupka, J. Berkowitz, and D. Gutman, J. Chem. Phys. 55, 2724 (1971).

[17] R. M. Reese, V. H. Dibeler, and J. L. Franklin, J. Chem. Phys. 29, 880 (1958).

[18] R. M. Reese and V. H. Dibeler, J. Chem. Phys. 24, 1175 (1956).

[19] S. N. Foner and R. L. Hudson, J. Chem. Phys. 58, 581 (1973).

[20] K. A. G. MacNeil and J. C. J. Thynne, J. Phys. Chem. 74, 2257 (1970).

[21] J. A. D. Stockdale, R. D. Nelson, F. J. Davis, and R. N. Compton, J. Chem. Phys. 56, 3336 (1972).

[22] J. E. Hesser and K. Dressler, J. Chem. Phys. 47, 3443 (1967).

[22] (a) T. E. Sharp and J. T. Dowell, J. Chem. Phys. 50, 3024 (1969).

[23] G. Herzberg, *Electronic Spectra and Electronic Structure of Polyatomic Molecules* (Van Nostrand, New York, 1966).

[24] K. A. G. MacNeil and J. C. J. Thynne, Int. J. Mass Spectrom. Ion. Phys. 3, 445 (1970).

[25] F. M. Page and G. C. Goode, *Negative Ions and the Magnetron* (Wiley-Interscience, New York, 1969).

[26] K. A. G. MacNeil and J. C. J. Thynne, Int. J. Mass Spectrom. Ion Phys. 2, 1 (1969).

[27] J. W. Hastie and J. L. Margrave, J. Phys. Chem. 73, 1105 (1969).

[28] J. Ling-Fai Wang, J. L. Margrave, and J. L. Franklin, J. Chem. Phys. 58, 5417 (1973).

[29] M. M. Bibby and G. Carter, Trans. Faraday Soc. 59, 2455 (1963).

[30] R. Milstein and R. S. Berry, J. Chem. Phys. 55, 4146 (1971).

[31] J. W. Coomber and E. Whittle, Trans. Faraday Soc. 63, 1394 (1967).

[32] V. H. Dibeler, R. M. Reese, and F. L. Mohler, J. Res. Natl. Bur. Stand. 57, 113 (1956).

[33] C. Lifshitz and R. Grajower, Int. J. Mass Spectrom. Ion Phys. 3, 211 (1969).

[34] P. W. Harland and J. C. J. Thynne, Int. J. Mass Spectrom. Ion Phys. 9, 253 (1972).

[35] W. M. D. Bryant, J. Polym. Sci. 56, 277 (1962).

[36] P. W. Harland and J. C. J. Thynne, Int. J. Mass Spectrom. Ion Phys. 10, 11 (1973).

[37] C. Lifshitz and R. Grajower, Int. J. Mass Spectrom. Ion Phys. 10, 25 (1973).

[38] J. Ling-Fai Wang, J. L. Margrave, and J. L. Franklin, J. Chem. Phys. 60, 2158 (1974).

[39] J. L. Franklin, P. M. Hierl, and D. A. Whan, J. Chem. Phys. 47, 3148 (1967).

Advances in Mass Spectrometry 6, 319-325 (1974)

36

Studies of the Energies of Negative Ions at High Temperatures

By J. L. FRANKLIN, JOHN LING-FAI WANG,
S. L. BENNETT, P. W. HARLAND and
J. L. MARGRAVE

(Department of Chemistry, Rice University, Houston, Texas, U.S.A.)

INTRODUCTION

NEGATIVE ions formed in the gas phase from inorganic compounds have been studied relatively little and those from materials that vaporize only at elevated temperatures have been almost completely neglected. However, it would be expected that various of the metallic halides, oxides, sulphides, nitrates, etc. would form negative ions under the appropriate conditions and that considerable information of interest might be obtained from them. This study has been undertaken to separate negative ions from inorganic materials at high temperatures by dissociative resonance capture processes and to determine their thermochemistry.

When an electron of the proper energy contacts a molecule it may form an unstable ion that will break up in one or more ways in a very short time, thus

$$e + \mathrm{ABC} \rightarrow \mathrm{ABC}^{-*} \rightarrow \mathrm{A}^- + \mathrm{BC}$$

If the dissociation asymptote for A^- falls opposite the intersection of the potential energy curve with the Franck–Condon region, it is possible to detect the decomposition products in their ground states. The appearance potential can then be taken as the heat of reaction. If the dissociation asymptote falls below the intersection of the potential energy curve with the Franck–Condon region the appearance potential will include some excess energy which must be detected and deducted in order to obtain the heat of reaction. A portion of any excess energy that is involved will appear as translational energy of the products and this is readily measured. It has been shown by Haney and Franklin[1] with positive ions and by DeCorpo, Bafus and Franklin[2] with negative ions, that the average total translational energy at onset, $\bar{\varepsilon}_t$, is related to the total excess energy, E^*, by the equation

$$E^* = \alpha N \bar{\varepsilon}_t \tag{1}$$

where N is the number of vibrational modes and α is an empirically determined constant having an average value of 0·43. $\bar{\varepsilon}_t$ is obtained from the measured value $\bar{\varepsilon}_i$, the translational energy of the ion by means of the equation

$$\bar{\varepsilon}_i = \frac{m_i}{m_i + m_n} \times 3/2\, kT + \frac{m_n}{m_i + m_n}\,\bar{\varepsilon}_t \tag{2}$$

It has subsequently been shown[3] that α in eqn (1) may vary considerably from compound to compound. However, by measuring the translational energy in a dissociative resonance capture process, as a function of the electron energy (and hence of E^*) α can be determined for each process, and considerable improvement in accuracy achieved.

EXPERIMENTAL

A Bendix time-of-flight mass spectrometer model 14-107, modified with a Bendix model 3015 output scanner was used in these studies. Neutral molecules were generated in a Bendix Knudsen Cell Sample Inset System with a tantalum cell/Lucalox liner holding the solid sample for heating by a tungsten wire filament through either radiation or electron bombardment. The temperature of the cell was determined with a tungsten/tungsten-26% rhenium thermocouple inserted in the base of the cell. Gaseous samples were introduced through a conventional handling system.

Appearance potentials were determined by deconvolution of the ion intensities with the MacNeil–Thynne modification[4] of Morrison's[5] method. The electron energy scale was calibrated with O^-/CO, O^-/CO_2, O^-/SO_2 and F^-/SF_6 and the energy distribution of the ionizing electrons was determined from SF_6^-/SF_6 to be approximately 0·8 eV full width at half maximum. Translational energies were determined from peak shape analysis by the method of Franklin, Hierl and Whan.[6]

For each of the solids investigated the sample was thoroughly degassed and then the temperature of the Knudsen cell increased slowly until shutterable negative ions were observed. The temperature was then further increased until the intensity of the ions was sufficient to permit measurement of the appearance potential and, where possible, the translational energies of the ions.

RESULTS AND DISCUSSION

Figure 1 gives a typical dissociative resonance capture curve (for F^- from GeF_4) along with a plot of the average translational energy of F^- as a function of electron energy. The vertical arrow shows the appearance potential obtained after deconvolution. The translational energy of F^- at onset is 3·5 kcal/mole. The marked flattening of the translational energy at about 6 kcal/mole is due to the fact that at this energy, the more energetic ions begin to strike the wall and are not collected. Over a range of nearly one volt of electron energy the translational energy increases linearly with electron energy. This is characteristic of the behaviour of all of the systems studied. From the slope of the line we compute α for this process to be 0·56 and with

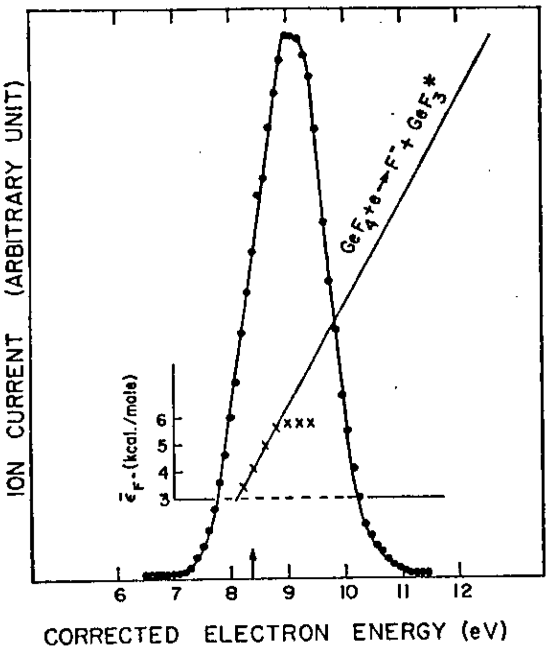

FIG. 1 Resonance and translational energy of F^- ion from GeF_4.

this and the translational energy at onset the excess energy is computed to be 18 kcal/mole.

Group IV Fluorides

The electron affinities of the MF_3 radicals from the Group IV fluorides, except SnF_4, and the heats of formation of the corresponding MF_3^- ions have been similarly determined and the results given in Table I.

Since CF_4, SiF_4 and GeF_4 are gases the measurements were made on them at room temperature. SnF_4 and PbF_4 are solids and had to be vaporized from the Knudsen cell at a temperature of about 520°C.

TABLE I

Thermochemistry of MF_3^- from Group IV Fluorides (kcal/mole).

	Ap	$\bar{\varepsilon}_t$	α	E^*	$\Delta H_f(MF_3^-)$	$EA(MF_3)$
$CF_4 + e \rightarrow CF_3^- + F$	125	15·3	0·33[a]	46	−163·3	50·7
$SiF_4 + e \rightarrow SiF_3^- + F$	247	33	0·43[b]	123	−281	47
$GeF_4 + e \rightarrow GeF_3^- + F$	187	23	0·43[b]	88	−205	37
$SnF_4 + e \rightarrow SnF_3^- + F$	115	—	—	(?)	−156[c]	5[c]
$PbF_4 + e \rightarrow PbF_3^- + F$	5	Thermal	—	0	−212	100

[a] Determined from the slope of ε_i versus electronvolt line.

[b] Taken as the average value at onset.

[c] Experimental values. See text for more probable values.

It is noteworthy that the carbon, silicon and germanium compounds all involved large amounts of excess energy at onset. PbF_3^-, which was formed at a very low appearance potential, appeared to be formed with thermal energy. SnF_3^- was formed with very low intensity and this combined with the multiplicity of interfering isotopic species made it impossible to measure the translational energy of the ion. It is evident from Table I that $\Delta H_f(SnF_3^-)$ should be about −212 kcal/mole and, when this is combined with $\Delta H_f(SnF_3)$ of −151 kcal/mole (see below), we estimate the electron affinity to be approximately 61 kcal/mole. This value is, of course, speculative, but appears reasonable in the light of the other values.

TABLE II

Processes and Energies (kcal/mole) for the Formation of F^- from the Group IV Fluorides.

	Ap	$\bar{\varepsilon}_t$	α	$E^*_{v,t}$	$\Delta H_f(MF_3)$	E^*_{el}
$CF_4 + e \rightarrow F^- + CF_3$	111	19·6	0·43[a]	74·1	−120	—
$SiF_4 + e \rightarrow F^- + SiF_3^*$	246	8·4	0·43[a]	32	−235	128
$GeF_4 + e \rightarrow F^- + GeF_3^*$	194	3·5	0·56[b]	18	−168	123
$SnF_4 + e \rightarrow F^- + SnF_3^*$	124	Thermal	—	0	(−63)[c]	88
$PbF_4 + e \rightarrow F^- + PbF_3$	21	Thermal	—	0	−112	0

[a] Average values at onset.
[b] From the slope of the curve of $\bar{\varepsilon}_i$ against eV.
[c] Experimental value which includes E^*_{el}.

The most intense ion from all of the Group IV fluorides is F^- and our measurements on it are given in Table II. Considerable amounts of translational energy were found with the first three members of the group and so the total excess translational and vibrational energy, $E^*_{v,t}$, was large with each of these. The tin and lead compounds gave F^- with thermal energy at onset. The heat of formation of CF_3 is in fair agreement with the accepted value of −112·4 kcal/mole.[7] This is not true of the silicon, germanium and tin compounds. Thus, in the case of SiF_4 the thermochemical equation for the reaction fails to balance unless an allowance is made for electronic excitation of the SiF_3 product, *i.e.*

$$SiF_4 + e = F^- + SiF_3 - (Ap - E^*_{v,t} - E^*_{el})$$
$$-386 = -65 - 235 - (246 - 32 - E^*_{el})$$

from which E^*_{el} is found to be 128 kcal/mole or about 5·5 eV. Wang, Krishnan and Margrave[8] have reported a value of 5·47 eV for the energy of the electronic transition $^2B \rightarrow X^2A$ in SiF_3, in excellent agreement with our determination. It should be mentioned that there is strong evidence for a similar excited electronic state of CF_3 which falls in the same resonance region as the one reported above. Similarly, one would expect GeF_3 to be formed in an electronically excited state. When we combine our appearance potential corrected for $E^*_{v,t}$ and apply Wang, Krishnan and Margrave's[9] energy of 5·37 eV for the $^2B - {}^2A$ transition of GeF_3, we compute $\Delta H_f(GeF_3)$ to be −168 kcal/mole.

TABLE III

Thermochemical Values (kcal/mole) of Negative Ions from Arsenic.

	Ap	α (slope)	$\bar{\varepsilon}_t$	E^*	ΔH_f (ion)	EA
$As_4 + e \rightarrow As_2^- + As_2$	70 ± 1·2	0·43	6·9 ± 0·7	17·8 ± 0·7	43·8 ± 4·1	2·3 ± 2·3
$As_4 + e \rightarrow As_3^- + As$	81 ± 2·3	0·43	4·1 ± 0·9	10·6 ± 0·9	38·1 ± 5·2	18·8 ± 7
$As_4 + e \rightarrow As^- + As_3$	83 ± 2·3	0·43	4·5 ± 0·7	11·5 ± 0·7	56·9 ± 4·9[a]	—

[a] Neutral As_3 combined with $\Delta H_f(As_3^-)$ gives $EA(As_3)$ to be 18·8 ± 7 kcal/mole.

The F^- ion from PbF_4 is formed with thermal energy at an appearance potential of only 0·9 eV. It is apparent that this process yields PbF_3 in the ground electronic state and the computed heat of formation is -112 kcal/mole. From the appearance potential of F^- from SnF_4, it seems probable that the process results in an electronically excited SnF_3. Unfortunately, there is no reliable value of $\Delta H_f(SnF_3)$ which we can use to compute E^*_{el}. From the sequence $D(F{-}MF_3)$ of 130, 170, 135 and 105 for C, Si, Ge and Pb, a reasonable estimate of $D(F{-}SnF_3)$ would be about 120 kcal/mole which would give $\Delta H_f(SnF_3)$ to be -151 kcal/mole. Since Ap F^-/SnF_4 gives $\Delta H_f(SnF_3)$ to be -63 kcal/mole, we would then estimate the energy of the $^2B - {}^2A$ transition to be about 88 kcal/mole. The result, while speculative, is not unreasonable.

In further support of the idea that the neutral fragment in certain dissociative resonance capture processes may be electronically excited, we cite other observations of similar behaviour. Thus, Harland, Carter and Franklin[10] attributed the second resonance of O^-/SO_2 to the $^1\Delta$ state of SO, and Petty *et al.*[11] found that the MF_2 neutrals formed along with F^- ion from the Group III fluorides were electronically excited. Indeed, it now appears that this is a phenomenon that will frequently be experienced.

Arsenic

Arsenic vapour at about 520°C is made up principally of As_4 with small amounts of As_2 also present. As will be seen in Table III, there are three

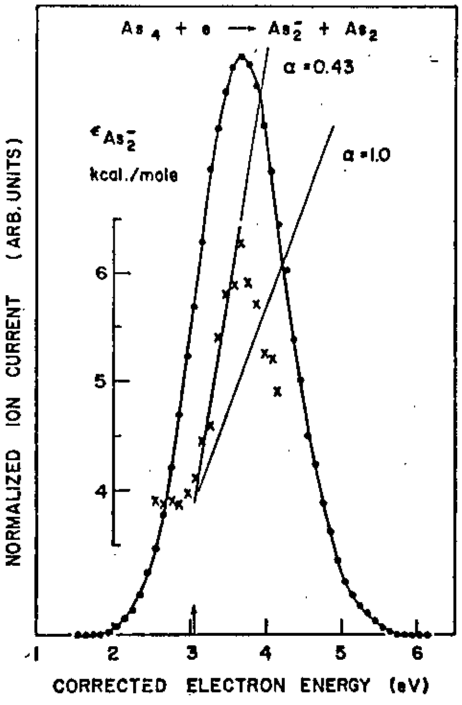

FIG. 2 Resonance and translational energy of As_2^- from As_4.

negative ions formed by dissociative resonance capture, all in our experiment from As_4.

As will be seen in Fig. 2, the translational energy of As_2^- rises linearly over the greater part of the resonance and then breaks downward sharply. The downward break is attributable to an instrumental artifact. The slope of the upward portion of the line gives a value of α in eqn (1) of 0·43. Similar behaviour was observed with As^- and As_3^-. From the computed E^* and Murray, Pupp and Pottie's[12] value of 54·26 kcal/mole for $D(As_4 - As_2)$, we compute the electron affinity of As_2 to be 0·1 eV.

As_3^- can come only from As_4 and its heat of formation is $-38{\cdot}1 \pm 5{\cdot}2$ kcal/mole. $\Delta H_f(As_3)$ has not previously been determined. Combining our appearance potential and excess energy measurement with Feldman's[13] recent value of $0{\cdot}75 \pm 0{\cdot}10$ eV for the electron affinity of As yields $\Delta H_f(As_3)$ to be $56{\cdot}9 \pm 4{\cdot}9$ kcal/mole and $EA(As_3) = 18{\cdot}7 \pm 7$ kcal/mole (0·8 eV). Thus, the electron affinities of As and As_3 are very nearly the same and are considerably greater than that of As_2.

It will be evident from Table III that all three of the processes studied involved considerable excess energy and that serious errors would have resulted had it not been possible to determine and correct for it.

ACKNOWLEDGMENT

The authors are pleased to acknowledge the support of this work by the Office of Naval Research, U.S. Navy, under Contract No. 67-A-0145-0002.

REFERENCES

1. Haney, M. A. and Franklin, J. L., *J. Chem. Phys.*, 1968, **48**, 4093.
2. DeCorpo, J. J., Bafus, D. A. and Franklin, J. L., *J. Chem. Phys.*, 1971, **54**, 1592.
3. Harland, P. W. and Franklin, J. L., to be published.
4. MacNeil, K. A. G. and Thynne, J. C. J., *Int. J. Mass Spectrom. Ion Phys.*, 1969, **3**, 35.
5. Morrison, J. D., *J. Chem. Phys.* 1963, **39**, 200.
6. Franklin, J. L., Hierl, P. M. and Whan, D. A., *J. Chem. Phys.*, 1967, **47**, 3148.
7. JANAF Tables, D. R. Stull, Ed., 1970.
8. Ling-Fai Wang, J., Krishnan, C. N. and Margrave, J. L., *J. Mol. Spectros.*, to be published.
9. Ling-Fai Wang, J., Krishnan, C. N. and Margrave, J. L., to be published.
10. Harland, P. W., Franklin, J. L. and Carter, D. E., *J. Chem. Phys.*, 1973, **58**, 1430.
11. Petty, F., Ling-Fai Wang, J., Steiger, R. P., Harland, P. W., Franklin, J. L. and Margrave, J. L., *High Temp. Science*, 1973, **5**, 25.
12. Murray, J. J., Pupp, C. and Pottie, R. F., *J. Chem. Phys.*, 1973, **58**, 2569.
13. Feldman, D., Reported by W. C. Lineberger at Conference of American Society for Mass Spectrometry, San Francisco, Calif., May, 1973.

Copyright 1974. All rights reserved

Reprinted from
ANNUAL REVIEW OF PHYSICAL CHEMISTRY
Volume 25, 1974

GASEOUS NEGATIVE IONS

*2595

J. L. Franklin
Department of Chemistry, Rice University, Houston, Texas 77001

Peter W. Harland
Division of Physics, National Standards Laboratory, Chippendale, Australia

INTRODUCTION

This article is intended to cover a wide range of gaseous negative ion studies and briefly describe experimental techniques, their objectives and, where possible, their relative merits and limitations. This is done in two parts: the first concerned with low pressure experiments, i.e. those conducted under single collision conditions, and the second with high pressure experiments and ion-molecule reactions. The theoretical approaches to negative ion resonances and the theoretical calculations of electron affinities are not discussed in detail, but sources of this information are presented. The relevance of negative ions and their chemistry in the solar system, the atmosphere, and terrestial phenomena are not included, as such details can be readily obtained elsewhere (1).

NEGATIVE ION MASS SPECTRA

Negative ion mass spectra, which are generally much simpler than positive ion spectra, have received little attention. Flesch & Svec (2) constructed a small scale model of a dual horizontal plane 60° magnetic sector mass spectrometer capable of simultaneously detecting and recording positive and negative ion mass spectra with a mass resolution of 60. A study of CF_2Cl_2 with this instrument, however, identified Cl^- as the only species in the negative ion mass spectrum. Later publications using a large scale instrument with a resolution of 200 include much improved data for chromyl fluoride and chromyl chloride (3, 4).

Thynne et al (5, 6) have tabulated and discussed the negative ion mass spectra of several polyatomic molecules and later presented and discussed several negative ion mass spectra (7–11).

SUMMARY OF REVIEWS PUBLISHED SINCE 1950

The review articles summarized in this section are listed in the bibliography (12–27). The first of these reviews in chronological order, the monograph on *Negative Ions* by Massey in 1950 (12), is a landmark in the field and provides an authoritative introduction to the theoretical implications and the mechanistics of negative ion formation. Pritchard's review (13) includes an excellent historical review of the experimental techniques prior to 1953 and their inherent limitations. Particular attention is directed to the estimation of electron affinities from lattice energy calculations and surface ionization or equilibrium studies. With the exception of the halide atoms, the electron affinities favored at that time are quite different from currently accepted values, as will be evident from comparisons of the tabulations given by Pritchard (13) and those included in the reviews by Branscomb in 1962 (14) and Moiseiwitsch in 1965 (15). The later review (15) is primarily devoted to detailed descriptions of the empirical and semi-empirical extrapolation methods and to quantum mechanical calculations for atomic species and the H_2^- ion.

A 1965 review of the theoretical approaches resulting in expressions for the calculation of atomic electron affinities by Smirnov (16) includes informative comparisons between computed and experimental atomic electron affinities. An excellent review of "Resonant Scattering of Electrons by Molecules" by Bardsley & Mandl (17) in 1968 covers qualitative and theoretical concepts of associative and dissociative resonance attachment. Resonances are classified into shape resonances and Feshbach resonance types followed by a discussion of experimentally observed resonances in terms of the classification. Resonance scattering theory is reviewed in some detail and the advantages and limitations of each approach considered. An earlier paper by Taylor et al (18) in 1966 also expounds useful qualitative descriptions for resonant electron attachment. Two distinct types of resonances in atoms and molecules are recognized from analogies to nuclear physics, core-excited and single particle resonances, synonymous with the electron-excited Feshbach and shape resonances of Bardsley & Mandl (17). The paper by Taylor et al (18) is devoted primarily to atomic systems, whereas that of Bardsley & Mandl (17) relates to both atomic and polyatomic systems.

A review of "Small Free Negative Ions" by Berry (19) in 1969 considers atomic species and in particular the hydride, halide, and oxygen ions. The optical photodetachment methods used to determine electron affinities are discussed in detail and other less precise techniques in outline. A tabulation of electron affinities includes 18 polyatomic species.

The proceedings of a conference on laboratory measurements of aeronomic interest contain several contributions which make reference to various negative ion measurements (20a–20c).

Several reviews of electron affinities and electron attachment phenomena have been presented by Christophorou et al (21–25), including a 1971 book entitled *Atomic and Molecular Radiation Physics* by Christophorou (1). Two chapters of this publication are devoted entirely to negative ions and many more indirect references to related negative ion phenomena appear throughout the text. This book is highly recommended and contains excellent tables of atomic and molecular electron affinities. The table of molecular electron affinities is weighted toward the heavier and biologically interesting molecules, particularly the aromatic and multiring molecules and derivatives, which therefore are not listed in this review. Hasted's book (26) devotes one chapter to negative ions. Finally, the review of "Negative Ion Mass Spectrometry" by Dillard (27) in 1973 is directed toward polyatomic ions, concentrating on the analytical aspects, evaluation of thermochemical data, and the use of mass spectrometry in structural analysis; it includes an extensive review of the literature.

ENERGY SPREAD IN ELECTRON BEAMS

A common feature of all ionization studies is a source of ionizing radiation which must be of variable incident energy and sufficient flux density to create measurable ion signals. Electron beams generated from heated filaments, usually tungsten, rhenium, or iridium wire (often thoria coated to reduce surface temperature and to enhance emission characteristics) have been used almost exclusively in the experiments discussed in this article.

Electron beams generated from heated filaments possess a Maxwell-Boltzman distribution of energies in the range 1.0 to 1.5 eV width at half maximum. When such a beam is used to ionize a gas sample, an energy-integrated ion signal about the nominal electron energy is obtained. Appearance potentials become smeared out and any fine structure which may be present is obscured. This energy spread thus poses a limit on the resolution and scope of the experiment conducted. This type of electron source, however, has the advantage of high stability and high electron densities which are important ingredients for negative ion investigations when electron capture cross sections rarely exceed 10^{-16} cm^2.

Early attempts to resolve this problem met with limited success, but fine structure in the ionization efficiency curves of some positive ions was observed. In 1939 Nottingham (28), using a magnetic selector, observed fine structure in the ionization efficiency curves of Hg^+. Sugden & Price (29) in 1948 used a photoelectron beam in the study of aldehydes and ketones, and in 1954 Clarke (30) obtained an energy spread of 0.2 eV using a 127° electrostatic selector enabling fine structure in the curves of N_2^+ and N^+ from nitrogen to be observed.

Two types of electrostatic velocity selectors have received attention in recent years. Parallel plate selectors, of the type used by Hutchison (31) in 1963, suffer from poor transmission which, although tolerable for positive ion investigations, is unsuitable for negative ion studies. The 127° electrostatic selector, however, was improved in 1960 by Marmet & Kerwin (32), who obtained a beam of 10^{-7} A with an energy spread of 0.02 eV. This selector was successfully applied by Marmet & Morrison (33) in 1962, and the difficulties they experienced have now been largely overcome in the advanced design of Brion et al (34, 35) in 1964 and 1966. Brion has used this selector in 1969 to study electron attachment processes in the group VI hexafluorides (36). Using an electron beam with an energy spread of 0.1 eV, the SF_6^- resonance appears as a facsimile of the electron energy distribution reversed on the energy scale, and the SF_5^- resonance consists of two overlapping resonances in the 0–1.0 eV range. A similar study of tetracyanoethylene has also been published (37). In the absence of counting equipment and long averaging times, a balance between low transmission and high resolution imposes severe limitations on the application of this technique to negative ion studies.

The most widely used method is the retarding potential difference (RPD) technique of Fox et al (38–40). In this, an extra grid, the retarding electrode, is added to the conventional electron gun and is biased slightly negative (~ 0.5 V) with respect to the filament, resulting in a sharp, low energy cutoff in the beam profile. This bias is then increased by a small amount, ΔV (typically 0.1 V), resulting in the removal of a further energy slice of width ΔV. The resulting change in ion current Δi, which occurs when ΔV is applied, is then attributed to the band of electrons homogeneous in energy to within ΔV eV. Significant improvements by Cloutier & Schiff (41) in 1959, and automation by Stockdale et al (42) in 1969, Chantry (43) in 1969, and in 1973 by Lifshitz et al (44) have removed the tedium from RPD operation.

Although the RPD approach offers a convenient method for obtaining a quasi-monoenergetic electron source, frequent ambiguities arise in data interpretation. Partial relaxation of the sharp cutoff due to space-charge effects in the ion source (45), negative difference currents (40), nonlinear variation of ion signal with electron energy and spurious maxima in ionization efficiency curves (46, 47), and resonance focusing described by Simpson (48) have all been discussed by Gordon et al (49) in 1969 in terms of a theoretical model developed for the RPD gun.

Despite the automation introduced, RPD still requires long and careful adjustments to the ion source. Noise is a serious problem because it results from the total transmitted electron current rather than the difference in electron current, whereas the differential ion signal has greatly reduced intensity. Applicability to conventional mass spectrometers without major structural modifications is a big advantage of this method and, when used in conjunction with signal averaging equipment, RPD is one of the best quasi-monoenergetic electron sources available for negative ion studies.

A recent innovation is the trochoidal electron monochromator of Stamatovic & Schulz (50). This device overcomes the noise problems inherent in the RPD technique and delivers an improved energy distribution with a half-width of about 0.02 eV at 10^{-10} A transmission. Electrons emitted from a thoria-coated iridium filament and aligned by a magnetic field of 100 G enter the monochromator off-axis by 0.3 mm through two collimating orifices. The beam is dispersed and describes a trochoidal motion in the electric field maintained between two parallel plates. Electrons with a specific velocity reach the axis and are transmitted through a series of plates into the collision chamber. Although long averaging times (15 hr for C^- from CO) are required for negative ion signals, Stamatovic & Schulz (51) have used this device coupled to a quadrupole mass filter to examine dissociative resonance attachment in carbon monoxide with good results.

A further approach to this problem has been the use of analytical methods to remove or reduce the energy spread of the electron beam. In 1963 Morrison (52) applied a deconvolution method to positive ion formation and showed, from tests on several artificial examples and two actual cases, that the method was promising and suggested structure in the ionization efficiency curves of the inert gases and of oxygen. Morrison considered two methods for the deconvolution procedure: the iterative equations of van Cittert (53) and the use of Fourier transforms. Both approaches offer advantages and disadvantages, but in both iterative smoothing of the original function is essential to the recovery of quantitative data. Ioup & Thomas (54) investigated in 1967 the two methods and found the iterative method preferable for the analysis of noisy data and for cases in which the position of the function on the energy axis is required. The Fourier method proved particularly suitable for treatment of very smooth data, but single stage unfolding was found to result in a sudden disastrous increase in the noise level. Iterative deconvolution is accompanied by a gradual buildup of noise with each successive step. Termination before the noise becomes restrictive is then possible. MacNeil & Thynne (55) applied the iterative deconvolution techniques to negative ion resonance curves in 1969. Tests on artificial functions yielded an accurate recovery of appearance potentials, resonance peak maxima and widths, and also showed that the amount of random noise which could be introduced without an adverse effect far exceeded that expected in data acquisition. The application of this method to real systems (56) in 1970 revealed hidden resonances in broad capture curves and resulted in more accurate estimation of thermochemical data.

The applicability of deconvolution to different experimental techniques has been discussed by Dromey & Morrison (57) in 1970, and an automated time averaging deconvolution method has since been developed by Morrison and co-workers (58, 59). Inverse convolution utilizing the Fourier method has been applied to low resolution mass spectra by Dromey & Morrison (60) in 1971 and to ionization efficiency curves by Vogt & Pascul (61) in 1972.

Deconvolution offers the advantage of requiring neither instrument modifications nor physical manipulation of the electron beam, which can thus be used without loss in intensity. This method requires knowledge of the electron energy profile, usually obtained by reversing the SF_6^- attachment curve on the energy scale, and only partially removes the effect of the distribution; i.e. 15 smoothing and 20 deconvolution iterations reduce an electron energy distribution with a natural width of 1 eV to an effective width of 0.3 eV.

Winters et al's (62, 63) energy distribution difference (EDD) method has met with some success for positive ion applications. This technique has found little application to negative ion studies and an evaluation of EDD and deconvolution by Giessner & Meisels (64) showed deconvolution to be superior for conventional instruments where the simple quasi-Boltzman distribution does not suffice to describe the instrument function.

ELECTRON ATTACHMENT PROCESSES

When a low energy electron (less than ~ 100 eV) interacts with a molecule under single collision conditions, depending on the energy of the electron and the nature of the molecule, negative ions may be produced by (*a*) associative resonance capture (thermal electrons), (*b*) dissociative resonance capture (0–15 eV electrons), and (*c*) pair production (> 10 eV). All processes may produce vibrationally excited products and *b* and *c* can also produce translationally excited ones. This review is primarily concerned with the first two processes. Photodetachment, used for the determination of precise atomic electron affinities and radical and molecule vertical detachment energies, is also discussed and an up-to-date table of electron affinities included.

ASSOCIATIVE RESONANCE ATTACHMENT

In the absence of collisional stabilization, associative resonance attachment results in the formation of metastable molecular ions exhibiting autodetachment lifetimes in the range 10^{-15}–10^{-3} sec which decay by electron detachment and, in some cases, by spontaneous dissociation. Such resonances are narrow and, depending on their lifetimes, are observed by different experimental techniques. The shorter-lived species are indirectly observed by inelastic electron scattering and the longer-lived species by collisional stabilization or conventional mass spectrometric techniques. Qualitative descriptions and theoretical discussions are given by Massey (12), Taylor et al (18), Bardsley & Mardl (17), and Christophorou (1). A semitheoretical model was presented by Compton et al (65) in 1966. In this, the principle of detailed balance is invoked to derive an expression which relates the average autodetachment lifetime, the associative attachment cross section, and the electron affinity. Using experimental determinations of the former two parameters, a lower limit to the molecular electron affinity can be calculated if the vibrational frequencies for the neutral molecule (assumed equivalent to the ion) are known. This model is described in more detail below.

Resonances exhibited by transient molecular negative ions with lifetimes too short for conventional mass spectrometric techniques, $\leq 10^{-6}$ sec, have been measured by various methods including the trapped electron, inelastic electron scattering, SF_6 scavenging methods, and a recent photoelectron spectroscopic method. Transient negative ion states are important intermediaries in the vibrational excitation of neutral molecules under electron impact and the first two techniques are particularly suited to the accurate determination of vibrational excitation functions.

TRAPPED ELECTRON METHOD

This method was developed by Schulz (66) in 1958 and consists basically of an RPD electron gun with two concentric cylinders along the axis of the electron beam. A trapping potential well depth of ~ 0.1 eV is created through field penetration between the electron collection cylinder and the mesh grid cylinder composing the collision chamber wall. Energy resolution of better than 0.2 eV was achieved with the first apparatus, and complete electronic energy spectra were obtained for He, Hg, and H_2. The technique was extended by Schulz (67) in 1959 to permit control of the well depth up to 4 V, thereby facilitating the study of excitation functions to this level above threshold. Transient negative ion states were identified in N_2 and CO at 2.3 and 1.7 eV, respectively, and N_2O at 2 eV (68). The latter correlates with the formation of O^- from N_2O by dissociative resonance capture at this energy.

An automated version of Schulz's apparatus claiming an energy resolution of better than 0.1 eV was described by Brongersma & Oosterhoff (69) in 1967, and in 1969 Bensimon et al (70) succeeded in resolving vibrational structure up to $V = 6$ for the N_2^- state at 2.3 eV, suggesting an autodetachment lifetime $> 10^{-12}$ sec. Schulz et al (71) have restudied N_2 and CO with improved resolution and measured the vibrational structure in the resonance. Pisanias et al (72) have used this method with quinoline, isoquinoline, and naphthalene. Two resonances below 2 eV were found in each molecule and evidence for vibrational structure obtained.

ELECTRON TRANSMISSION SPECTROSCOPY

The derivative of the transmitted electron current from an RPD source reflects any temporary negative ion resonances with a resolution adequate for the measurement of vibrational structure. Boness et al (73) observed vibrational structure in the energy range 1.0–1.8 eV for temporary negative ion resonances in CH_4, C_2H_4, and C_6H_6 and obtained well-resolved vibrational progressions for the resonance states of N_2^-, CO^-, NO^-, and O_2^- (74). Sanche & Schulz (75–78) have used this method extensively to measure vibrational progressions and Rydberg series of O_2^-, NO^- (75), the rare gases (76), diatomic molecules (77), triatomics, and hydrocarbons (78). The spacings and Franck-Condon factors for O_2^- and NO^- agreed respectively with those of $O_2^+(^4\pi_u^*)$ and $NO^+(X^1\Sigma^+)$, indicating that these states consist of two Rydberg electrons loosely attached to the ion core. Similar conclusions also apply to the negative ion states of the inert gases, N_2, CO, H_2O, H_2S, N_2O, CO_2, and C_2H_4. Broad and featureless shape resonances[1] were also identified for N_2O, H_2S, and C_2H_4, all below 6 eV.

SULFUR HEXAFLUORIDE SCAVENGING TECHNIQUE

SF_6 undergoes associative attachment of thermal electrons with a high cross section (79–81), $\sim 10^{-14}$ cm^2, exhibiting a narrow resonance (the full width at half maximum $\leq$ 0.02 eV) (50). Curran (82) exploited the electron scavenging property of SF_6 as a detector for thermalized electrons produced by the inelastic scattering of an electron beam off a target gas. Using a mass spectrometer equipped with a high pressure ion source (20 μ SF_6 and 180 μ Hg N_2) and an RPD gun, Curran (82) was able to reproduce the electronic energy level data for N_2 in agreement with those reported by Schulz (67) using the trapped electron method. This technique can be applied using any negative ion mass spectrometer equipped with a high pressure source. Because of the ease of application this method has been used extensively for studying energy loss spectra and many new transient molecular negative ion states of polyatomic molecules have been identified (83–91).

PHOTOELECTRON SPECTROSCOPIC METHOD

Price et al (92) observed anomalous peaks in the photoelectron spectra of certain diatomic and triatomic molecules at elevated ionization chamber pressures. These peaks were attributed to collisions between emitted photoelectrons (monochromatic) and neutral molecules leading to the formation of temporary negative ion states. Both vibrational excitation and resonant electron transmission phenomena are reported with a resolution (10–20 mV) superior to that obtained with the above electron impact methods. Irradiation of argon, ionization potentials (IPs) 15.76 ($^2P_{3/2}$) and 15.94 eV ($^2P_{1/2}$), or N_2, IP 18.75 eV, with helium resonance radiation, 21.22 eV, results in the liberation of monochromatic electrons of energy 5.46 and 5.28 or 2.47 eV, respectively. Inelastic collision losses of these electrons with a high density sample gas, such as N_2, may then occur. The transient molecular negative ions so formed are unstable and re-emit the electron with a quantized energy loss reflecting the vibrational energy level spacings of the neutral molecule.

[1] Shape resonances occur when the negative ion is formed by the incoming electron moving in the field of the target ground state. A combination of polarization, exchange, and centrifugal barrier effects lead to the electron being trapped for a short time. The resulting potential is considerably weaker than that of core-excited resonances, and it exhibits broad resonances. Lifetimes vary from 10^{-10} sec for O_2^- to 10^{-15} sec for H_2^-.

Using different inert gases to provide the monochromatic electrons, the potential energy surface of the neutral molecule can be probed and the vibrational excitation functions mapped. In a complementary experiment a polyatomic molecule that gives rise to a broad continuous spectrum, such as CH_4 or C_5H_{12}, is introduced into the ionization chamber with the N_2 and the subsequent absorptions from the continuous background reflect the vibrational energy level spacings in the N_2^- ion. Price et al (92) have deduced a potential surface to fit the experimental observations which are consistent with a maximum cross section for absorption for electron impact at 2.2 ± 0.1 eV as observed by Schulz (67, 71). Linewidth analysis indicated a lifetime of approximately 2×10^{-14} sec for $N_2^{-*}(^2\Pi_g)$. This method has considerable potential both as a source of monochromatic electrons and as an accurate means for investigating the potential energy surfaces of amenable species.

Transient molecular negative ions with lifetimes in the intermediate range, $\sim 10^{-7}$–10^{-10} sec, can be observed following collisional stabilization in a swarm beam apparatus or a mass spectrometer. Longer-lived species, lifetimes $\geq 10^{-6}$ sec, can be observed directly using a mass spectrometer with suitable transit time characteristics. The existence of long-lived ($> 10^{-6}$ sec) negative ions was first demonstrated in 1962 by Edelson et al (93), who showed that the SF_6^- has an average autodetachment lifetime of approximately 10 μsec. Asundi & Craggs (94) and Hickam & Fox (95) suggested that the energy of the captured electron is shared among the many degrees of freedom of the molecule for a time amenable to mass spectrometric observation. Compton et al (65, 96) extended the number of long-lived molecular negative ions to include $C_6H_5NO_2^-$, $(CHO)_2^-$, $(CH_3CO)_2^-$, and several perfluorocarbons with autodetachment lifetimes from 2.5 μsec for $(CHO)_2^-$ to 800 μsec for c-$C_6F_{11}CF_3^-$. Compton et al (65) also considered the energy to be redistributed throughout the ion, thus requiring some time before relocation of the energy into a mode favorable to autodetachment. The proposed model relates the attachment cross section (σ_a), the average autodetachment lifetime (T_a), and the molecular electron affinity (EA) at equilibrium through the expression

$$T_a = \rho^-/\rho^0(1/v\sigma_a) \qquad 1.$$

where ρ^- and ρ^0 are the respective densities of states for the ion and its fragments of relative velocity v. Measurement of T_a and σ_a and a knowledge of the vibrational frequencies can then be used to calculate the electron affinity, which is the dominant parameter in the term ρ^-/ρ^0. This model has been discussed by Compton et al (65), Collins (97), and Klots (98) in 1967.

The attachment cross sections used in such calculations have been determined by the combination swarm-beam method of Christophorou et al (99) described in (1). Harland & Thynne (100) determined relative cross sections by comparing the cross sections ion signals to that of SF_6 whose absolute cross section is known (81). "Long-lived" molecular negative ions have been extensively investigated by Compton, Christophorou, and co-workers. These studies include attachment in the field of the ground and excited electronic states (101, 102), the energy dependence of cross sections and lifetimes (103, 104), and the formation of metastable CO_2^- from molecules containing the carboxylic grouping in the correct stereospecific configuration (105). Theoretical papers on CO_2^- have been presented by Krauss & Neumann (106) and by Taylor et al (107).

SURFACE EQUILIBRIUM STUDIES

The Magnetron method for the determination of electron affinities is a development of the original method of Mayer et al (108–110) by Page and co-workers (111–119). The Magnetron consists of a co-axial triode-type valve, with the filament along the axis and the co-axial anode on the outside, mounted in a solenoid coil. In the absence of the magnetic field the thermionically emitted electrons and the negative ions pass through the grid and are collected by the anode. Following the application of a sufficiently intense magnetic field, the electrons move in circular paths and are collected by the grid, whereas the ions continue to be collected at the anode. The ratio of the anode currents at a series of filament temperatures can then be used to deduce the electron affinity of the attaching species. Page and co-workers have compiled an impressive list of electron affinities using this technique which have been published in book form by Page & Goode (119). In the absence of mass identification, however, some of the values deduced using this method are subject to unknown uncertainties.

A similar technique has been used by Fine & Scheer (120, 121) in the determination of the electron affinities for molybdenum, tungsten, and rhenium (see Table 1).

A technique developed by Wentworth et al (122–132) uses a gas chromatographic detector designed by Lovelock (133) to examine electron scavenging by polyatomic molecules. Using the cell in the pulsed mode, called the pulse sampling technique (125), 17–19 keV electrons emitted from a tritium-β foil are thermalized in a buffer gas of CH_4/Ar mixtures. Following a 1 msec stabilization period, a 0.4 μsec sampling pulse is applied and the electrons in the cell are collected. The experiment is repeated after a trace of the material under investigation has been admitted to the cell through a gas chromatograph and the difference in the electron current is attributed to loss by electron attachment. From a study of the temperature dependence of capture on electron affinities, activation energies and, in some cases, details on dissociative capture processes have been deduced. Although Wentworth (134) uses elaborate gas chromatographic purification procedures, trace contaminants pose a difficult problem generally unrecognized by other workers in this area. Electron affinities determined by Wentworth's method, mainly for aromatic molecules, have been listed (1) and are not included in Table 1 of electron affinities.

Table 1 Experimental atomic, radical, and molecular electron affinities[a]

m/e	Species	Electron affinity (eV)	Ref.	Method	Year
1	H	0.75415	(197)	C	1962
		0.756 ± 0.130	(198)	AS	1964
		0.77	(199)	C	1969
		0.776 ± 0.050	(186)	P	1970
4	He	0.080 ± 0.002	(200)	P	1967
7	Li	$0.65 < EA < 1.05$	(201)	SI	1969
		0.62	(199, 202)	C	1968, 1969
12	C	1.2	(203)	S	1954
		1.25 ± 0.03	(173)	P	1962‡
		1.29	(199)	C	1969
	C*	$< 0.5 \pm 0.05$	(186)	P	1970
13	CH	≥ 1.4	(204)	EI	1937
		~ 1.65	(205)	EI	1958
		0.74 ± 0.05	(186)	P	1970
14	CH_2	-0.95	(205)	EI	1958
15	CH_3	1.08	(119)	SI	1969
16	O	1.5	(206)	EI	1964
		1.461 ± 0.024	(207)	P	1965
		1.478 ± 0.002	(208)	P	1968‡
		1.42–1.35	(119)	SI	1969
16	NH_2	1.21 or 1.12	(119)	SI	1969
		0.74	(185)	P	1971
		0.744 ± 0.022	(209)	P	1972‡
17	OH	1.80	(210)	EI	1966
		1.78 – 1.82	(119, 211)	SI	1966
		1.83 ± 0.04	(182)	P	1966
		1.91	(212)	C	1967
		1.94	(213)	P	1969
19	F	3.448 ± 0.005	(158)	P	1963
		3.400 ± 0.002	(214, 215)	ES	1965, 1967‡
		3.45	(119)	SI	1966
		3.50	(199)	C	1969
		3.398 ± 0.002	(216)	AS	1971‡

[a] The species for which only calculated values are available are listed at the bottom of the table. The list of atomic electron affinities is incomplete, as previous reviews (e.g. 1) have included such tabulations. Aromatic molecules and their derivatives have been discussed in detail by Christophorou (1, 24) and have been omitted from this table.

Table 1 (*continued*)

m/e	Species	Electron affinity (eV)	Ref.	Method	Year
24	C_2	3.10 ± 1.00	(203)	EI	1954
		3.54 ± 0.05	(186)	P	1970
25	C_2H	2.70	(119)	SI	1969
		3.73 ± 0.05	(186)	P	1970
		2.2	(217)	CT	1972
		2.16 ± 0.4	(192)	ECT	1973
26	CN	3.6 ± 0.4	(13)	LE	1953
		3.7 ± 0.2	(218)	SI	1959
		3.2 ± 0.17	(219)	EI	1960
		3.16 ± 0.04	(119, 220)	SI	1968, 1969
		3.82 ± 0.02	(221)	PI	1969‡
		3.2	(145)	EI	1971
30	NO	0.87	(222)	CT	1961
		0.9 ± 0.1	(118)	SI	1964
		≥ 0.86	(223)	EI	1968
		≥ 0.65	(224)	EI	1969
		0.83	(119)	SI	1969
		0.09	(225)	ECT	1971
		$0.024^{+0.010}_{-0.005}$	(226)	P	1972
		0.015 ± 0.1	(192)	ECT	1973
31	CF	≥ 3.3	(227)	EI	1970
32	O_2	0.95 ± 0.07	(13)	LE	1953
		0.15 ± 0.05	(228)	P	1958
		~ 0.15	(229)	C	1959
		≥ 0.58	(230)	EI	1961
		0.43 ± 0.02	(231, 232)	EA	1961, 1966‡
		≥ 1.1	(224)	EI	1969
		> 1.2	(190, 233)	CT	1969
		$1.05 < O_2 < \sim 1.2$	(234)	CT	1970
		≥ 0.48	(225)	ECT	1971
		$\geq 0.45 \pm 0.1$	(235)	ECT	1971
		0.43 ± 0.03	(236)	P	1971‡
		$\geq 0.46 \pm 0.05$	(237)	MB	1971
		0.42	(238)	C	1972
32	S	2.07 ± 0.07	(177)	P	1956
		1.81	(119)	SI	1969
		2.0772 ± 0.0005	(184)	P	1970‡

Table 1 (*continued*)

m/e	Species	Electron affinity (eV)	Ref.	Method	Year
33	SH	≥ 1.8	(239)	EI	1961
		2.25	(212)	C	1967
		2.319 ± 0.010	(240)	P	1968
		2.19	(119)	SI	1969
		2.28 ± 0.15	(213)	P	1969
33	PH_2	1.60	(119)	SI	1969
		1.25 ± 0.03	(185, 241)	P	1971, 1972
35	Cl	3.613 ± 0.003	(158)	P	1963‡
		3.48, 3.70	(111, 242)	SI	1960, 1966
35	OF	$\geq 1.4 \pm 0.5$	(243)	EI	1970
36	C_3	1.8	(203)	S	1954
38	F_2	~ 3.0	(244)	EI	1958
		~ 2.8	(55)	EI	1969
		2.9 ± 0.22	(146)	EI	1971
		3.08 ± 0.10	(195)	ECT	1971
		2.94 ± 0.10	(149)	EI	1973
42	NCO	~ 1.56	(245)	EI	1968
		$\geq 2.6 \pm 0.4$	(246)	EI	1971
44	CS	≤ 1.2	(247)	EI	1969
45	FCN	$\geq 2.8 \pm 1.7$	(246)	EI	1971
46	NO_2	$\geq 3.82 \pm 0.06$	(248)	EI	1962
		3.9	(210)	EI	1966
		3.91	(119)	SI	1969
		$2.32 \geq NO_2 \geq 1.83$	(249)	CT	1969
		3.10 ± 0.05	(250)	P	1969
		2.45	(251)	CI	1970
		< 3.9	(252)	P	1970
		2.7 ± 0.2	(253)	CI	1971
		2.04	(225)	ECT	1971
		2.5 ± 0.1	(254)	CI	1972
		2.38 ± 0.06	(191)	CT	1972
		2.28 ± 0.10 2.30 ± 0.15	(192)	ECT	1973
		2.50 ± 0.05	(193)	MB	1973
47	CFO	~ 2.7	(55)	EI	1969
		~ 3.3	(256)	EI	1970
48	SO	≥ 1.1	(239)	EI	1961
		1.09 ± 0.05	(186)	P	1970
		1.1	(147)	EI	1973

Table 1 (*continued*)

m/e	Species	Electron affinity (eV)	Ref.	Method	Year
48	O_3	2.89	(257)	EA	1950
		~ 3.0	(230)	EI	1961
		$3.06 \geq O_3 \geq 1.96$	(225)	ECT	1971
50	CF_2	2.65	(119)	SI	1969
		≥ 0.2	(227)	EI	1970
		≤ 1.3 ± 0.8	(8)	EI	1972
52	NF_2	3.0	(119)	SI	1969
		1.58 ± 0.21	(149)	EI	1973
54	FCl	1.5 ± 0.4	(258)	EI	1969
		≥ 1.04	(258)	C	1969
58	SCN	3.51	(245)	EI	1968
		2.17	(119)	SI	1969
59	CH_3CO_2	3.3	(210)	EI	1966
		3.36	(128)	EA	1968
60	CO_3	1.8 ± 0.2	(187)	P	1972
62	NO_3	3.88	(259)	LE	1947
		≥ 2.48	(39)	CT	1971
64	S_2	≥ 0.84	(260)	EI	1968
64	SO_2	$1.12 > SO_2 > 1.0$	(189)	EI	1961
		1.0 ± 0.5	(186)	P	1970
		0.99	(192)	ECT	1973
65	C_5H_5	≤ 2.2 ± 0.3	(261)	EI	1972
69	CF_3	1.74 – 2.21	(119)	SI	1969
		~ 2.0	(262)	EI	1969
		1.8 ± 0.2	(243)	EI	1970
		2.1 ± 0.3	(227)	EI	1970
		2.2 ± 0.3 2.05 ± 0.2	(149)	EI	1973
70	Cl_2	2.5 ± 0.5	(251)	CI	1970
		2.52 ± 0.17	(146)	EI	1971
		2.38 ± 0.10	(195)	ECT	1971
		2.3, 2.45, 2.5	(254)	CT	1972
		2.35 ± 0.15	(191)	CT	1972
		2.32 ± 0.10	(192)	ECT	1973
76	CS_2	$1.12 > CS_2 > 1.0$	(189)	CT	1961
		0.5 ± 0.2	(192)	ECT	1973
77	AsH_2	1.27 ± 0.03	(209)	P	1972
78	$CO_3 \cdot H_2O$	2.1 ± 0.2	(187)	P	1972
80	Br	3.363 ± 0.003	(158)	P	1963‡
80	SeH	≤ 2.8 ± 0.5	(263)	C	1970
		2.21 ± 0.03	(264)	P	1972

Table 1 (*continued*)

m/e	Species	Electron affinity (eV)	Ref.	Method	Year
81	C_2F_3	2.0 ± 0.2	(227)	EI	1970
		2.0 ± 0.4	(265)	EI	1972
85	CF_3O	1.35	(119)	SI	1969
		1.9 ± 0.1	(243)	EI	1970
		≥ 1.9 ± 0.2	(266)	EI	1972
89	SF_3	2.71	(119)	SI	1969
		2.95 ± 0.05	(100)	EI	1971
96	Mo	1.0 ± 0.2	(120, 121)	SI	1967
97	CF_3CO	≤ 0.6	(256)	EI	1970
98	$SiCl_2$	≥ 2.6	(267)	EI	1947
99	CF_3NO	≥ 2.1 ± 0.3	(246)	EI	1971
108	SF_4	≥ 1.2	(246)	EA, C	1971
117	CCl_3	≥ 2.10 ± 0.35	(268)	EI	1961
		1.22	(119)	SI	1969
119	C_2F_5	~ 2.4	(269)	EI	1951
		~ 2.4	(270)	EI	1969
		~ 2.3	(262)	EI	1969
		2.2 ± 0.3	(246)	EI	1971
		2.1 ± 0.2	(7)	EI	1972
123	$C_6H_5NO_2$	≥ 0.4	(65)	EA, C	1966
		≥ 0.7 ± 0.2	(196)	ECT	1973
127	I	3.17	(112, 119)	SI	1961
		3.076 ± 0.005	(179)	P	1962
		3.063 ± 0.003	(158)	P	1963‡
127	SF_5	~ 3.39	(271)	EI	1961
		3.66 ± 0.04	(117)	SI	1964
		≥ 2.8 ± 0.1	(196)	ECT	1973
128	$C_2(CN)_4$	2.88 ± 0.06	(119)	SI	1969
131	C_3F_5	2.5 ± 0.3	(246)	EI	1971
		2.6 ± 0.4	(265)	EI	1972
		2.7 ± 0.2	(7)	EI	1972
146	SF_6	≥ 1.1	(65)	EA, C	1966
		1.43	(119)	SI	1969
		≥ 1.29	(102)	EA, C	1970
		≥ 1.4	(246)	EA, C	1971
		≥ 0.6 ± 0.1	(196)	ECT	1973
150	As_2	0.1 ± 0.18	(403)	EI	1973
152	CCl_4	2.06	(119)	SI	1969

Table 1 (*continued*)

m/e	Species	Electron affinity (eV)	Ref.	Method	Year
160	Br_2	2.3 ± 0.1	(170)	CI	1969
		2.87 ± 0.14	(146)	EI	1971
		2.51 ± 0.10	(195)	ECT	1971
		2.6, 2.55	(254)	CI	1972
		2.62 ± 0.2	(192)	ECT	1973
162	ICl	1.43	(222)	CT	1961
169	C_3F_7	1.99	(119)	SI	1969
		~ 2.4	(262)	EI	1969
		2.2 ± 0.2	(246)	EI	1971
		2.3 ± 0.2	(7)	EI	1972
181	C_4F_7	2.69	(119)	SI	1969
		2.6 ± 0.5	(246)	EI	1971
184	W	0.5 ± 0.3	(120, 121)	SI	1967
186	Re	0.15 ± 0.10	(120, 121)	SI	1967
186	C_6F_6	1.20	(119)	SI	1969
		≥ 0.2	(246)	EA, C	1971
		≥ 1.8 ± 0.3	(196)	ECT	1973
200	C_4F_8-2	≥ 0.7	(196)	ECT	1973
200	c-C_4F_8	≥ 0.4	(196)	ECT	1973
207	IBr	2.7 ± 0.2	(195)	ECT	1971
225	As_3	0.84 ± 0.35	(403)	EI	1973
231	C_5F_9	~ 3.1	(170)	EI	1970
		3.1 ± 0.3	(246)	EI	1971
236	C_7F_8	≥ 1.7 ± 0.3	(196)	ECT	1973
254	I_2	2.6 ± 0.1	(146)	EI	1971
		2.58 ± 0.10	(195)	ECT	1971
		2.5, 2.55, 2.3, 2.54	(254)	CI	1972
		2.42 ± 0.2	(192)	ECT	1973
260	WF_4	≥ 2.3	(272)	EI	1973
262	c-C_6F_{10}	≥ 1.4 ± 0.3	(196)	ECT	1973
279	WF_5	0.8 ± 0.2	(272)	EI	1973
298	WF_6	2.74	(119)	SI	1969
353	UF_6	2.91	(119)	SI	1969
Species for which only theoretical derivations of the election affinity are available					
2	H_2	−2.85	(273)		1936
		−3.58	(274)		1956
		−0.72	(205)		1958

Table 1 (*continued*)

m/e	Species	Electron affinity (eV)	Ref.	Method	Year
23	Na	0.54	(202)		1968
		0.35	(199)		1969
33	NF	0.6 ± 0.5	(275)		1971
39	K	0.47	(202)		1968
		0.30	(199)		1969
46	NS	1.3 ± 0.3	(255)		1971
50	PF	1.4 ± 0.3	(275)		1971
51	SF	2.5 ± 0.5	(263)		1970

Method key:

AS = absorption spectroscopy
C = calculation
CI = chemical ionization
CT = charge transfer
EA = electron attachment (equilibrium methods and low energy impact)
EA, C = calculations based on experimentally determined autodetachment lifetimes, attachment cross sections, and available vibrational frequencies (65)
ECT = endothermic charge transfer
EI = electron impact
ES = emission spectra
LE = lattice energies [only a few values included, see Pritchard (13)]
MB = molecular beam techniques
P = photodetachment
PI = photoionization mass spectrometry
PS = pulse-sampling method [Wentworth et al (122–133)]
S = sublimation
SI = surface ionization [magnetron technique (119)]
‡ = values frequently used in the literature

DISSOCIATIVE RESONANCE ATTACHMENT

Dissociative resonance attachment is considered to take place as follows:

$$AB + e \rightleftharpoons AB^{-*} \longrightarrow A^{-} + B \qquad 2.$$

Holstein (135) proposed that the cross section for dissociative electron attachment, σ_{da}, be given by the product of the cross section for capture into a repulsive state of the molecular ion, σ_a, and the probability, e^{-T_s/T_a}, that AB^{-*} will then dissociate without autodetachment, i.e.

$$\sigma_{da} = \sigma_a e^{-T_s/T_a} \qquad 3.$$

where T_a is the autodetachment lifetime. The survival time, T_s, is the time taken for the dissociating negative ion to cross the potential energy surface of the neutral. Recent theoretical treatments of dissociative attachment, e.g. O'Malley (136, 137) based on the resonance scattering theory of Feshbach (138, 139), have provided an explicit expression for σ_a in Holstein's equation. O'Malley's (136, 137) treatment predicts the isotope effects of σ_{da} observed by Rapp et al (140) and the striking temperature effects observed for O_2 by Fite et al (141, 142). Christophorou & Stockdale (143) have classified dissociative attachment reactions into three categories on the basis of a plot of the log dissociative attachment cross sections at resonance maximum, *ln* $\sigma_{da}(E_{max})$, against the resonance energy, E_{max}, for over 30 molecules. Each category has a distinct range for the ratio T_s/T_a in Holstein's (135) equation and consequently involves different degrees of isotope effect on σ_{da}.

ELECTRON IMPACT MASS SPECTROMETRY

The basic apparatus used in these studies includes an electron gun, a collision chamber where ions are formed, a mass analyzer, and an electron multiplier with associated electronics for ion measurements. The electron gun may be one of the quasi-monochromatic types and the instrument may or may not operate in a pulsed mode. The time-of-flight mass spectrometer has been used extensively in negative ion studies and is particularly suitable for studies of metastable ions. This, and other types of mass spectrometers have been described in some detail by Kiser (144) in 1965, and the reader is referred to this text for further details.

An evaluation of the energetics of negative ion formation by dissociative resonance capture processes can provide a wealth of thermochemical information such as electron affinities and heats of formation for radicals, ions, and molecules, which would otherwise be difficult to obtain.

$$AB + e \longrightarrow A^- + B \qquad 4.$$

$$\Delta H_{min} = A_p - E_e = \Delta H_f(A^-) + \Delta H_f(B) - \Delta H_f(AB) \qquad 5.$$

or

$$A_p = D(A - B) - EA(A) + E_e \qquad 6.$$

Where ΔH_{min} is enthalpy of reaction, A_p is appearance potential, and E_e, the excess energy, is the sum of the electronic, vibrational, rotational, and translational energies. Accurate determination of an unknown thermochemical parameter depends upon the accurate determination of both A_p and E_e. Partitioning of excess energy among the various degrees of freedom in polyatomic molecular ion intermediates is the subject of much discussion (147, 149–153) and the importance of this problem cannot be overemphasized. The absence of vibrational and rotational excitation in the dissociative capture products of a diatomic molecule greatly simplifies this problem, and in most cases electronic excitation can be inferred from the appearance potential. The excess energy term is then reduced to ϵ_t, the translational energy distributed between the dissociation products. Early attempts to measure translational energies conducted by Tate & Lozier (154, 155) and by Blewett (156) used a retarding potential method in a total ionization apparatus. This approach was highly successful and may be illustrated by Buchdahl's (157) determination of 3.0 ± 0.2 eV for the electron affinity of the iodine atom. The presently accepted photodetachment value is 3.063 ± 0.003 eV (158).

The difficulties of experimental measurements of the excess energy terms in polyatomic molecules have been largely responsible for their neglect and appearance potentials have been used to estimate limiting values for unknown parameters. Chantry & Schulz (159) have pointed out the importance of including the thermal motion of the target gas when applying translational energy corrections, and Chantry (160) has demonstrated the potency of combined appearance potential and translational energy measurements for analyses of reaction energetics. Haney & Franklin (161) used a time-of-flight technique (162) to measure the translational energy of the positive ion fragmentation products of 16 reactions and proposed an empirical relationship based on the quasi-equilibrium theory of Rosenstock et al (163, 164) for partitioning the excess energy among the various degrees of freedom of the intermediate molecular ion

$$E^* = \bar{\epsilon}_t \, \alpha N = A_p - \Delta H_{\min} \qquad 7.$$

In this expression, E^* is the excess energy, excluding electronic excitation and corrected for the thermal motion of the target gas; $\bar{\epsilon}_t$ is the total average translational energy distributed between the dissociation products; α is an experimentally determined coefficient less than unity which has the effect of reducing N, the vibrational degrees of freedom for the molecular ion, to an effective number of degrees of freedom. Experimental determinations of $\bar{\epsilon}_t$, using the time-of-flight method, and α are used to calculate E^* which is combined with the appearance potential, determined by deconvolution of the experimental resonance curve, to obtain a value for $\Delta H_{\min}$, the minimum enthalpy requirement for the process (137, 139). Franklin and co-workers have used this approach to evaluate the energetics of dissociative resonance attachment in diatomic (146, 147, 165), triatomic (147), and a wide variety of polyatomic (145, 148, 149, 166, 167, 402, 403) molecules. The rate of change of ion translational energy, as a function of excess energy above the resonance threshold, is found to be constant and to vary from one dissociative attachment process to the next. Abrupt changes in the translational energy over the resonances have been attributed to contributions from competing reactions and in some cases to the appearance of electronically excited neutral products. In such cases where spectroscopic information is available, agreement exists with the electronic energy spacings deduced from this method. Accurate electron affinities (and ground state heats of formation) have been determined and included in Table 1.

The effect of temperature on attachment cross sections has been studied for O^- formed from O_2 by Fite et al (141, 142), for O^- formation from N_2O by Chantry (168) and Chaney & Christophorou (169), for some perfluorocarbons by Lifshitz et al (170), and for a group of partially halogenated methane derivatives and sulfur hexafluoride by Spence & Schulz (171).

Fite et al (141, 142) have found the resonance maximum and onset for O^- from O_2 to be reduced by 1 and 2 eV, respectively, when the temperature is increased to 2100°K. O'Malley (137) has confirmed this by a semi-empirical method. The change was attributed to the increase in nuclear separation with increasing vibrational excitation. This also brings about a reduction in survival time with a consequent increase in cross section. Thus between 87 and 1040°K the cross section for O^- formation from N_2O increases from $< 10^{-19}$ to $\sim 10^{-15}$ cm^2 (168). Ferguson et al (172) have discussed the formation of the N_2O^{-*} ion and suggested that a geometric deformation of the neutral N_2O molecule would be necessary. The results of Chantry (168) and of Chaney & Christophorou (169) support these suggestions, the activation energy for deformation determining the temperature dependence of the cross section. The $(^2\Pi)$ N_2O^- state having a bond angle of ~ 134° is involved. The O^- ion exhibits a second resonance maximizing at 2.3 eV which is independent of temperature and is postulated to result from the linear $N_2O^-(^2\Sigma)$ state.

ELECTRON AFFINITY DETERMINATIONS

The measurement of electron affinities has proved a formidable task. Tabulations of up-to-date values may show significant annual changes as different techniques are applied to the same problem. Atomic electron affinities can now be measured accurately using the photodetachment method which may also yield adiabatic electron affinities for some small radicals. The majority of known radical electron affinities, however, have been determined by electron impact and surface equilibrium techniques and are accordingly limited in accuracy. The only electronically excited negative ion reported is C^{-*}, probably the ^2D state corresponding to the first excited level of the isoelectronic nitrogen atom, from the photodetachment studies of Seman & Branscomb (173). Further excited states are predicted from the extrapolation techniques (174–176) based on the assumption that the energies of isoelectronic species having different nuclear charge Z can be expressed in terms of Z plus a number of parameters specific to the configuration. The following states so predicted have not yet been experimentally verified: $Al^-(^1D)$, $Si^-(^2D)$, $Si^-(^2P)$, and $P^-(^1D)$.[2]

PHOTODETACHMENT

Branscomb & Smith (177) developed a crossed negative ion-photon beam apparatus at the National Bureau of Standards (NBS) which incorporated a double focusing mass spectrometer, a xenon-arc lamp, and a monochromator with phase-sensitive detection. A beam of mass analyzed negative ions generated

---

[2] Indirect experimental evidence for this state has recently been obtained (402).

in a discharge ion source was crossed with a modulated high intensity monochromatic light beam of variable frequency. The attenuation of the negative ion signal when the photon energy equals the binding energy of the extra electron is then determined and yields the electron affinity. Berry (19) and Christophorou (1) have discussed the threshold behavior. The NBS apparatus has yielded electron affinities of C (173), O (178), S (177), I (179), O_2 (180, 181), OH (182), and SH (183).

Lineberger & Woodward (184) used a tunable dye laser in place of Branscomb's arc lamp source to improve the accuracy of the electron affinity determination.

Smyth et al (185) used an ion cyclotron resonance spectrometer in place of Branscomb's mass spectrometer and the photon beam generated by a tunable dye laser was directed along the length of the analyzer cell. The electron affinities determined by these authors and by Feldmann (186) and Burt (187), using variations of Branscomb's technique, are included in Table 1.

Berry & Riemann (158) developed a different photodetachment technique to determine accurate electron affinities for the halogen and oxygen atoms. Halide negative ions were generated from their alkali halide salts in shock heated argon. A flash lamp source of continuous radiation is triggered by the wave in the shock tube and the absorption spectrum recorded photographically on a spectrograph. In the case of O^- the experiments were conducted at higher temperatures due to low ion currents in the shock tube and the emission spectrum for the process $O + e \rightarrow O^- + h\nu$ recorded. An accuracy of ±5 mV is claimed with this technique and the electron affinities determined are included in Table 1.

CHARGE TRANSFER

Charge transfer (or charge exchange) reactions are conducted in the high pressure source of a mass spectrometer or other suitable apparatus and provide information on the relative electron affinities of reactant and target species (188–191). A series of charge transfer reactions carried out using a combination of reactant ions of known electron affinity and target species can be used to compile a table of relative values from which an unknown electron affinity may be estimated. Thus, the fact that EA(NO_2) is greater than that of O (188), S, or SH (191) and less than that of Cl or Cl_2 (191) results in EA(NO_2) ≈ 2.3 eV in accord with the most recently published values: 2.28 ± 0.10 (192), 2.30 ± 0.15 (192), and 2.50 ± 0.05 eV (193). Such a favorable series of reactant ions with reasonably established electron affinities converging on that of the target gas is not typical and usually only limiting values are reported.

A recent development of this method is endothermic or endoergic charge transfer. The reaction is initiated by increasing the translational energy of the reactant ion beam until the secondary ion is detected. Following the application of instrumental corrections (192, 194) the electron affinity of the target gas is deduced from the charge transfer cross-section threshold. This technique has been used by Chupka et al (195) for the halogen molecules and by Tiernan et al (192, 194, 196) for a number of diatomic, triatomic, and selected fluorocarbon molecules.

Polyatomic negative ions produced by electron impact may be vibrationally excited and, in the case of molecular negative ions, undergo rapid autodetachment. The excess energy involved in a charge exchange collision is shared between the two scattered particles and consequently molecular negative ions in low lying vibrational states can be produced and used in subsequent reactions. Such results can then be compared with electron impact data to obtain information on the reactivity of vibrationally excited species.

Electron affinities determined by endothermic charge transfer and selected values deduced by conventional charge transfer are included in Table 1.

ION-MOLECULE REACTIONS

Introduction

Ions react readily upon collision with many neutral atoms or molecules. Such ion-molecule reactions were observed and a few identified (276, 373) in the earliest days of mass spectrometry. Interest lapsed, however, and was not revived until the mid-1950s when several laboratories undertook investigations, principally of positive ion-molecule reactions. The surprising nature of several of the reactions observed and their very large rate constants induced many mass spectrometrists to study ion-molecule reactions so that the literature expanded explosively. In the intervening years several reviews of the subject have been published, starting with Lampe et al (374). Chapters in books have been written by Stevenson (375), Melton (376), and Futrell (377). A symposium on ion-molecule reactions was held as part of the American Chemical Society meeting in 1966 and the papers published as a book (378). Recently, books by McDaniel et al (309) and a collection of review papers edited by Franklin (310) have been devoted entirely to ion-molecule reaction and present the current state of the subject in considerable detail. None of these reviews is devoted exclusively to reactions of negative ions, but they do include these as part of the general subject. In addition, there have been several reviews of specific aspects of the field, especially those of aeronomic importance (379, 380) and summaries of results by specific methods such as the ion cyclotron resonance (381) and flowing afterglow (382) techniques.

Experimental Methods

The first "modern" study of a negative ion reaction was that of Muschlitz (277) who used a molecular beam apparatus to study the reaction $H^-(H_2O, H_2)OH^-$. This was followed rapidly by reports of Melton & Rupp (278) of the reaction

$HCO_2^-(N_2, HNO_2)CN^-$ and of Henglein & Muccini (279) of several reactions. They studied abstraction of I atoms from several iodides by O^-; H^+ and H_2^+ transfer reactions of O^- with nitro methane, and charge exchange reactions of O^- with NO_2, of SO^- with SO_2, and of $C_6H_5NO_2^-$ with SO_2. They determined the rate constant of each of these reactions and found them to be comparable in magnitude with those of positive ion molecule reactions.

Early studies of ion molecule reactions were made with the ionization chamber of a mass spectrometer as the reactor. These instruments used continuous extraction of the ions so that the collision energy varied over the ion path in the source. This procedure was incapable of providing rate constants of thermal ions, and at the same time it could give only an approximate indication of the effect of collision energy upon reaction rate.

In order to secure more meaningful results, various experimenters have used equipment designed to give more precise knowledge and control of the reaction conditions. Thus, the time-of-flight mass spectrometer utilizes a pulsed-ion source and can be fitted with a variable time delay of the extraction pulse. Ions are formed by a short (normally 0.25 μsec) electron pulse and may be held in the source for up to 2 or 3 μsec before extraction. The variation of ion intensity with time and pressure gives the rate constant which is thus freed of the uncertainty of the collision energy inherent in the results of the continuous withdrawal source (280, 281). However, most of the reactions studied by this method used ions formed at the peak of the dissociative resonance capture curve. As shown by Harland et al (147), ions formed at resonance maximum will be translationally excited and, if polyatomic, vibrationally excited also. These effects can influence the reaction rate and unless care is taken to determine the translational and internal energies, the meaning of the rate constant is obscure.

In order to control the collision energy, several investigators have used tandem mass spectrometer devices. Such an apparatus was first used by Lindholm (282) for the study of charge exchange with positive ions. This method utilizes a mass spectrometer to select ions of the proper mass. These ions, usually after passing through a lens to reduce their energy, are injected into a collision chamber where they may react with the gas present. The product ions are extracted and analyzed in a second mass spectrometer. For studies of charge exchange the secondary ions are extracted at right angles to the path of the primary ions. In studies of ion molecule reactions, the product ions (together with the residual primaries) are extracted collinearly with the primary ions since the transverse extraction method discriminates against reactions involving the exchange of massive entities (283, 284). The instrument designed by Futrell & Miller (284) is also equipped for velocity analysis of the product ions. A number of such instruments have been built, those of Paulson (283), Chupka (195), and Tiernan using the instrument designed by Futrell & Miller (284) having been especially productive of results on negative ions. This method permits control of the collision energy over a wide range, but is limited to a minimum energy of about 0.3 eV. It also suffers from the fact that the internal energy of primary polyatomic ions cannot be controlled. The method has the great advantage of establishing unequivocally the identity of the precursor of the product ions. The control of collision energy makes possible the precise measurement of the onset of endothermic reactions and thus determinations of electron affinity or ionic heats of formation. Chupka et al (195) determined the electron affinities of the halogen molecules, and Paulson (283, 285) and Tiernan and his associates (192, 194, 196, 286) studied a large number of reactions by this method.

The most successful and productive method of studying thermal ion-molecule reactions is the flowing afterglow method developed by Ferguson and his associates (287, 288). In this method ions, usually He^+, are produced in a microwave discharge which may be either continuous or pulsed. A reactant gas is injected downstream from the discharge and reacts with He^+ or excited He atoms to produce the ions to be studied. These pass down the reactor tube along with the helium carrier gas and are thermalized. A second reactant gas is introduced downstream from the first and reacts with the primary reactant ions. The pressure of the reactant gas, the temperature, and the flow rate can be controlled. Reaction time is determined by the gas flow rate. The second reactant gas may be an unstable one, such as an atom or a free radical, which may be generated immediately before injection into the flowing gas stream. At the end of the reaction chamber the ions are sampled into a quadrupole mass filter and analyzed. This is the method of choice for studying thermal reactions and is probably the only method available for studying reactions of ions with unstable species. It has been used largely to study ion-molecule reactions of atmospheric interest but is in no sense limited to such reactions.

Ion-molecule reactions can be studied with a drift tube, but this method has been relatively little used with negative ions. The method uses a drift space with grids or ring electrodes which provide a controllable electric field that causes any ions present to drift through the gas at a controlled rate. It is possible to maintain a field strength and pressure such that ion-molecule collisions are essentially thermal. The method must be used with great care unless it is combined with mass analysis to identify the various ions present. Phelps et al (289) and Parkes (290) have used drift tube reactors in several studies.

One of the most interesting and original recent instrument developments in mass spectrometry has been the ion-cyclotron resonance (ICR) method of Wobschall (291, 292), Llewellyn (293), and Baldeschwieler (294, 295). By this method ions are formed in a conventional source and injected at low velocity into an ICR cell. Here the ions are subject to crossed electric and magnetic fields which cause them to move in a spiral path with a frequency that depends upon the mass of the ion and the magnetic field strength. A radiofrequency electric field is applied normal to the magnetic field. When the radiofrequency is the same as the frequency of revolution of the ion, the ion will absorb energy from the field. Thus, by measuring the power absorbed from the rf field while sweeping the electric or magnetic field, a mass spectrum can be obtained. Field strengths are small and the energy of the ions is never large, so collisions occur at near thermal energies. The path length in the cell and consequently the retention time is long. The pressure must be kept relatively low, but the long time makes it possible to observe ion-molecule reactions. The variation in intensity of primary or secondary ions with retention time permits determination of the reaction rate, and some variation in collision energy is possible. The method has been extended by Baldeschwieler (294, 296) by the application of a second rf field. If this is set at the frequency of the primary ion while the first or main rf field is set at the frequency of a suspected product ion, a change in the reaction rate will occur if the first is indeed reacting to form the second. Thus, the precursors of various product ions are readily identified. The method has the advantage of analysis in situ so that extraction and discrimination are not a problem, and absolute values of ion concentration are measured. It suffers from the disadvantage of relatively poor resolution and under some conditions from the quite complex mathematics required to interpret the results.

Early studies of ion-molecule reactions in single source mass spectrometers showed the rate constants for many reactions to be quite large ($> 10^{-9}$ cc/molec sec) (297) and suggested there would be extensive further reactions if the source pressure could be increased substantially. Several investigators have achieved higher source pressures by closing the source slits and installing differential pumping. Some instruments are operated at 1 atm and several at pressures of 1 to 10 torr. Probably the first to use this technique was Field (298), who studied positive ion-molecule reactions in ethylene at pressures up to a few tenths torr. Further studies by Munson & Field (299) showed that with methane at about 1 torr source pressure, very small amounts of impurities resulted in extensive reaction with, in most instances, relatively simple spectra. This technique, called chemical ionization, has proved to be a powerful tool for the detection and identification of very small quantities of complex molecules, especially those of biological or medical interest such as might be present in body fluids. Most chemical ionization has been carried out with positive ions; however, Dougherty (300, 301, 302) has shown that the technique can also be used with negative ions. At sufficiently high pressure the electrons, either primary or secondary, will ultimately attach to a suitable molecule with or without dissociation. Thus, the number of negative ions formed will be greater than the number of positive ions and consequently the technique will be more sensitive for negative than for positive ions. The primary ions thus formed can then undergo ion-molecule reactions, usually at energies approaching thermal. The method is being applied with considerable success by Dzidic (303), but as yet little has been published.

In all studies at elevated pressure, i.e. greater than a few tenths torr, difficulties are experienced in injecting electrons into the ionization chamber and investigators have found it necessary to increase the electron energy to 300–400 V in order to obtain useful ion intensities. Because of this problem, some mass spectrometrists have used a radioactive material, usually a small sheet or foil of the radioactive materials, as a source of ions or of ionizing radiation. Thus, Kebarle

(304, 305) has used polonium, Yang & Conway (306) have used tritium, and Dzidic (303) has used nickel as ionizing media. An alternative method, available to only a few experimenters, is the use of a beam of high energy ions. Kebarle (307) and Wexler (308) used this method but it apparently is not very satisfactory and has been used very little. In most of his experiments Kebarle has used electrons accelerated to 4000 V and focused by a specially designed electron gun.

More complete descriptions of the methods used to study ion-molecule reactions are given in McDaniel et al (309) and Franklin (310).

Kinetics

The early observation that ion-molecule reactions proceed at unusually high rates has made the study of their kinetics both interesting and important. In nearly all the systems studied the ion concentration is much smaller than that of the reactant molecules. Consequently all ion-molecule reactions, whether second or higher order, can be treated by pseudo-first order kinetics. In all cases it is assumed that the measured intensity of an ion is proportional to its concentration.

In molecular beam, tandem mass spectrometer, and ICR experiment, the precursor to each product ion is established. With drift tube, flowing afterglow, and single source mass spectrometer, some care in preparing the reactant ions is necessary and some chemical intuition is helpful in relating precursor to product. At pressures below about 0.1 torr appearance potentials are useful for this purpose, but at higher pressures this is impossible.

In order to determine the rate constant, the retention time must be known. In continuous extraction sources at low pressures, the time is computed from the free fall time of the ion in the electric field of the source. At elevated pressure (above about 0.2 torr) it is necessary in both standard single source and drift tube instruments to use mobility to determine drift velocity. Unfortunately, these are usually not known and must be estimated, so the results are necessarily approximate. The time in a pulsed source is determined from the length of time between application of the electron injection and ion withdrawal pulses and is usually variable.

Negative ions undergo all of the same kinds of reactions that positive ions do, including the transfer of neutral atoms, negatively and positively charged atomic ions, negatively charged diatomic ions, charge transfer, and reactions requiring structural rearrangement. In addition, negative ions can undergo associative capture reactions and will do so if the reaction is exothermic.

Although not exhaustive, Table 2 contains rate data on a large number of negative ion-molecule reactions and includes several examples of each kind. Rate constants for reactions of each type vary from about 2×10^{-9} to about 10^{-15} cm^3 molecule^{-1} sec^{-1}. In spite of the deficiencies of the various methods, rate constants for a given exothermic reaction determined by various methods are in better than order-of-magnitude agreement.

Table 2 Rate constants and reaction cross sections

Reaction	Method[a]	$10^{10}k$ (cc/molec. sec)	$Q(\text{Å}^2)$	Ref.
Associative Detachment				
1. $H^- + H \rightarrow H_2 + e$	FA	13	—	311
2. $H^- + O_2 \rightarrow HO_2 + e$	FA	15; 12	—	318
3. $H^- + CO \rightarrow HCO + e$	FA	0.5	—	318
4. $H^- + NO \rightarrow HNO + e$	FA	4.6	—	318
5. $C^- + CO \rightarrow C_2O + e$	FA	4.1	—	319b
6. $C^- + CO_2 \rightarrow 2CO + e$	FA	0.047	—	319b
7. $C^- + N_2O \rightarrow CO + N_2 + e$	FA	9	—	319b
8. $O^- + O \rightarrow O_2 + e$	FA	3, 1.9	—	312, 313
9. $O^- + N \rightarrow NO + e$	FA	2.2	—	313
10. $O^- + H_2 \rightarrow H_2O + e$	FA	15.0, 6.0	—	312, 314, 315
11. $O^- + H_2 \rightarrow H_2O + e$	DT	11, 7.2	—	316, 317
12. $O^- + H_2 \rightarrow H_2O + e$	ES	3.6	—	349
13. $O^- + D_2 \rightarrow D_2O + e$	ES	4.3	—	349
14. $O^- + O_2 \rightarrow O_3 + e$	ES	< 0.01	—	349
15. $O^- + CO \rightarrow CO_2 + e$	ES	7	—	349
16. $O^- + CO \rightarrow CO_2 + e$	FA	5, 4.4	—	312, 315
17. $O^- + CO \rightarrow CO_2 + e$	DT	8, 6.5	—	316, 317
18. $O^- + NO \rightarrow NO_2 + e$	FA	5, 1.6	—	312, 314, 315
19. $O^- + NO \rightarrow NO_2 + e$	DT	1.5, 2.4	—	316, 317
20. $O^- + NO \rightarrow NO_2 + e$	ES	1.4	—	349
21. $O^- + N_2 \rightarrow N_2O + e$	FA	< 0.01	—	312
22. $O^- + N_2 \rightarrow N_2O + e$	DT	< 0.005	—	316
23. $O^- + SO_2 \rightarrow SO_3 + e$	ES	9.25	—	349
24. $O^- + CH_4 \rightarrow CH_4O? + e$	ES	< 0.01	—	349
25. $O^- + C_2H_2 \rightarrow C_2H_2O + e$	ES	17	—	349
26. $O^- + C_2H_2 \rightarrow C_2H_2O + e$	FA	13	—	319c
27. $O^- + C_2H_4 \rightarrow C_2H_4O + e$	FA	4.05	—	319c
28. $O^- + C_2H_6 \rightarrow C_2H_6O + e$	ES	0.21	—	349
29. $O^- + C_2H_4 \rightarrow C_2H_4O + e$	ES	4.7	—	349
30. $O^- + C_3H_6 \rightarrow C_3H_6O + e$	ES	10.9	—	349
31. $O^- + 1\text{-}C_4H_8 \rightarrow C_4H_8O + e$	ES	18.5	—	349

[a] *Method Key*

FA = flowing afterglow
MS = mass spectrometry
MRPD = modulated RPD ion source
TMS = tandem mass spectrometer system
DMS = mass spectrometer equipped with a drift space for ions from refractory materials to pass through reactant gas
DT = drift tube
ICR = ion cyclotron resonance
MB = molecular beam
ES = electron scavenging

[b] Measured at 0.3 eV.

[c] Maximum value at 8–15 eV.

[d] At 1 eV.

[e] At 0.25–0.3 eV.

[f] This reaction is endothermic by about 20 kcal/mole.

[g] $\sigma \approx 0$ below 2.5 eV; σ max at 8 eV.

[h] Probably endothermic since k increase slightly as repeller voltage increased.

[i] At 0.8 eV.

Table 2 (*continued*)

Reaction	Method[a]	$10^{10}k$ (cc/molec. sec)	$Q(\text{Å}^2)$	Ref.
32. $O^- + 2\text{-}C_4H_8 \rightarrow C_4H_8O + e$	ES	20.4	—	349
33. $O^- + (CH_3)_2CO \rightarrow C_3H_6O_2 + e$	ES	11.4	—	349
34. $S^- + O_2 \rightarrow SO_2 + e$	ES	0.07	—	349
35. $S^- + O_2 \rightarrow SO_2 + e$	FA	0.3	—	319a
36. $Cl^- + H \rightarrow HCl + e$	FA	9	—	315
37. $O_2^- + O \rightarrow O_3 + e$	FA	5, 3.3	—	312, 313
38. $O_2^- + N \rightarrow NO_2 + e$	FA	5	—	312
39. $O_2^- + N \rightarrow NO + O + e$	FA	4	—	315
40. $O_2^- + O_2(^1\Delta g) \rightarrow 2O_2 + e$	FA	2	—	320
41. $OH^- + H \rightarrow H_2O + e$	FA	10	—	315
42. $OH^- + O \rightarrow HO_2 + e$	FA	2	—	312
43. $OH^- + N \rightarrow HNO + e$	FA	< 0.01	—	312
44. $CN^- + H \rightarrow HCN + e$	FA	0.8	—	315
Charge Transfer				
1. $H^- + O_2 \rightarrow O_2^- + H$	FA	< 0.1	—	312
2. $H^- + NO_2 \rightarrow NO_2^- + H$	FA	29	—	315
3. $D^- + NO_2 \rightarrow NO_2^- + D$	TMS	12^b	—	192
4. $D^- + SF_6 \rightarrow SF_6^- + D$	TMS	0.48^b	—	196
5a. $O^- + NO_2 \rightarrow NO_2^- + O$	FA	12	—	315
	MS	...	8–70	321
	B	—	60	322
	TMS	12^b	—	192
	MS	22	—	279
5b. $O^- + O_3 \rightarrow O_3^- + O$	FA	5.3	—	315
6. $O^- + N_2O \rightarrow N_2O^- + O$	MS	0.02	—	323
7. $O^- + CO_2 \rightarrow CO_2^- + O$	TMS	—	0.35^c	344
8. $O^- + SF_6 \rightarrow SF_6^- + O$	TMS	0.0024^b	—	196
9. $F^- + NO_2 \rightarrow NO_2^- + F$	B	—	0.3	322
10. $S^- + NO_2 \rightarrow NO_2^- + S$	MS	4.8	—	325
11. $Cl^- + SF_6 \rightarrow SF_6^- + Cl$	TMS	$< 8 \times 10^{-5\,b}$	—	196
12. $Cl^- + NO_2 \rightarrow NO_2^- + Cl$	MS	—	8–70	321
	FA	< 0.06	—	324
13. $I^- + SF_6 \rightarrow SF_6^- + I$	TMS	$< 2 \times 10^{-4\,b}$	—	196
13a. $O_2^- + O_3 \rightarrow O_3^- + O_2$	FA	3	—	318
14. $O_2 + NO_2 \rightarrow NO_2^- + O_2$	B	20	5	322
15. $O_2^- + NO_2 \rightarrow NO_2^- + O_2$	FA	8	—	315
16. $O_2^- + CO_2 \rightarrow CO_2^- + O_2$	TMS	—	0.26^c	344
17. $O_2^- + SO_2 \rightarrow SO_2^- + O_2$	FA	5.4	—	326
18. $O_2^- + SF_6 \rightarrow SF_6^- + O_2$	FA	0.7	—	313
19. $O_2^- + SF_6 \rightarrow SF_6^- + O_2$	TMS	0.36^b	—	196
20. $OH^- + NO_2 \rightarrow NO_2^- + OH$	FA	19'	—	315
21. $OH^- + SF_6 \rightarrow SF_6^- + OH$	TMS	$< 0.002^b$	—	196
22. $NO^- + O_2 \rightarrow O_2^- + NO$	FA	9, 5	—	312, 327
23. $NO^- + NO_2 \rightarrow NO_2^- + NO$	DT	7.4	—	327
24. $NO^- + CO_2 \rightarrow CO_2^- + NO$	TMS	—	0.8^c	344

Table 2 (*continued*)

Reaction	Method^{a}	$10^{10}k$ (cc/molec. sec)	$Q(\text{Å}^2)$	Ref.
25. $NO^- + SF_6 \rightarrow SF_6^- + NO$	TMS	1.5^{b}	—	196
26a. $NO^- + N_2O \rightarrow N_2O^- + NO$	TMS	—	0.5 max.^{d}	347
26b. $SH^- + NO_2 \rightarrow NO_2^- + SH$	MS	11	—	325
27. $SH^- + NO_2 \rightarrow NO_2^- + SH$	TMS	7.8^{b}	—	192
28. $SO^- + SO_2 \rightarrow SO_2^- + SO$	MS	2.4 rel.	—	279
29. $O_3^- + NO_2 \rightarrow NO_2^- + O_3$	B	7	—	322
30. $NH_2^- + NO_2 \rightarrow NO_2^- + NH_2$	FA	10	—	315
31. $SO_2^- + NO_2 \rightarrow NO_2^- + SO_2$	TMS	4.3^{b}	—	192
32. $CS_2^- + NO_2 \rightarrow NO_2^- + CS_2$	TMS	4.1^{b}	—	192
33. $O_4^- + O \rightarrow O^- + 2O_2$	FA	—	—	329
34. $CF_3^- + NO_2 \rightarrow NO_2^- + CF_3$	TMS	3.7^{b}	—	192
35. $C_2F_5^- + NO_2 \rightarrow NO_2^- + C_2F_5$	TMS	3.2^{b}	—	192
36. $C_2H_2^- + SF_6 \rightarrow SF_6^- + C_2H_2$	TMS	0.31^{b}	—	196
37. $SF_5^- + NO_2 \rightarrow NO_2^- + SF_5$	MS	—	8–70	321
38. $SF_6^- + NO_2 \rightarrow NO_2^- + SF_6$	MS	—	8-70	321
39. $SF_6^- + NO_2 \rightarrow NO_2^- + SF_6$	B	—	0.1	322
40. $SF_6^- + O \rightarrow O^- + SF_6$	FA	0.5	—	328
41. $SF_6^- + UF_6 \rightarrow UF_6^- + SF_6$	MRPD	15	—	345
42. $SF_6^- + SeF_6 \rightarrow SeF_6^- + SF_6$	MRPD	2.1	—	345
43. $SF_6^- + TeF_6 \rightarrow TeF_6^- + SF_6$	MRPD	1.9	—	345
44. $SF_6^- + TeF_6 \rightarrow TeF_5^- + SF_6 + F$	MRPD	1.1	—	345
45. $UF_5^- + UF_6 \rightarrow UF_6^- + UF_5$	MRPD	14	—	345
Atom Transfer				
1. $H^- + H_2O \rightarrow OH^- + H_2$	MS	38	—	329a
2. $H^- + H_2O \rightarrow OH^- + H_2$	B	—	0.3	277
3. $D^- + D_2O \rightarrow OD^- + D_2$	MS	45	—	323
4. $H^- + O_2 \rightarrow OH^- + O$	FA	< 0.1	—	318
5. $H^- + N_2O \rightarrow OH^- + N_2$	FA	11	—	318
6. $O^- + H_2 \rightarrow OH^- + H$	DT	0.33	—	319c
7. $O^- + H_2O \rightarrow OH^- + OH$	MS	14	—	329a
8. $O^- + N_2O \rightarrow O_2^- + N_2$	TMS	—	0.7 max^{g}	347
9. $O^- + N_2O \rightarrow NO^- + NO$	FA	2.2	—	330
	ICR	2.5	—	330
	DT	1.95	—	331
	TMS	—	1.2^{e}	347
10. $O^- + NO_2 \rightarrow O_2^- + NO$	MS	0.18	—	323
11. $O^- + CO_2 \rightarrow O_2^- + CO$	TMS	—	0.2 max^{c}	344
12. $O^- + I_2 \rightarrow OI^- + I$	MS	21	—	279
13. $O^- + IBr \rightarrow OI^- + Br$	MS	0.6	—	279
14. $O^- + CH_4 \rightarrow OH^- + CH_3$	DT	1.1	—	319c
	FA	1.0	—	332
15. $O^- + CH_3I \rightarrow OI^- + CH_3$	MS	10	—	279
16. $O^- + C_2H_4 \rightarrow OH^- + C_2H_3$	MS	0.6^{e}	—	338
17. $O^- + C_2H_6 \rightarrow OH^- + C_2H_5$	FA	7.0	—	332
18. $O^- + C_2H_2 \rightarrow OH^- + C_2H$	MRPD	3.5^{e,f}	—	338

Table 2 *(continued)*

Reaction	Method[a]	$10^{10}k$ (cc/molec. sec)	$Q(\text{Å}^2)$	Ref.
19. $O^- + C_3H_8 \rightarrow OH^- + C_3H_7$	FA	9.3	—	382
20. $O^- + n\text{-}C_4H_{10} \rightarrow OH^- + C_4H_9$	FA	12	—	332
21. $S^- + COS \rightarrow S_2^- + CO$	MS	3	—	351
22. $NO^- + N_2O \rightarrow NO_2^- + N_2$	DT	0.0003	—	331
23. $NO_2^- + NO_2 \rightarrow NO_3^- + NO$	FA	0.004	—	329
24. $NO_2^- + O_3 \rightarrow NO_3^- + O_2$	FA	0.18	—	324
25. $CO_4^- + O \rightarrow CO_3^- + O_2$	FA	0.48	—	329
26. $NO_3^- + NO \rightarrow NO_2^- + NO_2$	DT	0.00005	—	334
27. $NO_3^- + NO \rightarrow NO_2^- + NO_2$	FA	0.15	—	333
28. $WO_3^- + Cl_2 \rightarrow WO_3Cl^- + Cl$	DMS	15	—	348
29. $(WO_3)_2^- + Cl_2 \rightarrow (WO_3)_2Cl^- + Cl$	DMS	6	—	348
30. $(WO_3)_3^- + Cl_2 \rightarrow (WO_3)_3Cl^- + Cl$	DMS	4	—	348
31. $WO_3^- + NO_2 \rightarrow WO_4^- + NO$	DMS	6	—	348
32. $(WO_3)_2^- + NO_2 \rightarrow (WO_3)_2O^- + NO$ $\rightarrow (WO_3)NO_2^- + WO_3$	DMS	4	—	348
33. $(WO_3)_3^- + NO_2 \rightarrow (WO_3)_3O^- + NO$ $\rightarrow (WO_3)_2NO_2^- + WO_3$	DMS	3	—	348
34. $ReO_3^- + Cl_2 \rightarrow$	DMS	13	—	348
35. $ReO_3^- + NO_2 \rightarrow ReO_4^- + NO$	DMS	7	—	348
Transfer of Negative Atomic Ions				
1. $O_2^- + NO \rightarrow NO_2^- + O$	FA	< 0.01	—	315
2. $O_2^- + CO_2 \rightarrow CO_3^- + O$	TMS	—	0.2 max.[c]	344
3. $F_2^- + BF_3 \rightarrow BF_4^- + F$	MPRD	6	—	339
4. $O_3^- + H \rightarrow OH^- + O_2$	FA	8.4	—	335
5. $O_3^- + CO_2 \rightarrow CO_3^- + O_2$	FA	4.0	—	313
	DT	5.5	—	336
6. $O_3^- + SO_2 \rightarrow SO_3^- + O_2$	FA	17	—	337
7. $NO_2^- + H \rightarrow OH^- + NO$	FA	3.0; 4.0	—	337, 337a
8. $CO_3^- + O \rightarrow O_2^- + CO_2$	FA	0.8	—	313
9. $CO_3^- + NO \rightarrow NO_2^- + CO_2$	FA	0.09; 0.18	—	313, 337
10. $CO_3^- + NO_2 \rightarrow NO_3^- + CO_2$	FA	0.8	—	326
11. $CO_3^- + SO_2 \rightarrow SO_3^- + CO_2$	FA	2.3	—	337
12. $SF_6^{-*} + BF_3 \rightarrow BF_4^- + SF_5$	MRPD	18	—	339
13. $SF_6^{-*} + BCl_3 \rightarrow BCl_3F^- + SF_5$	MRPD	16		339
14. $SF_6^- + POF_3 \rightarrow POF_4^- + SF_5$	MS	0.25	—	352
15. $SF_6^- + PSF_3 \rightarrow PSF_4^- + SF_5$	MS	0.025[h]	—	352
Transfer of Positive Atomic Ions				
1. $H^- + O_2 \rightarrow O^- + OH$	FA	> 0.1	—	318
2. $C^- + O_2 \rightarrow O^- + CO$	FA	4.0	—	318
3. $O^- + CNCl \rightarrow CN^- + OCl$	MS	20	—	353
4. $O^- + C_2H_2 \rightarrow C_2H^- + OH$	DT	8	—	319c
	MRPD	13–24[b]	—	338
5. $O^- + C_2D_2 \rightarrow C_2D^- + OD$	MS	8–18[b]	—	338

Table 2 (*continued*)

Reaction	Method[a]	$10^{10}k$ (cc/molec. sec)	$Q(\text{Å}^2)$	Ref.
6. $O^- + CH_3NO_2 \rightarrow CH_2NO_2^- + OH$	MS	—	2.6	279
7. $O^- + CH_3NO_2 \rightarrow CH_2NO_2^- + OH$	MS	21	—	354
8. $O_2^- + HCl \rightarrow Cl^- + HO_2$	FA	16	—	342
9. $NO^- + HCl \rightarrow Cl^- + HNO$	FA	16	—	342
10. $NO_2^- + HCl \rightarrow Cl^- + HNO_2$	FA	14	—	342
11. $NO_2^- + HBr \rightarrow Br^- + HNO_2$	FA	19	—	342
12. $NO_3^- + HCl \rightarrow Cl^- + HNO_3$	FA	> 0.01	—	342
13. $NO_3^- + HBr \rightarrow Br^- + HNO_3$	FA	6.3	—	342
14. $CH_3O^- + CD_3CH_2F \rightarrow$ $^-CD_2CH_2F + CH_3OD$	ICR	0.4	—	343
Displacement and Rearrangement Reactions				
1. $O^- + CNCl \rightarrow OCN^- + Cl$	ICR	0.4	—	343
2. $O^- + C_2H_3 \rightarrow C_2OH^- + H_2$	DT	0.8	—	319c
	MRPD	0.46^b	—	338
3. $O^- + C_2D_2 \rightarrow C_2OD^- + D$	MRPD	0.42^b	—	338
4. $O^- + CH_3Cl \rightarrow Cl^- + CH_3O$	FA	12	—	346
5. $O^- + C_2H_4 \rightarrow C_2H_2^- + H_2O$	DT	1.9	—	319c
	MRPD	$\leq 4.2^f$	—	338
6. $O^- + CH_3NO_2 \rightarrow HCNO_2^- + H_2O$	MS	10	—	354
7. $O^- + C_6H_6 \rightarrow C_6H_4^- + H_2O^b$	MRPD	1.1	—	338
8. $O^- + C_6D_6 \rightarrow C_6D_4 + D_2O^b$	MRPD	2.6	—	338
9. $O^- + C_6H_6 \rightarrow C_6H_5O^- + H$	MRPD	0.84	—	338
10. $O^- + C_6D_6 \rightarrow C_6D_5O^- + D$	MRPD	1.7	—	338
11. $F^- + CD_3CH_2F \rightarrow DF_2^- + CD_2CH_2$	ICR	1.3	—	343
12. $OH^- + CH_3Cl \rightarrow Cl^- + CH_3OH$	FA	19	—	346
13. $NH_2^- + CS_2 \nearrow CS_2^- + NH_2$ $\searrow HS^- + HNCS$	MS	9.5	—	350
14. $NH_2^- + COS \nearrow HS^- + HNCO$ $\searrow NH_2S^- + CO$	MS	4.6	—	350
15. $NO_2^- + CH_3NO_2 \rightarrow OH^- + ?$	MS	1.2	—	354
16. $O_4^- + CO \rightarrow CO_3^- + O_2$	FA	< 0.2	—	333
17. $O_4^- + CO_2 \rightarrow CO_4^- + O_2$	FA	2.5	—	333
18. $O_4^- + CO_2 \rightarrow CO_4^- + O_2$	FA	4.3	—	333
19. $O_4^- + H_2O \rightarrow O_2^- \cdot H_2O + O_2$	MS	15	—	340
	DT	14	—	341
20 $CH_3O^- + CD_3CH_2F \rightarrow$ $CH_3ODF^- + CD_2CH_2$	ICR	0.4	—	343
21. $CH_3O^- + CD_3CH_2F \rightarrow$ $F^- + CH_3OCH_2CD_3(?)$	ICR	0.4	—	343

Determination of Acidity

The free energy of the reaction

$$HAB = H^+ + AB^-$$

is a measure of the acid strength of HAB. If the free energies of formation of HAB and AB^- are known, the equilibrium constant or acid strength is determined. This is seldom the case and so the acidity of a compound usually cannot be determined in this way. However, relative acidities can be obtained by observing whether or not proton transfer occurs between a certain molecule and a negative ion; thus

$$B^-(HA, HB)A^-$$

If the reaction is carried out at near thermal energies and proceeds as shown, then the proton affinity (B^-) is greater than the proton affinity (A^-) and HA is a stronger acid than HB. By studying a homologous series of compounds in this way, a qualitative understanding of the effect of structure upon acid strength can be established.

Brauman & Blair (355) have used the ICR double resonance technique (294, 296) to ascertain the direction of proton transfer in mixtures of CN^- and CH_3CN, of HCN and $^-CH_2COCN$, and of both ions with the enol form of $CH_3COCH_2COCH_3$. Their results show the acid strength to increase in the order $HCN < CH_3COCN < CH_3COCH_2COCH_3$. Brauman & Blair (356, 357) have also determined the order of acidities in several normal alcohols and found that the acidity increases with chain length. Similar results were obtained by Tiernan & Hughes (358), who used a tandem mass spectrometer to determine the rates of forward and reverse proton transfer reactions for several alcohols. The equilibrium constant (K_{eq}) was determined from the ratios of the rate constants with acidities in agreement with those of Brauman & Blair (356, 357) and McIver et al (360). Bohme et al (359) have found a similar order of acidities of alcohols using the flowing afterglow method. The order of acid strengths of the alcohols in the gas phase is thus the reverse of that in solution. This undoubtedly reflects the effect of solvent upon reactivity.

Haney & McIver (361) have studied S_N2 reactions in a number of systems using the pulsed ICR method. They measured the ratio of reaction of chloride ion with several alkyl bromides and of methyl chloride with several ions of elements from the first and second rows of the periodic table. The results disagreed seriously with those obtained in solution. Bohme & Young (362) have also studied the reaction of several negative ions with methyl chloride and found that the principal reaction was displacement of Cl^-. Smaller ions such as O^- and OH^- and larger ions having the electron localized reacted rapidly, whereas ions having the charge delocalized reacted relatively slowly.

Several other studies of proton transfer and relative acidity have been reported. McIver et al (363) have determined the acidities of several acetylenes and have gotten further values for the alcohols. Jäger et al (364) have also studied various reactions of O^- with several alcohols and gotten relative intensities of various product ions. By using deuterium substitution on the hydroxyl, the rate of removal of the hydrogen atom from the oxygen was found to be somewhat greater than that of a hydrogen attached to carbon.

Along somewhat similar lines, Dillard & Rhyne (365) have observed F^- ion transfer from SF_6^- to PF_3 and PF_5, and Dillard (366) has studied F^- transfer from SF_6^- to several methyl fluoro silanes. Haartz & McDaniel (367), using the ICR double resonance technique, have studied F^- transfer in several reactions and established an order of F^- affinities.

Endothermic Charge Transfer

In a previous section the determination of electron affinity by endothermic charge transfer was discussed. It should be mentioned that measurement of the onset for collisional decomposition will often yield valuable information concerning bond dissociation energies or electron affinities. In the course of measuring charge transfer and collisional decomposition, it is also possible to determine cross sections or reaction rate constants for the reactions. Several such results are included in Table 2. In addition to those previously mentioned, studies have been reported by Clow & Tiernan (368), Vogt (369), Paulson (344, 370, 371), and Martin & Bailey (372). In certain of these investigations exothermic reactions have exhibited a threshold, indicating an energy barrier to reaction (371, 372). Several investigators, using labeled compounds, have studied isotope distribution in the reaction products (192, 347, 369, 389) and Paulson (323) has shown that the reaction

$$O^-(O_2, O)O_2^{-\prime}$$

proceeds by both charge transfer and ion-atom exchange.

Equilibrium Studies

The availability of various kinds of equipment (flowing afterglow, drift tube, and high pressure ion source and ICR) that permit relatively long retention times and/or high pressures makes it possible to determine equilibrium constants and free energies of reaction. Some instruments can operate over a wide range of temperatures and thus permit the determination of heat of reaction. A large number of thermodynamic studies of exchange reactions of positive ions have been made, but relatively few exchange reactions of negative ions have been studied. Several studies of equilibrium in proton transfer reactions were discussed above. In a study of flames seeded with potassium and cesium, Gould & Miller (383) observed equilibrium to occur in several reactions of negative ions of chromium and rhenium oxides and determined their heats of reaction.

It early became evident that H_3O^+ and NH_4^+ added H_2O or NH_3 molecules successively as the pressure increased. Kebarle (384) among others has shown that it is possible to determine the equilibrium constants and their temperature dependence for each successive addition and has reported values for clusters up to eight solvent molecules.

Clustering reactions of negative ions have also been studied and Table 3 gives typical results for the enthalpy and entropy of several H_2O additions to OH^- and the halide ions. The enthalpy of each water addition decreases as the molecule becomes larger. The solvation of monatomic positive ions is greater than that of negative ions in the same period of the periodic table. This is to be expected as the positive ions are considerably smaller than the negative ions (387). However, F^- and K^+, and Cl^- and Cs^+ have similar ionic radii and exhibit similar enthalpies and entropies of solvation. In a further study Yamdagni & Kebarle have studied clustering of several other molecules around Cl^- (388, 389) and Payzant et al (390) have studied clustering around CN^-, NO_2^- and NO_3^-.

Table 3 $A^-(H_2O)_n = A^-(H_2O)_{n-1} + H_2O$

$n,n-1$	F^-(385)		Cl^-(385)		Br^-(385)		I^-(385)		OH^-(386)	
	ΔH	ΔS	ΔH	ΔS	ΔH	ΔS	ΔH	ΔS	ΔH	ΔS
1,0	83.3	17.4	13.1	16.5	12.6	18.4	10.2	16.3	22.5	19.1
2,1	16.6	18.7	12.7	20.8	12.3	22.9	9.8	19.0	16.4	19.3
3,2	13.7	20.4	11.7	23.2	11.5	24.5	9.4	21.3	15.1	24.8
4,3	13.5	36.9	11.1	25.8	10.9	26.8			14.2	29.5
5,4	13.2	30.7							14.1	33.2

Theory of Ion-Molecule Reactions

For a large number of ion-molecule reactions the rate constant agrees well with the classical collision rate treatment of Langevin (391) and its later modification by Gioumousis & Stevenson (392). Eyring, Hirschfelder & Taylor (393) obtained similar results using absolute rate theory. These treatments all result in the relation

$$\sigma = 2\pi(\alpha/\mu)^{\frac{1}{2}}e/v \qquad 8.$$

where σ is cross section, v is relative velocity, e is the unit electric charge, α is the polarizability of the neutral, and μ is reduced mass. Theard & Hamill (394) and Moran & Hamill (395) modified the treatment to include molecules with a permanent dipole.

The σ above is a collision cross section and corresponds to reaction cross section only when the rate of decomposition of the collision complex to products exceeds the collision rate. Statistical treatments of the decay of the complex have been developed by Light et al (396, 397, 398), Tannenwald (399), and Wolf (400). None of these is completely satisfactory. A complete review of the theories of ion-molecule reaction rates is beyond the scope of this review. The subject has been extensively treated in McDaniel et al (309) and various methods have been subjected to careful evaluation in light of available theories by Henchman (401). The reader is referred to those for more detailed information.

Literature Cited

1. Christophorou, L. G. 1971. *Atomic and Molecular Radiation Physics*, Chap. 6, 7. New York: Wiley
2. Flesch, G. D., Svec, H. J. 1963. *Rev. Sci. Instrum.* 34:897
3. Svec, H. J., Flesch, G. D. 1968. *Int. J. Mass Spectrom. Ion Phys.* 1:41
4. Flesch, G. D., White, R. M., Svec, H. J. 1969. *Int. J. Mass Spectrom. Ion Phys.* 3:339
5. MacNeil, K. A. G., Thynne, J. C. J. 1968. *Trans. Faraday Soc.* 64:2112
6. Thynne, J. C. J., MacNeil, K. A. G., Caldwell, K. J. 1969. *Time of Flight Mass Spectrometry*, ed. D. Price, J. E. Williams, 117. Oxford/New York: Pergamon
7. Harland, P. W., Thynne, J. C. J. 1972. *Int. J. Mass Spectrom. Ion Phys.* 9:253
8. Harland, P. W., Thynne, J. C. J. 1972. *Int. J. Mass Spectrom. Ion Phys.* 10:11
9. Harland, P. W., Cradock, S., Thynne, J. C. J. 1972. *Int. J. Mass Spectrom. Ion Phys.* 10:169
10. Harland, P. W., Thynne, J. C. J. 1973. *Inorg. Nucl. Chem. Lett.* 9:265
11. Thynne, J. C. J., Harland, P. W. 1973. *Int. J. Mass Spectrom. Ion Phys.* 11:127
12. Massey, H. S. W. 1950. *Negative Ions*. London: Cambridge Univ. Press
13. Pritchard, H. O. 1953. *Chem. Rev.* 52:529
14. Branscomb, L. M. 1962. *Atomic and Molecular Processes*, ed. D. R. Bates, 100–40. New York: Academic
15. Moiseiwitsch, B. L. 1965. *Advan. At. Mol. Phys.* 1:61
16. Smirnov, B. M. 1965. *High Temp.* 3:716
17. Bardsley, J. N., Mandl, F. 1968. *Rep. Progr. Phys.* 31:471
18. Taylor, H. S., Nazaroff, G. V., Golebiewski, A. 1966. *J. Chem. Phys.* 45:2872
19. Berry, R. S. 1969. *Chem. Rev.* 69:533

20a. Schoen, R. I. 1969. *Can. J. Chem.* 47:1879

20b. Phelps, A. V. 1969. *Can. J. Chem.* 47:1783

20c. Fehsenfeld, F. C., Albritton, D. L., Burt, J. A., Schiff, H. I. 1969. *Can. J. Chem.* 47:1793

21. Christophorou, L. G., Compton, R. N. 1967. *Health Phys.* 13:1277
22. Christophorou, L. G. 1970. *Proc. 10th Czechoslovak Ann. Meeting on Radiation Chem*, June 22–25, Mariánske Lázne, Czechoslovakia
23. Christophorou, L. G., Blaunstein, R. P. 1971. *Chem. Phys. Lett.* 12:173
24. Blaunstein, R. P., Christophorou, L. G. 1971. *Radiat. Res. Rev.* 3:69
25. Christophorou, L. G. 1972. *J. Phys. Chem.* 76:3730
26. Hasted, J. B. 1972. *Physics of Atomic Collisions*, Chap. 8, p. 451. London: Butterworth. 2nd ed.
27. Dillard, J. G. 1973. *Chem. Rev.* 73:583
28. Nottingham, W. B. 1939. *Phys. Rev.* 55:203
29. Sugden, T. M., Price, W. C. 1948. *Trans. Faraday Soc.* 44:108
30. Clarke, E. M. 1954. *Can. J. Phys.* 32:764
31. Hutchison, D. A. 1963. *Advan. Mass Spectrom.* 2:527
32. Marmet, P., Kerwin, L. 1960. *J. Appl. Phys.* 31:2071
33. Marmet, P., Morrison, J. D. 1962. *J. Chem. Phys.* 36:1238
34. Brion, C. E. 1964. *J. Chem. Phys.* 40:2995
35. Brion, C. E., Frost, D. C., McDowell, C. A. 1966. *J. Chem. Phys.* 44:1034
36. Brion, C. E. 1969. *Int. J. Mass Spectrom. Ion Phys.* 3:197
37. Brion, C. E., Olsen, L. A. R. 1972. *Int. J. Mass Spectrom. Ion Phys.* 9:413
38. Fox, R. E., Hickam, W. M., Kjeldaas, T. Jr., Grove, D. J. 1951. *Phys. Rev.* 84:859
39. Fox, R. E., Hickam, W. M., Kjeldaas, T. Jr. 1953. *Phys. Rev.* 89:555
40. Fox, R. E., Hickam, W. M., Grove, D. J., Kjeldaas, T. Jr. 1955. *Rev. Sci. Instrum.* 26:1101
41. Cloutier, G. G., Schiff, H. I. 1959. *J. Chem. Phys.* 31:793
42. Stockdale, J. A. D., Compton, R. N., Reinhardt, P. W. 1969. *Phys. Rev.* 184:81
43. Chantry, P. J. 1969. *Rev. Sci. Instrum.* 40:884
44. Lifshitz, C. et al 1973. *Int. J. Mass Spectrom. Ion Phys.* 11:243
45. Marmet, P. 1964. *Can. J. Phys.* 42:2102
46. Frost, D. C., McDowell, C. A. 1955. *Proc. Roy. Soc. London A* 232:227

47. Frost, D. C., McDowell, C. A. 1958. *J. Chem. Phys.* 29:964
48. Simpson, J. A. 1961. *Rev. Sci. Instrum.* 32:1283
49. Gordon, S. M., Haarhoff, P. C., Krige, G. J. 1969. *Int. J. Mass Spectrom. Ion. Phys.* 3:13
50. Stamatovic, A., Schulz, G. J. 1968. *Rev. Sci. Instrum.* 39:1752
51. Stamatovic, A., Schulz, G. J. 1970. *J. Chem. Phys.* 53:2663
52. Morrison, J. D. 1963. *J. Chem. Phys.* 39:200
53. van Cittert, P. H. 1931. *Z. Phys.* 69:298
54. Ioup, G. E., Thomas, B. S. 1967. *J. Chem. Phys.* 46:3959
55. MacNeil, K. A. G., Thynne, J. C. J. 1969. *Int. J. Mass Spectrom. Ion Phys.* 3:35
56. Harland, P. W., MacNeil, K. A. G., Thynne, J. C. J. 1970. *Dynamic Mass Spectrometry*, ed. D. Price, J. E. Williams, 1: Chap. 8. London: Heyden & Son
57. Dromey, R. G., Morrison, J. D. 1970. *Int. J. Mass Spectrom. Ion Phys.* 4:475
58. Dromey, R. G., Morrison, J. D., Traeger, J. C. 1971. *Int. J. Mass Spectrom. Ion Phys.* 6:57
59. Morrison, J. D., Traeger, J. C. 1973. *Int. J. Mass Spectrom. Ion Phys.* 11:77
60. Dromey, R. G., Morrison, J. D. 1971. *Int. J. Mass Spectrom. Ion Phys.* 6:253
61. Vogt, J., Pascul, C. 1972. *Int. J. Mass Spectrom. Ion Phys.* 9:441
62. Winters, R. E., Collins, J. H., Courchene, W. L. 1966. *J. Chem. Phys.* 45:1931
63. Collins, J. H., Winters, R. E., Engerholm, G. G. 1968. *J. Chem. Phys.* 49:2469
64. Giessner, B. G., Meisels, G. G. 1971. *J. Chem. Phys.* 55:2269
65. Compton, R. N., Christophorou, L. G., Hurst, G. S., Reinhardt, P. W. 1966. *J. Chem. Phys.* 45:4634
66. Schulz, G. J. 1958. *Phys. Rev.* 112:150
67. Schulz, G. J. 1959. *Phys. Rev.* 116:1141
68. Schulz, G. J. 1961. *J. Chem. Phys.* 34:1778
69. Brongersma, H. H., Oosterhoff, L. J. 1967. *Chem. Phys. Lett.* 1:169
70. Bensimon, J. et al 1969. *3e Colloque. Nat. Phys. Coll. Atom et Electr.*, Toulouse
71. Spence, D., Mauer, J. L., Schulz, G. J. 1972. *J. Chem. Phys.* 57:5516
72. Pisanias, M. N., Christophorou, L. G., Carter, J. G. 1972. *Chem. Phys. Lett.* 13:433
73. Boness, M. J. W., Larkin, I. W., Hasted, J. B., Moore, L. 1967. *Chem. Phys. Lett.* 1:292
74. Boness, M. J. W., Hasted, J. B. 1966. *Phys. Lett.* 21:526
75. Sanche, L., Schulz, G. J. 1971. *Phys. Rev. Lett.* 27:1333
76. Sanche, L., Schulz, G. J. 1972. *Phys. Rev. A* 5:1672
77. Sanche, L., Schulz, G. J. 1972. *Phys. Rev. A* 6:69
78. Sanche, L., Schulz, G. J. 1973. *J. Chem. Phys.* 58:479
79. Mahan, B. H., Young, C. E. 1966. *J. Chem. Phys.* 44:2192
80. Fehsenfeld, F. C. 1970. *J. Chem. Phys.* 53:2000
81. Christophorou, L. G., McCorkle, D. L., Carter, J. G. 1971. *J. Chem. Phys.* 54:253
82. Curran, R. K. 1963. *J. Chem. Phys.* 38:780
83. Compton, R. N., Christophorou, L. G., Huebner, R. H. 1966. *Phys. Lett.* 23:656
84. Brion, C. E., Eaton, C. R. 1968. *Int. J. Mass Spectrom. Ion Phys.* 1:102
85. Compton, R. N., Huebner, R. H., Reinhardt, P. W., Christophorou, L. G. 1968. *J. Chem. Phys.* 48:901
86. Begun, G. M., Compton, R. N. 1969. *J. Chem. Phys.* 51:2367
87. Lifshitz, C., Grajower, R. 1970. *Int. J. Mass Spectrom. Ion Phys.* 4:92
88. Hubin-Franskin, M.-J., Collin, J. E. 1970. *Int. J. Mass Spectrom. Ion Phys.* 5:163
89. Hubin-Franskin, M.-J., Collin, J. E. 1970. *Int. J. Mass Spectrom. Ion Phys.* 5:255
90. Stockdale, J. A. D., Nelson, D. R., Davis, F. J., Compton, R. N. 1972. *J. Chem. Phys.* 56:3336
91. Pisanias, M. N., Christophorou, L. G., Carter, J. G., McCorkle, D. L. 1973. *J. Chem. Phys.* 58:2110
92. Streets, D. G., Potts, A. W., Price, W. C. 1972. *Int. J. Mass Spectrom. Ion Phys.* 10:123
93. Edelson, D., Griffiths, J. E., McAfee, K. B. Jr. 1962. *J. Chem. Phys.* 37:917
94. Asundi, R. K., Craggs, J. D. 1964. *Phys. Soc. London* 83:611
95. Hickam, W. H., Fox, R. E. 1956. *J. Chem. Phys.* 25:642
96. Naff, W. T., Cooper, C. D., Compton, R. N. 1968. *J. Chem. Phys.* 49:2784
97. Collins, P. M. 1970. PhD thesis. Univ. of Tennessee, Knoxville, Tennessee
98. Klots, C. E. 1967. *J. Chem. Phys.*

46:1197
99. Christophorou, L. G., Compton, R. N., Hurst, G. S., Reinhardt, P. W. 1965. *J. Chem. Phys.* 43:4273
100. Harland, P. W., Thynne, J. C. J. 1971. *J. Phys. Chem.* 75:3517
101. Christophorou, L. G., Carter, J. G., Christodoulides, A. A. 1969. *Chem. Phys. Lett.* 3:237
102. Chaney, E. L., Christophorou, L. G., Collins, P. M., Carter, J. G. 1970. *J. Chem. Phys.* 52:4413
103. Collins, P. M., Christophorou, L. G., Chaney, E. L., Carter, J. G. 1970. *Chem. Phys. Lett.* 4:646
104. Christophorou, L. G., Carter, J. G., Collins, P. M., Christodoulides, A. A. 1971. *J. Chem. Phys.* 54:4706
105. Cooper, C. D., Compton, R. N. 1972. *Chem. Phys. Lett.* 14:29
106. Krauss, M., Neumann, D. 1972. *Chem. Phys. Lett.* 14:26
107. Claydon, C. R., Segal, G. A., Taylor, H. S. 1970. *J. Chem. Phys.* 52:3387
108. Sutton, P. P., Mayer, J. E. 1935. *J. Chem. Phys.* 3:20
109. Mitchell, J. J., Mayer, J. E. 1940. *J. Chem. Phys.* 8:282
110. McCallum, K. J., Mayer, J. E. 1943. *J. Chem. Phys.* 11:56
111. Page, F. M. 1960. *Trans. Faraday Soc.* 56:1742
112. Page, F. M. 1961. *Trans. Faraday Soc.* 57:359
113. Page, F. M. 1961. *Trans. Faraday Soc.* 57:1254
114. Andsell, D. A., Page, F. M. 1962. *Trans. Faraday Soc.* 58:1084
115. Napper, R., Page, F. M. 1963. *Trans. Faraday Soc.* 59:1086
116. Gaines, A. F., Page, F. M. 1963. *Trans. Faraday Soc.* 59:1266
117. Kay, J., Page, F. M. 1964. *Trans. Faraday Soc.* 60:1042
118. Farragher, A. L., Page, F. M., Wheeler, R. C. 1964. *Discus. Faraday Soc.* 37:203
119. Page, F. M., Goode, G. C. 1969. *Negative Ions and the Magnetron.* New York: Wiley
120. Fine, J., Scheer, M. D. 1967. *J. Chem. Phys.* 47:4267
121. Scheer, M. D., Fine, J. 1967. *J. Chem. Phys.* 46:3998
122. Wentworth, W. E., Becker, R. S. 1962. *J. Am. Chem. Soc.* 84:4263
123. Becker, R. S., Wentworth, W. E. 1963. *J. Am. Chem. Soc.* 85:2210
124. Wentworth, W. E., Chen, E. 1963. *J. Phys. Chem.* 67:2201
125. Wentworth, W. E., Chen, E., Lovelock, J. E. 1966. *J. Phys. Chem.* 70:445
126. Wentworth, W. E., Chen, E. 1967. *J. Phys. Chem.* 71:1929
127. Wentworth, W. E., Becker, R. S., Tung, R. 1967. *J. Phys. Chem.* 71:1652
128. Wentworth, W. E., Chen, E., Steelhammer, J. C. 1968. *J. Phys. Chem.* 72:2671
129. Wentworth, W. E., Ristau, W. 1969. *J. Phys. Chem.* 73:2126
130. Steelhammer, J. C., Wentworth, W. E. 1969. *J. Chem. Phys.* 51:1802
131. Wentworth, W. E., George, R., Keith, H. 1969. *J. Chem. Phys.* 51:1791
132. Wentworth, W. E., Chen, E., Freeman, R. 1971. *J. Chem. Phys.* 55:2075
133. Lovelock, J. E. 1961. *Nature* 189:729
134. Wentworth, W. E. 1973. Private communication
135. Holstein, T. 1951. *Phys. Rev.* 84:1073
136. O'Malley, T. F. 1966. *Phys. Rev.* 150:14
137. O'Malley, T. F. 1967. *Phys. Rev.* 155:59
138. Feshbach, H. 1958. *Ann. Phys.* 5:357
139. Feshbach, H. 1962. *Ann. Phys.* 19:287
140. Rapp, D., Sharp, T. E., Briglia, D. D. 1965. *Phys. Rev. Lett.* 14:533
141. Fite, W. L., Brackmann, R. T. 1963. *Proc. Int. Conf. Ioniz. Phenomena Gases, 6th, Paris* 1:21
142. Henderson, W. R., Fite, W. L., Brackmann, R. T. 1969. *Phys. Rev.* 183:157
143. Christophorou, L. G., Stockdale, J. A. D. 1968. *J. Chem. Phys.* 48:1956
144. Kiser, R. W. 1965. *Introduction to Mass Spectrometry and Its Applications.* Englewood-Cliffs, NJ: Prentice-Hall
145. De Corpo, J. J., Bafus, D. A., Franklin, J. L. 1971. *J. Chem. Phys.* 54:1592
146. De Corpo, J. J., Franklin, J. L. 1971 *J. Chem. Phys.* 54:1885
147. Harland, P. W., Franklin, J. L., Carter, D. E. 1973. *J. Chem. Phys.* 58:1430
148. Petty, F. et al 1973. *High Temp. Sci* 5:25
149. Harland, P. W., Franklin, J. L. 1974. *J. Chem. Phys.* In press
150. Klots, C. E. 1964. *J. Chem. Phys.* 41:117
151. Haney, M. A., Franklin, J. L. 1968. *J. Chem. Phys.* 48:4093
152. Spotz, E. L., Seitz, W. A., Franklin, J. L. 1969. *J. Chem. Phys.* 51:5142
153. Klots, C. E. 1973. *J. Chem. Phys.* 58:5364
154. Tate, J. T., Lozier, W. W. 1932. *Phys. Rev.* 39:254

155. Lozier, W. W. 1934. *Phys. Rev.* 46:268
156. Blewett, J. P. 1936. *Phys. Rev.* 49:900
157. Buchdahl, R. 1941. *J. Chem. Phys.* 9:146
158. Berry, R. S., Reimann, C. W. 1963. *J. Chem. Phys.* 38:1540
159. Chantry, P. J., Schulz, G. J. 1967. *Phys. Rev.* 156:134
160. Chantry, P. J. 1968. *Phys. Rev.* 172:125
161. Haney, M. A., Franklin, J. L. 1968. *J. Chem. Phys.* 48:4093
162. Franklin, J. L., Hierl, P. M., Whan, D. A. 1967. *J. Chem. Phys.* 47:3148
163. Rosenstock, H. M., Wallenstein, M. B., Wahrhaftig, A. L., Eyring, H. 1952. *Proc. Nat. Acad. Sci. USA* 38:677
164. Rosenstock, H. M., Krauss, M. 1963. *Mass Spectrometry of Organic Ions*, ed. F. W. McLafferty, 2–64. New York: Academic
165. De Corpo, J. J., Steiger, R. P., Franklin, J. L., Margrave, J. L. 1970. *J. Chem. Phys.* 53:936
166. Wang, J. Ling-Fai, Margrave, J. L., Franklin, J. L. 1973. *J. Chem. Phys.* 58:5417
167. Wang, J. Ling-Fai, Margrave, J. L., Franklin, J. L. 1973. *Chem. Phys.* 60: 2158
168. Chantry, P. J. 1969. *J. Chem. Phys.* 51:3369
169. Chaney, E. L., Christophorou, L. G. 1969. *J. Chem. Phys.* 51:883
170. Lifshitz, C., Peers, A. M., Grajower, R., Weiss, M. 1970. *J. Chem. Phys.* 53:4605
171. Spence, D., Schulz, G. J. 1973. *J. Chem. Phys.* 58:1800
172. Ferguson, E. E., Fehsenfeld, F. C., Schmeltekopf, A. L. 1967. *J. Chem. Phys.* 47:3085
173. Seman, M. L., Branscomb, L. M. 1962. *Phys. Rev.* 125:1602
174. Johnson, H. R., Rohrlich, F. 1959. *J. Chem. Phys.* 30:1608
175. Edlen, B. 1960. *J. Chem. Phys.* 33:98
176. Clementi, E., McLean, A. D., Raimondi, D. L., Yoshimine, M. 1964. *Phys. Rev. A* 133:1274
177. Branscomb, L. M., Smith, S. J. 1956. *J. Chem. Phys.* 25:598
178. Branscomb, L. M., Burch, D. S., Smith, S. J., Geltman, S. 1963. *Phys. Rev.* 111:504
179. Steiner, B., Seman, M. L., Branscomb, L. M. 1962. *J. Chem. Phys.* 37:1200
180. Burch, D. S., Smith, S. J., Branscomb, L. M. 1958. *Phys. Rev.* 112:171
181. Burch, D. S., Smith, S. J., Branscomb, L. M. 1959. *Phys. Rev.* 114:1652
182. Branscomb, L. M. 1966. *Phys. Rev.* 148:11
183. Steiner, B. 1968. *J. Chem. Phys.* 49:5097
184. Lineberger, W. C., Woodward, B. W. 1970. *Phys. Rev. Lett.* 25:424
185. Smyth, K. C., McIver, R. T. Jr., Brauman, J. I., Wallace, R. W. 1971. *J. Chem. Phys.* 54:2758
186. Feldmann, D. 1970. *Z. Naturforsch. A* 25:621
187. Burt, J. A. 1972. *J. Chem. Phys.* 57:4649
188. Henglein, A., Muccini, G. A. 1959. *J. Chem. Phys.* 31:1426
189. Kraus, K. A., Müller-Duysing, W., Neuert, H. 1961. *Z. Naturforsch. A* 16:1385
190. Lifshitz, C., Grajower, R. 1969. *Int. J. Mass Spectrom. Ion Phys.* 3:Appen. 5
191. Dunkin, D. B., Fehsenfeld, F. C., Ferguson, E. E. 1972. *Chem. Phys. Lett.* 15:257
192. Hughes, B. M., Lifshitz, C., Tiernan, T. O. 1973. *J. Chem. Phys.* 59:3162
193. Leffert, C. B., Jackson, W. M., Rothe, E. W. 1973. *J. Chem. Phys.* 58:5801
194. Lifshitz, C., Hughes, B. M., Tiernan, T. O. 1970. *Chem. Phys. Lett.* 7:469
195. Chupka, W. A., Berkowitz, J., Gutman, D. 1971. *J. Chem. Phys.* 55:2724
196. Lifshitz, C., Tiernan, T. O., Hughes, B. M. 1973. *J. Chem. Phys.* 59:3182
197. Pekeris, C. L. 1962. *Phys. Rev.* 126: 1470
198. Woolf, M. J., Schwarzschild, M., Rose, W. K. 1964. *Astrophys. J.* 140:833
199. Zollweg, R. J. 1969. *J. Chem. Phys.* 50:4251
200. Hall, J. L. 1967. *Phys. Rev. Lett.* 19:737
201. Scheer, M. D. 1969. *J. Chem. Phys.* 50:4343
202. Weiss, A. 1968. *Phys. Rev.* 166:70
203. Hornig, R. E. 1954. *J. Chem. Phys.* 22:126
204. Smith, L. G. 1937. *Phys. Rev.* 51:263
205. Buchel'nikova, N. I. 1958. *Usp. Fiz. Nauk* 65:351
206. Chantry, P. J., Schulz, G. J., 1964. *Phys. Rev. Lett.* 12:449
207. Elder, F. A., Villarejo, D., Inghram, M. G. 1965. *J. Chem. Phys.* 43:758
208. Berry, R. S., Mackie, J. C., Taylor, R. L., Lynch, P. 1965. *J. Chem. Phys.* 43:3067
209. Smyth, K. C., Brauman, J. I. 1972. *J. Chem. Phys.* 56:4620
210. Tsuda, S., Hamill, W. H. 1966. *Advan. Mass Spectrom.* 3:249

211. Kay, J., Page, F. M. 1966. *Trans. Faraday Soc.* 62:3081
212. Cade, P. E. 1967. *J. Chem. Phys.* 47:2390
213. Brauman, J. I., Smyth, K. C. 1969. *J. Am. Chem. Soc.* 91:7778. This value was given as a wavelength cutoff at 6400 Å in the paper.
214. Popp, H. P. 1965. *Z. Naturforsch. A* 20:642
215. Popp, H. P. 1967. *Z. Naturforsch. A* 22:254
216. Milstein, R., Berry, R. S. 1971. *J. Chem. Phys.* 55:4146
217. Bohme, D. K., Lee-Ruff, E., Young, L. B. 1972. *J. Am. Chem. Soc.* 94:5153
218. Buchel'nikova, N. J., Ionov, N. I. 1959. *Russ. J. Phys. Chem.* 33:286
219. Heron, J. T., Dibeler, V. H. 1960. *J. Am. Chem. Soc.* 82:1555
220. Page, F. M. 1968. *J. Chem. Phys.* 49:2466
221. Berkowitz, J., Chupka, W. A., Walter, T. A. 1969. *J. Chem. Phys.* 50:1497
222. Jortner, J., Sokolov, U. 1961. *Nature* 190:1003
223. Williams, J. M., Hamill, W. H. 1968. *J. Chem. Phys.* 49:4467
224. Stockdale, J. A. D., Compton, R. N., Hurst, G. S., Reinhardt. P. W. 1969. *J. Chem. Phys.* 50:2176
225. Chupka, W. A., Berkowitz, J., Gutman, D. 1971. *J. Chem. Phys.* 55:2733
226. Siegel, M. W., Celotta, R. J., Hall, J. L., Levine, J., Bennett, R. A. 1972. *Phys. Rev. A* 6:607
227. MacNeil, K. A. G., Thynne, J. C. J. 1970. *Int. J. Mass Stectrom. Ion Phys.* 5:329
228. Burch, D. S., Smith, S. J., Branscomb, L. M. 1958. *Phys. Rev.* 112:171
229. Mulliken, R. S. 1959. *Phys. Rev.* 115:1225
230. Curran, R. K. 1961. *J. Chem. Phys.* 35:1849
231. Phelps, A. V., Pack, J. L. 1961. *Phys. Rev. Lett.* 6:111
232. Pack, J. L., Phelps, A. V. 1966. *J. Chem. Phys.* 44:1870
233. Lifshitz, C., Grajower, R. 1969. *Int. J. Mass Spectrom. Ion Phys.* 3:Appen. 5 Authors suggest EA(O_2) > EA(C_6F_6) which is taken to be 1.2 eV from (119). Later work (196) has shown EA(C_6F_6) $\geq 1.8 \pm 0.3$ eV, or ≥ 0.2 (246).
234. Vogt, D., Hauffe, B., Neuert, H. 1970. *Z. Physik.* 232:439
235. Tiernan, T. O., Hughes, B. M., Lifshitz, C. 1971. *J. Chem. Phys.* 55:5692
236. Celotta, R., Bennett, R., Hall, J., Levine, J., Siegel, M. W. 1971. *Bull. Am. Phys. Soc.* 16:212
237. Nolley, S. J., Compton, R. N. 1971. *Chem. Phys. Lett.* 9:529
238. Zemke, W. T., Das, G., Wahl, A. C. 1972. *Chem. Phys. Lett.* 14:310
239. Kraus, K. 1961. *Z. Naturforsch. A* 16:1378
240. Steiner, B. 1968. *J. Chem. Phys.* 49:5097
241. Smyth, K. C., Brauman, J. I. 1972. *J. Chem. Phys.* 56:1132
242. Gaines, A. F., Kay, J., Page, F. M. 1966. *Trans. Faraday Soc.* 62:874
243. Thynne, J. C. J., MacNeil, K. A. G. 1970. *Int. J. Mass Spectrom. Ion Phys.* 5:95
244. Reese, R. M., Dibeler, V. H., Franklin, J. L. 1958. *J. Chem. Phys.* 29:880
245. Dillard, J. G., Franklin, J. L. 1968. *J. Chem. Phys.* 48:2353
246. Harland, P. W. 1971. PhD thesis. Edinburgh Univ., England
247. MacNeil, K. A. G., Thynne, J. C. J. 1969. *J. Phys. Chem.* 73:2960
248. Curran, R. K. 1962. *Phys. Rev.* 125:910
249. Vogt, D. 1969. *Int. J. Mass Spectrom. Ion Phys.* 3:81
250. Warneck, P. 1969. *Chem. Phys. Lett.* 3:532
251. Lacmann, K., Herschbach, D. R. 1970. *Chem. Phys. Lett.* 6:106
252. Milligan, D. E., Jacox, M. E., Guillory, W. A. 1970. *J. Chem. Phys.* 52:3864
253. Lacmann, K., Herschbach, D. R. 1971. *Bull. Am. Phys. Soc.* 16:213
254. Baede, A. P. M. 1972. *Physica* 59:541
255. O'Hare, P. A. G. 1971. *J. Chem. Phys.* 54:4124
256. Harland, P. W., Thynne, J. C. J. 1970. *J. Phys. Chem.* 74:52
257. Nikol'skii, G. P., Kazarnovskaya, L. I., Bagdasar'yan, Z. A., Kazarnovskii, I. A. 1950. *Dokl. Akad. Nauk SSSR* 72:713
258. Harland, P. W., Thynne, J. C. J. 1969. *J. Phys. Chem.* 73:4031. Value of 1.04 eV calculated from stability of FCl^- to the decomposition process resulting in a Cl^- ion and an F atom.
259. Yatsimirskii, K. B. 1947. *J. Gen. Chem. USSR* 17:2019
260. Dillard, J. G., Franklin, J. L. 1968. *J. Chem. Phys.* 48:2349
261. di Domenico, A., Harland, P. W, Franklin, J. L. 1972. *J. Chem. Phys.* 56:5299

262. Lifshitz, C., Grajower, R. 1969. *Int. J. Mass Spectrom. Ion Phys.* 3:211
263. O'Hare, P. A. G., Wahl, A. C. 1970. *J. Chem. Phys.* 53:2834
264. Smyth, K. C., Brauman, J. I. 1972. *J. Chem. Phys.* 56:5993
265. Lifshitz, C., Grajower, R. 1972. *Int. J. Mass Spectrom. Ion Phys.* 10:25
266. MacNeil, K. A. G., Thynne, J. C. J. 1972. *Int. J. Mass Spectrom. Ion Phys.* 9:135
267. Vought, R. H. 1947. *Phys. Rev.* 71:93
268. Curran, R. K. 1961. *J. Chem. Phys.* 34:2007
269. Lossing, F. P., Tickner, A. W., Bryce, W. A. 1951. *J. Chem. Phys.* 19:1254
270. MacNeil, K. A. G., Thynne, J. C. J. 1969. *Int. J. Mass Spectrom. Ion Phys.* 2:1
271. Curran, R. K. 1961. *J. Chem. Phys.* 34:1069
272. Harland, P. W., Thynne, J. C. J. 1973. *Int. J. Mass Spectrom. Ion Phys.* 11:137
273. Eyring, H., Hirschfelder, J. O., Taylor, H. S. 1936. *J. Chem. Phys.* 4:479
274. Dalgarno, A., McDowell, M. R. C. 1956. *Proc. Phys. Soc. A* 69:615
275. O'Hare, P. A. G., Wahl, A. C. 1971. *J. Chem. Phys.* 54:4563
276. Hogness, T. R., Harkness, R. W. 1928. *Phys. Rev.* 32:784
277. Muschlitz, E. E. 1957. *J. Appl. Phys.* 28:1414
278. Melton, C. E., Rupp, G. 1958. *J. Am. Chem. Soc.* 80:5573
279. Henglein, A., Muccini, G. A. 1929. *J. Chem. Phys.* 31:1426
280. Dillard, J. G., Franklin, J. L. 1968. *J. Chem. Phys.* 48:2349
281. Stockdale, J. A., Compton, R. N., Rheinhardt, P. W. 1969. *Phys. Rev.* 184:81
282. Lindholm, E. 1954. *Z. Naturforsch. A* 9:535
283. Paulson, J. F. 1970. *J. Chem. Phys.* 52:959
284. Futrell, J. H., Miller, C. D. 1966. *Rev. Sci. Instrum.* 37:1521
285. Paulson, J. F. 1970. *J. Chem. Phys.* 52:963
286. Tiernan, T. O., Hughes, B. M., Lifschitz, C. 1971. *J. Chem. Phys.* 55:5692
287. Fehsenfeld, F. C., Schmeltekopf, A. L., Goldan, P. D., Schiff, H. I., Ferguson, E. E. 1966. *J. Chem. Phys.* 44:4087, 4095
288. Fehsenfeld, F. C., Ferguson, E. E., Schmeltekopf, A. L. 1966. *J. Chem. Phys.* 44:3022
289. Voshall, R. E., Pack, J. L., Phelps, A. V. 1965. *J. Chem. Phys.* 43:1990
290. Parkes, D. A. 1971. *Trans. Faraday Soc.* 67:711
291. Wobschall, D., Graham, J. R., Malone, D. P. 1963. *Phys. Rev.* 131:1565
292. Wobschall, D. 1965. *Rev. Sci. Instrum.* 36:466
293. Llewellyn, P. M. 1965. *ASTM Conference on Mass Spectrometry*, St. Louis, Missouri
294. Anders, L. R., Beauchamp, J. L., Dunbar, R. C., Baldeschwieler, J. D. 1966. *J. Chem. Phys.* 45:1062
295. Beauchamp, J. L., Anders, L. R., Baldeschwieler, J. D. 1967. *J. Am. Chem. Soc.* 89:4569
296. Baldeschwieler, J. D. 1966. Paper presented at the 152nd Annual Meeting of Am. Chem. Soc., New York
297. See, for example, the review by Lampe, F. W., Franklin, J. L., Field, F. H. 1961. *Progr. React. Kinet.* 1:68
298. Field, F. H. 1961. *J. Am. Chem. Soc.* 83:1523

299a. Munson, M. S. B., Field, F. H. 1965. *J. Am. Chem. Soc.* 87:3294

299b. Munson, M. S. B., Field, F. H. 1966. *J. Am. Chem. Soc.* 88:2621

300. Dougherty, R. C., Weisenberger, C. R. 1968. *J. Am. Chem. Soc.* 90:6570
301. Dougherty, R. C., Roberts, J. D. *Proceedings of the 1972 Conference on Mass Spectrometry*, 259. Sponsored by ASMS
302. Dannenbaum, H. P., Dougherty, R. C. Ibid, p. 243
303. Dzidic, I. Private communication
304. Kebarle, P., Goodbole, E. W. 1963. *J. Chem. Phys.* 39:1131
305. Kebarle, P., Hogg, A. M. 1965. *J. Chem. Phys.* 42:789
306. Yang, J. H., Conway, D. C. 1964. *J. Chem. Phys.* 40:1729
307. Kebarle, P., Haynes, R. M., Collins, G. J. 1967. *J. Am. Chem. Soc.* 89:5753
308. Wexler, J., Lifschitz, A., Quattrochi, A. 1966. *Advan. Chem. Ser.* 58:193
309. McDaniel, E. W., Čermák, V., Dalgarno. A., Ferguson, E. E., Friedman, L. 1970. *Ion-Molecule Reactions.* New York: Wiley
310. Franklin, J. L., Ed. 1972. *Ion-Molecule Reactions.* New York: Plenum
311. Schmeltekopf, A. L., Fehsenfeld, F. C., Ferguson, E. E. 1967. *Astrophys. J.* 148:L155
312. Schmeltekopf, A. L., Fehsenfeld, F. C., Ferguson, E. E. 1966. *J. Chem. Phys.* 45:1844

313. Fehsenfeld, F. C., Schmeltekopf, A. L., Schiff, H. I., Ferguson, E. E. 1967. *Planet. Space Sci.* 15:373
314. Fehsenfeld, F. C., Schmeltekopf, A. L., Gilman, G. I., Puls, L. G., Ferguson, E. E. 1966. *Bull. Am. Phys. Soc.* 11:501
315. Ferguson, E. E., Fehsenfeld. F. C., Schmeltekopf, A. L. 1969. *Advan. Chem. Ser.* 80:83
316. Moruzzi, J. L., Phelps, A. V. 1966. *Bull. Am. Phys. Soc.* 11:506; 1966. *J. Chem. Phys.* 45:4617
317. Moruzzi, J. L., Ekin, J. W., Phelps, A. V. 1968. *J. Chem. Phys.* 48:3070.
318. Dunkin, D. B., Fehsenfeld, F. C., Ferguson, E. E. 1970. *J. Chem. Phys.* 53:987
319a. Fehsenfeld, F. C., Ferguson, E. E. 1969. *J. Chem. Phys.* 51:3512
319b. Fehsenfeld, F. C., Ferguson, E. E. 1970. *J. Chem. Phys.* 53:2614
319c. Parkes, D. A. 1972. *J. Chem. Soc. Faraday Trans. I* 68:613
320. Fehsenfeld, F. C., Albritton, D. L., Burt, J. A., Schiff, H. I. 1969. *Can. J. Chem.* 47:1793
321. Curran, R. K. 1962. *Phys. Rev.* 125:910
322. Rutherford, J. A., Turner, B. R. 1967. *J. Geophys. Res.* 72:3795
323. Paulson, J. F. 1966. *Advan. Chem. Ser.* 58:28
324. Fehsenfeld, F. C., Ferguson, E. E. 1968. *Planet. Space Sci.* 16:701
325. Paulson, J. F. quoted in McDaniel et al (309), table 6-2
326. Ferguson, E. E. 1969. *Can. J. Chem.* 47:1815
327. McFarland, M., Dunkin, D. B., Fehsenfeld, F. C., Schmeltekopf, A. L., Ferguson, E. E. 1972. *J. Chem. Phys.* 56:2358
328. Fehsenfeld, F. C. 1971. *J. Chem. Phys.* 54:438
329. Fehsenfeld, F. C., Ferguson, E. E., Bohme, D. K. 1969. *Planet. Space Sci.* 17:1759
329a. Melton, C. E., Neece, G. A. 1971. *J. Am. Chem. Soc.* 93:6757
330. Marx, R., Mauclaire, G., Fehsenfeld, F. C., Dunkin, D. B., Ferguson, E. E. 1973. *J. Chem. Phys.* 53:3267
331. Parkes, D. A. 1973. *J. Chem. Soc. Faraday Trans. I* 68:2103
332. Bohme, D. K., Fehsenfeld, F. C. 1969. *Can. J. Chem.* 47:2717
333. Adams, N. G., Bohme, D. K., Dunkin, D. B., Fehsenfeld, F. C., Ferguson, E. E. 1970. *J. Chem. Phys.* 52:3133
334. Parkes, D. A., Sugden, T. M. 1972. *Trans. Faraday Soc. II* 68:600
335. Fehsenfeld, F. C., Howard, C. J., Ferguson, E. E. 1973. *J. Chem. Phys.* 58:5841
336. Parkes, D. A. 1972. *J. Chem. Soc. Faraday Trans. I* 68:627
337. Fehsenfeld, F. C., Ferguson, E. E. 1974. *J. Chem. Phys.* To be published
337a. Fehsenfeld, F. C., Ferguson, E. E. 1972. *Planet. Space Sci.* 20:295
338. Stockdale, J. A. D., Compton, R. N., Reinhardt, P. W. 1970. *Int. J. Mass Spectrom. Ion Phys.* 4:401
339. Stockdale, J. A., Nelson, D. R., Davis, F. J., Compton, R. N. 1972. *J. Chem. Phys.* 56:3336
340. Payzant, J. D., Kebarle, P. 1972. *J. Chem. Phys.* 56:3482
341. Pack, J. L., Phelps, A. V. 1971. *Bull. Am. Phys. Soc.* 16:214
342. Ferguson, E. E., Dunkin, D. B., Fehsenfeld, F. C. 1972. *J. Chem. Phys.* 57:1459
343. Ridge, D. P. 1973. *Proc. ASMS Conf. ICR Mass Spectrom.*, San Francisco, California
344. Paulson, J. F. 1970. *J. Chem. Phys.* 52:963
345. Stockdale, J. A. D., Compton, R. N., Schweinler, H. C. 1970. *J. Chem. Phys.* 53:1502
346. Bohme, D. K., Young, L. B. 1970. *J. Am. Chem. Soc.* 92:7354
347. Paulson, J. F. 1970. *J. Chem. Phys.* 52:959
348. Center, R. E. 1972. *J. Chem. Phys.* 56:371
349. Haartz, J. C., Lifschitz, C., Tiernan, T. O. 1973. See Ref. 343
350. Dillard, J. G., Franklin, J. L. 1968. *J. Chem. Phys.* 48:2353
351. Dillard, J. G., Franklin, J. L. 1968. *J. Chem. Phys.* 48:2349
352. Rhyne, T. C., Dillard, J. G. 1971. *Int. J. Mass Spectrom. Ion Phys.* 7:371
353. Dillard, J. G., Seitz, W. A., Franklin, J. L. 1968. *J. Chem. Phys.* 48:3828
354. di Domenico, A., Franklin, J. L. 1972. *Int. J. Mass Spectrom. Ion Phys.*
355. Brauman, J. I., Blair, L. K. 1968. *J. Am. Chem. Soc.* 90:5636
356. Brauman, J. I., Blair, L. K. 1968. *J. Am. Chem. Soc.* 90:6561
357. Brauman, J. I., Blair, L. K. 1970. *J. Am. Chem. Soc.* 92:5986
358. Tiernan, T. O., Hughes, B. M. 1969. *Proc. 17th Ann. Conf. Mass Spectrom.*, Dallas, Texas. Sponsored by ASMS
359. Bohme, D. K., Lee-Ruff, E., Young, L. B. 1971. *J. Am. Chem. Soc.* 93:4608
360. McIver, R. T., Scott, J. A., Riveros, J. A. 1973. *J. Am. Chem. Soc.* 95:2706

361. Haney, M. A., McIver, R. T. 1971. *Proc. 19th Ann. Conf. Mass Spectrom.*, Atlanta, Georgia. Sponsored by ASMS
362. Bohme, D. K., Young, L. B. 1970. *J. Am. Chem. Soc.* 92:7354
363. McIver, R. T., Scott, J. A., Silvers, J. H. 1973. *Proc. 21st Ann. Conf. Mass Spectrom.*, San Francisco, California. Sponsored by ASMS
364. Jäger, K., Sewic, M., Henglein, A. 1967. *Z. Naturforsch. A* 22:961
365. Dillard, J. G., Rhyne, T. C. 1969. *J. Am. Chem. Soc.* 91:6521.
366. Dillard, J. G. 1973. See Ref. 363
367. Haartz, J. C., McDaniel, D. H. 1973. *J. Am. Chem. Soc.* 95:8562
368. Clow, R. P., Tiernan, T. O. 1972. *Proc. 20th Ann. Conf. Mass Spectrom.*, Dallas, Texas. Sponsored by ASMS
369. Vogt, D. 1969. *Int. J. Mass Spectrom. Ion Phys.* 3:81
370. Paulson, J. F. Unpublished results
371. Paulson, J. F. 1972. See Ref. 310
372. Martin. G. D., Bailey, T. L. 1968. *J. Chem. Phys.* 49:1977
373. Dempster, A. J. 1916. *Phil. Mag.* 31:438
374. Lampe, F. W., Franklin, J. L., Field, F. H. 1961. *Progr. React. Kinet.* 1:68
375. Stevenson, D. P. 1963. *Mass Spectrometry*, ed. C. A. McDowell, 589. New York: McGraw
376. Melton, C. E. 1963. *Mass Spectrometry of Organic Ions*, ed. F. W. McLafferty, 65. New York: Academic
377. Futrell, J. H., Tiernan, T. O. 1968. *Fundamental Processes in Radiation Chemistry*, ed. P. Ausloos, 171. New York: Interscience
378. Ausloos, P., Ed. 1966. *Symposium on Ion-Molecule Reactions*, Vol. 58. Washington. DC: Am. Chem. Soc.
379. Ferguson, E. E. 1970. *Accounts Chem. Res.* 3:402
380. Ferguson, E. E. 1973. *Atomic Nuclear Data Tables* 12:159
381. Beauchamp, J. L. 1971. *Ann. Rev. Phys. Chem.* 22:527
382. Ferguson, E. E., Fehsenfeld, F. C., Schmeltekopf, A. L. 1969. *Advan. At. Mol. Phys.* 5:1
383. Gould, R. K., Miller, W. J. 1973. See Ref. 363
384. See Kebarle, P. (310, p. 315) for a general survey of this work.
385. Arshadi, M., Yamdagni, R., Kebarle, P. 1970. *J. Phys. Chem.* 74:1475
386. Arshadi, M., Kebarle, P. 1970. *J. Phys. Chem.* 74:1483
387. Pauling, L. 1948. *The Nature of the Chemical Bond*, 346. Ithaca, New York: Cornell Univ. Press
388. Yamdagni, R., Kebarle, P. 1971. *J. Am. Chem. Soc.* 93:7139
389. Yamdagni, R., Kebarle, P. 1972. *J. Am. Chem. Soc.* 94:2940
390. Payzant, J. D., Yamdagni, R., Kebarle, P. 1971. *Can. J. Chem.* 49:3308
391. Langevin, M. P. 1905. *Ann. Chim. Phys.* 5:245. An English translation is given as Appendix I in McDaniel, E. W. 1964. *Collision Phenomena in Ionized Gases.* New York: Wiley
392. Gioumousis, G., Stevenson, D. P. 1958. *J. Chem. Phys.* 29:294
393. Eyring, H., Hirschfelder, J. O., Taylor, H. S. 1936. *J. Chem. Phys.* 4:479
394. Theard, L. P., Hamill, W. H. 1962. *J. Am. Chem. Soc.* 84:730
395. Moran, T. F., Hamill, W. H. 1963. *J. Chem. Phys.* 39:1413
396. Light, J. C. 1964. *J. Chem. Phys.* 40:3221
397. Pechukas, P., Light, J. C. 1965. *J. Chem. Phys.* 42:3281
398. Light, J. C., Lin, J. 1965. *J. Chem. Phys.* 43:3209
399. Tannenwald, A. 1966. *Proc. Phys. Soc.* 87:109
400. Wolf, F. A. 1966. *J. Chem. Phys.* 44:1619
401. Henchman, M. 1972. See Ref. 310, p. 101
402. Bennett, S. L., Margrave, J. L., Franklin, J. L. 1974. *J. Chem. Phys.* In press
403. Bennett, S. L., Margrave, J. L., Franklin, J. L., Hudson, J. E. 1973. *J. Chem. Phys.* 59:5814

International Journal of Mass Spectrometry and Ion Physics, 15 (1974) 197–213
© Elsevier Scientific Publishing Company, Amsterdam – Printed in the Netherlands

IONIC COLLISION PROCESSES IN MIXTURES OF METHANE WITH CARBON DIOXIDE AND NITROUS OXIDE

K. R. RYAN AND P. W. HARLAND
National Standards Laboratory, Sydney 2008 (Australia)

(Received 4 June 1974)

ABSTRACT

Ionic collision processes which occur in weakly ionized mixtures of methane with nitrous oxide and carbon dioxide have been studied while the ions are contained in a potential well generated by an electron space charge. Where comparison is possible the results are in reasonable agreement with other recent measurements. In addition, the present study has allowed an assessment of the relative importance of electron transfer and hydrogen atom abstraction processes when either N_2O^+ or CO_2^+ react with methane. Within the experimental error, the combined rate coefficient for hydrogen atom abstraction and electron transfer reactions with methane is the same for both N_2O^+ and CO_2^+. However for N_2O^+ only one reactive collision in 15 results in electron transfer, while for CO_2^+ electron transfer occurs for one reactive collision in four.

In mixtures of nitrous oxide with methane evidence has been obtained for the production of m/e 30. Threshold measurements reveal that both N_2O^+ and CH_4^+ are possible precursor ions. In the same mixtures it has been found that CH_3^+ will react with N_2O but that the observed rate coefficient rises from 0 to 0.53×10^{-9} cm^3 molecule^{-1} sec^{-1} as the ionizing electron energy is increased from the threshold for CH_3^+ production to 20 eV. This observation is taken as evidence for a reaction pathway which involves only internally excited CH_3^+ ions.

INTRODUCTION

In mixtures of methane with either carbon dioxide or nitrous oxide, the following rapid ionic reactions are possible.

$CH_4^+ + X \rightarrow$ products (A)
$CH_5^+ + X \rightarrow$ products (B)
$X^+ + CH_4 \rightarrow$ products (C)

where X represents CO_2 or N_2O. Reactions represented by (A), (B) and (C) have been studied by high-pressure mass spectrometry [1], ion cyclotron resonance mass spectrometry [2], flowing afterglow methods [3, 4] and, quite recently, by the trapped ion method [5]. Not all of the reactions have been studied by all of these techniques but sufficient overlap exists to demonstrate significant discrepancies in the rate coefficient measurements.

Two sources of these discrepancies are readily recognizable. The first stems from systematic errors associated with a particular investigation. The second source of discrepancy is a more fundamental one brought about by differences in the energy of the reactant ion. It is well known that some ionic reaction rates are influenced by both the internal and translational energy of the reactant species [6]. Since, in general, the available experimental methods do not allow the unique specification of the energy state of the ion, differences in measured rate coefficients are to be expected. Some of the difficulties associated with the evaluation of the relative importance of these two sources of discrepancy are discussed further below with reference to some recent measurements of simple reactions in methane.

Because the proton affinities of methane and carbon dioxide are about equal [4], it is found that when the equilibrium

$$CO_2H^+ + CH_4 \rightleftharpoons CH_5^+ + CO_2 \qquad (1)$$

is reached, measurable quantities of both CO_2H^+ and CH_5^+ coexist. This has allowed the measurement of the equilibrium coefficient K_p by Kasper and Franklin [1], using high-pressure mass spectrometry, by Bohme et al. [3] and by Hemsworth et al. [4] using flowing afterglow methods and, more recently, by Harrison and Blair [5] using the trapped ion technique. The large discrepancies observed in the value obtained for K_p have been attributed to the fact that neither the method of Kasper and Franklin nor that of Harrison and Blair allows the ions to attain thermal equilibrium.

Presented below are the results for rate coefficient measurements for several reactions in pure methane, in methane and carbon dioxide mixtures, and in methane and nitrous oxide mixtures. These measurements have all been made using the ion trapping technique and by controlling the parameters so that the mean translational energy of the primary ions is kept to ~0.1 eV. This point is discussed further in the Experimental section.

EXPERIMENTAL

All the reactions discussed here have been studied using the technique for ion trapping described by Bourne and Danby [7] and developed for ion–molecule studies by Herod and Harrison [8]. The performance of the National Standards Laboratory research mass spectrometer when set up for ion trapping has been

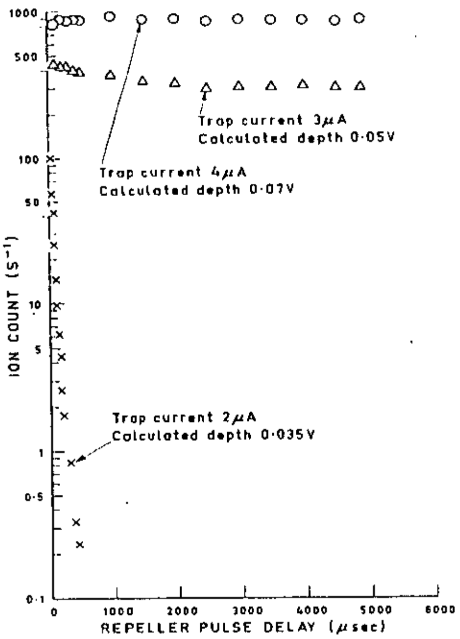

Fig. 1. Trapping characteristics obtained for Ar^+ in pure argon. The well depth is expected to be proportional to the trap current and the calculated depths are shown on the figure.

described by Ryan and Graham [9]. No changes have been made either to the apparatus or in the conditions employed in that study. Calculations indicate that the space charge well is less than 0.1 V in depth and the results for Ar^+ in pure argon shown in Fig. 1 support this. The well depth, which is expected to be proportional to electron current [10], is seen to be too shallow to trap any ions when the current is 2 μamp, but when this is increased to 4 μamp quite good trapping characteristics are obtained. For an ion source temperature of 340 K the argon ions formed at any point in the electron beam will have an initial mean kinetic energy of 0.043 eV. The effect of the space charge well will be to modify this distribution, but it is clear from the 2 μamp results (Fig. 1) that those ions formed at the bottom of the well (and hence unable to derive kinetic energy from it) possess sufficient kinetic energy to escape from the well. From this we conclude that the well depth for the 2 μamp case is <0.043 V. Because of the assumed proportionality between depth and electron current, we expect the depth at 4 μamp to be <0.086 V.

The relationship between the pressure in the inlet reservoir and the collision chamber density has been established using the method of Stevenson and Schissler [11] with argon as the calibrating gas. This procedure yields a rate coefficient of $(1.22 \pm 0.02) \times 10^{-9}$ cm^3 molecule^{-1} sec^{-1} for the reaction of CH_4^+ with methane. Here the errors shown represent reproducibility and not accuracy. Henchman has made a compilation of values for this reaction coefficient (Table IV ref. [6]) and concludes that it is 1.2×10^{-9} cm^3 $molecule^{-1}$ sec^{-1} with an uncertainty of 1×10^{-10} cm^3 $molecule^{-1}$ sec^{-1}. Thus the measurement made here is in close agreement with values obtained by other methods.

Measurements show that the gas flow is molecular and this is supported by the results of Ryan and Graham [9] which show that a fourfold increase in the reservoir pressure had no significant effect on the rate coefficients obtained for the reaction of CH_4^+ with methane or H_2^+ with hydrogen. For gas mixtures the sum of the % composition for each component has been $(100 \pm 1)\%$ in all cases, while the error in the composition of any component is $\leq 1\%$ of its value.

RESULTS AND DISCUSSION

Reactions in pure methane

Before the results obtained for mixtures of methane with nitrous oxide or carbon dioxide can be interpreted, allowance must be made for those reactions which occur in pure methane. We have measured the rate coefficients for reactions of both CH_4^+ and CH_3^+ and observations of the secondary ions produced indicate that, under the prevailing conditions, the only reactions which occur are:

$$CH_4^+ + CH_4 \rightarrow CH_5^+ + CH_3 \qquad (2)$$

$$CH_3^+ + CH_4 \rightarrow C_2H_5^+ + H_2 \qquad (3)$$

Measurement of the rate coefficients for these two reactions yield $(1.22 \pm 0.02) \times 10^{-9}$ cm^3 $molecule^{-1}$ sec^{-1} and $(1.31 \pm 0.04) \times 10^{-9}$ cm^3 $molecule^{-1}$ sec^{-1} for reactions (2) and (3) respectively. As pointed out in the Experimental section, reaction (2) is used to calibrate the flow system and all other rate coefficients are referred to it.

Table 1 illustrates the difficulty in assessing the reliability of rate coefficient measurements even for the relatively uncomplicated reactions in methane. All of the measurements reported there have been made by observing the attenuation of the primary ion rather than the production of the secondary ion. Furthermore, with the exception of Herod and Harrison [8], all authors claim that their measurements are made under conditions for which the primary ions have low translational energy (i.e. a mean energy ~0.1 eV). The table, while it is by no means exhaustive (a more comprehensive compilation is given by Huntress and Pinizzotto [14]), does illustrate the amount of variation to be found among recent measurements. In fact the two most recent measurements for the CH_3^+ reaction, those of Huntress and Pinizzotto and of Futrell [13], lie close to the opposite ends of the distribution of the literature values tabulated by Huntress and Pinizzotto.

TABLE 1

COMPILATION OF RECENT VALUES FOR THE RATE COEFFICIENTS OF CH_4^+ AND CH_3^+ DECAY IN PURE METHANE

Reaction	*Reaction rate coefficients (cm³ molecule⁻¹ sec⁻¹ × 10⁹)*				
	Fluegge [12]	*Herod and Harrison [8]*	*Futrell [13]*	*Huntress and Pinizzotto [14]*	*This work*
$CH_4^+ + CH_4 \xrightarrow{k_{CH_4^+}} CH_5^+ + CH_3$	1.2	1.20	1.20	1.11±0.04[a]	1.22
$CH_3^+ + CH_4 \xrightarrow{k_{CH_3^+}} C_2H_5^+ + H_2$	1.3±0.1	1.15±0.05	1.30	0.89±0.03[a]	1.31±0.04
Reaction rate coefficient ratio					
$k_{CH_4^+}/k_{CH_3^+}$	0.92±0.07	1.04±0.05	0.92±0.05	1.25±0.05	0.93±0.04

[a] Pressure measured using a capacitance manometer attached directly to the reaction region; other values in table obtained using indirect pressure measurements.

There is ample evidence [6] to show that the rate coefficient for the reaction of CH_4^+ does not vary within the range of conditions represented by the measurements in Table IV of [6]. If $k_{CH_4^+}$ does not vary but there is a real variation in $k_{CH_4^+}/k_{CH_3^+}$, then $k_{CH_3^+}$ must vary according to the experimental conditions employed.

Factors which may affect the rate of reaction of CH_3^+ are the internal and translational energy of the ion. In order to determine the effect of excess internal energy on $k_{CH_3^+}$ we have studied reaction (3) as a function of the electron energy near the threshold for CH_3^+. Our results, shown in Table 2, make it clear that the energy of the electrons used to produce the CH_3^+ ion has no measurable effect, in our apparatus, on the subsequent rate of reaction of that ion. Table 2 shows that exactly the same conclusions may be drawn for the CH_4^+ ion. Whether the variation observed in Table 1 for $k_{CH_4^+}/k_{CH_3^+}$ is caused by the undoubted differences in ion velocity distributions or by unknown instrumental effects is uncertain. However, it seems likely that some instrumental effect has not been taken into account in the work of Huntress and Pinizzotto.

TABLE 2

RATE COEFFICIENT FOR CH_4^+ AND CH_3^+ DECAY IN PURE METHANE AS A FUNCTION OF UNCORRECTED ELECTRON ENERGY

Reaction	*k (cm³ molecule⁻¹ sec⁻¹ × 10⁹) for electron energy (eV) (in parenthesis)*			
$CH_4^+ + CH_4 \rightarrow CH_5^+ + CH_3$	1.20 (13),	1.23 (15),	1.22 (17),	1.22 (20)
$CH_3^+ + CH_4 \rightarrow C_2H_5^+ + H_2$	1.32 (13.5),	1.32 (15),	1.28 (17),	1.31 (20)

Reactions in mixtures of methane with nitrous oxide

It is to be expected that the ionic chemistry of these mixtures will be dominated by reactions (2), (4), (5) and (6).

$$CH_4^+ + CH_4 \rightarrow CH_5^+ + CH_3 \qquad (2)$$

$$CH_4^+ + N_2O \rightarrow N_2OH^+ + CH_3 \qquad (4)$$

$$N_2O^+ + CH_4 \rightarrow N_2OH^+ + CH_3 \qquad (5)$$

$$CH_5^+ + N_2O \rightarrow N_2OH^+ + CH_4 \qquad (6)$$

Ion cyclotron resonance, ICR, studies have made it clear that both CH_4^+ and N_2O^+ react rapidly [2] and, in addition to reactions (2) to (6), the much slower reactions

$$CH_4^+ + N_2O \rightarrow NOH^+ + CH_3N \qquad (7)$$

and

$$N_2O^+ + CH_4 \rightarrow NOH^+ + CH_3N \qquad (8)$$

have been proposed.

Typical results from the present study are shown in Figs. 2 to 5. For N_2O^+ the removal rate is uncomplicated by opposing reactions and the ion intensity is seen to decay in a simple exponential manner yielding a rate coefficient of $(1.17 \pm 0.07) \times 10^{-9}$ cm^3 molecule^{-1} sec^{-1} which is in satisfactory agreement with a combined coefficient of $(0.98) \times 10^{-9}$ cm^3 molecule^{-1} sec^{-1} found by McAllister [2] for reactions (5) and (8). Examination of Curve (A) Fig. 3 reveals that for

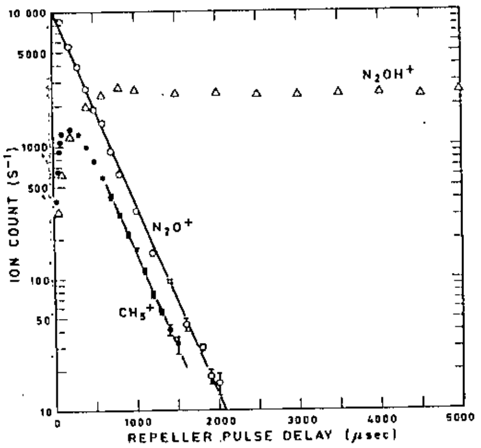

Fig. 2. Typical characteristics obtained for N_2O^+, CH_5^+ and N_2OH^+ in ~1:1 mixture of N_2O with CH_4. Ionizing electron energy 20 eV; collision chamber density 7.1×10^{12} molecules cm^{-3}. The counts shown for N_2O^+ and CH_5^+ are to be divided by 10.

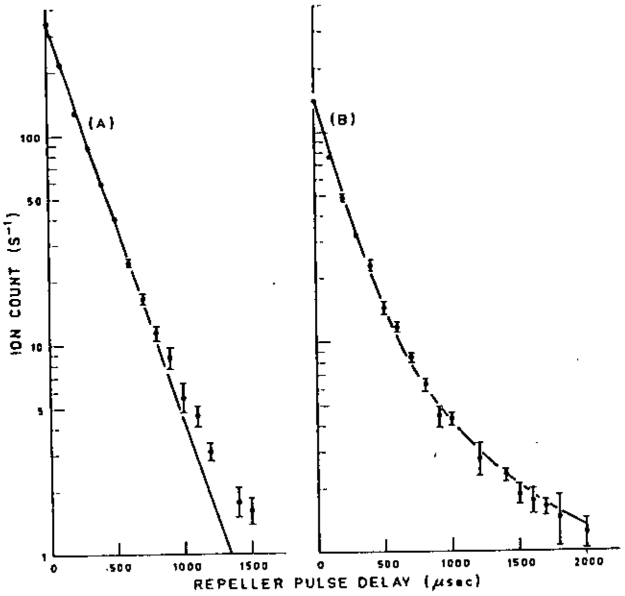

Fig. 3. CH_4^+ decay curves in N_2O/CH_4 mixtures. Curve (A) obtained from ~1:1 mixture; the straight line represents a least squares fit out to 700 μsec delay. Curve (B) obtained from ~4:1 N_2O:CH_4 mixture. The smooth curve through the points represents a fit according to eqn. (10) (see text). Ionizing electron energy 20 eV; collision chamber density 3.4×10^{12} molecules cm^{-3}.

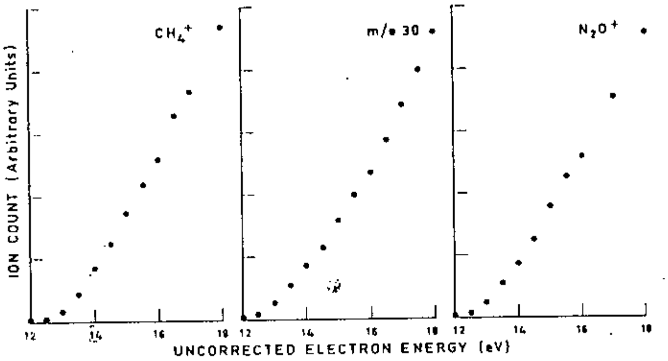

Fig. 4. Ionization efficiency curves for CH_4^+, N_2O^+ and m/e 30 from 1:1 mixture of N_2O with CH_4. Collision chamber density 3.4×10^{12} molecules cm^{-3}.

CH_4^+ in a 1:1 mix there is a slight but significant deviation from a simple exponential decay. To emphasize this deviation a least squares plot has been drawn through the points for reaction times to 700 μsec. It can be seen readily that the values for CH_4^+ counts at reaction times greater than 700 μsec are systematically higher than those predicted from the initial slope. These observations, which have been quite reproducible, are similar to those which we have recently attributed to charge

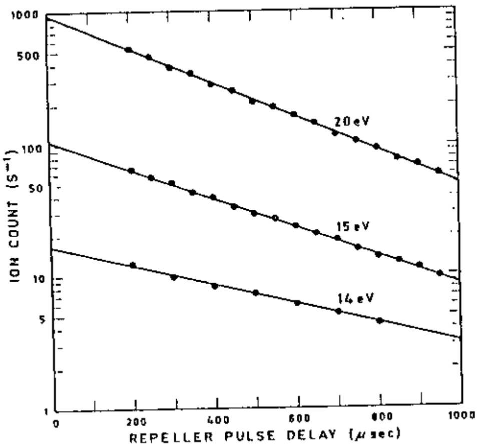

Fig. 5. CH_3^+ decay curves in ~1:1 mixture of N_2O with CH_4. Electron energy as shown; collision chamber density 3.4×10^{12} molecules cm^{-3}.

transfer phenomena [9]. In this particular case the observations can be explained if the reaction

$$N_2O^+ + CH_4 \rightarrow CH_4^+ + N_2O \tag{9}$$

occurs. Support for this interpretation is given by the results in Curve (B) Fig. 3 which have been obtained in ~4:1 mixture of nitrous oxide and methane. In this mixture the relative importance of the charge transfer reaction is increased, thereby causing a complete departure from a simple exponential behaviour for the CH_4^+ decay curve.

If reactions (4), (7) and (9) all occur, the expected dependence of CH_4^+ on time is given by

$$[CH_4^+]_t = [CH_4^+]_0 \exp[-((k_4+k_7)[N_2O]+k_2[CH_4])t] + \frac{k_9[CH_4][N_2O^+]_0[\exp[-[CH_4](k_5+k_8+k_9)t]-\exp[-((k_4+k_7)[N_2O]+k_2[CH_4]t))]]}{[N_2O](k_4+k_7)+[CH_4](k_2-(k_5+k_8+k_9))} \tag{10}$$

where k_X is the rate coefficient for reaction (X) and [Y] is the particle density of species Y.

An expression of the form given by eqn. (10) has been fitted to the experimental observations and the result is the smooth curve through the points for CH_4^+ in curve (B) Fig. 3. From this analysis one obtains a value of $(1.5\pm0.2)\times10^{-9}$ cm^3 $molecule^{-1}$ sec^{-1} for k_4+k_7, which is to be compared with the combined value of 1.04×10^{-9} cm^3 $molecule^{-1}$ sec^{-1} found by McAllister. Analysis of the decay curve for CH_4^+ also yields a value of $(0.08\pm0.04)\times10^{-9}$ cm^3 $molecule^{-1}$ sec^{-1} for k_9, the charge transfer rate coefficient. The low value of the rate coefficient for charge transfer relative to the high value for CH_4^+ reactions leads to large errors in the estimate of $(k_5+k_8+k_9)$

by these curve fitting procedures. Thus the direct measurement of $(k_5+k_8+k_9)$ results in a value of $(1.17 \pm 0.07) \times 10^{-9}$ cm^3 molecule^{-1} sec^{-1}, whereas curve fitting procedures yields a value of $(1.8 \pm 0.9) \times 10^{-9}$ cm^3 molecule^{-1} sec^{-1}.

Figure 2 shows a typical result for CH_5^+ which is produced by reaction (2) and removed by reactive collisions with N_2O. For repeller delay times greater than 700 μsec, production of CH_5^+ can no longer be detected and the intensity of this ion then decays exponentially. A least squares fit to this exponential decay yields a rate coefficient of $(0.79 \pm 0.10) \times 10^{-9}$ cm^3 molecule^{-1} sec^{-1} and measurement of the secondary ion intensities shows that CH_5^+ is removed almost exclusively by reaction (6).

The production of a secondary ion with a mass-to-charge ratio of 31 has been observed in this study. This is probably NOH^+ which has been reported in the ICR studies of McAllister. Using double resonance methods he concluded that both reactions (7) and (8) occur and do so with the same rate coefficient of 3.0×10^{-11} cm^3 molecule^{-1} sec^{-1}. In principle it is possible to estimate the contributions of both CH_4^+ and N_2O^+ to the production of NOH^+ in our experiments but its low intensity makes this impractical. However it is possible to set upper limits for the rate coefficients of reactions (7) and (8). If it is first assumed that reaction (7) is the only process leading to the production of NOH^+, then it can be shown readily that

$$\frac{[NOH]^+_\infty}{[CH_4^+]_0 + \frac{k_9}{k_5+k_9}[N_2O^+]_0} = \frac{k_7[N_2O]}{(k_7+k_4)[N_2O]+k_2[CH_4]} \tag{11}$$

where the subscripts outside the concentration brackets refer to reaction time and the subscripts on the rate coefficients refer to the appropriate reaction. This treatment leads to an upper limit of $(\sim 2.0) \times 10^{-11}$ cm^3 molecule^{-1} sec^{-1} for reaction (7), which agrees within experimental error with the value of $(3 \pm 1.5) \times 10^{-11}$ cm^3 molecule^{-1} sec^{-1} reported by McAllister.

If it is now assumed that reaction (8) is the sole means of production of NOH^+, one obtains an upper limit of $\sim 6 \times 10^{-12}$ cm^3 molecule^{-1} sec^{-1}, in poor agreement with the value of $(3 \pm 1.5) \times 10^{-11}$ cm^3 molecule^{-1} sec^{-1} found by McAllister.

This study has also revealed the production of a secondary ion with a mass-to-charge ratio of 30. After allowing for contributions from $^{13}C^{12}CH_5^+$ and from NO^+, mass 30 accounts for $\sim 2\%$ of all secondary ion production. Attempts to use threshold measurements to establish the identity of the primary ion which leads to mass 30 have been unsuccessful. In Fig. 4 are shown crude ionization efficiency curves obtained in a 1:1 mixture of CH_4 with N_2O. The electron energy scale has not been corrected but it is clear from the figure that the process which produces mass 30 has a threshold close to thresholds of N_2O^+ and CH_4^+. The precision of the experiment does not allow either of these ions to be excluded as a possible precursor, and all that can be said is that at least one of them is probably responsible for the production of mass 30. Furthermore it is not possible to be certain of the composition of this secondary ion but we note that it may be CH_4N^+ since both

$$N_2O^+ + CH_4 \rightarrow CH_4N^+ + NO \qquad (12)$$

and

$$CH_4^+ + N_2O \rightarrow CH_4N^+ + NO \qquad (13)$$

are exothermic.

Shown in Fig. 5 are decay curves obtained for the CH_3^+ ion in a 1:1 mixture of CH_4 with N_2O for ionizing electron energies of 20, 15 and 14 eV. It can be seen that the slope of these sets of results depends upon the energy of the ionizing electron. This increase in slope with increasing electron energy may be caused by reactions of internally excited CH_3^+ ions. Because we have shown, in Table 2, that the rate coefficient for the CH_3^+ reaction in pure methane is independent of electron energy, we interpret the results in Fig. 5 as evidence for a reaction of excited CH_3^+ ions with N_2O. From a consideration of reactions which would be endothermic for the ground state ion one or more of the following ions may be suggested as possible reaction products: CHN_2^+ (*m/e* 41), $CH_3N_2^+$ (*m/e* 43), CH_3NO^+ and N_2OH^+ (*m/e* 45). The absence of ion signals for *m/e* 41 and *m/e* 43 excludes these ions as reaction products and the masking of *m/e* 45 by N_2OH^+ formed from reactions (4), (5) and (6) precludes conclusions regarding the last two ions. An additional possibility is that exothermic reaction channels for the ground state ion may be suppressed by insurmountable activation energy barriers. Consideration of these, and the opening of such channels to the internally excited CH_3^+ ions, suggests N_2H^+ (*m/e* 29) and CH_3O^+ (*m/e* 31) as further possible reaction products. However, as in the case of *m/e* 45 above, the N_2H^+ ion would be masked by the $C_2H_5^+$ ion formed by reaction (3) and the CH_3O^+ ion is excluded because the low ion signal detected at *m/e* 31, and attributed to NOH^+

TABLE 3

REACTION RATE COEFFICIENTS (cm^3 $molecule^{-1}$ $sec^{-1} \times 10^9$) FOUND FOR THE REACTION: $CH_3^+ + N_2O \rightarrow$ products

Uncorrected electron energy (eV)	*Reaction rate coefficient*[a]
20	0.53±0.01
18	0.50±0.02
16	0.43±0.02
15	0.34±0.02
14	0[b]

[a] Values computed using the measured value of 1.31×10^{-9} cm^3 $molecule^{-1}$ sec^{-1} for reaction (3).

[b] Actual value obtained −0.04±0.04.

(see above), is insufficient above the threshold for CH_3^+ to support this possibility. Table 3 summarizes measurements made for this rate coefficient as a function of electron energy.

Reactions in mixtures of methane with carbon dioxide

Ionic reactions in methane/carbon dioxide mixtures have been studied recently by flowing afterglow [3 and 4], high pressure mass spectrometry [1], and trapped ion techniques [5]. It is clear from these studies that the most rapid processes are

$$CH_4^+ + CO_2 \rightarrow CO_2H^+ + CH_3 \quad (14)$$

$$CH_4^+ + CH_4 \rightarrow CH_5^+ + CH_3 \quad (15)$$

$$CO_2^+ + CH_4 \rightarrow CO_2H^+ + CH_3 \quad (16)$$

$$CO_2H^+ + CH_4 \rightarrow CH_5^+ + CO_2 \quad (17)$$

$$CH_5^+ + CO_2 \rightarrow CO_2H^+ + CH_4. \quad (18)$$

Primary ion reactions

The experimental results of the present study are summarized in Figs. 6 to 8. It is clear from Fig. 6 that CO_2^+ decays in a simple exponential manner and the value obtained for the rate coefficient, $(1.15 \pm 0.1) \times 10^{-9}$ cm^3 molecule^{-1} sec^{-1}, is in good agreement with the value of $(1.07 \pm 0.09) \times 10^{-9}$ cm^3 molecule^{-1} sec^{-1} obtained by Harrison and Blair [5]. There seems little doubt that an error in the estimate of the ion source residence time is responsible for the high value of 2.3×10^{-9} cm^3 molecule^{-1} sec^{-1} reported by Kasper and Franklin [1].

Some results for CH_4^+ removal are shown in Fig. 7. Harrison and Blair have reported that the rate of disappearance of CH_4^+ depends strongly on the ionizing electron energy and they have attributed this to the charge transfer process

$$CO_2^+ + CH_4 \rightarrow CH_4^+ + CO_2. \quad (19)$$

The experimental conditions chosen by Harrison and Blair were such that the amount of CH_4^+ ions decayed by a factor of about 10 during the reaction time employed. Further, while it is true that the rate of disappearance of the CH_4^+ ion depended on the electron energy used, it is also true that their results appear to follow a simple exponential law for a given electron energy. Harrison and Blair were unable to assess the relative importances of reactions (16) and (19).

Our analysis for those systems in which charge transfer occurs concurrently with ion–molecule reaction is given by eqn. (10). It is clear from this analysis that, provided the charge transfer reaction has sufficient cross section, one would expect CH_4^+ ions to decay in a complicated way rather than in a simple exponential

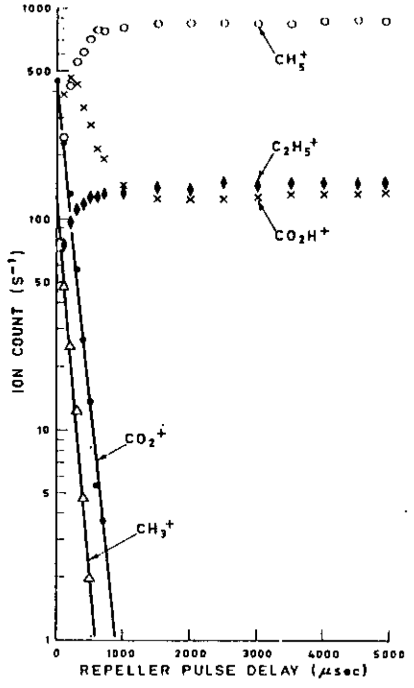

Fig. 6. Typical characteristics obtained for CH_3^+, CO_2^+, CH_5^+, $C_2H_5^+$ and CO_2H^+ obtained in ~1:1 mixture of CO_2 with CH_4. Ionizing electron energy 16 eV; collision chamber density 1.7×10^{12} molecules cm^{-3}.

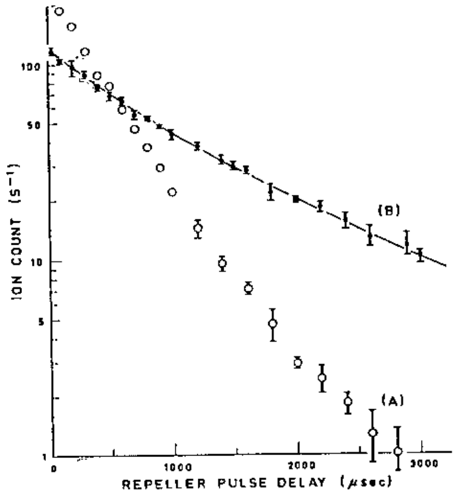

Fig. 7. CH_4^+ decay curves in CO_2/CH_4. Curve (A) obtained from ~1:1 mixture of curve (B) obtained from ~4:1 CO_2:CH_4 mixture. The smooth curve through the points represents a fit to an equation analogous to (10). Ionizing electron energy 20 eV; collision chamber density 3.4×10^{12} molecules cm^{-3}.

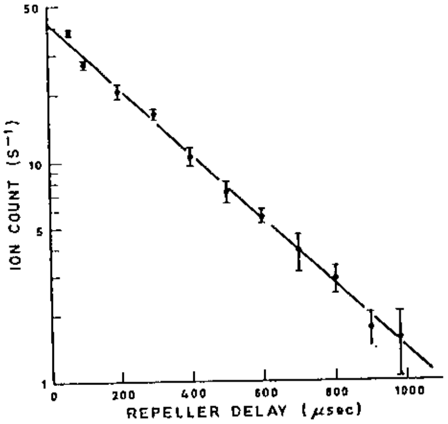

Fig. 8. CH_4^+ decay characteristic from ~1:1 mixture of CO_2 with CH_4. Nominal ionizing electron energy 13 eV; collision chamber density 3.4×10^{12} molecules cm^{-3}.

manner. A typical result for CH_4^+ decay in a 1:1 mixture at 20 eV ionizing electron energy is shown in curve (A) Fig. 7. Two points are immediately obvious. First, the dependence of CH_4^+ on time does not follow a simple exponential behaviour over the 200-fold reduction of intensity shown. Secondly, over the first order o magnitude of reduction of CH_4^+, no departure from a simple exponential behaviour can be detected.

Curve (B) Fig. 7 shows results obtained in a 4:1 CO_2/CH_4 mixture which has been chosen to accentuate the effect of the charge transfer reaction on the decay of the CH_4^+ ion. The smooth curve through the experimental points represents the fit obtained using an expression analogous to equation (10). This treatment yields a value of $(1.13\pm0.05)\times10^{-9}$ cm^3 $molecule^{-1}$ sec^{-1} for the combined reactions of CO_2^+, $(3\pm1.5)\times10^{-10}$ cm^3 $molecule^{-1}$ sec^{-1} for the charge transfer reaction and $(0.6\pm0.2)\times10^{-9}$ for the reaction of CH_4^+ with CO_2.

The high signal-to-noise ratio of our apparatus allows a measurement to be made of the CH_4^+ decay under conditions such that the initial ratio of CH_4^+/CO_2^+ is ~10:1. This ratio is obtained for a nominal electron ionizing energy of 13 eV and a typical result is shown in Fig. 8. Under these conditions the contribution of the charge transfer reaction (19) to the initial slope of the CH_4^+ ion decay should be negligible and thus a direct measurement for the rate coefficient of reaction (14) is possible. In this way a rate coefficient of $(0.8\pm0.1)\times10^{-9}$ cm^3 $molecule^{-1}$ sec^{-1} has been obtained for reaction (14) and this is in reasonable agreement with the value of $(0.6\pm0.2)\times10^{-9}$ cm^3 $molecule^{-1}$ sec^{-1} obtained from the curve fitting procedure.

Reactions of the CO_2H^+ and CH_5^+ ions

Reactions of these species have been studied by high pressure mass spectrometry [1], flowing afterglow [3 and 4], and trapped ion methods [5]. All of these investigations have shown that the proton affinities of methane and carbon dioxide are almost equal and, for this reason, a steady state can be obtained in which measurable quantities of both ionic species are present. The flowing afterglow method allows the ion to attain thermodynamic equilibrium and this permits an accurate measurement of K_p, the equilibrium coefficient for

$$CO_2H^+ + CH_4 \rightleftharpoons CH_5{}^+ + CO_2 . \tag{1}$$

Recent flowing afterglow studies have shown that K_p depends strongly on temperature within the range of 196 K to 533 K [4].

Although a steady state can be reached in both the trapped ion and high pressure mass spectrometric studies, an accurate measurement of K_p is not possible by these methods. This is because the internal and translational energy carried by the CO_2H^+ and $CH_5{}^+$ ions will affect their relative intensities when the steady state is attained. A comparison of the apparent values of K_p so obtained with values from the flowing afterglow may lead to qualitative information about the departure from thermodynamic equilibrium.

Typical results for CO_2H^+ and $CH_5{}^+$ obtained in our apparatus are shown in Fig. 6. We obtain a value of (9.5 ± 1) for K_p at 340 K, which is to be compared with 7.4 measured by Kasper and Franklin and ~ 20 derived from flowing afterglow measurements. Harrison and Blair, working at 373 K, obtained a value of 3.8 compared with a value of ~ 16 derived from flowing afterglow measurements at the same temperature.

Some comments on the qualitative effects of departure from Maxwell-Boltzmann energy distribution are possible. Under suitable conditions of pressure and composition, all primary ions are removed rapidly and the dependence of CO_2H^+ and $CH_5{}^+$ on time is then described by

$$-\frac{d[CO_2H^+]}{dt} = k_{17}[CO_2H^+][CH_4] - k_{18}[CO_2][CH_5{}^+] \tag{20}$$

which has the solution

$$\ln[(CO_2H^+)_t - (CO_2H^+)_\infty] = \ln[(CO_2H^+)_0 - (CO_2H^+)_\infty] - (k_{17}(CH_4) + k_{18}(CO_2))t \tag{21}$$

Measurement of the slope of a plot of $\ln[(CO_2H^+)_t - (CO_2H^+)_\infty]$ against reaction time together with the value of $k_{17}/k_{18} = 9.5$ leads to separate values k_{17} and k_{18}. In this way the results of fifteen measurements have led to values of $(5.5 \pm 0.8) \times 10^{-10}$ cm^3 molecule^{-1} sec^{-1} and $(5.9 \pm 1.0) \times 10^{-11}$ cm^3 molecule^{-1} sec^{-1} for k_{17} and k_{18} respectively.

From the work of Kasper and Franklin, the flowing afterglow studies, as well as the trapped ion measurements of Harrison and Blair, one may also obtain an estimate of both k_{17} and k_{18} during the approach to a steady state. The results of these determinations are summarized in Table 4.

TABLE 4

RATE COEFFICIENTS FOR THE FORWARD AND BACKWARD REACTIONS IN THE EQUILIBRIUM: $CO_2H^+ + CH_4 \rightleftharpoons CH_5^+ + CO_2$

Investigator[a]	*Rate coefficient (cm³ molecule⁻¹ sec⁻¹ × 10⁹)*		k_{17}/k_{18}
	k_{17}	k_{18}	
Kasper and Franklin[b] (340 K)	0.13	0.018[c]	7.4
Bohme et al.[e] (300 K)	0.78	0.033	23.6
Harrison & Blair[f] (373 K)	0.61[d]	0.15[d]	4.0
This work (340 K)	0.56[d]	0.06[d]	9.5

[a] Temperature at which the investigation was carried out is shown in parenthesis.
[b] Ref. 1.
[c] Deduced from a measurement of k_{17} and the ratio k_{17}/k_{18}.
[d] Deduced from a measurement of $(k_{17}+k_{18})$ and the ratio k_{17}/k_{18}.
[e] Ref. 3.
[f] Ref. 5.

Harrison and Blair have pointed out that internal and translational energy are likely to have a greater effect on the rate coefficient for the endothermic reaction (18) than on the rate coefficient of the reverse reaction.

The results in Table 4 make it difficult to decide if this is true. Certainly the values obtained for k_{17} by Bohme et al., by Harrison and Blair, and by us are in reasonable agreement. On the other hand the value of Kasper and Franklin is lower by about a factor of 5. Unless this value may be discounted, it is not possible to say that k_{17} is unaffected by the energy of the ions. However, in comparing our measurements with those of Harrison and Blair we feel that some conclusions may be drawn. The experimental procedures used are similar and this suggests that the internal energy of the ions will not vary significantly between both sets of experiments. Accordingly the significant difference in the value of k_{18} between this work and that of Harrison and Blair is probably related to differences in the mean translational energy of the CH_5^+ ion. Harrison and Blair point out that the rate of the endothermic reaction (18) would be expected to increase with increasing energy of the CH_5^+ ion. If this interpretation is correct then we conclude that the mean translational energy for the CH_5^+ ion in our work is significantly lower than that for the experiments of Harrison and Blair.

CONCLUSION

In Table 5 are summarized those rate coefficients measured in this study but not reported in Tables 1 to 4. In this table as for all others, the rate coefficients reported for this work are derived from an assumed value of 1.22×10^{-9} cm³ molecule⁻¹ sec⁻¹ for the reaction of CH_4^+ with methane. Some aspects of Table 5

TABLE 5

RATE COEFFICIENTS MEASURED IN THIS STUDY BUT NOT INCLUDED IN TABLES 1 TO 4

Reaction	*Reaction rate coefficient (cm^3 molecule^{-1} sec^{-1} $\times 10^9$)*[a]	
	This work	*Other measurements*
$N_2O^+ + CH_4 \rightarrow$ products	1.17 ± 0.07	0.98 ± 0.2[b]
$N_2O^+ + CH_4 \rightarrow CH_4^+ + N_2O$	0.08 ± 0.04	—
$N_2O^+ + CH_4 \rightarrow NOH^+ + CH_3N$	≤ 0.006	0.03 ± 0.015[b]
$CH_4^+ + N_2O \rightarrow$ products	1.5 ± 0.2	1.04 ± 0.2[b]
$CH_4^+ + N_2O \rightarrow NOH^+ + CH_3N$	≤ 0.02	0.03 ± 0.015[b]
$CH_5^+ + N_2O \rightarrow$ products	0.79 ± 0.1	—
$CO_2^+ + CH_4 \rightarrow$ products	1.15 ± 0.1	1.07 ± 0.09[c], 2.3[d]
$CO_2^+ + CH_4 \rightarrow CH_4^+ + CO_2$	0.3 ± 0.15	—
$CH_4^+ + CO_2 \rightarrow$ products	0.8 ± 0.1	—

[a] Referred to a value of 1.22 for reaction (2), see text.

[b] Ref. 2.

[c] Ref. 5.

[d] Ref. 1.

need further clarification. In many of the reactions the products are unspecified. The rate coefficient in those cases represents the sum of the rate coefficients for all possible reaction pathways. For N_2O^+ and CO_2^+ separate measurements provide rate coefficients for the electron transfer processes.

Where comparisons are possible in Table 5, the agreement is about as good as can be expected. It must be assumed that the rate coefficient for reactive collision between CO_2^+ and methane reported by Kasper and Franklin is in error because of an under-estimation of the ionic reaction time. However for all of the other major rate coefficients, satisfactory agreement is obtained when the experimental errors are considered. Thus for these exothermic processes, differences in the internal and translational energy of the ions, which may exist between the results compared, would appear to affect the rate coefficient by less than 15%. This finding is in marked contrast to the observations for the endothermic reaction (18) whose rate coefficient appears to be strongly dependent upon the experimental conditions.

The only major discrepancies in Table 5 are for the minor reactions which produce NOH^+. The low rate coefficients for these reactions render them correspondingly more difficult to measure and it is possible that the error limits are greater than shown. Equally likely however is that these minor pathways are most sensitive to the energy carried into the reactive collision.

REFERENCES

1 S. F. Kasper and J. L. Franklin, *J. Chem. Phys.*, 56 (1972) 1156.
2 T. McAllister, *Int. J. Mass Spectrom. Ion Phys.*, 10 (1973) 419.

3 D. K. Bohme, R. S. Hemsworth, H. W. Rundle and H. I. Schiff, *J. Chem. Phys.*, 58 (1973) 3504

4 R. S. Hemsworth, H. W. Rundle, D. K. Bohme, H. I. Schiff, D. B. Dunkin and F. C. Fehsenfeld, *J. Chem. Phys.*, 59 (1973) 61.

5 A. G. Harrison and S. Blair, *Int. J. Mass Spectrom. Ion Phys.*, 12 (1973) 175.

6 M. Henchman, in J. L. Franklin (editor), *Ion-Molecule Reactions*, Vol. 1, Plenum Press, New York 1972.

7 A. J. Bourne and C. J. Danby, *J. Sci. Instrum., Ser.* 2, 1 (1968) 155.

8 A. A. Herod and A. G. Harrison, *Int. J. Mass Spectrom. Ion Phys.*, 4 (1970) 415.

9 K. R. Ryan and I. G. Graham, *J. Chem. Phys.*, 59 (1973) 4260.

10 F. A. Baker and J. B. Hasted, *Phil. Trans. Roy. Soc.*, A261 (1966) 33.

11 D. P. Stevenson and D. O. Schissler, *J. Chem. Phys.*, 29 (1958) 282.

12 R. A. Fluegge, *J. Chem. Phys.*, 50 (1969) 4373.

13 J. H. Futrell, *J. Chem. Phys.*, 59 (1973) 4061.

14 W. T. Huntress Jr and R. F. Pinizzotto, *J. Chem. Phys.*, 59 (1973) 4742.

International Journal of Mass Spectrometry and Ion Physics, 18 (1975) 215–227
© Elsevier Scientific Publishing Company, Amsterdam – Printed in The Netherlands

SOME LOW ENERGY ELECTRON TRANSFER PROCESSES FOR CO_2 AND N_2O

P. W. HARLAND AND K. R. RYAN
National Measurement Laboratory, CSIRO, Sydney 2008 (Australia)

(Received 22 April, 1975)

ABSTRACT

Electron transfer from the molecules N_2O and CO_2 to the ions Kr^+, Ar^+ and $N_2{}^+$ has been studied for primary ions of near thermal energy. The rate coefficient for the reaction between Kr^+ and N_2O has been found to depend strongly upon the electronic state of Kr^+. For the $^2P_{3/2}$ state the rate coefficient is fast and about twenty times higher than the coefficient for the $^2P_{1/2}$ state. As a consequence it has been possible to determine the initial relative abundance of the $^2P_{1/2}$ state as a function of the ionizing electron energy.

For the systems $(Kr^+ + N_2O)$, $(Ar^+ + CO_2)$, $(Ar^+ + N_2O)$, $(N_2{}^+ + CO_2)$ and $(N_2{}^+ + N_2O)$ the amount of excess translational energy detected in the products indicates that the initial and final states differ in energy by ~ 0.1 eV. Even though the Franck–Condon factors are unfavourable, the following systems have been found to react with high rate coefficients: $(Kr^{+\,2}P_{3/2} + N_2O)$, $(Kr^{+\,2}P_{1/2} + CO_2)$, $(Ar^{+\,2}P_{3/2}$, $Ar^{+\,2}P_{1/2} + N_2O)$, $(Ar^{+\,2}P_{3/2}$, $Ar^{+\,2}P_{1/2} + CO_2)$, $(N_2{}^+ + CO_2)$ and $(N_2{}^+ + N_2O)$. From this we conclude that, for fast electron transfer in these systems, it is not a necessary condition that favourable Franck–Condon factors should couple the reactant molecule to the product ion.

INTRODUCTION

At ion energies greater than about 5 eV electron transfer is thought to occur by an electron jump mechanism from a non-orbiting collision [1]. Smith and Kevan [2, 3] have studied a number of these electron transfer processes using primary ions with an average energy of 50 eV. Their results show that the cross section for the process

$$A^+ + B \rightarrow B^+ + A \qquad (1)$$

is high if

(a) an energy state for the ion B^+ corresponds to the recombination energy of A^+, and

(b) if the transition from B to this energy state of B^+ has favourable Franck–Condon (F.C.) factors.

Gauglhofer and Kevan [1] measured electron transfer reactions between several ions and CH_4 at near thermal ion energies. A strong resonance effect was found and the rate coefficients at resonance appear to be ~ 3 times those deduced from simple polarization theory [4]. They concluded from these observations that both energy resonance and favourable F.C. factors are required for fast electron transfer from CH_4 under these conditions. A shift in the observed resonance away from the F.C. manifold for $CH_4{}^+$ production was assumed to be caused by the perturbation of CH_4 by the slowly moving ion. Bowers and Elleman [5] reported a similar shift in the resonance peak when electron transfer processes were studied for a number of ions with SiH_4.

Recently Laudenslager et al. [6] have attempted further to discover the relative importance of F.C. factors and energy resonance for thermal electron transfer processes. They chose a variety of diatomic and simple polyatomic molecules for reaction with rare gas ions. The F.C. manifolds of these molecules consist of a few discrete vibrational levels for each electronic state thereby allowing a more critical test of the importance of resonance and F.C. effects.

In general Laudenslager et al. concluded that both favourable F.C. factors and energy resonance must obtain in order to observe a fast charge transfer reaction. Notable exceptions were the reactions of Ar^+ with both CO_2 and N_2O which are fast yet have unfavourable F.C. factors. On the other hand Kr^+ was found to have a high rate coefficient with CO_2 (where energy resonance for Kr^+-${}^2P_{\frac{1}{2}}$ is within 0.1 eV and the F.C. factors are favourable) and a low rate coefficient with N_2O where the F.C. factors are unfavourable for transitions to N_2O^+ near the energy of $Kr^{+\,2}P_{\frac{1}{2}}$.

The analysis for Kr^+ assumed that the relative abundance of $Kr^{+\,2}P_{\frac{1}{2}}$ is negligible. We report here measurements which show that, when the abundance of $Kr^{+\,2}P_{\frac{1}{2}}$ is taken into account, the results obtained for reactions of Kr^+ with both N_2O and CO_2 cannot be explained in terms of F.C. factors.

EXPERIMENTAL

The reactions discussed here have been studied by an ion trapping technique using apparatus which has been described previously [7]. Ions are produced during a short pulse of energetic electrons and are then trapped in the space charge well created by an electron beam whose energy is below that necessary to produce additional ions. The trapping interval, and hence the time available for ion–molecule interaction, is terminated by a voltage pulse applied to the ion repeller electrode.

For an electron beam of circular cross section, Baker and Hasted [8] have derived an approximate expression for the space-charge well depth which is given by

$$V_{(r)} = I_e r^2 / 4 V_0^{\frac{1}{2}} \pi e_0 a^2 (2\eta)^{\frac{1}{2}} + V_0 \tag{2}$$

where I_e is the electron current, r the distance from the centre of the beam, V_0 the potential on the axis of the beam, e_0 the permittivity of free space, a the radius of the beam, and η is the electron charge/ mass ratio. This expression does not consider the case where the space charge well extends beyond the dimensions of the electron beam. Normally the cross section of the electron beam will be significantly less than that of the ion source through which it is moving. Under these conditions the space charge well extends beyond the dimensions of the electron beam and out to the walls of the ion chamber. Preliminary calculations [9] show that, for our ion source, the major fraction of the space charge well occurs outside the electron beam. For example when the trapping electron current is 5μA the trap depth is ~ 0.025 V from the centre to the edge of the electron beam. For the same conditions positive ions encounter an additional trapping potential of ~ 0.063 V between the edge of the beam and the chamber wall. With the electron current raised to 12 μA these potentials become 0.07 V and 0.15 V respectively. The calculations apply for an electron energy of 4 eV and to that part of the electron beam sampled by the ion exit slit.

From these considerations it is apparent that while primary ions can gain little translational energy from the trap, secondary ions with significant translational energy may be retained. Thus secondary ions may have velocity distributions which are quite different from those of the primary ions. This will occur for those reactions which yield products with substantial kinetic energy. In the experiments described below we have attempted to examine the products for kinetic energy by varying the trap depth through changes in the electron current density. The minimum electron density employed is that required to produce trapping conditions such that an unreactive ion formed with thermal energy may be trapped for 5 milliseconds with less than 5 % attenuation in ion intensity. Typical trapping characteristics for Ar^+ in pure argon have been reported earlier [7b]. There it may be seen that the electron trap in the source here will not meet the above trapping requirement when the electron current is reduced below 4 μA.

All rate coefficients reported here are based upon a value of 1.2×10^{-9} cm^3 molecule^{-1} s^{-1} for the reaction of CH_4^+ with CH_4. Errors shown for rate coefficients represent reproducibility and not accuracy.

RESULTS AND DISCUSSION

(*a*) *Reactions of Kr$^+$ ions*

In Figs. 1–4 are shown typical results obtained in mixtures of krypton with nitrous oxide. Figure 3 shows a family of curves illustrating how the rate of remo-

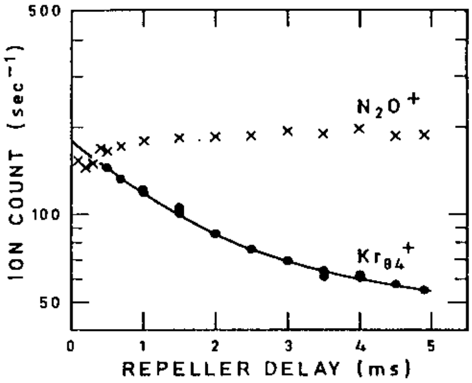

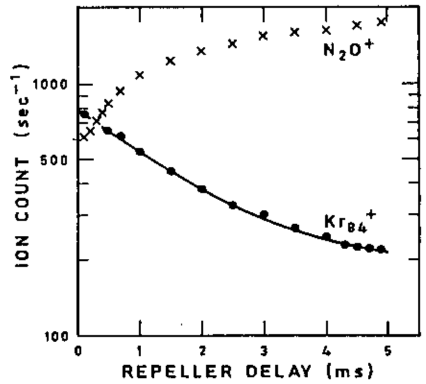

Fig. 1. (left) Dependence of N_2O^+ and $Kr_{84}{}^+$ intensities on reaction time for ~ 1 : 1 mix of N_2O with Kr. Ionizing electron energy 20 eV, trapping electron current 5μA, collision chamber density 3.4×10^{12} molecule cm^{-3}.

Fig. 2. (right) Ion intensities of N_2O^+ and $Kr_{84}{}^+$ for ~1 : 1 mix of N_2O with Kr. Ionizing electron energy 20 eV, trapping electron current 12 μA, collision chamber density 3.4×10^{12} molecule cm^{-3}.

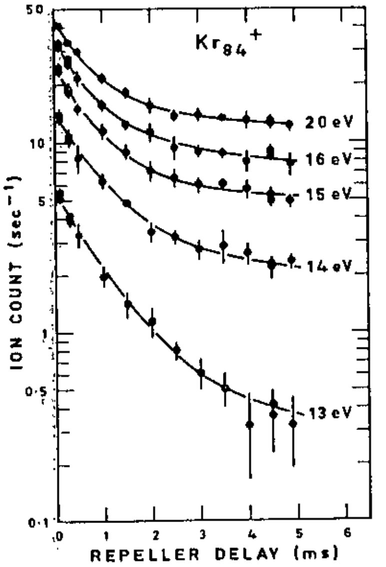

Fig. 3. The effect of ionizing electron energy on the shape of the $Kr_{84}{}^+$ decay curve in ~ 1 : 10 mixture of Kr with N_2O. Collision chamber density 3.4×10^{12} molecule cm^{-3}. Smooth curves through points represent fits according to eqn (3) (see text).

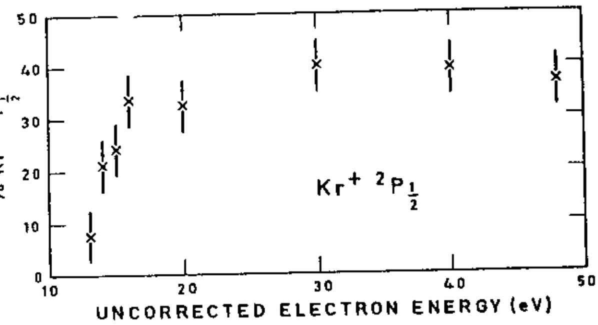

Fig. 4. The percentage abundance of $Kr^{+2}P_{\frac{1}{2}}$ following electron impact of Kr. The values shown are deduced from the reaction of Kr^+ with N_2O.

al of $Kr_{84}{}^+$ is influenced by the energy of the electrons used to generate the $Kr_{84}{}^+$ ions. It is clear that the ions do not decay in a simple exponential manner and that the degree of departure from this simple form increases as the electron energy is increased from 13 eV up to about 20 eV. The $Kr^{+2}P_{\frac{1}{2}}$ and $Kr^{+2}P_{\frac{3}{2}}$ states have energies of 14.665 eV and 13.999 eV respectively and we assume that the departure from simple exponential decay may reflect differing rates of reaction for each of these ionic species with N_2O. If the rate coefficients for the $^2P_{\frac{3}{2}}$ and the $^2P_{\frac{1}{2}}$ state are k_1 and k_2 respectively, then it follows that

$$\begin{aligned}&[Kr^{+2}P_{\frac{3}{2}}]_t+[Kr^{+2}P_{\frac{1}{2}}]_t\\&=[Kr^{+2}P_{\frac{3}{2}}]_0\exp(-k_1[N_2O]_t)+[Kr^{+2}P_{\frac{1}{2}}]_0\exp(-k_2[N_2O]_t),\end{aligned}\tag{3}$$

where $[X]_t$ is the number density of species X at time t.

If this interpretation is correct then the data can be fitted to yield k_1 and k_2. In addition $[Kr^{+2}P_{\frac{3}{2}}]_0$ and $[Kr^{+2}P_{\frac{1}{2}}]_0$ can be evaluated and thus a measure of the relative abundances of these two states as a function of the electron impact energy can be obtained. The smooth curves through the experimental points in Fig. 3 represent a fit to the data according to eqn (3). From the analysis of 20 determinations with electron energies ranging from 13 to 50 eV rate coefficients of $(3.7\pm0.7)\times10^{-10}$ cm^3 molecule^{-1} s^{-1} and $(2.0\pm0.7)\times10^{-11}$ cm^3 molecule^{-1} s^{-1} result for the $^2P_{\frac{3}{2}}$ and $^2P_{\frac{1}{2}}$ states respectively. These rates have been found to be independent of the value chosen for the trapping electron current and thus insensitive to changes in the primary ion velocity distributions associated with these changes in current.

In Fig. 4 the values obtained for $[Kr^{+2}P_{\frac{1}{2}}]_0/\{[Kr^{+2}P_{\frac{1}{2}}]_0+[Kr^{+2}P_{\frac{3}{2}}]_0\}$ plotted against uncorrected electron energy are given. As can be seen, the contribution to the total current from the higher state rises rapidly from threshold to about 20 eV and only minor increases are detected at higher energies. If we assume that near threshold the ionization efficiency curve has a linear dependence on energy, then

$$I_s \propto g_s(E - E_s)$$

where I_s is the ion current produced by electron impact for state s, g_s is the statistical weight, E_s is the threshold energy, and E is the electron energy. Setting

$$\frac{g_{\frac{3}{2}}}{g_{\frac{1}{2}}} = \frac{2}{1}$$

one can calculate the expected abundance of the $^2P_{\frac{1}{2}}$ state as a function of electron energy. Allowance has to be made for the energy distribution of the electron beam. If the filament temperature is taken as 2000 K one finds that the predicted abundance of the $^2P_{\frac{1}{2}}$ state rises rapidly from threshold to a value of 31 % of total ion intensity at 20 eV. Naturally this simple analysis is only of qualitative usefulness but it does predict the general features of the experimental results given in Fig. 4.

Laudenslager et al. [6] conclude that the reason their measured rate coefficient for Kr^+/N_2O is 6 times smaller than their value for Kr^+/CO_2 is because, for the $Kr^{+\,2}P_{\frac{3}{2}}$ state, both energy resonance and favourable F.C. factors apply in the latter case but not in the former. Our measurements indicate that collisions between $Kr^{+\,2}P_{\frac{3}{2}}$ and CO_2 are only about 1.5 times as efficient in promoting electron transfer as are collisions between $Kr^{+\,2}P_{\frac{3}{2}}$ and N_2O. Furthermore our $Kr^{+\,2}P_{\frac{1}{2}}$ and $Kr^{+\,2}P_{\frac{3}{2}}$ rate coefficients with N_2O appear to be difficult to explain on the grounds of energy resonance and favourable F.C. factors. The photoelectron spectrum for N_2O indicates entirely unfavourable F.C. factors for both the $^2P_{\frac{1}{2}}$ and $^2P_{\frac{3}{2}}$ states of Kr^+ [10] and yet we find that the $^2P_{\frac{3}{2}}$ state reacts with a relatively fast rate coefficient which is 20 times the value for the $^2P_{\frac{1}{2}}$ state. In order to explain the rate coefficient for the $^2P_{\frac{3}{2}}$ state in terms of F.C. factors one would have to assume perturbation of the molecule by the ion before the vertical transition required to produce the new ionic species. Laudenslager et al. have invoked this perturbation mechanism to explain the high rate coefficient for Ar^+/CO_2 and Ar^+/N_2O collisions. The necessity to invoke such perturbation effects seems to limit the usefulness of F.C. factors for the prediction of electron transfer rates.

Inspection of Figs. 1 and 2 reveals that not all of the $Kr_{84}{}^+$ ions removed can be accounted for by a corresponding increase in N_2O^+. In fact since $Kr_{84}{}^+$ represents only 57 % of all Kr^+ ions only 30 % and 73 % of the N_2O^+ ions produced are retained for electron trap currents of 5 μA and 12 μA respectively. We believe that the 70 % of ions unaccounted for at 5 μA are those formed with sufficient translational energy to escape from the trap. Increasing the trap current to 12 μA increases the trap depth and accounts for the greater ion retention at this higher current. A crude calculation based upon the assumed trap depths indicates that ~ 0.1 eV of translational energy is released following Kr^+/N_2O collisions.

Typical results for reactions of Kr^+ with CO_2 are shown in Figs. 5 and 6.

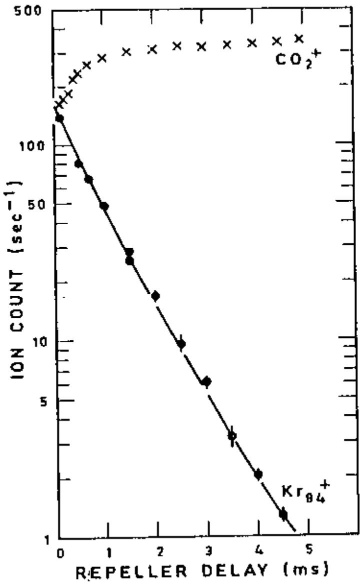

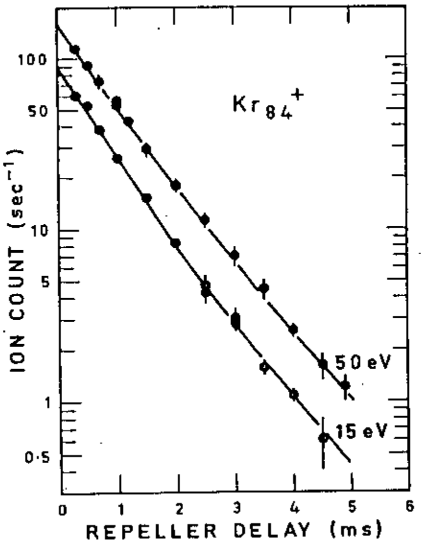

Fig. 5. (left). Observed ion intensities for CO_2^+ and Kr_{84}^+ in ~ 1 : 1 mix of CO_2 with Kr. Ionizing electron energy 20 eV, trapping electron current 5μA, collision chamber density 3.4×10^{12} molecule cm^{-3}. The smooth curve through the points represents a fit to an eqn analogous to eqn (3) (see text).

Fig. 6. (right). Decay characteristics for Kr_{84}^+ in ~ 1 : 1 mix of CO_2 with Kr obtained for ionizing electron energies of 50 eV and 15 eV. The smooth curves through the points represent fits according to an equation analogous to eqn (3) (see text). Collision chamber density 3.4×10^{12} molecule cm^{-3}.

The Kr^+ decay shows a significant and reproducible departure from a simple exponential behaviour. We assume that this is because the $^2P_{\frac{3}{2}}$ and the $^2P_{\frac{1}{2}}$ states react with differing rate coefficients. In the case of Kr^+/N_2O collisions it has been possible to obtain the rate coefficients for each state as well as the relative abundances for the production of these states by electron impact. In the Kr^+/CO_2 collisions however the relatively small changes in slope as a function of time make it difficult to obtain all of this information. Instead we have used the ratios for the states obtained in the Kr^+/N_2O study as fixed parameters and then fitted the curves to obtain the values of the rate coefficients.

In this way one obtains rate coefficients of $(7.9 \pm 0.7) \times 10^{-10}$ cm^3 molecule^{-1} s^{-1} and $(4.9 \pm 0.4) \times 10^{-10}$ cm^3 molecule^{-1} s^{-1} for the $^2P_{\frac{3}{2}}$ and $^2P_{\frac{1}{2}}$ states respectively. Laudenslager et al. have also observed a high rate coefficient for the reaction of Kr^+ with CO_2 and have assumed that this is good evidence for the increased reaction probability for a reaction that has both energy resonance and favourable F.C. factors. However conclusions of this kind must be modified when our rate coefficient for the $^2P_{\frac{1}{2}}$ state is taken into account. This indicates that for Kr^+/CO_2 collisions F.C. factors are not of paramount importance in determining a high rate coefficient. The $Kr^{+2}P_{\frac{3}{2}}$ recombination energy lies within 0.1 V of a peak in the photoelectron spectrum of CO_2^+ [10]. This spectrum reveals that the vibrational level corresponding to this peak accounts for about 15 % of the vertical transitions from the CO_2 molecule to the $\tilde{X}^2\pi_g$ state of the CO_2^+ ion. There are no detectable vertical transitions for $CO_2 \rightarrow CO_2^+$ in the vicinity of the recombination energy of the $Kr^{+2}P_{\frac{1}{2}}$ state. Nevertheless measurements here show that both states of Kr^+ react rapidly with CO_2. Certainly the $^2P_{\frac{1}{2}}$ state reacts more rapidly than the $^2P_{\frac{3}{2}}$ state but both reactions must be considered as fast. Consequently F.C. factors of the undistorted CO_2 molecule would appear to be of little help in predicting the rate coefficients in this case.

The results for the CO_2^+ ion curve shown in Fig. 5 are in marked contrast to the observation for N_2O^+ production on reaction with Kr^+. In the case of CO_2^+ at least 90 % of the ions are retained even at the low trapping current of 5μA. From this we conclude that the electron transfer process involves the release of an insignificant amount of translational energy irrespective of the state of Kr^+ concerned.

(*b*) *Reactions of Argon ions*

Experimental results for the reaction of Ar^+ with N_2O are shown in Figs. 7 and 8. For this reaction the rate coefficient was found to be $(2.8 \pm 0.11) \times 10^{-10}$ cm^3 $molecule^{-1}$ s^{-1} in good agreement with earlier measurements [6]. The rate

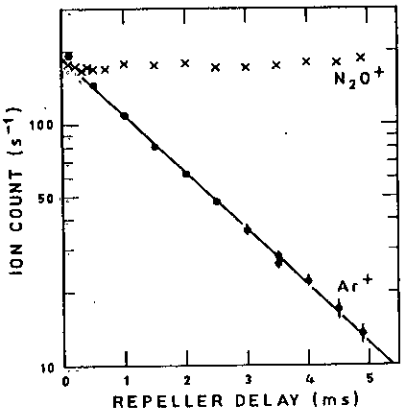

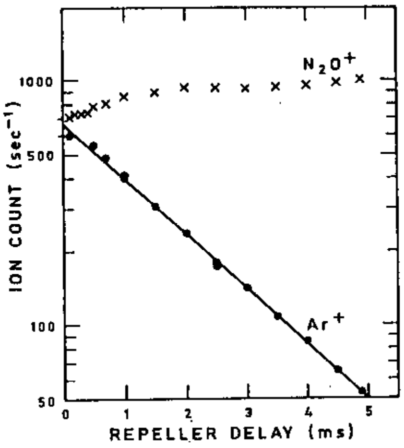

Fig. 7. (left) Dependence of N_2O^+ and Ar^+ intensities on reaction time for ~ 1 : 1 mix of N_2O with Ar. Ionizing electron energy 20 eV, trapping electron current 6 μA, collision chamber density 3.4×10^{12} molecule cm^{-3}.

Fig. 8. (right) Ion intensities of N_2O^+ and Ar^+ for ~ 1 : 1 mix of N_2O with Ar. Ionizing electron energy 20 eV, trapping electron current 12 μA, collision chamber density 3.4×10^{12} molecule cm^{-3}.

coefficient was unaffected by the value of the electron trap current and therefore it is insensitive to the changes in primary ion distribution brought about in this way. Examination of the N_2O^+ curves reveals that for 6 μA only ~ 10 % of the Ar^+ ions removed can be accounted for as N_2O^+ product. For trap currents of 12 μamp about 50 % of the Ar^+ removed can be accounted for as N_2O^+. Although electron transfer between N_2O and Ar^+ has dissociative channels it has been shown that at least 90 % of reactive collisions lead to the production of the molecular ion [11]. Consequently our experimental results are interpreted in terms of loss of N_2O^+ ions with excess translational energy. By comparison of the amount of product ion retained, it is apparent that on average, Ar^+/N_2O collisions release more translational energy than do $Kr^{+\,2}P_{\frac{3}{2}}/N_2O$ collisions. Nevertheless the amount of energy released is still ~ 0.1 eV.

Typical results for Ar^+/CO_2 collisions are shown in Figs. 9 and 10. The rate coefficient for Ar^+ removal was found to be independent of trapping electron current and in good agreement with the value obtained by Laudenslager et al. [6]. Evidence for the production of secondary ions with excess translational energy may be seen from the results. The amount of CO_2^+ retained rose from ~ 20 % at 5 μA to ~ 95 % at 12 μA trapping current. These results again indicate the

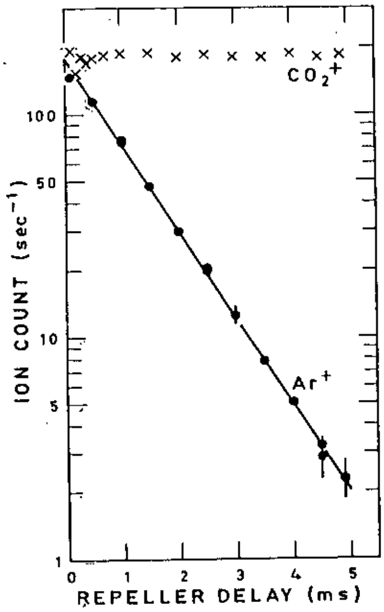

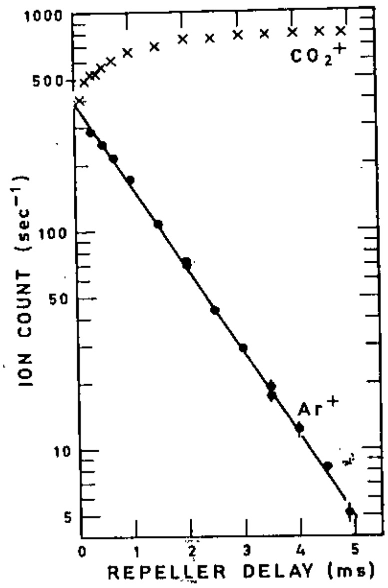

Fig. 9. (left) Ion intensities for CO_2^+ and Ar^+ for ~ 1 : 1 mix of CO_2 with Ar. Ionizing electron energy 20 eV, trapping electron current 5 μA, collision chamber density 3.4×10^{12} molecule cm^{-3}.

Fig. 10. (right) Ion intensities for CO_2^+ and Ar^+ for ~ 1 : 1 mix of CO_2 with Ar. Conditions as for Fig. 9 except that the trapping electron current has been increased to 12 μA.

liberation of translational energy of ~ 0.1 eV but with a narrower distribution than that for Ar^+/N_2O collisions.

(c) *Reactions of N_2^+ ions*

As is the case for Ar^+, the expected recombination energy of N_2^+ does not correspond to a region of favourable F.C. factors for either N_2O or CO_2. We estimate that ~ 75 % of N_2^+ ions have recombination energies between 15.56 and 15.58 eV. The remainder fall into two groups having recombination energies between 15.24 and 15.29 eV and 15.81 and 15.85 eV respectively. These figures were obtained in the following manner. The initial distributions following electron impact of the electronic states $N_2^+B^2\Sigma_u^+$, $N_2^+A^2\pi_u$ and $N_2^+X^2\Sigma_g^+$ as well as the relative populations of vibrational levels within these states were estimated. Transitions from the vibrational levels of the $B^2\Sigma_u^+$ and $A^2\pi_u$ states to the $X^2\Sigma_g^+$ state may then be calculated from the appropriate F.C. factors. The $B^2\Sigma_u^+$ is strongly coupled to the $X^2\Sigma_g^+$ state and will decay rapidly to it by emission. The $A^2\pi_u$ state is metastable with respect to the $X^2\Sigma_g^+$ state but the mean lifetime has been measured to be ~ 10 μs [12]. Thus for times appropriate to these experiments (> 100 μs) both the upper electronic states will have decayed into the $X^2\Sigma_g^+$ state.

The initial relative abundance of the $A^2\pi_u$ state was taken as 30 % [12]. The initial ratio of $X^2\Sigma_g^+/B^2\Sigma_u^+$ is taken as ~ 2.5 : 1 [13]. The initial relative intensities of vibrational levels within these electronic states were taken from Moran and Friedman [13]. The relative populations of the vibrational levels within the $N_2^+X^2\Sigma_g^+$ state following the decay of the B and A states were calculated using the F.C. factors given by Nicholls [14].

Recombination energies at times appropriate to the electron transfer process are obtained by combining the vibrational distribution for the $N_2^+X^2\Sigma_g^+$ state with the F.C. factors calculated by Nicholls [15] for $N_2^+X^2\Sigma_g^+ \rightarrow N_2X^1\Sigma_g^+$. It is important to realise that this last step assumes that the electron transfer occurs by a vertical transition from the unperturbed N_2^+ ion. This point will be discussed further below.

Reactions of N_2^+ with either N_2O or CO_2 showed quite similar behaviour to the corresponding reactions of Ar^+. The N_2^+ reactions gave high rate coefficients in agreement with earlier measurements [11,16, 17] and evidence for the release of translational energy ~ 0.1 eV. A simple exponential decay was observed for the N_2^+ ion with a slope which was independent of the electron energy. From this we conclude that despite whatever states of N_2^+ are present and whatever transitions they undergo on electron capture, state-dependent differences in the rates of these processes are undetectable. Since neither N_2O nor CO_2 have favourable F.C. factors in the region of the expected vertical recombination energies for the N_2^+ ions, it is clear that unperturbed F.C. factors cannot be used to predict rate coefficients for either N_2^+/N_2O or N_2^+/CO_2.

CONCLUSIONS

Table 1 summarizes the values obtained for the electron transfer rate coefficients found in this study and compares them with earlier measurements. The work here indicates that the rate coefficients are insensitive to changes in primary ion translational energy distributions within the range of trapping currents used in the experiments. In general good agreement is seen between measurements here and those from both the flowing afterglow and low energy ICR. This indicates that these electron transfer rate coefficients are insensitive to the differences in primary ion velocity distributions which obtain in these different techniques. For electron transfer in the systems ($N_2O+N_2^+$) and (N_2O+Ar^+) Ryan has shown that the rate coefficients are insensitive to primary ion translational energy over a much broader range than that encountered in any of the three low energy methods [11].

TABLE 1

SUMMARY OF ELECTRON TRANSFER REACTIONS. RATE COEFFICIENTS EXPRESSED AS cm^3 $molecule^{-1}$ $s^{-1} \times 10^{10}$

Reaction[a]		*Previous measurements*	*This work*[b]
$Kr^{+2}P_{\frac{1}{2}}+N_2O$	$\rightarrow N_2O^++Kr$		0.2 ± 0.07
$Kr^{+2}P_{\frac{3}{2}}+N_2O$	$\rightarrow N_2O^++Kr$	1.0[c]	3.7 ± 0.7
$Kr^{+2}P_{\frac{1}{2}}+CO_2$	$\rightarrow CO_2^++Kr$		4.9 ± 0.4
$Kr^{+2}P_{\frac{3}{2}}+CO_2$	$\rightarrow CO_2^++Kr$	6.0[c]	7.9 ± 0.7
$Ar^+\{^2P_{\frac{1}{2}}, {}^2P_{\frac{3}{2}}\}+N_2O$	$\rightarrow N_2O^++Ar$	2.6[d], 3.1[c]	2.8 ± 0.1
$Ar^+\{^2P_{\frac{1}{2}}, {}^2P_{\frac{3}{2}}\}+CO_2$	$\rightarrow CO_2^++Ar$	7.0[c], 7.6[f], 4.2[c]	4.7 ± 0.1
$N_2^++N_2O$	$\rightarrow N_2O^++N_2$	4.0[g], 5.7[d]	7.6 ± 0.2
$N_2^++CO_2$	$\rightarrow CO_2^++N_2$	9.0[h]	8.3 ± 0.4

[a] Rate coefficient measurements refer to primary ion removal. In some cases dissociative paths exist but are of minor significance.

[b] Errors quoted represent reproducibility. All measurements are referred to a value of 12.0 for CH_4^+ removal in CH_4.

[c] Ref. 6.

[d] Ref. 11.

[e] P. Warneck, *J. Chem. Phys.*, 46 (1967) 513.

[f] F. C. Fehsenfeld, E. E. Ferguson and A. L. Schmeltekopf, *J. Chem. Phys.*, 45 (1966) 404.

[g] Reference 16.

[h] Reference 17.

For the reaction

$$X^+ + M \rightarrow M^+ + X$$

to occur with high probability, transitions from the potential energy surface for (X^++M) to one corresponding to (M^++X) must occur readily. If this transition takes place for X^+ sufficiently far removed that the perturbation by it of M is negligible, then the electron transfer will be a near resonant-process. It also follows that, under these conditions, the F.C. factors coupling M with M^+ must be favourable. In those systems where the energy levels of M^+ which are near resonant with the recombination energy of X^+ do not have favourable F.C. factors with M, one would expect little electron transfer at large separation. However as X^+ approaches M more closely, perturbation may occur to the extent that the required transition takes place. The difference in energy between $(X^+ + M)$ and $(X + (M^+)^*)$, measured at complete separation of the reactant and product partners, will be seen as excess translational energy of the products.

The observation of excess translational energy of the products by the methods employed in these experiments reveals little infomation about the collision mechanism. Certainly all the rate coefficients measured are less than that calculated from simple orbiting theory which suggests that the reactants can approach sufficiently close to allow considerable perturbation. There is no evidence to show that the reactants come together to form an entity which exists for times which are long compared to vibrational or rotational motion. All that one can say is that for those systems where translational energy is detected, i.e. $(Kr^+ + N_2O)$, $(Ar^+ + CO_2)$, $(Ar^+ + N_2O)$, $(N_2{}^+ + CO_2)$ and $(N_2{}^+ + N_2O)$, the states involved are off resonance by ~ 0.1 eV at infinite separation.

From the reactions of Kr^+ with N_2O we have been able to measure the ratio $[Kr^{+\,2}P_{\frac{1}{2}}]_0/\{[Kr^{+\,2}P_{\frac{1}{2}}]_0 + [Kr^{+\,2}P_{\frac{3}{2}}]_0\}$ as a function of electron energy and obtain a value of (0.4 ± 0.05) in the electron energy range of 30–50 eV. This is higher than the value expected from statistical weights (0.33) but is in reasonable agreement with a value of 0.37 obtained from photoelectron spectroscopy [10]. Recognizing the abundance of $Kr^{+\,2}P_{\frac{1}{2}}$ at 50 eV allows one to conclude that electron transfer in the collisions $(Kr^{+\,2}P_{\frac{1}{2}} + N_2O)$ and $(Kr^{+\,2}P_{\frac{1}{2}} + CO_2)$ is rapid even though the F.C. factors are unfavourable. Thus the following systems examined in this study have high electron transfer rate coefficients even though the F.C. factors are unfavourable: $(Kr^{+\,2}P_{\frac{3}{2}} + N_2O)$, $(Kr^{+\,2}P_{\frac{1}{2}} + CO_2)$, $(Ar^{+\,2}P_{\frac{3}{2}}$, $Ar^{+\,2}P_{\frac{1}{2}} + N_2O)$, $(Ar^+\,{}^2P_{\frac{3}{2}}$, $Ar^{+\,2}P_{\frac{1}{2}} + CO_2)$, $(N_2{}^+ + CO_2)$ and $(N_2{}^+ + N_2O)$.

We conclude from this that the use of F.C. factors in attempting to predict charge transfer rate coefficients for either CO_2 or N_2O is of little value.

REFERENCES

1 J. Gauglhofer and L. Kevan, *Chem. Phys. Lett.*, 16 (1972) 492.
2 D. L. Smith and L. Kevan, *J. Amer. Chem. Soc.*, 93 (1971) 2113.
3 D. L. Smith and L. Kevan, *J. Phys. Chem.*, 55 (1971) 2290.
4 G. Gioumousis and D. P. Stevenson, *J. Chem. Phys.*, 29 (1958) 294.
5 M. T. Bowers and D. D. Elleman, *Chem. Phys. Lett.*, 16 (1972) 486.
6 J. B. Laudenslager, W. T. Huntress and M. T. Bowers, *J. Chem. Phys.*, 61 (1974) 4600.
7 (a) K. R. Ryan and I. G. Graham, *J. Chem. Phys.*, 59 (1973) 4260.
7 (b)K. R. Ryan, *J. Chem. Phys.*, 61 (1974) 1559.

8 F. A. Baker and J. B. Hasted, *Philos. Trans. R. Soc. Lond. A*, 261 (1966) 33.
9 I. G. Graham, H. M. Stock, and K. R. Ryan, (in preparation).
10 D. W. Turner, C. Baker, A. D. Baker and C. R. Brundle, *Molecular Photoelectron Spectroscopy*, Wiley-Interscience 1970.
11 K. R. Ryan, *J. Chem. Phys.*, 57 (1972) 271.
12 R. F. Holland and W. B. Maier, *J. Chem. Phys.*, 56 (1972) 5229.
13 T. F. Moran and L. Friedman, *J. Chem. Phys.*, 42 (1965) 2391.
14 R. W. Nicholls, *J. Res. Natl. Bur. Stand.*, A 65 (1961) 451.
15 R. W. Nicholls, *J. Quant. Spectrosc. Radiat. Trans.*, 2 (1962) 433.
16 G. A. Derwish, A. Galli, A. Giardini-Guidoni and G. G. Volpi, *J. Chem. Phys.*, 40 (1964) 3450.
17 F. C. Fehsenfeld, A. L. Schmeltkopf and E. E. Ferguson, *J. Chem. Phys.*, 46 (1967) 2019.

International Journal of Mass Spectrometry and Ion Physics, 25 (1977) 61–70 61
© Elsevier Scientific Publishing Company, Amsterdam — Printed in The Netherlands

ELECTRON ATTACHMENT TO THE STABLE FREE RADICAL BIS-TRIFLUOROMETHYLNITROXIDE IN THE GAS PHASE

PETER W. HARLAND *

Chemistry Department, Edinburgh University, Edinburgh EH9 3JJ (Gt. Britain)

(Received 25 January 1977)

ABSTRACT

Associative and dissociative electron attachment to the gaseous free radical bis-trifluoromethylnitroxide, $(CF_3)_2NO$, over the electron energy range 0—10 eV, has been investigated. In contrast to molecular negative ions with an equivalent number of vibrational degrees of freedom, where the electron-capture peak is narrow and the ions exhibit autodetachment lifetimes in the range 10—ca. 60 μs, $(CF_3)_2NO^-$ was formed over a 2-eV energy range with a mean autodetachment lifetime of ca. 650 μs. Analysis of the dissociative attachement curves for the fragmentation ions F^-, CF_3^- and CF_3NO^- formed over the energy range 0—10 eV has resulted in the estimation of limiting values for a number of thermochemical properties of the free radical and its decomposition products.

INTRODUCTION

The stable free radical bis-trifluoromethylnitroxide was first synthesized in 1965 [1—3]. The radical exists as a purple gas at room temperature, condensing at −25°C to a purple-brown liquid which freezes to a yellow crystalline solid at −70°C; it is unaffected by storage in pyrex or stainless steel vessels, thermally stable to 350°C and is unreactive with air, water, weak acidic or basic solutions, fluorotrichloromethane and benzene [1,4]. Although this radical has been the subject of an electron diffraction study [5], MO calculation [6], photoelectron spectroscopic investigation [7], theoretical and experimental ESR studies [8—11] fluorine NMR [1,12] and numerous gas phase and heterogeneous reactions [13], this is the first report of electron attachment to the free radical and of estimates for basic thermochemical parameters.

EXPERIMENTAL

The experiments were performed on a Bendix time-of-flight mass spectrometer, Model 3015. The procedures adopted in the measurement of auto-

---

* Present address: Chemistry Department, University of Canterbury, Christchurch, New Zealand.

detachment lifetimes, dissociative attachment peaks and the treatment of results have been previously described [14—16] and comments will be restricted to special precautions adopted in this study. A sample of bis-trifluoromethylnitroxide was purchased in a sealed ampoule (Pierce Chemical Company, but no longer available from this source) and used within 48 h of breaking the seal. The chemical reactivity of the nitroxide with the gases employed for energy scale calibration have not been reported in the literature and so the mass spectrum of the pure gas was compared to those of 1 : 1 mixtures with Ar, CO, SO_2 and SF_6. All mixtures were prepared at room temperature in a prebaked stainless steel inlet assembly to a total pressure of 1 torr using a Baratron capacitance manometer. Ion source pressures were maintained below 1×10^{-5} torr and typically $<2 \times 10^{-6}$ torr for lifetime measurements. Initially all experiments were carried out with the pure nitroxide with all ions intracalibrated before use of the calibration mixtures and intercalibration of the energy scale. There were no discernible differences between the dissociative attachment data taken with the mixtures and the pure gas, from which it was concluded that significant chemical reaction with these molecules does not take place at room temperature in the period required for an ionization efficiency run — ca. 2 h.

RESULTS AND DISCUSSION

Bis-trifluoromethylnitroxide proved to be an abundant source of negative ions, the average cross-section for dissociative electron attachment being several orders-of-magnitude higher than that found for $(CF_3)_2CO$ [17,18] i.e. comparable with SF_6, ca. 10^{-15} cm^2 [16]. The ions detected in this study were F^-, CF_3^-, CF_3O^-, CF_3NO^-, $(CF_3)_2N^-$ and $(CF_3)_2NO^-$ with relative abundances in the ratios shown in Table 1. The relative magnitudes and shapes of the CF_3O^- and $(CF_3)_2N^-$ peaks observed below 1.5 eV, which were typically 50 times more intense than the other ions at this energy, were found to be sensitive functions of the electron-trap current and ion-source pressure whilst the relative peak heights and dimensions of the remaining ionization efficiency curves remained unaffected by source conditions.

TABLE 1

Relative intensities of negative ions produced from $(CF_3)_2NO$ at respective dissociative attachment maxima and at 70 eV. See text for discussion of CF_3O^- and $(CF_3)_2N^-$ ion formation at 0 eV

m/e	Ion	70 eV	Res. max.
19	F^-	100	74
69	CF_3^-	55	100
85	CF_3O^-	12	—
99	CF_3NO^-	17	40
152	$(CF_3)_2N^-$	24	—
168	$(CF_3)_2NO^-$	1	24

Regulated trap currents in the range 0.0025 to 0.05 μA were employed and 'negative electron energies' up to 3 V achieved by inserting a mercury dry battery into the filament bias circuit. Even with such low trap-current demands the filament temperature rises very rapidly as the electron energy is reduced towards O eV (as evidenced by rapid filament erosion when operating for prolonged periods below 1 eV). Since $(CF_3)_2NO$ decomposes to $(CF_3)_2NOCF_3$, tris-trifluoromethylhydroxylamine and $CF_3{-}N{=}CF_2$, perfluoromethylmethyleneimine, above 350°C [4], it is evident that such decomposition products will be formed in the region of the filament and that the importance of pyrolysis products and resulting surface ionization and/or electron capture by such products will increase rapidly as the electron energy is reduced towards negative values. This phenomenon has been reported in a study of carbonyl sulphide and carbon disulphide [19] where the polymeric sulphur ions S_n^- ($n \leqslant 6$) were detected below 1 eV and attributed to the thermal decomposition of the CS_2 and COS on the filament.

The formation of $(CF_3)_2N^-$ and CF_3O^- at ca. 0 eV is thus attributed to the pyrolysis product $(CF_3)_2NOCF_3$. The possibility of such a contribution to the weaker F^-, CF_3^- and CF_3NO^- signals, also measured below 1 eV, cannot be excluded but the overall consistency of the peak height ratios of these ions to the molecular $(CF_3)_2NO^-$ ion confirm the latter as a source of these fragment ions by spontaneous dissociative attachment from the metastable $(CF_3)_2NO^-$ ion state(s) involved:

$$\begin{array}{l}(CF_3)_2NO + e(\text{ca. } 0\text{ eV}) \rightarrow [(CF_3)_2NO^-]^* \rightarrow (CF_3)_2NO + e \\ \qquad\qquad\qquad\qquad\qquad\qquad\quad \downarrow \\ \qquad\qquad\qquad\qquad\qquad F^-, CF_3^-, CF_3NO^- \end{array} \tag{1}$$

Associative attachment

This molecule was of particular interest as the molecular negative ion, if formed, would be isoelectronic with CF_3OOCF_3 and $(CF_3)_2NF$ which are both stable molecules. Further, as electron attachment could involve lone-pair formation it might also be expected to exhibit unusual stability for a molecular negative ion with only 24 vibrational degrees of freedom. These suspicions were realized and the average autodetachment lifetime of the molecular ion, which was formed at 0 eV with a broad resonance maximising at 1.2 ± 0.1 eV as shown in Fig. 1, was found to be 650 ± 100 μs. This may be compared with the autodetachment lifetimes of the following ions which also have 24 vibrational degrees of freedom; perfluoropropyne-2 molecular ion, $C_4F_6{-}2^-$ (16.3 μs) [20], perfluorocyclobutene molecular ion, $c{-}C_4F_6^-$ (11.2 μs) [20] and hexafluoroacetone molecular ion, $(CF_3)_2CO^-$ (ca. 60 μs) [21]. Although it is apparent from these examples that the carbonyl group exerts a strong influence on the stability of the negative ion state (with respect to autoionization), reconcilation of the nitroxide lifetime can only be found with the stability incurred as a consequence of electron attachment to a free radical acceptor.

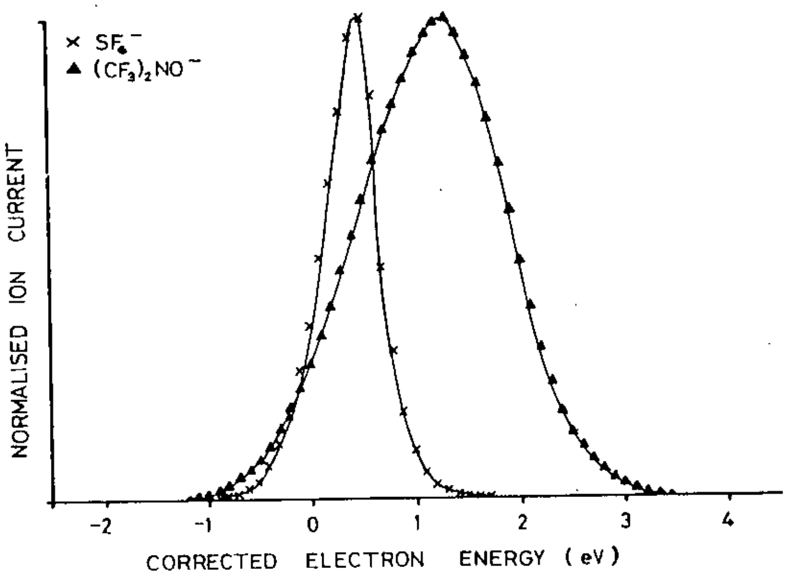

Fig. 1. Associative attachment curves for $(CF_3)_2NO$ and SF_6.

Numerical MO calculations carried out in this laboratory * with the unrestricted SCF method [22] in the INDO approximation [23] lend support to the contention that the increased stability of the $(CF_3)_2NO^-$ metastable ion is the result of lone-pair formation. The computations also reveal that the triplet state may also be involved in associative attachment. The free electron in the neutral molecule appears in an antibonding NO π-orbital with the electron mainly localized on the oxygen atom, a result reported earlier by Morokuma [6]. The charge density is distributed over the molecule as indicated in Table 2 which shows the effective number of valence electrons on each atom. Most of the charge density appears on the electronegative fluorine atoms with a net charge depletion on the carbons. The calculations for $(CF_3)_2NO^-$ show the singlet to be the lower energy and more favoured state, the captured electron pairing with the free electron in the NO π^*-orbital on the oxygen atom with very little disturbance to the overall molecular

TABLE 2

Calculated charge density for $(CF_3)_2NO$ and $(CF_3)_2NO^-$

	Charge Z	Spin S	Charge density (number of valence electrons)			
			N	O	C	F
$(CF_3)_2NO$	0	$\frac{1}{2}$	5.14	6.11	3.13	7.25
$(CF_3)_2NO^-$	−1	0	5.18	6.62	3.18	7.30
$(CF_3)_2NO^-$	−1	1	5.22	6.26	3.29	7.32

---

* Chemistry Department, University of Canterbury, Christchurch, New Zealand

charge distribution, and consequently little effect on the nuclear geometry of the nitroxide. In the triplet state the captured electron goes into an orbital centered on the nitrogen atom to form a higher energy (lower electron affinity) state with a more evenly distributed charge density over the molecular ion, a situation which would be consistent with the formation of a nuclear excited Feshbach resonance state [24]. The possibility then exists that both singlet and triplet ion states are formed, each with a distinct attachment cross-section and stability.

The smearing effect of the thermionically generated electron energy distribution [25] in these experiments precluded a detailed exploration of the broad resonance for evidence of fine structure. This problem and the small neutral-peak to ion-peak ratio also precluded attempts to measure lifetime as a function of electron energy across the resonance. This technique has been successfully employed by Christophorou [21] and other workers for the analysis of molecular ions formed in the field of excited states (electron-excited Feshbach resonances) using a quasi-monoenergetic electron beam. Christophorou and co-workers have demonstrated that electron attachment in the field of an excited molecular state can occur at electron energies above thermal and produce broad capture peaks slightly below the energy of the corresponding excited state of the neutral species. However, the high stability (relatively long lifetime) measured for the $(CF_3)_2NO^-$ ion cannot be explained by an electron excited Feshbach resonance since the molecular ions so formed have been shown to have shorter lifetimes than the corresponding nuclear-excited Feshbach resonance state [21]. The broad resonance measured in this work may nevertheless encompass a number of unresolved overlapping resonances including both nuclear and electron-excited Feshbach resonance states. Support for this suggestion may be found in the experimental capture curves: the molecular ion and 0-eV dissociative attachment peaks cannot be superimposed over the whole electron capture range as would be anticipated for the dissociation of a single molecular ion state. Further studies of this molecular ion are planned and some of these possibilities will be investigated.

Dissociative attachment

The experimental results for F^-, CF_3^- and CF_3NO^- over the energy range 0—10 eV are shown in Fig. 2(a) and the unfolded curves in Fig. 2(b). The absence of an independent source of thermochemical data for this radical restricts unambiguous analysis of the dissociative attachment results to the first and second appearance potentials for each ion measured. Despite this limitation a number of previously unknown thermochemical parameters have been estimated using the following energy balance expression written for the general dissociative attachment process, $AB + e \rightarrow A^- + B$

$$AP(A^-) \geqslant D(A\text{—}B) - EA(A) \qquad (2)$$

$$\geqslant \Delta H_f(A^-) + \Delta H_f(B) - \Delta H_f(AB) \qquad (3)$$

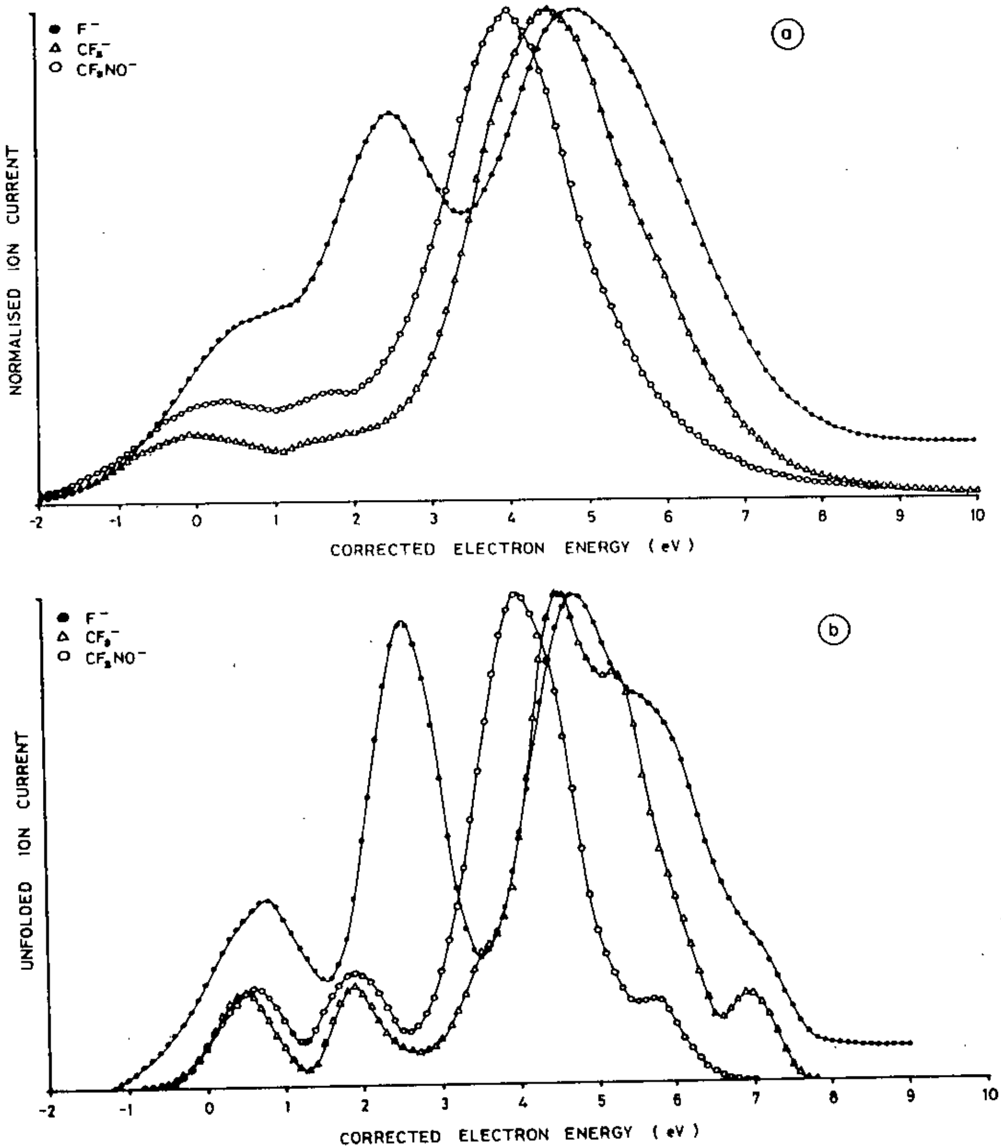

Fig. 2. Dissociative attachment curves for F^-, CF_3^- and CF_3NO^- ion formation from $(CF_3)_2NO$; (a) experimentally measured curves, (b) deconvoluted curves using 15 smoothing and 20 unfolding iterations.

where, $AP(A^-)$ is the appearance potential measured for the ion A^-, $D(A{-}B)$ the bond dissociation energy of AB, $EA(A)$ the electron affinity of fragment A, and ΔH_f the heat of formation of the species indicated. The inequality sign in the above expression, which results from a neglect of excess energy terms [26,27], results in the estimation of upper limits for bond dissociation energies, lower limits for electron affinities and limiting values for heats of formation.

Table 3 lists the negative ion appearance potential data for $(CF_3)_2NO$ with the processes considered responsible for ion formation. The origin of dissociative attachment products at 0 eV has been discussed above and the following reactions involving single bond cleavage are proposed to account for ion formation:

$$[(CF_3)_2NO^-]^* \rightarrow F^- + CF_3NO \cdot CF_2 \tag{4}$$

$$\rightarrow CF_3^- + CF_3NO \tag{5}$$

$$\rightarrow CF_3NO^- + CF_3 \tag{6}$$

Application of eqn. (2) leads directly to the following parameters: $D(F—CF_2\text{-}NO.CF_3) \leqslant EA(F)$; $D(CF_3—NO.CF_3) \leqslant EA(CF_3)$; and $EA(CF_3NO) \geqslant D(CF_3—NO.CF_3)$, where $EA(F) = 3.40$ eV and $EA(CF_3) = 2.0 \pm 0.2$ eV [25].

The (C—F) bond dissociation energy thus appears to be considerably weaker than those of the analogous bonds in the perfluoroalkanes which are around 5.2 eV. This difference must be attributed to the distribution of charge density in the $(CF_3)_2NO$ molecule where there is large depletion of effective valance electrons on the carbon atoms and a surplus on the fluorines, Table 2. The weakening effect of a large charge polarization on bond strength has been previously reported by Gowenlock and co-workers [28] to account for the weak (C—N) bond in CF_3NO. These authors make reference

TABLE 3

Dissociative Attachement Data for $(CF_3)_2NO$

Ion	*AP* (eV)	Mechanism	Parameters deduced
F^-	0	$\rightarrow F^- + CF_2NO \cdot CF_3$	$D(C—F) \leqslant 3.40$ eV
	1.6 ± 0.1	$\rightarrow F^- + CF_2 + CF_3NO$	
		$\rightarrow F^- + CF_3 + CF_2NO$	
		$\rightarrow (F^-)^*_{trans} + (CF_2NO \cdot CF_3)^*_{vib,trans}$	
	3.5		
	~5.2		
	~6.5		
CF_3^-	0	$\rightarrow CF_3^- + CF_3NO$	$D(C—N) \leqslant 2.0 \pm 0.2$ eV
	1.3 ± 0.1	$\rightarrow CF_3^- + CF_3 + NO$	$D(CF_3—NO) \leqslant 1.3 \pm 0.1$ eV
	2.7		
	~5.0		
	~6.5		
CF_3NO^-	0	$\rightarrow CF_3NO^- + CF_3$	$EA(CF_3NO) \geqslant 2.0 \pm 0.2$ eV
	1.2 ± 0.1	$\rightarrow (CF_3NO^-)^*_{vib,trans} + (CF_3)^*_{vib,trans}$	$E^* \geqslant 1.2 \pm 0.1$ eV
	2.6		
	~5.4		

to the electron diffraction study of Davis et al. [29] who showed that a similar charge distribution in CF_3NO was such that the ionic form $CF_3^-NO^+$ could be suggested to contribute to the molecular structure and thereby account [28] for the unusually weak (C—N) bond in this molecule.

The value of $\leqslant 2.0 \pm 0.2$ eV deduced for the D(C—N) bond dissociation energy in $(CF_3)_2NO$ is in accord with the correlation between (C—N) bond energy and (C—N) bond length suggested by Gowenlock and co-workers [29] from a study of monomeric C-nitroso-compounds and di-t-butylnitroxide. (C—N) bond dissociation energies in the range 1.3—2.7 eV were reported * where $D(CF_3\text{—}NO) = 1.34$ eV for $r(CN) = 1.555$ Å, and D(Ph—NO) = 1.78 eV for $r(CN) = 1.44$ Å, cf. $r(CN)$ for $(CF_3)_2NO = 1.441$ Å [5]. It is pertinent at this point to consider the second appearance potential for the CF_3^- ion at 1.3 ± 0.1 eV since further bond cleavage according to reaction (7)

$$(CF_3)_2NO + e(1.3 \pm 0.1\ \text{eV}) \rightarrow CF_3^- + CF_3 + NO \tag{7}$$

requires $D(CF_3\text{—}NO) \leqslant 1.3 \pm 0.1$ eV in agreement with the value of 1.34 ± 0.1 eV reported by Gowenlock and co-workers [28] for this bond.

There are no other values with which $EA(CF_3NO) \geqslant 2.0 \pm 0.2$ eV estimated from reaction (6) may be compared, although stability of the CF_3NO^- ion to the dissociation

$$CF_3NO^- \rightarrow CF_3^- + NO \tag{8}$$

requires $EA(CF_3NO) \geqslant 0.7$ eV.

The second resonance peak for F^- ion formation has an appearance potential at 1.6 ± 0.1 eV. Reactions (9) or (10) may be tentatively suggested to satisfy this onset, thereby requiring that the dissociation energy of the (C—N) bond involved must be $\leqslant 1.6 \pm 0.1$ eV:

$$(CF_3)_2NO + e(1.6 \pm 0.1\ \text{eV}) \rightarrow F^- + CF_2 + CF_3NO \tag{9}$$

$$\rightarrow F^- + CF_3 + CF_2NO \tag{10}$$

Since the possibility also exists that excited products of reaction (4) account for this appearance potential (in the absence of translational energy measurements [26,27]) these experiments cannot be used to differentiate between reactions (9)—(11).

$$(CF_3)_2NO + e(1.6 \pm 0.1\ \text{eV}) \rightarrow (F^-)^*_{\text{trans}} + (CF_3NOCF_2)^*_{\text{vib,trans}} \tag{11}$$

The formation of excited products must be proposed to satisfy the energetics for the second CF_3NO^- appearance potential since insufficient energy is available for further bond cleavage.

Thermochemical parameters discussed above and heats of formation

---

* Since the analysis used in ref. 28 is subject to the same assumptions employed in this work, the bond dissociation energies given in this ref. are also upper limits only.

TABLE 4

Summary of thermochemical parameters measured and deduced

Parameter	Value
$D(\mathrm{F{-}CF_2NO\cdot CF_3})$	$\leqslant 3.40$ eV
$D(\mathrm{CF_3{-}NO\cdot CF_3})$	$\leqslant 2.0 \pm 0.2$ eV
$D(\mathrm{CF_3{-}NO})$	$\leqslant 1.3 \pm 0.1$ eV
$EA(\mathrm{CF_3NO})$	$\geqslant 2.0 \pm 0.2$ eV
$\Delta H_f^0((\mathrm{CF_3})_2\mathrm{NO})$	$\geqslant -1190 \pm 40$ kJ mol^{-1}
$\Delta H_f^0(\mathrm{CF_3NO\cdot CF_2})$	$\leqslant -\ 940 \pm 40$ kJ mol^{-1}
$\Delta H_f^0(\mathrm{CF_3NO})$	$\geqslant -\ 510 \pm 10$ kJ mol^{-1}
$IP(\mathrm{CF_3})_2\mathrm{NO}$	$= 10.5 \pm 0.2$ eV

deduced using eqn. (3) are listed together in Table 4. The value ΔH_f^0 (CF_3NO) was obtained from the value of $D(CF_3{-}NO)$ which was then used in conjunction with known heats of formation [30] in reactions (5) and (7) to estimate a value of $\geqslant -12.4 \pm 0.4$ eV ($\geqslant -1190 \pm 40$ kJ mol^{-1}) for ΔH_f^0-$[(CF_3)_2NO]$. The ionization potential of $(CF_3)_2NO$ was also measured relative to an energy scale calibrated against the appearance potential of Ar^+ at 15.76 eV. This result, $IP = 10.5 \pm 0.2$ eV, is also included in Table 4 and may be compared to a value of 10.7 ± 0.1 eV determined by photoelectron spectroscopy [7].

ACKNOWLEDGEMENT

The author would like to thank Dr. R.G.A.R. Maclagan of the Chemistry Department, University of Canterbury, for the provision and running of the INDO program employed in this paper.

REFERENCES

1 W.D. Blackley and R.R. Reinhard, J. Am. Chem. Soc., 87 (1965) 802.
2 S.P. Makarov, A. Ya. Yakubovitch, S.S. Dubov and A.N. Medvedev, Dokl. Akad. Nauk SSSR, 160 (1965) 1319.
3 S.P. Makarov, A. Ya. Yakubovitch, S.S. Dubov and A.N. Medvedev, Zh. Vses. Khim. Obshchest., 10 (1965) 106.
4 D.P. Babb and J.M. Shreeve, Intra-Sci. Chem. Rep., 5 (1971) 55.
5 C. Glidewell, D.W.H. Rankin, A.G. Robiette, G.M. Sheldrick and S.M. Williamson, J. Chem. Soc. A, (1971) 478.
6 K. Morokuma, J. Am. Chem. Soc., 91 (1969) 5412.
7 A.B. Cornford, D.C. Frost, F.G. Herring and C.A. McDowell, Faraday. Discuss. Chem. Soc., 54 (1972) 56.
8 G.R. Underwood and V.L. Vogel, Mol. Phys., 19 (1970) 621.
9 T.J. Schaafsma, Magn. Reson. Relat. Phenom., Proc. Congr. Ampère, 18th, 1974, 2 (1975) 497.

10 T.J. Schaafsma and D. Kievelson, J. Chem. Phys., 49 (1968) 5235.
11 W.R. Knolle and J.R. Bolton, J. Am. Chem. Soc., 19 (1969) 5411.
12 P.V. Schastev, A.V. Balaev and G.M. Zhidomirov, Zh. Strukt. Khim., 12 (1971) 719.
13 See review article, ref. 4 above, and refs. therein.
14 P.W. Harland, K.A.G. Macneil and J.C.J. Thynne, in D. Price and J.E. Williams (Eds.), Dynamic Mass Spectrometry, Vol. 1, Heyden and Son Ltd., London, 1970, Ch. 8.
15 K.A.G. Macneil and J.C.J. Thynne, Int. J. Mass Spectrom. Ion Phys., 3 (1969) 35.
16 P.W. Harland and J.C.J. Thynne, J. Phys. Chem., 75 (1971) 3517.
17 P.W. Harland and J.C.J. Thynne, J. Phys. Chem., 73 (1969) 2791.
18 P.W. Harland and J.C.J. Thynne, J. Phys. Chem., 74 (1970) 52.
19 K.A.G. Macneil and J.C.J. Thynne, J. Phys. Chem., 73 (1969) 2960.
20 P.W. Harland, Ph.D. Thesis, Edinburgh University, 1971.
21 L.G. Christophorou, Atomic and Molecular Radiation Physics, Wiley—Interscience, New York, 1971, Ch. 6.
22 J.A. Pople and R.K. Nesbet, J. Chem. Phys., 22 (1954) 57.
23 J.A. Pople, D.L. Beveridge and D.A. Dobosh, J. Chem. Phys., 47 (1967) 2026.
24 J.N. Bardsley and F. Mandl, Rep. Progr. Phys., 31 (1968) 471.
25 J.L. Franklin and P.W. Harland, Ann. Rev. Phys. Chem., 25 (1974) 485.
26 P.W. Harland, J.L. Franklin and D.E. Carter, J. Chem. Phys., 58 (1973) 1430.
27 P.W. Harland and J.L. Franklin, J. Chem. Phys., 61 (1974) 1621.
28 P.J. Carmichael, B.G. Gowenlock and C.A.F. Johnson, J. Chem. Soc. Perkin II, (1973) 1853.
29 M.I. Davis, J.E. Boggs, D. Coffey and H.P. Hanson, J. Phys. Chem., 69 (1965) 3727.
30 J.L. Franklin, J.G. Dillard, H.M. Rosenstock, J.T. Heron, K. Draxl and F.H. Field, Ionization Potentials, Appearance Potentials and Heats of Formation of Gaseous Positive Ions, NSRDS-NBS 26, Washington, D.C., 1969.

International Journal of Mass Spectrometry and Ion Physics, 27 (1978) 77–82 77
© Elsevier Scientific Publishing Company, Amsterdam — Printed in The Netherlands

THE EQUILIBRIUM $H_3S^+ + HCN \rightleftharpoons H_2CN^+ + H_2S$ AND THE RELATIVE PROTON AFFINITIES OF HCN AND H_2S

C.G. FREEMAN, P.W. HARLAND and M.J. MCEWAN

Department of Chemistry, University of Canterbury, Christchurch (New Zealand)

(Received 30 September 1977)

ABSTRACT

The reaction $H_3S^+ + HCN \rightleftharpoons H_2CN^+ + H_2S$ has been studied at 300 K in a flowing afterglow system from both the forward and reverse directions. Equilibrium was readily attained under most reaction conditions enabling a value for the equilibrium constant $K = 5.2 \pm 1.0$ to be determined, and hence $\Delta G^0_{300K} = -4.1 \pm 0.5$ kJ mol^{-1}. The forward and reverse rate coefficients are $k_f = 1.9 \times 10^{-9}$ and $k_r = 3.4 \times 10^{-10}$ cm^3 molecule^{-1} s^{-1}. Using an estimate of the entropy change, ΔS^0, for the reaction, the relative proton affinities of H_2S and HCN were found (PA (H_2S) $<$ PA (HCN) by 2.5 kJ mol^{-1}).

INTRODUCTION

Earlier studies carried out in this laboratory using the FA technique reported rate coefficient measurements for ion—molecule reactions of a number of sulphur-containing and cyanide-derived species [1—3]. Attempts to measure the rate coefficient for proton transfer from the parent species H_3S^+ to HCN showed marked curvature in the plots of log [H_3S^+] versus HCN flow. This curvature led us to suspect that the reverse reaction was contributing to the observed H_3S^+ ion signals. Such a situation occurs if both forward and reverse reactions have rapid rates, thus bringing about an equilibrium state. This is typical of reactions that are close to isoenergetic and indicates that the proton affinities of H_2S and HCN have similar values. Measurements reported in the literature for the proton affinities of H_2S and HCN show that whereas a number of determinations have been made for H_2S, the proton affinity of HCN is not well established [4—6].

In this paper we report the results of a kinetic study of the equilibrium system (1) from both directions:

$$H_3S^+ + HCN \rightleftharpoons H_2CN^+ + H_2S \qquad (1)$$

We have determined the rate coefficients for the forward and reverse directions, ΔG^0 for reaction (1) and the relative proton affinities of H_2S and HCN.

EXPERIMENTAL

The experiments reported here were performed using a FA system which has been described elsewhere [2]. Typical flow-rates of the hydrogen carrier gas were in the range 150—200 atm $cm^3 s^{-1}$. In this study the precursor ion H_3^+ was generated in the hydrogen carrier gas by an electron gun at the upstream end of the 9.48-cm i.d. reaction tube. Two reactant gases (H_2S and HCN) were added via fixed inlet jets downstream of the electron gun. When reaction (1) was studied in the forward direction, H_2S gas was added at the first inlet converting the primary ion, H_3^+, into H_3S^+ by the rapid proton transfer reaction [1]

$$H_3^+ + H_2S \rightarrow H_3S^+ + H_2 \qquad (2)$$

The neutral reactant HCN was introduced at the second inlet jet and the ensuing reaction between H_3S^+ and HCN was followed by continuous sampling of small quantities of gas into a quadrupole mass spectrometer. Typical concentrations of reactant species are ca. 1×10^{16} molecules cm^{-3} for the H_2 carrier gas, ca. 1×10^8 ions cm^{-3} for the ions and ca. 5×10^{11} molecules cm^{-3} for the neutral reactant. Pseudo-first-order kinetics therefore apply and the rate constant is readily obtained from the logarithmic decay of reactant ion signal as a function of neutral reactant flow.

Industrial grade dry hydrogen was used as the carrier gas after further drying over a molecular sieve trap at 77 K. H_2S and HCN were prepared in this laboratory by adding sodium sulphide and sodium cyanide respectively to *o*-phosphoric or sulphuric acids. These gases were purified by drying over P_2O_5 and repeated trap-to-trap distillation.

RESULTS AND DISCUSSION

The method of Bohme et al. [7] was used to determine the equilibrium constant of reaction (1) from both forward and reverse directions. In each direction it was possible to determine K by two independent methods as illustrated in Figs. 1—3. In Figs. 1 and 2 the variations in ion signals with neutral reactant concentration are shown for the approach to equilibrium in the forward direction (Fig. 1) and in the reverse direction (Fig. 2). At very low concentrations of the product neutral species (the back-reactant) equilibrium is not established. Under these conditions the slope of the logarithmic decay of either the H_3S^+ signal (for the forward direction) or the H_2CN^+ signal (for the reverse direction) gives values for k_f or k_r respectively. One of these rate coefficients is then used as an input parameter in a computer program which adjusts the remaining rate coefficient to find the curve of best fit through the observed data. This iterative procedure is used on those sets of data where equilibrium is established at all concentrations of reactant neutral species, i.e. when high concentrations of back-reactant are present. The computer fit, which is shown by the solid lines in Figs. 1 and 2,

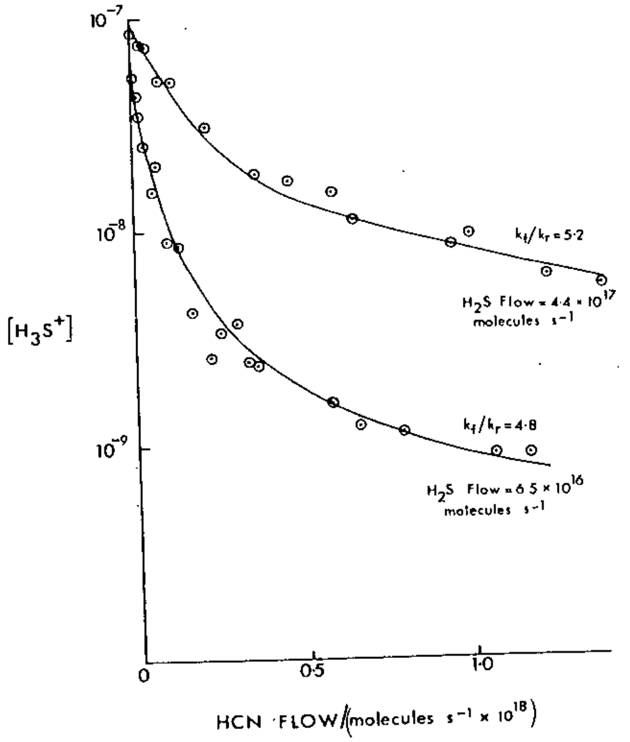

Fig. 1. The variation in the H_3S^+ signal with HCN flow at two flows of H_2S. The points are experimental and the curves calculated using the values indicated for k_f/k_r.

then provides a value for the equilibrium constant which is independent of any mass discrimination in the detection system.

Figure 3 shows a plot of the ion ratio $[H_3S^+]/[H_2CN^+]$, corrected for mass discrimination, against H_2S flow for two flows of back-reactant HCN. The linearity of this plot shows that equilibrium is attained over almost all of the range of H_2S concentrations. No corrections have been made in this work for any differences between the ambipolar diffusion coefficients of the ions H_3S^+ and H_2CN^+ in H_2. This neglect of differences in the diffusion coefficients should not introduce a large error in the equilibrium constant since the diffusion coefficients for these ions are not expected to be widely different. The results of equilibrium constant calculations are summarized in Table 1. Rate coefficients for the forward and reverse directions have been found to be $k_f = (1.9 \pm 0.3) \times 10^{-9}$ cm^3 molecule^{-1} s^{-1} and $k_r = (3.4 \pm 0.3) \times 10^{-10}$ cm^3 molecule^{-1} s^{-1}. These reaction rates do not appear to have been reported previously. The uncertainties shown are the standard deviations of the measurements and do not include systematic errors which increase the uncertainty to ± 30% [2].

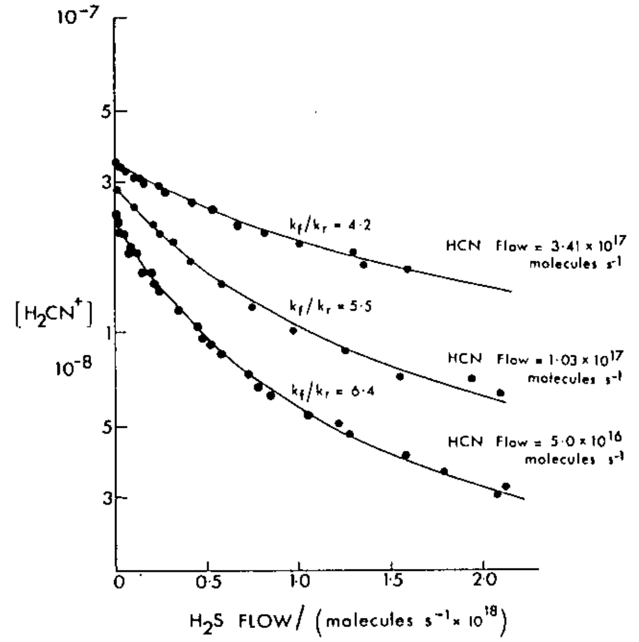

Fig. 2. The variation in H_2CN^+ signal with H_2S flow at three different flows of HCN. The points are experimental and the curves calculated using the values indicated for k_f/k_r.

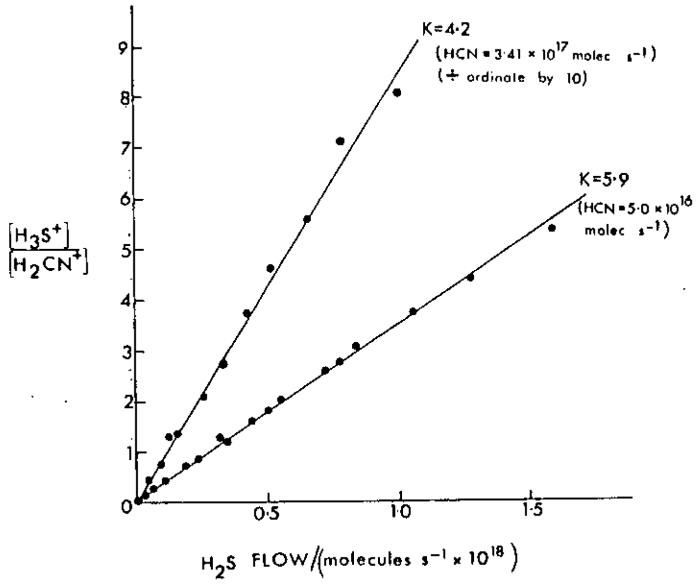

Fig. 3. The variation in the observed ion concentration ratio $[H_3S^+]/[H_2CN^+]$ as a function of H_2S flow showing the attainment of equilibrium. The best straight lines through the points at high H_2S flow yields the values of K shown. The ratio of ion concentrations is determined from the measured ion signal ratio corrected for mass discrimination.

TABLE 1

Equilibrium constants K for the reaction $H_3S^+ + HCN \rightleftharpoons H_2CN^+ + H_2S$ at 300 K

Direction studied	No. of determinations	K ($=k_f/k_r$)	K (ratio plot)
Forward	3	4.8 ± 0.4	5.4 ± 0.3
Reverse	6	5.5 ± 1.4	4.9 ± 0.9

An equilibrium constant of $K = 5.2 \pm 1.0$ leads to a standard free energy change for reaction (1) of $\Delta G^0_{300K} = -4.1 \pm 0.5$ kJ mol^{-1}. Standard entropies for the ions H_2CN^+ and H_3S^+ are not known but an estimate for the entropy change occurring in reaction (1), ΔS^0, can be calculated using the method of Lias and Ausloos [8]. Estimates for Z_f and Z_r (the collision rate coefficients for the forward and reverse reactions) can be found using the ADO $\overline{\cos\theta}$ model [9]. These estimates are $Z_f = 2.72 \times 10^{-9}$ and $Z_r = 1.46 \times 10^{-9}$ cm^3 molecule^{-1} s^{-1} respectively. The entropy change during reaction (1) is then $\Delta S^0 = 5.2$ J K^{-1} mol^{-1} which when combined with our measured ΔG^0 leads to $\Delta H^0 = -2.5 \pm 0.5$ kJ mol^{-1}. (The uncertainty in ΔS^0 has not been included.) As ΔH^0 for reaction (1) represents the difference between the proton affinities of H_2S and HCN it is found that the proton affinity of $H_2S <$ the proton affinity of HCN by 2.5 kJ mol^{-1}.

A number of measurements have been reported in the literature for the proton affinity of H_2S derived from gas-phase ion equilibrium measurements. Kebarle et al. [4,5] report the proton affinity of H_2S as 720 ± 8 kJ mol^{-1} from relative measurements based on an absolute value for the proton affinity of isobutene. Combining their result for H_2S with our relative measurement we find the proton affinity of HCN to be 723 ± 8 kJ mol^{-1} (172.7 kcal mol^{-1}). Haney and Franklin [6] estimated proton affinities for both H_2S and HCN of 711 ± 13 kJ mol^{-1} from appearance potential measurements and from observations of the non-occurrence of particular ion—molecule reactions. Our results however provide an inherently more accurate determination for the difference in proton affinity between H_2S and HCN.

ACKNOWLEDGEMENT

This work was given financial support by the New Zealand Universities Research Committee.

REFERENCES

1 J.P. Liddy, C.G. Freeman and M.J. McEwan, Astrophys. Lett., 16 (1975) 155.

2 J.P. Liddy, C.G. Freeman and M.J. McEwan, Int. J. Mass Spectrom. Ion Phys., 23 (1977) 153.

3 J.P. Liddy, C.G. Freeman and M.J. McEwan, Mon. Notic. Roy. Astron. Soc., 180 (1977) 683.
4 P. Kebarle, R. Yamdagni, K. Hiraoka and T.B. McMahon, Int. J. Mass Spectrom. Ion Phys., 19 (1976) 71.
5 R. Yamdagni and P. Kebarle, J. Am. Chem. Soc., 98 (1976) 1320.
6 M.A. Haney and J.L. Franklin, J. Phys. Chem., 73 (1969) 4328.
7 D.K. Bohme, R.S. Hemsworth, H.W. Rundle and H.I. Schiff, J. Chem. Phys., 58 (1973) 3504.
8 S.G. Lias and P. Ausloos, J. Am. Chem. Soc., 99 (1977) 4831.
9 L. Bass, T. Su, W.J. Chesnavich and M.T. Bowers, Chem. Phys. Lett., 34 (1975) 119.

Aust. J. Chem., 1978, 31, 963–6

Some Ion–Molecule Reactions of Hydrogen Cyanide

Colin G. Freeman, Peter W. Harland, John P. Liddy and Murray J. McEwan

Department of Chemistry, University of Canterbury, Christchurch, New Zealand.

Abstract

Rate coefficients for the reactions of several positive ions with HCN in the gas phase have been measured by the flowing afterglow technique. The reactions are all of the form

$$X^+ + HCN \rightarrow \text{products}$$

where X^+ and the corresponding rate coefficient, in units of cm^3 $molecule^{-1}$ s^{-1}, are: $X^+ = HCN^+$ (k $9 \cdot 8 \times 10^{-10}$); C_2N^+ (k $3 \cdot 1 \times 10^{-10}$); CN^+ (k $2 \cdot 8 \times 10^{-9}$); CH^+ (k $3 \cdot 2 \times 10^{-9}$); H_3O^+ (k $4 \cdot 5 \times 10^{-9}$) and HCO^+ (k $3 \cdot 9 \times 10^{-9}$).

Introduction

Earlier studies carried out in this laboratory by means of the flowing afterglow (FA) technique reported rate coefficients of a number of ion–molecule reactions of species derived from HCN (i) with H_3^+,[1] and (ii) of relevance to interstellar chemistry.[2] We include in this report the results and a brief discussion of rate coefficient measurements of other positive ions with HCN and compare the observed rate coefficients with those calculated from the ADO $\overline{\cos\theta}$ model.[3] These ion–molecule reactions are of the general type

$$X^+ + HCN \rightarrow \text{products} \qquad (1)$$

where $X^+ = HCN^+$, C_2N^+, CN^+, CH^+, H_3O^+ and HCO^+.

Experimental

The rate coefficient measurements were carried out in a FA system which has been described previously.[1] Ions produced by electron impact on a carrier gas of hydrogen or helium are allowed to attain thermal energies (300 K) by collision with the carrier gas molecules before their entry into the reaction region. The reactant ion concentration is monitored by a quadrupole mass spectrometer after sampling of the flow stream through a 0·03 cm diameter hole in a molybdenum-tipped sampling port. As the neutral reactant concentration (*c.* 10^{12} molecules cm^{-3}) is much larger than the ion concentration (*c.* 10^8 ions cm^{-3}), pseudo-first-order kinetics prevail. The rate coefficients are then readily found from the linear logarithmic decays of the reactant ion signal as a function of neutral reactant flow.

---

[1] Liddy, J. P., Freeman, C. G., and McEwan, M. J., *Int. J. Mass Spectrom. Ion Phys.*, 1977, **23**, 153.

[2] Liddy, J. P., Freeman, C. G., and McEwan, M. J., *Mon. Not. R. Astron. Soc.*, 1977, **180**, 683.

[3] Bass, L., Su, T., Chesnavich, W. J., and Bowers, M. T., *Chem. Phys. Lett.*, 1975, **34**, 119.

Either helium (Matheson 99·995%) or industrial grade dry hydrogen (after drying over a molecular sieve trap at 77 K) was added directly to the reaction tube at flow rates between 150–200 atm cm^3 s^{-1}. Hydrogen cyanide was prepared in this laboratory by adding sodium cyanide to orthophosphoric acid and purified after drying by repeated trap-to-trap distillation. The absolute accuracy of the measured rate coefficients is estimated at ±30% and the reproducibility was better than ±10%.

Results and Discussion

The following ion–molecule reactions were studied:

$$HCN^+ + HCN \rightarrow H_2CN^+ + CN \qquad (k_2\ 9{\cdot}8\times10^{-10}\ \text{cm}^3\ \text{molecule}^{-1}\ \text{s}^{-1}) \qquad (2)$$

$$C_2N^+ + HCN \rightarrow \text{products} \qquad (k_3\ 3{\cdot}1\times10^{-10}\ \text{cm}^3\ \text{molecule}^{-1}\ \text{s}^{-1}) \qquad (3)$$

$$CN^+ + HCN \rightarrow HCN^+ + CN \qquad (k_4\ 2{\cdot}8\times10^{-9}\ \text{cm}^3\ \text{molecule}^{-1}\ \text{s}^{-1}) \qquad (4)$$

$$CH^+ + HCN \rightarrow \left[\begin{array}{l} H_2CN^+ + C \\ C_2N^+ + H_2 \end{array}\right. \qquad (k_5\ 3{\cdot}2\times10^{-9}\ \text{cm}^3\ \text{molecule}^{-1}\ \text{s}^{-1}) \qquad (5)$$

$$H_3O^+ + HCN \rightarrow H_2CN^+ + H_2O \qquad (k_6\ 4{\cdot}5\times10^{-9}\ \text{cm}^3\ \text{molecule}^{-1}\ \text{s}^{-1}) \qquad (6)$$

$$HCO^+ + HCN \rightarrow H_2CN^+ + CO \qquad (k_7\ 3{\cdot}9\times10^{-9}\ \text{cm}^3\ \text{molecule}^{-1}\ \text{s}^{-1}) \qquad (7)$$

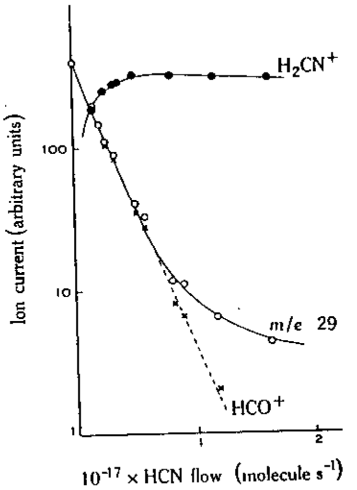

Fig. 1. The variation in the HCO$^+$ signal with HCN flow. The circles represent the observed ion signals at *m/e* 29. The crosses are the observed ion signals corrected for the isotope contribution from H$_2$CN$^+$ at *m/e* 28.

All of the results were obtained in a similar manner but as reaction (7) provided an added difficulty the *m/e* 29 (HCO$^+$) decay curve is presented. The reactant ion HCO$^+$ was produced by the addition of CO into hydrogen carrier gas downstream from the electron gun, so that the primary H_3^+ ion was converted into HCO$^+$ by the rapid reaction

$$H_3^+ + CO \rightarrow HCO^+ + H_2 \qquad (k_8\ 1{\cdot}4\times10^{-9}\ \text{cm}^3\ \text{molecule}^{-1}\ \text{s}^{-1})^4 \qquad (8)$$

HCN was added further downstream from the CO inlet and the ensuing reaction (7) was followed by monitoring the peak at *m/e* 29. The logarithmic decay of this mass peak showed pronounced curvature with large amounts of added HCN (see Fig. 1)

---

[4] Burt, J. A., Dunn, J. L., McEwan, M. J., Sutton, M. M., Roche, A. E., and Schiff, H. I., *J. Chem. Phys.*, 1970, 52, 6062.

because of the contribution to *m/e* 29 from three isotopes of the product ion H_2CN^+ (normally at *m/e* 28). These isotopes ($^2H^1H^{12}C^{14}N^+$, $^1H_2{}^{13}C^{14}N^+$ and $^1H_2{}^{12}C^{15}N^+$) contribute 1·5% of the H_2CN^+ signal at *m/e* 28 to the peak at *m/e* 29. Subtracting this isotope contribution from the observed *m/e* 29 signal we obtain a linear decay over more than two decades (broken line of Fig. 1).

The results for all reactions are summarized in Table 1 together with measurements reported by other workers[2,5–7] and the calculated capture rate coefficients from the ADO cos θ model.[3]

Table 1. Rate coefficients (cm³ molecule⁻¹ s⁻¹) at 300 K for reactions of the type $X^+ + HCN \rightarrow$ products

X^+ ion	Reaction number	k_{obs} (this work)	k_{obs} (others)	k(ADO) (ref. 3)
HCN^+	(2)	$9{\cdot}8\times10^{-10}$	$6{\cdot}0\times10^{-10\,A}$	$2{\cdot}9\times10^{-9}$
C_2N^+	(3)	$3{\cdot}1\times10^{-10}$		$2{\cdot}7\times10^{-9}$
CN^+	(4)	$2{\cdot}8\times10^{-9}$		$2{\cdot}9\times10^{-9}$
CH^+	(5)	$3{\cdot}2\times10^{-9}$		$3{\cdot}6\times10^{-9}$
H_3O^+	(6)	$4{\cdot}5\times10^{-9}$	$3{\cdot}5\times10^{-9\,B}$	$3{\cdot}2\times10^{-9}$
HCO^+	(7)	$3{\cdot}9\times10^{-9}$	$3{\cdot}5\times10^{-9}$,^{C} $4{\cdot}0\times10^{-9}$,^{D} $3{\cdot}0\times10^{-9\,D}$	$2{\cdot}8\times10^{-9}$

^A Ref. 5. ^B Ref. 7. ^C Ref. 6. ^D Ref. 2.

Few measurements of the rates of these reactions have been reported but good agreement is obtained where comparison is possible. Inoue and Cottin[8] made a study of several ion-molecule reactions of C_2N_2 and HCN but did not measure directly thermal rate coefficients for reaction. From their measurements of appearance potentials and the variation in ion current with pressure they predicted the following products from reactions (3), (4) and (5):

$$C_2N^+ + HCN \rightarrow C_3N_2{}^+ + H \tag{3a}$$

$$CN^+ + HCN \rightarrow C_2N_2{}^+ + H \tag{4a}$$

$$CH^+ + HCN \rightarrow \begin{cases} C_2N^+ + H_2 & \text{(5a)} \\ C_2NH^+ + H & \text{(5b)} \end{cases}$$

Although we could not identify the products of reaction (3) because of interference from competing reactions, we did not observe an appreciable mass signal at *m/e* 64 corresponding to Inoue and Cottin's observation of $C_3N_2{}^+$.

The most likely product ion(s) of reaction (4) at thermal energies is HCN^+ and of reaction (5) are H_2CN^+ and C_2N^+ all of which we observed. The probable reason for these differences between our results and those of Inoue and Cottin[8] are: (i) their measurements were made at relatively high pressures (10^{-2} Torr) making it very difficult to measure primary ions; and (ii) their conditions were non-thermal due to a

---

[5] Harrison, A. G., and Thynne, J. C. J., *Can. J. Chem.*, 1967, **45**, 1321.

[6] Huntress, W. T., and Anicich, V. G., *Astrophys. J.*, 1976, **208**, 237.

[7] Mackay, G. I., Betowski, L. D., Payzant, J. D., Schiff, H. I., and Bohme, D. K., *J. Phys. Chem.*, 1976, **80**, 2919.

[8] Inoue, M., and Cottin, M., *Adv. Mass Spectrom.*, 1966, **3**, 339.

voltage gradient of between 5 and 20 V cm^{-1} being applied to ions in the high-pressure region.

A comparison of our measured rates with the calculated collision rates shows reasonable agreement in most cases with one notable exception. In reaction (3) the observed rate coefficient is a factor of 9 less than the collision rate. The heat of formation of C_2N^+ is not well established and hence exothermic pathways cannot be identified. This relatively low efficiency of collisions in producing a reaction (*c.* 1 in 9) may be due to orientation requirements in the collision complex if extensive molecular rearrangement is required to form the product ion. Such deviations between observed rate coefficients and those calculated on the basis of collision rates are not uncommon.[9]

Acknowledgment

We wish to thank the New Zealand Universities Research Committee for financial support.

Manuscript received 24 October 1977

---

[9] Tanaka, K., Mackay, G. I., Payzant, J. D., and Bohme, D. K., *Can. J. Chem.*, 1976, **54**, 1643.

International Journal of Mass Spectrometry and Ion Physics, 28 (1978) 19—25 19
© Elsevier Scientific Publishing Company, Amsterdam — Printed in The Netherlands

THE EQUILIBRIUM SYSTEMS H_3CO^+ (HCN, HCHO)H_2CN^+, H_3CO^+ (H_2S, HCHO)H_3S^+ AND THE RELATIVE PROTON AFFINITIES OF HCHO, HCN AND H_2S

C.G. FREEMAN, P.W. HARLAND and M.J. McEWAN

Department of Chemistry, University of Canterbury, Christchurch (New Zealand)

(Received 15 November 1977)

ABSTRACT

The two reaction systems, $H_3CO^+ + H_2S \rightleftharpoons H_3S^+ + HCHO$ and $H_3CO^+ + HCN \rightleftharpoons H_2CN^+ + HCHO$, have been studied at 300 K in a flowing afterglow system in both the forward and reverse directions. From the measured equilibrium constants and calculated entropies the relative proton affinities have been determined as: $PA(\text{HCHO}) = PA(\text{HCN}) + 1.6(\pm 0.4)$ kJ mol^{-1}; $PA(\text{HCHO}) = PA(H_2S) + 4.0(\pm 0.4)$ kJ mol^{-1}. Rate constants were also measured in the forward and reverse direction for both reaction systems.

INTRODUCTION

The versatility of the flowing afterglow (FA) method has been adequately demonstrated in recent years. An illustration of this is the study of proton transfer systems in which equilibrium is established between the forward and reverse directions as reported by Bohme et al. [1] and Fehsenfeld et al. [2]. From the observed values of the equilibrium constants and estimated or measured entropy changes, the enthalpy changes for proton transfer processes and hence proton affinities were obtained. (The proton affinity of a molecule X, $PA(X)$, is usually defined as ΔH° for the process $XH^+ \rightarrow X + H^+$.) A study of reactions where neutral reactants and products have similar proton affinities may be used to establish relative proton affinities in a similar way to those established by high-pressure mass spectrometric methods [3].

In earlier FA studies we measured the rate coefficients of a number of ion—molecule reactions of cyanide-derived species [4,5] and also the relative proton affinities of HCN and H_2S from the equilibrium constant for the reaction [6]

$$H_3S^+ + HCN \rightleftharpoons H_2CN^+ + H_2S \tag{1}$$

We have since observed both H_2S and HCN to accept protons readily from protonated formaldehyde, H_3CO^+. We report here equilibrium constants and rate coefficients in both the forward and reverse directions for reactions (2) and (3) at 300 K:

$$H_3CO^+ + H_2S \rightleftharpoons H_3S^+ + HCHO \quad (2)$$

$$H_3CO^+ + HCN \rightleftharpoons H_2CN^+ + HCHO \quad (3)$$

EXPERIMENTAL

The details of the FA technique have been described elsewhere [4,7]. In these experiments hydrogen carrier gas is passed through the reaction tube at flow rates in the range 150—200 cm^3 atm s^{-1} and total pressures around 0.3 torr. Electron impact on the hydrogen carrier gas provides the precursor H_3^+ ion which readily donates a proton to one of the neutral species, HCHO, H_2S or HCN, added downstream from the electron gun, to form the appropriate reactant ion. For example, in the study of reaction (2) in the forward direction, HCHO is added at a first inlet jet, thus converting all of the H_3^+ ion into H_3CO^+. The neutral reactant H_2S is added through a second inlet which is placed sufficiently far downstream from the first inlet that the reaction between H_3^+ and HCHO is essentially complete before H_2S addition. The reaction between H_3CO^+ and H_2S is allowed to proceed along an additional length of reaction tube before a small portion of the reacting gases is sampled into a quadrupole mass filter. Typical concentrations of reacting species are: carrier gas, 10^{16} molecule cm^{-3}; reactant ion, 10^8 ion cm^{-3}; neutral reactant, 10^{12} molecule cm^{-3}.

Industrial grade hydrogen was dried over a molecular sieve trap at 77 K before entry to the reaction tube. H_2S and HCN were prepared in this laboratory by the addition of sodium sulphide and sodium cyanide respectively to orthophosphoric or sulphuric acids. These gases were further purified by drying over P_2O_5 and repeated trap-to-trap distillation. Formaldehyde, HCHO, which was prepared by heating paraformaldehyde, was stored and used in the form of $HCHO/H_2$ mixtures. The partial pressure of HCHO in all mixtures with H_2 was maintained below 18 torr to preclude polymerization, the total pressure of the mixtures being, typically, 500—600 torr. Formaldehyde vapour stored in this way showed no deterioration attributable to paraformaldehyde formation over a period of 24 h, after which time the gas mixture was discarded. All rate measurements involving formaldehyde were repeated with at least two mixtures of different composition.

RESULTS AND DISCUSSION

The method of determining the equilibrium constant, K, from experimental observation has been described by Bohme et al. [1]. Two independent methods are used to determine K in both the forward and reverse directions for each reaction system, thus giving four distinct estimates of K. In one method, the ratio of the rate constants, k_f/k_r, is found by measuring k_f under non-equilibrium conditions and computing, using an iterative technique,

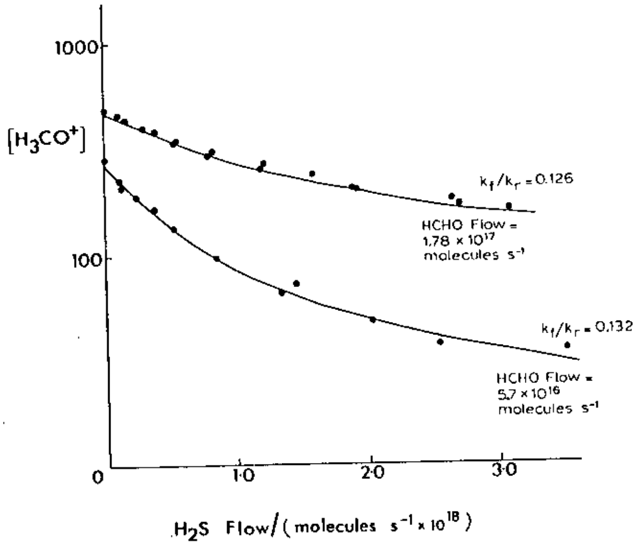

Fig. 1. The variation in the H_3CO^+ signal with H_2S at 2 flows of HCHO. The points are experimental and the curves calculated using the values indicated for k_f/k_r.

the best value of k_r to fit the results observed under equilibrium conditions. The computed (solid line) and the observed (individual points) ion signals are compared in Figs. 1 and 2 and are independent of any mass discrimination in the detection system. In the second method K is found directly from the

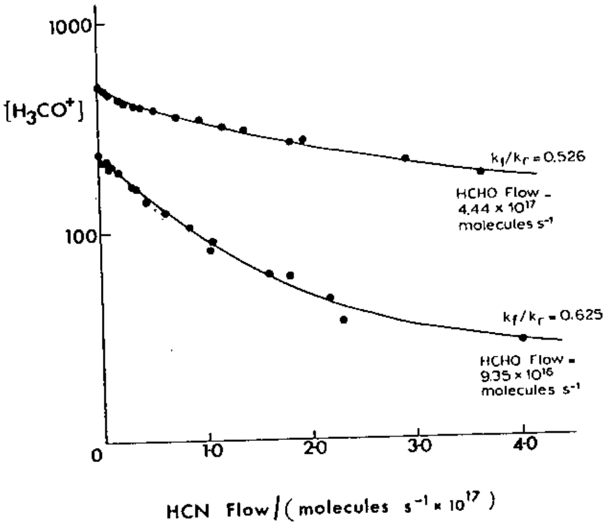

Fig. 2. The variation in the H_3CO^+ signal with HCN at 2 flows of HCHO. The points are experimental and the curves calculated using the values indicated for k_f/k_r.

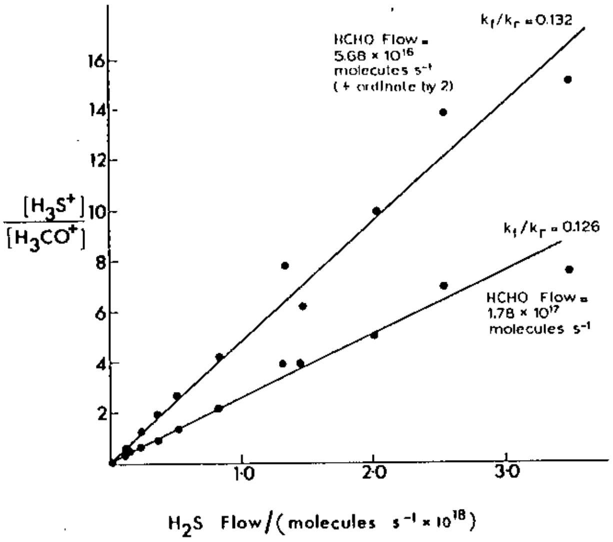

Fig. 3. The ratio plot for reaction (2) in the forward direction. $[H_3S^+]/[H_3CO^+]$ versus H_2S flow. The ratio of ion concentrations has been corrected for mass discrimination. The best straight lines through the points at high H_2S flows yield the values of K shown.

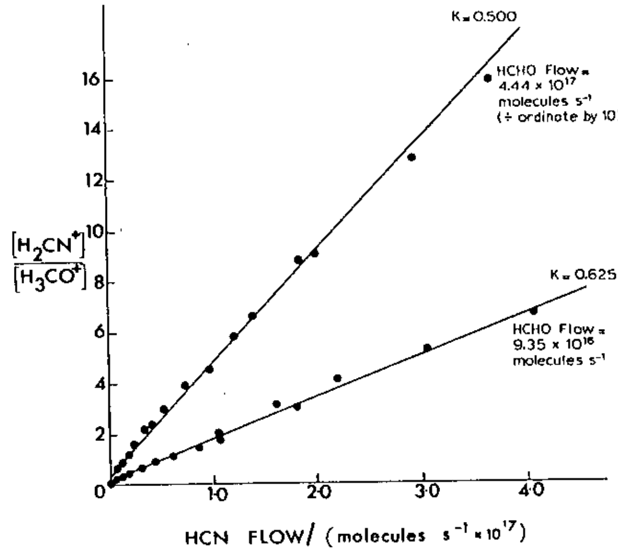

Fig. 4. The ratio plot for reaction (3) in the forward direction. $[H_2CN^+]/[H_3CO^+]$ versus HCN flow. The ratio of ion concentrations has been corrected for mass discrimination. The best straight lines through the points at high HCN flows yield the values of K shown.

TABLE 1

Equilibrium constants, K, for the reactions $H_3CO^+ + H_2S \rightleftharpoons H_3S^+ + HCHO$, and $H_3CO^+ + HCN \rightleftharpoons H_2CN^+ + HCHO$

Direction studied	No. of determinations	K ($=k_f/k_r$)	K (ratio plot)
$H_3CO^+ + H_2S \rightleftharpoons H_3S^+ + HCHO$			
Forward	7	0.13 ± 0.02 *	0.14 ± 0.03
Reverse	5	0.13 ± 0.03	0.13 ± 0.02
		(Overall mean 0.13 ± 0.02 **)	
$H_3CO^+ + HCN \rightleftharpoons H_2CN^+ + HCHO$			
Forward	7	0.63 ± 0.08 *	0.63 ± 0.12
Reverse	4	0.56 ± 0.15	0.76 ± 0.12
		(Overall mean 0.64 ± 0.09 **)	

* Standard deviation of the group of measurements.

** Standard deviation of all 4 groups of measurements.

slope of the plot [product ion]/[reactant ion] versus flow of neutral reactant. In this method it is necessary to correct the observed ion signals for mass discrimination (Figs. 3 and 4). As in our earlier work [6], no correction has been made for any difference between the ambipolar diffusion coefficients of the ions H_3CO^+, H_2CN^+ and H_2S^+. The neglect of these differences is not expected to introduce a large error in K.

The results of the equilibrium constant measurements are summarized in Table 1 and those of the observed rate coefficients and calculated collision rates in Table 2.

$H_3CO^+ + H_2S \rightleftharpoons H_3S^+ + HCHO$

The variation in H_3CO^+ ion concentration with H_2S flow is shown in Fig. 1. Only proton transfer type reactions were observed to occur at low H_2S or HCHO flow rates but at higher neutral flows small peaks at $m/e = 69$ and $m/e = 65$ owing to $H_3S^+ \cdot H_2S$ and $H_3CO^+ \cdot H_2S$ clusters were observed. As

TABLE 2

Rate coefficients for the reactions of H_3CO^+ with H_2S and HCN in units of cm^3 molecule^{-1} s^{-1}

Reaction	Rate coefficient	k_{calc} *
$H_3CO^+ + H_2S \rightarrow H_3S^+ + HCHO$	5.0×10^{-10}	1.42×10^{-9}
$H_3S^+ + HCHO \rightarrow H_3CO^+ + H_2S$	3.4×10^{-9}	2.19×10^{-9}
$H_3CO^+ + HCN \rightarrow H_2CN^+ + HCHO$	1.3×10^{-9}	2.70×10^{-9}
$H_2CN^+ + HCHO \rightarrow H_3CO^+ + HCN$	2.1×10^{-9}	2.24×10^{-9}

* Calculated using the ADO $\overline{\cos\theta}$ model [8].

the rate of cluster formation was very slow compared with the reverse reaction no correction for ion clustering was necessary. The ratio plot $[H_3S^+]/[H_3CO^+]$ versus H_2S flow (after correction for mass discrimination) is shown in Fig. 3 at two different HCHO flows. Rate coefficients for the forward and reverse reactions measured directly under non-equilibrium conditions were found to be $k_f = (5 \pm 1) \times 10^{-10}$ cm^3 molecule^{-1} s^{-1} and $k_r = (3.4 \pm 0.8) \times 10^{-9}$ cm^3 molecule^{-1} s^{-1}, respectively. Neither of these reaction rates appears to have been reported previously. The uncertainties shown are the standard deviations of the measurements. The absolute accuracy of the rate coefficients has earlier been estimated as ±30% [4].

$H_3CO^+ + HCN \rightleftharpoons H_2CN^+ + HCHO$

Again only proton transfer reactions are observed at low HCN or HCHO flows and the variation in the H_3CO^+ signal with HCN flow is given in Fig. 2 for two different flows of the back reactant HCHO. Ion cluster formation at $m/e = 55$, attributable to $H_2CN^+ \cdot HCN$, was noticeable when the equilibrium system was being studied in the forward direction at high HCN flows, and it became necessary to correct the H_2CN^+ signal for cluster formation. The ratio plot $[H_2CN^+]/[H_3CO^+]$ versus HCN flow, after correcting for ion cluster formation ($H_2CN^+ \cdot HCN$) and mass discrimination, is given in Fig. 4. Rate coefficients for the forward and reverse directions are $k_f = (1.3 \pm 0.2) \times 10^{-9}$ cm^3 molecule^{-1} s^{-1} and $k_r = (2.1 \pm 0.5) \times 10^{-9}$ cm^3 molecule^{-1} s^{-1}.

Proton affinities

Equilibrium constants of $K_2 = 0.13 \pm 0.02$ and $K_3 = 0.64 \pm 0.09$ lead to standard free energy changes of $\Delta G^\circ_{300K} = 5.1 \pm 0.4$ kJ mol^{-1} and 1.1 ± 0.4 kJ mol^{-1} for reactions (2) and (3), respectively. From the values for the collision rate coefficients for the forward and reverse directions, Z_f and Z_r as shown in Table 2, and the method of Lias and Ausloos [9] we estimated the entropy changes during reactions (2) and (3) as $\Delta S^\circ_{(2)} = -3.6$ and $\Delta S^\circ_{(3)} = +1.6$ J K^{-1} mol^{-1}, respectively. Combining these ΔS° values with the ΔG° measurements, we obtained standard enthalpy changes for the two reactions as $\Delta H^\circ_{(2)} = 4.0 \pm 0.4$ kJ mol^{-1} and $\Delta H^\circ_{(3)} = 1.6 \pm 0.4$ kJ mol^{-1}. (Uncertainties in ΔS° have not been included in the standard deviations shown for enthalpy changes.) As ΔH° for the reaction is equal to the difference in proton affinities of product neutral and reactant neutral then we have: $PA(\mathrm{HCHO}) = PA(\mathrm{H_2S}) + (4.0 \pm 0.4)$ kJ mol^{-1}; $PA(\mathrm{HCHO}) = PA(\mathrm{HCN}) + (1.6 \pm 0.4)$ kJ mol^{-1}. From these figures we deduced indirectly that $PA(\mathrm{HCN}) = PA(\mathrm{H_2S}) + 2.4$ kJ mol^{-1}, which is in excellent agreement with out earlier direct measurement of 2.5 ± 0.5 kJ mol^{-1} [6].

Few measurements have been reported in the literature of the proton affinity of formaldehyde. Haney and Franklin [10] quote 703 kJ mol^{-1} for $PA(\mathrm{HCHO})$ using the photoionization measurements on lower aliphatic alcohols of Refaey and Chupka [11]. The value of $\Delta H^\circ_f(\mathrm{CH_2OH^+}) = 7.38$ eV (712 kJ mol^{-1}) derived by Refaey and Chupka from the appearance of the

CH_2OH^+ peak in photoionization of methyl and ethyl alcohols corresponds to the proton affinity of HCHO quoted by Haney and Franklin. From appearance potential measurements and observations of the occurrence and non-occurrence of particular proton transfer reactions Haney and Franklin [10] then assigned the proton affinities of both H_2S and HCN as 8.4 kJ mol^{-1} greater than that of HCHO. However, it is evident from the present work that proton transfer to HCHO from H_2CN^+ and H_3S^+ occurs readily in both directions and hence their method is not always a reliable guide to relative proton affinities. The determination of equilibrium constants is inherently more accurate.

In summary, we have established the order of proton affinities as $PA(\text{HCHO}) = PA(\text{HCN}) + 1.6$ kJ mol^{-1}; $PA(\text{HCN}) = PA(H_2S) + 2.4$ kJ mol^{-1}. Combining the measurements of Kebarle et al. [3] with our relative proton affinities, we have $PA(H_2S) = 720 \pm 8$ kJ mol^{-1}; and $PA(\text{HCHO}) = 724 \pm 8$ kJ mol^{-1}.

ACKNOWLEDGEMENT

This work was given financial support by the New Zealand Universities Research Committee.

REFERENCES

1 D.K. Bohme, R.S. Hemsworth, H.W. Rundle and H.I. Schiff, J. Chem. Phys., 58 (1973) 3504.
2 F.C. Fehsenfeld, W. Lindinger, H.I. Schiff, R.S. Hemsworth and D.K. Bohme, J. Chem. Phys., 64 (1976) 4887.
3 P. Kebarle, R. Yamdagni, K. Hiraoka and T.B. McMahon, Int. J. Mass Spectrom. Ion Phys., 19 (1976) 71.
4 J.P. Liddy, C.G. Freeman and M.J. McEwan, Int. J. Mass Spectrom. Ion Phys., 23 (1977) 153.
5 C.G. Freeman, P.W. Harland, J.P. Liddy and M.J. McEwan, Aust. J. Chem., 31 (1978) in press.
6 C.G. Freeman, P.W. Harland and M.J. McEwan, Int. J. Mass Spectrom. Ion Phys., 27 (1978) 77.
7 E.E. Ferguson, F.C. Fehsenfeld and A.L. Schmeltekopf, Advan. At. Mol. Phys., 5 (1969) 1.
8 L. Bass, T. Su, W.J. Chesnavich and M.T. Bowers, Chem. Phys. Lett., 34 (1975) 119.
9 S.G. Lias and P. Ausloos, J. Am. Chem. Soc., 99 (1977) 4831.
10 M.A. Haney and J.L. Franklin, J. Phys. Chem., 73 (1969) 4328.
11 K.M.A. Refaey and W.A. Chupka, J. Chem. Phys., 48 (1968) 5205.

International Journal of Mass Spectrometry and Ion Physics, 28 (1978) 377—388 377
© Elsevier Scientific Publishing Company, Amsterdam — Printed in The Netherlands.

GAS PHASE PROTON-TRANSFER EQUILIBRIA IN BINARY MIXTURES OF CH_3OH, CH_3NO_2 AND HCOOH AND THE RELATIVE PROTON AFFINITIES OF CH_3OH, CH_3NO_2 AND HCOOH

C.G. FREEMAN, P.W. HARLAND and M.J. McEWAN

Department of Chemistry, University of Canterbury, Christchurch (New Zealand)

(Received 24 April 1978)

ABSTRACT

The reaction systems

$CH_3NO_2H^+ + CH_3OH \rightleftharpoons CH_3OH_2^+ + CH_3NO_2$

$HCOOH_2^+ + CH_3NO_2 \rightleftharpoons CH_3NO_2H^+ + HCOOH$

and

$HCOOH_2^+ + CH_3OH \rightleftharpoons CH_3OH_2^+ + HCOOH$

have been studied at 300 K in a flowing afterglow system in both the forward and reverse directions. We report forward and reverse rate coefficients for each system, equilibrium constants and three-body association rates for the process

$BH^+ + B + M \rightarrow (B)_2 \cdot H^+ + M$

where B = CH_3OH, CH_3NO_2 and HCOOH. The equilibrium constant determination yielded the relative proton affinities $PA(CH_3OH) = PA(CH_3NO_2) + 2.2$ kJ mol^{-1}; $PA(CH_3NO_2) = PA(HCOOH) + 2.8$ kJ mol^{-1}; $PA(CH_3OH) = PA(HCOOH) + 5.7$ kJ mol^{-1}.

INTRODUCTION

Over the past 10 years or so, several attempts have been made to establish proton affinities of organic acids and bases from mass spectrometric studies of ion—molecule equilibria [1—4] such as

$$B_1H^+ + B_2 \rightleftharpoons B_2H^+ + B_1 \qquad (1)$$

where B_1 and B_2 are two bases. Yamdagni and Kebarle [2] used a high-pressure ion source mass spectrometer to measure the ratio B_1H^+/B_2H^+ under equilibrium conditions from which they determined equilibrium constants and hence proton affinities for a range of bases having proton affinities between those of H_2O and NH_3. To avoid complications from ion clusters of the type $(B_2)_nH^+$ Yamdagni and Kebarle made their measurements at 600 K. Very recently Wolf et al. [4] applied the same principle of measurement to determine equilibrium constants for reaction (1) where B_1 and B_2 were again a series of bases having proton affinities between those of H_2O and NH_3. The experimental conditions of the two studies were widely different. Wolf et al. [4] used a pulsed ion cyclotron resonance (ICR) technique with partial pressures of B_1 and B_2 in the 10^{-7}—10^{-6}-torr range, whereas the partial pressure in the ion source of Yamdagni and Kebarle was typically 10—200 mtorr. Despite the great difference in experimental conditions the agreement between the two groups was good: Yamdagni and Kebarle [2] report $PA(NH_3)—PA(H_2O) = 133 \pm 8$ kJ mol^{-1} at 600 K and Wolf et al. [4] report the difference as 134 ± 4 kJ mol^{-1} at 300 K. However, within the ladder of bases required to determine the difference between the *PA* values of NH_3 and H_2O a number of discrepancies in relative proton affinities are evident. For example, Yamdagni and Kebarle estimate $PA(MeOH)—PA(HCOOH) = 17$ kJ mol^{-1} whereas Wolf et al. give the difference as 9 kJ mol^{-1}. The flowing afterglow (FA) technique has also been employed to determine accurate measurements of relative proton affinities for a number of systems [5,6]. We have conducted investigations of proton-transfer equilibria in the following systems using an FA system:

$$CH_3NO_2H^+ + CH_3OH \rightleftharpoons CH_3OH_2^+ + CH_3NO_2 \tag{2}$$

$$HCOOH_2^+ + CH_3NO_2 \rightleftharpoons CH_3NO_2H^+ + HCOOH \tag{3}$$

$$HCOOH_2^+ + CH_3OH \rightleftharpoons CH_3OH_2^+ + HCOOH \tag{4}$$

A study of these systems allows us to provide further information on differences in the relative proton affinities reported by the high-pressure mass spectrometer method and the low-pressure ICR method. We report for each reaction system, equilibrium constants, relative proton affinities and rate coefficients for the forward and reverse directions. The inclusion of reaction (4) adds a very useful cross-check on the relative proton affinities of HCOOH and CH_3OH with the value obtained by the combination of reactions (2) and (3).

EXPERIMENTAL

The experimental details of our FA system have been described previously [7]. The primary ion H_3^+ is produced by electron impact on a stream of hydrogen at flow rates in the range 150—200 cm^3 atm s^{-1} and total pressures around 0.3 torr. The reactant ion of interest is produced by proton transfer from H_3^+ to the appropriate base (CH_3OH, CH_3NO_2 or HCOOH) and the reactant neutral is added further downstream. The ensuing proton-transfer reaction is followed by monitoring reactant and product ion signals as the neutral reactant flow varies.

Gases used are industrial-grade, dry hydrogen which is further dried over a molecular sieve trap at 77 K before entry to the reaction tube. Suitable mixtures in hydrogen of commercially obtained (spectroscopic grade or analytical grade) CH_3OH, CH_3NO_2 and HCOOH were prepared such that the partial pressures of these species in the mixture were always well below their saturation vapour pressure at room temperature. In the case of formic acid, which exists mainly as the dimer at room temperature and moderate pressures but as the monomer at reaction tube pressures, it was necessary to correct all our flows of HCOOH for dimer formation. The equilibrium measurements of Halford [8] showed that, in a typical $HCOOH/H_2$ mixture in which the partial pressure of acid is 33 torr, 88% of the vapour is in its dimer form $(HCOOH)_2$.

DATA ANALYSIS

Under favourable conditions the equilibrium constant K for reaction (1)

$$B_1H^+ + B_2 \rightleftharpoons B_2H^+ + B_1 \tag{1}$$

can be estimated by 5 distinct measurements with the FA technique. (a) By direct measurement of k_f and k_r under non-equilibrium conditions from which $K = k_f/k_r$. (b) By monitoring the reactant ion signal (B_1H^+) for reaction (1) in the forward direction and using calculated ion densities and an iterative procedure to find the best value of k_r to fit the observed reactant ion concentration as a function of B_2 flow. $K = k_{f(obs)}/k_{r(iterated)}$. (c) By monitoring both reactant and product ion signals in the forward direction under equilibrium conditions as a function of neutral reactant flow. After correcting for mass discrimination $K = [B_2H^+][B_1]/[B_1H^+][B_2]$. (d) Repeat (b) in the reverse direction. (e) Repeat (c) in the reverse direction. In cases where the forward and reverse reactions are the only reactions competing for the ions B_1H^+ and B_2H^+, good estimates may be found for calculated ion densities from the analytical solution to the differential equations which include radial and axial diffusive loss (model 1) [5]. However, in the systems investigated in this work we had also to include contributions from clustering reactions of the type

$$B_2H^+ + B_2 + M \rightleftharpoons (B_2)_2 \cdot H^+ + M \tag{5}$$

which proceed sufficiently rapidly to prevent equilibrium from becoming established. In an earlier investigation of $HCN/HCHO/H_2S$ equilibria [9], the effect of clustering reactions was minimised by carefully controlling the experimental conditions. However, the very rapid rate of reaction (5) when $B_2 = CH_3OH$, CH_3NO_2 and HCOOH required the inclusion of this B_2H^+ loss mechanism as an additional chemical loss term in the model. The three first-order differential equations that summarise the kinetic scheme (reactions (1), (−1) and (5)) have an exact solution which was used as the basis for a chemical model (model 2) to account for the observed variation in reactant ion signal with neutral reactant flow. In model 2 diffusion is included only as an empirical correction. The magnitude of this correction was calculated by comparing the rate coefficient k_r, iterated using model 1, with that obtained for k_r from model 2 under conditions where clustering reactions are of only minor importance. Values of k_r obtained from model 2 are estimated to be within a factor of 2 of the value produced when model 1 is applied to the observed data. The results of model 2 calculations were not rigorous, being intended only as an aid for interpretation of the measurements and they were not used for the determination of equilibrium constants.

RESULTS AND DISCUSSION

The determination of K by method (c) above was precluded as a consequence of the rapid clustering reaction (5). However, by carefully controlling conditions, method (a) was used to determine k_f and k_r for each reaction system from the slopes of linear semilogarithmic decays of reactant ion with neutral reactant flow (Fig. 1). These results are summarised in Table 1. The ratio of k_f/k_r is the value of K listed in the third column of Table 2.

$CH_3NO_2H^+ + CH_3OH \rightleftharpoons CH_3OH_2^+ + CH_3NO_2$ *[Reaction (2)]*

In Fig. 2 we show the raw data from one series of measurements for reac-

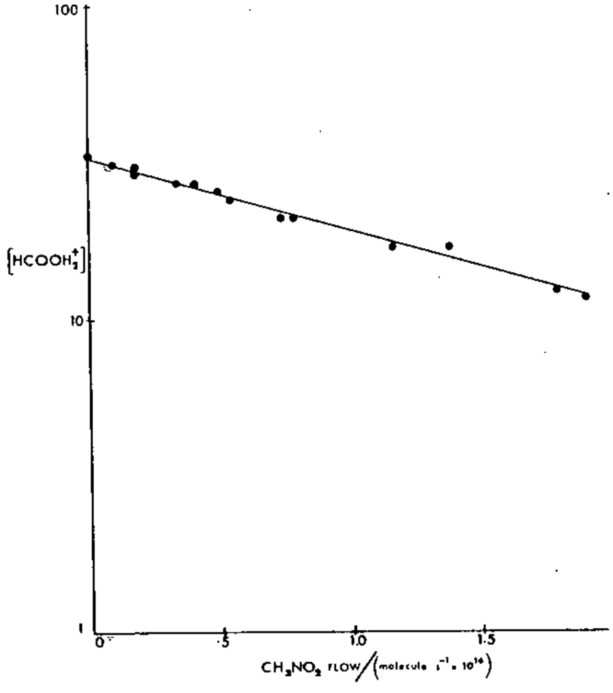

Fig. 1. The slope of the semilogarithmic decay of $HCOOH_2^+$ ions with added CH_3NO_2 yields a value of k_3 = 4.05 × 10^{-9} cm^3 molecule^{-1} s^{-1}. The flow of HCOOH = 6.43 × 10^{15} molecule s^{-1}.

TABLE 1

Rate coefficients for proton transfer in units of 10^{-9} cm^3 molecule^{-1} s^{-1}

Reaction number	Reaction	k_{obs}
(2)	$CH_3NO_2H^+ + CH_3OH \rightarrow CH_3OH_2^+ + CH_3NO_2$	2.3
(−2)	$CH_3OH_2^+ + CH_3NO_2 \rightarrow CH_3NO_2H^+ + CH_3OH$	1.6
(3)	$HCOOH_2^+ + CH_3NO_2 \rightarrow CH_3NO_2H^+ + HCOOH$	4.0
(−3)	$CH_3NO_2H^+ + HCOOH \rightarrow HCOOH_2^+ + CH_3NO_2$	0.7
(4)	$HCOOH_2^+ + CH_3OH \rightarrow CH_3OH_2^+ + HCOOH$	3.8
(−4)	$CH_3OH_2^+ + HCOOH \rightarrow HCOOH_2^+ + CH_3OH$	0.37

tion (2). In Fig. 3 the variation in $CH_3OH_2^+$ ion concentration with CH_3NO_2 flow is shown for two different flows of CH_3OH. The solid curves are computer-fitted curves to the experimental data using model 2 and allowing the values of k_2 and k_5 to vary independently until a minimum deviation is found between the calculated and observed profiles. Proton transfer was found to be the main reaction in the reverse direction (>90%) although a product peak at $m/e = 30$ indicates that a minor channel producing NO^+ + (?) is also occurring. At higher flows of CH_3OH (in the forward direction) or CH_3NO_2 (in the reverse direction), removal of the product ion by clustering became very noticeable (see Fig. 2). From the decrease in $CH_3OH_2^+$ signal with increasing CH_3OH flow resulting from the reaction

$$CH_3OH_2^+ + CH_3OH + H_2 \rightleftharpoons (CH_3OH)_2 \cdot H^+ + H_2 \qquad (6)$$

a clustering rate of $k_6 = 6 \times 10^{-26}$ cm^6 molecule^{-2} s^{-1} was determined for a range of H_2 pressures from 0.15 to 0.4 torr. Grimsrud and Kebarle [10] have measured the equilibrium constant of reaction (6) and found $\Delta G^0_{300K} = -100$ kJ mol^{-1}. Combining our value for k_6 and their equilibrium measurement we obtain $k_{-6} = 5.7 \times 10^{-24}$ cm^3 molecule^{-1} s^{-1}. Independent measurements of the rate coefficients for the forward and reverse reactions gave k_2 =

TABLE 2

Equilibrium constants, K, and the corresponding values of ΔG^0_{300K} for proton-transfer equilibria in $CH_3OH/CH_3NO_2/HCOOH$

Reaction number	Equilibrium	K	ΔG^0_{300K} (kJ mol^{-1})
2	$CH_3NO_2H^+ + CH_3OH \rightleftharpoons CH_3OH_2^+ + CH_3NO_2$	1.4	−0.9
3	$HCOOH_2^+ + CH_3NO_2 \rightleftharpoons CH_3NO_2H^+ + HCOOH$	5.7	−4.3
4	$HCOOH_2^+ + CH_3OH \rightleftharpoons CH_3OH_2^+ + HCOOH$	10.3	−5.8

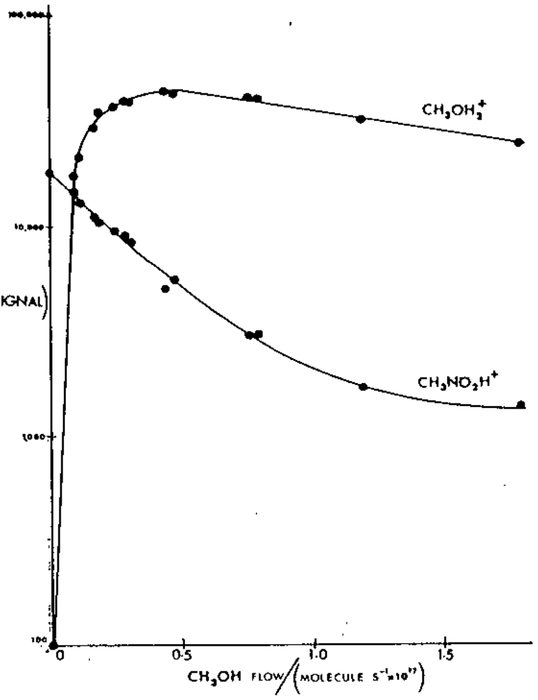

Fig. 2. Raw data for the equilibrium system $CH_3NO_2H^+ + CH_3OH \rightleftharpoons CH_3OH_2^+ + CH_3NO_2$ studied from the forward direction. The flow of $CH_3NO_2 = 2.58 \times 10^{16}$ molecule s^{-1}. The effect of removal of the $CH_3OH_2^+$ ion by clustering is clearly seen although the cluster peak at $m/e = 65$ is not shown.

2.3×10^{-9} and $k_{-2} = 1.6 \times 10^{-9}$ cm^3 $molecule^{-1}$ s^{-1} respectively. These rate coeffients were obtained from the slopes of semilogarithmic decays of the reactant ion concentration as the neutral concentration varied. Very low reactant gas flows were maintained to prevent contributions to the reactant ion signals from the reverse reaction and from the three-body association process.

$HCOOH_2^+ + CH_3NO_2 \rightleftharpoons CH_3NO_2H^+ + HCOOH$ [Reaction (3)]

Proton transfer was the only process observed in either direction at low reactant flows. When investigating reaction (3) in the reverse direction at high flows of HCOOH, the $HCOOH_2^+$ signal was observed to decrease owing to the clustering process

$$HCOOH_2^+ + HCOOH + H_2 \rightleftharpoons (HCOOH)_2 \cdot H^+ + H_2 \qquad (7)$$

The observed rate of decrease gave a value of $k_7 \sim 2.0 \times 10^{-26}$ cm^6 $molecule^{-2}$ s^{-1}. Similarly, in the forward direction, $CH_3NO_2H^+$ was also observed to undergo the association reaction

$$CH_3NO_2H^+ + CH_3NO_2 + H_2 \rightleftharpoons (CH_3NO_2)_2 \cdot H^+ + H_2 \qquad (8)$$

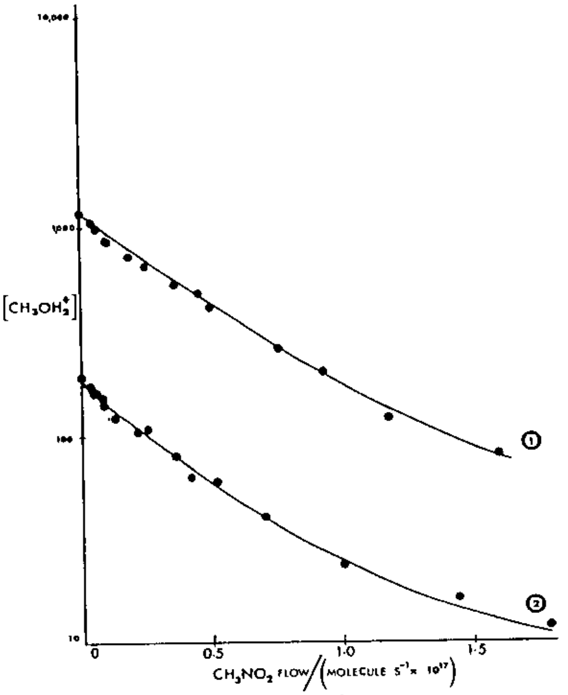

Fig. 3. Variation of $[CH_3OH_2^+]$ with CH_3NO_2 flow at 2 different flows of CH_3OH. The points are experimental and the curves calculated using model 2. k_2 and k_5 are adjustable parameters for achieving minimum deviation. For curve (1) $CH_3OH = 7.6 \times 10^{15}$ molecule s^{-1}, $k_2 = 3.4 \times 10^{-9}$ cm^3 $molecule^{-1}$ s^{-1} and $k_5 = 3.8 \times 10^{-26}$ cm^6 $molecule^{-2}$ s^{-1}. For curve (2) $CH_3OH = 1.7 \times 10^{16}$ molecule s^{-1}, $k_2 = 1.1 \times 10^{-9}$ cm^3 $molecule^{-1}$ s^{-1} and $k_5 = 1.1 \times 10^{-26}$ cm^6 $molecule^{-2}$ s^{-1}.

Measurements of the rate of removal of $CH_3NO_2H^+$ with large flows of added CH_3NO_2 were made during studies of reaction (3) in the forward direction and of reaction (2) in the reverse direction. These yielded a value of $k_8 \sim 4.5 \times 10^{-26}$ cm^6 $molecule^{-2}$ s^{-1}.

The direct measurement of k_3 and k_{-3} gave 4.0×10^{-9} and 0.7×10^{-9} cm^3 $molecule^{-1}$ s^{-1} respectively. A computer fit to the observed decay of $CH_3NO_2H^+$ with HCOOH flow based on model 2 is shown in Fig. 4 for two CH_3NO_2 flows.

$HCOOH_2^+ + CH_3OH \rightleftharpoons CH_3OH_2^+ + HCOOH$ [Reaction (4)]

Again proton transfer was the only reaction observed at low reactant flows in either direction. In the forward direction at higher flows of CH_3OH and in the reverse direction at higher flows of HCOOH the presence of rapid three-body association was again evident. Within the limits of the data treatment provided by model 2, reasonable values were obtained for k_4 and k_6 in the forward direction and k_{-4} and k_7 for the reverse direction when the devi-

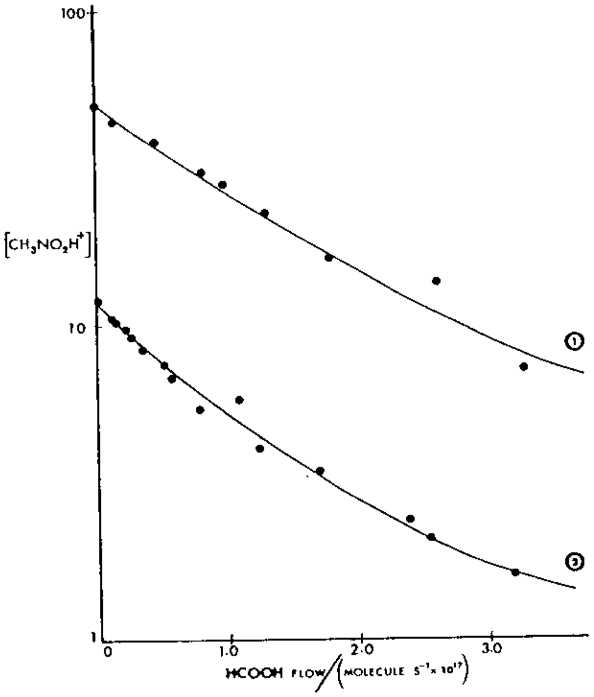

Fig. 4. Variation of [$CH_3NO_2H^+$] with HCOOH flow at 2 different flows of CH_3NO_2. The points are experimental and the curves calculated using model 2. k_3 and k_7 are adjustable parameters for achieving minimum deviation. For curve (1) CH_3NO_2 = 1.1 × 10^{17} molecule s^{-1}, k_3 = 1.0 × 10^{-9} cm^3 $molecule^{-1}$ s^{-1} and k_7 = 2.8 × 10^{-26} cm^6 $molecule^{-2}$ s^{-1}; for curve (2) CH_3NO_2 = 1.5 × 10^{16} molecule s^{-1}, k_3 = 3.0 × 10^{-9} cm^3 $molecule^{-1}$ s^{-1} and k_7 = 1.0 × 10^{-26} cm^6 $molecule^{-2}$ s^{-1}.

ation between the observed and calculated profiles was minimized (see Fig. 5). The direct measurement of the forward and reverse rate coefficients gave $k_4 = 3.8 \times 10^{-9}$ and $k_{-4} = 0.37 \times 10^{-9}$ cm^3 $molecule^{-1}$ s^{-1} respectively.

Free energy and proton affinity

From the ratio of the forward and reverse rate coefficients for each of reactions (2)–(4) we obtain the equilibrium constants K_2 = 1.4 (±20%), K_3 = 5.7 (±20%) and K_4 = 10.3 (±20%). These values of K lead to the standard free energy changes at 300 K $\Delta G^0_{(2)}$ = (−0.9 ± 0.4) kJ mol^{-1}; $\Delta G^0_{(3)}$ = (−4.3 ± 0.5) kJ mol^{-1} and $\Delta G^0_{(4)}$ = (−5.8 ± 0.5) kJ mol^{-1}. From the values for the collision rate coefficients for the forward and reverse directions and the method of Lias and Ausloos [11] we estimate the entropy changes ($\Delta S^0_{\mathrm{coll}}$) during each reaction as $\Delta S^0_{\mathrm{coll}(2)}$ = −4.4 J K^{-1} mol^{-1}, $\Delta S^0_{\mathrm{coll}(3)}$ = 5.1 J K^{-1} mol^{-1} and $\Delta S^0_{\mathrm{coll}(4)}$ = −0.3 J K^{-1} mol^{-1}. The ADO cos θ model [12] was used to calculate collision rates. Calculated values for the average polarizability of CH_3NO_2 and HCOOH, using the δ-function potential model of

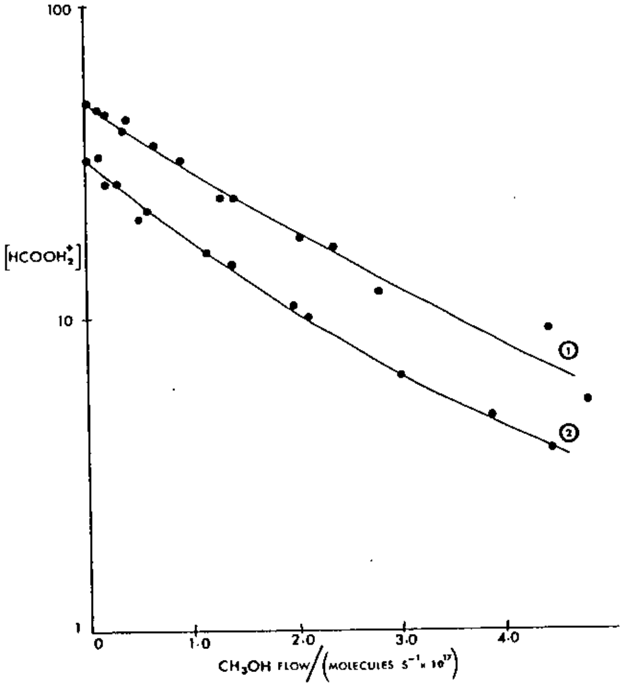

Fig. 5. Variation of [$HCOOH_2^+$] with CH_3OH flow at 2 different flows of back-reactant HCOOH. The points are experimental and the curves calculated using model 2. k_4 and k_6 are adjustable parameters for achieving minimum deviation. For curve (1) $CH_3OH = 3.2 \times 10^{16}$ molecule s^{-1}, $k_4 = 1.3 \times 10^{-9}$ cm^3 molecule^{-1} s^{-1} and $k_7 = 1.2 \times 10^{-26}$ cm^6 molecule^{-2} s^{-1}. (2) $CH_3OH = 1.5 \times 10^{16}$ molecule s^{-1}, $k_4 = 3.1 \times 10^{-9}$ cm^3 molecule^{-1} s^{-1}, and $k_7 = 2.1 \times 10^{-26}$ cm^6 molecule^{-2} s^{-1}.

Lippincott and Stutman [13], were 46.8×10^{-25} and 30.7×10^{-25} cm^3 respectively. The measured average polarizability of CH_3OH is 32.3×10^{-25} cm^3 [14]. As other workers have used rotational symmetry numbers to estimate ΔS^0 changes for reaction (1) using the expression $\Delta S^0_{rs} = R \ln\{\sigma(B_1H^+)\sigma(B_2)/\sigma(B_2H^+)\sigma(B_1)\}$ we have compared our calculated entropies with those of ΔS^0_{rs} in Table 3. Rotational symmetry numbers of 1 were chosen for the protonated bases $CH_3OH_2^+$, $CH_3NO_2H^+$ and 2 for $HCOOH_2^+$. Although the entropy contribution to ΔG^0 is small, the values assumed for ΔS^0 are very important to the evaluation of enthalpy changes as the equilibrium constants are close to unity and consequently $|\Delta G^0|$ values are small. The method of calculation of ΔS^0 therefore has a marked influence on relative proton affinities as can be seen from Table 3. Detailed comparison between different groups is therefore best made on the basis of ΔG^0 values which are obtained directly from experiment rather than from proton affinities. Combining our calculated ΔS^0_{coll} values with our ΔG^0 measurements we obtain the standard enthalpy changes shown in column (5) of Table 3. Thus

TABLE 3

Calculated ΔS^0 (J mol^{-1} K^{-1}) and ΔH^0 (kJ mol^{-1}) of reaction

Reaction number	Reaction system	ΔS^0_{coll} *	ΔS^0_{rs} **, ***	ΔH^0 (calc, ΔS^0_{coll})	ΔH^0 *** (calc, ΔS^0_{rs})	ΔH^0 ** (calc, ΔS^0_{rs})
2	$CH_3NO_2H^+ + CH_3OH \rightleftharpoons CH_3OH_2^+ + CH_3NO_2$	−4.4	0	−2.2	−0.9	−0.9
3	$HCOOH_2^+ + CH_3NO_2 \rightleftharpoons CH_3NO_2H^+ + HCOOH$	5.1	5.8	−2.8	−4.3	−2.6
4	$HCOOH_2^+ + CH_3OH \rightleftharpoons CH_3OH_2^+ + HCOOH$	−0.3	5.8	−5.7	−5.8	−4.1

* Estimated using the method of ref. 11.

** Estimated using $\Delta S^0_{rs} = R\ln\{\sigma(B_1H^+)\sigma(B_2)/\sigma(B_2H^+)\sigma(B_1)\}$ and the rotational symmetry number (σ) = 1 for all species except $HCOOH_2^+$ for which a value of $\sigma = 2$ has been assumed.

*** If σ 1 for all species then $\Delta S^0_{rs} = 0$ and $\Delta G^0 = \Delta H^0$ for all reactions.

the proton affinities are $PA(CH_3OH) = PA(CH_3NO_2) + 2.2$ kJ mol^{-1}; $PA(CH_3NO_2) = PA(HCOOH) + 2.8$ kJ mol^{-1}; and $PA(CH_3OH) = PA(HCOOH) + 5.7$ kJ mol^{-1} (direct measurement). The internal consistency of the relative proton affinities of CH_3OH and HCOOH is within experimental error. However our measurement of $\Delta G^0_{(4)} = (-5.8 \pm 0.5)$ kJ mol^{-1} is greater than either of that reported by Yamdagni and Kebarle (—17 kJ mol^{-1}) [2] or by Wolf et al. (—10 kJ mol^{-1}) [4]. Neither of these references mentions a correction for dimer formation in HCOOH which, if neglected under experimental conditions favourable to dimerisation, will result in experimental values of ΔG^0 which are larger (more positive) than the true value. If this consideration was neglected in the work of Wolf et al. and Yamdagni and Kebarle it would tend to increase the discrepancy between ΔG^0 reported in this work and the results reported by the other two groups. It is also interesting that two systems in which Wolf et al. have noted [4] that marked irregularities occur between measured and calculated entropies are those in which there is significant dimerisation of the neutral molecule: viz. HCOOH—MeOH and H_2O—CF_3COOH.

If we accept a value of 762 kJ mol^{-1} for the proton affinity of CH_3OH [15] then $PA(CH_3NO_2) = 760$ kJ mol^{-1} and $PA(HCOOH) = 756$ kJ mol^{-1}. Two recent ICR studies of CH_3NO_2 gave estimates for the proton affinity (on the basis of whether particular ion—molecule reactions were observed) as 753 ± 17 kJ mol^{-1} [16] and ~753 kJ mol^{-1} [17].

ACKNOWLEDGEMENTS

This work was given financial support by the New Zealand Universities Research Committee.

REFERENCES

1 M.A. Haney and J.L. Franklin, J. Phys. Chem., 73 (1969) 4328.
2 R. Yamdagni and P. Kebarle, J. Am. Chem. Soc., 98 (1976) 1320.
3 P. Kebarle, R. Yamdagni, K. Hiraoka and T.B. McMahon, Int. J. Mass Spectrom. Ion Phys., 19 (1976) 71.
4 J.F. Wolf, R.H. Staley, I. Koppel, M. Taagepera, R.T. McIver, J.L. Beauchamp and R.W. Taft, J. Am. Chem. Soc., 99 (1977) 5417.
5 D.K. Bohme, R.S. Hemsworth, H.W. Rundle and H.I. Schiff. J. Chem. Phys., 58 (1973) 3504.
6 C.G. Freeman, P.W. Harland and M.J. McEwan, Int. J. Mass Spectrom. Ion Phys., 27 (1978) 77.
7 J.P. Liddy, C.G. Freeman and M.J. McEwan, Int. J. Mass Spectrom. Ion Phys., 23 (1977) 153.
8 J.O. Halford, J. Chem. Phys., 10 (1942) 582.
9 C.G. Freeman, P.W. Harland and M.J. McEwan, Int. J. Mass Spectrom. Ion Phys., 28 (1978) 19.
10 E.P. Grimsrud and P. Kebarle, J. Am. Chem. Soc., 95 (1973) 7939.
11 S.G. Lias and P. Ausloos, J. Am. Chem. Soc., 99 (1977) 4831.

12 L. Bass, T. Su, W.J. Chesnavich and M.T. Bowers, Chem. Phys. Lett., 34 (1975) 119.
13 E.R. Lippincott and J.M. Stutman, J. Phys. Chem., 68 (1964) 2926.
14 J.O. Hirschfelder, C.F. Curtis and R.B. Bird, Molecular Theory of Gases and Liquids, Wiley, New York, 1964.
15 P. Kebarle, Ann. Rev. Phys. Chem., 28 (1977) 445.
16 P. Kriemler and S.E. Buttrill, J. Am. Chem. Soc., 95 (1973) 1365.
17 T. McAllister and P. Pitman, Int. J. Mass Spectrom. Ion Phys., 19 (1976) 241.

Aust. J. Chem., 1978, **31**, 2157–60

Ion–Molecule Reactions of Formic Acid. I
Proton-Transfer Reactions

Colin G. Freeman, Peter W. Harland and Murray J. McEwan

Department of Chemistry, University of Canterbury,
Christchurch, New Zealand.

Abstract

Rate coefficients are reported for a number of proton-transfer reactions with formic acid. These reactions can be represented by the general equation

$$XH^+ + HCOOH \rightarrow (HCOOH)H^+ + X$$

($X = CH_4$, H_2O, N_2, CO, HCN, HCHO, CH_3OH and H_2S). Reasonable agreement was obtained between our observed results and predictions based on the average-dipole-orientation (ADO) model except that ADO theory may slightly underestimate the collision rate.

Introduction

Several studies have been made of proton-transfer reactions in organic acids and bases in the gas phase.[1–3] Following an equilibrium study of several reactions of protonated molecules with formic acid[4] we were encouraged to investigate proton-transfer reactions directly. In this study we have confined ourselves to measurements of rate coefficients of simple proton-transfer reactions of formic acid which can be represented by the equation

$$XH^+ + HCOOH \rightarrow (HCOOH)H^+ + X \qquad (1)$$

In reaction (1) $X = CH_4$, H_2O, N_2, CO, HCN, HCHO, CH_3OH and H_2S. Proton-transfer reactions of this type generally have high (close to 100%) reaction efficiencies and are usually free from the complications introduced by multiple reaction channels. These features make proton-transfer reactions a particularly useful means of testing models of reaction rates.[5–7] Although the average-dipole-orientation (ADO) theory of Su, Bowers *et al.*[5,8] provides the most realistic model of collision rates for proton-transfer reactions a number of reactions have been noted where ADO theory under-

---

[1] Kebarle, P., *Annu. Rev. Phys. Chem.*, 1977, **28**, 445.

[2] Yamdagni, R., and Kebarle, P., *J. Am. Chem. Soc.*, 1976, **98**, 1320.

[3] Wolf, J. F., Staley, R. H., Koppel, I., Taagepera, R. T., McIver, R. T., Beauchamp, J. L., and Taft, R. W., *J. Am. Chem. Soc.*, 1977, **99**, 5417.

[4] Freeman, C. G., Harland, P. W., and McEwan, M. J., *Int. J. Mass Spectrom. Ion Phys.*, 1978a, in press.

[5] Su, T., and Bowers, M. T., *Int. J. Mass Spectrom. Ion Phys.*, 1973, **12**, 347.

[6] Betowski, D., Payzant, J. D., Mackay, G. I., and Bohme, D. K., *Chem. Phys. Lett.*, 1975, **31**, 321.

[7] Liddy, J. P., Freeman, C. G., and McEwan, M. J., *Int. J. Mass Spectrom. Ion Phys.*, 1977, **23**, 153.

[8] Bass, L., Su, T., Chesnavich, W. J., and Bowers, M. T., *Chem. Phys. Lett.*, 1975, **34**, 119.

estimates the collision rate up to 40%.[9] The study reported here allows us to make comparisons of theory and experiment with a system of moderate dipole moment and polarizability and also to examine the effect of exothermicity on reaction efficiency.

Experimental

The rate coefficients of the reactions reported were measured by the flowing afterglow technique at 300 K which has been described previously.[7] Primary ions are produced by electron impact on a hydrogen carrier gas and quickly attain thermal energies by collisional deactivation. The ion of interest is formed by adding a suitable neutral reactant downstream from the electron impact source thus producing the reactant ion from the primary ion. Further downstream the reactant neutral (formic acid in this case) is added and the reactant and product ion concentrations are monitored by a quadrupole mass spectrometer. Typical operating conditions are: total gas pressure c. 0·3 Torr; gas velocity c. 7000 cm s^{-1}; reaction length 56 cm; reactant ion concentration c. 10^8 ions cm^{-3} and neutral reactant concentration c. 10^{12} molecules cm^{-3}. The overall accuracy of the rate measurements is estimated as ±30% but the precision is within ±10%.[7]

Hydrogen (industrial dry grade) was used as carrier gas after passage through a molecular sieve trap at 77 K before entry to the reaction tube. The neutral reactants used to form the ion XH^+ were nitrogen (Matheson, 99·999%), carbon monoxide (Matheson, 99·5%), ammonia (N.Z. Gas, 99·9%), methane (Matheson, 99%), distilled water, methanol (Koch-Light spectroscopic grade) and formaldehyde (BDH, reagent grade). Hydrogen sulfide and hydrogen cyanide were prepared in this laboratory by the addition of sulfuric acid to potassium sulfide or potassium cyanide respectively and after drying were purified by trap-to-trap distillation. Mixtures of formic acid (Merck, analytical grade) were prepared with hydrogen so that at all times the vapour pressure of formic acid was well below its saturation vapour pressure at room temperature. In most cases the experiments were repeated with mixtures having widely different mole fractions of formic acid to eliminate potential problems arising from mixture contamination. At the pressures of formic acid used in the preparation of mixtures in this work the dimeric form predominates[10] (for example, at 300 K and a partial pressure of 40 Torr, formic acid is present as c. 88% dimer). Allowance was made for this in the monitoring of the formic acid flow rates with the assumption that after expansion into the flow system complete dissociation to the monomer occurs rapidly.

Results and Discussion

The rate coefficients measured for the proton-transfer reactions studied are summarized in the second column of Table 1. Each reported value is the mean of at least four separate observations. We are not aware of any other values reported for these rate coefficients. In most cases determination of the rate of proton transfer was straightforward with no complications arising from alternative reaction channels. The one exception was the reaction with H_3^+ where the exothermicity of reaction (323 kJ) was sufficiently great for fragmentation of the product ion to occur to give HCO^+ as the main channel:

$$H_3^+ + HCOOH \rightarrow HCO^+ + H_2O + H_2 \tag{2}$$

Although this exothermic channel to form the HCO^+ product was also open to the N_2H^+ reaction, the proton-transfer process was the dominant channel.

The three most widely used classical physical theories for collision rates between ions and molecules can be represented by the equation

$$k = (2\pi q/\mu^{1/2})[\alpha^{1/2} + c\mu_D(2/\pi k_B T)^{1/2}] \tag{3}$$

---

[9] Mackay, G. I., Betowski, L. D., Payzant, J. D., Schiff, H. I., and Bohme, D. K., *J. Phys. Chem.*, 1976, **80**, 2919.

[10] Halford, J. O., *J. Chem. Phys.*, 1942, **10**, 582.

where k is the calculated capture rate coefficient, q the ionic charge, α the average electronic polarizability of the neutral molecule, μ the reduced mass of the ion–neutral pair, μ_D the permanent dipole moment, and k_B is the Boltzmann constant. Parameter c is a parameter which has the value zero in simple Langevin theory, the value one in the locked-dipole limit[11] and intermediate values that have been parameterized by

Table 1. $10^9 \times$ **rate coefficients** (cm^3 **molecule**$^{-1}$ s^{-1}) **at 300 K for proton-transfer reactions of the type** $XH^+ + HCOOH \rightarrow (HCOOH)H^+ + X$

XH^+	k_{obs}	k(ADO)^A	k(LD)^B	k_{obs}/k(ADO)	k_{obs}/k(LD)	$-\Delta H^{\circ\,C}$
$H_3^{+\,D}$	3·9	3·9	10·1	1·0	0·39	323, 132^D
CH_5^+	3·0	1·9	4·8	1·6	0·63	209
H_3O^+	2·2	1·8	4·6	1·2	0·48	35
N_2H^+	1·7	1·6	4·0	1·1	0·43	270
HCO^+	1·9	1·6	4·0	1·2	0·48	163
H_2CN^+	1·4	1·6	4·1	0·88	0·34	16
H_3CO^+	2·0	1·5	3·9	1·3	0·51	26
$CH_3OH_2^+$	0·37	0·15^E	0·38^E	2·5	0·97	−5·7^E
H_3S^+	2·0	1·50	3·8	1·3	0·53	19

[A] Calculated by average-dipole-orientation theory and the $\overline{\cos\theta}$ model[8] ($c = 0·192$).

[B] Calculated by 'locked-dipole' theory ($c = 1·0$) (from Gupta, S. K., Jones, E. G., Harrison, A. G., and Myher, J. J., *Can. J. Chem.*, 1967, **45**, 3107).

[C] The proton affinities adopted in this work (in kJ mol^{-1}) are based on values previously tabulated (ref. 1 and Freeman, C. G., Harland, P. W., and McEwan, M. J., *Int. J. Mass Spectrom. Ion Phys.*, 1978b, in press), unless otherwise stated.

[D] Although not a proton-transfer reaction, as noted in the text, we have included the reaction of H_3^+ to emphasize any trend in deviation between theory and experiment. $\Delta H^\circ = -323$ kJ mol^{-1} applies to proton transfer and $\Delta H^\circ = -132$ kJ mol^{-1} applies to formation of HCO^+.

[E] We have measured the enthalpy of this reaction directly as $\Delta H^\circ = 5·7$ kJ mol^{-1} (ref. 4). The ADO and LD rate coefficients have been calculated from an Arrhenius-type expression in which the activation energy is set equal to the endothermicity of reaction.

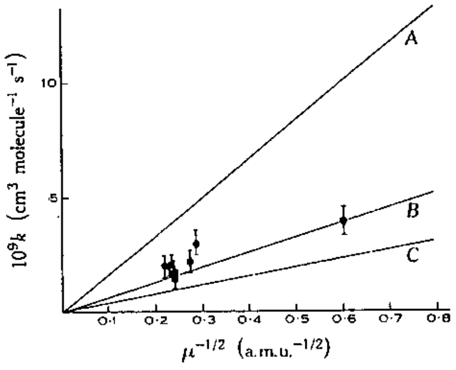

Fig. 1. A comparison of observed rate coefficients of formic acid with the capture rates predicted by *A*, 'locked-dipole' ($c = 1$); *B*, ADO ($c = 0·192$); *C*, Langevin ($c = 0$) theories. The points are experimental.

Bass *et al.*[8] in ADO theory. Thus at one extreme ($c = 0$), Langevin theory ignores ion–permanent dipole interaction while at the other extreme ($c = 1$) there is complete alignment or 'locking in' of the dipole as considered by Gupta *et al.*[11] There is now a considerable body of evidence to support the case that most proton-transfer reaction

---

[11] Gupta, S. K., Jones, E. G., Harrison, A. G., and Myher, J. J., *Can. J. Chem.*, 1967, **45**, 3107.

rates are best described by ADO theory where c has intermediate values which lie between 0 and 0·26.[8]

Formic acid has a dipole moment of 1·41 D.[12] The average polarizability of formic acid has been calculated by means of the δ-function potential model of Lippincott and Stutman[13] and the resulting value of $30 \cdot 7 \times 10^{-25}$ cm^3 used in the present work. The collision capture rate coefficients calculated from the ADO model which assumes 100% reaction efficiency and an average angle θ between the dipole and the line of centre of collision are shown in the third column of Table 1. Rate coefficients based on the locked-dipole limit model are shown in the fourth column. As expected from similar studies[5,7,9] we find that ADO theory gives the best approximation to the degree of permanent dipole interaction whereas locked-dipole theory overestimates the interaction (see Fig. 1). Although we do not observe any major difference between calculated collision capture coefficients (which assume 100% reaction efficiency) and experiment, no trend is observed in the series with reaction exothermicity which indicates all reactions studied proceed at close to 100% efficiency.

Acknowledgment

We wish to acknowledge the New Zealand Universities Research Committee for financial support.

Manuscript received 3 April 1978

---

[12] 'Selected Values of Electric Dipole Moments for Molecules in the Gas Phase' (Compiled by Nelson, Lide and Maryott, NSRDS-NBS10, Washington, 1967).

[13] Lippincott, E. R., and Stutman, J. M., *J. Phys. Chem.*, 1964, **68**, 2926.

Aust. J. Chem., 1978, **31**, 2593–9

Ion–Molecule Reactions of Formic Acid. II[†] Rearrangement Reactions

Colin G. Freeman, Peter W. Harland and Murray J. McEwan

Department of Chemistry, University of Canterbury, Christchurch, New Zealand.

Abstract

Rate coefficients for a number of rearrangement reactions of positive ions with HCOOH are reported. These reactions may be represented by the general equation

$$Y^+ + HCOOH \rightarrow \text{products}$$

Most reactant ions resulted in the fragmentation product HCO^+ and five reactant ions, N^+, O^+, CN^+, N_2^+ and CO^+, were observed to have rate coefficients much greater than predicted by the ADO model. An explanation for the high rates observed for these reactant ions is proposed and involves dissociative charge transfer by a non-orbiting electron-jump mechanism.

Introduction

In an earlier investigation into the rates of ion–molecule reactions of gas-phase formic acid,[1] we made a study of a series of proton transfer reactions which can be represented by the general equation

$$XH^+ + HCOOH \rightarrow (HCOOH)H^+ + X \tag{1}$$

Proton transfer reactions usually have high reaction efficiency and are generally free from the complications introduced by multiple reaction paths. As formic acid has been observed in the interstellar region towards Sgr B2[2] together with closely related molecules such as methyl formate,[3] we have extended the range of reactions of formic acid to include rearrangement-type reactions. When the reactant ion has no transferable protons or alternatively has sufficient energy to initiate fragmentation of the formic acid molecule, the possibility of multiple reaction pathways exists (e.g. reaction (2)):

$$\begin{aligned} Y^+ + HCOOH &\rightarrow HCO^+ + Y + OH \\ &\rightarrow HCOOH^+ + Y \\ &\rightarrow YH^+ + CO_2 + H \\ &\rightarrow YH_2^+ + CO_2 \end{aligned} \tag{2}$$

[†] Part I, *Aust. J. Chem.*, 1978, **31**, 2157.

[1] Freeman, C. G., Harland, P. W., and McEwan, M. J., *Aust. J. Chem.*, 1978, **31**, 2157.

[2] Winnewisser, G., and Churchwell, E., *Astrophys. J. Lett.*, 1975, **200**, L33.

[3] Brown, R. D., Crofts, J. G., Gardner, F. F., Godfrey, P. D., Robinson, B. J., and Whiteoak, J. B., *Astrophys. J. Lett.*, 1975, **197**, L29.

Very few detailed investigations have been reported of the rates of ion–molecule reactions involving organic acids. Only one earlier investigation of reactions of formic acid appears to have been undertaken.[4] In that study the ions chosen were generated from the HCOOH molecule itself and proton transfer was the main reaction channel as in our earlier study.[1] In the present investigation, however, proton transfer (where possible) proved to be the exception rather than the rule.

Experimental

The rate coefficients reported in this work have been measured by the flowing afterglow technique which has been described elsewhere.[5] In all the reactions studied, the ions were generated by electron impact on a helium carrier gas rather than in hydrogen as described in Part I.[1] Typical operating conditions were: total gas pressure *c.* 0·3 Torr; gas velocity *c.* 7000 cm s^{-1}; reaction length 56 cm; reactant ion concentration *c.* 10^8 ions cm^{-3} and formic acid concentration *c.* 10^{12} molecules cm^{-3}. The overall accuracy of the rate measurements is estimated as ±30%[5] but the precision is within ±10%.

The reagents used were helium (N.Z. Ind. Gases 99·995%), NH_3 (N.Z. Gas Co., 99·9%), CO (Matheson, 99·5%), N_2 (Matheson, 99·999%), O_2 (Matheson, 99·95%), CH_4 (Matheson, 99%) and C_2H_4 (Matheson, 99·5%). HCN was prepared by the action of sulfuric acid on KCN, dried over P_2O_5 and further purified by trap-to-trap distillation. Mixtures of HCOOH (Merck, analytical grade) in hydrogen were prepared as described earlier[1] so that at all times the vapour pressure of HCOOH was well below its saturation vapour pressure at room temperature. Corrections were applied for dimer formation of HCOOH as previously described.[1]

Results and Discussion

Table 1 summarizes the reactions studied and compares the results observed with those calculated by various methods.[6–9] Each rate coefficient reported is the mean of at least three separate determinations. Although many of the reactions had two or more ion products, the major pathway for most reactions led to the initial production of HCO^+ which subsequently underwent secondary reaction with formic acid to produce $(HCOOH)H^+$ at *m/e* 47:[1]

$$HCO^+ + HCOOH \rightarrow (HCOOH)H^+ + CO \tag{3}$$
$$k_3 = 1{\cdot}9\times10^{-9}\ cm^3\ molecule^{-1}\ s^{-1}$$

The formation of HCO^+ was endothermic in four of the five reactions in which HCO^+ was not the major ion product, viz. $Y^+ = O_2^+$, $C_2H_5^+$, NH_2^+ and NH_3^+. Only reaction (8), where $Y^+ = CH_3^+$, was the exothermic pathway leading to HCO^+ formation much less important than hydrogen atom abstraction and, instead of HCO^+, CH_5^+ was the major product. In Fig. 1 we show the raw data for reaction of CO^+ with HCOOH. The slope of the linear semilogarithmic decay of CO^+ with formic acid flow gives the rate coefficient for reaction (16). The rapid increase in HCO^+ signal at low formic acid flows indicates that HCO^+ is the primary ion product which subsequently reacts with HCOOH to produce a secondary ion $HCOOH_2^+$ (reaction (3)).

[4] Pritchard, H., Thynne, J. C. J., and Harrison, A. G., *Can. J. Chem.*, 1968, **46**, 2141.

[5] Liddy, J. P., Freeman, C. G., and McEwan, M. J., *Int. J. Mass Spectrom. Ion Phys.*, 1977, **23**, 153.

[6] Bass, L., Su, T., Chesnavich, W. J., and Bowers, M. T., *Chem. Phys. Lett.*, 1975, **34**, 119.

[7] Gupta, S. K., Jones, E. G., Harrison, A. G., and Myher, J. J., *Can. J. Chem.*, 1967, **45**, 3107.

[8] Rosenstock, H. M., Draxl, K., Steiner, B. W., and Herron, J. T., *J. Phys. Chem. Ref. Data*, 1977, **6**, (Suppl. No. 1), 1.

[9] Freeman, C. G., Harland, P. W., and McEwan, M. J., *Int. J. Mass Spectrom. Ion Phys.*, 1978, in press.

In those reactions where two or more primary product ions were produced, we were unable to determine accurately the relative importance of each reaction channel and instead can only provide approximate branching ratios. Three factors are mainly responsible for this approximation. (*a*) The sensitivity of the sampling system and mass spectrometer varied non-uniformly with the mass of the ion. (*b*) In all reactions, the reactant ion is formed by reaction of He 2^3S metastable atoms and He^+ ions with

Table 1. Rate coefficients in units of 10^{-9} cm³ molecule⁻¹ s⁻¹ at 300 K for reactions of the type $Y^+ + HCOOH \rightarrow$ products

Reaction number	Y^+	Major ion products[A]	k_{obs}	k_{ADO}[B]	k_{LD}[C]	$-\Delta H^{\circ}$[D] (kJ mol⁻¹)
(4)	H_3^+	HCO^+	3·9	3·9	10·1	323
(5)	He^+	HCO^+, HCO_2^+, $HCOOH^+$	4·1	3·4	8·9	1138
(6)	C^+	HCO^+	3·3	2·1	5·5	615
(7)	N^+	HCO^+	6·2	2·0	5·2	167
(8)	CH_3^+	CH_5^+	2·1	2·0	5·1	195
(9)	O^+	HCO^+, HO_2^+	5·0	1·9	5·0	78
(10)	NH_2^+	NH_4^+, ($HCOOH_2^+$?)	2·7	1·9	5·0	425
(11)	NH_3^+	NH_4^+, ($HCOOH_2^+$?)	0·9	1·9	4·8	103
(12)	CN^+	HCO^+	5·3	1·6	4·2	126
(13)	HCN^+	HCO^+	2·5	1·6	4·1	79
(14)	N_2^+	HCO^+	4·6	1·6	4·1	270
(15)	$C_2H_5^+$	$HCOOH_2^+$	1·5	1·6	4·0	92[E]
(16)	CO^+	HCO^+	4·1	1·6	4·0	115
(17)	O_2^+	$HCOOH^+$, HCO_2^+	1·8	1·5	3·9	69

[A] See text for details of products.

[B] Calculated by using average-dipole-orientation theory and the $\overline{\cos\theta}$ model ($c = 0{\cdot}192$) as outlined in ref. 6.

[C] Calculated by using the 'locked-dipole' limit model as described in ref. 7.

[D] Unless otherwise indicated, the ΔH° values shown were estimated from ΔH_f° values of ref. 8. Where multiple ion products are obtained, the ΔH° value shown is for the channel producing HCO^+ as the product ion.

[E] ΔH_f° ($HCOOH_2^+$) was calculated from the proton affinity of HCOOH in ref. 9.

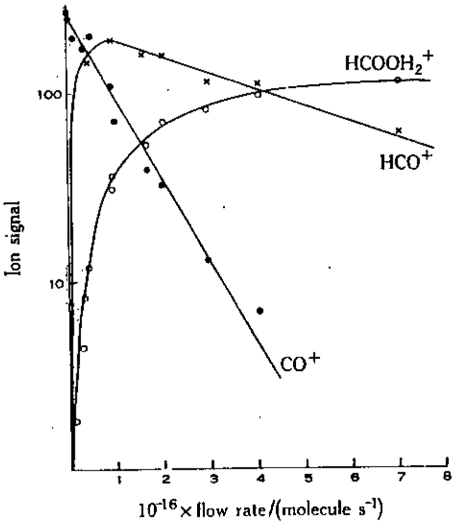

Fig. 1. Raw results for reaction (16) $CO^+ + HCOOH \rightarrow HCO^+ + CO + OH$. The slope of the linear semilogarithmic CO^+ signal gave $k_{16} = 4{\cdot}1 \times 10^{-9}$ cm³ molecule⁻¹ s⁻¹.

a reactant gas. Often several primary product ions are produced and each may react further with formic acid thus making product analysis difficult. (*c*) Secondary reactions of the product ion with formic acid may also occur. In some cases it was possible to eliminate potential reaction pathways from a knowledge of the thermochemistry of reactants and products. A brief outline of the more complex reactions follows. (We would point out that no neutral product analysis has been undertaken.)

Reaction (5)

$$\mathrm{He^+ + HCOOH \xrightarrow{c.\ 70\%} HCO^+ + He + OH} \qquad \Delta H^\circ = -1138\ \mathrm{kJ\ mol^{-1}} \qquad (5a)$$

$$\mathrm{\xrightarrow{c.\ 30\%} HCO_2^+ + He + H} \qquad \Delta H^\circ \approx -1127\ \mathrm{kJ\ mol^{-1}} \qquad (5b)$$

The rate coefficient for removal of He^+ was found to be $k_{5(a+b)} = 4{\cdot}1 \times 10^{-9}$ cm^3 molecule^{-1} s^{-1}. Product ions from the reaction were observed at *m/e* 29 (HCO^+), 45 (HCO_2^+), 46 ($HCOOH^+$) and 47 ($HCOOH_2^+$). Protonated formic acid, $HCOOH_2^+$, cannot be formed as a primary product of the reaction but is derived in reaction (3) from HCO^+. From relative peak heights we estimate the main products as HCO^+ (*c*. 70%) and HCO_2^+ (*c*. 30%). A smaller signal corresponding to $HCOOH^+$ showed that charge transfer was less than 10%.

Reactions (7) and (14)

$$\mathrm{N^+ + HCOOH \rightarrow HCO^+ + N + OH} \qquad \Delta H^\circ = -167\ \mathrm{kJ\ mol^{-1}} \qquad (7)$$

$$\mathrm{N_2^+ + HCOOH \rightarrow HCO^+ + N_2 + OH} \qquad \Delta H^\circ = -270\ \mathrm{kJ\ mol^{-1}} \qquad (14)$$

When trace amounts of N_2 were added to the helium flow downstream from the electron gun, N^+ and N_2^+ ions were produced. Both of these ions exhibited linear semilogarithmic decays with increasing formic acid flow to give $k_7 = 6{\cdot}2 \times 10^{-9}$ and $k_{14} = 4{\cdot}6 \times 10^{-9}$ cm^3 molecule^{-1} s^{-1}. A small signal corresponding to $HCOO^+$ (< 10% of total product signal) was also observed but may have been due to residual He^+, He 2^3S species in the carrier gas.

Reactions (9) and (17)

$$\mathrm{O^+ + HCOOH \xrightarrow{c.\ 70\%} HCO^+ + O + OH} \qquad \Delta H^\circ = -78\ \mathrm{kJ\ mol^{-1}} \qquad (9a)$$

$$\mathrm{\xrightarrow{c.\ 30\%} HO_2^+ + HCO} \qquad \Delta H^\circ = -90\ \mathrm{kJ\ mol^{-1}} \qquad (9b)$$

$$\mathrm{O_2^+ + HCOOH \xrightarrow{c.\ 65\%} HCOOH^+ + O_2} \qquad \Delta H^\circ = -69\ \mathrm{kJ\ mol^{-1}} \qquad (17a)$$

$$\mathrm{\xrightarrow{c.\ 35\%} HCO_2^+ + HO_2} \qquad \Delta H^\circ \approx -115\ \mathrm{kJ\ mol^{-1}} \qquad (17b)$$

Small amounts of O_2 added to the helium flow produced the ions O^+ and O_2^+. From their linear semilogarithmic decays we obtained $k_{9(a+b)} = 5{\cdot}0 \times 10^{-9}$ and $k_{17(a+b)} = 1{\cdot}8 \times 10^{-9}$ cm^3 molecule^{-1} s^{-1}. Product ions observed from the joint reaction of O^+ and O_2^+ with HCOOH were at *m/e* 29 (HCO^+), 33 (HO_2^+), 45 (HCO_2^+), 46 ($HCOOH^+$) and 47 ($HCOOH_2^+$). As noted already $HCOOH_2^+$ cannot be formed in the primary reaction and is derived from a secondary reaction between HCO^+ and HCOOH. Only two exothermic pathways exist for the reaction of O_2^+ with formic acid, i.e. charge transfer and the formation of HCO_2^+. The product at *m/e* 46 was attributed entirely to reaction (17a) after a comparison of peak heights corrected for mass discrimination. Although HCO_2^+ is also a possible product ion of reaction (9) on energetic grounds, the relatively small amplitude of the HCO_2^+ signal caused us to assign the entire signal to reaction (17b). We did not therefore consider HCO_2^+ to be a major product of reaction (9).

Reactions (10) and (11)

$$NH_2^+ + HCOOH \rightarrow NH_4^+ + CO_2 \qquad \Delta H^\circ = -425\ \text{kJ mol}^{-1} \quad (10a)$$

$$\rightarrow HCOOH_2^+ + NH \qquad \Delta H^\circ = -161\ \text{kJ mol}^{-1} \quad (10b)$$

$$NH_3^+ + HCOOH \rightarrow NH_4^+ + CO_2 + H \qquad \Delta H^\circ = -103\ \text{kJ mol}^{-1} \quad (11a)$$

$$\rightarrow HCOOH_2^+ + NH_2 \qquad \Delta H^\circ \approx -1\cdot5\ \text{kJ mol}^{-1} \quad (11b)$$

Traces of ammonia added to the helium flow produced the ions NH_2^+, NH_3^+ and NH_4^+. We established from separate experiments, using a hydrogen carrier gas, that no simple reaction of NH_4^+ with formic acid occurs. The slope of the semi-logarithmic decays of NH_2^+ and NH_3^+ with formic acid gave values for $k_{10(a+b)}$ and $k_{11(a+b)}$ of $2\cdot7\times10^{-9}$ and $9\cdot0\times10^{-10}$ cm^3 molecule^{-1} s^{-1} respectively. Product ions observed from the joint reactions of NH_2^+ and NH_3^+ with HCOOH were at m/e 18 (NH_4^+), 29 (HCO^+), 45 (HCO_2^+) and 47 ($HCOOH_2^+$). To obtain acceptable concentrations of NH_2^+ and NH_3^+ it was necessary to retain small He^+ signals and thus the HCO^+ and HCO_2^+ product ions were attributed to products of the He^+ + HCOOH reaction. This assignment was confirmed by the fact that no exothermic channels exist for the formation of HCO^+ from HCOOH by NH_2^+ or NH_3^+. The product ion at m/e 47 ($HCOOH_2^+$) appeared to be produced as a primary product of the reaction but we could not establish relative channel efficiencies.

Dissociative Charge-Transfer Reactions

An interesting feature of these measurements are the large rate coefficients observed for reactions (7) (N^+), (9) (O^+), (12) (CN^+), (14) (N_2^+) and (16) (CO^+) compared with collision rates calculated by using the average-dipole-orientation (ADO) model.[6] Although most tests of the theory of ion–molecule reaction rates have been carried out for proton-transfer reactions, as long as the reaction proceeds at close to unit efficiency, the classical theories should also be able to provide adequate descriptions of the physical interactions of the simple ions of this study. It is apparent from Table 1 that ADO theory does not model correctly the interaction of the ion with formic acid. In the extreme case of 'dipole locking' where the permanent dipole of HCOOH is considered to be continuously locked along the line of centres of the collision pair, the corresponding calculated rate coefficient k_{LD}, is substantially greater than k_{ADO}. For reactions (7), (9), (12), (14) and (16) the 'locked dipole' limit approximation gives values that are close to the observed rate coefficients. We feel however that this agreement is fortuitous as there is no obvious reason why the degree of 'dipole locking' should be greater for N^+ than, say, for C^+.

However, an alternative mechanism may involve a non-orbiting exoergic long-range charge-transfer process. At ion energies greater than about 5 eV[10–12] charge transfer by an electron-jump mechanism may occur at distances outside the classical capture

[10] Gauglhofer, J., and Kevan, L., *Chem. Phys. Lett.*, 1972, **16**, 492.
[11] Smith, D. L., and Kevan, L., *J. Am. Chem. Soc.*, 1971, **93**, 2113.
[12] Smith, D. L., and Kevan, L., *J. Phys. Chem.*, 1971, **55**, 2290.

limit and consequently rate coefficients may be greater than those estimated by simple polarization models.[10] Gauglhofer and Kevan,[10] using atomic ions, concluded from their measurements on methane that (i) energy resonance must exist between the reactant ion system ($Y^+ + HCOOH$ in this work) and the product system ($Y + HCOOH^+$) at the recombination energy of Y^+; and (ii) that there be favourable Franck–Condon factors for the reactant molecule to its ion. Laudenslager *et al.*[13] demonstrated the applicability of this mechanism and the above criteria for thermal energy charge transfer and Harland and Ryan[14] showed that for some cases rapid thermal energy charge transfer may occur despite unfavourable Franck–Condon factors. If we assume an electron-jump mechanism for the system $Y^+ + HCOOH$ and that HCO^+ is to be a major product of the reaction, then the reaction exothermicity, ionization potential $I_p(Y) - I_p(HCOOH)$, must be greater than the endothermicity of the autodissociation channel forming HCO^+:

$$Y^+ + HCOOH \rightarrow Y + (HCOOH^+)^* \tag{18}$$

$$(HCOOH^+)^* \rightarrow HCO^+ + OH \tag{19}$$

$$\Delta H^\circ_{18} + \Delta H^\circ_{19} < 0$$

This simple argument takes no account of any partitioning of the excess energy in the charge-transfer step. When the reactant ion Y^+ is atomic, it seems reasonable to presume that most of the reaction exoergicity will end up as internal excitation of the polyatomic product $HCOOH^+$ although, in those cases where a diatomic or polyatomic ion is involved, then energy partitioning between products may be expected.

Table 2. **Enthalpy changes for dissociative charge transfer to formic acid**

$Y^+ + HCOOH \rightarrow Y + HCOOH^+$ (18) $HCOOH^+ \rightarrow HCO^+ + OH$ (19)

$\Delta H_{19}^\circ = 139$ kJ mol^{-1}

Reaction	Reactant	ΔH_{18}° (kJ mol^{-1})^A	($\Delta H_{18}^\circ + \Delta H_{19}^\circ$) (kJ mol^{-1})
(4)	H_3^+	207	>0
(5)	He^+	−1278	−1139
(6)	C^+	13	>0
(7)	N^+	−306	−167
(8)	CH_3^+	140	>0
(9)	O^+	−217	−78
(10)	NH_2^+	−2	>0
(11)	NH_3^+	107	>0
(12)	CN^+	−266	−127
(13)	HCN^+	−218	−79
(14)	N_2^+	−409	−270
(15)	$C_2H_5^+$	285	>0
(16)	CO^+	−255	−116
(17)	O_2^+	−69	>0

^{A} ΔH_f values of reactants and products are taken from ref. 8. In most cases values are accurate to ±20 kJ mol^{-1}.

Table 2 lists the reactant ions studied in this work, the standard enthalpy change for the charge-transfer reaction (18), and the overall enthalpy change for the formation of HCO^+ by dissociative charge transfer, reactions (18)+(19).

[13] Laudenslager, J. B., Huntress, W. T., and Bowers, M. T., *J. Chem. Phys.*, 1974, **61**, 4600.

[14] Harland, P. W., and Ryan, K. R., *Int. J. Mass Spectrom. Ion Phys.*, 1975, **18**, 215.

The only reactant ions for which this mechanism is energetically favourable are He^+, N^+, O^+, CN^+, HCN^+, N_2^+ and CO^+. Once the energy requirement is fulfilled the reaction is still dependent upon the following two conditions: (i) the resonance criterion is met and (ii) most of the reaction exoergicity appears as internal excitation of the $HCOOH^+$ ion from (18). With the exception of He^+, all these ions exhibit rate coefficients significantly exceeding the predictions of the ADO model. The high recombination energy of He^+, 24·6 eV (2374 kJ mol^{-1}), may not correspond to a region of the potential energy surfaces where accidental resonance with $HCOOH \rightarrow (HCOOH^+)^*$ occurs, in which case the resonance criterion would not be satisfied. All excited states of HCOOH above the I_p, 11·33 eV (1094 kJ mol^{-1}), will be autoionizing or autodissociating. Unfortunately the dearth of spectroscopic data precludes a meaningful assessment of the probability of energy resonance occurring in the reactions studied.

Smith and Futrell[15] have recently shown that exothermic charge transfer is the main channel in the reactions of C^+ ions of near thermal energy with various polyatomic molecules including acetone and biacetyl. Dissociative charge transfer of C^+ and acetone accounts for 42% of products and C^+ and biacetyl for 96%. The electron-jump dissociative charge-transfer mechanism considered as a possible explanation of our results may also be applied to C^+ on acetone and biacetyl. In both cases the process would be exothermic, the reaction with acetone by *c.* 100 kJ mol^{-1} and the reaction with biacetyl by *c.* 145 kJ mol^{-1}. However, no rate measurements were undertaken by Smith and Futrell which precludes any further comparison.

In summary, we have determined rate coefficients for 14 rearrangement-type ion–molecule reactions of formic acid. A number of these reactions had rate coefficients much in excess of rate coefficients calculated from the ADO model and all showed HCO^+ as the major product ion. These increased rate coefficients have been interpreted in terms of an electron transfer process in which an energetic intermediate complex $HCOOH^{+*}$ undergoes autodissociation to form the fragmentation products $HCO^+ + OH$.

Manuscript received 12 July 1978

---

[15] Smith, R. D., and Futrell, J. H., *Int. J. Mass Spectrom. Ion Phys.*, 1978, **26**, 111.

Astrophysical Letters
1978, Vol. 19, pp. 133–135

© Gordon and Breach Science Publishers Ltd., 1978
Printed in Great Britain

The Interstellar Synthesis of HC_3N and HC_5N

COLIN G. FREEMAN, PETER W. HARLAND and MURRAY J. McEWAN
Department of Chemistry, University of Canterbury, Christchurch, New Zealand

(*Received May 10, 1978*)

A laboratory investigation of a number of ion-molecule reactions leading to the possible synthesis of the cyanoacetylene-type molecules HC_3N and HC_5N has been undertaken. Although a simple mechanism was observed for the production of HC_3N, no such simple mechanism could be found for HC_5N involving only gas phase ion-molecule reactions.

INTRODUCTION

In 1971 Turner reported the first identification of the molecule cyanoacetylene, HC_3N, in the interstellar region towards Sgr B2. This was followed in 1976 by the 7 atom molecule cyanodiacetylene, HC_5N, (Avery *et al.*, 1976) and in 1977 by the 9 atom molecule ethyl cyanide, C_2H_5CN (Johson *et al.*, 1977). The synthesis of the simpler cyanides such as HCN and their observed densities can be accounted for by an ion-molecule reaction mechanism (Herbst and Klemperer, 1973; Huntress and Anicich, 1976; Liddy *et al.*, 1977a and Watson, 1974). However it is not yet evident whether similar ion-molecule reactions may also explain the presence of the larger polyatomic cyanides. Anders *et al.* (1974) and Hayatsu *et al.* (1972) have demonstrated that in the laboratory, under conditions markedly different from those prevailing in interstellar clouds, many interstellar molecules including HC_3N can be formed by surface catalysis on clay catalysts at 250–300 °C. Huntress (1977) using the ion cyclotron resonance technique has measured the reaction rate of $C_2H_2^+$ with HCN and found a product ion at m/e 52 which he suggests could be protonated cyanoacetylene.

$$C_2H_2^+ + HCN \longrightarrow H_2CN^+ + C_2H \qquad (1a)$$

$$\qquad\qquad \longrightarrow C_2H_2.CN^+ + H \qquad (1b)$$

Winnewisser (1977) has also commented that a possible production mechanism for the larger polyatomic cyanides is via the reaction sequence reaction (1b), (2a) and (3) followed by dissociative recombination (4).

$$C_2H_2^+ + HC_3N \longrightarrow H_2C_5N^+ + H \qquad (2a)$$

$$C_2H_2^+ + HC_5N \longrightarrow H_2C_7N^+ + H \qquad (3)$$

$$H_2C_5N^+ + e \longrightarrow HC_5N + H \qquad (4)$$

Allen and Wilse Robinson (1977) on the other hand, suggest that large molecules such as HC_3N and HC_5N can form on grain surfaces by a free radical-type mechanism where activation energies are generally negligible.

We report here the results of a laboratory investigation of some ion-molecule reactions related to the possible synthesis of HC_3N and HC_5N in interstellar clouds solely from gas phase ion-molecule reactions.

EXPERIMENTAL METHOD

The rate coefficients reported here have been determined at 300K by the flowing afterglow technique which has been described in detail elsewhere (Liddy *et al.*, 1977b). In brief, primary ions are produced by electron impact on a carrier gas and are carried down a reaction tube in a stream of helium or hydrogen. Typical flow velocities are $\sim 7 \times 10^3$ cm s^{-1} at a total pressure ~ 0.3 Torr. The rate coefficient for the ion-molecule reaction is determined by monitoring the ion concentration as a function of added neutral reactant flow. The total uncertainty in the measurements is believed to be ± 30 per cent.

TABLE 1
Rate coefficients in units of cm^3 $molecule^{-1}$ s^{-1} measured at 300 K

Reaction number	Reaction	Rate coefficient
1a	$C_2H_2^+ + HCN \xrightarrow{\sim 0.85} H_2CN^+ + C_2H$	7.1 (−10)[a]
1b	$C_2H_2^+ + HCN \xrightarrow{\sim 0.15} H_2C_3N^+ + H$	
2b	$C_2H_2^+ + HC_3N \longrightarrow H_2C_3N^+ + C_2H$	1.9 (−9)
5	$H_3^+ + HC_3N \longrightarrow H_2C_3N^+ + H_2$	9.1 (−9)
6	$H_2C_3N^+ + C_2H_2 \longrightarrow$ products (see text)	<1 (−13)
7	$H_2C_3N^+ + NH_3 \longrightarrow NH_4^+ + HC_3N$	2.3 (−9)[b]

[a] 7.1 (−10) = 7.1×10^{-10} cm^3 $molecule^{-1}$ s^{-1}.
[b] $H_2C_3N^+$ was generated in two different ways — see text.

RESULTS AND DISCUSSION

The results of our rate coefficient measurements are summarised in Table 1. In dense clouds, simple hydrocarbons may be formed in the sequence of reactions (8) to (12) which require an initial radiative association step between C^+ and H_2 (Black and Dalgarno, 1977).

$$C^+ + H_2 \longrightarrow CH_2^+ + h\nu \qquad (8)$$

$$CH_2^+ + H_2 \longrightarrow CH_3^+ + H \qquad (9)$$

$k_9 = 7.2 \times 10^{-10}$ cm^3 $molecule^{-1}$ s^{-1} (Huntress, 1977)

$$CH_3^+ + C \longrightarrow C_2H^+ + H_2 \qquad (10)$$

$$C_2H^+ + H_2 \longrightarrow C_2H_2^+ + H \qquad (11)$$

$k_{11} = 7.8 \times 10^{-10}$ cm^3 $molecule^{-1}$ s^{-1} (Huntress, 1977)

$$C^+ + CH_4 \left\{ \begin{array}{l} \xrightarrow{0.33} C_2H_2^+ + H_2 \\ \xrightarrow{0.67} C_2H_3^+ + H \end{array} \right\} \qquad (12)$$

$k_{12} = 1.2 \times 10^{-9}$ cm^3 $molecule^{-1}$ s^{-1} (Smith and Adams, 1977)

One possible mechanism for the interstellar production of HC_3N is via reaction (1b)

$$C_2H_2^+ + HCN \longrightarrow C_2H_2.CN^+ + H \qquad (1b)$$

$k_{1b} \sim 1 \times 10^{-10}$ cm^3 $molecule^{-1}$ s^{-1} (this work)

followed by dissociative recombination

$$H_2C_2.CN^+ + e \longrightarrow HC_3N + H \qquad (13)$$

Our measured rate coefficient for reaction (1b) is in disagreement with the determination of Huntress (1977) who reported the overall rate of removal of $C_2H_2^+$ by HCN to be 5.3×10^{-11} cm^3 $molecule^{-1}$ s^{-1} compared with our overall rate of 7.1×10^{-10} cm^3 $molecule^{-1}$ s^{-1}. Our estimate of the product ratio was also more in favour of H_2CN^+ (~85 percent) than $H_2C_2.CN^+$ (~15 percent) compared with the corresponding ratios of 41 and 59 percent respectively of Huntress. We point out however, that in our FA system we could not eliminate completely the occurrence of secondary reactions. It is clear from both measurements that reaction (1b) occurs much more slowly than the collision rate at 300 K. It is possible that reaction (1b) may exhibit a temperature dependence with the rate increasing at the lower temperatures of interstellar clouds. To investigate whether the ion product of reaction (1b), $H_2C_2.CN^+$, is identical with that of protonated cyanoacetylene $H_2C_3N^+$ (formed by reaction (5)) we measured the proton transfer rates of both ions with NH_3 and found they exhibited identical rates (reaction (7)).

$$H_2C_3N^+ + NH_3 \longrightarrow NH_4^+ + HC_3N \qquad (7)$$

$k_7 = 2.3 \times 10^{-9}$ cm^3 $molecule^{-1}$ s^{-1} (this work)

Although not conclusive, the evidence supports the suggestion that both protonated cyanoacetylene, $H_2C_3N^+$ from reaction (5) and $H_2C_2.CN^+$ from reaction (1b) are identical.

We did not observe the addition of $C_2H_2^+$ to HC_3N (reaction (2a)).

$$C_2H_2^+ + HC_3N \not\longrightarrow C_2H_2.C_3N^+ + H \qquad (2a)$$

Instead the relatively high proton affinity of HC_3N ensured that proton transfer was rapid and $H_2C_3N^+$ was the only ion product observed.

$$C_2H_2^+ + HC_3N \longrightarrow H_2C_3N^+ + C_2H \quad (2b)$$
$$k_{2b} = 1.9 \times 10^{-9}\ \mathrm{cm^3\ molecule^{-1}\ s^{-1}}\ \text{(this work)}$$

Our failure to observe any product ion at m/e = 76 corresponding to $C_2H_2.C_3N^+$ ensures that $k_{2a} < 10^{-13}\ \mathrm{cm^3\ molecule^{-1}\ s^{-1}}$. HC_3N was also observed to accept protons readily from a number of $C_mH_n^+$ hydrocarbon ions and other hydrogen-containing ions (Freeman *et al.*, 1978) *e.g.*

$$H_3^+ + HC_3N \longrightarrow H_2C_3N^+ + H_2 \quad (5)$$
$$k_5 = 9.1 \times 10^{-9}\ \mathrm{cm^3\ molecule^{-1}\ s^{-1}}\ \text{(this work)}$$

All attempts to increase the number of C atoms in the cyanoacetylene molecule by an ion-molecule process failed and resulted in either proton transfer or fragmentation of HC_3N. Similarly, the reactions of protonated cyanoacetylene with suitable hydrocarbon molecules also failed to increase the length of the carbon chain, *e.g.*

$$H_2C_3N^+ + C_2H_2 \longrightarrow ? \quad (6)$$
$$k_6 < 1 \times 10^{-13}\ \mathrm{cm^3\ molecule^{-1}\ s^{-1}}\ \text{(this work)}$$

A small observed decrease in the $H_2C_3N^+$ signal was attributed to trace impurities of acetone in the C_2H_2 and not to any reaction of $H_2C_3N^+$ with C_2H_2. It is thus apparent from the reactions included here and from a more extensive study of the positive ion chemistry of HC_3N (Freeman *et al.*, 1978), that the synthesis of acetylene-type cyanides having greater than 5 atoms, through ion-molecule reactions involving hydrocarbon ions and cyanide-derived species is not likely. Instead, the mechanism for producing HC_5N possibly requires a heterogeneous mechanism involving neutral-neutral reactions on grain surfaces or, alternatively, radiative association processes.

ACKNOWLEDGEMENTS

We wish to thank Miss C. H. Foo who prepared the samples of HC_3N.

REFERENCES

Allen, M., and Wilse Robinson, G., 1977, *Astrophys. J.*, **212**, 396.

Anders, E., Hayatsu, R., and Studier, M. H., 1974, *Astrophys. J. Letters*, **192**, L101.

Avery, L. W., Broten, M. W., MacLeod, J. M., Oka, T., and Kroto, H. W., 1976, *Astrophys. J. Letters*, **205**, L173.

Black, J. H., and Dalgarno, A., 1977, *Astrophys. J. Supp. Ser.*, **34**, 405.

Freeman, C. G., Harland, P. W., and McEwan, M. J., 1978. (To be published).

Hayatsu, R., Studier, M. H., Matsuoka, S., and Anders, E., 1972, *Geochim. Cosmochim. Acta*, **36**, 555.

Herbst, E., and Klemperer, W., 1973, *Astrophys. J.*, **185**, 505.

Huntress, W. T., 1977, *Astrophys. J. Supp. Ser.*, **33**, 495.

Huntress, W. T., and Anicich, V. G., 1976, *Astrophys. J.*, **208**, 237.

Johson, D. R., Lovas, F. J., Gottlieb, C. A., Gottlieb, E. W., Litvak, M. M., Guelin, M., and Thaddeus, P., 1977, *Astrophys. J.*, **218**, 370.

Liddy, J. P., Freeman, C. G., and McEwan, M. J., 1977a, *Mon. Not. Roy. Astron. Soc.*, **180**, 683.

Liddy, J. P., Freeman, C. G., and McEwan, M. J., 1977b, *Int. J. Mass Spectrom. Ion Phys.*, **23**, 153.

Smith, D., and Adams, N. G., 1977, *Astrophys. J.*, **217**, 741.

Turner, B. E., 1971, *Astrophys. J. Letters*, **163**, L35.

Watson, W. D., 1974, *Astrophys. J.*, **188**, 35.

Winnewisser, G. W., 1977, Paper delivered at Int. Free Radical Symp. Southampton, England.

Mon. Not. R. astr. Soc. (1979) 187, 441–444

Laboratory investigation of ion–molecule reactions of HC_3N in dense interstellar clouds

C. G. Freeman, P. W. Harland and M. J. McEwan
Department of Chemistry, University of Canterbury, Christchurch, New Zealand

Received 1978 October 2; in original form 1978 July 11

Summary. Rate coefficients from laboratory measurements at 300 K are reported for reactions of cyanoacetylene, HC_3N, with 18 ions of interstellar significance. Reactions between HC_3N and ions of the type YH^+ were found to be exclusively proton transfer except in the case where $Y = NH_3$ where no reaction occurred. These observations limit the proton affinity of HC_3N to the range between 824 and 866 kJ/mol. Reactions between HC_3N and ions with non-transferable protons, Y^+, were exclusively charge transfer with rate coefficients in most cases exceeding the predictions of the simple polarization and orientated dipole models. A further consequence of the high proton affinity of HC_3N is that HC_5N will not be formed from HC_3N via the reaction $C_2H_3^+ + HC_3N \rightarrow H_2C_5N^+ + H_2$.

Introduction

Within the past 10 years a series of molecular species that contain the –CN group linked to acetylene-type hydrocarbons have been identified in interstellar regions. The simplest of these molecules is cyanoacetylene (HC_3N) which was first identified by Turner (1971) in the region towards Sgr B2. More recently cyanodiacetylene (HC_5N) has been observed (Avery *et al.* 1976) and in 1977 cyanotriacetylene (HC_7N) was first reported (Kroto *et al.* 1978). The mechanism by which these molecules are formed in interstellar clouds is uncertain. Although participation in molecular synthesis by ion–molecule reactions has been shown as a possibility for smaller polyatomic molecules (Herbst & Klemperer 1973; Watson 1977) the importance of ion–molecule reactions in the synthesis of large polyatomic species has yet to be ascertained. We have recently measured in the laboratory, rate coefficients of several ion–molecule reactions relating to the formation and reactions of cyanoacetylene (Freeman, Harland & McEwan 1978a). We observed that whereas HC_3N has a possible source in reactions of the type

$$C_2H_2^+ + HCN \rightarrow H_2C_3N^+ + H \tag{1}$$

$$H_2C_3N^+ + e \rightarrow HC_3N + H \tag{2}$$

no such likely source exists for the formation of HC_5N.

an upper limit of 866 kJ/mol on PA (HC_3N). Our observation that proton transfer is rapid between CH_3^+ and HC_3N suggests that the PA of HC_3N is greater than that of CH_2, i.e. greater than 824 kJ/mol (Rosenstock *et al.* 1977). We estimate therefore 824 kJ/mol < PA(HC_3N) < 866 kJ/mol, from which we conclude that only SiH and NH_3 of the simple interstellar molecules have higher proton affinities (Huntress 1977). Our earlier observation of proton transfer from $H_2C_3N^+$ to NH_3 is in agreement with this suggestion that PA(HC_3N) < PA(NH_3) (Freeman *et al.* 1978a).

$$H_2C_3N^+ + NH_3 \rightarrow NH_4^+ + HC_3N \qquad (23)$$

$k_{23} = 2.3 \times 10^{-9}\,cm^3\,molecule^{-1}\,s^{-1}$.

(b) Where the reactant ion did not contain a transferable proton, charge transfer was the main process observed.

$$Y^+ + HC_3N \rightarrow HC_3N^+ + Y. \qquad (24)$$

It is evident from Table 1 that for ions such as C^+ and CN^+ the rate coefficient for charge transfer is significantly greater than the collision capture rate, k_{ADO}, calculated using the average dipole orientation (ADO) model of Bass *et al.* (1975). To calculate values for k_{ADO} we estimated the polarizability of HC_3N as $47 \times 10^{-25}\,cm^3$ using δ-function potentials (Lippincott & Stutman 1964). The polarizability combined with the measured dipole moment (Landolt-Bornstein 1967) gave a value for the ADO parameter, *C*, of 0.246. In an investigation of ion–molecule rearrangement reactions of HCOOH (Freeman, Harland & McEwan 1978b) we observed that dissociative charge transfer rate coefficients for neutral molecules containing four or more atoms can be considerably larger than collision capture rate coefficients calculated using classical models. In that work we observed rates which were up to a factor of 6 greater than those calculated from the Langevin model and up to 3 times the corresponding values of k_{ADO}. This discrepancy was attributed to the possibility of the electron transfer process taking place by an electron-jump mechanism at distances outside the classical capture limit. Such a process could also be occurring here.

Churchwell, Winnewisser & Walmsley (1978) have detected HC_3N, HC_5N and HC_7N in emission in a dark cloud in the Taurus complex. As all three of these, cyanoacetylene-type molecules have been observed in the same region they suggested that each of the molecules, $CN{-}(C)_n{-}H$, is formed in a single step from $CN{-}(C)_{n-2}{-}H$ possibly via reactions of the type

$$C_2H_3^+ + HC_3N \rightarrow H_2C_5N^+ + H_2 \qquad (14a)$$

followed by dissociative recombination. Our observations show, however, that proton transfer (reaction (14)) is the only channel observed for both $C_2H_2^+$ and $C_2H_3^+$ ions and therefore synthesis of higher cyanoacetylenes will not occur by this process.

$$C_2H_3^+ + HC_3N \rightarrow H_2C_3N^+ + C_2H_2. \qquad (14)$$

A further consequence of the high PA of HC_3N is that few ion–molecule channels are available for removal of $H_2C_3N^+$ whereas HC_3N will accept protons readily from most interstellar ions of the type YH^+. In a dense cloud, dissociative recombination of $H_2C_3N^+$ (reaction (25)) will prevent a substantial

$$H_2C_3N^+ + e \rightarrow \text{products} \qquad (25)$$

fraction of HC_3N from being converted into $H_2C_3N^+$. If the dense cloud conditions can be represented by $[H_2] \sim 3 \times 10^4\,cm^{-3}$, $[HCO^+] \sim 2 \times 10^{-4}\,cm^{-3}$ and $[e] = 3 \times 10^{-3}\,cm^{-3}$ (Herbst & Klemperer 1973; Watson 1976) and if $k_{25} \sim 10^{-7}\,cm^{-3}\,s^{-1}$ then $[H_2C_3N^+]/[HC_3N] \sim 2 \times 10^{-3}$.

We have extended our laboratory measurements of the reactions of HC_3N and report here rate coefficients for reaction of HC_3N with a number of ions of relevance to interstellar chemistry.

Experimental technique and results

All rate coefficients were measured at 300 K in a flowing afterglow system which has been described elsewhere (Liddy *et al.* 1977). HC_3N was prepared in this laboratory by ammonolysis of methyl propiolate followed by dehydration with P_2O_5 as described by Moureu & Bongrand (1920). Although HC_3N was stored in vacuum to prevent polymerization, some deterioration was observed after several weeks. Therefore, immediately before use, the sample of HC_3N was purified by trap-to-trap distillation and then, after mixing with helium, was added directly to the flow system.

The observed rate coefficients for all reactions studied are summarized in Table 1. We are not aware of any previous measurement of these reaction rate coefficients although we have included our earlier results (Freeman *et al.* 1978a) in Table 1 for completeness.

Table 1. Rate coefficients measured at reactant temperatures of 300 K in units of $10^{-9}\,\mathrm{cm^3\,molecule^{-1}\,s^{-1}}$.

Reaction number	Reaction	Observed rate coefficient	Calculated rate coefficient, k_{ADO}[a]
(3)	$H_3^+ + HC_3N \rightarrow H_2C_3N^+ + H_2$	9.1	7.9
(4)	$He^+ + HC_3N \rightarrow HC_3N^+ + He$	8.2	6.8
(5)	$C^+ + HC_3N \rightarrow HC_3N^+ + C$	8.7	4.2
(6)	$CH_2^+ + HC_3N \rightarrow H_2C_3N^+ + CH$	4.1	4.0
(7)	$CH_3^+ + HC_3N \rightarrow H_2C_3N^+ + CH_2$	2.7	3.9
(8)	$CH_4^+ + HC_3N \rightarrow H_2C_3N^+ + CH_3$	2.5	3.8
(9)	$CH_5^+ + HC_3N \rightarrow H_2C_3N^+ + CH_4$	4.5	3.7
(10)	$H_3O^+ + HC_3N \rightarrow H_2C_3N^+ + H_2O$	4.0	3.6
(11)	$CN^+ + HC_3N \rightarrow HC_3N^+ + CN$	5.3	3.2
(12)	$C_2H_2^+ + HC_3N \rightarrow H_2C_3N^+ + C_2H$	1.9	3.2
(13)	$HCN^+ + HC_3N \rightarrow H_2C_3N^+ + CN$	2.5	3.2
(14)	$C_2H_3^+ + HC_3N \rightarrow H_2C_3N^+ + C_2H_2$	1.8	3.2
(15)	$C_2H_4^+ + HC_3N \rightarrow H_2C_3N^+ + C_2H_3$	1.1	3.1
(16)	$CO^+ + HC_3N \rightarrow HC_3N^+ + CO$	2.3	3.1
(17)	$H_2CN^+ + HC_3N \rightarrow H_2C_3N^+ + HCN$	3.4	3.1
(18)	$HCO^+ + HC_3N \rightarrow H_2C_3N^+ + CO$	3.7	3.1
(19)	$C_2H_5^+ + HC_3N \rightarrow H_2C_3N^+ + C_2H_4$	3.8	3.1
(20)	$N_2H^+ + HC_3N \rightarrow H_2C_3N^+ + N_2$	4.2	3.1
(21)	$NH_4^+ + HC_3N$ – no reaction observed	$< 1 \times 10^{-14}$	3.6

(a) Calculated using the average dipole orientation theory model and $C = 0.246$ (Bass *et al.* 1975).

Discussion

The reactions listed in Table 1 can be considered as belonging to either of two classes.

(a) If the reactant ion contains a proton (YH^+), then the high proton affinity of HC_3N ensures that proton transfer is the only process taking place.

$$YH^+ + HC_3N \rightarrow H_2C_3N^+ + Y. \qquad (22)$$

Of the ions of type YH^+ studied in this work, the only exception to the occurrence of proton transfer was in the case of NH_4^+, where no reaction was observed. From this observation and the known proton affinity (PA) of NH_3, 866 kJ/mol (Kebarle 1977), we can place

In summary, the positive ion chemistry of HC_3N is dominated by either proton-transfer or charge-transfer reactions.

Acknowledgments

We wish to thank Miss C. H. Foo who prepared the samples of HC_3N. We also thank Dr G. Winnewisser, Max-Planck-Institute für Radioastronomie, Bonn, for sending preprints of his work.

References

Avery, L. W., Broten, N. W., MacLeod, J. M., Oka, T. & Kroto, H. W., 1976. *Astrophys. J.*, **205**, L173.
Bass, L., Su, T., Chesnavich, W. J. & Bowers, M. T., 1975. *Chem. Phys. Lett.*, **34**, 119.
Churchwell, E., Winnewisser, G. & Walmsley, C. M., 1978. *Astr. Astrophys.*, **67**, 139.
Freeman, C. G., Harland, P. W. & McEwan, M. J., 1978a. *Astrophys. Lett.*, **19**, 133.
Freeman, C. G., Harland, P. W. & McEwan, M. J., 1978b. *Aust. J. Chem.*, in press.
Herbst, E. & Klemperer, W., 1973. *Astrophys. J.*, **185**, 505.
Huntress, W. T., 1977. *Astrophys. J. Suppl. Ser.*, **33**, 495.
Kebarle, P., 1977. *Ann. Rev. Phys. Chem.*, **28**, 445.
Kroto, H. W., Kirby, C., Walton, D. R. M., Avery, L. W., Broten, N. W., MacLeod, J. M. & Oka, T., 1978. *Astrophys. J.*, **219**, L133.
Landolt-Bornstein (new series), 1967. Group II, Vol. 4, *Molecular Constants from Microwave Spectroscopy*, Springer-Verlag.
Liddy, J. P., Freeman, C. G. & McEwan, M. J., 1977. *Int. J. Mass Spectrom. Ion Phys.*, **23**, 153.
Lippincott, E. R. & Stutman, J. M., 1964. *J. Phys. Chem.*, **68**, 2926.
Moureu, C. & Bongrand, J. C., 1920. *Ann. Chemie*, **14**, 47.
Rosenstock, H. M., Draxl, K. Steiner, B. W. & Herron, J. T., 1977. *J. Phys. Chem. Ref. Data*, **6**, Suppl. No. 1.
Turner, B. E., 1971. *Astrophys. J.*, **163**, L35.
Watson, W. D., 1976. *Rev. Mod. Phys.*, **48**, 513.
Watson, W. D., 1977. *Accnts. Chem. Res.*, **10**, 221.

International Journal of Mass Spectrometry and Ion Physics, 30 (1979) 285—291 285
© Elsevier Scientific Publishing Company, Amsterdam — Printed in The Netherlands

THE POSITIVE ION CHEMISTRY OF TRIFLUORONITROSOMETHANE, CF_3NO

C.G. FREEMAN, P.W. HARLAND and M.J. McEWAN

Chemistry Department, University of Canterbury, Christchurch (New Zealand)

(Received 7 August 1978)

ABSTRACT

The positive ion chemistry of trifluoronitrosomethane, CF_3NO, has been investigated at 300 K in a flowing afterglow system. Dissociative ionization dominates the ion chemistry of CF_3NO and this may be attributed to the low C—N bond dissociation energy, $\leqslant 130$ kJ mol^{-1}, in this molecule. Generally, reactant ions with non-transferable protons undergo dissociative charge transfer and those with transferable protons undergo dissociative proton transfer and/or proton transfer. The occurrence or non-occurrence of proton transfer for reactant ions of the type XH^+, for which the proton affinities, PA(X), covered the range 423—747 kJ mol^{-1}, restricts the PA(CF_3NO) to the range bounded by H_2O and HCN, i.e.,

$$PA(HCN) = 723 \text{ kJ mol}^{-1} > PA(CF_3NO) > PA(H_2O) = 708 \text{ kJ mol}^{-1}$$

INTRODUCTION

Trifluoronitrosomethane is a blue gas with a boiling point of —84°C. Monomeric C-nitroso-compounds have characteristically low C—N bond dissociation energies, the value for F_3C—NO being $\leqslant$130 kJ mol^{-1} (31 kcal mol^{-1}) [1,2]. The weak bond in CF_3NO may be attributed to depletion of electron density in the C—N bond by the electron-withdrawing effects of the CF_3 and NO groups. This depletion results in an unusually long C—N bond length of 0.1555 nm (1.555 Å), which led Davis et al. [3] to suggest that the ionic form $CF_3^-NO^+$ may be considered to contribute to the CF_3NO structure. Although the ionization potential [1], electron affinity [2] and heat of formation [2] of CF_3NO have been determined by photoelectron spectroscopy and low pressure mass spectrometry, the ion—molecule chemistry has not been studied. In this work, thermal energy (300 K) rate coefficients have been measured for the reaction of 17 different positive ions with trifluoronitrosomethane, and the effects of reaction exothermicity on reaction efficiency and multiple reaction channels have been determined.

EXPERIMENTAL

The rate coefficients reported in this paper were measured at 300 K using the flowing afterglow technique, which has been described previously [4]. Briefly, primary ions are generated by electron impact on an H_2 or He carrier gas upstream from the first gas inlet jet, where the appropriate reactant ion is produced by ion—molecule reaction with the primary carrier gas ions. The reactant neutral, CF_3NO in these experiments, is added at a second inlet jet further downstream and the reaction progress is followed by sampling the flow stream through a small orifice in a molybdenum-tipped nose cone into a quadrupole mass filter. Typical operating conditions are: total gas pressure ~0.3 torr; gas velocity ~7000 cm s^{-1}; reaction length 77 cm; reactant ion concentration ~10^8 cm^{-3} and neutral reactant concentration ~10^{12} cm^{-3}.

The carrier gases, industrial dry grade H_2 and 99.995% He, were passed through a molecular sieve trap maintained at 77 K before entry into the reaction tube. With the exception of HCN and CF_3NO, which were prepared in the laboratory, and H_2O (distilled water) all reagent gases were obtained commercially. Hydrogen cyanide was prepared by the addition of sulphuric acid to potassium cyanide, the product dried over P_2O_5 and purified by repeated trap-to-trap distillation. Trifluoronitrosomethane was prepared by decarboxylation of nitrosyltrifluoroacetate (CF_3CO_2NO) at 200°C in a stream of dry nitrogen, (150 cm^3 min^{-1}) using the method of Taylor et al. [5]. The product was purified by repeated trap-to-trap distillation and stored in blackened pyrex bulbs. Experiments were then conducted using mixtures of CF_3NO in He.

The reproducibility of rate coefficients for repeated determinations is better than 10% and the overall accuracy is estimated to be ±30% [4,6].

RESULTS AND DISCUSSION

The reactions studied are summarized in Table 1, with the rate coefficients (each value being the mean of at least three determinations), the products with the percentage channel efficiency in parentheses, and the rate coefficients calculated from the simple polarization theory of Langevin [7], k_L, and the average-dipole-orientation model of Bowers et al. [8], k_{ADO}. The mean molecular polarizability of CF_3NO was calculated to be 44.7×10^{-25} cm^3 using the δ-function potential model of Lippincott and Stutman [9] and the dipole moment was estimated to be 1.6 D from the literature values [10,11] for CF_3NO_2, CH_3NO_2, CH_3NO and the value for the $-NO_2$ group contribution [12].

Generally, the overall reaction efficiency is low, all measured rate coefficients being less than the value of k_{ADO} and in most cases also less than k_L. With the exception of reaction 12, all reactions result in the dissociative ionization of CF_3NO to NO^+, and also to CF_3^+ in those cases where this channel

TABLE 1

Rate coefficients in units of 10^{-9} cm^3 molecule^{-1} s^{-1} and primary product distributions (% total products) for reactions $Y^+ + CF_3NO \rightarrow$ products at 300 K

Reaction number	Y^+	Products and (%) distribution	k_{exp}	k_L [a]	k_{ADO} [b]
1	H_3^+	NO^+ (~80), CF_3^+ (<5), CF_3NOH^+ (~15)	3.1	2.9	4.5
2	He^+	NO^+ (~55), CF_3^+ (~45)	2.1	2.5	3.9
3	CH_3^+	[c]	0.66	1.3	2.0
4	CH_5^+	NO^+ (~40), m/z 67 (~20) [c], CF_3NOH^+ (~40)	0.94	1.4	2.1
5	H_3O^+	NO^+ (~100) [c]	0.01	1.2	1.9
6	$C_2H_2^+$ [d]	NO^+ (~50), CF_3^+ (~25), m/z 95 (~25) [c]	0.52	1.1	1.7
7	$C_4H_3^+$		0.25	0.85	1.3
8	C^+ [c,g]	NO^+ (~70), CF_3^+ (~25), CF_3NO^+ (<5)	1.2	1.1	1.6
9	CO^+		2.1	1.5	2.3
10	H_2CN^+	No reaction observed	[f]	1.1	1.6
11	N_2H^+	NO^+ (~65), CF_3^+ (~1), CF_3NOH^+ (~35)	1.2	1.0	1.6
12	HCO^+	m/z 67 (~45) [c], CF_3NOH^+ (~55)	0.78	1.0	1.6
13	$C_2H_5^+$ [e]	NO^+ (~90), CF_3NOH^+ (~10)	0.10	1.0	1.6
14	$C_4H_9^+$	No reaction observed	[f]	0.50	0.77
15	HNO^+	NO^+ (~80), CF_3^+ (<5), CF_3NOH^+ (~15)	1.3	1.0	1.6
16	Ar^+	NO^+ (~60), CF_3^+ (~40)	0.79	0.93	1.4
17	$HCOF_2^+$	[c]	0.39	0.78	1.2

[a] Calculated from $k_L = 2\pi q(\alpha/\mu)^{1/2}$ as given in ref. 7.

[b] Calculated using average-dipole-orientation theory and the $\overline{\cos\theta}$ model (C = 0.185) as outlined in ref. 8.

[c] See text for details.

[d] $C_2H_2^+$ and $C_4H_3^+$ generated simultaneously from C_2H_2 in a He afterglow.

[e] $C_2H_5^+$ and $C_4H_9^+$ are both generated from C_2H_4 in a H_2 afterglow.

[f] No reaction detected, thereby placing an upper limit of ~10^{-14} cm^3 molecule^{-1} s^{-1} on the rate coefficient.

[g] C^+ and CO^+ generated simultaneously from CO in a He afterglow, thereby precluding the assignment of product distribution to either reactant ion.

is exothermic. Reactant ions having non-transferable protons undergo dissociative charge transfer to CF_3NO^+ and, with the exception of CH_3^+ (see below), reactant ions with transferable protons undergo proton transfer and/or dissociative proton transfer.

Charge transfer and dissociative charge transfer

These reactions are of the general type:

$$X^+ + CF_3NO \rightarrow X + CF_3NO^+ \begin{array}{l} \nearrow NO^+ + CF_3 \\ \searrow CF_3^+ + NO \end{array}$$

Reactions 2, 8, 9 and 16 (Table 1) fall into this category:

$$\mathrm{He^+ + CF_3NO \rightarrow NO^+(\sim 55\%),\ CF_3^+(\sim 45\%)} \qquad (2)$$

$$\left.\begin{matrix}\mathrm{C^+} \\ \mathrm{CO^+}\end{matrix}\right\} \mathrm{+ CF_3NO \rightarrow NO^+(\sim 70\%),\ CF_3^+(\sim 25\%),\ CF_3NO^+(<5\%)} \qquad \begin{matrix}(8)\\(9)\end{matrix}$$

$$\mathrm{Ar^+ + CF_3NO \rightarrow NO^+(\sim 60\%),\ CF_3^+(\sim 40\%)} \qquad (16)$$

The exothermicities for charge transfer in the above reactions are —1371, —348, —260 and —502 kJ mol^{-1} respectively. Only in the case of C^+, CO^+ was the charge transfer product CF_3NO^+ detected. The agreement between the measured rate coefficients and the values calculated from the simple polarization model, k_L, is reasonably good, which may suggest that a close-encounter mechanism is involved. This close-encounter mechanism is in contrast to the long range electron-jump mechanism which has been suggested to account for the dissociative charge transfer reactions of formic acid [13], which exhibit rate coefficients greatly exceeding the predictions of the ADO model.

Proton transfer and dissociative proton transfer

Since the C—N bond in CF_3NO is very weak, proton transfer may be expected to lead to dissociation of the protonated species for those cases where the exothermicity is large. Proton transfer was manifest by the formation of the dissociation products NO^+ or CF_3^+ with CF_3NOH^+ appearing, in most cases, as a minor reaction channel. Proton transfer may then be considered as the two step process:

$$\mathrm{XH^+ + CF_3NO \rightarrow X + (CF_3NOH^+)^*} \begin{array}{l} \nearrow \mathrm{NO^+ + CF_3H + X} \\ \rightarrow \mathrm{CF_3^+ + NOH + X} \\ \overset{}{\underset{\mathrm{M}}{\searrow}} \mathrm{CF_3NOH^+ + X} \end{array}$$

The formation of the fragmentation ion NO^+ is 221 kJ mol^{-1} more exothermic than the formation of CF_3^+. Except for CH_5^+, $C_2H_5^+$, H_2CN^+ and $C_4H_9^+$, all ions with transferable protons underwent dissociative proton transfer and/or proton transfer. These processes may only occur where the proton affinity (PA) of CF_3NO exceeds, or is very close to, that of the neutral species X. The ions of type XH^+ are listed in Table 2 in order of increasing proton affinity. It is evident that only those ions, XH^+, with $PA(X) \leqslant 708$ kJ mol^{-1} (H_2O) undergo a proton transfer reaction with CF_3NO, while for reactant ions with $PA(X) \geqslant 723$ kJ mol^{-1} (HCN) no reaction with CF_3NO is observed.

We therefore conclude that the proton affinity of CF_3NO lies in the range 708—723 kJ mol^{-1} i.e:

$$723 \text{ kJ mol}^{-1} > PA(CF_3NO) > 708 \text{ kJ mol}^{-1}$$

In addition, the observation of CF_3NOH^+ in these experiments means that it

TABLE 2

The occurrence or non-occurrence of proton transfer to CF_3NO by ions of the type XH^+, in order of ascending PA(X) ($kJ\ mol^{-1}$)

Reaction number	Reactant ion, XH^+	PA(X) [a] ($kJ\ mol^{-1}$)	Reaction
1	H_3^+	423	REACTION
11	N_2H^+	476	
15	HNO^+	481 [b]	
4	CH_5^+	536	
12	HCO^+	582	
13	$C_2H_5^+$	669 [b]	
5	H_3O^+	708	
10	H_2CN^+	723 [c]	NO REACTION
14	$C_4H_9^+$	747 [d]	

[a] Proton affinities without superscripts taken from ref. 15.

[b] Ref. 14.

[c] PA(HCN) = 723 $kJ\ mol^{-1}$, ref. 17.

[d] $C_4H_9^+$ is generated from C_2H_4 in an H_2 afterglow; $C_2H_5^+ + C_2H_4 \xrightarrow{H_2}$ sec-$C_4H_9^+$. Assuming the ion to be sec-$C_4H_9^+$ the PA is calculated from ref. 16.

must be stable to the autodissociation process:

$$CF_3NOH^+ \rightarrow NO^+ + CF_3H$$

which places an upper limit of 295 $kJ\ mol^{-1}$ for $\Delta H_f^\circ(CF_3NOH^+)$. Using the value $\Delta H_f^\circ(CF_3NO) \geqslant -510 \pm 10\ kJ\ mol^{-1}$ [2], we can estimate that $PA(CF_3NO) \approx 720\ kJ\ mol^{-1}$, which is consistent with our experimental observations which place an upper limit of 723 $kJ\ mol^{-1}$ on the proton affinity of CF_3NO.

Reaction of CH_3^+ with CF_3NO

The method used for the generation of CH_3^+ from CH_4 in an He afterglow also produces CH_2^+, CH_4^+ and $C_2H_5^+$ ions, thereby preventing an unambiguous assignment of products to the specific reactant ion CH_3^+. However, the main product observed in these experiments was NO^+. The low ionization potential (IP) of CH_3, 9.8 eV, renders charge transfer to CF_3NO, IP = 10.4 eV, endothermic and the high proton affinity of CH_2, ~825 $kJ\ mol^{-1}$, precludes proton transfer. The following reaction, 107 $kJ\ mol^{-1}$ exothermic, is proposed to account for the observed rate coefficient

$$CH_3^+ + CF_3NO \rightarrow CH_3F + CF_2 + NO^+$$

Reactions of $C_2H_2^+$ with CF_3NO

We cannot differentiate between charge transfer and dissociative proton transfer for this ion since both channels are exothermic $IP(C_2H_2) -$

IP(CF_3NO) = 1.0 eV and PA(C_2H) = 677 kJ mol^{-1}. The product ion at m/z 95 may tentatively be assigned the structure $CF_3C_2H_2^+$ and attributed to the displacement reaction:

$C_2H_2^+ + CF_3NO \rightarrow CF_3C_2H_2^+ (m/z\ 95) + NO$

Reactions of HCO⁺ and CH₅⁺ with CF₃NO

Both of these reactants resulted in a primary product ion at m/z 67, which underwent secondary reaction with CF_3NO. We identify this product ion as $HCOF_2^+$ from a consideration of the reactants available. This behaviour is shown in Fig. 1 for the reaction of HCO^+, where NO^+ was formed, not as a primary product, but solely as a result of the reaction of $HCOF_2^+$ with CF_3NO. In the case of CH_5^+, NO^+ was produced both as a primary product and as a secondary product from the decay of $HCOF_2^+$. The rate of removal of $HCOF_2^+$ was determined for these two cases to be 4.0×10^{-10} and 3.7×10^{-10} cm^3 molecule^{-1} s^{-1} respectively and a mean value of 3.9×10^{-10} cm^3 molecule^{-1} s^{-1} is included as reaction 17 in Table 1.

$HCOF_2^+ + CF_3NO \rightarrow NO^+$ + neutral products (17)

Reactions of C⁺ with CF₃NO

The reactant ions C^+ and CO^+ were generated simultaneously from CO in an He afterglow. The ratio of C^+ to CO^+ could be controlled to some extent by variation of the ionizing electron energy, although neither ion could be

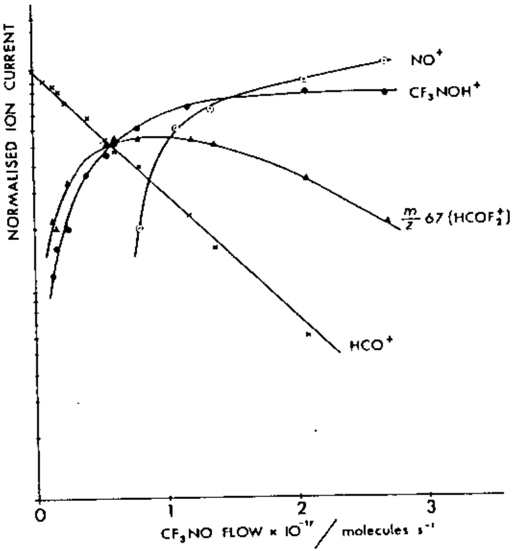

Fig. 1. Experimental data for the reaction of HCO^+ with CF_3NO. The slope of the linear semilogarithmic HCO^+ signal gave $k_{12} = 7.8 \times 10^{-10}$ cm^3 molecule^{-1} s^{-1}.

produced exclusively over the electron energy range at our disposal (10—100 eV). The reactions of CO^+ were conducted using an electron energy of 30 eV, for which the ratio $C^+/CO^+ \sim 10^{-2}$. The products observed under these conditions are those given in Table 1. Operation of the electron gun at 100 eV results in the ratio $C^+/CO^+ \sim 0.15$ and the rate of removal for C^+ was determined under these conditions. The same products were observed under both conditions, although an extra minor product (<10%) at *m/z* 66 appeared when operating with the ion ratio used in the C^+ studies. We attribute this product to a reaction between C^+ and CF_3NO.

$$C^+ + CF_3NO \rightarrow COF_2^+ (m/z\ 66) + FCN$$

The above process is ~520 kJ mol^{-1} exothermic if the following thermodynamic data are assumed:

$\Delta H_f^\circ(COF_2) = -531$ kJ mol^{-1} [18], $IP(COF_2) = 13.2$ eV [16] and

$\Delta H_f^\circ(FCN) = 23.4$ kJ mol^{-1} [16] .

ACKNOWLEDGEMENT

This work was supported by the New Zealand Universities Grants Committee.

REFERENCES

1 P.J. Carmichael, B.G. Gowenlock and C.A.F. Johnson, J. Chem. Soc., Perkin Trans. 2, (1973) 1853.
2 P.W. Harland, Int. J. Mass Spectrom. Ion Phys., 25 (1977) 61.
3 M.I. Davis, J.E. Boggs, D. Coffey and H.P. Hanson, J. Phys. Chem., 69 (1965) 3727.
4 J.P. Liddy, C.G. Freeman and M.J. McEwan, Int. J. Mass Spectrom. Ion Phys., 23 (1977) 153.
5 C.W. Taylor, T.J. Brice and R.L. Wear, J. Org. Chem., 27 (1962) 1064.
6 A.E. Roche, M.M. Sutton, D.K. Bohme and H.I. Schiff, J. Chem. Phys., 55 (1971) 5480.
7 G. Gioumousis and D.P. Stevenson, J. Chem. Phys., 29 (1958) 294.
8 L. Bass, T.Su, W.J. Chesnavich and M.T. Bowers, Chem. Phys. Lett., 34 (1975) 119.
9 E.R. Lippincott and J.M. Stutman, J. Phys. Chem., 68 (1964) 2926.
10 A.L. McClellan, Tables of Experimental Dipole Moments, W.H. Freeman, San Francisco, 1963.
11 Handbook of Chemistry and Physics, R.C. Weast (Ed.), 56th edn., CRC Press, Cleveland, Ohio, 1975—1976.
12 P. Debye, The Dipole Moment and Chemical Structure, Blackie, Glasgow, 1931, Chap. 4.
13 C.G. Freeman, P.W. Harland and M.J. McEwan, Aust. J. Chem., 31 (1978) 2593.
14 W.T. Huntress, Astrophys. J., Suppl. Ser., 33 (1977) 495.
15 P. Kebarle, Ann. Rev. Phys. Chem., 28 (1977) 445.
16 H.M. Rosenstock, K. Draxl, B.W. Steiner and J.T. Herron, J. Phys. Chem. Ref. Data, 6 (1977).
17 C.G. Freeman, P.W. Harland and M.J. McEwan, Int. J. Mass Spectrom. Ion Phys., 27 (1978) 77.
18 JANAF Thermochemical Tables, Dow Chemical Co., Midland, Mich., 1971.

Volume 64, number 3 CHEMICAL PHYSICS LETTERS 15 July 1979

THERMAL ENERGY CHARGE TRANSFER REACTIONS OF ACETONE AND BIACETYL

Colin G. FREEMAN, Peter W. HARLAND and Murray J. McEWAN *
Department of Chemistry, University of Canterbury, Christchurch, New Zealand

Received 26 October 1978; in final form 3 May 1979

Rate coefficients up to a factor of 2.5 times larger than the capture collision rate are reported for a series of thermal energy, positive ion–molecule reactions of acetone and biacetyl. These rapid rates are interpreted in terms of a dissociative charge transfer process in which an electron is transferred in a non-spiralling collision from outside the classical capture limit. The factors which lead to this type of mechanism are discussed briefly.

1. Introduction

The mechanism of thermal energy charge transfer between positive ions and large polyatomic molecules is not well understood. Various approaches have been developed to describe these interactions but as yet, no theory satisfactorily accounts for all charge transfer reactions of ions with polyatomic molecules. Ion–molecule collisions are usually classified according to their reaction mechanism as either a persistent complex mechanism or a direct mechanism. In the persistent complex case, the complex survives for more than a rotational period. In a direct mechanism the collision between the particles is sudden: i.e., the collision time is shorter than a rotational period. At energies greater than thermal, beam studies have provided evidence that a mechanism can change from a complex formation to an impulse interaction as the energy increases [1]. In some examples such as the reaction between Ar^+ and D_2, the direct mechanism has been found to operate at energies as low as 0.05 eV [2]. It has also been pointed out that at very low energies, the long-range ion–induced dipole forces accelerate the reactants together so that even at zero initial velocity the actual energy of impact is a few tenths of an eV [2]. In beam studies with more complex ions and molecules, however, persistent complex formation has been observed up to several eV [3].

At *thermal energies*, most of the information on charge transfer processes has been derived from mass spectrometric investigations of the rate coefficients which unfortunately reveal few details of the reaction dynamics. At best, a large divergence between a measured rate coefficient and a predicted value based on a particular model may indicate the non-validity of the model. Measured rate coefficients of the many hundreds of thermal energy ion–molecule reactions reported have usually been compared with the capture rates of the classical models [4,5]. These models are based upon a potential function that varies as the inverse fourth power of the separation. For molecules possessing a permanent dipole moment, a correction factor has been added to the potential function to include the long range interaction between the ionic charge and the permanent dipole [5]. The rate coefficient of these models is thus an encounter rate and provides an upper limit for the rate coefficient. Although they are plausible but not rigorous models, predictions based on them have nevertheless shown reasonable agreement with many measurements on different systems. Because of the success of these classical theories for reactions at thermal energies, it is customary to talk in terms of a model in which the interaction time is sufficiently long for spiralling collisions [6] (sometimes called "orbiting") to occur with the formation of complexes that survive long enough to undergo several rotational or vibrational periods.

---

* Presently on leave as a National Research Council Research Associate at the Jet Propulsion Laboratory, California Institute of Technology, Pasadena, California 91103, USA.

In the special case of *charge transfer* reactions for which Langevin rate coefficients cannot be used as an upper bound, the model is modified to include two alternative mechanisms: (i) a spiralling collision of the type considered in the classical theories [4,5] (alternatively, a small impact parameter collision); or (ii) an electron transfer from a non-spiralling collision where the electron transfer may originate at a distance outside the classical orbiting collision limit (alternatively, a large impact parameter collision) [7,8]. Evidence for the second mechanism has been provided from observations of resonance effects and from rate coefficients that are larger than the classical models predict. It has been suggested that the important factors contributing to the second mechanism for the charge transfer process

$$A^+ + B \rightarrow B^+ + A \qquad (1)$$

are (i) that energy resonance should exist between $A^+ + B$ and $B^+ + A$ at the recombination energy of A^+, and (ii) that the transition between B and B^{+*} should have a favourable Franck–Condon factor [8,9]. The Franck–Condon restriction has been shown to be unimportant in several reactions of triatomic molecules [10]. In large polyatomic molecules, the high density of states ensures that the energy resonance requirements are readily met. There are usually a great number of available energy states linked to the ground state of B by favourable Franck–Condon factors and thus both requirements for long distance electron transfer should usually be satisfied. It therefore appears that the main evidence for a non-spiralling or large impact parameter collision is whether the observed rate coefficient for charge transfer is larger than the collision rate of the classical theories. A further complication can arise when charge transfer is only one of several available reaction pathways. The observed large rate coefficient may then be mainly due to the competing processes rather than charge transfer and this criticism has been levelled at some studies reporting apparent charge transfer rate coefficients that are larger than the classical collision rates [11]. Some controversy still surrounds the proposed electron jump mechanism at thermal energies. Ausloos et al. [11] in a study of thermal energy charge transfer reactions concluded "there was no firm evidence in the literature for the occurrence of asymmetric charge transfer reactions of thermal ions at rates higher than the capture collision rate".

In a study of rearrangement reactions of formic acid of the type

$$Y^+ + HCOOH \rightarrow HCO^+ + OH + Y\,, \qquad (2)$$

we observed several reactions that had rate coefficients between two and three times greater than the collision rate based on the ADO model [12]. These rapid reactions all produced HCO^+ as the major product ion and were interpreted as dissociative charge transfer reactions in which the electron was transferred in a non-spiralling collision. We noted that all reactions of positive ions with formic acid having rates significantly greater than collision theory were exothermic to dissociative charge transfer. All other reactions had rate coefficients in accord with classical collision models. In the formic acid study we also pointed out that a similar type of non-orbiting long distance transfer could occur in reactions of C^+ with acetone and biacetyl. Smith and Futrell [13] had earlier reported that the ion CH_3CO^+, which is a dissociative charge transfer product ion, was the major product ion of the C^+–acetone or biacetyl reaction. Although Smith and Futrell measured branching ratios, they did not undertake rate coefficient measurements. In this study we report measurements of the rate coefficients for reactions of several atomic, diatomic and tetratomic positive ions with acetone and biacetyl.

2. Experimental

The experiments were carried out with a flowing afterglow system in the usual manner [14]. Positive ions were generated by adding an appropriate reactant gas to a helium plasma in which He^+ ions and He $2\,^3S$ metastable atoms were present. In this way the ions C^+, CO^+, CN^+, $C_2N_2^+$, O^+, N^+ and N_2^+ were generated by the addition of CO, C_2N_2, O_2 or N_2 to the reaction tube downstream from the electron gun. Further downstream, mixtures of either acetone, CH_3COCH_3, or biacetyl $CH_3COCOCH_3$, in helium were added to the reaction tube. Rate coefficients were determined in the usual way from the logarithmic decay of the ion signal with increasing acetone or biacetyl flow. The relative ion concentration was monitored by a quadrupole mass spectrometer which continuously sampled a small portion of the reactant gases from the downstream end of the reaction tube.

3. Results and discussion

Rate coefficients measured at thermal energies (298 K) for reactions (3) and (4) are summarized in table 1 for acetone and table 2 for biacetyl:

$$Y^+ + CH_3COCH_3 \begin{array}{ll} \nearrow CH_3COCH_3^+ + Y & (3a) \\ \searrow CH_3CO^+ + CH_3 + Y & (3b) \end{array}$$

$$Y^+ + CH_3COCOCH_3 \begin{array}{ll} \nearrow CH_3COCOCH_3^+ + Y & (4a) \\ \searrow CH_3CO^+ + CH_3CO + Y & (4b) \end{array}$$

$(Y^+ = C^+, N^+, O^+, CN^+, N_2^+, CO^+, C_2N_2^+)$.

The calculated orbiting collision rates are listed in tables 1 and 2 for comparison. As biacetyl has no permanent dipole moment the Langevin–Gioumousis–Stevenson equation has been used to estimate the capture rates in table 2. The effect of including the quadrupole moment of biacetyl will increase this capture rate coefficient by no more than 20% [16]. The molecular polarizability of acetone is 63.3×10^{-25} cm^3 [17] and of biacetyl is 81.5×10^{-25} cm^3 (calculated using the method of additivity of bond polarizabilities [18]). Estimates of the enthalpy changes for dissociative charge transfer (reactions (3b) and (4b)) have also been included and these are exothermic in all cases. The corresponding charge transfer reactions ((3a) and (4a)) are more exothermic than dissociative charge transfer.

We were not able to determine relative efficiencies of possible product channels with any accuracy because of two difficulties that are inherent to the flowing afterglow technique. It was not possible to generate a clean source of reactant ions free from the presence of other ions of different mass. Also, primary product ions of the reaction under study spend sufficient time in the reaction region to react further with the neutral reactant. Nevertheless, we did establish that the primary product ion of reaction (9) in table 1 and of reactions (16) and (17) in table 2 was CH_3CO^+. In all reactions studied the most important reaction channel appeared to produce CH_3CO^+ (dissociative charge transfer). Smith and Futrell [13] using a tandem Dempster–ICR mass spectrometer found reaction (5) yielded almost equal ion signals corresponding to CH_3CO^+ and $CH_3COCH_3^+$ with only small contributions from ions at m/e = 44$(C_3H_8^+)$ or m/e = 27$(C_2H_3^+)$. For reaction (12) they observed CH_3CO^+ as the major product in agreement with our results.

It is apparent from tables 1 and 2 that several reactions occur with rate coefficients substantially greater than the estimates based on the classical model of collision rates in which spiralling collisions are assumed. We have now reported a number of such reactions of atomic and diatomic ions with HCOOH [12], HC_3N [19], acetone and biacetyl (this work) which all have rate coefficients much larger than the collision capture rates. These observations therefore provide evidence

Table 1
Rate coefficients in units of 10^{-9} cm^3 molecule^{-1} s^{-1} at 298 K for reaction $Y^+ + CH_3COCH_3 \rightarrow$ products

Reaction number	Y^+	Major ion products	k_{obs}	k_{ADO} a)	$\frac{k_{obs}}{k_{ADO}}$	$-\Delta H^0$ b) (kJ mol^{-1})
(5)	C^+	$CH_3COCH_3^+, CH_3CO^+$ c)	8.3	3.7	2.2	89
(6)	N^+	$CH_3CO^+, CH_3COCH_3^+$ d)	7.6	3.5	2.2	409
(7)	O^+	$CH_3CO^+, CH_3COCH_3^+$ d)	7.1	3.3	2.2	374
(8)	CN^+	$CH_3CO^+, CH_3COCH_3^+$ d)	2.5	2.8	0.9	368
(9)	CO^+	CH_3CO^+ e)	2.9	2.7	1.1	357
(10)	N_2^+	$CH_3CO^+, CH_3COCH_3^+$ d)	3.1	2.7	1.2	512
(11)	$C_2N_2^+$	$CH_3CO^+, CH_3COCH_3^+$ d)	2.6	2.2	1.2	298

a) Calculated using average-dipole-orientation theory and the cos θ model (c = 0.22) as outlined in ref. [5].
b) ΔH^0 values are taken from ref. [11] and refer to the dissociative charge transfer reaction $Y^+ + CH_3COCH_3 \rightarrow CH_3CO^+ + CH_3 + Y$. Charge transfer is more exothermic by ≈ 55 kJ mol^{-1}.
c) Main products are $CH_3COCH_3^+$ ≈ 50% and CH_3CO^+ ≈ 50%.
d) Both ions, CH_3CO^+ and $CH_3COCH_3^+$ were observed but channel efficiencies could not be determined – see text.
e) The main product was found to be CH_3CO^+ > 90%.

Table 2
Rate coefficients in units of 10^{-9} cm^3 molecule^{-1} s^{-1} at 298 K for reaction $Y^+ + CH_3COCOCH_3 \rightarrow$ products

Reaction number	Y^+	Major ion products	k_{obs}	k_{LGS} a)	$\frac{k_{obs}}{k_{LGS}}$	$-\Delta H^0$ b) (kJ mol^{-1})
(12)	C^+	CH_3CO^+, $CH_3COCOCH_3^+$ c)	5.2	2.1	2.5	799
(13)	N^+	CH_3CO^+, $CH_3COCOCH_3^+$ d)	3.3	1.9	1.7	1118
(14)	O^+	CH_3CO^+, $CH_3COCOCH_3^+$ d)	4.7	1.8	2.6	1029
(15)	CN^+	CH_3CO^+, $CH_3COCOCH_3^+$ d)	4.1	1.5	2.7	1078
(16)	CO^+	CH_3CO^+ e)	2.9	1.4	2.1	1067
(17)	N_2^+	CH_3CO^+ e)	2.4	1.4	1.7	1221
(18)	$C_2N_2^+$	CH_3CO^+, $CH_3COCOCH_3^+$ d)	2.5	1.2	2.1	1008

a) Calculated using the Langevin–Gioumousis–Stevenson equation in ref. [4].

b) ΔH^0 values are taken from ref. [15] and refer to the dissociative charge transfer reaction $Y^+ + CH_3COCOCH_3 \rightarrow CH_3CO^+ + CH_3CO + Y$. Charge transfer is more exothermic by ≈ 45 kJ mol^{-1}.

c) Product ratios are $CH_3CO^+ > 90\%$, $CH_3COCOCH_3^+ \approx 5\%$.

d) Main products are CH_3CO^+ and $CH_3COCOCH_3^+$ but relative channel efficiencies could not be determined – see text.

e) The main product ion observed $CH_3CO^+ > 90\%$.

that asymmetric charge transfer reactions at thermal energies can occur via large impact parameter collisions if it is assumed the observed product ions are produced by a dissociative charge transfer mechanism.

In most cases the deviations between the observed rate coefficients and the calculated capture rate coefficient are largest for atomic and diatomic ions possibly because the higher charge density on these ions encourages electron transfer from greater distances. All the reactions in this study are sufficiently exothermic to disguise any trends in rate coefficient or product distribution as a function of reaction exothermicity. We might also expect a series of ions having increasing degrees of freedom but similar exothermicities would show an increasing tendency to non-dissociative charge transfer due to the energy partitioning amongst the internal modes of the products. In this way energy partitioning can lower the pool of energy left on the product ion as a result of the encounter, thereby diminishing the possibility of a dissociative charge transfer process.

The energy resonance requirement and, if necessary, the Franck–Condon requirement appear to be met in most reactions of ions with large polyatomic molecules. It therefore appears that one of the most important features in controlling the rate of electron transfer is the charge density on the reactant ion. This work indicates that a rapid process occurs when the charge density is high (i.e. atomic and diatomic ions) but that the rate falls off as the size of the ion increases. Support for this suggestion is also provided by the study of Lias et al. [20] which reports low reaction rates for positive ion charge transfer reactions of C_3–C_9 alkanes and cycloalkanes.

Acknowledgement

The authors gratefully acknowledge helpful discussions with V.G. Anicich and J.B. Laudenslager.

References

[1] W.S. Koski, Advan. Chem. Phys. 30 (1975) 185.
[2] Z. Herman, J. Kersetter, T.L. Rose and R. Wolfgang, Discussions Faraday Soc. 44 (1966) 123.
[3] Z. Herman and K. Birkinshaw, Ber. Bunsenges. Physik. Chem. 75 (1971) 413.
[4] G. Gioumousis and D.P. Stevenson, J. Chem. Phys. 29 (1958) 294.
[5] L. Bass, T. Su, W.J. Chesnavich and M.T. Bowers, Chem. Phys. Letters 34 (1975) 119.
[6] J.V. Dugan and J.L. Magee, Advan. Chem. Phys. 22 (1971) 209.
[7] M.T. Bowers and D.D. Elleman, Chem. Phys. Letters 16 (1972) 486.
[8] J. Gauglhofer and L. Kevan, Chem. Phys. Letters 16 (1972) 492.

[9] J.B. Laudenslager, W.T. Huntress and M.T. Bowers, J. Chem. Phys. 61 (1974) 4600.

[10] P.W. Harland and K.R. Ryan, Intern. J. Mass Spectrom. Ion Phys. 18 (1975) 215.

[11] P. Ausloos, J.R. Eyler and S.G. Lias, Chem. Phys. Letters 30 (1975) 21.

[12] C.G. Freeman, P.W. Harland and M.J. McEwan, Australian J. Chem. 31 (1978) 2593.

[13] R.D. Smith and J.H. Futrell, Intern. J. Mass Spectrom. Ion Phys. 26 (1978) 111.

[14] J.P. Liddy, C.G. Freeman and M.J. McEwan, Intern. J. Mass Spectrom. Ion Phys. 23 (1977) 153.

[15] H.M. Rosenstock, K. Draxl, B.W. Steiner and J.T. Herron, J. Phys. Chem. Ref. Data 6 (1977) Suppl. No. 1, p. 1.

[16] T. Su and M.T. Bowers, Intern. J. Mass Spectrom. Ion Phys. 17 (1975) 309.

[17] Landolt-Börnstein, Zahlenwerte und Functionen, Vol. 1, Part 3 (Springer, Berlin, 1951) p. 510.

[18] J.O. Hirschfelder, C.F. Curtiss and R.B. Bird, Molecular theory of gases and liquids (Wiley, New York, 1954).

[19] C.G. Freeman, P.W. Harland and M.J. McEwan, Monthly Notices Roy. Astron. Soc. (1978), to be published.

[20] S.G. Lias, P. Ausloos and Z. Horvath, Intern. J. Chem. Kinetics 8 (1976) 725.

International Journal of Mass Spectrometry and Ion Processes, 54 (1983) 217–223 217
Elsevier Science Publishers B.V., Amsterdam – Printed in The Netherlands

Short Communication

SOFTWARE-CONTROLLED MULTIPLE PULSE GENERATOR AND ITS APPLICATION TO A DRIFT TUBE GATING SYSTEM

P.W. HARLAND and B.J. McINTOSH
Chemistry Department, University of Canterbury, Christchurch (New Zealand)

(Received 9 March 1983)

Figure 1 shows a block diagram of the control system described in this communication. It was designed to satisfy the requirements of a versatile drift-tube mass spectrometer instrument [1] constructed for the measurement of ion transport parameters and ion–molecule studies. The resultant low cost (~ $1500) microprocessor-based system may be readily adapted to any experiment which requires pulsed-mode operation, mass spectrometer control and data collection facilities. The novel feature of the unit lies in the machine-language controlled use of the 8-bit 6502 CPU-based microcom-

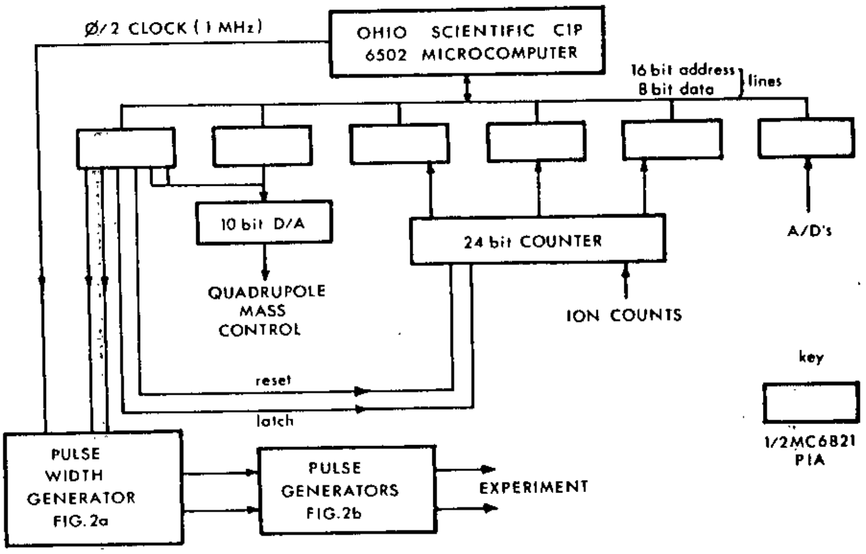

Fig. 1. Schematic diagram of microcomputer-controlled pulse generator, mass programmer and ion counter.

0168-1176/83/$03.00 © 1983 Elsevier Science Publishers B.V.

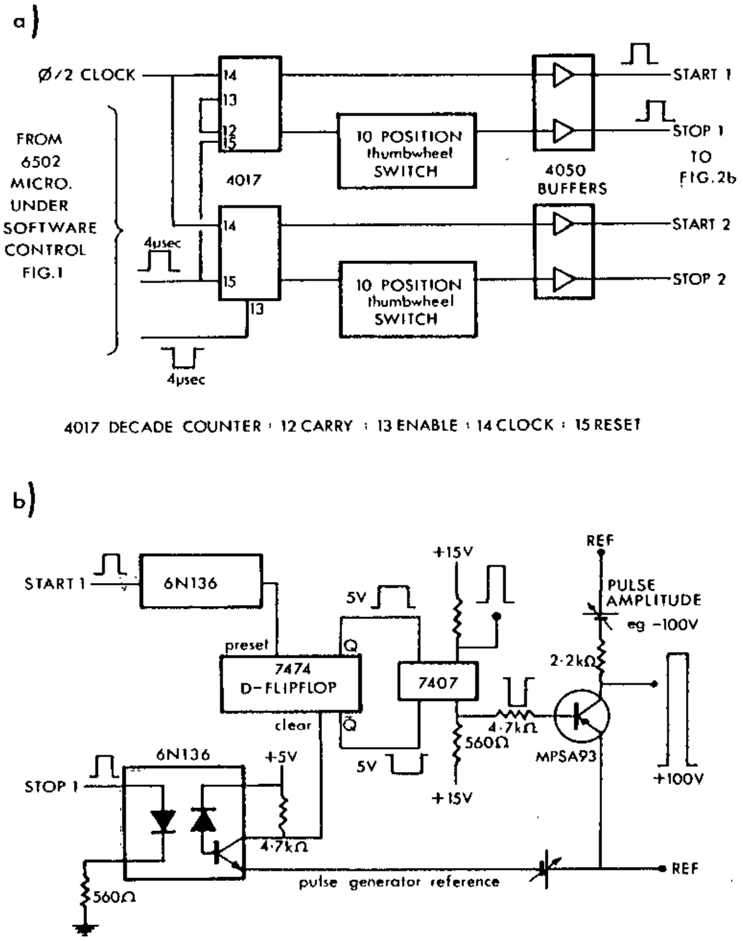

Fig. 2. (a) Pulse width selector circuit; (b) pulse generator and amplifier circuit. To increase clarity in the diagrams the following omissions were made: in Fig. 2a (count 1) pin 2 of the 4017 decade counter provides the start pulse to the 4050 buffers and the remaining 8 counts plus carry provide the stop via the 10-position switch; in Fig. 2b the pulse amplitude and pulse generator references are both at the common reference (to ground) shown as REF in the figure and both resistors in the + 15 V lines are 560 Ω (one only labeled). Note that the tops of positive-going pulses correspond in potential to the base of negative-going pulses. (7407: Hex buffers/drivers with open collector high-voltage outputs.)

puter* with circuits designed to generate independently-floatable bipolar square-wave pulses of variable width and amplitude. The pulse widths for

---

* Ohio Scientific Superboard II supporting 32K RAM and one disc drive with OS-65D V3.2 DOS. The program requirement of this communication is 4K RAM only (excluding the 16K utilized for the DOS and that used for large data arrays).

this system (Figs. 1 and 2) are variable from 1 μs to 9 μs in 1 μs steps and the delay between pulses may be incremented in 1 μs steps to 10 ms. The minimum delay is 6 μs imposed by the time required for the 6502 microprocessor to execute the assembly language instructions used to set up the

```
 10         *= $6000
 20         P2B=$E30A      ;6821 PIA  Bit7=1st pulse
 30         CR= $E30B      ;          Bit6=2nd pulse
 40         V = $48        ;No. of cycles (16 bit)
 50 INIT    LDA #0         ;Initialize cycle count
 60         STA V
 70         STA V+1
 80         LDA #%01010000    ;Reset ion count(bit4 HI)
 90         STA P2B
100         LDA #%01000000    ;Both pulses inactive
110         STA P2B
120         LDX #%11000000    ;1st pulse active (HI)
130         LDY #%00000000    ;2nd pulse active (LO)
140 PULSE   STX P2B       ;RESET system & start 1st 4017
150         STA P2B
160         NOP           ;PHA for ODD times
170          ;
180          ;
190         NOP
200         STY P2B       ;Enable 2nd 4017 for 10us
210         NOP           ;This section of code moved
220         NOP           ;by BASIC calling program
230         NOP
240         STA P2B
250         NOP
260          ;
270          ;
280         NOP
290         JMP DLYEND      ;Maximum time (POKEd in from
300         NOP             ;                  BASIC program)
310          ;
320          ;
330         NOP
340 DLYEND  PHA           ;NOP for ODD times
350         PLA
360         CLC
370         LDA V
380         ADC #1        ;Increment no. of cycles
390         STA V
400         LDA V+1
410         ADC #0
420         STA V+1
430         CMP #$FF     ;Data POKEd here from BASIC
440         BEQ NEXT
450         LDA #%01000000   ;Both OFF state
460         JMP PULSE
470 NEXT    LDA #%01100000   ;Latch ion count (bit5 HI)
480         STA P2B
490         LDA #$90
500         STA P2B
510         RTS
```

Fig. 3. 6502 assembly language control program.

second pulse and to make provision for 1 μs delay intervals (lines 160 and 200 in Fig. 3). The ultimate constraint on the speed (frequency) of the system is the 1 MHz clock in the microcomputer and the use of 1 MHz peripheral interface adaptors (PIA) in the interface unit. However, a 2 MHz clock and 2 MHz PIA permit 0.5 μs pulse widths and 0.5 μs delays and so on. The gating requirements of the drift tube were met with undistorted bipolar pulses of amplitude in the range 15–200 V. The circuits shown above provide for variable pulse amplitudes over this range and could be readily adjusted in either direction with the appropriate floatable power supplies.

The microcomputer was also used to control the mass setting of the quadrupole mass filter via a 10-bit D/A channel and to store ion pulses accumulated by a 24-bit (3 × 8-bit) counter in the interface unit (Figs. 1 and 2). Opto-coupled A/D and D/A channels were also used to generate voltages and read instruments such as an MKS Baratron pressure transducer.

PROGRAM AND CIRCUIT DESCRIPTION

The digital circuitry is shown in Figs. 2a and 2b. Pulses generated by the microcomputer under software control (Fig. 3) enter the two-channel pulse width generator (Fig. 2a) where the output of 4017 decade counters selected by 10-position thumbwheel switches provides for output pulse widths over the range 1–9 μs in 1 μs steps. This is achieved through the generation of start (clock) and stop (delayed) pulses for each channel. Each start pulse serves as a trigger for a 7474 d-flipflop in the pulse generator–amplifier circuit, shown in Fig. 2b, to generate the leading edge of the final output pulse. The stop pulse similarly acts as an edge-trigger to define the trailing edge for the final output pulse of the preselected width. Figure 2b illustrates only one of the two opto-coupled pulse generator–amplifier circuits required for the two-channel system used in these experiments. The 5 V pulses from the 7474 are buffered to 15 V (or less if required) and further amplified using a switching transistor and a floating power supply referenced by the pulse generator bias, as shown in Fig. 2b.

When loaded from disk, the object code shown in Fig. 3 contains 200 NOP instructions between lines 160 and 330. The first pulse is initiated by instruction 140 and the code for the second pulse, lines 200–240, is inserted by the BASIC calling program to coincide with the chosen minimum time. Similarly, parameters input to the BASIC program are used by the JMP instruction in line 290 for the maximum time and by the CMP instruction in line 430 for the number of sweeps. After pulse output, lines 200–240 are moved along by the BASIC program and an NOP inserted. An NOP instruction requires 2 clock cycles (2 μs for a 1 MHz clock) giving rise to 2 μs delay increments between pulses. For 1 μs steps (odd times) the first NOP in line 160 is replaced by a PHA instruction which requires 3 clock cycles (3 μs) and the PHA at line 340 is replaced by an NOP. These are then alternated to give 1 μs steps.

The ion pulse counter is reset when the routine is entered (line 80) and the data latched through to the PIA in line 470 before returning to BASIC in line 510.

EXPERIMENTAL RESULTS

The system described above permits the automated collection of ion arrival time distributions in the drift tube instrument [1]. A 2 μs pulse of electrons is generated in a moveable ion source within the drift region by application of a typically 150 V positive-going pulse of 2 μs duration to a control grid normally biased negative with respect to the cathode. Ions generated by the electron pulse drift out of the ion source and into the drift tube under the influence of a uniform electric field. A fine-mesh grid, biased 2 V positive or negative, depending on the ion polarity, located in the exit aperture of the drift tube inhibits passage of arriving ions to the mass spectrometer until overridden by a 15 V pulse of 1 or 2 μs duration and the appropriate polarity (negative for positive ions). The delay between these two gating pulses is incremented in 1 μs steps under software control as described above. The BASIC part of the program provides for selection of ion counting time at each delay interval after which the counter is latched and the data transferred to the appropriate element of a one-dimensional array set up by the BASIC program. The repetition frequency is set at a convenient time after the last delay selected in response to the initial setup of program parameters. In this way multiple scans are readily accommodated with a corresponding accumulation of ion counts for each time increment, in the same way that a multichannel analyzer operates. Calculations may be performed on the accumulated data as shown in Fig. 4, which is a printout of experimental ion counts and smoothed ion counts using a fifth-degree seven-point smoothing routine [2]. The left-hand column labeled "Time" is the delay in μs between the two pulses generated by the system. Figure 4 shows data taken for the He^+ ion drifting through pure He for an uncorrected geometric distance [3] of 5.87 cm under the conditions indicated in the printout. The data shown are the accumulated ion counts from 3 scans at 10 counts per delay increment per scan. The arrival time distributions collected over the drift range 1–10 cm are used to calculate the drift velocity, v_d, and the reduced mobility K_0.

The drift tube constructed is being used to determine ion transport parameters for primary and secondary ions and where comparisons with

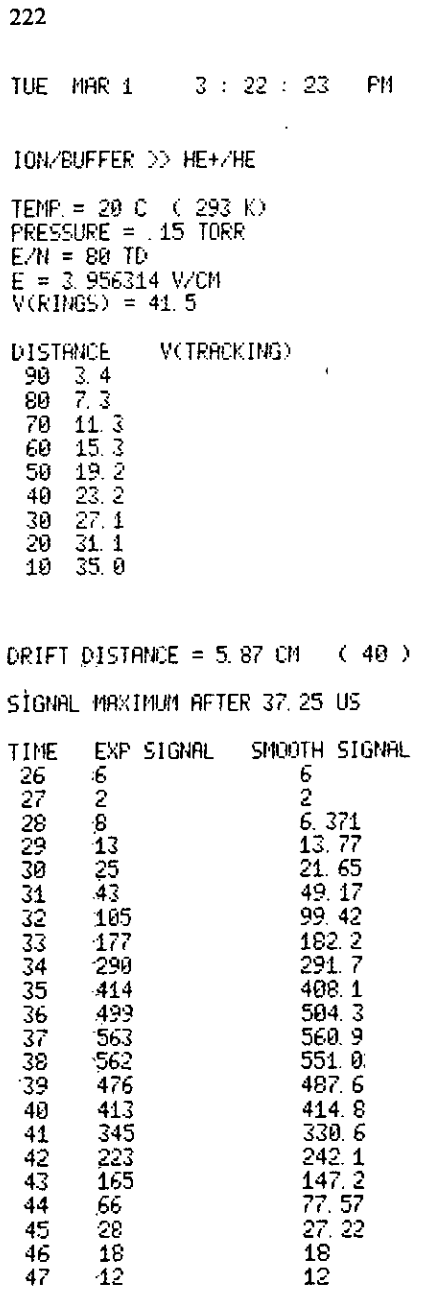

```
222

TUE  MAR 1      3 : 22 : 23   PM

ION/BUFFER >> HE+/HE

TEMP. = 20 C  ( 293 K)
PRESSURE = .15 TORR
E/N = 80 TD
E = 3. 956314 V/CM
V(RINGS) = 41. 5

DISTANCE     V(TRACKING)
 90  3. 4
 80  7. 3
 70  11. 3
 60  15. 3
 50  19. 2
 40  23. 2
 30  27. 1
 20  31. 1
 10  35. 0


DRIFT DISTANCE = 5. 87 CM   ( 40 )

SIGNAL MAXIMUM AFTER 37. 25 US

TIME   EXP SIGNAL   SMOOTH SIGNAL
 26    6             6
 27    2             2
 28    8             6. 371
 29    13            13. 77
 30    25            21. 65
 31    43            49. 17
 32    105           99. 42
 33    177           182. 2
 34    290           291. 7
 35    414           408. 1
 36    499           504. 3
 37    563           560. 9
 38    562           551. 0
 39    476           487. 6
 40    413           414. 8
 41    345           330. 6
 42    223           242. 1
 43    165           147. 2
 44    66            77. 57
 45    28            27. 22
 46    18            18
 47    12            12
```

Fig. 4. Direct printout for the arrival time of He^+ ions drifting through pure He gas for $E/N = 80$ Td, $P = 0.15$ Torr, $T = 293$ K and uncorrected drift distance 5.87 cm. V(rings) and V(tracking) are the voltages supplied to the drift tube ring stack and moveable ion source, respectively, to maintain the preselected value for E/N.

literature values are possible, agreement is usually within 2–3% [1]. The data above, taken with that recorded over the full drift range available in the instrument, yields $K_0 = 8.02 \pm 0.30$ cm^2 V^{-1} s^{-1} at 80 Td. The value given in the compilation of gas-phase ion transport properties [4] is 8.12 ± 0.24 cm^2 V^{-1} s^{-1}.

Copies of the BASIC program and further details on the circuits may be obtained from the authors on request.

REFERENCES

1 P.W. Harland and B.J. McIntosh, Int. J. Mass Spectrom. Ion Phys., submitted.

2 L.G. Kelly, Handbook of Numerical Methods and Applications, Addison–Wesley Pub. Co., 1967, p. 84.

3 E.W. McDaniel, J. Chem. Phys., 52 (1970) 3931.

4 H.W. Ellis, R.Y. Pai, E.W. McDaniel, E.A. Mason and L.A. Viehland, Atomic Data and Nuclear Data Tables, 17 (1976) 177–210; 22 (1978) 179–217.

International Journal of Mass Spectrometry and Ion Processes, 57 (1984) 283–297 283
Elsevier Science Publishers B.V., Amsterdam – Printed in The Netherlands

MOBILITIES OF $HCN^{+\cdot}$, H_2CN^+, C_2N^+, $C_2N_2^{+\cdot}$ AND $C_2H_3N^{+\cdot}$ IN HELIUM AT 293 K

P.W. HARLAND and B.J. McINTOSH
Chemistry Department, University of Canterbury, Christchurch (New Zealand)

(Received 7 November 1983)

ABSTRACT

A drift tube incorporating a movable ion source for the measurement of ion transport properties and the study of ion/molecule interactions is described. The drift tube has the facility for variable gas temperature and an operating pressure range up to 5 Torr. Ion velocities and mobilities have been determined for $HCN^{+\cdot}$, H_2CN^+, C_2N^+, $C_2N_2^{+\cdot}$ and $C_2H_3N^{+\cdot}$ in helium at 293 K for the E/N range 10–140 Td using dilute mixtures of HCN, C_2N_2, CH_3CN and CH_3NC in helium.

INTRODUCTION

There are a number of excellent reviews which consider the theory and application of drift tube techniques to the determination of ion transport properties and ion/molecule kinetics [1–3]. A knowledge of ion transport parameters as a function of E/N for the gas temperature and composition of the experiment is a necessary prerequisite to the elucidation of rate coefficients from drift tube data. Blanc's law [1] may be employed to estimate ion mobilities for binary gas mixtures of known composition providing data exist for the ion of interest in both pure components. Such data are sparse and Blanc's law cannot usually be applied unless experimental measurements are conducted on the pure components. As a consequence, accurate measurements for the gas mixtures used in the kinetic experiments must usually be performed.

The drift tube described in this article was designed for the measurement of ion drift velocities and ion/molecule rate coefficients over a wide range of variable experimental parameters: drift distance, ion temperature, gas temperature and operating pressure up to 5 Torr with independent sample admittance to the movable ion source and the drift ring assembly. This article describes the drift tube assembly and presents data for the drift

0168-1176/84/$03.00 © 1984 Elsevier Science Publishers B.V.

velocities of several primary and secondary positive ions produced from dilute mixtures of the cyanocompounds HCN, C_2N_2, CH_3CN and CH_3NC in helium at 293 K.

EXPERIMENTAL

Instrument description

Figure 1 is a schematic diagram of the drift tube mass spectrometer employed in this study. The microcomputer control and data collection facility which is included in Fig. 1 has been previously described in detail [4]. A scaled drawing of the drift tube and movable ion source is shown in Fig. 2. The system is constructed of high-vacuum-compatible materials which may be baked to 400°C: stainless steel, molybdenum, silver, gold, glass ceramic and mica. The ring assembly comprises eleven 1 cm gold-plated stainless steel interlocking rings of internal diameter 5 cm separated by precision ground glass ceramic insulators and interconnected by 100 kΩ vacuum-compatible bakeable resistors enclosed in a stainless steel vacuum envelope. The vacuum envelope is also a dewar for the circulation of fluids and a heating jacket carrying four 150 W cartridge heaters. Temperature is monitored by iron–constantan thermocouples attached to the third and ninth rings (numbered from the bellows end), a free-standing thermocouple in the gas space below the ring assembly and a fourth on the drift tube vacuum

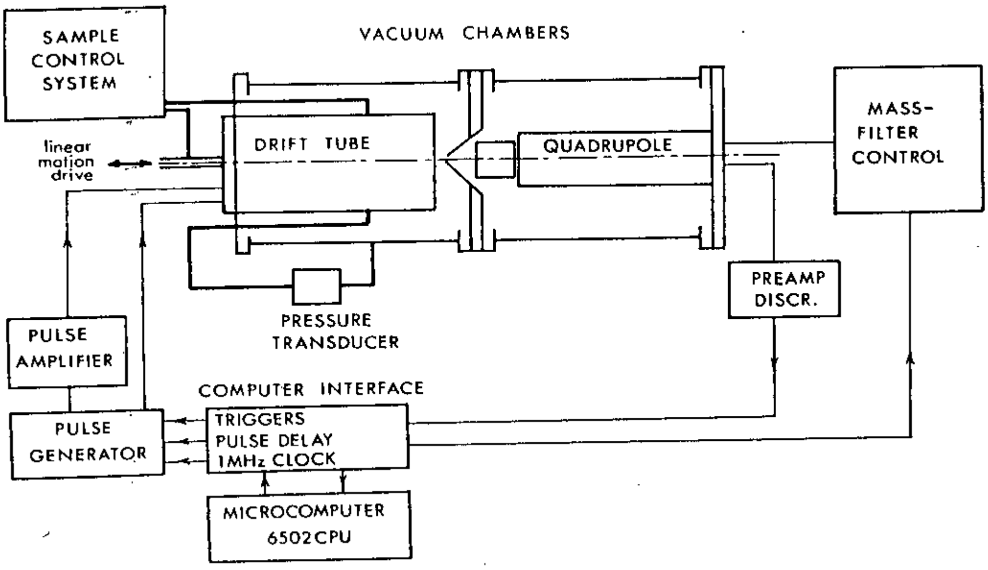

Fig. 1. Schematic diagram of the computer-controlled drift tube mass spectrometer.

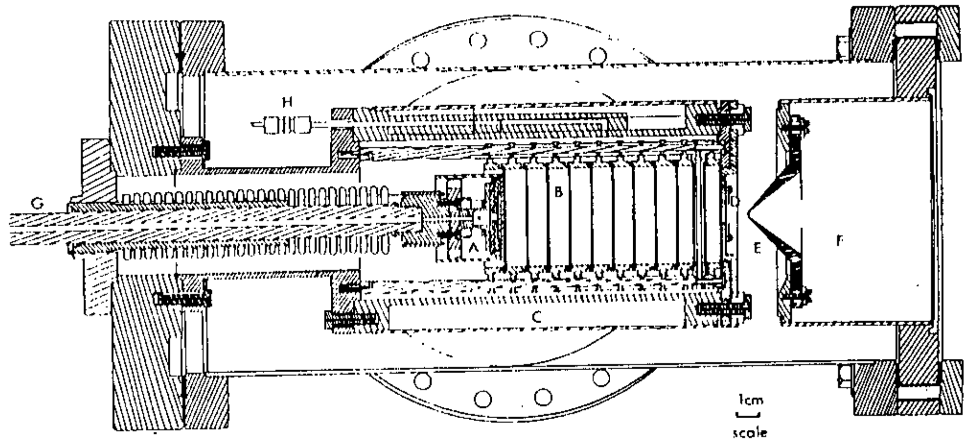

Fig. 2. Scale drawing of the drift tube. A, Movable ion source; B, drift rings; C, drift tube vacuum envelope–dewar; D, ion exit gate; E, skimmer; F, mass spectrometer chamber; G, linear-drive shaft for the ion source (details of drive mechanism have been excluded); H, one of two diametrically opposite sample lines used to admit samples to the drift tube and for the measurement of the drift tube pressure using a Model 170M-49 MKS Baratron.

envelope. For the results reported here, the drift tube temperature was maintained at 293 K (20°C) by the circulation of water through the dewar. Sample admittance and pressure monitoring lines pass through the dewar and open into the drift tube behind the ring assembly at diametrically opposite points close to the middle drift ring. A separate inlet channel drilled through the linear motion drive shaft forms part of a line-of-sight laser alignment path along the instrument axis and communicates directly into the movable ion source which is electrically insulated from the bellows assembly by a glass ceramic disc. The ion source carries an electron gun perpendicular to the drift tube axis, an electron control gate of 90% transmission gold-plated copper mesh and an ion gate of the same material which can be used as a two-element plane lens. The filament is mounted on molybdenum rods and housed in a stainless steel enclosure separated from the collision chamber by the electron-control grid and a mica heat shield. The filament material normally used to achieve high emission currents is platinum ribbon but, for operation with cyanocompounds in this study, 0.013 cm diameter iridium wire was found to be the only suitable material. The inevitable temperature gradient produced in the vicinity of the electron gun was minimised by the application of barium zirconate [5] to the filament and by operation of the ion source with emission currents $< 50\ \mu A$. Under these conditions, a temperature rise of 1–2° was measured on leaving the ion source positioned adjacent to one of the drift rings on to which a thermocouple was attached. The drift ring rapidly recovered to the temperature of the drift tube envelope on repositioning the ion source. The linear drive mechanism is used to move the ion source continuously through the full length of the drift ring assembly where it may be positioned to an accuracy better than 0.1 mm. The ion exit flange, which is also gold-plated, carries a 1.5 cm diameter molybdenum disc of 0.025 cm thickness recessed into the drift ring side through which a conically shaped ion exit aperture of minimum diameter 0.025 cm is drilled. The ion exit gate is constructed from 90% transmission gold-plated copper electroformed mesh sandwiched between two stainless steel shims which are electrically isolated from, but attached to, the vacuum side of the exit flange. The distance between the exit orifice and the gold-plated skimmer which separates the drift tube and mass spectrometer vacuum chambers is 1.0 cm. The quadrupole mass filter is an Extranuclear Model 4-270-9 with a mass range of 0–800 u. Vacuum seals are made from 0.5 mm diameter pure silver wire which appears to be a perfectly adequate and affordable substitute for gold.

The drift tube and mass spectrometer vacuum chambers, which are separated by a skimmer with a 2 mm diameter orifice, are individually pumped by 2000 $\mathrm{l\ s^{-1}}$ (for helium) liquid-air-trapped oil diffusion pumps. For a drift tube pressure of 1 Torr helium (133 Pa), the drift tube and mass spectrometer chambers operate at 5×10^{-5} Torr (6×10^{-3} Pa) and 4×10^{-7} Torr (5×10^{-5} Pa), respectively. The admission of helium to the drift tube via a liquid-air-cooled molecular sieve trap following overnight baking at 150°C and 10^{-7} Torr (10^{-5} Pa) results in a mass spectrum comprising $> 99.5\%$ m/z 4, $\mathrm{He}^{+\cdot}$, $< 0.2\%$ m/z 8, $\mathrm{He}_2^{+\cdot}$ and $< 0.1\%$ each of m/z 16, 17 and 18, $\mathrm{O}^{+\cdot}$, OH^{+} and $\mathrm{H_2O}^{+\cdot}$, respectively.

Drift tube operation

The drift tube may be operated either in continuous mode with variable drift distance at constant pressure or variable pressure at fixed drift distance for ion/molecule reaction studies or, alternatively, it may be operated in pulsed mode for drift velocity measurements. Electron and ion gating is achieved by the application of square-wave pulses to override small blocking bias voltages on the gate elements. The start-gate pulse may be applied either to the electron gun control grid or the elements between the ion extractor and the ion source sleeve, which is maintained at the appropriate potential to its location on the drift tube axis. For the work reported here, the electron gun control grid was used to gate 2 μs pulses of 70 eV electrons into the source. $\mathrm{He}^{+\cdot}$ ions generated by electron impact undergo charge transfer reactions with the trace component in the gas mixture to produce the ions of interest which drift out of the source under the influence of a uniform electric field whose magnitude is determined by the E/N ratio at the drift tube temperature. The exit gate, which is normally reverse biassed a few volts with respect to the ion exit plate, is opened by the application of a 2 µs 15 V pulse delayed with respect to the electron control pulse [4]. The ion count is linear with respect to the width of either gate pulse and passes through the origin (zero counts) for zero pulse widths.

The arrival-time distributions for primary ions measured using this instrument are in good accord with those calculated using the drift equations developed by McDaniel and Mason for a drift tube of cylindrical geometry and a point source of ions [1]:

$$I^+(z,t)=\frac{C(v_d+z/t)}{4(\pi D_L t)^{1/2}}\left[\exp -\frac{(z-v_d t)^2}{4D_L t}\right]\left[1-\exp\left(-\frac{r_0^2}{4D_T t}\right)\right] \qquad (1)$$

where $I^+(z,t)$ is the normalised ion count for drift distance z and drift time t, C is the normalisation factor, v_d is the ion drift velocity, r_0 the radius of the point source of ions, and D_L and D_T are the longitudinal and transverse diffusion coefficients, respectively. The term in D_T is small and can be neglected for this drift tube where the radius of the ion exit orifice in the movable ion source is 1.0 mm. The longitudinal diffusion coefficient, D_L, was calculated from the expression [1]

$$D_L = D_0 + \left(\frac{M+3.72m}{3N(M+1.908m)}\right)\frac{Mv_d^3}{q(E/N)} \qquad (2)$$

where D_0 is the diffusion coefficient under zero field conditions, m is the ion mass and M the buffer gas mass. Experimental and calculated arrival time distributions for $He^{+\cdot}$ in He for a total drift tube pressure of 0.4 Torr, $E/N = 80$ Td (1 Td $= 10^{-21}$ V m^2) and two drift distances are shown in Fig. 3. The experimental arrival time distributions are in good accord with the

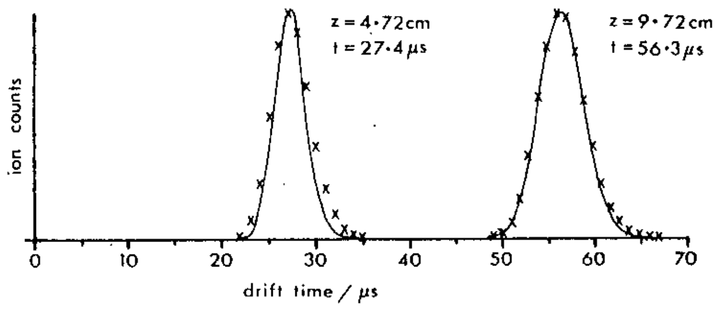

Fig. 3. Experimental (×) and calculated (———) arrival time distributions for $He^{+\cdot}$ in helium for E/N 80 Td. Total drift tube pressure 0.40 Torr, gas temperature 293 K and the two drift distances 4.72 and 9.72 cm. The drift velocity and reduced mobility calculated for $He^{+\cdot}$ at 80 Td are 1.72×10^5 cm s^{-1} and 8.0 cm^2 V^{-1} s^{-1}, respectively, compared with literature values [6] of 1.75×10^5 cm s^{-1} and 8.12 cm^2 V^{-1} s^{-1}, respectively.

predictions of Eq. (1) for the longer drift paths and are slightly broader for the shorter drift distances. The effect of the gate widths on the arrival time distribution was examined both experimentally and by deconvolution using fast Fourier transforms (FFT). There were no discernible differences between arrival time distributions for $He^{+\cdot}$ in helium measured with 1 or 2 μs gate widths. A slight broadening effect became evident for a 3 μs electron gate width or a 4 μs ion exit width, in agreement with the calculations. In this study, both gates were operated with 2 μs widths and the arrival time spectra collected with 1 μs delay increments.

Drift velocities were determined from the slope of arrival time maxima versus drift distance plots over the geometric drift path range 2–10 cm. Linear plots with correlation coefficients > 0.995 are typical (Fig. 4) although extrapolation to zero drift time did not always correspond to zero

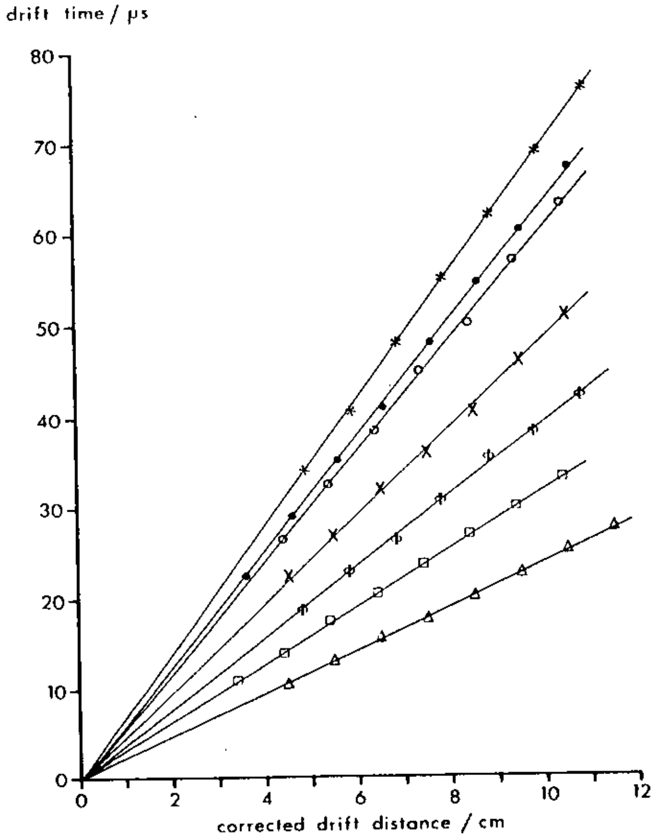

Fig. 4. Plots of maximum ion-arrival time versus corrected ion drift distance. *, HCN^+ 25 Td; ●, $C_2N_2^+$ 40 Td; O, C_2N^+ 40 Td; ×, $C_2H_3N^+$ 60 Td; Φ, $C_2H_3N^+$ 80 Td; □, H_3O^+ 80 Td; Δ, H_2CN^+ 120 Td.

geometric drift distance. Plots for $He^{+\cdot}$ in pure helium for $E/N > 50$ Td extrapolated through the origin, but this was not found to be the case for secondary and tertiary ions (e.g. $H_2O^{+\cdot}$, H_3O^+, and $N_2^{+\cdot}$) or for $He^{+\cdot}$ below 50 Td, although the values of the drift velocity, v_d, determined from the slopes were in excellent agreement, better than ±3%, with published values [6]. These end effects result from field inhomogeneities in the vicinity of the gates and, for the products of ion/molecule reactions involving dissociative charge transfer from $He^{+\cdot}$, a contribution from the finite distance over which the ions are generated along the drift tube axis. The end effects are not reproducible from day to day, although the values of v_d obtained from the slopes are reproducible from month to month to better than ±2% over wide ranges of total drift tube pressure and E/N. Intercepts give apparent drift distances up to 15% greater than the geometric value at 5 cm. Although this discrepancy decreases for increasing geometric drift distances, in the absence of a movable ion source it would carry through to the ion transport properties [1,7]. A recent measurement of the mobility of NH_2^+ in helium using a drift tube with a fixed path length of 11 cm noted a 10% discrepancy from an earlier result by the same authors using a fixed drift path of 5.65 cm [8,9]. Discrepancies of similar magnitude are evident for the mobility of Cl^- in nitrogen where values from a fixed drift path drift tube cell [10] and the drift-SIFT apparatus [11] lie outside their combined uncertainties.

Materials used

The hydrogen cyanide, HCN, used in this work was prepared by the reaction of sulphuric acid on sodium cyanide and the crude product was dried over P_2O_5 prior to repeated vacuum distillation. Dicyanogen, C_2N_2, was vacuum distilled from the Matheson technical grade. Methyl cyanide, CH_3CN, was vacuum distilled from the British Drug Houses reagent grade and methyl isocyanide, CH_3NC, was prepared from the reaction of methyl iodide on silver cyanide. Gas mixtures were prepared on a high vacuum gas-handling line using an MKS capacitance manometer to measure gas pressures. The cyanocompound was admitted to an evacuated 5 l glass bulb and the associated vacuum lines to a known pressure. Dry helium was then admitted at high pressure to make up the mixture which was then allowed to mix over a period of several hours before sealing the bulb. Mass spectra were then recorded as a check of mixture purity.

RESULTS

Arrival time distributions for each ion were measured for seven or eight drift distances for each value of E/N. The maxima were located by fitting a seven-point Lagrange interpolation formula to the individual distributions about the experimental maxima. Interpolation of the experimental data to find the true maximum in the peak was then performed in order to increase the time scale resolution. Drift velocities, v_d, were determined from plots of arrival time maxima against drift distance, shown in Fig. 4 for ions at selected values of E/N at 293 K. Ion mobilities, K, and the reduced mobilities, K_0, were calculated using the equations [1]

$$K = v_d/E \tag{3}$$

$$K_0 = K(P/760)(273/T) \tag{4}$$

where, E is the electric field gradient applied to the drift tube, P is the total drift tube pressure in Torr and T is the drift tube temperature in degrees Kelvin.

The cyano ions reported in this study were generated by consecutive ion/molecule reactions initiated by dissociative charge transfer from $He^{+\cdot}$ ions to the precursor molecule present in the drift tube as a dilute mixture with helium. The extent of reaction was controlled by adjustment of the mixture dilution and the total drift tube pressure to maximise ion formation in the ion source and the first few centimetres of the drift region. The ion profiles for each gas mixture were examined as a function of drift distance in order to establish conditions and to optimise mixture compositions. With the exception of H_2CN^+, where a mixture composition of 0.2% HCN in helium was used, all measurements were repeated for a series of mixture compositions over the range 0.04–0.16% cyano compound in helium. The drift velocities were independent of composition and the data presented are representative of ion transport in pure helium.

The $HCN^{+\cdot}$ and H_2CN^+ ions are formed by reactions (5)–(7) for dilute HCN in helium mixtures.

$$He^{+\cdot} + HCN \rightarrow CN^+ + H^\cdot + He \tag{5}$$

$$CN^+ + HCN \rightarrow HCN^{+\cdot} + CN^\cdot \tag{6}$$

$$HCN^{+\cdot} + HCN \rightarrow H_2CN^+ + CN^\cdot \tag{7}$$

The rate constants have been reported to be $\sim 3.9 \times 10^{-9}$ or $\sim 3.1 \times 10^{-9}$ $cm^3\ molec^{-1}\ s^{-1}$ for reaction (5) [12,13], $2.5 \pm 0.6 \times 10^{-9}$ $cm^3\ molec^{-1}\ s^{-1}$ for reaction (6) [14] and 9.8×10^{-10} $cm^3\ molec^{-1}\ s^{-1}$ for reaction (7) [15]. There are additional small contributions to the CN^+ and $HCN^{+\cdot}$ ion signals from direct electron impact. The drift time versus drift distance, t–z, plots for $HCN^{+\cdot}$ were non-linear for dilute mixtures of less than 0.05% HCN in helium and $E/N > 60$ Td at 0.4 Torr total pressure. Under these conditions of short ion residence and low partial pressures, the arrival time distributions are diffuse, due to ion formation occurring down-field from the ion source region. Narrow arrival-time distributions and linear t–z plots were obtained for $HCN^{+\cdot}$ using a series of mixture compositions to span the E/N range from 20 to 140 Td. Dilute mixtures, 0.05% HCN in helium, gave linear plots for the E/N range 20–50 Td with total drift tube pressures of 0.4–0.5 Torr. Mixtures of composition 0.1% HCN in He were used to overlap this range in E/N and to extend the data to E/N 140 Td where the ion residence times are much shorter. These results are shown with data collected for a 0.16% HCN in helium mixture in Fig. 5 as the reduced mobility against E/N. A typical t–z plot for the $HCN^{+\cdot}$ ion formed from a 0.05% HCN in helium mixture at 25 Td and 0.4 Torr total drift tube pressure is shown in Fig. 4.

The H_2CN^+ ion is the terminal ion for the HCN system. Linear t–z plots could not be obtained for mixtures with compositions $< 0.15\%$ in HCN for drift tube pressures < 0.5 Torr. The t–z plot for H_2CN^+ for E/N 120 Td shown in Fig. 4 was determined for a 0.2% HCN in helium mixture at 0.5 Torr drift tube pressure. Figure 6 shows experimental arrival time distributions for E/N 15, 25, 50 and 110 Td under these conditions compared with those calculated using Eq. (1) which assumes a point source of ions originating along the electron beam axis. The broader experimental distributions are a consequence of a diffuse H_2CN^+ ion source. Ions arriving at the exit gate are a mixture of those which have been formed within the movable ion source and those which have spent varying times as the less mobile $He^{+\cdot}$ ion and as the more mobile CN^+ and $HCN^{+\cdot}$ ions along the drift path. Equation

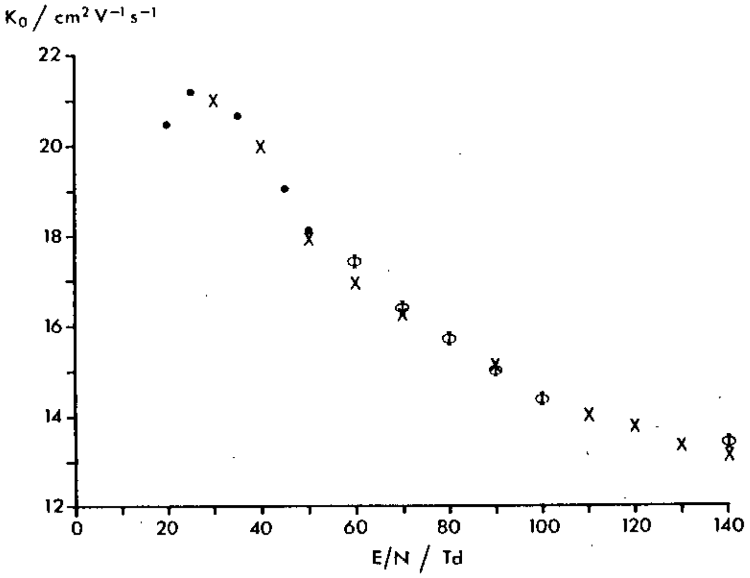

Fig. 5. Plot of the reduced mobility of the $HCN^{+\cdot}$ ion versus E/N for three dilute mixtures of HCN in helium at 293 K. ●, 0.05% HCN–He; ×, 0.10% HCN–He; Φ, 0.16% HCN–He.

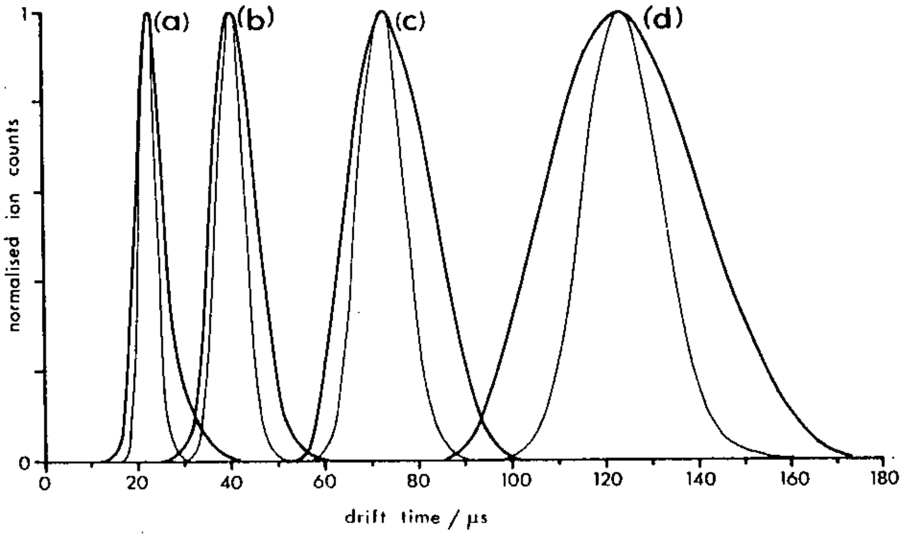

Fig. 6. Experimental (▬) and calculated (——) arrival time distributions for H_2CN^+ over a drift distance of 8.72 cm and four valves of E/N (a) 110 Td; (b) 50 Td; (c) 25 Td; (d) 15 Td at 293 K.

(1) was modified by the addition of a kinetics term derived from the reaction series (5)–(7) and the arrival-time distributions recalculated. The overall effect was a small increase in the width of the distributions which were still narrower than those measured experimentally, as found above for $He^{+\cdot}$ in helium. Experiments were performed using HCN mixtures contaminated with water vapour to facilitate reactions (8)–(13) as additional pathways to the H_2CN^+ ion.

$$He^{+\cdot} + H_2O \rightarrow H_2O^{+\cdot} + He \tag{8}$$

$$H_2O^{+\cdot} + H_2O \rightarrow H_3O^+ + OH \tag{9}$$

$$H_2O^{+\cdot} + HCN \rightarrow H_2CN^{+\cdot} + OH \tag{10}$$

$$H_3O^+ + HCN \rightarrow H_2CN^+ + H_2O \tag{11}$$

$$CN^+ + H_2O \rightarrow H_2CN^+ + O \tag{12}$$

$$\rightarrow H_2O^{+\cdot} + CN \tag{13}$$

The drift velocities detemined for wet mixtures were the same as those measured for anhydrous mixtures, i.e. the velocities were independent of the reaction pathway. A plot of reduced mobility for the H_2CN^+ ion over the E/N range 10–140 Td is shown in Fig. 7.

The C_2N^+ ion is formed directly from the dissociative charge transfer of $He^{+\cdot}$ on C_2N_2 in the reaction

$$He^{+\cdot} + C_2N_2 \rightarrow C_2N^+ + N^\cdot + He \tag{14}$$

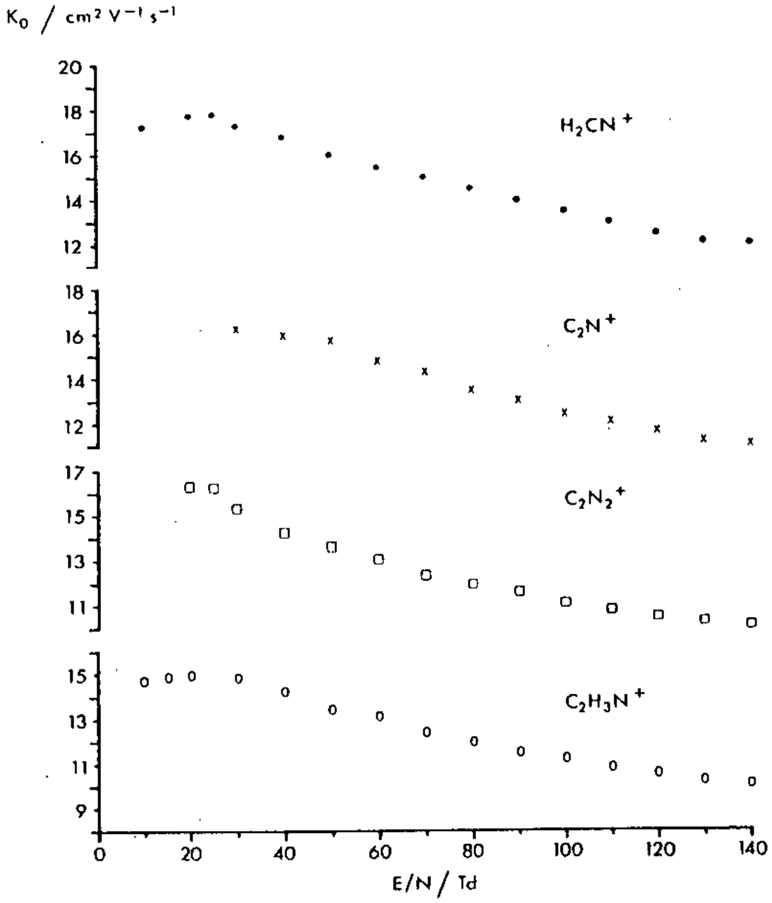

Fig. 7. Plots of reduced mobility versus E/N for the ions H_2CN^+, C_2N^+, $C_2N_2^{+\cdot}$ and $C_2H_3N^{+\cdot}$ in helium at 293 K.

The arrival-time distributions were narrow and the t–z plots linear over the full range of mixture compositions used in this study. A t–z plot for a 0.05% mixture of C_2N_2 in helium for a drift tube pressure of 0.4 Torr and E/N 40 Td is shown in Fig. 4. Drift velocities for m/z 38, C_2N^+, were also measured from dilute methyl cyanide and methyl isocyanide mixtures in helium. The values measured were independent of the source molecule and self-consistent within the ±2% reproducibility of the instrument over a period of several months.

The $C_2N_2^+$ ion is formed from cyanogen by reactions (15) and (16), reaction (16) representing the major pathway.

$$He^{+\cdot} + C_2N_2 \rightarrow C_2N_2^{+\cdot} + He \qquad (15)$$

$$CN^+ + C_2N_2 \rightarrow C_2N_2^{+\cdot} + CN^\cdot \qquad (16)$$

TABLE 1

Ion transport properties for $HCN^{+\cdot}$ in helium at 293 K

E/N (Td)	v_d [a] (10^4 cm s^{-1})	K_0 (cm^2 V^{-1} s^{-1})	T_{eff} (K)	$\Omega(T_{eff})$ (10^{-15} cm^2)
20	11.0	20.5	587	2.00
25	14.3	21.2	785	1.67
30	16.9	21.0	988	1.50
35	19.4	20.6	1203	1.39
40	21.2	19.7	1380	1.36
45	23.0	19.0	1573	1.32
50	24.2	18.0	1711	1.33
60	27.8	17.2	2158	1.24
70	30.7	16.3	2573	1.20
80	33.8	15.7	3055	1.14
90	36.6	15.1	3527	1.11
100	38.7	14.4	3924	1.10
110	41.4	14.0	4446	1.06
120	44.2	13.7	5026	1.02
130	46.9	13.4	5606	0.99
140	50.1	13.3	6364	0.94

[a] Reproducibility ±2%; absolute accuracy better than ±5%.

TABLE 2

Ion transport properties for H_2CN^+ in helium at 293 K

E/N (Td)	v_d [a] (10^4 cm s^{-1})	K_0 (cm^2 V^{-1} s^{-1})	T_{eff} (K)	$\Omega(T_{eff})$ (10^{-15} cm^2)
10	4.6	18.3	345	3.08
20	9.6	17.8	515	2.45
25	12.0	17.8	640	2.20
30	14.0	17.4	770	2.05
40	18.2	16.9	1093	1.77
50	21.7	16.1	1428	1.63
60	25.0	15.5	1807	1.50
70	28.4	15.1	2249	1.38
80	31.4	14.6	2682	1.31
90	33.9	14.0	3073	1.28
100	36.6	13.6	3532	1.22
110	38.8	13.1	3929	1.21
120	40.7	12.6	4296	1.20
130	42.7	12.2	4698	1.18
140	45.7	12.1	5318	1.12

[a] Reproducibility ±2%; absolute accuracy better than ±5%.

TABLE 3

Ion transport properties for C_2N^+ in helium at 293 K

E/N (Td)	v_d [a] (10^4 cm s^{-1})	K_0 (cm^2 V^{-1} s^{-1})	T_{eff} (K)	$\Omega(T_{eff})$ (10^{-15} cm^2)
30	13.1	16.2	707	2.26
40	17.2	16.0	1010	1.91
50	21.2	15.8	1386	1.66
60	23.9	14.8	1674	1.61
70	26.9	14.3	2048	1.50
80	29.0	13.5	2335	1.49
90	31.7	13.1	2727	1.42
100	33.6	12.5	3029	1.42
110	36.1	12.2	3447	1.36
120	37.8	11.7	3745	1.36
130	39.5	11.3	4072	1.35
140	42.2	11.2	4598	1.28

[a] Reproducibility ±2%; absolute accuracy better than ±5%.

The $C_2N_2^{+\cdot}$ ion was the terminal ion under the conditions used in this work. A t–z plot for E/N 40 Td using a 0.1% mixture of C_2N_2 in helium at a drift tube pressure of 0.4 Torr is shown in Fig. 4 and a plot of the reduced mobility against E/N is shown in Fig. 7.

The $C_2H_3N^{+\cdot}$ ion is formed predominantly by CN^+ charge transfer to

TABLE 4

Ion transport properties for $C_2N_2^{+\cdot}$ in helium at 293 K

E/N (Td)	v_d [a] (10^4 cm s^{-1})	K_0 (cm^2 V^{-1} s^{-1})	T_{eff} (K)	$\Omega(T_{eff})$ (10^{-15} cm^2)
20	8.8	16.4	481	2.67
25	11.0	16.3	584	2.44
30	12.3	15.3	662	2.44
40	15.4	14.3	866	2.28
50	18.3	13.6	1103	2.13
60	21.1	13.1	1375	1.98
70	23.3	12.4	1612	1.93
80	25.8	12.0	1907	1.83
90	28.1	11.6	2202	1.77
100	29.9	11.1	2450	1.75
110	32.0	10.8	2764	1.69
120	33.6	10.4	3020	1.68
130	36.0	10.3	3432	1.59
140	38.0	10.1	3794	1.54

[a] Reproducibility ±2%; absolute accuracy better than ±5%.

CH_3CN or CH_3NC, analogous to the situation for $C_2N_2^{+\cdot}$ in reactions (15) and (16). Figure 4 shows two t–z plots for CH_3CN^+ for E/N 60 and 80 Td and Fig. 7 shows a plot of reduced mobility versus E/N.

Compilations of gas phase ion transport properties [6] include the ion temperature, T_{eff}, and the collision-averaged momentum-transfer cross-section, $\Omega(T_{\text{eff}})$, calculated from the two-temperature theory of ion transport developed by Viehland and Mason [3,16]. The relationship between the ion mobility, K, and $\Omega(T_{\text{eff}})$ is given by

$$K = \frac{3q}{8N}\left(\frac{\pi}{2m_r k_B T_{\text{eff}}}\right)^{1/2} \frac{1+\alpha}{\Omega(T_{\text{eff}})} \tag{17}$$

where q is the charge on the electron, N is the particle density in the drift tube, m_r is the ion–neutral (helium) reduced mass, k_B the Boltzmann constant, α a correction factor which is less than 0.1 and T_{eff} is the ion temperature given by

$$T_{\text{eff}} = T + \frac{Mv_d^2}{3k_B}(1+\beta) \tag{18}$$

where M and T are the buffer gas mass and temperature, respectively, and β is a second correction factor which is also < 0.1. Both α and β were set to zero for the calculated values of T_{eff} and $\Omega(T_{\text{eff}})$ included in Tables 1–5.

TABLE 5

Ion transport properties for $C_2H_3N^{+\cdot}$ in helium at 293 K

E/N (Td)	v_d (10^4 cm s^{-1})	K_0 (cm^2 V^{-1} s^{-1})	T_{eff} (K)	$\Omega(T_{\text{eff}})$ (10^{-15} cm^2)
10	4.0	14.7	331	3.63
15	6.0	14.9	380	3.34
20	8.1	15.0	451	3.05
30	12.0	14.9	643	2.57
40	15.4	14.3	866	2.31
50	18.2	13.5	1091	2.18
60	21.3	13.2	1391	1.97
70	23.3	12.4	1612	1.95
80	25.6	11.9	1880	1.88
90	28.1	11.6	2202	1.78
100	30.4	11.3	2529	1.71
110	32.3	10.9	2810	1.68
120	34.2	10.6	3126	1.64
130	35.7	10.2	3372	1.64
140	37.7	10.0	3725	1.59

[a] Reproducibility ±2%; absolute accuracy better than ±5%.

ACKNOWLEDGEMENTS

The authors should like to acknowledge the DSIR Physics and Engineering Workshops, Petone, for construction of the drift tube, Mr. Gordon Collins of the Chemistry Department electronics workshop who assembled the electronics modules and Mr. Kevin Gillard of the Chemistry Department mechanical workshops for his advice. One of us, P.W.H., would like to acknowledge the University Grants Committee and the New Zealand Lottery Board for the provision of research grants in support of this work.

REFERENCES

1 E.W. McDaniel and E.A. Mason, The Mobility and Diffusion of Ions in Gases, Wiley, New York, 1973.
2 D.L. Albritton, NATO Adv. Study Inst. Ser. B, 40 (1979) 119.
3 L.A. Viehland, Mass Spectrometry, Specialist Periodicals Report, Vol. 6, Royal Society of Chemistry, London, 1981, Chap. 3.
4 P.W. Harland and B.J. McIntosh, Int. J. Mass Spectrom. Ion Processes. 54 (1983) 217.
5 D. MacNair, Rev. Sci. Instrum., 38 (1967) 124.
6 H.W. Ellis, E.W. McDaniel, D.L. Albritton, L.A. Viehland, S.L. Lin and E.A. Mason, At. Data Nucl. Data Tables, 22 (1978) 179; 17 (1976) 177.
7 E.W. McDaniel, J. Chem. Phys., 52 (1970) 3931.
8 R. Thomas, J. Barassin and A. Barassin, Int. J. Mass Spectrom. Ion Phys., 41 (1981) 95.
9 J. Barassin, A. Barassin and R. Thomas, Int. J. Mass Spectrom. Ion Phys., 49 (1983) 51.
10 T. Fuju and G.G. Meisels, J. Chem. Phys., 75 (1981) 5067.
11 L.A. Viehland and D.W. Fahey, J. Chem. Phys., 78 (1983) 435.
12 J.P. Liddy, C.G. Freeman and M.J. McEwan, Mon. Not. R. Astron. Soc., 180 (1977) 683.
13 W.T. Huntress and V.G. Anicich, Astrophys. J., 208 (1976) 237.
14 M.J. McEwan, V.G. Anicich and W.T. Huntress, Jr., Int. J. Mass Spectrom, Ion Phys., 50 (1983) 179.
15 C.G. Freeman, P.W. Harland, J.P. Liddy and M.J. McEwan, Aust. J. Chem., 31 (1978) 963.
16 L.A. Viehland and E.A. Mason, Ann. Phys. (N.Y.), 499 (1975); 110 (1978) 287.

J. Chem. Soc., Faraday Trans. 2, 1985, 81, 169-176

The Mobility of CN^+ in Helium at 293 K

By Peter W. Harland* and Bruce J. McIntosh†

Chemistry Department, University of Canterbury, Christchurch, New Zealand

Received 6th June, 1984

Arrival-time distributions of CN^+ ions in dilute mixtures of HCN and C_2N_2 in helium at 293 K have been measured in a drift-tube mass spectrometer with a movable ion source. The mobility of the CN^+ ion in helium was evaluated over the range of E/N from 40×10^{-21} to 140×10^{-21} m^2 V by comparison of the experimental distributions with curves calculated from ion-transport equations. The reliability of the mobilities were tested by comparison of calculated and experimental arrival-time distributions for a variation of the total drift-tube pressure over the range 0.2-0.5 Torr.‡

Drift tubes may be utilised both for the determination of ion-transport properties and for the study of ion-molecule interactions over a wide range of effective ion temperatures. The two-temperature theory of Viehland and Mason[1] quantitatively describes the equivalence of ion temperature and the ratio of the electric-field gradient to the particle density, E/N, a parameter readily variable over a wide range in the drift tube. The measurement of drift velocities as a function of E/N is a necessary prerequisite to the implementation of this theory; for example, in order to study an ion-molecule reaction at a given ion temperature the drift velocity of the ion is required in order to establish the appropriate electric-field gradient.

The drift tube used in this work has been previously employed to determine the mobilities of ions formed in dilute mixtures of small cyano-compounds in helium.[2] The CN^+ ion is generated and depleted by rapid reactions yielding low ion signals and broad ion arrival-time distributions which cannot be analysed from plots of the mean arrival time against total ion drift distance normally employed. CN^+ arrival-time distributions were recorded for 7 or 8 drift distances for each value of E/N sampled and compared with distributions calculated using ion-transport equations developed by Snuggs *et al.*[3,4] in which the CN^+ mobility was the variable parameter.

Cyano-compounds are being studied because of their role in extraterrestrial systems. The $CN^·$ radical and HCN have been detected in interstellar dust clouds and in comets, and HCN has recently been identified in the atmosphere of Titan.[5] Complex cyano-molecules, including the series HC_xN, where $x=3$, 5, 7 and 9, CH_3CN, NH_2CN and CH_2CHCN, have also been observed and the mechanisms for their production is of considerable interest.[6,7] The importance of ion-molecule reactions in the synthesis of these interstellar polyatomic molecules has been demonstrated and the relative abundances of several molecules successfully modelled.[8,9]

EXPERIMENTAL

The drift-tube mass spectrometer used in this study has been previously described.[2,10] The drift tube comprises eleven 1 cm gold-plated interlocking drift rings of 5 cm internal diameter enclosed in a temperature-controlled vacuum envelope. A movable electron-impact

---

† Present address: CSIRO, Division of Chemical Physics, Clayton, Victoria, Australia.

‡ 1 Torr = 101 325/760 Pa.

ion source, incorporating an electron-beam control grid and a two-element plane ion lens, is enclosed in a shield electrically biased according to its position in the drift tube. The ion source may be positioned anywhere along the drift-tube axis to within better than 0.1 mm. Ions gated from the drift tube are mass-analysed by an Extranuclear model 4-270-9 quadrupole mass filter and detected by pulse counting.

Electron and ion gating are achieved by the application of square-wave pulses to the electron-control and ion-exit grids to over-ride small blocking bias voltages on these elements. $He^{+\cdot}$ ions, generated in the helium buffer gas by 70 eV electron pulses, undergo charge-transfer and dissociative charge-transfer reactions with trace amounts of hydrogen cyanide, HCN, or dicyanogen, C_2N_2, in the gas mixture. The ions of interest drift out of the ion source and traverse the drift tube under the influence of a uniform electric field whose magnitude is determined by the ratio E/N [expressed in the unit townsend (Td), where $1\ \text{Td} = 10^{-21}\ \text{m}^2\ \text{V}$]. The arrival-time distributions of ions arriving at the drift-tube end plate were sampled at 1 μs increments and the mass-selected ion pulses accumulated for repetitive scans. The operating frequency was set at 10 kHz with typical total counting times of 20–40 s per increment.

The hydrogen cyanide used in this work was prepared by the reaction of sulphuric acid on sodium cyanide and the crude product was dried over P_2O_5 prior to multistep vacuum distillation. Dicyanogen was vacuum distilled from Matheson technical grade. Dilute mixtures of HCN or C_2N_2 in helium with compositions in the range 0.04–0.20% were prepared on a high-vacuum gas-handling line using an MKS capacitance manometer to measure gas pressures. Mass spectra were then recorded as a check of mixture purity.

RESULTS AND DISCUSSION

Drift velocities are normally determined from the slope of plots of linear mean drift time against drift distance ($\bar{t}$–z plots), and the reduced mobility, K_0, calculated by the equation[11]

$$K_0 = \frac{v_d}{E}\left(\frac{p}{760}\right)\left(\frac{273.15}{T}\right) \tag{i}$$

where v_d is the ion drift velocity, p the total drift-tube pressure in Torr and T the gas temperature in the drift tube. The measured arrival-time distributions for $He^{+\cdot}$ and many secondary and tertiary ions are narrow and almost symmetrical. The arrival-time maxima can be accurately located by fitting a seven-point Lagrange interpolating polynomial about the peak of each distribution and the maximum found by interpolation. The resulting $\bar{t}$–z plots for $He^{+\cdot}$ extrapolate through the origin where z is the sum of the geometric drift-tube distance and the distance between the transverse electron-beam track and the ion-source exit orifice. Ions generated by charge transfer from $He^{+\cdot}$, or by subsequent reactions along the drift-tube axis, exhibit negative intercepts, having travelled part-way in the form of the low-mobility $He^{+\cdot}$. The value of the negative intercept, which is dependent upon the relative ion mobilities, the number of reactions involved and E/N, extended to 1.6 cm for H_2CN^+ generated from the following sequence of reactions in dilute mixtures of HCN in helium at high E/N (short residence time in the drift tube):

$$He^{+\cdot} + HCN \rightarrow CN^+ + H^\cdot + He \tag{1}$$

$$CN^+ + HCN \rightarrow HCN^{+\cdot} + CN^\cdot \tag{2}$$

$$HCN^{+\cdot} + HCN \rightarrow H_2CN^+ + CN^\cdot. \tag{3}$$

Table 1. Reactions in HCN + He and C_2N_2 + He mixtures

reaction		k/cm^3 molecule^{-1} s^{-1}	ref.
$He^{+\cdot} + HCN \rightarrow CN^+ + \cdots$	(1)	3.9×10^{-9} (±30%)	13
		3.1×10^{-9}	9
$CN^+ + HCN \rightarrow HCN^{+\cdot} + \cdots$	(2)	$(2.5 \pm 0.6) \times 10^{-9}$	14
$HCN^{+\cdot} + HCN \rightarrow H_2CN^+ + \cdots$	(3)	9.8×10^{-10} (±30%)	15
$He^{+\cdot} + C_2N_2 \rightarrow CN^+ + \cdots$	(4)	3.5×10^{-9} (±30%)	16
$CN^+ + C_2N_2 \rightarrow C_2N_2^{+\cdot} + \cdots$	(5)	$(2.1 \pm 0.4) \times 10^{-9}$	5

The $\bar{t}$–z plots for product ions exhibiting negative intercepts are non-linear for short drift distances, <2 cm, and the drift velocities are determined from measurements made over the drift-distance range 3–11 cm.

It has been shown that the present instrument can be used to determine the mobilities of product ions such as $HCN^{+\cdot}$ and H_2CN^+ over a wide range of E/N by careful selection of the gas-mixture composition.[12] Reactions (1) and (2) are both fast (see table 1), whereas reaction (3) is relatively slow. Dilute mixtures of HCN in helium (0.05–0.10%) were used to optimise the $HCN^{+\cdot}$ ion population, and less dilute mixtures (0.15–0.20%) were used to favour the terminal ion H_2CN^+. The CN^+ ion, however, which is both formed and depleted by rapid reactions, gave rise to broad, unsymmetrical arrival-time distributions that precluded an unambiguous assignment of the arrival-time maxima. Dilute mixtures, <0.10%, of HCN or C_2N_2 in helium gave rise to arrival-time distributions extending out to the drift time for the precursor $He^{+\cdot}$ ions, and less dilute mixtures (>0.10%) resulted in a rapid depletion of the CN^+ ion signal owing to reaction (2) or (5), table 1. Fig. 1 shows a typical set of data for a 0.04% mixture of HCN in helium over a range of drift distances for $E/N = 80$ Td, $p = 0.4$ Torr and $T = 293$ K.

The $CN^{+\cdot}$ ion mobilities were evaluated from the experimental arrival-time distributions by comparison with distributions calculated using an analytic solution of the ion-transport equation which was developed by Snuggs *et al.*[3,4] for the determination of rate coefficients. The flux of secondary ions (B^+) passing through the axial drift-tube exit aperture of area a, at time t, for a drift distance z, is given by

$$I_B(z, t) = sa\alpha_A \int_0^t (\pi b_A)^{-1/2} \left(\frac{2 D_{LB}(z - c_A)}{b_A} + v_{dB} \right) \exp\left(-d_A - \frac{(z - c_A)^2}{b_A} \right) \times \left(1 - \exp \frac{-r_0^2}{a_A} \right) \mathrm{d}u \qquad \text{(ii)}$$

where

$$a_A = 4 D_{TA} t - 4(D_{TA} - D_{TB}) u \qquad \text{(iii)}$$

$$b_A = 4 D_{LA} t - 4(D_{LA} - D_{LB}) u \qquad \text{(iv)}$$

$$c_A = v_{dA} t - (v_{dA} - v_{dB}) u \qquad \text{(v)}$$

$$d_A = \alpha_A t - (\alpha_A - \alpha_B) u. \qquad \text{(vi)}$$

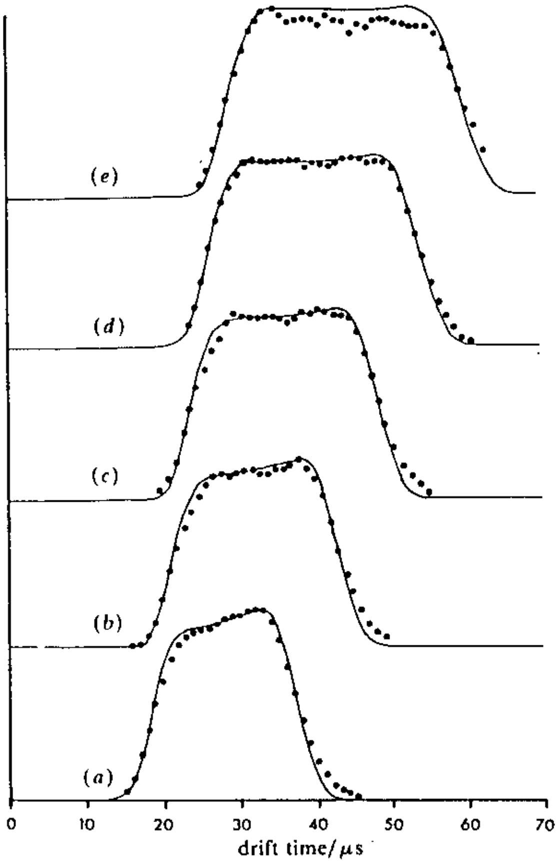

Fig. 1. Calculated (——) and experimental (●) arrival-time distributions for CN$^+$ in 0.04% HCN+He for a range of drift distances, z: (a) 6.5, (b) 7.5, (c) 8.5, (d) 9.5 and (e) 10.5 cm. $E/N = 80$ Td, $p = 0.4$ Torr, $T = 293$ K, $K_0(\mathrm{He}^{+\cdot}) = 8.12\ \mathrm{cm^2\,s^{-1}\,V^{-1}}$ and $K_0(\mathrm{CN}^+) = 16.3\ \mathrm{cm^2\,s^{-1}\,V^{-1}}$.

All ions are assumed to be introduced as a delta-function burst with initial uniform surface density s through the ion entrance aperture of radius r_0. Primary ions, A$^+$, with drift velocity v_{dA} are removed by reaction with frequency α_A ($=kN_r$, where k is the second-order rate coefficient and N_r is the number density of the neutral reactant in the drift tube). Secondary ions, B$^+$, with drift velocity v_{dB} are depleted in turn with frequency α_B, and the time of drift spent by an ion in form B$^+$ is denoted by u, the variable of integration. The longitudinal and transverse diffusion coefficients of A, D_{LA} and D_{TA}, respectively, and of B, D_{LB} and D_{TB}, respectively, were calculated from the generalized Einstein relationships[11]

$$D_L = D(0) + \frac{(M+3.72m)Mv_d^3}{3(M+1.908m)qE} \qquad \text{(vii)}$$

$$D_T = D(0) + \frac{(M+M)Mv_d^3}{3(M+1.908m)qE} \qquad \text{(viii)}$$

where $D(0)$, the zero-field mobility, was calculated from the Einstein equation

$$D(0)=\frac{v_d}{E}\left(\frac{kT}{q}\right). \tag{ix}$$

m and M are the ion and neutral masses, respectively, q is the charge on the electron, k is Boltzmann's constant and E is the electric-field gradient applied to the drift-tube assembly.

Eqn (ii) was integrated numerically using Simpson's rule. Drift-velocity data for $He^{+\cdot}$ had been previously measured with this instrument and found to be in good agreement with values in the literature.[2,12] The rate coefficients, which were used for the evaluation of α_A and α_B, are shown in table 1 for both HCN and C_2N_2 as neutral reactant. The effective drift distance for use in these computations was taken as the value which gave a good fit to the trailing edge of the experimental distribution. The trailing edge results from CN^+ ions which were produced by $He^{+\cdot}$ ions that survived along virtually the entire length of the drift tube and this is almost coincident with the trailing edge of $He^{+\cdot}$ arrival-time distributions recorded under identical conditions. For each value of E/N the difference between the optimal effective drift distance and the geometric drift distance determined by this procedure was found to be independent of the ion-source position and the gas-mixture composition. This difference is equivalent to the negative intercept of the $\bar{t}$–z plots and was equal to 0.76 cm for HCN mixtures at 80 Td (fig. 1). The leading edge of the calculated distributions was fitted to the experimental data by adjusting the drift velocity of the secondary ion, CN^+. This procedure was then repeated for arrival-time data collected as a function of drift distance over the full range of E/N accessible within the limits imposed by the kinetics and the necessity to use dilute mixtures. The fitting procedure was very sensitive to the value selected for the secondary-ion drift velocity and a change of 0.2 $cm^2\,s^{-1}\,V^{-1}$ in the reduced mobility was sufficient to reduce the fit on the leading edge significantly. The choice of rate coefficients determined the relative amplitudes of the early and late part of the calculated distributions without exerting a large influence on the leading and trailing edges. The mobilities found to yield the closest fit were relatively insensitive to the rate coefficients within the range of experimental uncertainties associated with the reported values. They were also independent of the precursor neutral species and therefore representative of the mobility in pure helium. The uncertainty in the reduced mobilities determined by this method is estimated to be better than 5%.

Fig. 2 shows a plot of $K_0(CN^+)$ against E/N over the range 40–140 Td compared with the values determined for $HCN^{+\cdot}$ and H_2CN^+ from $\bar{t}$–z plots.[2] The zero-field values for the reduced mobility of each ion, calculated from the Langevin equation:[11]

$$K_0(0)=\frac{13.876}{\alpha^{1/2}}\left(\frac{m+M}{mM}\right)^{1/2} \tag{x}$$

are marked on the ordinate. In eqn (x) α is the polarizability of helium in units of $Å^3$ and the ion and neutral masses are in atomic mass units.

The reliability of the fitting procedure and of the CN^+ mobility data were assessed by comparison of calculated arrival-time distribution curves with experimental data collected over a range of total drift-tube pressures for fixed drift distance and E/N. The mobility data in fig. 2 were used in eqn (ii) to calculate arrival-time distributions for CN^+ ions for total drift-tube pressures from 0.2 to 0.5 Torr. The typical set of calculated and experimental CN^+ arrival-time distributions shown in fig. 3, for a 0.07% mixture of HCN, an effective drift distance of 10.5 cm, $E/N=100$ Td and

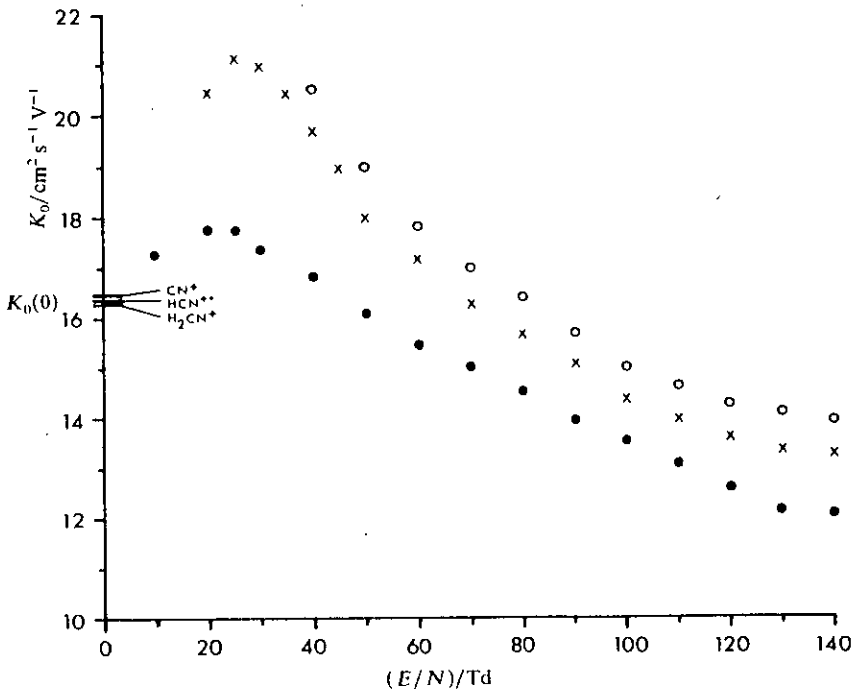

Fig. 2. Plots of reduced mobility against E/N for the ions CN^+ (O), $HCN^{+\bullet}$ (×) and H_2CN^+ (●) in helium at 293 K. The Langevin values for the zero-field reduced mobilities, calculated from eqn (x), are shown on the ordinate.

$K_0(CN^+) = 15.3$ cm^2 s^{-1} V^{-1}, illustrate the good agreement obtained. These data also serve to show the effect of the rate coefficients on the general shape of the distributions. The higher pressures promote reaction (1) with a subsequent decline in the $He^{+\bullet}$ ion population surviving the full length of the drift tube and a relative decline in the amplitude of the late part of the distribution.

The mobility data for CN^+ plotted in fig. 1 are also tabulated with the effective ion temperatures, T_{eff}, and the collision-averaged momentum-transfer cross-sections, $\Omega(T_{eff})$, calculated from the two-temperature theory of ion transport,[1] in table 2. The relationship between the drift velocity and $\Omega(T_{eff})$ is given by

$$v_d = \frac{3q^E}{8N}\left(\frac{\pi}{2m_r kT_{eff}}\right)^{1/2} \frac{1+a}{\Omega(T_{eff})} \qquad \text{(xi)}$$

where m_r is the ion-molecule reduced mass and a is here a correction factor which is <0.1. T_{eff} is given by

$$T_{eff} = T + \frac{Mv_d^2}{3k}(1+b) \qquad \text{(xii)}$$

where b is a second correction factor which is also <0.1. Both a and b were set to zero for the calculated values of T_{eff} and $\Omega(T_{eff})$ included in table 2.

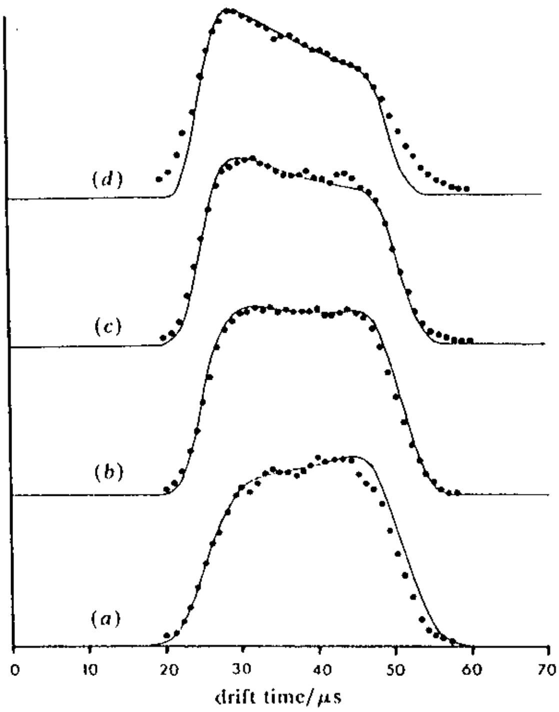

Fig. 3. Calculated (——) and experimental (●) arrival-time distributions for CN^+ in 0.07% HCN + He for a range of drift-tube pressures, *p*: (*a*) 0.2, (*b*) 0.3, (*c*) 0.4 and (*d*) 0.5 Torr. $E/N = 100$ Td, $z = 10.5$ cm, $T = 293$ K, $K_0(He^+) = 7.67\ cm^2\ s^{-1}\ V^{-1}$ and $K_0(CN^+) = 15.3\ cm^2\ s^{-1}\ V^{-1}$.

Table 2. Ion-transport properties for CN^+ in helium at 293 K

(E/N) /Td	v_d /10^4 cm s^{-1}	K_0 /$cm^2\ s^{-1}\ V^{-1}$	T_{eff} /K	$\Omega(T_{eff})$ /$10^{-16}\ cm^2$
40	22.1	20.5	1470	12.6
50	25.6	19.0	1873	12.1
60	28.7	17.8	2290	11.7
70	32.0	17.0	2773	11.1
80	35.1	16.3	3270	10.7
90	38.0	15.7	3789	10.3
100	41.1	15.3	4392	9.8
110	43.5	14.7	4871	9.7
120	46.5	14.4	5522	9.3
130	49.7	14.2	6260	8.9
140	52.7	14.0	7019	8.5

---

[1] L. A. Viehland and E. A. Mason, *Ann. Phys. (N.Y.)*, 1975, **91**, 499; 1978, **110**, 287.

[2] P. W. Harland and B. J. McIntosh, *Int. J. Mass Spectrom. Ion Processes*, 1984, **57**, 283.

[3] R. M. Snuggs, D. J. Volz, J. H. Schummers, D. W. Martin and E. W. McDaniel, *Phys. Rev. A*, 1971, **3**, 477.

[4] R. M. Snuggs, D. J. Volz, I. R. Gatland, J. H. Schummers, D. W. Martin and E. W. McDaniel, *Phys. Rev. A*, 1971, **3**, 487.

[5] M. J. McEwan, V. G. Anicich, W. T. Huntress Jr, P. R. Kemper and M. T. Bowers, *Int. J. Mass Spectrom. Ion Phys.*, 1983, **50**, 179.

[6] R. H. Gammon, *Chem. Eng. News*, 1978, **56**, 20.

[7] C. G. Freeman, P. W. Harland and M. J. McEwan, *Astrophys Lett.*, 1978, **19**, 133.

[8] E. Herbst and W. Klemperer, *Astrophys. J.*, 1973, **185**, 505.

[9] W. T. Huntress and V. G. Anicich, *Astrophys. J.*, 1976, **208**, 237.

[10] P. W. Harland and B. J. McIntosh, *Int. J. Mass Spectrom. Ion Processes*, 1983, **54**, 217.

[11] E. W. McDaniel and E. A. Mason, *The Mobility and Diffusion of Ions in Gases* (Wiley, New York, 1973).

[12] H. W. Ellis, R. Y. Pai, E. W. McDaniel, E. A. Mason and L. A. Viehland, *At. Data Nucl. Data Tables*, 1976, **17**, 177.

[13] J. P. Liddy, C. G. Freeman and M. J. McEwan, *Mon. Not. R. Astron. Soc.*, 1977, **180**, 683.

[14] M. J. McEwan, V. G. Anicich and W. T. Huntress Jr, *Int. J. Mass Spectrom. Ion Phys.*, 1983, **50**, 179.

[15] C. G. Freeman, P. W. Harland, J. P. Liddy and M. J. McEwan, *Aust. J. Chem.*, 1978, **31**, 963.

[16] C. G. Freeman, P. W. Harland and M. J. McEwan, unpublished results.

(PAPER 4/938)

International Journal of Mass Spectrometry and Ion Processes, 67 (1985) 29–46 29
Elsevier Science Publishers B.V., Amsterdam – Printed in The Netherlands

ENTHALPIES OF FORMATION FOR THE ISOMERIC IONS H_xCCN^+ AND H_xCNC^+ ($x = 0$–3) BY "MONOCHROMATIC" ELECTRON IMPACT ON C_2N_2, CH_3CN AND CH_3NC

P.W. HARLAND and B.J. McINTOSH *
Chemistry Department, University of Canterbury, Christchurch (New Zealand)

(Received 24 January 1985)

ABSTRACT

Enthalpies of formation determined from ionization efficiency curves and kinetic energy distributions for the ion series $H_xC_2N^+$ ($x = 0$–3) from "monochromatic" electron impact on C_2N_2, CH_3CN and CH_3NC provide evidence for the retention of the carbon–nitrogen skeletal framework in two stable sets of isomers, H_xCCN^+ and H_xCNC^+. The ionization efficiency curves for the C_2N^+ ion from C_2N_2 and CH_3NC exhibit two thresholds, the first appearance energy corresponding to the formation of the lowest energy CNC^+ isomer with a second channel, ~ 1.1 eV above the first appearance energy, corresponding to co-production of the more energetic CCN^+ isomer. The CNC^+ isomer is estimated to represent ~ 30% and ~ 60% of the C_2N^+ ion populations produced by electron impact on C_2N_2 and CH_3NC, respectively, for electron energies 3–4 eV above the threshold.

INTRODUCTION

Cyano compounds are considered to play an important role in the chemistry of extraterrestrial systems. The $CN^{\cdot}$ radical and HCN have been detected in comet tails, HCN has recently been identified in the atmosphere of Titan [1] and complex cyano molecules, including the series HC_xN, where $x = 1$, 3, 5, 7 and 9, CH_3CN, NH_2CN and CH_2CHCN, have been detected in interstellar dust clouds where the mechanisms for their synthesis are of considerable interest [2,3]. The importance of ion/molecule reactions in the synthesis of these interstellar polyatomic molecules has been demonstrated and the relative abundances of several molecules successfully modelled [4,5].

---

* Present address: CSIRO, Division of Chemical Physics, Clayton, Victoria, Australia.

0168-1176/85/$03.30 © 1985 Elsevier Science Publishers B.V.

The models devised to interpret the experimental observations rely heavily on published enthalpy and rate data for the neutral and ionic species considered to play a role in molecular synthesis. However, a large proportion of the thermochemical data for gaseous positive and negative ions was determined by electron impact ionization using thermonically generated electron beams exhibiting broad energy distributions and with no consideration of excess energy at the ionization threshold. There are large discrepancies between the appearance energy data reported in different studies which involve a variety of data treatment techniques such as linear extrapolation, energy distribution difference and analytical deconvolution [6,7]. It is not uncommon to find discrepancies of 0.5–1.0 eV between literature reports of the same ionization threshold with an equivalent range for the difference in the calculated ionic enthalpies of formation. Fortuitously, a neglect of excess energy tends to an over-estimation of the true threshold and the use of an electron beam with a broad energy distribution results in an underestimation of the true threshold. The combination of these factors can, in some cases, such as the formation of C_2N^+ from C_2N_2, result in a value for the enthalpy of formation which is in good agreement with the true value. This is, however, the exception rather than the rule.

The existence of geometric isomers may be inferred from collisional activation spectra, differences in ion/molecule rate coefficients and product ratios, theoretical calculations of ion structure or by measurement of the enthalpies of formation by photoionization or electron impact. Each of these techniques suffers from limitations and uncertainties; the differences between the fragmentation patterns used to identify geometric isomers in collisional-induced activation analysis are often minimal and differences in the rate coefficients and/or produced ratios for ions generated from different sources may reflect differences in their internal energy. Photoionization eliminates the uncertainties inherent in the use of thermonically generated electron beams but suffers from low photoionization cross-sections. A study of dicyanogen [8], C_2N_2, by photoionization gave relative intensities of $C_2N_2^{+\cdot}$, C_2N^+, CN^+ and $C_2^{+\cdot}$ ions of 1.0 : 0.01 : 0.07 : 0.2, respectively, at 58.4 nm (21.23 eV). The C_2N^+ ion was noted to be immeasurably small and the CN^+ ion to be observed only over a short wavelength region near 60 nm (20.66 eV). In contrast, all of the positively charged ions from dicyanogen, including C_2N^+, were readily measured using the "monochromatic" electron source in this study and the negative ions C_2^-, CN^-, $C_2N_2^-$ were detected. The relatively high ionization cross-section for the formation of the CN^- ion facilitated the use of the monochromatic electron source and the determination of the translational energy of the ion over the resonance capture peak [9]. All of these methods are therefore complementary and no one technique leads directly to a complete picture.

EXPERIMENTAL

The low pressure monochromatic electron impact ion source and ion retarding lens system are illustrated in Fig. 1. The hemispherical electrostatic electron velocity analyser which serves as the electron energy monochromator has an electron track radius of 25 mm, a gap of 5 mm with entrance and exit apertures of 5 mm × 0.5 mm. These dimensions were selected to yield symmetrical electron energy distributions with a theoretical width of ~ 35 meV at half maximum [10,11]. The hemispheres were machined from phosphor-bronze and polished to a tolerance of better than 2.5×10^{-3} mm on the radius, better than 1 part in 10^4, gold-plated and coated with aquadag (colloidal graphite). They were mounted on to a 10 mm thick stainless steel support plate with 3 mm precision sapphire balls and clamped into place. The stainless steel support also carried the electron beam entrance and exit apertures, an enclosed filament assembly, the monochromatic electron beam acceleration/deceleration lenses and a mu-metal shield to isolate the electron gun from stray electro-magnetic fields. All of the elements on the electron beam track were coated with aquadag and sooted over a fuel rich benzene flame in order to minimise surface scattering. The monochromator is biased positive with respect to the cathode, the reference bias, and the voltage on each hemisphere adjusted for maximum transmission of a beam with a nominal electron energy equal to the reference bias selected. The maximum electron transmission is always obtained when the inner and outer hemi-

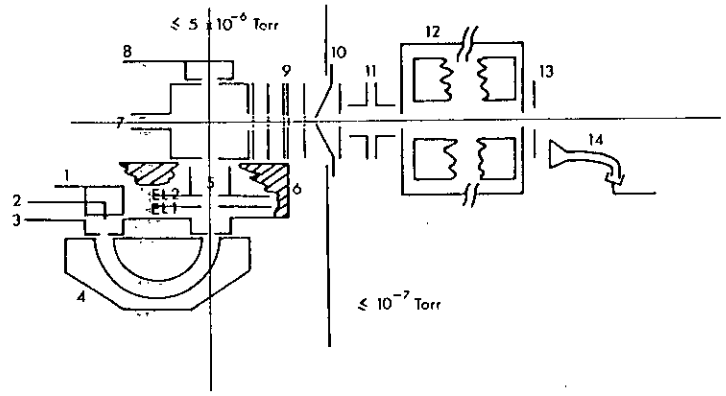

Fig. 1. Instrument layout. 1, Filament enclosure; 2, barium zirconate-coated rhenium filament; 3, monochromator support and voltage reference; 4, hemispherical electrostatic electron monochromator; 5, electron beam focussing lens assembly; 6, partial view of magnetic field shield; 7, collision chamber and gas inlet; 8, electron collector; 9, ion withdrawal and focussing lens assembly; 10, ion beam retarding element; 11, ion beam lens; 12, quadrupole mass filter; 13, ion focus element; 14, ion counting channeltron.

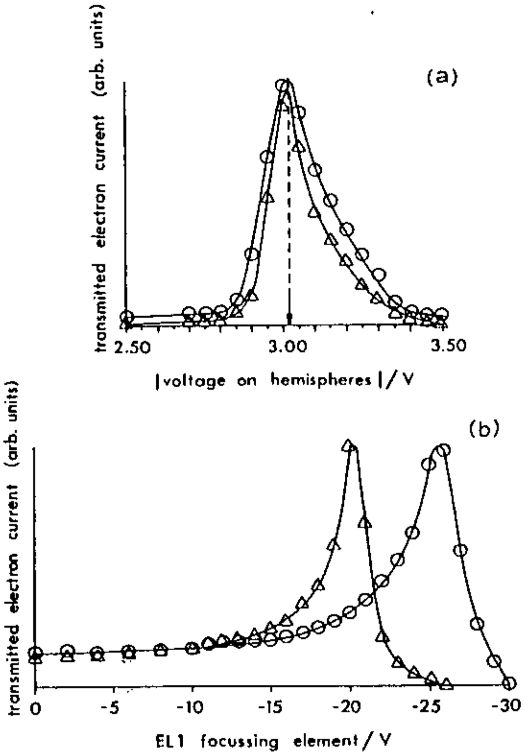

Fig. 2. Characteristics of the "monochromatic" electron gun. (a) Effect of independent variation of the hemisphere potential on the transmitted electron beam for an electron energy of 16.00 eV and initially optimised hemisphere potentials of ±3.02 V. ○, Variation of the outer hemisphere with the inner hemisphere fixed at +3.02 V; △, the variation of the inner hemisphere with the outer hemisphere fixed at −3.02 V. (b) Focussing characteristics of the electron lens element EL1 with EL2 held at the monochromator reference potential. ○, 23.00 eV beam; △, 20.00 eV beam.

spheres are of equal and opposite polarities, inner hemisphere positive and outer hemisphere negative, with respect to the monochromator reference bias (electron energy). The effect of varying the voltage applied to the hemispheres from the optimum value is shown in Fig. 2(a). These data were recorded for an electron beam energy of 16.00 eV with maximum beam transmission for hemisphere potentials of ±3.02 V with respect to this reference (+19.02, −12.98 V with respect to the cathode). The monochromator exit aperture and the second electron lens element, EL2 in Fig. 1, are maintained at the reference bias and EL1 is used to focus the beam into the collision chamber. The focussing characteristics of EL1, which acts as a convex lens, are shown in Fig. 2(b) for electron beam energies of 20.00 and 23.00 eV. Operation of the electron gun involves manual tuning of the monochromator for maximum transmission of an electron beam with a preselected electron energy. This beam is then accelerated or decelerated in small steps over a 2–3 V range by computer control of the bias between EL2 and the collision chamber. The electron beam current, which is typically in the range 1–10 nA for a filament emission of 10–100 μA, is regulated throughout data collection by a feedback loop to the filament current circuit.

The electron energy distribution was measured by retardation of the electron beam at the collision chamber and the full width at half maximum found to be 50–60 meV. Ionization efficiency curves collected by acceleration and deceleration of the electron beam were superimposable, indicating that significant degradation of the electron energy distribution does not occur over the acceleration–deceleration range of 3 eV usually employed. Positive ions created by electron impact in the collision chamber are accelerated into the ion lens assembly with an extractor biased at −1 V with respect to the collision chamber potential and ions transmitted by the quadrupole mass filter [43] are counted for a period of 10–45 s depending on the ionization cross-section. The accumulated ion count is stored in the system computer and the electron energy advanced or retarded as selected. Ionization efficiency data were collected for electron energy steps of 0.04 and 0.08 eV and each ionization efficiency curve was repeated between 5 and 10 times with a reproducibility of ±0.08 eV on the first threshold. The background ion count rate using an off-axis Galileo type 4816 pulse counting channeltron operating with a gain of 10^6 at a pressure of 3×10^{-7} Torr was better than 0.2 c.p.s. Ionization efficiency curves for CO^+, Ar^+ and Ne^+ measured simultaneously are shown in Fig. 3. The differences between the thresholds, marked with arrows in the figure, are within 0.04 eV of the spectroscopic values for CO^+ and Ar^+ and better than 0.08 eV between CO^+ and Ne^+, despite an absolute difference of 7.55 eV between their respective thresholds.

The ion lens assembly, labelled 9 in Fig. 1, may be used as an ion beam retarding lens in which ions from the collision chamber enter an equipotential region defined by the two elements sandwiching the double grid retarding element, as described by Locht and Schopman [12]. The poor transmission properties of this retarding ion beam arrangement have been noted by Locht and Schopman who report that counting times up to 72 h are required for retarding curves close to the threshold. The inclusion of a conical retarding element (Fig. 1) with the preceding elements used as an ion lens led to a large enhancement in the ion signal and retarding curves were indistinguishable in shape from those obtained using the double grid plane lens arrangement. The first element of the einzel lens following the conical ion beam retarding element was operated at a potential close to that on the collision chamber (the retarding element potential reference) to minimize

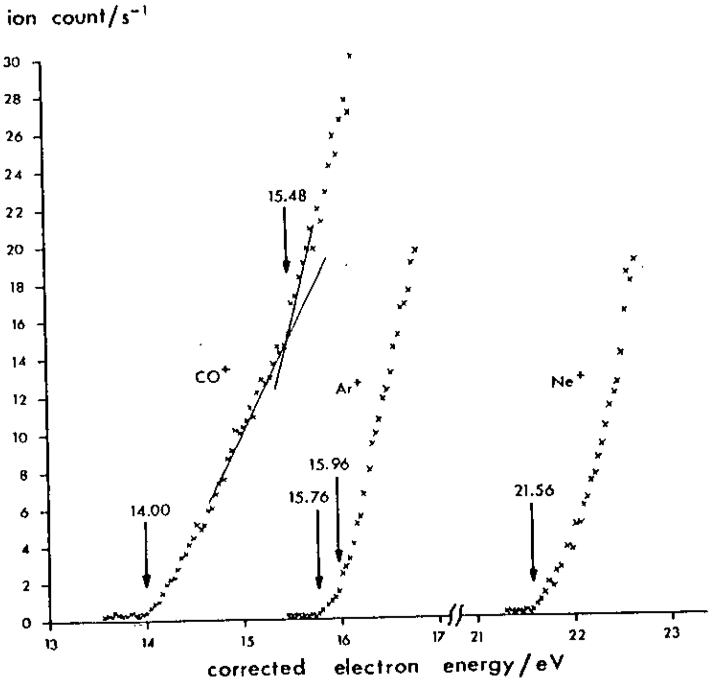

Fig. 3. Typical ionization efficiency curves measured for the three electron energy scale calibrants CO^+/CO, Ar^+/Ar and Ne^+/Ne. The vertical arrows point to the $CO^+(X^2\Sigma^+)$ threshold at 14.01 eV and the autoionizing level at 15.48 eV, to the spin-orbit states of $Ar^+(^2P_{3/2})$ at 15.76 eV and $(^2P_{1/2})$ at 15.96 eV and to the Ne^+ (^2P) threshold at 21.56 eV.

stray field effects. The resultant ion stopping curves and their differentials, produced automatically using a differential op-amp, were recorded simultaneously in real time on a multichannel UV recorder. The differentiated retarding curve for the O^+ ion formed from O_2 by 60 eV electron impact is compared with the data of Locht and Schopman [12] in Fig. 4. The retarding potential corresponding to the peak maxima are in good agreement with the values reported earlier with the addition of a peak at 3.5 V, which has not been previously reported. The retarding curve for the O_2^+ ion is also shown in Fig. 4 on an expanded scale. The peak width at the half-maximum of 170 meV is determined largely by the potential gradients and space charge in the region of the electron beam. Variation of the weak ion extraction field has no effect on the shape of the distribution, although the retarding potential scale, V_R, shifts by the corresponding change in the extractor voltage. The zero in the retarding potential scale is taken to correspond to the maximum in the dI^+/dV_R curves for ions formed with zero excess energy, or thermal ions. This procedure corrects for contact potentials and provides a molecular

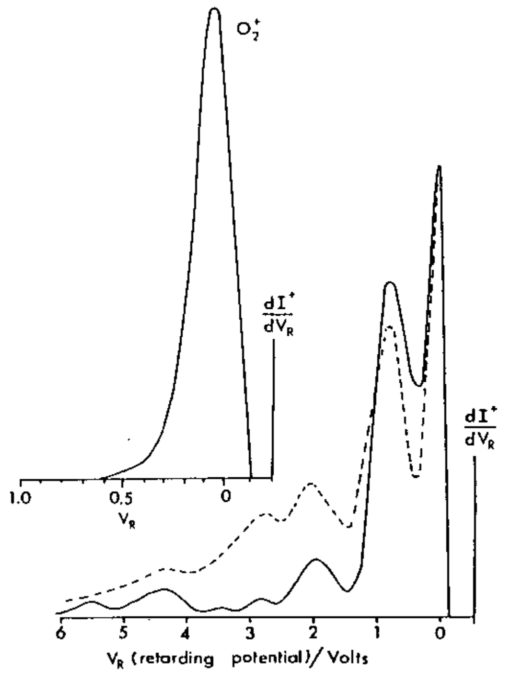

Fig. 4. Differentiated ion beam retarding curves (kinetic energy distributions) for O^+/O_2 and O_2^+/O_2. ———, This work; - - - - - -, data from ref. 12.

ion reference scale for the fragmentation products of each molecule studied. The differentiated retarding curves for O_2^+, N_2^+, H_2O^+, Ar^+, Ne^+, $C_2N_2^+$, CH_3CN^+ and CH_3NC^+ are all superimposable on the curve for O_2^+ shown in Fig. 4 and no scale adjustments are required for matching the peaks of these molecular ions run simultaneously from mixtures. The translational energy of ions at the ionization threshold was estimated from an extrapolation of measurements made over the electron energy range from 2 eV above the threshold to 70 eV. The kinetic energy distributions for the cyano ions were similar in shape to that shown for the O_2^+ molecular ion in Fig. 4. There was no complex structure and only a slight variation of translational energy with electron energy was evident. In contrast to dissociative resonance capture processes, where the total translational energy of the captured electron is distributed between the fragmentation products [13,14], positive ion formation involves the release of two electrons which are available to carry away excess energy. No attempts have been made to explore the possibility of internal excitation of the fragmentation products except that the enthalpy of formation for CNC^+ and CCN^+ from these separate source molecules would have shown inconsistencies had internal excitation been a significant factor.

MATERIALS USED

Dicyanogen, C_2N_2, was vacuum distilled from the Matheson technical grade and methyl nitrile, CH_3CN, was vacuum distilled from the British Drug Houses reagent grade. Methyl isonitrile, CH_3NC, was prepared from the reaction of *N*-methylformamide with *p*-toluene sulphonyl chloride in the presence of freshly distilled quinoline at 75°C under reduced pressure [15]. The crude product was collected in a dry ice–acetone trap followed by vacuum distillation on a high vacuum gas handling line and stored at liquid nitrogen temperature. The mass spectra of all three compounds were in good agreement with the literature [16,17]. All experiments were performed with collision chamber pressures of $\leqslant 5 \times 10^{-6}$ Torr.

RESULTS AND DISCUSSION

The electron impact ionization threshold or appearance energy, AE, for positive ion formation, process (1), is related to the enthalpies of formation of the parent molecule and the fragmentation products by the energy balance equation (2).

$$\begin{array}{l} AB + e^- \rightarrow (AB^+)^* + 2\,e^- \\ \qquad\qquad\quad \downarrow \\ \qquad\qquad (A^+ + B)^* \end{array} \tag{1}$$

$$AE(A^+) = \Delta H_f(A^+) + \Delta H_f(B) - \Delta H_f(AB) + E^* \tag{2}$$

$$E^* = E_{tr} + E_{int} \tag{3}$$

The excess energy involved in the process at the threshold, E^*, is the sum of the translational and internal energy terms given by Eq. (3). The total translational energy, E_{tr}, is related to the translational energy of the ion at threshold, $E_{tr}(A^+)$, by the principle of conservation of momentum in Eq. (4).

$$E_{tr} = \{[m(A^+) + m(B)]/m(B)\}\, E_{tr}(A^+) \tag{4}$$

$AE(A^+)$ is measured directly in these experiments and $E_{tr}(A^+)$ is the value of the translational energy of the ion at the threshold. There is no simple conservation of momentum principle for the case of the multiple fragmentation process (5).

$$\begin{array}{l} ABC + e^- \rightarrow (ABC^+)^* + 2\,e^- \\ \qquad\qquad\quad\;\; \downarrow \\ \qquad\qquad\; A^+ + B + C \end{array} \tag{5}$$

TABLE 1

Appearance energy data for C_2N_2, CH_3CN and CH_3NC

Molecule	Ion	AE (eV)	Literature		Method [a]
			AE (eV)	Ref.	
C_2N_2	C_2N^+	18.84 ± 0.05	19.5 ± 0.1	17	b, d, e, g
		19.92 ± 0.10	19.5 ± 0.3	32	b, d, e, h
CH_3CN	C_2N^+	20.00 ± 0.08	–		
	$HC_2N^{+\cdot}$	15.90 ± 0.08	15.7 ± 0.1	33	b, d, e, h
			15.1 ± 0.1	33	b, d, e, h
			15.1 ± 0.1	34	c, e
	$H_2C_2N^+$	14.38 ± 0.04	14.30 ± 0.02	33	b, d, e, h
			14.47 ± 0.06	33	b, d, e, h
			14.72	16	b, e, h
			14.01 ± 0.02	34	c, e
			14.28 ± 0.05	35	b, d, e
			13.54 ± 0.08	36	b, d, e
	$H_3C_2N^{+\cdot}$	12.38 ± 0.04	12.65	16	b, d, e, h
			12.205 ± 0.004	37	c, e
			12.46	37	a, e
			12.52 ± 0.02	33	b, d, e, h
			12.77 ± 0.03	33	b, d, e, h
			12.3 ± 0.25	22	b, d, e, h
CH_3NC	C_2N^+	18.33 ± 0.06	18.28	16	b, e, h
		19.46 ± 0.09			
	$HC_2N^{+\cdot}$	14.56 ± 0.08	14.46	16	b, e, h
	$H_2C_2N^+$	13.21 ± 0.04	13.21	16	b, e, h
	$H_3C_2N^{+\cdot}$	11.53 ± 0.04	11.24	39	c, e
			11.83	16	b, e, h
			11.32	38	a, e
			11.5 ± 0.25	22	b, d, e, h

[a] Method key: a, photoelectron spectroscopy; b, electron impact ionization; c, photoionization; d, broad electron energy distribution; e, kinetic energy of the ion assumed to be zero; f, analysis by the extrapolated voltage difference method; g, semi-log plot analysis; h, extrapolation of ionization efficiency curve to zero signal.

Process (5) could also be written in terms of the two-step processes shown in (6).

$$\begin{tikzcd}[column sep=small]
ABC + e^- \arrow[r] & (ABC^+)^* \arrow[dl] \arrow[dr] & + 2\,e^- \\
(AB^+)^* + C \arrow[d] & & (AC^+)^* + B \arrow[d] \\
A^+ + B & & A^+ + C
\end{tikzcd} \qquad (6)$$

TABLE 2

Enthalpies of formation for H_xCCN^+ and H_xCNC^+ for $x = 0$–3

Isomer	ΔH_f [a] (kJ mol^{-1})
CNC^+	1620 ± 11
CCN^+	1726 ± 12
$HCNC^+$	1554 ± 9
$HCCN^+$	1622 ± 9
H_2CNC^+	1206 ± 5
H_2CCN^+	1257 ± 5
H_3CNC^+	1261 ± 5
H_3CCN^+	1282 ± 5

[a] Uncertainties refer to standard deviations and reflect the reproducibility.

The distribution of excess energy in the form of internal excitation and relative translational motion of the fragmentation products may well depend upon the fragmentation mechanism. Since this cannot be determined, the conservation of linear momentum principle has been applied in this study to the two multifragmentation processes where excess translational energy was found; C_2N^+/CH_3CN and C_2N^+/CH_3NC, giving a lower limit to the total translational energy deduced for these processes.

The appearance energies measured in this study are compared with literature values in Table 1 and the enthalpies of formation derived for the structural isomers H_xCNC^+ and H_xCCN^+ are listed in Table 2.

C_2N^+ ($m/z = 38$) from C_2N_2, CH_3CN and CH_3NC

Molecular orbital calculations by Haese and Woods [18] on the structural isomers of C_2N^+ gave standard enthalpies of formation of 1556 ± 84 and 1761 ± 105 kJ mol^{-1} for the CNC^+ and CCN^+ isomers, respectively, with an isomerization barrier of 272 kJ mol^{-1} above the metastable CCN^+ state. The high activation barrier to isomerization suggests that, once formed, the isomers will retain their original identity and exhibit distinct kinetic properties. Haese and Woods noted that the appearance energy for the C_2N^+ ion from C_2N_2, reported by Franklin and co-workers [17] to be 19.5 ± 0.1 eV, gave an enthalpy of formation for the assumed CCN^+ isomeric form of 1720 ± 17 kJ mol^{-1}, in good agreement with their calculations. They also suggested that the reaction of C^+ ions with HCN and HNC would produce the CNC^+ and CCN^+ isomers according to the reactions

$$C^+ + HCN \rightarrow CNC^+ + H \tag{7}$$

$$C^+ + HNC \rightarrow NCC^+ + H \tag{8}$$

Two recent studies of the ion–molecule chemistry of C_2N^+ have been reported [19,20]. Schiff and Bohme [19] used reaction (7) in a SIFT study and McEwan et al. [20] employed electron impact on C_2N_2 "near" threshold in an ICR study where the identity of the isomer was assumed to be CCN^+. Differences in the products observed in the reaction of C_2N^+ with NH_3 were tentatively attributed in the ICR study to the effects of the different isomers, although it was concluded from the general agreement between the rate coefficients in the two studies that the isomers were of equivalent reactivity, contrary to the predictions of Haese and Woods who suggest that the more energetic carbene-like CCN^+ isomer may be considerably more reactive than the lower energy CNC^+ isomer.

Ionization efficiency curves for the C_2N^+ ion formed from C_2N_2, CH_3CN and CH_3NC are shown in Fig. 5. The appearance energy for the formation of the C_2N^+ ion from CH_3CN has not been reported previously (Table 1) probably due to the low ionization cross-section, which is approximately one third of that for C_2N^+ ion formation from CH_3NC. The ionization effi-

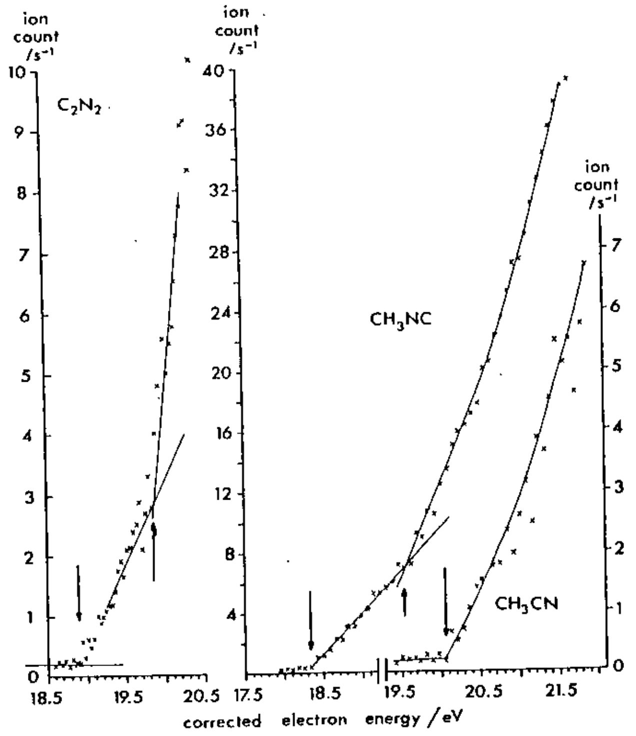

Fig. 5. Ionization efficiency curves for the C_2N^+ ion formed from C_2N_2, CH_3NC and CH_3CN.

ciency curve exhibits a single threshold at 20.00 ± 0.08 eV. The kinetic energy distribution for the C_2N^+ ion is broader than the CH_3CN^+ thermal ion distribution with the maximum displaced towards higher retarding potential. The integrated mean C_2N^+ ion translational energy extrapolated to the threshold is $\geqslant 5.6 \pm 1.0$ kJ mol^{-1}, giving a total excess energy of $\geqslant 76.3$ kJ mol^{-1}.

$$CH_3CN + e^- \rightarrow CCN^+ + H_2 + H + 2\,e^- \tag{9}$$

For ion formation according to process (9), the enthalpy of formation of the C_2N^+ ion is calculated to be $\leqslant 1724 \pm 9$ kJ mol^{-1}. The uncertainty associated with the calculated enthalpy limit is not the error but the standard deviation over 6 repeated determinations of the appearance energy and 5 repeated determinations of the differentiated ion retarding curves. Assuming that the carbon–nitrogen skeletal structure of the CH_3CN molecule is preserved in the ionization process, this value of the enthalpy of formation would correspond to the CCN^+ isomer, in good agreement with the value of 1761 ± 105 kJ mol^{-1} calculated by Haese and Woods [18].

The ionization efficiency curve for C_2N^+ ion formation from CH_3NC exhibits a threshold at 18.33 ± 0.06 eV followed by a break at 19.46 ± 0.09 eV corresponding to a second appearance energy 109 kJ mol^{-1} above the first. The integrated mean C_2N^+ ion translational energy extrapolated to the appearance energy at 18.33 eV is $\geqslant 6.1 \pm 1.0$ kJ mol^{-1}, giving an enthalpy of formation of $\leqslant 1617 \pm 8$ kJ mol^{-1} for the C_2N^+ ion according to the process

$$CH_3NC + e^- \rightarrow CNC^+ + H_2 + H + 2\,e^- \tag{10}$$

This value for the enthalpy of formation of the C_2N^+ ion is 107 ± 17 kJ mol^{-1} lower than the value obtained from process (9) and falls within the limits calculated for the CNC^+ isomer, 1556 ± 84 kJ mol^{-1}, by Haese and Woods [18]. Agreement between the calculated and experimental enthalpy values tends to sustain the assumption that the C_2N^+ ion formed from CH_3CN and CH_3NC, at the first appearance energy, retains the C–N skeletal structure of the neutral molecules.

The difference between the two appearance energies for the C_2N^+ ion from CH_3NC is, within the respective experimental uncertainties, equal to the difference between the calculated enthalpies of formation for the two C_2N^+ isomers. Since there is insufficient energy available at the second appearance energy for the dissociation of the neutral H_2 fragmentation product, it seems likely that this second process corresponds to the formation of the higher energy CCN^+ isomer by a rearrangement mechanism, viz.

$$CH_3NC + e^- \rightarrow CCN^+ + H_2 + H + 2\,e^- \tag{11}$$

The enthalpy of formation of the CCN^+ isomer according to process (11) is $\leqslant 1726 \pm 12$ kJ mol^{-1}, cf. $\leqslant 1724 \pm 9$ kJ mol^{-1} for CCN^+/CH_3CN.

The formation of the C_2N^+ ion from dicyanogen was studied primarily to provide a cross-check on the enthalpy of formation of the CCN^+ isomer determined from the C_2N^+/CH_3CN appearance energy. Two previous studies had reported a single appearance energy at 19.5 eV (Table 1). The ionization efficiency curve measured in this study is shown in Fig. 5. The first appearance energy at 18.84 ± 0.05 eV is nearly 0.7 eV lower than the previously reported value and the break at 19.92 ± 0.10 eV is 0.4 eV higher. The kinetic energy distribution for the C_2N^+ ion is broader than the thermal $C_2N_2^+$ (and O_2^+, Fig. 4) distribution with an integrated mean translational energy of 8.7 ± 1.0 kJ mol^{-1} at the threshold. The only C_2N^+ fragmentation process involves the loss of a nitrogen atom, which gives an enthalpy of formation of 1622 ± 8 kJ mol^{-1} for the C_2N^+ ion. This value is very close to the value of 1617 ± 8 kJ mol^{-1} calculated for the CNC^+ isomer from process (10) and the separation between the two appearance energies, 104 ± 14 kJ mol^{-1}, is the same as that found for the C_2N^+/CH_3NC ionization efficiency curve, Fig. 5. Processes (12) and (13), corresponding to the appearance energies at 18.84 and 19.92 eV, respectively, would satisfy these observations and yield an enthalpy of formation of 1727 ± 13 kJ mol^{-1} for the CCN^+ isomer, cf. $\leqslant 1724 \pm 9$ kJ mol^{-1} for CCN^+/CH_3CN and $\leqslant 1726 \pm 12$ kJ mol^{-1} for CCN^+/CH_3NC.

$$C_2N_2 + e^- \rightarrow CNC^+ + N + 2\,e^- \tag{12}$$

$$C_2N_2 + e^- \rightarrow CCN^+ + N + 2\,e^- \tag{13}$$

This result for C_2N^+ ion formation from C_2N_2 was unexpected in light of the published appearance energy data and the rearrangement necessary to produce the CNC^+ isomer. The two earlier studies of C_2N_2 employed conventional electron impact ion sources and the fragmentation products were assumed to have no excess kinetic energy (Table 1). Compensation for the broad electron energy distributions were not made and the ionization efficiency curves were analysed by the semi-log plot method [17] and by an extrapolation of a curve-fitted ionization efficiency curve to zero cross-section [31]. The smearing of the true ionization efficiency curve by the high energy tail of the thermonically generated electron energy distribution would lead to an underestimation of the true threshold and the data analysis techniques employed are insensitive to low cross-section structure in the vicinity of the threshold. Extrapolation of the C_2N^+ ionization efficiency curves measured in this study from several eV above the break to the ion dark count level gave an "apparent" appearance energy of 19.6 eV, in good agreement with the earlier values of 19.5 ± 0.1 eV [17] and 19.5 ± 0.3 eV [31].

In the absence of kinetic energy data and assuming the exclusive formation of the CCN^+ isomer, an appearance energy at 19.6 eV gives an enthalpy of formation of 1728 kJ mol^{-1} for the CCN^+ isomer. The agreement between this value, the value determined in this study and that calculated by Haese and Woods [18] is fortuitous since it is based on incomplete data.

The formation of the lowest energy isomer, CNC^+, at the first appearance energy either requires a rearrangement in the transition state or the presence of the isodicyanogen molecule [21]. There is evidence for rearrangement ions in most mass spectra, e.g. $C_2H_x^+$ from CH_3SCH_3 where $x = 0–5$, although mass spectral scans are blind to rearrangements producing structural isomers. The possible existence of the isodicyanogen molecule, NCNC, has been considered by Haese and Woods [21]. Their calculations indicate that isodicyanogen would have a dipole moment of 4.7×10^{-30} C m and an isomerization energy of 58 kJ mol^{-1} for the process NCCN $\rightarrow$ NCNC. The difference between the zero point energies (NCCN–NCNC) was found to be dependent upon the basis set selected giving a range of values from 59 to -449 kJ mol^{-1}, cf. ΔH_f (NCCN) = 308.95 kJ mol^{-1} (Table 3). The existence of NCNC in the C_2N_2 samples used is not suggested, but the existence of the HNC and CH_3NC isomers and the low isomerization energy calculated for the dicyanogen–isodicyanogen rearrangement lends support to a mechanism in which the skeletal framework of the dicyanogen molecule may be rearranged in the ionization process.

The C_2N^+ ionization efficiency curves are reasonably linear within a few eV of the threshold. The relative slopes for the C_2N^+ curves from CH_3CN and C_2N_2 above and below the breaks have been used to provide a rough estimation for the relative isomeric populations 3–4 eV above the first appearance energy. These measurements provide an estimation of $\sim 30\%$ CNC^+ in C_2N_2 and $\sim 60\%$ CNC^+ in CH_3NC at 22 eV. The formation of the C_2N^+ ion from C_2N_2 "near" threshold should therefore yield a mixture of the two isomers weighted in favour of the CCN^+ species. Despite the low

TABLE 3

Enthalpy of formation data used from ref. 7

Species	ΔH_f (kJ/mol^{-1})
H	217.97
N	472.70
C_2N_2	308.95
CH_3CN	87.4
CH_3NC	149.0

ionization cross-section, CH_3CN would be the most appropriate choice as a source of CCN^+ ions for kinetic studies and the reaction of C^+ on HCN, process (7), would be the cleanest source of the CNC^+ isomer, as suggested by Haese and Woods [18].

$H_xC_2N^+$ from CH_3CN and CH_3NC

The hydrogen-containing ions $HC_2N^{+\cdot}$, $H_2C_2N^+$ and $H_3C_2N^{+\cdot}$ from both CH_3CN and CH_3NC gave single appearance energies (Table 1) with thermal energy at the threshold. The enthalpy of formation calculated for each ion type according to ionization processes (14)–(19) is dependent upon the precursor molecule, i.e. the carbon–nitrogen skeletal arrangement.

$$CH_3CN + e^- \rightarrow HCCN^{+\cdot} + H_2 + 2\,e^- \tag{14}$$

$$CH_3NC + e^- \rightarrow HCNC^{+\cdot} + H_2 + 2\,e^- \tag{15}$$

$$CH_3CN + e^- \rightarrow H_2CCN^+ + H + 2\,e^- \tag{16}$$

$$CH_3NC + e^- \rightarrow H_2CNC^+ + H + 2\,e^- \tag{17}$$

$$CH_3CN + e^- \rightarrow CH_3CN^{+\cdot} + 2\,e^- \tag{18}$$

$$CH_3NC + e^- \rightarrow CH_3NC^{+\cdot} + 2\,e^- \tag{19}$$

The data are consistent with non-interconverting H_xCCN^+ and H_xCNC^+ isomers with the enthalpies of formation shown in Table 2. Although the energy differences between the isomers of $H_2C_2N^+$ and of $HC_2N^{+\cdot}$ are less than for C_2N^+, there were no discernible breaks in the ionization efficiency curves of the H_2CNC^+ or $HCNC^{+\cdot}$ ions to suggest the onset of rearrangement channels to the higher energy isomeric forms. A study of the collisional-induced activation spectra of alkyl nitrile and isonitrile cations by Chess et al. [22] provided evidence for at least four stable isomers of the $H_3C_2N^{+\cdot}$ ion, including the radical cations $CH_3CN^{+\cdot}$ and $CH_3NC^{+\cdot}$. Estimates of the enthalpies of formation based on extrapolated ionization efficiency curves using a normal electron impact ion source gave values of 1276 ± 24 and 1259 ± 24 kJ mol^{-1} for the enthalpies of formation of the $CH_3CN^{+\cdot}$ and $CH_3NC^{+\cdot}$ ions, respectively, in good accord with the values of 1282 ± 4 and 1262 ± 4 kJ mol^{-1} reported here. The $H_2C_2N^+$ ion was also examined as a fragmentation product from the four stable, non-interconverting isomers of the radical cation $H_3C_2N^{+\cdot}$, i.e. $CH_3CN^{+\cdot}$, $CH_2CNH^{+\cdot}$, $CH_3NC^{+\cdot}$ and $CH_2NCH^{+\cdot}$. The collision-induced spectra were found to be independent of the $H_3C_2N^{+\cdot}$ isomer and a single cyclic structure for the $H_2C_2N^+$ ion was proposed. However, the appearance energy measurements determined in this work, and all the others listed in Table 1, provide evidence for two non-interconnecting isomers, possibly structures **I** and **II**,

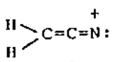

I

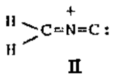

II

III

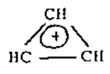

IV

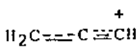

V

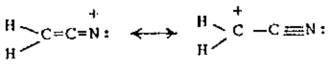

I **VI**

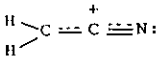

VII

which retain the carbon–nitrogen skeletal framework of the precursor molecule.

The isoelectronic cyclopropenyl ion, structure **IV**, is a highly stable species [23–26] which is considered to be the simplest case of a Huckel $(4n+2)$ electron system, where $n=0$. The ion is planar with the two electrons delocalised in the sp^2 hybridised carbon p-orbitals located above and below the ring plane. The resonance stabilisation energy conferred by delocalisation results in the enthalpy of formation, 1075 ± 15 kJ mol^{-1}, being 100 kJ mol^{-1} lower than that of the linear propargyl isomer, structure **V** [23,27,28]. Unlike the isoelectronic c-$C_3H_3^+$ ion, the $H_2C_2N^+$ ion also carries a pair of electrons on the nitrogen. The nitrogen may then be either sp^2 hybridised without participation of the resulting lone pair in the establishment of a pseudo-aromatic ring structure, or the nitrogen may be sp^3 hybridised to minimise the electron repulsive forces between the electrons on the nitrogen, in which case the vacant p-orbital would no longer be available to participate in a delocalised molecular orbital of an "aromatic" ring system. Any departure from pure sp^2 hybridisation would be a departure from the $(4n+2)$ requirement due to an increased electron density contribution from the two nitrogen electrons into the ring plane. This would consequently increase the enthalpy of formation of such a structure relative to the linear imine- and carbene-type structures shown as **I** and **II**. Structure **I** has been the subject of three theoretical studies to investigate the stabilization effect of the cyano group on the H_2CCN^+ carbonium ion [29–31]. These molecular orbital calculations suggest that the H_2CCN^+ ion is a stable entity existing in the resonance forms **I** and **VI**, which may be represented by structure **VII**.

This is presumably the species formed from electron impact on CH_3CN in this study.

Preliminary SCF calculations [40] of the structure and relative energies of the $C_2H_2N^+$ ions, using a double zeta Cartesian Gaussian basis set with polarization functions (DZP), suggest that the cyclic isomer would be the lowest energy structure followed by the linear isomers H_2CNC^+ and H_2CCN^+, 43 and 77 kJ mol^{-1} less stable, respectively. The energy difference between the more stable cyclic structure and the linear isomers is less than the corresponding difference for the cyclic and linear isomers of $C_3H_3^+$. The enthalpy difference between the two linear isomers determined from the appearance energy data, 51 ± 10 kJ mol^{-1}, compares reasonably well with the difference of 34 kJ mol^{-1} obtained from the calculations.

CONCLUSIONS

Thermochemical information, calculations of ion structure and data on the relative stabilities of structural isomers for ions in the gas phase form an important data base for the assessment of complex ion/molecule reaction schemes. Large uncertainties inherent in many of the earlier enthalpy of formation measurements for gaseous ions have been discussed above and illustrated by recent kinetic studies [41,42], which have shown that the previously accepted enthalpy of formation for the $C_3H_2^+$ ion was 117 kJ mol^{-1} too high. Near "monochromatic" electron impact or photoionization coupled with translational energy measurements can be used to obtain accurate enthalpy of formation data and to provide information on the existence of multiple isomeric ion forms, which can be further explored by molecular orbital calculations and kinetic studies.

ACKNOWLEDGEMENTS

P.W.H. would like to acknowledge the University Grants Committee and the New Zealand Lottery Board for the provision of research grants in support of this work.

REFERENCES

1 R. Hanel, B. Conrath, F.M. Flasar, V. Kunde, W. Maguire, J. Pearl, J. Pirraglia, R. Samuelson, L. Herath, M. Allison, D. Cruickshank, D. Grantier, P. Gierasch, L. Horn, R. Koppany and C. Pomamperuma, Science, 212 (1981) 192.
2 R.H. Gammon, Chem. Eng. News, 56 (1978) 20.
3 C.G. Freeman, P.W. Harland and M.J. McEwan, Astrophys. Lett., 19 (1978) 133.
4 E. Herbst and W. Klemperer, Astrophys. J., 185 (1973) 505.
5 W.T. Huntress, Jr. and V.G. Anicich, Astrophys. J., 208 (1976) 237.

46

6 J.L. Franklin and P.W. Harland, Ann. Rev. Phys. Chem., 25 (1974) 485.
7 H.M. Rosenstock, K. Draxl, B.W. Steiner and J.T. Heron, J. Phys. Chem. Ref. Data Suppl. 1, 6 (1977).
8 V.H. Dibeler and S.K. Liston, J. Chem. Phys., 47 (1967) 4548.
9 P.W. Harland and B.J. McIntosh, Aust. J. Chem., in press.
10 D. Roy and J.-D. Carette, Appl. Phys. Lett., 16 (1970) 413.
11 D. Roy and J.-D. Carette, J. Appl. Phys., 42 (1971) 3601.
12 R. Locht and J. Schopman, Int. J. Mass Spectrom. Ion Phys., 15 (1974) 361.
13 P.W. Harland, J.L. Franklin and D.E. Carter, J. Chem. Phys., 58 (1973) 1430.
14 P.W. Harland and J.L. Franklin , J. Chem. Phys., 61 (1974) 1621.
15 R.E. Schuster, J.E. Scott and J. Casanova, Jr., Org. Synth., 5 (1973) 772.
16 W. Heerma, J.J. de Ridder and G. Dijkstra, Org. Mass Spectrom., 2 (1969) 1103; 3 (1970) 1439.
17 V.H. Dibeler, R.M. Reese and J.L. Franklin, J. Am. Chem. Soc., 83 (1961) 1813.
18 N.N. Haese and R.C. Woods, Astrophys. J., 246 (1981) L51.
19 H.I. Schiff and D.K. Bohme, Astrophys. J., 232 (1979) 740.
20 M.J. McEwan, V.G. Anicich and W.T. Huntress, Jr., Int. J. Mass Spectrom. Ion Phys., 50 (1983) 179.
21 N.N. Haese and R.C. Woods, J. Chem. Phys., 73 (1980) 4521.
22 E.K. Chess, R.L. Lapp and M.L. Gross, Org. Mass Spectrom., 17 (1982) 475.
23 K. Raghavachari, R.A. Whiteside, J.A. Pople and P.v.R. Schleyer, J. Am. Chem. Soc., 103 (1981) 5649.
24 M.L. Gross, J. Am. Chem. Soc., 94 (1972) 3744.
25 T. McAllister and A.J.C. Nicholson, J. Chem. Soc. Faraday Trans. 1, 77 (1981) 821.
26 F.P. Lossing, Can. J. Chem., 50 (1972) 3973.
27 J.L. Holmes and F.P. Lossing, Can. J. Chem., 57 (1979) 249.
28 P.J. Ausloos and S.G. Lias, J. Am. Chem. Soc., 103 (1981) 6505.
29 D.A. Dixon, P.A. Charlier and P.G. Gassman, J. Am. Chem. Soc., 102 (1980) 3957.
30 J.B. Moffat, Chem. Phys. Lett., 76 (1980) 304.
31 M.N. Paddon-Row, C. Santiago and K.N. Houk, J. Am. Chem. Soc., 102 (1980) 6561.
32 O.I. Smith, Int. J. Mass Spectrom. Ion Processes, 54 (1983) 55.
33 C.A. McDowell and J.W. Warren, Trans. Faraday Soc., 48 (1952) 1084.
34 V.H. Dibeler and S.K. Liston, J. Chem. Phys., 48 (1968) 4765.
35 R.F. Pottie and F.P. Lossing, J. Am. Chem. Soc., 83 (1961) 4737.
36 J.L. Franklin, Y. Wada, P. Natalis and P.M. Hierl, J. Phys. Chem., 70 (1966) 2353.
37 K. Watanabe, T. Nakuyama and J. Mottl, J. Quant. Spectrosc. Radiat. Transfer, 2 (1962) 369.
38 L. Asbrink, W. Von Niessen and G. Bieri, J. Electron Spectrosc. Relat. Phenom., 21 (1980) 93.
39 R.F. Lake and H.W. Thompson, Spectrochim. Acta Part A, 27 (1971) 783.
40 R.G.A.R. Maclagan and P.W. Harland, to be published.
41 D. Smith, N.G. Adams and E.E. Ferguson, Int. J. Mass Spectrom. Ion Processes., 61 (1984) 15.
42 E.E. Ferguson, D. Smith and N.G. Adams, J. Chem. Phys., 81 (1984) 742.
43 Extranuclear Laboratories, Inc., Pittsburgh, PA, quadrupole mass filter Model 4-270-9.

Aust. J. Chem., 1985, **38**, 967–76

The Attachment of Low-Energy Electrons to Dicyanogen in the Gas Phase

Peter W. Harland[A] *and Bruce J. McIntosh*[A,B]

[A] Chemistry Department, University of Canterbury, Christchurch, New Zealand.
[B] Present address: Division of Chemical Physics, CSIRO, Clayton, Vic. 3168.

Abstract

The negative ions C^-, CN^- and C_2N^- formed by the dissociative resonance attachment of low-energy electrons to dicyanogen in the gas phase have been studied over the electron impact energy range from 0 to 15 eV. The formation of the CN^- ion was studied by using a 'monochromatic' electron gun and the translational energy of the ion measured as a function of the electron energy across the dissociative resonance capture curve. An energy balance analysis for CN^- ion formation has been used to propose the electron capture processes and to construct a potential energy diagram (for C–C internuclear separation) for CN^- ion formation. The molecular ion, $C_2N_2^{-\cdot}$, has been shown to result from the associative resonance attachment of thermalized electrons scattered from the collision chamber surfaces and to exhibit an autodetachment lifetime in the microsecond time-range.

Introduction

Studies of negative ion formation from dicyanogen, C_2N_2, by electron impact have been relatively few compared with the attention devoted to other small, stable molecules. The reasons for this are twofold. Dicyanogen is a 'dirty' gas which causes a rapid deterioration in the performance of the ion source and electrostatic lens assemblies as well as undergoing an efficient thermal decomposition process on the hot filament to produce metal carbides which ensure a short filament lifetime. Secondly, the attachment cross-section is very low and previous studies have only reported detection and measurements for the CN^- ion by resonance attachment under single collision conditions.[1–4] The CN^- resonance measured by using a broad electron energy distribution[1–3] exhibits an apparent threshold in the range 4·2–4·4 eV with a peak maximum at *c.* 6·0 eV and a long trailing edge to *c.* 10 eV. This broad electron capture peak was resolved into two distinct dissociative resonance peaks[4] in a study of the differential scattering of CN^-/C_2N_2 in a crossed electron–molecule experiment in which the CN^- ion translational energy distribution was measured as a function of the scattering angle and the electron impact energy. The primary negative ions

---

[1] McDowell, C. A., and Warren, J. W., *Trans. Faraday Soc.*, 1952, **48**, 1084.
[2] Craggs, J. D., McDowell, C. A., and Warren, J. W., *Trans. Faraday Soc.*, 1952, **48**, 1092.
[3] Inoue, M., *J. Chim. Phys. Phys.-Chim. Biol.*, 1966, **63**, 1061.
[4] Tronc, M., and Azria, R., *Chem. Phys. Lett.*, 1982, **85**, 345.

0004-9425/85/060967$02.00

C^-, CN^-, C_2N^- and $C_2N_2^{-\bullet}$ were detected in this study with the relative intensities 0·2, 100·0, 0·1, 0·1 at 70 eV, respectively. The dissociative resonance attachment curve for the CN^- ion was measured by means of a hemispherical electrostatic electron monochromator and the integrated mean translational energy of the ion was determined over the resonance by retardation of the negative ion beam. The low cross-section for the formation of the remaining negative ions below 15 eV precluded use of the 'monochromatic' electron source. The dissociative resonance attachment curves for the C_2N^- and C^- ions were measured by using a conventional magnetically constrained electron gun and the C_2N^- curve was deconvoluted to minimize the broadening effect of the electron energy distribution.

There has been renewed interest in the study of gas phase cyano ions and their chemistry[5–12] following the recognition that cyano compounds and their ions play an important role in the chemistry of planetary atmospheres and interstellar molecular synthesis.[13–15] The contribution, if any, of negative cyano ions in these environments has not yet been explored, although the corresponding positive ions have been shown to play an important role in molecular synthesis.

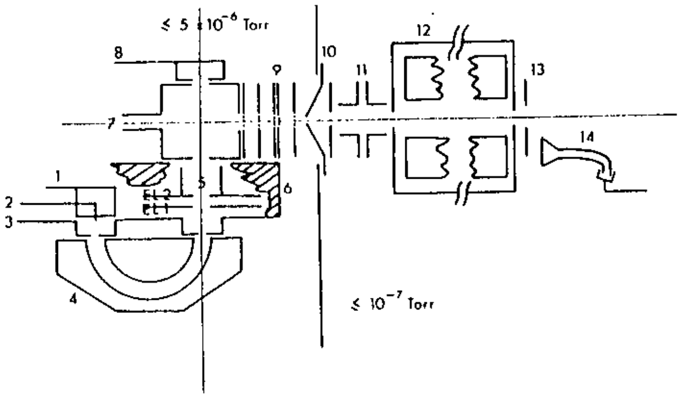

Fig. 1. Instrument layout. **1**, Filament enclosure; **2**, barium zirconate coated rhenium filament; **3**, monochromator support and voltage reference; **4**, hemispherical electrostatic electron monochromator; **5**, electron beam focusing lens assembly; **6**, partial view of magnetic field shield; **7**, collision chamber and gas inlet; **8**, electron collector; **9**, ion withdrawal and focusing lens assembly; **10**, ion beam retarding element; **11**, ion beam lens; **12**, quadrupole mass filter; **13**, ion focus element; **14**, ion counting channeltron.

[5] Gammon, R. H., *Chem. Eng. News*, 1978, **56**, 20.

[6] Haese, N. N., and Woods, R. C., *J. Chem. Phys.*, 1980, **73**, 4521.

[7] Haese, N. N., and Woods, P. C., *Astrophys. J.*, 1981, **246**, L51.

[8] Schiff, H. I., and Bohme, D. K., *Astrophys. J.*, 1979, **232**, 740.

[9] Freeman, C. G., Harland, P. W., and McEwan, M. J., *Astrophys. Lett.*, 1978, **19**, 133.

[10] McEwan, M. J., Anicich, V. G., and Huntress, W. T., Jr, *Int. J. Mass Spectrom. Ion Phys.*, 1983, **50**, 179.

[11] Harland, P. W., and McIntosh, B. J., *Int. J. Mass Spectrom. Ion Procs*, 1984, **57**, 283.

[12] Harland, P. W., and McIntosh, B. J., *Int. J. Mass Spectrom. Ion Procs*, in press.

[13] Herbst, E., and Klemperer, W., *Astrophys. J.*, 1973, **185**, 505.

[14] Huntress, W. T., Jr, and Anicich, V. G., *Astrophys. J.*, 1976, **208**, 237.

[15] Hanel, R., Conrath, B., Flasar, F. M., Kunde, V., Maguire, W., Pearl, J., Pirraglia, J., Samuelson, R., Herath, L., Allison, M., Cruickshank, D., Grantier, D., Gierasch, P., Horn, L., Koppany, R., and Pomamperuma, C., *Science*, 1981, **212**, 192.

Experimental

The low pressure 'monochromatic' electron impact ion source and ion retarding lens system illustrated in Fig. 1 have been described in detail previously.[12] A rhenium ribbon filamant coated with barium zirconate,[16] to reduce the operating temperature and to minimize chemical attack, proved satisfactory for the study of dicyanogen delivering small (c. 60 μA) but reasonably stable emission currents. The lowest collision-chamber pressure consistent with measurable ion signals was used to optimize the filament lifetime to several days, typically $<5\times10^{-6}$ Torr ($<7\times10^{-4}$ Pa). Exposure of an untreated rhenium filament to C_2N_2 under these conditions gave a rapidly declining emission current and a filament lifetime of an hour or so. The quadrupole mass filter, Extranuclear 4-270-9, and the off-axis ion counting channeltron were housed in a separate differentially pumped vacuum chamber maintained at a working pressure of $<1\times10^{-7}$ Torr ($<1\times10^{-5}$ Pa). This minimized contact with the sample and allowed operation of the Galileo 4816 pulse-counting multiplier at a gain of 10^7 in the absence of excessive noise.

Dicyanogen was vacuum distilled from the Matheson technical grade and used without further purification.

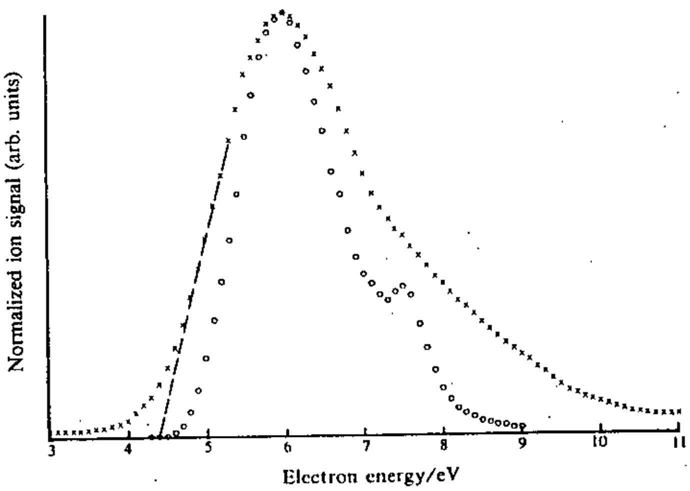

Fig. 2. Dissociative resonance attachment curve for the CN^- ion;
× conventional electron gun;
o 'monochromatic' electron gun.

Results

CN^- Ion

The dissociative resonance attachment curve for the CN^- ion measured with the 'monochromatic' electron gun and with the conventional electron gun are shown in Fig. 2 for comparison. The full width of the electron beam energy distribution at half-maximum ($W_{h/2}$) produced by the conventional electron gun is between 0·9 and 1·0 eV, compared to 0·12 eV for the 'monochromatic' electron gun operating below 10 eV. The broad CN^- ion capture curve is a composite of two overlapping curves with maxima at 6·0 and c. 7·5 eV and with thresholds at 4·5±0·1 and c. 7 eV, respectively. The electron energy scale was calibrated against the threshold at 4·2 eV and the maximum at 4·9 eV for the formation of the O^- ion from SO_2[17,18] which was measured simultaneously with the CN^- ion produced from a mixture of sulfur dioxide and dicyanogen. The integrated mean translational energy of the CN^- ion

[16] MacNair, D., *Rev. Sci. Instrum.*, 1967, **38**, 124.
[17] Kraus, K., *Z. Naturforsch.*, 1961, **16**, 1378.
[18] Harland, P. W., and Thynne, J. C. J., *J. Phys. Chem.*, 1970, **74**, 52.

across the resonance curve was determined by differentiation of the retarded negative ion beam as a function of electron impact energy[12] (Fig. 3), with CN^-/HCN serving as a thermal ion reference.

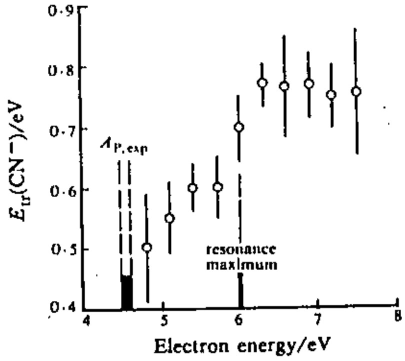

Fig. 3. Mean translational energy of the CN^- ion as a function of electron energy across the resonance peak.

The earlier mass spectrometric studies of CN^-/C_2N_2 in which conventional electron guns were used report a broad capture peak maximizing at *c.* 6 eV with a threshold at 4·4±0·2 eV,[1] 4·4 eV [2] and 4·4±0·25 eV.[3] Extrapolation of the leading edge of the CN^- resonance curve measured with the conventional electron gun in this study to zero ion signal also yields an appearance potential of 4·4 eV (Fig. 2). The threshold determined from the 'monochromatic' electron impact study is 4·5±0·1 eV. The smearing effect of the high-energy tail in the full electron energy distribution on the resonance curve in the threshold region is clearly evident in Fig. 2.

The mean translational energy of the CN^- ion at the threshold is 0·50±0·05 eV, in agreement with the value of 0·52 eV reported in the electron–molecule scattering experiment of Tronc and Azria.[4] The resonance maximum was reported to be 5·3 eV with a threshold at 4·0 eV (taken from Fig. 2 in ref.[4]), the O^-/CO resonance maximum at 10·04 eV being used as the electron energy scale calibrant. The advantage of using O^-/SO_2 is the close proximity of the O^- resonance to the CN^-/C_2N_2 resonance of interest; this minimizes the errors incurred by non-linear deviations in the energy scale with absolute electron beam energy.

Table 1. Enthalpy of formation data

From Rosenstock, H. M., Draxl, K., Steiner, B. W., and Heron, J. T., *J. Phys. Chem. Ref. Data*, 1977, **6**, Suppl. No. 1. Electron affinities used to calculate the negative ion enthalpy of formation values taken from Franklin, J. L., and Harland, P. W., *Annu. Rev. Phys. Chem.*, 1974, **25**, 485

Species	ΔH_f/kJ mol^{-1}	Species	ΔH_f/kJ mol^{-1}	Species	ΔH_f/kJ mol^{-1}
$C^\cdot$	716·68	$N^\cdot$	472·70	CN^-	66·4
C^-	598·03	$CN^\cdot$	435·1	C_2N_2	308·95

The minimum energy required for the formation of ground state fragmentation products, equation (1), is calculated from equation (2), by using the enthalpy data in Table 1, to be 1·99 eV.

$$C_2N_2(X^1\Sigma_g^+)+e^- \rightarrow CN^-(X^1\Sigma^+)+CN^\cdot(X^2\Sigma^+) \qquad (1)$$

$$A_{P,min} = \Delta H_f[CN^-(X^1\Sigma^+)]+\Delta H_f[CN^\cdot(X^2\Sigma^+)]-\Delta H_f(C_2N_2) \qquad (2)$$

This value for the appearance potential, $A_{P,min}$, assumes internally cold fragmentation products with zero recoil energy. Equation (2) is rewritten in terms of the experimental appearance potential, $A_{P,exp}$, by the addition of the excess energy term E^* in equation (3),

$$A_{P,exp} = \Delta H_f[CN^-(X^1\Sigma^+)] + \Delta H_f[CN^\bullet(X^2\Sigma^+)] - \Delta H_f(C_2N_2) + E^* \tag{3}$$

where E^* is the sum of the total translational energy of the fragmentation products, E_{tr}, and the total electronic, vibrational and rotational energy terms, E_{int}. The total excess energy partitioned into translational motion of the fragments at the CN^- threshold, E_{tr}, is calculated from the mean CN^- translational energy, $E_{tr}(CN^-)$, according to the conservation of linear momentum (4).

$$E_{tr} = \{[m(CN^-)+m(CN^\bullet)]/m(CN^\bullet)\}E_{tr}(CN^-) \tag{4}$$

where $m(CN^-)$ and $m(CN^\bullet)$ are the masses of the CN^- ion and the $CN^\bullet$ radical, respectively. Since $m(CN^-) \approx m(CN^\bullet)$ the total translational energy at the threshold is equal to $1{\cdot}0 \pm 0{\cdot}1$ eV. By taking $A_{P,exp}$ to be $4{\cdot}5 \pm 0{\cdot}1$ eV and E_{tr} $1{\cdot}0 \pm 0{\cdot}1$ eV, E_{int} is found from equation (3) to be $1{\cdot}50 \pm 0{\cdot}20$ eV. The internal excitation energy calculated from the threshold at 4·0 eV with the mean translational energy of 1·04 eV reported by Tronc and Azria[4] would be 0·97 eV. The C_2N_2 electronic ground state is ${}^1\Sigma_g^+$ for an electronic configuration .... $1\pi_u^4$, $1\pi_g^4$. The lowest vacant orbital available to accommodate the electron will be either $2\pi_u$ or $5\sigma_u$[19] to give a molecular negative ion in the ${}^2\Pi$ or ${}^2\Sigma$ states, respectively. Unlike the $C_2N_2{}^{-\bullet}({}^2\Sigma)$ state in equation (5) the $C_2N_2{}^{-\bullet}({}^2\Pi)$ state does not correlate with the $CN^-(X^1\Sigma^+)$ and $CN^\bullet(X^2\Sigma^+)$ electronic ground states and Tronc and Azria concluded that the first dissociative attachment resonance is a consequence of the dissociation of a $C_2N_2{}^{-\bullet}({}^2\Pi)$ shape resonance to the $CN^-(X^1\Sigma^+)$ ground state and the $CN^\bullet(A^2\Pi)$ excited state which lies 1·145 eV above the ground state (6).

$$C_2N_2(X^1\Sigma_g^+) + e^- \rightarrow C_2N_2{}^{-\bullet}({}^2\Sigma) \rightarrow CN^-(X^1\Sigma^+) + CN^\bullet(X^2\Sigma^+) \tag{5}$$

$$C_2N_2(X^1\Sigma_g^+) + e^- \rightarrow C_2N_2{}^{-\bullet}({}^2\Pi) \rightarrow CN^-(X^1\Sigma^+) + CN^\bullet(A^2\Pi) \tag{6}$$

This proposal can certainly be sustained from the excess energy available for internal excitation determined in this study, although it is doubtful whether this is so for the data of Tronc and Azria where the mean excess internal energy of $<1{\cdot}0$ eV is below the $CN^\bullet(A^2\Pi) \leftarrow CN^\bullet(X^2\Sigma^+)$ transition energy. Assuming experimental uncertainties allow for the difference, this energy balance would preclude any partitioning of excess energy into the rotational and vibrational states of the fragments. The second CN^- resonance was attributed to reaction (5) which would require E^* to be 5·0 eV at the threshold. Since the mean CN^- ion translational energy was also found to be 0·52 eV at 7·0 eV,[4] approximately 4 eV must be consigned to vibrational–rotational excitation of the fragments.

The distribution of excess energy amongst the internal degrees of freedom cannot be determined directly. However, the total energy available in the molecular ion transition state and its final distribution between the various degrees of freedom in the fragmentation products can be estimated by using a semiempirical relationship

---

[19] Bell, S., *Chem. Phys. Lett.*, 1979, 67, 498.

devised by Franklin *et al.*[20–22] from theoretical considerations.[23–25] Equation (7) relates the fraction of the excess energy, E^*, partitioned into translational motion of the fragments, E_{tr}, to the effective number of oscillators, N, available in the molecular ion transition state.

$$E^* = E_{tr}\alpha N \qquad (\alpha \leqslant 1) \tag{7}$$

N is the number of fundamental vibrational modes, $3n-5 = 7$ for the linear $C_2N_2^{-\bullet}$ ion, and α is an experimentally determined parameter which reduces N to an effective number of oscillators. The rate of change of the mean translational energy with total excess energy above the threshold can be used to determine the proportionality factor α, which is found to be 0·4, a typical value. E^* at the threshold is then calculated to be *c.* 2·8 eV from equation (7) of which 1·0±0·1 eV is partitioned into translational motion. The balance, *c.* 1·8 eV, is in good agreement with the internal energy of 1·5±0·2 eV deduced from equation (3) above. These deductions are consistent with the dissociative attachment process in which vibrotationally–translationally excited ground state fragmentation products follow electron capture at 4·5 eV according to (5).

The second resonance with a threshold at *c.* 7·0 eV may then correspond to the formation of the CN• radical in its first excited state (6). If the mean CN^- ion translational energy is taken as *c.* 0·75 eV at the second threshold, E_{tr} is 1·5 eV and E_{int} about 3·5 eV. If α is assumed to be 0·4 in equation (7), E^* is then *c.* 4·2 eV and the excess energy partitioned into the vibrational degrees of freedom is estimated to

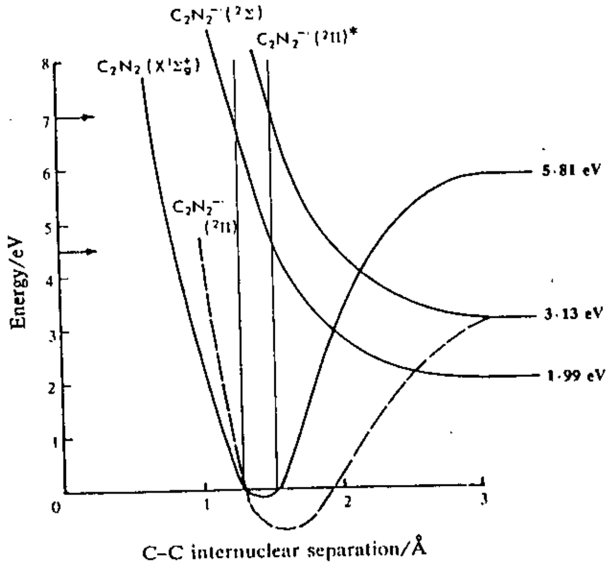

Fig. 4. Potential energy diagram for the C–C internuclear separation in C_2N_2 and $C_2N_2^{-\bullet}$. The Franck–Condon region is indicated by the vertical lines about the $v = 0$ level in the ground electronic state of C_2N_2.

---

[20] Haney, M. A., and Franklin, J. L., *J. Chem. Phys.*, 1968, **48**, 4093.
[21] Spotz, E. L., Seitz, W. A., and Franklin, J. L., *J. Chem. Phys.*, 1969, **51**, 5142.
[22] Harland, P. W., Franklin, J. L., and Carter, D. E., *J. Chem. Phys.*, 1973, **58**, 1430.
[23] Carter, D. E., Ph.D. Thesis, Rice University, Houston, Texas, 1977.
[24] Carter, D. E., *J. Chem. Phys.*, 1976, **65**, 2584.
[25] Klots, C. E., *J. Chem. Phys.*, 1964, **41**, 117.

be *c.* 2·7 eV. Considering the uncertainties in the threshold, the difference of 0·8 eV between the internal energy deduced from the experimental data and the calculated vibrational excitation energy, from equation (7), is in reasonable accord with the $CN^{\bullet}(A^2\Pi) \leftarrow CN^{\bullet}(X^2\Sigma^+)$ transition energy of 1·145 eV.

Considering these deductions and the detection of a long-lived $C_2N_2^{-\bullet}$ ion state the potential energy diagram shown in Fig. 4 has been constructed for the following sequence of attachment processes.

$$C_2N_2(X^1\Sigma_g^+)+e^-(c.\ 0\ eV) \rightleftharpoons C_2N_2^{-\bullet}(^2\Pi) \qquad (8)$$

$$C_2N_2(X^1\Sigma_g^+)+e^-(4\cdot5\ eV) \rightarrow C_2N_2^{-\bullet}(^2\Sigma) \rightarrow CN^-(X^1\Sigma^+)+CN^{\bullet}(X^2\Sigma^+) \qquad (9)$$

$$C_2N_2(X^1\Sigma_g^+)+e^-(c.\ 7\ eV) \rightarrow C_2N_2^{-\bullet}(^2\Pi)^* \rightarrow CN^-(X^1\Sigma^+)+CN^{\bullet}(A^2\Pi) \qquad (10)$$

C_2N^- *Ion*

The dissociative resonance attachment curve for the C_2N^- ion measured with the conventional electron gun is shown in Fig. 5. There are three main resonance peaks with maxima at 5·5, 7·0 and 8·6 eV with a shoulder at 10·8 eV which may be a further dissociative attachment process. The low cross-section for C_2N^- ion formation precluded data collection by means of the 'monochromatic' electron gun or the measurement of translational energies. An attempt was made to reduce the broadening effect of the electron energy distribution on the attachment curve by deconvolution of the experimental data according to the iterative method developed by Goursaud and Abouaf.[26] Analytical unfolding techniques have been used successfully for the deconvolution of negative ion resonance data, although their effectiveness diminishes as the width of the resonance curves exceed several times the $W_{h/2}$ of the electron energy distribution. Both the CN^- and C_2N^- resonance curves are broad and a com-

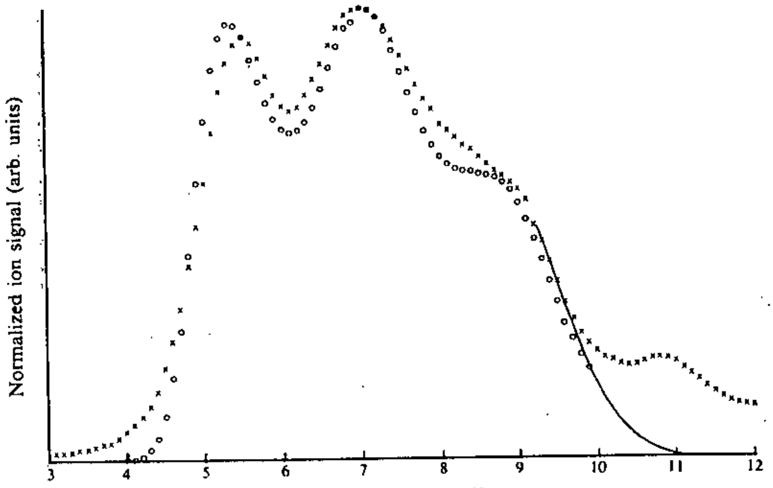

Fig. 5. Experimental (×) dissociative resonance attachment curve for the C_2N^- ion compared with the deconvoluted curve (o) after 20 smoothing and 20 unfolding iterations.

---

[26] Goursaud, S., and Abouaf, R., *Int. J. Mass Spectrom. Ion Phys.*, 1981, 40, 351.

parison between the deconvoluted CN^- resonance shown in Fig. 6 with the direct measurements by means of the 'monochromatic' electron source shown in Fig. 2 serve to illustrate the improvement to be expected from 20 smoothing and 20 deconvolution iterations. An increase in the number of iterative cycles above 20 caused divergence of the fit and the appearance of spurious bumps and excessive noise. There has been an improvement in the resolution of the resonance curves although the shift in the peak maxima along the electron energy scale in the course of the unfolding is a feature of this technique. The first threshold for C_2N^- ion formation is probably not too different from the CN^- threshold at 4·5±0·1 eV, which suggests a common molecular ion intermediate exhibiting multiple dissociation channels (11).

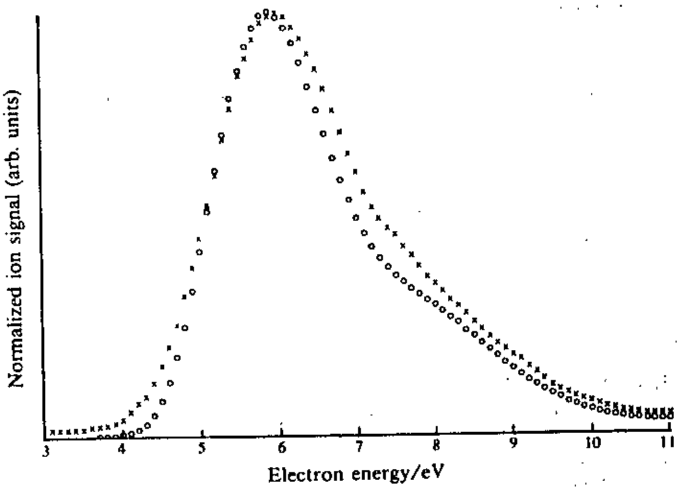

Fig. 6. Experimental (×) dissociative resonance attachment curve for the CN^- ion compared with the deconvoluted curve (○) after 20 smoothing and 20 unfolding operations.

$$C_2N_2(X^1\Sigma_g^+)+e^-(4\cdot 5\,\text{eV}) \rightarrow C_2N_2^{-\bullet}(^2\Sigma) \rightarrow \begin{cases} CN^-(X^1\Sigma^+)+CN^\bullet(X^2\Sigma^+) \\ C_2N^-+N^\bullet(^4S) \end{cases} \qquad (11)$$

In the absence of translational energy measurements the E^* term in the energy balance equation is unknown. However, the observation of the C_2N^- ion can be used to predict a lower limit to the electron affinity of the $C_2N^\bullet$ radical, $E_A(C_2N^\bullet)$, from equation (12).

$$E_A(C_2N^\bullet) \geqslant D(NCC \equiv N) - A_{P,\text{exp}}(C_2N^-) \qquad (12)$$

If the experimental appearance potential is taken as 4·5 eV and the C–N bond energy as 7·5 eV,[27] the electron affinity of the $C_2N^\bullet$ radical is deduced to be >3·0 eV. This value may be compared with values reported for other cyano species: $E_A(CN^\bullet) = 3\cdot 82\pm 0\cdot 02$ eV, $E_A(FCN) > 2\cdot 8\pm 1\cdot 7$ eV, $E_A(SCN^\bullet) = 3\cdot 51$ eV, 2·17 eV, and $E_A[C_2(CN)_4] = 2\cdot 88\pm 0\cdot 06$ eV.[28] The higher-energy resonances probably include the formation of the nitrogen atom in the (^2D) and (^2P) electronic states which lie 2·38 eV and 3·58 eV above the (^4S) ground state, respectively.

[27] Herzberg, G., 'Molecular Spectra and Molecular Structure. III. Electronic Spectra and Electronic Structure of Polyatomic Molecules' p. 615 (Van Nostrand-Reinhold: New York 1966).

[28] Franklin, J. L., and Harland, P. W., *Annu. Rev. Phys. Chem.*, 1974, **25**, 485.

$C_2N_2^{-\bullet}$ Ion

The molecular ion has been previously reported by Inoue[3] as the product of an ion–molecule reaction at elevated dicyanogen pressures. It was detected in this study under single collision conditions as a weak signal from 70 eV to <10 eV. Attempts made to detect an associative resonance attachment peak around 0 eV were unsuccessful, probably due to the deleterious effect of C_2N_2 on the electron and ion optics.

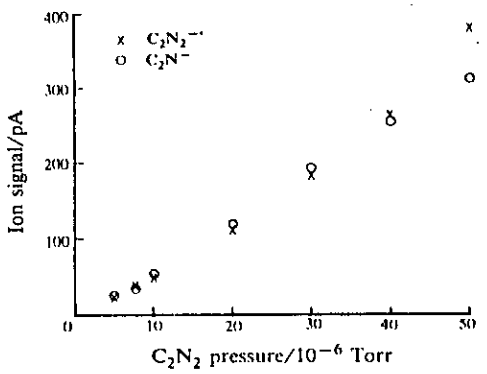

Fig. 7. Pressure dependence of the $C_2N_2^{-\bullet}$ and C_2N^- ion signals as a function of the dicyanogen pressure for 70 eV electron impact. An ion current of 400 pA is equivalent to an ion count rate of 250 s^{-1}.

Ultra-clean conditions and uniform electric fields are essential for the establishment of very-low-energy (<1·0 eV) electron beams and these conditions are incompatible with the study of dicyanogen. The SF_6^- attachment peak at 0 eV could not be established after exposure of the ion source to dicyanogen. The pressure dependence of the $C_2N_2^{-\bullet}$ signal at 70 eV was used to establish the mechanism for molecular ion formation. The $C_2N_2^{-\bullet}$ signal as a function of C_2N_2 pressure from 5×10^{-6} Torr to 5×10^{-5} Torr is plotted together with the C_2N^- ion signal in Fig. 7. The linear dependence of the ion signal with pressure indicates a primary electron capture process and is due to the associative capture of scattered, thermalized electrons in the collision chamber (13).

$$e^-(70\ \mathrm{eV}) \xrightarrow{\text{surface scattering}} e^-(\text{thermal})$$

$$e^-(\text{thermal}) + C_2N_2 \rightleftharpoons (C_2N_2^{-\bullet})^* \qquad (13)$$

The formation of $C_2N_2^{-\bullet}$ by secondary electron capture (14), collisional stabilization (15) or ion–molecule reaction would give rise to a quadratic or higher order pressure dependence and there is evidence for this at the higher pressure shown in Fig. 7, where the deviation of the $C_2N_2^{-\bullet}$ signal from linearity was reproducible.

$$C_2N_2 + e^-(>13\cdot3\ \mathrm{eV}) \rightarrow C_2N_2^{+} + 2e^-(\text{near thermal})$$

$$e^-(\text{near thermal}) \xrightarrow{\text{wall}} e^-(\text{thermal})$$

$$C_2N_2 + e^-(\text{thermal}) \rightleftharpoons (C_2N_2^{-\bullet})^* \qquad (14)$$

$$(C_2N_2^{-\bullet})^* + C_2N_2 \rightarrow C_2N_2^{-\bullet} + (C_2N_2)^* \qquad (15)$$

The autodetachment lifetime of the molecular ion must be in the microsecond time range to survive passage through the ion lens and quadrupole mass filter assemblies.

An SCFMO calculation in the INDO approximation[29,30] was carried out for the $C_2N_2^{-\bullet}$ ion. The minimum energy prediction is for a linear ion with the electron density distributed symmetrically about the centre of mass, each nitrogen atom carrying 0·45 e⁻ and each carbon atom 0·05 e⁻. This delocalization of the electron density must account for the stability of the ion.

C^- Ion

The C^- ion is formed by dissociative resonance attachment between 10·5 and 16 eV with a maximum cross-section at 13·4 eV. Either or both (16) and (17) with minimum energy requirements of 10·42 eV and 12·40 eV, respectively, may contribute to the observed signal:

$$C_2N_2 + e^- \rightarrow C^- + C + N_2 \qquad (16)$$

$$C_2N_2 + e^- \rightarrow C^- + CN^\bullet + N \qquad (17)$$

Acknowledgments

One of us, P.W.H., would like to acknolwledge the University Grants Committee and the New Zealand Lottery Board for the provision of research grants in support of this work.

Manuscript received 5 February 1985

---

[29] Pople, J. A., and Nesbit, R. K., *J. Chem. Phys.*, 1954, **22**, 57.
[30] Pople, J. A., Beveridge, D. L., and Dobash, D. A., *J. Chem. Phys.*, 1967, **47**, 2026.

Reprinted from The Journal of Physical Chemistry, 1986, 90, 944.
Copyright © 1986 by the American Chemical Society and reprinted by permission of the copyright owner.

Reaction of K Atoms with Oriented CF_3Br

Howard S. Carman,[†] Peter W. Harland,[‡] and Philip R. Brooks*

Department of Chemistry and Rice Quantum Institute, Rice University, Houston, Texas 77251
(Received: September 17, 1985)

A beam of oriented CF_3Br molecules is prepared by passing a randomly oriented beam through an appropriate series of inhomogeneous and homogeneous electric fields. An atomic K beam crosses the beam of oriented CF_3Br and the angular distribution of the reactively scattered KBr is measured with a differential surface ionization detector. The "heads" orientation (Br end closest to incoming K) is about threefold more reactive than the "tails" orientation. The KBr is scattered backward in the "heads" orientation and forward in the "tails" orientation, qualitatively consistent with a "harpoon" type of mechanism in which the orientation affects either the electron jump or the breakup of the dissociating negative ion.

Introduction

Proper orientation of reagents as a prerequisite for chemical reaction seems to be widely accepted on an intuitive level. Almost all theories of reaction rates include "steric factors" in one form or another.[1] However, a detailed understanding of these factors is still lacking. Experimentally, recent advances in molecular beam and laser technology[2] have made possible the direct observation of a variety of steric effects in several reactions.

Polarized laser radiation can be used to prepare beams of *polarized* molecules, which are molecules whose plane of rotation can be oriented with respect to a fixed axis. This technique has been applied, for example, to Sr + HF and "broadside" attack of the plane-of-rotation of HF is observed[3] to yield more SrF (J' = 2) than "edge-on attack", suggesting a bent minumum energy configuration. Similarly, polarized light has been used[4] to produce atoms in which excited p- or d-orbitals are directed parallel or perpendicular to the relative velocity. In the case of Ca + HCl, the direction of the Ca* p-orbital strongly influences the branching into two different CaCl* states.

Electrostatic deflection techniques have been used to prepare beams of *oriented* molecules,[2a,5] which are molecules whose figure axes precess around a space-fixed axis. One "end" of the molecule can be distinguished from another, and can be pointed toward (or away from) an incoming atom so that chemical reactivity can be studied as a function of orientation. Examples of reactions studied using this technique are O_3 reacting with oriented NO,[6] K reacting with CH_3I and CF_3I,[7] and Rb reacting with CH_3I.[8] The latter

TABLE I: Operating Conditions

distances, cm	
K oven–scattering center	12
nozzle–scattering center	70
scattering center–detector	5
nozzle–skimmer	2.6
field length	54
temp, K	
gas nozzle	308
K oven	623
K nozzle	673
nozzle backing pressure, torr	110
hexapole voltage, kV	12
homogeneous field strengths, V/cm	80

[†] Robert A. Welch Predoctoral Fellow.

[‡] Permanent Address: Chemistry Department, University of Canterbury, Christchurch, New Zealand.

(1) See, e.g.: Hammes, G. G. "Principles of Chemical Kinetics"; Academic Press: New York, 1978; Chapter 2.

(2) For recent reviews see: (a) Stolte, S. *Ber. Bunsenges. Phys. Chem.* **1982**, *86*, 413. (b) Leone, S. *Annu. Rev. Phys. Chem.* **1984**, *35*, 109.

(3) Karny, Z.; Estler, R. C.; Zare, R. N. *J. Chem. Phys.* **1978**, *69*, 5199.

(4) (a) Rettner, C. T.; Zare, R. N. *J. Chem. Phys.* **1981**, *75*, 3636. (b) Schmidt, H.; Weiss, P. S.; Mestdagh, J. M.; Covinsky, M. H.; Lee, Y. T. to be published.

(5) Brooks, P. R. *Science* **1976**, *193*, 11.

(6) (a) van den Ende, D.; Stolte, S. *Chem. Phys. Lett.* **1980**, *76*, 13. (b) van den Ende, D.; Stolte, S.; Cross, J. B.; Kwei, G. H.; Valentini, J. J. *J. Chem. Phys.* **1982**, *77*, 2206.

(7) Brooks, P. R.; McKillop, J.; Pippen, H. G. *Chem. Phys. Lett.* **1979**, *66*, 144 and references therein.

0022-3654/86/2090-0944$01.50/0 © 1986 American Chemical Society

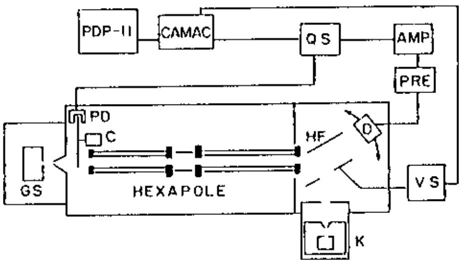

Figure 1. Schematic diagram of apparatus. GS, nozzle gas source; C, chopper; PD, photodiode assembly; HF, homogeneous orienting electric field plates; K, potassium atom source; D, detector; VS, voltage supply for homogeneous field; PRE, fast preamplifier; AMP, pulse amplifier/discriminator; QS, quad scalar. Relevant dimensions are given in Table I.

reaction has recently been probed in detail.

The CH_3I reactions are found to be qualitatively consistent with "chemical intuition": the alkali atom is most likely to react when the "heads" orientation (the I end) is approached, and for Rb + CH_3I, there is a sizable cone of no reaction[8] when the Rb approaches the "tails" end of the molecule. The product, MI, is scattered backward. In contrast, CF_3I appears[5] to be roughly equally reactive (to form KI) when K approaches in either the heads (I end) or tails (CF_3 end) orientations, but the products are backward scattered from the heads orientation and forward from the tails orientation. These observations are qualitatively consistent with an electron-jump model of reaction, and subsequent experiments on "sideways" orientations[7] have reinforced this interpretation.

The facility with which the electron is transferred to the oriented molecule is expected to depend on the electron affinity of the molecule. In order to assess the possible role played by the electron affinity, we have studied the reaction of K with oriented CF_3Br. This molecule has a smaller electron affinity[9] than CF_3I, and it was thought that a possible electron jump might be substantially different from CF_3I. We find a behavior somewhat intermediate between CF_3I and CH_3I.

Experimental Section

The apparatus is similar in concept to that used in previous investigations from this laboratory,[7] and is shown schematically in Figure 1. Relevant dimensions and operating parameters are shown in Table I.

Beams of CF_3Br and CF_3I are formed by supersonic expansion from a stainless steel oven with a 0.2-mm-diameter nozzle located in a separate cryopumped chamber. The beam is collimated with a 0.7-mm-diameter skimmer, modulated by a rotating wheel, and then enters an inhomogeneous hexapole electric field which transmits only molecules with negative values of $\langle \cos \theta \rangle$, where θ is the average classical angle between the dipole moment and electric field.[10] (Quantum mechanically, $\langle \cos \theta \rangle = MK/(J^2 + J)$.) The state-selected molecules then enter a region of uniform electric field created by two parallel plates tilted at an angle of 30° with respect to the CF_3Br velocity. The molecules make adiabatic transitions into this field where they are now oriented with respect to the relative velocity for K + CF_3Br collisions. (CF_3I was studied as a comparison and the field plates were not realigned to account for the different CF_3I speed, a correction of about 2°.) The direction of the molecule could be reversed by reversing the polarity of the uniform field.

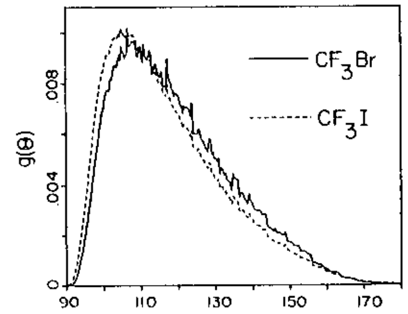

Figure 2. Distributions of orientation angles, θ, where θ is defined as arccos $(MK/(J^2 + J))$. Curves are smoothed quantum mechanical results. (See ref 11.)

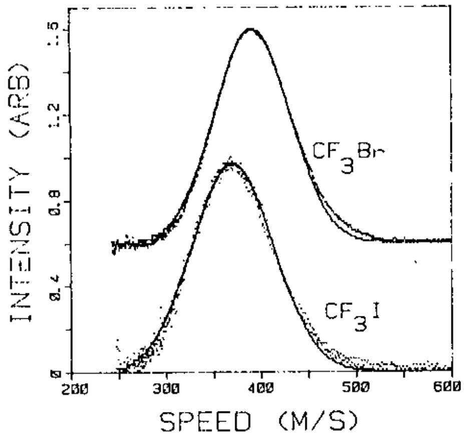

Figure 3. Experimental velocity distributions of supersonic CF_3X (X = I, Br) beams as measured by the time-of-flight technique. The solid curves are calculated by using eq 1 and temperatures of 29 and 45 K for CF_3Br and CF_3I, respectively.

The K beam was formed by effusion from a Monel oven and collimated with a 1-mm-diameter heated skimmer. The K beam passed through holes in the uniform field plates and intersected the CF_3Br (CF_3I) beam at right angles in the region of uniform electric field. Scattered K and KBr (KI) were detected by a surface ionization detector which rotated about the scattering center in the plane of the two beams. K and KBr (KI) were detected by ionization on a single crystal W wire. It was empirically determined that best results for ionization of KBr were obtained if the wire were operated at 1525 K, which is cooler than normally used for detection of KI (1775 K). Nonreactively scattered K atoms were detected on a 92% Pt-8% W alloy wire operated at 1500 K. The atomic ionization efficiencies of the two filaments were normalized by measuring scattering from beams of 1,1,1-trichloroethane and methanol which can be focused in the electric field but which are not reactive. The product KBr (KI) intensity was obtained as the difference between the count rate from the W filament and the count rate from the Pt filament (adjusted for different ionization efficiencies). The ions were detected by counting pulses from a Bendix Model 306 crossed-field multiplier. A PDP-11 computer collected the data and controlled the apparatus via a CAMAC interface.

---

[8] (a) Stolte, S.; Chakravorty, K. K.; Bernstein, R. B.; Parker, D. H. *Chem. Phys.* **1982**, *71*, 353. (b) Parker, D. H.; Chakravorty, K. K.; Bernstein, R. B. *Chem. Phys. Lett.* **1982**, *86*, 113. (c) Parker, D. H.; Chakravorty, K. K.; Bernstein, R. B. *J. Phys. Chem.* **1981**, *85*, 466 and references to earlier work listed therein.

[9] Compton, R. N.; Reinhardt, P. W.; Cooper, C. D. *J. Chem. Phys.* **1978**, *68*, 4360.

[10] The dipole moment is defined as pointing from the negative charge to the positive charge and the energy of interaction with an electric field is $W = -\mu\epsilon \cos \theta$ (Debye, P. "Polar Molecules"; Dover: New York, 1945). But regardless of the sign convention used for the dipole moment and $\cos \theta$, the state selected molecules will be oriented in the uniform field with their positive end toward the positive field plate since they are in states which increase in energy in an electric field. See ref 5 and: Bernstein, R. B. "Chemical Dynamics via Molecular Beam and Laser Techniques"; Oxford University Press: New York, 1982.

A distribution of orientations (all with negative[10] ⟨cos θ⟩) results from the state-selection process because the deflection in the field depends on both the rotational state and the speed of the molecules. Figure 2 shows distributions of θ for CF_3X (X = Br, I) which have been calculated[11] from the equations of motion through the field. These calculations require knowledge of the internal molecular temperature and the velocity distribution, so the velocity distribution was measured for the randomly oriented molecules incident on the hexapole field. For these measurements, the hexapole field was removed and the low-speed chopper was replaced with a 400-Hz wheel containing a narrow slit so that the beam could be pulsed and the velocity distribution measured by the time-of-flight technique. A small ionization gauge was used to detect the beam, and the pulses were averaged by using a Lecroy Model 2256A waveform digitizer. The velocity distributions are shown in Figure 3. The experimental distributions were fit to an expression of the form[12]

$$n(v) \propto \left(\frac{v}{v_s}\right)^2 e^{-[(v-v_s)/\alpha_s]^2} \qquad (1)$$

where $\alpha_s = (2kT_s/m)^{1/2}$. The hydrodynamic flow speed, v_s, and the translational temperature, T_s, (29 and 45 K for CF_3Br and CF_3I) were used as fitting parameters. The rotational temperature of the molecules is assumed equal to the translational temperature characterizing the velocity distribution.

Results

Laboratory angular distributions for scattering from CF_3Br and CF_3I are shown in Figure 4. The results from CF_3I are in qualitative agreement with those found previously in this laboratory[19] and are included only for comparison with the CF_3Br results. These data represent averages of data taken on several different days. The larger error bars at small angles arise from the subtraction procedure used to determine the KX signal. (The KBr signal at 40° was typically only ~7% of the total scattered flux, compared to ~70% at 90°.) These data were taken by using a focusing voltage of 12 kV and arise from the CF_3X orientations shown in Figure 2. The heads configuration is the distribution of orientations which result when the uniform field plate nearest the K beam is positive; the tails configuration is that which results when the polarity of the uniform field is reversed. As discussed below, heads refers to orientations in which the X atom (I or Br) is closest to the incoming K atom, and tails refers to orientations in which the CF_3 end is closest to the incoming K.

Figure 4 shows that an alkali halide molecule is formed in each reaction and that the angular distribution depends quite drastically on the orientation of the molecule. Unfortunately, two reaction products are possible in each case, KF and KX, and the surface ionization detector is unable to discriminate between the two possibilities. Nevertheless, we believe that each reaction proceeds to form KX (and not KF) for the following reasons:

(a) The C–F bond is stronger than either the C–I or C–Br bond (108 vs. 54 or 70 kcal/mol, respectively).[13] The classic Polanyi diffusion flame experiments[14a] showed no evidence of reactivity for the exothermic reaction of Na with CH_3F, and diffusion flame experiments on Na + CF_3X yielded[14b] mainly NaX with NaF formed only in secondary reactions with CF_3 radicals.

(b) Diffusion flame experiments from this laboratory[14c] on the K + CF_3I reaction showed that KI was the principal product and KF was formed in secondary reactions, and we concluded that K + CF_3I yields KI in either orientation of the molecule. Reactions with sideways oriented CF_3I molecules[7] (see Discussion) reinforce the conclusion that KI is the product.

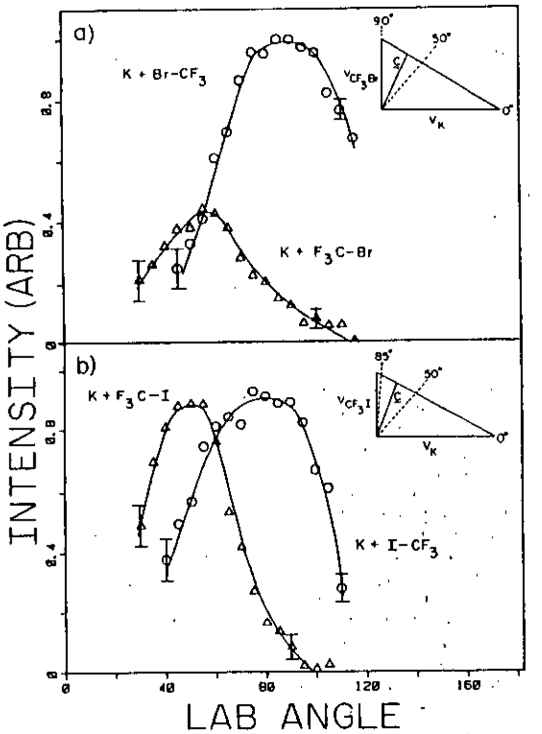

Figure 4. (a) Laboratory angular distribution of reactively scattered KBr from K + CF_3Br. (b) Laboratory angular distribution of reactively scattered KI from K + CF_3I. (○) heads orientation; (△) tails orientation. Smooth curves have been drawn through the points for clarity. Points shown are average values from several experiments. Representative error bars are drawn at small angles and at large angles. Inset nominal Newton diagrams show the lab angles where experimental intensity is maximum.

(c) The behavior of CF_3Br is similar to that for CF_3I, except that the "tails" configuration is less reactive. By analogy to the CF_3I case, we surmise that K + CF_3Br yields KBr in either orientation.

The hexapole electric field selects molecules in states for which the energy increases with applied field. In a uniform field the positive end of a state-selected molecule is thus closest to the positive field plate. The directions of the dipole moments of CF_3X are not known, but because of the high electron affinity of the F atom, we presume that the X ends of the molecules are positive. This assumption is consistent with the magnitude of the dipole moments[15] in various CF_3Y molecules. As Y is made more electropositive the dipole moment increases: μ = 0, 0.5, 0.65, 1.0, and 1.6 D for Y = F, Cl, Br, I, and H. Moreover, the reactive scattering itself strongly suggests that the positive end of CF_3X is the X end, since that end yields angular distributions which are strikingly similar to that from the I end of CH_3I. Our interpretation proceeds on the assumption that the positive end of each molecule is the X end.

The heads configuration for both molecules yields KX which peaks near 90° in the laboratory and which corresponds to backward scattering in the CM as shown by the nominal Newton diagrams in Figure 4. The tails orientation for both molecules yields KX which peaks near 50° in the laboratory and this corresponds to forward scattering in the CM. Unlike CF_3I, for which heads and tails seem to be roughly equally reactive, the heads end

---

[11] Strictly speaking, the distribution in Figure 2 is the distribution of molecules for which ⟨cos θ⟩ = $MK/J(J + 1)$, and is not the distribution of cos θ. This point is elaborated in ref 8a.

[12] Anderson, J. B. In "Molecular Beams and Low Density Gasdynamics"; Wegener, P. P., Ed.; Marcel-Dekker: New York, 1974.

[13] Benson, S. W. *J. Chem. Educ.* 1965, *42*, 502.

[14] (a) Polanyi, M. "Atomic Reactions"; Williams and Norgate: London 1932. (b) Reed, J. F.; Rabinovitch, B. J. *J. Am. Chem. Soc.* 1957, *61*, 598. (c) Hardee, J. R.; Brooks, P. R. *J. Phys. Chem.* 1977, *81*, 1031.

[15] Nelson, Jr., R. D.; Lide, Jr., D. R.; Maryott, A. A. "Selected Values of Electric Dipole Moments for Molecules in the Gas Phase"; *Nat'l Bur. Stand.* 1967, NSRDS-NBS10.

of CF_3Br is about threefold more reactive than the tails end.

Comparison of reactivity between CF_3Br and CF_3I was made on the basis of product count rate and crude flux measurements and also on the basis of stagnation pressures and the calculated hexapole field transmission. We roughly estimate the K + CF_3I reactive cross section to be about 1.5 times that for K + CF_3Br (17 Å^2 vs. 11 Å^2). This estimate for CF_3I agrees well with an earlier estimate of 15 Å^2 obtained from bulk gas-phase studies.[14c]

Discussion

The reactivity of both the molecules studied is very sensitive to the molecular orientation, especially considering that the nominal orientation, shown in Figure 2, is really rather poor. This point should be emphasized: even though the molecules are not perfectly oriented, reaction still occurs. This suggests that most reaction events do not proceed via collinear geometry, and this seems to be the case with the other oriented molecules studied. Certainly collinear reactivity in the heads orientation is quite likely, but since noncollinear orientations greatly outweigh the collinear, it is expected that most reactions will proceed through noncollinear collisions. (Collinear tails orientations have been shown[8] to be nonreactive in CH_3I.)

The angular distribution of reaction products from a *given* orientation in Figure 4 does not display symmetry about the CM and we conclude that long-lived complexes are not formed for either molecule in either configuration. Instead, when the X atom is nearest the incident K atom (heads), the product KX rebounds in the direction from whence the K came, and the KX is *backward* scattered and appears in the laboratory frame near 90° as is the case with heads (I end) scattering from CH_3I. Scattering from the tails orientation of either molecule, on the other hand, is forward scattered, and is *not* analogous to CH_3I.

This behavior can be rationalized on the basis of an impact parameter argument: for heads orientations the K may strike the X atom and product KX collide with the CF_3 moiety and rebound in the direction of the incident K atom. In the tails orientation, the molecule is not perfectly oriented and the obscuring CF_3 group may not completely shield the reactive site. Consequently, it can be expected that some trajectories incident at the CF_3 end may fly by the CF_3 group and strike the reactive X atom. Since the covalent radius of the I atom is larger[16] than that of the Br (1.33 Å vs. 1.14 Å), one might expect the Br to be more effectively shielded than the I and might expect the tails reactive cross section to be smaller than heads in CF_3Br, as is observed.

The Harpoon Mechanism. The electron-jump or "harpoon" mechanism was introduced[17] to explain the anomalously large cross sections for alkali metal–halogen reactions and has been extended[18] to cover other reactions as well. The features of the model can be qualitatively seen[18] by considering the interaction between an alkali atom M and a halogen atom X. At large distances the interaction is that between neutral species and can best be described in terms of a covalent potential energy surface. But the binding of MX is clearly ionic, so at distances corresponding to the stable molecule, the system can best be described in terms of an ionic potential surface. The hypothetical reaction between M and X thus proceeds at long range via a covalent interaction, but at some distance, r_c, the interaction switches to an ionic interaction, and M donates its valence electron (the "harpoon") to X. The Coulombic attraction between M^+ and X^- ensures reaction, so the cross section for reaction, σ_r, is approximately πr_c^2 where

$$e^2/r_c \simeq I(M) - E(X) \qquad (2)$$

where $I(M)$ is the ionization potential of M and $E(X)$ is the electron affinity of X.

For reaction with molecules the situation is a little more complicated. The surfaces for M–RX and $M^+(RX)^-$ must again cross, but the details will depend on the nature of the R group, and the appropriate electron affinity is the vertical electron affinity (evaluated at the bond distances which obtain when the electron jumps). The electron is expected to jump to the lowest unoccupied molecular orbital, which for many molecules is strongly antibonding. The molecular ion is thus likely to be formed in a repulsive state (or equivalently, high on the repulsive wall of a bound state) and the ion is expected to dissociate within one vibrational period in a manner strongly reminiscent of photodissociation.

In order to interpret our earlier results on the reactive scattering of oriented CF_3I we postulated[19] that an electron transfer occurred, leaving the CF_3I^- ion in a repulsive state. The ion was expected to decompose in much less than a rotational period, so the I^- ion was predicted to be ejected in the direction of the C–I bond which obtained at the instant of electron transfer. If the C–I bond were oriented such that the I were pointed toward (away from) the incoming K, the I^- ion would be ejected backward (forward) and the K^+ ion would be expected to follow. This correctly explains the observed backward scattering for the heads orientation and forward scattering for the tails orientation. This model also qualitatively predicted the drastic difference in angular distribution when the molecules were oriented sideways.[7] From the sideways scattering results we tentatively concluded that the *probability* of electron transfer and subsequent dissociation of the ion are independent of the orientation of the molecule, but the *direction* in which the product is ejected depends directly on the orientation.

CF_3Br exhibits both similarities and differences with respect to CF_3I. The electron affinity of CF_3Br is lower[9] (0.91 eV vs. 1.57 eV), and eq 2 predicts that the electron should jump at a shorter distance (4.2 vs. 5.2 Å), and πr_c^2 is 55 vs. 85 Å^2. The magnitudes of σ_r are only in rough agreement with our estimates for the reaction cross sections, 11 and 17 Å^2, but the ratios agree almost exactly. The KBr angular distributions from CF_3Br (backward for heads, forward for tails) are similar to that for KI from CF_3I and is in nice agreement with the notion that the molecular ion will dissociate in the direction in which it is pointing at the instant of the electron jump. But the forward, tails scattering is attenuated in the CF_3Br case, and this may result from several (presently indistinguishable) causes.

The probability of electron transfer (electron affinity) may be dependent on orientation. Even though the lowest unfilled orbital is mainly on the X atom, the electron is transferred to the entire molecule. At long range, as in the CF_3I case, the molecule may appear as an electron acceptor regardless of orientation. But at shorter range, as for CF_3Br, the electron transfer may be facilitated by having the Br closest to the incoming K, and reaction would thus be more probable in the heads orientation.

We should emphasize that the harpoon mechanism is a useful standard for comparison, but is a gross oversimplification for a very complicated process, especially at short range. Not only might the orientation affect the electron affinity, but also at close range the K^+ ion might affect the dissociation of the CF_3Br^-. Even if the electron affinity is not dependent on orientation, backside attack of the CF_3Br may result in a nonreactive event just because the K^+ cannot get by the CF_3 moiety in time to react.

Trajectory calculations[20] to model alkali metal (M)–halogen (XY) reactions found that the strong forward scattering associated with these reactions arose from charge migration, where an initial $M^+\cdots X^-$ interaction was followed by migration to yield M^+Y^- + X. In addition, the forward scattered products formed in such encounters were found to have enhanced translational energy. If charge migration were important here, backside attack of CF_3Br could give CF_3^-–Br followed by charge migration to Br and forward scattering of the KBr, which might be expected to recoil with higher energy than backscattered KBr from the heads orientation. The diminished forward scattered intensity experimentally observed in the LAB might thus result not only from a real dynamic effect, but also from a kinematic effect whereby

---

[16] Pauling, L. "The Nature of the Chemical Bond", 3rd ed.; Cornell University Press: Ithaca, NY, 1960.

[17] Magee, J. L. *J. Chem. Phys.* **1940**, *8*, 687.

[18] Herschbach, D. R. *Adv. Chem. Phys.* **1966**, *10*, 319.

[19] Brooks, P. R. *Faraday Discuss. Chem. Soc.* **1973**, *55*, 299.

[20] Kuntz, P. J.; Mok, M. H.; Polanyi, J. C. *J. Chem. Phys.* **1969**, *50*, 4623.

the CM cross sections for heads and tails scattering might be nearly equal, but the Jacobian factor $(u/v)^2$ in the CM → LAB transformation would favor a higher intensity in the lab for the slower backward scattered flux. Measurements on the product velocity distributions as functions of orientation may help to differentiate among these possibilities.

Acknowledgment. We gratefully acknowledge financial support of these experiments by the National Science Foundation and by the Robert A. Welch Foundation, and acknowledge a grant from the US–New Zealand Cooperative Science Program of the NSF for travel for P.W.H. P.R.B. thanks the Alexander von Humboldt Foundation for a Senior U.S. Scientist Award and Prof. J. P. Toennies and the members of the Max-Planck Institut für Strömungsforschung in Göttingen for their hospitality during the writing of this manuscript.

Registry No. K, 7440-09-7; CF_3Br, 75-63-8; KBr, 7758-02-3.

International Journal of Mass Spectrometry and Ion Processes, 70 (1986) 231–236 231
Elsevier Science Publishers B.V., Amsterdam – Printed in The Netherlands

Short Communication

APPEARANCE ENERGIES AND ENTHALPIES OF FORMATION FROM IONIZATION OF CYANOACETYLENE BY "MONOCHROMATIC" ELECTRON IMPACT

P.W HARLAND
Chemistry Department, University of Canterbury, Christchurch (New Zealand)

(Received 9 December 1985)

Cyanoacetylene, HC_3N, is a member of the HC_xN series of cyanopolyynes, where $x = 1, 3, 5, 7, 9$, which are of considerable interest as constituents of the dense interstellar cloud TMC-1 [1,2]. There are several recent reports of the ion/molecule chemistry of HC_3N^+, reactions involving HC_3N and possible mechanisms for its production and depletion in the interstellar environment [3–6]. Enthalpies of formation for several ionic fragmentation products of HC_3N reported in this work were employed in the selected ion flow tube studies of Knight et al. [3]. The only previous electron impact dissociative ionization studies of HC_3N were by Dibeler et al. [7] and Buchler and Vogt [8] using conventional electron impact ion sources.

EXPERIMENTAL

The low pressure monochromatic electron impact ion source used in this study, its performance characteristics and the measurement of ion translational energies have been previously described [9]. Briefly, a near monochromatic electron beam with a full width at half maximum energy distribution of 50–60 meV is produced using a hemispherical electrostatic monochromator. The electron beam is accelerated or decelerated into a collision chamber containing the sample at a pressure of $< 1 \times 10^{-6}$ Torr ($< 1 \times 10^{-4}$ Pa). Ion beam retarding curves are measured for each ion as a function of electron energy from 70 eV to within 1–2 eV of the threshold using a retarding lens assembly incorporating a conical retarding element. Ionization efficiency curves were measured in 40 or 80 meV steps, depending upon the ion count, using Ar^+, Ne^+ and He^+ as energy scale calibrants.

Cyanoacetylene, HC_3N, was prepared by the ammonolysis of methyl propiolate followed by dehydration of the amide product in xylene at 120°C under an atmosphere of dry nitrogen [10]. HC_3N polymerizes readily at

0168-1176/86/$03.50 © 1986 Elsevier Science Publishers B.V.

room temperature and was stored as dilute mixtures in Ar, Ne or He in the dark at liquid-N_2 temperature until used.

RESULTS

The experimental results are shown in Table 1 and a list of the enthalpies of formation calculated from the data are given in Table 2. The 70 eV, 0–60 u mass spectrum in Fig. 1 shows the doubly charged molecular ion peak at m/z 25.5 and the domination of the spectrum by C_3N^+ and $HC_3N^{+\cdot}$ at m/z 50 and 51, respectively.

The CN^+ ion is formed at 19.96 ± 0.08 eV with a mean translational energy of 48 meV. Assuming that the neutral fragmentation product is the $C_2H^\cdot$ radical, taking $\Delta H_f(CN^+)$ as 1794 kJ mol^{-1} [13] and $\Delta H_f(C_2H^\cdot)$ as 477 kJ mol^{-1} [14], then the enthalpy of formation of the cyanoacetylene molecule is calculated to be 354 kJ mol^{-1}.

The ionization efficiency curve for the C_2N^+ ion is shown in Fig. 2 with the ionization efficiency curve for Ne^+ which was used as an energy scale calibrant. An earlier study of C_2N^+ ion formation from C_2N_2, CH_3CN and CH_3NC [9] confirmed the theoretical prediction [15] that the C_2N^+ ion has two structural isomers, CNC^+ and CCN^+. The enthalpies of formation

TABLE 1

Appearance energies, AE, mean translational energies, E_{tr}, and ion formation mechanisms for electron impact ionization of HC_3N

m/z	Ion	AE (eV)	E_{tr} (meV)	Mechanism	AE(lit.) (eV)	
25	C_2H^+	18.84 ± 0.08	94	$C_2H^+ + CN^\cdot$	19.0 ± 0.2	[7]
					18.3	[8]
26	CN^+	19.96 ± 0.08	96	$CN^+ + C_2H^\cdot$	14.5 ± 0.5	[7]
					19.8 ± 0.2	[7]
37	C_3H^+	17.76 ± 0.08	~ 0	$C_3H^+ + N^\cdot$	18.0 ± 0.2	[7]
38	C_2N^+	(i) ~ 17.9		See text	(i) 18.0 ± 0.5	[7]
		(ii) 20.5 ± 0.10	157	$CCN^+ + CH^\cdot$		
		(iii) 23.1 ± 0.10		$CNC^+ + C + H^\cdot$		
		(iv) 24.0 ± 0.08		$CCN^+ + C + H^\cdot$	(ii) 24 ± 0.5	
50	C_3N^+	(i) 17.78 ± 0.08	~ 0	$C_3N^+ + H^\cdot$	18.2 ± 0.3	[7]
		(ii) 18.64 ± 0.08		$(C_3N^+)^* + H^\cdot$	17.7	[8]
51	$HC_3N^{+\cdot}$	11.56 ± 0.04	~ 0	$HC_3N^{+\cdot}$	11.6 ± 0.2	[7]
					11.62 ± 0.01	[10]
					11.6 ± 0.1	[11]
					11.6	[12]
25.5	HC_3N^{2+}	31.52 ± 0.15	~ 0	HC_3N^{2+}	32.3 ± 0.2	[7]

TABLE 2

Enthalpies of formation determined from the data in Table 1

Species	ΔH_f [a] (kJ mol^{-1})
C_2H^+	1728
C_3H^+	1598
C_2N^{+} [b] $\left.\right\}$ CNC^+	1620
CCN^+	1726
C_3N^{+} [b] $\left.\right\}$ C_3N^+ (1)	1850
C_3N^+ (2)	1935
$HC_3N^{+\cdot}$	1470
HC_3N^{2+}	3396
HC_3N	354

[a] Uncertainty better than ±15 kJ mol^{-1}.
[b] See text for discussion.

which were reported for these isomers [9] are given in Table 2. Using these values, $\Delta H_f(HC_3N) = 354$ kJ mol^{-1}, as determined above, and the literature enthalpy of formation values for C and $H^{\cdot}$ [13,14], the following minimum appearance energies are calculated for C_2N^+ ion formation processes from HC_3N

$$HC_3N + e^- \rightarrow CNC^+ + CH^{\cdot} + 2\,e^- \qquad AE = 19.3 \text{ eV} \tag{1}$$

$$HC_3N + e^- \rightarrow CCN^+ + CH^{\cdot} + 2\,e^- \qquad AE = 20.4 \text{ eV} \tag{2}$$

$$HC_3N + e^- \rightarrow CNC^+ + C + H^{\cdot} + 2\,e^- \qquad AE = 22.8 \text{ eV} \tag{3}$$

$$HC_3N + e^- \rightarrow CCN^+ + C + H^{\cdot} + 2\,e^- \qquad AE = 23.9 \text{ eV} \tag{4}$$

The experimental appearance energies at 20.40, 23.00 and 24.00 eV can be reconciled with processes (2), (3) and (4), respectively, providing support for the $\Delta H_f(C_2N^+)$ values reported in the previous study [9]. However, the experimental appearance energy for the low cross-section process at ~17.9 eV requires further consideration. It is possible that a threshold corresponding to ionization process (1) lies buried in the ionization efficiency data between 17.9 and 20.4 eV. It was noted that the threshold measured at ~17.9 eV varied up to ±0.2 eV from sample to sample and a mass spectral scan showed small ion signals for m/z 48 (C_4^+), 60 (C_5^+), 62 (C_4N^+), 72 (C_6^+), 74 (C_5N^+), 86 (C_6N^+) and 100 ($C_6N_2^+$), all less than 0.1% of the base peak at m/z 51 ($HC_3N^{+\cdot}$). It seems likely then, that traces of HC_3N polymerization products, such as C_6N_2, exist in the samples and that the low cross-section threshold at ~17.9 eV results from dissociative ionization of one or more of these species. Dibeler et al. [7] gave the appearance energy of the C_2N^+ ion as 18.0 ± 0.5 eV. The uncertainty assigned to this value is greater than any other appearance energy they reported with the exception

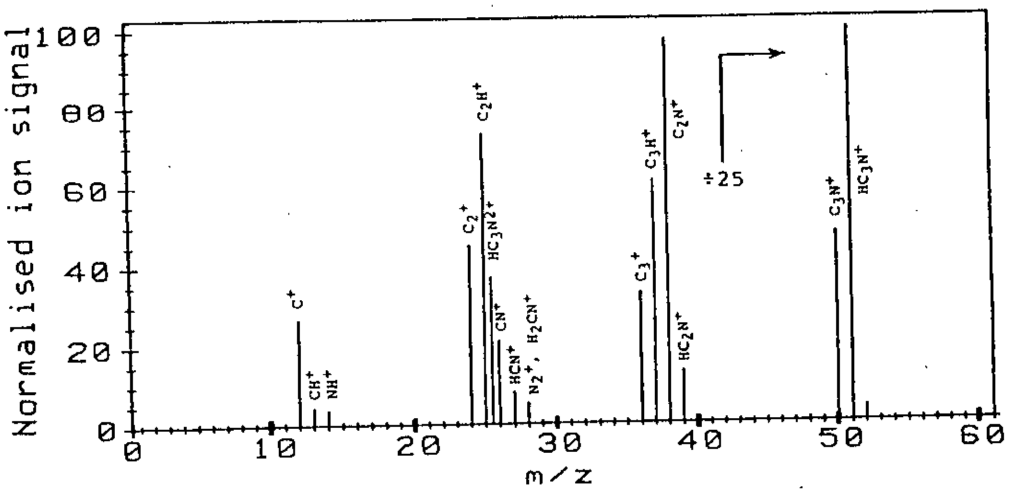

Fig. 1. 70 eV mass spectrum for HC_3N at 1×10^{-6} Torr (1×10^{-4} Pa). Note that the peaks for $m/z > 49$ have been divided by 25 to facilitate presentation.

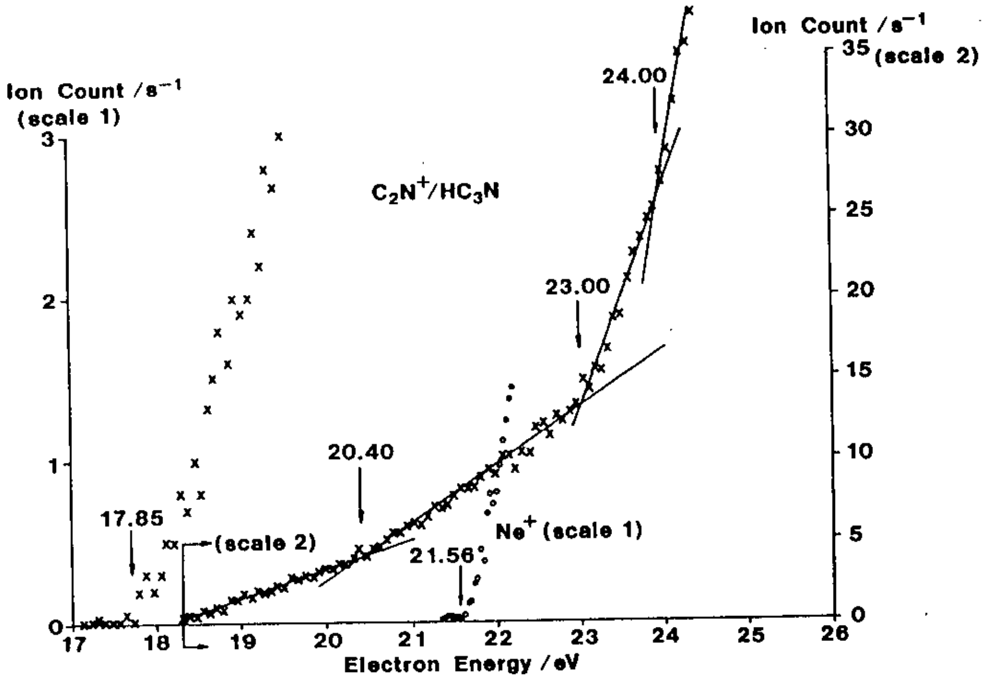

Fig. 2. Ionization efficiency curve for C_2N^+ from HC_3N. Ne^+ included as one of the energy scale calibrants used.

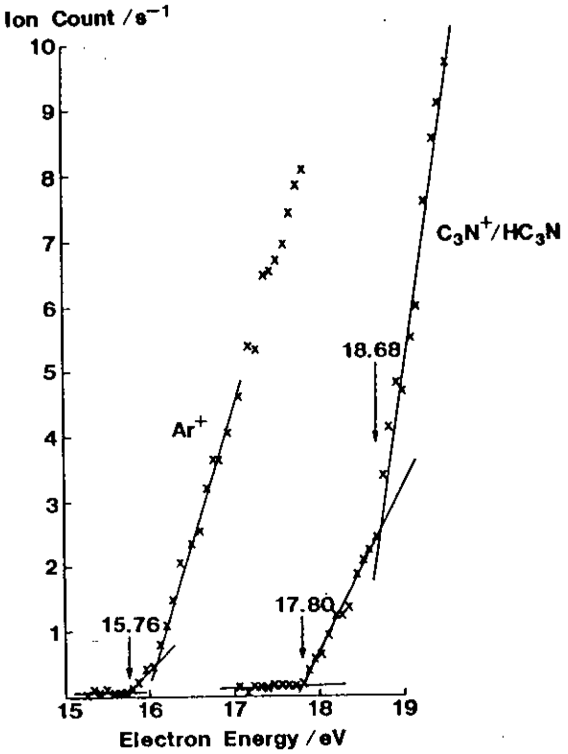

Fig. 3. Ionization efficiency curve for C_3N^+ from HC_3N. Ar^+ included as one of the energy scale calibrants used.

of 14.5 ± 0.5 eV for the appearance energy of the CN^+ ion which they assumed to be formed from $CN^·$ radicals generated on the surface of the hot filament. It therefore seems likely that irreproducibilities for this appearance energy were experienced, probably as a result of the same problem.

The ionization efficiency curve for the C_3N^+ ion is shown in Fig. 3 together with Ar^+ which was used as an energy scale calibrant. There is a threshold at 17.78 ± 0.08 eV followed by a break at 18.64 ± 0.08 eV. The values given in the figure correspond to the experimental run illustrated, whereas, the values given in Table 2 are averaged over six runs. Both thresholds were reproducible and independent of the sample. The trace polymerization products, discussed in terms of the first appearance energy for C_2N^+, do not appear to be responsible for the break observed for the C_3N^+ ion, leaving the possibility either of structural isomers or a metastable electronically excited state of the C_3N^+ ion (ion transit time to detector for m/z 50 at 10 eV ion energy is 70 μs). The reactivity of the C_3N^+ ion produced from HC_3N by electron impact was studied in a selected ion flow tube [16]. The pseudo-first-order log plot for the C_3N^+ ion decay was found to exhibit two linear sections for reaction with both H_2 and CH_4. This behaviour is characteristic of different isomeric forms of the ion [17] although the presence of excited states, such as a metastable electronically excited ion, could not be eliminated on this evidence. The enthalpies of formation for both species are given in Table 2.

The doubly charged molecular ion, HC_3N^{2+}, was initially reported by Dibeler et al. [7]. The first and second ionization potentials for HC_3N from the data in Table 1 are 11.56 and 20.74 eV, respectively.

REFERENCES

1 H.W. Kroto, C. Kirby, D.R.M. Walton, L.W. Avery, N.W. Broten, J.M. MacLeod and T. Oka, Astrophys. J., 219 (1978) L133.
2 N.W. Broten, T. Oka, L.W. Avery, J.M. MacLeod and H.W. Kroto, Astrophys. J., 223 (1978) L105.
3 J.S. Knight, C.G. Freeman, M.J. McEwan, N.G. Adams and D. Smith, Int. J. Mass Spectrom. Ion Processes, 67 (1985) 317.
4 J.S. Knight, C.G. Freeman, M.J. McEwan, S.C. Smith, N.G. Adams and D. Smith, Mon. Not. R. Astron. Soc., in press.
5 A.B. Raksit and D.K. Bohme, Int. J. Mass Spectrom. Ion Processes, 57 (1984) 211.
6 D.K. Bohme and A.B. Raksit, Mon. Not. R. Astron. Soc., 213 (1985) 717.
7 V.H. Dibeler, R.M. Reese and J.L. Franklin, J. Am. Chem. Soc., 83 (1961) 1813.
8 U. Buchler and J. Vogt, Org. Mass. Spectrom., 14 (1979) 503.
9 P.W. Harland and B.J. McIntosh, Int. J. Mass Spectrom. Ion Processes, 67 (1985) 29.
10 C. Moren and J.C. Bongrand, Ann. Chem., 14 (1920) 47.
11 C. Baker and D.W. Turner, Proc. R. Soc. London Ser. A, 308 (1968) 19.
12 B. Naragan, Proc. Indian Acad. Sci. Sect. A, 75 (1972) 92.
13 H.M. Rosenstock, K. Draxl, B.W. Steiner and J.T. Herron, J. Phys. Chem. Ref. Data Suppl. 1, 6 (1977).
14 D.R. Stull and H. Prophet, JANAF Thermochemical Tables, NSRDS-NBS, 2nd edn., 1971.
15 N.N. Haese and R.C. Woods, Astrophys. J., 246 (1981) L51.
16 J.S. Knight, Ph.D. Thesis, University of Canterbury, New Zealand, 1986.
17 J.S. Knight, C.G. Freeman and M.J. McEwan, J. Am. Chem. Soc., in press.

J. Chem. Soc., Faraday Trans. 2, 1986, **82**, 2039-2046

The Effect of Ion Structure on Gas-phase Ion Transport Properties

Peter W. Harland,* Bruce J. McIntosh,† Richard W. Simpson and Noel R. Thomas
Chemistry Department, University of Canterbury, Christchurch, New Zealand

Drift theory has been used with a simple interaction potential to predict the relative effects of structural parameters on the ion transport properties of polyatomic ions drifting in helium. Experimental data measured using a static drift tube for ions of dissimilar chemical composition are in accord with the qualitative predictions of theory, the spatial volume of the ion being the dominant factor on the ion transport properties. Differences in the mobilities of some of the structural isomers of $C_2H_4O^+$ and $C_2H_5O^+$ ions have been measured and rationalised in terms of their structural differences.

A recent review of gas-phase ion transport by McDaniel and Viehland[1] traces the development of drift theory and describes the static drift tube technique employed for the determination of ion drift velocities over the energy range from thermal to *ca.* 10 eV.

Chapman and Enskog[2] developed a theoretical treatment for spherically symmetric ions undergoing elastic collisions with a similarly characterised buffer gas under the influence of a weak, uniform electric field. This showed that the ion mobility is inversely proportional to the momentum-transfer integral which, in turn, depends on the interaction potential between the ion and the neutral buffer gas [eqn (1)-(4)]:

$$K = \frac{3}{8}\frac{q}{N}\left(\frac{\pi}{2\mu kT}\right)^{1/2}\frac{(1+\alpha)}{\bar{\Omega}^{(1,1)}(T)} \tag{1}$$

$$\bar{\Omega}^{(1,1)}(T) = \tfrac{1}{2}(kT)^{-3}\int_0^\infty E'^2 Q^{(1)}(E')\exp(-E'/kT)\,\mathrm{d}E' \tag{2}$$

$$Q^{(1)}(E') = 2\pi\int_0^\infty [1-\cos\theta(b,E')]b\,\mathrm{d}b \tag{3}$$

$$\theta(b,E') = \pi - 2b\int_{r_0}^\infty \left(1-\frac{b^2}{r^2}-\frac{V(r)}{E'}\right)^{-1/2}\frac{\mathrm{d}r}{r^2} \tag{4}$$

where the ion mobility, K, is related to the experimentally determined drift velocity, v_d, by

$$K = v_d/E. \tag{5}$$

E is the electric field gradient in the drift tube, q is the charge on the electron, μ is the reduced ion-neutral mass, k is Boltzmann's constant, T is the absolute temperature, $\Omega^{(1,1)}(T)$ is the energy-averaged momentum-transfer collision integral, α is a correction factor (which is typically < 0.04), N is the particle density in the drift tube, $Q^{(1)}(E')$ is a transport cross-section for the relative energy, E', of the ion-buffer collision, $\theta(b, E')$ is the deflection angle for an ion-buffer collision of energy E' and impact parameter b,

---

† Present address: CSIRO, Chemical Physics Division, Clayton, Victoria, Australia.

and $V(r)$ is the ion-buffer interaction potential. The ion mobility is usually expressed as the standard or reduced (to s.t.p.) mobility, K_0, given by

$$K_0 = \frac{v_d}{E}\left(\frac{p}{760}\right)\left(\frac{273.15}{T}\right) \tag{6}$$

where p is the drift tube pressure in Torr.

These relationships show that the temperature dependence of ion mobility is sensitive to the nature of the ion-neutral interaction potential. However, there was no distinction made between the ion and buffer-gas temperatures. Refinements of the theory by Viehland and coworkers[3-6] have addressed this and other deficiencies resulting in the two- and three-temperature theories. The two-temperature theory can be accurately applied to swarms of atomic (spherically symmetrical) ions moving in a single-component atomic buffer gas. The mobility of these ions are given by the Chapman-Enskog type of equation, which incorporates an effective ion temperature given by

$$kT_{\text{eff}} = kT + Mv_d^2(1+\beta)/3. \tag{7}$$

where β is a second correction factor, which is typically <0.1, and M is the neutral mass.

Although the two-temperature model has been successful for the modelling of mobilities over a wide range of E/N, the ratio of the electric field to the particle density, the theory has failed to provide an acceptable description of transverse and longitudinal diffusion. The three-temperature model was developed to address this discrepancy, and these theories are now as accurate for atomic ion-buffer-gas systems as the most accurate experimental measurements.

Two- and three-temperature theories have also been developed for molecular systems[5,6] from which a number of important qualitative features have emerged, although quantitative predictions have been precluded by the difficulties in calculating the collision cross-sections. The intimate relationship between the ion mobility and the ion-buffer-gas interaction potential, predicted for atomic systems by the Chapman-Enskog theory, remains an essential feature. For a fixed gas temperature there are a number of system properties which influence the interaction potential and hence the magnitude of the ion mobility; the buffer-gas polarizability, the dipole moment of the ion precursor, the effective size and shape of the ion and the ion-neutral reduced mass.

Ions of the same nominal mass but of dissimilar chemical composition and structure, N_2^+ and H_2CN^+ for example, may exhibit different ion transport properties as a consequence of differences in their interaction potentials with the buffer-gas atoms. Preliminary calculations have been carried out to assess the relative effect of ion dimension, dipole moment and the depth of the well in the interaction potential on the ion mobility in helium using eqn (1)-(7). The generalised potential

$$V(r) = \varepsilon\left[\left(\frac{r_m}{r}\right)^{12} - 2\left(\frac{r_m}{r}\right)^{6}\right] - \frac{\alpha_p dq}{8\pi\varepsilon_0 r^5} - \frac{\alpha_p q^2}{8\pi\varepsilon_o r^4} \tag{8}$$

was used to determine the effect of individually varying the well depth ε, the ion-atom separation corresponding to the minimum in the potential, r_m, and the dipole moment d. The ion-atom separation is r, ε_0 is the permittivity of free space and α_p is the polarizability of the neutral target. Collision integrals were calculated from this potential using the program of Smith and O'Hara,[7] from which the dependence of the drift velocity on E/N was calculated using the two-temperature theory, which included the calculation of α and β to first order. The results of these calculations suggest that, for a given E/N, an increase in the dipole moment from 0 to 26×10^{-30} C m (0 to 8 Debye) would result in an increase of $<1\%$ in the drift velocity. An increase in r_m by 0.01 nm would result in a decrease of *ca.* 6% and that an increase of 0.1 eV in the well depth would give a decrease of 10%. The mass, size and shape of an ion will influence both r_m and

ε in an undetermined way; however, an increase in the radius of an ion of $m/z = 45$ of 0.01 nm (0.21 to 0.22 nm, for example) would translate into a decrease of *ca.* 10% in the ion mobility for E/N in the range 10–100 Td.†

The mobilities of chemically dissimilar ions of the same nominal mass and structural isomers of the general type $C_2H_xO^+$, where $x = 3$–5, have been measured or taken from the literature to illustrate the effect of ion structure on ion transport properties.

Experimental

The drift-tube mass spectrometer used in this study has been previously described.[8,9] Briefly, the drift tube comprises eleven 1 cm gold-plated interlocking drift rings of 5 cm internal diameter enclosed in a temperature-controlled vacuum envelope. A movable electron impact ion source, incorporating an electron-beam control grid and a two-element plane lens, is enclosed in a stainless steel sleeve which is electrically biased according to its position in the drift tube. The ion source may be positioned along the drift-tube axis to an accuracy of better than 0.1 mm. Ions gated from the drift-tube axis pass through a skimmer into a second vacuum chamber for mass analysis by an Extranuclear model 4-270-9 quadrupole mass filter and detection by pulse counting.

The drift tube was operated within the pressure range 0.3–0.5 Torr (40–67 Pa). Dilute gas mixtures of the sample of interest in helium, 0.04–0.1%, were prepared on a high-vacuum gas-handling line using an MKS Baratron capacitance manometer. Electron and ion gatings are achieved by the application of square-wave voltage pulses to the electron beam control grid and the ion exit grid to over-ride small blocking bias voltages on these elements. He^+ ions, generated in the helium buffer gas by 80 eV electron pulses of 2 μs duration, undergo charge-transfer and dissociative charge-transfer reactions with the trace component. The ions formed drift out of the ion source under the influence of a uniform electric field whose magnitude is determined by the ratio E/N, where E is the electric field gradient in Vm^{-1} and N is the particle density in the drift tube in m^{-3}. The arrival-time distributions of ions arriving at the drift-tube exit orifice are sampled at 1 μs intervals and the mass-selected ion pulses accumulated for repeated scans. The operating frequency is typically 10 kHz, with counting times of 30–60 s per increment. Drift velocities are determined from the slopes of mean arrival time *vs.* drift distance plots for 8–10 drift distances at each value of the E/N[8].

Dimethylether was prepared by the reaction of 98% sulphuric acid on methanol at 135 °C and the product purified by vacuum distillation. Ethylene oxide and acetaldehyde were vacuum distilled from B.D.H. reagent-grade products, and spectroscopic-grade ethanol was used without further purification.

Results and Discussion

The influence of ion structure on the reduced mobilities for ions of dissimilar composition is illustrated in fig. 1 for positive ions of m/z 16, 18, 28 and 41. The data were taken from the literature[10–12] and from measurements made in this laboratory.[8] Except for NH_2^+, which is rapidly removed by reaction, and ArH^+, which requires gas mixtures with substantial partial pressures of hydrogen, the drift velocities for all of the ions shown in the figure have been measured in this laboratory at several values of the E/N for comparative purposes against the literature. The agreement was better than 3%, with the relative values for each pair of ions of the same m/z being in the direction shown in the figure, *i.e.* H_2O^+ more mobile than NH_4^+ *etc.*

Drift theory for polyatomic ions in atomic gases has not been developed with sufficient sophistication to provide quantitative comparisons between the behaviour of ions of

---

† E/N is usually expressed in the unit townsend, Td, where 1 Td = 10^{-21} Vm^2.

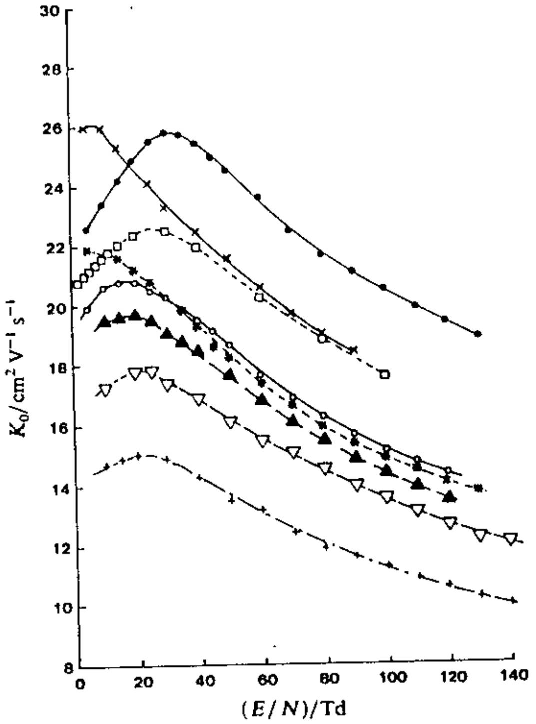

Fig. 1. Reduced mobilities as a function of E/N for pairs of chemically dissimilar positive ions of $m/z = 16$, 18, 28 and 41, in helium at or close to 300 K. ●, O^+(16); X, NH_2^+(16); □, H_2O^+(18); ○, CO^+(28); *, NH_4^+(18); ▲, ArH^+(41); ▽, H_2CN^+(28); +, $C_2H_3N^+$(41).

the type plotted in fig. 1. Interaction potentials have not been determined for such ions, and the data for atomic ions are very limited. The calculations outlined in the introduction provide only a qualitative guide to the expected effect of dipole moment, ion dimension *etc.*, although the figures quoted for the relative magnitude of these effects on the mobility are reliable within the constraints of the chosen form for the interaction potential. In the absence of realistic interaction potentials for the ions studied it is not feasible to unfold the individual contributions of these parameters on the experimentally observed mobilities. However, it is possible to rationalise the results in terms of the theoretical calculations given above.

The mobility curves for the ions of m/z 16, O^+ and NH_2^+, and for the ions of m/z 41, ArH^+ and $C_2H_3N^+$, provide the most graphic illustration of the effect of ion spacial volume on mobility. For ions of m/z 41 a difference of 0.06 nm in the effective diameter of the ions would be sufficient to account for these observations. This is equivalent to a change of 0.05 nm in r_m for a fixed well depth, ε, or a change of 0.3 eV in the well depth for a fixed r_m.

The literature values for the reduced mobilities of N_2^+ and CO^+, $m/z = 28$, are in close agreement as might be anticipated for ions of the same shape, the small dipole moment of 3.9×10^{-31} C m (0.117 D) for CO exerting only a minor influence on the CO^+-He interaction potential. The H_2CN^+ ion of the same nominal mass is a larger ion which would exhibit a higher collision cross-section and therefore a lower mobility. The dipole moment of the H_2CN species will be *ca.* 3×10^{-30} C m (*ca.* 1 D) and would not be a significant influence on the interaction potential. The observed differences in

Table 1. Isomers of $C_2H_5O^+$

	structure	relative *ab initio*[19] energy/ kJ mol^{-1}	experimental relative[15-18] energy/kJ mol^{-1}
(D)	$^+CH_2CH_2OH$	182	—
(C)	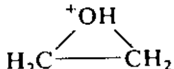	132	109
(B)	$CH_3\overset{+}{O}CH_2$	—	63
(A)	$CH_3CH\overset{+}{O}H$	0	0

the mobilities of the CO^+ and H_2CN^+ ions may be attributed directly to the effect of the ion structure on the interaction potential, *i.e.* ε and r_m.

According to the calculations the dipole moment of H_2O, 6.2×10^{-30} C m (1.85 D), would tend to an increase in the mobility of the H_2O^+ ion, $m/z = 18$, over a spherically symmetrical 'hard-sphere' ion of the same m/z, whereas the greater size of the NH_4^+ ion, $m/z = 18$, would lead to a decrease in the mobility, *i.e.* an increase in the energy averaged momentum transfer collision integral. The experimental result is a mobility difference of 11% for $E/N = 30$ Td and 18% for $E/N = 100$ Td, relative to the mobility of the NH_4^+ ion. The curves of reduced mobility *vs.* E/N cross at low E/N, the H_2O^+ curve exhibiting a maximum which is characteristic for helium data. The shape of the NH_4^+ curve is quite different, this is a reflection of the difference between the interaction potentials of these ions in the vicinity of the potential minimum, the competing influences of the attractive and repulsive components of the potential.

The mobilities of several structural isomers of the $C_2H_xO^+$ series, where $x = 3$-5, were determined in order to investigate the effect of more subtle structural differences on the transport properties of ions. The choice of isomers was restricted by the requirements for ions formed with a high dissociative charge transfer cross-section from He^+ and high isomerisation barriers to interconversion. The recombination energy of helium is 24.6 eV, and the appearance energies for the $C_2H_xO^+$ ions from the precursor molecules, acetaldehyde, ethylene oxide, dimethyl ether and ethanol, all lie within the energy range from 10.2 to 14.5 eV.[13,14] The neutral products of the ionisation process are helium with either or both hydrogen atoms and hydrogen molecules. These light fragmentation products will carry away a substantial fraction of the excess energy released in the dissociative charge-transfer process in the form of recoil energy with any internal ion energy being thermalised in collisions with the helium buffer gas (pressure 0.5 Torr). The structural isomers studied have been shown to exist as non-interconverting species in kinetic and collisional dissociation studies, and both experimental and theoretical values for the enthalpies of formation are available (tables 1 and 2).

$C_2H_5O^+$ ($m/z = 45$)

Four stable structures for the $C_2H_5O^+$ ion are shown in table 1 with experimental[15-18] and theoretical[19] relative enthalpies of formation. The absolute enthalpy of formation for the protonated acetaldehyde molecular ion, structure (A), was reported to be 598 kJ mol^{-1}.[15] Drift velocities were determined for the $C_2H_5O^+$ fragmentation ion from dilute mixtures (0.2%) of ethanol and dimethyl ether in helium and for the protonated molecular ion of acetaldehyde for mixtures <0.5% of acetaldehyde in helium. Plots of reduced mobility *vs.* E/N are shown in fig. 2. The mobility of the $C_2H_5O^+$ ion produced from dimethyl ether, which has a C—O—C skeletal structure, is between 3 and 6% lower than the mobility determined for the same ion produced from ethanol and proton transfer to acetaldehyde, which have a C—C—O skeletal framework. The actual

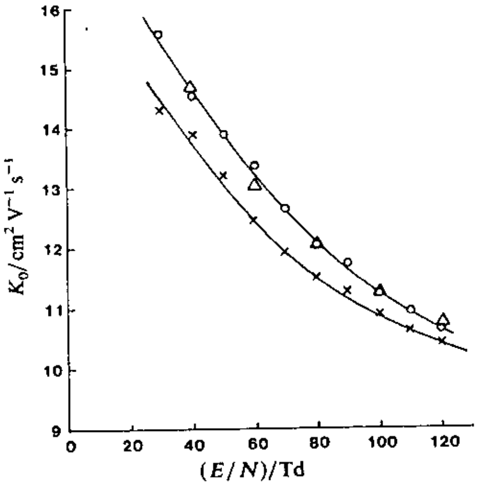

Fig. 2. Reduced mobilities as a function of E/N for the $C_2H_5O^+$ ion produced from three different precursor molecules in helium at 293 K. ×, CH_3OCH_3; ○, C_2H_5OH; △, CH_3CHO.

structures for the ions can only be inferred from the information in table 1; the ion produced from dimethyl ether is assumed to be the C—O—C isomer (B) and the species formed from ethanol and acetaldehyde, which have the same ion transport properties, is assumed to be isomer (A). This being the case, then the C—O—C isomer exhibits a higher momentum transfer collision integral, and therefore a lower mobility, than the C—C—O isomer. This may be rationalised in terms of the structures shown in table 1. Terminal carbon atoms carry at least two hydrogen atoms projecting away from the carbon-oxygen skeleton, whereas a terminal oxygen carries only one hydrogen atom. The oxygen atom in structure (A) also carries the charge which further constrains the spacial volume at the oxygen end of the ion. The magnitude of $\Omega^{(1,1)}(T)$ reflects the spacial volume, and hence the collision cross-section of the ions on helium, in the same way as discussed above for chemically dissimilar ions of the same nominal mass (fig. 1). The effect of the number of terminal hydrogen atoms on mobility is well illustrated by a comparison of the mobilities of the CN^+, HCN^+ and H_2CN^+ ions, where the difference in mobility are far greater than would be anticipated on the basis of their unit-mass changes.[9]

$C_2H_4O^+(m/z=44)$

The structures, relative *ab initio*[20] and experimental[15,21-23] energies for the $C_2H_4O^+$ isomers are shown in table 2. The four structural isomers shown correspond to the molecular ions of vinyl alcohol (A), acetaldehyde (B) and ethylene oxide (D). Structure (C) corresponds to a ring-opened ethylene oxide or a fragmentation product of dimethyl ether. The relative enthalpies of formation shown in table 2 are referenced to an absolute value of 757 kJ mol^{-1} for isomer (A), which was determined by 'monochromatic' electron impact.[23] Mobility data for $C_2H_4O^+$ ions from dilute (<0.2%) mixtures of ethanol and ethylene oxide are shown with data for CO_2^+ ($m/z=44$) in fig. 3. The electron-impact study identified the $C_2H_4O^+$ ion from ethanol as the vinyl alcohol structure (A) and two ion cyclotron resonance studies[16,21] both proposed that the $C_2H_4O^+$ isomer from ethylene oxide is the ring-opened structure (C). The isomerisation barrier for conversion of the closed ethylene oxide structure (D) to the more stable ring-opened structure (C) has been estimated to be 105-120 kJ mol^{-1}.[20] The exothermicity of the charge-transfer reaction of He^+ on $(CH_2)_2O$ is 1.45MJ mol^{-1}. This would certainly provide enough

Table 2. Isomers of $C_2H_4O^+$

	structure	relative *ab initio*[22] energy/kJ mol^{-1}	experimental relative[16,21,23] energy/kJ mol^{-1}
(D)	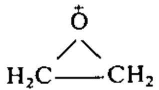	182.6	209
(C)	$CH_2\overset{+}{O}CH_2$	124.9	101
(B)	$CH_3CH{=}\overset{+}{O}$	52.3	63
(A)	$CH_2CH\overset{+}{O}H$	0	0

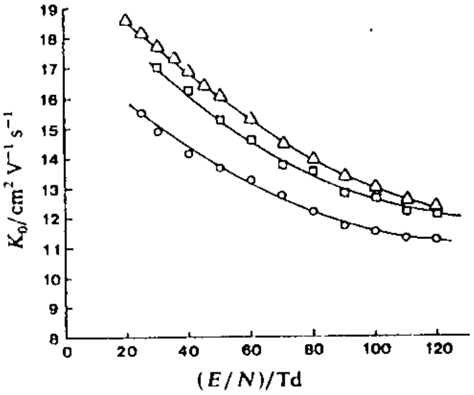

Fig. 3. Reduced mobilities as a function of E/N for the $C_2H_4O^+$ ion produced from two different precursor molecules in helium and for CO_2^+ produced from CO_2 in helium at 293 K. △, $m/z = 44$, CO_2^+/CO_2; □, $C_2H_4O^+/C_2H_5OH$(A); ○, $C_2H_4O^+/(CH_2)_2O$(C).

internal energy to drive isomerisation. The mobility curves shown in fig. 3 have been labelled according to these considerations. The difference in mobilities between the two isomers is *ca.* 10%, the C—O—C isomer exhibiting a lower mobility (higher collision cross-section) than the C—C—O isomer in accord with the $C_2H_5O^+$ results. Data for the mobility of CO_2^+ in helium were taken from the literature.[10]

$C_2H_3O^+$ ($m/z = 43$)

The $C_2H_3O^+$ ion is a minor product (*ca.* 1%) of total He^+ dissociative charge transfer ionisation of dimethyl ether and (*ca.* 9%) from ethanol. The ion density in the drift tube must be maintained low enough (*ca.* 10^{-4} cm^{-3}) to preclude Coulombic repulsion and the distortion of the arrival-time profiles. This seriously limited the $C_2H_3O^+$ ion signal and the reliability of the measurements. Nevertheless, the mobility of the $C_2H_3O^+$ ion produced from ethanol and dimethyl ether were measured over the range 80-140 Td, the values for the C—O—C isomer from dimethyl ether being consistently *ca.* 3% lower than the C—C—O isomer from ethanol.

Conclusion

The effects of ion structure on ion transport properties in helium have been qualitatively predicted from drift theory and confirmed experimentally. Significant differences between the mobilities of chemically dissimilar ions of the same mass-to-charge ratio, *m*/*z*, have been rationalised in terms of dipole moment, ion size (shape) and structure in accord with the predictions of the calculations. Smaller differences in mobility have been found for the structural isomers of $C_2H_xO^+$, where $x = 3$-5. The experimental mobility data may be used to estimate the interaction potential for the ion or *vice versa* for the few cases where an *ab initio* or experimental interaction potential is available. *Ab initio* and semi-empirical interaction potentials are currently under consideration for atomic and polyatomic positive and negative ions. The comparison of experimental ion transport properties with calculated values will provide information on ion structure, particularly for negative ions where few molecular-orbital calculations have been performed.

References

1 E. W. McDaniel and E. A. Mason, *Phys. Rep.*, 1984, **10**, 333.
2 S. Chapman and T. G. Cowling, *The Mathematical Theory of Non-uniform Gases* (Cambridge University Press, London, 3rd edn, 1970).
3 L. A. Viehland and E. A. Mason, *Ann. Phys.* (*N.Y.*), 1975, **91**, 499.
4 S. L. Lin, L. A. Viehland and E. A. Mason, *Chem. Phys.*, 1979, **37**, 411.
5 L. A. Viehland, S. L. Lin and E. A. Mason, *Chem. Phys.*, 1981, **54**, 341.
6 L. A. Viehland, *Chem. Phys.*, 1986, **101**, 1.
7 F. J. Smith and H. O'Hara, *Comput. Phys. Commun.*, 1971, **2**, 47.
8 P. W. Harland and B. J. McIntosh, *Int. J. Mass Spectrom. Ion. Phys.*, 1983, **54**, 217; 1984, **57**, 283.
9 P. W. Harland and B. J. McIntosh, *J. Chem. Soc., Faraday Trans. 2*, 1985, **81**, 169.
10 H. W. Ellis, R. Y. Pai, E. W. McDaniel, E. A. Mason and L. A. Viehland, *At. Data Nucl. Data Tables*, 1976, **16**, 177.
11 H. W. Ellis, E. W. McDaniel, D. L. Albritton, L. A. Viehland, S. L. Lin and E. A. Mason, *At. Data Nucl. Data Tables*, 1978, **22**, 179.
12 J. Barassin, A. Barassin and R. Thomas, *Int. J. Mass Spectrom. Ion Phys.*, 1983, **49**, 51.
13 J. L. Franklin, J. G. Dillard, H. M. Rosenstock, J. T. Heron and K. Draxl, *Natl Stand. Ref. Data Ser.* (*U.S.*), 1969, **26**.
14 H. M. Rosenstock, K. Draxl, B. W. Steiner and J. T. Heron, *J. Phys. Chem. Ref. Data Suppl.*, 1977, **1**, 6.
15 R. R. Corderman, P. R. LeBreton, S. E. Butrill, A. D. Williamson and J. L. Beauchamp, *J. Chem. Phys.*, 1976, **65**, 4929.
16 A. G. Harrison, C. D. Finney and J. A. Stark, *Org. Mass Spectrom.*, 1971, **5**, 1313.
17 R. H. Staley, P. R. Corderman, M. S. Foster and J. L. Beauchamp, *J. Am. Chem. Soc.*, 1974, **96**, 1260.
18 K. M. A. Refeay and W. A. Chupka, *J. Chem. Phys.*, 1968, **48**, 5205.
19 H. Lischka and J. Kohler, *Chem. Phys. Lett.*, 1979, **63**, 326.
20 W. J. Bouma, J. K. McLeod and L. Radom., *J. Am. Chem. Soc.*, 1979, **101**, 5540.
21 C. C. Van de Sande and F. W. McLafferty, *J. Am. Chem. Soc.*, 1975, **97**, 4613.
22 W. J. Bouma, J. K. McLeod and L. Radom, *J. Chem. Soc., Chem. Commun.*, 1978, 724.
23 J. L. Holmes, J. K. Terlouw and F. P. Lossing, *J. Phys. Chem.*, 1976, **80**, 2860.

Paper 6/535; Received 17th March, 1986

J. Phys. B: At. Mol. Phys. 20 (1987) 2723-2731. Printed in the UK

Ab initio calculation of the mobility of F^- in helium

Richard W Simpson, Robert G A R Maclagan and Peter W Harland
Department of Chemistry, University of Canterbury, Christchurch, New Zealand

Received 17 October 1986, in final form 10 December 1986

Abstract. The mobility of F^- in helium has been calculated using the two-temperature theory of ion transport. The interaction potential required by this theory was calculated at the MP4SDQ/6-311+G(3df, 3pd) level of theory. In order for the theoretical results to fall within the experimental error of the corresponding experimental results, a high level of theory is required in the calculation of the interaction potential.

1. Introduction

The classical theories describing ion transport in gases are well known and have been the subject of a recent review (McDaniel and Viehland 1984). In particular, the two- and three-temperature theories are capable of accurately describing the relationship that exists between the ion-neutral interaction potential and the observed mobility and diffusion coefficients. Thus, it is possible to use these theories to test proposed interaction potentials for a particular ion-neutral system through a comparison of the calculated ion transport coefficients with the corresponding experimentally determined values. This method has been applied several times (for example, Viehland and Lin 1979, Viehland and Mason 1984, Gatland *et al* 1977) usually with interaction potentials obtained from scattering experiments. The two- and three-temperature theories have also been used in an inversion-type procedure to extract the ion-neutral interaction potential directly from experimental mobility measurements (Viehland *et al* 1976). These theories have also been applied to ion-neutral systems using an *ab initio* interaction potential (for example, Viehland 1983). Such calculations require an accurate potential surface over a large range of internuclear separation. In this paper we will show how application of the two-temperature theory of ion mobility, as applied to F^- ions drifting in helium using an *ab initio* interaction potential, can give results in agreement with experiment when the interaction potential is calculated at a high level of theory. The sensitivity of the calculated mobility to small changes in the interaction potential will be shown.

2. Two-temperature theory

Viehland and Mason (1975, 1978) provided the first rigorous kinetic theory of ion mobility in neutral gases in which the ions are allowed to have a temperature different from the neutral-gas temperature. This is the two-temperature theory and is known to adequately describe mobility but not the transverse or longitudinal diffusion coefficients for which the three-temperature theory was developed (Lin *et al* 1979).

0022-3700/87/122723+09\$02.50 © 1987 IOP Publishing Ltd

The two-temperature theory was used in this paper principally because it is much easier to apply than the three-temperature theory (McDaniel and Viehland 1984) and also because, as shown below, there is little to be gained by using the three-temperature theory when relatively large changes in the calculated ion-transport properties are caused by small adjustments to the interaction potential.

The mobility, K, of an ion is written, according to the two-temperature theory, as

$$K = \frac{3}{8}\frac{q}{N}\left(\frac{\pi}{2\mu k_B T_{\rm eff}}\right)^{1/2}\frac{1+\alpha}{\Omega^{(1,1)}(T_{\rm eff})} \tag{1}$$

where q is the ion charge, N is the gas density, μ is the reduced mass, k_B is Boltzmann's constant and $\Omega^{(1,1)}(T_{\rm eff})$ is the first in a series of momentum-averaged collision integrals. The temperature $T_{\rm eff}$ is the effective ion temperature which is related to the ion temperature T_i but is normally given by

$$\tfrac{3}{2}k_B T_{\rm eff} = \tfrac{3}{2}k_B T + \tfrac{1}{2}Mv_d^2(1+\beta) \tag{2}$$

where the buffer gas temperature is T and M is the neutral gas atomic or molecular mass. It can be seen in (2) that as the drift velocity v_d of an ion increases the effective ion temperature also increases. The quantities α and β present in equations (1) and (2) depend in a complicated way on higher-order collision integrals, the ion and neutral gas masses and other experimental parameters. To a first approximation they may be written as (Viehland and Mason 1978):

$$\alpha = \frac{m(m+M)}{5(3m^2+M^2)+8mMA^*}\left(\frac{10(m+M)}{5m+3MA^*} - \frac{5(m-M)+4MA^*}{m+M}\right)\frac{\mathrm{d}\ln K}{\mathrm{d}\ln(E/N)} \tag{3}$$

$$\beta = \frac{mM(5-2A^*)}{5(m^2+M^2)+4mMA^*}\,\frac{\mathrm{d}\ln(K)}{\mathrm{d}\ln(E/N)}. \tag{4}$$

The mass of the ion is m. The quantities A^*, B^* and C^* are ratios of higher-order collision integrals and are defined as

$$A^* = \Omega^{(2,2)}/\Omega^{(1,1)} \tag{5}$$

$$B^* = (5\Omega^{(1,2)} - 4\Omega^{(1,3)})/\Omega^{(1,1)} \tag{6}$$

$$C^* = \Omega^{(1,2)}/\Omega^{(1,1)}. \tag{7}$$

Equations (8), (9) and (10) show how the collision integrals required by this theory are related through three levels of integration to the interaction potential (McDaniel and Mason 1972):

$$\Omega^{(l,s)}(T) = [(s+1)!]^{-1}\int_0^\infty \exp(-x)x^{s+1}Q_l(kTx)\,\mathrm{d}x \tag{8}$$

$$Q_l(E') = 2\pi\left(1-\frac{1+(-1)^l}{2(1+l)}\right)^{-1}\int_0^\infty b(1-\cos^l\chi(b,E'))\,\mathrm{d}b \tag{9}$$

$$\chi(b,E') = \pi - 2b\int_{r_0}^\infty\left(1-\frac{b^2}{r^2}-\frac{V(r)}{E'}\right)^{-1/2}\frac{\mathrm{d}r}{r^2}. \tag{10}$$

Equation (10) is the classical deflection function, which determines the deflection angle in an ion–neutral collision as a function of the impact parameter b and the relative energy E'. This classical deflection function depends on the interaction potential $V(r)$

that exists between the ion and neutral-gas molecules. The lower integration limit r_0 is the outermost root of equation (11):

$$1-\frac{b^2}{r_0^2}-\frac{V(r_0)}{E'}=0. \tag{11}$$

The second and third integrations average over impact parameters and energies, respectively, to produce collision integrals as a function of temperature. In the two-temperature theory the temperature used here is the effective temperature T_{eff}. The collision integrals were evaluated using the program developed by O'Hara and Smith (1970, 1971). Slight modifications were made to the program to enable an interaction potential known only at a discrete number of points to be used; these will be discussed later. The program evaluates the reduced collision integrals $\Omega^{(l,s)*}$ as a function of a reduced temperature T^*. These integrals are related to the actual collision integrals and effective temperatures by the following equations, where r_m and ε have units of distance and energy, respectively, and $V'(r)$ is the interaction potential actually used by the program:

$$V'(r)=\varepsilon^{-1}V(r/r_m) \tag{12}$$

$$\Omega^{(l,s)}(T_{\mathrm{eff}})=\pi r_m^2\Omega^{(l,s)*}(T^*) \tag{13}$$

$$T^*=\varepsilon^{-1}k_B T_{\mathrm{eff}}. \tag{14}$$

It can be shown that the collision integrals, $\Omega^{(l,s)}(T_{\mathrm{eff}})$, do not depend on the choice of values for r_m or ε. Given an interaction potential, and choosing r_m and ε one can use the O'Hara–Smith program to evaluate the reduced collision integrals $\Omega^{(l,s)*}$ as a function of the reduced temperature T^*. After scaling one obtains the collision integrals as a function of the effective temperature. These integrals can then be used in our two-temperature theory program to determine the reduced mobility as a function of the parameter E/N. The parameter E/N is the average electric field experienced by each ion and is usually reported in units of townsends (Td), where $1\,\mathrm{Td}=10^{-21}\,\mathrm{V\,m^2}$.

The mobility, K, and reduced mobility, K_0, of an ion are defined as

$$K=v_d/E \tag{15}$$

$$K_0=K\frac{P}{760}\,\frac{273.16}{T} \tag{16}$$

where v_d is the average ion drift velocity, E is the electric field, and P and T are the experimental pressure in Torr and temperature in kelvin, respectively.

We can therefore write the reduced mobility as

$$K_0=0.372\,20\,v_d/(E/N) \tag{17}$$

where the drift velocity v_d is in units of $\mathrm{m\,s^{-1}}$ and E/N is in Td, K_0 then has units of $10^{-4}\,\mathrm{m^2\,V^{-1}\,s^{-1}}$. The two-temperature theory program used reads a tabulated interaction potential and a set of temperatures. Following this the O'Hara–Smith program determines collision integrals at these temperatures to a specified accuracy (in the present paper an accuracy of 0.01% was used). Values of α and β are calculated and used to obtain the second approximation of the drift velocity or reduced mobility at discrete values of E/N. Intermediate values of the drift velocity or reduced mobility can be obtained by interpolation on this calculated set. Using this method we were able to compare calculated reduced mobilities with their experimental counterparts at the values of E/N at which the experiments were performed.

3. The HeF$^-$ interaction potential

The ground-state interaction potential of HeF$^-$, separating at infinity to He ^{1}S and F$^-$ ^{1}S, was calculated using the Gaussian 82 program (Binkley *et al* 1983) at the MP4SDQ/6-311+G(3df, 3pd) level of theory, excluding core contributions to the correlation energy. At this level of theory the electron affinity of fluorine was calculated to be 3.157 eV, as compared with the experimental value of 3.399 eV and the error in the energy of the He atom is 0.13 eV. The results of the calculation at the HF, MP2 and MP4SDQ levels of theory are given in table 1. Calculations were also performed at the same level of theory using the 6-311+G** basis set. A natural cubic spline was used to transform the calculated potential points into the analytic function required by the O'Hara-Smith program. Analytic functions were fitted to both ends of the spline to ensure that the potential function was defined for all internuclear separations. Outside $r_{\min}$ and $r_{\max}$ the functions used were

$$V(r)=\frac{a}{r^m}+b \qquad 0<r\leqslant r_{\min} \tag{18}$$

$$V(r)=\frac{c}{(r-d)^n} \qquad r_{\max}\leqslant r<\infty. \tag{19}$$

The constants a, b, c and d were determined during the fitting procedure for given values of m and n; a and b were chosen so that function (18) matched the spline and

Table 1. Hartree-Fock, MP2 and MP4SDQ total energies as a function of internuclear separation for HeF$^-$.

r (Å)	E (HF)	E(MP2) (Hartree)	E (MP4SDQ)
0.875	−101.735 086	−102.081 608	−102.083 380
1.000	−101.905 339	−102.250 593	−102.251 498
1.125	−102.045 273	−102.379 418	−102.382 096
1.250	−102.141 120	−102.468 781	−102.472 140
1.375	−102.202 732	−102.526 809	−102.530 412
1.500	−102.241 556	−102.563 573	−102.567 240
1.625	−102.265 880	−102.586 701	−102.590 348
1.750	−102.281 073	−102.601 225	−102.604 807
1.875	−102.290 532	−102.610 340	−102.613 838
2.000	−102.296 412	−102.616 072	−102.619 482
2.250	−102.302 361	−102.621 997	−102.625 253
2.500	−102.304 661	−102.624 385	−102.627 529
2.750	−102.305 525	−102.625 332	−102.628 402
3.000	−102.305 827	−102.625 683	−102.628 708
3.125	−102.305 880	−102.625 749	−102.628 759
3.250	−102.305 897	−102.625 773	−102.628 772
3.375	−102.305 893	−102.625 771	−102.628 761
3.500	−102.305 875	−102.625 751	−102.628 736
4.000	−102.305 771	−102.625 620	−102.628 595
4.500	−102.305 687	−102.625 510	−102.628 480
5.000	−102.305 637	−102.625 443	−102.628 411
5.500	−102.305 608	−102.625 407	−102.628 374
∞	−102.305 551	−102.625 345	−102.628 311

derivative at $r = r_{min}$; c and d were determined by requiring that function (19) match the two interaction potential points at the large-r end of the spline. Tests showed that the values of the collision integrals were relatively insensitive to the values of m and n chosen. The results presented here were determined with $m = n = 5$, since $n = m = 5$ appeared to give the best fit to the calculated values. The degree of fit was independent of n and m to less than 0.1% over the range from 4 to 7. For internuclear separations important in determining the values of the collision integral at low E/N, the dispersion r^{-6} term appears to have a significant contribution as well as the ion-induced dipole r^{-4} term. The calculated points and the interpolated and extrapolated interaction energy curve are shown in figure 1. The modifications to the O'Hara-Smith program enabled the cubic spline coefficients as well as the values of a, b, c and d to be read into a COMMON block. The modified potential function and derivative function in the program could then take their values directly from this extended spline interpolating function.

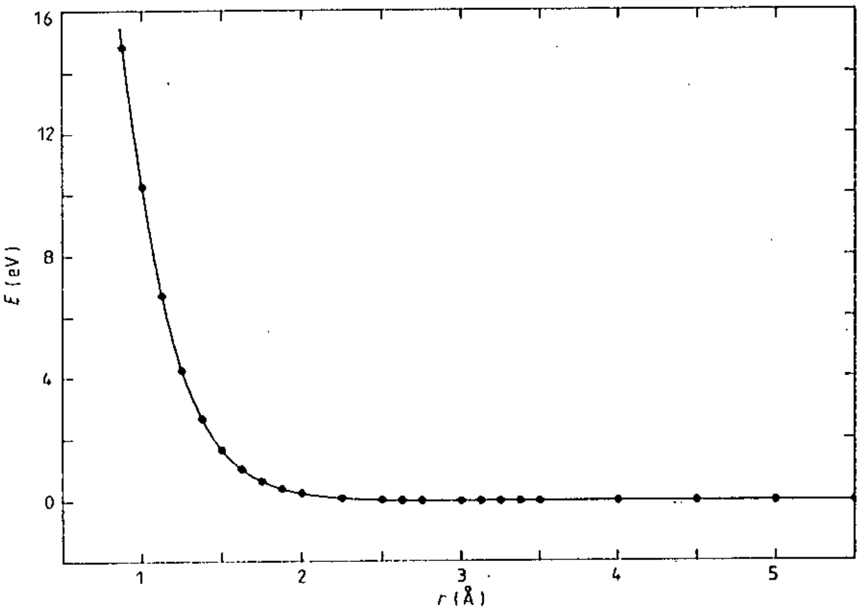

Figure 1. Interaction potential of $^1\Sigma$ HeF⁻. ●, MP4SDQ/6-311+G(3df, 3pd) values.

4. Results and discussion

The reduced mobiltiy of F⁻ in helium as a function of E/N has been reported by Dotan *et al* (1977, 1979) and included in a compilation of mobility data by Ellis *et al* (1978). We have used these values as the basis for our comparison of theory and experiment. We have applied the two-temperature theory, calculating α and β to first order, to several related HeF⁻ interaction potentials, thus determining the theoretical dependence of both the reduced mobility K_0 and drift velocity v_d on the parameter E/N. The following interaction potentials were used in our two-temperature theory calculations:

(i) MP4SDQ/6-311+G(3df, 3pd);

(ii) HF/6-311+G(3df, 3pd);
(iii) same as (i) except only points lying on a purely repulsive curve were used;
(iv) same as (i) except the well depth was halved.

In table 2 are listed the results from the two-temperature theory calculation using potential (i); the T_{eff} values used were determined by setting β to zero and using equation (2) to convert the experimental drift velocities to approximate effective temperatures. Table 3 compares the reduced mobilities from all calculations and the drift velocity from the calculation using potential (i) with the corresponding experimental quantities; the raw calculated reduced mobilities and drift velocities were interpolated using a cubic spline to provide values at the experimental values of E/N in this tabulation.

Table 2. Calculated momentum-transfer collision integrals, drift velocities, reduced mobilities and related quantities for $He+F^-$.

T_{eff}	$\Omega^{(1,1)}(T_{\text{eff}})$ (10^{-20} m^2)	α	β	v_d (ms^{-1})	E/N (Td)	K_0 (10^{-4} m^2 V^{-1} s^{-1})
298.0	23.51	0.000	−0.000	78.94	1.171	25.09
310.0	23.07	0.000	−0.000	284.6	4.226	25.07
360.0	21.56	0.003	−0.002	627.2	9.356	25.95
450.0	19.65	0.008	−0.006	979.4	14.81	24.62
534.0	18.42	0.013	−0.010	1221	18.75	24.24
590.0	17.77	0.016	−0.012	1359	21.12	24.96
770.0	16.25	0.022	−0.016	1731	27.92	23.07
870.0	15.63	0.024	−0.018	1907	31.39	22.62
990.0	15.02	0.026	−0.019	2098	35.32	22.11
1 277.0	13.92	0.030	−0.021	2497	44.09	21.08
1 750.0	12.69	0.032	−0.023	3044	57.24	19.76
2 321.0	11.69	0.033	−0.023	3593	71.58	18.69
3 170.0	10.66	0.034	−0.023	4281	90.86	17.54
4 600.0	9.517	0.033	−0.023	5238	119.6	16.30
5 500.0	8.999	0.033	−0.022	5758	136.1	15.75
6 400.0	8.573	0.032	−0.023	6235	151.5	15.32
7 400.0	8.176	0.031	−0.021	6724	167.7	14.93
8 600.0	7.777	0.030	−0.020	7267	186.0	14.55
10 700.0	7.215	0.029	−0.019	8130	215.6	14.04
12 200.0	6.888	0.028	−0.018	8692	235.2	13.75

The theoretical and experimental values of the reduced mobility, K_0, as a function of E/N are compared graphically in figure 2. The graphical comparison of the theoretical and experimental drift velocities as a function of E/N is shown in figure 3.

The MP4SDQ potential (i) was in good agreement with the experimental values of K_0 at large E/N but was poorer than the Hartree-Fock potential (ii) at very low E/N. The reason for this is explained by the results from potential curves (iii) and (iv) as shown in figure 2. The two-temperature theory calculations based on these curves show the effect of partially or fully neglecting the very small well ($D_e = 0.0126$ eV; $r_e = 3.25$ Å) found in potential (i). Thus we conclude that although correlation energy makes an important contribution to the interaction energy, it must be determined consistently over a wide range of internuclear distance for the interaction potential to be useful in mobility calculations. It would appear that the MP4SDQ potential has overestimated the depth of the potential well by about 0.007 eV. Comparison of the

Table 3. Theoretical and experimental values for the reduced mobility of F^- in He.

	$K_0(10^{-4}\ m^2\ V^{-1}\ s^{-1})$					$v_d(10^2\ ms^{-1})$	
E/N(Td)	MP4SDQ	HF	Half well	Repulsive	Experiment	MP4SDQ	Experiment
2.0	25.1	27.1	29.7	33.6	29.2	1.35	1.57
4.0	25.1	27.0	29.5	33.2	28.9	2.69	3.10
6.0	25.0	26.9	29.2	32.5	28.5	4.04	4.60
8.0	25.0	26.7	28.8	31.8	28.2	5.37	6.06
10.0	24.9	26.5	28.4	30.9	27.8	6.70	7.47
12.0	24.8	26.2	27.9	30.1	27.5	8.00	8.86
15.0	24.6	25.8	27.2	28.9	27.0	9.92	10.9
20.0	24.1	24.9	25.9	27.2	26.1	13.0	14.0
30.0	22.8	23.2	23.8	24.5	24.6	18.4	19.8
40.0	21.5	21.8	22.2	22.6	23.2	23.2	24.9
60.0	19.6	19.6	19.9	20.1	20.9	31.5	33.7
80.0	18.1	18.1	18.3	18.5	19.3	39.0	41.5
100.0	17.1	17.0	17.2	17.3	18.0	45.9	48.4
120.0	16.3	16.2	16.4	16.4	17.0	52.5	54.8
140.0	15.6	15.5	15.7	15.7	16.3	58.8	61.3
160.0	15.1	15.0	15.2	15.2	15.7	64.9	67.4
180.0	14.7	14.5	14.7	14.7	15.1	70.9	73.0
200.0	14.3	14.2	14.3	14.3	14.6	76.8	78.5
220.0	14.0	13.8	14.0	14.0	14.2	82.6	83.9

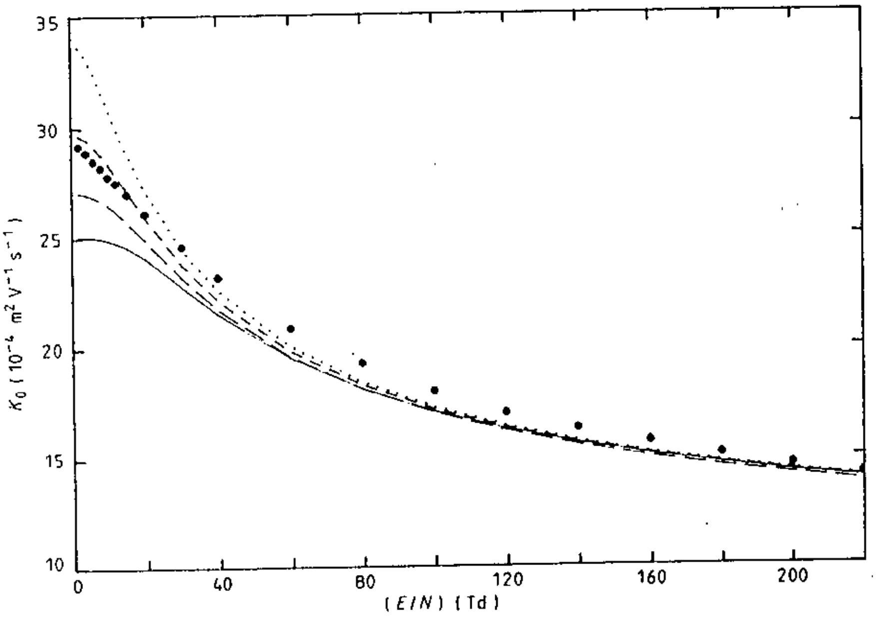

Figure 2. Calculated and experimental reduced mobilities of F^- in helium. ●, experiment; (——), MP4SDQ; (— —), HF; (- - -), half well; (· · · · ·), repulsive curve.

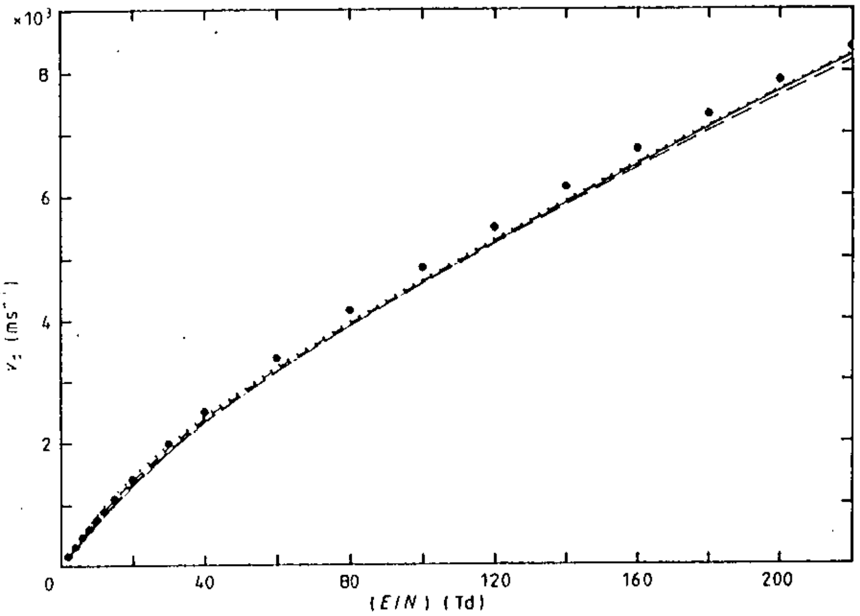

Figure 3. Calculated and experimental drift velocities of F^- in helium. ●, experiment; (——), MP4SDQ; (— —), HF; (- - -), half well; (· · · · ·), repulsive curve.

MP4SDQ and HF potentials suggests that at small internuclear separation the calculated interaction potentials are not steep enough.

The drift-velocity comparisons, as shown in figure 3, do not show the effect of the size of the potential well and it appears that agreement with experiment is good for v_d values at low E/N but not as good at high E/N. However, at a given value of E/N, the percentage errors between the calculated drift velocities and the experimental measurements are the same as the percentage errors between the calculated reduced mobilities and the experimental measurements.

Very small fluctuations in an interaction potential especially at larger distance can have a major effect on the calculated mobility. However, once an accurate interaction potential has been obtained, it can then be used to calculate the depence of the reduced mobility, K_0, or drift velocity, v_d, as a function of E/N, at any temperature, including temperatures outside the range accessible to experimentalists.

Calculations are currently underway to explore the effect on the ion transport properties of low-lying excited-state interaction potentials, with the aim of determining which ion–neutral interactions are important in accounting for experimentally observed mobility data and for the prediction of previously unmeasured ion transport properties.

References

Binkley J S, Frisch M J, DeFrees D J, Raghavachari K, Whiteside R A, Schlegel H B, Fluder E M and Pople J A 1983 *Gaussian 82* (Pittsburgh: Carnegie-Mellon University)

Dotan I, Albritton D L and Fehsenfeld F C 1977 *J. Chem. Phys.* **66** 2232

—— 1979 *J. Chem. Phys.* **71** 4762

Ellis H W, McDaniel E W, Albritton D L, Viehland L A, Lin S L and Mason E A 1978 *At. Data Nucl. Data Tables* **22** 179

Gatland I R, Viehland L A and Mason E A 1977 *J. Chem. Phys.* **66** 537

Lin S L, Viehland E A and Mason E A 1979 *Chem. Phys.* **37** 411
McDaniel E W and Mason E A 1972 *The Mobility and Diffusion of Ions in Gases* (New York: Wiley)
McDaniel E W and Viehland L A 1984 *Phys. Rep.* **110** 333
O'Hara H and Smith F J 1970 *J. Comput. Phys.* **5** 328
—— 1971 *Comput. Phys. Commun.* **2** 47
Viehland L A 1983 *Chem. Phys.* **78** 279
Viehland L A, Harrington M M and Mason E A 1976 *Chem. Phys.* **17** 433
Viehland L A and Lin S L 1979 *Chem. Phys.* **43** 135
Viehland L A and Mason E A 1975 *Ann. Phys., NY* **91** 499
—— 1978 *Ann. Phys., NY* **110** 287
—— 1984 *J. Chem. Phys.* **80** 416

J. Chem. Soc., Faraday Trans. 2, 1987, 83(11), 2133-2137

The Structure and Energetics of the C_3N^+ Ion

Peter W. Harland and Robert G. A. R. Maclagan*

Department of Chemistry, University of Canterbury, Christchurch, New Zealand

Ab initio calculations of the relative energies for various structures and electronic states of the C_3N^+ ion have been performed and the results used to interpret the C_3N^+ ionization efficiency curve measured by the 'near-monochromatic' electron-impact ionization of cyanoacetylene, HC_3N. The calculated lowest-energy isomer, which is reconciled with the experimental appearance energy of the C_3N^+ ion at 17.78 ± 0.08 eV, is a $^3\Sigma^-$ state of the $CCCN^+$ isomer, corresponding to an experimentally determined C_3N^+ enthalpy of formation of 1850 kJ mol^{-1}. A sharp break in the experimental ionization efficiency curve 0.9 eV above the appearance energy is in accord with the formation of a cyclic C_3N^+ isomer which is calculated to lie 1.0 eV above the ground state. There is no conclusive experimental support for the electron-impact formation of the isocyano $CCNC^+$ isomers, which are calculated to lie 0.15 and 0.50 eV above the ground state.

The ionization efficiency curve for the cyanoethynyl ion, C_3N^+, investigated by the monochromatic electron-impact ionization of cyanoacetylene, HC_3N, revealed a sharp break 0.9 eV above the threshold.[1] Such an increase in the ionization cross-section with a distinctive threshold is characteristic of an additional channel for ion formation. This may involve further fragmentation of the dissociating molecular ion, the formation of an electronically excited neutral or ionic fragmentation product or the production of a higher-energy isomer. When several possibilities are energetically favourable it may be difficult to elucidate the ionization mechanism unambiguously. Complementary information from other experimental techniques, such as collision-induced dissociation and kinetic studies, as well as theoretical calculations of the structures and relative energies of the fragmentation products must be taken into account.

An experimental investigation of the C_2N^+ ion formed from electron-impact ionization of C_2N_2, CH_3CN and CH_3NC,[2] and from HC_3N[1] has identified two isomers, CNC^+ and the higher-energy isomer CCN^+, in agreement with the earlier predictions of *ab initio* calculations.[3] The difference in value between the enthalpies of formation for the isomers of the series H_xCNC^+/H_xCCN^+, where $x = 0$ to 3, range from -106 kJ mol^{-1} for $\Delta H_f(CNC^+) - \Delta H_f(CCN^+)$ to -21 kJ mol^{-1} for $\Delta H_f(H_3CNC^+) - \Delta H_f(H_3CCN^+)$[2] with an inversion of relative isometric stability for $x = 4$, where a kinetic study showed that $\Delta H_f(H_3CNCH^+) - \Delta H_f(H_3CCNH^+)$ is 43 kJ mol^{-1}.[4] The relative stabilities for this series of isomers could not have been predicted from the experimental enthalpy data and chemical intuition alone.

The only neutral fragmentation product from the formation of the C_3N^+ ion from HC_3N is the hydrogen atom. This eliminates the possibility that either electronic excitation or isomeric forms of the neutral fragmentation product could account for the second threshold occurring 0.9 eV above the first appearance energy for the ion. The second channel must involve either a metastable electronic state of the lowest-energy isomer formed at the first threshold or a stable, higher-energy isomer of C_3N^+. The experimental results cannot be used to differentiate between these two possibilities or to identify the structure of the lowest-energy isomer. *Ab initio* calculations have been carried out to determine the relative energies of available electronic states and isomeric structures.

Table 1. HF/6-311G*//HF/6-311G*, MP4SDQ/6-311G*//HF/6-311G* and relative energies of various structures and states of C_3N^+

structure	E (HF) /hartree	E (MP4SDQ) /hartree	relative energy (MP4SDQ) /eV
		$CCCN^+$	
$^3\Sigma^-$	−167.536 581	−167.994 082	0.000
$^3\Pi$	−167.532 524	−167.992 722	0.037
$^1A'$	−167.461 219	−167.974 995	0.519
		$CCNC^+$	
$^3\Sigma^-$	−167.514 026	−167.988 506	0.152
$^3\Pi$	−167 521 785	−167.975 715	0.500
		c-C_3N^+	
$^3B_1$	−167.456 338	−167.954 854	1.067
$^1A_1$	−167.424 636	−167.953 489	1.105

The structure of several species isoelectronic to C_3N^+ has been the subject of considerable theoretical interest recently. Calculations on C_4 have been reported by Whiteside *et al.*,[5] Magers *et al.*,[6] Wang *et al.*[7] and Lammertsma.[8] Calculations on Si_2C_2 have been reported by Trucks and Bartlett.[9] Lammertsma also reported calculations on related four-membered ring structures. For C_4 it was found that the relative energy of the linear ($^3\Sigma_g^-$) and rhombus (bicyclic ^1A_g) structures was very sensitive to the basis set used and, to a lesser degree, the level of theory used. For both C_4 and Si_2C_2, it appears that the singlet rhombic structures are lower in energy than the triplet linear structure, although the linear structures are lower in energy at the Hartree–Fock level of theory.

Calculations

The geometries of the C_3N^+ isomers were optimised at the RHF (singlets) or UHF (triplets) level of theory using GAUSSIAN 82[10] with the standard 6-311G* basis set. Calculations reported at the MP4SDQ level of theory used the optimised HF geometries. Some calculations were carried out with smaller basis sets. In particular, vibrational frequencies were calculated at the HF/6-31G* level of theory.

Results and Discussion

Table 1 lists the optimised Hartree–Fock energies, the MP4SDQ energies calculated at the optimised HF geometries, and relative energies of various structures and states of C_3N^+. Unlike C_4 and Si_2C_2, the lowest-energy structure is the $^3\Sigma^-$ state of $CCCN^+$ at both the HF and MP4SDQ levels of theory. Just 0.04 eV above this state is a $^3\Pi$ state. The configuration of the lowest-energy structure is

$$1\sigma^2 2\sigma^2 3\sigma^2 4\sigma^2 5\sigma^2 6\sigma^2 7\sigma^2 8\sigma^2 9\sigma^2 1\pi^4 2\pi^2.$$

The configuration of the $^3\Pi$ state is

$$1\sigma^2 2\sigma^2 3\sigma^2 4\sigma^2 5\sigma^2 6\sigma^2 7\sigma^2 8\sigma^2 9\sigma 1\pi^4 2\pi^3.$$

The ground state of the parent neutral molecule radical was found by Wilson and Green[11] to be the

$$1\sigma^2 2\sigma^2 3\sigma^2 4\sigma^2 5\sigma^2 6\sigma^2 7\sigma^2 8\sigma^2 9\sigma 1\pi^4 2\pi^4\ {}^2\Sigma^+$$

Table 2. Equilibrium bond lengths and bond angles for various structures and states of C_3N^+

structure	C_1-C_2 /Å	C_2-C_3 /Å	C_2-N /Å	C_3-N /Å
		$CCCN^+$		
$^3\Sigma^-$	1.335	1.292	—	1.223
$^3\Pi$	1.256	1.317	—	1.173
$^1A'$	1.346	1.310	—	1.164
		$CCNC^+$		
$^3\Sigma$	1.337	—	1.240	1.204
$^3\Pi$	1.264	—	1.241	1.204
		c-C_3N^+		
$^3B_1$	1.386	1.542	1.350	1.350
	(67.6)[a]	(111.4)[b]	(69.7)[c]	
$^1A_1$	1.513	1.542	1.310	1.310
	(61.3)[a]	(113.3)[b]	(72.1)[c]	

[a] $\angle C_2C_1C_3$/°. [b] $\angle C_1C_2N$/°. [c] $\angle C_2NC_3$/°.

state. The $^3\Pi$ state is formed by removing an electron from a 2π orbital, but the formation of the $^3\Sigma^-$ state involves the excitation of an electron from a 2π to the 9σ orbital as well. Von Niessen *et al.*[12] found that the lowest ionisation potential of cyanoacetylene is associated with the loss of an electron from the 2π orbital. The virtually linear $^1A'$ state is also derived from a $\cdots 9\sigma^2 1\pi^4 2\pi^2$ configuration. We were unable with the GAUSSIAN 82 program to investigate properly the open-shell singlet state derived from the same configuration as the $^3\Sigma^-$, $^3\Pi$ or $^3B_1$ states of C_3N^+. At the Hartree-Fock level of theory, the ground state of $CCNC^+$ is the $^3\Pi$ state, but when electron correlation is included the $^3\Sigma$ state is lower, lying only 0.15 eV above the triplet ground state of $CCCN^+$ in energy. The kite-shaped structure is again a triplet with the configuration

$$1a_1^2 2a_1^2 3a_1^2 1b_2^2 4a_1^2 5a_1^2 2b_2^2 6a_1^2 1b_1^2 3b_2^2 7a_1^2 2b_1 8a_1.$$

The $^1A_1$ structure, which is only just above the $^3B_1$ state, has the $8a_1$ orbital doubly occupied.

The energies quoted do not include any vibrational or rotational component. An estimate of the effect of including these contributions was obtained by calculating harmonic vibrational frequencies at the HF/6-31G* level of theory. Relative to the $CCCN^+$ $^3\Sigma^-$ state, the $^3\Pi$ state is raised 0.024 eV at 0 K and 0.025 eV at 298 K. At high temperatures the population of the $^3\Pi$ state will be greater than that of the $^3\Sigma^-$ state. Relative to the $CCCN^+$ $^3\Sigma^-$ state, the $^1A'$ state is raised by 0.005 eV at 0 K and 0.007 eV at 298 K. Relative to the $CCCN^+$ $^3\Sigma^-$ state the $^3B_1$ state is lowered 0.008 eV at 0 K and 0.023 eV at 298 K. The calculated harmonic frequencies for the $^3\Sigma^-$ $CCCN^+$ state were 234 (π), 509 (π), 937 (σ), 1531 (σ) and 2046 cm^{-1} (σ). The calculated rotational constant for $(^{12}C^{12}C^{12}C^{14}N)^+$ was 4773 MHz at the HF/6-311G* level of theory. The calculated harmonic frequencies for the $^3\Pi$ $CCCN^+$ state were: 198 (π), 250 (π), 496 (π), 530 (π), 996 (σ), 1896 (σ) and 2042 cm^{-1} (σ). The calculated rotational constant for $(^{12}C^{12}C^{12}C^{14}N)^+$ was 4994 MHz at the HF/6-311G* level of theory. The harmonic vibrational frequencies for $^3B_1$ C_3N^+ were: 498 (b_2), 616 (b_1), 980 (a_1), 995 (b_2), 1328 (a_1) and 1455 cm^{-1} (a_1). The calculated rotational constants for $(^{12}C^{12}C^{12}C^{14}N)^+$ were 35 410, 15 288 and 10 678 MHz. The rotational constant for $^3\Sigma^-(^{12}C^{12}C^{14}N^{12}C)^+$ was 5269 MHz and that for $^3\Pi$ $(^{12}C^{12}C^{14}N^{12}C)^+$ was 5461 MHz.

Table 2 gives the calculated parameters for the structures and electronic states calculated at the HF/6-311G* level of theory. When compared with the calculated

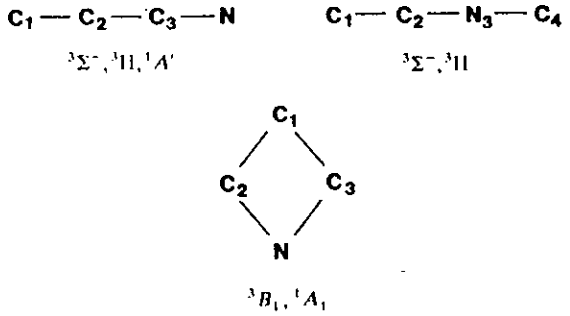

Fig. 1. Calculated states and structures of the C_3N^+ ion.

structural parameters for C_3N[11] and the calculated[13,14] and experimental[15,16] parameters for HC_3N, the parameters for the $^3\Sigma^-$ and $^3\Pi$ $CCCN^+$ structures are significantly different. The C_1—C_2 bond lengths are longer than those in C_3N and HC_3N and the C_2—C_3 bond lengths are shorter. The bond lengths in C_3N and HC_3N are very similar. In preliminary calculations, it was found that with bond lengths set initially to those in C_3N, the optimised triplet structure obtained had bond lengths similar to those in C_3N and HC_3N, but had the configuration $\ldots 7\sigma^2 8\sigma 9\sigma 1\pi^4 2\pi^4$ and was 2.13 eV above the ground-state configuration at the HF/6-311G level of theory. Another singlet configuration, 5.25 eV above the triplet ground state at the HF/6-311G level of theory, had the configuration $\ldots 8\sigma^2 1\pi^4 2\pi^4$. It also had a geometry similar to that in C_3N and HC_3N. The differences in geometry may be attributed to the unfilled 2π orbital in the triplet C_3N^+ state which is filled in C_3N and HC_3N. While the C_1—C_2 and C_2—C_3 bond lengths are similar for the $^3\Sigma^-$ state, for the $^3\Pi$ state the C_1—C_2 bond length is *ca.* 0.05 Å shorter and the C_2—C_3 bond length is *ca.* 0.04 Å longer than those found for the $^3\Sigma_g^-$ structure of C_4.[8,9] In the $^1A_1$ structure the C_1—C_2 bond length is 0.05–0.08 Å longer than found for the corresponding C_4 structure. In the $^3B_1$ structure it is 0.05–0.07 Å shorter than in the singlet C_4 structure.

Conclusion

The calculations at both the HF and MP4SDQ levels of theory indicate that the lowest-energy, ground-state structure of the C_3N^+ ion is the $^3\Sigma^-$ state of the $CCCN^+$ isomer (table 1 and fig. 1). Just above it is a $^3\Pi$ state which may be more populated at higher temperatures. The $^3\Sigma^-$ state of the isocyano isomer $CCNC^+$ lies *ca.* 0.15 eV above the ground state. The electronically excited $^1A'$ state of the $CCCN^+$ isomer and the $^3\Pi$ state of the isocyano isomer, $CCNC^+$, lie close together in energy at 0.5 eV above the ground state. A cyclic isomer, existing in both triplet and singlet states, lies 1.0 eV above the ground state, the triplet being of marginally lower energy. It is difficult to access the error in these theoretical energy differences between various C_3N^+ states. Certainly it should be better than the *ca.* 0.1 eV error found by Hehre *et al.*[17] in a comparison of calculations done at the MP4SDQ/6-31G*//HF/3-21G level of theory.

The first threshold in the C_3N^+ ionization efficiency curve at 17.78 ± 0.08 eV is consistent with the formation of the $^3\Sigma^-$ or the $^3\Pi$ state of the $CCCN^+$ isomer with an enthalpy of formation of 1850 kJ mol^{-1}:

$$HC_3N + e^-(17.78\ \text{eV}) \rightarrow CCCN^+(^3\Sigma^-) + H'(^2S) + 2e^-. \qquad (1)$$

The second threshold, at 18.64 ± 0.08 eV, lies 0.86 ± 0.16 eV above the appearance energy, in good accord with the calculated difference in energy between the ground state and the $^3B_1$ state of the cyclic isomer lying 1.07 eV (or 1.04 eV when thermal energies are included) above the ground state:

$$\mathrm{HC_3N} + \mathrm{e}^-(18.64\ \mathrm{eV}) \rightarrow \text{c-}\mathrm{C_3N}^+(^3B_1) + \mathrm{H}^{\cdot}(^2\mathrm{S}) + 2\mathrm{e}^-. \qquad (2)$$

The enthalpy of formation for the $^3B_1$ state of the c-C_3N^+ isomer calculated from the experimental results is 1935 kJ mol^{-1}.[1]

Ionization efficiency curves generated by low-intensity 'near-monochromatic' electron–molecule collisions suffer from significant statistical fluctuations because of the low ion count rates. Consequently, processes with low ionization cross-sections can be missed and the failure to observe a threshold for a known state of the ion or neutral fragmentation product does not eliminate such channels. The absence of a threshold 0.15 or 0.50 eV above the appearance energy corresponding to the $^3\Sigma^-$ or $^3\Pi$ CCNC$^+$ isomers may indicate either low-cross-section processes or an absence of the CCNC$^+$ isomer under electron-impact ionization.

References

1 P. W. Harland, *Int. J. Mass Spectrom. Ion Process.*, 1986, **70**, 231.
2 P. W. Harland and B. J. McIntosh, *Int. J. Mass Spectrom. Ion Process.*, 1985, **67**, 29.
3 N. N. Haese and R. C. Woods, *Astrophys. J.*, 1981, **246**, L51.
4 J. S. Knight, C. G. Freeman and M. J. McEwan, *J. Am. Chem. Soc.*, 1986, **108**, 1404.
5 R. A. Whiteside, R. Krishnan, D. J. DeFrees, J. A. Pople and P. v. R. Schleyer, *Chem. Phys. Lett.*, 1981, **78**, 538.
6 D. H. Magers, R. J. Harrison and R. J. Bartlett, *J. Chem. Phys.*, 1986, **84**, 3284.
7 Z. Z. Wang, R. N. Diffenderfer and I. Shavitt, paper presented at 25th Sanibel Symposium, March 1985.
8 K. Lammertsma, *J. Am. Chem. Soc.*, 1986, **108**, 5127.
9 G. W. Trucks and R. J. Bartlett, *J. Mol. Struct.*, 1986, **135**, 423.
10 J. S. Binkley, M. J. Frisch, D. J. DeFrees, K. Raghavachari, R. A. Whiteside, H. B. Schlegel, E. M. Fluder and J. A. Pople, GAUSSIAN 82 (Carnegie Mellon University, Pittsburgh, 1983).
11 S. Wilson and S. Green, *Astrophys. J.*, 1977, **212**, 87.
12 W. Von Niessen, L. S. Cederbaum, J. Schirmer, G. H. F. Diercksen and W.P. Kraemer, *J. Electron Spectrosc. Relat. Phenom.*, 1982, **28**, 45.
13 R. J. Boyd, W. E. Jones and K. W. Ling, *Chem. Phys.*, 1981, **58**, 203.
14 R. D. Brown and E. H. N. Rice, *J. Am. Chem. Soc.*, 1984, **106**, 6475.
15 R. A. Westenberg and E. B. Wilson, *J. Am. Chem. Soc.*, 1950, **72**, 199.
16 J. K. Tyler and J. Sheridan, *Trans. Faraday Soc.*, 1976, **59**, 175.
17 W. J. Hehre, L. Radom, P. v. R. Schleyer and J. A. Pople, *Ab Initio Molecular Orbital Theory* (Wiley, Interscience, New York, 1985).

Paper 7/345; Received 23rd February, 1987

Interaction potentials and mobility calculations for the HeO$^+$ system

R. W. Simpson, R. G. A. R. Maclagan, and P. W. Harland
Department of Chemistry, University of Canterbury, Christchurch, New Zealand

(Received 29 May 1987; accepted 16 July 1987)

Valence bond, SCF, and MP4SDQ calculations are reported for three low lying states of the HeO$^+$ molecular ion; $^4\Sigma(^4S)$, $^2\Pi(^2D)$, and $^2\Pi(^2P)$. Together with the two-temperature theory of ion transport, these interaction potentials have been used to calculate the drift velocity and reduced mobility of O$^+$ in helium as a function of the electric field to gas number density ratio. The calculated HeO$^+$ ($^4\Sigma$) interaction potentials adequately describe the mobility of ground state O$^+$ in helium, however, the O$^+$ (^2D) mobility calculated using the $^2\Pi(^2D)$ interaction potential does not match the experimental mobility measurements for the metastable O^{+*} ion which have been reported as the O$^+$ (^2D) state. An interaction potential is reported for HeO$^+$ [$^2\Pi(^2P)$] which will reproduce the experimental mobility of O^{+*}.

I. INTRODUCTION

The He–O$^+$ system has previously been investigated by both experimental techniques (mobility measurements and beam experiments) and using *ab initio* calculations. The relationship between ion transport properties, such as the ion mobility, and the interaction potential between the ion and neutral gas atoms or molecules is provided by ion transport theory.[1] Thus, mobility measurements of O$^+$ in helium serve as a probe to investigate the HeO$^+$ interaction potential, and conversely *ab initio* or otherwise determined HeO$^+$ interaction potentials can be used to calculate the mobility of O$^+$ in helium. The O$^+$ ion is one of the most abundant ions in the ionosphere[2] where satellite measurements have found 38% of O$^+$ is in the ^2D state and 20% in the ^2P state.[3] Consequently, it has been desirable to determine rate coefficients for reactions involving these electronic states of the O$^+$ ion. The determination of rate coefficients of ion–neutral reactions using inert gas buffered flow tubes or static drift tubes requires a knowledge of the ion mobility over the experimental range of electric field to particle density ratio E/N.

A number of experimental investigations of the mobility of O$^+$ in helium have been reported including several recent studies in which a less mobile ion of $m/z = 16$ was observed and assigned to the excited ^2D state of the O$^+$ ion. Following on from our earlier experimental and theoretical studies into the effect of ion structure on gas phase ion transport properties,[4,5] we have calculated interaction potentials for the $^4\Sigma(^4S)$, $^2\Pi(^2D)$, and $^2\Pi(^2P)$ states of HeO$^+$. The two-temperature theory of ion mobility[6,7] has been used with these interaction potentials to calculate the mobility of the three lowest electronic states of O$^+$ (^4S, ^2D, and ^2P). Our results indicate that the previously assigned O$^+$ (^2D) ion is not responsible for the experimental observations and we are confident that the ^2P state of O$^+$ is the ion observed.

II. PREVIOUS WORK

The mobility of O$^+$ in He has been of continuing interest in experimental gas phase ion chemistry. Mobility measurements are required so that reaction rate data from flow tubes can be analyzed to obtain rate coefficients. Heimerl *et al.*[8] and Johnsen *et al.*[9] reported drift tube mass spectrometer measurements of the mobility of O$^+$ in helium. Later these were improved by McFarland *et al.*[10] and Lindinger *et al.*[11] to the stage where the mobility of ground state O$^+$ in helium was well characterized. In 1975, Kosmider and Hasted[12] realized that their ion drift tube could produce an appreciable proportion of excited O$^+$ ions. Using a test reaction for excited O$^+$ ions[13] they were able to control their ion source conditions to produce exclusively ground state O$^+$. The resulting mobility measurements agreed well with those of McFarland *et al.*[10] It was not until satellite data were analyzed[3] that the importance of excited states of O$^+$ in the ionosphere was realized, and consequently it was desirable to measure rate coefficients for reactions involving both ground and excited states of the O$^+$ ion. Johnsen and Biondi[14] reported a difference in ionic mobilities of metastable-state and ground-state ions in helium, the first case in which state specific mobilities have been observed for ions in a chemically different gas. Following this, Rowe *et al.*[15] used a selected ion flow tube to measure some reaction rates and the mobility of O^{+*} with an experimental error of 7%. During the mobility measurements slightly skewed O$^+$ arrival time distributions were observed, consistent with two ions of $m/z = 16$ being present in the flow tube. The major ion appeared to be the ^4S ground state and the slower minor ion was assigned as the ^2D state of O$^+$. The mobility of this metastable ion in helium was determined over the electric field to gas density ratio (E/N) range 5 to 100 Td, where 1 Td $\equiv 10^{-21}$ V m^2. Johnsen *et al.*[16] returned to the problem of measuring the mobility of O^{+*} in helium but they could only observe it over a limited field range, $E/N < 40$ Td. In the most recent study on O$^+$ and O^{+*} mobility to date, Fhadil *et al.*[17] reproduced the data of Lindinger *et al.*[11] for the ground state O$^+$ ion, and also extended the data of Rowe *et al.*[15] for O^{+*} up to 150 Td, but with reduced errors (less than 5%). They used an injected ion drift tube to make these measurements. The identity of the O^{+*} ion in all these studies is still debated although evidence from a number of different sources suggested that the O^{+*} ions were most likely in the ^2D state. However, this assignment was not unambiguous. In particular satellite data for the reaction of O$^+$ (^2D) ions with N$_2$ cannot be reconciled with ion flow tube measurements of O^{+*} with N$_2$ [15] which implies that the O^{+*} ions are largely

© 1987 American Institute of Physics

in the O$^+$(^2P) state. It should be noted that the experimental observation of excited states of ions in a flow or drift tube is very difficult and the presence or absence of these ions can be strongly dependent upon the ion source conditions during the experiment.[10,18]

There have been several attempts at calculating interaction potentials for the HeO$^+$ ion. SCF molecular orbital calculations have been carried out on the $^2\Pi$ and $^2\Sigma$ states using Gaussian orbitals[19] and on the $^2\Pi$ state using Slater orbitals.[20] A Monte Carlo simulation of ion motion[21] has been used to determine a ground-state interaction potential for HeO$^+$ by fitting calculation results to the observed mobility of O$^+$ in He.[10] An empirical (n,6,4) potential has been determined[22] which will reproduce the experimental mobility of O$^+$ in He[11] when used with the two-temperature theory of ion mobility. The most extensive *ab initio* calculation on HeO^{+}[23] used a minimal basis set and full CI to calculate potential curves corresponding to all the valence states of HeO$^+$, as well as an O($6s$,$4p$,$1d$), He($2s2p$) basis set for more accurate calculations on a few selected states, but did not include enough information on each state for these interaction potentials to be useful in calculating ion mobility. The lack of very accurate mobility data (1%–2% error) for O^{+*} in He over a wide range of E/N precludes the possibility of obtaining an interaction potential by inverting such data.[24]

III. DETAILS OF CALCULATIONS

The ground-state interaction potential of HeO$^+$, separating at infinity to He (^1S) and O$^+$(^4S), was calculated using the GAUSSIAN82 program[25] at the MP4SDQ/6-311 + G($3df$,$3pd$) level of theory, excluding core contributions to the correlation energy. The results of the calculation are given in Table I. At 1.191 Å we estimate an energy of −77.256 38 hartree which compares well with the MP4SDTQ/6-311G($2df$,$2pd$) calculation by Koch and Frenking[26] who obtained −77.258 58 hartree. For ground-state O$^+$(^4S) there is only one molecular ion state formed with He(^1S) which is HeO$^+$($^4\Sigma$). However, there are three states of HeO$^+$ which dissociate to give O$^+$(^2D) + He(^1S). These are the $^2\Pi(^2D)$, $^2\Sigma(^2D)$, and $^2\Delta(^2D)$ states. Similarly, there are two states of HeO$^+$, $^2\Pi(^2P)$ and $^2\Sigma(^2P)$, which dissociate to give O$^+$(^2P) and He(^1S). In the present work we only consider the lowest energy molecular ion state which dissociates to each of the three low energy states of O$^+$. The rationale behind this choice is that during a collision between O$^+$, in a particular state, and He(^1S) the HeO$^+$ molecular ion formed will naturally adopt the state of lowest energy if more than one molecular state is accessible. Consequently, the mobility of O$^+$ will be dominated by the two-body collisions whose interaction potential energy corresponds to the lowest energy molecular ion state which will dissociate into the particular state of O$^+$ being studied. All of the molecular ion states which dissociate to O$^+$ (^2P) and He(^1S) and to O$^+$(^2D) and He(^1S) require multiple reference functions to describe this process correctly. The GAUSSIAN 82 program is not able to describe interaction potentials which require more than one reference function to correctly describe molecular dissociation so a different theoretical method was required for the doublet states of HeO$^+$. Valence bond methods do not have this limitation so this approach was used. The valence bond program has been described previously.[27] The integrals required were calculated with Steven's integral package.[28] In a preliminary valence bond study a minimum basis set calculation was carried out to identify the electronic configurations of HeO$^+$ which dissociate to give doublet O$^+$ and He(^1S) and to assign these to the various molecular ion states available. It was found, as expected, that the $^2\Pi(^2P)$ and $^2\Pi(^2D)$ molecular states arise from the $1s^2_{\mathrm{He}}\,1s^2_{\mathrm{O}}\,2s^2_{\mathrm{O}}\,2p_{x,\mathrm{O}}\,2p^2_{y,\mathrm{O}}$ and $1s^2_{\mathrm{He}}\,1s^2_{\mathrm{O}}\,2s^2_{\mathrm{O}}\,2p^2_{z,\mathrm{O}}$ configurations. The $^2\Delta(^2D)$ molecular state arises from the $1s^2_{\mathrm{He}}\,1s^2_{\mathrm{O}}\,2s^2_{\mathrm{O}}\,2p^2_{x,\mathrm{O}}\,2p_{z,\mathrm{O}}$, $1s^2_{\mathrm{He}}\,1s^2_{\mathrm{O}}\,2s^2_{\mathrm{O}}\,2p^2_{y,\mathrm{O}}\,2p_{z,\mathrm{O}}$, and $1s^2_{\mathrm{He}}\,1s^2_{\mathrm{O}}\,2s^2_{\mathrm{O}}\,2p_{x,\mathrm{O}}\,2p_{y,\mathrm{O}}\,2p_{z,\mathrm{O}}$ configurations. The $^2\Sigma(^2P)$ state arises from the $1s^2_{\mathrm{He}}\,1s^2_{\mathrm{O}}\,2s^2_{\mathrm{O}}\,2p^2_{x,\mathrm{O}}\,2p_{z,\mathrm{O}}$ and $1s^2_{\mathrm{He}}\,1s^2_{\mathrm{O}}\,2s^2_{\mathrm{O}}\,2p^2_{y,\mathrm{O}}\,2p_{z,\mathrm{O}}$ configurations. The $^2\Sigma(^2D)$ state arises from the $1s^2_{\mathrm{He}}\,1s^2_{\mathrm{O}}\,2s^2_{\mathrm{O}}\,2p_{x,\mathrm{O}}\,2p_{y,\mathrm{O}}\,2p_{z,\mathrm{O}}$ configuration. This preliminary study provided the necessary base functions from which excitations using a better basis set could yield a large number of configurations to be included in more extensive valence bond calculations of He + O$^+$ interaction potentials. Valence bond calculations were performed to determine the interaction potential energies of the $^4\Sigma$, $^2\Pi(^2D)$, and $^2\Pi(^2P)$ states of HeO$^+$ using a double-zeta (DZ) basis set with orbital exponents from Huzinaga and Arnau.[29] This basis was contracted to He($1s$,$2s$) and O($1s$,$2s$,$3s$,$2p$,$3p$) using contraction coefficients which had been determined from atomic calculations on He(^1S), O$^+$(^4S), and O$^+$(^2D) using the program of Roos *et al.*[30] Table II lists the contraction coefficients. For the $^2\Pi(^2P)$ state of HeO$^+$, the O$^+$(^2D) contraction coefficients were used. This basis set was augmented with the addition of polarization functions (p on He, d on O) and diffuse functions on each center ($2s$ on He; $3s$ and $3p$ on O). The diffuse func-

TABLE I. MP4SDQ and HF energies for the HeO$^+$($^4\Sigma$)

	E(hartree)	
r(Å)	HF	MP4SDQ
0.875	−76.751 470 2	−76.922 271 6
1.000	−76.938 016 3	−77.106 569 1
1.125	−77.051 414 0	−77.217 285 4
1.25	−77.120 739 1	−77.283 381 6
1.375	−77.163 602 0	−77.322 966 7
1.5	−77.190 050 3	−77.346 652 3
1.625	−77.206 135 1	−77.360 686 2
1.75	−77.215 724 4	−77.368 854 9
1.875	−77.221 300 8	−77.373 476 4
2.0	−77.224 430 8	−77.375 969 6
2.25	−77.226 932 6	−77.377 756 4
2.375	−77.227 302 1	−77.377 927 8
2.5	−77.227 427 6	−77.377 915 0
2.625	−77.227 429 0	−77.377 818 7
2.75	−77.227 371 5	−77.377 691 1
3.0	−77.227 203 3	−77.377 431 1
3.5	−77.226 902 2	−77.377 045 3
4.0	−77.226 699 3	−77.376 804 4
4.5	−77.226 583 0	−77.376 671 3
5.0	−77.226 523 9	−77.376 605 1
∞	−77.226 436 9	−77.376 511 0

(1 hartree = 27.210 7 eV)

TABLE II. Basis set for valence bond calculations on HeO^+.

Contraction coefficients

	O^+ ($^4\Sigma$)	He(^1S)	O^+ (^2D)
1s	0.717 389		0.717 282
	0.291 325		0.291 490
	0.002 191 74		0.002 313 99
	−0.002 599 88		−0.002 832 06
2s	−0.326 755		−0.327 532
	0.027 576 3		0.027 710 9
	0.241 122		0.236 383
	0.840 833		0.845 501
2p	0.662 810		0.673 097
	0.424 228		0.412 989
3s	−0.551 153		−0.549 790
	0.199 934		0.199 358
	−2.143 20		−2.143 63
	2.132 09		2.130 04
3p	1.186 07		1.180 26
	−1.290 78		−1.294 42
1s		0.844 778	
		0.179 640	
2s		1.621 28	
		−1.819 32	

Additional functions included in basis set:

Center	polarization functions	diffuse functions
He	$2p(\xi = 1.5)$	$2s(\xi = 0.687)$
O	$3d(\xi = 1.0)$	$3s(\xi = 1.342)$
		$3p(\xi = 0.794)$

TABLE III. Valence bond energies for HeO^+.

	E (hartree)		
r (bohr)	$^4\Sigma$	$^2\Pi(^2D)$	$^2\Pi(^2P)$
1.5	−76.477 195 77	−76.827 690 60	−75.578 930 59
2.0	−76.981 859 93	−77.045 408 42	−76.525 758 87
2.25	−77.089 365 67	−77.076 385 31	−76.743 129 48
2.5	−77.151 707 48	−77.088 207 85	−76.870 921 45
2.75	−77.187 718 94	−77.092 157 16	−76.943 902 11
3.0	−77.208 307 85	−77.094 204 93	−76.983 420 83
3.25	−77.219 882 80	−77.096 419 63	−77.003 238 26
3.5	−77.226 237 41	−77.098 626 44	−77.012 483 25
4.0	−77.231 333 04	−77.101 359 00	−77.018 397 97
4.5	−77.232 473 41	−77.102 168 18	−77.019 415 97
5.0	−77.232 537 95	−77.102 247 18	−77.019 467 56
5.5	−77.232 363 16	−77.102 156 27	−77.019 355 58
6.0	−77.232 163 84	−77.102 055 87	−77.019 244 41
6.5	−77.231 985 06	−77.101 976 19	−77.019 159 77
7.0	−77.231 832 13	−77.101 915 87	−77.019 097 84
7.5	−77.231 705 18	−77.101 872 27	−77.019 054 47
8.0	−77.231 599 69	−77.101 840 22	−77.019 023 34
10.0	−77.231 386 43	−77.101 776 86	−77.018 962 73
∞	−77.231 234 82	−77.101 729 32	−77.018 916 96

(1 bohr = 0.529 177 Å)

tions were based upon the diffuse Gaussian orbitals used in a study on HeO.[31] The details of these additional functions are also contained in Table II. For the $^4\Sigma$ state, 64 configurations were chosen. The majority of these being single excitations from three base configurations: $1s_{\rm He}^2 1s_{\rm O}^2 2s_{\rm O}^2 p_{x,{\rm O}} p_{y,{\rm O}} p_{z,{\rm O}}$, $1s_{\rm He}^2 1s_{\rm O}^2 2s_{\rm O} p_{x,{\rm O}} p_{y,{\rm O}} p_{z,{\rm O}}^2$, and $1s_{\rm He} 1s_{\rm O}^2 2s_{\rm O}^2 p_{x,{\rm O}} p_{y,{\rm O}} p_{z,{\rm O}}^2$. These included all the $p \rightarrow p$, $s \rightarrow s$, and $p \rightarrow d$ excitations possible from the base configurations. Also included in the configurations list were a number of double excitations of *s* functions.

For the two doublet states a similar procedure was used resulting in a total of 71 configurations. Five base functions were used: $1s_{\rm He}^2 1s_{\rm O}^2 2s_{\rm O}^2 p_{x,{\rm O}} p_{y,{\rm O}}^2$, $1s_{\rm He}^2 1s_{\rm O}^2 2s_{\rm O}^2 p_{x,{\rm O}} p_{z,{\rm O}}^2$, $1s_{\rm He} 1s_{\rm O}^2 2s_{\rm O}^2 p_{x,{\rm O}} p_{y,{\rm O}}^2 p_{z,{\rm O}}$, $1s_{\rm He}^2 1s_{\rm O}^2 2s_{\rm O} p_{x,{\rm O}} p_{y,{\rm O}}^2 p_{z,{\rm O}}$, and $1s_{\rm He} 1s_{\rm O}^2 2s_{\rm O} p_{x,{\rm O}} p_{y,{\rm O}}^2 p_{z,{\rm O}}^2$. Twenty-five configurations were generated by single and double excitation from each of bases 1 and 2, 12 from base 3, and the remainder from bases 4 and 5. Valence bond calculations were performed over the range 1.5 to 10.0 bohr. The results of the valence bond calculations are summarized in Table III.

IV. DISCUSSION

Both the quartet and doublet calculations exhibited the correct separation behavior: $HeO^+(^4\Sigma) \rightarrow He(^1S) + O^+(^4S)$, $HeO^+[^2\Pi(^2D)] \rightarrow He(^1S) + O^+(^2D)$ and $HeO^+[^2\Pi(^2P)] \rightarrow He(^1S) + O^+(^2P)$. The two doublet-state calculations were performed simultaneously because only one calculation was required to get energies for each state. With the exception of calculations performed at small internuclear separation, the lowest energy and eigenfunction corresponded to the $^2\Pi(^2D)$ and the second lowest to the $^2\Pi(^2P)$ state. In a similar calculation on the $^2\Delta(^2D)$ and $^2\Sigma(^2P)$ states at several distances, the energies obtained were higher than the corresponding $^2\Pi(^2D)$ and $^2\Pi(^2P)$ energies. This agrees with a previous calculation[19] and we are confident that the $^2\Pi(^2D)$ and $^2\Pi(^2P)$ states of HeO^+ are the lowest energy molecular states dissociating to give $O^+(^2D)$ and $O^+(^2P)$, respectively. The VB calculated energy separations between the states compare well with the atomic energy levels. We calculate that the $O^+(^2D)$ state lies 28 400 cm^{-1} above and the $O^+(^2P)$ state 46 600 cm^{-1} above the ground state compared with 26 819 and 40 468 cm^{-1} observed spectroscopically.[32] The calculated interaction potentials were used as input to our two-temperature theory program which calculates the dependence of the reduced mobility on E/N for a tabulated interaction potential, the details of which have been described.[5] It was necessary to carry out a valence bond calculation on the ground state of $HeO^+(^4\Sigma)$ in order to compare the quality of the mobility calculated from an interaction potential at this level of theory with the mobility calculated from the more accurate MP4SDQ/6-311 + G(3*df*,3*pd*) $HeO^+(^4\Sigma)$ interaction potential. The confidence we have in our results for the doublet state mobilities of O^+ in helium is based on the good agreement between the mobilities calculated for ground-state O^+ in helium by both the valence bond and fourth-order Moller–Plesset methods.

The calculated reduced mobility of O^+ in helium as a function of E/N from the MP4SDQ interaction potential of $HeO^+(^4\Sigma)$, shown in Fig. 1, accurately reproduces the experimental measurements on ground-state O^+ in helium.[11,17] The corresponding VB calculation is 12% too low at 5 Td, but above 25 Td the agreement is better than 7%. Valence bond calculations with an extended basis set employing a suitably chosen set of configurations should there-

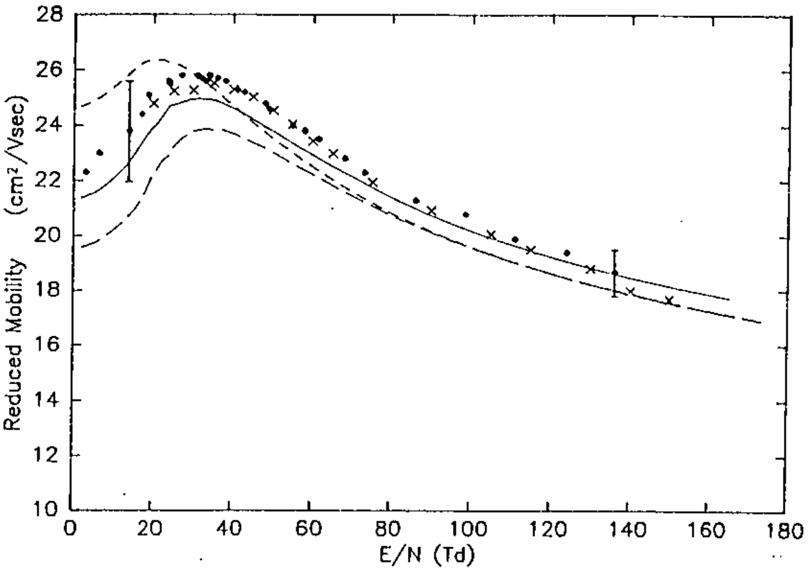

FIG. 1. Reduced mobility of O^+ in He. ●, experimental values (Ref. 11); ×, experimental values (Ref. 17); (—), calculation using MP4SDQ potential; (– –), calculation using VB ($^4\Sigma$) potential; (---), calculation using HF potential.

fore provide an interaction potential which can accurately describe the mobility of an ion above 30 Td. The reduced mobility calculated from the HF interaction potential is higher than the experimental measurements at low values of E/N and is less suitable for determining the position of the maximum in the experimental reduced mobility than either of the calculations based on the MP4SDQ or VB interaction potentials. On the basis of previous mobility calculations[5] we know that this HF interaction potential well depth is too small resulting in a calculated reduced mobility which is higher than the experiment results at low values of E/N. Table IV lists some parameters derived from the interaction potentials in the present study; r_m is the distance corresponding to the minimum energy, ϵ the well depth, and σ the internuclear separation at which the energy is zero. It can be seen in Table IV that the well depth of the HF interaction potential is significantly less than the well depth of the other $^4\Sigma$ calculations. We have found previously[4,5] that low field reduced mobilities are very sensitive to minor changes in the position r_m and depth ϵ of the interaction potential well, and a high level of theory is required to estimate these quantities accurately. A small change in r_m or ϵ may lead to a relatively large change in the long range part of the interaction potential, the region known to affect the calculated low field mobilities.[24] In contrast experimental mobilities for atomic ions measured at values of E/N above 30 Td can be reproduced within experimental error using the two-temperature theory of ion mobility with interaction potentials generated using *ab initio* methods.[5] Valence bond calculations performed on the two low lying doublet states of HeO^+ were used to calculate the reduced mobility curves shown in Fig. 2. It is immediately obvious that the mobility calculated using the $HeO^{+2}\Pi(^2P)$ interaction potential is remarkably close to the experimental values for the mobility of O^{+*} in helium except at low values of E/N. The correlation between the mobility calculated using the $HeO^{+2}\Pi(^2D)$ interaction potential and the experimental values is very poor and certainly well outside the maximum discrepancies expected from application of the second approximation of the two-temperature theory.[5] From Table IV it is not possible to account for the difference in the calculated mobilities of $O^+(^2P)$ and $O^+(^2D)$ on the basis of r_m and ϵ values. The difference in the interaction potentials which is responsible for the higher calculated mobility of $O^+(^2D)$ than $O^+(^2P)$ appears to be a significantly "harder" repulsive wall in the $HeO^{+2}\Pi(^2P)$ interaction potential as compared with the $HeO^{+2}\Pi(^2D)$ interaction potential. The third curve in Fig. 2 was obtained by scaling the negative energies (relative to the separated atoms) of the $HeO^{+2}\Pi(^2P)$ curve by a factor of 2.4. This has the effect of decreasing the well depth by only 0.02 eV and has a dramatic effect on the low field reduced mobility but only a small effect above 40 Td. No reasonable amount of adjustment of the $HeO^{+2}\Pi(^2D)$ potential well will ever bring the calculated reduced mobility of $O^+(^2D)$ in helium within the experimental errors of the measurement of the reduced mobility of O^{+*} in helium. Figure 3 shows the drift velocity v_d of O^+ in helium as a function of E/N calculated for the three states of O^+ considered in this study together with the experimental results for O^+ and O^{+*} drifting in helium. This dramatically illustrates our conclusion from

TABLE IV. Interaction potential parameters for HeO^+.

State	Method	σ (Å)	r_m (Å)	ϵ (eV)
$^4\Sigma$	MP4SDQ	2.04	2.42	0.0388
$^4\Sigma$	HF	2.16	2.56	0.0273
$^4\Sigma$	VB	2.11	2.53	0.0363
$^2\Pi(^2D)$	VB	2.19	2.55	0.0145
$^2\Pi(^2P)$	VB	2.20	2.51	0.0162

where $V(\sigma) = 0$ and $V(r_m) = -\epsilon$

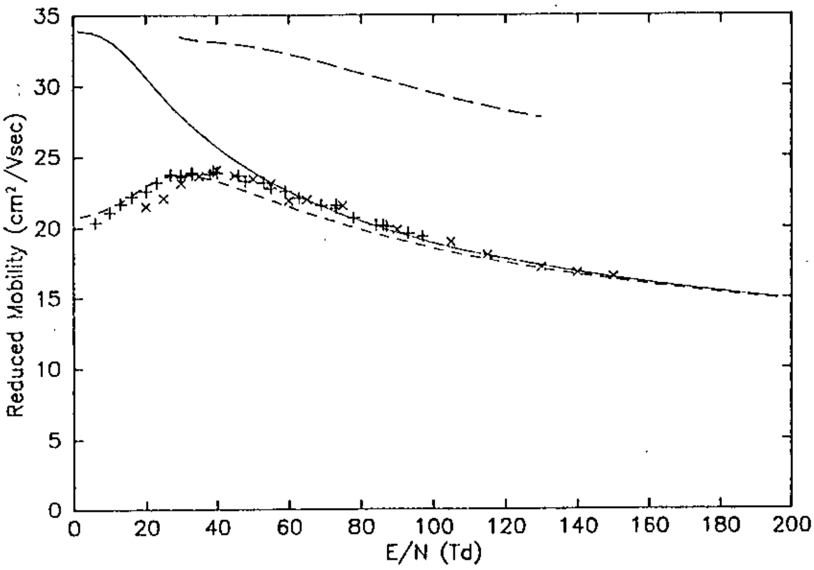

FIG. 2. Reduced mobility of O^{+*} in He. +, experimental values (Ref. 15); ×, experimental values (Ref. 17); (—), calculation using VB $^2\Pi(^2P)$ potential; (– –), calculation using VB$^2\Pi(^2D)$ potential; (---), calculation using VB $^2\Pi(^2P)$ potential with the well increased in depth by 0.02 eV.

this work that the O^{+*} ion observed in experiments[15–17] and assigned as O$^+(^2D)$ should be reassigned as the O$^+(^2P)$ state.

Previous experimental evidence used in justifying the O$^+(^2D)$ state assignment included comparison of photorelaxation lifetimes and energy levels for each possible state. However, a typical ion source producing O^{+*} will be forming both the ^2P and ^2D states as they are only 13 650 cm^{-1} (1.7 eV) apart. Both states have photorelaxation lifetimes several orders of magnitude longer than flow-drift tube transit times so neither state will be significantly depleted by this process. The apparent state selection of O$^+(^2P)$ can be explained in terms of the potential energy surface crossing between the $^2\Pi(^2D)$ state and the $^4\Sigma$ ground state of HeO$^+$. This occurs at 2.2 bohr and is 0.8 eV above the energy of O$^+(^2D)$ + He(^1S) and 4.3 eV above the energy of O$^+(^4S)$ + He(^1S). The presence of this curve crossing provides an effective channel for depletion of the $^2\Pi(^2D)$ state. There is no equivalent curve crossing from the $^2\Pi(^2P)$ state of HeO$^+$ to lower lying surfaces. The presence of the $^2\Pi(^2D)$ state and $^4\Sigma$ state curve crossing has been predicted[23] to result in quenching of the ^2D state of O$^+$ by He but not the ^2P

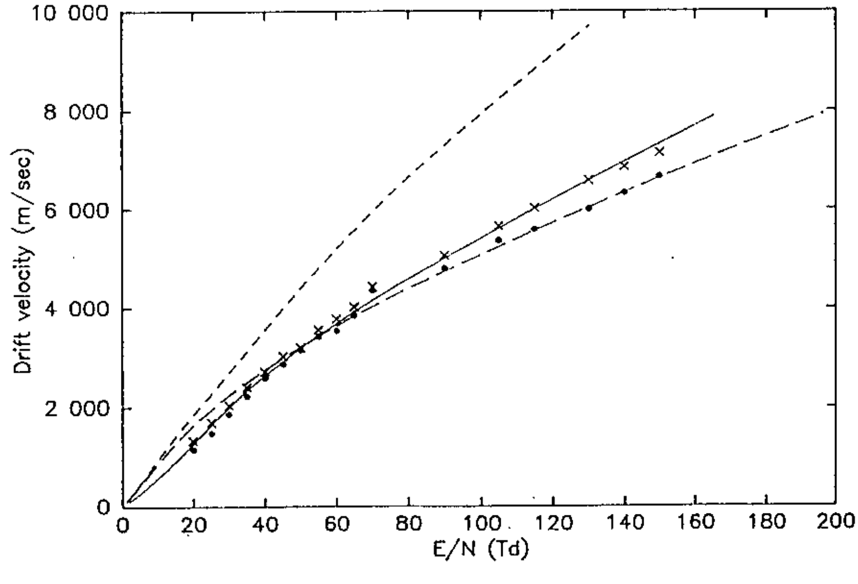

FIG. 3. Drift velocity of O$^+$ and O^{+*} in He. ×, O$^+$ experimental values (Ref. 17); ●, O^{+*} experimental values (Ref. 17); (—), calculation using MP4SDQ ($^4\Sigma$) potential; (– –), calculation using VB$^2\Pi(^2P)$ potential; (---), calculation using VB$^2\Pi(^2D)$ potential.

state. This quenching process is written as follows:

$$\mathrm{He} + \mathrm{O}^+(^2D) \rightarrow \mathrm{He} + \mathrm{O}^+(^4S).$$

The assignment of O^{+*} observed in flow tube studies to the ^2D state of O$^+$ is based upon limited evidence and is in direct conflict with some experimental results. Based upon our mobility calculations, using *ab initio* interaction potentials, we believe that it is in fact O$^+(^2P)$ which has been observed. This can be explained since both O$^+(^2P)$ and O$^+(^2D)$ will be formed in an ion source producing O^{+*} but only the ^2D state of O$^+$ can be quenched by collision with He.

ACKNOWLEDGMENTS

We wish to acknowledge computational assistance from Chemistry Division, D.S.I.R. and the University Grants Committee for the provision of a postgraduate scholarship to R.W.S.

[1] L. A. Viehland and E. A. Mason, J. Chem. Phys. **80**, 416 (1984).

[2] E. E. Ferguson, F. C. Fehsenfeld, and D. L. Albritton, Gas Phase Ion Chem. **1**, 45 (1971).

[3] M. Oppenheimer, E. R. Constantinides, K. Kirby-Docken, G. A. Victor, and A. Dalgarno, J. Geophys. Res. **82**, 5485 (1977).

[4] P. W. Harland, B. J. McIntosh, R. W. Simpson, and N. R. Thomas, J. Chem. Soc. Faraday Trans. 2 **82**, 2039 (1986).

[5] R. W. Simpson, R. G. A. R. Maclagan, and P. W. Harland, J. Phys. B **20**, 2723 (1987).

[6] L. A. Viehland and E. A. Mason, Ann. Phys. **91**, 499 (1975).

[7] L. A. Viehland and E. A. Mason, Ann. Phys. **110**, 287 (1978).

[8] J. Heimerl, R. Johnsen, and M. A. Biondi, J. Chem. Phys. **51**, 5041 (1969).

[9] R. Johnsen, H. L. Brown, and M. A. Biondi, J. Chem. Phys. **52**, 5080 (1970).

[10] M. McFarland, D. L. Albritton, F. C. Fehsenfeld, E. E. Fergusson, and A. L. Schmeltekopf, J. Chem. Phys. **59**, 6610 (1973).

[11] M W. Lindinger and D. L. Albritton, J. Chem. Phys. **62**, 3517 (1975).

[12] R. G. Kosmider and J. B. Hasted, J. Phys. B **8**, 273 (1975).

[13] P. P. Ong and J. B. Hasted, J. Phys. B **2**, 91 (1969).

[14] R. Johnsen and M. A. Biondi, J. Chem. Phys. **73**, 190 (1980).

[15] B. R. Rowe, D. W. Fahey, F. C. Fehsenfeld, and D. L. Albritton, J. Chem. Phys. **73**, 194 (1980).

[16] R. Johnsen, M. A. Biondi, and M. Hayashi, J. Chem. Phys. **77**, 2545 (1982).

[17] H. A. Fhadil, D. Mathur, and J. B. Hasted, J. Phys. B **15**, 1443 (1982).

[18] H. A. Fhadil, A. T. Numan, T. Shuttleworth, and J.B. Hasted, Int. J. Mass Spectrom. Ion. Proc. **65**, 307 (1985).

[19] J. F. Liebman and L. C. Allen, Int. J. Mass Spectrom. Ion. Phys. **7**, 27 (1971).

[20] D. L. Cooper and S. Wilson, Mol. Phys. **44**, 161 (1981).

[21] S. L. Lin and J. N. Bardsley, J. Chem. Phys. **66**, 435 (1977).

[22] L. A. Viehland and E. A. Mason, J. Chem. Phys. **66**, 422 (1977).

[23] S. D. Augustin, W. H. Miller, P. K. Pearson, and H. F. Schaefer III, J. Chem. Phys. **58**, 2845 (1973).

[24] L. A. Viehland, M. M. Harrington, and E. A. Mason, Chem. Phys. **17**, 433 (1976).

[25] J. S. Binkley, M. J. Frisch, D. J. DeFrees, K. Raghavachari, R. A. Whiteside, H. B. Schlegel, E. M. Fluder, and J. A. Pople, GAUSSIAN 82 (Carnegie–Mellon University, Pittsburgh, 1983).

[26] W. Koch and G. Frenking, J. Chem. Soc. Chem. Comm. **1986**, 1095.

[27] R. G. A. R. Maclagan and G. W. Schnuelle, J. Chem. Phys. **55**, 5431 (1971).

[28] R. M. Stevens, J. Chem. Phys. **55**, 1725 (1971).

[29] S. Huzinaga and C. Arnau, J. Chem. Phys. **53**, 451 (1970).

[30] B. Roos, C. Salez, A. Veillard, and E. Clementi (IBM Research Laboratory, San Jose, 1968).

[31] V. Staemmler and R. Jaquet, Chem. Phys. **92**, 141 (1985).

[32] C. Moore, U. S. Dept. Comm., NBS Atomic Energy Levels **45** (1971).

Aust. J. Phys., 1988, **41**, 545–8

Dependence of Zero-field Ion Mobilities on Well Depth and Minimum Position in the Ion–Neutral Interaction Potential

Peter W. Harland, Robert G. A. R. Maclagan and Richard W. Simpson

Department of Chemistry, University of Canterbury,
Christchurch 1, New Zealand.

Abstract

The dependence, at fixed temperature, of the zero-field ion mobility on well depth ϵ and minimum position r_{m} in the ion–neutral interaction potential is explored. For large values of r_{m} the mobility is very sensitive to small changes in ϵ, but at small r_{m} the mobility varies only slightly from the Langevin value.

1. Introduction

The interaction of an atomic ion and a neutral atom at short–medium range is either attractive or repulsive. If the interaction is attractive, there will be a definite minimum in the potential energy curve $V(r)$. At long range the interaction energy is dominated by the attractive ion-induced dipole term $\frac{1}{2}\alpha^2 q^2/4\pi\epsilon_0 r_{\mathrm{m}}^4$. At very short range the potential is always repulsive. Thus, even for a repulsive interaction, there will always be a minimum in the potential energy curve. We have found previously (Harland *et al.* 1986; Simpson *et al.* 1987) that the calculated low-field ion mobility can be very sensitive to small changes in the magnitude of a long range van der Waals attractive well in the interaction potential. To investigate this behaviour further we have performed low-field two-temperature theory mobility calculations using a number of different hypothetical potentials. We have found that for certain values of the well depth ϵ and minimum position r_{m} the interaction potential need only be changed slightly to effect large changes in the calculated mobility, but this sensitivity varies significantly over the ranges of r_{m} and ϵ considered.

2. Theory and Method

Given $V(r)$, it is possible to calculate the drift velocity v_{d} and the ion mobility reduced to STP, K_0, as a function of electric field strength E/N (Mason and Schamp 1958):

$$K_0 = \frac{v_{\mathrm{d}}}{E} = \frac{3q}{8N_0}\left(\frac{\pi}{2\mu k_{\mathrm{B}}\, T_{\mathrm{eff}}}\right)^{\frac{1}{2}} \frac{1+\alpha'}{\Omega^{(1,1)}(T_{\mathrm{eff}})}, \tag{1}$$

where N_0 is the particle density reduced to STP, q is the charge on an electron and

0004-9506/88/040545$03.00

k_B is Boltzmann's constant. The temperature T_{eff} can be written as

$$T_{\mathrm{eff}} = T + \tfrac{1}{3} M v_d^2 (1+\beta), \tag{2}$$

where T is the buffer gas temperature and M is the mass of the buffer gas. The collision integral $\Omega^{(1,1)}(T_{\mathrm{eff}})$ can be written as

$$\Omega^{(1,1)}(T_{\mathrm{eff}}) = \tfrac{1}{2}(k_B T_{\mathrm{eff}})^{-3} \int_0^\infty E'^2 Q^{(1)}(E') \exp\left(\frac{E'}{k_B T_{\mathrm{eff}}}\right) \mathrm{d}E', \tag{3}$$

where the cross section $Q^{(1)}(E')$ is an integral of the classical deflection function $\chi(b, E')$,

$$Q^{(1)}(E') = 2\pi \int_0^\infty \{1 - \cos\chi(b, E')\}\, b\, \mathrm{d}b; \tag{4}$$

and b is the impact parameter, E' is the centre of mass energy and the deflection function $\chi(b, E')$ is

$$\chi(b, E') = \pi - 2b \int_{r_0}^\infty \left(1 - \frac{b^2}{r^2} - \frac{V(r)}{E'}\right)^{-\frac{1}{2}} \frac{\mathrm{d}r}{r^2}. \tag{5}$$

The lower integration limit r_0 in (5) is defined as the outermost root of

$$1 - \frac{b^2}{r_0^2} - \frac{V(r_0)}{E'} = 0. \tag{6}$$

To evaluate equations (3) to (5) we initially calculate the dimensionless reduced collision integrals $\Omega^{(l,s)*}(T^*)$ using a dimensionless interaction potential $V'(r')$. This is related to the actual interaction potential by

$$V'(r') = \frac{1}{\epsilon''} V(r/r''_m). \tag{7}$$

The required collision integrals $\Omega^{(l,s)}(T_{\mathrm{eff}})$ are obtained by a second use of the scaling factors ϵ'' and r''_m:

$$\Omega^{(l,s)}(T_{\mathrm{eff}}) = \pi r''^2_m \Omega^{(l,s)*}(T^*), \tag{8}$$

where the reduced temperature T^* is given by

$$T^* = k_B T_{\mathrm{eff}}/\epsilon''. \tag{9}$$

The collision integrals are independent of the values of these scale factors. The scale factors have no relationship with the actual well depth ϵ or position of the potential minimum r_m.

The dimensionless parameters α' and β in equations (1) and (2) respectively are negligible at zero field strength. It is also possible to go from mobility data to $V(r)$ (Viehland *et al.* 1976). It has been shown (Gatland *et al.* 1977) that the ion mobility at large E/N is principally determined by $V(r)$ at low r, while the ion mobility at small E/N is determined principally by $V(r)$ at large internuclear separation. It might therefore be expected that the reduced mobility at zero field strength, $K_0(0)$, would be given by the Langevin model where the potential is just the ion-induced dipole term. This would mean that at zero field strength, the effect of other short range terms is negligible. This is not the case as is demonstrated in this paper.

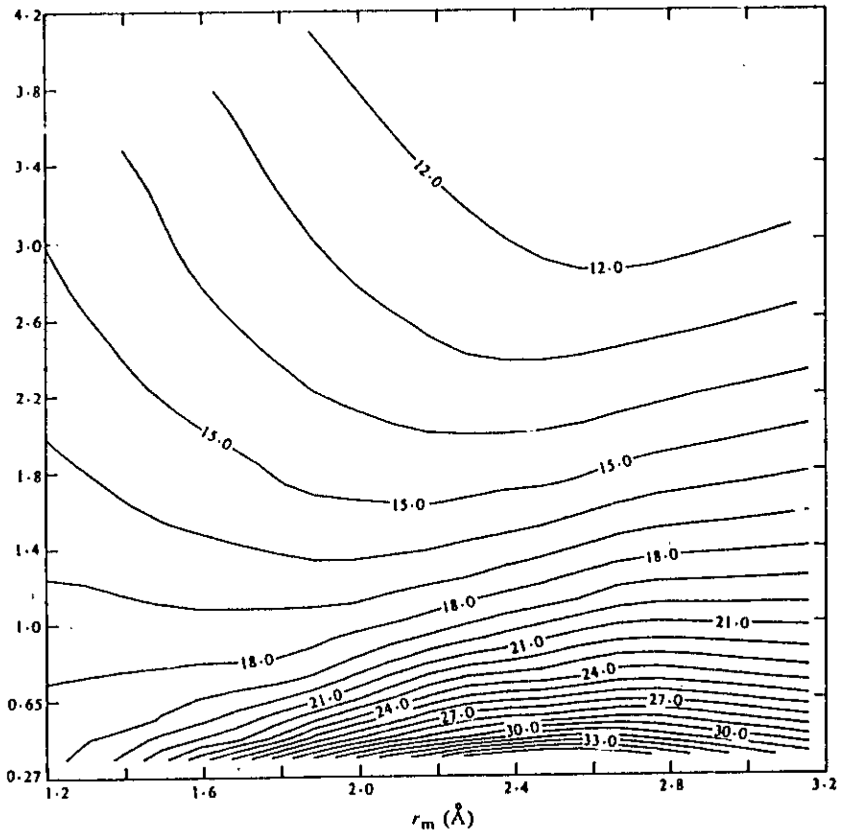

Fig. 1. Contour plot of the zero-field reduced ion mobility $K_0(0)$ over the range 12·0 to 33·0 $\mathrm{cm^2\,V^{-1}\,s^{-1}}$, shown as a function of the reduced well depth ϵ/ϵ' and the minimum position r_m.

3. Results and Discussion

To explore the effect of the position and depth of the potential energy minimum on the zero-field mobility we used, for a model helium-F^+/F^- interaction potential, an $(n, 6, 4)$ potential of the form

$$V(r) = \frac{n\epsilon}{n(3+\gamma)-12(1+\gamma)}\left\{\frac{12}{n}(1+\gamma)\left(\frac{r_m}{r}\right)^n - 4\gamma\left(\frac{r_m}{r}\right)^6 - 3(1-\gamma)\left(\frac{r_m}{r}\right)^4\right\}, \qquad (10)$$

where ϵ and r_m are the depth and position of the potential energy minimum respectively, and the value of the dimensionless parameter γ has been constrained so that the r^4 term corresponds to the value appropriate to an ion interacting with helium (polarisability is $\alpha = 0\cdot204$ Å^3); that is,

$$3\epsilon(1-\gamma)r_m^4 = \alpha q^2/4\pi\epsilon_0\,,$$

where ϵ_0 is the vacuum permittivity. In presenting the results of the calculations of zero-field ion mobilities, it was found useful to scale the well depth ϵ by a factor $\epsilon' = \frac{1}{2}\alpha q^2/4\pi\epsilon_0\, r_m^4$, the value of the ion-induced dipole term at the minimum. In Fig. 1 a contour plot of $K_0(0)$ as a function of ϵ/ϵ' and r_m is presented, obtained using a (12-6-4) potential and a room temperature value of $T = 300$ K. Where the minimum in the potential r_m is at small r, a very large change in ϵ is required to vary $K_0(0)$ by a large amount from the Langevin value for the F^+/F^- ion of $16\cdot90$ cm^2 V^{-1} s^{-1}. At $r_m = 1\cdot2$ Å, $\epsilon' = 0\cdot708$ eV ($68\cdot3$ kJ mol^{-1}), but at $3\cdot2$ Å, $\epsilon' = 0\cdot0140$ eV $= 1\cdot35$ kJ mol^{-1}. At large r_m, a very small change in ϵ has a very large effect on $K_0(0)$. For the (12-6-4) potential, at $r_m = 3\cdot2$ Å, doubling ϵ from $\epsilon = \epsilon'$ to $\epsilon = 2\epsilon'$, a difference of $0\cdot014$ eV to give a slightly more attractive potential, decreases $K_0(0)$ from $21\cdot1$ to $15\cdot2$ cm^2 V^{-1} s^{-1}. Halving ϵ from $\epsilon = \epsilon'$ to $\epsilon = \epsilon'/2$, to give a slightly more repulsive short range potential, a difference of only $0\cdot007$ eV, increases $K_0(0)$ from $21\cdot1$ to $27\cdot9$ cm^2 V^{-1} s^{-1}. At $r_m = 1\cdot2$ Å, the values of $K_0(0)$ at $\epsilon'/2$, ϵ' and $2\epsilon'$ are $18\cdot5$, $17\cdot5$ and $16\cdot0$ cm^2 V^{-1} s^{-1} respectively. If a (8-6-4) potential is used, where the repulsive term is not as steep, essentially the same contour diagram is obtained with the mobilities at small r_m being slightly smaller.

The influence of the ion–atom interaction potential on the macroscopic ion transport properties and the collision dynamics must be taken into account in the estimation of errors in rate coefficients obtained from flow-tube experiments where the diffusion correction is estimated using the Langevin equation.

These observations also have an important consequence when *ab initio* methods are used to calculate $V(r)$. To obtain accurate estimates of $K_0(0)$, the values of $V(r)$ at about 3 Å need to be very accurate [to within better than $0\cdot001$ eV to obtain $K_0(0)$ correct to two significant figures]. A basis set that is adequate to describe a bond of length 1–2 Å may not be adequate at a separation of 3 Å. The dependence of the correlation energy on internuclear separation must be correct. These criteria are rarely met in *ab initio* calculations.

References

Gatland, I. R., Viehland, L. A., and Mason, E. A. (1977). *J. Chem. Phys.* **66**, 537–41.

Harland, P. W., McIntosh, B., Simpson, R. W., and Thomas, N. J. (1986). *J. Chem. Soc. Farad. Trans.* **82**, 2039–46.

Mason, E. A., and Schamp, H. W. (1958). *Ann. Phys. (NY)* **4**, 233–70.

Simpson, R. W., Maclagan, R. G. A. R., and Harland, P. W. (1987). *J. Phys.* B **20**, 2723–31.

Viehland, L. A., Harrington, M. M., and Mason, E. A. (1976). *Chem. Phys.* **17**, 433–44.

Manuscript received 10 November 1987, accepted 29 January 1988

J. Chem. Soc., Faraday Trans. 2, 1988, **84**(11), 1847–1853

Ab Initio $HeF^+(^3\Sigma, {}^3\Pi)$ Interaction Potentials and Calculations of the Mobility of $F^+(^3P)$ and $F^-(^1S)$ in Helium

Peter W. Harland,* Robert G. A. R. Maclagan* and Richard W. Simpson
Chemistry Department, University of Canterbury, Christchurch, New Zealand

The mobility of $F^+(^3P)$ in helium has been calculated using both the two-temperature and three-temperature theories of ion transport. The interaction potentials for the two possible molecular states $HeF^+(^3\Sigma)$ and $HeF^+(^3\Pi)$ required by the transport theories were calculated at the MP4SDQ/6-311+G(3df, 3dp) level of theory. The mobility of F^+ in helium derived by summing over the appropriate statistical weights for the two molecular ion states separating to $He(^1S)+F^+(^3P)$ is in good agreement with experimental data. The mobility of the $F^-(^1S)$ ion in helium has been calculated at the three-temperature level of theory using an interaction potential calculated at the MP4SDQ/6-311+G (3df, 3dp) level of theory and refined by fitting to low-field experimental mobility measurements. The mobilities calculated with this potential were found to be in good accord with the values calculated using an $HeF^-(^1\Sigma)$ MBPT(4) interaction potential incorporating a very large basis set.

The classical theories describing ion transport in gases have been the subject of a recent review.[1] The two-temperature theory of Viehland and Mason[2,3] is capable of accurately describing the relationship that exists between the ion–neutral interaction potential and the observed mobility. *Ab initio* interaction potentials calculated by molecular orbital and valence bond methods have been previously used with the two-temperature theory of ion transport to calculate the mobilities of both ground-state and electronically excited ions in helium.[4-7] Agreement between the calculated and experimental mobilities are generally within the reported experimental uncertainties and for the case of the O^{+*} ion in helium the calculated mobilities for the $O^+(^2D)$ and $O^+(^2P)$ states suggested a reassignment of the ion state which had been deduced from the experimental measurements.[6] The calculation of mobilities using two-temperature theory has been shown to successfully reproduce experimental data for electric field to particle density ratios, E/N, above 30 Td,[5,6] where $1\ \mathrm{Td} \equiv 10^{-21}\ \mathrm{V\ m^2}$. Below 30 Td the mobility is particularly sensitive to small changes in the attractive region of the potential and adjustments of only a few meV in the well depth is required to bring the calculated low-field mobilities into line with the experimental measurements.[5,6] The three-temperature theory of ion transport[8,9] was developed to overcome deficiencies in the two-temperature theory. At high field strengths the convergence of the calculated mobility as a function of the level of approximation may be slow, but more significantly the theory does not adequately describe ion diffusion. This is due to the description of the ion swarm in terms of a single temperature, the second temperature in the two-temperature theory describing the random motions of the buffer gas. The diffusion coefficients are more intimately connected to the anisotropic nature of the ion swarm than ion mobilities and the use of a single ion temperature constrains the ion distribution to be isotropic. In the three-temperature theory two temperature variables are used to describe the ion temperature, both parallel, $T_\parallel$, and perpendicular, $T_\perp$, to the direction of the applied field, thus allowing the ion distribution to be anisotropic. As well as providing more acceptable estimates for the longitudinal and transverse diffusion coefficients than the two-temperature theory, the three-temperature theory exhibits improved convergence properties as the level of approximation is increased, especially for the high-field ion mobilities. Veihland and Lin[8,9] have shown that the fourth approximation of this theory is of comparable accuracy to the most accurate experimental measurements for both mobilities (1-2%) and diffusion coefficients (5-10%). Although this theory leads to equations with no obvious physical interpretation, it has been employed with success to test the accuracy of proposed interaction potentials for ion–neutral systems by comparison of calculated transport properties with the corresponding experimental quantities.[10,11] We have calculated the mobility of the F^+ ion in helium using both the two- and three-temperature theories with *ab initio* interaction potentials. Three-temperature theory calculations are also included for the mobility of F^- in helium for comparison with the two-temperature calculations previously reported.[5] The agreement with experimental measurements of ion mobility is within the experimental uncertainties for both the F^- and F^+ in helium calculations, where the theoretical F^+ mobility used in the comparison is derived by summing the mobilities calculated for the $HeF^+(^3\Sigma)$ and $HeF^+(^3\Pi)$ interaction potentials with the statistical weighting of 1:2.

Ion-transport Theory

The two-temperature theory of ion transport has been used in our earlier work because it is much easier to apply than the three-temperature theory.[1] We also suggested from an investigation of the effect of small changes to the interaction potential on the mobility of F^- in helium that since relatively large changes in the calculated ion-transport properties result from small adjustments to the interaction potential there would be little to be gained by use of the three-temperature theory.[5] The mobility of the $F^-(^1S)$ ion in helium has been recalculated using the three-temperature theory with the *ab initio* interaction potential previously calculated and a complete fourth-order many-body perturbation theory, MBPT(4), interaction potential published recently.[12] As shown below, our earlier conclusions are shown to be justified.

The two-temperature theory used in this work has been described in detail in the previous paper.[5]

Three-temperature calculations were performed using the program MOBDIF supplied by L. A. Viehland (1987). The same *ab initio* interaction potentials were used in both the two- and three-temperature calculations and the mobilities interpolated for comparison with the experimental values reported in the literature.

$HeF^-(^1\Sigma)$

The ground-state interaction potential of $HeF^-(^1\Sigma)$, separating at infinity to $He(^1S)$ and $F^-(^1S)$, has been previously calculated[5] using the GAUSSIAN82 program[13] at the MP4SDQ/6-311+G (3df, 3pd) level of theory, excluding core contributions to the correlation energy. The mobility of the F^- ion in helium calculated using two-temperature theory with this interaction potential was found to be within the reported experimental uncertainty above 30 Td. Below 30 Td the calculated mobility deviated from −7% at 30 Td to −14% at 2 Td. The negative deviation in the calculated values for low E/N characterises an overestimation of the well depth, which was calculated to be 0.0126 eV. A very close fit of the calculated low-field mobility experimental data was obtained by reducing the shallow well by 0.007 eV. This adjustment to the potential leaves the high-field calculated mobilities virtually unchanged.[5] The calculations have now been repeated using three-temperature theory with the interaction potential calculated at the MP4SDQ/6-311+G (3df, 3pd) level of theory and a recently published high-level (fourth-order) many-body perturbation theory, MBPT(4), interaction potential.[12] The

Table 1. Two- and three-temperature calculations of the reduced mobility of F^- in helium using two different $^1\Sigma$ HeF^- interaction potentials

	K_0/cm^2 V^{-1} s^{-1}					
			MP4SDQ		MBPT(4)	
(E/N)/Td	exptl	MP4SDQ(adj) 2-T	3-T	2-T	3-T	2-T
2	29.2	29.7	25.13	25.09	27.88	27.92
4	28.9	29.5	25.12	25.08	27.82	27.85
6	28.5	29.5	25.09	25.05	27.72	27.85
8	28.2	28.8	25.04	25.00	27.57	27.57
10	27.8	28.4	24.97	24.93	27.37	27.38
12	27.5	27.9	24.86	24.82	27.12	27.10
15	27.0	27.2	24.66	24.61	26.69	26.60
20	26.1	25.9	24.19	24.09	25.84	25.62
30	24.6	23.8	23.04	22.80	24.07	23.68
40	23.2	22.2	21.87	21.55	22.50	22.03
60	20.9	19.9	19.87	19.56	20.10	19.64
80	19.3	18.3	18.45	18.14	18.45	18.07
100	18.0	17.2	17.42	17.09	17.28	16.97
120	17.0	16.4	16.57	16.28	16.41	16.16
140	16.3	15.7	15.91	15.64	15.75	15.56
160	15.7	15.2	15.36	15.11	15.23	15.09

All reduced mobilities are in cm^2 V^{-1} s^{-1}.

MBPT(4) interaction potential has been calculated using a very large polarized basis set of Gaussian-type orbitals. For helium the basis included four contracted s orbitals to which were added a diffuse s orbital and both p- and d-orbital functions. A similar contracted basis set was used for fluorine and this was extended by diffuse s- and p-orbital functions as well as d- and f-polarisation functions. The resulting interaction potential has a well depth of 0.008 eV at 3.45 Å compared to 0.006 eV at 3.25 Å for the MP4SDQ interaction potential adjusted for a fit of the calculated mobility curve to the low-field experimental data. Two- and three-temperature theory calculations of the reduced mobility of F^- in helium at 297 K using the unchanged MP4SDQ and the MBPT(4) $HeF^-(^1\Sigma)$ interaction potentials are shown in table 1 with the experimental data. The calculations using the adjusted MP4SDQ potential, MP4SDQ (adj) and two-temperature theory are also included for comparison. It can be seen that the three-temperature theory is slightly better than the two-temperature theory for estimating the mobility at high values of E/N, for both interaction potentials, but the improvement is not dramatic. The calculated values still fall below the experimental values, although well within the experimental uncertainty. The collision cross-section, $Q^{(l)}(E')$, were calculated to an accuracy of 0.1% for the three-temperature calculations and the reduced mobility converged to an accuracy of 0.75%. In a comparison of computer processor usage it was found that a three-temperature theory calculation is at least an order of magnitude slower than the corresponding two-temperature theory calculation.

$HeF^+(3\Sigma, {}^3\Pi)$

The mobility of the F^+ ion in helium has been measured by Hamdan and Birkinshaw[14] over the range 6–94 Td using a selected ion-flow drift tube, SIFDT. The reduced mobility data for F^+ as a function of E/N was found to exhibit a broad maximum over the range 25–70 Td in contrast to the mobility curves for the other halogen ions which show the behaviour characteristic of strongly repulsive interaction potentials. An *ab initio*

Table 2. Interaction potential energies for the $^3\Sigma$ state of HeF^+ calculated at the MP4SDQ/6-311+G(3df, 3pd) level of theory

r/Å	E/hartree	r/Å	E/hartree
1.50	−98.823 479	3.00	−98.880 956
1.75	−98.863 379	3.50	−98.880 593
2.00	−98.876 280	4.00	−98.880 351
2.50	−98.881 038	4.50	−98.880 232
2.625	−98.881 126	5.00	−98.880 177
2.75	−98.881 110	∞	−98.880 091

Table 3. Interaction potential energies for the $^3\Pi$ state of HeF^+ calculated at the MP4SDQ/6-311+G(3df, 3pd) level of theory

r/Å	E/hartree	r/Å	E/hartree
0.875	−98.534 913	2.50	−98.881 924
0.9375	−98.628 480	2.75	−98.881 457
1.000	−98.698 098	3.00	−98.881 097
1.25	−98.834 063	3.25	−98.880 621
1.50	−98.971 239	4.00	−98.880 364
1.75	−98.880 859	4.50	−98.880 240
1.875	−98.882 221	5.00	−98.880 181
2.00	−98.882 651	6.00	−98.880 133
2.125	−98.882 637	∞	−98.880 091
2.25	−98.882 441		

SCF calculation of the interaction potentials for the HeF^+ molecular ion has been reported by Liebman and Allan.[16] The interaction of the ground-state F^+ ion, $F^+(^3P)$, with $He(^1S)$ can result in two possible molecular ion states:

$$F^+(^3P)+He(^1S) \rightarrow HeF^+(^3\Sigma) \tag{1}$$

$$F^+(^3P)+He(^1S) \rightarrow HeF^+(^3\Pi). \tag{2}$$

The interaction potentials reported by Liebman and Allan were calculated at a low level of theory with insufficient points to be suitable for accurate mobility calculations. The interaction potentials for the $^3\Sigma$ and $^3\Pi$ states of HeF^+ calculated at the MP4SDQ/6-311+G (3df, 3pd) level of theory using GAUSSIAN82 are shown in tables 2 and 3. The interaction potentials are represented graphically in fig. 1. The HeF^+ ($^3\Pi$) interaction potential has a relatively deep narrow well at 2.04 Å of depth 0.070 eV. The HeF ($^3\Sigma$) state exhibits a shallow broad minimum centred at 2.625 Å with a depth of 0.028 eV. These interaction potentials were used to calculate the mobility for $F^+(^3P)$ in helium at both the two-temperature and three-temperature levels of theory. Results from the two- and three-temperature theory calculations are shown for $He+F^+(^3P)$ [$HeF^+(^3\Sigma)$] in table 4 and $He+F^+(^3P)$ [$HeF^+(^3\Pi)$] in table 5. Assuming that the orientation of the fluorine atom is random, the statistical weight of the two molecular states HeF^+ ($^3\Sigma$) and $HeF^+(^3\Pi)$ will be 1:2. The average cross-section is one third of that for the $^3\Sigma$ state plus two thirds of that for the $^3\Pi$ state. The averaged mobility is thus given by

$$1/K_0\ (\text{averaged}) = \tfrac{1}{3}/K_0(^3\Sigma)+\tfrac{2}{3}/K_0(^3\Pi). \tag{20}$$

The agreement with experiment is good and well within the quoted experimental uncertainty of ±7% for $E/N < 30$ Td and ±5% for $E/N > 30$ Td. We have found

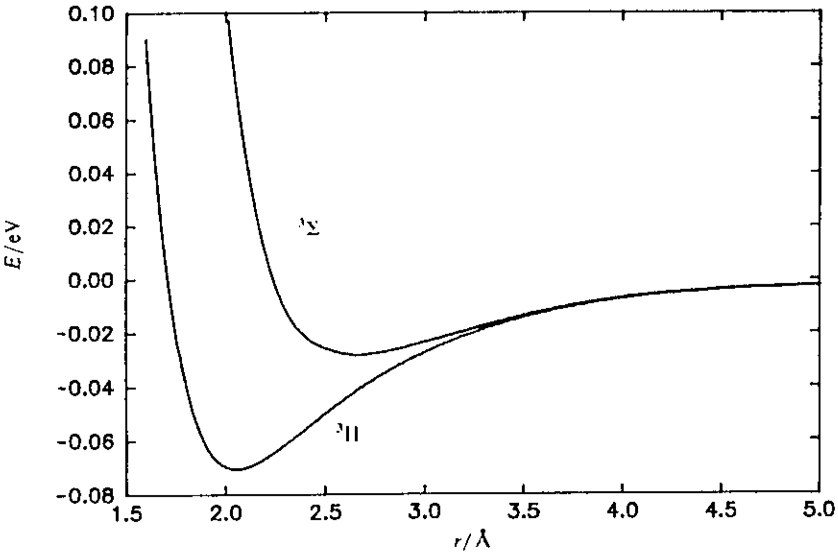

Fig. 1. Interaction potentials for the $^3\Sigma$ and $^3\Pi$ states of HeF^+.

Table 4. Calculated momentum-transfer collision integrals, drift velocities, reduced mobilities and related quantities for $He + F^+(^3P)$ [$HeF^+(^3\Sigma)$]

T_{eff}	$\Omega^{(1,1)}(T_{eff})$ /10^{-20} m^2	α	β	(E/N) /Td	$K_0(2\text{-}T)$	$K_0(3\text{-}T)$
					/10^{-4} m^2 V^{-1} s^{-1}	
299.5	26.12	−0.0002	0.0001	1.60	22.51	22.52
333.1	24.38	−0.0035	0.0027	7.62	22.00	22.79
376.1	22.62	−0.0057	0.0044	11.22	23.08	23.09
431.1	20.85	−0.0058	0.0045	14.47	23.37	23.36
501.6	19.18	−0.0036	0.0028	17.72	23.62	23.60
591.8	17.62	0.0010	−0.0008	21.19	23.78	23.75
707.3	16.19	0.0073	−0.0056	25.03	23.82	23.81
855.1	14.95	0.0134	−0.0104	29.54	23.60	23.69
1044.4	13.84	0.0197	−0.0151	34.85	23.21	23.40
1286.8	12.87	0.0250	−0.0190	41.28	22.60	22.89
1597.1	12.02	0.0293	−0.0221	49.09	21.81	22.20
1994.3	11.26	0.0326	−0.0244	58.58	20.91	21.37
2502.9	10.56	0.0350	−0.0259	70.09	19.94	20.42
3154.0	9.92	0.0363	−0.0266	84.05	18.94	19.41
3987.7	9.32	0.0370	−0.0269	100.81	17.95	18.39
5054.9	8.74	0.0371	−0.0267	120.84	17.00	17.41
6421.3	8.18	0.0368	−0.0261	144.65	16.11	16.44
8170.7	7.64	0.0361	−0.0254	172.82	15.28	15.52
10 410.3	7.11	0.0352	−0.0245	205.97	14.52	14.83
13 277.7	6.61	0.0343	−0.0237	244.91	13.83	14.05

Table 5. Calculated momentum-transfer collision integrals, drift velocities, reduced mobilities and related quantities for $He + F^+(^3P)[HeF^+(^3\Pi)]$

T_{eff}	$\Omega^{(1,1)}(T_{eff})$ $/10^{-20}\,m^2$	α	β	(E/N) /Td	$K_0(2\text{-}T)$	$K_0(3\text{-}T)$
					$/10^{-4}\,m^2\,V^{-1}\,s^{-1}$	
299.5	32.62	−0.0003	0.0003	2.00	18.02	18.02
333.1	29.86	−0.0076	0.0058	9.36	18.54	18.42
376.1	27.28	−0.0178	0.0136	13.64	18.90	18.99
431.1	24.39	−0.0288	0.0219	17.18	19.52	19.67
501.6	21.56	−0.0405	0.0305	20.41	20.23	20.47
591.8	18.94	−0.0503	0.0381	23.55	20.99	21.33
707.3	16.42	−0.0500	0.0377	26.34	22.15	22.24
855.1	14.34	−0.0466	0.0355	29.43	23.15	23.26
1044.4	12.49	−0.0343	0.0262	32.54	24.35	24.24
1286.8	10.98	−0.0205	0.0157	36.20	25.33	25.13
1597.1	9.72	−0.0062	0.0047	40.56	26.05	25.91
1994.3	8.69	0.0059	−0.0045	45.98	26.38	26.40
2502.9	7.86	0.0145	−0.0109	52.83	26.26	26.50
3154.0	7.16	0.0214	−0.0158	61.22	25.85	26.23
3987.7	6.57	0.0259	−0.0190	71.55	25.18	25.65
5054.9	6.05	0.0288	−0.0208	84.11	24.36	24.84
6421.3	5.59	0.0305	−0.0218	99.19	23.44	23.92
8170.7	5.16	0.0314	−0.0221	117.18	22.50	22.93
10 410.3	4.77	0.0315	−0.0219	138.48	21.57	21.97
13 277.7	4.40	0.0309	−0.0212	163.55	20.69	21.03

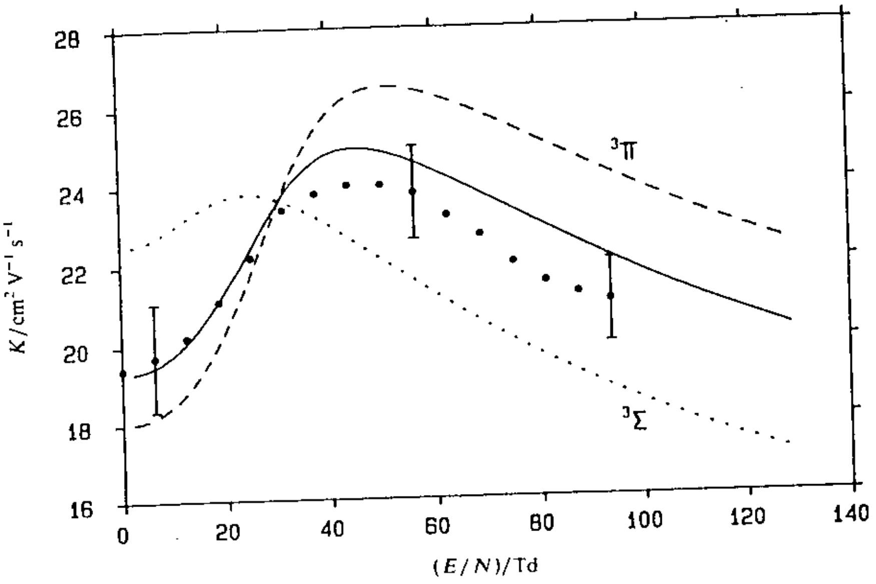

Fig. 2. Calculated reduced mobility of F^+ in helium as a function of E/N arising from the $^3\Sigma(\cdots)$ and $^3\Pi(---)$ states of HeF^+ together with the average mobility (——) and the experimental values (●) (Hamdan and Birkinshaw, 1986).

equally good accord between experiment and theory for both the ground state and electronically excited state of C^+ in helium, where both states correlate to molecular states of the HeC^+ molecular ion.[7] These calculations demonstrate the successful application of *ab initio* interaction potentials for the calculation of ion-transport properties for atomic ions in helium when the mobility of the ion in helium correlates with more than one state of the diatomic ion.

We thank L. A. Viehland for a copy of his program MOBDIF.

References

1 E. W. McDaniel and L. A. Viehland, *Phys. Rep.*, 1984, **110**, 333.
2 L. A. Viehland and E. A. Mason, *Ann. Phys.*, 1975, **91**, 499.
3 L. A. Viehland and E. A. Mason, *Ann. Phys.*, 1978, **110**, 287.
4 L. A. Viehland, *Chem. Phys.*, 1983, **78**, 279.
5 R. W. Simpson, R. G. A. R. Maclagan and P. W. Harland, *J. Phys. B*, 1987, **20**, 2723.
6 R. W. Simpson, R. G. A. R. Maclagan and P. W. Harland, *J. Chem. Phys.*, 1987, **87**, 5419.
7 S. T. Grice, P. W. Harland, R. G. A. R. Maclagan and R. W. Simpson, *Int. J. Mass Spectrom Ion Processes*, in press.
8 S. L. Lin, L. A. Viehland and E. A. Mason, *Chem. Phys.*, 1979, **37**, 411.
9 L. A. Viehland and S. L. Lin, *Chem. Phys.*, 1979, **43**, 135.
10 L. A. Viehland, E. A. Mason and S. L. Lin, *Phys. Rev. A*, 1981, **24**, 3004.
11 L. A. Viehland and E. A. Mason, *J. Chem. Phys.*, 1984, **80**, 416.
12 G. H. F. Diercksen and A. J. Sadlej, *Mol. Phys.*, 1986, **59**, 889.
13 J. S. Binkley, M. J. Frisch, D. J. DeFrees, K. Raghavachari, R. A. Whiteside, H. B. Schlegel, E. M. Fluder and J. A. Pople, 1983, GAUSSIAN82 (Pittsburgh: Carnegie-Mellon University).
14 M. Hamdan and K. Birkinshaw, *Int. J. Mass Spectrom. Ion Phys.*, 1986, **70**, 221.
15 J. F. Liebman and L. C. Allen, *J. Am. Chem. Soc.*, 1970, **92**, 3539.

Paper 8/01282B; *Received* 29*th March*, 1988

International Journal of Mass Spectrometry and Ion Processes, 87 (1989) 181–186 181
Elsevier Science Publishers B.V., Amsterdam – Printed in The Netherlands

AB INITIO CALCULATION OF THE MOBILITY OF $C^+(^2P)$ AND $C^+(^4P)$ IN HELIUM

STEPHEN T. GRICE, PETER W. HARLAND, ROBERT G.A.R. MACLAGAN
and RICHARD W. SIMPSON

Department of Chemistry, University of Canterbury, Christchurch (New Zealand)

(First received 4 March 1988; in final form 13 June 1988)

ABSTRACT

The mobility of the ^2P ground state and the ^4P excited state of C^+ in helium have been calculated using the two-temperature theory of ion transport and HeC^+ interaction potentials calculated at the MP4SDQ/6311+G(3*df*,3*pd*) level of theory. Agreement with experimental data is very good. The results confirm a recent experimental observation of the ^4P state of C^+.

INTRODUCTION

The values of the mobility of the C^+ ion are important for the experimental determination of the ion/molecule rate constants of reactions of C^+. The reaction of C^+ and H_2 to form CH^+ is of particular astrophysical interest.

The mobility of C^+ in helium has been measured by Thomas et al. [1], Dotan et al. [2], Peska et al. [3] and Twiddy et al. [4]. Not only are the reactions of the $2s^2p\ ^2P$ ground state of C^+ of interest, but also the $2sp^2\ ^4P$ excited state. Twiddy et al. were able to measure the mobility of a species in helium that they claimed was metastable C^+ (^4P). If confirmed, this was one of the first measurements of the mobility of an excited state of an ion.

Ab initio interaction potentials of He and C^+ (^2P) have been reported by a number of workers. SCF calculations have been reported for the $^2\Pi$ state of HeC^+ by Harrison et al. [5] and Copper and Wilson [6]. Koch and Frenking [7] have reported calculations at the MP2/6-31G(d,p) and MP4/6311G(d,p) levels of theory on the optimised structures of the $^2\Pi$, $^2\Sigma^+$ and $^4\Sigma^-$ states of HeC^+. The optimisations were at the MP2/6-31G(d,p) level of theory. The HeC^+ $^2\Pi$ state was shown to be weakly bound with a D_e of about 200–400 cm^{-1} and an r_e of about 2.4 Å. A gas phase ion of nominal mass 16 u generated from a helium discharge between carbon electrodes has been assigned to a stable HeC^+ or $He_2C_2^{2+}$ ion by Young and Coggiola [8] using high resolution mass spectrometry.

0168-1176/89/$03.50 © 1989 Elsevier Science Publishers B.V.

TABLE 1

HF/6-311+G(3*df*,3*pd*) and MP4SDQ/6-311+G(3*df*,3*pd*) energies for the HeC^+ $^2\Pi$ and $^2\Sigma^+$ states

R_{HeC} (Å)	E (hartree)			
	$^2\Pi$		$^2\Sigma^+$	
	HF	MP4SDQ	HF	MP4SDQ
1.00	−40.03507	−40.15541	–	–
1.25	−40.10512	−40.22379	–	–
1.50	−40.13415	−40.24956	–	–
1.75	−40.14690	−40.25970	–	–
2.00	−40.15191	−40.26313	−40.13942	−40.25112
2.25	−40.15364	−40.26401	−40.14843	−40.25898
2.50	−40.15402	−40.26392	−40.15186	−40.26185
2.75	−40.15391	−40.26357	−40.15302	−40.26272
3.00	−40.15371	−40.26322	−40.15332	−40.26286
3.25	–	–	−40.15334	−40.26279
3.50	−40.15338	−40.26277	−40.15329	−40.26268
4.00	−40.15319	−40.26253	−40.15316	−40.26251
4.50	−40.15308	−40.26240	−40.15307	−40.26239
5.00	−40.15301	−40.26232	−40.15301	−40.26231
∞	−40.15291	−40.26220	−40.15291	−40.26220

The two temperature theory was developed by Viehland and Mason [9,10]. It allows the mobility, K, to be calculated as a function of electric field strength E/N if the interaction potential $V(r)$ is known. The two temperature theory and the program used in this work has been described by Simpson et al. [11,12]. The work of Simpson et al. demonstrated that if a high level of theory was used to calculate the interaction potential, the calculated mobilities were, within experimental error, in agreement with the experimental results. This allows one to predict with confidence the experimental mobilities of gaseous atoms.

In this paper calculations are reported on the C^+ ($2s^2p$ ^2P) + He ($1s^2$ ^1S) $^2\Pi$ and $^2\Sigma^+$ states of HeC^+ and the C^+ ($2sp^2$ ^4P) + He ($1s^2$ ^1S) $^4\Sigma^-$ and $^4\Pi$ states. The interaction potentials are used to calculate the mobilities of the C^+ ^2P and ^4P states in a helium buffer gas.

CALCULATION OF INTERACTION POTENTIALS

The interaction potentials were calculated using the GAUSSIAN 82 program [13] at the MP4SDQ/6-311 + G(3*df*,3*pd*) level of theory, excluding core contributions to the correlation energy.

The results of the calculations are given in Table 1 for the $^2\Pi$ and $^2\Sigma^+$ states of HeC^+ arising from interaction with the C^+ ^2P state and in Table 2

TABLE 2

HF/6-311+G(3*df*,3*pd*) and MP4SDQ/6-311+G(3*df*,3*pd*) energies for the HeC^+ $^4\Sigma^-$ and $^4\Pi$ states

R_{HeC} (Å)	E (hartree)			
	$^4\Sigma^-$		$^4\Pi$	
	HF	MP4SDQ	HF	MP4SDQ
0.875	−39.97539	−40.05254	–	–
1.00	−40.02952	−40.10586	–	–
1.125	−40.04514	−40.11957	–	–
1.25	−40.04607	−40.11765	–	–
1.375	−40.04221	−40.11050	–	–
1.50	−40.03740	−40.10246	−39.96854	−40.03228
2.00	−40.02478	−40.08180	−40.00117	−40.06819
2.50	−40.02114	−40.07607	−40.01886	−40.07369
2.75	–	–	−40.01946	−40.07405
2.875	–	–	−40.01954	−40.07406
3.00	−40.01996	−40.07444	−40.01955	−40.07402
3.25	–	–	−40.01949	−40.07389
3.50	−40.01950	−40.07386	−40.01940	−40.07376
4.00	−40.01929	−40.07360	−40.01925	−40.07357
4.50	−40.01917	−40.07347	−40.01916	−40.07345
5.00	−40.01910	−40.07338	−40.01909	−40.07338
∞	−40.01899	−40.07326	−40.01899	−40.07326

for $^4\Sigma^-$ and $^4\Pi$ states of HeC^+ arising from interaction with the C^+ ^4P state. The values of the interaction potentials calculated at the Hartree–Fock level of theory are also given. The HeC^+ $^2\Pi$ state is calculated to have a D_e of 406 cm^{-1} and an r_e of 2.329 Å. The $^2\Sigma^+$ state has a D_e of 147 cm^{-1} and an r_e of 2.978 cm^{-1}. The $^4\Sigma^-$ state has a D_e of 10254 cm^{-1} and an r_e of 1.158 Å. The $^4\Pi$ state has a D_e of 175 cm^{-1} and an r_e of 2.805 Å. These values should be regarded as improvements on the previously published values [5–7]. The ^4P state of C^+ is calculated to be 41 466 cm^{-1} above the ^2P state, compared with the 43000 cm^{-1} determined spectroscopically.

MOBILITY CALCULATIONS

The two temperature program, based upon the program of O'Hara and Smith [14,15], was described in detail by Simpson et al. [11]. The mobility, K, and reduced mobility, K_0, of an ion are defined as

$$K = v_d/E \tag{1}$$

$$K_0 = K\left(\frac{P}{760}\right)\left(\frac{273.15}{T}\right) \tag{2}$$

where v_d is the average ion drift velocity, E is the electric field, and P and T are the experimental pressure in Torr and temperature in Kelvin, respectively. The reduced mobility can be written as

$$K_0 = 0.37220\ v_d/(E/N) \tag{3}$$

where the drift velocity v_d is in units of m s^{-1} and E/N is in Td. K_0 then has units of 10^{-4} m^2 V^{-1} s^{-1}.

There are two states of HeC^+ that correlate with He $1s^2\ {}^1S + C^+\ 2s^2p\ {}^2P$, the ${}^2\Pi$ and ${}^2\Sigma^+$ molecular states. In an earlier investigation of the HeO^+ system [12], where the interaction potentials for the different states are very similar, the mobilities calculated for the $O^+({}^2D)$ and $O^+({}^2P)$ ions in helium taking the interaction potential for the states of lowest energy were virtually the same as the values calculated assuming a statistically weighted mixing of HeO^+ states. This led to the conclusion that the molecular ion could be assumed to adopt the state of lowest energy for the purposes of a mobility calculation. However, this conclusion, on reflection, does not apply where the interaction potentials for the molecular ion states exhibit quite different characteristics, as they do for the HeC^+ molecular ion states. Assuming that the orientation of the carbon atom is random, the statistical weight of the two states will be 2 : 1. It cannot be assumed that the behaviour of the HeC^+ ions will be described only in terms of the lowest energy state. In Fig. 1 the reduced mobility of $C^+\ {}^2P$ in helium as a function of E/N is shown. At large E/N the mobility calculated using the ${}^2\Pi$ potential curve is greater than the experimental value, but that calculated using the ${}^2\Sigma^+$ curve is less

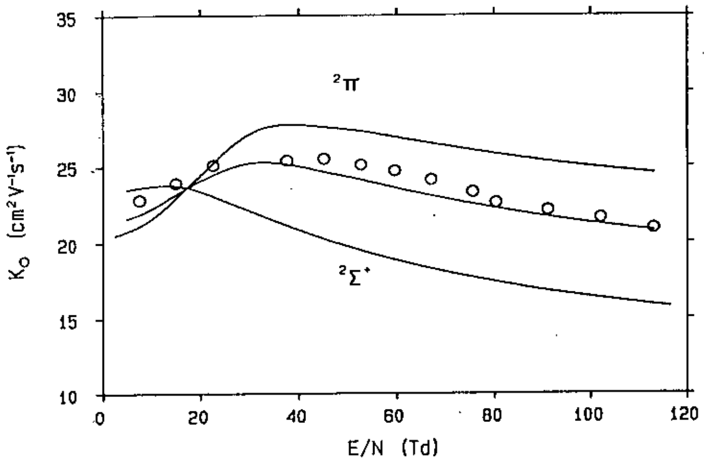

Fig. 1. Experimental and calculated reduced mobilities of $C^+\ {}^2P$ in helium. Solid lines show the mobility calculated using the ${}^2\Pi$ and ${}^2\Sigma^+$ potential curves as the interaction potential, and the weighted sum of these two calculated mobilities.

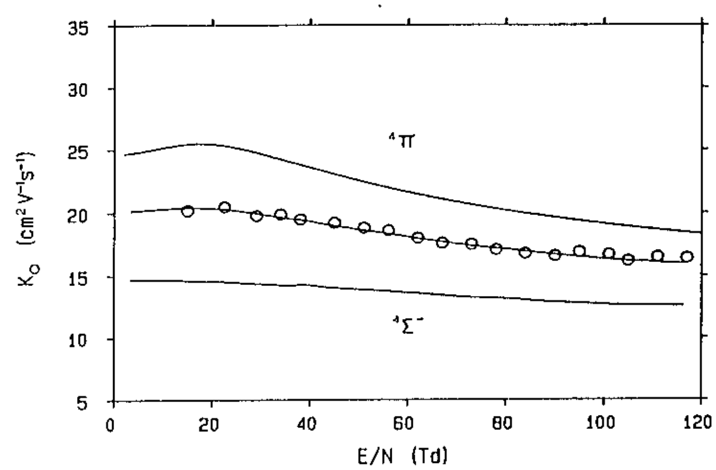

Fig. 2. Experimental and calculated reduced mobilities of $C^+\ ^4P$ in helium. Solid lines show the mobility calculated using the $^4\Sigma^+$ and $^4\Pi$ potential curves as the interaction potential, and the weighted sum of these two calculated mobilities.

than the experimental value. At low E/N the mobility calculated with the $^2\Sigma^+$ curve is greater than that calculated with the $^2\Pi$ curve. The effective collision integral $\Omega^{(1,1)}$ is summed with statistical weights of 2/3 for the collision integral calculated using the $^2\Pi$ curve and 1/3 for the collision integral calculated using the $^2\Sigma^+$ curve. This gives for the reduced mobility

$$1/K_0 = 1/3K_0(^2\Sigma^+) + 2/3K_0\ (^2\Pi) \tag{4}$$

Agreement with experiment is very good. This procedure is valid since in any given collision a definite potential curve will apply, although the actual surface over which the collision occurs will be random. The results of Simpson et al. [11] for He + F^- showed that very good agreement can be expected at large E/N.

The same procedure was adopted for the two states of HeC^+ that correlate with $C^+\ ^4P$ + He ^1S, the $^4\Sigma^-$ and $^4\Pi$ molecular states. The reduced mobility of $C^+\ ^4P$ in helium is shown in Fig. 2. Agreement with the measured mobilities of Twiddy et al. [4] is again very good. The mobility calculated with the state of Π symmetry is greater than that with Σ symmetry as found for the doublet states. The variation of the mobility with electric field strength is mainly due to the contribution from the $^4\Pi$ state. The change from 20 to 120 Td is about 2 cm^2 V^{-1} s^{-1} with the $^4\Sigma^-$ curve but about 7 cm^2 V^{-1} s^{-1} with the $^4\Pi$ curve. Kusonoki and Ottinger [16] estimate the lifetime of $C^+\ ^4P$ to be at least of the order of 10^{-5}. Thus it should be certainly observable in a drift tube. The mobility of CH^+ has been shown by Thomas et al. [1] to have a greater dependence on electric field strength and higher values than the species observed by Twiddy et al. These calculations give further confirmation that the species observed by Twiddy et al. was $C^{+}\ {}^{4}P$.

These calculations show that it is possible to calculate the mobility of an ion in helium that correlates with more than one state of the diatomic species and to obtain results in good agreement with experiment. They also demonstrate that the mobility of an excited state of an ion, which may be difficult to measure experimentally, may be calculated with some confidence.

ACKNOWLEDGEMENTS

The authors acknowledge computational assistance from Chemistry Division, D.S.I.R. and the Department of Civil Engineering, University of Canterbury, and the University Grants Committee for the provision of a postgraduate scholarship to R.W.S.

REFERENCES

1 R. Thomas, J. Barassin and A. Barassin, Int. J. Mass Spectrom. Ion Phys., 31 (1979) 227.
2 I. Dotan, F.C. Fehsenfeld and D.L. Albritton, J. Chem. Phys., 71 (1979) 4762.
3 K. Peska, G. Sejkora, H. Stori, F. Egger, H. Ramier, M. Kriegel and W. Lindinger, in W. Lindinger (Ed.), 3rd Symp. Atomic and Surface Physics, Innsbruck, 1982, p. 318.
4 N.D. Twiddy, A. Mohebati and M. Tichy, Int. J. Mass Spectrom. Ion Processes, 74 (1986) 251.
5 S.W. Harrison, G.A. Henderson, L.J. Massa and P. Solomon, Astrophys. J., 189 (1974) 605.
6 D.L. Cooper and S. Wilson, Molec. Phys., 44 (1981) 161.
7 W. Koch and G. Frenking, Int. J. Mass Spectrom. Ion Processes, 74 (1986) 133.
8 S.E. Young and M.J. Coggiola, Int. J. Mass Spectrom. Ion Processes, 74 (1986) 137.
9 L.A. Viehland and E.A. Mason, Ann. Phys. (N.Y.), 91 (1975) 499.
10 L.A. Viehland and E.A. Mason, Ann. Phys. (N.Y.), 110 (1978) 287.
11 R.W. Simpson, R.G.A.R. Maclagan and P.W. Harland, J. Phys. B, 20 (1987) 2723.
12 R.W. Simpson, R.G.A.R. Maclagan and P.W. Harland, J. Chem. Phys., 87 (1987) 5419.
13 J.S. Binkley, M.J. Frisch, D.J. DeFrees, K. Raghavachari, R.A. Whiteside, H.B. Schlegel, E.M. Fluder and J.A. Pople, GAUSSIAN 82, Carnegie-Mellon University, Pittsburgh, PA, 1983.
14 H. O'Hara and F.J. Smith, J. Comput. Phys., 5 (1970) 328.
15 H. O'Hara and F.J. Smith, Comput. Phys. Commun., 2 (1971) 47.
16 I. Kusonoki and Ch. Ottinger, J. Chem. Phys., 73 (1980) 2069.

Aust. J. Chem., 1989, **42**, 9–15

Kinetic and Electron Impact Studies of the HCO^+/COH^+ Isomers

Peter W. Harland, Nick D. Kim and Simon A. H. Petrie

Chemistry Department, University of Canterbury,
Christchurch, New Zealand.

Abstract

The ionization efficiency curve for the CHO^+ ion, *m/z* 29, formed from the near-monochromatic electron impact ionization of CH_3OH has been found to exhibit two distinct appearance energies (thresholds) which can be assigned to the formyl, HCO^+, and the higher energy isoformyl, COH^+, isomers. The energy separation between the appearance energies of 138 kJ mol^{-1} provides an estimate of the difference between the enthalpies of formation of the formyl–isoformyl isomers. Acetaldehyde undergoes dissociative ionization to yield only the lower energy, formyl, isomer. This has been confirmed from a study of the energetics of the proton transfer reaction of CHO^+ on N_2O over the centre-of-mass collision energy range 0·3–4 eV measured by using a drift-tube mass spectrometer.

Introduction

The formyl ion, HCO^+, and more recently the isoformyl ion, COH^+, have been detected spectroscopically in interstellar dust clouds, and their identification has been confirmed by laboratory experiments.[1-6] There have been a series of theoretical calculations[7-16] concerned with the electronic structure of the isomers, the energy difference between the isomers, the activation barrier to isomerization, and the proton affinity of CO for proton attachment to the

---

[1] Green, S., *Annu. Rev. Phys. Chem.*, 1981, **32**, 103.
[2] Woods, R. C., *J. Mol. Struct.*, 1983, **97**, 195.
[3] Woods, R. C., *Astrophys. J.*, **270**, 583.
[4] Gudeman, C. S., and Woods, R. C., *Phys. Rev. Lett.*, 1982, **48**, 1344.
[5] Blake, G. A., Helminger, P., Herbst, E., and DeLucia, F. C., *Astrophys. J. Lett.*, 1983, **264**(2, Part 2), L69.
[6] Woods, R. C., Gudeman, C. S., Dickman, R. L., Goldsmith, P. F., Huguenin, G. R., Irvine, W. M., Hjalmason, A., Hymein, L. A., and Olofsson, H., *Astrophys. J.*, 1983, **270**, 583.
[7] Bruna, P. J., Peyerimhoff, S. D., and Beunker, R. J., *Chem. Phys.*, 1975, **10**, 323.
[8] Jansen, H. B., and Ros, P., *Theor. Chim. Acta*, 1971, **21** 199.
[9] Vasudevan, K., Peyerimhoff, S. D., and Beunker, R. J., *Chem. Phys.*, 1974, **5**, 149.
[10] Summers, N. L., and Tyrrell, J., *Theor. Chim. Acta*, 1978, **47**, 223.
[11] Nobes, R. H., and Radom, L., *Chem. Phys.*, 1981, **60**, 1.
[12] Del Bene, J. E., Frisch, M. J., Raghavachari, K., and Pople, J. A., *Phys. Chem.*, 1982, **86**, 1529.
[13] DeFrees, D. J., Loew, G. H., and McLean, A. D., *Astrophys. J.*, 1982, **257**, 376.
[14] Dixon, D. A., Komornicki, A., and Kraemer, W. P., *J. Chem. Phys.*, 1984, **81**, 3603.
[15] DeFrees, D. J., McLean, A. D., and Herbst, E., *Astrophys. J.*, 1984, **279**, 322.
[16] DeFrees, D. J., and McLean, A. D., *J. Comput. Chem.*, 1986, **7**, 321.

0004-9425/89/010009$03.00

carbon and oxygen end of the molecule. The reactivities of the isomers have been studied experimentally, and the proton affinity of CO to form HCO^+ and COH^+ has been reported.[17-24] The kinetic experiments have provided rate constants, product distributions, and evidence for vibrational excitation of the ions.[22] An electron impact induced dissociation study of a series of oxygen containing compounds by Haney and Franklin[25] provided a mean value of 828±8 kJ mol^{-1} for the enthalpy of formation of the formyl ion. A more recent experimental determination of the enthalpies of formation for the HCO^+ and COH^+ ions by McMahon and Kebarle[23] by proton transfer equilibria gave values of 812 and 962 kJ mol^{-1}, respectively, and a value of 990 kJ mol^{-1} has been reported for the enthalpy of formation of the isoformyl ion by Freeman *et al.*[24] using the SIFT technique to determfine relative proton affinities. The above experimental values reported for the enthalpies of formation of the two isomers yield an energy difference over the range 134–178 kJ mol^{-1} or a value of 150 kJ mol^{-1} by using the values reported by McMahon and Kebarle.[23]

The formyl and isoformyl ions have been the subject of many *ab initio* molecular orbital calculations over the past 20 years.[7-16] The earlier calculations concerned the electronic structure and protonation energies for the isomers,[7,8] *ab initio* SCF methods being used to the double-zeta level. These calculations indicated that the isoformyl ion should be a stable high energy isomer. Vasudevan *et al.*[9] employed a contracted Gaussian basis set of double-zeta quality and CI to calculate the absolute energies for the isomers giving an energy difference of 77 kJ mol^{-1}. Summers and Tyrrell used the GAUSSIAN 70 program[10] with a 4-31G basis set to calculate an energy difference of 91 kJ mol^{-1}. Higher levels of theory with more sophisticated basis sets have resulted in a series of calculations for the energy difference which lie within the range from 138 kJ mol^{-1} (ref. 15) to 175 kJ mol^{-1} (ref. 16), with a calculated activation barrier to the isomerization from HCO^+ to COH^+ of approximately 300 kJ mol^{-1}.[11] Nobes and Radom[11] used GUASSIAN 80 with the MP3/6-311G** basis set to calculate an energy difference of 157 kJ mol^{-1} between the isomers, and an activation barrier of 150 kJ mol^{-1} above the HOC^+ energy level. Del Bene *et al.*[12] performed a Hartree–Fock calculation with a 6-31G** basis set with correlation energies calculated at the MP4SDQ level of theory giving an energy difference of 149 kJ mol^{-1} and an activation barrier of 156 kJ mol^{-1} above the HOC^+ energy level. CI(SDQ) calculations carried out by DeFrees *et al.*[13] and by Dixon *et al.*[14] gave the energy spacing between isomers as 159 kJ mol^{-1},[13] and 165 kJ mol^{-1} (valence CI)[14] or 161 kJ mol^{-1} (all electron CI).[14] The most recent

---

[17] Roche, A. E., Sutton, M. W., Bohme, D. K., and Schiff, H. I., *J. Chem. Phys.*, 1971, **55**, 5480.

[18] Adams, N. G., Smith, D., and Grief, D., *Int. J. Mass Spectrom. Ion Phys.*, 1978, **26**, 405.

[19] Tanner, S. D., Mackay, G. I., Hopkinson, A. C., and Bohme, D. K., *Int. J. Mass Spectrom. Ion Phys.*, 1979, **29**, 157.

[20] Semo, N., Osheroff, M. A., and Koski, W. S., *J. Phys. Chem.*, 1983, **87**, 2302.

[21] Illies, A. J., Jarrold, M. F., and Bowers, M. T., *J. Am. Chem. Soc.*, 1983, **105**, 2562.

[22] Wagner-Redeker, W., Kemper, P. R., Jarrold, M. F., and Bowers, M. T., *J. Chem. Phys.*, 1985, **83**, 1121.

[23] McMahon, T. B., and Kebarle, P., *J. Chem. Phys.*, 1985, **83**, 3919.

[24] Freeman, C. G., Knight, J. S., Love, J. G., and McEwan, M. J., *Int. J. Mass Spectrom. Ion Processes*, 1988, in press.

[25] Haney, M. A., and Franklin, J. L., *Trans. Faraday Soc.*, 1969, **65**, 1974.

calculations by DeFrees *et al.*[16] using the MP4SDQ level of theory with a series of 6-311++G(*x,y*) basis sets with various polarization functions (*x,y*) yield an energy difference of 175 kJ mol^{-1}.

Despite the spread in both the calculated and experimental values reported for the enthalpy of formation of the HCO^+ isomers, the protonation reaction of CHO^+ on N_2O may be used as a probe for the presence of both or only one isomer. The reaction of the COH^+ isomer on N_2O being exothermic (see below) should be fast even at thermal collision energies whereas the reaction of the HCO^+ isomer will be endothermic for thermal collision energies, an increase in the total collision energy being required to overcome the endothermicity. We report in this communication the results of a near-monochromatic electron impact study of the CHO^+ ionization efficiency curve generated from CH_3OH and CH_3CHO, and the dependence of the cross-section for the reaction of the CHO^+ isomers with N_2O on the total centre-of-mass collision energy over the range 0·3–4 eV measured by using a drift-tube mass spectrometer.

Experimental

Ionization efficiency curves were measured by using a low pressure 'monochromatic' electron impact ion source which has been previously described in detail.[26] Briefly, a near-monochromatic electron beam with a full width at half maximum energy distribution of 50–60 meV is produced by means of a hemispherical electrostatic monochromator. The electron beam is accelerated or decelerated into a collision chamber containing the sample at a pressure of $<1\times10^{-6}$ Torr ($<1\times10^{-4}$ Pa). Ion beam retarding curves are measured to assess the translational energy of ions under investigation. Ionization efficiency curves were measured in 80 meV steps, Ar^+ and Kr^+ being used as energy scale calibrants. The reactive cross-sections for the CHO^+ isomers on N_2O were measured by using a drift-tube mass spectrometer which has been previously described for the determination of ion transport properties.[27] CHO^+ ions were generated by He^+ ion chemical ionization of 0·5% mixtures of methanol or acetaldehyde in helium and the N_2O admitted into the drift tube through a separate inlet system. The ion signal corresponding to the CHO^+ ion (*m/z* 29) was recorded as a function of the N_2O partial pressure (milliTorr) for a constant total drift-tube pressure of 0·3 Torr helium at 298 K. Pressures were measured by means of a 310 Baratron capacitance manometer with a 10 Torr head, and the temperature of the drift tube was maintained constant at 298 K by the circulation of water through the outer jacket and monitored with three thermocouples which were attached on two separate drift rings and one in the gas space.

Results

A typical ionization efficiency curve for Kr^+ and CHO^+ measured for a 1 : 2 mixture of krypton and methanol at a source pressure of $<1\times10^{-6}$ Torr is shown in Fig. 1. The appearance energies for $Kr^+(^2P_{3/2})$ at 13·999 eV and $Kr^+(^2P_{1/2})$ at 14·665 eV were chosen as the energy scale calibrants due to their close proximity to the experimental appearance energies found for CHO^+/CH_3OH. The energy difference between the two spin–orbit states of the Kr^+ ion found from 10 runs was 0·65±0·08 eV, in good accord with the spectroscopic value of 0·666 eV.[28] The ionization efficiency curve for the

---

[26] Harland, P. W., and McIntosh, B. J., *Int. J. Mass Spectrom. Ion Processes*, 1985, **67**, 29.

[27] Harland, P. W., and McIntosh, B. J., *Int. J. Mass Spectrom. Ion Processes*, 1984, **57**, 283.

[28] Rosenstock, H. M., Draxl, K., Steiner, B. W., and Herron, J. T., *J. Phys. Chem. Ref. Data Suppl.*, 1977, **1**, 6.

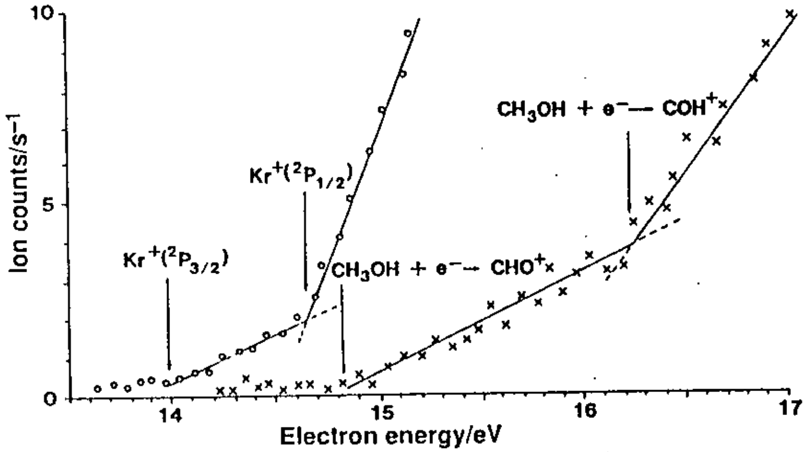

Fig. 1. Ionization efficiency curves for Kr^+ and CHO^+ from a 1 : 2 mixture of krypton and methanol. The electron energy scale has been calibrated to the spectroscopically determined appearance energy for $Kr^+(^2P_{3/2})$ at 13·999 eV (14·00 eV).

CHO^+ ion exhibits an appearance energy or threshold at 14·82±0·20 eV and a break at 16·25±0·27 eV with a mean separation between the thresholds of 1·43 eV (138 kJ mol^{-1}).

The ionization mechanism for the formation of the CHO^+ ion from methanol is shown in equation (1):

$$CH_3OH + e^- \rightarrow CHO^+ + H_2 + H + 2e^- \qquad (1)$$

where CHO^+ corresponds to the formyl isomer, HCO^+, at the first threshold and to the isoformyl isomer, COH^+, at the second threshold. In the absence of excess recoil energy and internal excitation of the ionization fragments the energy separation of these thresholds would correspond to the difference in the enthalpies of formation for the two isomers. However, if the enthalpy of formation of the formyl ion is taken as 828 kJ mol^{-1}, the minimum appearance energy (first threshold) for the formyl isomer is calculated to be 12·88 eV, almost 2 eV lower than the experimental value of 14·82 eV. The experimental value found here, however, is in good agreement with the range of values, 14·3–14·7 eV and the calculated value of 14·76 eV, reported by Lifshitz *et al.*,[29] that incorporated the excess tranlational energy of 1·42 eV found in the fragmentation process by Beynon *et al.*[30] The ion beam retarding curve for CHO^+ indicated excess translational energy for the ion, although this was insufficient to account for all of the excess energy evident from the high displacement of the threshold from the minimum calculated value. These observations can only be reconciled if the non-atomic fragmentation products (CHO^+ and/or H_2) also carry vib-rotational energy. Wagner-Redeker *et al.*[22] have reported kinetic evidence that CHO^+ ions are generated in vibrationally excited states. Since neither the distribution of the excess energy between internal modes and

---

[29] Lifshitz, C., Shapiro, M., and Sternberg, R., *Isr. J. Chem.*, 1969, **7**, 291.

[30] Beynon, J. H., Fontaine, A. E., and Lester, G. R., *Int. J. Mass Spectrom. Ion Phys.*, 1968, **1**, 1.

translational energy nor the excess energy for the individual thresholds can be determined in these experiments the difference of 138 kJ mol^{-1} between the thresholds can only be reported as an estimate to the enthalpy difference between the isomers. This value falls into the lower end of the range for values deduced from *ab initio* calculations but is certainly in agreement with the value of 150 kJ mol^{-1} reported by McMahon and Kebarle,[23] within the respective uncertainties.

The ionization efficiency curve for CHO^+ produced by the dissociative electron impact ionization of acetaldehyde, CH_3CHO, did not exhibit any breaks which could be attributed to the higher energy isomer. The threshold, at 12·64±0·13 eV, was not sharp, lying 0·9 eV above the minimum calculated appearance energy for the formation of the formyl isomer by the dissociative ionization of CH_3CHO. The kinetic studies reported below confirm the absence of the higher energy isoformyl isomer from the ionization of CH_3CHO. Acetaldehyde would be a useful precursor molecule for the preparation of the formyl ion free from the higher energy isomer. Bowers *et al.*[21] have found isomeric mixes of the CHO^+ ion from electron impact or helium ion chemical ionization of HCHO, CH_3OH, CH_3COOH, $(CH_3)_2O$ and $HCOOCH_3$ and from the reaction of H_3^+ on CO.

The proton transfer reaction (2) is endothermic, the calculated endothermicity depending on the value chosen for the enthalpy of formation of the formyl ion:

$$HCO^+ + N_2O \rightarrow N_2OH^+ + CO \qquad (2)$$

From the value of 828 kJ mol^{-1} proposed by Haney and Franklin and the value of 812 kJ mol^{-1} reported by McMahon and Kebarle, reaction (2) is found to be endothermic by 20 or 36 kJ mol^{-1}, respectively. The experimental uncertainty on each of these individual values would be about ±10 kJ mol^{-1}. The enthalpy of formation for protonated N_2O was taken to be 1041 kJ mol^{-1}.[31] Reaction (3), in contrast, is exothermic, the degree of exothermicity depending on the value taken for the enthalpy of formation of the isoformyl ion:

$$COH^+ + N_2O \rightarrow N_2OH^+ + CO \qquad (3)$$

From the values 962 and 990 kJ mol^{-1}, respectively,[23,24] the enthalpy of reaction (3) is calculated to be either −114 or −142 kJ mol^{-1}.

The attentuation of the CHO^+ ion signal in the drift tube of drift distance z as a function of the N_2O particle density, n_{N_2O}, is given by:

$$I_{CHO^+} = I_{CHO_0^+} \exp(-\sigma(E) . n_{N_2O} . z) \qquad (4)$$

where $\sigma(E)$ is the reaction cross-section for the mean centre-of-mass collision energy E. Attenuation curves were measured as a function of the electric field to particle density ratio, E'/N, which is a measure of the ion energy in the drift tube, over the range 40–200 Td (1 Td ≡ 10^{-21} V m^2 where Td denotes

---

[31] Lias, S. G., Liebman, J. F., and Levin, R. D., *J. Phys. Chem. Ref. Data*, 1984, **13**, 695.

the unit known as the townsend) for methanol as the CHO^+ precursor and 30–200 Td for acetaldehyde as the CHO^+ precursor. The lower limit to E'/N accessible in the drift tube is imposed by the magnitude of the ion signal. E' is the electric field gradient in the drift tube, and N the total particle density. These E'/N ranges are equivalent to a range of centre-of-mass collision energies[32] from 0·3 to 4 eV (30–390 kJ mol^{-1}). Endothermic ion–molecule reactions can be switched on as the centre-of-mass collision energy exceeds the reaction endothermicity. The reaction cross-section for an endothermic process increases from the threshold to a maximum value and then declines towards a hard-sphere limit following the same behaviour as an exothermic process with increasing collision energy (E'/N).

When CH_3OH is used as the CHO^+ precursor both isomers are present in the drift tube. The plots of log(ion signal) against n_{N_2O} were found to be non-linear and characteristic of a double exponential decay according to equation (5):

$$I_{CHO^+} = I_{HCO_0^+} \exp(-\sigma(E)_{HCO^+} . n_{N_2O} . z) + I_{COH_0^+} \exp(-\sigma(E)_{COH^+} . n_{N_2O} . z) \qquad (5)$$

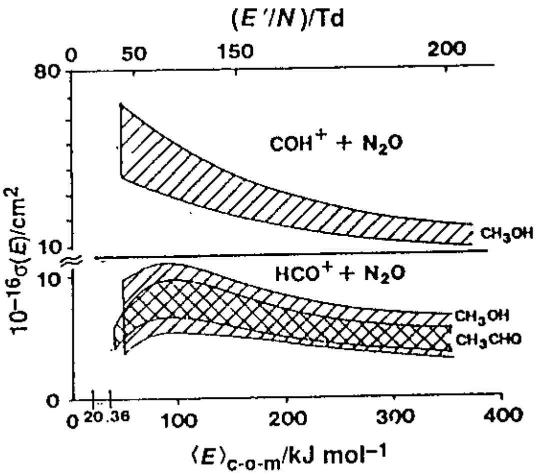

Fig. 2. Cross-sections for the protonation of N_2O by the isomers of CHO^+ as a function of E'/N or mean total collision energy <E>. The areas filled by the right-sloping cross-hatch incorporate values obtained from the double exponential ion attenuation curves by using the iterative fitting procedure. The area filled by the left-sloping cross-hatch incorporates cross-section values determined for reaction of the CHO^+ ion formed from CH_3CHO. The range of endothermicities or threshold energies for the reaction of HCO^+ on N_2O obtained from literature enthalpies of formation are shown on the abscissa.

The cross-sections for the protonation of N_2O by the individual isomers as a function of E'/N (total collision energy, E) obtained from fitting equation (5) to the experimental attenuation curves are shown in Fig. 2. The excitation function, plot of reaction cross-section against collision energy, for one set of cross-sections obtained from the fitting procedure exhibits the typical behaviour expected for an exoergic reaction, presumably for the exothermic proton transfer reaction involving the higher energy COH^+ isomer, and the second set exhibiting the characteristics of an endothermic reaction with a threshold corresponding to the lower energy HCO^+ isomer. The uncertainty

---

[32] McFarland, M., Albritton, D. L., Fehsenfeld, F. C., Ferguson, E. E., and Schmeltekopt, A. L., *J. Chem. Phys.*, 1973, **59**, 6620.

on the cross-sections derived from the Simplex iterative fitting procedure is estimated to be 30–40%. The attenuations of the CHO$^+$ ion derived from the CH_3CHO precursor by reaction with N_2O were simple exponential curves yielding more accurate reactive cross-sections (estimated ±20%). These data are in general agreement with the low reactivity component generated from the CH_3OH precursor which we have attributed to the HCO$^+$ ion (Fig. 2) in accord with the results from the electron impact study. The accuracy of these data precludes a meaningful extrapolation of the cross-section curve for the HCO$^+$ isomer to the threshold although we could conclude that it is not inconsistent with the reaction endothermicity in the range 20–36 kJ mol^{-1} calculated from the enthalpy of formation values deduced from proton transfer experiments.

Manuscript received 15 February 1988

International Journal of Mass Spectrometry and Ion Processes, 90 (1989) 193–196 193
Elsevier Science Publishers B.V., Amsterdam – Printed in The Netherlands

Short Communication

THEORETICAL CALCULATION OF THE HeB$^+$ MOLECULAR ION INTERACTION POTENTIAL AND THE MOBILITY OF B$^+$ IONS IN HELIUM

R.W. SIMPSON, P.W. HARLAND * and R.G.A.R. MACLAGAN
Chemistry Department, University of Canterbury, Christchurch (New Zealand)

D. SMITH and N.G. ADAMS
Department of Space Research, The University of Birmingham,
Birmingham B15 2TT (Gt. Britain)

(Received 7 October 1988)

Interaction potentials for many of the first-row atomic positive ions and stable negative ions in helium have been calculated by ab initio molecular orbital and valence bond methods at the University of Canterbury, Christchurch [1–5]. These interaction potentials have then been used with the two-temperature [6,7] and three-temperature [8,9] theories of ion transport to calculate ion mobilities in helium for comparison with experimental measurements made in the laboratory and taken from the literature. The agreement between the theoretical and experimental ion drift velocities and mobilities has been within the quoted experimental uncertainties and in the case of the O$^+$ ion in helium the calculated mobility curve for the O$^+$(^2P) ion could be closely matched with literature measurements for the O^{+*} ion, which had been tentatively identified as the O$^+$(^2D) ion [2]. The mobilities of ions such as C$^+$, N$^+$, O$^+$ and F$^+$, which exhibit multiple ion/helium molecular states, have been calculated from the ab initio interaction potentials for each state using the appropriate statistical weighting of states in Blanc's Law. The success of this approach is demonstrated by the close agreement between the experimental measurements for the F$^+$(^3P), C$^+$(^4P) and C$^+$(^2P) ions in helium and the mobilities calculated from the statistical weighting of the available HeF$^+$ and HeC$^+$ molecular ion states. The attraction of a theoretical computational approach to ion mobility data based on reliable ab initio interaction potentials lies in the wide range and combinations of buffer gas, ion temperature (the ratio of the electric field to

---

* Author to whom correspondence should be addressed.

0168-1176/89/$03.50 © 1989 Elsevier Science Publishers B.V.

the particle density, E/N) and electronic states of ions that can be explored easily and which may not be readily amenable to experimental study.

The mobility of the B^+ ion in helium had not previously been measured and an attempt to rectify this situation using the static drift tube at the University of Canterbury, Christchurch was met with unexpected technical difficulties. Boron compounds introduced in trace amounts into the drift tube (1–5 parts per thousand in helium at a pressure of 0.3 torr) resulted in a rapid increase in the work function of the filament with a corresponding reduction in the thermionic electron emission and a subsequent loss of the B^+ ion signal. This effect was found for bare iridium and rhenium, thoriated iridium and for both iridium and rhenium coated with barium zirconate, irrespective of whether the boron-carrying molecule was B_2H_6, BCl_3 or BF_3. The effect is fully reversible, the filament emission and normal drift tube operating characteristics recovering within minutes of pumping out the boron sample. The problem was solved using the selected ion flow drift tube at the University of Birmingham [10]. The mobility of the $^{11}B^+$ ion in helium was measured at five points over the range of E/N from 11 to 32 Td (1 Td $= 10^{-21}$ V m^2) with an estimated experimental uncertainty of ±5%.

The HeB^+ molecular ion interaction potential was calculated using the GAUSSIAN 82 program [11] at the MP4SDQ/6-311 + G(3*df*,3*pd*) level of theory, excluding core contributions to the correlation energy. The results of this calculation are given in Table 1 and plotted in Fig. 1. This interaction potential was used with the three-temperature theory of ion transport to calculate the $^{11}B^+$ ion mobility over the range of E/N from 2 to 160 Td. The collision cross-sections were calculated to an accuracy of 0.1% and the three-temperature theory calculation for the mobility converged to within 0.8%. The theoretical curve of reduced mobility vs. E/N and the experimental data points, including the ±5% error bars, are shown in Fig. 2. The

TABLE 1

Interaction potential energies for the ground state of the HeB^+ molecular ion calculated at the MP4SDQ/6-311 + G(3*df*,3*pd*) level of theory

Internuclear separation (Å)	Energy (hartree)	Internuclear separation (Å)	Energy (hartree)
1.50	−27.154654	3.25	−27.189733
1.75	−27.174503	3.50	−27.189590
2.00	−27.183922	3.75	−27.189469
2.25	−27.187931	4.00	−27.189375
2.50	−27.189437	4.50	−27.189247
2.75	−27.189860	5.00	−27.189168
2.875	−27.189889	∞	−27.189029
3.00	−27.189861		

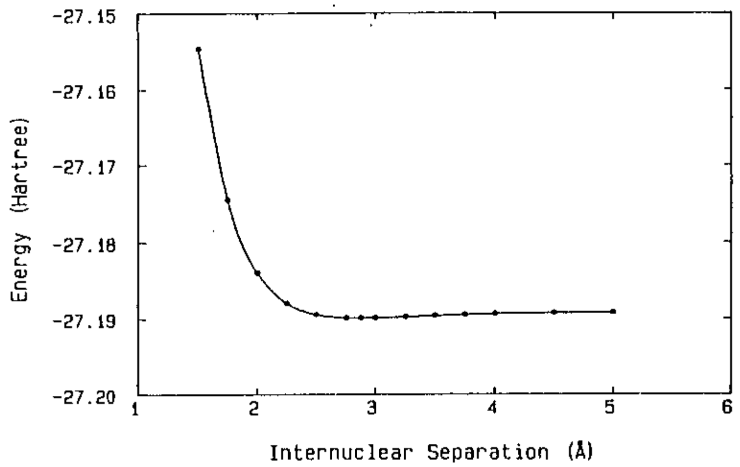

Fig. 1. Interaction potential for the ground state of the HeB^+ molecular ion using the theoretical data given in Table 1.

experimental measurements have been made over a relatively narrow range of E/N owing to experimental limitations. However, there is agreement with the theoretically calculated curve within the estimated uncertainty and both the experimental data and the theoretical curve exhibit a maximum at 20 Td. These results reinforce conclusions based on our previous calculations and comparisons with experimental data measured using both static and selected ion drift tubes. The theoretical calculations give mobilities within 1–2% for

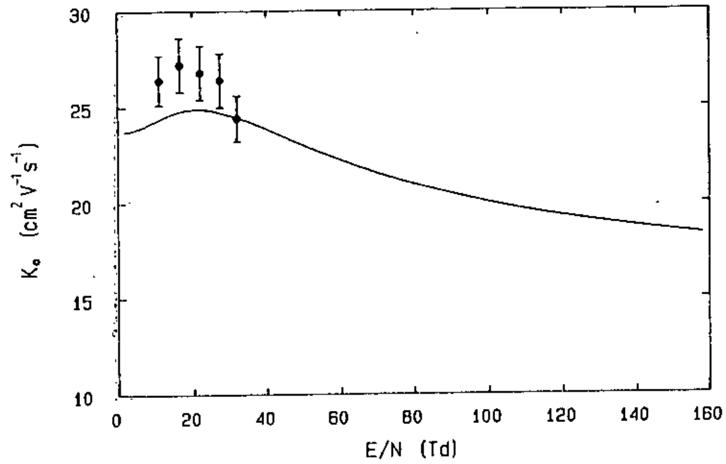

Fig. 2. Calculated (———) and experimental (●) reduced mobility of B^+ ions in helium as a function of E/N.

$E/N > 30$ Td, where the repulsive part of the interaction potential is dominant, and within the range of published experimental uncertainties, 5–7%, for $E/N < 30$ Td, where small changes in the potential translate into significant changes in the ion mobility.

REFERENCES

1 R.G.A.R. Maclagan, R.W. Simpson and P.W. Harland, J. Phys. B, 20 (1987) 2723.
2 R.W. Simpson, R.G.A.R. Maclagan and P.W. Harland, J. Chem. Phys., 87 (1987) 5419.
3 S.T. Grice, P.W. Harland and R.G.A.R. Maclagan, Int. J. Mass Spectrom. Ion Processes, 87 (1989) 181.
4 P.W. Harland, R.G.A.R. Maclagan and R.W. Simpson, J. Chem. Soc., Faraday Trans. 2, 84 (1988) 1847.
5 R.W. Simpson, Ph.D. Thesis, University of Canterbury, Christchurch, New Zealand, 1988.
6 L.A. Viehland and E.A. Mason, Ann. Phys., 91 (1975) 499.
7 L.A. Viehland and E.A. Mason, Ann. Phys., 110 (1978) 287.
8 S.L. Lin, L.A. Viehland and E.A. Mason, Chem. Phys., 37 (1979) 711.
9 L.A. Viehland and S.L. Lin, Chem. Phys., 43 (1979) 135.
10 D. Smith and N.G. Adams, Adv. At. Mol. Phys., 24 (1988) 1.
11 J.S. Binkley, M.J. Frisch, D.J. DeFrees, K. Raghavachari, R.A. Whiteside, H.B. Schlegel, E.M. Fluder and J.A. Pople, GAUSSIAN 82, Carnegie-Mellon University, Pittsburgh, PA, 1983.

J. Chem. Soc., Faraday Trans. 2, 1989, 85(3), 187-193

Structures and Energies of $C_2NH_2^+$ Isomers

Peter W. Harland, Robert G. A. R. Maclagan*
Chemistry Department, University of Canterbury, Christchurch, New Zealand
Henry F. Schaefer III
Center for Computational Quantum Chemistry, †School of Chemical Sciences, University of Georgia, Athens, Georgia 30602, U.S.A.

Ab initio calculations of the structures and relative energies of the isomers of $C_2NH_2^+$ show three low-energy isomers. The lowest-energy form is a cyclic isomer with two higher-energy stable linear forms, H_2CNC^+ and H_2CCN^+. The relative energies calculated at the MP4SDQ/6-311G** level of theory are 0, 60 and 52 kJ mol^{-1}, respectively. Interconversion between the cyclic isomer and the linear isocyano isomer H_2CNC^+ involves an intermediate structure calculated using CISD energies to be 141 kJ mol^{-1} above the cyclic structure and interconversion between the cyclic and cyano isomer involves an intermediate 226 kJ mol^{-1} above the cyclic isomer. Vibrational frequencies and infrared intensities have been calculated for the three stable isomers at the SCF DZP level of theory. The theoretical energies are compared with experimental measurements for the formation of the $C_2NH_2^+$ ion from CH_3CN and CH_3NC which provided evidence for two isomers separated in energy by 51 ± 10 kJ mol^{-1}, that from CH_3NC being the cyclic isomer and that from CH_3CN being the linear isomer.

The ionisation threshold for the formation of the $C_2NH_2^+$ ion has been measured from both methyl cyanide, CH_3CN, and methyl isocyanide, CH_3NC, precursor molecules. The literature values for the appearance energy of the $C_2NH_2^+$ ion from CH_3CN cover the range from 13.54 to 14.72 eV. The most recent value from a monochromatic electron-impact ionisation study of CH_3CN and CH_3NC is 14.38 ± 0.04 eV.[1] The same study determined the appearance energy for the formation of the $C_2NH_2^+$ ion from CH_3NC, methyl isonitrile, to be 13.21 ± 0.04 eV, in accord with the only other literature value. These appearance energies used with known standard enthalpies of formation for the precursor molecules and the hydrogen-atom fragmentation product gave the enthalpy of formation for the $C_2NH_2^+$ ion from CH_3CN as 1257 ± 5 kJ mol^{-1} and from CH_3NC as 1206 ± 5 kJ mol^{-1}.

The difference of 51 ± 10 kJ mol^{-1} between these two precursor molecules was interpreted in terms of two stable isomeric forms of the ion. Using the results of SCF calculations of the isomeric structures and relative energies as a guide, it was argued that skeletal integrity of the precursor molecule may well be retained, giving rise to the H_2CCN^+ ion from ionisation of CH_3CN and the H_2CNC^+ ion from ionisation of CH_3NC. The cyclic isomer, c-$C_2NH_2^+$, has been previously suggested to account for the collision-induced spectra of the $C_2NH_2^+$ ion generated from a series of $H_3C_2N^+$ isomers.[2] The attraction of the cyclic form lies in its potential stabilisation as the simplest example of a Hückel $(4n+2)\pi$ electron system, where $n = 0$. The isoelectronic cyclopropenyl ion, c-$C_3H_3^+$, is a well studied stable gas-phase ion.[3-6] The resonance stabilisation energy conferred by delocalisation results in an enthalpy of formation 100 kJ mol^{-1} lower than

---

† Contribution CCQC no. 25.

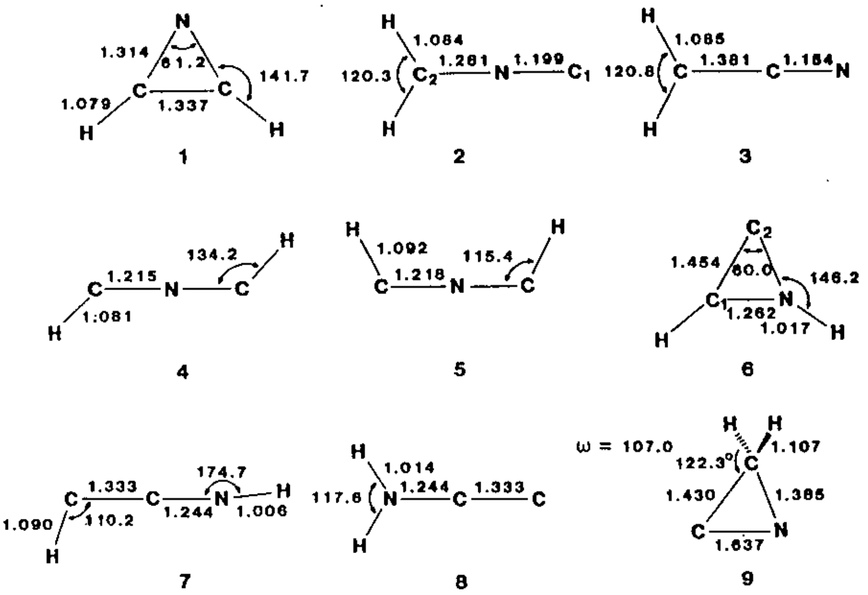

Fig. 1. Optimised geometries for structures 1–9 (distances in Å, angles in degrees).

that for the linear propargyl isomer.[3,7,8] The preliminary SCF calculations for the $C_2NH_2^+$ isomers[1] gave the cyclic isomer as the lowest-energy structure, followed by the two linear isomers H_2CNC^+ and H_2CCN^+, 43 and 77 kJ mol^{-1} less stable, respectively. Assignment of the isomers formed from the monochromatic electron-impact ionization of CH_3CN and CH_3NC to the linear isomers was based on the conservation of the C, N skeletal framework of the precursor molecule as discussed above, and the apparant reasonable accord between the experimental energy separation, 51 ± 10 kJ mol^{-1}, and the SCF calculation of 34 kJ mol^{-1}.

$C_2H_2N^+$ has been the subject of several other theoretical studies: STO-3G calculations were reported by Moffat for the two isomers H_2CCN^{+9} and H_2CNC^+.[10] Swanton *et al.*[11] reported geometries optimised with a 4-21G basis set for nine isomers of $C_2H_2N^+$. In addition, they reported HF energies calculated using 6-31G, DZ and DZ+P basis sets for the isomers lowest in energy (structures 1, 2, 3 and 7 in fig. 1). The 4-21G optimised geometries were used for these calculations. MP3/4-21G correlation energies were also reported for the three isomers lowest in energy (structures 1–3 in fig 1). Only with the DZ+P basis set, which includes polarisation functions, is the cyclic structure (1) predicted to be the lowest in energy. The isocyano isomer (2) is lower in energy than the cyano isomer (3).

$C_2H_2N^+$ is isoelectronic with C_3H_2 and C_2H_2Si. Related structures include $C_3H_3^+$, ethynamine (NH_2C_2H) and ketene (H_2C_2O). The laboratory identification of cyclopropenylidene by Reisenauer *et al.*[12] was facilitated by the calculation of infrared band frequencies and the relative intensities by Lee *et al.*[13] Lee *et al.* found that there were important contributions from the excited $6a_1^2 \rightarrow 2b_1^2$ configuration in a TCSCF study. We would hope that the vibrational data included in this paper might permit some laboratory identification of $C_2H_2N^+$ ions. Frenking *et al.*[14] made an extensive study of five different isomers of C_2H_2Si. They found that the lowest-energy isomer was the cyclic silacyclopropenylidene. The isomer next lowest in energy was vinylidenesilene H_2CCSi, *ca.* 71.3 kJ mol^{-1} above the lowest-energy isomer. The next lowest-energy isomer was silenylacetylene, $HSiC_2H$.

Table 1. SCF, CISD and CISD+Q energies for $C_2NH_2^+$ species with a DZ+P basis set

structure	*E*(SCF)/hartree	*E*(CISD)/hartree	*E*(CISD+Q)/hartree
1	−130.990 486	−131.389 029	−131.430 102
2	−130.974 061	−131.367 678	−131.410 465
3	−130.960 932	−131.361 831	−131.407 589
4	−130.902 226	−131.308 156	−131.356 588
5	−130.884 668	−131.291 554	−131.340 660
6	−130.933 242	−131.291 996	—
7	−130.920 852	−131.275 691	—
8	−130.890 052	−131.256 585	—
9	−130.760 341	−131.155 675	−131.203 990

Theoretical Details

Equilibrium structures were obtained at the self-consistent field (SCF) level of theory using analytic gradient techniques.[15] The basis sets chosen were standard double-zeta plus polarisation (DZ+P) sets. On the carbon and nitrogen atoms the (9s5p) set of Huzinaga[16] was contracted following Dunning[17] to [4s2p]. A full set of six d-like functions was added with orbital exponents of $\alpha_C = 0.75$ and $\alpha_N = 0.80$. For the hydrogen atoms, a 4s set, scaled by 1.2 was contracted to [2s],[17] with a set of p functions added with orbital exponent $\alpha = 0.75$. For structures 1–3 of fig. 1 harmonic vibrational frequencies were calculated using analytic second derivatives[18] from the SCF optimum geometries. Configuration interaction (CI) calculations were performed at the SCF optimum geometry. The CI wavefunctions included all interacting singly and doubly excited configurations (CISD) relative to the Hartree–Fock reference configuration. Some calculations were also performed at the HF/6-311G** and MP4SDQ/6-311G** levels of theory using the GAUSSIAN82[19] program.

Results and Discussion

The DZ+P SCF optimised geometries for nine isomers of $H_2C_2N^+$ are given in fig. 1. Comparison of the geometry of structure (1) with the 4-21G geometry of Swanton *et al.*[11] and STO-3G calculations show that improving the basis set decreases both the CC and CN bond lengths. The 4-21G and DZ+P optimised structures are very similar for structure (2). For structure (3), the CC bond length is significantly smaller with the 4-21G basis set than with the STO-3G and DZ+P basis sets. The CC bond length in structure (1) is similar to that calculated for the corresponding isomers of C_3H_2 (1.317 Å) and C_2SiH_2 (1.343 Å) with DZ+P basis sets. Owing to the longer SiC bond length, the CSiC bond angle in C_2SiH_2 of 43.6° is smaller than that for C_3H_2 of 55.6° or $H_2C_2N^+$ of 53.9°. The CC bond length of 1.381 Å for isomer (3) is slightly longer than the 1.318 Å found in the C_2SiH_2 isomer and 1.316 Å found for ketene.[20]

In table 1 are listed the HF, CISD energies, and the CISD+Q energies calculated using Davidson's correction[21] for the structures given in fig. 1. The lowest-energy structure is the cyclic structure (1), as was found for C_2SiH_2 and $C_3H_3^+$.[22] Structure (2) is calculated to be 51.6 kJ mol^{-1} (47.7 kJ mol^{-1} when the calculated zero-point vibrational energy is included) higher in energy, with structure (3) slightly higher at 59.1 kJ mol^{-1} (53.7 kJ mol^{-1} with the zero-point vibrational energies included) above the cyclic structure. At the SCF level of theory with a 4-21G basis set, the isocyano ion (2) is lowest in energy. The calculations of Swanton *et al.*[11] showed that only with the inclusion of polarisation functions in the basis set is the cyclic structure calculated to be the lowest in energy. The formation of structure (1) from ions formed initially as either isomers

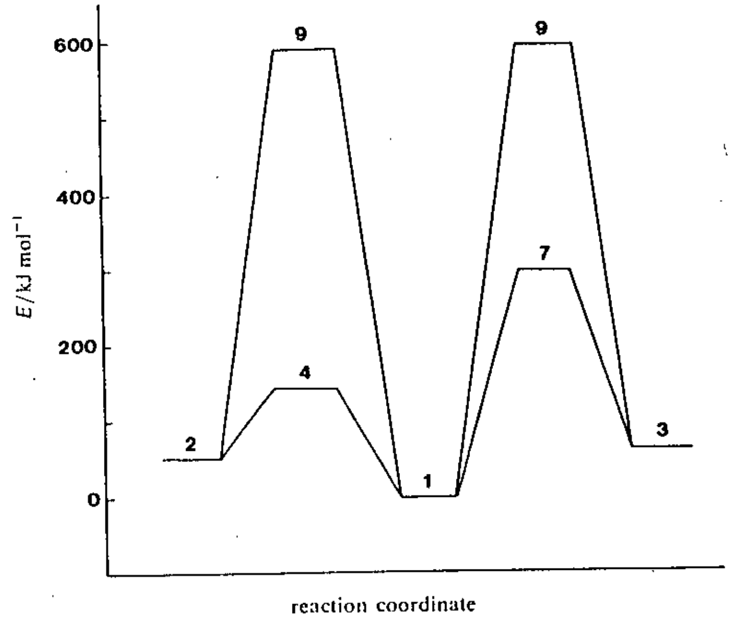

Fig. 2. Relative CISD energies of structures 1-3 and possible intermediates between them.

Table 2. Relative energies (in kJ mol^{-1}) for the three lowest-energy structures of $C_2NH_2^+$

structure	DZ+P SCF	DZ+P CISD	DZ+P CISD+Q	6-311G** SCF	6-311G** MP4SDQ
1	0.0	0.0	0.0	0.0	0.0
2	43.1	56.1	51.6	45.7	60.2
3	77.6	71.4	59.1	71.7	51.6

(2) or (3) will be slow, with the formation from the cyano ion being much slower than from the isocyano ion as the energy of the intermediate structures (and hence transition states) are much higher for the conversion of (3) to (1). Structure (9), which is a possible intermediate formed by simple ring closure, lies 593.7 kJ mol^{-1} above structure (1). Structure (4), formed by a 1-3 hydrogen shift from structure (2), lies 141.5 kJ mol^{-1} above structure (2). This would be a possible intermediate in the transition from structure (2) to the cyclic structure (1). Structure (9) is the only obvious intermediate structure between (3) and (1). A more indirect route involves structure (7), which is predicted to lie 226.2 kJ mol^{-1} above structure (3) using CISD energies. The relative energies of these isomers are shown in fig. 2. The isomerisation barriers indicate that structures (1) and (3), once formed, would exist as stable, non-interconverting isomers in the absence of external influences.

In the CISD calculations on structures (1)-(3) the coefficients of the most important configuration were 0.9471, 0.9441 and 0.9412, respectively, indicating that a single reference treatment is satisfactory.

Calculations were also performed at the MP4SDQ/6-311G**//HF/6-311G** level of theory for structures (1)-(3). This is a slightly larger basis set and a different level of theory from the previously described CISD calculations. For structure (1), E(SCF) = −130.999 896 hartree; E(MP4SDQ) = −131.412 693 hartree; R(C—C) = 1.331 Å,

Table 3. Theoretically determined vibrational wavenumbers/(cm^{-1}) and i.r. intensities at the DZ+P SCF level for structures 1, 2 and 3

	structure 1			structure 2			structure 3		
	wavenumber	intensity[a]	symmetry	wavenumber	intensity[a]	symmetry	wavenumber	intensity[a]	symmetry
1	3451	0.41	a_1	3409	0.97	b_2	3407	2.00	b_2
2	3390	4.06	b_2	3284	0.06	a_1	3286	0.73	a_1
3	1857	0.27	a_1	2233	28.25	a_1	2335	16.10	a_1
4	1507	0.68	a_1	1641	0.02	a_1	1569	0.01	a_1
5	1323	1.95	b_2	1321	0.04	b_1	1265	0.03	b_1
6	1096	0.00	b_2	1311	0.87	a_1	1131	4.77	a_1
7	1078	0.00	a_2	1236	0.32	b_2	1108	0.01	b_2
8	1030	1.30	a_1	303	0.26	b_1	374	0.03	b_2
9	932	0.58	b_1	283	0.46	b_2	278	0.06	b_1

[a] $(D/\text{Å})^2/\text{amu} = 42.25 \text{ km mol}^{-1}$.

R(C—N) = 1.307 Å, R(C—H) = 1.075 Å, ∠NCH = 141.5° and ∠CNC = 68.0°. For structure (2), E(SCF) = −130.982 475 hartree; E(MP4SDQ) = −131.389 769 hartree; R(C—N) = 1.279 Å, R(N—C) = 1.194 Å. R(C—H) = 1.082 Å, and ∠HCH = 120.3°. For structure (3), E(SCF) = 130.972 593 hartree; E(MP4SDQ) = −131.393 022 hartree; R(C—C) = 1.371 Å, R(C—N) = 1.145 Å, R(C—H) = 1.082 Å, and ∠HCH = 120.1°. The relative energies of the three lowest-energy structures, as predicted by the various levels of theory are given in table 2. At the MP4SDQ level structure (3) is now 8.5 kJ mol^{-1} lower than structure (2) and 51.6 kJ mol^{-1} higher in energy than structure (1). On the basis of these calculations and the enthalpies of formation obtained from appearance energies it would appear that the cyclic isomer, structure (1), is formed from CH_3NC with the linear isomer, structure (3), formed from CH_3CN. Presumably, rearrangement of the CH_3NC^+ intermediate state is able to facilitate formation of the cyclic isomer, whereas the corresponding process is unfavourable from the CH_3CH^+ molecular ion intermediate. Once the ions are formed under single-collision conditions in the ionisation experiments isomerisation is precluded by the high barriers.

In table 3 are given the harmonic vibrational frequencies calculated at the SCF level of theory for structures 1-3. Along with the frequencies, the calculated infrared intensities for each vibrational mode are given. For structure (1) the three most intense bands are the CH asymmetric stretch mode at 3390 cm^{-1}, the mode at 1323 cm^{-1}, which has CH rock and CN asymmetric stretch character, and the in-plane symmetric CH bend mode at 1030 cm^{-1}. The most intense band for structure (2) is the asymmetric CN stretch mode at 2335 cm^{-1} and the symmetric CH bend mode at 1131 cm^{-1} The zero-point vibrational energies (within the harmonic approximation) for structures 1-3 are 93.7, 89.9 and 88.2 kJ mol^{-1}, respectively.

Conclusion

This paper demonstrates the value of the interplay of experiment and theory. On their own the experiments are unable to differentiate different structural isomers of the ions under study and intuitive judgements are not always substantiated following theoretical calculations of the possible ion structure energies. Our calculations show that while the ion formed from CH_3NC is the lowest-energy isomer(1), this isomer cannot be formed from CH_3CN owing to the height of possible intermediates (and hence transition states) above the CH_2CN^+ isomer energy for the conversion to the cyclic isomer. These barriers are not too large for the CH_2 NC^+ isomer. The difference between the infrared spectrum for (1), (2) and (3) might allow experimental determination.

H.F.S. thanks the U.S. National Science Foundation for support.

References

1 P. W. Harland and B. J. McIntosh, *Int. J. Mass Spectrom. Ion Process.*, 1985, **67**, 29.
2 E. K. Chess, R. L. Lapp and M. L. Gross, *Org. Mass Spectrom*, 1982, **17**, 475.
3 K. Raghavachari, R. A. Whiteside, J. A. Pople and P. v. R. Schleyer, *J. Am. Chem. Soc.*, 1981, **103**, 5649.
4 M. L. Gross, *J. Am. Chem. Soc.*, 1972, **94**, 3744.
5 T. McAllister and A. J. C. Nicholson, *J. Chem. Soc., Faraday Trans. I*, 1981, 77, 821.
6 F. P. Lossing, *Can. J. Chem.*, 1972, **50**, 3973.
7 J. L. Holmes and F. P. Lossing, *Can. J. Chem.*, 1979, **57**, 249.
8 P. J. Ausloos and S. G. Lias, *J. Am. Chem. Soc.*, 1981, **103**, 6505.
9 J. B. Moffat, *Chem. Phys. Lett.*, 1980, **76**, 304.
10 J. B. Moffat *J. Am. Chem. Soc.*, 1982, **104**, 3949.
11 D. J. Swanton, G. B. Bacskay, G. D. Willett and N. S. Hush, *J. Mol. Struct.* (*Theochem.*), 1983, **91**, 313.
12 H. P. Reienauer, G. Maier, A. Riemann and R. W. Hoffmann, *Angew. Chem. Int. Ed. Engl.*, 1984, **23**, 641.
13 T. J. Lee, A. Bunge and H. F. Schaefer *J. Am. Chem. Soc.*, 1985, **107**, 137.

Effect of molecular orientation on electron transfer

Peter W. Harland,[a)] Howard S. Carman, Jr.,[b)] Leon F. Phillips,[a)]
and Philip R. Brooks
Department of Chemistry & Rice Quantum Institute, Rice University, Houston, Texas 77251

(Received 23 January 1989; accepted 23 February 1989)

The effect of molecular orientation on chemical reactivity has been studied in crossed beams for several systems.[1] For K + (oriented) CF_3I, the KI is forward scattered for attack at the "tails" (CF_3) end and backward scattered for attack at the "heads" (I) end. These experimental results[2] are nicely accounted for by the "harpoon mechanism"[3]: electron transfer from an electropositive atom to an electron accepting molecule; break-up of the negative molecular ion in the field of the incoming positive ion; and completion of reaction via the Coulomb attraction of the resulting ions. Because the decomposition of the negative ion occurs within one vibrational period, the I^- ion is ejected in the instantaneous direction of the CF_3I axis, giving backward scattering for heads approach, forward scattering for tails approach, and also nicely accounting for the scattering from the sideways approach.[4]

Extension of the same argument to K + (oriented) CF_3Br is not in complete accord with experiment,[1(a)] suggesting that the electron jump might be affected by the molecular orientation. Since the dominant forces after the jump are Coulombic, chemical specificity would seem indeed to be reflected in the initial transfer. To investigate this effect directly, we have studied collisions of fast K atoms[5] with oriented CF_3I and CH_3I molecules over the CM energy range ≈ 5–25 eV. These reactions are known[6] to produce K^+ and I^-; we report here that for both molecules the probability of forming K^+ is greater for attack at the I end.

Beams of fast K atoms are generated by charge exchange[7] of K^+, and after residual K^+ ions are swept out of the beam, the fast K atoms intersect a supersonic beam of RI molecules ($R = CF_3$, CH_3) which have been state selected in an inhomogeneous six-pole electric field[8] and oriented[9] in a uniform field. Positive ions formed in the collision are detected by one of two channeltrons (C_{180} or C_0) arranged

0021-9606/89/095201-03$02.10 © 1989 American Institute of Physics

schematically as shown in Fig. 1. The "uniform" field is generated by two plates parallel to the RI beam with holes to pass the K atom beam, and to allow access to the channeltron cones. This arrangement was necessary both to orient the molecules and to collect the K^+ ions. The active channeltron cone was biased at -1200 V while its uniform plate was held at -50 V. The opposing plate and cone were held at $+50$ V, and both channeltron anodes were held at $+800$ V.

The six-pole electric field transmits RI molecules with negative values of $\langle \cos\theta \rangle$, where θ is the average classical angle between the dipole moment and the electric field. Although individual rotational states have been resolved for other molecules in a similar apparatus,[10] our emphasis was to observe reactive scattering which for intensity considerations required the use of neat beams resulting in a distribution of orientations. The distribution [Refs. 1(a) and 8] is broad and is calculated to have the most probable $\langle \cos\theta \rangle \approx -0.15$ but in the uniform field the negative ends of all these molecules point towards the negative field plate. The orientation may be reversed by reversing the polarity of the uniform field. In the following, 0° refers to the field configuration with the positive field plate nearest the K oven (ions counted by C_0), and 180° refers to the negative field plate nearest the K oven (ions counted by C_{180}). For CH_3I the I end is negative and points towards the incoming K atoms in the 180° configuration.

The raw signals, S_0 and S_{180}, are the six-pole (HV) focusing field (on–off) differences in counts, i.e., $[S_0(5\ \text{kV}) - S_0(0\ \text{kV})]$, typically a few cps. These signals are different and suggest that the threshold for electron transfer is lower at the I end (by ≈ 0.5 eV for CF_3I), although signal limitations prevent extrapolation to threshold. Comparison between S_0 and S_{180} is complicated by different channeltron and ion collection efficiencies. To decouple these from orientation effects, the relative detection efficiency, $F(\varepsilon) = (S_{180}/S_0)_{0\,\text{kV}}$, is measured (for each energy) using the small flux of randomly oriented molecules obtained when no voltage is applied to the six-pole field (0 kV). $F(\varepsilon)$ is roughly independent of the molecule (RI and SF_6) used, but because of nonreproducible contact potentials on the field electrodes and multipliers, its measurement was interspersed with measurement of S. The relative signal due to the oriented molecules, S', is the HV on-HV off signal difference corrected for the multiplier efficiencies: $S'_{180} = S_{180}$ and $S'_0 = F \cdot S_0$.

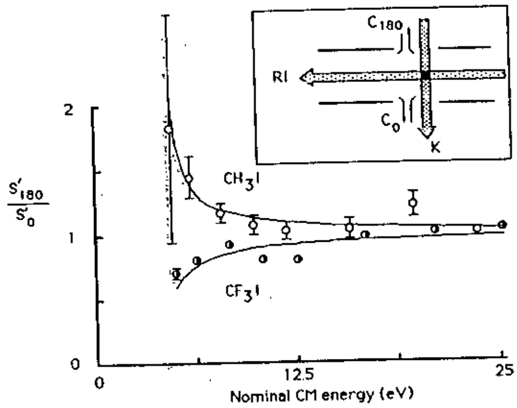

FIG. 1. Inset: uniform field electrodes and channeltron cones. Plot: K^+ signal in 0° orientation relative to that in 180° orientation, $G = S'_{180}/S'_0$, vs nominal cm energy. If there is no effect of orientation, $G = 1$. Curves are line-of-centers plots with energy thresholds: I end $= 3.3$ eV; R end $= 4.0$ eV.

Figure 1 shows the ratio of corrected signals, $G = S'_{180}/S'_0$ for CH_3I and CF_3I vs CM energy (mass factor×lab energy[11]). Both molecules exhibit a pronounced steric effect near threshold. For CH_3I, G is greater than one, showing that production of K^+ is most efficient when K is incident on the *negative* end (I) of CH_3I. For CF_3I impact at the *positive* end is most effective, and this is once again the I end of the molecule.[12] No effect of focusing voltage was observed for SF_6, a spherical top not focused by the six-pole field, showing that the results are due to focused molecules. The curves in Fig. 1 are calculated using a line-of-centers energy dependence of the cross section, $\sigma_i = \sigma_0(1 - E_i/E)$, for each orientation. E_i are the thresholds for the I or R ends and are very roughly determined by fitting the data: $E_R \approx 4.0$ eV, and $E_I \approx 3.3$ eV.

We conclude that the electron jump is not governed solely by the polarity of the molecule, otherwise G would show the same behavior for the two cases. In both cases the negative molecular ion fragments[6] and the major product is the I^- ion, so the electron seems to prefer to jump to the *leaving* group. The electron jump and ion decomposition thus seem to be concerted processes, suggesting that K atom attack at the I end may cause a distortion of the molecule which facilitates its decomposition. The nominal threshold energy for the I end of these molecules (as fitted above) is consistent with the thermodynamic threshold for I^- production ($E_I = \text{IP} + \Delta D - \text{EA}_I = 4.34 + 2.0 - 3.06 = 3.3$ eV).[13,14] This notion parallels the suggestion of Los and coworkers[5(d)] that in collisional ionization of halogens, the halogen bonds stretch during the electron jump, increasing the effective electron affinity of the molecule.

We gratefully acknowledge financial support from NASA and from the Robert A. Welch Foundation. This work is dedicated to the memory of Jim Grannan.

---

[a] Permanent address: Chemistry Department, University of Canterbury, Christchurch, New Zealand.

[b] Permanent address: Chemical Physics Section, Health & Safety Research Division, Oak Ridge National Laboratory, P.O. Box 2008, Oak Ridge, Tennessee 37831.

[1] See the following and references cited therein: (a) H. S. Carman, P. W. Harland, and P. R. Brooks, J. Phys. Chem. 90, 944 (1986); (b) D. H. Parker, K. K. Chakravorty, and R. B. Bernstein, Chem. Phys. Lett. 86, 113 (1982); (c) D. H. Parker, H. Jalink, and S. Stolte, J. Phys. Chem. 91, 5427 (1987); (d) R. B. Bernstein, D. R. Herschbach, and R. D. Levine, *ibid.* 91, 5365 (1987).

[2] P. R. Brooks, Faraday Discuss. Chem. Soc. 55, 299 (1973).

[3] D. R. Herschbach, Adv. Chem. Phys. 10, 319 (1966).

[4] P. R. Brooks, J. McKillop, and H. G. Pippen, Chem. Phys. Lett. 66, 144 (1979).

[5] For reviews of collisional ionization, see (a) A. W. Kleyn, J. Los, and E. A. Gislason, Phys. Rep. 90, 1 (1982); (b) K. Lacmann, in *Potential Ener-*

gy Surfaces, edited by K. P. Lawley (Wiley, New York, 1980), p. 513; (c) A. P. M. Baede, Adv. Chem. Phys. 30, 463 (1975); (d) J. Los and A. W. Kleyn, in *Alkali Halide Vapors*, edited by P. Davidovits and D. L. McFadden (Academic, New York, 1979), p. 279.

[6] (a) R. N. Compton, P. W. Reinhardt, and C. D. Cooper, J. Chem. Phys. **68**, 4360 (1978); (b) S. Y. Tang, B. P. Mathur, E. W. Rothe, and G. P. Reck, *ibid.* **64**, 1270 (1976); (c) P. E. McNamee, K. Lacman, and D. R. Herschbach, Faraday Discuss. Chem. Soc. **55**, 318 (1973); (d) A. W. Kleyn, M. N. Hubers, and J. Los, 10th ICPEAC Abstracts of Papers, Paris, 1977, p. 1162.

[7] R. K. B. Helbing and E. W. Rothe, Rev. Sci. Instrum. 39, 1948 (1968).

[8] H. S. Carman, Ph.D. thesis, Rice University, 1986.

[9] P. R. Brooks, Science **193**, 11 (1976).

[10] S. R. Gandhi, Q.-X. Xu, T. J. Curtiss, and R. B. Bernstein, J. Phys. Chem. **91**, 5437 (1987), and references cited therein.

[11] The *nominal* lab energy was given by the voltage in the source.

[12] S. R. Gandhi and R. B. Bernstein, J. Chem. Phys. **88**, 1472 (1988).

[13] S. W. Benson, J. Chem. Ed. **42**, 502 (1965).

[14] H. Hotop and W. C. Lineberger, J. Phys. Chem. Ref. Data Ser. **4**, 539 (1975).

Electron transfer to oriented molecules: $K+CF_3I$ and $K+CH_3I$

Peter W. Harland,[a] Howard S. Carman, Jr.,[b] Leon F. Phillips,[a]
and Philip R. Brooks
Department of Chemistry and Rice Quantum Institute, Rice University, Houston, Texas 77251

(Received 23 January 1990; accepted 10 April 1990)

K^+ ions have been detected from the intersection of a beam of K atoms (5–30 eV) with beams of CH_3I and CF_3I molecules which had been oriented prior to the collision. Collisional ionization is found to be favored for both molecules when the fast K is incident at the I end of the molecule, even though the electrical polarity of the I end is different for the two molecules. For both molecules, the effect of molecular orientation is most pronounced near threshold (≈ 5 eV) and almost disappears at higher (30 eV) energies. For CF_3I, the threshold for impact at the I end is ≈ 0.7 eV less than the threshold for impact at the CF_3 end. We interpret these results using a "harpoon" mechanism in which the electron jump during the initial approach is probably *independent* of orientation, but as the charged particles separate, the electron may jump *back* to the K^+. For impact at the I or "head" end, the I^- is ejected backwards towards the incoming K^+. This increases the final relative velocity of the ions and lowers the probability of neutralization. The ion signal is greater and the electron thus *appears* to favor the I end of the molecule.

INTRODUCTION

Proper orientation of reagents during collision has been considered crucial to chemical reaction and energy transfer. Just what constitutes "proper" orientation has largely been a matter of speculation (called "chemical intuition") because experiments usually include all possible orientations of the reagents, but in the isolated environment of a molecular beam, it has been possible to produce beams of molecules which are oriented in space[1] and several different chemical reactions of the type $M + CR_3X$ (where M is an alkali or alkaline earth, R is a radical, and X a halogen) have now been studied using oriented molecule reagents.[2] In almost all cases, large differences in reactivity have been observed for impact at the different "ends" of a dipolar molecule.

We have been especially fascinated with the reaction of K with oriented CF_3I. KI is formed with about equal probability for impact at either end of the molecule,[3] but impact on the I (or "heads") end yields KI scattered backward in the center-of-mass (c.m.) system and impact on the "tails" end (CF_3) yields KI scattered forwards in the c.m. system. This is in sharp contrast to the behavior observed[4] for CH_3I, where the KI rebounds backwards in the c.m. regardless of the orientation, although heads attack does produce the most KI.

The observations for CF_3I have been rationalized in terms of the harpoon or curve crossing model. We proposed that the electropositive K atom would donate an electron to the electronegative CF_3I at long range (≈ 5 Å) relatively independent of orientation. The CF_3I^- was expected to be formed in a repulsive state or high on the repulsive wall of a bound state. In either case, the molecular ion was expected to immediately dissociate, ejecting the fragments along the initial direction of the C–I axis. The K^+ ion would follow along with the ejected I^- ion and would thus produce KI scattered forwards when I was pointing forwards (the "tails" orientation) and produce KI scattered backwards when I was pointing backwards (the heads orientation). This model predicted that if the molecule were oriented sideways with respect to the incoming K atom that the angular distribution would be completely changed and this was confirmed by experiment.[5]

This explanation is less successful in interpreting the behavior observed for other molecules. For CH_3I and *t*-butyl I, only rebound scattering is observed for either orientation, although the heads end is more reactive. For CF_3Br, the experimental results show[1(a)] that once again tails attack yields KBr scattered in the forward direction and heads attack yields KBr rebounding in the backward direction. In this case, however, the tails orientation is less reactive than heads and we postulated that electron transfer might depend on the orientation of the molecule (or alternatively, the decomposition of the molecular ion might be inhibited if the CF_3 were between K^+ and I^-, i.e., the tails configuration.).

Electron transfer is the first step in the harpoon mechanism[6] as well as being a fundamental chemical process itself. In order to understand how molecular orientation might affect electron transfer, we have investigated[7] collisions of oriented CF_3I and CH_3I with K atoms which are fast enough to enable the ions to separate. These reactions had been studied previously[8] without orientation of the molecule and the dominant processes found to be

$$K + CF_3I \rightarrow K^+ + I^- + CF_3, \qquad (1)$$

$$K + CH_3I \rightarrow K^+ + I^- + CH_3. \qquad (2)$$

In the experiments reported here, K^+ ions were observed as a function of initial energy and initial orientation. We find the greatest K^+ signals arise when K is incident on the I end of either molecule, although our initial expectation

---

[a] Permanent address: Chemistry Department, University of Canterbury, Christchurch, New Zealand.

[b] Permanent address: Chemical Physics Section, Health & Safety Research Division, Oak Ridge National Laboratory, P.O. Box 2008, Oak Ridge, Tenn. 37831.

J. Chem. Phys. 93 (2), 15 July 1990 0021-9606/90/141089-09$03.00

© 1990 American Institute of Physics

was that the electron would be transferred to the positive end of the dipole, which is the CH_3 end in CH_3I. We interpret this behavior as follows: The electron is apparently transferred regardless of orientation as the reagents approach. The negative molecular ion dissociates impulsively and the resulting I^- fragment is ejected along the direction of the C–I axis. In the heads orientation, I^- is ejected in the backward hemisphere, increasing the relative velocity between K^+ and I^-, and there is little propensity for K^+ to be neutralized. In the tails orientation, I^- is ejected roughly in the same direction as K^+ is traveling, the relative velocity is smaller, the electron is more likely to hop back to neutralize the ion pair, and therefore fewer ions are observed in this orientation.

EXPERIMENTAL

A beam of fast K atoms ($\approx$5–25 eV Lab) was crossed with a beam of CH_3I or CF_3I molecules which had been oriented in the laboratory. Positive ions (K^+) resulting from the collision were observed for orientations in which K approached the I end (heads) or the alkyl end (tails). The molecular beam apparatus is schematically shown in Fig. 1 and is a modification of that described earlier.[1(a)] The details of construction are described in Carman's thesis.[9]

Oriented molecule beam

A beam of RX is generated by supersonic expansion from nozzle N, defined by the skimmer, and passed through a differentially pumped buffer chamber where it is modulated by a 45 Hz chopper. The beam then passes into a third differentially pumped chamber containing the electric fields necessary to provide state selection and orientation.

Symmetric top molecules such as CH_3I rotate in an electric field like a child's top in a gravitational field. The symmetry axis precesses about an applied field and the dipole moment does not average to zero. (In contrast, most diatomic molecules rotate like a baton in a plane perpendicular to the angular momentum vector. The dipole moment points in all directions in the course of this rotation and averages to zero.[10] The rotating diatomic molecule thus appears to have zero dipole moment in a space-fixed axis system.) In the collision-free environment of the molecular beam, each symmetric top molecule is therefore oriented with respect to a weak applied field, but all orientations are present, giving a sample with no net orientation. To produce an oriented sample, it is only necessary to remove the orientations that are not wanted, and this is accomplished by passing the beam through an inhomogeneous electric field in which the deflection of a molecule depends upon its orientation with respect to the local electric field direction.

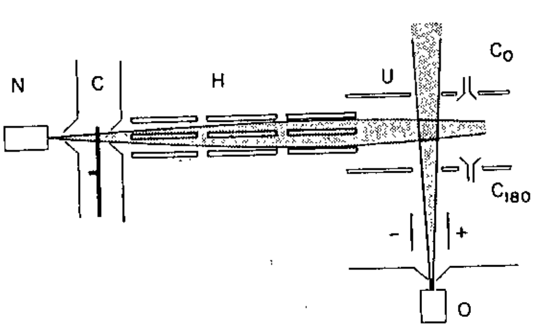

FIG. 1. A schematic diagram of apparatus. N = RX nozzle source, C = beam chopper, H = hexapole electric field array, U = uniform electric field, O = hyperthermal K atom source oven, C_0 and C_{180} channeltrons.

The energy of interaction $W = -\boldsymbol{\mu}\cdot\mathbf{E}$ of a symmetric top molecule with an applied field is given by the first order Stark effect[11] $W = -\mu_0 E MK/J(J+1) = -\mu_0 E\langle\cos\theta\rangle$, where μ_0 is the dipole moment and J,K, and M are, respectively, quantum numbers for the total angular momentum, the component along the top axis, and the component along the field. Classically, $\langle\cos\theta\rangle$ is the average angle between the symmetry axis and the electric field. In an inhomogeneous field, a molecule will experience a force $\mathbf{F} = -\nabla W$ such that each molecule will move to minimize its energy and molecules with negative $\langle\cos\theta\rangle$ are separated from those with positive $\langle\cos\theta\rangle$. *Any* inhomogeneous field will suffice in principle, but it is useful experimentally to use a hexapole field because molecules with negative $\langle\cos\theta\rangle$ are focused by the field.[12]

The high voltage state-selecting field is 137 cm long, constructed of three 45.7 cm long sections, each section consisting of six 6.4 mm stainless steel rods held in plexiglass insulators. The rods are located on a 15.9 mm diam. circle and are equally spaced and alternately charged to $\pm V$, typically $\approx$5 kV. Polar molecules entering the inhomogeneous electric field are subject to a radial force $F_r = -\partial W/\partial r$. A symmetric top molecule thus experiences a radially inward or outward force depending on the *sign* of $M\cdot K$ (or $\langle\cos\theta\rangle$) and the hexapole field serves as a state-selecting filter, rejecting molecules in states with positive values of $\langle\cos\theta\rangle$, and passing molecules in states with negative values of $\langle\cos\theta\rangle$. These molecules are oriented with respect to the local, nonuniform electric field inside the hexapole field. Laboratory orientation is obtained by allowing the molecules to fly into a region in which the electric field direction, and consequently the axis of orientation, is uniform. This is discussed in greater detail below.

Molecules are actually focused by the hexapole field and, if only a few J,K,M states are populated, it is possible to select individual J,K,M states.[13] This degree of refinement was not possible in the experiments reported here. In order to obtain reactive scattering signals, it was necessary to maximize the intensity of the oriented molecules by using neat rather than seeded supersonic expansions and by eliminating all apertures in the hexapole field. Thus, many rotational states are populated ($T\approx$45 K) and the hexapole acts mainly in a "filter" mode, passing molecules in states with negative values of $\langle\cos\theta\rangle$. The current level of experimental sophistication does not require determination of the distribution of $\langle\cos\theta\rangle$, but an approximate distribution can be calculated by averaging the field transmission over the incident thermal distribution[4(b),12(c)] and this is shown in Fig. 2.

Fast K atoms

Beams of fast potassium atoms are generated by charge exchange[14] of K^+ inside oven O. Atoms are surface ionized

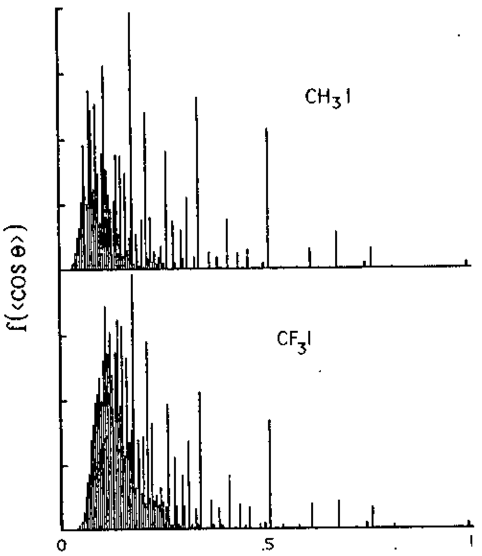

FIG. 2. Calculated distribution of average orientations $\langle \cos\theta \rangle = MK/J(J+1)$ transmitted by the hexapole field at 5 kV.

on a hot W filament located inside the oven and the resulting K^+ ions are accelerated to a grid ≈ 1 mm away. Neutral K atoms with the same energy as the ions are produced by resonant charge exchange as the K^+ drifts through the low pressure (≈ 0.01 Torr) potassium gas in the same oven. The beam which results contains thermal K, fast K, and K^+ ions. The residual ions are swept out of the beam by a deflecting field of ≈ 20 V/cm. Although the neutral atomic beam contains a small fraction of thermal energy atoms, their energy is far below threshold for ionization, and since they produce no ions, they do not interfere with the experiments described here.

The beam intensity is monitored by surface ionization on a cool W filament (0.13 mm × 6 mm) located 0.7 m from the source. Ions from the wire are passed through a grid with a small (≈ 1 V) bias which discriminates against any ions resulting from surface ionization of thermal atoms. The resulting ions are then counted by a crossed-field multiplier. Typical beam intensities are extremely low at energies of a few eV, as shown in Fig. 3. Rough measurements of the energy distribution of this beam suggested that [full width at half-ΔE(FWHM)]/E was $\approx 10\%$. The accelerating voltage in the source was used as the nominal laboratory energy.

Beam intersection and ion collection

The beams intersect about 10 cm from the K oven inside a region of uniform field U generated by two plates parallel to the RI beam ≈ 5 cm apart. The *direction* of the local field determines the *direction* of the molecular axis, and to provide uniform laboratory orientation, a weak (≈ 20 V/cm) field is applied by the uniform field plates U. The laboratory

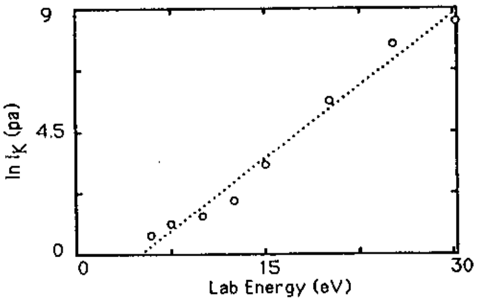

FIG. 3. The intensity of the fast K atom beam (pA) plotted vs lab energy. The dotted line is for illustration.

orientation of the molecules can be reversed by reversing the polarity of this uniform field.[15] Holes are cut in the plates to pass the K atom beam and to allow viewing of the intersection by two channeltron cones.

K^+ ions formed in the collision are detected by one or the other of the two channeltrons(C_{180} or C_0) arranged schematically as shown in Fig. 1. The voltage applied depended upon the orientation studied. The active channeltron was the one that peeked through whichever uniform plate was negatively biased. The active cone was biased at -1200 V, while its uniform plate was held at -50 V. The opposing plate and cone were held at $+50$ V and both channeltron anodes were held at $+800$ V. This arrangement was used to satisfy simultaneously two conditions: (1) in order for the molecules to be oriented, they must be located in a region where the electric field direction is reasonably uniform and well defined; and (2) in order for the ions to be detected, the nascent positive ions need to reach a channeltron. For these operating conditions, the field at the intersection region is roughly determined by the parallel plates because it was observed that the channeltron counts decreased if the plates were biased much above 50 V, indicating that at higher voltages the ions would be collected only by the plates and not the channeltrons. Ions are less efficiently detected by channeltron C_{180}, apparently because the K^+ ions formed in the collision zone are initially moving away from C_{180}.

The orientation of the molecules may be reversed by reversing the polarity of the uniform field. The polarities used, together with the active channeltrons, are shown in Fig. 4. 0° refers to the field configuration with the positive field plate nearest the K oven (ions counted by C_0), and 180° refers to the negative field plate nearest the K oven (ions counted by C_{180}). For CH_3I, the I end is negative and points towards the incoming K atoms in the 180° configuration. For CF_3I, the I end is positive[16] and points towards the incoming K atoms in the 0° orientation.

Data acquisition

The active channeltron is capacitively coupled to a quad scaler which counts signal pulses and pulses from a 2^{18} Hz clock. Two channels of the quad scaler record signal and clock counts continuously and the other two count only when the oriented beam is on. The scalers are enabled by a

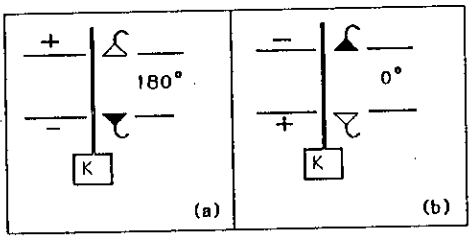

FIG. 4. A schematic view of uniform field polarities. The active channeltron is shown darkened; in the 180° arrangement, the channeltron nearest the K oven is active and the negative end of the molecule is nearest the K oven.

trigger signal from the beam modulator, which is delayed several ms to account for the time the molecules require to traverse the 1.4 m hexapole. Beam-on signals $S(V)_{\mathrm{on}}$ are thus measured directly and beam-off signals $S(V)_{\mathrm{off}}$ are calculated using the clock counts to account for the fraction of pulses acquired with the beam off. The signal difference for channeltron $i(i = 0 \text{ or } 180)$, $S(V)_i = [S(V)_{\mathrm{on}} - S(V)_{\mathrm{off}}]_i$ is the signal due to ionizing collisions of oriented molecules at hexapole voltage V as measured on channeltron i.

The raw signals $S(V)_0$ and $S(V)_{180}$ are measured with *different* channeltrons with different multiplication efficiencies and different ion collection efficiencies. To decouple these from orientation effects, the *relative* detection efficiency $F(\epsilon) = S(0)_{180}/S(0)_0$, is measured for each energy using the small flux of randomly oriented molecules obtained when no voltage is applied to the six-pole field (0 kV). As shown in Fig. 5, $F(\epsilon)$ is roughly the same for CF_3I, CH_3I, and SF_6. Because of nonreproducible contact potentials on the field electrodes and multipliers, measurements of $F(\epsilon)$ were interspersed with measurements of S. The *relative* signal due to the oriented molecules $S'(V)$ is the (HVon)-(HV off) signal difference corrected for the multiplier efficiencies at beam energy ϵ: $S'(V)_{180} = S(V)_{180}$ and $S'(V)_0 = F \cdot S(V)_0$.

RESULTS

Relative signals for CH_3I and CF_3I are shown in Fig. 6. There is a clear difference between S'_0 and S'_{180}. For CH_3I, the 180° orientation is more reactive, but for CF_3I, the opposite is true. We conclude that the difference in relative signals arises from a real molecular effect and not from any electrical switching artifacts because the experimental configuration corresponding to maximum signal corresponds to different polarities of the uniform field (and therefore different channeltrons). Since the two molecules have different polarity (the I end is negative in CH_3I and positive in CF_3I), the data displayed in Fig. 6 show that *ionization is more likely for impact at the I end of both molecules*. The data suggest that there are different thresholds for the two orientations and linear extrapolation of the low energy signals give I end thresholds ≈ 0.2 eV lower for CH_3I and ≈ 0.7 eV lower for CF_3I. These threshold differences must be regarded as very tentative because, as shown in Fig. 3, the flux of K atoms (and the signal-to-noise ratio) is extremely low near threshold.

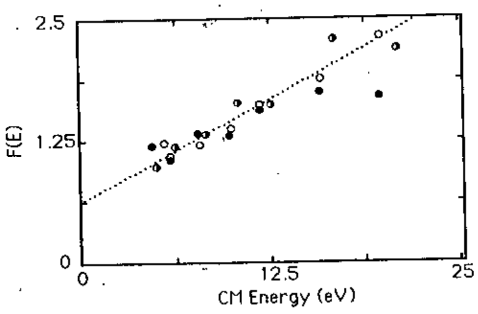

FIG. 5. Relative channeltron detection efficiency $F(\epsilon)$ vs c.m. collision energy for SF_6 (open circles), CH_3I (closed circles), and CF_3I (half-filled circles). The dashed line is drawn through SF_6 data for purposes of illustration.

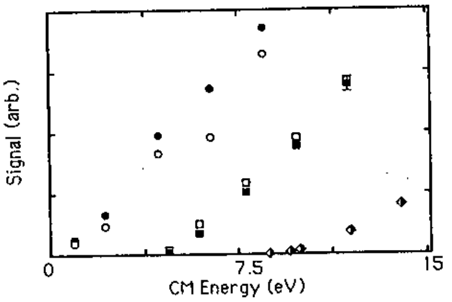

FIG. 6. Signal counts vs c.m. collision energy for CH_3I (squares: open = 180°, closed = 0°). For CF_3I (circles: open = 180°, closed = 0°), the data are displaced 4 eV to lower energy and for SF_6 (diamonds, both electrical configurations give identical orientations), the data are displaced 4 eV to higher energy. Most error bars are smaller than the symbols.

The relative dependence of the cross sections on orientation and energy is shown in Fig. 7. The difference in molecular orientation is still apparent. The cross section for SF_6 was measured to provide an experimental consistency check. SF_6 is a spherical top with no dipole moment and is unaffected by the hexapole field. A low flux of SF_6 molecules passes through the hexapole field at zero voltage, (because there are no beam stops) and we are able to see ions from this tiny flux of SF_6. These molecules are *not* oriented and the ion signals are unaffected by the hexapole voltages, showing that any stray electric fields from the hexapole have no effect on the detection of the ions formed in the collision center. The data reduction procedure insures that $S'_0 = S'_{180}$ for SF_6 at 0 kV and, since the hexapole voltage has no effect on the SF_6 signal, $S'_0 = S'_{180}$ at other voltages as well. We are presently unable to determine if the orientation affects the energy at which the cross section is a maximum.

The effect of molecular orientation is quite large, but is masked by the energy dependence of the cross section. In order to emphasize the salient features of the orientation, we plot the normalized signal difference $G \equiv [S'_{180} - S'_0]/[S'_{180} + S'_0]$ in Fig. 8. Here the difference in polarity between CH_3I and CF_3I is readily apparent.

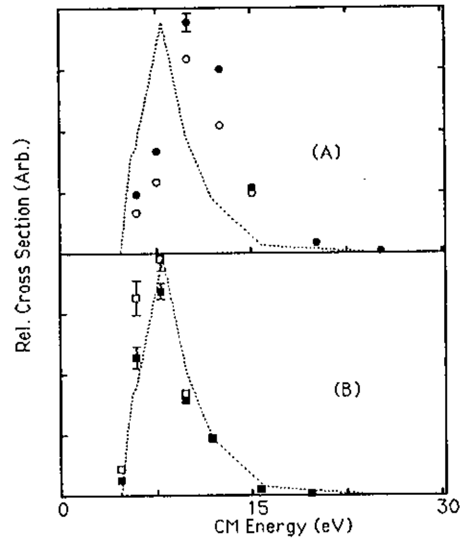

FIG. 7. Relative cross sections (signal counts/K intensity) for (A) CF_3I and (B) CH_3I in the 180° and 0° orientations. Open symbols denote 180° orientation, closed symbols denote 0° orientations. The dashed lines are drawn through data for SF_6 and that data is normalized to the same peak height as that for the comparison gas. Rough measurements indicate the cross sections are in the order $SF_6 > CF_3I > CH_3I$. Most error bars are smaller than the symbols.

$|G|$ is largest near threshold and is almost negligible at energies greater than about 15 eV. Note that since G must lie in the range $-1 < G \leq +1$, orientation makes quite a large difference near threshold (especially given the expected distribution shown in Fig. 2).

DISCUSSION

Our initial expectation was that the electron would jump to the positive end of the molecule, but we observe that the electron appears to prefer the *negative* end of the CH_3I molecule. We also thought that orientation might be more important at higher energies because there would be less time during the collision for the molecule to twist into a favorable configuration. However, we observe just the opposite: at high energies the orientation seems almost irrelevant.

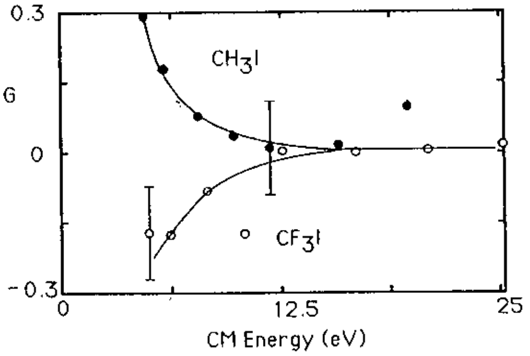

FIG. 8. $G \equiv [S'_{180} - S'_0]/[S'_{180} + S'_0]$ plotted vs c.m.energy in eV. $G > 1$ for CH_3I indicates that the greater signal comes when K is incident on the negative or the I end of the molecule. For CF_3I, $G < 1$ indicates that the positive or I end gives the greater signal. Error bars shown are typical of all points.

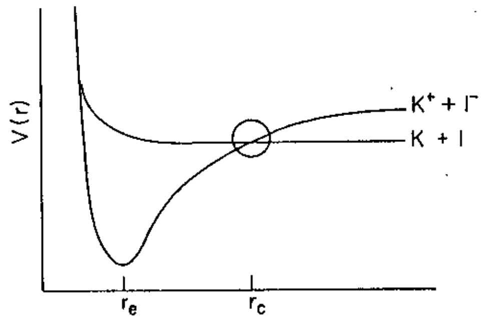

FIG. 9. Schematic ionic and covalent potential energy curves for K colliding with I. A complete collision is represented by a trajectory which will traverse the crossing twice, once on the way in and once on the way out. The curve crossing is shown enlarged in Fig. 10.

We should emphasize that these experiments do not determine which end of the molecule initially receives the electron, because the electron could be transferred back to K^+. The experiments do tell us in which orientation the molecular moiety is most likely to accept *and keep* the electron.

Electron transfer results from the crossing of a covalent and ionic potential energy surface.[17] Figure 9 shows schematic potential curves for the *atomic* system $K + I \rightarrow K^+ + I^-$. At internuclear distances near the bond distance in the stable KI molecule r_e, the system is highly polar, K^+I^-, and bonding is largely described by the ionic potential. At large distances, the molecule is best described by the covalent potential because the molecule dissociates to give neutral atoms. At r_c, these zeroth order (diabatic) ionic and covalent curves appear to cross, representing a breakdown in the Born–Oppenheimer approximation. The adiabatic curves resulting from ionic covalent coupling do not cross, as shown in Fig. 10, and the character of the system

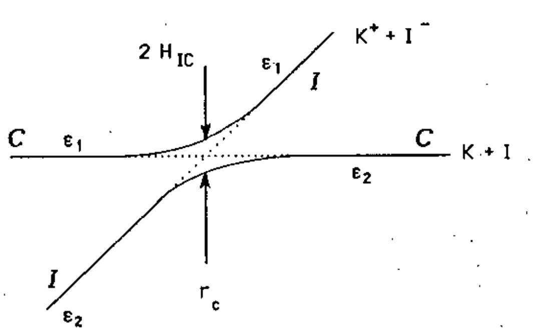

FIG. 10. An enlarged view of the avoided crossing between the ionic (I) and covalent (C) curves for K + I. The adiabatic curves are shown as solid lines which change smoothly from "covalent" to "ionic"; the diabatic curves are denoted by dotted lines.

can change smoothly from covalent at long range to ionic at short range.

The behavior of a colliding system at the avoided crossing depends on the speed at which the crossing is traversed, as well as the separation and slopes of the adiabatic curves. Figure 10 shows an enlarged view of the avoided crossing. If the atoms approach slowly enough on the covalent curve, the uncertainty principle allows the energy to be well defined and the system stays on the lowest, adiabatic curve. The adiabatic process results in what we loosely call an electron "jump." On the other hand, if the atoms approach at high speed and traverse the crossing quickly, the energy will be less well defined and it is possible that the system will make a nonadiabatic, or diabatic crossing and will continue to be described by the covalent potential. (The diabatic crossing represents a "hop" from one potential curve to the other, but the electron stays on the K atom and does not jump.)

The probability of a diabatic hop P_d is given to good approximation by the Landau–Zener relation[18]

$$P_d \approx e^{-\kappa/v}, \tag{3}$$

where $\kappa = (2\pi H_{1C})^2/h\Delta S$, $\Delta S = |\partial E_I/\partial r - \partial E_C/\partial r|$, v is the speed, and H_{IC} is the matrix element in the Hamiltonian that couples the two states.

For the simplest crossing of an ionic curve with a covalent curve, the slope of the covalent potential can be regarded as zero with zero energy compared to the separated atoms. The crossing radius is given approximately by $r_c = e^2/\Delta E_0$, where $\Delta E_0 =$ ionization potential (IP)-electron affinity (EA), the difference between the ionization potential of the donor (K) and the electron affinity of the acceptor (I). $\Delta S = (e/r_c)^2$ and κ becomes

$$\kappa = (4\pi^2 e^2/h)[H_{IC}(r_c)/\Delta E_0]^2. \tag{4}$$

Thus low speeds or large separation between the curves (H_{IC}) gives a small probability of a diabatic hop between potential curves. Without such a hop, the system passes adiabatically through the crossing, smoothly changing from a covalent to an ionic description.

The coupling matrix element depends exponentially on r_c and is given semiempirically[17] by

$$H^*_{IC} = c_1 r^*_c \exp(-c_2 r^*_c), \tag{5}$$

where $H^*_{IC} = H_{IC}/\sqrt{I \cdot EA}$, $r^*_c = r_c(\sqrt{I} + \sqrt{EA})/\sqrt{2}$ and $c_1 = 1, c_2 = 0.86$. [For molecules $r^*_c = r_c\sqrt{2I}, c_1 = 1.73$, and $c_2 = 0.875$, where all quantities are in atomic units.]

The complete collision process requires the crossing to be traversed twice, once on the way in and once on the way out. In order to produce ions starting with neutrals, the atomic system must traverse one crossing adiabatically and the other diabatically. For the *atomic* system shown in Fig. 9, the two crossings are identical and the overall probability of ionization is $P = (1 - P_{nd})P_{nd}$, but for atom–*molecule* collisions, the internal state of the molecule can change between the crossings. Indeed, if the electron jumps at the first crossing, complete dissociation of the molecular ion may occur between the crossings, leaving only the atomic ions to undergo a diatomic crossing. This is shown very schematically in Fig. 11. Note that the atom–molecule system is multidimensional and "r" is not the same for the reagents and the products.

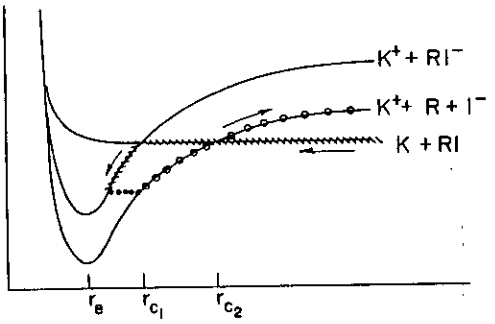

FIG. 11. A very schematic one-dimensional illustration of electron jump in a molecular system. The crossing between the neutral reagents and molecular ions occurs at r_{c_1} and an adiabatic transition (represented by the picket fence trajectory) could lead to a distortion of the molecule ion (heavy dots) yielding a different crossing between the distorted molecule ion and the neutral products (open dots). As illustrated here, the molecule could dissociate and "r" represents distances in different dimensions for the reagents and the products.

Both CH_3I and CF_3I undergo dissociative electron attachment[18] and in collisional ionization give I^- ions in $\approx 98\%$ yield.[8] The scenario suggested above (the electron jumps at the first crossing and the molecular ion dissociates before the second crossing is encountered) is thus very likely to occur. Consider the first electron jump. Using electron affinities and ionization potentials, we can calculate the first crossing distance $r_{c_1} = e^2/\Delta E_0$ and the semiempirical results of Eq. (5) allow an estimate of H_{IC}. The IP, EA, and resulting estimates for the crossing distances and matrix elements are given in Table I.

At the nominal collision speeds used in these experiments, $v_r \approx 5.6$ km/s (56 Å/ps) for CH_3I at 5 eV, the Landau–Zener relation, Eq. (3) predicts that the first crossing will be completely adiabatic and the electron will jump to the molecule. The electron is expected to occupy an antibonding C–I σ^* orbital and the molecular ions produced CF_3I^- and CH_3I^- are expected to dissociate within a vibrational period.

If the molecule were to remain intact upon the addition of the electron, the second crossing could be equivalent to the first and would be traversed completely adiabatically. The electron would be smoothly transferred back to K^+, the products would separate on the covalent surface, and *no* ions

TABLE I. First crossing radii and H_{IC} values.

Atom	IP(eV)[a]	Molecule	EA(eV)[a]	r_{c_1}(Å)	H_{IC}(meV)
K	4.349	CH_3I	0.35	3.6	280
K		CF_3I	0.91	4.2	308
K		I	3.06	11.3	3

[a] *Handbook of Chemistry & Physics*, 66th ed., edited by R. C. Weast (Chemical Rubber, Boca Raton, 1985).

would be produced. If, on the other hand, the molecule ion decomposes explosively, the second curve crossing would be an asymptotic crossing between the emerging I^- ion and the incident K^+. The LZ relation then predicts that the second crossing would be completely diabatic, i.e., that the electron would stay on the I^- ion and the products would separate on the ionic surface. In this latter limiting case, every collision would lead to ionization and the orientation would not be important.

The behavior observed is clearly intermediate between these two limits. Because there is an orientation effect, every collision does not lead to ionization. From the data of Table I, we expect the electron to be transferred adiabatically at the first crossing, but at the second crossing, the K^+ ion must be encountering something intermediate between a bound CF_3I^- molecule and a free I^- atom. It must encounter a species in the act of breaking apart and we can use the experimental orientation data to extract some information about this species.

We assume since the first crossing is completely adiabatic, that the probability of the K escaping as K^+ is the probability that the second curve crossing is traversed diabatically $P_d \approx e^{-\kappa/v}$. We note that this is sensitive to the *relative speed* of the crossing. The orientation of the dissociating ion will influence the relative speed as shown in Fig. 12.

The electron probably enters an antibonding σ^* orbital centered on the C–I bond and the molecule ion fragments in a time comparable to a vibrational period. Since the C–I bond does not have time to rotate, I^- will be ejected in the instantaneous direction of the C–I axis. In the heads orientation, the I^- ion will be ejected *towards* the incoming K^+, increasing the relative speed between the ions, whereas in the tails orientation, I^- will be ejected in the same direction as K^+, decreasing the relative speed between the ions, and making neutralization more likely in the latter case than in the former. As the incident K velocity increases, the velocity imparted to the I^- ion will play a smaller role and the effect of initial orientation will become less important at higher energies, as is observed.

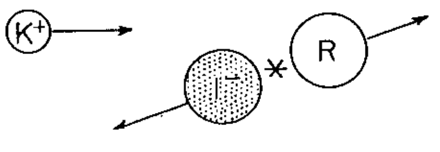

a) Heads

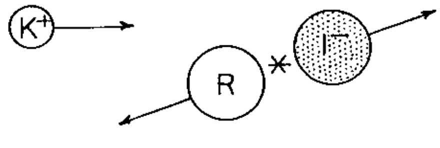

b) Tails

FIG. 12. (a) Velocity relationship between K^+ incident on the heads end of the RI molecule. I^- is ejected backwards in the c.m. system. Relative speed between ions is greater, reducing chances of electron returning to K^+, resulting in a greater chance of making ions. (b) The velocity relationship between K^+ incident on the tails end of the RI molecule. I^- is ejected forwards in the c.m. system. Relative speed between ions is less, increasing changes of neutralizing the charges.

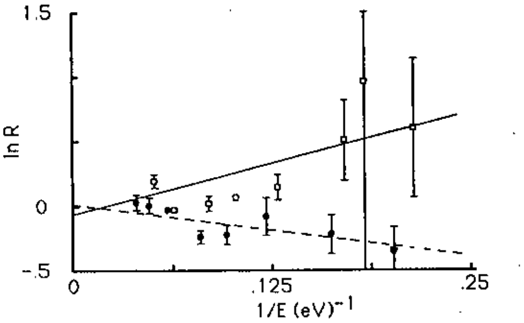

FIG. 13. The plot of ln R vs $1/E$ for CH_3I (squares) and CF_3I (circles). $R \equiv S'_{180}/S'_0$ and is P_H/P_T for CH_3I and P_T/P_H for CF_3I. Lines are least-squares fits to experimental points and are forced through zero.

Thus, assuming that κ in Eq. (4) is the same in both orientations, the probability of traversing the second crossing diabatically in the heads orientation is given by $P_H = \exp(-\kappa/V_H)$, that in the tails orientation by $P_T = \exp(-\kappa/V_T)$, and the ratio

$$R = P_H/P_T = \exp(-\kappa\Delta v/v^2). \qquad (6)$$

Here V_H is the relative velocity between K^+ and I^- in the heads orientation (I^- is assumed for simplicity to be ejected backwards along the K^+ velocity), V_T the relative velocity in the tails orientation (I^- ejected forwards), $\Delta v = V_T - V_H$, and $v^2 = V_H V_T \approx \sqrt{2E/\mu}$, where E is the initial collision energy and μ the initial reduced mass. Thus, a plot of ln R vs $1/E$ is expected to be linear with a slope of $\kappa\Delta v$ and such a plot is shown in Fig. 13.

Within experimental accuracy, the data are reasonably fit by a straight line, suggesting that the mechanism shown in Fig. 12 is reasonable. As the product ions recede, there is thus a curve crossing where there is a difference in the nonadiabatic transition probability depending on the direction in which I^- is ejected. The nature of this crossing is indicative of the species involved, the negative ion being a species intermediate between the molecular ion CF_3I^- (CH_3I^-) and the bare atomic ion I^-.

We can now use the experimental data obtained here to

TABLE II. Parameters for "second" curve crossing.

Molecule	$\kappa\Delta v(km/s)^2$	$\Delta v(km/s)$	$(H_{1C}/\Delta E_0)$	r_{c_2} (Å)
CH_3I	20	0.62[a]	0.045	4.6
CF_3I	−10	1.3[a]	0.023	7.1

[a] C. W. Walter, B. G. Lindsay, K. A. Smith, and F. B. Dunning, Chem. Phys. Lett. **154**, 409 (1989).

learn something about this intermediate species. The slopes of the curves of Fig. 13 give $\kappa\Delta v$. The energy released in the dissociation of CH_3I^- and CF_3I^- has been determined[19] following attachment of essentially free electrons from K atoms in high Rudberg states, so Δv and then κ can be separately evaluated. From Eq. (4), an experimental value $H_{1C}/\Delta E_0$, can be extracted.

Because the negative ion species is not well known, ΔE_0 is not known and is taken to be e^2/r_{c_2}, where r_{c_2} is the radius of the second crossing. An experimental value of $H_{1C}r_{c_2}$ is thus obtained and, together with the semiempirical relation given in Eq. (5), an approximate value of r_{c_2} is obtained. These values are listed in Table II.

Comparison of Tables I and II shows that for CH_3I the first and second crossing radii are essentially the same, whereas for CF_3I, the second crossing occurs at a much larger distance than the first. These crossing radii are calculated based on a highly simplified one-dimensional model. The real system is, of course, multidimensional and while caution should be exercised in pursuing in depth the properties of the reacting system, some insight may result from elaboration of this one-dimensional model. The distance the K^+ travels during the collision is $z \approx r_{c_2} - r_{c_1} \approx 1$ Å for CH_3I and ≈ 2.9 Å for CF_3I. At 56 Å/ps, K^+ requires ≈ 50 fs between crossings for CF_3I, but only ≈ 20 fs in CH_3I. In this time, assuming a nominal repulsive force ≈ 5 eV/Å, the C–I distance would increase by ≈ 1.3 Å in CF_3I, but by only ≈ 0.7 Å in CH_3I. As anticipated, CF_3I^- is a moiety clearly in the act of disintegration, whereas CH_3I^- is less disturbed.

The mechanism deduced here and sketched in Fig. 12 also nicely accounts for the angular distribution of KI found in the *thermal* energy experiments with CF_3I.[1(a),3,5] There the incoming K^+ was much slower than in these experiments and the momentum of I^- as the molecule–ion dissociates largely determines the direction in which the neutral product emerges.

In the thermal experiments on CH_3I, on the other hand, the angular distribution (but not the yield) of KI was roughly independent of the initial orientation. This is consistent with our finding that the first and second curve crossings in CH_3I are essentially the same. In CH_3I, the dissociation of the molecule ion apparently cannot be viewed as an independent process, because K^+ is too close, but in CF_3I, the crossings are at larger separations and the electron jump–negative ion dissociation mechanism is a much better description, as exemplified by the completely different heads and tails angular distributions observed in the thermal energy CF_3I experiments.

Independent support for the conclusions exemplified in Fig. 12 is provided by the beam-gas experiments of Kalamarides, *et al.*[20] in which the angular distribution of I^- ions formed in the reaction

$$K^{**} + CF_3I \rightarrow K^+ + I^- + CF_3$$

was measured, where K^{**} denotes a K atom in a high Rydberg state. In these experiments, a beam of K^{**} was passed through a scattering gas containing low pressure CF_3I and the angular distribution of the resulting I^- ions was measured with a microchannel plate and position sensitive detector.

For large principal quantum numbers $n \approx 26$, the Rydberg electron is essentially free of the core and behaves as a free electron. Since CF_3I was a gas, all orientations of the molecule were equally likely and CF_3I^- ions were expected to be formed in all orientations by attachment of the "free" electron. Dissociation of CF_3I^- should eject I^- along the randomly oriented molecular axes and the I^- ions were expected to be distributed isotropically, which was confirmed by experiment. But as n decreased to 9, the angular distribution became anisotropic, with fewer I^- moving in the direction of the initial K^{**}. These atoms are more similar to those of this study ($n = 4$). The Rydberg electron in this case is not free, but carries with it the positively charged core. Kalamarides, *et al.* thus concluded that fewer I^- ions were observed in the forward direction because if I^- were ejected in the forward direction [see Fig. 12.(b)], I^- and the positive core would more likely interact to form neutral products and the ion signal would decrease.

CONCLUSIONS

CH_3I and CF_3I are collisionally ionized by fast (a few eV) K atoms. We have measured the K^+ ion signal for K atoms incident on these molecules oriented in either the heads or tails orientations and find that in both molecules the maximum signal occurs when K is incident on the I end of the molecule. The effect of orientation disappears at collision energies above about 15 eV. We interpret these findings as an exit channel interaction. The intermediate negative molecular ion decomposes and ejects the I^- either parallel or antiparallel to the incident K^+. If K^+ and I^- are moving parallel (which occurs in the tails orientation), there is an enhanced probability of neutralization, so fewer ions are observed. The orientation effect allows us to estimate the distance at which the ionic and covalent surfaces cross in the exit channel; this is found to be ≈ 4 Å for CH_3I and ≈ 7 Å for CF_3I.

ACKNOWLEDGMENTS

We gratefully acknowledge financial support from the Robert A. Welch Foundation and the National Science Foundation.

[1] See the following and references cited therein: (a) H. S. Carman, P. W. Harland, and P. R. Brooks, J. Phys. Chem. 90, 944 (1986); (b) D. H. Parker, K. K. Chakravorty, and R. B. Bernstein, Chem. Phys. Lett. 86, 113 (1982); (c) D. H. Parker, H. Jalink, and S. Stolte, J. Phys. Chem. 91, 5427 (1987); (d) R. B. Bernstein, D. R. Herschbach, and R. D. Levine, *ibid.* 91, 5365 (1987); (e) D. H. Parker and R. B. Bernstein, Annu. Rev. Phys. Chem. 40, 561 (1989); (f) S. Stolte, in *Atomic and Molecular Beam Methods*, edited by G. Scoles (Oxford, New York, 1988), Vol. 1, p. 631; (g) H. Ohoyama, T. Kasai, K. Ohashi, and K. Kuwata, Chem. Phys. Lett. 136, 236 (1987).

[2] See Ref. 1. The Nijmegen group has studied molecules other than CR_3X and reactions with Ar^* has been studied in Osaka.

[3] P. R. Brooks, Faraday Discuss. Chem. Soc. 55, 299 (1973).

[4] (a) P. R. Brooks, Science 193, 11 (1976); (b) K. K. Chakravorty, D. H. Parker, and R. B. Bernstein, Chem. Phys. 68, 1 (1982). These latter experiments have been reinterpreted in terms of a steric cone of nonreaction of $\approx 53°$ by S. E. Choi and R. B. Bernstein, J. Chem. Phys. 83, 4463 (1985).

[5] P. R. Brooks, J.McKillop, and H. G.Pippen, Chem. Phys. Lett. **66**, 144 (1979).

[6] D. R.Herschbach, Adv. Chem. Phys. **10**, 319 (1966).

[7] For a preliminary report see P. W. Harland, H. S. Carman, Jr., L. F. Phillips, and P. R. Brooks, J. Chem. Phys. **90**, 5201 (1989).

[8] For collision with K: (a) P. E.McNamee, K. Lacman, and D. R.Herschbach, Faraday Discuss. Chem. Soc. **55**, 318 (1973); (b) A. W. Kleyn, M.N.Hubers, and J. Los, *10th ICPEAC Abstracts of Papers* (Commissariat a l'Energie Atomique, Paris, 1977), p. 1162; for collision with other alkali metals; (c) R.N. Compton, P. W. Reinhardt, and C. D. Cooper, J. Chem. Phys. **68**, 4360 (1978); (d) S.Y. Tang, B.P.Mathur, E. W. Rothe, and G. P. Reck, *ibid.* **64**, 1270 (1976).

[9] H. S. Carman, Jr., Ph.D. thesis, Rice University, 1986.

[10] One end of the dipole thus cannot be distinguished from the other end, but it is possible (with polarized light, e.g.) to select the plane of rotation, resulting in a *polarized*, but unoriented sample.

[11] C. H., Townes and A. L. Schawlow, *Microwave Spectroscopy* (Dover, New York, 1975).Hyperfine structure complicates this description, but is important mainly for $J \approx 1$.

[12] (a) H. G. Bennewitz, W. Paul, and Ch. Schlier, Z. Phys. **141**, 6 (1955); (b) K. H. Kramer and R. B. Bernstein, J. Chem. Phys. **42**, 767 (1965); (c) P. R. Brooks, E. M. Jones, and K. Smith, *ibid.* Phys. **51**, 3073 (1969).

[13] S. R. Gandhi, Q.-X. Xu, T. J. Curtiss, and R. B. Bernstein, J. Phys. Chem. **91**, 5437 (1987), and references cited therein.

[14] R. K. B. Helbing and E. W. Rothe, Rev. Sci. Instrum. **39**, 1948 (1968).

[15] We use the commonly accepted convention that the dipole moment points towards the positive charge. Regardless of convention, the molecules transmitted by the field are in high energy states, so the positive end of the molecule points towards the positive field plate in region *U*.

[16] Electronegativity, dipole moment trends, and reactivity of the oriented molecule make this clear (Ref. 3) and the polarity has been determined by photodissociation of the oriented molecule by S. R. Gandhi and R. B. Bernstein, J. Chem. Phys. **88**, 1472 (1988).

[17] For reviews of collisional ionization, see (a) A. W. Kleyn, J. Los, and E. A. Gislason, Phys. Rep. **90**, 1 (1982); (b) K. Lacmann, in *Potential Energy Surfaces*, edited by K. P. Lawley (Wiley, New York, 1980), p. 513; (c) A. P. M. Baede, Adv. Chem. Phys. **30**, 463 (1975); (d) J. Los and A. W. Kleyn, in *Alkali Halide Vapors*, edited by P. Davidovits and D. L. McFadden (Adacemic, New York, 1979), p.279.

[18] (a) J. A. Stockdale, F. J. Davis, R. N. Compton, and C. E. Klots, J. Chem. Phys. **60**, 4279 (1974); (b) M. Heni and E. Illenberger, Chem. Phys. Lett. **131**, 314 (1986).

[19] C. W. Walter, B. G. Lindsay, K. A. Smith, and F. B. Dunning, Chem. Phys. Lett. **154**, 409 (1989).

[20] A. Kalamarides, C. W. Walter, B. G. Lindsay, K. A. Smith, and F. B. Dunning, J. Chem. Phys. **91**, 4411 (1989).

International Journal of Mass Spectrometry and Ion Processes, 107 (1991) 215–224 215
Elsevier Science Publishers B.V., Amsterdam

EXPERIMENTAL MEASUREMENTS AND THEORETICAL CALCULATIONS OF THE MOBILITY OF THE N$^+$ ION IN HELIUM

STEPHEN T. GRICE, PETER W. HARLAND, JOHN A. HARRISON,
ROBERT G.A.R. MACLAGAN and RICHARD W. SIMPSON

Department of Chemistry, University of Canterbury, Christchurch 1 (New Zealand)

(First received 6 August 1990; in final form 30 November 1990)

ABSTRACT

The mobility of the ^{3}P ground state of N$^+$ in helium has been calculated using the three-temperature theory of ion transport. The relevant adiabatic interaction potentials of the HeN$^+$ species have been calculated at the MP4SDQ/6-311G+(3df, 3pd) level of theory. Two limiting methods for calculating the mobility of an atomic ion in an atomic gas with orbital angular momentum greater than zero are developed and discussed.

INTRODUCTION

The atomic ion/helium interaction potentials for many of the first-row positive ions and stable negative ions have been calculated by ab initio molecular orbital and valence bond methods [1–6]. These interactions have been used with the two- [7,8] and three-temperature [9,10] theories of ion transport to calculate ion mobilities in helium for comparison with laboratory experiments. The comparison between theory and experiment serves as a sensitive test of the computed interaction potential [11]. The interaction potentials calculated for electronically excited ions and for ion states which correlate with more than one molecular ion state can also be effectively used to calculate ion mobilities in agreement with experimental results over a wide range of ion energies, given the assumption that the ion/helium interaction follows a single adiabatic path for the duration of the collision. Typically, calculated ion mobilities for values of the electric field to particle density ratio, E/N, greater than 30 Td (1 Td $= 10^{-21}$ V m^2), where the repulsive part of the interaction potential dominates the collisions, are within the experimental uncertainties for such data. The calculated mobilities for E/N less than 30 Td, where the attractive part of the interaction potential plays an increasingly dominant role, are usually within 5–7% of the measurements.

This paper is concerned with the ion transport properties of the N$^+$ ion in helium. When the lowest electronic state of the ion, N$^+$(^{3}P), interacts with

0168-1176/91/$03.50 © 1991 Elsevier Science Publishers B.V.

He(^{1}S) there are two possible adiabatic eigenstates of the electronic hamiltonian, HeN$^+$($^3\Sigma$) and HeN$^+$($^3\Pi$). The methodology of previous calculations [3–5] was to obtain the mobility of the ion from the ab initio interaction potentials for each state and then using the appropriate statistical weightings of these states to combine them using Blancs Law. This approach has been very successful in reproducing experimental measurements for the C$^+$(^{4}P) and C$^+$(^{2}P) [3], O$^+$(^{2}P) and O$^+$(^{2}D) [4], and F$^+$(^{3}P) [5] ions. Initial theoretical mobility curves for N$^+$ in helium determined in this way exhibited an unusual step feature in the mobility versus E/N curve between 40 and 60 Td.

With the exception of a single set of measurements by Fahey et al. [12] extending to an E/N value of 145 Td, the literature measurements all terminate around 60 Td with a range of values for the reduced mobility at 60 Td, from 16–24 cm^2 V^{-1} s^{-1} [13–16]. Data sets in the region of interest exhibited a wide variation in the experimental measurements precluding a definitive judgement of the mobility of N$^+$ in helium. This provided the incentive to remeasure the mobility of N$^+$ in helium using the Canterbury static drift-tube mass spectrometer operating in pulsed mode as previously described [17,18].

EXPERIMENTAL MOBILITIES AND RATE COEFFICIENTS

The N$^+$ ion is produced by thermal energy charge transfer [19] of He$^+$ on N$_2$ in the drift-tube (eqn. 1a) giving the (C $^2\Sigma_u^+$) excited state of N$_2^+$ which either radiates to the ground state N$_2^+$(X $^2\Sigma_g^+$) (eqn. 1b) or predissociates according to eqn. 1c:

$$\mathrm{He^+(^2S) + N_2(X\ ^1\Sigma_g^-) \rightarrow He(^1S) + N_2^+(C\ ^2\Sigma_u^+)} \tag{1a}$$

$$\mathrm{N_2^+(C\ ^2\Sigma_u^+) \rightarrow N_2^+(X\ ^2\Sigma_g^+)} \tag{1b}$$

$$\mathrm{N_2^+(C\ ^2\Sigma_u^+) \rightarrow N^+(^3P) + N(^4S)} \tag{1c}$$

The dissociative charge transfer reaction took place in a 1% N$_2$ mixture in helium with a total drift-tube pressure of 0.4 Torr and at a regulated temperature of 298 K. The drift-tube is constructed of ultra-high vacuum compatible materials and maintains a base pressure of 1 × 10^{-8} Torr prior to experiments. The He$^+$ ions are produced in the movable ion source of the drift-tube by a 2 μs electron pulse. The He$^+$ ions move through the ion source into the drift region under the influence of the uniform electric field gradient maintained from the ion source to the ion exit aperture. Reaction with N$_2$ molecules can occur throughout the drift path which is continuously variable from 1 to 11 cm. The determination of the N$^+$ ion drift velocity for any selected value of E/N involved measurement of the N$^+$ ion arrival time distribution for seven or eight different values of drift distance. The drift velocity and the He$^+$ ion removal rate via reaction 1a are the variable

TABLE 1

Mobility measurements of N^+ in helium

E/N(Td)	35.0	40.0	45.0	50.0	55.0	60.0	65.0	70.0	75.0	80.0	85.0
K_0(cm^2 V^{-1} s^{-1})	21.1	21.2	21.4	21.6	21.3	21.3	20.7	20.7	20.0	19.8	19.7
E/N (Td)	90.0	95.0	100.0	105.0	110.0	115.0	120.0	125.0	130.0	135.0	140.0
K_0(cm^2 V^{-1} s^{-1})	19.6	19.1	18.8	18.5	18.4	18.3	18.2	18.0	17.9	17.9	17.6

parameters used to fit the experimental arrival time curves to those emerging from the model calculation [20]. The mobility of the N^+ ion was calculated from the experimental drift velocities obtained by fitting the ion arrival time distributions based on the geometry of the drift-tube, the physical conditions selected for the experimental measurements and the ion/neutral kinetics of the N_2–He system [20,21]. The He^+ ion mobilities measured in this laboratory are within 2% of the values listed in the compilation of Ellis et al. [22] and the depletion rate of the N^+ ion by reaction with N_2 was taken to be 1.8×10^{-10} cm^3 s^{-1} [23].

The results of the arrival time modelling for the measurements over the range of E/N from 35 to 140 Td are shown in Table 1. The mobilities are listed as the values reduced to STP, the reduced mobility K_0. The mobility data from Table 1 are plotted together with the literature data in Fig. 2. The error bars on the data corresponding to ref. 12 reflect the experimental uncertainty in the absolute values of that study. The results of this study lie within the respective uncertainties of the two data sets and are almost superimposable for $E/N < 60$ Td. It is immediately evident from the table that the variation of the N^+ mobility with E/N is a smoothly changing curve.

THEORETICAL CALCULATIONS OF INTERACTION POTENTIALS AND ION MOBILITIES

The adiabatic interaction potentials for the $HeN^+(^3\Sigma)$ and the $HeN^+(^3\Pi)$ molecular ion states correlating with the $N^+(^3P)$ ion and the $He(^1S)$ atomic ground states were calculated using the Gaussian 82 program [24] at the MP4SDQ/6-311+G(3df, 3pd) level of theory, excluding core contributions to the correlation energy, and accounting for basis set superposition error (BSSE) by counterpoise. The results of these calculations are presented in Tables 2 and 3 and compared graphically in Fig. 1. The $HeN^+(^3\Sigma)$ state exhibits a deep and narrow well, $D_e = 0.194$ eV (1563 cm^{-1}), $r_e = 1.596$ Å, from MP4SDQ/6-311G+(3df, 3pd), and $D_e = 0.174$ eV (1407 cm^{-1}), $r_e = 1.611$ Å, $\omega_e = 383$ cm^{-1}, from MP4SDQ/6-311G+(3df, 3pd) + BSSE. The depth of this well suggests that collisional stabilisation of the ion may be expected at low temperatures, and this appears to be the case. Smith and Adams [25] have observed an m/z 18 signal when N_2 is introduced into the

TABLE 2

MP4SDQ/6-311G+(3df, 3pd) energy calculations for N^+ ($^3\Sigma$) including helium basis set, He ($^1\Sigma$) including N basis set and HeN^+ ($^3\Sigma$) as a function of internuclear separation

R_{HeN^+} (Å)	E(hartree)		
	$^3\Sigma$(MP4SDQ) N^+ (He basis)	$^1\Sigma$(MP4SDQ) He (N basis)	$^3\Sigma$(MP4SDQ) N^+
0.875	−53.97860	−2.89945	−56.76625
0.9375	−53.97842	−2.89941	−56.80451
1.00	−53.97825	−2.89937	−56.83015
1.125	−53.97796	−2.89930	−56.85966
1.25	−53.97777	−2.89923	−56.87375
1.3125	−53.97770	−2.89920	−56.87763
1.375	−53.97764	−2.89917	−56.88017
1.50	−53.97754	−2.89914	−56.88259
1.625	−53.97744	−2.89914	−56.88296
1.75	−53.97735	−2.89909	−56.88242
2.00	−53.97720	−2.89906	−56.88072
2.125	−53.97714	−2.89905	−56.87992
2.50	−53.97703	−2.89902	−56.87812
3.00	−53.97700	−2.89898	−56.87693
3.50	−53.97700	−2.89896	−56.87644
4.00	−53.97699	−2.89894	−56.87618
5.00	−53.97697	−2.89891	−56.87597
6.00	−53.97697	−2.89890	−56.87591
∞			−56.87587

helium buffer flow in the Birmingham selected ion flow drift tube (SIFDT) at 80 K. In contrast, the HeN^+ ($^3\Pi$) interaction potential exhibits a shallow minimum, $D_e = 0.022$ eV, $r_e = 2.715$ Å, from MP4SDQ/6-311G+(3df, 3pd) + BSSE.

Previous theoretical investigations of the HeN^+ species include SCF calculations by Cooper and Wilson [26] and also by Liebman and Allen [27]. More recently, Koch et al. [28] report a thermodynamic study to find the geometry and energy of the HeN^+ ($^3\Sigma_g^-$) species at the MP4SDTQ/6-311G (2df, 2pd)//MP2/6-31G(d, p) level of theory. The dissociation energy from the calculation of Koch et al. (0.191 eV) is practically identical to that of our own but we estimate that this is lowered 10.3% to 0.174 eV when correcting for BSSE. However, the difference in the equilibrium internuclear distances between the result of Koch et al. (1.749 Å) and the result of this work (1.611 Å) is significant and is most probably due to the larger basis set used in the present study, as the levels of theory are very similar.

Theoretical N^+ mobility curves using our earlier approach [3] are shown in Fig. 2. Two points must be made in relation to these calculations. Firstly, the

TABLE 3

MP4SDQ/6-311G+(3df, 3pd) energy calculations for N^+ ($^3\Pi$) with helium basis set, He ($^1\Sigma$) with N basis set and HeN^+ ($^3\Pi$) as a function of internuclear separation

R_{HeN^+} (Å)	E (hartree)		
	$^3\Pi$(MP4SDQ) N^+ (He basis)	$^1\Sigma$(MP4SDQ) He (N basis)	$^3\Pi$(MP4SDQ) N^+
1.25	−53.97799	−2.89923	−56.74190
1.50	−53.97772	−2.89914	−56.82614
1.75	−53.97751	−2.89909	−56.85924
2.00	−53.97732	−2.89906	−56.87152
2.25	−53.97720	−2.89904	−56.87564
2.50	−53.97710	−2.89902	−56.87673
2.75	−53.97705	−2.89900	−56.87683
3.00	−53.97702	−2.89898	−56.87669
3.25	−53.97702	−2.89897	−56.87652
3.50	−53.97701	−2.89896	−56.87638
4.00	−53.97700	−2.89894	−56.87617
5.00	−53.97697	−2.89891	−56.87597
6.00	−53.97697	−2.89890	−56.87591
∞			−56.87587

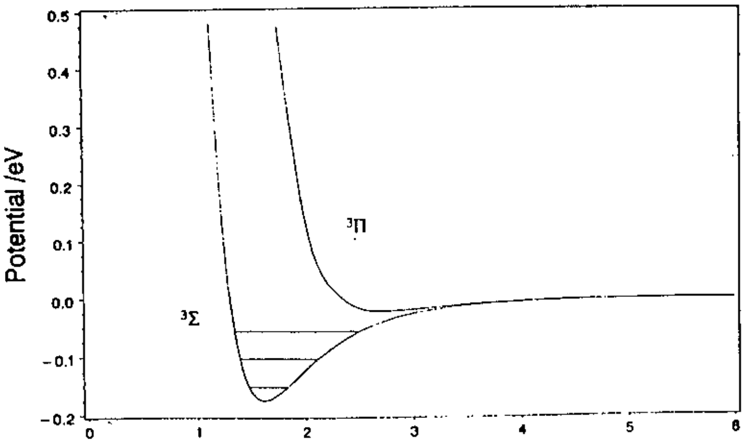

Fig. 1. Interaction energy of the HeN^+ ($^3\Sigma$) and HeN^+ ($^3\Pi$) systems calculated at the MP4SDQ/6-311G+(3df, 3pd) + BSSE level of theory. The HeN^+ ($^3\Sigma$) interaction shows the first ($v = 0$), second ($v = 1$), and third ($v = 2$) vibrational levels calculated assuming a harmonic oscillator model at the MP4SDQ/6-311G+(3df, 3pd) level of theory.

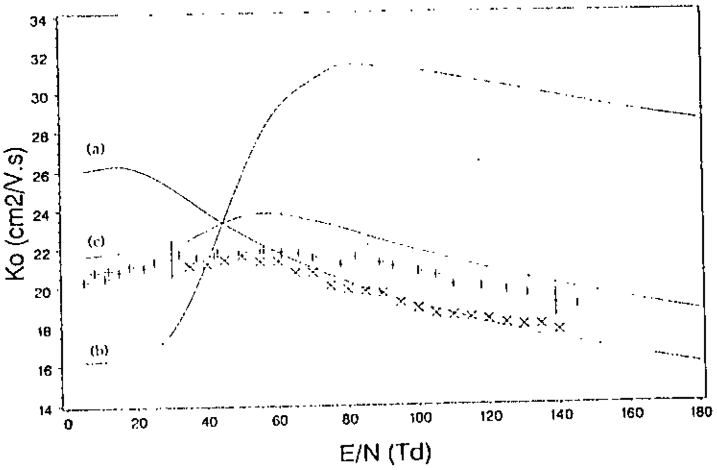

Fig. 2. Experimental measurements and theoretical calculations of the mobility of N^+ in helium. +, measurements of Fahey et al. [12]; ×, this work; solid lines represent theoretical three-temperature calculation results. (a) Mobility function derived from $^3\Pi$ potential interaction. (b) Mobility function derived from $^3\Sigma$ potential interaction. (c) Mobility function obtained from combining (a) and (b) using Blancs Law.

three temperature calculations for the $^3\Sigma$ state did not converge in the range 30–100 Td where the mobility rises rapidly. However, the mobility calculations converged elsewhere. Secondly, the calculation of the overall mobility by Blanc's law for the neutral gas mixtures is an approximation. Blanc's law is justified at low fields where the mean collision energy is largely thermal and thus ratios of mean collision energies of the ions in the different gases (or in this case different states of the same gas) are unity. Blanc's law is also valid when the collision cross-sections are independent of the collision energy. This is true when the ratio of collision energy to well depth of the potential interaction for the calculation tends to infinity, i.e. the high field limit. Blanc's law is a valid approximation for these two extremes and for when the ratio of the mean collision energies are close to unity, implying that application is justified for the medium field only when the mobilities are similar. This has been true of systems which we have reported to date. We suggest that these approximations are accurate to well within 10%. In the N^+–He system the mobility curves for the two different interactions differ widely and thus we anticipate that Blanc's law will be invalid. To negate the problem of non-convergence of the mobility curve resulting from the $^3\Sigma$ interaction the three-temperature theory implementation (MOBDIF) of Viehland and Kumar [29] was used. This has been shown to have superior convergence properties to a previous three-temperature theory implementation (MOBILDIF) [30]. All calculations were performed with 24 Gauss–Laguerre and 32 Gauss–Legendre

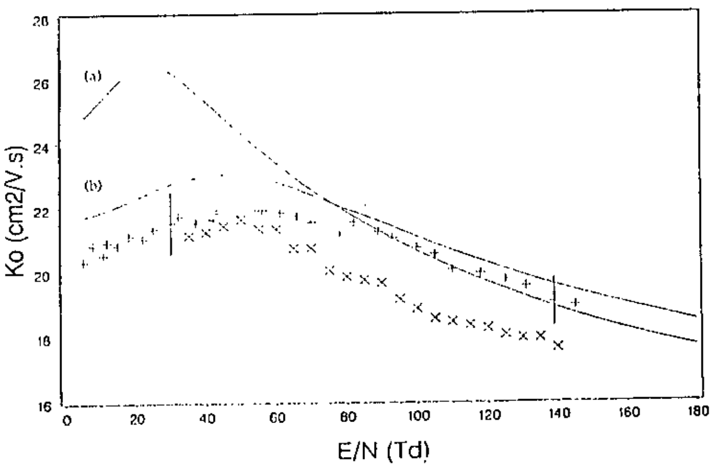

Fig. 3. Experimental measurements and theoretical calculations of the mobility of N^+ in helium. +, measurements of Fahey et al. [12]; ×, this work; solid lines represent theoretical three-temperature calculation results. (a) Assumes transition frequency between Born–Oppenheimer states to be infinite. (b) Assumes transition frequency between Born–Oppenheimer states to be zero.

quadrature points and with mobilities and diffusion coefficients to an accuracy of 1% and 5% respectively. All transport coefficients were calculated to at least the third approximation. This narrowed the window of non-convergence for the $^3\Sigma$ mobility curve to 30–60 Td. The identical curve to that shown in Fig. 2 is obtained if we interpolate through the region of non-convergence using only converged points. However, the mobility functions for the two interactions still differed significantly, thus undermining Blanc's law. The calculation of the mobility of an ion with orbital angular momentum greater than zero where the weighted cross-sections for the different interactions were averaged as a function of collision energy resulted in solution of both the convergence problems of the numerical solution and the problem of the validity of Blanc's law (see Fig. 3). This approach assumes that each collision proceeds along a single potential surface, that is an eigenstate of the electronic hamiltonian. It is well known that if the nuclear motion is large enough, coupling between adiabatic electronic states induces transitions from one Born–Oppenheimer state to another [31–33]. In terms of ion transport we cannot specify the state of an ion with orbital angular momentum greater than zero during the collision process, and as a result we cannot apply a single potential required for a classical transport theory. We can, however, assume the frequency of transitions between the possible Born–Oppenheimer states to be great enough for an ion to act according to an effective potential that can be obtained by averaging over the adiabatic potential surfaces with the appropriate weightings given by the correct degeneracies. Thus we have a method for calculating transport phenomena at two extremes, that is, assuming the transition frequency between Born–Oppenheimer states is either zero or infinite. This limitation is a direct result of using quantum mechanics to calculate the potentials and a classical method to calculate the mobility.

The mobility curves calculated using the two- and three-temperature theories of ion transport by averaging the weighted cross-sections and assuming the transition frequency between Born–Oppenheimer states to be zero gave the best agreement with the experimental measurements below 30 Td (see Fig. 3). For comparison we also calculated the mobility curves assuming the frequency of transitions between the Born–Oppenheimer states to be infinite, by averaging the potentials assuming that the HeN$^+$ interaction was given by

$$V_{\mathrm{eff}}(r) \;=\; 1/3V(r, {}^3\Sigma) + 2/3V(r, {}^3\Pi) \tag{2}$$

The effective potential is dominated by the HeN$^+$ ($^3\Pi$) interaction as this interaction becomes steeply repulsive for internuclear distances in the region of the HeN$^+$ ($^3\Sigma$) well, that is less than 2.0 Å.

The mobility curves were then calculated using both two- and three-temperature theories of ion transport in the same way. The derived mobility curve giving the correct qualitative features gave the best agreement with the experimental errors of the literature measurements at large E/N.

These results are not surprising as by raising E/N we are increasing the drift velocity and on average increasing the relative collision energy. We can expect that at low E/N, where, on average, the collision velocity is smallest, coupling, which results from the relative motion of the nuclei, will be negligible. Thus in the region of low E/N we expect that the mobility function obtained by assuming a transition frequency of zero will correspond well to experimental mobility measurements. As E/N is increased and with it the relative collision velocity, we would expect this assumption to break down. However, as E/N is increased, we can expect the transition frequency between Born–Oppenheimer states to become significant and increasingly important in determining the mobility of the ion. Thus in the region of large E/N we can expect that the mobility function obtained by assuming the transition frequency to be infinite to correspond well to experimental mobility measurements (see Fig. 3).

CONCLUSIONS

In calculating bulk transport properties of ions in gases the possibility of transitions between Born–Oppenheimer states due to coupling resulting from the motion of the nuclei in the collision event should be taken into account. We have outlined two limiting cases for calculating the mobility of an ion in a neutral gas where the orbital angular momentum of the collision partner is greater than zero. These two limiting cases are a natural consequence of confining the description of ion mobility classically. The cases for which the transition frequency is neither effectively zero nor effectively infinite can only be dealt with adequately using a quantum theory of ion transport. Thus the mobility of N^+ in helium is a warning not to oversimplify the theory of atom–atomic ion systems, and as an example that caution must be applied in experiments that are designed to gain knowledge of the interaction potential between species via collision events.

ACKNOWLEDGEMENT

We thank A. David Buckingham for helpful discussions.

REFERENCES

1 R.G.A.R. Maclagan, R.W. Simpson and P.W. Harland, J. Phys. B, 20 (1987) 2723.
2 R.W. Simpson, R.G.A.R. Maclagan and P.W. Harland, J. Chem. Phys., 87 (1987) 5419.
3 S.T. Grice, P.W. Harland and R.G.A.R. Maclagan, Int. J. Mass Spectrom. Ion Processes, 87 (1989) 181.
4 R.W. Simpson, Ph.D. thesis, University of Canterbury, New Zealand, 1988.
5 P.W. Harland, R.G.A.R. Maclagan and R.W. Simpson, J. Chem. Soc., Faraday Trans. 2, 84 (1988) 1847.
6 R.W. Simpson, P.W. Harland, R.G.A.R. Maclagan, D. Smith and N.G. Adams, Int. J. Mass Spectrom. Ion Processes, 90 (1989) 193.
7 L.A. Viehland and E.A. Mason, Ann. Phys., 91 (1975) 499.
8 L.A. Viehland and E.A. Mason, Ann. Phys., 110 (1978) 287.
9 S.L. Lin, L.A. Viehland and E.A. Mason, Chem. Phys., 37 (1979) 411.
10 L.A. Viehland and S.L. Lin, Chem. Phys., 43 (1979) 135.
11 C.E. Dykstra, Ab initio Calculation of the Structure and Properties of Molecules, Elsevier, Amsterdam, 1988.
12 D.W. Fahey, F.C. Fehsenfeld and D.L. Albritton, J. Chem. Phys., 74 (1981) 2080.
13 R. Johnson, H.L. Brown and M.A. Biondi, J. Chem. Phys., 52 (1970) 5080.
14 M. McFarland, D.L. Albritton, F.C. Fehsenfeld, E.E. Ferguson and A.L. Schmeltekopf, J. Chem. Phys., 59 (1973) 6610.
15 Y. Kaneko, T. Koizumi and N. Kobayashi, Mass Spectrosc. (Tokyo), 26 (1978) 35.
16 H.A. Fahdil, A.T. Numan, T. Shuttleworth and J.B. Hasted, Int. J. Mass Spectrom. Ion Processes, 65 (1985) 307.
17 P.W. Harland and B.J. McIntosh, Int. J. Mass Spectrom. Ion Processes, 54 (1983) 217.
18 P.W. Harland and B.J. McIntosh, Int. J. Mass Spectrom. Ion Processes, 57 (1984) 283.
19 J.B. Laudenslager, W.T. Huntress, Jr. and M.T. Bowers, J. Chem. Phys., 61 (1974) 4600.
20 P.W. Harland and B.J. McIntosh, J. Chem. Soc., Faraday Trans. 2, 81 (1985) 169.
21 P.W. Harland, N. Kim and S.A.H. Petrie, Aust. J. Chem., 42 (1989) 9.
22 H.W. Ellis, R.Y. Pai, E.W. McDaniel, E.A. Mason and L.A. Viehland, At. Data Nucl. Data Tables, 17 (1976) 177.
23 F.C. Fehsenfeld, D.L. Albritton, Y.A. Bush, P.G. Fournier, T.R. Govers and J. Fournier, J. Chem. Phys., 61 (1974) 2150.
24 J.S. Binkley, M.J. Frisch, D.J. DeFrees, K. Raghavachari, R.A. Whiteside, H.B. Schlegel,

E.M. Fluder and J.A. Pople, Gaussian 82, Carnegie-Mellon University, Pittsburgh, PA, 1983.
25 D. Smith and N.G. Adams, Department of Space Research, University of Birmingham, UK, private communication, 1988.
26 D.L. Cooper and S. Wilson, Mol. Phys., 44 (1981) 161.
27 J.F. Liebman and L.C. Allen, J. Am. Chem. Soc., 92 (1970) 3539.
28 W. Koch, G. Frenking, J. Gauss, D. Cremer and J.R. Collins, J. Am. Chem. Soc., 109 (1987) 5917.
29 L.A. Viehland and K. Kumar, Chem. Phys., 131 (1989) 295.
30 L.A. Viehland, Chem. Phys., 70 (1982) 149.
31 T. Pacher, C.A. Mead, L.S. Cederbaum and H. Köppel, J. Chem. Phys., 91 (1989) 7057.
32 B. Zygelman, Phys. Lett. A, 125 (1987) 476.
33 D.R. Bates and R. McCarrol, Proc. R. Soc. London Ser. A, 245 (1958) 175.

J. CHEM. SOC. FARADAY TRANS., 1991, 87(8), 1069–1073 1069

Flow Dynamics of Supersonic Molecular Beams and the Measurement of Rotational–Translational Coupling Parameters for N_2 and H_2

Brett R. Cameron and Peter W. Harland
Chemistry Department, University of Canterbury, Christchurch, New Zealand

Collision frequency, flow velocity, particle density, mean-free path, axial and radial temperatures in supersonic atomic and homonuclear diatomic beams have been calculated for various species within the framework of the thermal conduction model using realistic interaction potentials and collision cross-sections obtained from scattering theory. Comparison between numerical results and measured velocity distributions are made to estimate values of rotational–translational coupling parameters for N_2 and H_2.

A frequently cited property of supersonic molecular beams is the collision-free nature of the flow far downstream from the nozzle exit plane; the beam may be considered to consist simply of a stream of molecules moving along parallel paths in the complete absence of any collisions. To the extent that this is a valid description of the true situation, it facilitates the preparation of state-selected and oriented species for the investigation of scattering processes,[1,2] and the investigation of radiationless processes in large isolated molecules. In reality, the supersonic flow will only approach a collision-free situation;[3] free molecular flow will never actually occur due to the finite width of the velocity distribution, causing some molecules to overtake and collide with others.

Since the development and use of molecular beams as a research tool some two or three decades ago, a number of workers have addressed the problem of calculating collision rates within such systems. Probably the first in this regard was Troitskii,[4] who reported that the collision frequency of molecules at any point in an effusive beam is approximately one-third that found in a bulk gas of the same number density. Using a similar formalism Lubman *et al.*[5] developed general expressions for the collision frequency in effusive and supersonic molecular beams. Their calculations showed that, when characterized by the same density and temperature, the collision rates in an effusive beam, supersonic beam, and a bulb are approximately in the ratio of 1 : 1.5 : 3, indicating that the directionality of the nozzle beam source does little to reduce the collision frequency by any more than a factor of two below that in a gas bulb.

While exact for the case of an effusive beam, the expressions given by Lubman pertaining to the supersonic system were obtained using a greatly simplified treatment of the expansion process and, although completely general, cannot be considered particularly accurate. Velocity components perpendicular to the beam axis were assumed to contribute little to the overall number of collisions and were neglected in Lubman's analysis.

In this paper, the thermal conduction model[6] is used to provide a more realistic description of the expansion process. The model has been modified to incorporate a variable flow velocity and extended using Klots approach[7] to include rotational degrees of freedom. Results obtained from the thermal conduction model are used in conjunction with accurately calculated collision cross-sections to derive theoretical values of collision frequency as a function of distance from the nozzle for supersonic beams of the monatomics He, Ne, Ar and Kr, and homonuclear diatomics H_2 and N_2. Klots rotational–translational coupling parameter has been determined for N_2 and H_2 by fitting parameters calculated using the thermal conduction model to experimental data determined by the time-of-flight method described below. The value determined for N_2 was in excellent accord with previously published results and the value found for H_2 is consistent with the expectations of previous work.[8]

Theoretical Considerations

The free expansion of a gas into a vacuum is one of the fundamental theoretical and experimental problems of rarefied gas dynamics. Accordingly, many theories have been developed to explain the dynamics of the expansion, ranging in sophistication from a simple hard-sphere treatment of the collision dynamics[9] through to the incorporation of subtle quantum effects.[10] At an intermediate level one finds the collision dynamics treated solely in terms of long-range van der Waals forces, generally assuming an interaction potential of the form

$$V(r) = -C_6 r^{-6} \tag{1}$$

One such model which has been employed by a number of workers in recent years is the thermal conduction model, originally proposed by Habets[11] and Beijerinck and Verster[6] to describe the breakdown of translational equilibrium in free-jet expansions of monatomic gases. The model has been extended by Klots[7] to include rotational degrees of freedom through the application of unimolecular decomposition theory which, as applied to collision complexes, provides a natural means for describing the coupling between rotational and translational modes. The thermal conduction model is particularly appealing both from the point of view of its relatively simple form and its ability to produce results in good agreement with those obtained by experiment.

In common with most other models of the expansion process, the thermal conduction model assumes that the local number density in the core of the expansion at a distance z from the nozzle is given by

$$n(z) = n_0\left(\frac{z}{z_0}\right)^{-2}\left(\frac{u}{u_\infty}\right)^{-1} \tag{2}$$

where n_0 is the stagnation density and z_0 is related to the nozzle throat radius by the expression

$$z_0^2 = r_0^2\kappa\left[\left(\frac{\gamma-1}{\gamma+1}\right)^{1/2}\left(\frac{2}{\gamma+1}\right)^{1/(\gamma-1)}\right]$$

where γ is the heat capacity ratio C_p/C_v, and κ is the nozzle peaking factor, a complicated function of γ. Table 1 gives κ for several values of γ, as calculated by Beijerinck. The value

Table 1 Peaking factors for various γ

γ	5/3	7/5	8/6	9/7
κ	1.98	1.38	1.08	1.10

of u_∞ is given by the expression

$$u_\infty = \left(\frac{\gamma}{\gamma - 1}\right)^{1/2}\left(\frac{2k_B T_0}{m}\right)^{1/2} \tag{3}$$

and represents the thermodynamic limiting value of the streamline or directed flow velocity u.

In order to simplify the solution to the expansion problem, Beijerinck *et al.* introduced a source parameter Ξ which is a function of the reservoir parameters and the interaction potential:

$$\Xi = \frac{16}{15} n_0 z_0 c_{2,2}\left(\frac{2k_B T_0}{m}\right)^{1/2}\left(\frac{C_6}{k_B T_0}\right)^{1/3}\frac{1}{u_\infty}; \qquad c_{2,2} \approx 2.99$$

Introducing the reduced variables

$$\tau = \frac{T}{T_0}\,\Xi^{6(\gamma-1)/(\gamma+2)}$$

and

$$\zeta = \frac{z}{z_0}\,\Xi^{-3/(\gamma+2)}$$

the appropriate set of differential equations to be solved under the thermal conduction model for the attractive C_6 potential are:

$$\begin{aligned}\frac{d\tau_\perp}{d\zeta} = {} & -\frac{2\tau_\perp}{\zeta} + p(\tau_\perp, \tau_\parallel, \tau_r)\frac{\tau_m^{1/6}}{2\zeta^2}\\ & \times\left\{\frac{1}{2}(\tau_\parallel - \tau_\perp)(1 + \xi\alpha) + \xi\beta(\tau_r - \tau_m)\right.\\ & \left.\times\left[1 - \frac{1}{18}\left(\frac{\tau_\parallel - \tau_\perp}{t_m}\right)\right]\right\}\end{aligned} \tag{4a}$$

$$\begin{aligned}\frac{d\tau_\parallel}{d\zeta} = {} & p(\tau_\perp, \tau_\parallel, \tau_r)\frac{\tau_m^{1/6}}{\zeta^2}\\ & \times\left\{(\tau_\parallel - \tau_\perp)(1 + \xi\beta) - \xi\beta(\tau_r - \tau_m)\right.\\ & \left.\times\left[1 + \frac{1}{9}\left(\frac{\tau_\parallel - \tau_\perp}{\tau_m}\right)\right]\right\}\end{aligned} \tag{4b}$$

$$\frac{d\tau_r}{d\zeta} = -p(\tau_\perp, \tau_\parallel, \tau_r)\frac{3\xi\beta}{R}\frac{\tau_m^{1/6}}{\zeta^2}(\tau_r - \tau_m) \tag{4c}$$

$$\tau_m = \frac{2\tau_\perp + \tau_\parallel}{3}$$

where $\tau_\parallel$, $\tau_\perp$ and τ_r pertain to the parallel, perpendicular and rotational temperatures respectively, R is the number of rotational degrees of freedom and ξ relates to the efficiency of rotational to translation energy transfer, as discussed below. The two coefficients α and β are defined as

$$\alpha = \frac{1}{\Gamma}\frac{3}{80}\left(\frac{R}{R + 1}\right)$$

and

$$\beta = \frac{1}{\Gamma}\frac{1}{16}\left(\frac{R}{R + 1}\right)$$

respectively, with $\Gamma \approx 0.5813$ for the C_6 potential.

In most previous studies involving the use of the thermal conduction model, it has been assumed that the directed flow velocity reaches its terminal value only a few nozzle diameters downstream of the nozzle leading to a simplification of eqn. (2):

$$n(z) = n_0\left(\frac{z}{z_0}\right)^{-2}$$

In fact, the flow velocity can never attain its terminal value since to do so would require the conversion of all the energy associated with the translational and internal modes of the particles into the kinetic energy $\frac{1}{2}mu^2$ of the directed mass flow. Rather, u asymptotically approaches its terminal value as the expansion proceeds. Assuming that the expansion is truly isentropic, conservation of energy gives that[12]

$$\frac{5}{2}k_B T_0 + \frac{R}{2}k_B T_0 = \frac{3}{2}k_B T_\parallel + \frac{2}{2}k_B T_\perp + \frac{R}{2}k_B T_r + \frac{1}{2}mu^2 \tag{5}$$

assuming $\frac{1}{2}k_B T$ per rotational degree of freedom and neglecting all vibrational contributions. In eqn. (4), the function $p(\tau_\perp, \tau_\parallel, \tau_r)$ represents the ratio u/u_∞ which can be simply determined from eqn. (5) to be

$$p(\tau_\perp, \tau_\parallel, \tau_r) = \left(\frac{(R + 5)\tau_0 - 3\tau_\parallel - 2\tau_\perp - R\tau_r}{(R + 5)\tau_0}\right)^{1/2}$$

The rotational–translational coupling is described in terms of the single parameter ξ, which represents the fraction of capture collisions (those pertaining to classical capture cross-sections) that lead to a quasiequilibrium distribution of energy. Although somewhat naive, the assumption that ξ is independent of all other collision parameters is made attractive by its simplicity and the success of eqn. (4) to yield results which are in excellent agreement with those obtained by experiment. While eqn. (4) does allow solutions for $\xi > 1$, it is most unlikely that rotational relaxation will ever be more efficient than translational relaxation and it would therefore appear reasonable to suggest that $\xi = 1$ represents a lower limit to the terminal rotational temperature obtainable in a given expansion.

In order to calculate the mean collision rate, the local velocity distribution of the atoms or molecules in the beam must be known or approximated. The most frequently used distribution is an ellipsoidal function of the form

$$\begin{aligned}f(\mathbf{v})\,d\mathbf{v} = {} & \frac{1}{\pi^{3/2}}\left(\frac{m}{2k_B T_\perp}\right)\left(\frac{m}{2k_B T_\parallel}\right)^{1/2}\\ & \times \exp(-mv_x^2/2k_B T_\perp)\exp(-mv_y^2/2k_B T_\perp)\\ & \times \exp(-m(v_z - u)^2/2k_B T_\parallel)\,d\mathbf{v}\end{aligned} \tag{6}$$

where v_x and v_y are the velocity components perpendicular to the beam axis and v_z is the velocity component parallel to the beam axis. The use of this ellipsoidal model has become a standard technique in many theoretical and experimental studies[13,14] as it simplifies the analysis of the parallel and perpendicular profiles by allowing their characterization in terms of separate uncoupled Maxwellian distribution functions.

Assuming that all molecules in the beam have a normalised velocity distribution given by eqn. (6), the mean collision rate for a single atom or molecule was calculated by averaging the product $n\sigma c_r$ over all classes of the relative speed c_r:

$$\begin{aligned}\nu &= n\int_0^\infty \sigma(c_r)c_r\,g(c_r)\,dc_r\\ &= \overline{n\sigma(c_r)c_r}\end{aligned} \tag{7}$$

where g is the relative speed distribution function derived from eqn. (6). Mean-free paths are calculated in an analogous manner:

$$\lambda = \left(n \int_0^\infty \sigma(c_r) g(c_r)\, \mathrm{d}c_r\right)^{-1}$$

The collision cross-sections were calculated according to the integral

$$\sigma^l(c_r) = 2\pi \int_0^\infty b(1 - \cos^l \chi)\, \mathrm{d}b \qquad (8)$$

for $l = 2$, where b is the impact parameter and χ is the classical deflection angle. Evaluations of the integral (8) were performed using the quadrature techniques described by O'Hara and Smith.[15] Lennard-Jones (12,6) potentials were used in the calculation of collision cross-sections for the diatomic species using the parameters given in ref. 16, while for the monatomic gases a modified Buckingham potential was employed.[17]

Time-of-flight Measurements

Measurement of the parallel beam temperature was performed using a synchronous time-of-flight (TOF) technique.[18] A modified Honda Civic fuel-injection valve fitted with a cylindrical 70 μm nozzle was used to generate the supersonic beams. The pulsed beam was passed through a 1 mm diameter skimmer (Beam Dynamics) into a differentially pumped flight tube housing the beam chopper assembly and terminated with a quadrupole mass filter (Vacuum Generators SXP300). The chopper wheel, with two diametrically opposed slits of width 1 mm, was rotated by a synchronous 400 Hz motor. A photodiode residing diametrically opposed to the beam axis emitted a pulse-train having twice the rotational frequency of the chopper wheel which was divided down to give a resultant frequency sufficiently low (typically 10 Hz) to trigger the pulsed nozzle and associated electronics. The chopped gas pulse was then allowed to evolve in time over a fixed flight path of 0.70 m and the resulting mass-selected waveform (analogue output current of the electron multiplier passed through a 1 MHz amplifier) captured by a transient digitizer capable of averaging repetitive waveforms (LeCroy 8013A). The resultant averaged data were stored as a permanent file using a dedicated microcomputer.

The stored TOF waveforms were fitted to the speed distribution function

$$h(v) = Av^2 \exp(-m(v - u)^2/2k_B T_\parallel) \qquad (9)$$

where u is the directed flow velocity of the beam and A is a normalisation constant. Fitting was performed using an iterative least-squares procedure. The effect of the amplifier response function and the chopper (or gate) function on the measured TOF signal[19] was investigated by deconvolution and found to be negligible. The flight times of ions through the quadrupole mass filter were measured in a separate experiment and the flight time for the neutral species corrected accordingly.

Results and Discussion

Fig. 1 shows experimental and fitted TOF waveforms for H_2 and N_2. The nozzle temperature for these measurements was 300 K, with source pressures of 4 atm for H_2 and 1 atm for N_2. For H_2, fitting the experimental data to eqn. (9) gave $T_\parallel = 4.4$ K and $u = 2659$ m s^{-1} and for N_2 under the above conditions we obtain $T_\parallel = 13.1$ K and $u = 753$ m s^{-1}.

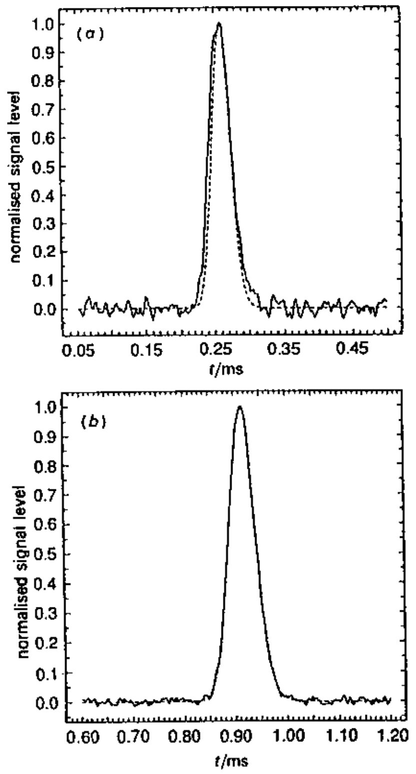

Fig. 1 Experimental (——) and fitted (– – –) TOF waveforms for (*a*) H_2 and (*b*) N_2

A comparison between the measured parallel temperatures and numerical results obtained using the thermal conduction model gave values for the rotational–translational coupling parameter ξ of 0.015 for H_2 and 0.39 for N_2. The theoretical fits for values of ξ exceeding *ca.* ±5% difference from the values quoted are substantially degraded in comparison to those shown in Fig. 1. We would suggest a maximum uncertainty of ±10% for the values quoted. The value of 0.39 measured for N_2 is in good agreement with that of 0.41 suggested by Randeniya.[20] Fig. 2 illustrates the calculated temperature profiles for H_2 with $\xi = 0.015$ and N_2 with $\xi = 0.39$ under the experimental conditions specified above. The rotational temperature freezes out very rapidly for both gases, the final rotational temperatures being 154.7 and 26.9 K for H_2 and N_2, respectively. The low value of ξ for H_2 indicates that rotational relaxation is extremely inefficient. This is well known to be the case, with high collision numbers having been determined for both vibrational–translational and rotational–translational relaxation processes. The total number of collisions experienced by an atom or molecule during the expansion would appear to be of the order of 10^2–10^3. Any kinetic process requiring this number of collisions will be subject to relaxation effects during the course of the expansion and may freeze. The vibrational relaxation of simple diatomic molecules typically requires in excess of 10^4 collisions, indicating that the vibrational modes of such species do not participate in the expansion. The explicit consideration of vibrational degrees of freedom has thus been ignored in our analysis, the assumption being that either these modes very rapidly freeze out or that they contain insufficient energy to significantly alter any flow character-

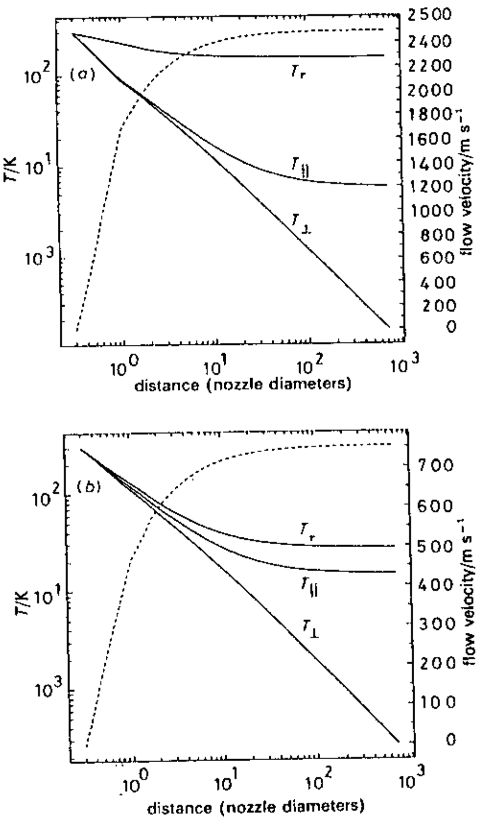

Fig. 2 Calculated temperature profiles for (*a*) H_2 and (*b*) N_2

istics. In fact, for thermal equilibrium at a nozzle temperature of 300 K, statistical thermodynamical considerations show a negligible population of anything but the ground vibrational level for the diatomic systems considered in this paper. The vibrational collision numbers of large polyatomic molecules and the rotational collision numbers of most diatomics tend to be of the order of 10–100, so that such modes can exchange energy and cool to some extent during the initial part of the expansion before freezing. Our calculated value for the final rotational temperature of H_2 compares well with that obtained from the work of Gallagher and Fenn.[8] A more sophisticated theoretical investigation into the rotational relaxation of small molecules in supersonic molecular beams, along with the possible extension to gas mixtures, is currently being pursued.

Fig. 3–5 present a set of curves showing the variation of collision frequency and mean-free paths as a function of distance for several species under various conditions. From the curves it is evident that even at large distances from the nozzle the collision frequency remains quite high. Fig. 3 gives a set of curves calculated for argon at three reservoir pressures and illustrates the point that, for a fixed nozzle diameter, the collision frequency scales as P_0. The variations of normalised beam density as a function of the axial distance from the nozzle in nozzle diameters calculated using eqn. (2) are shown for helium and nitrogen in Fig. 6. For the machine used in this study the particle density for a helium jet 3.9 cm from the nozzle corresponds to a beam pressure of 3×10^{-3} Torr for a stagnation pressure of 1 atm. Realistic values for

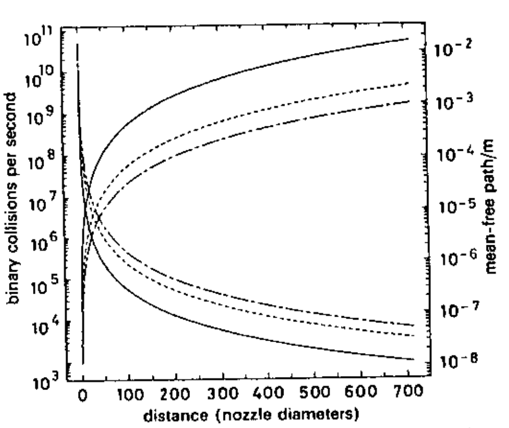

Fig. 3 Collision frequencies and mean-free paths as a function of stagnation pressure for beams of Ar for a source temperature of 300 K. (——) $P_0 = 1$ atm, (---) $P_0 = 5$ atm, (—-—) $P_0 = 10$ atm

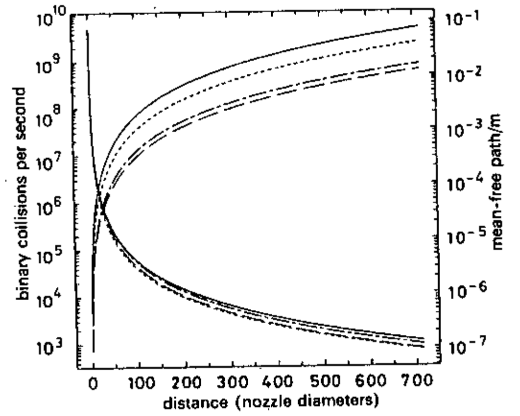

Fig. 4 Calculated collision frequencies and mean-free paths for He (——), Ne (---), Ar (—-—) and Kr (——). $P_0 = 1$ atm, $T_0 = 300$ K

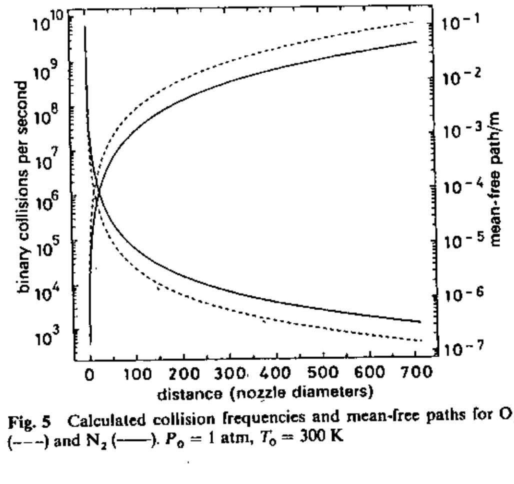

Fig. 5 Calculated collision frequencies and mean-free paths for O_2 (---) and N_2 (——). $P_0 = 1$ atm, $T_0 = 300$ K

Table 2 Comparison between measured and calculated TOF parameters

system	P_0/atm	T_0/K	u_{calc}/m s^{-1}	$T_{\parallel,calc}$	u_{expt}/m s^{-1}	$T_{\parallel,expt}$
He	1	300	1745	5.8	1740	5.5
Ne	1	300	781	3.3	773	3.2
Ar	1	300	557	1.4	552	1.3
Kr	1	300	385	1.1	381	1.1
H_2	4	300	2493	5.9	2659	4.4
N_2	1	300	753	14.6	753	13.1

beam density as a function of axial distance from the nozzle, are an essential prerequisite for the determination of collision cross-sections from crossed beam experiments.

Collision frequencies in a bulb were calculated in an analogous manner to those in the beam according to the integral (7), using a Maxwellian speed distribution function for $g(c_r)$. A plot of the ratio $\nu_{beam}:\nu_{bulb}$ as a function of the mean kinetic temperature T_m is given in Fig. 7 for argon. The oscillations in the curve result only from the integration procedure used and also reflect the greater density of points calculated for the lower temperatures. The collision frequency in the beam is always lower than that in the bulb, although the ratio does not remain constant at a value of *ca.* 1/2 as originally suggested by Lubman. The major reason for this difference comes from our use of realistic, energy-dependent, collision cross-sections in place of constant hard-sphere values. Our calculations indicate that the size of $\sigma(c_r)$ can change by a factor of as much as 5–10 during the course of a typical expansion starting at room temperature. The reason that $\nu_{beam} < \nu_{bulb}$ is due to the fact that the magnitude of the relative velocity between two particles in a supersonic beam is significantly less than that between two particles in a bulb. Quite clearly atoms and molecules can never be taken as being completely isolated in a supersonic beam simply because of the finite width of the velocity distribution, causing some particles to overtake and collide with others. What is of importance however, is whether or not the beam species are suitably well isolated on the timescale relevant to the experiment of interest.

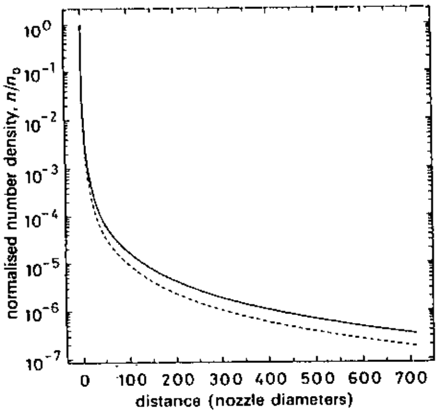

Fig. 6 Calculated normalised number density profiles for He (——) and N_2 (– – –)

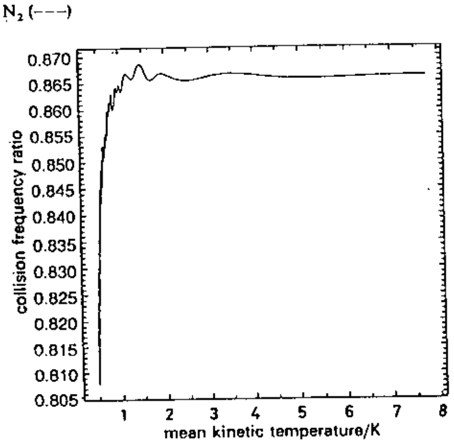

Fig. 7 $\nu_{beam}:\nu_{bulb}$ as a function of T_m

The comparison between experimentally determined and calculated time-of-flight parameters demonstrated for the inert gases and the diatomics H_2 and N_2 in Table 2 and the agreement found between the rotational–translational coupling parameter for N_2 with the mean literature value afford us some confidence that the collision frequencies and particle densities calculated from the thermal conduction model using realistic collision cross-sections and interaction potentials closely reflect the characteristics of a skimmed supersonic beam along the axis.

References

1 P. W. Harland, H. S. Carman, L. F. Phillips and P. R. Brooks, *J. Chem. Phys.*, 1990, **93**, 1089.
2 H. S. Carman, P. W. Harland and P. R. Brooks, *J. Phys. Chem.*, 1986, **90**, 944, and references therein.
3 B. B. Hamel and D. R. Willis, *Phys. Fluids*, 1966, **9**, 829.
4 V. S. Troitskii, *Soc. Phys. JETP (Engl. Transl.)*, 1962, **14**, 281.
5 D. M. Lubman, C. T. Rettner and R. N. Zare, *J. Phys. Chem.*, 1982, **86**, 1129.
6 H. C. W. Beijerinck and N. F. Verster, *Physica C*, 1981, **111**, 327.
7 C. E. Klots, *J. Chem. Phys.*, 1980, **72**, 192.
8 R. J. Gallagher and J. B. Fenn, *J. Chem. Phys.*, 1973, **60**, 3492.
9 J. B. Anderson and J. B. Fenn, *Phys. Fluids*, 1965, **8**, 780.
10 J. P. Toennies and K. Winkelmann, *J. Chem. Phys.*, 1977, **66**, 3965.
11 A. H. M. Habets, PhD Thesis, Eindhoven University of Technology, Eindhoven, 1977.
12 H. Haberland, U. Buck and M. Tolle, *Rev. Sci. Instrum.*, 1985, **56**, 1712.
13 D. R. Willis, B. B. Hamel and J. T. Lin, *Phys. Fluids*, 1972, **15**, 573.
14 R. Engelhardt, T. Lorenz, K. Bergmann, T. Mietzner and A. Palczewski, *Chem. Phys.*, 1985, **95**, 417.
15 F. J. Smith and R. J. Mann, *J. Chem. Phys.*, 1964, **41**, 3560, and references therein.
16 J. O. Hirschfelder, C. F. Curtiss and R. B. Bird, *Molecular Theory of Gases and Liquids*, John Wiley, Chichester, 1954.
17 K. T. Tang and J. P. Toennies, *J. Chem. Phys.*, 1977, **66**, 1496.
18 B. D. Weaver and D. R. Frankl, *Rev. Sci. Instrum.*, 1987, **58**, 2115.
19 W. S. Young, *Rev. Sci. Instrum.*, 1973, **44**, 715.
20 L. K. Randeniya, X. K. Zeng, R. S. Smith and M. A. Smith, *J. Chem. Phys.*, 1989, **93**, 8031.

Paper 0/04880A; *Received* 30*th October*, 1990

Observation of structure in transition state spectra of the bimolecular reactions $K+XNa \rightarrow KX+Na$ ($X=Br,Cl$)

Michael D. Barnes,[a] Philip R. Brooks, R. F. Curl, Jr., and Peter W. Harland[b]
Chemistry Department and Rice Quantum Institute, Rice University, Houston, Texas 77251

(Received 27 December 1990; accepted 31 January 1991)

Experimental studies of chemical reaction dynamics usually attempt to draw inferences about the reaction process by monitoring the product states formed from reactant states prepared as specifically as possible. Recently, several experimental techniques have been developed[1] to observe directly the spectra of species in the process of chemical reaction. The early studies[2] in this field focused primarily on establishing the possibility of making experimental observations of such "transition region species" (TRS). Little new insight was obtained into the reaction event, largely because the spectra were essentially featureless. It was widely believed that featureless spectra would always result for bimolecular reactions because it seemed impossible to avoid averaging over a wide range of impact parameters.

Photodissociation or "half-collision" experiments avoid such averaging by preparing a dissociative state in a known geometry. The beautiful experiments of Kinsey,[3] Neumark,[4] and Zewail[5] have produced specific information which can be interpreted in terms of the dynamics of the dissociation process. In a nice extension of these photodissociation experiments, Bernstein and Zewail[6] have observed the time evolution of OH formed by reacting CO_2 with H atoms prepared by Wittig's technique[7] of photodissociating the van der Waals molecule, $HI \cdots CO_2$. This latter approach has the significant advantage of reducing the averaging over the impact parameter but this advantage is obtained at the expense of constraining the geometry of the reaction system in ways which may not be representative of free space reactions.

Because most chemical reactions involve a full collision with its attendant range of impact parameters, it seems important to develop experiments which probe full bimolecular reaction processes. Therefore, we have continued studies of transition region species formed in bimolecular collisions, in spite of their inherent limitations, in hopes of obtaining some insights into the reactive collision which might enlarge and complement that obtained in the photodissociation experiments. We report here spectra for the KClNa and KBrNa bimolecular transient systems. We find that the spectra of the TRS obtained are not featureless: clear structure is observed in the TRS spectrum in the bromide case.

The reactions studied are $K + XNa \rightarrow [KXNa]^{\ddagger} \rightarrow KX + Na$. In the experiment, the transition region species, $[KXNa]^{\ddagger}$, are continuously produced in crossed beams of K and NaX. A tiny fraction of the TRS's are electronically excited by a cw dye laser to $[KXNa]^{\ddagger *}$. This species decomposes to give either $KX + Na^*$ or $K^* + XNa$. Decay into the electronically excited reactive channel is monitored by measuring the intensity of the Na^* emission at 589 nm.

The apparatus is similar to that previously described,[8] with several changes which have improved the stability and run-to-run reproducibility. Quasieffusive beams of K and NaX ($X = Cl$ or Br) were crossed inside the extended cavity of a cw dye layer where the circulating power density was estimated to be ≈ 3 kW/cm^2. Light from the crossing region was collimated by an f/1.5 achromat, passed through an interference filter with a bandwidth of 0.3 nm centered at 589.0 nm (passing only one Na D line), and pulse counted with a cooled C31034 PMT. Excitation by dye fluorescence of Na atoms present as impurities in both beams is eliminated by placing a Na heat pipe oven inside the cavity. Each of the 3 beams was separately flagged and data was acquired in all 8 beam-on, beam-off combinations. The "3-beam" signal (3BS) is the signal with all three beams on after contributions from processes involving all 0, 1, and 2 beam signals are subtracted. The 3BS can be thought of as a three-body process

$$K + XNa + h\nu \rightarrow KX + Na^*, \tag{1}$$

and the "3-beam" signals are normalized by dividing by each beam intensity to yield the three-body analogue of a cross section.

The excitation spectra for KXNa are shown in Fig. 1, where the normalized 3BS (Na^* fluorescence intensity at 589 nm) are plotted vs the excitation laser wavelength. It is immediately apparent that the spectrum for KBrNa is different from that for KClNa. Our earlier Cl spectrum appeared rather featureless, but with improved beam stability we observe a minimum near 600 nm. (The collective data[8] suggest a broad maximum ≈ 660 nm.) For the Br case, a minimum near 600 nm is again observed, but the maximum is ≈ 608 nm and is well resolved.

In previous work on the K + NaCl system a number of tests were performed to eliminate possible artifact sources of the 3-beam signal. Experiments such as magnetic (Stern–Gerlach) deflection experiments[9] allowed us to rule out the possibility that Na^* arose from reactions of laser-excited K_2. We concluded from these tests that we had

---

[a] Robert A. Welch Foundation Predoctoral Fellow.

[b] Permanent address: Chemistry Department, University of Canterbury, Christchurch, New Zealand.

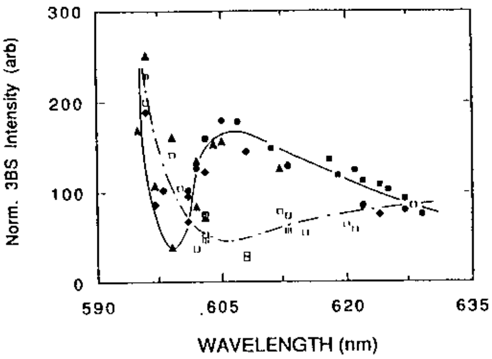

FIG. 1. Normalized 3-beam signals at the Na D line 589 nm in the NaCl + K and NaBr + K systems as a function of excitation wavelength. The dark points are bromide system signals and the open points are chloride system signals. The different point symbols correspond to data obtained on different runs. The curves are drawn only for illustration.

observed excitation of [KClNa].[‡] In going from the chloride to the bromide system, nothing is changed except the salt beam; therefore, only artifacts which might involve changes in species in the salt beam need to be considered. There is no salt beam photoluminescence at the Na D line for either system. The concentration of Na atoms in the NaBr beam is observed by using direct excitation to be less than that in the NaCl beam. It was verified that the 3-beam signal in K + NaBr is from Na* (as had already been established for K + NaCl) by tilting the interference filter which changes the wavelength transmitted. We therefore believe that the Br spectrum in Fig. 1 is that of [KBrNa].[‡] Experiments were run alternating the salts and the spectra were found to be reproducible. The Br and Cl signals shown in Fig. 1 are obtained under similar conditions[10] permitting meaningful comparison of the signals from the two systems.

The cross-sections for the dark reactions, $K + XNa \rightarrow KX + Na$, are large with reaction occurring on every gas kinetic collision without activation barriers. Thus the systems move quite freely on the $1\,^2A'$ ground state potential energy surface (pes) exploring a wide range of configurations in the reaction process. The laser field can induce transitions to excited pes's. There are two low-lying excited surfaces, the $2\,^2A'$, and $3\,^2A'$, but it is believed that only the $3\,^2A'$ is accessible at the wavelengths used here (600–700 nm). In the Born–Oppenheimer, stationary phase approximation, for a given instantaneous nuclear configuration $\{r_i\}$, the reacting system can absorb a photon only if the laser is tuned very near the frequency, $\nu = h^{-1}(V_3\{r_i\} - V_1\{r_i\})$. Equivalently, for a given laser frequency, systems will be excited only if they pass through nuclear configurations $\{r_i\}$ on the $1\,^2A'$ pes which are resonant with the laser. Once excited to the $3\,^2A'$ surface, the system can evolve to either K* or Na*. The latter (reactive) process is observed by monitoring fluorescence from the Na*.

The structure shown in Fig. 1 has survived in spite of averaging over thermal distributions, orientations, and impact parameters and clearly differs for the two chemical systems. Such a spectral feature could arise from (a) a region of the pes which is traversed by a reasonable fraction of collisions where the potential energy surfaces are relatively parallel (so that many nuclear configurations can absorb at basically the same frequency) or from (b) a region of the lower potential surface where the evolving system lingers, increasing the probability of transition.[11]

The 3-beam signal rises steeply in both systems as the laser is tuned towards the Na atom D line. This might arise from excitation of the newly formed Na atom in the exit channel while it is still perturbed by the salt molecule, but we regard this as only a tentative conclusion. These signals could also be due to collision-broadened absorption of Na atoms (impurities in both beams), although our signal estimates for this process are much smaller than the signals observed. If the rise near the D line is associated with excitation of the TRS in the exit channel, the interaction shifting the frequency from the D line center is most likely due to dipole-induced dipole or dispersion effects differing only mildly between systems. Indeed, the normalized signals are observed to differ only slightly. Such features can be classified as type (a) arising from parallel surfaces.

The maxima in the spectra (near 608 for the Br and ≈660 for Cl) clearly depend on the reaction and probably come from excitation in the heart of the reaction region. At present it is unclear whether they can be better characterized as representing type (a) behavior (parallel pes's) or by type (b) behavior (ground state dynamics). The $M + M'X$ exchange reactions are known to occur via collision complexes with lifetimes on the order of the rotational periods[12] and stable MXM' species have been observed experimentally[13] and predicted theoretically.[14] Trajectory calculations on ground pes's suggest[15] that some trajectories become "trapped" in snarled trajectories in limited regions of the pes and excitation from these "pools" might be expected to produce maxima in the spectrum.

For the KClNa reaction, surface hopping trajectory calculations[16] of the Na* excitation spectrum have been carried out and do not predict a maximum to the red of the Na D lines, but instead show only a monotonic decline in the probability of forming Na* as the wavelength is tuned to the red. It is not known what modifications, if any, of the pes's used in these calculations could result in the prediction of a maximum. An interesting conjecture is that the maxima observed might arise through collisional nonadiabatic transitions to the $2\,^2A'$ electronic surface.[17] Once accessed, systems in the $2\,^2A'$ state would be trapped for a considerable time with a consequent increase in excitation probability.

It thus appears that the blue feature of the excitation spectrum seems understandable from simple theory, but that the origin of the red feature is as yet unknown. Observation of clear structure in the NaBr + K system brings renewed hope that these experiments will provide useful information on bimolecular systems in the process of reaction.

Support by the National Science Foundation and the Robert A. Welch Foundation is gratefully acknowledged.

[1] P. R. Brooks, R. F. Curl, and T. C. Maguire, Ber. Bunsen-Ges. Phys. Chem. **35**, 109 (1982); H. J. Foth, J. C. Polanyi, and H. H. Telle, J. Phys. Chem. **86**, 5027 (1982).

[2] P. R. Brooks, Chem. Rev. **88**, 407 (1988).

[3] D. Imre, J. L. Kinsey, A. Sinha, and J. Krenos, J. Phys. Chem. **88**, 3956 (1984).

[4] S. E. Bradforth, A. Weaver, D. W. Arnold, R. B. Metz, and D. M. Neumark, J. Chem. Phys. **92**, 7205 (1990), and references cited therein.

[5] L. R. Khundkar and A. H. Zewail, Annu. Rev. Phys. Chem. **41**, 15 (1990) and references cited therein.

[6] N. F. Scherer, L. R. Khundkar, R. B. Bernstein, and A. H. Zewail, J. Chem. Phys. **87**, 1451 (1987).

[7] S. Buelow, G. Radhakrishnan, J. Catanzarite, and C. Wittig, J. Chem. Phys. **83**, 444 (1985).

[8] T. C. Maguire, P. R. Brooks, R. F. Curl, Jr., J. H. Spence, and S. Ulvick, J. Chem. Phys. **85**, 844 (1986).

[9] S. Kaesdorf, P. R. Brooks, R. F. Curl, Jr., J. H. Spence, and S. Ulvick, Phys. Rev. A **34**, 4418 (1986).

[10] The NaBr source temperature is 1150 K vs 1300 K for NaCl.

[11] Similar conclusions arise in the quasi-static theory of atomic line broadening. Intensity in the wings of a spectral line of atom A which are collision broadened by B are due to transitions from one state of the AB molecule to another. Features (called satellites) on the spectral lines arise when the potential energy curves are parallel, and the intensity observed at a particular frequency $\nu = [V_1(r) - V_2(r)]/h$ depends on the time the colliding systems spend at a particular distance r.

[12] W. B. Miller, S. A. Safron, and D. R. Herschbach, Discuss Faraday Soc. **44**, 108 (1967).

[13] K. I. Peterson, P. D. Dao, and A. W. Castleman, Jr., J. Chem. Phys. **79**, 777 (1983); M. M. Kappes, P. Radi, M. Schär, and E. S. Schumacher, Chem. Phys. Lett. **113**, 243 (1985).

[14] (a) A. C. Roach and M. S. Child, Mol. Phys. **14**, 1 (1968); (b) W. S. Struve, *ibid.* **25**, 777 (1973); (c) K. Yamashita and K. Morokuma, J. Phys. Chem. **92**, 3109 (1988).

[15] G. H. Kwei, B. P. Boffardi, and S. F. Sun, J. Chem. Phys. **58**, 1722 (1973).

[16] K. Yamashita and K. Morokuma, J. Chem. Phys. **91**, 7477 (1989).

[17] S. K. Neoh and D. R. Herschbach, J. Chem. Phys. **63**, 1030 (1975).

Reprinted from The Journal of Physical Chemistry, 1991, *95*.
Copyright © 1991 by the American Chemical Society and reprinted by permission of the copyright owner.

Effects of Molecular Orientation on Electron-Transfer Collisions

Peter W. Harland,[†] Howard S. Carman, Jr.,[‡] Leon F. Phillips,[†] and Philip R. Brooks[*]

Department of Chemistry & Rice Quantum Institute, Rice University, Houston, Texas 77251

(Received: February 12, 1991)

K^+ ions have been detected from the intersection of a beam of K atoms (5–30 eV) with beams of various simple molecules, such as CH_3Br and CF_3Br, which had been oriented prior to the collision. Production of ions in the collision is found to be highly dependent on orientation. The effect is most pronounced near threshold (~5 eV) and almost disappears at higher (30 eV) energies. Attack at the "reactive" halogen end produces the most ions, *regardless* of the polarity of that end. For each molecule, the reactive end seems to have the lower threshold energy. These observations may be a result of the electron being transferred to a specific end of the molecule, but the experiments measure only the net result of an electron transfer *followed* by the separation of the ions. Whether or not electron jump per se depends on orientation is still an open question, but we are able to qualitatively interpret the experimental results as being due to interactions between the ions as they separate in the exit channel. Most of the negative molecular ions dissociate, ejecting a halogen X^- in the direction of the (oriented) molecular axis. If the X end is oriented away from the incoming K atom, the ejected X^- will travel in the same direction as the K^+, making the electron more likely to return to the K^+ ion and reducing the K^+ signal in this unfavorable orientation.

I. Introduction

"Chemical intuition", as well as a growing amount of direct experimental observation, tells us that chemical reaction depends on the orientation of the molecules involved. By "orientation" we mean a spatial configuration where one end of a molecule can be distinguished from another. Although reactive species differentiate between ends by not reacting with the "wrong" end, we have little experimental guidance for what constitutes the "right" end because most experiments include all possible orientations during collision and isolation of orientation effects has not been possible.

Several molecular beam techniques have arisen to prepare reagent molecules in known orientations.[1] The simplest (and most recent) is the "brute force" method of merely applying a strong electric field on extremely cold polar molecules,[2] but this method is highly restrictive.[3] Most experiments so far have been done with symmetric top molecules, such as CH_3Br. The orientation is defined by a weak electric field because these molecules precess in an applied electric field in the same way a child's top precesses in a gravitational field. Each molecule is oriented. Even though all orientations are present in a beam, passing the beam through an inhomogeneous electric field filters out molecules in orientations such that $\langle \cos\theta \rangle > 0$, where θ is the angle between the dipole moment and electric field. The molecules passed by the inhomogeneous field have $\langle \cos\theta \rangle < 0$, and are reacted with an atomic beam in a weak uniform electric field. The weak field is applied parallel or antiparallel to the relative velocity and determines which end of the molecule is presented to the atoms.

Orientation effects are large and varied. For example, at thermal energies, CH_3I reacts with K or (Rb^4) preferentially on the I end, but CF_3I and CF_3Br react at both ends, with different angular distributions. The "harpoon" model[5] of electron transfer has been invoked[6] to describe the CF_3I reaction, and this nicely explains the different angular distributions observed in the "heads" and "tails" orientations. In this model, the K is expected to donate an electron (the harpoon) to the CF_3I, followed by explosive decomposition of the CF_3I^-, after which the Coulomb attraction causes the K^+ and I^- to combine:

$$K + CF_3I \rightarrow K^+ + CF_3I^- \quad \text{electron transfer} \qquad (1)$$

$$CF_3I^- \rightarrow CF_3 + I^- \quad \text{ion dissociation} \qquad (2)$$

$$I^- + K^+ \rightarrow KI \quad \text{ionic recombination} \qquad (3)$$

Because the cross section for reaction at the two ends was roughly equal, step 1 was assumed to be independent of orientation. The dependence on orientation was assumed to be in step 2 because the I^- would be ejected in the known direction of the molecular dipole. After we accounted for the momentum of all the partners, this mechanism qualitatively reproduced the experimental angular distribution, not only for heads and tails orientations, but also for sideways orientations.[7]

For the K + CF_3Br reaction the angular distributions are in qualitative accord with this harpoon model, but the reactive probability is less at the tails (CF_3) end, leading us to speculate[8] that the electron-transfer process might be orientation dependent.

Electron-transfer processes are important to many different kinds of reactions as well as to the harpoon reaction, and we have begun to investigate how orientation might affect electron transfer. We have now studied several reactions, including K + CF_3X (X = I, Br), at energies of a few (5–30) eV, so that the ions move fast enough that they can escape from their Coulomb attraction and be detected directly. Collisional ionization has been studied in some detail previously[9] (for unoriented molecules) and the products of these[10] fast-atom collisions are predominantly K^+, CF_3, and X^-. In the experiments reported here, we orient symmetric top molecules prior to collision, and we detect the K^+ ion.

[†] Permanent address: Chemistry Department, University of Canterbury, Christchurch, New Zealand.

[‡] Permanent address: Chemical Physics Section, Health & Safety Research Division, Oak Ridge National Laboratory, P. O. Box 2008, Oak Ridge, TN 37831.

(1) For reviews see: (a) Brooks, P. R. *Science* 1976, *193*, 11. (b) Bernstein, R. B.; Herschbach, D. R.; Levine, R. D. *J. Phys. Chem.* 1987, *91*, 5365. (c) Parker, D. H.; Bernstein, R. B. *Annu. Rev. Phys. Chem.* 1989, *40*, 561. (d) Stolte, S. In *Atomic and Molecular Beam Methods*; Scoles, G., Ed.; Oxford: New York, 1988; Vol. 1, p 631.

(2) (a) Loesch, H. J.; Remscheid, A. *J. Chem. Phys.* 1990, *93*, 4779. (b) Friedrich, B.; Herschbach, D. R. *Z. Phys.*, in press.

(3) This method can be used if $E_{rot} \ll \mu E$ and requires either very cold molecules or very high fields, but it is the only method available for orienting Σ-state molecules. For these Σ molecules, various optical methods have been used to produce *polarization*, where the plane of rotation is selected but one end is not distinguished from the other (described in ref 1b).

(4) Chakravorty, K. K.; Parker, D. H.; Bernstein, R. B. *Chem. Phys.* 1982, *68*, 1. These latter experiments have been reinterpreted in terms of a steric cone of nonreaction of ~53°: Choi, S. E.; Bernstein, R. B. *J. Chem. Phys.* 1985, *83*, 4463.

(5) Herschbach, D. R. *Adv. Chem. Phys.* 1966, *10*, 319.

(6) Brooks, P. R. *Faraday Discuss. Chem. Soc.* 1973, *55*, 299.

(7) Brooks, P. R.; McKillop, J.; Pippen, H. G. *Chem. Phys. Lett.* 1979, *66*, 144.

(8) Carman, H. S.; Harland, P. W.; Brooks, P. R. *J. Phys. Chem.* 1986, *90*, 944.

(9) For reviews of collisional ionization, see: (a) Kleyn, A. W.; Los, J.; Gislason, E. A. *Phys. Rep.* 1982, *90*, 1. (b) Lacmann, K. I. *Potential Energy Surfaces*; Lawley, K. P.; Ed.; Wiley: New York, 1980, p 513. (c) Baede, A. P. M. *Adv. Chem. Phys.* 1975, *30*, 463. (d) Los, J.; Kleyn, A. W. *Alkali Halide Vapors*; P. Davidovits, P., McFadden, D. L., Eds.; Academic Press: New York, 1979; p 279.

(10) For collision with K: (a) McNamee, P. E.; Lacman, K.; Herschbach, D. R. *Faraday Discuss. Chem. Soc.* 1973, *55*, 318. (b) Kleyn, A. W.; Hubers, M. N.; Los, J. 10th ICPEAC Abstracts of Papers, Paris, 1977; p 1162. For collision with other alkali metals: (c) Compton, R. N.; Reinhardt, P. W.; Cooper, C. D. *J. Chem. Phys.* 1978, *68*, 4360. (d) Tang, S. Y.; Mathur, B. P.; Rothe, E. W.; Reck, G. P. *J. Chem. Phys.* 1976, *64*, 1270.

0022-3654/91/2095-8137$02.50/0 © 1991 American Chemical Society

Preliminary results have been obtained for CH_3I and CF_3I.[11,12] Here we report on a survey of related molecules, CH_3X (X = F, Cl, Br, and I); CF_3Y (Y = Cl, Br, and I); *t*-butyl Z (Z = Cl, Br); and CX_3H (X = Cl, F). We find in all cases a strong dependence on orientation at energies near threshold, and this effect decreases as the energy is increased. *Regardless* of the polarity of the dipole, the end producing the most ions is the "heads" end (the end with the most labile halogen). These results may stll be understood in terms of the orientation of the dissociating molecular ion.

II. Experimental Section

The experimental apparatus and procedure for data collection have been previously discussed in paper I (ref 12), and we provide here only a brief summary of the experiment.

A beam of fast (≈ 5–30 eV) K atoms intersects a beam of symmetric top molecules RX, such as CH_3Br. Molecules in the molecular beam are oriented before the collision by passing them through a series of inhomogeneous and uniform electric fields. Collisions in this energy range are sufficiently energetic to ionize the reagents, and the negative molecular ions usually dissociate, giving as products K^+, X^-, and R, where X is a halogen and R an alkyl radical. The orientation of the molecule with respect to the incoming K atom is controlled by applying a weak (≈20 V/cm) field in the collision zone. The positive K^+ ions are detected by one of two channeltrons, depending on the polarity of the collision zone.

Because of intensity limitations, neat beams of RX were used, with translational temperatures ≈45 K. Individual *JKM* states are not resolved for the molecules, and the high voltage hexapole field acts as a filter to pass molecules having negative values of $\langle \cos \theta \rangle = MK/J(J+1)$, where *J*, *K*, and *M* are the standard symmetric top quantum numbers.[13] In the collision zone each molecule is oriented and precesses about the applied electric field, which is either parallel or antiparallel to the incoming atom. A distribution of precession angles results, but all of the molecules precess with their positive ends directed toward the positive field plate. (This high-energy configuration is the one passed by the hexapole field.) The orientation of the molecule with respect to the incoming atoms is reversed by reversing the direction of the applied electric field. Representative distributions of molecular orientations are shown in paper I.

K^+ ions were detected by different channeltrons, depending on the direction of the applied field. Thus, comparison between one orientation of the molecule and the other requires that allowance be made for different ion collection efficiencies and different multiplication efficiencies. As described in paper I, this comparison is accomplished by using as a reference K^+ formed in collision with SF_6. Since SF_6 is a spherical top, no orientation effects are possible, and the different experimental signals directly account for the ion collection and detection efficiency. The relative detection efficiency $F(\epsilon)$ is measured at each energy, and measurements of $F(\epsilon)$ are interspersed with signal measurements to minimize effects due to nonreproducible contact potentials on field electrodes and multipliers. The relative signal due to the oriented molecules $S'(V)$ is the (hexapole field on) − (hexapole field off) signal difference $S(V)$ corrected for the multiplier efficiencies at beam energy ϵ: $S'(V)_{180} = S(V)_{180}$ and $S'(V)_0 = F(\epsilon)S(V)_0$.

III. Results

Relative signals for several representative molecules are shown in Figure 1. For each molecule there is a clear difference between the 180° and 0° orientations. As in paper I, the "180°" orientation corresponds to having the negative plate of the uniform field closest to the incoming K atom, and the "0°" orientation corresponds to having the positive plate of the uniform field closest to the incoming K atom. As previously mentioned, the oriented molecules are in high-energy states, so the positive end of the molecule points towards the incoming K atom in the 0° orientation.

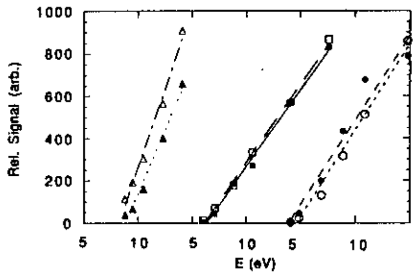

Figure 1. Relative signal vs center-of-mass energy at low energies for *t*-BuCl (triangles), CH_3Br (squares), and CF_3Br (circles). Filled symbols correspond to 0° orientation, and open symbols to 180° orientation. Lines are least-square fits to the data.

TABLE I: Molecules Reacted with Fast K Atoms

molecule	polarity[a] +···−	more reactive orientation	more reactive end	approx. threshold, eV 180°	approx. threshold, eV 0°
CH_3I[b]	$CH_3\cdots I$	180°	I	4.7	4.9
CH_3Br	$CH_3\cdots Br$	180°	Br	6.1	6.3
CH_3Cl[c]	$CH_3\cdots Cl$	180°	Cl	8.6	8.7
CH_3F[d]c	$CH_3\cdots F$	180°	F	7.4	7.8
CF_3I[b]	$I\cdots CF_3$	0°	I	4.8	4.5
CF_3Br	$Br\cdots CF_3$	0°	Br	5.6	5.0
CF_3Cl	$Cl\cdots CF_3$	0°	Cl	7.4	7.0
t-BuBr[c]	*t*-Bu···Br	180°	Br	5.2	5.3
t-BuCl	*t*-Bu···Cl	180°	Cl	8.3	8.8
CCl_3H[c]	$H\cdots CCl_3$	180°	Cl	6.7	6.7
CF_3H[c]	$H\cdots CF_3$	180°	F		

[a] Polarities are determined from electronegativity difference and dipole moment trends in homologous series and thermal energy reactivity of oriented molecules. See ref 6. The polarity of CF_3I has been directly measured (Gandhi, S. R.; Bernstein, R. B. *J. Chem. Phys.* **1988**, *88*, 1472), and the I end is found to be positive. [b] Paper I. [c] Extrapolation to threshold is unreliable.

For CH_3Br and *t*-BuCl, signals for the 180° orientation are greater, and the *negative* end (Br or Cl) is the more reactive. Signals for the 0° orientation are greater for CF_3Br, and the *positive* (Br) end is the more reactive. The orientation of greatest reactivity is thus dependent upon the molecule being studied and not merely a manifestation of an electrical artifact.

As shown also in Figure 1, linear extrapolation of the signals to zero suggests that there is a difference in threshold for the two orientations. This difference is most pronounced for *t*-BuCl but is apparent in other molecules as well. In Table I are listed the molecules reported here, together with their polarities, the end observed here to be more reactive in forming ions, and our estimate of the thresolds for each orientation. We regard these thresholds as very tentative: these preliminary data are quite noisy and different values may be obtained depending on which points are emphasized. Moreover, the energy scale has not been calibrated. It does seem, however, that in almost every case the more reactive end has a lower threshold.

Representative relative cross sections (signal/K intensity) for CH_3Br and CF_3Br are plotted in Figure 2. The difference in molecular orientation is still apparent and persists to some 15 or 20 eV. The cross section for SF_6 is displayed for comparison. Other molecules in Table I show similar behavior, although CCl_3H and CF_3H peak at higher energy.

The effect of molecular orientation is masked by the energy dependence of the cross section and the strong variation of the K beam intensity with energy. In order to decouple the dependence of orientation from this dependence on energy, we plot in Figures 3 and 4 the normalized signal difference, *G*, where $G \equiv (S'_{180} -$

---

[11] Harland, P. W.; Carman, H. S.; Phillips, L. F.; Brooks, P. R. *J. Chem. Phys.* **1989**, *90*, 5201.

[12] Harland, P. W.; Carman, H. S.; Phillips, L. F.; Brooks, P. R. *J. Chem. Phys.* **1990**, *93*, 1089 (referred to as paper I).

[13] Townes, C. H.; Schawlow, A. L. *Microwave Spectroscopy* Dover: New York, 1975. We use the convention that the dipole points towards the positive charge, but regardless of convention the molecules transmitted by the hexapole field are in high-energy states, so the positive end of the dipole points toward the positive field plate.

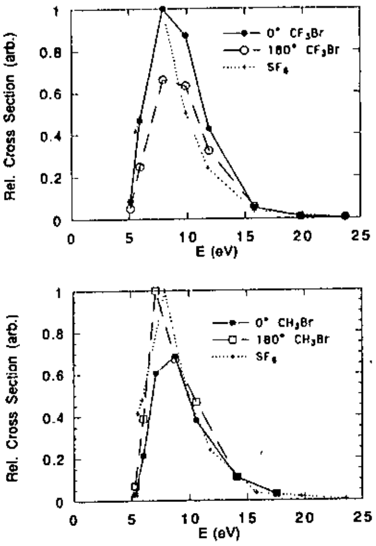

Figure 2. Relative cross section vs. collision energy: (a, Top) CF$_3$Br; (b, Bottom) CH$_3$Br. Filled symbols correspond to 0° orientation, and open symbols to 180° orientation. Dotted lines are experimental values for SF$_6$ normalized to the peak and are included for comparison.

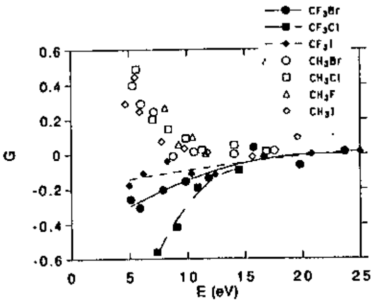

Figure 3. Relative orientation effect (difference/sum) $G = [S'_{180} - S'_0]/[S'_{180} + S'_0]$ vs energy for various molecules. Curves are drawn through data points for ease in identifying trends.

$S'_0)/(S'_{180} + S'_0)$. This plot makes the effect of orientation quite apparent and graphically illustrates the data entries in Table I. G is positive for all molecules except for the trifluoro compounds, for which G is negative. In all cases, $|G|$ is largest near threshold and decreases to zero for energies $\approx$15 eV. For molecules with positive G, collision with the *negative end* of the molecule is more likely to yield ions.

G must lie in the range $-1 \leq G \leq +1$, and the maximum value of $|G|$ for some molecules is found to be greater than 0.5. This is especially surprising in view of the distribution of molecular orientations present in the collision zone. Semiclassically, the molecules precess in a cone of half angle θ about the applied electric field lines where $\langle \cos\theta \rangle = MK/J(J+1)$. Filtering the beam through the hexapole electric field results in the removal of positive values of $\langle \cos\theta \rangle$, but a distribution of negative values of $\langle \cos\theta \rangle$ still results and this is discussed in paper I. Very roughly speaking, this distribution peaks for $\langle \cos\theta \rangle \approx -0.2$, corresponding to a cone of half-angle $\approx$100°, or 80° if the direction is reversed.[14]

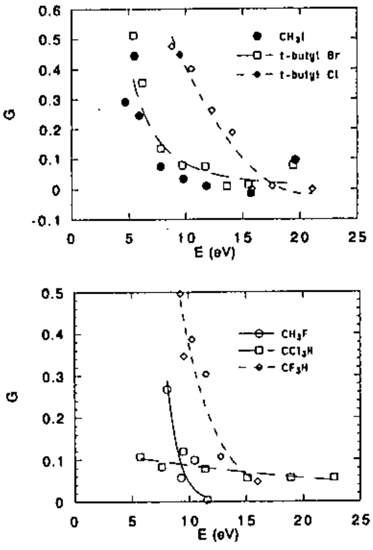

Figure 4. Relative orientation effect (difference/sum) $G = [S'_{180} - S'_0]/[S'_{180} + S'_0]$ vs energy for various molecules. Curves are drawn through data points for ease in identifying trends.

In any case, very few molecules are completely oriented, yet the experimental effect is large. This suggests that some unfavorable orientations are completely unreactive, and a similar conclusion was reached for the thermal-energy reaction of Rb with CH$_3$I.[4]

IV. Discussion

The data displayed in Table I and Figures 3 and 4 clearly show that the probability of ion formation depends on the orientation of the target. But the data cannot be rationalized by simply claiming that the electron hops to the positive end of the molecular dipole, because the experiments conclusively show that the *negative* end of most molecules is the most reactive. (The direct experimental observation is the polarity of the end that is more reactive, and we must use dipole moment information to infer which end that is.)

We emphasize that the experiments tell us the polarity of the end that, when attacked by a fast K atom, yields the most positive ions. These processes can be regarded as electron-transfer processes, but we do not directly observe which end of the molecule receives the electron. We observe the entire process of the electron jumping followed by the ions separating. The more reactive end of the molecule must somehow maximize the likelihood of an electron jumping followed by the ions separating from one another. The end of the molecule that receives the electron can, at best, only be *inferred* from the experiments.

A. Entrance Channel Effects. At long range, we expect the interaction between the polarizable K atom and the oriented molecule to be dependent on dipole-induced dipole forces. These are always attractive because the polarity of the induced dipole is opposite in polarity to the fixed dipole. Thus, either orientation of the molecule will produce an attraction and the orientations do not differ.

Chemical "intuition", which often works best after all the facts are in, suggests that the potential must be different for different orientations as the reagents approach. The different thresholds listed in Table I support this view, although it is important to remember that these are thresholds for the entire process, not just for an initial encounter. Nevertheless, we were able to model the kinetic energy dependence of G by a line-of-centers energy dependence, $\sigma = \sigma_0(1 - E_h^*/E)$, where E_h^* (or E_t^*) was the threshold parameter for the "heads" (tails) orientation.[11] This functional form has the same qualitative dependence on energy as the data shown in Figures 3 and 4, but the E^* parameters

---

[14] A quantum-mechanical description (Stolte, S.; Chakravorty, K. K.; Bernstein, R. B.; Parker, D. H. *Chem. Phys.* **1982**, *71*, 353), of course, provides a (small) probability that the axis of the molecule will actually be pointing in the opposite direction. For the heavy molecules and comparatively high rotational temperatures used in these experiments, many rotational levels are populated, and the semiclassical picture is appropriate.

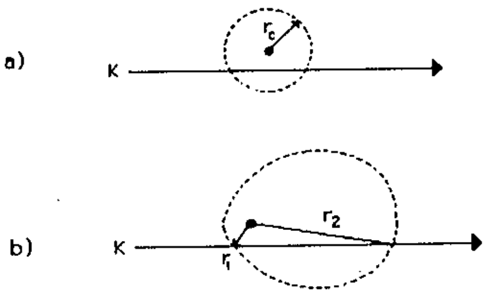

Figure 5. Electron jump radii. (a) For atoms the ionic and covalent potential curves cross at r_c (illustrated by the dashed circle) and as the K atom passes the target (I) it encounters this curve crossing twice. In order for ions to be formed, an electron must hop to the molecule at one crossing, but must not hop at the other. (b) For molecules potential surfaces cross and more dimensions need to be considered. As this figure suggests, the first crossing is closer and the electron is more likely to hop. But if the molecule dissociates along another coordinate, the second crossing (r_2) can be quite different from the first.

TABLE II: First Crossing Radii

atom	IP, eV	molecule	EA,[10] eV	r_{C_1}, Å
K	4.349	CH_3I	0.2	3.5
K		CF_3I	1.57	5.2
K		CF_3Br	0.91	4.2
K		I	3.06	11.3

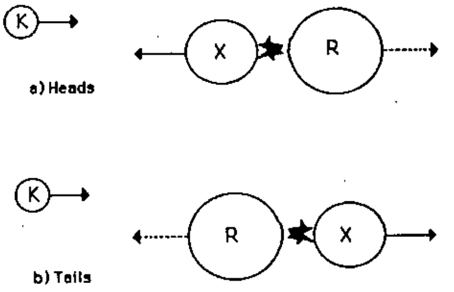

Figure 6. Schematic illustration of velocity relationships as molecular ion dissociates. (a) In the heads orientation, the X^- is ejected toward the incoming K^+ and the relative velocity is increased. (b) In the tails orientation, the relative velocity is decreased, making neutralization of the ions more likely, and this orientation produces fewer ions.

required cannot be determined by fitting the present data. The thresholds so required are not those of Table I, although the more reactive end must, of course, have the lower threshold.

We believe that orientation effects can be important in the entrance channel, but at present we are able to interpret the experiments almost solely on the basis of interactions in the exit channel. We defer further comment on the entrance channel until more facts are in.

B. Exit Channel Effects. In our earlier studies of the angular distributions of the thermal-energy reactive scattering for the reaction

$$K + (\text{oriented})\ CF_3I \rightarrow KI + CF_3 \tag{4}$$

we found[6] that the KI signal was approximately equal for reaction in the "heads" (I end) or "tails" (CF_3 end) orientations. But "heads" end attack on the molecule yielded backscattered KI, whereas "tails" attack gave forward scattered KI. We rationalized this via the "harpoon mechanism" by *postulating* that the probability of an electron hop from K to CF_3I would occur *independnt* of orientation. (This ad hoc assumption was made in an attempt to avoid introducing too many variables, but it makes the yield about the same at each end.) The electron almost certainly enters a strongly antibonding C–I orbital, and the molecular ion was expected to dissociate impulsively in less than a vibrational period. This ejects the I^- fragment in the direction of the C–I axis of the oriented molecule. The slow-moving K^+ was expected to be pulled along by the I^-, and the resulting KI was predicted to be found in the general direction of the original C–I axis. After we take into account the initial momenta of the reagents, this prediction is in reasonable accord with experiment. This same explanation successfully accounts for the completely different angular distribution that occurs for reaction 4 when the molecule is oriented sideways with respect to the incoming K beam.[7]

The angular distributions for the thermal reaction of K with oriented CF_3Br is qualitatively similar[8] to that for CF_3I, although the reaction probability is no longer equal at the two ends of the molecule. The similar angular distribution thus suggests that impulsive recoil of the CF_3 and Br^- fragments is similar to that in CF_3I^-. The different reaction probability for the two ends could be a consequence of an interference of the neighboring K^+ or might indicate that the initial electron transfer depended on orientation.

In paper I we suggested that the harpoon mechanism and impulsive dynamics also dominated these higher energy experiments. Figure 5 very schematically summarizes the discussion given in paper I. Part a shows an interaction between two *atoms*. An electron can be transferred from the K to the I at a distance r_c where the covalent and ionic potential curves cross. The crossing radius is given approximately by $r_c = e^2/\Delta E$, where ΔE = IP − EA, the difference between the ionization potential (IP) of one atom and electron affinity (EA) of the other. The probability that the electron will hop, P_a (that the transition is adiabatic), is given to a good approximation by the Landau–Zener relation.[9]

$$P_a = 1 - P_d \approx 1 - e^{-\kappa/v} \tag{5}$$

where P_d is the probability of a diabatic transition, $\kappa = (2\pi H_{IC})^2/h\Delta S$, $\Delta S = |\partial E_I/\partial_r - \partial E_C/\partial_r|$, v is the speed, and H_{IC} is the matrix element in the Hamiltonian that couples the two states.

Regardless of whether or not the electron hops at r_c, the system encounters a second curve crossing identical with the first. The probability that ions will be formed in the collision is the probability that the electron hops at one crossing and does not hop at the other, so

$$P_{ions} = 2P_aP_d = 2P_d\,(1 - P_d) \tag{6}$$

If the electron hops at the first crossing it must not hop at the second, and vice versa. For atoms the first crossing and second crossing are identical, potential curves describe the interaction, and eq 6 applies. But for molecules the second crossing can be quite different because the molecular ion can distort significantly or even dissociate (as many do) by the time the second crossing is reached. The second crossing can thus occur between *species* different from those existing at the first crossing.

Part b of Figure 5 very schematically shows the atom–molecule case. (The greater dimensionality makes even qualitative arguments more complicated, and we very roughly approximate the molecule as another atom.) The electron affinity of most molecules is smaller than that of halogen atoms, and as shown in Table II, the first crossing occurs at closer distances. Qualitative estimates for energies of a few eV suggest that at this close distance P_d = 0: the transition is completely adiabatic (the electron hops). But in order for the ions to separate, the electron must stay on the negative ion, so the second crossing must be diabatic. If the second crossing were between a bare halogen ion and a K^+, the crossing distance would be so large as to always be diabatic (P_d = 1) and *no* orientation effect would be observed. But if the second crossing were between a K^+ and a molecular ion *in the process of dissociating*, P_d would be intermediate between 0 and 1 and according to eq 5 would depend on the relative velocity. This is now orientation dependent, because the velocity acquired by the halogen ion in the dissociation process is directed either (roughly) parallel or antiparallel to the incoming K^+, depending on whether the orientation is tails or heads. In the limiting heads orientation,

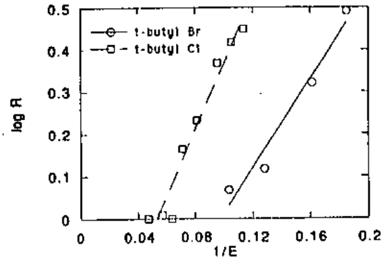

Figure 7. Plot of log R ($\equiv S_{180}/S_0$) vs $1/E$ for *tert*-butyl halides. Lines are least-square fits.

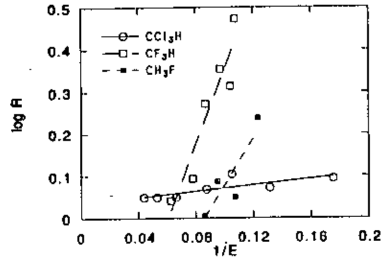

Figure 8. Plot of log R ($\equiv S_{180}/S_0$) vs $1/E$ for haloforms and methyl fluoride. Lines are least-square fits.

the halogen ion velocity is directed backward and the relative velocity is increased over the initial relative velocity. In the tails orientation the halogen ion is directed forward, decreasing the relative velocity. (See Figure 6.) The probability that the electron will be transferred back to the K^+ is thus greater for the tails orientation, as observed experimentally.

If this explanation applies and the orientation dependence is determined by the relative velocity at the second curve crossing, then the experimental data give information about this second crossing. The probability of producing ions is the probability that one crossing is adiabatic and the second is diabatic. For molecules (at a few eV) the first crossing is almost completely adiabatic, $P_a = 1$, and $P_{ions} = P_d$, where P_d is evaluated at the second crossing. The probability of making ions in the heads orientation is thus the velocity-dependent probability for a diabatic transition at the second crossing, $P_H = P_{d2H} = \exp(-\kappa/v_H)$, and similarly for the tails orientation. The ratio

$$R = P_H/P_T = \exp(-\kappa\Delta v/v^2) \tag{7}$$

Here v_H is the relative velocity between K^+ and I^- in the heads orientation (the I^- is assumed for simplicity to be ejected backward along the K^+ velocity), v_T the relative velocity in the tails orientation (I^- ejected forward), $\Delta v = v_T - v_H$, and $v^2 = v_H v_T = 2E/\mu$, where E is the initial collision energy and μ the initial reduced mass. Thus, a plot of log R vs $1/E$ is expected to be linear with a slope of $\kappa\Delta v$, and several such plots are shown in Figures 7–9.

The data plotted in Figures 7–9 are fit reasonably well by eq 7 and lend credence to this impulsive model. For CF_3I and CH_3I results plotted in paper I, we forced the line to pass through the origin as required by eq 7, and the RBr plots in Figure 9 have lines coming close to the origin. But it is clear from Figures 7 and 8, that while data for many molecules are linear, they do not behave according to eq 7. This probably[15] arises because in the derivation of eq 7 we assumed that the initial speed was low enough that the first crossing was completely adiabatic ($P_a = 1$), and this assumption breaks down at higher energies. Thus eq 7 applies only in the low-energy limit and the data in Figures 7–9 are not extrapolated to high energy. The slopes of these plots yield experimental values for $\kappa\Delta v$, and these values are given in Table III. (Values for CH_3I and CF_3I differ from those from paper I, because they are obtained from the least-square slopes without the restriction that the lines pass through the origin.)

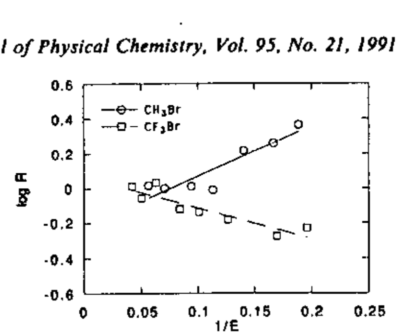

Figure 9. Plot of log R ($\equiv S_{180}/S_0$) vs $1/E$ for methyl and trifluoromethyl bromide. $S_{180}/S_0 = P_H/P_T$. (For CF_3Br, $S_{180}/S_0 = P_T/P_H$.) Lines are least-square fits.

TABLE III: Results of Plotting log R vs $1/E$

molecule	$\kappa\Delta v$, (km/s)^2	Δv, km/s	R_1, Å	R_2, Å
CH_3I	40	0.62	3.5	2.8
CH_3Br	75			
CH_3Cl	93			
CH_3F	140			
CF_3I	20	1.3	4.2	5.9
CF_3Br	18	1.3	5.2	6.1
CF_3Cl	114			
CCl_3H	5			
CF_3H	160			
t-BuBr	95			
t-BuCl	110			

The energy released in translation following the attachment of an electron has been measured in a few cases,[16] giving experimental values of Δv and consequently κ. As described in I, an experimental value of the product $H_{IC}r_2$ can be extracted from κ in this quasi-diatomic treatment if it is assumed that the diabatic curves are essentially a covalent curve and a Coulomb curve (i.e., $\Delta S = e^2/r_2^2$). A second (approximate) relation between H_{IC} and r_2 is given by a semiempirical correlation and these two relations may be solved to yield an approximate value for the second crossing distance, which is given in Table III.

The second crossing distance in CH_3I is roughly the same as the first, probably reflecting the inadequacy of this treatment for the close-range interactions in CH_3I. The qualitative picture of Figure 6 also does not describe the thermal-energy reactive scattering angular distributions, because the KI is backscattered in either orientation, although the tails orientation is less reactive. For CF_3I and CF_3Br, however, the second crossing is found to be 1–1.5 Å larger. These crossing radii are calculated on a highly simplified one-dimensional model, and caution needs to be exercised to avoid over-interpreting their significance. With this caveat in mind, we can roughly estimate the distortion of the molecule at the second crossing. The distance between crossings is roughly $z \approx |r_1 - r_2|$. The nominal relative velocity at 5 eV energy is ≈50 Å/ps, so the time that elapses between crossings is ≈40 fs for CF_3I, about 20 for CF_3Br, and less for CH_3I. If the C–X bond breaks with a nominal repulsive force of ≈5 eV/Å, then by the time the K^+ gets to the second crossing, the C–X bond would increase ≈1.3 Å for CF_3I, ≈0.7 Å for CF_3Br, and still less for CH_3I. The $R-X^-$ molecule is thus considerably distorted at

---

(15) Channels leading to other products may also become open.

(16) Walter, C. W.; Lindsay, B. G.; Smith, K. A.; Dunning, F. B. *Chem. Phys. Lett.* **1989**, *154*, 409.

(17) Walter, C. W.; Smith, K. A.; Dunning, F. B. *J. Chem. Phys.* **1989**, *90*, 1652.

(18) (a) Kalamarides, A.; Walter, C. W.; Lindsay, B. G.; Smith, K. A.; Dunning, F. B. *J. Chem. Phys.* **1989**, *91*, 4411. (b) Kalamarides, A; Marawar, R. W.; Durham, M. A.; Lindsay, B. G.; Smith, K. A.; Dunning, F. B. *J. Chem. Phys.* **1990**, *93*, 4043.

the second crossing and is indeed in the process of coming apart.

Finally, we note that the relative orientation effects, G, shown in Figures 3 and 4 are comparable for different molecules. Thus, for the CF_3X series of Figure 3, $|G|$ increases as I → Br → Cl, which may suggest that smaller halogen ions are more completely shielded by the CF_3 group. A similar trend is not apparent in the methyl halides, suggesting that shielding by the CH_3 is less effective. However, the S/N is poorer for this family, and this suggestion is tentative.

There are polarity differences between the CH_3X and CF_3X families that we hope are explained here. There are apparently smaller differences among other families, but further interpretation is not possible at this time because of signal-to-noise limitations and lack of ancillary data such as EAs. But the behavior of CCl_3H seems to be qualitatively different from the rest of the molecules studied. As shown in Figures 4 and 8, G and R are small and relatively independent of energy. Even though log R vs $1/E$ is fairly linear we thought perhaps CCl_3H simply does not dissociate impulsively. Both CCl_4 and $CFCl_3$ have long-lived molecular ions,[17] and our previous thermal energy reactive scattering experiments showed no measurable effect of orientation for the reaction K + CCl_3H and are consistent with this supposition. But in the recent experiments of Kalamarides, et al.[18] with high-Rydberg-state K^{**} atoms, impulsive behavior for CCl_3H similar to that observed in CF_3I was found. It thus appears that this behavior cannot be ascribed simply to a long-lived molecular ion.

V. Conclusions

Collisional ionization has been observed as a function of energy and molecular orientation for fast K atoms colliding with a number of different molecules. In all cases the orientation makes a large difference in the ionization probability, especially at low energies. There seems to be a difference in threshold for different molecular orientations, but this is not well established.

Ionization is most likely for impact on the "heads" end (the most labile halogen) that would be reactive in a lower energy collision. In many instances this is the negative end of the dipole. These findings, together with reactive scattering experiments at lower energies, can be interpreted as a result of an electron transfer (which may be orientation independent), followed by an impulsive decomposition of the molecular anion. If K^+ attacks in the tails orientation, a halogen anion is ejected in the same direction as the K^+, and there is an enhanced probability of neutralization and concomitant loss of ion signal.

The orientation effect, plus a knowledge of the amount of energy relased in the decomposition of the molecular ion, allows us to estimate the distances at which the ionic and covalent surfaces cross in the exit channel and this is found to be ≈6 Å for CF_3I and CF_3Br and ≈3 Å for CH_3I. For other molecules the energy release data are not known.

Acknowledgment. We gratefully acknowledge financial support from the National Science Foundation and the Robert A. Welch Foundation.

Registry No. K, 7440-09-7; CH_3Br, 74-83-9; CH_3F, 593-53-3; CH_3Cl, 74-87-3; CH_3I, 74-88-4; CF_3I, 2314-97-8; CF_3Br, 75-63-8; CF_3Cl, 75-72-9; *t*-BuBr, 507-19-7; *t*-BuCl, 507-20-0; CCl_3H, 67-66-3; CF_3H, 75-46-7.

Collision Dynamics of Alkali-Metal Atoms with Oriented Symmetric-Top Molecules

Philip R. Brooks,[†] **Peter W. Harland, Leon F. Phillips,***
Chemistry Department, University of Canterbury, Christchurch, New Zealand

and Howard S. Carman, Jr.
Oak Ridge National Laboratory, Oak Ridge, Tennessee *(Received: July 2, 1991)*

Theoretical calculations based on the long-range dynamics of the harpoon model have been used to predict the effects of reactant orientation upon ionization yields and angular distributions of product MX for reactions of alkali-metal atoms M with oriented symmetric-top molecules of general formula CY_3X, where X is a halogen and Y is H, F, or methyl. Large effects of orientation upon ionization yield near threshold are found to result from differences in the partitioning of kinetic energy between relative motion and center-of-mass motion, depending on whether the X^- ion ejected by the unstable CY_3X^- ion is traveling in the same direction as the incoming M^+ ion or the opposite direction. For most systems for which comparison is possible, excellent agreement is obtained with experimental data on the effect of orientation upon ionization yield. For ionizing collisions of fast K atoms with CH_3I and CH_3F, and for product angular distributions found with thermal K atoms and oriented CF_3I and CF_3Br, the theory is less successful and it appears that orientation-dependent short-range interactions must play a major role.

Introduction

Molecular beam studies of collisions of alkali-metal atoms M with oriented CY_3X molecules, where X is Cl, Br, or I, comprise a number of measurements of angular distributions of the product MX from reactions of thermal alkali-metal atoms,[1-10] and of the effect of orientation on ionization yields obtained with fast (5–30 eV) potassium atoms.[11-13] Angular distributions of products have often been interpreted in terms of what chemists intuitively think of as steric factors, amounting to a substantial "cone of no reaction" for the case of a rubidium atom approaching a methyl iodide molecule on the side of the methyl group.[6] An alternative, dynamic interpretation in terms of the harpoon mechanism has arisen from work at Rice University.[7] In this alternative picture, the electron transfer proceeds independently of orientation, but the direction of the CY_3–X axis at the instant the "harpoon" electron is transferred from the approaching metal atom fixes the direction in which the X^- ion is ejected by the resulting unstable CX_3Y^- ion. The direction of ejection of the X^- in turn has a major influence on the direction in which the MX product is observed to be scattered. This same model has been used to interpret the results of measurements of the effect of orientation on ionization

---

[†] Permanent address: Department of Chemistry and Rice Quantum Institute, Rice University, Houston, TX.

(1) Brooks, P. R. *Faraday Discuss. Chem. Soc.* **1973**, *55*, 299. Brooks, P. R. *Science* **1976**, *193*, 11.
(2) Brooks, P. R.; McKillop, J.; Pippen, H. G. *Chem. Phys. Lett.* **1979**, *66*, 144.
(3) Parker, D. H.; Chakravorty, K. K.; Bernstein, R. B. *J. Phys. Chem.* **1981**, *85*, 446.
(4) Parker, D. H.; Chakravorty, K. K.; Bernstein, R. B. *Chem. Phys. Lett.* **1982**, *86*, 113.
(5) Stolte, S.; Chakravorty, K. K.; Bernstein, R. B.; Parker, D. H. *Chem. Phys.* **1982**, *71*, 353.
(6) Choi, S. E.; Bernstein, R. B. *J. Chem. Phys.* **1985**, *83*, 4463.
(7) Carman, H. S., Jr.; Harland, P. W.; Brooks, P. R. *J. Phys. Chem.* **1986**, *90*, 944.
(8) Parker, D. H.; Jelink, H.; Stolte, S. *J. Phys. Chem.* **1987**, *91*, 5427.
(9) Bernstein, R. B.; Herschbach, D. R.; Levine, R. D. *J. Phys. Chem.* **1987**, *91*, 5635.
(10) Parker, D. H.; Bernstein, R. B. *Annu. Rev. Phys. Chem.* **1989**, *40*, 561.
(11) Harland, P. W.; Carman, H. S., Jr.; Phillips, L. F.; Brooks, P. R. *J. Chem. Phys.* **1989**, *90*, 5201.

0022-3654/92/2096-1557$03.00/0 © 1992 American Chemical Society

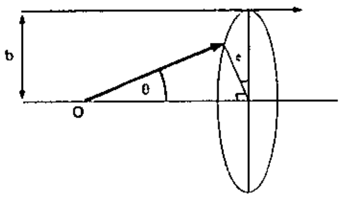

Figure 1. Angular relationships in the collision of a fast M atom with an oriented CY_3X molecule. The angle θ is selected by the hexapole focusing system; b is the impact parameter.

yields from collisions of fast potassium atoms with a number of oriented symmetric-top molecules.[12,13] For these systems, the direction of ejection of X^- relative to the incoming M^+ has been assumed to affect the ionization yield through its effect on the relative velocity, v, in the Landau–Zener expression

$$P = \exp[-4\pi^2 H_{12}^2/(hv|\Delta F|)] \qquad (1)$$

for the probability of curve-crossing at the intersection of the $M^+ + X^-$ potential with the neutral MX potential. When the X^- ion is ejected toward the incoming M^+ ion, the magnitude of the relative velocity v is much greater than when it is ejected in the same direction as the M^+ is traveling, so that P, representing the probability that the system will remain on the diabatic potential curve leading to ions, is larger.

It seems likely that the two kinds of mechanism, which we will term *steric* and *dynamic*, represent ideal limiting cases and a real reaction system can be expected to show behavior which is intermediate between the two extremes. The interpretation in terms of ordinary steric effects emphasizes the short-range behavior of the system during a collision of M with CY_3X, whereas the dynamic interpretation emphasizes the long-range features of the picture provided by the harpoon mechanism. The present paper gives the results of numerical calculations based purely on the dynamic model, the aim being to establish how well the experimental results can be accounted for on the basis of this model alone. The results show that, as might have been expected, the dynamic mechanism accounts for many but not all of the features of the experimental results. An interesting additional outcome of these calculations has been the identification of a second kind of dynamic mechanism which can lead to an orientation dependence of the ionization yield. The new mechanism depends on the circumstance that partitioning of the energy of the M^+,X^- system into kinetic energy of relative motion and kinetic energy of motion of the center of mass is strongly dependent on the direction of relative motion of M^+ and X^-. If the two ions are moving in the same direction, the kinetic energy of the center of mass will be much greater than if the ions are traveling in opposite directions. Consequently, at collision energies close to the threshold for ion production, the kinetic energy of relative motion is more likely to be insufficient to enable the charges to separate, when they are traveling in the same direction, and the observed ionization yield will therefore be lower than when they are traveling in opposite directions. The present calculations show that this effect is likely to be more important when the mass of M is comparable with or larger than that of X, and when species Y of the CY_3 group is the heavier F or CH_3 rather than H.

Calculations

(a) Ionization Yields with Fast M Atoms. Data used in the calculations, and derived curve-crossing radii, are given in Table I. For these calculations the CY_3X molecule was regarded as a stationary target, oriented at some angle θ with respect to the collision axis, and rotated by an angle ϕ with respect to the plane of the collision (Figure 1). The distribution over θ was calculated for the species CY_3X with values of hexapole dimensions and other beam parameters chosen to correspond to the experimental system as previously described.[12,13] The distribution over ϕ was assumed to be uniform. For each (θ,ϕ) combination the ionization cross section was calculated by summing the product of area and ionization probability over a range of impact parameters between zero and the first curve-crossing radius R_1. This radius was calculated as the intersection of the $M^+ + CY_3X^-$ Coulomb potential with an essentially flat $M + CY_3X$ neutral potential (Figure 2). The CY_3X^- ion was assigned an arbitrary lifetime τ, which was taken to be 10^{-13} s for the results reported here. Results obtained with assumed lifetimes between 10^{-11} and 10^{-14} s differed in detail but were qualitatively very similar.

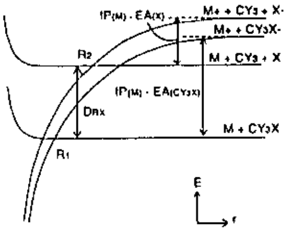

Figure 2. Section through potential energy surfaces showing energy relationships and crossing radii R_1 and R_2 in the $M + CY_3X$ system.

TABLE I: (a) Data Used in Calculations and (b) Calculated Curve-Crossing Radii

(a) Data Used in Calculations

ionization potentials,[a] eV: Li (5.392), K (4.341), Cs (3.894)
electron affinities,[a] eV: F (3.399), Cl (3.617), Br (3.365), I (3.060), CF_3Br (0.91), CF_3I (1.57), CH_3I (0.2)
electron affinities,[b] eV: CF_3Cl (0.75), CH_3F (0.75), CH_3Cl (0.75), *t*-BuCl (0.75), CH_3Br (0.5), *t*-BuBr (0.5), *t*-BuI (0.25)
dipole moments,[a] D: CF_3Cl (0.50), CF_3Br (0.65), CF_3I (0.92), CH_3F (1.79), CH_3Cl (1.869), CH_3Br (1.822), CH_3I (1.62), *t*-BuCl (2.15), *t*-BuBr (2.21), *t*-BuI (2.13)
dissociation energies,[c] D_{RX}, kJ/mol: CF_3Cl (328), CF_3Br (276), CF_3I (240), CH_3F (452), CH_3Cl (349), CH_3Br (280), CH_3I (234), *t*-BuCl (328), *t*-BuBr (276), *t*-BuI (240)
CY_3-lifetimes[b]: all 10^{-13} s

(b) Calculated Curve-Crossing Radii

first-crossing radius R_1, Å:
Li + CF_3I (3.77), CF_3Br (3.21), CF_3Cl (3.10), CH_3Cl (3.10), CH_3F (3.10), CH_3Br (2.94), *t*-BuBr (2.94), *t*-BuCl (2.91), *t*-BuI (2.80), CH_3I (2.77)
K + CF_3I (5.18), CF_3Br (4.19), CF_3Cl (4.00), CH_3Cl (4.00), CH_3F (4.00), CH_3Br (3.74), *t*-BuBr (3.74), *t*-BuCl (3.69), *t*-BuI (3.51), CH_3I (3.47)
Cs + CF_3I (6.20), CF_3Br (4.83), CF_3Cl (4.58), CH_3Cl (4.58), CH_3F (4.58), CH_3Br (4.24), *t*-BuBr (4.24), *t*-BuCl (4.18), *t*-BuI (3.95), CH_3I (3.90)
second-crossing radius R_2, Å:
$Li^+ + F^-$ (7.22), Cl^- (8.11), Br^- (7.10), I^- (6.17)
$K^+ + F^-$ (15.2), Cl^- (19.7), Br^- (14.6), I^- (11.2)
$Cs^+ + F^-$ (29.1), Cl^- (52.0), Br^- (27.2), I^- (17.3)

[a] Reference 17. [b] Assumed values. [c] Reference 18.

The $M^+ + CY_3X^-$ trajectory for each impact parameter was calculated on an uneven radial grid with a hard-sphere core located at some arbitrary minimum radius (typically 1.5 Å), and the trajectory was continued until either less than 1% of the negative ion remained to dissociate, or the second crossing radius R_2, given by the intersection of the $M^+ + X^-$ Coulomb potential with a flat $M + CY_3 + X$ potential (see Figure 2), had been reached. The kinetic energy of the X^- ion was calculated from the exothermicity $\Delta E = EA_X - D_{RX}$ of the CY_3X^- dissociation process (Figure 3), with no contribution from the kinetic energy of the incoming M atom. Such long-range energy transfer might occur as a result of polarization of the anion by the Coulomb field of the cation,[14] but calculations in which an amount of the order of 15% of the

---

[12] Harland, P. W.; Carman, H. S., Jr.; Phillips, L. F.; Brooks, P. R. *J. Chem. Phys.* **1990**, *93*, 1089.

[13] Harland, P. W.; Carman, H. S., Jr.; Phillips, L. F.; Brooks, P. R. *J. Phys. Chem.*, in press.

[14] Kendall, G. M.; Grice, R. *Mol. Phys.* **1972**, *24*, 1373.

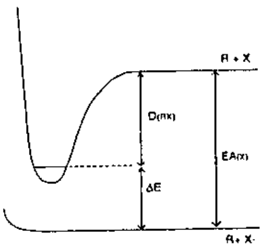

Figure 3. Section through potential energy surfaces showing the relationship between the dissociation energy D_{RX} of the CY_3–X bond, the electron affinity EA_X of the X atom, and the exothermicity ΔE of the CY_3X^- dissociation.

energy of a K atom was assumed to be transferred to the CY_3X^- gave results which did not differ qualitatively from those obtained with no energy transfer at long range, and this effect has been assumed negligible.

At each point on the radial grid, the fraction of CY_3X^- dissociated since the previous grid point was calculated, and the kinetic energy of the center of mass of the M^+ and X^- ions was found. This center of mass energy was then subtracted from the sum of the kinetic energies of the metal ion and the ejected X^- to give the amount of energy remaining as kinetic energy of relative motion of M^+ and X^-. For trajectories in which the kinetic energy of relative motion failed to exceed the energy of the $M^+ + X^-$ dissociation limit (the majority of trajectories were in this category at energies close to the ionization threshold) the contribution to the ionization cross section was zero. For the remaining trajectories, an effective impact parameter for the $M^+ + X^-$ collision was calculated from the initial velocity vectors of the ions at the time of dissociation of CY_3X^-, this quantity being needed to calculate the centrifugal energy contribution to the effective potential at R_2. Trajectories in which the kinetic energy of relative motion failed to exceed the effective potential at R_2 also made no contribution to the ionization cross section. For the remainder, the Landau–Zener crossing probability was calculated from the relative velocity of M^+ and X^- at R_2, using the matrix element H_{12} given by the formula of Baede.[15] Values of H_{12} given by Baede's formula were also used, with less justification, to calculate the crossing probability for $M + CY_3X$ forming $M^+ + CY_3X^-$ at R_1. Because of the relatively small first-crossing radii, the calculated values of H_{12} were quite large and the corresponding transition probabilities were of the order of unity. Ideally, values of H_{12} for the first crossing would be calculated from the observed dependences of relative ionization cross-sections on collision energy, but this cannot be done on the basis of the available data because the experimental arrangement[12,13] did not permit accurate measurement of the metal atom flux as a function of energy. Errors in the calculated first-crossing probabilities would affect the absolute values found for ionization cross sections but would not affect the calculations of relative ionization yields for different orientations of CY_3X. The relative yield was expressed in terms of the quantity G, defined by

$$G = (\sigma_{180} - \sigma_0)/(\sigma_{180} + \sigma_0) \qquad (2)$$

where the subscript 0 denotes the orientation in which the CY_3 group points towards the incoming M atom and the subscript 180 denotes the opposite orientation. With this definition the quantity G is always positive but is otherwise identical with G as defined in ref 12, where the subscripts related to the direction of the dipole moment of CY_3X rather than to the direction in which the X^- was ejected.

In order to assess the relative importance of the various possible reasons for the calculated values of G to differ from zero, the program kept count of the number of trajectories which failed to reach the $M^+ + X^-$ dissociation limit, the number of trajectories which failed to reach the second crossing radius, and the number of trajectories in which the Landau–Zener crossing probabilities at the second curve-crossing differed by more than 20% between the two orientations.

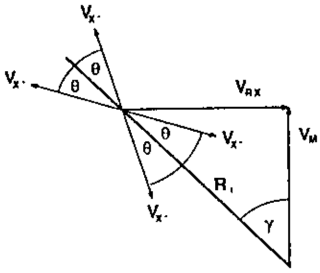

Figure 4. Representative vector diagram for dissociation of CY_3X^- in the $M + CY_3X$ system at low M-atom energies. The angle γ defines the direction of the relative velocity vector of M and CY_3X; θ is the orientation angle of CY_3X with respect to the relative velocity vector.

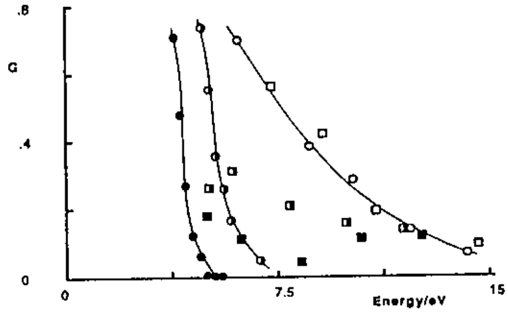

Figure 5. Experimental (squares) and theoretical (circles) values of G as a function of metal-atom energy for $K + CF_3Cl$ (unfilled points), $K + CF_3Br$ (half-filled points), and $K + CF_3I$ (solid points).

(b) Product Angular Distributions. In these calculations, the velocity distributions of both the CY_3X beam and the thermal beam of M atoms were taken into account. As before, the experimental distribution[7] over the orientation angle θ was used, θ being defined with respect to the relative velocity vector of M and CY_3X (Figure 4). The acceptance angle of the MX detector was assumed to be small enough that only products traveling in the plane of the collision need be considered, so that for each value of θ with given orientation there were two possible velocity vectors for the ejected X^- ion, corresponding to the two intersections of a cone of apex angle 2θ with the plane of the collision. In the very simple calculations to be discussed here, the M^+ ion was assumed to proceed undeflected and there was no integration over impact parameter. The direction of the velocity vector of the MX product in the laboratory frame was calculated from the resultant of the M^+ and X^- momenta in this frame, using the trigonometric relationships implicit in Figure 4, and converted to a deflection angle α relative to the M^+ velocity vector.

Results and Discussion

Experimental and calculated values of G, as defined in eq 3, are shown in Figure 5 as a function of metal atom energy for collisions of potassium atoms with CF_3X where X = Cl, Br, and I. For CF_3Cl the agreement between theory and experiment is seen to be remarkably good, a result that is probably fortuitous in view of both experimental error and the uncertainty in such quantities as the CF_3Cl electron affinity and the CF_3–Cl^- bond energy and lifetime. Nevertheless, the qualitative agreement between theory and experiment shown by the relative magnitudes of G values for X = Cl, Br, and I is certainly significant and can be taken as implying that the dynamic mechanism does play a major role in deciding the value of G for these systems. The

---

(15) Baede, A. P. M. *Adv. Chem. Phys.* **1975**, *30*, 463.

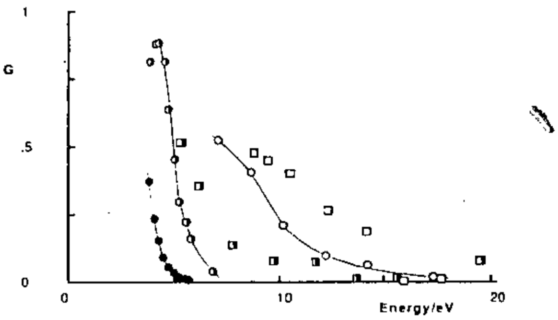

Figure 6. Experimental (squares) and calculated (circles) values of G for K + t-BuCl (unfilled points), K + t-BuBr (half-filled points), and K + t-BuI (solid points).

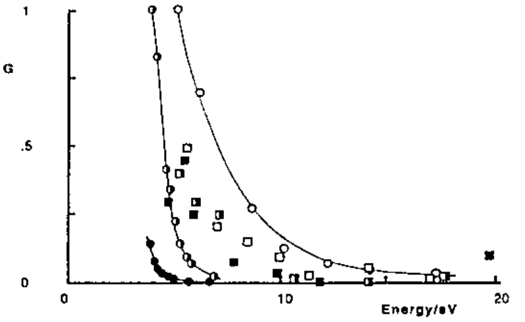

Figure 7. Experimental (squares) and calculated (circles) values of G for K + CH_3Cl (unfilled points), K + CH_3Br (half-filled points), and K + CH_3I (solid points).

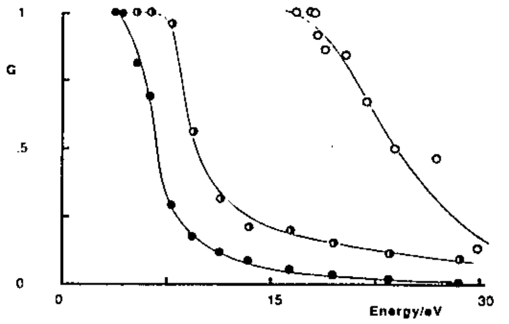

Figure 8. Calculated values of G for Cs + CF_3Cl (unfilled points), CF_3Br (half-filled points), and CF_3I (solid points).

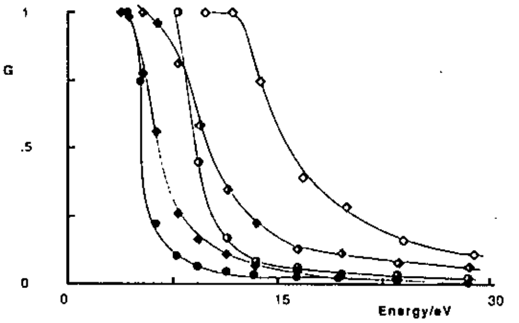

Figure 9. Calculated values of G for Cs + CH_3Br (half-filled circles), CH_3I (solid circles), t-BuCl (unfilled diamonds), t-BuBr (half-filled diamonds), and t-BuI (solid diamonds).

trajectory counts show that the effect of orientation on ionization cross section is mainly, perhaps even entirely, due to the effect of orientation on the number of trajectories which are able to reach the $M^+ + X^-$ dissociation limit, there being no pairs of successful trajectories for which the Landau–Zener crossing probabilities differed by more than 20%. The experimental G values greater than zero found at relatively high energies are possibly attributable to the presence of a significant number of lower energy K atoms in the fast atom beam, which was formed by charge exchange of K^+ in a cloud of neutral K. They might also be due to short-range effects which are not included in the model. The usual kind of steric effects, which are specifically excluded from the dynamic model, could lead to a dependence of ionization yield on orientation because they inhibit the formation of MX in one orientation and not the other, and formation of MX competes with production of ions. However, the direction of any steric effect would be expected to be similar to that found for the Rb + CH_3I system, which is such that more MX, and therefore fewer ions, should be formed when the X^- ion is ejected toward the incoming K^+ ion, and this is opposite to the observed effect of orientation on ionization yield.

Calculated and experimental G values for collisions of potassium atoms with tertiary butyl halides are shown in Figure 6. Experimental data is lacking for tertiary butyl iodide; for the other halides the agreement between theory and experiment is seen to be comparable with that shown by the results in Figure 5. Again the calculated orientation effects have no contribution from pairs of trajectories in which the Landau–Zener crossing probabilities differ by more than 20%.

Figure 7 shows experimental and calculated G values for collisions of potassium atoms with methyl halides. Agreement between theory and experiment is seen to be tolerable for methyl chloride and methyl bromide, but very poor for methyl iodide. For methyl iodide, the calculated departure of G from zero arises mainly from differences in Landau–Zener crossing probabilities, in marked contrast to all the other results considered so far. The experimental results for methyl fluoride[13] are not shown here. According to the model we are using, with no long-range energy transfer, there should be no F^- produced from methyl fluoride because the CH_3–F bond energy exceeds the electron affinity of F^- and the CH_3F^- ion should therefore be stable (Figure 3). Attempts were made to model the K + CH_3F system by allowing long-range transfer of an energy-dependent fraction (typically 20% near threshold) of the K atom energy to the CH_3F, but it proved impossible to reproduce the experimental results on the basis of such a model. Thus, in order to account for an orientation-dependent ion production in collisions of CH_3F with K atoms, it appears to be necessary to postulate the transfer of kinetic energy from the K atom to the CH_3F as the result of a short-range collisional interaction in which steric effects are important. It is noteworthy that the experimental ionization cross sections for the K + CH_3F system were very small,[16] which suggests that the short-range mechanism is important only when the dynamic mechanism is either inefficient, as for K + CH_3I, or ineffective, as for K + CH_3F.

Predicted G values for Cs colliding with CF_3Cl, CF_3Br, and CF_3I are shown in Figure 8. The effects of orientation on ionization yield are seen to be much more pronounced than for potassium, and to persist to much higher metal atom energies. At higher energies the total ion signal is larger, so that the signal-to-noise ratio for measurements of G should be much better with Cs than with K, and experiments with cesium should therefore provide a better test of the theory. Significant differences in

---

(16) Harland, P. W., unpublished data.

(17) *Handbook of Chemistry and Physics*, 71st ed.; Lide, D. R., Ed.; Chemical Rubber Co.: Boca Raton, FL, 1990.

(18) Lias, S. G.; Bartmess, J. E.; Liebman, J. F.; Holmes, J. L.; Levin, R. D.; Mallard, W. G. *J. Phys. Chem. Ref. Data* **1978**, *17*, Suppl. No. 1. Pauling, L. *Nature of the Chemical Bond*, 3rd ed.; Cornell University Press: Ithaca, NY, 1960.

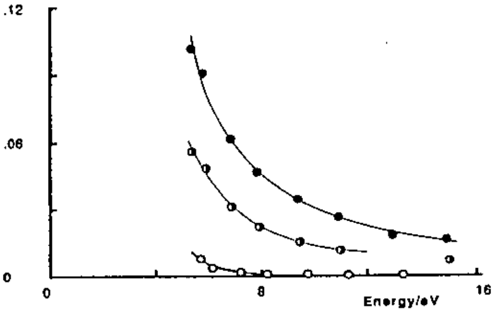

Figure 10. Calculated G values for Li + CF_3Cl (unfilled points), CF_3Br (half-filled points), and CF_3I (solid points).

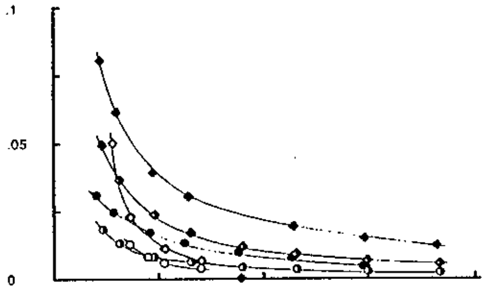

Figure 11. Calculated G values for Li + CH_3Cl (unfilled circles), CH_3Br (half-filled circles), CH_3I (solid circles), t-BuCl (unfilled diamonds), t-BuBr (half-filled diamonds), and t-BuI (solid diamonds).

ionization thresholds between the two orientations, indicated by the presence of energy ranges over which G is unity, are also predicted.

Similar conclusions can be drawn from the data in Figure 9, which shows predicted G values for Cs colliding with CH_3Br and CH_3I and with the three tertiary butyl halides. For CH_3Cl the dynamic constraints on the system are such that the calculations gave a zero yield of ions for both orientations at all Cs energies tried (up to 30 eV). This implies that any ionization which is observed experimentally for Cs + CH_3Cl must be the result of short-range interactions. Differences greater than 20% in Landau–Zener crossing probabilities for the two orientations played no part in the calculated orientation effects for cesium.

Predicted G values for lithium with CF_3Cl, CF_3Br, and CF_3I are shown in Figure 10. The variation of the magnitude of G with the nature of the halogen is seen to be in the opposite direction from that found with potassium and cesium, and the predicted differences of G from zero are quite small. Also in contrast to the results for K and Cs, the trajectory counts show that the major cause of the calculated orientation effects is differences in Landau–Zener crossing probabilities, as originally postulated. Figure 11 shows similar predicted G values for lithium with the three methyl halides and the three tertiary butyl halides. As with the fluoromethyl halides, the G values are all close to zero, the difference of G from zero is greatest for I and least for Cl, and the differences are almost entirely due to differences in Landau–Zener crossing probability. Because of the smallness of the orientation effects that are predicted to arise from long-range interactions in these systems, experiments with lithium atoms appear to be best suited for investigations of the orientation dependence of short-range interactions.

Product angular distributions for K + CF_3Br and K + CF_3I predicted by the long-range mechanism are shown in Figures 12 and 13, respectively. When these predictions are compared with

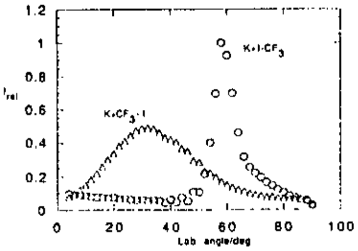

Figure 12. Calculated product angular distributions for K + oriented CF_3I.

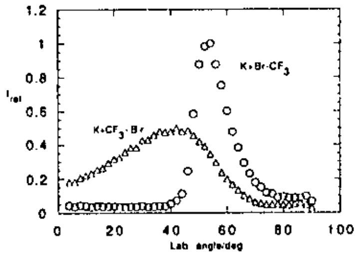

Figure 13. Calculated product angular distributions for K + oriented CF_3Br.

the experimental data,[7] the general form of the results is found to be qualitatively correct, with approach from the bromine or iodine end of the molecule leading to scattering at larger angles, and the ratio of the peak scattering cross sections is reproduced quite well for the bromide, although not for the iodide. However, quantitative agreement with the experimental angular distributions is poor, in that the peak scattering angles are about 30° too small, and this is undoubtedly a result of the failure of the model to take account of short-range interactions of the kind that lead to large-angle scattering.

Thus it would appear that the dynamic theory is much better at predicting the outcome of experiments with high-energy metal atom beams than with beams of thermal energy but, even at high energies, there are cases such as K + CH_3F where the experimental results cannot be understood without invoking collisions in which steric effects operate at short range. In an attempt to include some of the short-range behavior of the collision system, product deflection angles were also calculated by a more elaborate procedure in which detailed trajectories were calculated for M + CY_3X collisions over the range of impact parameters from zero to the first crossing radius R_1 and the deflection angle of M^+ was included in the calculation of the direction of the resultant MX velocity vector. (For a given impact parameter there were then two possible deflection angles for M^+, because the approach of M to CY_3X could occur on either side of the collision axis in Figure 1.) The more elaborate calculation was expected to lead to larger predicted product deflection angles but so far the improvement in agreement with experiment has not been significant, even with a core radius of several angstroms and an assumed lifetime of 10^{-11} s for the CY_3X^- ion. Clearly this is not a simple problem and more work is required.

Acknowledgment. We are grateful to the University of Canterbury for the award of an Erskine Fellowship to P.R.B., and to the U.S. National Science Foundation and the Robert Welch Foundation for support of the experimental studies from which this paper derives.

Registry No. K, 7440-09-7; Cs, 7440-46-2; Li, 7439-93-2; CF_3Cl, 75-72-9; CF_3Br, 75-63-8; CF_3I, 2314-97-8; CH_3Cl, 74-87-3; CH_3Br, 74-83-9; CH_3I, 74-88-4; t-BuCl, 507-20-0; t-BuBr, 507-19-7; t-BuI, 558-17-8.

Photoexcitation spectra of transition region species in reactions of potassium with sodium halides

Michael D. Barnes,[a),b)] Philip R. Brooks, R. F. Curl, Peter W. Harland,[c)]
and Bruce R. Johnson
Department of Chemistry and Rice Quantum Institute, Rice University, Houston, Texas 77251

(Received 28 October 1991; accepted 29 November 1991)

Emission at 589.0 nm from Na atoms is observed when beams of K and NaX (X = Cl, Br, I) are crossed inside the cavity of a cw dye laser tuned to wavelengths not resonant with either the isolated reagents or products. This emission is interpreted as the signature of light absorption by a system in the process of chemical reaction, and the variation of this emission intensity with probe wavelengths is an excitation spectrum of "transition region species" formed in these reactions. Each spectrum displays a "blue" feature where the emission intensity increases sharply as the probe wavelength approaches the Na *D* lines. A second "red" feature is also observed in all of the spectra. This feature appears as a well resolved maximum for the Br and I systems peaked at ~610 nm, and is much broader for the Cl system with the maximum at ~640 nm. Definitive assignment of these features is not yet possible, but several possible mechanisms are proposed which may give insight into the reaction dynamics.

I. INTRODUCTION

During the last 30 years a variety of experimental techniques for studying "state-to-state" chemistry have led to great advances in the understanding of the dynamics of chemical reaction events. Even though these experiments can often be very sophisticated, the observations are almost always made on reagents *before* the reaction or products *after* the reaction, and details of the reaction event must be *inferred* from these measurements. Direct probes of the reaction event are clearly desirable, and recently progress[1] has been made toward the direct study of species in the process of reaction. In this paper, we present the results of experiments in which the reaction event is probed directly for the reactions K + NaX→KX + Na, where X = Cl, Br, or I.

As the nuclei evolve from "reagents" to "products" in a chemical reaction, they pass through many nuclear configurations which are neither reagents nor products. We call these transient nuclear configurations transition region species (TRS) defined as the set of all configurations intermediate between reagents and products.[2] The goal of these studies has been to experimentally probe these TRS's in hopes of obtaining insight into the motions of the nuclei during chemical reaction.

The extremely short duration of the reaction event (typically < 1 ps) makes spectroscopic interrogation of the chemical system during the reactive collision very difficult. A second difficulty, of perhaps equal magnitude, is that interpretation of any experimental spectra of transition region species requires some knowledge of the potential energy surfaces (PES's) involved. In most cases, this information is either unavailable or is insufficiently accurate to allow an unambiguous interpretation. Furthermore, an experimental TRS spectrum is likely to probe many nuclear configurations, not just one "transition state," and is likely to be severely broadened by averaging over the initial distribution of impact parameters, internal states of the reactants, and collision energies. This suggests that such a spectrum would be unlikely to exhibit any discernible features.

The difficulties just described can be partially circumvented by studying unimolecular processes in which a stable species is photoexcited to a dissociative state and the decomposition of the system on the excited surface is observed. These "half-collision" experiments offer several advantages: stable species can be made in higher concentration than bimolecular TRS's and stable species can usually be prepared at low temperatures in *known* geometries so photoexcitation accesses a *limited* set of final states and avoids averaging over a broad range of initial conditions. Moreover, for stable species extensive spectroscopic data are often available and more accurate PES's are likely to be available to assist in the interpretation.

Several groups have now reported elegant studies on such unimolecular systems. In the experiments of Kinsey and co-workers (Ref. 3), CH_3I and O_3 were irradiated in bands which normally lead to prompt photodissociation. But despite the short photodissociation lifetime (< 1 ps), very weak fluorescence from the *dissociating* molecule was observed which, combined with information about the excited potential surface, enabled the time evolution of the wave packet in the dissociative state to be extracted.

In a similar spirit (but using a completely different technique), Neumark and co-workers[4] have photodetached negative ions XHY^- (where X and Y are halogen atoms) to form an *unstable* neutral XHY species. The neutral surface corresponds to that for reactions X + HY→XH + Y and the XHY species is prepared on that reactive surface with roughly the same geometry as the negative ion. The kinetic energy distribution of the photodetached electrons was measured, and in some instances this distribution shows vibrational structure in coordinates orthogonal to the reaction

---

[a)] Robert A. Welch Pre- and Postdoctoral Fellow.
[b)] Current address: Analytical Chemistry Division, Oak Ridge National Laboratory, Oak Ridge, Tennessee 37831.
[c)] Permanent address: Chemistry Department, University of Canterbury, Christchurch, New Zealand.

0021-9606/92/053559-10$06.00 © 1992 American Institute of Physics

coordinate, giving detailed information on the scattering states supported by the neutral potential energy surface.

Zewail and co-workers[5] have been able to examine the motion of a photodissociating system on a femtosecond (fs) time scale by using one fs laser pulse to produce the excited state and then using a second (delayed) fs pulse to probe the dynamics of the molecule in the excited state. In the photodissociation of NaI, for example, the fluorescence of Na atoms showed an oscillation with probe delay (≈ 1 ps) which was a manifestation of the oscillation of the NaI wave packet in a quasiwell created by an avoided crossing between the ionic and covalent potential curves. An extension of this technique to bimolecular reactions (which lack a time zero) has been made by Bernstein and Zewail[6(a)] in the study of OH formed in the $H + CO_2$ reaction, where the reaction was initiated using Wittig's technique[7] of photolyzing a van der Waals molecule, in this case $HI\cdots CO_2$. Their method has most recently been extended[6(b)] to a study of the $Br + I_2$ reaction (initiated by photolysis of $HBr\cdots I_2$) in which they find a complex lifetime ≈ 50 ps.

Photodissociation experiments are half-collision experiments, and it can be argued that for a complete picture of bimolecular chemical reaction, the full collision must be investigated. The investigation of bimolecular reactions by the photolysis of van der Waals precursors appears to be a step in this direction. In this photolytic method, the region of the reactive potential surface probed is limited by the geometry of the stable ground state of the van der Waals precursor. This is simultaneously both an asset and a liability; an asset because it removes much of the averaging over impact parameters and relative orientation of the reagents in the reactive collision; a liability because the regions thus selected cannot be easily varied and might not be important in the full bimolecular collision. For this reason, we have continued to develop direct probes of transition region species formed in full collisions recognizing the inherent complications associated with averaging over initial conditions.

We have previously investigated TRS's in the K + NaCl system.[8] Molecular beams of K and NaCl were crossed inside the cavity of a cw dye laser tuned to wavelengths where neither products nor reactants absorb. The reaction, $K + NaCl \rightarrow KCl + Na$ which is ≈ 0.2 eV exoergic, occurs on roughly every gas kinetic collision, and goes through a complex with a lifetime measured[9] to be about one rotational period and calculated[10] to be ~ 1–10 ps. The combination of large reaction cross section and long TRS lifetime maximizes the steady state concentration of TRS's available to be probed and thus the expected spectroscopic

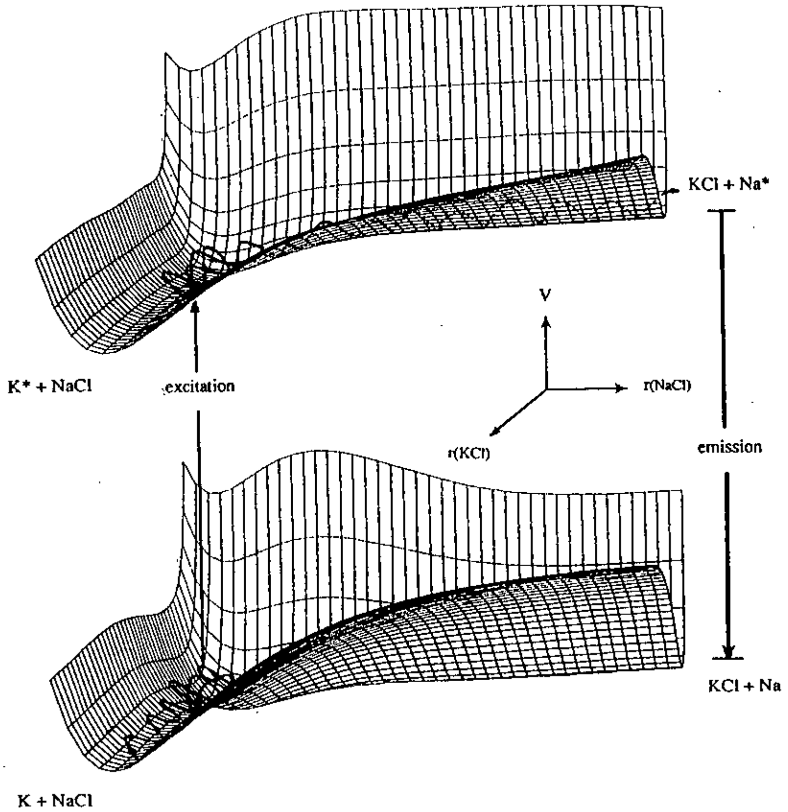

FIG. 1. Fixed angle potential energy surfaces for the K + NaCl surfaces of Yamashita and Morokuma (Ref. 12). A schematic reactive trajectory is shown to illustrate the formation of the TRS on the lower surface, excitation to the upper surface, and the reactive decay of the TRS on the upper surface.

signal. Generally we have probed the TRS spectrum by cw dye laser excitation of the system to the red of the Na *D* lines. The sum of reaction exoergicity, collision energy, and photon energy provides the energy required to open the channel to formation of Na*(3*p*) atoms, which can only occur in the presence of a radiation field. The resulting emission from Na* indicates that light absorption by the reacting system has taken place.

The process observed can be viewed in a stepwise fashion as

$$\begin{aligned}&\mathrm{K}+\mathrm{NaX}\rightarrow[\mathrm{KXNa}],\\&[\mathrm{KXNa}]+h\nu_{\mathrm{probe}}(595\text{–}700\ \mathrm{nm})\rightarrow[\mathrm{KXNa}]^{*},\qquad(1)\\&[\mathrm{KXNa}]^{*}\rightarrow\mathrm{KX}+\mathrm{Na}^{*}({}^{2}P_{3/2,1/2}),\\&\mathrm{Na}^{*}\rightarrow\mathrm{Na}+h\nu(589.0,589.6\ \mathrm{nm}),\end{aligned}$$

where [KXNa] represents TRS's formed in collisions of K and NaX, and [KXNa]* represents the electronically excited TRS following photon absorption.

The set of Eqs. (1) is an unusual sort of kinetic mechanism. A pictorial view of the process may be useful. Figure 1 shows potential energy surfaces for ground and excited states of the KClNa system, and the motion of the nuclei during a collision is represented by a schematic trajectory on the ground state surface. If the collision occurs in a radiation field, the colliding system can absorb a photon, provided that the trajectory passes through a nuclear configuration (a TRS) which is connected to the upper surface by that photon of wavelength λ. The photon will not need to be resonant with either the reagents or the products, and the wavelengths that excite the TRS will depend not only on the potential surfaces for the system but also on the dynamics on the ground potential surface. If excitation occurs, the system will continue to evolve on the upper surface, and *may* undergo reactive decay to yield Na* as shown in Fig. 1. Observation of Na* will also depend on the dynamics on the upper surface as well.

The excitation spectrum previously observed for X = Cl exhibits a sharp rise near the *D* line and a threshold at ~735 nm, but is otherwise relatively featureless as might be expected in view of the averaging over the collision parameters. It was difficult to reach any conclusions regarding the nature of the TRS or of the PES's involved in the K + NaCl reaction from this structureless spectrum. Nevertheless, we decided to investigate other K + NaX systems in the hope that differences among the photoexcitation spectra might be found which could give some insight into the nature of the TRS's in these reactions. In this paper, we report a refined photoexcitation spectrum of TRS's formed in the K + NaBr reaction previously communicated,[11] and, in addition, a TRS photoexcitation spectrum for K + NaI. We find that all of the spectra display a similar "blue" feature where the emission intensity rises sharply at laser wavelengths between 600 and 595 nm. In each spectrum a second "red" feature is also observed which is well resolved for the NaBr and NaI systems. Even the NaCl system is, upon closer inspection, revealed to have a "red" feature, which is much broader and less distinct than either the Br or I features.

In an effort to ascertain whether the clear red features of the Br and I systems might be the result of a pure mass effect, we have extended the surface hopping trajectory calculations performed by Yamashita and Morokuma[12] to larger masses. No significant mass effect was found, and these calculations modeling TRS excitation give poor agreement with the experimental chloride spectra, suggesting inadequacies in either the PES or the surface-hopping model. Thus, an unambiguous assignment of these features cannot yet be made. However, some possible origins of these features will be discussed which may give insight into the dynamics of these reactions.

II. EXPERIMENT

The apparatus has been previously described in detail.[7,13] In this experiment, beams of K atoms and NaX (X = Cl, Br, I) molecules were crossed inside the cavity of a cw dye laser tuned between 595 and 635 nm. Excited Na* atoms formed by the laser assisted reaction

$$\mathrm{K}+\mathrm{NaX}+h\nu\rightarrow\mathrm{KX}+\mathrm{Na}^{*}\qquad(2)$$

were detected by fluorescence at 589.0 nm, and the emission intensity was measured as a function of the dye laser wavelength. In order to separate out the portion of the observed signal which arises from the process of interest, it was necessary to measure the photomultiplier count rate for each of the eight possible combinations of beam on/off conditions for the three beams.

The K beam source was operated at ≈350 °C corresponding to a vapor pressure ≈3 Torr. Assuming effusive flow, the particle density at the crossing region was $\approx 2\times10^{11}\ \mathrm{cm}^{-3}$. The NaX source temperature used depended on the choice of the alkali halide, and was 1000, 850, and 750 °C for NaCl, NaBr, or NaI, respectively. These temperatures correspond roughly to a vapor pressure ≈4 Torr and a particle density at the crossing region roughly equal to that of the potassium.

A Spectra-Physics 375 dye laser was modified by replacing the standard output-coupler with a 150 cm radius high reflector 150 cm from the beam waist to allow insertion of the vacuum chamber into the dye laser cavity. The dye laser was typically pumped by 9 W of 514 nm light from an argon ion laser giving tunable intracavity power ≈ 100 W. As reported previously, direct excitation of Na atom impurities by dye fluorescence at the Na *D* lines was avoided by placing a sodium heat pipe in the laser beam between the dye jet and the beam intersection region.

Light from the beam intersection region was collected by an f1.4 achromat and passed through a narrow bandwidth (0.27 nm FWHM) interference filter transmitting only the 589.0 nm *D* line. The light transmitted by the filter was focused onto a cooled C31034A photomultiplier (PMT) and pulses from the anode of the PMT were amplified, discriminated, and input into a pulse counter/timer.

The TRS signal requires all three beams to be present. However, other sources not requiring the presence of all three beams such as photomultiplier dark counts, and emission from oven heaters gave rise to PMT counts. To account for the contributions of such zero, one, and two beam processes, counts were accumulated for each of the eight beam on/off combinations using flags to block each beam when appropriate. The three-beam signal (3BS) was obtained by subtracting contributions from all zero, one, and two-beam processes from the count rate for all three beams on, as described in Refs. 8 and 13.

In order to account for small changes in beam intensities and laser power during an experiment and to compare experiments run at different times, each 3BS was normalized by dividing by the product of three beam monitor measurements. This "normalized" 3BS corresponds to a relative (Ref. 14) three-body rate coefficient. The laser power was monitored by steering the reflection from one of the Brewster windows into a power meter.[15] The K and NaX beam intensities were monitored by surface ionization on hot tungsten filaments. The surface ionization efficiency, however, is not the same for the three sodium halides. The absorption of halogen atoms into the tungsten filament lowers the work function of the surface, and it has been shown[16] that the relative surface ionization efficiencies of the three sodium halides NaCl:NaBr:NaI is 1:1.14:1.50. Beam monitor signals corrected for surface ionization efficiency were used to calculate the normalized 3BS.

III. RESULTS

Typical unnormalized count rates for the KXNa systems acquired over an 8 min total counting time are shown in Table I. For the three columns of Table I corresponding to the three chemical systems, the molecular and laser beam intensities were approximately equal. As can be seen by comparing the columns in Table I, most of the corresponding one and two-beam signals are of similar magnitude in the three chemical systems. The NaX background signal, which arises from the glow from heater wires on the NaX collimator and which is consequently extremely sensitive to skimmer temperature, tends to be one of the largest and most variable signals. For approximately equal fluxes, the different sodium halides require different skimmer temperatures; therefore significant differences in this background signal are observed among the three systems. As mentioned above, the signal of interest is the 3BS. These data show that the 3BS is always one of the largest and can be the largest of the eight signals.

TABLE I. Count rates (s^{-1}) of Na D line emission at 589.0 nm for K + NaX irradiated at 608 nm.

Signal[a]	Origin	X = Cl	X = Br	X = I
R000	Dark current	55 ± 1	21 ± 1	21 ± 1
R100	Scattered light	21 ± 2	29 ± 2	57 ± 2
R010	K background	5 ± 2	3 ± 1	1 ± 1
R001	NaX background	581 ± 4	336 ± 4	29 ± 2
R110	K photoluminescence	42 ± 3	16 ± 2	61 ± 3
R101	NaX photoluminescence	− 11 ± 6	4 ± 5	− 3 ± 3
R011	Chemiluminescence	4 ± 5	1 ± 5	− 2 ± 2
R111	Three beam signal	114 ± 8	237 ± 8	234 ± 5

[a] Denotes elementary rates for laser, K, and NaX on/off (1/0) beam combinations. See Ref. 8 for a complete description of signal nomenclature and calculation of elementary rates from measured sums.

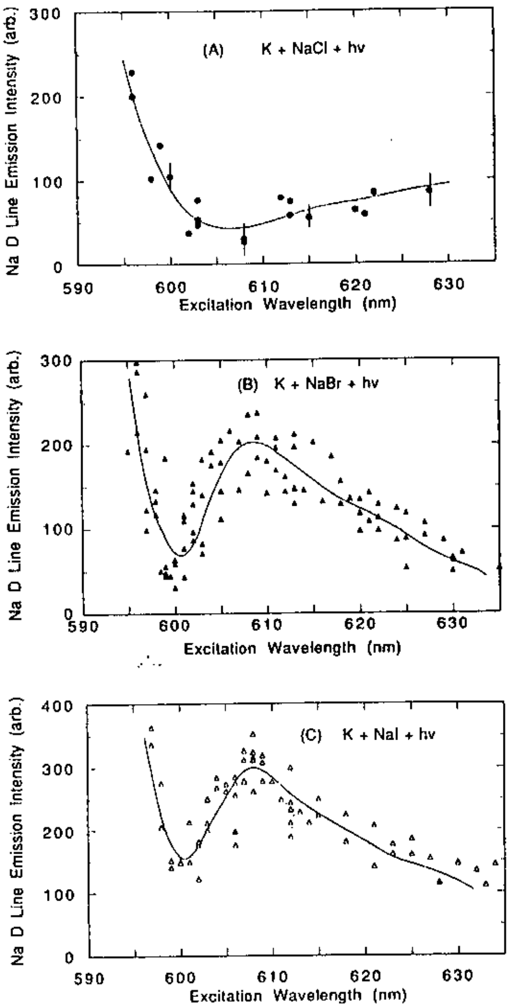

FIG. 2. Normalized three-beam signals (corrected for NaX surface ionization efficiency) vs excitation wavelength for (a) K + NaCl + $h\nu$; (b) K + NaBr + $h\nu$; and (c) K + NaI + $h\nu$. Curves are drawn for illustration only.

Normalized 3BS vs laser wavelength for the K + NaX systems are shown in Fig. 2. We believe these are excitation spectra of the TRS [KXNa]. The spectra arising from the three chemical systems show striking differences as well as similarities. Each spectrum shows a sharp increase in signal as the laser wavelength is scanned from 600 to 595 nm, which we call the blue feature. In addition, each spectrum displays a broad peak or red feature. This red feature is well-resolved in the [KBrNa] and [KINa] spectra, with a maximum occurring at ~610 nm, and appears to be quite similar in shape and width for these two systems. The red feature is considerably broader and less distinct in the [KClNa] spectrum, with the collective data[8] suggesting that the maximum occurs at ~640 nm. It is clear that the characteristics of the red feature depend on the chemical system under study, and the difference between the observed spectrum of [KClNa] and those of the Br and I systems suggests that the reaction dynamics are quite different for the heavier sodium halides.

Because of the high photon flux ($\approx 10^{22}\ \mathrm{s}^{-1}\,\mathrm{cm}^{-2}$) there is a possibility that the 3BS could arise from other (less interesting) processes involving light absorption by some impurity present in very small concentration. Potassium dimer was present in the K beam and free Na atoms were present in both beams, and it was necessary to verify that the 3BS does not arise from some process involving these impurities. The tests performed to verify that the 3BS indeed arises from excitation of TRS's were aimed at establishing one of the following three points: (1) identification of the 3BS emitter as Na*, (2) elimination of the possibility that energy transfer processes involving free Na atoms was giving rise to the 3BS; and (3) elimination of processes involving dimers.

We have performed several tests that strongly support our interpretation of the 3BS as excitation spectra of TRS. These tests are described in detail in the Appendix. Briefly, filters are used to show that the source of emission is excited sodium atoms, and energy transfer processes involving Na impurities are shown to be unlikely because adding Na to the K beam does not change the 3BS. Finally, magnetic deflection experiments demonstrate that the 3BS arises from a paramagnetic species in the K beam, which rules out the participation of K dimers. These tests show that the 3BS is not a result of processes involving the artifact sources considered above.

Thus, we conclude that the spectra shown in Fig. 2 represent an excitation of the TRS [KXNa]. The steeply rising blue feature between 600 and 595 nm was observed in the early KClNa experiments,[8] but not emphasized because our attention was focused on determining whether or not observation of TRS's was possible. (When the laser is tuned far to the red of the Na *D* lines, many artifacts are either ruled out or become less plausible. In the early experiments, we tended to discount signals near the *D* lines where the energy defect could easily be made up by collisional energy without requiring energy to be supplied by the reaction exoergicity.) The tests we have made here and the similarity of the feature for all three systems lead us to conclude that the blue feature *is a spectroscopic feature of the TRS.*

The distinct red feature in the [KBrNa] and [KINa] spectra suggests that the dynamics of these reactions are different from the K + NaCl reaction. The potential surfaces for these reactions are expected to be similar, but at this stage we have little idea how sensitive the spectra are to the details of the potential surfaces involved. A possible explanation for the accentuated red feature in the heavier halides is that the increased mass decreases the speed of the system resulting in some critical region being traversed more slowly. The longer time spent in such a "critical" region might result in an increased probability for light absorption. This was explored by performing surface hopping classical trajectory calculations modeling both the ground and excited state dynamics using the procedure of Ref. 12.

IV. SURFACE HOPPING TRAJECTORY CALCULATIONS

Surface hopping trajectory calculations on slightly modified[17] surfaces[12,18] were carried out to investigate the possibility of a mass effect as the origin of the red feature and to explore the role exit-channel excitation[13] plays in the blue feature. Because potential energy surfaces (PES's) for the K + NaBr and NaI reactions are as yet unavailable, trajectory calculations were performed using the K + NaCl potential energy surfaces calculated in Ref. 18. Generally, the method employed for calculating the TRS spectra was the same as that used by Yamashita and Morokuma.[12] The effect of increased mass and decreased mean speed for the Br and I systems was investigated using the same (K + NaCl) PES and changing the mass of the halogen atom and the velocity distribution of the sodium halide molecule. In order to understand the results of these calculations, it is useful to first examine some of the details of the K + NaCl PES's.

There are four low lying adiabatic PES's in the K + NaCl reaction ($1\,^2A'$, $2\,^2A'$, $3\,^2A'$, and $1\,^2A''$) of possible significance to the present experiments. Yamashita and Morokuma[18] argued on the basis of their calculations that the TRS spectrum of this system should involve primarily a transition from the ground $1\,A'$ to the second excited $3\,A'$ state (omitting the doublet designation). They calculated 241 *ab initio* points[12,18] which were then fit to parameterized Murrel–Sorbie analytical functions,[19] although parameters were only provided for the $1\,A'$ and $3\,A'$ states. In Fig. 3, their minimum energy paths along these A' surfaces are shown. The curve drawn for the $2\,A'$ state is based on the well depth reported[12] and is therefore only approximate. No parameters are available for the $1\,A''$ surface, although it does correlate with the same product asymptote as the $3\,A'$.

As seen in Fig. 3, each of the A' states has a potential well, and the excited states correlate with K*(4*p*) + NaCl and Na*(3*p*) + KCl in the reagent and product asymptotes,

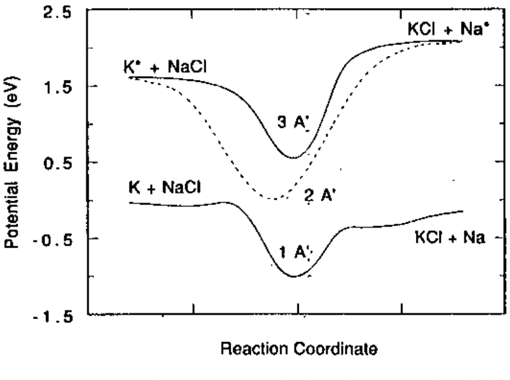

FIG. 3. Schematic minimum energy paths along the $1\,A'$ and $3\,A'$ PES's for the K + NaCl reactions. Since the parameters for the $2\,A'$ state are not available, an approximate curve is drawn showing the well depth reported for this surface. The geometry changes for the minimum energy configurations for each state, and the K–Cl–Na angles of these configurations are 85°, 180°, and 135° for the $1\,A'$, $2\,A'$, and $3\,A'$ states, respectively. The $1\,A''$ surface, which correlates with K* + NaCl and KCl + Na*, is not shown.

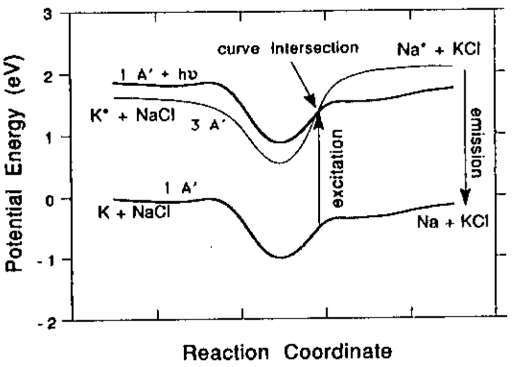

FIG. 4. Schematic minimum energy path description of the intersection of a "dressed" 1 A' potential with the 3 A' potential. The "dressed" 1 A' potential is simply the curve corresponding to the 1 A' state moved up by the energy of the photon (≈ 1.8 eV in this figure). The "crossing" depicted is actually avoided because of coupling between the surfaces caused by the laser field. The adiabatic potential would evolve smoothly from the 1 $A' + h\nu$ state of the reagents to the excited potential, 3 A' for the products.

respectively. The 2 A' level correlates adiabatically with the lower $^2P_{1/2}$ fine structure level of the atom and the 3 A' and 1 A'' levels correlate adiabatically with the $^2P_{3/2}$ level. These experiments involve measurements of emission intensity at 589.0 nm, corresponding to the higher energy $^2P_{3/2}$ fine structure state. Thus to the extent that nonadiabatic transitions in the exit channel may be neglected, only reactive trajectories on the 3 A' and 1 A'' state should be experimentally observed.

The process of light absorption by the reacting system was treated[12] as a surface hopping process between the "laser-dressed"[20] ground state and the 3 A' excited state. The "laser-dressed" ground state PES is created by adding the laser photon energy to the ground state, and as suggested in Fig. 4, the dressed surface can intersect an excited surface. Near such intersections the electric field of the radiation couples the two surfaces through the electric dipole transition moment causing an avoided crossing. Thus a trajectory begun on the dressed ground state could (schematically) remain on the adiabatic surface and ultimately emerge on the 3 A' surface giving Na*. (Previous calculations suggest that this trajectory is likely to be snarled[10,12] and may encounter a surface crossing many times.) This surface-hopping process was examined, using a standard Monte Carlo method,[21] by propagating the classical trajectory on the laser dressed surface until a point of intersection with the 3 A' surface was encountered. The adiabatic transition probability (representing a transition to the 3 A' surface) was estimated using the Landau–Zener relation[22,23]

$$P_a = 1 - \exp[-4\pi^2 d_{12}^2/h(d\Delta W/dt)], \qquad (3)$$

where $d_{12} = \mu \cdot E$ and ΔW is the difference in energy between the crossing surfaces. If this transition probability was greater than a freshly generated random number, the trajectory was continued on the upper surface (corresponding to the excited state PES) until it was determined to be reactive or nonreactive. If a transition was not made, the trajectory was continued on the laser dressed ground state until another crossing was encountered or until the criteria for ending the trajectory were satisfied. This approach of sometimes jumping to the 3 A' surface and sometimes remaining on the 1 A' surface takes into account the possibility that a given trajectory on the 1 A' surface might go through several crossings. Although this procedure neglects effects such as interference between waves on the excited surface, extensive averaging over many trajectories makes such interference almost certainly unimportant.

No effort has been made to produce absolute cross sections for the process. Therefore, the magnitude of the coupling term is relevant only in comparison with the range of random numbers used as the surface hopping criterion. The coupling term[24] ($\mu E = 0.1$ kcal/mol) used was the same as that used by Yamashita and Morokuma, and the random number range was adjusted to provide a reasonable division between hopping and continuing on the 1 A' surface. The fact that this coupling term corresponds to a laser power much higher than that used in the experiments is irrelevant.

The ratio of reactive trajectories on the excited state to the total number of trajectories as a function of photon energy was used to calculate a model excitation spectrum. Figure 5 shows the results of these calculations with 500 excited state/reactive trajectories accumulated for each photon energy. The results obtained for the K + NaCl system are in good agreement with those of Ref. 12 in the wavelength range between 600 and 650 nm. The agreement between the KClNa results and the results calculated for the heavier mass shows that there is no effect of mass on the calculated spectrum, as the minor differences seen are within the Monte Carlo sampling error.

The overall agreement between the model and experimental spectra is poor, and these calculations seem to give no clues as to the origin of either the red or the blue feature. The sharp rise evident in the experimental spectrum near the Na D lines is specifically *not* predicted, even in the [KClNa]

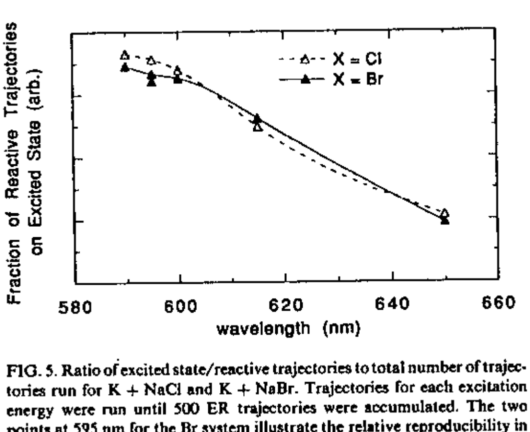

FIG. 5. Ratio of excited state/reactive trajectories to total number of trajectories run for K + NaCl and K + NaBr. Trajectories for each excitation energy were run until 500 ER trajectories were accumulated. The two points at 595 nm for the Br system illustrate the relative reproducibility in the calculations. The small differences between the Cl and Br calculations are not significant.

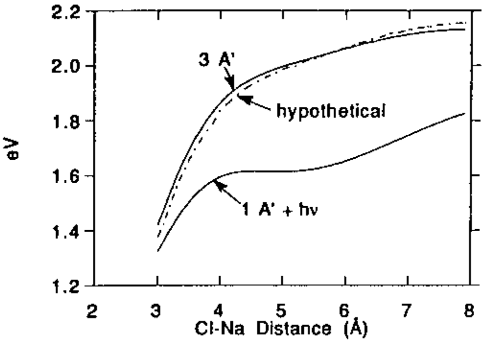

FIG. 6. Product asymptote region of 3 A' state and 1 A' ground state (augmented with photon energy corresponding to wavelength of 595 nm) for KClNa. Curves represent variation of potential energy as a function of Cl–Na distance with K–Cl distance fixed for a fixed K–Cl–Na angle of 90°. The dashed, hypothetical curve would be expected to give a strong feature at the Na D line. The zero of energy is defined here to be ground state products.

spectrum. The calculated difference in Na* emission between 595 and 600 nm is only ~5%, whereas the experimental difference is approximately a factor of 3. Even with an excitation wavelength of 590 nm, only 1 nm from the Na D line, the calculated signal increases only by about another 5%.

It seems most likely that the blue feature is an exit channel phenomenon. Figure 6 compares the 3 A' surface for a K–Cl–Na angle of 90° together with the corresponding 1 A'-plus-photon-energy curve. Also shown is a hypothetical laser-dressed 1 A' curve at 90° with a shape more nearly parallel to the 3 A' surface. The small crossing angles between the hypothetical 1 A' and the 3 A' surface would lead to large Landau–Zener adiabatic transition probabilities (photoexcitation) because $d\Delta W/dt$ in Eq. (3) becomes small. For the actual potential surfaces, no such nearly parallel crossings are found in this region. Thus for the actual potential surfaces used in the calculations, no dramatic increase in the photoexcitation cross section is anticipated or found from the calculations, in contrast to the experimental observations.

V. DISCUSSION

The TRS spectra of the three sodium halide reactions with potassium have been investigated here in the hope that differences among the spectra could be observed and interpreted in terms of the underlying dynamics. This hope has been partially realized in that features have been observed in all three spectra whose characteristics depend on the choice of sodium halide. The next task is then the interpretation of the observed features in terms of the reaction dynamics. As a tentative step in this direction, it is useful to consider how it may be possible to observe structure in this type of spectrum.

As shown in Fig. 1, the reacting system may absorb a photon if the laser is tuned to a frequency corresponding to the potential energy difference between the ground (V_1) and an excited state (V_2) for a given instantaneous nuclear configuration (R_t), that is, where $V_2(R_t) - V_1(R_t) = h\nu$. In this picture[25] (assuming a constant transition moment) the intensity of light absorption by the TRS depends on (a) the number of configurations R_t for which $\Delta V = h\nu$, and (b) the time spent in nuclear configurations similar to R_t (where a similar configuration is one in which the energy difference between the crossing dressed surfaces $\lesssim$ the strength of the dipole coupling to the field).

Thus, there are three principal ways in which features may arise in this type of spectrum.[26]

(1) There may be a region of the lower PES where the system remains trapped for a period of time resulting in a "persistent" configuration which will increase the probability of absorption at the wavelength corresponding to $\Delta V(R_{\mathrm{trap}})$.

(2) There may be certain configurations that are explored by all trajectories en route from reactants to products. For example, a "bottleneck" in the ground state surface may force trajectories with widely different initial conditions through a narrow region of phase space.

(3) There may be regions of the ground and excited PES's traversed by the system which are relatively parallel so that many different configurations may absorb light of the same frequency. Thus, increases in absorption strength by the TRS may result from an increase of the number of similar configurations, i.e., from regions where the PES's are parallel.

A. The blue feature

It has been previously suggested that the blue feature arises from excitation in the exit channel of the ground state PES where the two surfaces should become more parallel.[11,27] Such excitation of the newly formed Na atom perturbed by the KX dipole presumably could occur at relatively long (>5 Å) Na–X distances and should vary only slightly among chemical systems. Indeed, the blue features in all three spectra appear to be quite similar. We attribute these features to chemical reactions; we have shown experimentally that the blue feature does not arise from an artifact associated with Na impurities in either beam and therefore cannot be nonreactive collision broadening of Na atoms.

Atomic resonance lines are broadened by collisions and frequently show a "blue" feature similar to that found in the reactive systems. In the atomic case, the potential curves for the ground and excited states of the atom-collider pair become asymptotically parallel and an increasing number of nuclear configurations become resonant for a given λ as $R \to \infty$. (The photon dressed ground state curve would coincide with an ever-increasing segment of the excited state curve as $\lambda \to \lambda_{\mathrm{atom}}$, as suggested in Fig. 6 by the hypothetical curve.) If both attractive and repulsive curves can correlate with the excited atomic state, as is expected for a p state, the resonance line will be broadened both to the red and to the blue, as observed by Gallagher and co-workers for the broadening of the Rb resonance line by Xe.[28] By analogy to this process, we expect the newly formed Na* atom to be perturbed by the departing KX. Such reactive line broadening was observed in the early experiments of Polanyi *et al.*,[29] where the broadening of the Na* resonance line was observed in the chemiluminescent reaction $\mathrm{F} + \mathrm{Na}_2 \to \mathrm{Na}^* + \mathrm{NaF}$. In those experiments, Na* was observed to fluoresce at $\lambda > \lambda_{\text{atom}}$, with intensity falling rapidly in the 590–595 nm interval.

As noted earlier, the trajectory surface hopping calculations do not predict such a blue feature and this may reflect slight inaccuracies in the properties of the K + NaCl surfaces used. (Given accurate *ab initio* points, it is still difficult to construct global analytical polyatomic PES's free of unphysical features.) It is also possible that the surface-hopping model may be inadequate to simulate light absorption by the reacting system. For example, significant differences between classical and quantum dynamics calculations have been reported in reactions[30] such as F + H_2, although for heavier systems such as K + NaBr the differences between classical and quantum mechanics could reasonably be expected to be smaller. Furthermore, in the classical calculations, the Landau–Zener model may fail in certain domains that are well understood[31] (at least for one-dimensional problems). It is unlikely, however, that such inadequacies could be the sole cause of suppression of the blue feature.

Regardless of possible inadequacies of either the surface-hopping method or the details of the A' PES's, it is also possible that other surfaces play a role in the blue feature. The $1A''$ surface is particularly relevant here since it also correlates to Na $^2P_{3/2}$ state which is observed in the experiments. It is not possible to examine this in more detail here since no calculations have been reported for this surface.

B. The red feature

The presence of a distinct red feature in the [KBrNa] and [KINa] spectra which appears much broadened and less apparent in the [KClNa] spectrum, indicates that the reaction dynamics are quite different for the heavier sodium halides. It is significant that this feature has survived in spite of averaging over initial orientations, impact parameters, and thermal distributions of speeds and internal energies, and this suggests that the spectral feature arises from some relatively coarse-grained property of the system. Identifying this property remains a difficult task since little is known about the PES's for the heavier sodium halides.

It is possible that the regions of the potential surface responsible for the observed red feature may be completely different for the heavier halides. For example, the ground state surface for the K + NaCl reaction is predicted to have a potential well bound by ~0.5 eV with respect to products.[18,32] The K + NaBr and NaI systems may have much deeper ground state wells capable of trapping trajectories with a wider variety of initial conditions. Excitation from these quasibound states might give rise to the structure in the experimental spectrum if the probability distribution were more localized.

An interesting conjecture[11] is that the red feature might arise from trajectories which first make nonadiabatic transitions into the deeply bound $2A'$ state, and which are then photoexcited to the $3A'$ state. For the K + NaCl system, the first excited state ($2A'$) is predicted to be bound by ~1.6 eV with respect to excited state reactants[18,31] and comes within ~5 kcal/mol of the $1A'$ surface. If a nonadiabatic transition to the $2A'$ state occurs, the system does not have enough energy to dissociate on this surface[33] to either excited atom, and it might be effectively trapped in the $2A'$ first excited electronic state. Since these trapped species might have a limited range of nuclear configurations, laser excitation to the second excited state ($3A'$) might then result in a feature in the spectrum.

The Landau–Zener probability for a nonadiabatic transition from the $1A'$ state to the $2A'$ is given by

$$P_{n-a} = \exp[-4\pi^2 d_{12}^2/h(d\Delta W/dt)], \tag{4}$$

where d_{12} is the coupling term causing the diabatic surfaces to split,[34] and $(d\Delta W/dt)$ is the time derivative of the potential energy difference between the two diabatic surfaces, which is directly related to the nuclear velocities. The nonadiabatic transition probability is obviously maximized where the magnitude of d_{12} is small, or where the nuclear velocities are large. If the magnitude of the nonadiabatic coupling term were approximately the same for all the sodium halides, the lower mean speed of NaBr and NaI relative to NaCl would favor *adiabatic* passage through the crossing region and trajectories for the heavier halides would be less likely to jump to the $2A'$ surface. Thus, for a collisional nonadiabatic mechanism to be responsible for the red feature, the magnitude of the nonadiabatic coupling term (corresponding to the separation between nonadiabatic states) would have to be smaller for the heavier sodium halides.

Chemiluminescence experiments performed by Moulton and Herschbach[35] on the Na + $KX^\dagger \rightarrow NaX + K^*$ system (where X = Cl, Br, † denotes vibrational excitation and * denotes electronic excitation) showed that the yield of K^* was greater by approximately a factor of 3–5 for the Br system even though more vibrational energy in the KX reagent is available in the Cl system. Since the formation of K^* involves a transition to an excited electronic state ($2A'$ or $3A'$), a nonadiabatic transition must be made at some point during the collision. These results were interpreted by Struve[36] in terms of differences in the coupling between the ground and first excited states for these reactions. He extended the Roach and Child[32] pseudopotential method to various alkali + alkali–halide systems, and his results (cf., the discussion on p. 799) make it plausible that the interaction between the states is stronger for the Br system than for the Cl system. Thus he rationalized the Herschbach results in terms of an enhanced nonadiabatic transition probability for the Br reaction.

The experiments[32,34] thus show that collisions in higher energy systems can populate the $2A'$ state and suggest that nonadiabatic transitions are more likely for Br than Cl systems. This lends credence to the idea that the red feature in the [KBrNa] and [KINa] spectra arises from nonadiabatic transitions to the first excited state followed by laser excitation to the $3A'$ state which dissociates to give Na^*.

VI. SUMMARY AND CONCLUSIONS

Photoexcitation spectra of TRS formed in the bimolecular reactions of K + NaCl, NaBr, and NaI have been measured. All of the spectra show a common blue feature which is thought to arise from excitation in the exit-channel at long Na–X distances. Surface-hopping trajectory calculations performed on slight modifications of the K + NaCl PES's of

Yamashita and Morokuma do not predict that such a feature should occur.

The spectra obtained for the NaBr and NaI systems show an additional red feature which appears greatly broadened and less distinct in the NaCl system. A possible explanation for this red feature based on collisional nonadiabatic transitions has been proposed. The differences among the spectra suggest that the reaction dynamics and the nature of TRS's vary from system to system, and we believe that the differences observed reflect differences in the potential surfaces involved.

APPENDIX: ELIMINATION OF POSSIBLE ARTIFACT SOURCES

A. Identification of the emitter

It is fairly straightforward to establish that the optical fluorescence at 589.0 nm comes from excited Na atoms as opposed to some other broad band source. By tilting the interference filter with respect to the plane defined by the three beams, the peak wavelength transmitted by the filter is blue-shifted by ~0.2 Å per degree tilt and light from a sodium lamp is extinguished when the filter is tilted ~10°. It was previously shown that the 3BS for the KClNa system was extinguished by the same tilt, verifying that excited Na atoms are the source of emission. This test was repeated at the peak of the 3BS (≈ 611 nm) for the K + NaBr experiments reported here, and again we conclude that the emitter is atomic Na. Results of various cutoff filter tests also indicated that the observed emission arises from excited Na atoms.

B. Elimination of energy transfer processes

Establishing that excited Na atoms are responsible for the observed emission does not, of itself, guarantee that the 3BS arises from excitation of TRS. The presence of Na atom impurities (in the parts per million range) in both molecular beams allows for the possibility of some collisional process transferring energy to a sodium atom and thereby producing Na*. Direction excitation of Na atoms is avoided by inserting a heat pipe oven in the laser cavity.[6] In previous studies[8] on the K + NaCl system, it was shown that chemically reactive species were necessary to produce a 3BS. The possibility that the 3BS results from an energy transfer process producing Na* through collisions of Na atoms with laser excited species was explored in earlier work[8] by replacing in one experiment the NaCl beam with a weak Na beam and then in a second experiment seeding the K beam with Na. No 3BS was observed, ruling out the possibility that the observed 3BS was due to energy transfer processes involving sodium atoms.

Since the bond energy of NaBr is ~10 kcal/mol lower than that of NaCl,[37] it was thought that there might have been a much higher concentration of Na atoms in the NaBr beam increasing the probability of an energy transfer artifact signal. By removing the heat pipe oven from the laser cavity, it was possible to use the spontaneous fluorescence of the dye to probe the Na atom concentration in the beam. It was found that the concentration of Na atoms in the NaCl beam was about three times larger than that of the NaBr beam.[38] Since energy transfer processes in NaCl do not seem responsible for the 3BS and since [Na] is less in the NaBr system, it seems reasonable to conclude that the signals for the NaBr and NaI systems are also not due to energy transfer processes involving Na atoms in the salt beams.

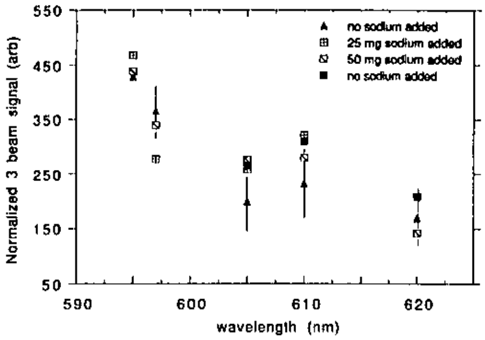

FIG. 7. Normalized three-beam signals for K + NaI + $h\nu$. Different symbols denote different levels of Na added to 20 g K charge as indicated in the legend. Error bars are $\pm 1\sigma$.

As a final test for energy transfer processes involving Na atoms, several experiments were run with NaI with varying amounts of additional sodium (0, 25, and 50 mg) *added* to the 20 g potassium charge. The results of these experiments are shown in Fig. 7, and it can be seen that there is no correlation between the magnitude of the 3BS and the level of sodium impurity. Our conclusion from the results of these tests is that the emission does not arise from energy transfer processes involving free Na atoms in either the K beam or the salt beam.

C. Elimination of dimer contributions

Several tests for artifactual sources of the three-beam signal involving the small (0.1%) amount of K dimers in the K beam have previously been performed.[8] The well known $B \leftarrow X$ electronic transition for K_2 occurs at wavelengths between 615 and 650 nm making it necessary to rule out processes of the type,

$$K_2 + h\nu \rightarrow K_2^*,$$

$$K_2^* + \text{NaX(or Na)} \rightarrow \text{Na}^* + \text{other products.} \qquad (A1)$$

It was previously observed that there was no correlation between K dimer fluorescence and magnitude of the 3BS. But since K_2 might be excited to some other state which might interfere but not fluoresce, an inhomogeneous magnet was used to separate the atoms from *all* of the dimers. The results of these magnetic focusing experiments[39] demonstrated that magnetically focusable species, which almost certainly must be K atoms, are required for signals observed in the K + NaCl system, conclusively ruling out possible artifactual 3BS involving K dimers.

D. Role of $(NaX)_2$

It is also known that NaX dimers are present in the sodium halide beam, perhaps in concentrations as high as

5%.[40] Little is known of the spectroscopy of NaX dimers, which like the monomers, should be transparent to visible light. Direct excitation of the dimer and energy transfer processes involving excited $(NaX)_2$ therefore seem unlikely. It is, however, possible that the 3BS observed is due to TRS's formed in the reaction $K + (NaX)_2$, although we believe the 3BS arises mainly from the monomer reaction. The dimer concentration depends sensitively on the temperature of the nozzle chamber of the oven, but the 3BS does not. Experiments at different oven temperatures for NaI allow comparison of the 3BS for different dimer concentrations as calculated from the thermodynamic parameters given in Ref. 36. This comparison *suggests* that dimers are not responsible for the 3BS. (Fluctuations in the 3BS are large enough that this result is not yet definitive.)

ACKNOWLEDGMENTS

We gratefully acknowledge the financial support of the Robert A. Welch Foundation, and the National Science Foundation under Grant Nos. CHE87-19403 and CHE89-09777. The authors wish to thank Koichi Yamashita, for helpful discussions pertaining to the K + NaCl PES's. We would also like to thank James Spence, Sydney Ulvick, Carter Kitrell, and David Blunt for many helpful discussions and assistance.

---

[1] P. R. Brooks, Chem. Rev. **88**, 407 (1988).

[2] This definition includes the "transition state" of some chemical theories.

[3] D. Imre, J. L. Kinsey, A. Sinha, and J. Krenos, J. Phys. Chem. **88**, 3956 (1984).

[4] S. E. Bradforth, A. Weaver, D. W. Arnold, R. B. Metz, and D. M. Neumark, J. Chem. Phys. **92**, 7205 (1990), and references therein.

[5] L. R. Khundkar and A. Zewail, Annu. Rev. Phys. Chem. **41**, 15 (1990), and references therein.

[6] (a) N. F. Scherer, L. R. Khundkar, R. B. Bernstein, and A. H. Zewail, J. Chem. Phys. **87**, 1451 (1987); (b) M. Gruebele, I. R. Sims, E. D. Potter, and A. H. Zewail, *ibid.* **95**, 7763 (1991).

[7] S. Buelow, M. Noble, G. Radhakrishnan, H. Reisler, and C. Wittig, J. Phys. Chem. **90**, 1015 (1986).

[8] T. C. Maguire, P. R. Brooks, R. F. Curl, Jr., J. H. Spence, and S. J. Ulvick, J. Chem. Phys. **85**, 844, (1986), and references therein.

[9] W. B. Miller, S. A. Safron, and D. R. Herschbach, Discuss Faraday Soc. **44**, 108 (1967).

[10] G. Kwei, B. P. Boffardi, and S. F. Sun, J. Chem. Phys. **58**, 1722 (1973).

[11] M. D. Barnes, P. R. Brooks, R. F. Curl, Jr., and P. W. Harland, J. Chem. Phys. **94**, 5245 (1991).

[12] K. Yamashita and K. Morokuma, J. Chem. Phys. **91**, 7477 (1989).

[13] M. D. Barnes, Ph.D. thesis, Rice University, 1991.

[14] The true three-body rate coefficient would require knowledge of the beam geometries, speeds, and absolute detection efficiencies and these have not been measured.

[15] This reflection is horizontally polarized whereas the standing wave in the reaction center is mainly vertically polarized. We have shown that monitoring this polarization provides a reliable measure of the intensity of both polarizations. (See T. C. Maguire, Ph.D. thesis, Rice University, 1984]. The laser power closely follows the gain curve of Rh6G and the spectral features shown in Fig. 1 are evident in the raw data. These features are *not* artifacts of normalization.

[16] A. A. Johnson and T. E. Phipps, J. Chem. Phys. **7**, 1039 (1939).

[17] The K^* excitation energy used as input to the $3\,A'$ surface was chosen to be 1.6104 eV instead of 1.423 eV as used by Ref. 12, and a typographical error of a factor of 2 in the one-body switching function was corrected [K. Yamashita (private communication)].

[18] K. Yamashita and K. Morokuma, J. Phys. Chem. **92**, 3109 (1988).

[19] N. Murrel, S. Carter, S. C. Farantos, P. Huxley, and A. J. C. Varandas, *Molecular Potential Energy Functions* (Wiley, New York, 1984).

[20] T. F. George, J. Phys. Chem. **86**, 10 (1982).

[21] M. Karplus, R. N. Porter, and R. D. Sharma, J. Chem. Phys. **43**, 3259 (1965).

[22] L. D. Landau, Phys. Z. Sowjetunion **2**, 46 (1932); C. Zener, Proc. R. Soc. London, Ser. A **137**, 696 (1932).

[23] J. R. Stine and J. T. Muckerman, J. Chem. Phys. **65**, 3975 (1976), and references therein.

[24] The transition dipole moment for the $1\,A'$–$3\,A'$ transitions was found in Ref. 18 to be relatively smoothly varying over a wide range of geometries and was assumed constant for convenience by Yamashita and Morokuma (Ref. 12). This approximation should be explored in any future *ab initio* calculations, since spectroscopic structure could conceivably arise from certain configurations being more heavily weighted by the transition moment.

[25] If the ground surface is dressed by a photon of frequency ν, it is moved up by energy $h\nu$ and will intersect the upper surface at the configurations for which $\Delta V = h\nu$. The time spent in the region where the difference in potential energy is comparable to μE is given by $t = \mu E/(d\Delta W/dt)$ which appears in Eq. (3), the Landau–Zener formula.

[26] These are largely analogous to the effects which lead to features in the broadening of atomic lines (see Ref. 1) and were also explored in model trajectory studies by J. C. Polanyi and R. J. Wolf, J. Chem. Phys. **75**, 5951 (1981).

[27] H. R. Mayne, R. A. Poirer, and J. C. Polanyi, J. Chem. Phys. **80**, 4025 (1984).

[28] See A. Gallagher, in *Atomic Physics*, edited by G. zu Putlitz *et al.* (Plenum, New York, 1975), and references therein.

[29] P. Arrowsmith, F. E. Bartoszek, S. H. P. Bly, T. Carrington, Jr., P. E. Charters, and J. C. Polanyi, J. Chem. Phys. **73**, 5895 (1980); P. Arrowsmith, S. H. P. Bly, P. E. Charters, and J. C. Polanyi, *ibid.* **79**, 283 (1983).

[30] M. Baer, I. Last, and Y. Shima, Chem. Phys. Lett. **110**, 163 (1984).

[31] J. Light and A. Szöke, Phys. Rev. A **18**, 1363 (1978).

[32] A. C. Roach and M. S. Child, Mol. Phys. **14**, 1 (1968).

[33] In systems with higher energy [translation, S. K. Neoh and D. R. Herschbach, J. Chem. Phys. **63**, 1030 (1975); vibration, Ref. 35] electronically excited atoms are observed, and are apparently produced by this nonadiabatic jump followed by dissociation on the $2\,A'$ surface.

[34] This splitting is due to the molecular electronic structure and is not dependent upon the laser.

[35] M. C. Moulton and D. R. Herschbach, J. Chem. Phys. **44**, 3010 (1967).

[36] W. S. Struve, Mol. Phys. **25**, 777 (1973).

[37] P. Davidovits and D. L. McFadden, *Alkali Halide Vapors* (Academic, New York, 1979).

[38] The free Na atoms in the alkali–halide beams are formed from thermal dissociation in the nozzle. Therefore, the increased nozzle temperature for NaCl is probably responsible for the larger relative amount of Na atoms.

[39] S. Kaesdorf, P. R. Brooks, R. F. Curl, J. H. Spence, and S. J. Ulvick, Phys. Rev. A **34**, 4418 (1986).

[40] NaCl dimers, R. J. Mawhorter, M. Fink, and J. G. Hartley, J. Chem. Phys. **83**, 4418 (1985). NaBr dimers, J. G. Hartley and M. Fink, *ibid.* **87**, 5477 (1987). NaI dimers, J. G. Hartley and M. Fink, *ibid.* **89**, 6053 (1988). The NaX vapor in our experiments is superheated by 200–300 °C and the dimer concentration is expected to be much lower than in the experiments of Fink *et al.*

Chemical Physics 165 (1992) 73–87
North-Holland

Calculation of the potential energy surface of Li^+–N_2

Stephen T. Grice, Peter W. Harland and Robert G.A.R. Maclagan
Department of Chemistry, University of Canterbury, Christchurch, New Zealand

Received 9 March 1992

A new potential energy surface for the Li^+–N_2 system is presented at the Hartree–Fock and Møller–Plesset levels of theory. Improvements in the basis set and in the electron correlation are outlined. The potential energy surface has an energy minimum in the linear configuration of 0.522 eV at 4.926 bohr, and a saddle point energy in the perpendicular arrangement of 0.113 eV at 4.615 bohr at the Hartree–Fock level of theory. An increase in the size of the basis sets and the addition of more polarization functions has resulted in improvements in the electric multipole moments and polarization properties of the separated species. Electron correlation does not alter the positions of the stationary points or the energies markedly but it does lower the energy minimum by 0.035 eV. The potential is expanded into its angular components and compared with existing expansions.

1. Introduction

The first ab initio study of the complete potential energy surface of the species Li^+–N_2 by Staemmler [1] provided valuable input for a number of fitting [2,3] and scattering [4–10] studies. The availability of this potential energy surface provided opportunities to compare theory with experiments and to examine the relationship between expectations based on the potential energy surface and the experimental measurements. Most results showed adequate correspondence between experiment and theory for the authors [5–7,9] to conclude that the Hartree–Fock (HF) potential energy surface of Staemmler was reasonably accurate in the 1–20 eV energy range. However, other authors [8] have reported contradictory results.

The analytic expression for the rigid rotor potential energy surface of Billing [6] has been tested [11] at energies below 1 eV. Although this potential energy surface was fitted to Staemmler's HF data using twelve parameters, it failed to reproduce the absolute experimental values [12] of the transport properties of Li^+ in N_2. However, the general form was the same [11]. A number of theoretical investigations [13–19] of the thermodynamic and structural properties of the Li^+–N_2 system have been reported since Staemmler's paper. These studies have supplied data for the potential energy surface in the regions about stationary points, but give limited information about the behaviour of the potential energy surface elsewhere.

Hartree–Fock calculations have been shown to be unreliable in reproducing electric multipole moments [20], which are important in long-range interaction effects. Similarly, binding energies in the region of a potential energy minimum are not adequately described although the short-range repulsive interaction is described with moderate success [21]. Since there are reservations over the ability of Staemmler's potential energy surface to model accurately measured transport data over a wide energy range, and considering the advances in computer speed in the time since Staemmler reported his results, we have undertaken a detailed examination of the Li^+–N_2 potential energy surface.

In this paper we report ab initio calculations of the Li^+–N_2 potential energy surface. In section 2 we describe improvements in the properties of the separate species Li^+ and N_2 with differing basis sets. The potential energy surface is presented and a discussion of the effects of inclusion of electron correlation is presented in section 3. Analysis of the potential en-

Correspondence to: R.G.A.R. Maclagan, Department of Chemistry, University of Canterbury, Christchurch, New Zealand.

0301-0104/92/$ 05.00 © 1992 Elsevier Science Publishers B.V. All rights reserved.

ergy surface and its Legendre expansion, with emphasis on a break down of the angular components of the long-range interaction energy, is given in section 4.

2. Basis set and properties

Foremost in our choices of a basis set was the consideration of the properties of the separate Li^+ and N_2 species. Particularly important are the polarization and electric multipole moments which dominate the long-range interactions between these two subsystems. Staemmler [1] has commented that polarization functions are critical in reproducing experimental binding energies, quadrupole moments and polarizabilities for the N_2 subsystem. In order to improve on the potential energy surface that Staemmler generated it has been necessary to obtain reasonable properties for N_2 using a more sophisticated basis set and a more elaborate treatment of electron correlation.

The major part of this study involved calculations using the 6-311+G(2df) basis set. This basis set includes an extra f function on the N atomic centres and two extra d's and an extra f function on the Li atomic centre when compared to Staemmler's best basis set. The addition of extra d polarization functions to all atomic centres was studied, with the 6-311+G(3df) basis set. This basis set has been shown to be reliable in studies of the interactions between atomic ion/atom systems [22–26]. An extensive list of the electrical properties obtained with these basis sets is given in table 1 along with other experimental and theoretical results.

The basis set with a HF quadrupole moment, Q, in best agreement with the experimental measurement of Hout and Bose [27], is the 6-311+G(2df) basis set. The correlated MP2 wavefunctions have similar quadrupole moments ($Q \approx -1.2$ au) for each basis set considered here. The reliability of the quadrupole moment is crucial to the accuracy of the long-range interactions between N_2 and any other ionic system. The hexadecapole moment, H, increases in magnitude with the addition of polarization functions from -6.47 to -7.71 au with basis sets 6-311+G(df) to 6-311+G(3df) respectively, at the HF level of theory, but remains relatively constant for the basis sets considered when including electron correlation to a MP2 level of theory. Staemmler's own result of -6.78 au is consistent with that reported here if you compare the size of the basis sets with respect to the number of polarization functions included. To our knowledge there is no experimental measurement of the hexadecapole moment of N_2 in the literature.

The dipole polarizability in table 1 also shows an increase in magnitude with an increase in the size of the basis set. Greater agreement with experiment is achieved with the inclusion of more polarization functions in the basis sets. The parallel component of the dipole polarizability, $\alpha_\parallel$, compares favourably with the experimental value, with 2.9%, 4.6%, and 4.6% errors for the 6-311+G(df), 6-311+G(2df), and 6-311+G(3df) basis sets, respectively, at the MP4SDTQ level of theory. The perpendicular component of the dipole polarizability, $\alpha_\perp$, approaches the experimental value with 25.4%, 15.0%, and 4.6% errors for the 6-311+G(df), 6-311+G(2df), and 6-311+G(3df) basis sets, respectively, at the MP4SDTQ level of theory.

In addition to the reproduction of the electric multiple moments and the dipole polarizabilities, important to the long-range interaction of N_2 with any ionic species, it is also important to model the structural and thermodynamic properties of N_2. The equilibrium bond distance, the dissociation energy, the force constant, and the total energy of N_2 are presented in table 2.

The equilibrium bond distances calculated for the basis sets used in this study are slightly shorter than the experimental value, by approximately 0.05 bohr. Dixon [19] reported an equilibrium bond distance of 2.03 bohr using a (11s7p1d)/[5s4p1d] basis set which increased approximately 0.05 bohr with inclusion of electron correlation in his configuration interaction (CISD) calculations. We have not optimised the bond distance past the HF level of theory, but it seems reasonable to expect that an inclusion of electron correlation would improve our bond distances in a similar manner.

Electron correlation is also important in the determination of binding energies, as HF calculations cannot adequately describe the dissociation of the closed shell N_2 (X, $^1\Sigma_g^+$) molecule into two open shell N ^3S atoms [20]. HF potentials have been shown to give dissociation energies that are too small and force

Table 1
Electric properties of N_2 [a]

Basis set	Q	H	$\alpha_\parallel$	$\alpha_\perp$
HF/6-311+G(df)	−1.26	−6.47	14.68	7.01
MP2/6-311+G(df)	−1.22	−6.75	13.81	7.59
MP4SDTQ/6-311+G(df)	–	–	14.39	7.61
HF/6-311+G(2df)	−1.03	−7.35	14.29	8.12
MP2/6-311+G(2df)	−1.27	−6.69	13.67	8.54
MP4SDTQ/6-311+G(2df)	–	–	14.13	8.57
HF/6-311+G(3df)	−0.98	−7.71	14.19	9.32
MP2/6-311+G(3df)	−1.22	−6.74	13.67	9.66
MP4SDTQ/6-311+G(3df)	–	–	14.12	9.73
Staemmler's results [1]	−0.94 [b]	−6.78 [b]	13.46 [b]	8.20 [b]
best experimental results	(−1.093±0.05) [c]	–	14.81 [d]	10.20 [d]

[a] All electric properties in au.
[b] Basis set A of that work; see ref. [1].
[c] Hout and Bose [27].
[d] Mason and McDaniel [21].

Table 2
Structural and thermodynamic properties of N_2 [a]

Basis set	r_e	D_e (eV)	k_e	E
HF/6-311+G(df)	2.018	4.87	106.6 [b]	−108.97689
MP4SDTQ/6-311+G(df)	–	9.40	–	−109.34721
HF/6-311+G(2df)	2.016	5.06	105.9 [b]	−108.98391
MP4SDTQ/6-311+G(2df)	–	9.48	–	−109.36929
HF/6-311+G(3df)	2.016	5.09	105.9 [b]	−108.98486
MP4SDTQ/6-311+G(3df)	–	9.54	–	−109.37427
Staemmler's results	2.018 [c]	9.0 [c]	110.3 [c]	−109.2754 [c]
best experimental results	2.074	9.77 [d]	99.87 [e]	–

[a] All structural and thermodynamic properties in au, except D_e.
[b] HF force constants scaled by $(0.89)^2$; see text.
[c] Basis set A of that work; see ref. [1].
[d] Huber and Herzberg [34].
[e] Cade and Wahl [35].

constants that are too large. The MP4SDTQ bond energies in table 2 are nearly double the HF values with the same basis set. Again, the bond energies approach the experimental value, with 3.8%, 3.0%, and 2.4% error using the 6-311+G(df), 6-311+G(2df), and 6-311+G(3df) basis sets, respectively, at the MP4SDTQ level of theory.

The force constants have been calculated at the HF level of theory, and scaled as recommended by DeFrees and McLean [28]. The total energy of the lithium ion in the ground electronic state is −7.23584 au and the major requirement of the lithium basis set is that it remains flexible enough to describe any medium-range bonding interactions.

In the following work we have used the 6-311+G(2df) basis set, unless otherwise stated. This represents the best compromise between the accuracy of the molecular properties describing the subsystems, and expense of characterizing the entire rigid rotor potential energy surface. The 6-311+G(2df) basis set has similar MP2 multipole moments to the other basis sets considered and polarizabilities that are comparable with the experiment values. The bond energy and force constants are in good accord with the experimental measurements. It seems likely that the short-range coulombic repulsion interaction is described well by any of the basis sets studied here.

All calculations have been performed using the GAUSSIAN 90 series of programs [29].

3. The potential energy surface of Li^+–N_2

The calculations reported here were performed with the bond distance of N_2 fixed to the value optimised at the HF level of theory. The post-HF method used to include electron correlation was Møller–Plesset fourth order perturbation theory, with a frozen core that included 1s functions on both N atomic centres. The magnitude of R, the vector connecting the centre of mass of the N_2 molecule and the centre of the Li^+ ion, and θ, the angle between the internuclear vector, r, of N_2, and R, were varied. R was varied to completely characterize the potential energy surface over the energy range 10^{-3}–10^{1} eV for all values of θ. Enough angles were computed to completely characterize the dominant interactions of the Legendre expansion in this energy range. This required calculation of four angles, $\theta = 0°$, 22.5°, 45°, 90°. Tables 3 and 4 contain the total energies for the Li^+–N_2 calculations as a function of R and θ for the HF and the MP4SDTQ levels of theory, respectively.

These potentials have been spline fitted to determine the values of the critical points of the potential energy surface. The spline functions have been determined in a similar fashion to that described by Simpson et al. [30]. Each potential function has been tabulated as a series of points (R_i, V_i), where $V_i = V(R_i)$. These points have been fitted using piece-wise cubic splines by developing equations that ensure that (a) the function interpolates the points (R_i, V_i) and (b) that first and second derivatives are continuous. Two additional equations are required for a complete solution of the cubic spline system of equations and these usually involve constraints on the derivatives at the end points. We have set the second derivatives of the short-range end point to equal zero thus achieving a "natural" cubic spline. Then we have extrapolated to shorter R with the potential

$$V(R) = \frac{a}{R^m} + b, \quad \text{for } R < R_1 , \tag{1}$$

which was fitted using (R_1, V_1), and $(R_1, \partial V_1/\partial R)$ attained after solving the cubic spline system of equations. In this work m was set to equal 6. This extrapolation function was chosen because it closely approximated the behaviour of the short-range ab initio points. Enough ab initio points were calculated to characterize the repulsive wall of the potential energy surface.

The long-range potential was determined by fitting the extrapolating function

$$V(R) = \frac{c}{(R-d)^n}, \quad \text{for } R > R_n , \tag{2}$$

to the points (R_{n-1}, V_{n-1}) and (R_n, V_n). The first derivative of this function at R_n was then used to set the final condition needed to solve the cubic spline system of equations. For the potential energy surface functions n was set to equal 3. The leading long-range interaction terms for the Li^+–N_2 potential energy surface are the ion-quadrupole and the ion-induced dipole interactions. When eq. (2) is expanded in inverse powers of R the ion–quadrupole and the ion–induced-dipole terms are represented as c/R^3, and $3cd/R^4$, respectively. The values of c and d, which are given in table 5, closely correspond to the quadrupole moment and the polarizabilities of the N_2 molecule for the 6-311+G(2df) basis set given in table 1. Enough ab initio points were calculated at large separation to ensure the extrapolation function exhibited the correct long-range behaviour. The value of c in the linear arrangement is very similar to the quadrupole moment calculated to the MP2 level of theory. Because the ion-induced dipole interaction is attractive we expect d to have an opposite sign to c. The value of $3cd$ in the linear arrangement is also very close to the value of $\frac{1}{2}\alpha_{\parallel}$, where $\alpha_{\parallel}$ is given in table 1. In the perpendicular arrangement the value of c is negative because the quadrupole interaction is repulsive. This repulsive interaction leads to a local maximum. Several ab initio points have been calculated beyond the maximum in order to improve the correspondence between the calculated polarizability given in table 1 and the values obtained from the fitting function. The value of c is reasonable but the value of d is not in accord with the calculated polarizabilities. Because the leading asymptotic term (the ion–quadrupole term) is reasonable and the extrapolation function is fitted at large R, we have concluded

Table 3
HF/6-311+G(2df) total energies (in au)

R (Å)	$\theta=0.0°$	$\theta=22.5°$	$\theta=45.0°$	$\theta=90.0°$
1.000	–	–	–	–115.65949
1.100	–	–	–	–115.83856
1.200	–	–	–115.51758	–
1.300	–	–115.23747	–	–116.04877
1.350	–	–	–	–116.08099
1.400	–115.28865	–115.54091	–115.88558	–116.10764
1.500	–115.61167	–115.76920	–115.99939	–116.14779
1.625	–115.87413	–	–116.09464	–116.18025
1.700	–115.97860	–	–	–
1.750	–116.03225	–116.07988	–116.15366	–116.19985
2.000	–116.17998	–116.19218	–116.20988	–116.21799
2.250	–116.22686	–116.22785	–116.22731	–116.22319
2.375	–116.23494	–	–	–
2.500	–116.23825	–116.23609	–116.23071	–116.22386
2.750	–116.23812	–	–116.22968	–116.22318
3.000	–116.23499	–116.23263	–116.22769	–116.22228
3.500	–116.22896	–116.22746	–116.22436	–116.22095
4.000	–116.22532	–116.22440	–116.22246	–116.22028
5.000	–116.22218	–116.22176	–116.22068	–116.21978
6.000	–116.22100	–116.22078	–116.22029	–116.21969
6.500	–	–	–	–116.21968
7.000	–	–	–	–116.21968
8.000	–116.22021	–116.22013	–116.21994	–116.21969
10.000	–116.21997	–116.21993	–116.21984	–116.21971
12.000	–116.21987	–	–	–116.21973
∞	–116.21975	–116.21975	–116.21975	–116.21975

that the error involved in the incorrect fitted polarizability is negligible.

The following general features are exhibited, and listed in table 6, for HF, MP2, and MP4SDTQ levels of theory undertaken in this study. There exists an absolute minimum in the potential energy surface for all the levels of theory at $R \approx 4.9$ bohr, $\theta = 0°$. The depth of the minimum is 0.522 eV at the HF level of theory which increases 6.3% to 0.557 eV with the inclusion of electron correlation at the MP4SDTQ level of theory. The MP4SDTQ potential energy surface minimum reported here is very similar to Staemmler's own HF potential energy surface minimum which he quotes at $R \approx 5.0$ bohr, $\theta = 0°$ with a depth of 0.56 eV. Between the two minima in the linear arrangement exists a col in the perpendicular arrangement. The col is located at $R \approx 4.6$ bohr, $\theta = 90°$ with a relative energy of 0.113 eV at the HF level of theory which decreases slightly (0.9%) to 0.112 eV at the MP4SDTQ level of theory. The col in Staemmler's HF potential energy surface was located slightly shorter at $R \approx 4.5$ bohr but much lower at 0.20 eV suggesting that the magnitude of the quadrupole moment is very important in defining the height of the saddle. Staemmler's quadrupole moment for basis set A was 15% smaller in magnitude than the best experimental value available [27]. This leads to overestimation of the relative energy of the col in the perpendicular arrangement by almost a factor of 2.

The quadrupole moment is important in determining the character of the long-range interaction which is repulsive at large R in the perpendicular arrangement. The quadrupolar repulsion is then dominated by a charge-induced-dipole interaction at smaller R, resulting in a net attraction. Therefore we find a single local maximum exists at $R \approx 12.4$ bohr of 1.89×10^{-3} eV at the HF level of theory, and at $R \approx 11.8$ bohr of 2.74×10^{-3} eV at the MP4SDTQ level of theory. Staemmler reported a local maximum at $R \approx 15$ bohr of 1.3×10^{-3} eV which is again

Table 4
MP4SDTQ/6-311+G(2df) total energies (in au)

R (Å)	$\theta=0.0°$	$\theta=22.5°$	$\theta=45.0°$	$\theta=90.0°$
1.000	–	–	–	−116.05489
1.100	–	–	–	−116.23128
1.200	–	–	−115.89033	–
1.300	–	−115.61827	–	−116.43808
1.350	–	–	–	−116.46967
1.400	−115.70788	−115.92658	−116.26847	−116.49576
1.500	−116.00134	−116.15496	−116.38348	−116.53499
1.625	−116.26123	–	−116.47942	−116.56663
1.700	−116.36492	–	–	–
1.750	−116.41823	−116.46519	−116.53882	−116.58575
2.000	−116.56544	−116.57771	−116.59563	−116.60344
2.250	−116.61278	−116.61397	−116.61354	−116.60853
2.375	−116.62117	–	–	–
2.500	−116.62474	−116.62267	−116.61716	−116.60923
2.750	−116.62488	–	−116.61613	−116.60859
3.000	−116.62176	−116.61932	−116.61402	−116.60771
3.500	−116.61538	−116.61377	−116.61035	−116.60634
4.000	−116.61137	−116.61037	−116.60820	−116.60563
5.000	−116.60786	−116.60738	−116.60637	−116.60512
6.000	−116.60654	−116.60629	−116.60573	−116.60503
6.500	–	–	–	−116.60503
7.000	–	–	–	−116.60503
8.000	−116.60565	−116.60556	−116.60534	−116.60505
10.000	−116.60537	−116.60533	−116.60522	−116.60508
12.000	−116.60526	–	–	−116.60509
∞	−116.60513	−116.60513	−116.60513	−116.60513

Table 5
Fitting parameters for long-range extrapolations

	c (au)	d (au)
HF		
$\theta=0°$	−1.164	+1.429
$\theta=22.5°$	−0.889	+1.840
$\theta=45°$	−0.396	+2.330
$\theta=90°$	+0.491	−4.666
MP4SDTQ		
$\theta=0°$	−1.208	+1.947
$\theta=22.5°$	−0.985	+1.966
$\theta=45°$	−0.418	+2.598
$\theta=90°$	+0.899	−7.524

smaller than the energy reported here and at larger R. Features of the potential energy surface in table 6 show that the geometries of the critical points are not very dependent on the treatment of electron correlation, except for the region about the local maximum.

Other comparisons of the potential energy surface are best observed graphically. Fig. 1 displays the potential energy surface for $\theta=0°$, 45°, and 90° at the MP4SDTQ level of theory. The $\theta=22.5°$ potential energy surface was omitted for clarity. Staemmler's HF potential points are also plotted in fig. 1. Staemmler's $\theta=0°$ potential closely matches the MP4SDTQ potential reported here, however his $\theta=90°$ potential differs significantly from both the HF and MP4SDTQ potentials, which are very close together. It seems intermolecular correlation (dispersion energy) is negligible in the perpendicular approach. Staemmler's points for $\theta=45°$ also suggest values substantially different to the potentials reported here although not enough points were published to draw further conclusions. Comparisons of short-range repulsion are made in fig. 2. Again the $\theta=22.5°$ potential energy surface was omitted for clarity. From fig. 2 it can be seen that the exponential

Table 6
Critical points of the potential energy surface

Critical points	HF	MP2	MP4SDTQ
$\theta=0°$			
$R\ (V=0)$	4.129 [a]	4.129	4.124
$R\ (\partial V/\partial R=0)$	4.926	4.955	4.948
$V\ (\partial V/\partial R=0)$	−0.01919 [b]	−0.02031	−0.02046
$R\ (\partial^2 V/\partial R^2=0)$	5.626	5.659	5.654
$\theta=22.5°$			
$R\ (V=0)$	4.079	4.079	4.071
$R\ (\partial V/\partial R=0)$	4.912	4.938	4.929
$V\ (\partial V/\partial R=0)$	−0.01677	−0.01478	−0.01808
$R\ (\partial^2 V/\partial R^2=0)$	5.601	5.580	5.577
$\theta=45°$			
$R\ (V=0)$	3.971	3.968	3.957
$R\ (\partial V/\partial R=0)$	4.758	4.782	4.769
$V\ (\partial V/\partial R=0)$	−0.01097	−0.01182	−0.01205
$R\ (\partial^2 V/\partial R^2=0)$	5.522	5.559	5.550
$\theta=90°$			
$R\ (V=0)$	3.879	3.902	3.877
$R\ (\partial V/\partial R=0)$	4.615	4.646	4.627
$V\ (\partial V/\partial R=0)$	−0.00415	−0.00382	−0.00413
$R\ (\partial^2 V/\partial R^2=0)$	5.375	5.446	5.432
$R\ (V=0)$	12.387	11.564	11.815
$R\ (\partial V/\partial R=0)$	9.794	9.128	9.413
$V\ (\partial V/\partial R=0)$	−0.00007	−0.00012	−0.00010
$R\ (\partial^2 V/\partial R^2=0)$	16.079	14.777	15.087

[a] All bond distances in bohr.

[b] All energies in au and relative to $R=\infty$.

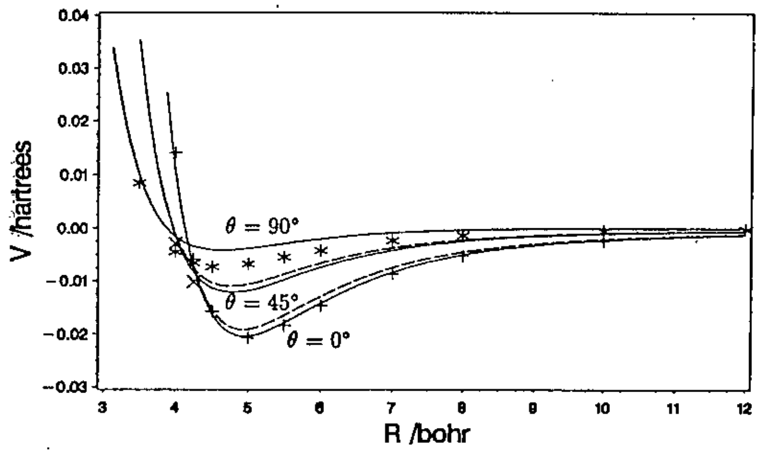

Fig. 1. The potential energy surface of Li^+-N_2 for $\theta=0°$, 45°, and 90°. The dashed curves represent the calculations at the HF level of theory. The solid lines represent the calculations at the MP4SDTQ level of theory. Staemmler's points are represented as +, ×, and • for $\theta=0°$, 45° and 90° respectively.

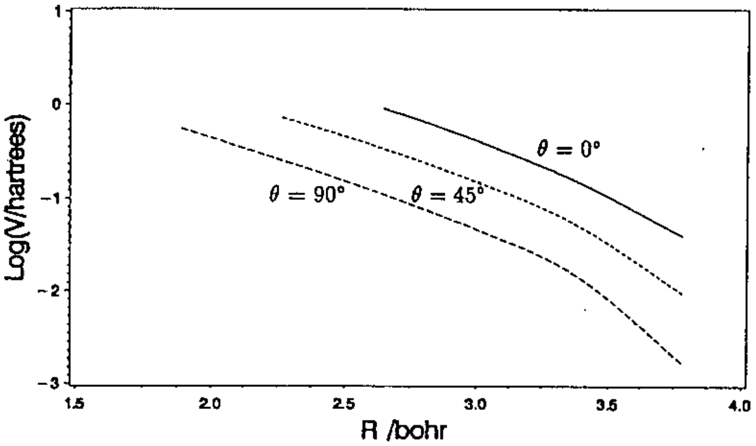

Fig. 2. The short-range potential energy surface of Li^+–N_2. The three curves represent the potential energy surface with $\theta = 0°$, 45°, and 90° for the solid line, the short dashed line and the long dashed line respectively, at the MP4SDTQ level of theory.

repulsion behaviour begins for $R < 3$ bohr.

4. The Legendre expansion

The potential energy surface of Li^+–N_2 results from a number of interactions that are best analysed by decomposing the angular variation of these interactions in a truncated Legendre expansion. This is achieved by

$$V(R, \theta_m) = \sum_{n=0}^{k} P_{m,n} V_n(R) , \qquad (3)$$

where $P_{m,n}$ is the nth degree Legendre polynomial of $\cos\theta_m$, and θ_m are the angles for which ab initio calculations have been performed, namely

$$\theta_m \in \{0°, 22.5°, 45°, 90°\} . \qquad (4)$$

The Legendre expansion was performed for the series up to $k=6$. The odd terms of n vanish in the series as N_2 is a member of the $D_{\infty h}$ point group. The radial functions are obtained using the inverted matrix elements $P^{-1}_{2n,m}$ as radial coefficients:

$$V_{2n}(R) = \sum_{m=0}^{k/2} P^{-1}_{2n,m} V(R,\theta_m) . \qquad (5)$$

The points for which all θ were calculated for a given R have been inverted directly and shown in table 7, and table 8 for the HF and MP4SDTQ levels of theory, respectively. These data are plotted in fig. 3, and some general features are outlined here. The radial functions have also been spline fitted in a similar manner to that described for the potential energy surface. The long-range exponent n of eq. (2) was set to 4, 3, and 5 for V_0, V_2, and V_4 respectively. These exponents are consistent with the ion–induced-dipole, ion–quadrupole, and ion–hexadecapole interactions which are the leading terms for each radial function respectively. For the V_6 radial function n was set equal to 7.

As expected the potential energy surface exhibits a large anisotropic radial function V_2. It is evident from a comparison between fig. 3 of this work and fig. 4 of Staemmler's work that the potential energy surfaces reported here are substantially more anisotropic. At long range this is mainly due to the larger quadrupole moment of our basis set compared to Staemmler's, again emphasizing the importance of electrical behaviour of the isolated subunits. In the region of the radial functions' minimum the anisotropic radial function V_2, is in fact deeper than the isotropic radial function V_0 in contrast with Staemmler's result. The

Table 7
HF/6-331+G(2df) Legendre expansions

R (Å)	V_0 [a]	V_2	V_4	V_6
1.400	293204 [b]	432995	144150	60496
1.500	190728	291156	95869	30070
1.750	56374	92801	31368	6705
2.000	8623	19913	9127	1850
2.250	−6053	−3737	1819	608
2.500	−8950	−9596	−398	190
3.000	−6524	−8088	−845	−36
3.500	−3813	−5076	−523	−48
4.000	−2285	−3219	−302	−22
5.000	−1022	−1539	−106	−17
6.000	−600	−854	−47	−5.3
8.000	−362	−343	−11	−0.7
10.000	−300	−169	−3.0	−0.1

[a] Zeroth order Legendre expansion; see text.
[b] All bond energies are in 1×10^6 au.

Table 8
MP4SDTQ/6-311+G(2df) Legendre expansion

R (Å)	V_0 [a]	V_2	V_4	V_6
1.400	287420 [b]	440228	138274	31322
1.500	190356	292648	92878	27901
1.750	56443	93323	30842	6294
2.000	8629	19867	9443	1748
2.250	−6280	−4323	2375	574
2.500	−9341	−10533	84	180
3.000	−6891	−9067	−636	−38
3.500	−3962	−5802	−443	−49
4.000	−2257	−3700	−266	−23
5.000	−847	−1762	−98	−22
6.000	−379	−986	−46	−7.1
8.000	−116	−399	−11	−0.9
10.000	−47	−197	−2.9	−0.1

[a] Zeroth order Legendre expansion; see text.
[b] All bond energies are in 1×10^6 au.

magnitude of the anisotropic radial function V_2 is also greater than that of the isotropic radial function V_0 at short range, in agreement with Staemmler's result, although this behaviour is not unexpected, considering the N_2 bond distance is of the order of the inter-nuclear distance between the two sub-units. We can also see the Legendre expansion converges rapidly as a series in n, justifying truncating the series at $n=6$.

The improvements in the long-range potential energy surface reported here are supported by the total cross-section measurements of Gislason et al. [10]. Gislason et al. have fitted their scattering data to an analytic expression for the deflection function, from which they have inferred an isotropic radial function, which they claim is valid over the range $2.9 \leqslant R \leqslant 10.2$ bohr. Their isotropic radial function is compared to the one we have derived in table 9 and figs. 4 and 5. Excellent agreement at long range between our isotropic radial function and the isotropic radial function derived by Gislason et al. for $R \geqslant 7$ bohr justifies our choice of basis set and method in this region. Gislason et al. have suggested that Staemmler's HF

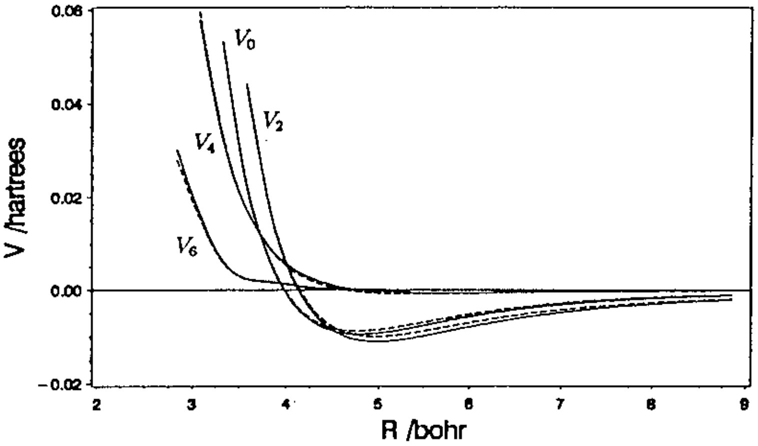

Fig. 3. The radial functions of Li^+–N_2. The dashed lines represent calculations at the HF level of theory, and the solid lines represent calculations at the MP4SDTQ level of theory for the radial functions of the Legendre expansion. At short-range the curves represent in order of increasing repulsion, V_6, V_4, V_0, and V_2.

Table 9
Critical points of the Legendre radial functions

Critical points	HF	MP4SDTQ	Staemmler's	Gislason's	Waldman's
V_0					
$R\ (V_0=0)$	3.990 [a]	3.979	3.932	3.928	3.836
$R\ (\partial V_0/\partial R=0)$	4.759	4.773	4.764	4.793	4.535
$V\ (\partial V_0/\partial R=0)$	−0.00870 [b]	−0.00936	−0.01187	−0.01166	−0.00802
$R\ (\partial^2 V_0/\partial R^2=0)$	5.450	5.481	5.738	5.644	–
V_2					
$R\ (V_2=0)$	4.120	4.109	4.209	–	–
$R\ (\partial V_2/\partial R=0)$	4.990	5.002	5.024	–	–
$V\ (\partial V_2/\partial R=0)$	−0.01018	−0.01120	−0.00939	–	–
$R\ (\partial^2 V_2/\partial R^2=0)$	5.620	5.640	5.585	–	–
V_4					
$R\ (V_4=0)$	4.581	4.759	–	–	–
$R\ (\partial V_4/\partial R=0)$	5.294	5.457	–	–	–
$V\ (\partial V_4/\partial R=0)$	−0.00095	−0.00066	–	–	–
$R\ (\partial^2 V_4/\partial R^2=0)$	5.651	6.411	–	–	–
V_6					
$R\ (V_6=0)$	5.348	5.534	–	–	–
$R\ (\partial V_6/\partial R=0)$	6.211	6.189	–	–	–
$V\ (\partial V_6/\partial R=0)$	−0.00005	−0.00006	–	–	–
$R\ (\partial^2 V_6/\partial R^2=0)$	6.996	6.942	–	–	–

[a] All bond distances in bohr.

[b] All energies in au and relative to $R=\infty$.

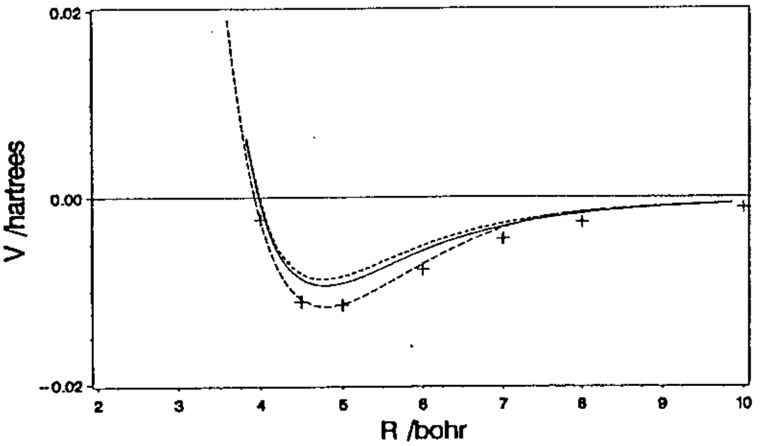

Fig. 4. The isotropic radial function of the Legendre expansion of Li^+-N_2. The + represent Staemmler's isotropic radial function. The short dashed line represents calculations at the HF level of theory and the solid line represents the calculations at the MP4SDTQ level of theory. The long dashed line represents the isotropic radial function derived from Gislason's work.

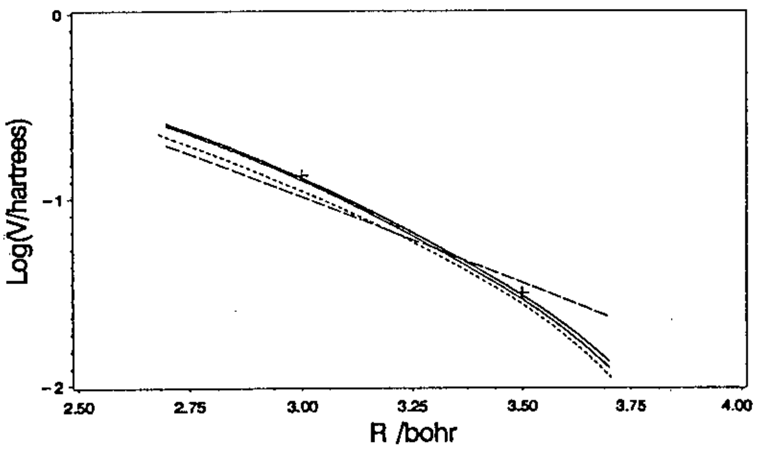

Fig. 5. The short-range radial isotropic function of Li^+-N_2. The long dashed line represents the potential fitted by Kita et al. to $V = \exp(-\alpha R)$. The short dashed line represents the isotropic radial function of Gislason et al. derived from scattering data. Both the HF and the MP4SDTQ levels of theory are represented by the upper solid line. These two levels of theory are sufficiently close to be represented as one line in this region of the potential energy surface. The lower solid line represents $V_{\mathrm{eff},0}$ representing the correction for nuclear polarization at short-range.

method "incorrectly obtains some covalent interaction between the two particles in this region", however our HF surface seems reasonable in this region and we have concluded that the improvement in the basis set was responsible for the agreement between experiment and theory. Waldman et al. [13] have used polarized electron-gas theory to calculate the Li^+-N_2 potential energy surface. Their results have been included in table 9 for comparison.

The well depth of the isotropic radial function is 0.237 eV at the HF level of theory. This increases to 0.255 eV with the inclusion of electron correlation at the MP4SDTQ level of theory. In the region about the well Gislason's isotropic radial function is approximately 20% deeper than the result reported here. This represents an absolute error of about 0.05 eV and is probably at the upper limit of the accuracy of our calculations. In order to estimate the error in treating the N_2 sub-unit as a rigid rotor, we have optimised the bond distance of the N_2 sub-unit with the value of R set at the well minima. This resulted in a lowering of energy of the minimum by 0.006 eV but is still in error by 18% when compared to Gislason's derived potential. We estimate that the well depth for this basis set is 0.261 eV when correcting for nuclear polarization [31]. The effect of increasing the basis set size was also investigated by estimating the well depth with a 6-311+G(3df) basis set, and we found the difference between the two potential energy surfaces to be less than the margin of error for these calculations. Simpson [32] has experienced similar discrepancies between ab initio potentials and the reported experimental values for spherically symmetric ions in inert gases. These discrepancies were treated by scaling the attractive part of the spherically symmetric potential to the experimentally reported well depths, resulting in improved agreement between theoretically derived mobility curves and experimental mobility measurements. Staemmler's isotropic radial function closely matches Gislason's isotropic radial function in the region of the well, but our previous attempts to match this accuracy with atomic ion/atom systems with the HF method have shown that this agreement is fortuitous.

At short range we have compared the isotropic radial functions for $R \leqslant 3.75$ bohr in fig. 5. Kita et al. [4] have made total scattering cross-section measurements of the Li^+–N_2 system in this energy range and fitted their scattering results to a function of the form $V(R) = A\exp(-\alpha R)$. This potential is plotted in fig. 5, along with Staemmler's ab initio points and Gislason's scattering results (which are extrapolated slightly beyond the range of reported validity). Gislason et al. have commented that the results of Kita et al. [4] "agree very well" with their own in this energy range. However Kita et al. appears to have overestimated the range of R for which his functional potential is valid and both Gislason's isotropic radial function and the isotropic radial functions reported here start to depart substantially from the function fitted by Kita et al. in the lower energy region of this energy range. The derivatives of the logarithms of the isotropic radial functions of our results and those of Gislason et al. are in excellent agreement. However the absolute values differed by an amount that is reasonably constant, suggesting that similar exponents would result when attempting to fit a potential of the form used by Kita et al.

We have used Billing's fitted procedure [2] and analytic expression [6], to fit our HF/6-311+G(2df) potential energy surface. Using 35 chosen points and minimizing the error using Powell's method [33] in an identical manner to Billing, and using his parameters as starting values we have managed to reduce the fitting error to 4.5%. Further improvement resulted when using the values of the long-range multipole moments reported here as starting parameters. Replacing the quadrupole and hexadecapole moments with the values listed in table 1, and then minimizing again resulted in an error of only 2.1%. This is an improvement on Billing's attempt to fit Staemmler's HF surface when an error of 6.7% resulted. The optimised parameters are listed in table 10.

We have optimised the N_2 bond distance at short Li^+–N_2 distances to check if nuclear polarization is important. Gislason [31] has commented that the nuclear contribution to long-range polarization effects is negligible, or nearly so, for small molecules such as N_2 and CO. However, with the approach of the Li^+ ion at short-range we should expect to see significant perturbation of the N_2 internuclear distance away from its equilibrium position and corresponding changes to the potential energy surface. Re-opti-

Table 10
Fitted Billing's potential parameters

α [a]	2.0626	B_{00}	−0.1322
β_{00}	0.7197	B_{20}	−86.7854
β_{02}	2.0082	α	9.9682
A_{00}	100.88	Q	−0.8110
A_{20}	250.37	H	−7.5793
A_4	48.046	$\frac{1}{3}(\alpha_\parallel - \alpha_\perp)$	4.7821

[a] All parameters in au.

mizing the bond length of the N_2 species with the Li^+ ion species at $R=2.75$ bohr with angles $\theta=0°$, 45°, 90°, has resulted in absolute bond distance changes to r of -0.221, -0.062, and $+0.005$ bohr, respectively, at the HF level of theory. Associated with these changes in bond distances are decreases in energy when comparing the optimized bond distance values with the corresponding value obtained when the bond distance of the N_2 molecule was fixed to its equilibrium distance. The energy is lowered by 2.603, 0.119, and 0.001 eV at the HF level of theory and 1.609, 0.034 and 0.021 eV at the MP4SDTQ level of theory for the angles $\theta=0°$, 45°, and 90° respectively. A pronounced decrease in the bond length (10%) occurs in the linear arrangement and a slight increase occurs in the perpendicular arrangement for $R=2.75$ bohr. These results are in accord with those described by Staemmler. The decrease in the absolute energy from optimizing the N_2 internuclear distance for the Li^+ ion at short-range appears to be over-estimated at the HF level of theory. A large part of this over-estimation is probably related to the failure of the HF approximation to provide accurate force constants. We have examined the likely changes to the Legendre expansion functions due to nuclear polarization. Using eq. (5) to transform these changes to the potential energy surface at $R=2.75$ bohr has resulted in a lowering of energy to the radial functions. The energy is lowered by 0.374, 0.448, and 0.579 eV at the HF level of theory and by 0.195, 0.050, and 0.448 eV at the MP4SDTQ level of theory for the radial functions V_0, V_2, and V_4, respectively. To account for the effect of nuclear polarization on the Legendre radial functions we have fitted an analytic function of the form of eq. (7) to correct the rigid rotor surface,

$$V_{\mathrm{eff},n}=V_n-V_{\mathrm{np},n}\,, \tag{6}$$

$$V_{\mathrm{np},n}=(V_n-V_{\mathrm{opt},n})\exp[-\alpha(R-r_{\mathrm{np}})]\,. \tag{7}$$

We have calculated the correction for nuclear polarization at $r_{\mathrm{np}}=2.75$ bohr, and we have approximated α with that reported by Kita et al. [4] (2.127 bohr^{-1}) for the radial functions V_0, V_2, and V_4 because log–linear plots of the potential as a function of R reveal similar slopes (see fig. 6). We have not attempted to theoretically justify this analytic form. However, this function is in accord with Staemmlers description of nuclear polarization at short range, is physically reasonable, and is exact at $R=2.75$ bohr. With this expression we have avoided expensive calculations optimizing r as a function of R and θ. The values of $V_n-V_{\mathrm{opt},n}$ are given in table 11, and $V_{\mathrm{eff},0}$ is plotted in fig. 5. Comparing the isotropic radial func-

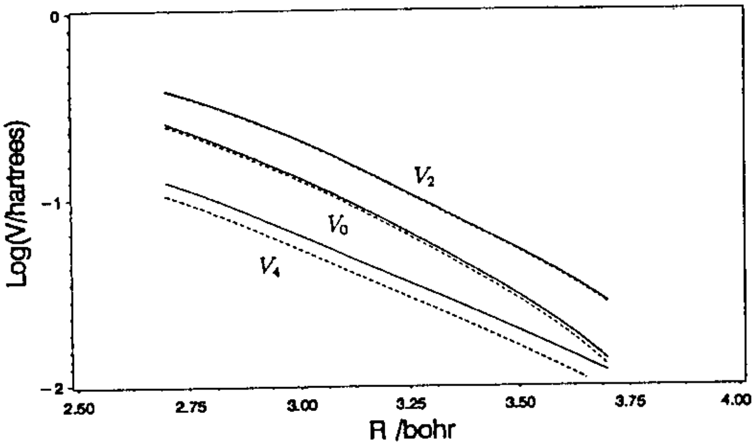

Fig. 6. The short-range radial functions V_4, V_0, and V_2 of $Li^+ + N_2$ in order of increasing repulsion. The solid lines represent the rigid rotor radial functions. The short dashed lines represent the corrections for nuclear polarization. Note that the gradients of the radial functions are similar at $R=2.75$ bohr.

Table 11
Parameters to correct for nuclear polarization

	HF	MP4SDQ	MP4SDTQ
$V_0 - V_{\mathrm{opt},0}$	0.01375 [a]	0.00751	0.00716
$V_2 - V_{\mathrm{opt},2}$	0.01646	0.00512	0.00183
$V_4 - V_{\mathrm{opt},4}$	0.02128	0.01745	0.01648

[a] All parameters in au.

tion which has been corrected for nuclear polarization with the experimentally derived isotropic radial function of Gislason shows improved agreement at short range. Our corrections for nuclear polarization have only slightly perturbed the values of the critical points listed in tables 6 and 9. The relative features have all remained similar to the uncorrected potential energy surface and the most significant differences appear at short range.

Estimation of the basis set superposition error (BSSE) by counterpoise correction has been examined for a few points on the potential energy surface. Previous experience with atomic-ion–atom systems has shown these effects on the potential energy surface to be comparatively small in the area about the well, and even less significant elsewhere. To fully calculate the BSSE by counterpoise correction for the entire potential energy surface is prohibitively expensive and we estimate that the correction would decrease the well depth of the isotropic radial function by less than 10%. Similar absolute corrections would result for V_2 and V_4.

5. Conclusion

We have reported ab initio calculations for the potential energy surface for the the Li^+–N_2 interaction at the HF and MP4SDTQ levels of theory with a 6-311+G(2df) basis set. We have selected our basis set and method to optimize agreement between the calculated and experimental electrical properties of the isolated sub-units. The calculated quadrupole moment, perpendicular and parallel polarizabilities for the N_2 sub-unit differ from the experimentally reported values by 5.8%, 15.9%, and 4.6%, respectively. The long-range interaction of the Li^+–N_2 system agrees well with the isotropic radial function derived from total scattering cross-sections reported by Gislason et al. [10]. The isotropic radial function has a well depth of 0.256 eV at 4.805 bohr at the MP4SDTQ level of theory. This is 19.4% less deep than Gislason's result. The short-range isotropic radial function corresponds well with Gislason's derived isotropic radial function although our values are more repulsive. This is explained to some extent by re-optimizing the N_2 bond length on approach of the Li^+ ion. The following paper tests the potential energy surface reported here by comparing transport coefficients calculated from it with the experimental values for Li^+–N_2.

Acknowledgement

We wish to thank Larry A. Viehland for suggesting this study and for his many helpful suggestions.

References

[1] V. Staemmler, Chem. Phys. 7 (1975) 17.
[2] G.D. Billing and A. Hunding, Chem. Phys. Letters 44 (1976) 30.
[3] T.F. Ewing, J. Detrich and R.W. Conn, J. Chem. Phys. 69 (1978) 4662.
[4] S. Kita, K. Noda and H. Inouye, Chem. Phys. 7 (1975) 156.
[5] L.D. Thomas, J. Chem. Phys. 67 (1977) 5224.
[6] G.D. Billing, Chem. Phys. 36 (1979) 127.
[7] D. Poppe and R. Böttner, Chem. Phys. 30 (1978) 375.
[8] G.A. Pfeffer and D. Secrest, J. Chem. Phys. 78 (1983) 3052.
[9] U. Gierz, J.P. Toennies and M. Wilde, Chem. Phys. Letters 110 (1984) 115.
[10] E.A. Gislason, P. Polak-Dingels and M.S. Rajan, J. Chem. Phys. 93 (1990) 2476.
[11] L.A. Viehland, in: Status and future developments in the study of transport properties, NATO ASI Series C, Vol. 361, eds. W.A. Wakeham, A.S. Dickinson, F.R.W. McCourt and V. Vesovic (Kluwer, Dordrecht, 1992).
[12] T.D. Selnaes, T.H. Løvaas and H.R. Skullerud, J. Phys. B 23 (1990) 2391.
[13] M. Waldman and R.G. Gordon, J. Chem. Phys. 71 (1979) 1353.
[14] J.E. Del Bene, M.J. Frisch, K. Raghavachari, J.A. Pople and P. von R. Schleyer, J. Phys. Chem. 87 (1983) 73.
[15] S. Ikuta, Chem. Phys. 95 (1985) 235.
[16] J. Sauer and P. Hobza, Theoret. Chim. Acta 65 (1984) 291.
[17] V.M. Pinchuk, J. Struct. Chem. 26 (1985) 350.
[18] J.E. Del Bene, J. Comput. Chem. 7 (1986) 259.
[19] D.A. Dixon, J.L. Cole and A. Komornicki, J. Phys. Chem. 92 (1988) 1378.

[20] A. Szabo and N.S. Ostlund, Modern quantum chemistry: introduction to advanced electronic structure theory (Macmillan, New York, 1982).

[21] E.A. Mason and E.W. McDaniel, Transport properties of ions in gases (Wiley–Interscience, New York, 1988).

[22] P.W. Harland, R.G.A.R. Maclagan and R.W. Simpson, J. Chem. Soc. Faraday Trans. II 84 (1988) 1847.

[23] R.W. Simpson, R.G.A.R. Maclagan and P.W. Harland, J. Chem. Phys. 87 (1987) 5419.

[24] R.W. Simpson, P.W. Harland and R.G.A.R. Maclagan, Intern. J. Mass Spectrom. Ion Processes 90 (1989) 193.

[25] S.T. Grice, P.W. Harland, R.G.A.R. Maclagan and R.W. Simpson, Intern. J. Mass Spectrom. Ion Processes 87 (1989) 181.

[26] S.T. Grice, P.W. Harland, J. Harrison, R.G.A.R. Maclagan and R.W. Simpson, Intern. J. Mass Spectrom. Ion Processes 107 (1991) 215.

[27] J. Hout and T.K. Bose, J. Chem. Phys. 94 (1991) 3849.

[28] D.J. DeFrees and A.D. McLean, J. Chem. Phys. 82 (1985) 333.

[29] M.J. Firsch, M. Head-Gordon, G.W. Trucks, J.B. Foresman, H.B. Schlegel, K. Raghavachari, M. Robb, J.S. Binkley, C. Gonzalez, D.J. DeFrees, D.J. Fox, R.A. Whiteside, R. Seeger, C.F. Melius, J. Baker, R.L. Martin, L.R. Kahn, J.J.P. Stewart, S. Topiol and J.A. Pople, GAUSSIAN 90, Revision F (Gaussian Inc., Pittsburgh, 1990).

[30] R.W. Simpson, R.G.A.R. Maclagan and P.W. Harland, J. Phys. B 20 (1987) 2723.

[31] G.A. Gislason, F.E. Budenholzer and A.D. Jorgensen, Chem. Phys. Letters 47 (1977) 434.

[32] R.W. Simpson, Ph.D. Thesis, University of Canterbury, New Zealand (1988).

[33] W.H. Press, B.P. Flannery, S.A. Teukolsky and W.T. Vetterling, Numerical recipes (Cambridge Univ. Press, Cambridge, 1986).

[34] K.P. Huber and G. Herzberg, Molecular spectra and molecular structure, Vol. 4. Constants of diatomic molecules (Van Nostrand Reinhold, New York, 1979).

[35] P.E. Cade, K.D. Sales and A.C. Wahl, J. Chem. Phys. 44 (1966) 1973.

J. CHEM. SOC. FARADAY TRANS., 1993, 89(12), 1903–1907

Application of the Thermal Conduction Model to Rotational Relaxation in Molecular Beams

Brett R. Cameron and Peter W. Harland
Chemistry Department, University of Canterbury, Christchurch, New Zealand

A simple approach to the estimation of rotational relaxation times and collision numbers in supersonic expansions based on the use of the thermal conduction model is presented. Expressions are derived for the calculation of these quantities and relaxation times are calculated as a function of mean kinetic temperature and axial distance from the nozzle exit for the homonuclear diatomic species H_2, N_2, O_2 and Cl_2.

Until recently, supersonic or nozzle molecular beam sources have been the exclusive domain of the molecular dynamicist. Once it was recognised that these devices provided a new technique for the generation of cooled molecules through seeding, such sources became a valuable tool in the study of the spectroscopy of polyatomic molecules[1,2] and for the study of ion–molecule chemistry at low temperatures. Experiments such as these which are designed to measure quantitative parameters in molecular beams rely on a knowledge of the beam density, collision frequency and temperature of the species involved as a function of distance from the nozzle exit. The thermal conduction model and the extensions described in this paper provide a convenient means by which these properties may be estimated. Such parameters cannot be routinely measured in the laboratory and rigorous solution of the Boltzmann equation results in expressions which cannot be easily applied.

The translational temperature of a molecular gas undergoing a supersonic expansion may decrease so rapidly that the rotational degrees of freedom of a molecule do not have sufficient time to relax completely.[3] It is these relaxation lags which are observed experimentally in the form of a difference between the terminal rotational temperature and the terminal parallel translational temperature of a supersonic molecular beam. An analysis of these rotational relaxation lags is useful for the study of energy-transfer processes between rotational and translation degrees of freedom and for the prediction of the internal states of molecules in molecular beams produced by supersonic expansion techniques. It would, for example, be desirable to be able to predict with some degree of accuracy the final distribution of rotational states of symmetric-top molecules used in molecular beam experiments employing a supersonic nozzle source in association with an upper Stark state selector.[4]

A number of workers have analysed the relaxation kinetics in supersonic expansions on the basis of the so-called Landau–Teller model[5] with the inherent assumption that the characteristic bulk rotational relaxation rate is approximately constant throughout the entire duration of the expansion. On the basis of experimental results this assumption is quite clearly incorrect.[6] Consequently, for any theoretical model to describe realistically the relaxation kinetics of supersonic expansions it must allow for the variation of the rotational relaxation time as a function of both the mean translational temperature and the rotational temperature. We show here that the thermal conduction model may be used to provide the required functionality in both a straightforward and reliable manner.

Theoretical Considerations

The differential equation used to describe the rate of change of the rotational temperature as a function of distance in our adaptation of the thermal conduction model has much in common with the following expression which has been frequently used for many years[7] to describe rotational relaxation phenomena:

$$\frac{dT_r}{dt} = \frac{1}{\tau_r}(T_m - T_r) \tag{1}$$

In this equation, τ_r is the mean rotational relaxation time, T_r is the rotational temperature at time t and T_m is the mean equilibrium temperature of the translational reservoir. Eqn. (1) has generally been applied to the analysis of bulk systems under thermodynamic equilibrium and has proved somewhat difficult to justify at the molecular level. Gallagher and Fenn[5] recognised, however, that the evolution of a distinct rotational temperature in a supersonic expansion is essentially a relaxation process having much in common with such bulk equilibrium processes. Comparing eqn. (1) with eqn. (4c) of ref. 3, which describes the change in rotational temperature as a function of reduced distance along the expansion axis, it can be shown that the expression for the inverse rotational relaxation time according to the thermal conduction model is

$$\tau_r^{-1} = u\frac{3\xi\beta}{R}p(T_\perp, T_\parallel, T_r)\Xi\left(\frac{T_m}{T_0}\right)^{1/6}\frac{z_0}{z^2} \tag{2}$$

$$= \frac{16}{15}\frac{3\xi\beta}{R}p(T_\perp, T_\parallel, T_r)^3 n(z) \times\left(\frac{2k_B T_m}{m}\right)^{1/2} c_{2,2}\left(\frac{C_6}{k_B T_m}\right)^{1/3}; \quad c_{2,2} \approx 2.99 \tag{3}$$

where $n(z)$ is the number density at distance z from the nozzle exit,[8] u is the mean flow velocity of the molecular beam and Ξ is the source parameter.[8,9] The coefficient β is given by the expression

$$\beta = \frac{1}{\Gamma}\frac{9}{16}\left(\frac{R}{R+1}\right)$$

with $\Gamma \approx 0.5813$ for the C_6 potential, and ξ is the rotational–translational coupling parameter, introduced by Klots[7] to represent the fraction of inelastic collisions experienced by a molecule. Note that eqn. (3) is applicable only to the evaluation of rotational relaxation times in an expanding jet, and that it is valid only at distances from the nozzle exit greater than or equal to the boundary condition value, z_0. The function $p(T_\perp, T_\parallel, T_r)$ in eqn. (2) and (3) has the following form:

$$p(T_\perp, T_\parallel, T_r) = \left[\frac{(R+5)T_0 - 3T_\parallel - 2T_\perp - RT_r}{(R+5)T_0}\right]^{1/2} \tag{4}$$

and must be evaluated using our variant of the thermal conduction model. In this expression T_0 is the source temperature, $T_\perp$ and $T_\parallel$ are the translational temperature components perpendicular and parallel to the beam axis, respectively, and R is the number of rotational degrees of freedom of the molecule.

The expression for the rotational relaxation time given in eqn. (3) is similar in form to eqn. (26) of ref. 10 derived by Randeniya and Smith, but with one important difference. In contrast to the expression derived by them, eqn. (3) accounts for the dependence of the rotational relaxation time on the translational and the rotational temperature of the system. The expression used by Randeniya and Smith includes only one temperature variable and essentially assumes that the function $p(T_\perp, T_\parallel, T_r)$ is a constant value. They go to considerable lengths to derive a set of moment equations from the generalized Boltzmann equation to predict the properties of a supersonic expansion and criticise the thermal conduction model for its failure to account properly for the total energy of the expanding jet as a result of fixing the flow velocity of the beam at its thermodynamic limiting value at all points in the expansion. Subsequent to Randeniya and Smith's publication, we introduced the function $p(T_\perp, T_\parallel, T_r)^3$ as a simple and effective means of incorporating a variable flow velocity into the thermal conduction model using basic conservation of energy principles. While it is true that $p(T_\perp, T_\parallel, T_r)$ rapidly tends to a constant value for most systems, it is by no means independent of temperature. In assuming a constant function for $p(T_\perp, T_\parallel, T_r)$, Randeniya and Smith have effectively incorporated into their model the point of their criticism regarding the thermal conduction model.

From eqn. (3) it follows that the inverse rotational collision number is given by the expression

$$Z_r^{-1} = \frac{16}{15}\frac{3\xi\beta}{R}\, p(T_\perp, T_\parallel, T_r)^3 \qquad (5)$$

which, like eqn. (3), is also a function of both the translational and rotational temperature of the expanding jet. In the approach adopted by Randeniya and Smith this quantity is assumed to be a constant value, independent of the rotational and translational energy of the system during the course of the expansion. The rotational collision number is defined as the product of the rotational relaxation time and the mean collision frequency. The collision number is therefore independent of pressure and dependent only upon T_r, T_m and the degree of non-equilibrium between the translational and rotational modes of the molecule.

The distribution of rotational energies of molecules in an expanding jet may exhibit distinctly non-Boltzmann character.[11] Although the thermal conduction model and the approach used by Randeniya and Smith to describe the expansion process freely use the term rotational temperature, this does not imply that a unique rotational temperature and, by inference, a well defined rotational-state distribution exist in an expanding jet.[7] The rotational temperature is merely a convenient short-hand notation used to describe the average rotational energy of the system.

Note that the approach described here represents only a first-order approximation of the rotational relaxation process in molecular beams and will become progressively less accurate with increasing distance from the nozzle exit. The inclusion of higher-order terms in the rate expression would require a knowledge of the exact state-to-state cross-sections for the rotational to translational energy transfer process. A complete evaluation of the differential cross-sections as a function of scattering angle and initial relative velocity would be necessary to evaluate the relaxation time properly. The use of full-scale trajectory calculations for the evaluation of such detailed information is currently being pursued for the case of atomic–homonuclear diatomic systems. The application of a simple direct-simulation Monte Carlo algorithm to the calculation of rotational relaxation data for larger non-polar polyatomic systems is also being investigated. The method described here is not applicable to polar molecules for which the interaction potential is decidedly non-spherical.

Results and Discussion

Rotational relaxation times calculated using eqn. (3) for the homonuclear diatomic species N_2, O_2, Cl_2 and H_2 are plotted in Fig. 1 as a function of the mean kinetic temperature, T_m, and in Fig. 2 as a function of axial distance expressed in nozzle diameters. All data were calculated for a

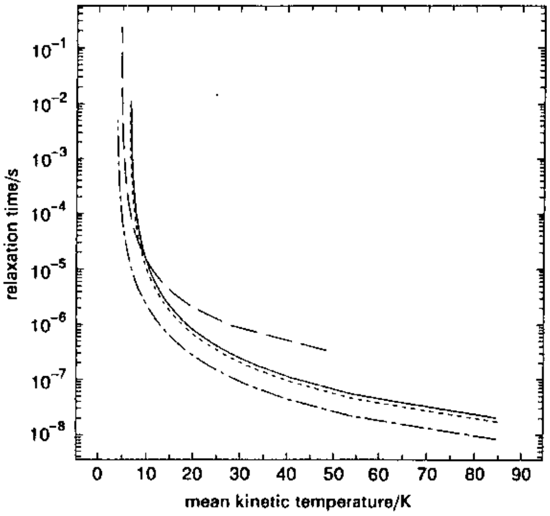

Fig. 1 Rotational relaxation times as a function of mean kinetic temperature for (——) N_2, (- - -) O_2, (-·-·) Cl_2 and (— —) H_2 calculated for a source pressure of 1 atm at 300 K

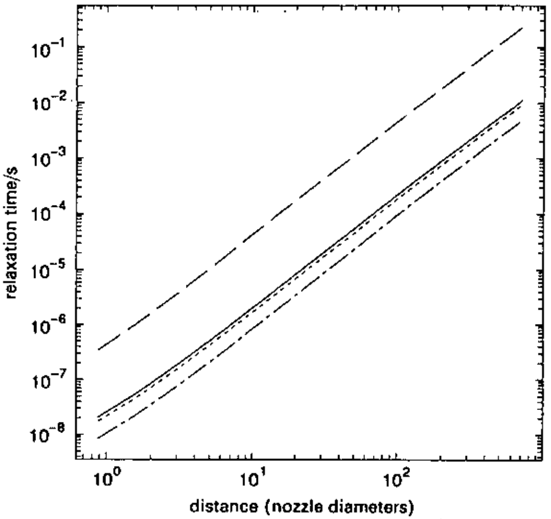

Fig. 2 Rotational relaxation times as a function of distance from the nozzle exit for N_2, O_2, Cl_2 and H_2 (key to lines as for Fig. 1)

Table 1 Rotational-translational coupling parameters used for the calculation of relaxation times and collision numbers

system	ξ
H_2	0.015
N_2	0.39
O_2	0.41
Cl_2	0.58

source pressure of 1 atm at a temperature of 300 K and a nozzle diameter of 7×10^{-5} m. The values of the rotational-translational coupling parameters, ξ, used for these calculations are given in Table 1. The Lennard-Jones C_6 potential parameters were taken from ref. 12. The values of ξ for H_2, N_2 and O_2 were taken from ref. 3 while the value of 0.58 for Cl_2 was estimated from the experimental data of ref. 13 using an iterative Monte Carlo procedure in which it is assumed that the amount of energy transferred between the rotational and translational degrees of freedom of each molecule in a binary collision is equal to a constant fraction multiplied by the difference in energy between the rotational and translational modes. The value of the constant fraction is varied in an iterative manner such that the calculated rotational relaxation time converges to the specified experimental figure. It can be shown that this fraction is, to a good approximation, directly proportional to ξ.[14] Given suitably reliable experimental rotational relaxation data, this technique provides a useful approach to estimating ξ for any system. A comment should be made regarding the observation that the values of ξ given by Randeniya and Smith[10] are approximately a factor of two smaller than those presented here in Table 1. This difference is essentially due to the implicit inclusion of the number of rotational degrees of freedom in the values stated by Randeniya and Smith.

The variation of rotational collision number as a function of distance from the nozzle exit is illustrated for the species considered in Fig. 3. It can be seen that the absolute change in rotational collision number during the course of the expansion is small but significant. For all the systems considered, the collision number is observed to decrease slightly during the expansion and then become essentially constant as the rotational and parallel translational temperature components begin to freeze out. The rotational collision number represents the average number of collisions required for a molecule to establish equilibrium between its rotational and translational degrees of freedom. As the rotational and parallel translational temperature components of the expanding jet freeze out, so too will the rotational collision number. It is, of course, true that the perpendicular component of the translational temperature does not freeze out but rather continues to decrease towards zero with increasing distance from the nozzle exit. However, the perpendicular temperature is so small compared with the parallel temperature at the point in the expansion where the parallel component becomes frozen that its effect on the collision number will be quite negligible beyond that point.

The behaviour of the N_2, O_2 and Cl_2 systems is quite similar, with the rotational collision numbers becoming almost constant at approximately the same point within the expansion. Rotational relaxation in H_2 is a far less efficient process with the rotational temperature becoming frozen relatively early in the expansion, close to the nozzle exit where the number density is still high. This is clearly illustrated in Fig. 4, which shows the variation of rotational temperature as a function of axial distance expressed in terms of nozzle diameters for the species considered here. As can be seen, the rotational temperature of H_2 drops by only a factor of 2 and attains its terminal value after just a few nozzle diameters while the rotational temperatures of the other species continue to drop well into the expansion. By definition, ξ represents the fraction of inelastic collisions experienced by a molecule, indicating that only one in about every 67 collisions between hydrogen molecules leads to an exchange of energy between rotational and translational modes. The magnitude of the rotational collision number is largely determined by the value of the rotational-translational coupling parameter ξ, which may be considered to represent a measure of the efficiency of rotational to translational energy transfer.

Unfortunately, it is difficult to compare the data shown in Fig. 1–3 with most other studies of rotational relaxation in

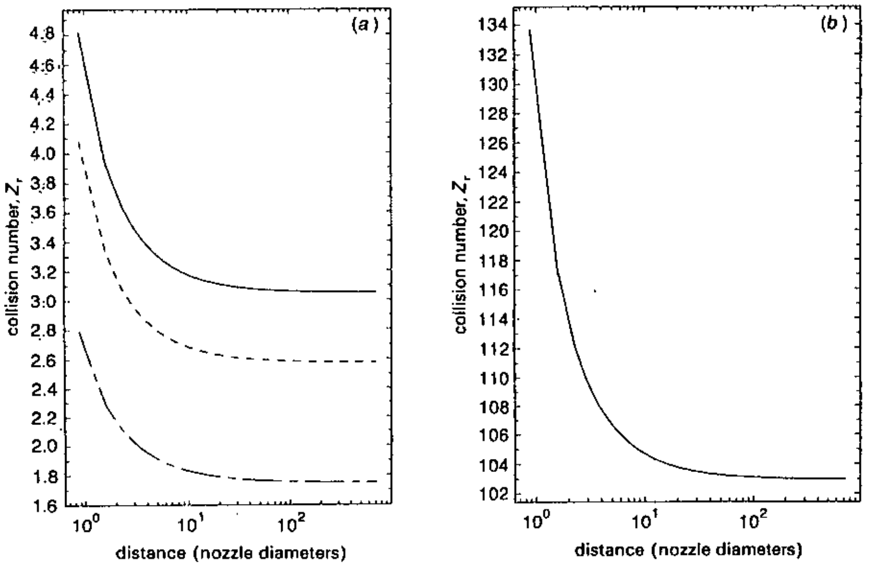

Fig. 3 Rotational collision numbers as a function of distance from the nozzle exit for (a) N_2, O_2 and Cl_2 (key to lines as for Fig. 1), and (b) H_2

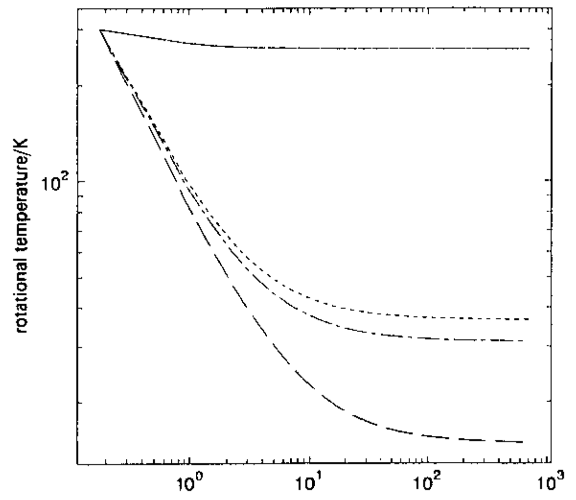

Fig. 4 Rotational temperatures as a function of distance from the nozzle exit for (---) N_2, (-·-·) O_2, (— —) Cl_2 and (——) H_2

molecular beams. The accuracy of results presented in many papers which discuss the calculation of relaxation times and collision numbers in molecular beams is uncertain. While the majority of such papers generally employ sophisticated and reliable models to calculate the relaxation times, the expansion process is often described in a very simple manner using basic isentropic flow relations to evaluate the axial number density and translational temperature of the molecular beam.[6] Such relations do not provide an accurate description of the expansion process and, as a consequence, rotational relaxation times calculated using number densities and translational temperatures determined in such a manner cannot be considered reliable.

The collision numbers presented in Fig. 3 for N_2 and O_2 close to the nozzle exit where the translational temperature of the gas is not greatly different from that of the source, are in good agreement with the calculations of Parker[15] and the experimental results of Sessler[16] and Greenspan.[17] The variation of Z_r with axial distance for N_2 is in qualitative agreement with the experimental results of Poulsen and Miller[18] for supersonic expansions of nitrogen–argon mixtures. The rotational collision numbers calculated for Cl_2 appear slightly high compared with the results of ref. 19 and 20, but are in reasonable agreement with Parker's results. The experimental data used to estimate ξ for Cl_2 were obtained from observations of shock front thickness and may not be entirely applicable to the molecular beam environment.[21] Experimental and theoretical studies indicate that rotational relaxation in Cl_2 is a very efficient process and the value for ξ of 0.58 may be somewhat conservative.

Studies for H_2 have generally been performed at higher temperatures than those considered here. The experimental data of Gallagher and Fenn[5] for H_2 extend only down to 77 K and the master equation calculations of Rabitz and Lam[21] down to *ca.* 100 K. In both cases the calculated rotational collision numbers are considerably higher than those that might be expected from extrapolation of the data shown in Fig. 3 for H_2 to higher temperatures. The results of Gallagher and Fenn suggest that the value of the rotational–translational coupling parameter for H_2 should possibly by closer to half the value stated in Table 1. The value of 0.015 was determined by comparing values of the terminal parallel translational temperature of the molecular beam calculated using the thermal conduction model with terminal temperatures measured by standard time-of-flight techniques.[3] While it may be argued that the resolution of such techniques is insufficient to measure accurately the extremely narrow speed distribution of hydrogen, considerable care was taken to ensure that all possible sources of distortion to the time-of-flight signal were either eliminated or properly taken into account, and we are confident that our value of ξ for H_2 is accurate to within ±10%. It is hoped that work currently being pursued using a higher level of theory will help to clarify this situation.

Table 2 Values of the parameter A in eqn. (6) calculated for $P_0 = 1$ atm and $T_0 = 300$ K

system	A/kg m^{-1} s^{-1} K^{-1}
H_2	1.45×10^{-4}
N_2	6.97×10^{-6}
O_2	5.81×10^{-6}
Cl_2	2.83×10^{-6}

It is evident from Fig. 2 that log–log plots of rotational relaxation time *vs.* axial distance are distinctly linear. Fitting these curves to a straight line yielded a linear least-squares correlation coefficient of better than 0.99 in all cases. To a good approximation, the rotational relaxation time may therefore be calculated as a function of axial distance for any set of source conditions using the following expression:

$$\tau_r = A\frac{T_0}{P_0}\left(\frac{z}{d_0}\right)^2; \quad \frac{z}{d_0} > \left(\frac{1}{A}\right)^{1/2}\left(\frac{P_0}{T_0}\right)^{1/2} \qquad (6)$$

where z is the distance from the nozzle along the beam axis, d_0 is the nozzle diameter, P_0 and T_0 are the source pressure and temperature, respectively, and A is a fitting parameter which is approximately constant over a moderate range of P_0 and T_0. The restriction imposed on the minimum value of z is relatively insignificant, corresponding to only a fraction of a nozzle diameter under most conditions. Values of A for the species considered in this paper based on a source pressure of 1 atm† and temperature of 300 K are given in Table 2. Further calculations at several sets of source conditions indicate that A is a weak function of P_0 and T_0, being inversely proportional to both quantities, but more sensitive to changes in the latter. For example, calculations for N_2 reveal that A changes by only 1% as a result of increasing P_0 from 1 atm to 2 atm, while increasing T_0 by a factor of two reduces the value of A given in Table 2 by *ca.* 5%. Eqn. (6) should be applied with some care and used as a guide only. It simply represents a convenient means of roughly estimating rotational relaxation times without the need for solving the differential equations used by the thermal conduction model to describe the expansion process.

Conclusion

This paper describes a relatively simple approach to the estimation of rotational relaxation times and collision numbers for non-polar molecules in a supersonic expansion based on the thermal conduction model. Results for the species considered are in general agreement with those of similar studies, giving us some confidence in the derived expressions for the rotational relaxation time and the rotational collision number. The use of the derived expressions requires the complete solution of the thermal conduction model. The empiri-

---

† 1 atm = 101 325 Pa.

cal expression given by eqn. (6) was obtained from analysis of calculated relaxation time data as a function of axial distance and may be used to estimate relaxation times for any set of source conditions. The method described in this paper is not restricted to diatomic species and may easily be applied to simple non-polar polyatomic molecules such as CO_2 and CH_4. Calculations for these and other species are currently being pursued.

References

1 R. D. Levine and R. B. Bernstein, *Molecular Reaction Dynamics*, Oxford, 1974.
2 *Atomic and Molecular Beam Methods*, ed. G. Scoles, Oxford, 1988.
3 B. R. Cameron and P. W. Harland, *J. Chem. Soc., Faraday Trans.*, 1991, **87**, 1069.
4 P. W. Harland, H. S. Carman Jr., L. F. Phillips and P. R. Brooks, *J. Chem. Phys.*, 1991, **95**, 8137, and references therein.
5 R. J. Gallagher and J. B. Fenn, *J. Chem. Phys.*, 1973, **60**, 3492.
6 S. Yamazaki, M. Taki and Y. Fujitani, *J. Chem. Phys.*, 1981, **74**, 4476.
7 C. E. Klots, *J. Chem. Phys.*, 1980, **72**, 192.
8 H. C. W. Beijerinck, G. H. Kaashoek, J. P. M. Beijers and M. J. Verheijen, *Physica C*, 1983, **121**, 425.
9 H. C. W. Beijerinck and N. F. Verster, *Physica C*, 1981, **111**, 327.
10 L. K. Randeniya and M. A. Smith, *J. Chem. Phys.*, 1990, **93**, 661.
11 P. V. Marrone, *Phys. Fluids*, 1967, **10**, 521.
12 J. O. Hirschfelder, C. F. Curtiss and R. B. Bird, Molecular Theory of Gases and Liquids, Wiley, Chichester, 1954.
13 W. H. Anderson and D. F. Hornig, Technical Report, Metcalf Research Laboratory, Brown University, 1958.
14 B. R. Cameron and P. W. Harland, 1993, unpublished results.
15 J. G. Parker, *Phys. Fluids*, 1959, **2**, 449.
16 G. Sessler, *Acustica*, 1958, **8**, 395.
17 M. Greenspan, *J. Acoust. Soc. Am.*, 1959, **31**, 155.
18 P. Poulsen and D. R. Miller, American Institute of Aeronautics and Astronautics, New York, 1977, p. 899.
19 E. Sittig, *Acustica*, 1960, **10**, 81.
20 H. J. Bauer and H. Kosche, *Acustica*, 1966, **17**, 1196.
21 H. Rabitz and S. H. Lam, *J. Chem. Phys.*, 1975, **63**, 3532.

Paper 3/00328K; *Received 19th January*, 1993

J. CHEM. SOC. FARADAY TRANS., 1993, 89(19), 3517-3525 3517

Monte Carlo Calculation of Rotational Relaxation in Small Molecules

Brett R. Cameron and Peter W. Harland
Chemistry Department, University of Canterbury, Christchurch, New Zealand

The application of a direct simulation Monte Carlo procedure to the investigation of rotational relaxation in homogeneous gases is described in which the rotational–translational energy transfer is assumed to be related to the fraction of inelastic collisions in terms of a rotational–translational coupling parameter. The energy dependence of the coupling parameter is investigated for the homonuclear diatomic molecules H_2, N_2, O_2 and Cl_2, and for the polyatomic species CO_2, OCS, NH_3, CH_4, CH_3Cl and C_2H_4. Rotational collision numbers are calculated for these molecules and the energy-dependent coupling parameter is used in thermal conduction model calculations to investigate the breakdown of translational and rotational equilibrium in supersonic expansions of CO_2, OCS and CH_3Cl.

The exchange of energy between translational and internal degrees of freedom in molecular collisions plays an important role in molecular processes, and has been an area of considerable theoretical and experimental interest for many years. The mechanism of rotational–translational energy transfer has not received as much attention as vibrational–translational transfer, due to the greater influence of the latter process on the kinetics of chemical reactions. The study of rotational–translational energy transfer and rotational relaxation processes of molecules in supersonic expansions is, however, of particular interest for several reasons. The low collision energies attainable in supersonic expansions provide a unique environment which is ideally suited to the synthesis of weakly bound van der Waals clusters and the spectroscopy of complex molecules. From a spectroscopic point of view, it would therefore be highly desirable to be able to predict with some degree of accuracy the populations of individual rotational energy levels for molecules at any location within the expanding jet, while in general, there is the hope that an improved understanding of both rotational relaxation phenomena and the expansion process itself may be gained from such studies.

In previous papers,[1,2] we examined the rotational relaxation of the homonuclear diatomic species H_2, N_2, O_2 and Cl_2 in a supersonic expansion on the basis of the thermal conduction model.[1,3] In this paper, we present some initial calculations of rotational relaxation times and collision numbers using a direct simulation Monte Carlo procedure in which the exchange of energy between the rotational and translational degrees of freedom is assumed to be simply related to the fraction of inelastic collisions experienced by a molecule at a particular energy in terms of Klots rotational–translational coupling parameter.[3] The energy dependence of the rotational–translational coupling parameter is investigated for the homonuclear diatomic species stated above, and for the polyatomic molecules CO_2, OCS, NH_3, CH_4, CH_3Cl and C_2H_4 using available experimental and theoretical data. The rotational and translational energy dependence of rotational relaxation times is examined for these species and the energy-dependent coupling parameter is incorporated into the thermal conduction model to investigate the breakdown of rotational and translational equilibrium in supersonic expansions of CO_2, OCS and CH_3Cl.

Relaxation Model

A number of classical dynamical and statistical theories have been developed for the investigation of relaxation phenomena in molecules of varying size and complexity. Dynamical calculations are generally observed to produce results which differ considerably from those obtained using statistical theories, with the latter often badly overestimating the average energy changes in a collision. The use of full-scale dynamical trajectory calculations is generally considered to be the most reliable means of investigating energy transfer or relaxation processes in a classical mechanical manner.[4] In order for the full potential of such methods to be realised, however, it is necessary to have detailed information describing the entire potential surface for the collision system of interest. Lack of suitable potential-energy surface data for many systems of interest coupled with the computational difficulties and time overhead associated with the use of such surfaces in full-scale three-dimensional trajectory calculations of relaxation times is sufficient to justify recourse to a phenomenological approach to the problem. The approach adopted in this paper makes use of the direct simulation Monte Carlo method and available relaxation data to predict rotational relaxation times under any set of conditions.

The direct simulation Monte Carlo method is a technique specifically devised for the computer modelling of complex gas flow phenomena. Flows are modelled by storing the velocity components and spatial coordinates of a representative population of simulated molecules and allowing these molecules to collide and move in accordance with their physical properties. The crux of the direct simulation Monte Carlo technique is the manner in which molecular motion and intermolecular collisions are uncoupled. Simulations of this type essentially proceed by uncoupling molecular motion and intermolecular collisions over some time interval Δt_m such that Δt_m is small compared to the inverse of the mean collision frequency. At time t all molecules are allowed to move freely over the time interval Δt_m and collisions appropriate to this time-span are then calculated by fixing the molecular positions.

The computation of a set of representative collisions is of crucial importance in the direct simulation Monte Carlo method. The total number of collisions N_t occurring in a uniform homogeneous gas during the time interval Δt_m is given by the expression

$$N_t = \frac{1}{2} N_m n \Delta t_m \overline{\sigma c_r} \qquad (1)$$

where N_m is the total number of simulated molecules present in the flow at time t, n is the number density and σ is the collision cross-section for a collision pair moving with relative speed c_r. The symmetry factor 1/2 is included in eqn. (1) as there are two molecules whose properties are recalculated after each collision. If the number of collisions calculated over Δt_m is $N_m/2$, then all of the N_m simulated molecules will have experienced a change of state.

The product $\overline{\sigma c_r}$ in eqn. (1) represents the mean collision rate per unit density. The evaluation of this quantity will be time consuming, particularly if N_m is large, as is usually the case. To negate this problem in the direct simulation Monte Carlo method each collision is given a collision lifetime Δt_c, determined by the expression

$$\Delta t_c = \frac{2}{N_m} (n\overline{\sigma c_r})^{-1} \tag{2}$$

and collisions are then calculated until the sum of the collision lifetimes equals or just exceeds the value of Δt_m. Collision pairs are chosen by application of the acceptance–rejection method[5] with probability proportional to σc_r and both molecules have their velocity components recalculated according to the conservation of energy and momentum.

Since its inception there has been some concern that the direct-simulation Monte Carlo method does not provide a solution to the Boltzmann equation. The method has been shown to produce results consistent with the Boltzmann equation, but equivalence has not been proved. The technique was developed from the point of view of simulating real gas flows rather than for the explicit purpose of solving the Boltzmann equation. The method is simple to apply to a particular problem and conceptually straightforward. It is computationally more efficient than other similar simulation schemes[6,7] and has been demonstrated by Bird[8,9] and others[10] to give excellent results when applied to a wide range of complex gas-flow problems.

The devised simulation is based on the energy sink model proposed by Bird,[11,12] and associates a single variable representing the total rotational energy summed over all rotational degrees of freedom with each simulated molecule. In a collision, the value of this variable is compared for each collision partner with the relative translational energy of the collision. If the rotational energy is not equal to the relative translational energy, a fraction of the energy difference is transferred between the rotational and translational modes in the direction which more nearly satisfies equilibrium according to the equation[3]

$$E_{t,f} = E_{t,i} + \xi\left(\frac{\mathscr{R}}{\mathscr{R}+1}\right)\left(k_b T_r - \frac{3}{5}\, 6E_{t,i}\right) \tag{3}$$

where $E_{t,i}$ and $E_{t,f}$ are the initial and final relative translational energies, respectively, $\mathscr{R}$ is the number of rotational degrees of freedom, T_r is the effective rotational temperature, and ξ is the rotational–translational coupling parameter. The rotational–translational coupling parameter was introduced by Klots[3] as a means of incorporating rotational degrees of freedom into the thermal conduction model used for investigating the breakdown of equilibrium in supersonic expansions,[1,13] and represents the fraction of collisions in which energy is transferred between the rotational and translational degrees of freedom of the colliding molecules.

As stated by Klots,[3] the assumption that the rotational relaxation process can be properly described by a single value of the coupling parameter, independent of all other collision parameters, is somewhat naive and open to improvement. As ξ represents the fraction of inelastic collisions experienced by a molecule, it seems reasonable to assume that it will be proportional to the mean collision cross-section, and we therefore suggest that ξ may be suitably approximated by an expression of the form

$$\xi = \begin{cases} a\bar{\sigma} & \bar{\sigma} \leqslant a^{-1} \\ 1 & \text{otherwise} \end{cases} \tag{4}$$

where $\bar{\sigma}$ is the mean collision cross-section and a is a constant scaling parameter for a particular collision system. According to the definition that ξ represents the fraction of inelastic collisions experienced by a molecule, it is required that $0 \leqslant \xi \leqslant 1$, and we assume that for energies below which $\bar{\sigma} > a^{-1}$, the coupling parameter is exactly equal to unity. In order to easily incorporate the functionality of ξ suggested by eqn. (4) into the thermal conduction model, we fit calculated values of ξ to an expression of the form

$$\xi = \begin{cases} (\beta T_m)^{\alpha} & T_m \geqslant \beta^{-1} \\ 1 & \text{otherwise} \end{cases} \tag{5}$$

where α and β are fitting parameters and T_m is the mean kinetic temperature. Collision cross-sections are often approximated by functions of the form T_m^{α} and, in fact, the thermal conduction model using an attractive C_6 interaction potential, inherently uses collision cross-sections proportional to $T_m^{-1/3}$.

Computational Procedure

The Monte Carlo procedure for the calculation of rotational relaxation times is primed with the initial temperatures of the rotational and translational reservoirs, the initial pressure of the system, a tabulated interaction potential, the molecular mass of the gas, the cross-section scaling parameter a, the number of rotational degrees of freedom, and a value specifying the time interval Δt_m at which the rotational and translational temperatures are to be sampled. The total number of sampling intervals is fixed at a value of 100.

The tabulated interaction potential consisted of up to 100 points, generally taken at regular intervals along the potential curve, and over a suitably wide range to ensure that little or no extrapolation of the supplied data was required. Cubic spline interpolation[14] was then used to evaluate the interaction potential at any intermolecular separation from the supplied list of points. Extrapolation of the supplied potential data with the correct behaviour at large and small intermolecular separations was performed when necessary by fitting inverse power functions to each end of the interpolating function such that

$$V(r) = \begin{cases} \dfrac{c_1}{r^p} + c_2\,; & 0 < r \leqslant r_1 \\[2ex] \dfrac{c_3}{(r - c_4)^q}\,; & r_n \leqslant r < \infty \end{cases} \tag{6}$$

where c_1, c_2, c_3 and c_4 are fitting parameters, and r_1 is the smallest and r_n the largest tabulated intermolecular separation. Values of the exponents p and q were generally chosen to be 12 and 6, respectively. Using a tabulated interaction potential in this way places no functional restrictions on the form of the potential and allows listed data to be taken directly from the literature if required. This method was used with considerable success by Simpson *et al.* to model accurately ion mobilities in helium using interaction potentials calculated at as few as 12 intermolecular separations.[15–17] A similar approach has been adopted by Viehland and Mason,[18] who used the somewhat more sophisticated method of Lagrange interpolation to calculate $V(r)$, although there appears to be little difference in terms of the results obtained using either interpolation scheme. The various advantages and disadvantages of these and other methods of interpolation are discussed in detail by Press *et al.*[19]

The number N_m of simulated molecules was set at 4096 for all of the calculations presented in this paper. In general, there is a square-law relationship between the error associated with an answer and the number of observations used in the determination of the answer in a Monte Carlo calculation. To reduce the error by a factor of k, it is therefore necessary to increase the number of observations by k^2. It was considered that 4096 simulated molecules was a sufficiently large number to produce answers with an acceptably small standard error but not so large as to incur a significant overhead in the overall computation time.

The initial velocity components for each simulated molecule were randomly selected from a Maxwellian velocity distribution function of the form

$$f(v_x, v_y, v_z)\,\mathrm{d}v_x\,\mathrm{d}v_y\,\mathrm{d}v_z = \left(\frac{m}{2\pi k_b T_m}\right)^{3/2} \times \exp[-m(v_x + v_y + v_z)^2/2k_b T_m]\,\mathrm{d}v_x \times \mathrm{d}v_y\,\mathrm{d}v_z \tag{7}$$

where m is the molecular mass and T_m is the translational temperature. The random selection of velocities from this distribution was performed using the method of Box and Muller,[19] which is generally considered to be the most efficient means of sampling from Gaussian distributions such as eqn. (7).

The distribution of rotational energies was approximated by a continuous probability distribution function of the form[20]

$$p(E_r)\,\mathrm{d}E_r \propto E_r^{(\vartheta/2-1)} \exp(-E_r/k_b T_r)\,\mathrm{d}E_r \tag{8}$$

Values for the initial rotational energy of each simulated molecule were randomly selected from this distribution using a variation on the algorithm described by Press *et al.*[19] for the selection of random deviates from the gamma distribution. While it may be somewhat unrealistic to describe the distribution of rotational energies in terms of a continuous function such as eqn. (8), it is computationally difficult and time consuming to sample from discrete distributions. We feel that results obtained using eqn. (8) are satisfactory in most circumstances.

The collision algorithm commences with the random selection of a pair of molecules with appropriate probability. For pairs which are accepted for a collision, the collision counter is advanced by unity, the time counter is advanced according to eqn. (2), and energy is transferred between the rotational and translational modes of the colliding molecules in accordance with eqn. (3).

Following the exchange of energy between the rotational and translational degrees of freedom, the post-collision components (u_r^*, v_r^*, w_r^*) of the relative velocity vector c_r^* are calculated according to the following set of equations[21]

$$u_r^* = u_r \cos\chi + (v_r^2 + w_r^2)^{1/2} \sin\chi \sin\varepsilon \tag{9}$$

$$v_r^* = v_r \cos\chi + (c_r w_r \cos\varepsilon - u_r v_r \sin\varepsilon)(v_r^2 + w_r^2)^{-1/2} \sin\chi \tag{10}$$

$$w_r^* = w_r \cos\chi - (c_r v_r \cos\varepsilon + u_r w_r \sin\varepsilon)(v_r^2 + w_r^2)^{-1/2} \sin\chi \tag{11}$$

and scaled to account for the exchange of energy. The solution of these equations requires the evaluation of the classical deflection angle, χ, at the initial relative translational energy and the azimuth angle ε. The azimuth angle is uniformly distributed on the interval $\{0, 2\pi\}$ and may be randomly selected according to the expression

$$\varepsilon = 2\pi R_f \tag{12}$$

where R_f is a uniform random deviate on the interval $\{0, 1\}$. The classical deflection angle is given by the integral

$$\chi = \pi - 2b \int_{r_m}^{\infty} \frac{1}{r^2}\left(1 - \frac{V(r)}{E} - \frac{b^2}{r^2}\right)^{-1/2} \mathrm{d}r \tag{13}$$

where b is the impact parameter and r_m is the outermost solution of the equation

$$\left(1 - \frac{V(r)}{E} - \frac{b^2}{r^2}\right)^{1/2} = 0 \tag{14}$$

for an interaction potential $V(r)$. The impact parameter for the collision was chosen at random from the probability distribution

$$p(b)\,\mathrm{d}b = \frac{1}{\pi b_{max}^2} 2\pi b\,\mathrm{d}b \tag{15}$$

with crude Monte Carlo selection.[5] Noting that the probability of obtaining a particular impact parameter is directly proportional to b, it is a straightforward matter to apply the transformation method[5] to eqn. (15) and show that

$$b = R_f^{1/2}/b_{max} \tag{16}$$

where R_f is a uniform random deviate on the interval $\{0, 1\}$ and b_{max} is a cut-off impact parameter chosen such that it is large enough to include all significant events, but not so large as to produce too many uninteresting collisions. It is important to note that calculated rotational relaxation times will depend to some extent upon the choice of b_{max}, and its value must therefore be chosen with some care. In previous simulations of this type, the value of b_{max} was generally chosen in a somewhat arbitrary manner and held constant for all collisions.[4] In this investigation we calculate a separate and more suitable b_{max} for each collision on the basis of the collision cross-section σ according to the expression

$$b_{max} = \frac{1}{\sqrt{\pi}} \sigma(c_r)^{1/2} \tag{17}$$

where c_r is the relative speed of the collision pair. Collision cross-sections were calculated according to the integral

$$\sigma^{(l)}(E) = 2\pi \int_0^{\infty} b(1 - \cos^l \chi)\,\mathrm{d}b \tag{18}$$

for $l = 2$. Evaluation of eqn. (13) and (18) was performed using an extensively modified version of the program employed by O'Hara and Smith for the calculation of collision integrals.[22,23]

It is important to emphasize that the deflection function described by eqn. (13) refers to elastic scattering while eqn. (9)–(11) are applicable to both elastic and inelastic collisions. The aim of the present model is to provide a reliable method for estimating rotational relaxation data without having to perform lengthy three-dimensional trajectory calculations requiring detailed information about the entire potential surface for a particular collision system and the solution of a large set of coupled differential equations. Instead of calculating complete trajectories, the exchange of energy between the rotational and translational modes of the collision pair is assumed to be separable from the determination of the post-collision velocity components. Energy is transferred between the rotational and translational modes according to eqn. (3) prior to the determination of the post-collision velocity components which are then scaled to ensure conservation of energy.

Owing to the large number of collisions which must be examined, the evaluation of the double integral describing the collision cross-sections clearly represents one of the more time-consuming aspects of the computational procedure. In order to reduce this computational overhead, collision cross-sections were calculated at 256 intervals over a suitably wide energy range and fitted to Chebyshev polynomials[19,24] prior to initiation of the Monte Carlo simulation. In this way, the solution of eqn. (18) was reduced to the evaluation of a simple polynomial expression, with a considerable saving in computation time. The energy range over which cross-sections were fitted was taken as three standard deviations either side of the mean of the relative velocity distribution at the initial translational temperature. The probability of a velocity lying outside this range is $<2.2 \times 10^{-5}$.[25]

The rotational and translational temperatures were sampled at the specified interval Δt_m and stored until the end of the run, whereupon they were fitted to the first-order relaxation equation

$$\frac{dT_r}{dt} = \frac{1}{\tau_r}(T_e - T_r) \qquad (19)$$

or

$$T_r = T_e - (T_e - T_{r,0})\exp(-t/\tau_r) \qquad (20)$$

in which τ_r is the mean rotational relaxation time, T_e is the equilibrium temperature, T_r is the rotational temperature at time t and $T_{r,0}$ is the initial rotational temperature at time $t = 0$. The equilibrium temperature is defined for a non-equilibrium gas as the weighted average of the translational and rotational temperatures according to the expression

$$T_e = \frac{1}{\mathcal{R} + 3}(3T_m + \mathcal{R}T_r) \qquad (21)$$

assuming $\frac{1}{2}k_b T$ of energy per rotational degree of freedom.

To estimate collision cross-section scaling parameters, the computational procedure was modified to solve the equation

$$\tau_r(a) = \tau_{r,\text{expt}} \qquad (22)$$

given an experimentally measured rotational relaxation time, $\tau_{r,\text{expt}}$, and two values of the scaling parameter, a, bridging the root. The value of the scaling parameter was then varied in an iterative manner using the algorithm of Dekker and Brent[19] within the specified range until the calculated relaxation time converged to within ±1% of the experimental figure. Having determined the collision cross-section scaling parameter, it is possible to calculate relaxation times under any set of conditions.

Results and Discussion

Collision cross-section scaling parameters and rotational relaxation times were calculated for the ten species given in Table 1. Relaxation times were determined by fitting the sampled rotational temperatures to eqn. (20) using a simple linear least-squares algorithm. The quality of the obtained fits was generally found to be very good, resulting in linear least-squares correlation coefficients of better than 0.95 in almost all cases. Poor correlation coefficients were invariably due to a bad choice of sampling interval, resulting in the rotational and translational degrees of freedom actually reaching equilibrium well before the end of the simulation. A sampling interval of *ca.* 0.1 mean collision times was found to be suitable for most calculations. Tabulated interaction potentials used in all of the calculations discussed below were constructed from the Lennard-Jones (12,6) parameters given by Hirschfelder *et al.*[21]

Values of the collision cross-section scaling parameter for the species listed in Table 1 were determined from experimental and theoretical relaxation data found in the literature. Unfortunately it was often difficult to use directly the data given by some authors without making assumptions regarding the initial rotational temperature or degree of non-equilibrium between the rotational and translational degrees of freedom, as such information was not always clearly stated, the assumption presumably being that the relaxation time is independent of the initial degree of non-equilibrium.† In such situations it was necessary to choose a suitable initial rotational temperature on the basis of how the system was displaced from equilibrium. Rotational relaxation times have been most commonly measured by supersonic expansion, sound absorption and shock tube techniques. As stated by Rabitz and Lam,[26] the temperature departures associated with these three techniques are $T_r > T_m$, $T_r \approx T_m$, and $T_r < T_m$, respectively. It was found that the relaxation model is not well behaved when $T_r \approx T_m$, making it difficult to use relaxation data obtained from sound absorption experiments reliably for the estimation of scaling parameters.

The scaling parameter of 7.41×10^{17} m^{-2} calculated for N_2 was derived from theoretical results of Mason and Monchick[27] and represents an average of values determined at seven relaxation times over a translational temperature range 100–1000 K. The resulting values of the rotational–translational coupling parameter and the mean collision cross-section $\bar{\sigma}$ at each of the seven temperatures are plotted in Fig. 1. The plotted values of $\bar{\sigma}$ represent the average of some 10^4 cross-sections calculated at energies sampled from the relative speed distribution at each temperature. The calculated variation of the coupling parameter is remarkably similar to the variation of the mean collision cross-section with temperature over the range considered, providing us with some confidence in the validity of eqn. (4). Also plotted in Fig. 1 is the curve fitted to the calculated values of ξ using eqn. (5).

Similarly, good agreement between the calculated variation of ξ and $\bar{\sigma}$ was found for CH_4 and C_2H_4 using the experimental data of Kelly and Hill and Winter[28,29] and for O_2 based on the sound absorption measurements of Sessler[30] and Greespan.[31] The value of the scaling parameter given for H_2 was estimated from the results of Gallagher and Fenn[32] who determined relaxation times at several temperatures between 300 and 1900 K from time-of-flight analysis of supersonic free jets and the ultrasonic measurements of Winter and Hill.[33] The scaling parameter for OCS was determined from the results of Unland and Flygare,[34] who determined rotational relaxation times for OCS from microwave double-resonance experiments over a wide range of pressures.

Calculations of the scaling parameter for the remaining species listed in Table 1 were made somewhat difficult owing to either the lack of sufficiently accurate experimental data or considerable discrepancies between values of relaxation times

Table 1 Calculated scaling and fitting parameters

system	$a/10^{17}$ m^{-2}	α	β/K^{-1}	system	$a/10^{17}$ m^{-2}	α	β/K^{-1}
H_2	0.34	−0.3348	2.924×10^{3}	O_2	6.81	−0.3827	3.499×10^{-2}
CH_4	1.05	−0.3842	2.372×10^{0}	CO_2	8.41	−0.3833	6.056×10^{-3}
NH_3	5.82	−0.3749	1.772×10^{-1}	CH_3Cl	6.50	−0.3315	6.981×10^{-3}
N_2	7.41	−0.3484	4.245×10^{-2}	OCS	6.06	−0.3698	7.036×10^{-3}
C_2H_4	1.15	−0.3831	7.563×10^{-1}	Cl_2	3.16	−0.3676	3.928×10^{-2}

---

† As will be discussed later, such an assumption is quite reasonable for most non-polar diatomic molecules, with the rotational relaxation time being only a weak function of the rotational temperature.

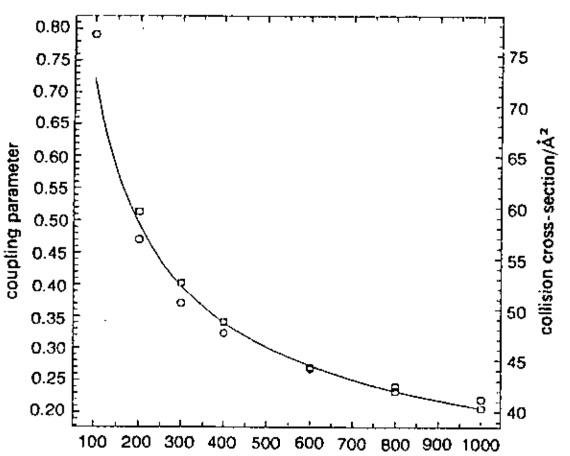

Fig. 1 Collision cross-sections (□) and calculated values of ξ (○) for N_2 from 100 to 1000 K

stated by different authors. The value of 3.16×10^{17} m^{-2} for Cl_2 was determined from the experimental results of Sittig,[35] resulting in a calculated collision number of *ca.* 3.3 at 300 K. This figure is significantly less than that of 4.9 calculated by Parker[36] and the upper limit of 5.5 suggested by Anderson and Hornig[37] from observations of shock front thickness. As stated by Miller and Andres,[38] rotational collision numbers obtained from shock-tube experiments are often observed to be slightly higher than may be expected. Owing to the close coupling of the rotational and translational modes of most molecules, it is frequently difficult to separate the contributions of rotational relaxation from those of translational relaxation in such experiments, meaning that the information obtained, while generally precise, is not totally unambiguous. The rotational energy levels of Cl_2 are considerably more closely spaced than those of N_2 or O_2 and since rotational–translational energy transfer is more efficient when the rotational levels of the species involved are closer, it seems reasonable to assume that rotational relaxation in Cl_2 should be somewhat more efficient than that of N_2 or O_2. We therefore consider that the scaling parameter calculated for Cl_2 from the experimental results of Sittig is likely to be quite reasonable.

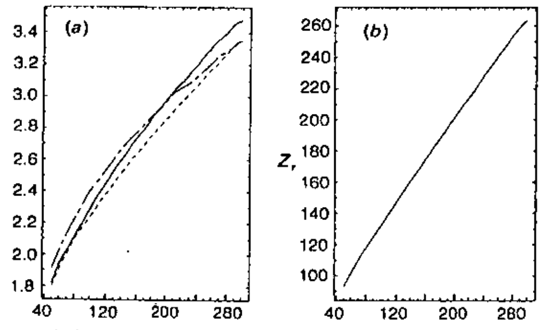

Fig. 2 Variation of rotational collision number with translational temperature for (*a*) N_2 (——), O_2 (– – –) and Cl_2 (–·–) and (*b*) H_2

The scaling parameter of 5.82×10^{17} m^{-2} for NH_3 was estimated from the results of Jones *et al.*[39] Little work has been done on the rotational relaxation of NH_3, making it somewhat difficult to assess the reliability of the calculated parameter, although the resulting values of ξ seem quite reasonable ($\xi \approx 0.23$ at 300 K) considering the fact that the rotational energy levels in NH_3 are some 3–4 times less closely spaced than those of N_2. One point to note, however, is that vibrational–rotational energy transfer in NH_3 is a highly efficient process due to the low-frequency umbrella motion peculiar to the NH_3 molecule, with $Z_v \approx Z_r$ at room temperature,[39] where Z_v is the vibrational collision number. Consequently, it may not be possible to ignore vibrational motion in the calculation of rotational relaxation times for NH_3. Detailed information is available on the vibrational transition probabilities of many species, and the possibility of extending the model described here to include vibrational degrees of freedom is currently being investigated.

The value of 8.41×10^{17} m^{-2} determined for CO_2 was based on the thermal transpiration measurements of Malinauskas *et al.*[40] and results in coupling parameter values similar to those of OCS.

The scaling parameter of 6.50×10^{17} m^{-2} for CH_3Cl was calculated from the theoretical results of Mason and Monchick[27] and should not be considered reliable. Mason and Monchick developed a simple expression relating the thermal conductivity of a polyatomic gas to its rotational relaxation time. Comparisons made with experimental data indicate that the expression produces good results for simple molecules such as homonuclear diatomics, but fails to provide an accurate description of the relaxation process for highly polar species. CH_3Cl is a highly polar molecule, having a dipole moment of 1.87 D,† close to the value for H_2O (1.85 D) and significantly greater than that of HCl (1.08 D). The relaxation model described here, with its incorporation of a spherical potential, may not be applicable either.

Values of the fitting parameters α and β for eqn. (5) given in Table 1 were determined from a linear least-squares fit of $\ln|\xi|$ *vs.* $\ln|T_m|$. The calculated values of α are approximately the same for all of the species considered and are reasonably close to 1/3, reflecting the attractive C_6 component of the Lennard-Jones potentials used in all of the calculations. The value of β is observed to vary by several orders of magnitude from 10^{-3} for CO_2, OCS and CH_3Cl through to 10^3 for H_2.

With the possible exception of CH_3Cl, the simulation procedure was found to reproduce reliably the majority of experimental and theoretical results used in the determination of the cross-section scaling parameters, giving us considerable confidence in the use of the model to predict rotational relaxation times at any set of initial conditions. Rotational collision numbers calculated using the direct simulation Monte Carlo procedure are presented in Fig. 2 and 3 as a function of translational temperature from 50 to 300 K for the species listed in Table 1. The rotational collision number is a useful and frequently stated quantity in the discussion of rotational relaxation phenomena. It is a dimensionless quantity, defined simply as the product of the rotational relaxation time and the mean collision frequency:

$$Z_r = \tau_r \nu \tag{23}$$

and represents the average number of collisions required for a molecule initially perturbed from equilibrium to re-establish equilibrium between its rotational and translational degrees of freedom. The collision number is independent of

---

† 1 D ≈ 3.33564×10^{-30} C m.

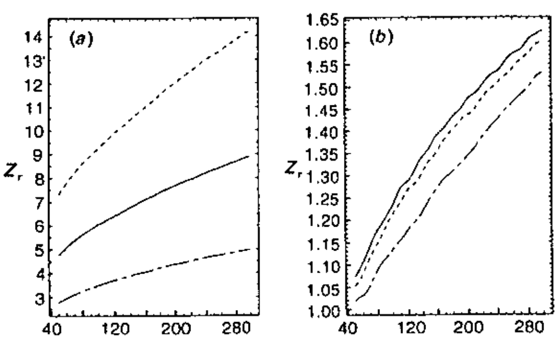

Fig. 3 Variation of rotational collision number with translational temperature for (*a*) C_2H_4 (——), CH_4 (– – –), NH_3 (– — –) and (*b*) CH_3Cl (——), OCS (– – –), CO_2 (– — –)

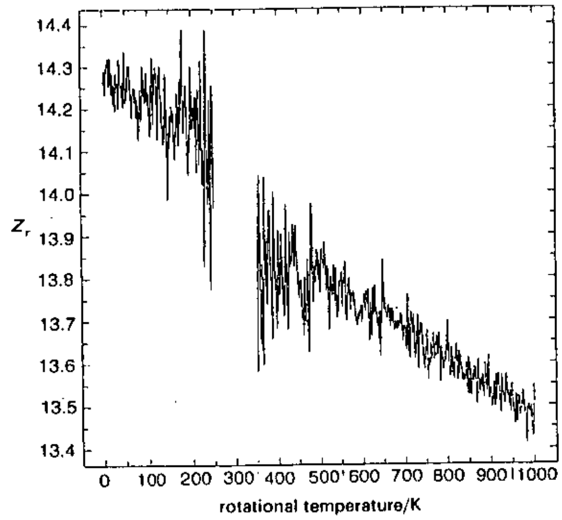

Fig. 4 Variation of rotational collision number with rotational temperature for CH_4

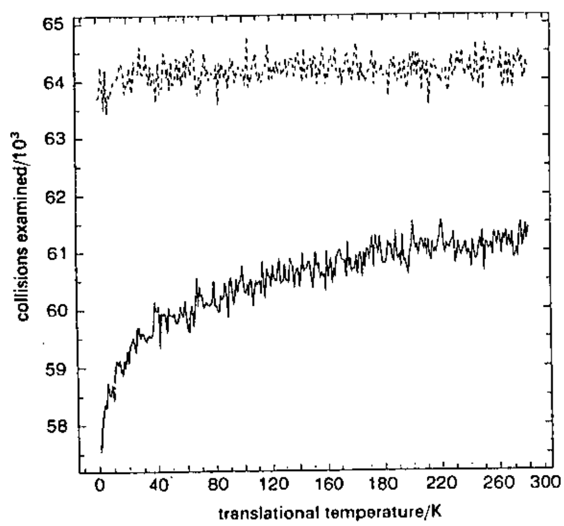

Fig. 5 Number of collisions examined as a function of translational temperature for H_2 (– – –) and N_2 (——)

density and thus provides a convenient means of comparing relaxation data measured under different conditions. With the exception of H_2 and some hydrides, the rotational energy level spacings of most molecules are quite small. Consequently, rotational–translational energy transfer is generally observed to be a relatively efficient process, with rotational collision numbers being in the range of 1 to 10 for most species at room temperature.

The relaxation times used to determine the collision numbers illustrated in Fig. 2 and 3 were calculated at a pressure of 1 atm with all of the energy associated with each simulated molecule initially contained in the translational modes so that the results could be directly compared with the theoretical predictions of Parker[36] and Zeleznik.[41] The values of the collision cross-section scaling parameter used for these calculations are given in Table 1 along with calculated values of the fitting parameters α and β used in eqn. (5). The data presented in Fig. 2 and 3 were smoothed to remove from the calculated curves much of the noise incurred through the use of Monte Carlo methods. As can be seen, the calculated collision numbers increase with increasing translational temperature for all of the species considered. The results are all in qualitative agreement with the predictions of Parker, although, as discussed by Carnevale *et al.*,[42] the expression derived by Parker generally underestimates the dependence of the collision number on the translational temperature. The calculated variation of collision number with translational temperature for CH_3Cl is in reasonable agreement with results obtained using the expression derived by Zeleznik for pure polar gases. This result for CH_3Cl should be treated with some degree of caution. While the expression given by Zeleznik and the model described in this paper both predict that the rotational collision number of CH_3Cl monotonically increases with translational temperature, experimental measurements of rotational relaxation in other highly polar species such as HCl indicate that this may not be the case, with the rotational collision number being observed to pass through a local minimum.[43,44]

The effect of rotational temperature on the relaxation time is illustrated in Fig. 4 for CH_4 at a translational temperature of 300 K. In this case, the effect is very small, with the collision number decreasing by *ca.* 0.8 over the 1000 K rotational temperature range considered. Analogous calculations were performed for the other species listed in Table 1 and similar trends were observed in all cases, with the collision number decreasing slightly with increasing rotational energy. It was found that the rotational energy dependence was more significant for species such as CO_2 and OCS for which rotational relaxation is a highly efficient process, while for H_2 the effect was negligible. It should be noted that relaxation times were not calculated between 250 and 300 K due to the poor behaviour of the computational procedure when the initial departure from equilibrium is small. This effect can be seen in Fig. 4, with the statistical noise increasing as the singularity at 300 K is approached. The data presented in Fig. 4 have not been smoothed, unlike those in Fig. 2 and 3.

It would appear that the dependence of the rotational relaxation time on the rotational temperature becomes negligible for most systems when the fraction of elastic collisions falls below *ca.* 2%. The assumption that ξ is independent of the rotational energy is quite reasonable for non-polar or slightly polar molecules. The rotational relaxation time is largely determined by the total collision cross-section, which is not significantly influenced by the rotational motion of such species. For highly polar molecules such as CH_3Cl, in which the total collision cross-section can be significantly affected by the rotational motion of the molecule, the applicability of the model described here is questionable.

Extremely large cross-sections are observed for rotational–translational energy transfer between strongly polar molecules due to the long range dipole–dipole interaction which dominates the scattering behaviour of such species and results in very large total collision cross-sections and unusually large rotational inelastic cross-sections.

Running on a MicroVAX 3100-30, the calculation of a single rotational relaxation time takes between 15 and 60 s, depending upon the number of collisions examined. Fig. 5 shows the number of collisions examined as a function of translational temperature from 1 to 300 K for H_2 and N_2 with no initial rotational energy. The number of collisions examined is observed in both cases to gradually increase with temperature and then level out. Owing to the inefficient and slow nature of rotational relaxation in H_2, the number of collisions examined at a given temperature is significantly greater for this species than for N_2.

In previous papers, the rotational–translational coupling parameter ξ was assumed to be a constant, independent of all other collision parameters, and was generally estimated from a comparison of terminal translational and rotational temperatures measured in supersonic expansions with temperatures calculated using the thermal conduction model or the theory developed by Randeniya and Smith.[1,3,45] In this paper we assume that ξ is proportional to the mean collision cross-section, according to eqn. (4). We suggest further that the previously determined constant values of ξ, based on terminal temperatures measured in a supersonic expansion, represent the maximum attainable value of the coupling parameter, ξ_{max}, under such conditions. In order to make use of the results presented in this paper for the prediction of expansion properties, it is therefore necessary to know or be able to estimate ξ_{max} for the species of interest. Reliable values of ξ_{max} have been determined for H_2, N_2, O_2 and CH_4,[1,45]† but for the remainder of the species listed in Table 1, there are little or no known experimental data on which to estimate ξ_{max} accurately. Huber-Wälchi *et al.*[46] observed a terminal rotational temperature of 40 K for C_2H_4 expanded through a 60 μm nozzle at 300 K with a source pressure of 0.6 atm. From this result we estimate ξ_{max} for C_2H_4 to be 0.18 ± 10%. The high efficiency of rotational relaxation observed for CO_2, CH_3Cl and OCS suggests that ξ_{max} for these species may be close to unity, while values of 0.2–0.25 and 0.55–0.6 for NH_3 and Cl_2, respectively, are probably reasonable.

The results of thermal conduction model calculations performed for OCS, CO_2 and CH_3Cl using the values of α and β given in Table 1 to describe the temperature dependence of the coupling parameter according to eqn. (5) are presented in Table 2. The variation of rotational temperature with axial distance, expressed in terms of nozzle diameters, is shown in Fig. 6 for CO_2 and OCS. All data were calculated for a source pressure of 1 atm at a temperature of 300 K with a nozzle diameter of 7×10^{-5} m. The rotational–translational coupling parameter was assumed to attain its maximum allowable value of unity in each case. The calculated variation of rotational temperature with axial distance for CH_3Cl was almost indistinguishable from that of OCS and is therefore not shown in Fig. 6 for reasons of clarity. Similarly, the parallel component of the translational temperature was virtually identical to the rotational temperature in all cases, illustrating the close coupling of the translational and rotational degrees of freedom in these molecules.

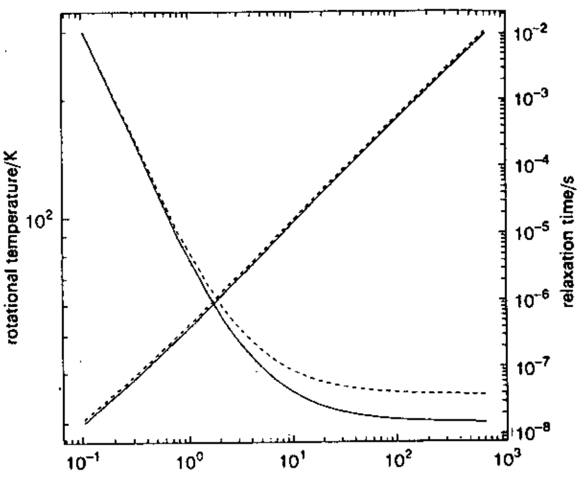

Fig. 6 Rotational temperatures and relaxation times as a function of distance from the nozzle exit for OCS (——) and CO_2 (– – –)

The calculated final translational temperature of CH_3Cl is in excellent agreement with the value of 29 K measured by Aitkin *et al.*[47] using time-of-flight techniques.[1] The calculated value of the flow velocity, however, was found to be some 10% greater than the measured value, indicating that the actual rotational temperature was *ca.* 170 K. We must conclude that the observed agreement between the calculated and measured temperatures was purely coincidental and that the supersonic expansion of such highly polar species cannot be accurately described by the thermal conduction model in its present form. In particular, it may be completely unrealistic to describe the distribution of rotational energies in terms of a single temperature. As was noted by Carman,[48] the rotational energy levels of CH_3Cl are widely spaced ($\mathscr{A} = 150000$ MHz, $\mathscr{B} = 13293$ MHz) and therefore non-equilibrium rotational distributions may be considerably more likely. Such deviations from Boltzmann distributions have been observed for rotational populations of a number of molecules in supersonic expansions.[49,50] In the thermal conduction model the rate of rotational–translational energy transfer is assumed to be proportional to the difference in temperature between the translational and rotational reservoirs. For highly polar symmetric top molecules, such as CH_3Cl with two very different rotational constants, it may be necessary to associate a separate rotational temperature with each unique rotational degree of freedom.

The calculated terminal parallel translational and rotational temperatures given in Table 2 for CO_2 and OCS seem reasonable. Previously reported thermal conduction model calculations for H_2, N_2 and O_2 were all found to be in good

Table 2 Temperatures and flow velocities calculated using the thermal conduction model with the variation

system	P_0/atm	T_0/K	u_{calc}/m s^{-1}	$T_{\parallel, calc}$	$T_{r, calc}$	ξ_{max}
CO_2	1	300	643	35.2	35.2	1.0
CH_3Cl	1	300	603	31.5	31.5	1.0
OCS	1	300	554	30.0	30.0	1.0

---

† Note that the coupling parameter values given by Randeniya and Smith[45] implicitly include the number of rotational degrees of freedom and therefore must be scaled accordingly to obtain values comparable with those presented in this paper.

agreement with experimental measurements,[1,46] and we are confident in the reliability of the computational procedure for species such as CO_2 and OCS.

Also shown in Fig. 6 is the variation of the rotational relaxation time with distance from the nozzle exit for CO_2 and OCS calculated using the thermal conduction model. log–log plots of rotational relaxation time in a supersonic molecular beam *vs.* axial distance are distinctly linear and may be estimated using an expression of the form[2]

$$\tau_r = A\frac{T_0}{P_0}\left(\frac{z}{d_0}\right)^2; \quad \frac{z}{d_0} > \left(\frac{1}{A}\right)^{1/2}\left(\frac{P_0}{T_0}\right)^{1/2} \tag{24}$$

where z is the distance from the nozzle exit along the beam axis, d_0 is the nozzle diameter, P_0 and T_0 are the source pressure and temperature, respectively, and A is a constant for a particular gas. Values of A for CH_3Cl, CO_2 and OCS are given in Table 3. Eqn. (24) should be used as a guide only, and it is important to emphasize this point. The equation is by no means accurate over a wide range of source conditions and simply represents a convenient method of estimating relaxation times in supersonic beams without the need for solving a complex set of equations describing the expansion process.

Rotational relaxation times in a bulb were also calculated for CO_2 using the Monte Carlo simulation procedure under analogous conditions of temperature and pressure to those employed for the calculation of relaxation times in a supersonic expansion using the thermal conduction model. The comparison, illustrated in Fig. 7, shows that rotational relaxation is significantly faster in a bulb. While it is somewhat difficult to compare critically results obtained using the thermal conduction model with those of the direct simulation Monte Carlo procedure, it seems reasonable to expect that rotational relaxation will be less efficient in a supersonic molecular beam due to the lower collision frequency[1] and the additional competing processes which redirect translational and internal energy into directed axial motion.

Table 3 A in eqn. (24) calculated for $P_0 = 1$ atm and $T_0 = 300$ K

system	$A/10^{-6}$ kg m^{-1} s^{-1} K^{-1}
CO_2	7.078
CH_3Cl	6.306
OCS	6.314

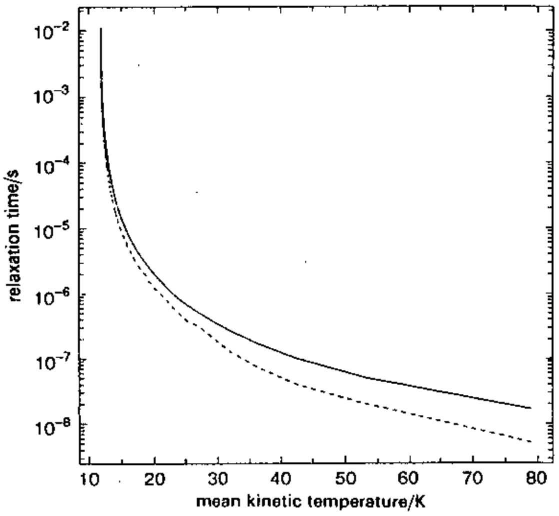

Fig. 7 Comparison of rotational relaxation times for CO_2 in a bulb (- - -) calculated using the Monte Carlo simulation procedure with relaxation times in a supersonic expansion estimated using the thermal conduction model (——)

Conclusion

An approximate direct simulation Monte Carlo procedure has been developed for the investigation of rotational relaxation in homogeneous gases. The devised simulation procedure runs several orders of magnitude faster than full-scale trajectory calculations of relaxation times and initial work indicates that the method gives good results for simple molecules such as homonuclear diatomic species and other small non-polar polyatomic molecules such as CO_2, CH_4 and C_2H_4. Results for the polar species OCS and NH_3 also appear reasonable. The model fails to produce reliable results for highly polar species such as CH_3Cl, where it is quite unrealistic to ignore the effects of dipole–dipole interactions. For symmetric-top molecules such as CH_3Cl, in which the two rotational constants $\mathscr{A}$ and $\mathscr{B}$ are significantly different, it is also somewhat unrealistic to assume that the coupling function ξ is the same for each unique rotational degree of freedom. The model described here may be extended to calculate separate relaxation times for each rotational degree of freedom having a unique coupling function, and it is hoped that work currently being pursued in this regard will improve the accuracy of the relaxation model for such species. The inclusion of dipole–dipole interactions is also being investigated.

Experimental and theoretical studies in the bulk have yielded valuable information on the overall rates of relaxation processes, although many important questions still remain largely unanswered. On the practical side, spectroscopists in particular would like to know or be able to predict with some degree of accuracy not just the overall rate, but also the individual rates of state–state energy-transfer processes. The model described in this paper is by no means capable of calculating such detailed information, but provides a quick and convenient method of obtaining useful qualitative and quantitative information on many important aspects of rotational relaxation phenomena.

References

1 B. R. Cameron and P. W. Harland, *J. Chem. Soc., Faraday Trans.*, 1991, **87**, 1069.
2 B. R. Cameron and P. W. Harland, *J. Chem. Soc., Faraday Trans.*, 1993, **89**, 1903.
3 C. E. Klots, *J. Chem. Phys.*, 1980, **72**, 192.
4 H. Hippler, H. W. Schranz and J. Troe, *J. Phys. Chem.*, 1986, **90**, 6158.
5 J. M. Hammersley and D. C. Handscomb, *Monte Carlo Methods*, Wiley, New York, 1964.
6 K. Nanbu, *J. Phys. Soc. Jpn.*, 1980, **49**, 2042.
7 K. Nanbu, *J. Phys. Soc. Jpn.*, 1983, **52**, 3382.
8 G. A. Bird, *Phys. Fluids*, 1963, **6**, 1518.
9 G. A. Bird, *AIAA J.*, 1970, **8**, 1998.
10 I. D. Boyd and J. P. W. Stark, *Phys. Fluids*, 1987, **30**, 3661.
11 G. A. Bird, *Proc. 7th Int. Symp. on Rarefied Gas Dynamics*, 1970.
12 G. A. Bird, *Molecular Gas Dynamics*, Clarendon Press, Oxford, 1976.
13 H. C. W. Beijerinck and N. F. Verster, *Physica C*, 1981, **111**, 327.
14 S. D. Conte and C. de Boor, *Elementary Numerical Analysis*, McGraw-Hill, Tokyo, 1980.
15 R. W. Simpson, R. G. A. R. Maclagan and P. W. Harland, *J. Phys. B*, 1987, **20**, 2723.
16 R. W. Simpson, Ph.D. Thesis, University of Canterbury, New Zealand, 1988.
17 R. W. Simpson, R. G. A. R. Maclagan and P. W. Harland, *J. Chem. Phys.*, 1988, **87**, 5419.

18 L. A. Viehland and E. A. Mason, *J. Chem. Phys.*, 1984, **80**, 416.
19 W. H. Press, B. P. Flannery, S. A. Teukolsky and W. T. Vetterling, *Numerical Recipes: The Art of Scientific Computing*, Cambridge University Press, Cambridge, 1986.
20 C. Borgnakke and P. S. Larsen, *J. Comput. Phys.*, 1975, **18**, 405.
21 J. O. Hirschfelder, C. F. Curtiss and R. B. Bird, *Molecular Theory of Gases and Liquids*, John Wiley, New York, 1954.
22 H. O'Hara and F. J. Smith, *J. Comput. Phys.*, 1970, **5**, 328.
23 H. O'Hara and F. J. Smith, *Phys. Commun.*, 1971, **2**, 328.
24 M. Abramowitz and I. A. Stegun, *Handbook of Mathematical Functions*, Dover Publications, Place, 1964.
25 L. Blank, *Statistical Procedures for Engineering, Management, and Science*, McGraw Hill, Tokyo, 1982.
26 H. Rabitz and S. H. Lam, *J. Chem. Phys.*, 1975, **63**, 3532.
27 E. A. Mason and L. Monchick, *J. Chem. Phys.*, 1962, **36**, 1622.
28 B. T. Kelly, *J. Acoust. Soc. Am.*, 1957, **29**, 1005.
29 G. L. Hill and T. G. Winter, *J. Chem. Phys.*, 1968, **49**, 440.
30 G. Sessler, *Acustica*, 1958, **8**, 395.
31 M. Greenspan, *J. Acoust. Soc. Am.*, 1959, **31**, 155.
32 R. J. Gallagher and J. B. Fenn, *J. Chem. Phys.*, 1974, **60**, 3492.
33 T. G. Winter and G. L. Hill, *J. Acoust. Soc. Am.*, 1967, **43**, 848.
34 M. L. Unland and W. H. Flygare, *J. Chem. Phys.*, 1966, **45**, 242.
35 E. Sittig, *Acustica*, 1960, **10**, 81.
36 J. G. Parker, *Phys. Fluids*, 1959, **2**, 449.
37 W. H. Anderson and D. F. Hornig, Technical Report, Metcalf Research Laboratory, Brown University, 1958.
38 D. R. Miller and R. P. Andres, *J. Chem. Phys.*, 1967, **46**, 3418.
39 D. G. Jones, J. D. Lambert, M.P. Suksena and J. L. Stretton, *Trans. Faraday Soc.*, 1969, **65**, 965.
40 A. P. Malinauskas, J. W. Gooch Jr., B. K. Annis and R. E. Fuson, *J. Chem. Phys.*, 1970, **53**, 1317.
41 F. J. Zeleznik, *J. Chem. Phys.*, 1967, **47**, 3410.
42 E. H. Carnevale, C. Carey and G. Larson, *J. Chem. Phys.*, 1967, **47**, 2829.
43 C. E. Baker and R. S. Brokaw, *J. Chem. Phys.*, 1964, **40**, 1523.
44 C. E. Baker and R. S. Brokaw, *J. Chem. Phys.*, 1965, **43**, 3519.
45 L. K. Randeniya and M. A. Smith, *J. Chem. Phys.*, 1990, **93**, 661.
46 P. Huber-Wälchi and J. W. Nibler, *J. Chem. Phys.*, *1982*, **76**, 273.
47 C. G. Aitkin, D. A. Blunt and P. W. Harland, unpublished results, 1993.
48 H. S. Carman Jr., Ph.D. Thesis, Rice University, Texas, 1986.
49 S. G. Kukolich, D. E. Oates and J. H. S. Wang, *J. Chem. Phys.*, 1974, **61**, 4686.
50 M. Maier, H. S. Lufman and J. S. Winn, *J. Phys. Chem.*, 1984, **88**, 5167.

Paper 3/02359A; *Received 26th April*, 1993

The potential energy surface of Li^+–CO

Stephen T. Grice, Peter W. Harland, and Robert G. A. R. Maclagan
Department of Chemistry, University of Canterbury, Christchurch, New Zealand

(Received 3 May 1993; accepted 19 July 1993)

A new potential energy surface for the Li^+–CO system calculated at the HF/6-311+G(2*df*) and MP4SDTQ/6-311+G(2*df*) levels of theory in a rigid rotor approximation is presented. The potential energy surface has an absolute energy minimum at $\theta = 0°$, and $R = 5.330$ bohr of -0.716 eV. There is also a minimum at $\theta = 180°$ and $R = 5.344$ bohr of -0.475 eV, and a col at $\theta = 87.2°$ and $R = 4.709$ bohr of 0.100 eV. The potential is expanded into its angular components in a truncated Legendre expansion. The effect of nuclear polarization on the bond length of CO is investigated.

INTRODUCTION

It has been nearly 20 years since Toennies and coworkers[1] completed inelastic scattering studies on the ion–molecule systems Li^+–CO and Li^+–N_2. These two systems were expected to behave similarly because they were isoelectronic, and had almost identical reduced masses and rotational/vibrational energy spacings. However, significant differences between the time-of-flight (TOF) mass spectra for the two systems were observed and they speculated that the greater probability for vibrational excitation in the Li^+–CO system was due to differences in the potential hypersurface. Kita *et al.*[2] have measured integral scattering cross sections at very high energy (500–4000 eV) and have shown that the parameters describing the potential energy surfaces that were derived from the cross sections were very similar for both systems. Support for the integral cross section measurements of Kita *et al.* have been reported by Gislason and co-workers.[3]

In order to rationalize the inelastic scattering results of Toennies and to explain the contrasting results of these two experiments, Staemmler[4] performed an *ab initio* study of the Li^+–CO system. Staemmler's study was limited by the processing power of the computers available at that time and this led his study to the "classic" compromise between the quality of the calculation with respect to the inclusion of electron correlation and the quality of the basis set. To complicate matters further the CO molecule has long been a challenge to quantum chemists because its dipole moment, μ, has the incorrect sign in the HF limit.[5] In fact the CO molecule is often used to test the merit of new post-self-consistent-field (SCF) methods of calculation. Scuseria *et al.*[6] have shown that in order to achieve a dipole moment for the CO molecule that converges on its experimental value both high levels of theory and very large basis sets are required. Staemmler conceded that the theoretical difficulty of calculating the potential energy surface for Li^+–CO led to incorrect long-range behavior but concluded that the HF results should be reasonably accurate at small intermolecular distances. Despite these short comings Staemmler's potential energy surface has been used to fit an analytic potential hypersurface.[7]

Thomas[8] has used a reasonably sized basis set to calculate a CISD potential energy surface for the Li^+–CO system. This potential energy surface was then fitted and used to calculate classical rotationally inelastic differential scattering cross sections. The calculated differential scattering cross sections were then compared to experimental measurements[9] with little success which persisted even after vibrational excitation,[10] and quantum effects[11] were taken into account. In a further study of low angle scattering Thomas *et al.*[12] suggested that the "unresolved discrepancy" at high scattering angle was due to inaccuracies in the potential energy surface, and that the lack of structure in the classically calculated TOF spectrum for low angle scattering was due to the neglect of quantum effects. However, a later study by Gierz *et al.*[13] reported new differential inelastic scattering cross section data and rationalized the "rotational rainbow" structure observed in the TOF spectrum using a simple classical model.

Several other authors[14–18] have reported *ab initio* studies of the structural and thermodynamic properties of the Li^+–CO system. These studies provide some information on the location and depth of the stationary points of the potential energy surface.

Hartree–Fock calculations have been shown to be inadequate when calculating the interaction energy at large intermolecular separation for the Li^+–CO system because of the large basis sets and sophisticated treatments of electron correlation which are required to reproduce the electric properties of the CO molecule. The HF results of Staemmler are also of questionable accuracy in the region of the well. Because the only post-SCF potential energy surface available[10] for the Li^+–CO system was of questionable accuracy at short-range, we have undertaken a detailed examination of the potential energy surface for this system.

We first summarize the advancements made to the quality of the theory and the basis set applied. Then the potential energy surface is presented and the requirements for a reliable potential energy surface and comparisons with existing potential energy surfaces are discussed. This is followed by an analysis of the potential energy surface and its Legendre expansion, and comparisons to the Li^+–N_2 Legendre expansions are made. Finally, a comparison between the potential energy surfaces of the Li^+–N_2 system recently reported by Grice *et al.*[19] and the Li^+–CO system is presented.

TABLE I. The electric properties of CO.

Basis set	μ[a]	Q[a,b]	Θ[a,b]	$\alpha_\parallel$[a]	$\alpha_\perp$[a]
HF/6-311+G(*df*)	0.076	−1.75	4.20	14.04	9.10
MP2/6-311+G(*df*)	−0.141	−1.71	3.33	15.07	9.74
MP4SDQ/6-311+G(*df*)	−0.078	···	···	14.81	9.58
HF/6-311+G(2*df*)	+0.061	−1.58	4.23	13.87	10.03
MP2/6-311+G(2*df*)	−0.138	−1.57	3.35	14.88	10.63
MP4SDQ/6-311+G(2*df*)	−0.080	···	···	14.65	10.45
HF/6-311+G(3*df*)	+0.058	−1.63	4.41	14.05	10.88
MP2/6-311+G(3*df*)	−0.135	−1.59	3.49	15.07	11.53
MP4SDQ/6-311+G(3*df*)	−0.084	···	···	14.89	9.95
Staemmler's HF results[c]	+0.100	−1.56	···	14.13	11.10
Scuseria's[d,e] results	−0.049	···	···	···	···
Best experimental results[f,g]	−0.044	−1.86	···	17.55	10.97

[a] All electric properties in a.u.

[b] Quadrupole and octapole moments calculated in center of mass coordinates.

[c] Basis set C of that work (Ref. 4).

[d] CCSD(T) results of that work.

[e] Reference 6.

[f] Mason and McDaniel (Ref. 22).

[g] Note that a negative dipole moment implies C$^-$–O$^+$ bond polarity.

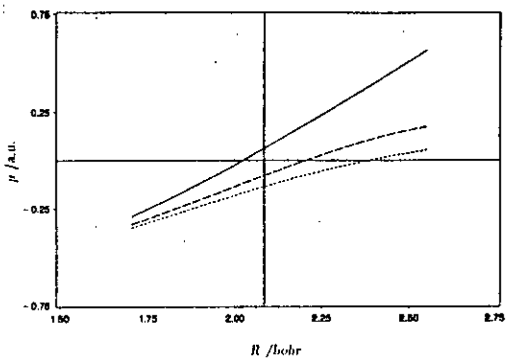

FIG. 1. The dipole moment of CO as a function of the internuclear distance *r*, for various level of theory. The HF dipole moment is represented as the solid curve, the dipole moment at the MP2 level of theory is represented as the short-dashed curve and the dipole moment at the MP4SDQ level of the theory is represented at the long-dashed curve. The solid vertical is drawn through the HF/6-311+G(2*df*) equilibrium bond distance r_e.

BASIS SET AND PROPERTIES

Particular attention must be paid to basis set choice and method when considering a theoretical study of the Li$^+$–CO system. The correct choice of basis set and method depends on the requirements that the potential energy surface must satisfy. For example, high energy inelastic/elastic scattering experiments probe only the repulsive parts of the intermolecular potential and do not require accurate values for the multipole moments and polarizabilities which dominate the medium and long-range interaction potential. In order to calculate transport data for comparison with experiment the potential energy surface is required to be accurate over a wide energy range (thermal to a few eV). Because of these constraints the calculated potential energy surfaces currently available[4,11] are not suitable. To calculate reliable polarizabilities for small molecules requires the addition of diffuse polarization functions, while the electric multipole moments require the addition of extra polarization functions with larger exponents. The addition of diffuse *s* and *p* functions is necessary for a complete description of medium-range bonding interactions.

All calculation reported here used the GAUSSIAN 90 program.[20]

The MP4SDTQ/6-311+G(2*df*) method used in the study of the Li$^+$–N$_2$ potential energy surface proved to be of sufficient accuracy to reproduce experimental transport data.[21] It is reasonable to expect that the same approach for Li$^+$–CO would result in equal success in light of the similarities between the two systems. However, the difficulty in describing the electric multipole moments of CO has presented new challenges for theory. An extensive list of the electric properties of the CO molecule for the various basis sets and methods examined in this study are given in Table I.

The dipole moment for CO, μ, has been calculated analytically for the HF and MP2 levels of theory and by central difference ($E=\pm 1\times 10^{-3}$ a.u.) (Ref. 6) for the MP4SDQ level of theory. These results are a subset of the extensive study of the CO dipole moment by Scuseria *et al.*[6] In that study Scuseria *et al.* have demonstrated the difficulty of attaining a converged dipole moment using Møller–Plesset methods as a function of the order of the theory. They also concluded that coupled cluster methods which successfully converged to the experimental value of the dipole moment of CO, did so only after using very large basis sets that included *d*, *f*, and *g* polarization functions. Such basis sets are currently impractical to use in the study of a potential energy surface. As well as the results listed in Table I, Fig. 1 displays the dipole moment of CO as a function the internuclear separation. The results that are plotted have been calculated using the 6-311+G(2*df*) basis set. The solid vertical line represents the equilibrium bond distance optimized at the HF level of theory. At this value of r_e the HF dipole moment is +0.076 a.u. (a negative sign implies the bond polarity, C$^-$–O$^+$). The wrong sign of the dipole moment in the HF approximation is over corrected if electron correlation at the MP2 level of theory is included. This is corrected for again when calculating the dipole moment using the MP4SDQ level of theory, where the dipole moment has a relative error of up to 80% compared with experiment,[22] although the absolute error is small.

The quadrupole moment of CO, Q, is in good agreement with the experimentally measured result,[22] and it appears to be more stable with regard to the level of theory used. The 6-311+G(2*df*) basis set value is in least agreement with experiment, but only differs by ~15%. The octapole moment of CO, Θ, is also listed in Table I although no experimental value is available for comparison.

The parallel component of the dipole polarizability, $\alpha_\parallel$, is in error of the experimental value by 20%, 14%, and 15% at the HF, MP2, MP4SDQ levels of theory, re-

TABLE II. The structural and thermodynamic properties of CO.

Basis set	r_e^a	D_e^a	k_e^a	E^a
HF/6-311+G(*df*)	2.086	7.57	81.3[b]	−112.776 11
MP2/6-311+G(*df*)	⋯	11.45	⋯	−113.109 20
MP4SDQ/6-311+G(*df*)	⋯	10.78	⋯	−113.117 07
HF/6-311+G(2*df*)	2.085	7.60	⋯	−112.778 77
MP2/6-311+G(2*df*)	⋯	11.48	⋯	−113.127 48
MP4SDQ/6-311+G(2*df*)	⋯	10.70	⋯	−113.133 96
HF/6-311+G(3*df*)	2.084	7.66	⋯	−112.781 26
MP2/6-311+G(3*df*)	⋯	11.57	⋯	−113.134 27
MP4SDQ/6-311+G(3*df*)	⋯	10.79	⋯	−113.140 26
Staemmler's results[c]	2.095	7.62	86.2	−112.733 04
Best experimental results[d]	2.132	11.09	82.9	⋯

[a] All structural and thermodynamic properties in a.u. except D_e which is in eV.

[b] HF force constants scaled by $(0.89)^2$ (Ref. 23).

[c] Basis set C of that work (Ref. 4).

[d] Huber and Herzberg (Ref. 26).

spectively. The perpendicular component of the dipole polarizability, $\alpha_\perp$, approaches the experimental value at the HF and MP2 levels of theory, but is in error by 12.7%, 8.6%, and 9.3% at the MP4SDQ level of theory, for the 6-311+G(*df*), 6-311+G(2*df*), and 6-311+G(3*df*) basis sets, respectively. The dipole polarizability in Table I is relatively constant with the inclusion of further *d* polarization functions. This suggests that inclusion of very diffuse *s* and *p* functions may be required in order to converge to experimental values. This has been investigated by the inclusion of extra diffuse *s* functions with Gaussian exponents of 0.039 63 and 0.076 67 for the carbon and oxygen centers, respectively, and extra diffuse *p* functions with Gaussian exponents of 0.026 17 and 0.051 56 for the carbon and oxygen centers, respectively. This only marginally improved the error in components of the dipole polarizability, $\alpha_\parallel$ and $\alpha_\perp$, when compared with experiment to 2.5% and 14.9% with absolute values of 10.70 and 14.94 a.u., respectively, at the MP2 level of theory.

The structural and thermodynamic properties of CO are listed in Table II. It is also important to closely reproduce the experimental values of the thermodynamic and structural properties to have confidence in the Li$^+$–CO potential energy surface. The equilibrium bond distance r_e has been calculated only at the HF level of theory for the basis sets listed in Table II. The HF approximation underestimates r_e by a small but significant amount. Inclusion of electron correlation in a study of the N_2 molecule increased r_e by a small amount.[17] An increase in the internuclear separation will impact on the electrical properties of the CO molecule and in particular should improve the agreement between theory and experiment for the dipole moment, see Fig. 1. This effect was examined with the smaller 6-31G* basis set. The HF/6-31G* equilibrium internuclear separation was calculated to be 2.105 a.u., which increased to 2.153 a.u. at the MP2/6-31G* level of theory. A similar increase in r_e for the basis sets listed in Table II would result in improved agreement with experiment for r_e and for the dipole moment, which has an estimated value of −0.049 a.u. at the experimental separation using MP4SDQ level of theory. This fortuitously agrees with the best results of Scuseria *et al.*[6]

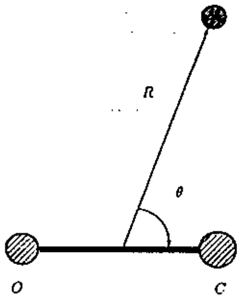

FIG. 2. The geometry coordinates of a rigid rotor/diatom atom collision.

Electron correlation is important in obtaining accurate values for the dissociation energy, D_0. The HF approximation is essentially useless, as it cannot adequately describe dissociation of the CO ($^1\Sigma^+$) into the C (^3P) and the O (^3P) atoms. The MP4SDQ results approach the experimental dissociation energy value with an error of 2.7% for the 6-311+G(3*df*) basis set.

The force constants have been calculated at the HF level of theory and scaled as recommended by DeFrees and McLean.[23] The total energy for CO compares favorably with that quoted by Staemmler in the HF approximation for all the basis sets.

THE POTENTIAL ENERGY SURFACE OF Li$^+$–CO

In the following work, the 6-311+G(2*df*) basis set was used unless otherwise stated. This basis set was chosen for its improved properties in the region of the well. Test calculations using the 6-311+G(*df*) basis set showed that the potential energy surface was underestimated in the region about the well by ~20%. Because of the increased anisotropy of the Li$^+$–CO potential energy surface compared with the Li$^+$–N_2 potential energy surface, due mainly to the nonzero dipole moment of CO, additional point calculations are required to fully characterize the rigid rotor potential energy surface. The MP4SDQ method was chosen because of the similarities of this surface and the MP4SDTQ surface in the Li$^+$–N_2 study,[19] and the considerable time savings this method offered. Both 1*s* orbitals on the carbon and oxygen atoms were frozen.

The calculations were performed with the bond distance of the CO fixed to the value optimized at the HF level of theory. The magnitude of R', the vector connecting the "center of distance" of the CO molecule and the lithium ion, and θ' the angles between the internuclear vector, r_e, and R' (see Fig. 2) was systematically varied to completely characterize the entire rigid rotor potential energy surface. The data for the potential energy surface are listed in Tables III and IV for the HF and the MP4SDQ levels of theory, respectively. A sufficient number of angles were calculated to fully characterize the angular dependence of the Li$^+$–CO potential energy surface.

TABLE III. The HF/6-311+G(2*df*) rigid-rotor potential energy surface of Li$^+$–CO.

	θ' [b,c]				
R' [a]	0°	22.5°	45°	67.5°	90°
1.150	···	···	···	−119.598 95	−119.722 58
1.200	···	···	···	···	
1.250	−118.266 29	···	−119.398 65	−119.714 03	−119.815 78
1.275	···	···	···	−119.738 15	···
1.300	···	···	−119.481 45	−119.760 60	−119.851 24
1.313	···	···	−119.500 97	−119.771 22	···
1.375	···	−119.182 75	−119.591 35	−119.818 76	−119.893 66
1.500	−119.258 30	−119.457 60	−119.736 70	−119.890 22	−119.942 79
1.750	−119.736 46	−119.803 73	···	···	···
2.000	−119.932 88	−119.953 13	−119.984 66	−120.001 55	−120.010 41
2.250	−120.007 16	−120.010 52	···	−120.013 66	−120.016 13
2.500	−120.031 58	−120.029 31	−120.023 01	−120.017 31	−120.017 29
2.750	−120.036 58	−120.032 87	···	−120.017 74	···
3.000	−120.034 72	−120.031 10	−120.023 19	−120.017 18	−120.016 31
3.125	···	···	−120.022 30	···	···
3.250	···	···	···	···	···
3.500	−120.027 57	−120.025 07	−120.019 75	−120.015 82	−120.015 26
4.000	−120.022 41	−120.020 81	−120.017 46	−120.014 99	−120.014 72
5.000	−120.017 69	−120.017 02	−120.015 58	−120.014 47	−120.014 39
6.000	−120.016 06	−120.015 72	−120.014 97	−120.014 41	−120.014 40
8.000	−120.015 05	−120.014 93	−120.014 66	−120.014 47	−120.014 48
10.000	−120.014 77	−120.014 72	−120.014 60	−120.014 52	−120.014 54
12.000	···	···	···	−120.014 55	−120.014 56
14.000	−120.014 64	···	−120.014 59	−120.014 56	−120.014 58
16.000	···	···	···	···	···
18.000	−120.014 61	···	−120.014 59	−120.014 58	−120.014 60
20.000	−120.014 61	···	−120.014 59	−120.014 59	−120.014 60
22.000	−120.014 60	···	···	···	···
24.000	···	···	···	···	···
26.000		···	···	···	···
∞	−120.014 61	−120.014 61	−120.014 61	−120.014 61	−120.014 61

	θ' [b,c]			
R' [a]	112.5°	135°	157.5°	180°
1.150	−119.612 34	···	···	···
1.200	−119.687 67	···	···	···
1.250	−119.750 10	−119.435 44	···	−118.274 56
1.275	···		···	···
1.300	−119.801 68	−119.547 26	···	−118.617 04
1.313	−119.813 10	···	···	···
1.375	−119.862 52	−119.680 33	−119.295 78	···
1.500	−119.931 16	−119.830 99	−119.616 23	−119.469 22
1.750	−119.996 42	−119.973 09	−119.913 68	−119.873 36
2.000	−120.017 52	−120.018 27	−120.007 46	−119.998 56
2.250	−120.022 68	−120.029 45	−120.032 31	−120.032 27
2.500	−120.022 60	−120.029 79	−120.035 41	−120.037 39
2.750	−120.021 14	···	−120.032 67	−120.034 76
3.000	−120.019 60	−120.024 64	−120.029 07	−120.030 85
3.125	···	−120.023 46	···	···
3.250	−120.018 34	···	−120.025 96	···
3.500	−120.017 40	−120.020 69	−120.023 55	−120.024 71
4.000	−120.016 23	−120.018 45	−120.020 38	−120.021 18
5.000	−120.015 20	−120.016 39	−120.017 42	−120.017 83
6.000	−120.014 88	−120.015 60	−120.016 21	−120.016 45
8.000	−120.014 71	−120.015 03	−120.015 31	−120.015 42
10.000	−120.014 66	−120.014 84	−120.014 99	−120.015 05
12.000	−120.014 64	−120.014 75	−120.014 85	−120.014 88
14.000	−120.014 63	−120.014 71	−120.014 77	−120.014 79
16.000	−120.014 63	−120.014 68	−120.014 72	−120.014 74
18.000	−120.014 63	−120.014 66	−120.014 70	−120.014 71
20.000	−120.014 62	−120.014 65	−120.014 68	−120.014 69
22.000	···	···	···	···
24.000	···	···	···	−120.014 66
26.000	···	···	···	−120.014 65
∞	−120.014 61	−120.014 61	−120.014 61	−120.014 61

[a] Energies in a.u.

[b] Bond distances in angstroms.

[c] Bond angles in degrees.

TABLE IV. The MP4SDQ/6-311+G(2df) rigid-rotor potential energy surface of Li⁺–CO.

	θ' [b,c]				
R' [a]	0°	22.5°	45°	67.5°	90°
1.150	···	···	···	−119.951 75	−120.076 17
1.200	···	···	···	···	···
1.250	−118.708 02	···	−119.756 80	−120.070 02	−120.170 78
1.275	···	···	···	−120.094 71	···
1.300	···	···	−119.841 49	−120.117 65	−120.206 65
1.3125	···	···	−119.861 39	−120.128 49	···
1.375	···	−119.556 72	−119.953 22	−120.176 94	−120.249 47
1.500	−119.648 61	−119.831 78	−120.099 81	−120.249 45	−120.298 90
1.750	−120.108 50	−120.171 51	···	···	···
2.000	−120.297 66	−120.316 71	−120.346 50	−120.361 28	−120.366 70
2.250	−120.368 73	−120.371 93	···	−120.373 04	−120.372 39
2.500	−120.391 79	−120.389 65	−120.383 27	−120.376 20	−120.373 46
2.750	−120.396 14	−120.392 59	···	−120.376 10	···
3.000	···	−120.390 31	−120.382 21	−120.375 03	−120.372 19
3.125	···	···	−120.381 04	···	···
3.250	···	···	···	···	···
3.500	−120.385 92	−120.383 38	−120.377 73	−120.372 84	−120.370 86
4.000	−120.380 04	−120.378 36	−120.374 68	−120.371 47	−120.370 15
5.000	−120.374 38	−120.373 65	−120.371 96	−120.370 39	−120.369 67
6.000	−120.372 29	−120.371 89	−120.370 97	−120.370 08	−120.369 63
8.000	−120.370 83	−120.370 67	−120.370 29	−120.369 91	−120.369 69
10.000	−120.370 34	−120.370 26	−120.370 06	−120.369 86	−120.369 73
12.000	···	···	···	−120.369 84	−120.369 75
14.000	−120.370 01	···	−120.369 91	−120.369 83	−120.369 77
16.000	···	···	···	···	···
18.000	−120.369 91	···	−120.369 86	−120.369 81	−120.369 78
20.000	−120.369 89	···	−120.369 85	−120.369 81	−120.369 78
22.000	−120.369 87	···	···	···	···
24.000	···	···	···	···	···
26.000	···	···	···	···	···
∞	−120.369 80	−120.369 80	−120.369 80	−120.369 80	−120.369 80

	θ' [b,c]			
R' [a]	112.5°	135°	157.5°	180°
1.150	−119.963 49	···	···	···
1.200	−120.038 77	···	···	···
1.250	−120.101 21	−119.779 64	···	−118.604 81
1.275	···	···	···	···
1.300	−120.152 85	−119.891 36	···	−118.947 53
1.3125	−120.164 27	···	···	···
1.375	−120.213 76	−120.024 72	−119.633 00	···
1.500	−120.282 53	−120.176 33	−119.954 85	−119.803 78
1.750	−120.348 22	−120.320 41	−120.256 86	−120.214 52
2.000	−120.369 90	−120.367 29	−120.353 89	−120.343 87
2.250	−120.375 60	−120.379 83	−120.381 05	−120.380 32
2.500	−120.375 96	−120.381 18	−120.385 70	−120.387 27
2.750	−120.374 83	···	−120.383 95	−120.385 78
3.000	−120.373 53	−120.377 23	−120.380 99	−120.382 58
3.125	···	−120.376 23	···	···
3.250	−120.372 44	···	−120.378 33	···
3.500	−120.371 61	−120.373 90	−120.376 25	−120.377 27
4.000	−120.370 62	−120.372 05	−120.373 56	−120.374 24
5.000	−120.369 84	−120.370 52	−120.371 26	−120.371 58
6.000	−120.369 68	−120.370 04	−120.370 43	−120.370 60
8.000	−120.369 67	−120.369 79	−120.369 94	−120.370 00
10.000	−120.369 70	−120.369 75	−120.369 82	−120.369 85
12.000	−120.369 73	−120.369 75	−120.369 78	−120.369 79
14.000	−120.369 74	−120.369 75	−120.369 77	−120.369 77
16.000	−120.369 75	−120.369 76	−120.369 76	−120.369 77
18.000	−120.369 76	−120.369 76	−120.369 77	−120.369 77
20.000	−120.369 77	−120.369 77	−120.369 77	−120.369 77
22.000	···	···	···	−0
24.000			···	−120.369 77
26.000		···	···	−120.369 78
∞	−120.369 80	−120.369 80	−120.369 80	−120.369 80

[a] Bond distances in angstroms.
[b] Bond angles in degrees.
[c] Energies in a.u.

TABLE V. Fitting parameters for long-range extrapolations of the Li$^+$–CO potential energy surface according to Eq. (2).

Fitting parameter	c	$2cd$[a]
MP4SDQ		
$\theta=0°$[b]	-0.0883	-1.12
$\theta=45°$	-0.0552	-0.481
$\theta=67.5°$	-0.0286	$+0.292$
$\theta=112.5°$	$+0.0318$	$+0.170$
$\theta=135°$	$+0.0601$	-0.958
$\theta=180°$	$+0.0867$	-3.22
Fitting parameter	c	$3cd$
$\theta=90°$[c]	-0.0083	-1.12

[a] All parameters in a.u.

[b] All bond angles in degrees.

[c] $\theta=90°$ is a special case.

The MP4SDQ potential has been transformed to "center of mass" coordinates such that the vector R connects the center of mass of the CO molecule with the Li$^+$ ion, where θ is the angle between R and the internuclear vector. The transformed potential energy surface was then spline fitted in a similar manner to that described in Grice *et al.*[19] The short-range extrapolation used was

$$V(R)=a\exp(-bR), \tag{1}$$

which was fitted using points (R_1,V_1), and $(R_1,\partial V_1/\partial R_1)$ obtained from solving the equation for a partial natural cubic spline. Enough *ab initio* points were calculated to characterize the repulsive wall of the potential energy surface. The same long-range interaction extrapolation function used in the Li$^+$–N$_2$ potential energy surface was adopted to fit the Li$^+$–CO potential energy surface,

$$V(R)=c/(R-d)^n \quad \text{for } R>R_n, \tag{2}$$

however, n was set to 2 for all angles except $\theta=90°$, where the ion-dipole interaction vanishes. In the perpendicular approach, n was set to 3, where the ion-quadrupole is the leading asymptotic term. When Eq. (2) is expanded in inverse powers of R for $n=2$, the leading ion-dipole and ion-quadrupole are represented by c/R^2, and $2cd/R^3$, respectively. The values of c and $2cd$ which are given in Table V, and correspond reasonably well with the known values of the dipole moment and quadrupole moments of CO, given in Table I. The parameters listed display the correct parity with respect to the angular variation of the leading asymptotic electrostatic terms. Again, enough *ab initio* points were calculated at large separation to ensure the correct behavior of the fitted asymptotic terms. This required calculations for R beyond 45 bohr, resulting in very small relative energies. The fitting parameters were very sensitive to the last few significant figures of the energy values, although these digits have been truncated in Tables III and IV.

The fitted center of mass potential energy surface for the MP4SDQ/6-311+G(2*df*) level of theory exhibited the following properties, which are also listed in Table VI. $R(V=0)$ is the value of R where the potential becomes repulsive and low R. There exists an absolute minimum at the geometry $R=5.330$ bohr, $\theta=0°$. The depth of the minimum is 0.716 eV. There exists a local minimum in the other colinear approach, at $\theta=180°$, $R=5.344$ bohr. The depth of this local minimum is 0.475 eV. Nearly 70% of the difference between these two well depths can be accounted for by the ion-dipole interaction. Between these two minima there exists a col. The geometry at the col is $\theta=87.2$, $R=4.709$ bohr, with a relative energy of 0.100 eV. There also exists an absolute maximum at large separation in the geometry $R=10.684$ bohr, $\theta=96.8°$, and with a relative energy of 0.006 eV. The maximum is a result of the slightly repulsive ion-dipole and repulsive ion-quadrupole interaction in this geometry at large separation. These repulsive interactions are then dominated largely by ion-induced dipole interactions resulting in a net attraction.

Figure 3 displays the MP4SDQ/6-311+G(2*df*) potential energy surface for Li$^+$–CO. The angles $\theta=22.5°$, 67.5°, 112.5°, and 157.5° have been omitted for clarity. Selected values of Staemmler's[4] HF data are also plotted. From a comparison of Staemmler's data to those reported here it is evident that the inaccuracies in the description of the electrical properties of the CO molecule have impacted on the Li$^+$–CO potential energy surface. The HF approximation which predicts the incorrect sign for the dipole moment of CO also incorrectly favors the Li$^+$–O–C minimum over the Li$^+$–C–O minimum. An accurate method for calculating the potential energy surface for Li$^+$–CO must account for electron correlation. The general features of the MP4SDQ/6-311+G(2*df*) calculations on Li$^+$–CO are evident in the surface plot graphed in Fig. 4. This figure graphs the potential energy surface as a function of the internuclear separation R, and angle θ. Other comparisons of the potential energy surface are best observed graphically.

The short-range potential energy surface of Li$^+$–CO is plotted in Fig. 5. It is evident that exponential repulsion begins for $R<3$ bohr. Comparing the short-range repulsive region of the potential energy surface of Li$^+$–CO with the results of Staemmler shows the discrepancies between the two calculations, particularly in the two colinear approaches. There is a substantial degree of anisotropy in the potential energy surface reported here, particularly at small intermolecular separation. The medium and long-range potential energy surface is largely dominated by electrostatic and polarization interactions. This is investigated in the next section.

THE LEGENDRE EXPANSION

The potential energy surface of Li$^+$–CO can be analyzed in terms of a number of interactions based on the decomposition of the angular variation in a truncated Legendre expansion, as given by Eq. (3),

$$V(R,\theta_m)=\sum_{m=0}^{k} P_{m,n}V_n(R). \tag{3}$$

We have calculated the potential energy surface for the angles

TABLE VI. Critical points of the Li$^+$–CO potential energy surface.[a,b]

Critical points	MP4SDQ	Critical points	MP4SDQ
$\theta=0$		$\theta=112.5$[c]	
$R,(V=0)$	4.413	$R,(V=0)$	3.711
$R,(\partial V/\partial R=0)$	5.330	$R,(\partial V/\partial R=0)$	4.462
$V,(\partial V/\partial R=0)$	−0.026 32	$V,(\partial V/\partial R=0)$	−0.006 66
$R,(\partial^2 V/\partial R^2=0)$	6.313	$R,(\partial^2 V/\partial R^2=0)$	5.225
		$R,(V=0)$	9.740
$\theta=45$[c]		$R,(\partial V/\partial R=0)$	13.270
$R,(V=0)$	4.201	$V,(\partial V/\partial R=0)$	+0.000 13
$R,(\partial V/\partial R=0)$	5.153	$R,(\partial^2 V/\partial R^2=0)$	15.181
$V,(\partial V/\partial R=0)$	−0.013 97		
$R,(\partial^2 V/\partial R^2=0)$	5.894	$\theta=135$[c]	
		$R,(V=0)$	3.736
$\theta=67.5$[c]		$R,(\partial V/\partial R=0)$	4.503
		$V(\partial V/\partial R=0)$	−0.011 80
$R,(V=0)$	4.123	$R,(\partial^2 V/\partial R^2=0)$	5.354
$R,(\partial V/\partial R=0)$	4.972	$R,(V=0)$	14.980
$V,(\partial V/\partial R=0)$	−0.006 17	$R,(\partial V/\partial R=0)$	21.653
$R,(\partial^2 V/\partial R^2=0)$	5.706	$V,(\partial V/\partial R=0)$	+0.000 05
		$R,(\partial^2 V/\partial R^2=0)$	29.133
$\theta=90$[c]		$\theta=180$[c]	
$R,(V=0)$	3.964	$R,(V=0)$	3.880
$R,(\partial V/\partial R=0)$	4.632	$R,(\partial V/\partial R=0)$	4.659
$V,(\partial V/\partial R=0)$	−0.003 73	$V,(\partial V/\partial R=0)$	−0.017 46
$R,(\partial^2 V/\partial R^2=0)$	5.527	$R,(\partial^2 V/\partial R^2=0)$	5.344
$R,(V=0)$	8.545	$R,(V=0)$	22.133
$R,(\partial V/\partial R=0)$	10.663	$R,(\partial V/\partial R=0)$	33.992
$V,(\partial V/\partial R=0)$	+0.000 17	$V,(\partial V/\partial R=0)$	+0.000 03
$R,(\partial^2/\partial R^2=0)$	13.497	$R,(\partial^2 V/\partial R^2=0)$	44.687

[a] All bond distances in a.u.

[b] All bond energies in a.u.

[c] All bond angles in degrees.

$$\theta=\{0^\circ,22.5^\circ,45^\circ,67.5^\circ,90^\circ,112.5^\circ,135^\circ,157.5^\circ,180^\circ\}. \quad (4)$$

Because the CO molecule belongs to the $C_{\infty v}$ point group, all terms are nonvanishing, unlike the Li$^+$–N$_2$ system. The radial functions are obtained from inverting Eq. (3) in the manner shown in Eq. (5),

$$V_n(R)=\sum_{m=0}^{k} P_{n,m}^{-1} V(R,\theta_m), \quad (5)$$

where $P_{n,m}^{-1}$ are the inverted matrix elements of the matrix $P_{n,m}=P_n(\cos\theta_m)$. The points for which all θ were calculated for a given R have been inverted directly and are listed in Table VII.

The expansion was tested for convergence in the expansion for k up to 8. First, there is a noticeably slow convergence in the series V_n, as a function of n, especially for $R\sim3$ bohr. Inclusion of the terms V_n $(0<n<4)$ calculated from the inversion of the data for $\theta=0^\circ$, 45°, 90°, 135°, 180°, resulted in a potential energy surface that is in error by 20% at short-range R and intermediate angle θ. Inclu-

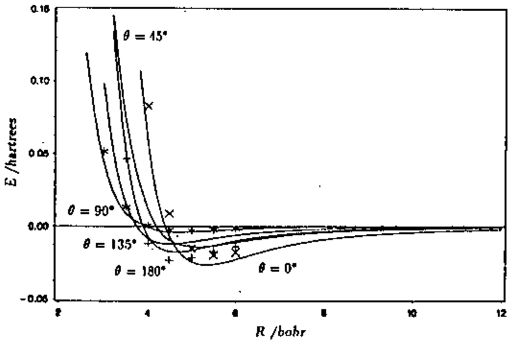

FIG. 3. The MP4SDQ/6-311+G(2df) potential energy surface for Li$^+$–CO as a function of R. The angles of θ have been graphed and marked in the figure. Staemmler's (Ref. 4) HF points are represented as +, *, and × for the angles $\theta=0^\circ$, 90°, and 180°, respectively.

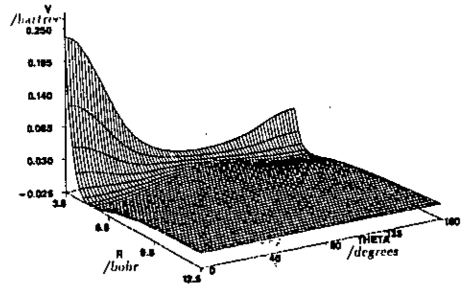

FIG. 4. The surface plot of the MP4SDQ/6-311+G(2df) potential energy surface as a function of the intermolecular distance and angle.

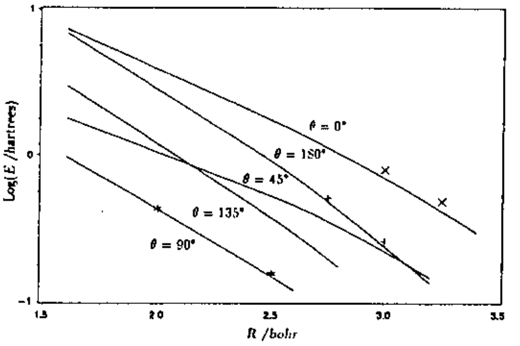

FIG. 5. The short-range MP4SDQ/6-311+G(2df) potential energy surface of Li$^+$–CO, as a function of R. The angles of θ have been graphed and labeled in the figure. Staemmler's (Ref. 4) HF points are represented as ×, *, and + for the angles $\theta=0°$, 90°, and 180°, respectively.

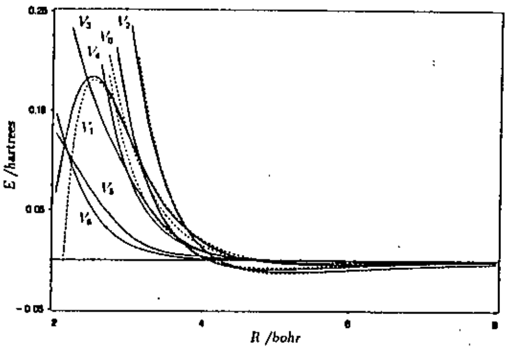

FIG. 6. The Legendre radial functions of the MP4SDQ/6-311+G(2df) potential energy surface for Li$^+$–CO. The radial functions V_n are labeled in the figure. The solid lines represent the MP4SDQ/6-311+G(2df) potential energy surface, while the dashed lines represent the CISD+Q data of Thomas *et al.* (Ref. 10).

sion of the V_5 and V_6 terms by including angles $\theta=67.5°$ and 112.5° improved the correspondence with the calculated potential energy surface to within an average error of $<1\%$. Further inclusion of V_7 and V_8 terms did not significantly improve the fit, and indeed these terms are comparatively small compared to other expansions in Table VII, at all internuclear separations. It was concluded that sufficient accuracy can be obtained by truncating the series at $k=6$. Critical points of the Legendre radial functions are listed in Table VIII and compared with other potential energy surfaces.

The radial functions have also been spline fitted in a similar manner to that described for the potential energy surface. The long-range exponent of Eq. (2) was set to 4, 2, 3, 4, and 5 for V_0, V_1, V_2, V_3, and V_4, respectively. The exponent n was set to 6 and 7 for V_5 and V_6, respectively. For all the expansions d was small compared with R_n, suggesting that the leading terms of the expansion in inverse powers of R were dominant. The MP4SDQ/6-311+G(2df) expansions $V_n(0<n<6)$ are plotted in Fig. 6 and at short-range in Fig. 7 with the expansions of Thomas *et al.*[10] $V_n(0<n<4)$ plotted as dashed lines.

The potential energy surface reported here is very anisotropic, especially in the region $R\sim3$ bohr. In this region of the potential energy surface a radial Legendre expansion including V_n only up to $n=4$ gives qualitatively the incorrect potential energy surface. This is in agreement with the findings of Thomas *et al.*[12] who in a later paper conceded that in the perpendicular approach his 5 angled Legendre expansion gave "the wrong sign for the slope meaning the force was in the wrong direction." The anisotropy of the Li$^+$–CO system decreases at large intermolecular separations where the potential energy surface is dominated by electrostatic and polarization interactions. For this reason we can expect that *ab initio* derived potential energy surfaces should converge providing they have similar values for the multipole moments and polarizabilities. This results in improved agreement between the expansion of Thomas *et al.* and those reported here, at long-range.

For $R<3$ bohr the anisotropy of the potential energy surface also decreases as the radial functions V_2, V_0, and V_4 become increasingly more dominant. Experiments that probe the potential energy surface about $R\sim3$ bohr are therefore very difficult to describe theoretically, and it is

TABLE VII. The radial Legendre expansion functions directly inverted from the Li$^+$–CO MP4SDQ/6-311+G(2df) potential energy surface according to Eq. (5).

R[a]	V_0[b]	V_1	V_2	V_3	V_4	V_5	V_6	V_7	V_8
1.5	196 125[c]	58 175	316 391	14 161	102 823	2 066	22 732	3 186	5 531
2.0	11 556	16 586	24 427	5 383	11 239	1 044	1 640	93	171
2.5	−9 393	−1 579	−11 121	−939	583	256	172	3	23
3.0	−7 476	−3 944	−10 521	−1 734	−459	30	36	17	5
3.5	−4 422	−3 042	−6 996	−1 281	−372	−18	−5	15	−1
4.0	−2 537	−2 066	−4 540	−839	−247	−2	−17	5	−2
5.0	−933	−1 093	−2 173	−321	−78	9	0	1	−1
6.0	−421	−695	−1 195	−153	−34	0	0	0	0
8.0	−128	−364	−482	−49	−8	0	0	0	0
10.0	−52	−226	−241	−20	−3	0	0	0	0

[a] All bond energies are in angstroms.
[b] Zeroth order Legendre expansion; see text.
[c] All bond energies are in μhartree.

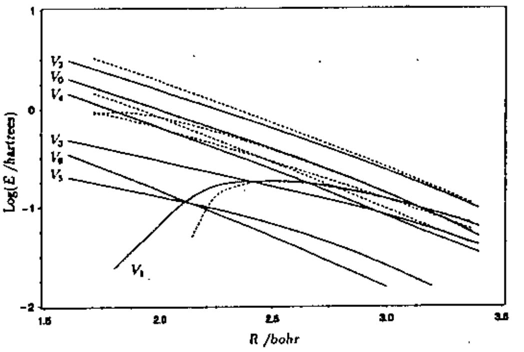

FIG. 7. The short-range Legendre radial functions of Li$^+$–CO. The radial functions V_n are labeled in the figure. The solid lines represent the MP4SDQ/6-311+G(2*df*) potential energy surface, while the dashed lines represent the CISD+Q data of Thomas *et al.* (Ref. 10).

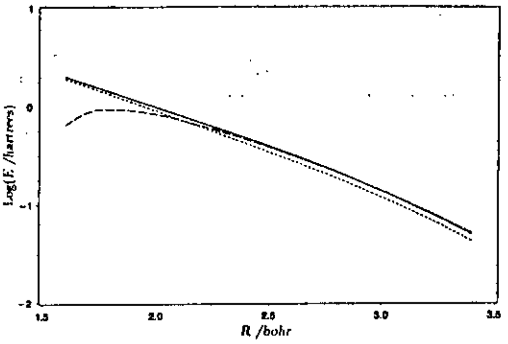

FIG. 9. The short-range isotropic radial function of Li$^+$–CO. The solid curve represents the isotropic radial function calculated to the MP4SDQ/6-311+G(2*df*) level of theory. The short dashed line represents the results of Gislason *et al.* (Ref. 3). Note that Gislason's results have been extrapolated beyond the range of reported validity. The long dashed line represents the fitted expansion of V_0 of Thomas *et al.* (Ref. 10).

not surprising that attempts to do so have met with mixed success.[8,10,12,13]

Now examining each expansion in turn, we can see that the correspondence between the MP4SDQ/6-311 +G(2*df*) isotropic radial function and the CISD+Q isotropic radial function of Thomas *et al.* is very good. This is supported by Fig. 8 where the two expansions are plotted along with the experimentally derived radial isotropic function of Gislason.[3] The same data sets are plotted at short range in Fig. 9. Note that while the correspondence between the two *ab initio* derived expansions is reasonably good for $R > 2.5$ bohr, the divergence at shorter intermolecular separation is only an artifact of the fitting function Thomas *et al.* used which is not valid in this region. Note the poor agreement between the two V_3 expansions. The disagreement in this region is most probably responsible for a large part of the error of the Thomas *et al.* expansion at short-range. Correspondence between the MP4SDQ/6-311+G(2*df*) expansion V_0 and the experimentally derived results of Gislason *et al.* are also good, even though Gislason *et al.* results have also been reported beyond the range of reported validity ($2.8 < R < 10.8$ bohr). These two expansions differ by a relatively small amount at small intermolecular separation as shown in the log–linear plot in Fig. 9. The effect of nuclear polarization on V_0 is examined later in this section.

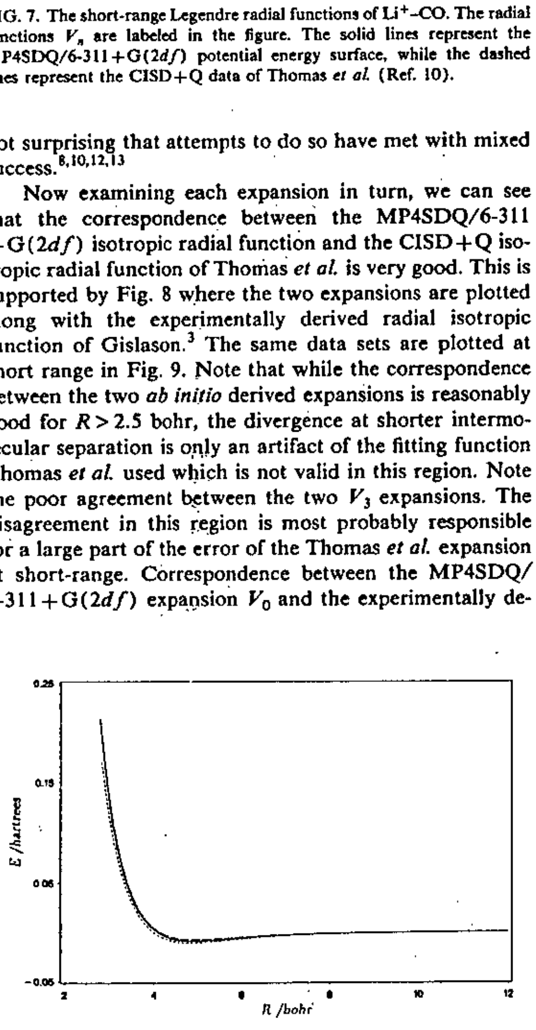

FIG. 8. The isotropic radial function of Li$^+$–CO. The solid curve represents the isotropic radial function calculated to the MP4SDQ/6-311 +G(2*df*) level of theory. The dashed line represents the results of Gislason *et al.* (Ref. 3). The long dashed line represents the fitted expansion of V_0 of Thomas *et al.* (Ref. 10).

Returning to the radial function V_1 of the Legendre expansion, it can be seen in Fig. 6 that correspondence between the MP4SDQ/6-311+G(2*df*) function and Thomas *et al.* results are good for $R > 3$ bohr, but they diverge at smaller intermolecular separations. This is most probably due to the nature of the fitting function Thomas *et al.* have employed. Another noticeable feature of the V_1 radial function is its maximum at $R \sim 2.8$ bohr. This results partly from the definition of the coordinate system which places the C atom of the CO molecule closer to the Li$^+$ ion for a given R, which favors the Li$^+$–OC configuration at short-range. At very large intermolecular separation the V_1 term dominates, and the fitted dipole moment, $\mu = -0.073$ a.u., is in reasonable agreement with the experimental result.[22]

The radial function V_2 also corresponds well with Thomas' own expansion, but diverges at short-range, see Fig. 7. The radial function V_2 is dominant in determining the potential energy surface from short to relatively large intermolecular separations. Note that the Thomas *et al.* CISD+Q expansion for V_2 does not diverge from the V_2 reported here until much smaller R than is plotted in Fig. 9 because of the extra fitting functions they used to ensure accuracy in this region.

The long-range fitted quadrupole moment, $Q \cong 1.4$ a.u. is also in reasonably good agreement with experiment,[22] and the polarization term $3cd$ displays the correct parity.

For the other radial function V_3 and V_4 the MP4SDQ/6-311+G(2*df*) expansion and the Thomas *et al.* expansion are not in agreement. Thomas *et al.* have stated that the convergence of their expansions is incomplete espe-

TABLE VIII. Critical points of the Legendre radial functions of Li$^+$–CO.

Critical points	MP4SDQ	Thomas's	Gislason's	Staemmler's
V_0				
$R,(V_0=0)$	4.074[a]	4.185	3.987	4.176
$R,(\partial V_0/\partial R=0)$	4.934	4.868	4.857	5.027
$V_0,(\partial V_0/\partial R=0)$	−0.009 20[b]	−0.008 11	−0.011 21	−0.007 97
$R,(\partial^2 V_0/\partial R^2=0)$	5.639	5.746	···	···
V_1				
$R,(\partial V_1/\partial R=0)$	2.487	2.377	···	···
$V_1,(\partial V_1/\partial R=0)$	+0.184 61	+0.193 24	···	···
$R,(\partial V_1/\partial R^2=0)$	2.954	2.497	···	···
$R,(V_1=0)$	4.695	4.889	···	···
$R,(\partial V_1/\partial R=0)$	5.713	5.731	···	···
$V_1,(\partial V_1/\partial R=0)$	−0.000 437	−0.002 87	···	···
$R,(\partial^2 V_1/\partial R^2=0)$	6.501	6.700	···	···
V_2				
$R,(V_2=0)$	4.236	4.193	···	···
$R,(\partial V_2/\partial R=0)$	5.163	5.174	···	···
$V_2,(\partial V_2/\partial R=0)$	−0.011 64	−0.013 04	···	···
$R,(\partial^2 V_2/\partial R^2=0)$	6.087	5.841	···	···
V_3				
$R,(V_3=0)$	4.657	4.742	···	···
$R,(\partial V_3/\partial R=0)$	5.613	5.667	···	···
$V_3,(\partial V_3/\partial R=0)$	−0.002 34	−0.002 46	···	···
$R,(\partial^2 V_3/\partial R^2=0)$	6.465	6.516	···	···
V_4				
$R,(V_4=0)$	5.062	5.106	···	···
$R,(\partial V_4/\partial R=0)$	5.963	5.917	···	···
$V_4,(\partial V_4/\partial R=0)$	−0.000 61	−0.000 63	···	···
$R,(\partial^2 V_4/\partial R^2=0)$	6.496	7.103	···	···

[a] All bond distances in bohr.

[b] All energies in a.u. and relative to $R=\infty$.

cially at short-range. This the MP4SDQ/6-311+G$(2df)$ results represent a significant improvement over the only other post-HF potential energy surface currently available.

NUCLEAR POLARIZATION OF Li$^+$–CO

The experimental TOF measurements of Toennies *et al.*[9] for the inelastic differential scattering of Li$^+$ from N_2 and CO investigated the rotational/vibrational inelastic cross sections for collision energies < 10 eV. They observed similar rotational excitation cross sections but very different vibrational excitation cross sections between the two systems. The TOF spectra showed an increased likelihood of vibrational inelastic scattering when Li$^+$ ions collided off CO, when compared to the TOF data for the Li$^+$–N_2 system. However, Kita *et al.*[2] measured integral elastic scattering cross sections for both Li$^+$–N_2 and Li$^+$–CO systems and showed that these cross sections and the potential energy surfaces derived from them were very similar. Staemmler[4] attempted to rationalize the increased likelihood of vibrational excitation of CO, despite the similarities of the short-range potential energy surface, by a study of the equilibrium bond distance of the diatomic (r_e) as a function of its geometry. This study showed, "pronounced," differences between the Li$^+$–CO and Li$^+$–N_2 systems at short-range.

The effects of nuclear polarization on the Li$^+$–CO system have been examined by optimizing the CO bond distance at short Li$^+$–CO distances to check if nuclear polarization is important, in a similar fashion to that reported for the Li$^+$–N_2 system.[19] Gislason *et al.*[24] have commented that long-range polarization effects are negligible, or nearly so for small molecules, however they quoted[25] values that suggested that nuclear polarizability, α_{np}, was significantly larger for the CO molecule (0.27 a.u.) than for the N_2 molecule (>0.03 a.u.). The greater polarizability of CO should be even more exaggerated at short-range where it is anticipated that significant perturbation of the CO bond distance away from its equilibrium position should lead to corresponding changes to the potential energy surface.

TABLE IX. Bond distance differences (Δr_e) and energy differences (Δ) for nuclear polarization of Li$^+$–CO.

	Δr_e[a]		ΔV[b]	
	HF	MP4SDQ	HF	MP4SDQ
θ'	/bohr		/hartree	
0°	−0.262	···	−0.115 82	−0.082 70
45°	−0.087	···	−0.007 08	−0.000 19
67.5°	−0.017	···	−0.000 21	−0.001 10
90°	+0.012	···	−0.000 10	−0.000 98
112.5°	+0.017	···	−0.000 22	−0.001 36
135°	−0.038	···	−0.001 19	−0.000 96
180°	−0.208	···	−0.066 76	−0.058 82

[a] All angles in degrees

[b] All parameters in a.u.

Reoptimizing the bond length of the CO species with the Li$^+$ species fixed at $R'=1.5$ Å (in the "center of distance" coordinate system) at various angles θ', lead to the following results. The bond length changes Δr for $\theta'=0°$, 45°, 67.5°, 90°, 112.5°, 135°, and 180° were −0.262, −0.087, −0.017, +0.012, +0.017, −0.038, and −0.208 bohr, respectively, at the HF level of theory. The bond length changes were associated with decreases in energy for these configurations of 3.152, 0.193, 0.006, 0.003, 0.006, 0.032, and 1.817 eV for the angles $\theta'=0°$, 45°, 67.5°, 90°, 112.5°, 135°, and 180°, respectively, at the HF level of theory. At the MP4SDQ//HF level of theory changes were 2.251, 0.005, 0.030, 0.027, 0.037, 0.026, and 1.601 eV for angles $\theta'=0°$, 45°, 67.5°, 90°, 112.5°, 135°, and 180°, respectively. These results are summarized in Table IX.

As with the Li$^+$–N_2 system, a pronounced decrease in the bond length (>10%) occurs in both linear arrangements, with the greatest decrease (−0.262 bohr) occurring as the Li$^+$ ion approaches the C center of the CO molecule. Small increases in r are observed in the region, $90° < \theta' < 112.5°$, about the perpendicular approach. Similar features are also observed in the Li$^+$–N_2 system. These results are in accord with the observations of Staemmler.[4] However, Staemmler correctly points out that the dipole moment of CO may play a crucial role in the behavior of nuclear polarization of Li$^+$–CO especially at short-range, thus complicating the numerical complexity of calculating its effect. These optimizations have been performed at the HF level of theory, where the dipole moment has the incorrect sign. Optimization of Li$^+$–CO in the Li$^+$–C–O geometry at the HF level of theory has resulted in a large

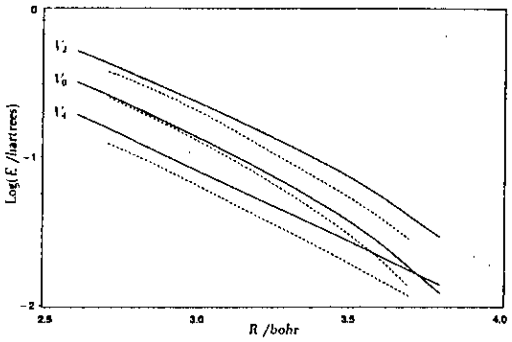

FIG. 10. Comparison of the short-range Legendre radial functions of the MP4SDQ/6-311+G(2*df*) potential energy surface of Li$^+$–CO and Li$^+$–N$_2$. The radial functions V_n are labeled in the figure. The Li$^+$–CO expansions are plotted as solid lines, and the Li$^+$–N$_2$ expansions are plotted in the dashed line.

bond length decrease because such a decrease changes the sign of the dipole moment (see Fig. 1) and allows a relatively stabilizing interaction. Optimization of the Li$^+$–CO system in the Li$^+$–O–C geometry has also resulted in a decrease in the CO bond length, although it is smaller than that for the Li$^+$–C–O geometry. Inclusion of electron correlation during the optimization is prohibitively expensive.

It is most likely that bond length dependence of the dipole moment of CO is the cause of the greater vibrational inelastic cross sections of Li$^+$–CO compared to Li$^+$–N$_2$. It is unfortunate that this interesting problem must await advances in computer speed and storage before an adequate treatment of electron correlation of the potential energy surface, particularly with respect to r and θ, will allow accurate calculations of vibrationally inelastic properties of these systems. If the *ab initio* method used could have provided the correct qualitative picture of nuclear polarization then the quantitative information obtained could be integrated into the potential energy surface with an expected improvement in the corresponding experimental properties calculated from this potential energy surface. Because of the uncertain reliability of these nuclear polarization calculations, the associated corrections to the rigid rotor potential energy surface have been neglected.

Calculations to estimate the BSSE by counterpoise correction have not been performed. The anticipated corrections are likely to be too small to justify expensive calculations.

COMPARISON OF THE POTENTIAL ENERGY SURFACES OF Li$^+$–CO AND Li$^+$–N$_2$

The radial functions V_2, V_0, and V_4 at the MP4SDQ/6-311+G(2*df*) level of theory for the Li$^+$–CO and at the MP4SDTQ/6-311+G(2*df*) level of theory for the Li$^+$–N$_2$ system are plotted in Fig. 10. There are similarities between the expansions which is not surprising considering the electronic similarities of the two systems. Bottner *et al.*[9] have already noted the similarities of these two potential energy surfaces, and commented that the greater amount of rotational excitation seen in the Li$^+$–CO system results from the presence of the V_1 term in the Legendre expansion. The agreement between the two systems is best at short-range and is best for the V_0 expansion. The well depths of the isotropic radial function for the two systems, namely 0.254 and 0.250 eV for Li$^+$–N$_2$ and Li$^+$–CO, respectively, and the dipole-polarizability for the two systems, namely, 10.42 and 11.85 a.u. for Li$^+$–N$_2$ and Li$^+$–CO, respectively, are also very similar. This suggests that the two potential energy surfaces are in fact very similar and this result is in accord with the results of Gislason *et al.*[3] who found the expansion for the isotropic radial function to be remarkably similar for two ion-molecule systems.

CONCLUSION

Ab initio calculations of the potential energy surface of the Li$^+$–CO system have been reported at the HF and MP4SDQ level of theory with a 6-311+G(2*df*) basis set. This basis set was selected to optimize agreement between the experimental and theoretical electrical properties of the isolated subunits. The calculated dipole moment, quadrupole moment, and parallel and perpendicular dipole polarizabilities differ from the experimentally reported values by 77.3% (MP4SDQ), 15.6% (MP2), 16.5% (MP4SDQ), and 4.7% (MP4SDQ), respectively. The apparently large difference between the experimental and theoretical results for the dipole moment of CO is due to the small absolute value of the dipole moment and while the ion-dipole interaction is the dominant long-range interaction the absolute error remains small. The isotropic radial function of the Legendre expansion agrees well with the experimental results of Gislason *et al.*[3] which were derived from total scattering cross sections. The isotropic radial function has a well depth of 0.250 eV at 4.934 bohr at the MP4SDQ level of theory.

While this study of the potential energy surface of Li$^+$–CO represents a significant improvement on any potential energy surface currently available, it has some deficiencies because of the inherent difficulties of describing this system. These deficiencies are a result of a complex interplay between the bond length of CO, the treatment of electron correlation of CO, and the dipole moment of CO. It has been shown that electron correlation has increased the bond length of CO and therefore makes the dipole moment more positive. Thus, electron correlation must be taken into account in the calculation of the bond length for an accurate calculation of the long-range potential energy surface. The dependence of the dipole moment of CO on the bond length should also impact on the potential energy surface via nuclear polarization at short-range. This is experimentally observed as the greater likelihood of vibrational excitation of the Li$^+$–CO system compared with the Li$^+$–N$_2$ system. The greater complexity of the Li$^+$–CO system compromises the accuracy of any practical calculation method which can be applied.

The potential energy surfaces of Li$^+$–CO and Li$^+$–N$_2$ have been calculated in order to derive the transport properties of Li^+ in the gases CO and N_2. It is anticipated that the Li^+–N_2 potential energy surface is of sufficient accuracy to reproduce the experimentally measured transport coefficients, however the Li^+–CO potential energy surface has been determined less confidently and it cannot be expected to perform to the same degree of accuracy. It is difficult to assess the component uncertainty of the calculated transport coefficients that is due to the known inaccuracies of the potential energy surface. However, a conservative estimate of not greater than 3%–5% at low E/N, may result from probing the parts of the potential energy surface with known errors due to the electric multipole moments of CO, reducing to substantially less than this for intermediate and high E/N, where the angular variation of the potential energy surface has been well characterized.

[1] R. Bottner, U. Ross, and J. P. Toennies, J. Chem. Soc. Faraday Discuss. 1, 221 (1973).

[2] S. Kita, K. Noda, and H. Inouye, Chem. Phys. 7, 156 (1975).

[3] E. A. Gislason, P. Polak-Dingels, and M. S. Rajan, J. Chem. Phys. 93, 2476 (1990).

[4] V. Staemmler, Chem. Phys. 17, 187 (1976).

[5] A. Szabo and N. S. Ostlund, *Modern Quantum Chemistry: Introduction to Advanced Electronic Structure Theory* (Macmillan, New York, 1982).

[6] G. E. Scuseria, M. D. Miller, F. Jesen, and J. Geertsen, J. Chem. Phys. 94, 6660 (1991).

[7] T. F. Ewing, J. Detrich, and R. W. Conn, J. Chem. Phys. 69, 4662 (1978).

[8] L. D. Thomas, J. Chem. Phys. 67, 5224 (1977).

[9] R. Bottner, U. Ross, and P. Toennies, J. Chem. Phys. 65, 733 (1976).

[10] L. D. Thomas, W. P. Kraemer, and G. H. F. Diercksen, Chem. Phys. 30, 33 (1978).

[11] L. D. Thomas, W. P. Kraemer, and G. H. F. Diercksen, Chem. Phys. 27, 237 (1978).

[12] L. D. Thomas, W. P. Kraemer, and G. H. F. Diercksen, Chem. Phys. Lett. 74, 445 (1980).

[13] U. Gierz, J. P. Toennies, and M. Wilde, Chem. Phys. Lett. 110, 115 (1984).

[14] J. E. Del Bene, M. J. Frisch, K. Raghavachari, J. A. Pople, and P. v. R. Schleyer, J. Phys. Chem. 87, 73 (1983).

[15] S. Ikuta, Chem. Phys. 95, 235 (1985).

[16] J. E. Del Bene, J. Comput. Chem. 7, 259 (1986).

[17] D. A. Dixon, J. L. Cole, and A. Komornicki, J. Phys. Chem. 92, 1378 (1988).

[18] S. Ikuta, Chem. Phys. Lett. 109, 115 (1984).

[19] S. T. Grice, P. W. Harland, and R. G. A. R. Maclagan, Chem. Phys. 165, 73 (1992).

[20] M. J. Frisch, M. Head-Gordon, G. W. Trucks, J. B. Foresman, H. B. Schlegel, K. Raghavachari, M. Robb, J. S. Binkley, C. Gonzalez, D. J. DeFrees, D. J. Fox, R. A. Whiteside, R. Seeger, C. F. Melius, J. Baker, R. L. Martin, L. R. Kahn, J. J. P. Stewart, S. Topiol, and J. A. Pople, GAUSSIAN 90, Revision F, Gaussian Inc., Pittsburgh, 1990.

[21] L. A. Viehland, S. T. Grice, R. G. A. R. Maclagan, and A. S. Dickinson, Chem. Phys. 165, 11 (1992).

[22] E. A. Mason and E. W. McDaniel, *Transport Properties of Ions in Gases* (Wiley-Interscience, New York, 1988).

[23] D. J. DeFrees and A. D. McLean, J. Chem. Phys. 82, 333 (1985).

[24] G. A. Gislason, F. E. Budenholzer, and A. D. Jorgensen, Chem. Phys. Lett. 47, 434 (1977).

[25] H. H. Landolt and R. Bornstein, Zahl. Funk. 1, 510 (1951).

[26] K. P. Huber and G. Herzberg, *Molecular Spectra and Molecular Structure. IV. Constants of Diatomic Molecules, 1979* (Van Nostrand Rienhold, New York, 1979).

Cross sections and transport numbers of Li^+–CO

Stephen T. Grice, Peter W. Harland, and Robert G. A. R. Maclagan
Department of Chemistry, University of Canterbury, Christchurch, New Zealand

(Received 3 May 1993; accepted 19 July 1993)

Transport cross sections for the collisions of positive lithium ions with carbon monoxide molecules have been computed from theoretical Li^+-CO interaction potentials. These cross sections have been combined with the kinetic theory of atomic ions in polyatomic gases to give the mobility and diffusion coefficients parallel and perpendicular to an external electric field. Comparison of the calculated values with experimental data show that theory and experiment agree within their mutual uncertainties.

I. INTRODUCTION

The interaction of atomic ions with diatomic neutrals is of considerable importance in the ionosphere. Although the fundamental quantity describing this interaction is the potential energy surface, accurate information about such surfaces is limited except for systems in which the diatom is H_2, HD, or D_2. This is due to the difficulties both of performing extensive *ab initio* calculations and of making accurate measurements of equilibrium, scattering, or transport data and then reliably inferring values for the potential energy surface.

We have recently reported calculations of the transport coefficients of Li^+ ions in N_2 gas[1] which were in agreement with the experimental values within their mutual uncertainties. Further more complicated calculations were required to test the theory and its implementation for atomic ion/diatom systems. The $Li^+ + CO$ system was chosen, because of the greater complexity of its potential energy surface due to the electronic structure of CO and its reduced symmetry compared to N_2. The similarity between the potential energy surfaces of the $Li^+ + N_2$ and the $Li^+ + CO$ systems has been outlined by Grice *et al.*[2] Very little accurate information has been published concerning both the potential energy surface and the transport properties of the $Li^+ + CO$ system. Thus this calculation is intended to be an *a priori* test of the theory and indication of the accuracy of the potential energy surface.

Toennies *et al.*[3] have reported inelastic scattering studies of both the $Li^+ + N_2$ and $Li^+ + CO$ systems. While there were similarities in the time of flight mass spectra of the two systems, the $Li^+ + CO$ system exhibited a greater probability for vibrational excitation in the energy range which they studied. The differences between the two spectra were rationalized in term of differences in the "potential hypersurface."

Staemmler has performed an *ab initio* self-consistent field (SCF) study of the $Li^+ + N_2$ (Ref. 4) and $Li^+ + CO$ (Ref. 5) systems in order to rationalize the differences in Toennies time-of-flight (TOF) spectra. Staemmler concluded that the dependence of the force constant of the diatomic molecule on the vector R was greater for the CO molecule than for N_2. Unfortunately further conclusions are precluded in the absence of a mechanistic approach to collisions using trajectory calculations, and it is unlikely that either of Staemmler's potential energy surfaces are accurate enough to be reliable in this regard.

Other authors[6,7] calculated the short-range isotropic potential energy surface from integral scattering cross section measurements and have concluded that the $Li^+ + CO$ and $Li^+ + N_2$ systems are very similar. Grice *et al.*[2] have performed an *ab initio* study of the $Li^+ + CO$ surface and compared the angular components of the full rigid rotor potential energy surface with the corresponding expansions for the $Li^+ + N_2$ system, and showed the similarities which support the results of Kita[6] and Gislason *et al.*[7] Unfortunately the rigid rotor potential energy surface contains little information about the internal vibrational coordinates of the system and as a result no conclusions about the differences in the inelastic differential scattering cross section results of Toennies *et al.*[3] can be made.

The aim of this study was to test the accuracy of the interaction potentials of Grice *et al.*[2] by comparing the experimental values of the transport coefficients with those derived from the potential energy surface for the $Li^+ + CO$ system. This was achieved with the use of a similar method to that described by Viehland *et al.*[1] Several of the statements presented supporting the calculation of the transport coefficients for the $Li^+ + N_2$ system are equally valid for the $Li^+ + CO$ system. This includes the validity of using classical mechanics to calculate the cross sections defined by the equations

$$Q^{(\lambda,\nu)}(\epsilon)=\frac{1}{kT}\int_0^\infty d\epsilon_0 \exp\left(-\frac{\epsilon_0}{kT}\right)q^{(\lambda,\nu)}(\epsilon,\epsilon_0), \quad (1)$$

$$\Sigma^{(\lambda,\nu)}(\epsilon)=\frac{1}{kT}\int_0^\infty d\epsilon_0 \exp\left(-\frac{\epsilon_0}{kT}\right)\sigma^{(\lambda,\nu)}(\epsilon,\epsilon_0), \quad (2)$$

and the use of the classical kinetic theory to calculate the transport cross sections. In Eqs. (1) and (2) ϵ is the precollisional kinetic energy and ϵ_0 is the precollisional rotational energy.

The details of the trajectory calculations are outlined followed by the calculations of the transport cross sections. In the following section transport coefficient calculations are described which in turn are followed by a discussion of the results. Particular attention is paid to the uncertainties of the experimental and theoretical transport coefficients.

II. CLASSICAL TRAJECTORY CALCULATIONS OF THE Li^+–CO SYSTEM

This section outlines the trajectory calculations that were required to calculate the transport cross sections that are defined by Eqs. (1) and (2). Full details of the procedure used have been given by Viehland *et al.*[1] The code of the program TRAJECK (Refs. 8 and 9) had to be slightly altered to account for the lower $C_{\infty v}$ symmetry of the CO molecule compared to the N_2 molecule. The greater anisotropy of the potential energy surface due to the lower symmetry is discussed by Grice *et al.*[2]

The numerical calculation of the cross sections defined by Eqs. (1) and (2) becomes a trade off between the accuracy required for the calculation of the transport coefficients and the available computer time. It has been shown that the accuracy of the theoretical transport coefficients will be limited by the accuracy of the potential energy surface. The electronic structure of the CO molecule has proven difficult to theoretically model using high level computational methods. For example, Scuseria *et al.*[10] have shown that the theoretical dipole moment of CO does not converge to the experimental value for the Møller–Plesset methods as a function of the order of the theory used. Careful attention was paid to the calculation of the cross sections using trajectory calculations in order that the numerical accuracy did not unnecessarily exceed the estimated accuracy of the $Li^+ + CO$ potential energy surface. To calculate the transport cross sections to an accuracy of that calculated for the $Li^+ + N_2$ system would have been expensive, while it would yield no additional information as to the real potential energy surface. Thus the trajectory parameters were systematically varied with the aim of calculating the transport cross sections with an uncertainty of not greater than 1%. This required several calculations of the cross sections defined by Eqs. (1) and (2), which are detailed in the following subsections.

III. CALCULATIONS OF ACCURATE CROSS SECTIONS FOR THE Li^+–CO SYSTEM

Because of the long-range ion-dipole interaction of this system, a slightly different strategy for varying the parameters to obtain accurate cross sections was adopted. The variation of the parameter R_s, the starting distance in the trajectory calculations of the Li^+ ion from the center of mass of the CO molecule, was primarily investigated for convergence before other parameters. Convergence of the cross sections was tested in each order of $y = \epsilon/k_b T$. A selection of the studies of the accuracies of the cross sections are given below.

A. Convergence of cross sections for $\log(y) = 3.0$

A study of the numerical effect of varying the parameter R_s on the values of some of the cross sections showed that R_s must be at least 120 bohr in order to obtain a convergence of the cross sections of $< 1\%$. The ion-dipole interactions are approximately the same strength at 120 bohr as the ion-quadrupole interaction at 40 bohr, which is the value used for this energy range in the cross section calculations for the $Li^+ + N_2$ system. A value of 1×10^{-8} for the accuracy parameter, ACC, which is used to determine the time steps in the integration procedure, was sufficient for convergence of the cross sections to $< 1\%$. The effect of the partitioning of the impact parameters was investigated on the number of impact parameters required in each region divided by the parameter b_s. By restricting the high impact parameters N2 to a minimum number of values, the value of b_s was set to the smallest possible value while retaining convergence of the cross sections to better than 1%. From the values of the cross sections it was concluded that with $b_s = 8$ a.u. at least 24 low impact parameters, N1 and 4 high impact parameters, N2 were required to calculate the cross sections to an accuracy better than 1%. As was found in the Li^+–N_2 calculations, the choice of the parameter c, used in the integration scheme in the larger impact region, is relatively unimportant when considering the accuracy of the calculated cross sections. Adequate accuracy of the cross sections required at least 6 angles of each of the three angular quadratures, χ, ϕ_L, and ϕ_j. The cross sections defined by Eqs. (1) and (2) are evaluated by averaging over the rotational energy by N6-point Gauss–Legendre integration at low w, and N7-point Gauss–Laguerre integration over high w, in an identical manner to that described by Viehland *et al.*[1] 4 high and 4 low rotational energy quadratures are sufficient to calculate the cross sections to an accuracy of better than 1%.

B. Convergence of cross sections for $\log(y) = 2.0$

In this energy range, R_s must be at least 160 bohr in order to obtain a convergence of the cross sections of $< 1\%$. A value of the accuracy parameter ACC of 1×10^{-9} was of sufficient accuracy to converge the cross sections to $< 1\%$. By restricting the high impact parameters to a minimum number of values, the value of b_s was set to the smallest possible value while retaining convergence of the cross sections to better than 1%. With $b_s = 10$ a.u., at least 32 low impact parameters, N1 and 6 high impact parameters, N2 were required to calculate the cross sections to an accuracy better than 1%. Adequate accuracy of the cross sections required at least 6 angles of each of the three angular quadratures, χ, ϕ_L, and ϕ_j, in this energy range. Eight high and eight low rotational energy quadratures are sufficient to calculate the average cross sections to an accuracy of better than 1%.

C. Convergence of cross sections for $\log(y) = 1.0$

As the kinetic energy of the collisions decreases it becomes more difficult to maintain a given accuracy in calculating the cross sections, due to the stability and convergence properties of solving the trajectory problem resulting from longer lasting and more convoluted interactions between the particles. Thus obtaining converged cross sections in the lowest kinetic energy region under study required a slightly different strategy to the other energy ranges. First, a study of the convergence of the parameter ACC was undertaken, on a small set of trajectories. It was found that the variable of $ACC = 1 \times 10^{-10}$ was of suffi-

TABLE I. Summary of $Li^+ + CO$ trajectory parameters used for the MP4SDQ/6-311G**(2*df*) potential energy surface.

Range of ϵ (10^{-3})	<9.5	9.5–95	>95
Number of ϵ values	2	8	15
Number of ϵ_0 values	20	16	8
ACC	1×10^{-8}	1×10^{-9}	1×10^{-10}
R_s a.u.	400	180	120
b_s a.u.	20.0	10.0	8.0
c	1.0	1.0	1.0
N1 and N2	48+6	32+6	24+4
N3=N4=N5	10	6	6
Number of trajectories	21 160 000	1 050 624	725 760

cient accuracy to converge the cross sections to $<1\%$, in this energy range. R_s must be at least 300 bohr in order to obtain a convergence of the cross sections of $<1\%$, in this energy range. At least 48 low impact parameters N1 and 6 high impact parameters N2 were required to calculate the cross sections to an accuracy of $\sim 1\%$. Adequate accuracy of the cross sections required at least 10 angles of each of the three angular quadratures, χ, ϕ_L, and ϕ_j, in this energy range.

These cross section calculations have been combined with several other calculations with the aim of maximizing the numerical accuracy with the minimum numerical effort. While the amount of time available to calculate the low kinetic energy cross sections is necessarily limited, this has led to a compromise in the accuracy of the cross sections and hence in the subsequent determination of the transport coefficients. Being mindful of the fact that the estimated accuracy of the cross sections should not exceed that estimated for the potential energy surface in a given energy range, the set of trajectories that are defined by the parameters in Table I represent the minimum number of trajectories possible to describe the transport coefficients to an accuracy of at least 1%. The final cross sections have been plotted in Fig. 1. It can be expected that the theoretical uncertainties should decrease at high *E/N*, where the convergence properties of the relevant cross sections and the potential energy surface that they probe were most accurate.

Improvements in the accuracy of the calculated cross sections may have to await the application of vector pipeline methods[11] in order to make large trajectory calculations feasible.

IV. TRANSPORT COEFFICIENTS OF $Li^+ + CO$

The transport coefficients of Li^+ ions in CO gas have recently been measured by Satoh *et al.*[12] The measured mobilities of the Li^+ ions in CO gas showed discrepancies with the only other data set in the literature reported by Tyndall[13] at zero field. Tyndall's measurements were also significantly smaller than those for the $Li^+ + N_2$ system, which he then interpreted in terms of the presence of the small dipole moment of the CO molecule. However transport measurements for other alkali-metal ions with N_2 and CO have revealed that the ratio of zero-field mobilities between the two systems were 1.10 for K^+,[14] and 1.11 for Cs^+.[15] Thus it seems likely that Tyndall's mobility measurements of Li^+ ions in CO gas are in error perhaps due to the presence of fast clustering reactions,[16] and that the permanent dipole moment affects the mobility to a small extent at small field strength.

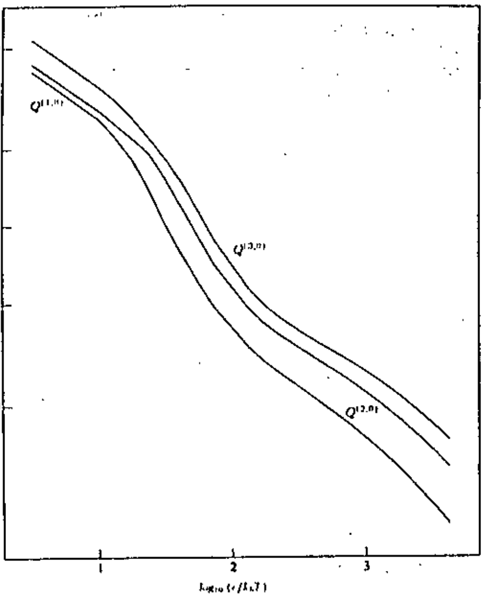

FIG. 1. The rotationally averaged transport cross sections of Li^+ ions in CO gas, as a function of the dimensionless relative kinetic energy. The transport cross sections are plotted as $\log_{10}$ and in a.u. The transport cross section curves for the cross sections $Q^{(1,0)}$, $Q^{(2,0)}$, and $Q^{(3,0)}$ are labeled in the figure.

The trajectories that are summarized in Table I were used to calculate the cross sections defined by the equations

$$q^{(\lambda,\nu)}(\epsilon,\epsilon_0)=2\pi\int_0^\infty db\,\frac{b}{2}\int_{-1}^{+1}d\cos\chi \times\frac{1}{2\pi}\int_0^{2\pi}d\phi_L\,\frac{1}{\pi}\int_0^{\pi}d\phi_j \times\left[1-\left(\frac{\epsilon'}{\epsilon}\right)^{\nu+\lambda/2}P_\lambda(\cos\theta)\right], \tag{3}$$

$$\sigma^{(\lambda,\nu)}(\epsilon,\epsilon_0)=2\pi\int_0^\infty db\,\frac{b}{2}\int_{-1}^{+1}d\cos\chi \times\frac{1}{2\pi}\int_0^{2\pi}d\phi_L\,\frac{1}{\pi}\int_0^{\pi}d\phi_j \times\left[1-\left(\frac{\epsilon'}{\epsilon}\right)^{\nu+\lambda/2}(\cos\theta)^{\lambda}\right] \times\left(\frac{\epsilon'}{\epsilon}\right)^{\nu}(\sin\theta)^{2\nu} \tag{4}$$

TABLE II. Transport properties of Li^+ ions in CO gas at $T=300$ K, as calculated from the MP4SDQ/6-311G**(2*df*) potential energy surface, at low field strength.

E/N (Td)	T_{ion} (K)	E_{lab} (eV)	v_d (km s^{-1})	K_0 (cm^2/V s)	$ND_\parallel$ 10^{18} cm s	$ND_\perp$
10.04	302.6	0.0391	0.098	3.62	2.23	2.22
11.29	303.3	0.0392	0.110	3.61	2.25	2.23
12.71	304.2	0.0393	0.123	3.61	2.27	2.24
13.48	304.7	0.0394	0.130	3.60	2.28	2.25
15.18	305.9	0.0396	0.147	3.59	2.30	2.27
17.10	307.5	0.0398	0.165	3.58	2.33	2.29
18.15	308.4	0.0399	0.174	3.58	2.35	2.30
19.27	309.5	0.0400	0.185	3.57	2.37	2.32
20.46	310.6	0.0402	0.196	3.56	2.40	2.33
23.09	313.4	0.0405	0.220	3.55	2.45	2.37
26.07	317.0	0.0410	0.247	3.53	2.52	2.42
29.47	321.4	0.0415	0.277	3.50	2.61	2.48
31.35	324.0	0.0419	0.294	3.49	2.66	2.52
33.35	327.0	0.0423	0.311	3.47	2.72	2.56
35.50	330.4	0.0427	0.330	3.46	2.78	2.60
37.79	334.1	0.0432	0.350	3.44	2.86	2.65
40.24	338.3	0.0437	0.371	3.43	2.93	2.70
42.87	343.1	0.0443	0.393	3.41	3.02	2.76
45.67	348.4	0.0450	0.416	3.39	3.13	2.83
48.68	354.4	0.0458	0.441	3.37	3.24	2.90
51.89	361.1	0.0467	0.468	3.35	3.38	2.98
55.33	368.6	0.0477	0.496	3.33	3.53	3.08
59.00	377.1	0.0487	0.526	3.31	3.70	3.18
62.92	386.6	0.0500	0.557	3.30	3.90	3.30
67.19	397.3	0.0514	0.591	3.27	4.14	3.43
71.77	409.4	0.0529	0.627	3.25	4.41	3.57
76.62	422.9	0.0547	0.665	3.23	4.78	3.73
81.79	438.1	0.0566	0.706	3.21	5.18	3.92
87.27	455.1	0.0588	0.750	3.20	5.68	4.13
93.05	474.3	0.0613	0.795	3.18	5.98	4.36
99.13	495.9	0.0641	0.844	3.17	6.34	4.63

TABLE III. Transport properties of Li^+ ions in CO gas at $T=300$ K, as calculated from the MP4SDQ/6-311G**(2*df*) potential energy surface, at high field strength.

E/N (Td)	T_{ion} (K)	E_{lab} (eV)	v_d (km/s)	K_0 (cm^2/V s)	$ND_\parallel$ 10^{18}/cm s	$ND_\perp$
303.98	6 050.4	0.7821	4.295	5.26	756.96	90.87
317.23	6 761.1	0.8740	4.546	5.33	825.92	123.42
332.38	7 559.7	0.9772	4.810	5.39	797.93	156.62
349.48	8 457.0	1.0932	5.123	5.46	729.67	193.06
368.75	9 465.2	1.2235	5.481	5.53	669.26	233.81
390.54	10 598.1	1.3699	5.869	5.59	635.40	278.31
415.02	11 870.9	1.5344	6.276	5.63	628.53	326.13
442.16	13 301.1	1.7193	6.702	5.64	641.62	378.13
471.91	14 908.0	1.9270	7.147	5.64	672.62	435.31
504.41	16 713.5	2.1604	7.611	5.62	714.61	498.48
539.58	18 742.3	2.4226	8.098	5.59	772.74	567.99
577.48	21 021.7	2.7173	8.609	5.55	845.09	644.74
618.13	23 582.9	3.0484	9.147	5.51	932.66	729.78
661.56	26 460.7	3.4203	9.715	5.47	1 036.12	824.411

using the potential energy surface given in Grice *et al.*[2] In Eqs. (3) and (4) ϵ is the precollisional kinetic energy, ϵ_0 is the precollisional rotational energy, ϵ' is the postcollisional kinetic energy, and θ is the scattering angle of the collision. The rotationally averaged cross sections were then used as input into the programs BIMAX (Ref. 17) and MOBDIF (Ref. 18), respectively, in order to calculate the transport coefficients of Li^+ ions in CO gas at $T=300$ K as a function of E/N.

V. TRANSPORT COEFFICIENTS CALCULATED FROM THE MØLLER–PLESSET POTENTIAL ENERGY SURFACE

The numerical results of the transport coefficients from the program MOBDIF at low E/N are displayed in Table II. Also displayed is the effective temperature of the ions, T_{ions}, the kinetic energy in the laboratory reference frame, E_{lab}, and the calculated drift velocity, v_d. Note that the mobility, K_0, and the parallel and perpendicular diffusion coefficients, $ND_\parallel$ and $ND_\perp$, respectively, have converged to an accuracy of 0.1%, 0.25%, and 0.25%, in this energy range.

Calculations of the transport coefficients at high field strength have been performed and the numerical results from the program MOBDIF are displayed in Table III. The theoretical accuracy of the calculated transport coefficients can be estimated from a comparison of the 7th- and 8th-order approximation results from the program. Note that the mobility K_0, and the parallel, and perpendicular diffusion coefficients, $ND_\parallel$ and $ND_\perp$, respectively, have converged to an accuracy of 0.1%, 0.25%, and 0.25% respectively, in this range.

To assess the degree of agreement between the theoretically and experimentally derived transport coefficients an estimate of the uncertainties of the calculations and experiments are required.

The theoretical accuracy of the calculated transport coefficients can be estimated from a comparison of the 7th- and 8th-order approximation results from the program MOBDIF. These results show that the mobility has converged to within 0.1% below 100 Td, and 0.1%–2% in the range 100–130 Td. There is a large region of inconvergence between ~130 and 300 Td, followed by between 10% and 2% accuracy for the mobility in the range of 300–400 Td, and between 2% and 0.6% in the range of 400–500 Td. The mobility converges to within 0.5% at field strengths beyond 500 Td.

The reduced perpendicular diffusion coefficient, $\tilde{D}_\perp$, converged to within 0.25% below 100 Td, within 0.25%–4% in the range 100–120 Td, and did not converge in the range 120–400 Td. In the range 400–500 Td the reduced perpendicular diffusion coefficient converged to an accuracy of within 10%–4%, and within 4%–2% in the 500–600 Td range.

The reduced parallel diffusion coefficient, $\tilde{D}_\parallel$, converged to within 0.25% below 90 Td, within 0.25%–50% in the range 90–120 Td, and did not converge in the range 120–400 Td. In the range 400–500 Td the reduced parallel diffusion coefficient converged to an accuracy of within 50%–20%, and within 20%–12% in the 500–600 Td range.

Other sources of uncertainties to the theoretically derived transport coefficients are from the accuracy of the potential energy surface. While the MP4SDQ/

6-311G**(2*df*) potential energy surface of Grice *et al.*[2] is not as accurate as the potential energy surface calculated for the $Li^+ + N_2$ system, a conservative estimate of the error would be a maximum of 5% at large separation and decreasing below 2%–3% at smaller separation. The greater uncertainty of the $Li^+ + CO$ potential energy surface results from the extra electronic complexity of the CO molecule, particularly with respect to establishing reliable electric multipole moments important in long-range interactions. The other main source of uncertainty in the theoretical calculations results from the choice of trajectory parameters which necessarily limits the number of the trajectory calculations. A conservative estimate of this source of uncertainty is $<1\%$. Therefore the combined theoretical uncertainty is greatest at 6% for small E/N, decreasing to $<3\%$ at high E/N.

Satoh *et al.*[12] estimates the uncertainties of their measurements as 3% at low and intermediate E/N, and 1.5% at high E/N. The major components of the uncertainties relate to the measurements of temperature and pressure throughout the course of the experiment. The uncertainties of the diffusion coefficients have been extrapolated from the uncertainties for the mobility using the equation

$$\tilde{D}=qD_{\parallel,\perp}/K_{\text{pol}}k_BT_{\text{pol}}. \tag{5}$$

Because the published graph of the transport coefficients had no associated table of data, the raw data was estimated from a magnified image of the figure. From the resulting variation of adjacent points on the experimental mobility and diffusion coefficient curves they have published, and from previous knowledge of the inherent errors in experimental measurements in drift-tubes, we estimate that the uncertainty in the mobility measurements to be $\sim 5\%$ below 100 Td, and $\sim 2\%$ above 100 Td.

The calculated mobilities and diffusion coefficients, which were made dimensionless by Eq. (5) and the equation

$$k_BT_{\text{pol}}=kT+1/3M(K_{\text{pol}}E)^2 \tag{6}$$

are compared to the results of Satoh *et al.*[16] in Figs. 2 and 3, respectively.

Several features are evident in the comparison of the experimentally and theoretically derived mobilities. The two mobility curves are within the mutual uncertainties almost over the entire range of E/N plotted. However, some systematic differences between the actual experimental points and the theoretical curve which were not present in the study of $Li^+ + N_2$ system suggest that the potential energy surface of $Li^+ + CO$ is comparatively more inaccurate. These findings are supported by the conclusions of our *ab initio* study[2] on $Li^+ + CO$. Note also that the agreement to within mutual uncertainties of the experimental and theoretical mobilities results mainly from the greater uncertainties in each data set, due partly to conservative estimates, compared to those for the $Li^+ + N_2$ system.

Considering each region of E/N separately it is apparent that the correspondence between the experimental and theoretical mobilities is reasonable at low E/N up to 100 Td. While there is a consistent displacement between the two data sets, the agreement is within the uncertainties of the experimental error, and the slight differences can easily be explained by the known difficulties of calculating accurate electric multipole moments of CO important in determining the long-range potential energy surface. Note that the fitted dipole moment of CO was larger than the experimental value and that this may be responsible for the smaller theoretical mobility at low E/N.

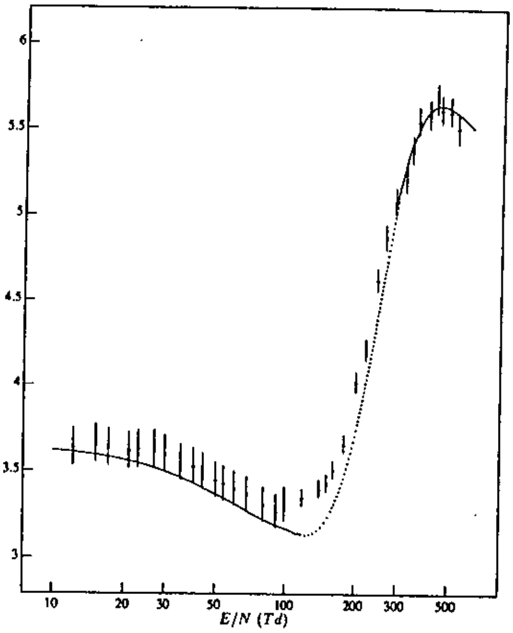

FIG. 2. The mobility of Li^+ ions in CO gas calculated using MP4SDQ/6-311G**(2*df*) potential energy surface, at $T=300$ K, as a function of E/N in units of Td. The points with error bars are the experimental data of Satoh *et al.* (Ref. 13). The solid curve was calculated with the program MOBDIF, using the cross sections calculated using the parameters as outlined in Table I. The mobility has been spline fitted through the region of inconvergence and is plotted using the dotted curve.

In the region directly after 100 Td, the problems of inconvergence associated with a rapid rise in mobility were encountered. The mobilities have been spline fitted through the region of inconvergence and plotted as a dotted line. It is clear that theoretical and experimental mobilities started to diverge to the limit of the mutual uncertainties that bound the agreement of these data sets. Because the uncertainties of the theoretical calculations are not as small as those corresponding to the $Li^+ + N_2$ system, and because of the inconvergence problems of the kinetic theory, any further conclusions about the potential energy surface are not possible. However it does seem likely that the possible disagreement in this region, which was also observed in the $Li^+ + N_2$ system, is due to the variation of correlation energy obtained from Møller–Plesset calculations as a function of molecular separation.[19] Other authors[17] have attempted to improve the convergence properties of kinetic equations by expanding the ion distribution function in

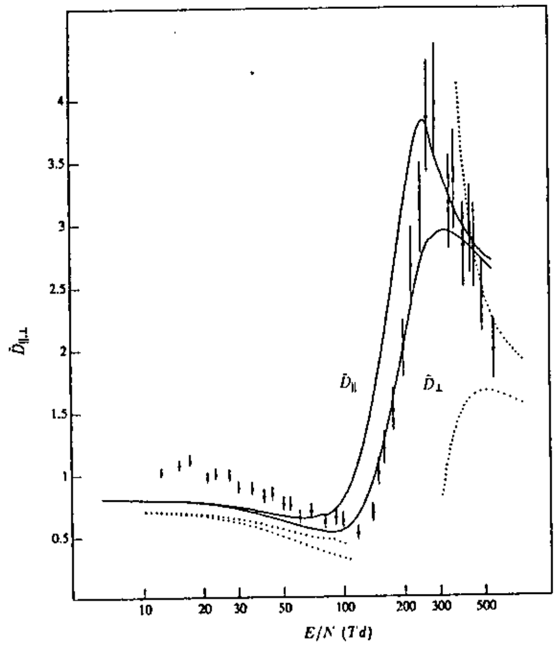

FIG. 3. The reduced diffusion coefficients of Li^+ ions in CO gas calculated using the MP4SDQ/6-311G**(2*df*) potential energy surface, at $T=300$ K, as a function of E/N in units of Td. The points with error bars are the experimental measurements of the parallel diffusion coefficients of Satoh *et al.* (Ref. 14). The solid curves, representing the reduced parallel, and perpendicular, diffusion coefficients, were calculated with the program BIMAX, using the cross sections calculated using the parameters as outlined in Table I. The results were spline fitted through the region of inconvergence. The dotted curves represent the reduced parallel and perpendicular diffusion coefficients calculated using the program MOBDIF, which were not plotted in the region of inconvergence. The reduced diffusion coefficients are dimensionless and defined by Eq. (5).

terms of a bimodel Maxwellian function, supposedly representing partial ion run away. These representations have improved the convergence properties of the kinetic equations of other systems that have been studied. Such methods could well result in improved convergence for the Li^+–CO system.

The agreement between the theoretical and experimental data sets at high E/N is excellent. The greater complexity of internal vibrational coordinates of the $Li^+ + CO$ potential energy surface at small separation meant that a simple semiempirical model could not be applied to simply account for the effect of nuclear polarization. Calculating the effect of nuclear polarization in this system requires more rigorous treatment of the internuclear coordinate of the CO molecule as a function of the intermolecular vector R. However, where such an effect produced a measurable improvement in the case of the $Li^+ + N_2$ systems' transport coefficients, it is doubtful if inclusion of this effect could improve the theoretically calculated mobilities for this system.

Turning to a discussion of the comparison of the experimental and theoretical diffusion coefficients plotted in Fig. 3, it is evident that there is no agreement between the data sets for the parallel diffusion coefficients except above 360 Td, where the correspondence between the reduced parallel diffusion coefficient calculated using the program BIMAX and the experimental results of Satoh *et al.* are good. These results complement those found for the mobilities. At low E/N, the consistent differences between the theoretical and experimental reduced diffusion coefficients are exaggerated and beyond the mutual uncertainties. The differences almost certainly result from the inaccuracies of the potential energy surface due to the difficulties of obtaining reliable electric multipole moments from Møller–Plesset methods. The comparison of the theoretical and experimental results for the reduced parallel diffusion coefficients at high E/N suggested that the potential energy surface is accurate. This conclusion is supported by the excellent agreement between the short-range isotropic radial function calculated by Grice *et al.*[2] and that determined by integral cross sections measurements by Gislason *et al.*[5] Note that no experimental data for the perpendicular diffusion coefficient have been reported.

VI. CONCLUSION

A complete report of the transport calculations of Li^+ ions in CO gas at $T=300$ K has been given. These results have allowed further conclusions about similar atomic ion-diatom transport systems to be made. The MP4SDQ/6-311G**(2*df*) potential energy surface of Grice *et al.*[2] was used to calculate the trajectories necessary to obtain kinetic theory cross sections with an inaccuracy not greater than 1%. These cross sections were then used to calculate the transport coefficients of Li^+ ions in CO gas. The comparison of the theoretical and experimental mobilities revealed that the data sets were within the mutual uncertainties although systematic differences were observed at low E/N. The differences between the experimental and theoretical reduced parallel diffusion coefficient were further exaggerated beyond the mutual uncertainties, suggesting that inaccuracies in long long-range potential energy surface were responsible. The fitted dipole moment of CO was larger than the experimental value and this may well be the cause of the slightly smaller low field theoretical mobilities and diffusion coefficients. Correspondence between the experimental and theoretical mobilities and diffusion coefficients was excellent at high E/N justifying the analysis of the angular anisotropy at short-range for the potential energy surface of Grice *et al.*

Comparison of the results for the $Li^+ + CO$ and the $Li^+ + N_2$ systems has shown some similarities. Inaccuracies in the calculated transport coefficients for these systems about 100 Td suggest that both potential energy surfaces are not accurate in the 6–10 bohr separation range. This observation is consistent with the known properties of Møller–Plesset calculations at nonequilibrium geometries.[19] The calculation of the transport properties is further complicated by the known difficulties in achieving convergence when calculating the dipole moment using Møller–Plesset theory. The accuracy of the potential energy surface could be improved with the application of a method with a more stable treatment of electron correlation as a function of separation, such as QCI methods. These methods have also been shown to have improved stability when calculating the electric multipole moments of the CO molecule.[10]

ACKNOWLEDGMENT

We wish to acknowledge valuable discussions with L. A. Viehland and thank him for the copies of his programs.

[1] L. A. Viehland, S. T. Grice, R. G. A. R. Maclagan, and A. S. Dickinson, Chem. Phys. 165, 11 (1992).

[2] S. T. Grice, P. W. Harland, and R. G. A. R. Maclagan, J. Chem. Phys. 99, 7619 (1993).

[3] R. Bottner, U. Ross, and J. P. Toennies, J. Chem. Soc. Faraday Discuss. 1, 221 (1973).

[4] V. Staemmler, Chem. Phys. 7, 17 (1975).

[5] V. Staemmler, Chem. Phys. 17, 187 (1976).

[6] S. Kita, K. Noda, and H. Inouye, Chem. Phys. 7, 156 (1975).

[7] E. A. Gislason, P. Polak-Dingels, and M. S. Rajan, J. Chem. Phys. 93, 2476 (1990).

[8] A. S. Dickinson and M. S. Lee, J. Phys. B 18, 4177 (1985).

[9] L. A. Viehland, in *Status and Future Developments in the Study of Transport Properties*, NATO ASI Series C, edited by W. A. Wakeham, A. S. Dickinson, F. R. W. McCourt, and V. Vesovic (Kluwer, Dordrecht, 1992), Vol. 361.

[10] G. E. Scuseria, M. D. Miller, F. Jesen, and J. Geertsen, J. Chem. Phys. 94, 6660 (1991).

[11] D. L. Cochrane and D. G. Truhlar, Parallel Comput. 6, 63 (1988).

[12] Y. Satoh, M. Takebe, and K. Iiunuma, J. Chem. Phys. 88, 3253 (1988).

[13] A. D. Tyndall, *The Mobility of Positive Ions in Gases* (Cambridge University, Cambridge, 1938).

[14] G. M. Thomson, J. H. Schummer, D. R. James, I. R. Gatland, M. R. Flannery, and E. W. McDaniel, J. Chem. Phys. 58, 2402 (1973).

[15] M. G. Thackston, F. L. Eisele, H. W. Ellis, and E. W. McDaniel, J. Chem. Phys. 67, 1276 (1977).

[16] Y. Satoh, M. Takebe, and K. Iiunuma, J. Chem. Phys. 87, 6520 (1987).

[17] K. F. Ness and L. A. Viehland, Chem. Phys. 148, 255 (1990).

[18] L. A. Viehland and K. Kumar, Chem. Phys. 131, 295 (1989).

[19] J. A. Pople, M. Head-Gordon, and K. Raghavachari, J. Chem. Phys. 87, 5968 (1987).

Deconvolution of unchopped time-of-flight waveforms

Brett R. Cameron and Peter W. Harland
Chemistry Department, University of Canterbury, Christchurch, New Zealand

(Received 12 May 1993; accepted for publication 18 September 1993)

A reliable method for deconvolving badly convoluted molecular beam time-of-flight waveforms using Fourier transform and Wiener filtering techniques is presented. The devised method places no restrictions on the functional form of any factors affecting the shape of the measured time-of-flight distribution, but rather uses an accurately determined distribution to estimate an overall response function for the system. The estimated response function may then be used to deconvolve any convoluted time-of-flight waveform measured under similar experimental conditions. The mathematical details of the method are discussed and examples of its application to the deconvolution of time-of-flight waveforms measured in unchopped pulsed supersonic beams of argon, krypton, $CHCl_3$, and CH_3Cl are presented.

I. INTRODUCTION

Time-of-flight techniques have been extensively used to determine speed distributions of atoms and molecules in molecular beam experiments for more than three decades. The importance and popularity of these methods are due not only to the simplicity and compactness of the experimental arrangements involved, but also to the wide range of experiments to which they are applicable. For example, time-of-flight techniques may be used for the characterization of molecular beam sources,[1] the investigation of inelastic scattering by energy loss methods,[2] or for the determination of reactant energy distributions in reactive scattering experiments.[3]

The accuracy with which the measured time-of-flight signal actually represents the true distribution of atomic or molecular speeds in a molecular beam has often been questioned.[4,5] In a time-of-flight experiment, the molecular beam must be modulated in some manner and the measured time-of-flight signal will therefore depend upon the geometry and frequency of the modulating device according to some modulator or *gate* function. Furthermore, since the beam signal is measured using an electronic circuit with a nonzero response time, the measured distribution of flight times will be distorted by the dynamic response of the electronic system. Due to these problems, it is often necessary to perform some kind of deconvolution on measured time-of-flight data in order to extract a more accurate representation of the true speed distribution. There are essentially three approaches which may be adopted to handle this problem. Apart from applying direct numerical deconvolution, it is possible to use moment methods, or to fit convolutions and transformations of empirical speed distribution functions to time-of-flight data.

Using Laplace transform methods, Alcalay and Knuth[4] derived expressions for the moments of typical speed distributions and gate functions. By evaluating moments of the measured time-of-flight data and subtracting those of the gate function, moments of the true speed distribution can be found. In principle, any function can be characterized to any degree by considering a sufficient number of moments. In practice, however, noise in the data generally limits the number of usable moments to only a few. The process is also time consuming and makes possibly invalid assumptions regarding the exact form of the gate function.

A quite general method for deconvolving time-of-flight data is to approach the problem from the reverse direction by fitting a parameterized convolution to the experimental data.[6] This approach is somewhat artificial and the solution derived in terms of the various parameters used may not be unique. Such an approach is also time consuming from a computational point of view, as numerically fitting the measured or observed signal in this manner for some assumed set of parameters may require many iterations in order to minimize the sum of the squares of the deviations between the experimental and fitted distributions.

While it may be necessary to make some assumptions regarding the form of the speed distribution in a supersonic molecular beam, it is not at all necessary to make any such assumptions regarding the form of the gate function or the electronic response function. Also, apart from these functions there may be any number of other factors that distort the time-of-flight waveform which cannot be adequately described in terms of any empirically derived expression. All of these factors combine to give an overall system response function which must be deconvolved from the measured time-of-flight signal in order to obtain the true distribution of flight times. In our laboratory, the situation is made worse by the fact that for some experiments it is not possible to fit a chopper assembly into the molecular beam apparatus to modulate the beam in an acceptable manner. It is therefore necessary to estimate flow velocities and parallel translational temperatures from highly convoluted time-of-flight waveforms measured in unchopped pulsed supersonic expansions.

In this communication we illustrate the use of Fourier transform and Wiener filtering techniques,[7] to reliably deconvolve measured time-of-flight waveforms. We show how an accurately measured, or theoretical, time-of-flight distribution may be deconvolved from a badly convolved distribution to estimate an overall response function for the system. This response function may then be used to deconvolute any time-of-flight distribution measured under sim-

0034-6748/94/65(1)/108/8/$6.00 © 1994 American Institute of Physics

ilar experimental conditions. The form of the system response function is briefly discussed and illustrative results obtained using the deconvolution procedure are presented for argon, krypton, $CHCl_3$, and CH_3Cl. The use of direct numerical deconvolution in this manner is made computationally efficient through the use of the fast Fourier transform algorithms,[8] and problems associated with high-frequency noise components in the experimental data are reduced by the application of a simple low-pass filtering function.

II. MATHEMATICAL CONSIDERATIONS

The effect of most factors that contribute to the distortion of time-of-flight waveforms may be expressed in terms of the convolution integral

$$g(t)=\int_0^t h(t)f(t-\tau)d\tau=\int_0^t h(t-\tau)f(t)d\tau, \qquad (1)$$

where $g(t)$ is the measured time-of-flight signal, $f(t)$ is the true time-of-flight waveform, and $h(t)$ some function which describes the dynamic response of the experimental apparatus at time t. Given sufficient knowledge regarding the form of the response function, Fourier transform techniques may be used to solve Eq. (1) to obtain $f(t)$ through the application of the convolution theorem, which states that the transform of the convolution is equal to the product of the transforms.

Defining the forward Fourier transform of a function $f(t)$ to be $F(\omega)$ such that

$$F(\omega)=\int_{-\infty}^{\infty} f(t)e^{2\pi i\omega t}dt, \qquad (2)$$

and the inverse Fourier transform as[9]

$$f(t)=\int_{-\infty}^{\infty} F(\omega)e^{-2\pi i\omega t}d\omega, \qquad (3)$$

the convolution theorem gives that

$$G(\omega)=H(\omega)F(\omega). \qquad (4)$$

The significance of the convolution theorem is that the process of convolution in the time domain is simplified to mere multiplication in the Fourier, or frequency, domain. Deconvolution of Eq. (1) to determine the true time-of-flight waveform therefore amounts to the calculation of $G(\omega)$ and $H(\omega)$ for a given $g(t)$ and $h(t)$, respectively, followed by the evaluation of $F(\omega)$ according to the equation

$$F(\omega)=\frac{G(\omega)}{H(\omega)}. \qquad (5)$$

Equation (3) may then be used to obtain $f(t)$. Despite the formal simplicity of this approach, considerable difficulties may arise in practice due to noise in the measured signal or the presence of zeros in $H(\omega)$.

It is a common problem that deconvolution will frequently result in the amplification of noise. Noise in the measured signal will produce high-frequency components in $G(\omega)$, causing $F(\omega)$ to diverge at high frequencies. Any such high-frequency components may be removed from the measured signal through the application of low-pass filtering, in which $G(\omega)$ is multiplied by some filtering function $L(\omega)$ with cut-off frequency ω_c. All components beyond the cut-off value will be removed, while those below ω_c may or may not be attenuated, depending upon the functional form of $L(\omega)$. The simplest low-pass filter is the rectangle function,

$$\Pi(\omega)=\begin{cases}1, & |\omega|<\omega_c\\ 0, & |\omega|>\omega_c\end{cases} \qquad (6)$$

which leaves all components of the filtered function unaltered for $|\omega|<\omega_c$. The use of rectangular filters, however, can frequently lead to the manifestation of undesirable features such as *ringing* in the corresponding time domain signal, and should therefore be applied with some caution. In this communication, experimentally measured time-of-flight signals were low pass filtered, when necessary, using a filter consisting of a rectangle function multiplied by a single cosine lobe,

$$L(\omega)=\Pi(\omega)\cos\left(\frac{\pi\omega}{\omega_c}\right), \qquad (7)$$

to provide a gradually increasing attenuation of $G(\omega)$ up to the chosen cut-off frequency. It was found that, with careful choice of ω_c, this filter was generally quite adequate for the removal of high-frequency noise components from measured time-of-flight waveforms, although in many applications involving more complicated signals, a considerably more sophisticated filtering function would probably be required.

Filtering of the measured time-of-flight signal may not always be required, and it is advisable to examine the Fourier transform of the measured signal to determine exactly what frequency components are present. Ideally the measured signal should be sufficiently smooth to avoid the need for any filtering, but obtaining a suitably smooth signal may often require a considerable amount of signal averaging, particularly if the signal is small, since to improve the signal-to-noise ratio by a factor of k the number of averages must be increased by k^2. If filtering is considered necessary, the choice of a suitable ω_c is to some extent a matter of trial and error. If the cut-off frequency is too low, information about $f(t)$ may be lost, while if it is too high no improvement in the quality of $F(\omega)$, and hence the deconvolved signal, may be gained. The transform of a measured signal may be compared with that of a perfectly smooth fitted curve, evaluated at *identical* time intervals, to estimate a reasonable lower limit for ω_c applicable to a series of experiments recorded with the same sampling frequency.

In order to deconvolve the experimental time-of-flight signal and obtain $f(t)$, it is necessary to know the form of the system response function, $h(t)$. The system response function will contain contributions from a large number of sources, many of which may be unknown. It is therefore impossible to predict the shape of this function with any real degree of accuracy. Instead, a reliable estimate, $\hat{h}(t)$, may be obtained by deconvolving an accurately measured, or theoretical, time-of-flight distribution from a convoluted distribution. This estimate of the system response function may then be applied to the deconvolution of other convoluted distributions measured in the *same* apparatus under *similar* experimental conditions. It is important to emphasize that a response function estimated in this manner will contain features peculiar to the apparatus in which the convoluted distribution was measured and may therefore not be applicable to results obtained using another apparatus. Further, the estimated response function will also depend to some extent upon the experimental conditions employed for a particular measurement, and care should be taken to ensure that pressures, temperatures, and detector settings are roughly the same for all measurements to which the estimated response function is to be applied.

In some cases it may be possible to make direct use of Eqs. (2), (3), and (5) to determine $f(t)$ using the estimated response function. Frequently, however, the Fourier transform of the response function will contain one or more points which are exactly zero, causing $F(\omega)$ to be undefined at those points. In such situations an acceptable deconvolution can generally be obtained through the application of Wiener filtering,[7] in which Eq. (5) is rewritten as

$$F(\omega)\approx G(\omega)\hat{W}(\omega), \tag{8}$$

where

$$\hat{W}(\omega)=\frac{\hat{H}^*(\omega)}{|\hat{H}(\omega)|^2+\phi}. \tag{9}$$

In this expression $\hat{H}^*(\omega)$ and $|\hat{H}(\omega)|$ are the complex conjugate and modulus of $\hat{H}(\omega)$, respectively, and ϕ is an adjustable parameter roughly equal to the noise-to-signal ratio associated with $g(t)$ such that

$$\phi\approx\frac{\Sigma c^2}{\Sigma f^2}, \tag{10}$$

for a signal with noise component $c(t)$. By improving the signal-to-noise ratio the ϕ term in the Wiener filter can be made very small resulting in a more highly resolved deconvolution. Unfortunately it is not always possible to make use of Eq. (10) and, as with the choice of low-pass filter cut-off frequency, the best choice of ϕ is to some extent a matter of trial and error. The optimum value of ϕ represents something of a compromise, as a value which is too small will cause $\hat{W}(\omega)$ to diverge for very small values of $|\hat{H}(\omega)|$, while a value that is too large will dominate $\hat{W}(\omega)$, resulting in a poor deconvolution. When it is difficult to estimate ϕ using Eq. (10), a simple and generally successful approach is to take ϕ as some small fraction ($\sim 10^{-6}$) of the maximum signal amplitude.

III. EXPERIMENTAL ARRANGEMENT

The experimental arrangement used to collect unchopped pulsed nozzle time-of-flight waveforms is illustrated schematically in Fig. 1. A commercially available pulsed value nozzle (General Valve Corporation, model 9-181) was employed for these measurements. The valve was modified to have a nominal nozzle diameter of 70 μm. The central core of the pulsed supersonic expansion was sampled by a 1-mm-diam skimmer (Beam Dynamics) positioned $\sim$15 mm downstream from the nozzle exit. The skimmed supersonic beam was then allowed to pass through a differentially pumped flight tube before entering the ion source of a Vacuum Generators SXP300 quadrupole mass filter. The output current of the channeltron electron multiplier generated by the impinging ion beam was converted into a voltage waveform and amplified using a custom built circuit having a gain of 5 and a flat frequency response across a bandwidth of 1 MHz. Amplified waveforms were monitored on a 20 MHz oscilloscope and sampled using a Thurlby digital storage adaptor. Digitized waveforms were stored on the hard disk of a personal computer. The frequency and duration of beam pulses was controlled by the beam source driver unit, which also provided the necessary trigger pulses for the digital storage adaptor and the oscilloscope. During operation of the pulsed nozzle, background pressures of 10^{-5} and 10^{-8} Torr were maintained in the expansion chamber and the flight tube, respectively.

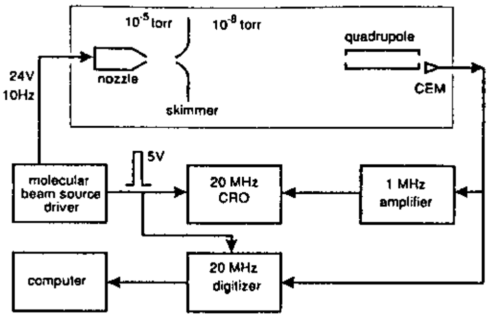

FIG. 1. Experimental arrangement employed for the collection of unchopped time-of-flight waveforms.

IV. RESULTS AND DISCUSSION

A number of special considerations apply to the measurement of time-of-flight waveforms in unchopped pulsed molecular beams. In particular, it is important to be aware of the time-dependent nature of the nozzle conductance, which implies that the speed distribution of an element of gas within a pulse is a function of the time at which that element passed through the nozzle. The width of the speed distribution will be relatively constant during the time that the pulsed nozzle is fully open. During the opening and closing of the nozzle, however, the width of the speed distribution will generally be somewhat greater, and time dependent. Because of this intrinsic time dependence, time-of-flight analysis of unchopped pulsed molecular beams is considerably more difficult than the analysis of well chopped beams, in which the speed distribution is separable from the beam modulating function.

It is also important to be aware of a number of points concerning the use of fast Fourier transform algorithms to convolve and deconvolve data. The fast Fourier transform algorithm used to obtain the results presented in this communication was that of Cooley and Tukey.[8] This algorithm may be used to perform discrete Fourier transforms on complex one-, two-, and three-dimensional data, requiring the number of points in each dimension to be a power of 2. It is a common feature of most fast Fourier transform algorithms that the number of data elements be a power of 2 for reasons of computational efficiency,[7] although there are algorithms available that place no such restriction upon the number of elements.[10] The output of the Thurlby digital storage adaptor used to collect the unchopped time-of-flight waveforms presented in this communication was 1024 regularly spaced samples, allowing us to make direct use of the Cooley–Tukey algorithm. In situations where the number of elements is not a power of 2, the measured data may be packed with an appropriate number of leading and trailing zeros to increase the number of samples to a suitable power of 2. Zero packing of the data in this manner results in an interpolation effect in the Fourier domain[7] which may often improve the resolution of spectral features. Indeed, in some instances, it may prove advantageous to perform zero packing on data sets already consisting of 2^N points for this very reason. It should be noted, however, that in some instances zero packing will be detrimental and therefore should not be applied in an indiscriminate manner.[7] No packing was performed on any of the data presented here.

The fast Fourier transform algorithm provides a discrete approximation of Eqs. (2) and (3), and assumes that the input is periodic with period equal to the number of data elements. The integration limits of Eqs. (2) and (3) extend from $-\infty$ to $+\infty$, while the fast Fourier transform is performed on waveforms which are discretely sampled within some window of finite size. If the sampled data do not adequately represent at least one entire period of the waveform, then spectral features pertaining to the shape of the window will be observed in the spectrum produced by the fast Fourier transform. This is of little consequence when performing simple deconvolutions such as those described in this communication, but is of considerable importance to experimental techniques, such as Fourier transform infrared spectroscopy, where detailed spectral analysis is required.

Unchopped pulsed nozzle time-of-flight waveforms were recorded for argon, krypton, CH_3Cl, and $CHCl_3$ using the experimental arrangement described in the previous section. All data were recorded for a source pressure of 1 atm at a temperature of 300 K. The pulsed nozzle was operated at a frequency of 10 Hz, with an estimated open time of not more than 2 ms. The time base of the Thurlby digital storage adaptor was set at 50 ms, corresponding to a sampling frequency of 20 kHz. Waveform averaging was performed to improve the signal-to-noise ratio of the recorded data, with 64 averages generally being sufficient to reduce the amplitude of any random noise superimposed on the observed signal to an acceptable level. Due to the high-frequency response of the amplifier and the digital storage adaptor employed for these measurements, it is unlikely that any distortion of the recorded signals was caused by the signal amplification and collection circuitry.

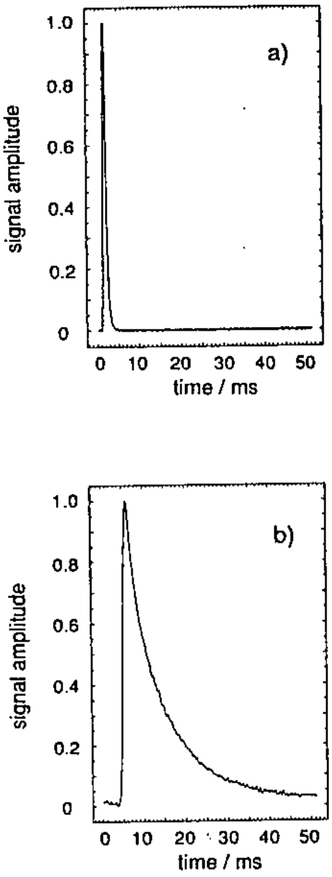

FIG. 2. Time-of-flight arrival time distributions for argon measured (a) with and (b) without a rotating chopper.

An overall response function for the system was estimated by deconvolving an accurate argon time-of-flight waveform determined in a previous study under identical source conditions,[11] from the corresponding argon distribution measured in the present study. As will be discussed later, a theoretical speed distribution could have been used in place of the accurately measured argon time-of-flight waveform to estimate the response function, but it was felt that the use of experimental data would provide a more severe test of the proposed deconvolution method. The chopped and unchopped argon waveforms are illustrated in Figs. 2(a) and 2(b), respectively. The width of the unchopped waveform is considerably greater than that of the chopped waveform, and the rise time of the unchopped signal, from the base of the leading edge to the most probable arrival time, is approximately twice that of the accurately measured curve. The greater width of the unchopped signal is a direct result of the long duration of the beam pulse, while the difference in rise times may be attributed to the finite time required for the pulsed nozzle to become fully open. The 2 ms duration of the beam pulse produced by the pulse nozzle was ~ 55 times longer than that of the chopped beam. It can also be seen from Fig. 2 that the most probable arrival time for the unchopped signal is some 4 ms greater than that of the chopped distribution. Apart from the time required for the pulsed nozzle to become fully open, there were a number of other factors responsible for this difference. In particular, the length of the flight path for the unchopped beam was ~ 1.2 m, while that of the chopped beam was only 0.89 m. The beam source driver unit used to control the pulsed nozzle and trigger the digital storage adaptor was the other major contributing factor to the observed difference in most probable arrival times, due to a fixed delay of 2 ms between the 5 V trigger pulse and the 24 V pulse supplied to the electromagnetic valve of the pulsed nozzle.

Despite the high signal-to-noise ratios observed for the chopped and unchopped waveforms shown in Fig. 2, both sets of data were low pass filtered prior to calculating the system response function to remove any frequency components above 5 kHz. Examination of the Fourier transforms of both the chopped and unchopped waveforms indicated the presence of noise components down to a frequency of ~ 1 kHz. It was found, however, that components below about 2.5 kHz could not be removed using the low-pass filter described by Eq. (7) without introducing considerable ringing into the corresponding time domain signal. This effect is clearly illustrated in Figs. 3(a) and 3(b), which show the chopped argon signal after the application of low-pass filtering according to Eq. (7), with cut-off frequencies of 500 Hz and 1 kHz, respectively. The period of the ringing is equal to the reciprocal of the filter cut-off frequency, while the amplitude of the introduced oscillations increases with decreasing cut-off frequency. This ringing is due to both the shape and cut-off frequency of the filtering function. It is important to realize that the act of filtering in the frequency domain corresponds to performing a convolution in the time domain. If the low-pass filter cut-off frequency is too low or the attenuation of frequency components up to the cut-off value is too rapid, then features of the filtering function will contribute significantly to the shape of the filtered signal in the time domain. In general, any abrupt attenuation performed in the frequency domain will produce ringing in the time domain. A raised cosine filter of the form

$$L(\omega)=\frac{\Pi(\omega)}{2}\left[1+\cos\left(\frac{2\pi\omega}{\omega_c}\right)\right] \tag{11}$$

may be used instead of the filter described by Eq. (7) to provide a considerably more gradual attenuation of frequency components up to the desired cut-off value. Results obtained using Eq. (7) with a cut-off frequency of 5 kHz were more than satisfactory, however, and the use of an alternative filter, such as that described by Eq. (11) was not considered necessary.

The deconvolution of the low-pass filtered chopped argon time-of-flight waveform from the filtered unchopped waveform to obtain the system response function was performed using a Wiener filter with an estimated noise-to-signal ratio of 3×10^{-4}. The spectrum of the resulting response function is illustrated in Fig. 4. It was observed that the value of ϕ, in this instance, was not particularly critical, with values ranging from 1×10^{-3} to 1×10^{-6} having an indiscernible effect of the shape of the estimated response function. The symmetry of Fig. 4 is due to the fact that we are working with purely real data. The Fourier transform of a real function is Hermitian,[7] and the real component of a Hermitian function is even. The sharp spike in the spectrum at 0 kHz was caused by the presence of a significant dc offset on the measured unchopped waveform; the Fourier transform of a constant function being the impulse function, $\delta(\omega)$. This offset is not reflected in Fig. 2(b) or any other plots of unchopped time-of-flight waveforms presented in this communication, as the y scales of these graphs have been adjusted to range from 0 to 1. The frequency components of the response function between $1<|\omega|<5$ kHz are due to noise which was not successfully

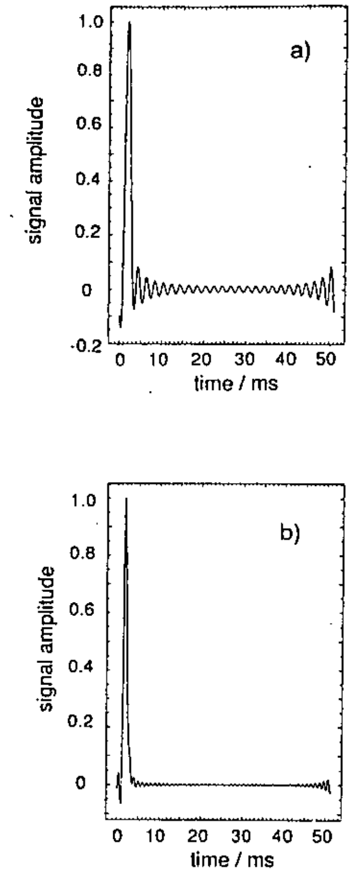

FIG. 3. Effect of badly chosen low-pass filter cut-off frequency: (a) $\omega_c=500$ Hz, (b) $\omega_c=1$ kHz.

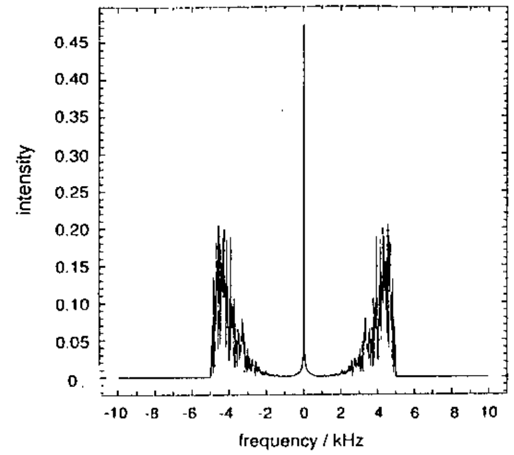

FIG. 4. Frequency domain spectrum of the estimated system response function.

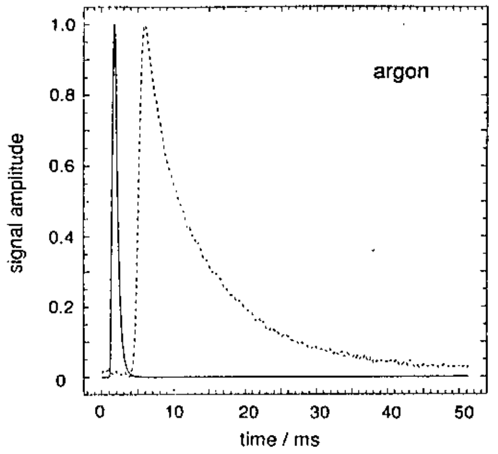

FIG. 5. Unchopped argon time-of-flight waveforms before (dashed curve) and after (continuous curve) deconvolution.

filtered from the chopped and unchopped waveforms. As can be seen, the noise level is observed to increase with increasing $|\omega|$ up to about 4.5 kHz, after which it drops rapidly, reaching zero at the low-pass filter cut-off frequency of 5 kHz. If no low-pass filtering had been performed on the data, the level of this noise would have continued to increase with $|\omega|$, resulting in a response function which could not be applied to the deconvolution of unchopped signals without introducing considerable noise, or amplifying existing noise. The observation that the noise level increases with increasing frequency suggests that high-frequency noise components were less effectively attenuated by the signal averaging process, and may be due to the existence of a timing instability between the internal clock of the digital storage adaptor and the internal clock of the beam source driver used to trigger the digital storage adaptor. By operating the system at higher frequencies, the effect of any such instability may be reduced, resulting in a more uniform attenuation of the noise components by the signal averaging process. The maximum operating frequency of the system is, however, restricted by the period of the waveform being measured. From Fig. 2(b), it can be seen that the period of the unchopped argon waveform is at least 50 ms, indicating that the system cannot be operated at above 20 Hz without significantly undersampling the waveform. A more precise value for the maximum operating frequency is given by the bandwidth of the system. The bandwidth may be estimated from the power spectrum,

$$\hat{P}(\omega)=\hat{H}(\omega)\cdot\hat{H}^*(\omega), \tag{12}$$

of the response function, being roughly equal to the full width at half maximum power. The power spectrum of Fig. 4 yielded a bandwidth of ~18.5 Hz.

The estimated response function was then used to deconvolve the unchopped argon signal. A comparison between the original and deconvolved unchopped signals is shown in Fig. 5. The deconvolved signal contains little or no noise, and appears identical to the chopped time-of-flight waveform in terms of rise time, width, and most probable arrival time. Deconvolution of the unchopped krypton signal also resulted in a considerable narrowing of the time-of-flight waveform and a similar shift of the most probable arrival time. As with argon, very little noise was observed on the deconvolved krypton signal.

The deconvolved argon and krypton signals were converted from the time domain into velocity space and least squares fitted to the speed distribution function

$$f(v)\,dv=Av^2e^{-m(v-u)^2/2k_bT_\parallel}\,dv, \tag{13}$$

where u and $T_\parallel$ represent the mean flow velocity and parallel translational temperature of the supersonic beam, respectively, and A is a normalization constant. Since deconvolution using the estimated response function adjusts the arrival times of the unchopped waveforms to correspond to those expected for chopped beams measured over a shorter flight path in the absence of any delaying effects introduced by the beam source driver and the action of the pulsed nozzle, speeds used in the fitting of the deconvolved waveforms were determined using the flight path of 0.89 m associated with the measurement of the chopped argon signal. The fitted values of u and $T_\parallel$, along with those obtained for accurately measured argon and krypton distributions,[11] are presented in Table I. The values of u

TABLE I. Estimated mean flow velocities and parallel translational temperatures for chopped and deconvoluted unchopped time-of-flight signals.

	Chopped		Deconvoluted unchopped	
System	u (m s^{-1})	$T_\parallel$ (K)	u (m s^{-1})	$T_\parallel$ (K)
Ar	552	1.4	552	1.4
Kr	381	1.1	381	1.2
$CHCl_3$	...	...	397	21.4
CH_3Cl	...	...	543	29.0

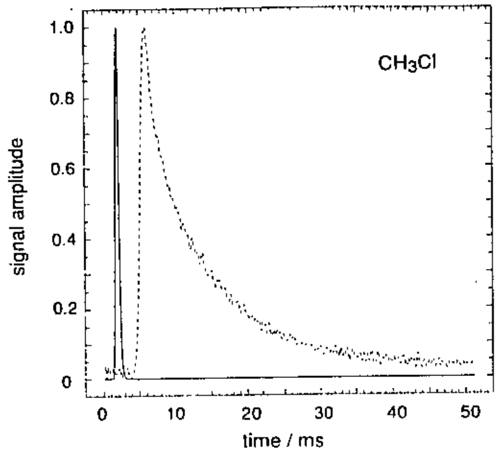

FIG. 6. Unchopped CH_3Cl time-of-flight waveforms before (dashed curve) and after (continuous curve) deconvolution.

and $T_{\parallel}$ calculated for the deconvolved argon signal were found to be virtually identical to those determined for the chopped data. Correspondingly good agreement was observed between the values of u and $T_{\parallel}$ determined for the accurately measured and the deconvolved krypton time-of-flight waveforms, providing us with considerable confidence in the validity of the proposed deconvolution strategy.

The estimated system response function was also used to deconvolve the unchopped time-of-flight waveforms measured for CH_3Cl and $CHCl_3$. The original unchopped and deconvolved signals for these species are illustrated in Figs. 6 and 7. The deconvolved distributions obtained for CH_3Cl and $CHCl_3$ were fitted to the speed distribution described by Eq. (13), and the resulting values of u and $T_{\parallel}$ are given in Table I. While accurate speed distribution measurements have not been performed in our laboratory for either of these species, the values of u and $T_{\parallel}$ obtained from the deconvoluted data appear quite reasonable. The values obtained for $CHCl_3$ are in good agreement with the predictions of thermal conduction model calculations,[11] assuming a rotational-translational coupling parameter of unity.

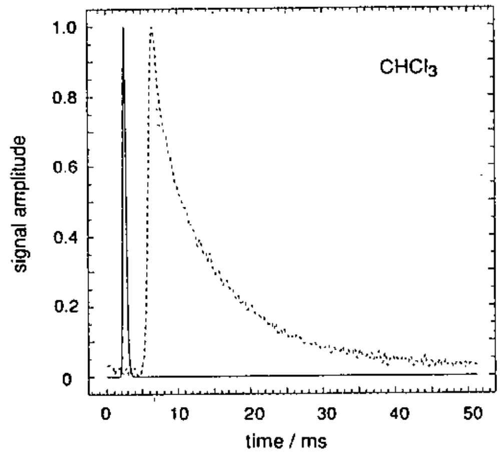

FIG. 7. Unchopped $CHCl_3$ time-of-flight waveforms before (dashed curve) and after (continuous curve) deconvolution.

A response function was also estimated using a theoretical argon time-of-flight waveform calculated according to the time domain equivalent of Eq. (13) using the fitted values of u and $T_{\parallel}$ given in Table I. The response function determined in this manner was found to produce identical deconvolutions to those obtained using the response function determined with the accurate experimental waveform. This result is of considerable importance with regard to the success of the deconvolution strategy, as accurate experimental time-of-flight data may not always be available for the estimation of the system response function, while theoretical terminal speed distributions may be reliably predicted for atomic species such as argon, neon, and krypton for any set of source conditions.[11]

In applying the same response function to the deconvolution of unchopped time-of-flight waveforms measured for a range of species, under identical experimental conditions, we have assumed that the influence of factors such as viscosity and the scattering of beam particles through collisions with background gases have a negligible effect on the shape of the measured time-of-flight waveform. For moderate source pressures ($P_0 \sim 1$ atm), it is reasonable to assume that the times required for the pulsed nozzle to fully open and to fully close are not significantly effected by the viscosity of the gas. Such an assumption may not be strictly valid at high source pressures ($P_0 > 10$ atm), and will depend considerably upon the design, and, in particular, the force constant of the pulsed nozzle. The scattering of beam particles through collisions with background gases will result in a narrowing of the speed distribution due to the preferential elimination of particles with lower momentum from the beam. The background pressures maintained in the apparatus used for the measurements described in this communication were sufficiently low to ensure that background scattering did not significantly affect the shape of the measured time-of-flight waveforms. It should also be recognized that as certain components of the system age, their characteristics and those of the system response function may change. This is particularly true of components such as electromagnetic values. More work is clearly required in order to determine the dependence of the system response function on both the experimental conditions and the nature of the gas.

A quite general method for deconvoluting badly convoluted supersonic molecular beam time-of-flight waveforms using Fourier transform and Wiener filtering techniques has been presented. The method makes no possibly invalid assumptions regarding the exact functional form of convolutions such as the chopper gating function or the response function of any detection electronics, but rather employs an overall system response function, estimated using accurate time-of-flight data, for the deconvolution of convoluted signals. In this communication, the method was successfully applied to the deconvolution of highly distorted argon, krypton, CH_3Cl, and $CHCl_3$ time-of-flight waveforms measured in an unchopped pulsed supersonic molecular beam, giving us considerable confidence in the reliability of the devised approach, although more work is required to determine the dependence of the estimated response function on experimental conditions. The use of direct numerical deconvolution in the manner described is considerably more efficient than the use of moment methods or the fitting of a parametrized convolution to experimental data. The problem of noise superimposed on the measured signal may be negated through the use of Wiener filtering and the application of a simple low-pass filter.

[1] H. S. Carman, Jr., Ph.D. thesis, Rice University, Texas, 1986.

[2] H. E. van den Bergh, M. Faubel, and J. P. Toennies, Faraday Disc. Chem. Soc. 55, 203 (1973).

[3] T. P. Schafer, P. E. Siska, J. M. Parson, F. P. Tully, Y. C. Wong, and Y. T. Lee, J. Chem. Phys. 53, 3385 (1970).

[4] J. A. Alcalay and E. L. Knuth, Rev. Sci. Instrum. 40, 438 (1969).

[5] W. S. Young, Rev. Sci. Instrum. 44, 715 (1973).

[6] D. B. Kay, T. Raymond, and J. Rice, Rev. Sci. Instrum. 57, 2266 (1986).

[7] R. N. Bracewell, *The Fourier Transform and its Applications* (McGraw-Hill, Singapore, 1986).

[8] J. W. Cooley and J. W. Tukey, Math. Comput. 19, 297 (1965).

[9] It should be noted that some authors define the forward transform with the minus sign, and the inverse transform without. This is of little consequence so long as consistency is maintained.

[10] W. H. Press, B. P. Flannery, S. A. Teukolsky, and W. T. Vetterling, *Numerical Recipes: The Art of Scientific Computing* (Cambridge University, Cambridge, 1986).

[11] B. R. Cameron and P. W. Harland, J. Chem. Soc. Faraday Trans. 87, 1069 (1991).

J. CHEM. SOC. FARADAY TRANS., 1994, 90(7), 935–939

Appearance Energies of Small Cluster Ions and their Fragments

Brett R. Cameron, Craig G. Aitken and Peter W. Harland*
Chemistry Department, University of Canterbury, Christchurch, New Zealand

Appearance energies of the cluster ions $(CO_2)_n^+$ $(2 \leqslant n \leqslant 4)$, $(N_2O)_n^+$ $(2 \leqslant n \leqslant 4)$ and $(NH_3)_nNH_4^+$ $(0 \leqslant n \leqslant 7)$, and the cluster ion fragments $(N_2O \cdot O)^+$ and $(N_2O \cdot NO)^+$ have been determined by electron impact ionization of neutral clusters formed in a supersonic molecular beam. Results obtained for $(CO_2)_n^+$ $(2 \leqslant n \leqslant 4)$, $(N_2O)_n^+$ $(2 \leqslant n \leqslant 4)$, $(N_2O \cdot NO)^+$ and $(NH_3)_nNH_4^+$ $(0 \leqslant n \leqslant 2)$ are in general agreement with previously reported appearance energies for these species, while the appearance energies of $(N_2O \cdot O)^+$ and $(NH_3)_nNH_4^+$ $(3 \leqslant n \leqslant 7)$ have been measured for the first time. Binding energies deduced from appearance energy measurements for the $(CO_2)_2^+$, $(CO_2)_3^+$ and $(N_2O)_2^+$ cluster ions are observed to be in accord with results obtained using ion–molecule equilibrium methods. Possible mechanisms for the formation of the cluster fragment ions $(N_2O \cdot O)^+$ and $(N_2O \cdot NO)^+$ are discussed.

Atomic and molecular clusters have been the subject of extensive experimental and theoretical research activity for more than 30 years. The fundamental aim of this research effort has been to gain an improved understanding of the evolution from the atomic or molecular properties of a system to its bulk phase properties with increasing cluster size. For example, atomic and molecular clusters represent small, isolated systems which may be used to test and further our understanding of amorphous solids, catalysis, liquid structure and solvation effects. Despite the intensive research activity involved, however, the characterization of cluster species is still in its early stages. Considerably more particle-specific information will be required in order to develop a complete understanding of the mechanisms of cluster formation and elucidate the factors governing the structure and stability of such species. The use of supersonic molecular beams to generate clusters which are rotationally and vibrationally cooled provides a suitable environment for obtaining this information. The essentially collision-free environment of the molecular beam provides the opportunity to investigate the clusters formed in the supersonic expansion in the absence of any further aggregation and problems relating to particle specificity may be largely resolved through the application of ionization and mass-filtering techniques.

In this paper we report an investigation of the appearance potentials for the cluster ions $(CO_2)_n^+$ $(2 \leqslant n \leqslant 4)$, $(N_2O)_n^+$ $(2 \leqslant n \leqslant 4)$ and $(NH_3)_nNH_4^+$ $(0 \leqslant n \leqslant 7)$, and the cluster ion fragments $(N_2O \cdot O)^+$ and $(N_2O \cdot NO)^+$. The chemistry of CO_2 cluster ions is of considerable interest in ionospheric studies of the predominantly CO_2 atmospheres of Mars and Venus,[1] while ammonia clusters are of interest with regard to the energetics of gas-phase proton solvation. Accurate appearance energies are required for the determination of binding energies and enthalpy changes associated with various steps in cluster formation. A knowledge of cluster-ion appearance energies may also be used to obtain information on rearrangement processes and internal cluster ion–molecule reactions which may follow from electron impact or photoionization of neutral clusters. Appearance energies for $(CO_2)_n^+$ $(2 \leqslant n \leqslant 4)$, $(N_2O)_n^+$ $(2 \leqslant n \leqslant 8)$, $(N_2O \cdot NO)^+$ and $(NH_3)_nNH_4^+$ $(0 \leqslant n \leqslant 2)$ have been previously reported,[2–8] while those determined for $(N_2O \cdot O)^+$ and $(NH_3)_nNH_4^+$ $(3 \leqslant n \leqslant 7)$ represent new results.

Experimental

The gas mixture under study was expanded from a high-pressure stagnation reservoir through a commercial electromagnetic pulsed valve (General Valve Corporation, model 9-181) into the first of two differentially pumped vaccum chambers. The valve was modified by the inclusion of a small stagnation volume between the 0.8 mm orifice in the valve and a 50 μm shaped orifice in the exit plate. This gave higher cluster densities than obtained from a valve fitted with a 50 μm orifice. The central core of the pulsed supersonic expansion was sampled by a 1.0 mm skimmer (Beam Dynamics) located *ca.* 300 nozzle diameters (15 mm) from the nozzle exit. The skimmed supersonic beam was allowed to enter the ion source of a Vacuum Generators SXP300 quadrupole mass filter located 10 cm downstream from the skimmer assembly in the second differentially pumped chamber. The electron energy distribution was estimated to be *ca.* 0.85 eV full width at half maximum (FWHM). Output pulses from the channeltron electron multiplier were passed through a high-*Q* 2 MHz notch filter to eliminate rf pick-up from the quadrupole driver circuitry and amplified with a fast preamplifier followed by an amplifier and pulse amplitude discriminator combination.

The signal-to-noise ratio of the beam signal was optimised using a simple gating arrangement. The TTL output pulses from the pulse-counting preamplifier were split and fed into two and-gates. Using a pulse generator and a pulse delay unit, two 5 V gates of identical width were independently delayed with respect to the nozzle trigger pulse in order to correspond with different regions of the signal pulse envelope. The first window was positioned over the ion arrival time distribution resulting from the pulsed supersonic beam in order to sample signal plus background, while the second was positioned somewhat later in time, sampling only background signal. Output pulses from the two and-gates were counted through a counter-timer. Computer control of electron energy and mass selection was implemented using custom-built 12-bit digital-to-analogue converters incorporated into the mass spectrometer control unit.

The pulsed nozzle was generally operated at a frequency of 10 Hz, with an open time of not more than 2 ms. Background pressures of 10^{-5} and 10^{-8} Torr were maintained in the expansion chamber and the mass spectrometer chamber during normal operation of the nozzle. The temperature of the nozzle was monitored using a thermocouple attached to the body of the valve. The potential difference across the thermocouple was calibrated and amplified using a simple fixed-gain circuit, the output of which was supplied to one of 16 14-bit analogue-to-digital conversion channels monitored. The reservoir pressure was monitored using an MKS Baratron (10000 Torr) connected to an MKS type 286 controller. Experiments were carried out automatically by scanning from low to high and from high to low electron energy for increments of 0.04 or 0.08 eV. Reproducibility from week to week was excellent and the ionization efficiency curves were automatically analysed using a linear least-squares procedure to locate and tabulate the threshold and any breaks in the curves. All of the ionization efficiency curves reported were calibrated against argon and the molecular ion recorded simultaneously.

Results

Neutral CO_2, N_2O and NH_3 clusters were produced by expanding gas mixtures containing 100 Torr of argon and 500 Torr of CO_2, N_2O or NH_3 made up to a total pressure of *ca.* 4000 Torr with helium at a reservoir temperature of 295 K. These mixtures were found to produce supersonic beams of sufficiently high cluster content for reliable determination of appearance energies for the cluster ions $(CO_2)_n^+$ $(2 \leqslant n \leqslant 4)$, $N_2O_n^+$ $(2 \leqslant n \leqslant 4)$ and $(NH_3)_nNH_4^+$ $(0 \leqslant n \leqslant 7)$. For the N_2O mixture it was also possible to determine the appearance potentials for the cluster ion fragments $(N_2O \cdot O)^+$ and $(N_2O \cdot NO)^+$. While monomer and cluster speed distributions were not measured, we would expect the parallel translational temperature of the cluster beams to be close to the value of *ca.* 6 K measured previously for a pure helium beam under the same source conditions.[9] The extent of rotational cooling which occurs during the supersonic expansion of these gas mixtures is unclear and will depend on the efficiency of rotational to translational energy transfer in collisions between the molecules and clusters and the rare-gas atoms. We tentatively suggest that the terminal rotational temperatures of the molecules and clusters will be less than 40 K in all cases. No clusters containing helium or argon atoms were observed for any of the gas mixtures examined.

Ion counts were measured at up to 100 points with a typical counting period of 5 s at each electron energy repeated some 15 to 20 times to obtain an average count with an acceptable standard error. Average ion counts were also recorded at an electron energy of 70 eV at the beginning and end of each run. Depending upon the number of ions examined, a run could take up to 3 or 4 h to complete and it was therefore necessary to consider any potential sources of long-term experimental instability that might adversely affect the accuracy of the measurements. In particular, it is known that the cluster content of supersonic molecular beams is highly sensitive to variations in source pressure and temperature,[10] and these variables were carefully monitored throughout each run. Owing to the small flow of gas through the 50 μm nozzle, the reservoir pressure was observed to drop by not more than 2 or 3% over a 4 h period of continuous operation and no change in nozzle temperature was detected.

The semi-log plot method[11,12] has been used in this study to determine the cluster-ion appearance potentials with an estimated accuracy of ±0.1 eV in all cases. This error limit includes both statistical and systematic errors. Although nominally less accurate than ideal photoionization measurements, reproducibility is excellent and certainly good enough to allow critical comparisons to be made between our results and those of previous experimental and theoretical investigations. The appearance potential of Ar^+ used as the primary electron energy scale calibrant for all of the appearance potential measurements was taken to be 15.76 ± 0.01 eV.[13]

CO_2 Clusters

Illustrative examples of ionization efficiency curves measured for $(CO_2)_2^+$, $(CO_2)_3^+$ and $(CO_2)_4^+$ are shown in Fig. 1, where every second point has been omitted for clarity. Calibration of the electron energy scale was achieved through a concurrent measurement of the ionization energy for Ar^+. The corrected values of the $(CO_2)_2^+$, $(CO_2)_3^+$ and $(CO_2)_4^+$ appearance energies and the calculated binding energies are shown in Table 1 with literature values for comparison.

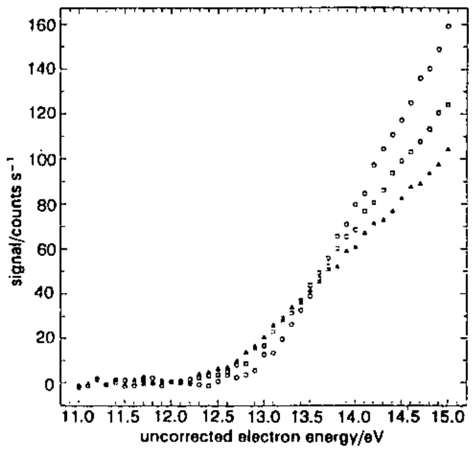

Fig. 1 Measured ionization efficiency curves for (○) $(CO_2)_2^+$, (□) $(CO_2)_3^+$ and (△) $(CO_2)_4^+$. Every second experimental point has been omitted for clarity.

N_2O Clusters

Ionization efficiency curves for $(N_2O)_n^+$ $(2 \leqslant n \leqslant 4)$ and the cluster ion fragments $(N_2O \cdot O)^+$ and $(N_2O \cdot NO)^+$ are illustrated in Fig. 2 and 3. The appearance energies determined for these species are summarized in Table 2. The value of 12.3 eV determined for the appearance energy of $(N_2O)_2^+$ is in

Table 1 Appearance energies (E_{app}) and binding energies (E_b) for $(CO_2)_n^+$ $(2 \leqslant n \leqslant 4)$

		E_b/eV for $(CO_2)_{n-1}^+ \cdot CO_2$	
ion	E_{app}/eV	this work	literature
$(CO_2)_2^+$	13.1 ± 0.1	0.73	0.675[a,b] 0.564[a,c]
$(CO_2)_3^+$	12.8 ± 0.1	0.36	0.32[b]
$(CO_2)_4^+$	12.6 ± 0.1	0.26	0.22[d]

[a] These values have been corrected to 0 K by Linn and Ng[4] and are therefore lower than the values stated by the authors. [b] Ref. 14. [c] Ref. 1. [d] Ref. 15.

Table 2 Appearance energies (E_{app}) and binding energies (E_b) for N_2O clusters

		E_b/eV	
ion	E_{app}/eV	this work	literature
$(N_2O \cdot O)^+$	14.6 ± 0.1		
$(N_2O \cdot NO)^+$	14.3 ± 0.1 17.0 ± 0.2		
$(N_2O)_2^+$	12.3 ± 0.1	0.61	0.56[a] 0.57[b,c]
$(N_2O)_3^+$	12.1 ± 0.1	0.22	
$(N_2O)_4^+$	12.0 ± 0.1	0.12	

[a] Ref. 4. [b] Ref. 18. [c] Corresponds to a temperature of 481 K and may not be directly comparable.

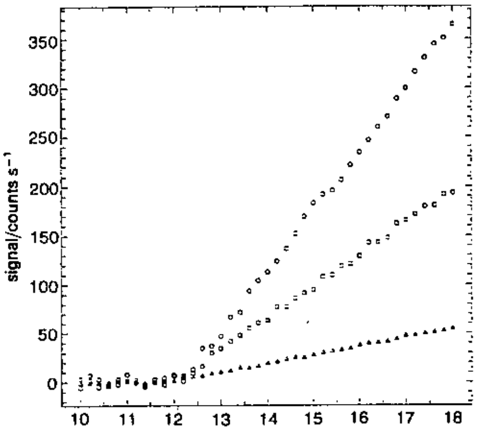

Fig. 2 Measured ionization efficiency curves for (○) $(N_2O)_2^+$, (□) $(N_2O)_3^+$ and (△) $(N_2O)_4^+$. Every second experimental point has been omitted for clarity.

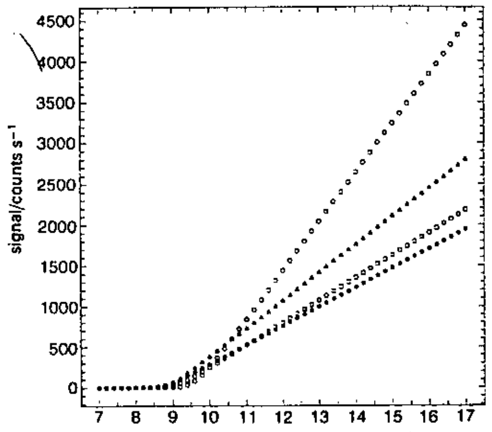

Fig. 4 Measured ionization efficiency curves for (○) NH_4^+, (□) $(NH_3)NH_4^+$, (△) $(NH_3)_2NH_4^+$ and (●) $(NH_3)_3NH_4^+$. Every second experimental point has been omitted for clarity.

excellent agreement with that of 12.35 ± 0.02 eV reported by Linn and Ng[4] and the value of 12.394 ± 0.015 eV reported by Kamke *et al.*[6] It can be seen from Fig. 4 that the shape of the ionization efficiency curve measured for the $(N_2O\cdot NO)^+$ cluster ion fragment is significantly different to the shape of the curves obtained for any of the other ions illustrated in Fig. 1–5. Apart from the ionization threshold at 14.3 eV, there is a sharp change of slope at *ca.* 17.0 eV, suggesting the presence of a second threshold for the formation of this ion. The shape of this curve was found to be totally reproducible. The $(N_2O\cdot NO)^+$ ion was also observed by Linn and Ng,[4] who estimated an appearance energy of 14.01 eV, in reasonable accord with the lowest-energy threshold of 14.3 eV determined in the present study. A second threshold at *ca.* 17.2 eV is also apparent on the $(N_2O\cdot NO)^+$ photoionization efficiency curve recorded by Linn and Ng. Although they attempted no interpretation of this, it lends support to our observation of a reproducible, higher-energy threshold. The appearance energy for the cluster fragmentation product $(N_2O\cdot O)^+$ has not been previously reported. In view of the agreement observed between the appearance energies of $(N_2O)_2^+$ and $(N_2O\cdot NO)^+$ determined in the present study and those obtained by Linn and Ng[4] using photoionization, we might expect the appearance energies of 12.1, 12.0 and 14.6 eV obtained for $(N_2O)_3^+$, $(N_2O)_4^+$ and $(N_2O\cdot O)^+$, respectively, to be equally reliable.

The appearance energies for $(N_2O)_3^+$ and $(N_2O)_4^+$ reported in the photoionization study of Kamke *et al.*[6] are 12.29 ± 0.02 and 12.26 ± 0.04 eV, respectively, or *ca.* 0.2 eV higher than the electron impact threshold reported here and listed in Table 2. Although, in principle, photoionization should yield more accurate thresholds with lower uncertainty, experimental photoionization data do not often measure up to these expectations. The appearance energies

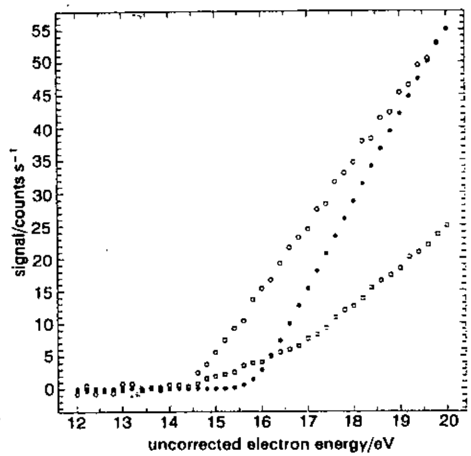

Fig. 3 Measured ionization efficiency curves for (○) $(N_2O\cdot O)^+$ and (□) $(N_2O\cdot NO)^+$, with Ar^+ (●) as reference. Every second experimental point has been omitted for clarity.

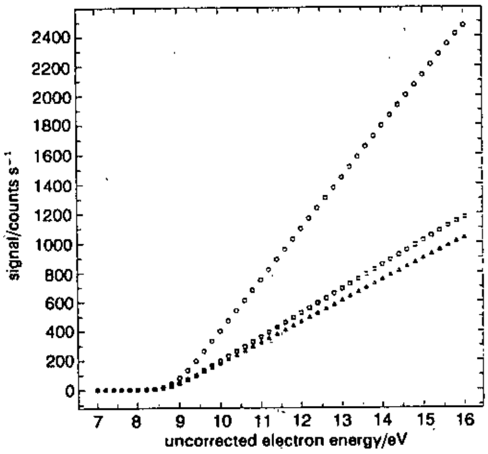

Fig. 5 Measured ionization efficiency curves for (○) $(NH_3)_4NH_4^+$, (□) $(NH_3)_5NH_4^+$ and (△) $(NH_3)_6NH_4^+$. Every second experimental point has been omitted for clarity. The ionization efficiency curve for $(NH_3)_7NH_4^+$ would be superimposed on that for $(NH_3)_6NH_4^+$ and has been omitted from the figure. The higher signal level for $(NH_3)_4NH_4^+$ over its neighbours, $(NH_3)_3NH_4^+$ (Fig. 5) and $(NH_3)_5NH_4^+$, reflects the higher stability of this cluster.

for the $(N_2O)_n^+$ ($1 \leqslant n \leqslant 8$) cluster ions are reported by Kamke *et al.*[6] with experimental uncertainties from ±0.015 eV for $n = 2$ to ±0.04 eV for $n = 8$. However, inspection of the experimental data shown in Fig. 1 of ref. 6 for the $(N_2O)_n^+$ ions shows little correspondence between the reported values and the thresholds anticipated from the data. The threshold regions are smeared, noisy and the shape of the curves varies considerably from $n = 1$ to $n = 8$. The reported thresholds and uncertainties are the result of an empirical multiparameter fitting procedure, which cannot gurantee a unique solution. So, despite photoionization thresholds quoted to two or three decimal places with uncertainties in the meV range, some consideration must be given to the data treatment. Electron impact ionization thresholds do return reliable values within the stated uncertainty, although it must be acknowledged that recoil energy and internal excitation in the ionization process are folded into the absolute values measured by either technique.

Using the appearance energy value of 12.3 eV measured for $(N_2O)_2^+$ with the ionization energy of 12.886 ± 0.002 eV for N_2O[16] and the estimated intermolecular binding energy of 0.02 eV for the neutral dimer,[17] the bond dissociation energy of $(N_2O)_2^+$ has been calculated to be 0.61 eV, in good agreement with the value of 0.56 eV reported by Linn and Ng[4] and the value of 0.57 eV determined by Illies[18] using ion–molecule methods. Note, however, that this latter value relates to a measurement of ΔH° for the association reaction of N_2O and N_2O^+ at 481 K and therefore may not be directly comparable. The $(N_2O)_2^+$ binding energy calculated using the photoionization data reported by Kamke *et al.*[6] would be 0.512 eV, which seems a little low. Assuming the same binding energy of 0.02 eV for $(N_2O)_3$ and $(N_2O)_4$, we calculate bond dissociation energies of 0.22 and 0.12 eV for $(N_2O)_2^+ \cdot N_2O$ and $(N_2O)_3^+ \cdot N_2O$, respectively, compared with values of 0.124 and 0.05 eV calculated using the photoionization thresholds reported by Kamke *et al.*[6]

The appearance energy of 14.6 eV determined for the $(N_2O \cdot O)^+$ cluster ion fragment is observed to be 2.3 eV greater than that of $(N_2O)_2^+$, close to the difference of 2.4 eV between the appearance energy of N_2O^+ from N_2O (12.886 eV) and the appearance energy of O^+ from N_2O (15.29 eV).[16] This observation may be rationalized by writing the structure of $(N_2O \cdot O)^+$ as $O^+ \cdot N_2O$ and to postulate that the formation of this species involves the ionization and fragmentation of one of the N_2O monomer units in $(N_2O)_2$ without any significant perturbation of the accompanying cluster molecule. Note that the same argument would also apply to the species $(CO \cdot CO_2)^+$ and $(NH_2 \cdot NH_3)^+$ observed by Stephan *et al.*[5,7] An alternative mechanism proposed by them for the formation of these cluster fragment ions involved an internal ion–molecule reaction. If the ion within the $(N_2O)_2$ cluster is initially formed in some electronically excited state N_2O^{+*}, then the $(N_2O \cdot O)^+$ ion may be produced by the following sequence of reactions:

$$(N_2O)_2 + e^- \rightarrow N_2O \cdot N_2O^{+*} + 2e^- \rightarrow N_2O_2^+ + N_2 \quad (1)$$

The $N_2O_2^+$ species produced in this manner would be expected to have an appearance energy greater than that of $(N_2O)_2^+$ by at least the additional energy required for the electronic excitation of the parent ion. Irrespective of whichever mechanism applies, we can use the measured appearance potential of 14.6 eV for $(N_2O \cdot O)^+$, the thermochemical threshold of 15.29 eV for the formation of O^+ from N_2O[16] and the binding energy of 0.02 eV for $(N_2O)_2$[17] to estimate a lower bound of 0.71 eV for the bond dissociation energy of $(N_2O \cdot O)^+$.

The lowest energy threshold observed for the formation of $(N_2O \cdot NO)^+$ corresponds to an appearance energy of 14.3 eV, while the break at higher electron energy equates to an ionization threshold of *ca.* 17.0 eV. Note that the differences of 2.0 and 4.7 eV observed between these thresholds and the appearance energy of 12.3 eV obtained for $(N_2O)_2^+$ correspond very well to the differences of 2.124 and 4.854 eV between the ionization energy of 12.886 eV for N_2O^+ and the thermochemical thresholds of 14.19 and 17.76 eV for the fragmentation processes

$$N_2O + e^- \rightarrow NO^+(X\,^1\Sigma^+) + N(^4S) + 2e^- \quad (2)$$

and

$$N_2O + e^- \rightarrow NO^+(X\,^1\Sigma^+) + N(^2P) + 2e^- \quad (3)$$

respectively.[16] Applying the same argument used for $(N_2O \cdot O)^+$, it seems reasonable to write the structure of $(N_2O \cdot NO)^+$ as $NO^+ \cdot N_2O$ and to describe the formation of this species as involving the ionization and fragmentation of one of the N_2O molecules in the neutral dimer without any significant perturbation of the other. Realistically, the molecules making up a cluster must exert an influence on one another. This might well be expected to include a lowering of the ionization energy with increase in cluster size, as observed in this and other studies. This adds support to the mechanism of cluster ionization described above. Linn and Ng[4] observed that the photoionization efficiency curve they measured for $(N_2O \cdot NO)^+$ had essentially the same profile as that of NO^+ produced from the fragmentation of N_2O^+. Such an observation indicates that the fragmentations of N_2O^+ and $(N_2O)_2^+$ to form NO^+ and $(N_2O \cdot NO)^+$, respectively, follow similar reaction pathways, further supporting the notion that ionization of the neutral N_2O dimer occurs on a single monomer unit to form $N_2O^+ \cdot N_2O$. The neutral monomer in $N_2O^+ \cdot N_2O$ then acts simply as a spectator in the fragmentation process leading to the formation of $(N_2O \cdot NO)^+$. Note that N_2O^+ may undergo another fragmentation process leading to the formation of $NO^+(X\,^1\Sigma^+)$ and $N(^2D)$. The thermochemical threshold for the formation of NO^+ by this process would be 16.57 eV,[16] suggesting that another break in the ionization efficiency curve of $(N_2O \cdot NO)^+$ may be expected between 14.3 and 17.0 eV. We were unable to detect this break, although there was some evidence for such a feature on the photoionization efficiency curve measured by Linn and Ng.[4] Our failure to observe this feature may be attributed to the low-energy resolution of the instrument employed for the present study. The fragmentation of $N_2O^+ \cdot N_2O$ may then be viewed as a set of energy-dependent unimolecular cluster ion dissociation reactions as shown in eqn. (4), analogous to eqn. (2) and (3).

$$\begin{array}{lll} & \text{—14.6 eV} \rightarrow & (N_2O)O^+ + N_2 + 2e^- \\ (N_2O)N_2O + e^- & \text{—14.3 eV} \rightarrow & (N_2O)NO^+ + N(^4S) + 2e^- \\ & \text{—16.6 eV} \rightarrow & (N_2O)NO^+ + N(^2D) + 2e^- \\ & \text{—17.0 eV} \rightarrow & (N_2O)NO^+ + N(^2P) + 2e^- \end{array} \quad (4)$$

NH_3 Clusters

Ionization efficiency curves for the ammonia clusters are shown in Fig. 4 and 5 and appearance energies are listed in Table 3 for $(NH_3)_nNH_4^+$ ($0 \leqslant n \leqslant 7$). Discrepancies between binding energies deduced from ion–molecule equilibria and from cluster-ion appearance energies suggest that electron impact and photoionization fail to yield the true adiabatic ionization energies of these weakly bound species.[2,5] Dissociation energies of the $(NH_3)_nNH_4^+$ ions deduced from appearance energy measurements were found to be in poor

Table 3 Appearance energies (E_{app}) for $(NH_3)_nNH_4^+$ ($0 \leqslant n \leqslant 7$)

ion	E_{app}/eV	
	electron impact[a]	photoionization[b]
NH_4^+	9.7	9.59 ± 0.02
$(NH_3)NH_4^+$	9.2	9.15 ± 0.04
$(NH_3)_2NH_4^+$	9.0	9.03 ± 0.04
$(NH_3)_3NH_4^+$	8.9	—
$(NH_3)_4NH_4^+$	8.8_5	—
$(NH_3)_5NH_4^+$	8.8_1	—
$(NH_3)_6NH_4^+$	8.7_8	—
$(NH_3)_7NH_4^+$	8.7_2	—

[a] Reproducibility ±0.1 eV or better (this work). [b] Ref. 8.

accord with those obtained by ion–molecule methods, indicative of this failure of electron impact ionization measurements to sample the true adiabatic ionization thresholds for the ammonia cluster ions.

Conclusion

Klots and Compton[2] suggested that the equilibrium geometry of van der Waals cluster ions produced by electron impact or photoionization may be considerably different from the equilibrium geometry of the neutral precursor. In such situations the Franck–Condon factors near the true adiabatic ionization threshold may be so small that the observation of the adiabatic threshold is precluded. It has been suggested that small Franck–Condon factors near threshold are not a particularly serious problem in the ionization of rare-gas cluster species owing to the close spacing of many Rydberg levels throughout the region between the adiabatic and the direct ionization thresholds which may decay *via* autoionization.[8,19] Rydberg states with lifetimes greater than 50 μs and principal quantum numbers $55 \leqslant n \leqslant 75$ have been reported for CO_2 clusters by Campbell and Tittes.[20] Such long-lived high Rydberg states can be observed only if there are some states for which non-radiative mechanisms of decay, such as autoionization and electronic predissociation, are significantly slower than radiative decay. It has been shown[21] that predissociation rates of molecular Rydberg states are considerably greater for states of low principal quantum number and while autoionization is the most probable non-radiative decay mechanism, the apparent absence of states with principal quantum number less than 55 observed in the experiment performed by Campbell and Tittes[20] indicates that predissociation may also be an important mechanism. It is therefore possible that lower Rydberg states of molecular clusters may, in fact, predissociate instead of decaying to levels of lower energy *via* the autoionization process. For this reason, unfavourable Franck–Condon factors may not be completely compensated for in the ionization of molecular cluster species, making the observation of their true adiabatic ionization potentials unlikely. Some knowledge of Franck–Condon factors for van der Waals clusters may therefore be required for the reliable interpretation of cluster-ion appearance potentials. The most probable mechanism for the formation of the cluster fragment ions $(N_2O \cdot O)^+$ and $(N_2O \cdot NO)^+$ would appear to involve the ionization and fragmentation of one of the N_2O molecules in the neutral N_2O dimer without any significant perturbation of the second molecule, although alternative mechanisms cannot be discounted. Despite these recognised deficiencies, electron impact ionization efficiency curves can provide significant mechanistic information, especially where breaks are found and where comparisons with monomer measurements and data collected using other techniques are available.

References

1 M. Mautner and F. H. Field, *J. Chem. Phys.*, 1977, **66**, 4527.
2 C. E. Klots and R. N. Compton, *J. Chem. Phys.*, 1978, **69**, 1636.
3 G. G. Jones and J. W. Taylor, *J. Chem. Phys.*, 1978, **68**, 1768.
4 S. H. Linn and C. Y. Ng, *J. Chem. Phys.*, 1981, **75**, 4921.
5 K. Stephan, J. H. Futrell, K. I. Peterson, A. W. Castleman Jr. and T. D. Märk, *J. Chem. Phys.*, 1982, **77**, 2408.
6 B. Kamke, W. Kamke, R. Herrmann and I. V. Hertel, *Z. Phys. D*, 1989, **11**, 153.
7 K. Stephan, J. H. Futrell, K. I. Peterson, A. W. Castleman Jr., H. E. Wagner, N. Djuric and T. D. Märk, *J. Mass Spectrom.*, 1982, **44**, 167.
8 S. T. Ceyer, P. W. Tiedemann, B. H. Mahan and Y. T. Lee, *J. Chem. Phys.*, 1979, **70**, 14.
9 B. R. Cameron and P. W. Harland, *J. Chem. Soc., Faraday Trans.*, 1991, **87**, 1069.
10 *Atomic and Molecular Beam Methods*, ed. G. Scoles, Oxford University Press, London, 1988.
11 C. A. McDowell, *The Ionization and Dissociation of Molecules*, McGraw-Hill, New York, 1963.
12 R. W. Kiser, *Introduction to Mass Spectrometry and its Applications*, Prentice-Hall, Englewood Cliffs, NY, 1965.
13 V. H. Dibeler and R. M. Reese, *Adv. Mass Spectrom.*, 1966, **3**, 471.
14 R. G. Keese and A. W. Castleman, *J. Phys. Chem. Ref. Data*, 1986, **15**, 1011.
15 K. Hiraoka, G. Nakajima and S. Shoda, *Chem. Phys. Lett.*, 1988, **146**, 535.
16 H. M. Rosenstock, K. Draxl, B. W. Steiner and J. T. Herron, *J. Phys. Chem. Ref. Data 6, Suppl. 1*, 1977, 70.
17 H. L. Johnston and K. E. McCloskey, *J. Phys. Chem.*, 1940, **44**, 1038.
18 A. J. Illies, *J. Phys. Chem.*, 1988, **92**, 2889.
19 C. Y. Ng, D. J. Trevor, P. W. Tiedemann, S. T. Ceyer, P. L. Kronebusch, B. H. Mahan and Y. T. Lee, *J. Chem. Phys.*, 1977, **62**, 4235.
20 E. E. B. Campbell and A. Tittes, *Chem. Phys. Lett.*, 1990, **165**, 289.
21 S. M. Tarr, J. A. Schiavone and R. S. Freund, *J. Chem. Phys.*, 1981, **74**, 2869.

Paper 3/05770D; *Received 24th September*, 1993

J. Chem. Phys., 1994, **101**: 11074-6.

Effect of molecular orientation on electron impact ionization and fragmentation

Craig G. Aitken, David A. Blunt, and Peter W. Harland

Chemistry Department, University of Canterbury, Christchurch, New Zealand

Abstract

Relative ionization cross-sections have been determined for the production of the molecular ion CH_3Cl^+ and the fragmentation product CH_3^+ from the 200 eV electron impact ionization of spatially oriented CH_3Cl molecules in a cross beam experiment. The ionization cross-section for CH_3Cl^+ formation is higher at the positive end, or CH_3-end, of the molecule while the cross-section for formation of the CH_3^+ fragmentation product is independent of spatial orientation, within experimental uncertainty.

The effect of molecular orientation on chemical reactivity[1], chemiluminescence[2], photoionization[3], Rydberg molecule formation[4] and, more recently, electron scattering[5] have been studied. The orientation asymmetry in most systems investigated has been significant, despite the use of oriented beams characterised by a distribution of spatial orientations[1]. In this communication we report preliminary results of an investigation into the effect of molecular orientation on electron impact ionization and fragmentation with results for the prolate symmetric top molecule CH_3Cl. We can report a significant asymmetry in the total ionization cross-section for CH_3Cl. Using a mass insensitive detector the cross-section for ionization at the CH_3-end of the molecule is 2.3 times higher than for ionization at the Cl-end. This is close to the ratio of 2.6 found for the formation of the molecular ion, CH_3Cl^+ using a mass filter detector. A ratio close to 1.0 is measured for the CH_3^+ fragment, i.e., the cross-section for the formation of the CH_3^+ fragmentation product is independent of electron - molecule orientation along the molecular axis, within experimental uncertainty.

Electron impact ionization was first used in mass spectrometry by Dempster[6] in 1918 in an attempt to generate reproducible mass spectra for use in analytical chemistry, an application of mass spectrometry suggested by J.J. Thomson[7] in 1913. Despite 80 years of experience in electron impact ionization, absolute ionization cross-sections cannot be routinely measured, fragmentation patterns are not always predictable using chemical intuition, and theoretical models of electron impact ionization fail to deliver either acceptable cross-sections or fragmentation patterns (mass spectra). The study of electron impact ionization of spatially oriented molecules has been initiated in order to gain a deeper insight into the electron impact ionization process and to provide data to test theoretical models.

Experiments are carried out using crossed beams of spatially oriented CH_3Cl and near-monochromatic electrons, see Figure 1. The molecular beam is produced by

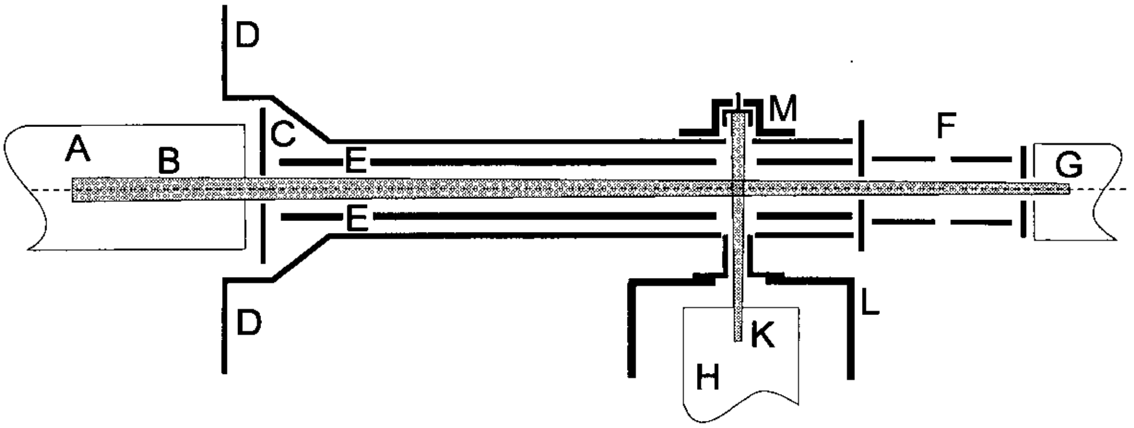

Figure 1 Diagram of the beam crossing region: A hexapole; B molecular beam; C hexapole exit aperture; D shielding plates; E homogeneous field plates; F ion guiding lens; G quadrupole mass filter; H electron gun; K electron beam; L shielded electron gun chamber; M shielded electron collector. Mesh shields at ground potential below the field plates and a copper shield at ground potential held at liquid nitrogen temperature above the field plates are not shown.

the expansion of CH_3Cl at 288 K from a stagnation pressure of 1,200 torr through a 70 μm nozzle in a pulsed General Valve Series 9 electromagnetic valve with an open time of 1.2 ms at a 10Hz repetition rate. The supersonic beam enters a buffer chamber through a 1.0 mm entrance skimmer and exits through a 3.6 mm skimmer that serves as the entrance orifice to a 0.833 m long hexapole filter with an inscribed radius of 5.5 mm (a second hexapole with an inscribed radius of 7.5 mm was used in some experiments). The inhomogeneous hexapole electric field (typically 10^6 V m^{-1}) transmits a focused beam of upper Stark-state selected CH_3Cl molecules through a 8.0 mm diameter exit aperture into a weak homogeneous orienting electric field (2,000 V m^{-1}) maintained between parallel field plates 200 mm long and 10 mm apart. The molecular beam is detected on axis by a Vacuum Generators SXP300 quadrupole mass filter which is also used as a mass sensitive ion detector after replacement of the ion source and lens with an Einzel lens assembly. An Amptektron Model 501-L low energy ion detector, which can be rotated about the electron beam - molecular beam intersection, is used for measuring beam profiles, alignment of the electron beam with respect to the molecular beam and as a mass insensitive detector for low energy ion counting. Deconvolution of the arrival time distribution gave a mean flow velocity of 543 ms^{-1} and a translational temperature of 29 K[8]. The on-axis quadrupole produced a mass spectrum dominated by the molecular ion, CH_3Cl^+ (100), with CH_3^+ (30) as the only other significant ion signal.

The electron beam is generated by an electron gun housed in a stainless steel chamber protruding into the scattering chamber. The gun has been designed to deliver pencil beams of 2-3 mm diameter over the energy range 20 - 300 eV (λ = 2.7 to 0.7 Å) with an electron energy distribution of <0.2eV FWHM. The electron beam is directed through a cylindrical snout which penetrates from the end of the chamber to the nearside homogeneous field plate. It passes through 10.0 mm diameter apertures in the field plates and enters a shielded Faraday cup coated with colloidal graphite (aquadag). The snout, homogeneous field plates, top and bottom shielding plates and shielding grids are all coated with colloidal graphite. In these experiments the electron beam was operated in continuous mode with a beam current of <300 nA at 200eV (0.87 Å) to minimise space charge effects. The field plates were energised at ±20V/gnd, and gnd/±20V combinations for field reversal and hence orientation reversal.

Collisions involving neutral reactants are unaffected by the presence of a uniform electric field in the crossing region. This is not the case where charged particles are involved. Ions formed between the homogeneous field plates would be accelerated towards the field plate of opposite polarity and be discharged. The K^+ ion products produced in collisions between fast K atoms and oriented symmetric top molecules[1(d)] were collected using channeltrons protruding through the field plates. This approach cannot be used for electron (or ion) impact where the proximity of the channeltron cones to the beam crossing would shatter the electron (ion) beam integrity and the geometry of the beam crossing volume. In these experiments one of the homogeneous field plates is maintained at ground potential and the second is set at ±20 V. Molecules are oriented such that the negative end of the dipole points towards the ground field plate when the configuration is gnd/+20 V and towards the energised field plate when the configuration is set to gnd/-20 V. In an experiment, the energised field plate is dropped to <0.1 V from ground (polarity preserved) in <100 ns as the leading edge of the gas pulse reaches the electron beam. Typically, the segment of oriented beam between the homogeneous field plates at the time the field is collapsed corresponds to 300 μs in flight time. Ions produced by the electron impact ionization of this 300 μs segment of spatially oriented beam are gated at a detector located 25 mm downstream on the molecular beam axis. A second gate of equal width intercepts ions produced from the electron impact ionization of a second 300 μs slice from the trailing segment of the gas pulse which did not sample the orienting field. This is repeated with the hexapole high voltage switched off and the rods set to ground potential, i.e., in the absence of the inhomogeneous field in the hexapole. This mode of operation assumes the integrity of the spatial orientation following collapse of the orienting field, at least on the μs time scale. Experiments designed to specifically explore this have not been performed, although the observation of reproducible orientation effects for symmetric top molecules and the absence of an effect for argon and the spherically symmetric molecule SF_6 under identical experimental conditions lends support to this assumption, at least qualitatively. The results for CH_3Cl are independent of the field plate polarity used, i.e., +20V/gnd gives the same results as gnd/-20V and gnd/+20V gives the same result as -20V/gnd.

The raw signals measured in the experiment are:

(i) ion counts, hexapole on, homo field on, for the +end of the molecule, $S_{hv,+}$;
(ii) ion counts, hexapole off, homo field on, for the +end of the molecule, $S_{0,+}$;
(iii) ion counts, hexapole on, homo field on, for the -end of the molecule, $S_{hv,-}$;
(iv) ion counts, hexapole off, homo field on, for the -end of the molecule, $S_{0,-}$.

S_+ is then defined as $S_{hv,+} - S_{0,+}$ and S_- is given by $S_{hv,-} - S_{0,-}$. The ratio, $S_{0,+}/S_{0,-}$, should ideally be unity but in practice it degrades from unity with time according to the condition of the electron gun and the elements making up the beam crossing region. The steric effect is expressed either as the steric ratio, S_+/S_-, which is equivalent to the ratio of the corrected signal for ionization at the positive end of the dipole to the signal for ionization at the negative end of the dipole, or as the steric factor $G = (S_- - S_+) / (S_+ + S_-)$ where $-1 \leq G \leq 1$. Equal ionisation probability at both ends of the molecule would give $G = 0$, preferential ionization at the positive end of the molecule would give a negative value for G and preference at the negative end a positive value for G.

Ions are counted over a 300 s period at a 10 Hz repetition rate with 300 µs gates. For CH_3Cl, total ion counts are around 2,000 for S_+ and 600 for S_-. The ion signals with hexapole on and hexapole off, with the homogeneous field plates grounded, are typically around 1,000 and 350 counts, respectively, resulting from a three-fold signal enhancement for a CH_3Cl beam through the hexapole inhomogeneous field. The data for CH_3Cl shown in Table 1 represent the average of 35 repeated determinations involving numerous disassembly - cleaning - assembly cycles of the machine, two different hexapoles, and experiments in which the energised electrode was both positive and negative. The ion counts for the spherically symmetric species Ar and SF_6 are independent of the hexapole high voltage and the homogeneous field conditions and since S_+ and S_- are small and almost equal for Ar and SF_6 under the same conditions as the CH_3Cl experiments, the steric ratios and factors are shown in the Table as ~ 0 and ~ 1, respectively.

Table 1 Steric factors and steric ratios for 200 eV electron impact ionization of CH_3Cl, Ar and SF_6 using a quadrupole mass filter detector.

System	Ion	$G=(S_--S_+)/(S_-+S_+)$	S_+/S_-
CH_3Cl	CH_3Cl^+	-0.42±0.12	2.58±0.81
	CH_3^+	-0.01±0.14	1.07±0.36
Ar	Ar^+	~0	~1
SF_6	SF_6^+	~0	~1

These experiments have shown that electron impact ionization is more efficient at the positive end of the CH_3Cl molecule for molecular ion formation and independent of orientation for the fragment ion CH_3^+. Although the distribution of orientations within the molecular beam is broad, the positive end of all molecules point towards the positive field plate and the negative end towards the negative field plate. Irrespective of the polarity on the field plates, the beam includes a substantial fraction of molecules which can best be described as sideways oriented[1]. In the case of CH_3^+ formation, a G factor of close to unity may point to the domination of sideways orientation in the fragmentation channel. Molecules of the general series CH_3X and

CF_3X are currently under investigation, the emergence of a coherent pattern will facilitate the construction of a theoretical model.

We should like to acknowledge Phil Brooks for his helpful advice, Barrie Wood for his machining skills, and the United States - New Zealand Cooperative Science Program and the National Science Foundation for travel grants.

[1] See the following and references cited therein: (a) P. W. Harland, H. S .Carman, Jr., L. F. Phillips, and P. R. Brooks, J.Chem.Phys., **90**, 944 (1986); *ibid.* (b) **96**, 1557 (1992); (c) **95**, 8137 (1991); (d) **93**, 1089 (1990).

[2] See the following and references cited therein: H. Ohoyama, T. Iguro, T. Kasai and K. Kuwata, Chem. Phys. Letters, **209**, 361 (1993); H. Ohoyama, T. Kasai, K. Ohasi, and K. Kuwata, Chem.Phys., **165**, 155 (1992); K. Ohashi, T. Kasai, D. Chil Che, and K. Kuwata, J. Phys. Chem., **93**, 5484 (1989).

[3] T. Kasai, T. Matsunami, T. Fukawa, H. Ohoyama, and K. Kuwata, Phys.Rev.Lett., **70**, 3864 (1993).

[4] See the following and references cited therein: S. R. Gandhi and R. B. Bernstein, Z.Phys.D, **10**, 179 (1988); S. E. Choi and R. B. Bernstein, J.Chem.Phys., **85**, 150 (1986); S. Kaesdorf, G. Schönhense, and U. Heinzmann, Phys.Rev.Lett., **54**, 885 (1985).

[5] M. Volkmer, Ch. Meier, A. Mihill, M. Fink, and N. Böwering, Phys.Rev.Lett., **68**, 2289 (1992); N. Böwering, M. Volkmer, C. Meier, J. Lieschke, and M. Fink, Z.Phys.D, **30**, 177(1994); C. Meier, M. Volkmer, J. Lieschke, M. Fink, and N. Böwering, Z.Phys.D, **30**, 183(1994).

[6] A. J. Dempster, Phys. Rev., **11**, 316 (1918).

[7] J. J. Thomson, Rays of Positive Electricity and Their Application to Chemical Analyses,Longmans, Green and Co., London, 1913.

[8] B. R. Cameron and P. W. Harland, Rev.Sci.Instrum., **65**, 108 (1994).

Advances in Gas Phase Ion Chemistry, Editors N. G. Adams and L. M. Babock,
Volume **2**, JAI Press Inc., London, 1995.

EFFECT OF MOLECULAR ORIENTATION ON ELECTRON TRANSFER AND ELECTRON IMPACT IONIZATION

Philip R. Brooks and Peter W. Harland

ABSTRACT

The influence of molecular orientation on electron transfer and electron impact ionization has been probed with oriented target molecules in crossed molecular beams. Electron transfer frequently occurs in thermal energy reactive collisions involving the harpoon or spectator-stripping mechanism, but at thermal energies charged species can rarely escape their mutual Coulomb attraction, and only neutral products are formed. By increasing the collision energy to a few eV, the charged species are

separated, and the role of orientation on the electron transfer process can be probed. Collisional ionization of fast (~3-25 eV) neutral K atoms has been measured for a variety of symmetric top molecules, such as CH_3I and CF_3Br, which were oriented prior to collision. It has been shown that the orientation of the molecular dipole drastically affects overall probability of ion production through a combination of entrance channel (electron transfer) and exit channel (ion recombination) effects. The electron transfers preferentially to the most labile substituent irrespective of its polarity, the negative Cl-end of CH_3Cl and the positive Br-end of CF_3Br. Electron ionization of several oriented symmetric top molecules has shown that ionization is favored for electron impact at the positive end of the dipole, the CH_3-end of CH_3Cl and the Br-end of CF_3Br, or for broadside collisions on the molecule. In a few cases, where the molecular ion and a fragment ion have been measured, it has been shown that the ratio of ions (the fragmentation pattern or mass spectrum) is orientation dependent.

ELECTRON TRANSFER

I. INTRODUCTION

The Simple Collision Theory for bimolecular gas phase reactions is usually introduced to students in the early stages of their courses in chemical kinetics. They learn that the discrepancy between the rate constants calculated using this model and the experimentally determined values may be interpreted in terms of a steric factor, which is defined to be the ratio of the experimental to the calculated rate constants! Despite its inherent limitations, the Collision Theory introduces the idea that molecular orientation (molecular shape) may play a role in chemical reactivity. We now have experimental evidence that molecular orientation plays a crucial role in many collision processes ranging from photoionization to thermal energy chemical reactions. Usually, processes involve a statistical distribution of orientations and information about orientation requirements must be inferred from indirect experiment. Over the last 25 years, two methods have been developed for orienting molecules prior to collision[1]: i) orientation by state selection in inhomogeneous electric fields, which will be discussed here, and ii) "brute force" orientation of polar molecules in extremely strong electric fields[2]. Several chemical reactions have been studied with one of the reagents oriented prior to collision[1,2].

Experimental studies of chemical reactions designed to explore the effect of spatial orientation have been heavily weighted toward the reactions between alkali metal atoms and alkyl halide molecules. The reagents have generally been prepared and introduced in cross particle beams where ultra-sensitive detection of alkali metal atoms and the alkali metal halide products is made possible by surface ionization on transition metal wires. This set of reactions involves an electropositive atom and an electronegative molecule and the first step in the reaction mechanism is considered to involve an electron transfer between the metal atom and the molecule. Reactions involving electron transfer are ubiquitous in chemistry and biology, but under normal circumstances (thermal energies) very few neutral species react to form ions because reactions are rarely energetic enough to cause the intermediate ions to separate as charged species. Ions normally recombine to form a salt, alkali halide in the case of alkali metal with alkyl halide reactions, but if the initial energy is increased to preclude recombination, the ions can be observed and the effect of molecular orientation on the electron transfer process can be probed more directly. We will discuss electron transfer collisions occurring with a collision energy of a few eV, where ions can be detected and where the processes are still expected to be similar to those applying at thermal energies.

II. THEORETICAL ASPECTS OF ELECTRON TRANSFER

Electron transfer can occur when ionic and covalent states of the same symmetry have the same energy. Coupling between these states results in an avoided crossing of the diabatic covalent and ionic potential energy surfaces[3] as shown in Figure 1 for the atomic system, $Na + I \rightarrow Na^+ + I^-$. At internuclear distances near the equilibrium bond distance in the NaI molecule, r_e, the system is highly polar, Na^+I^-, and bonding is largely described by an ionic potential. The ionic salt molecule dissociates to give neutral atoms[4], so at large distances the molecule is best described by a covalent potential. At r_c these zeroth order (diabatic) ionic and covalent curves appear to cross but a dissociating molecule must make a smooth transition from the ionic to covalent potential. For states of the same symmetry, the crossing is avoided by the adiabatic potentials, shown in Figure 1, which result from solution of the two-state Schrödinger equation using the Born-Oppenheimer approximation. The adiabats, ε_1 and ε_2 are given in terms of the diabats by

$$\varepsilon_i = \tfrac{1}{2}\,\{H_{11} + H_{22} \pm [(H_{11}-H_{22})^2 + 4H_{12}^2]^{1/2}\} \qquad (1)$$

The adiabatic curves resulting from ionic-covalent coupling do not cross, as shown in Figure 1, and the character of the system changes smoothly from covalent at long range to ionic at short range.

The behaviour of a colliding system at the avoided crossing depends on the speed with which the crossing is traversed, as well as the separation and slopes of the adiabatic curves. If the atoms approach slowly enough on the covalent curve, the uncertainty principle allows the energy to be relatively well-defined, and the system stays on the lowest, adiabatic curve. This adiabatic process results in what we loosely call an electron "jump". On the other hand, if the atoms approach at high speed and traverse the crossing quickly, the energy will be less well-defined and it is possible that the system will remain on the diabatic curve (making a non-adiabatic or diabatic crossing) and will continue to be described by the covalent potential. The diabatic crossing represents a "hop" from one adiabatic potential curve to the other, but the electron stays on the atom and doesn't jump.

The probability of a diabatic hop, P_d, is given to good approximation by the Landau-Zener relation[3],

$$P_d \approx e^{-\kappa/v} \qquad (2)$$

where $\kappa = (2\pi H_{IC})^2/\,h\Delta S$, and $\Delta S = |\partial E_I/\partial r - \partial E_C/\partial r|$, v is the speed, and H_{IC} is the matrix element in the Hamiltonian that couples the two states. For the simplest crossing of an ionic curve with a covalent curve, the slope of the covalent potential can be regarded as zero with zero energy compared to the separated atoms. The crossing radius is given approximately by the condition that $V(r_c)_{ionic} = V(r_c)_{covalent} = \Delta E_0 - e^2/r_c$, or

$$r_c = e^2 / \Delta E_0 \qquad (3)$$

where ΔE_0 = IP-EA, the difference between the ionization potential of the electron donor (Na) and the electron affinity of the acceptor (I) and e is the charge on the electron. $\Delta S = (e/r_c)^2$ and

$$\kappa = (4\pi^2 e^2/h)\,[H_{IC}(r_c) / \Delta E_0]^2 \qquad (4)$$

Thus from equation (2), low speeds or large κ (large H_{IC} or large separation between the curves) gives a small P_d, and the probability of a diabatic "hop" between potential curves is low. Under these circumstances the crossing is adiabatic and the system smoothly changes from a covalent to an ionic description. In this process the electron jumps from the Na atom to the I atom.

A complete collision requires the crossing to be traversed twice, once on the way in and once on the way out, as shown in Figure 2a). In order to produce ions starting with neutrals, the atomic system must traverse one crossing adiabatically, and the other diabatically. For the atomic system shown in Figures 1 and 2, the two crossings are identical, and the overall probability of ionization is $P = (1-P_d)P_d$. If the electron jumps at the first crossing the ions interact in close proximity to one another, leading to “ionic scattering”. If the first crossing is diabatic, the close proximity encounter occurs between weakly interacting neutrals leading to "covalent scattering", and the difference can be resolved in the differential scattering cross section. This has been extensively reviewed[3].

For atom-molecule collisions the situation is much more interesting. Many more dimensions need to be taken into consideration and the interaction is likely to be dependent upon the orientation. This is shown schematically in Figure 2b), where the radius of the second crossing is shown to be different from the first. Even a minute change in crossing distance can have a profound influence on the dynamics because the coupling matrix element, H_{12}, depends exponentially[3,5] on r_c and the LZ probability depends exponentially on H_{12}! Moreover, the internal state of the molecule can change between the crossings and the second crossing might be a crossing between surfaces quite different from those of the original system. This has been called "bond stretching" in the earlier work[3].

As an example of how the internal state of the molecule influences the crossing, consider the effect of adding an electron to a diatomic molecule, such as Br_2. The negative ion is less tightly bound than the neutral, and attachment of the electron (at fixed internuclear distance) results in a negative ion formed in a highly excited vibrational state. Following the electron jump, the Br nuclei begin to move apart which increases the apparent electron affinity of the Br_2. According to equation (3) this increases the crossing radius, decreases the ionic-covalent interaction, and greatly enhances the probability of the system making a diabatic transition. Since vibration of Br_2^- is periodic, the bond stretching causes the electron affinity and crossing radius to vary with time, and the electron transfer probability at the second crossing will depend on the time required (i.e., on the speed) for the atomic ion to arrive, as observed experimentally[6]. In the extreme limit of bond stretching, complete dissociation of the molecular ion may occur between the crossings, leaving only the atomic ions to undergo a diatomic crossing.

III. EXPERIMENTAL TECHNIQUE

A. Overview of the cross beam experiment

Collisions are studied between spatially oriented molecules neutral potassium atoms accelerated to energies of 3- 25 eV. The orientation of the molecule can be changed so that one end of the molecule or the other can be presented to the incoming K atom. Positive ions formed in the collision are detected by one of two particle multipliers, depending on the orientation, and pulse counted. The apparatus is schematically shown in Figure 3. Details concerning the construction may be found elsewhere.[7]

The molecular beam is formed from an expansion of a pure gas sample or a 10% seeded mixture in He from the nozzle N. The central core of the expanding jet is passed by a thin-walled skimmer into the buffer chamber, C, where it is modulated by the rotating chopper wheel. The beam then passes through a second skimmer into chamber H where it traverses an inhomogeneous hexapole electric field ($\approx \pm 5$ kV on adjacent rods) which filters out the lower Stark states of the symmetric top beam component and brings the upper Stark states to a focus at the exit aperture[8]. Symmetric top molecules such as CH_3I are good candidates for orientation because the criterion for quantum state filtering is that the dipole moment does not average to zero during the course of rotation. Unlike diatomic molecules (which rotate in a plane thereby causing the dipole moment to average to zero), symmetric top molecules rotate in an electric field like a child's top in a gravitational field, the symmetry axis precesses about the field and the dipole moment does not average to zero. The quantum state selected molecules in the beam make an adiabatic transition into an homogeneous field (20 V/cm) maintained between parallel field plates, U, held 5 cm apart. Molecular orientation is effected in the homogeneous field, the negative-end of the molecular dipoles pointing toward the negative field plate. Reversal of the polarity of the homogeneous field inverts the orientation such that either end of the molecule can be presented to the potassium atom beam passing through the molecular beam in the crossing region. Holes are cut in the field plates to pass the K atom beam, and to allow viewing of the intersection by two channeltron cones. A Quadrupole mass filter on axis is used for beam detection and characterisation. The beam of fast potassium atoms is generated by resonant charge transfer[9] of K^+ formed by surface ionization on a heated W filament in oven O. The K^+ ions are accelerated through the required potential and charge exchanged with K vapour at ≈ 0.01 mTorr in the same oven. Ions passing through the exit orifice of the oven are swept out of the beam with a deflecting field of 20 V/cm and thermal energy

K atoms are unable to form ions in collisions with the oriented molecules and do not interfere with the measurements[10].

B. Hexapole Characteristics and Orientation Distribution

Figure 4 shows the hexapole transmission of a CH_3Br beam at 10K calculated for two exit apertures dimensions for our experimental conditions. At these temperatures, the most populated state is |JK>=|00> which does not focus, but there is some population in the |11>, |21> and |31> states, and these states are transmitted individually at appropriate voltages as shown. Molecules are thus focused by the hexapole field. If only a few rotational states are populated, it is possible to select individual J, K, M states using appropriate combinations of applied voltage and beam apertures[11]. Focusing curves, such as that in Figure 4, have been measured experimentally and reactive scattering has been observed for a few cases in which the beam is in a single quantum state[12]. Unfortunately the intensity of such state-selected beams is extremely low, for this reason we have selected conditions which transmit oriented beams with a distribution of states in order to facilitate cross-beam studies of reactive systems.

Our experiments show that, although the beam intensity increases with the hexapole voltage, the hexapole voltage has no major qualitative effect upon the orientation distribution. Figure 5 compares calculated distributions for several molecules. As anticipated, the very prolate top CH_3Br (which, like a pencil, does not rotate stabily about its symmetry axis), represents the least well oriented sample, and the oblate top CF_3H (which, like a bicycle wheel, rotates easily about its symmetry axis) the best. Even though each resulting distribution is quite broad, a large effect is observed on the reaction.

C. Ion Detection

K^+ ions formed in the collision are detected by one or the other of the two channeltrons (C_{180} or C_0) arranged schematically as shown in Figure 6. The voltage applied depended upon the orientation studied. The channeltron that peeked through whichever uniform plate was negatively biased was activated to count positive ions. The active cone was biased at -1200 while its uniform plate was held at -50V. The opposing plate and cone were held at +50 V, and both channeltron anodes were held at +300 to +700 V, depending on gain requirements. For these operating conditions, the field at the intersection region is roughly determined by the parallel field plates because it was observed that the channeltron counts decreased if the plates were biased much above 50 V, indicating that at higher voltages the ions would be collected only by the plates and not the channeltrons. Ions are less efficiently detected by channeltron C_{180}, apparently because the K^+ ions formed in the collision zone are initially moving away from C_{180}.

The orientation of the molecules is determined by the direction of the uniform electric field and may be reversed by reversing the polarity of the uniform field plates. As shown in Figure 8, the positive end of the molecule is presented to the incoming K atom in the 0° configuration, and the ions counted by channeltron C_0. The negative end is presented in the 180° configuration and the ions counted by channeltron C_{180}. The experiments thus directly determine the polarity of the more reactive end, the chemical identity of the more reactive end must be deduced from electronegativities, dipole trends and the reactivity itself.

D. Data Acquisition

The active channeltron is capacitively coupled to a quad scaler which counts signal pulses and pulses from an 8^6 Hz clock. Beam on-off signal differences at focusing voltage V, $S(V)_i = [(S(V)_{on} - S(V)_{off})_i$ are measured for each channeltron i (i = 0 or 180) and then corrected for the different multiplication efficiencies and ion collection efficiencies of each channeltron. The relative detection efficiency, $F(\varepsilon) = S(0)_{180}/S(0)_0$, is measured for each energy, interspersed with measurements of S(V), using the small flux of randomly oriented molecules obtained when no voltage is applied to the 6-pole field (0kV). The relative signal due to the oriented molecules, S'(V), is the (HV on) - (HV off) signal difference corrected for the multiplier efficiencies at beam energy e: $S'(V)_{180} = S(V)_{180}$ and $S'(V)_0 = F \cdot S(V)_0$. For further details, see reference 7.

IV. RESULTS

A. Raw Signals

In every case studied, the orientation of the molecule clearly affects the signal, and examples of this effect are shown in Figure 7 for CH_3Br and CF_3Br. We compare the methyl- and perfluoromethyl- halides because the polarity of the molecules is different. The X-end in CH_3X is usually negative, whereas the X-end in CF_3X is usually positive. This demonstrates that these data arise from a real molecular effect, and not from stray electric fields. From the data in Figure 7 we conclude that the positive-end of CF_3Br is more reactive and the negative-end of CH_3Br is more reactive. The Br-end of CH_3Br is assumed to be the negative end, and dipole moment trends and reactivity suggest that in CF_3Br the Br is the positive end. In CF_3I the I has been directly[13] and indirectly[14] established (by using oriented molecules) to be the positive end. Both molecules are thus more reactive on the Br-end which we call the heads end (to emphasise the analog with the heads/tails orientation of a coin). Similar conclusions are reached, with less refined data, in comparisons of the CF_3I/CH_3I and CF_3Cl/CH_3Cl systems. The data are thus not explicable by the electron simply jumping to the positive end of the dipole.

B. Cross-Section

The energy dependence of the K beam intensity and the energy dependence of the reaction cross section obscure the orientation dependence of the signals themselves. It is thus useful to remove the beam intensity variation by comparing the relative cross sections S'/I(K) for heads/tails orientation as shown in Figure 8. The heads/tails difference is much more apparent and seems largest at low energies. The space charge limited relationship, $I_K \propto E^{3/2}$, is used here to normalize the ion signals at different K beam energies, because the neutral intensity is expected to be proportional to $E^{3/2}$, as experimentally observed by Aten, et al[15], and roughly confirmed here.

C. Steric Effect

The effect of orientation on the cross section is striking, but is still hidden by the variation of the cross section with energy. The Steric Factor, G, the signal difference normalized to the cross section

$$G = (S'_{180} - S'_0)/(S'_{180} + S'_0) \qquad (12)$$

emphasises the salient features of the orientation itself, and is shown in Figure 9 for the currently best-studied systems, CF_3Br and CH_3Br. The effect of orientation is striking: G must lie in the range $-1 \leq G \leq 1$, yet at low energy for both molecules G can clearly be extrapolated to 1. This means that at low energies one orientation is completely unreactive. At higher energies G tends to 0 and the orientation makes almost no difference. The difference in molecular polarity is immediately apparent, with the heads, or Br end being more reactive in either case. This difference persists throughout the CH_3X/CF_3X family, as shown in Figure 10. Other types of systems, such as t-butyl X and CX_3H, display somewhat similar features[10].

D. Threshold behaviour

Extrapolation of G to low energies yields $|G| = 1$, at least for CF_3Br, CF_3Cl and CH_3Br. This implies that at threshold one orientation is unreactive and is consistent with our early suspicion[10] that different orientations have different kinetic energy thresholds. This is indeed the case, as illustrated by the example shown in Figure 11.

V. DISCUSSION

All chemical reactions begin as the reagents approach and end as the products separate. The system must traverse both the entrance channel and the exit channel. Our hope is that by specifying the reagent orientation in the entrance channel and monitoring the appearance of ions in the exit channel, that we may learn how orientation affects the transfer of an electron from one species to another. Strictly speaking, we cannot separate the electron transfer, presumed to occur in the entrance channel, from the process of the ions separating, which is the exit channel. Under certain circumstances, one or the other of these interactions may dominate. We have thus interpreted the data under certain assumptions, but what we really learn is how the entire process is affected by the initial molecular orientation, and conclusions regarding the electron jump must be regarded in this light.

A. "Exit" Channel Interactions

Angular distributions of the products of many chemical reactions bear a resemblance to the distributions obtained from photodissociation, suggesting that the products are formed in an impulsive event similar to photolysis.[16] It has thus been useful to compare experiments with a "direct interaction with product repulsion" (DIPR) model. We have found this concept to be useful in interpreting the angular distributions of the neutral products of thermal energy collisions of oriented molecules. Early studies of the K + oriented CF_3I reaction suggested that the (uncharged) KI product molecule was scatted in the direction in which the CF_3I figure axis was originally pointing[14] The neutral KI molecule is found to be scattered backwards for K incident on the I end of the molecule and forwards for K incident on the CF_3-end. Cross sections for the "heads" and "tails" orientations were roughly equal. Because the LUMO receiving the electron might be rather diffuse, we had originally assumed (mainly for simplicity) that the initial electron jump might be relatively unaffected by the orientation of the molecule, and further analysis indicates that the angular distribution of heads, tails and sideways oriented molecules is primarily described by the distribution of directions of the molecular axes[17]. These experimental results are semi-quantitatively reproduced by the impulsive DIPR model sketched in Figure 12 when the effect of the incoming K atom's momentum is included. Moreover, this model also accounts for the totally different angular distribution observed if the molecule is oriented sideways[18]. It only partially accounts for the angular distribution observed for the analogous CF_3Br reaction[19], possibly because the orientation might affect the electron transfer. It thus appears that the breakup of the molecular negative ion plays an important role in determining the angular distribution of the products, and may be important also in describing the higher energy ionization collisions.

The collisional ionization experiments of unoriented molecules mentioned in Section II provide the key to understanding the exit channel interactions for oriented molecules: there must be two ionic/covalent surface crossings, one as the particles approach, and the second as they recede, qualitatively sketched in Figure 2b). In a limiting case of "bond stretching", the molecular ion might be in the process of dissociating by the time the second crossing is encountered. This is shown very schematically in Figure 13, where the covalent K+ RX surface crosses the ionic K^+ + RX^- surface at r_1. The first crossing distance $r_{c1} = e^2/\Delta E_0$ is calculated from ionization potentials and electron affinities to be ≈ 4 Å, and $H_{IC} \approx 300$ meV. At the nominal collision speeds used in these experiments, $v_r \approx 5.6$ km/sec (56Å/ps) for CH_3I at 5 eV, the Landau-Zener relation, equation (2), predicts that $P_d \approx 0$, and the first crossing will be completely adiabatic: the electron will jump to the molecule. The electron is expected to occupy an antibonding C-X σ^* orbital and the molecular ions produced, CF_3X^- and CH_3X^- are expected to dissociate promptly along yet another surface (in another dimension on the left panel), indicated as $K^+ + R + X^-$. This surface will intersect the K + R + X covalent surface at a much larger distance, r_{c2}. Since H_{IC} decreases exponentially with distance[5], this crossing is less avoided, and the system is more likely to traverse this crossing diabatically with the electron remaining on the X^- ion.

At energies a few volts above threshold, the CH_3I, CF_3I, CH_3Br and CF_3Br molecules undergo dissociative electron attachment[20] and in collisional ionization give X^- ions in ≈ 98% yield[21]. The scenario suggested above (the electron jumping at the first crossing and the molecular ion dissociating before the second crossing is encountered) is thus very likely to occur. If the molecule were to remain unchanged upon the addition of the electron, the second crossing would be exactly equivalent to the first and would again be traversed completely adiabatically. The electron would be smoothly transferred back to the K^+, the products would separate on the covalent surface, no ions would be produced, and there would be no dependence on orientation. If, on the other hand, the molecular ion were to decompose explosively, the second curve crossing would be an asymptotic crossing between the emerging X^- ion and the incident K^+. This second crossing occurs at large R where $H_{IC} \approx 0$. The LZ relation then predicts that the second crossing would be completely diabatic, the electron stays on the X- ion and the products separate on the ionic surface. In this latter limiting case every collision would lead to ionization and the orientation would again not be important.

The behaviour observed is clearly intermediate between these two limits: ions are produced and the orientation is important. The existence of an orientation effect shows that every collision does not lead to ionization. As discussed above, we expect the electron to be transferred adiabatically at the first crossing. But at the second crossing the K^+ ion must be encountering something intermediate between a bound CF_3Br^- molecular ion and a free Br^- atomic ion. It must encounter a species in the act of breaking apart, and we can use the experimental orientation data to extract some information about this species.

We assume the first crossing is completely adiabatic, and that the probability of the K escaping as K^+ is the probability that the second curve crossing is traversed diabatically,

$$P_d = e^{-\kappa/v}. \tag{13}$$

This is sensitive to the relative speed of ions at the crossing, which as shown in Figure 14, is different for the heads and tails orientation. Making the zeroth order approximation that κ is independent of orientation, then the probability of forming an ion in the heads or tails orientation is

$$P_\xi = P_d = \exp(-\kappa/v_\xi) \tag{14}$$

where ξ refers to either heads or tails. The heads/tails ratio then becomes

$$R = P_h/P_t = \exp(-k/v_h + k/v_t) = \exp(-\kappa\Delta v/v^2) \tag{15}$$

where $$\Delta v = v_t - v_h \text{ and } v^2 = v_h v_t \quad 2E'/\mu \tag{16}$$

A plot of lnR vs 1/E' is thus expected to be linear, where E' is the final translational energy, $E' < E-E_{th}$. This is shown for CF_3Br in Figure 15. For energies a few volts above threshold, the orientation effect is well described by equation (2). At high energies the first crossing may become diabatic thereby invalidating the assumption made in equation (13). Uncertainty in E_{th} and fluctuations in the very low signals probably accounts for deviations near E_{th}.

So, the impulsive model described in Figure 14 accounts nicely for the energy dependence of the orientation effect. In the exit channel the ions are trying to get away from one another, and this is easiest if they are travelling in opposite directions, which occurs in the heads orientation. The second ionic/covalent surface crossing occurs between species in the act of reacting, and an experimental value for κ at this second crossing can be obtained from the slope of a plot such as Figure 15. Semi-empirical estimates for H_{IC} have been used to obtain rough values of r_2, and suggest that r_2 may be an Å or two larger than r_1, consistent with the notion that the crossing is between a K^+ ion and a species in the act of coming apart[10].

Thus, many aspects of the collisional ionization experiments can also be described by the impulsive DIPR mechanism, provided the very strong interaction between the ions in the exit channel is recognised. This is qualitatively depicted in Figure 16, which differs from Figure 12 in two major respects: i) the incoming K atom is faster, and ii) ions are detected, not neutrals. As shown, the approach, the electron transfer, and the dissociation steps are similar to those at lower energy, and the negative atomic ion is again ejected in the direction of the molecular axis. The K atom is now much faster and the K^+ ion is more likely to continue in the forward direction. If the X^- ion is ejected antiparallel to the incoming K^+, the ions have less time to interact, and in the "heads" orientation the K^+ is more likely to escape the Coulomb attraction of the X^- and be detected as an ion. Similarly, in the tails orientation the X^- travels parallel to the K^+, the ions are more likely to either recombine or to neutralize one another, and fewer K^+ ions escape the Coulomb attraction.

Independent support for these conclusions regarding the orientation effects in the exit channel is provided by the experiments of Kalamarides, et al[22]. Reaction of K atoms in high Rydberg states with CF_3I , $K^{**} + CF_3I \rightarrow K^+ + I^- + CF_3$ was studied by passing a beam of K^{**} through a scattering gas containing low pressure CF_3I, and measuring the angular distribution of the resulting I^- ions with a microchannel plate and position sensitive detector. For large principal quantum numbers, $n \approx 26$, the Rydberg electron is essentially free of the core and behaves as a free electron. The CF_3I was a gas and all orientations of the molecules were equally likely, so CF_3I^- ions were expected to be formed in all orientations by attachment of the "free" electron. Dissociation of CF_3I^- would eject I^- along the randomly oriented molecular axes, and the I^- ions were expected be distributed isotropically, and this was confirmed by experiment. However, as n decreased to 9, the angular distribution became anisotropic, with fewer I^- moving in the direction of the initial K^{**}. The electron is more tightly bound for n=9, and is more comparable to those of this study (n=4): the Rydberg electron in this case is not free, but carries with it the positively charged core. Kalamarides, et al thus observed that fewer I^- ions were scattered in the forward direction and concluded that the diminution of I^- in the forward direction was due to a greater likelihood of charge neutralization if I^- and K^+ were travelling in the same direction as concluded from the oriented molecule experiments and shown in Figure 16.

B. "Entrance" Channel - Electron Transfer

The Landau-Zener theory is comparatively successful in explaining the overall behaviour of the reactions of oriented molecules at thermal energies where neutral products are formed and at elevated energies where the transient ions have enough energy to separate. This is, in a sense, frustratingly successful, because there seems to be no room to accommodate an orientation-dependent electron transfer, which chemical intuition suggests must be operative. The role of the electron transfer in the post-threshold behaviour discussed above is apparently overshadowed by the strong Coulomb forces in the exit channel. Orientation dependent exit channel interactions are possible when three or more species are produced in the collision as shown in Figure 14, and as discussed above, this is likely the case for several of the molecules studied. But if the collision energy is sufficiently low, decomposition of the molecular negative ion may not be allowed. If only two particles are formed, a positive ion and a negative ion, conservation of momentum requires that they must recede with antiparallel velocities regardless of the orientation. The strong, orientation-dependent forces in the exit channel suggested in Figure 14 are thus not present, and any orientation effect may be due to the electron transfer in the entrance channel.

The different threshold behaviour for heads and tails orientations shown in Figures 7 and 8 show that at very low energies reaction is restricted to only one end of the molecule. We directly observe that there is no reaction for attack in the unfavored orientation. The different thresholds for attack at different "ends" of these molecules requires the final state of the system, at the respective thresholds, to be somehow different for attack at the opposite ends of the molecule. For CF_3Br we believe that different products may be formed, depending on the end attacked, but the same species in different internal states could also be a possibility[23]. In these experiments there are two likely low energy reaction channels:

$$K + CX_3Y \rightarrow K^+ + Y^- + CX_3 \qquad (17)$$

$$\rightarrow K^+ + CX_3Y^- \qquad (18)$$

which we are not yet able to differentiate because only the K^+ positive ion was detected. (KY salt molecules might also be formed but since only charged particles are detected, the neutrals are not observed.) At energies a few volts above threshold, the fragmentation reaction (17) accounts for ≈ 95% of the products[21] and the early experiments were interpreted on the basis of reaction (17) At sufficiently low energies, however, the parent ion may not have enough energy to fragment and reaction (18) can be observed.

The negative ions formed in collisions of Na atoms with unoriented CF_3Br have been directly observed by Compton, Reinhardt & Cooper[21]. They observed the parent ion, CF_3Br^-, and determined the vertical electron affinity, EA_v, to be 0.91 ±0.20 eV. Their data predicts the threshold for electron transfer to CF_3Br to give the parent ion (18) is 3.43 eV and the threshold for fragmentation (17) to give Br^- is 3.97 eV. These threshold energies for formation of the parent ion, CF_3Br^-, and for fragmentation into CF_3 and Br^- agree closely with the apparent thresholds of 3.4 eV and 4.0 eV obtained for the oriented molecules. Since the threshold laws are not known, we have linearly extrapolated the data to yield apparent thresholds. The threshold differences are expected to be significant because the cross sections for heads and tails orientations are similar over a large energy range (Figure 8). We thus conclude that, at the lower (heads) threshold, parent CF_3Br^- is produced, and it is produced by attack at the Br-end of the molecule. In the energy range 3.4 - 4.0 eV, reaction occurs exclusively at the heads-end (Br) of the molecule producing only two particles, K^+ and CF_3Br^-, which must leave the collision travelling in opposite directions to conserve momentum. The strongly orientation-dependent 3-body exit channel interactions, which were adequate to explain the high energy (10 eV) orientation behaviour, are therefore absent. Effects of orientation between 3.4 and 4.0 eV must arise mostly from the electron transfer in the entrance channel, and we conclude that for energies near threshold the electron is transferred preferentially to the Br end of the molecule. At the higher (tails) threshold, tail-end attack results in fragmentation and produces Br^- fragments. Formation of the parent negative molecular ion by tails attack is apparently prevented by some barrier which can be overcome with 0.5 eV of translational energy. But the CF_3Br^- molecular ion is too weakly bound to accommodate this much energy, and the negative molecular ion breaks up according to reaction (17). Above the tails threshold, heads attack may also produce Br^- fragments because enough energy would likely be deposited in the parent ion to cause it to break apart, and above about 5 eV, Br^- is the dominant negative ion.

For the other molecules studied, less is known about the negative ions formed and their thresholds . It is, of course, tempting to speculate that different products are being formed for different orientations in a manner analogous to that for CF_3Br and for the electron bombardment experiments. For CF_3Cl the parent ion has been observed[24], and we have measured a difference between heads and tails thresholds of 0.6 eV. Again, the Cl-end is more reactive and at low energies only Cl-end attack produces ions. However, the apparent threshold is in poorer agreement with that calculated, possibly a result of the extrapolation or of our weaker signals because the reaction cross section is smaller than that for CF_3Br.

The parent CH_3Br ion has not been observed in previous studies[21,25]. Nevertheless, only one end of the molecule, the Br-end, is reactive at energies near threshold. The difference in thresholds is 0.2 eV, and the tails threshold is in rough agreement with the calculated threshold to produce Br^- and with the observations of Compton et al. for formation of Br^-. If the analogy with CF_3Br is pursued, these data indicate that the parent ion is bound only by 0.2 eV (±0.2eV), suggesting that the parent may be so fragile that it might not be observed. These data thus suggest that different products are formed by attack at different ends of the molecule, which are manifested here by different energetic thresholds for the two orientations.

The electron probably jumps to an antibonding pσ* orbital composed largely of p orbitals from carbon and bromine[24], which is expected to be more accessible from the Br-end of the molecule. The threshold results show that transfer through the CF_3-end is apparently impeded by a barrier of about 0.6 eV (14 kcal/mole), which can be overcome by increasing the collision energy, resulting in fragmentation of the anion. This is qualitatively illustrated by the potential curves in Figure 17 where the covalent potential for tails approach includes an extra repulsion term to account for the CF_3 group interposed between the K and Br. This extra repulsion forces the tails orientation crossing to be at larger distances (and higher energies) where electron transfer is much less likely because the orbital overlap is less. The interaction between the ionic and covalent configurations falls exponentially with distance[5], and at a given collision energy, the likelihood of an adiabatic crossing (electron jump) is greatly decreased, which mostly accounts for the lack of ions formed in the tails orientation. The higher energy of the crossing provides some rationale for the barrier to tails attack. This description and Figure 17 are highly simplified because additional dimensions, such as the C-Br distance, must be considered to explain salt formation as well as the fragmentation observed at higher energy.

The conclusion that electron transfer is localized is likely to apply to other systems, even at lower energies. As the energy is decreased towards thermal energy, the electron is more likely to "jump" although the electron will jump back if the energy is below threshold, which is likely the case for tails attack below tails threshold. Salt formation (exoergic by 20 kcal/mol) and ion production compete with one another above the ion threshold, and it is reasonable to conclude that these processes share the same entrance channel. The preference for the Br end is thus expected to extend to lower energies, and indeed in an earlier study of K + CF_3Br at thermal energies[19], we found that the neutral salt, KBr, was more likely to be formed by Br-end attack. While overall production of K^+ is greater at all energies for "heads" attack, we are as yet unable to assess the relative importance of "heads" vs "tails" attack on the Br-channel at the onset of Br^- formation.

In summary, ions are formed in electron transfer collisions between beams of neutral K atoms and beams of oriented target molecules. In every case studied so far, the orientation of the target molecule greatly affects the reactivity, consistent with "chemical intuition". The electron is not, however, simply transferred to the positive end of the molecule, because in the methyl halides the negative end is more reactive. At energies a few eV above threshold, where molecular negative ions might fragment, the dynamics seem to be dominated by the ions getting away from one another. More than two particles can form, and the initial molecular orientation can be manifested in the exit channel as ions travelling with parallel or antiparallel velocities. Ions with antiparallel velocities are most likely to survive as ions, consistent with observation. At low energies several molecules exhibit different thresholds for different orientations. There is consequently an energy region where no reaction occurs at the "wrong" end of the molecule.

ELECTRON IMPACT IONIZATION

I. INTRODUCTION

The experiments involving the collision of fast potassium atoms with oriented symmetric top molecules have demonstrated that the efficiency of the initial electron transfer step in the entrance channel is orientation dependent with the reaction threshold, cross-section and reaction products exhibiting an orientation dependence. The fast atom experiments were designed to probe the electron transfer step, although it is recognised that the LZ description of the electron transfer step in the entrance channel is an over-simplification. It is unlikely that a discrete electron particle "jumps" from the approaching alkali metal atom to the molecule at a well defined separation. The wavefunctions corresponding to the two particles mix during the approach and the system takes the characteristics of the transition state species in a smoothly changing manner with time. In impulsive encounters, such as these, it is likely that the electron transfer is only complete when the reaction products emerging from the transition state have assumed their asymptotic identities. Whether the electron is transferred as a discrete particle or not, these results beg the question, would the ionization of a molecule by a free electron also exhibit an orientation dependence? Recent cross beam experiments have shown[26] that this is indeed the case, the ionization cross-section and the fragmentation pattern exhibiting an orientation dependence.

A number of excellent reviews and books have included consideration of the fundamental electron impact ionization process[27-34] and the attention afforded the experimental measurement of ionization potentials and fragment ion appearance energies over the years is reflected in the comprehensive database of ionization potentials and gas phase ion enthalpies of formation published through the National Bureau of Standards in printed and electronic forms[35]. In contrast, few absolute ionization cross-sections have been measured. The most comprehensive compilation of molecular ionization cross-sections are relative values measured with a modified commercial electron impact mass spectrometer ion source using the cross-section for Ar as a reference[36].

II. EXPERIMENTAL TECHNIQUE

Experiments are carried out[26] using crossed beams of spatially oriented symmetric top molecules and near-monochromatic electrons. The dimensions of the hexapole were chosen to optimise transmission at the expense of specific quantum state selectivity. The focused beam of upper Stark-state selected molecules passes through an 8.0 mm diameter exit aperture into a highly screened weak homogeneous orienting electric field (20 V cm^{-1}) maintained between parallel field plates 200 mm long and 10 mm apart and is detected on axis by a) a quadrupole mass filter or b) a mass insensitive rotatable particle multiplier. The electron beam passes through apertures in the field plates, through the molecular beam and into a screened Faraday cup. The electron beam guiding elements, homogeneous field plates, screening grids and plates, Faraday cup assembly and the ion guiding lens are all coated with colloidal graphite. A diagram of the scattering region is shown in Figure 18.

Collisions involving neutral reactants and products are unaffected by the presence of a uniform electric field in the crossing region. This is not the case where charged particles are involved. Ions formed between the homogeneous field plates would be accelerated towards the field plate of opposite polarity and be discharged. The K^+ ion products produced in collisions between fast K atoms and oriented symmetric top molecules are collected using channeltrons protruding through the field plates. This approach cannot be used for electron impact, where the proximity of the channeltron cones to the beam crossing would shatter the electron beam integrity and the geometry of the beam crossing volume, and attract ions produced by ionization directly to the negative field plate. To overcome this problem, experiments are carried out using a pulsed nozzle operating at 10 Hz with a 1.8 ms open time. One field plate is maintained at ground potential and the other at ±20V. The energised field plate is switched to <0.1 V from ground (polarity preserved) in <1 μs as the leading edge of the gas pulse reaches the electron beam crossing. The segment of oriented beam between the homogeneous field plates at the time the field is collapsed corresponds to 300 μs in flight time. Ions produced by the electron impact ionization of this 300 μs segment of spatially oriented beam in the absence of the uniform orienting field are gated at the detector located 25 mm downstream on the molecular beam axis. An Einzel lens assembly fitted to the entrance of the quadrupole is designed to guide ions into the mass filter without disrupting the homogeneous field in the beam crossing region when it is energised. Measurements are repeated with the hexapole high voltage switched off and the rods set to ground potential, i.e., in the absence of the inhomogeneous field in the hexapole.

The method of data analysis is the same as that described above for the fast potassium experiments. The steric effect is expressed either as the steric ratio, $R = S_+/S_-$, which is the corrected (for background) signal for ionization at the positive end of the dipole to the signal for ionization at the negative end of the dipole, or as the steric factor G, equation (12). Equal ionisation probability at both ends of the molecule would give $R = 1$ and $G = 0$, preferential ionization at the positive end of the molecule would give $R > 1$ and $G < 0$, and preference at the negative end of the molecule would give $R < 1$ and $G > 0$.

III. RESULTS

The results for all experiments carried out todate are shown in Table 1. he symmetric top molecules exhibit a clear effect which disappears if the homogeneous field is switched off as the gas pulse enters the field plates. Under identical experimental conditions, the ion signal produced by the electron ionization of the non-polar molecules fails to display any effect on the field potentials or polarities. CH_3Cl exhibits the highest steric ratio for the molecules investigated. This is also found to be the case in studies of the elastic scattering of high energy electrons from oriented molecules[37]. Electron impact ionization is more efficient at the positive end for all of the molecules studied, with the possible exception of the CH_3^+ fragment ions formed from CH_3Cl and CH_3Br, which are independent of orientation or weakly favoured for electron impact on the negative end of the molecule. The CH_3Br results are preliminary, the experiments were carried out with a nozzle stagnation pressure determined by the vapour pressure of the liquid at room temperature resulting in low signal levels.

The distribution of orientations within the molecular beam is broad, however, the positive end of all molecules point towards the positive field plate and the negative end towards the negative field plate. Irrespective of the polarity on the field plates, the beam includes a substantial fraction of molecules which can best be described as sideways or broadside oriented. In the case of CH_3^+ formation, a G factor close to zero may point to the domination of sideways orientations in the fragmentation channel. To exclude the possibility that the ion guiding lens was somehow discriminating against CH_3^+ ion transmission, the Einzel lens and quadrupole detector were replaced by a mass insensitive particle multiplier detector fitted with a single plane electrostatic lens element. From the measured steric ratio for CH_3Cl (R = 2.58 for CH_3Cl^+ and R = 0.96 for CH_3^+) and the fragmentation pattern (CH_3Cl^+=100 and CH_3^+=54), a value of 1.78 can be calculated for the steric ratio for CH_3Cl (all ions) measured with a mass insensitive detector. The experimental result of R = 1.62 (G = -0.23) is considered to be in accord with the predicted value, showing that instrumental anomalies are not significant, and lending support to the evidence for fragment dependent steric ratios.

IV. THEORETICAL CONSIDERATIONS

Theoretical models of the electron impact ionization process have focused on the calculation of the ionization cross-section and its energy dependence, and can be characterized as quantum, semi-classical and semi-empirical. The theoretical treatment of the ionization process has been seen as a complex problem with the involvement of three charged particles in the exit channel[38]. Even for atomic hydrogen, the simplest ionization case, the long-range Coulomb force restricts free movement of the particles even at very large interparticle separations[39]. Quantum methods use a partial wave approximation. The Born approximation[33] considers the incident electron as a plane wave with limited interaction with the molecule and limited success[38]. A series of higher order approximations, including distorted wave theories[33,40], have found some success in describing the absolute electron ionization cross-section and the energy dependence for light neutral atoms such as H, He and Ne and light ion targets such as He^+, Be^+, Na^+ and Mg^{2+} (within about 25%). There has been limited success with heavier atoms and ions giving calculated ionization cross-sections within a factor of two or better of experiment[41].

A number of semi-classical and semi-empirical expressions[33] have been developed for modelling the energy dependence of the electron ionization cross-section for atoms, although no generally applicable model has yet emerged. There has been less effort invested in electron ionization of molecules resulting in models which exhibit limited success for specific examples. A simple qualitative model of the ionization process which describes the threshold behaviour involves the classical picture of the electron as a particle projectile transferring kinetic energy to the target molecule. At the ionization threshold all of the energy carried by the incident electron is transferred in a head-on collision. At higher incident electron energies, where only a fraction of the energy is transferred, glancing collisions become important with a concomitant increase in the (collision) ionization cross-section. This model could accommodate a spatial asymmetry in the cross-section through the influence of the molecular orbitals (shape of the molecule) on the impact parameters for the glancing collisions effective in the ionization process. One model proposed to account for the maximum in ionization efficiency curves considers that the passage of the incident electron subjects the molecule to a pulsed disturbance. The probability for energy transfer would depend on the magnitude of the Fourier component in the pulse in resonance with the transition energy in the molecule. As the electron energy increased, the ionization cross-section would decrease as the pulse width and the magnitude of the lower energy components decreased. Semi-empirical additivity rules have been devised to estimate ionization cross-sections for specific molecular groups with some success and a correlation between experimental ionization cross-section and polarizability, first reported by Lampe, Franklin and Field[36], has been more recently reported for several series of organic molecules by Bartmess and Georgiadis[42]. An inverse relationship between the product of ionization cross-section and the maximum in the ionization efficiency curve with the square of the ionization potential has been reported by Franco and Daltabuit[43]. Little progress has been made on the theoretical prediction of fragmentation patterns since the original Quasi-Equilibrium Theory which was based on statistical mechanics and transition state theory[44].

In summary, there is no simple model at present which adequately describes all aspects of the electron ionization process (threshold behaviour, total ionization cross-section, energy dependence of the cross-section, and fragmentation) in terms of simple equations that could be used confidently in a predictive manner. S. M. Younger comments on this situation in Reference 33 with the statement, "It may be said that there currently exists no rigorous theory of the electron impact ionization of atoms and ions. Indeed, developments since the early work of Thomson (1912) have concentrated on increasingly sophisticated approximations to an as yet undefined formal theory." Investigation of the electron impact ionization of spatially oriented molecules was initiated in order to extend the work on electron transfer, gain a deeper insight into the electron ionization process and to provide data useful for the development of semi-empirical models of practical value.

V. A MODEL FOR ELECTRON IONIZATION

The investigation of electron ionization is clearly in the early stages in comparison with the electron transfer studies and additional work of the influence of orientation on fragmentation will be required before a coherent pattern emerges and a model for fragmentation can be attempted. However, a simple model which considers ionization in terms of the Coulomb otential developed between the electron and the polar molecule, taking the electron transition probability into account, reproduces the main experimental features. This model accounts qualitatively for the steric effect measured and leads to simple, generally applicable, expressions for the maximum (70eV) ionization cross-section.

As the electron approaches the molecule an electric field is established which is described in terms of a Coulomb potential, ϕ_C. It is assumed that when the Coulomb potential reaches the electron transition energy, the ionization potential, E_0, the orbital electron involved in the transition absorbs from the field, the efficiency of the ionization depending on the transition probability, P_i. Neglecting the electron-induced dipole, a cross-section, σ_C, can be calculated from the interparticle separation when $\phi_C = E_0$. In order to find the maximum ionization cross-section, σ_i, σ_C must be multiplied by the transition probability P_i:

$$\sigma_i = \sigma_C P_i \tag{19}$$

A. An expression for σ_C

The target molecule is considered in terms of the isolated electron involved in the transition, charge q, and a charge, q", determined by the dipole moment of the molecule and its orientation with respect to the electron projectile. If the molecule is non-polar then q" = 0, and the electron is considered to be incident on a molecule exhibiting zero charge (electrically neutral). If the molecule has a permanent dipole moment μ and separation of charge centers l, then q" = $\pm\mu/l$, depending on the orientation of the dipole with respect to the projectile electron. The length of the dipole, l, for prolate and oblate symmetric top molecules, CY_3X, is taken arbitrarily as the distance along the C-X molecular axis between the centre of atom X and the Y atom plane perpendicular to the C-X axis. So, the magnitude of the effective Coulomb potential as a function of the electron-molecule separation depends on spatial orientation according to the following cases:

(i) zero dipole moment or the dipole perpendicular to the projectile electron (broadside),

$$\phi_{C,0} = \frac{q_{eff}}{(4\pi\varepsilon_0)\,r} = \frac{q}{(4\pi\varepsilon_0)\,r} \tag{20}$$

(ii) as the projectile electron approaches the positive end of the dipole, the field will be higher at a given separation and

$$\phi_{C,\delta+} = \frac{q_{eff}}{(4\pi\varepsilon_0)\,r} = \frac{(q+\mu/l)}{(4\pi\varepsilon_0)\,r} \tag{21}$$

(iii) as the projectile electron approaches the negative end of the dipole, the field will be lower at a given separation and

$$\phi_{C,\delta-} = \frac{q_{eff}}{(4\pi\varepsilon_0)\,r} = \frac{(q-\mu/l)}{(4\pi\varepsilon_0)\,r} \tag{22}$$

A plot of the Coulomb potentials for an electron approaching broadside, the CH_3-end (δ+) and the Cl-end (δ–) for CH_3Cl, according to equations (20) to (22), respectively, are shown in Figure 19.

When $\phi_C = E_0$, $r = b_{max}$, where b_{max} is the maximum impact parameter for the electron transition process (ionization). Then, assuming that $P_i = 1$, $\sigma_C = \pi b_{max}^2$, where σ_C is the calculated (Coulomb) maximum electron impact ionization cross-section

$$\sigma_C = \pi\left(\frac{q_{eff}}{(4\pi\varepsilon_0)\,E_0}\right)^2 \qquad \text{for } P_i = 1 \qquad (23)$$

Substituting the appropriate quantities

$$\sigma_C = 651.3\left(\frac{z_{eff}}{E_0}\right)^2 \text{ in units of Å}^2. \qquad (24)$$

where $z_{eff} = q_{eff}/q$. The model requires that ionization is favoured at the positive end of the molecule and this has been observed to be the case for CH_3X and CF_3X, even though the positive end of the dipole corresponds to the CH_3-end for CH_3X and the X-end for CF_3X.

Considering CH_3Cl in detail, the dipole moment is 6.24×10^{-30} Cm (1.87 D) and the effective dipole length is 215 pm giving the charge on the dipole as $\pm 2.90 \times 10^{-20}$ C or $\pm 0.18q$, where q is the electron charge. Using equation (24), the ionization cross-sections for electron impact on the +end, $\sigma_{i,\delta+}$, -end, $\sigma_{i,\delta-}$, and broadside, $\sigma_{i,0}$, orientations are calculated to be 7.2, 3.5 and 5.2 Å^2, respectively. So, these equations predict that the ionization cross-section will be higher for electron impact on the +end of the dipole, lowest for impact on the -end of the dipole and intermediate for broadside collisions. The calculated steric ratio $\sigma_{i,\delta+}/\sigma_{i,\delta-} = 2.1$ is close to the experimental ratio of 2.58 for the CH_3Cl^+ ion and 1.62 measured using the mass insensitive detector. Table 2 lists the calculated steric ratios for several polar molecules. For the systems which have been studied experimentally, CH_3Cl is predicted to exhibit the highest steric ratio in accord with experiment.

The experimental electron impact ionization cross-sections reported in the literature correspond to values for a random orientation of dipoles, $\sigma_{i,r}$. For this model, where $\Delta\phi/\Delta r$ ≈constant in the vicinity of $\phi = E_0$, then $(\sigma_{i,\delta+} - \sigma_{i,0}) \approx (\sigma_{i,0} - \sigma_{i,,\delta-})$ and $\sigma_{i,r} \approx \sigma_{i,0}$. Despite the simplicity of the model and its obvious limitations, the calculated cross-sections lie within a factor of two of the measured values[36], Figure 20.

B. An expression for P_i

If the transition probability, P_i, is taken to be proportional to $|\mu_{if}|^2$, where μ_{if} is the orbital overlap integral for the dipole transition from state *i* (neutral molecule) to state *f* (ion), then

$$\mu_{if} = \int \psi_i^* \,\tilde{\mu}\, \psi_f \, d\tau \qquad (25)$$

where $\tilde{\mu}$ is the electric dipole moment operator. $|\mu_{if}|^2$ is related to the quantum mechanical expression for mean molecular polarizability, α, by[45]

$$\alpha = \frac{2}{3}\sum_f \frac{|\mu_{if}|^2}{E_f - E_i} \tag{26}$$

Assuming discrete states

$$P_i \approx |\mu_{if}|^2 \approx \frac{3\alpha E_0}{2} = c\ \alpha'\ E_0 \tag{27}$$

This expression introduces a dependence of ionization efficiency on the polarization volume.

C. An expression for σ_i

An expression for the ionization cross-section, σ_i, can be written from equations (19), (24) and (27)

$$\sigma_i = \sigma_C\ P_i \approx c\ \sigma_C\ \alpha'\ E_0 \tag{28}$$

where c is a constant, α' is the polarizability volume ($\alpha = (4\pi\varepsilon_0)\ \alpha'$) and ε_0 is the permittivity of free space. Substituting from equation (23) for σ_C,

$$\sigma_i = c''\ z_{eff}^2\ \alpha' / E_0 \tag{29}$$

where c" is a constant. So, this model predicts a linear realtionship between ionization cross-section and α'/E_0 (Lampe, Field and Franklin[36] noted a linear relationship between their measured ionization cross-sections and the corresponding values for α' in 1957). Plots of the experimental 70 eV ionization cross-sections ($z_{eff} = 1$) reported by Lampe *et al*[36] versus α' and α'/E_0 are shown in Figure 21. The plots are linear and the equations obtained by least squares fitting are:

$$\sigma_i = 1.947\ \alpha' - 0.309 \tag{30}$$

$$\sigma_i = 18.79\ \alpha' / E_0 + 0.626 \tag{31}$$

where σ_i is expressed in units of Å^2, α' in units of Å^3 and E_0 in eV. Table 3 compares the ionization cross-sections for Ar, N_2, CH_4 and CH_3Cl calculated from equations (24), (30) and (31) with the experimental value reported by Lampe, Field and Franklin[36] (which are assumed to be accurate). The discrepancies between the calculated and experimental values, shown in parentheses in the Table, are well within the uncertainties expected from experimental measurements. The goodness of fits exhibited in Figure 21, covering a factor of 20 in cross-section, gives some confidence in the model.

In summary, preliminary experiments have demonstrated that the efficiency and outcome of electron ionization is influenced by molecular orientation. That is, the magnitude of the electron impact ionization cross-section depends on the spatial orientation of the molecule with respect to the electron projectile. The ionization efficiency is lowest for electron impact on the negative end of the molecular dipole. In addition, the mass spectrum is orientation dependent, for example, in the ionization of CH_3Cl the ratio CH_3Cl^+:CH_3^+ depends on the molecular orientation. There are both similarities and differences between the effect of orientation on electron transfer (as an elementary step in the harpoon mechanism) and electron impact ionization, but there is a substantial effect in both cases. It seems likely that other types of particle interactions, for example, free radical chemistry and ion-molecule chemistry, may also exhibit a dependence on relative spatial orientation. The information emerging from these studies should contribute one more perspective to our view of particle interactions and eventually to a deeper understanding of complex chemical and biological reaction mechanisms.

REFERENCES

[1] For reviews see: a) Brooks, P. R., *Science*, **1976**, 193, 11.; b) Bernstein, R. B., Herschbach, D. R., and Levine, R. D., *J. Phys. Chem.*, **1987**, 91, 5365.; c) Harren, F., Parker, D. H., and Stolte, S., *Comments At. Mol. Phys.*, **1991**, 26, 109.; d) Parker, D. H., and Bernstein, R. B., *Ann. Rev. Phys. Chem.*, **1989**, 40, 561.; e) Stolte, S., *Atomic and Molecular Beam Methods*, Vol 1., Scoles, G., editor, Oxford, New York, **1988**, 631.

[2] For example: a) Loesch, H. J., and Remscheid, A. J., *J. Chem. Phys.*, **1990**, 93, 4779.; b) *ibid* **1991**, 95, 8194.; c) Loesch, H. J., and Möller, J., *Chem. Phys.*, **1992**, 97, 9016.; d) Friedrich, B., and Herschbach, D. R., *Z. Physik*, **1991**, D18, 153.; e) Slenczka, A, Friedrich, B., and Herschbach, D. R., *Phys. Rev. Lett.*, **1994**, 72, 1806.

[3] For reviews of collisional ionization, see a) Kleyn, A. W., Los, J., and Gislason, E. A., *Physics Reports.*, **1982**, 90, 1.; b) Lacmann, K., *Potential Energy Surfaces*, Lawley, K. P., editor, John Wiley, New York, **1980**, 513.; c) Baede, P. M., *Adv. Chem. Phys.*, **1975**, 30, 463.; d) Los, J., and Klein, A. W., *Alkali Halide Vapors*, editors Davidovits, P., and McFadden, D. L., Academic Press, New York, **1979**, 279.

[4] Berry, R. S., *J. Chem. Phys.*, **1957**, 27, 1288.

[5] Grice, R., and Herschbach, D. R., *Mol Phys.*, **1974**, 27, 159.

[6] Kleyn, A. W., Khromov, V. N., and Los, J., *J. Chem.Phys.* **1980**, 72, 5282.

[7] a) Carman, Jr., H., Ph.D. Thesis, Rice University **1985**.; b) Xing, G., Ph.D. Thesis, Rice University **1993**.

[8] Bernstein, R. B., *Chemical Dynamics via Molecular Beam and Laser Techniques*, Oxford University Press, **1982**, 45.

[9] Helbing, R. K. B., and Rothe, E. M., *Rev. Sci. Instrum.* **1968,** 39 1948.

[10] a) Harland, P. W., Carman, H. S. Jr., Phillips, L. F., and Brooks, P. R., *J. Chem. Phys.*, **1989,** 90 5201; b) Harland, P. W., Carman, H. S. Jr., Phillips, L. F., and

Brooks, P. R., *J. Chem. Phys.*, **1990,** 93 1089; c) Harland, P. W., Carman, H. S. Jr., Phillips, L. F., and Brooks, P. R., *J. Phys. Chem.*, **1991,** 95 8137.

[11] a) Gandhi,S. R., Xu, Q.-X., Curtiss, T. J., and Bernstein, R. B., *J. Phys. Chem.* **1987,** 91, 5437.; b) Kasai, T., Fukawa, T., Matsunami, T., Che, D.-C., Ohashi, K.; Fukunishi, Y., Ohoyama, H., and Kuwata, K., *Rev. Sci. Instrum.*, **1993**, 64, 1150.

[12] Janssen, M. H. M., Parker, D. H., and Stolte, S., *J. Phys. Chem.*, **1991**, 95, 8142.

[13] Gandhi, S. R., and Bernstein, R.B., *J. Chem. Phys.* **1988**, 88, 1472.

[14] Brooks, P. R., *Faraday Disc. Chem. Soc.*, **1973**, 55, 299.

[15] Aten, J., and Los, J., *J. Phys. E*, **1975**, 8, 408.

[16] a) Kuntz, P.J., Mok, M. H., and Polanyi, J. C., *J. Chem. Phys.* **1969**, 50, 4623.; b) Herschbach, D. R., *Faraday Discuss. Chem. Soc.*, **1973**, 55, 233.

[17] Brooks, P. R., *J. Phys. Chem.*, **1993,** 97, 2153.

[18] Brooks, P. R., McKillop, J., and Pippen, H. G., *Chem. Phys. Lett.*, **1979,** 66, 144.

[19] Carman, H. S., Harland, P. W., and Brooks, P. R., *J. Phys. Chem.*, **1986,** 90, 944.

[20] a) Stockdale, J. A., Davis, F. J., Compton, R. N., and Klots,C. E., *J. Chem Phys*, **1974,** 60, 4279.; b) Heni, M., and Illenberger, E., *Chem Phys Lett.*, **1986,** 131, 314.

[21] Compton, R. N., Reinhardt, P.W., and Cooper, C. D., *J. Chem. Phys.* **1978,** 68, 4360.

[22] a) Kalamarides, A., Walter, C. W., Lindsay, B.G., Smith, K. A., and Dunning, F. B., *J. Chem. Phys.* **1989**, 91, 4411.; b) Kalamarides, A., Marawar, R. W., Ling, X., Walter, C. W., Lindsay, B.G., Smith, K. A., and Dunning, F. B., *J. Chem. Phys.*, **1990**, 92, 1672.

[23] a) Lobo, R. F. M., Moutinho, A. M. C., and Los, J., *Chem. Phys.* **1994**, 179, 179,; b) Lobo, R. F. M., Moutinho, A. M. C., Lacmann, K., and Los, J., *J.Chem. Phys.* **1991,** 95, 166.

[24] Hasegawa, A., and Williams, F., *Chem. Phys. Lett.* **1977**, 46, 66.

[25] McNamee, P.E., Lacman, K., and Herschbach, D.R., *Faraday Discuss. Chem. Soc.* **1973**, 55, 318.

[26] Aitken, C. G., Blunt, D. A., and Harland, P. W., *J. Chem. Phys.*, **1994**, 101, 11074.

[27] Massey, H. S.W., and Burhop, E. H. S., *Electronic and Ionic Impact Phenomena*, Oxford University Press, London, **1952**.

[28] Rudge, M. R. H., *Revs. Mod. Phys.*, **1968,** 40, 564.

[29] Massey, H. S. W., and Burhop, E. H. S., *Electronic and Ionic Impact Phenomena*, Volume 1, Oxford University Press, London, **1969**.

[30] Weingold, E., and McCarthy, I. E., *(e, 2e) Collisions, Advances in Atomic and Molecular Physics*, Volume **14**, edited by Bates, Sir. D. R. and Benderson, B., Academic Press, New York, **1978**.

[31] McCarthy, I .E., and Stelbovics, A.T., in *Theoretical Methods for Ionization in Atomic and Molecular Processes in Controlled Thermonuclear Fusion*, edited by McDowell, M. R. C., and Ferendeci, A. M., Plenum Press, New York, **1980**.

[32] Younger, S. M., *Comm. At. Mol. Phys.*, **1982**, 11, 193.

[33] Märk, T. D., and Dunn, G .H., editors, *Electron Impact Ionization*, Springer-Verlag, Wein and New York, **1985**.

[34] Christophorou, L. G., editor, *Electron-Molecule Interactions and Their Applications*, Volume 1, Academic Press, Inc., **1984**.

[35] a) Franklin, J. L., Dillard, J. G., Rosenstock, H. M., Heron, J. T., Draxl, K., and Field, F. H., *Ionization Potentials, Appearance Potentials, and Heats of Formation of Gaseous Positive Ions, Nat. Stand. Ref. Data Ser., NBS, US*, **1969**. b) Levin, R. D., and Lias, S. G., *Ionization Potential and Appearance Potential Measurements, 1971-1981, Nat. Stand. Ref. Data Ser., NBS, US*, **1982**. c) Lias, S. G., Bartmess, J. E., Liebman, J. F., Holmes, J. L., Levin, R. D., and Mallard, W. G., *Gas-Phase Ion and Neutral Thermochemistry, Nat. Stand. Ref. Data Ser., NBS, US*, **1988**.

[36] Lampe, F. W., Franklin, J. L., and Field, F. H., *J. Am. Chem. Soc.*, **1957**, 79, 6129.

[37] a) Volkmer, M., Meier, C., Mihill, A., Fink, M., and Böwering, N., *Phys.Rev.Lett.*, **1992**, 68, 2289. b) Böwering, N., Volkmer, M., Meier, C., Lieschke, J., and Fink, M., *Z.Phys.D*, **1994**, 30, 177. c) Meier, C., Volkmer, M., Lieschke, J., Fink, M., and Böwering, N., *Z.Phys.D*, **1994**, 30, 183.

[38] Ehrhardt, H., Jung, K., Knoth, G., and Schlemmer, P., *Z.Phys.D*, **1986**,1, 3.

[39] Brauner, M., Briggs, J. S., and Klar, H., *J.Phys.B*, **1989**, 22, 2265.

[40] Jones, S., Madison, D. H., Franz, A., and Altick, P.L., *Phys.Rev.A*, **1993**, 48, R22.

[41] McGuire, E. J., *Phys. Rev.*, **1977**, A16, 62., *ibid* **1977**, A16, 73., *ibid* **1979**, A20, 445.

[42] Bartmess, J. E., and Georgiadis, J. E., *Vacuum*, **1983**, 33, 149.

[43] a) Franco, J., and Daltabuit, E., *Rev. Mex. Astron. Astrof.*, **1978**, 2, 325. b) Franco, J., *Rev. Mex. Fisica*, **1981**, 27, 475.

[44] a) Rosenstock, H. M., and Krauss, M., *Quasi-Equilibrium Theory of Mass Spectra* in *Mass spectrometry of Organic Ions*, McLafferty, F. W., editor, Academic Press, New York, **1963**. b) Rosenstock, H. M., and Krauss, M., *Current Status of the Statistical Theory of Mass Spectra* in *Advances in Mass Spectrometry*, Volume 2, Elliott, R. M., editor, Pergamon Press, Oxford, **1963**.

[45] See for example, Atkins, P. W., *Physical Chemistry*, Fifth Edition, Oxford University Press, Chp 22, **1994**.

[46] Faist, M. B., and Levine, R. D., *J. Chem. Phys.*, **1976**, 64, 2953.

TABLES

Table 1 Steric factors and steric ratios for 200 eV electron impact ionization of oriented molecules, Ar and SF_6 using a quadrupole mass filter detector.

System	Ion	$G=(S_--S_+)/(S_-+S_+)$	$R = S_+/S_-$
Ar	Ar^+	0.004	0.99
SF_6	SF_6^+	~ 0	~ 1
CH_3Cl	CH_3Cl^+	-0.42 ± 0.12	2.58
	CH_3^+	+0.02 ± 0.03	0.96
CH_3Br	CH_3Br^+	~ -0.1	~1.2
	CH_3^+	~ 0	~ 1
CF_3Br	CF_3^+	-0.22 ± 0.20	1.80
$CHCl_3$	$CHCl_2^+$	-0.17 ± 0.08	1.36

Table 2 Calculated and experimental steric ratios.

Species	μ / 10^{-30} Cm	l / pm	R(calc)	R(expt)
$CH_3Cl^{\delta-}$	6.24	215	2.1	2.6
$CH_3Br^{\delta-}$	6.04	230	1.9	
$CH_3I^{\delta-}$	5.40	251	1.7	
$CHCl_3^{\delta-}$	3.37	168	1.6	1.4
$CHBr_3^{\delta-}$	3.30	175	1.6	
$CF_3Cl^{\delta+}$	1.67	220	1.2	
$CF_3Br^{\delta+}$	2.17	240	1.3	1.8
$HCl^{\delta-}$	3.60	129	1.8	
$NO^{\delta-}$	0.62	136	1.1	
$CO^{\delta+}$	0.39	121	1.1	

Table 3 Calculated and experimental maximum ionization cross-sections.

	$\sigma_{i,C}$ / Å^2	σ_i (a) / Å^2	σ_i (b) / Å^2	σ_i(expt) / Å^2
Ar	2.62 (-25.6%)	2.92 (-17.1%)	2.61 (-25.9%)	3.52
N_2	2.68 (-2.6%)	3.14 (+14.2%)	2.76 (+0.4%)	2.75
CH_4	4.16 (-2.3%)	4.75 (+10.5%)	4.53 (+5.3%)	4.30
CH_3Cl	5.17 (-45.3%)	8.34 (-11.8%)	8.06 (-14.8%)	9.46

FIGURE CAPTIONS

Figure 1.
Diabatic potential curves for NaI with an expanded view of the adiabatic potential curves, ε_1 and ε_2, near the diabatic curve crossing.

Figure 2.
Simplified picture of atom-atom collisional ionization with crossing distance R_c. Heavy solid lines represent trajectories of neutral systems. At the first crossing ($r=R_c$) some fraction ($1-P_d$) of trajectories make adiabatic transitions and are represented by dashed lines (ion pairs). Those making diabatic transitions remain neutral and continue their flight relatively unaffected. Each of these trajectories then encounters $r=R_c$ again, and again each trajectory can make an adiabatic or diabatic transition, resulting in ion pairs or neutrals depending on the trajectory. The ultimate production of ions requires one transition to be diabatic and one to be adiabatic, in either order. The inner circle represents the repulsive core.

Figure 3.
Illustration of the cross beam machine. N is the nozzle source for the molecular beam, C is the buffer chamber with a beam chopper (not shown), H is the hexapole electric field quantum state selector, U is the homogeneous electric field plates, Q is an on-axis quadrupole mass filter, O is the fast atom beam source, and C_0 and C_{180} are channeltrons.

Figure 4.
Calculated focusing curves (Intensity vs V) for CH_3Br at 10K for 1.4 m fields with exit aperture radii of 4.45mm and 0.145mm. Rotational states for the smaller aperture are resolved, the larger aperture completely loses rotational structure but gains in intensity.

Figure 5.
Distribution of orientations of molecules state selected by inhomogeneous hexapole electric field.

Figure 6.
Polarities of the homogeneous orienting field and channeltrons used for the 0° and 180° configurations. The orientation of the polar molecule is indicated for each configuration using CH_3Br and CF_3Br as examples.

Figure 7.
Relative signals for producing K^+ ions on collision with oriented CH_3Br and CF_3Br. The negative end of CH_3Br and the positive end of CF_3Br are more reactive.

Figure 8.
Relative cross section (corrected ion signal / K beam intensity) for heads and tails orientations of CH_3Br and CF_3Br.

Figure 9.
Steric Factor G vs CM energy for CF_3Br and CH_3Br. Horizontal line is G=0 (no steric effect) and dashed line is the negative of a smooth fit to the CH_3Br data plotted to compare the curvature of CH_3Br and CF_3Br.

Figure 10.
Comparison of experimental G values for CH_3X and CF_3X. The recent values of reference 7 b) are included as dashed lines, other data from reference 10.

Figure 11.
Relative cross sections for heads and tails orientations for the K + CF_3Br reaction near threshold for ion production.

Figure 12.
Schematic mechanism for impulsive reaction of thermal energy reaction of K with oriented CF_3I. The electron is assumed to be transferred at large distance to the molecule irrespective of orientation. The molecular ion is formed in a repulsive state which promptly dissociates, ejecting the I^- ion in the direction of the molecular axis and the K^+ is dragged off by the departing I^- resulting in backward scattering for heads orientation and forward scattering for tails as observed.

Figure 13.
Highly schematic one-dimensional representation of the electron jump in a dissociating molecular system. Neutral K and RX approach on a covalent surface on the right, crossing the ionic surface at r_{c1} which is at sufficiently short range for the surfaces to be separated and for the system to traverse the crossing adiabatically (the electron "jump"). After electron transfer, the negative ion can undergo a dissociation (migrating to the left panel), and the system evolves along another surface to give fragments K^+, X^-, and R. These undergo a crossing r_{c2} at larger distances with neutral fragments K, X and R, where the surfaces are not well separated. The system is more likely to traverse this crossing diabatically, and the fragments will separate as charged species.

Figure 14.
Schematic illustration of velocity components as the molecular ion dissociates in heads and tails orientations. In the heads orientation, the nascent ions collide head on with a higher relative velocity than in the tails orientation, where one ion must catch up with the other.

Figure 15.
Ln R vs $(E-E_{th})^{-1}$ for CF_3Br. Circles from reference 7 b) and squares from reference 10. Deviations from line are accentuated for low E.

Figure 16.
Schematic mechanism for impulsive reaction of high energy K with oriented CR_3X. Similar to Figure 12, but the higher energy K atom is much less perturbed by the lower energy X^-, although parallel trajectories (in the tails orientation) allow for

longer contact time resulting in some neutralization and a concomitant reduction in ion signal.

Figure 17.
Approximate one-dimensional ionic and covalent diabatic potentials adapted from reference 46 for CF_3Br. Solid and dashed ionic curves are Rittner-type potentials for parent and fragment ions respectively, and heads and tails are covalent curves. The ionic asymptotes are denoted by arrows. The crossings are avoided; dotted curves for the "crossing" near 4.3 Å are the adiabatic curves resulting from configuration interaction[5] between the diabatic ionic and covalent curves. (Adiabatic curves for the other crossings are omitted for simplicity.)

Figure 18.
Illustration of the molecular beam - electron beam crossing region used in the electron impact ionization experiments. The molecular beam source, buffer and hexapole chambers are similar to those shown in Figure 3.

Figure 19.
Coulomb potential versus the electron-molecule separation for three ideal orientations of the CH_3Cl molecule. The electron-molecule separations corresponding to an equivalence between the Coulomb potential and the ionization potential for CH_3Cl are shown by the vertical lines.

Figure 20.
Experimental ionization cross-section[36] versus the cross-sections calculated from equation (24) with $z_{eff} = 1$.

Figure 21.
Experimental ionization cross-section[36] versus the polarizabilty volume and versus the polarizabilty volume / ionization potential.

Figure 1

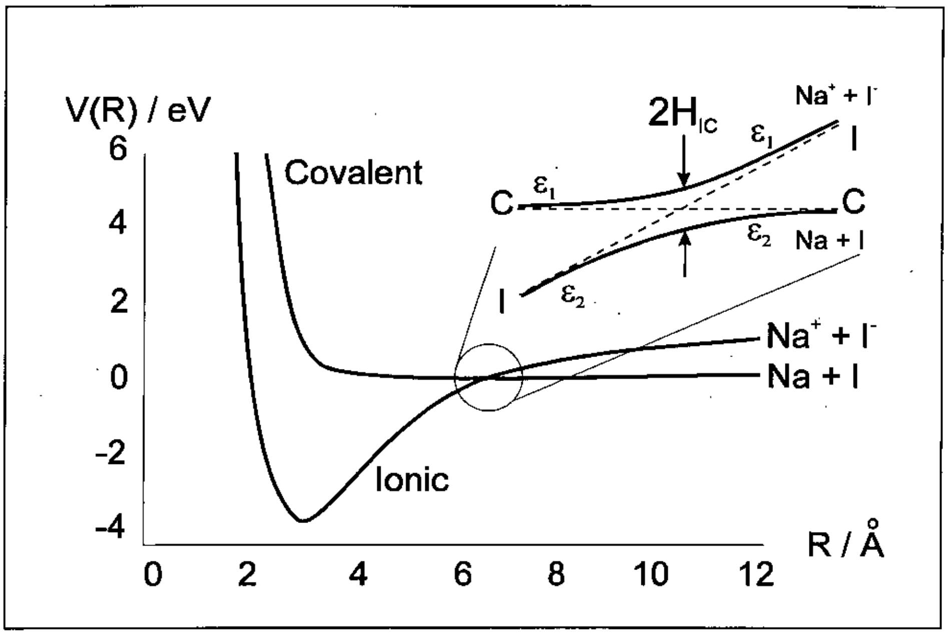

Figure 2

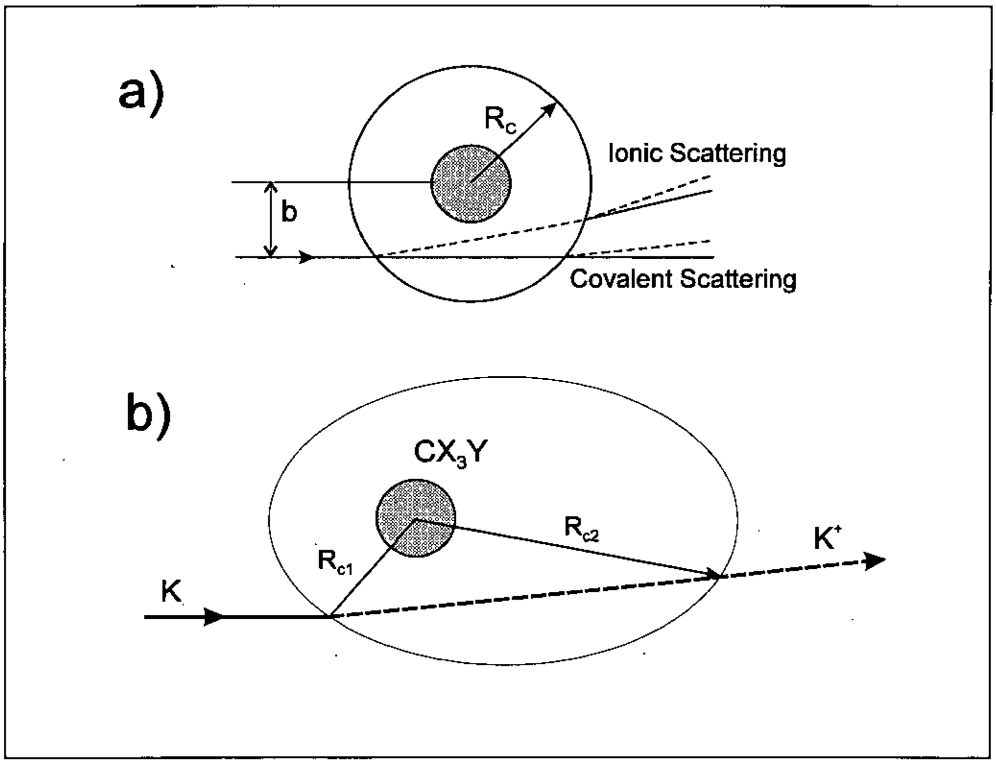

Figure 3

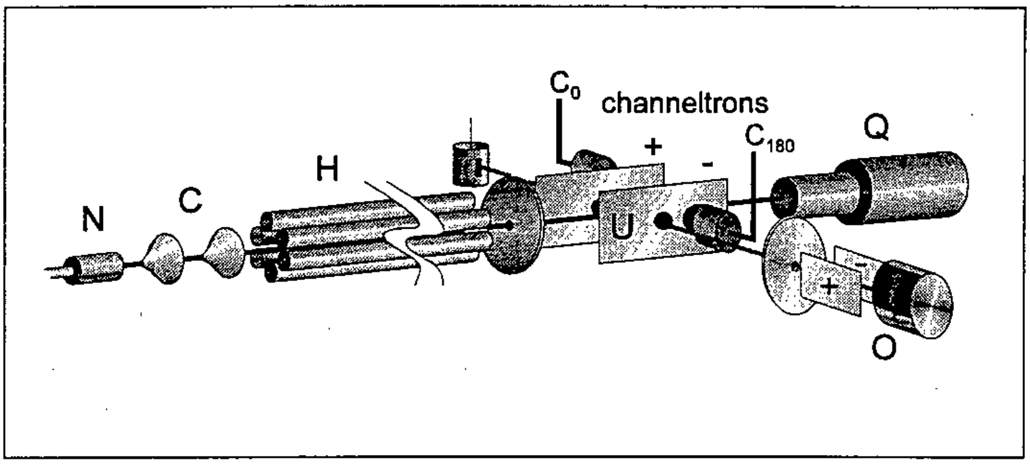

Figure 4

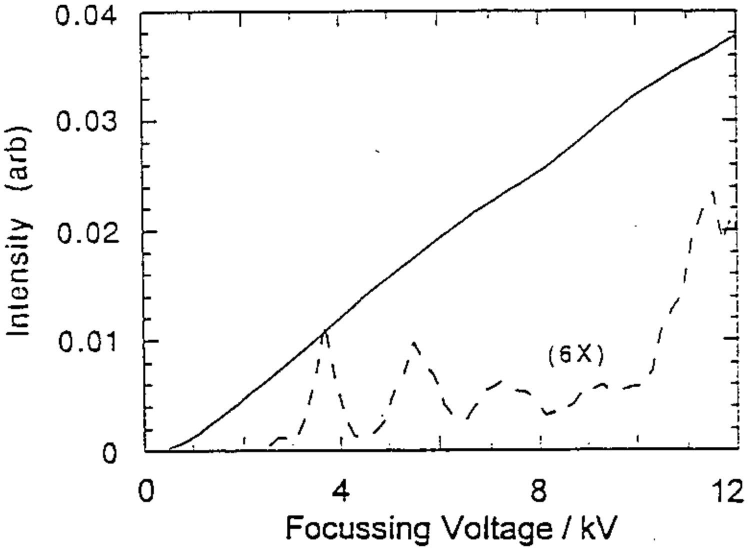

Figure 5

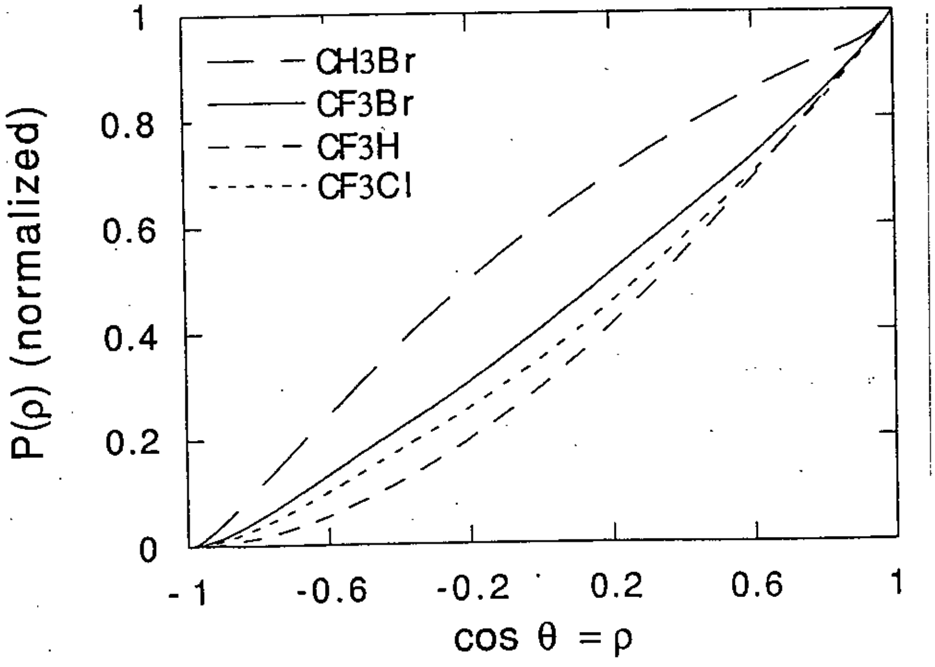

Figure 6

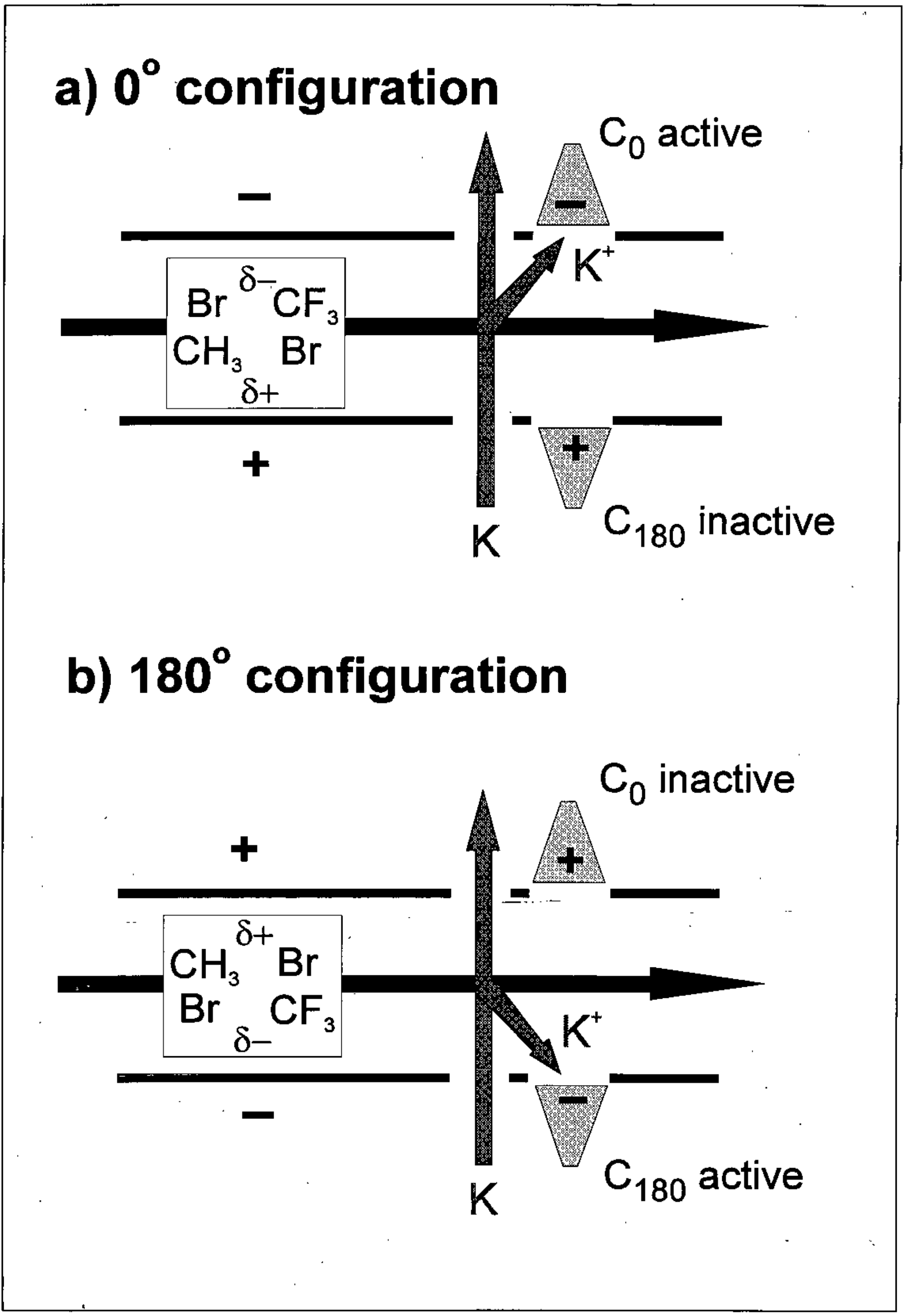
a) 0° configuration
C0 active
−
K+
Br δ− CF3
CH3 Br
δ+
+
K
C180 inactive
b) 180° configuration
C0 inactive
+
δ+
CH3 Br
Br CF3
δ−
K+
−
K
C180 active

Figure 7

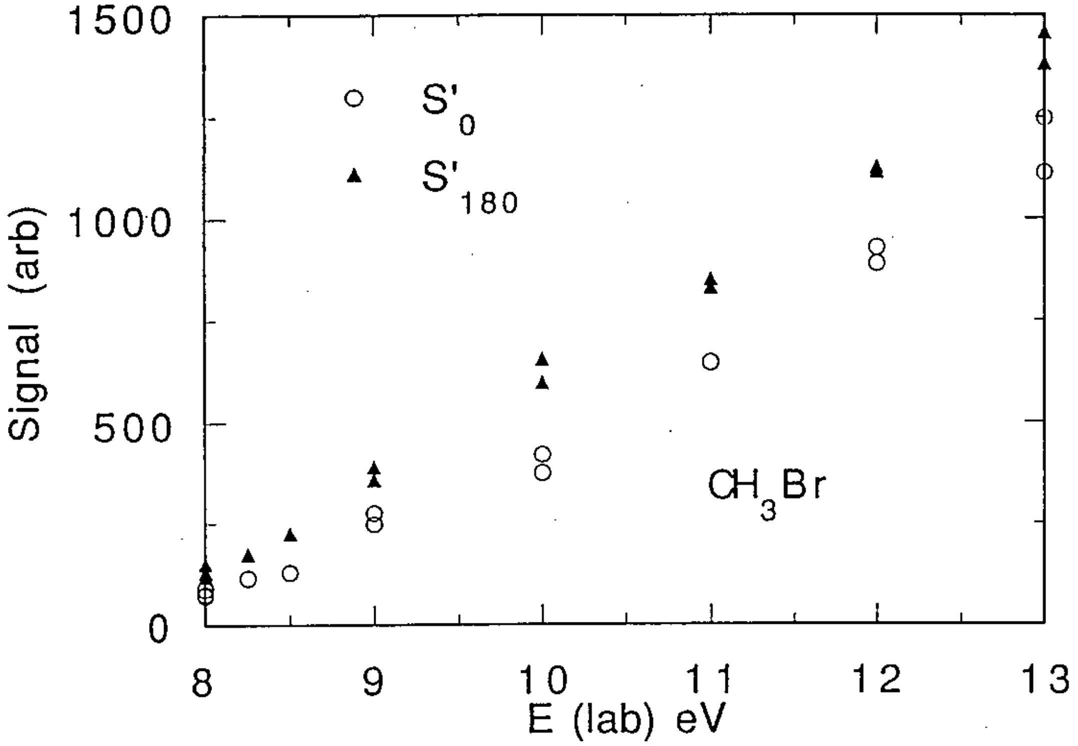
1500
1000
500
0
Signal (arb)
8
9
10
11
12
13
E (lab) eV
○ S'$_0$
▲ S'$_{180}$
CH$_3$Br

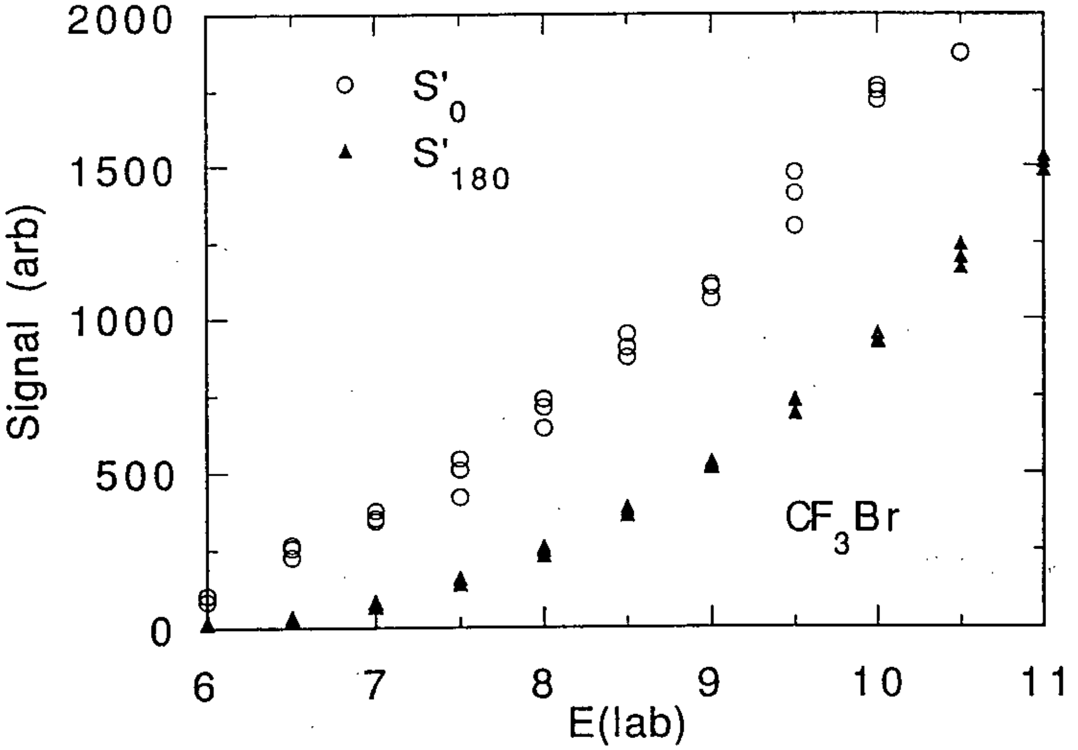
2000
1500
1000
500
0
Signal (arb)
6
7
8
9
10
11
E(lab)
○ S'$_0$
▲ S'$_{180}$
CF$_3$Br

Figure 8

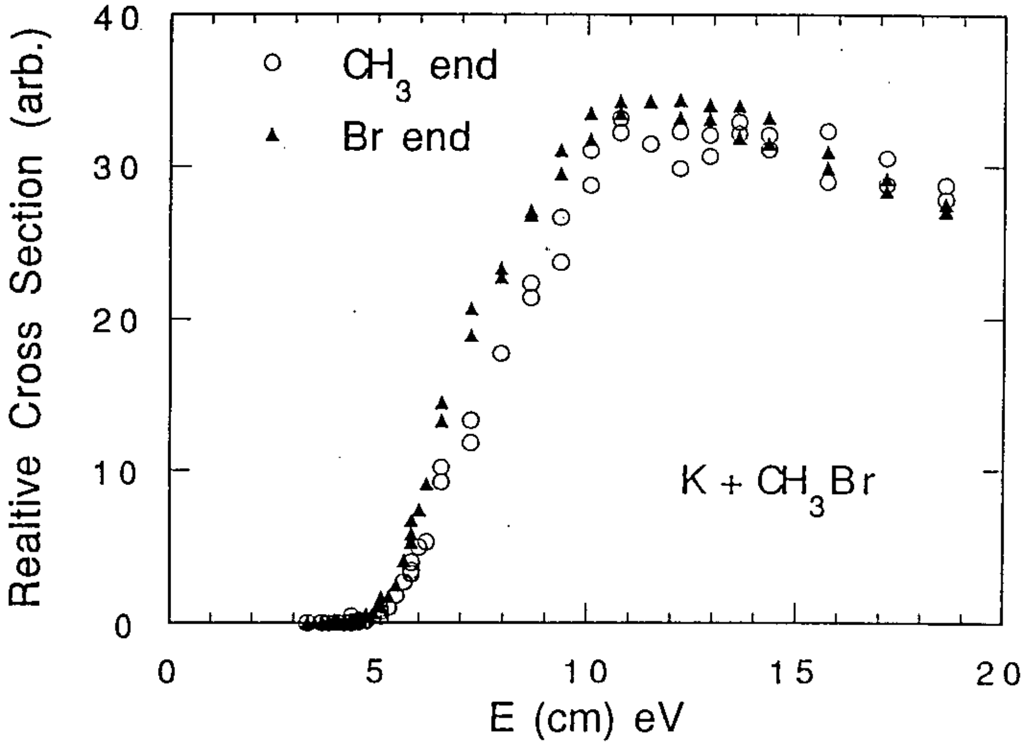
40
30
20
10
0
Realtive Cross Section (arb.)
○ CH_3 end
▲ Br end
K + CH_3Br
0
5
10
15
20
E (cm) eV

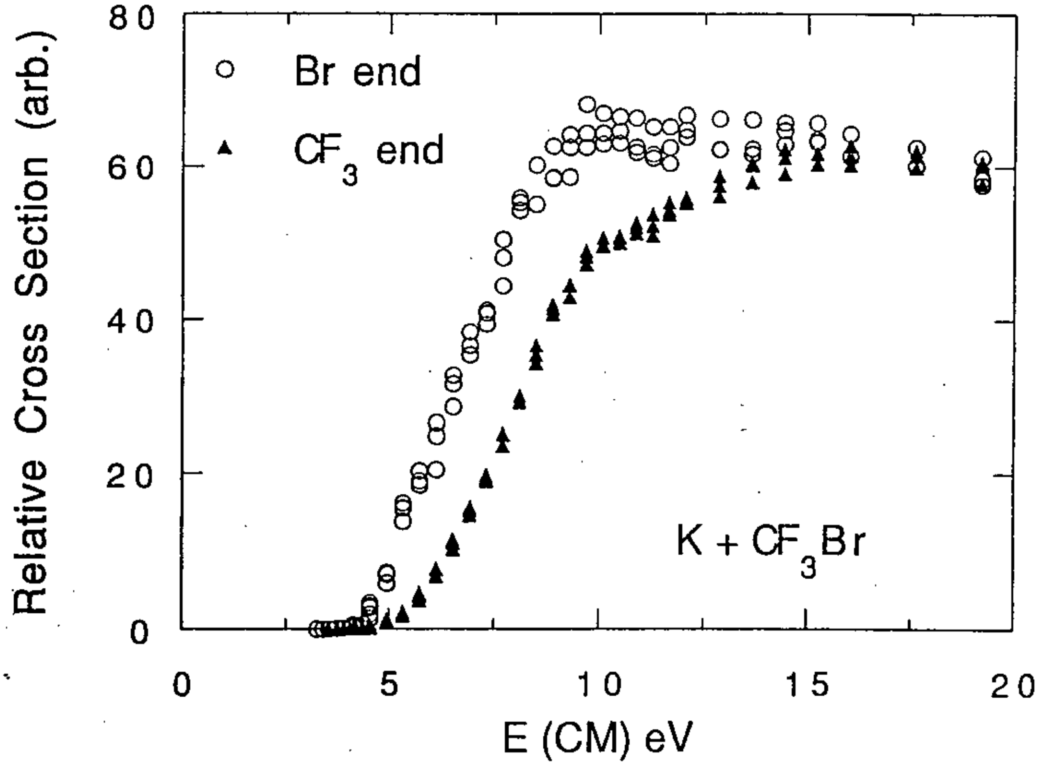
80
60
40
20
0
Relative Cross Section (arb.)
○ Br end
▲ CF_3 end
K + CF_3Br
0
5
10
15
20
E (CM) eV

Figure 9

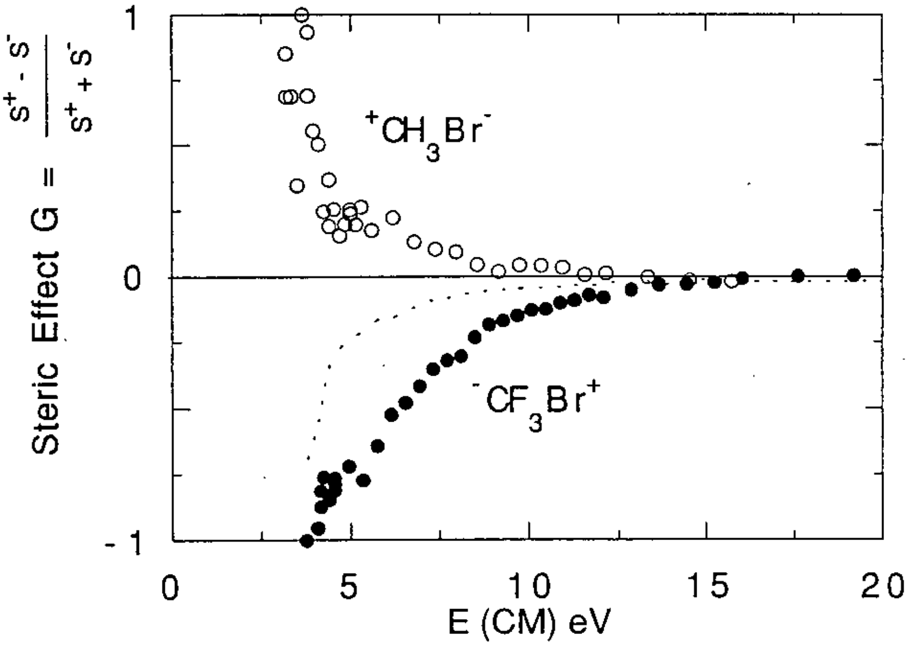

Figure 10

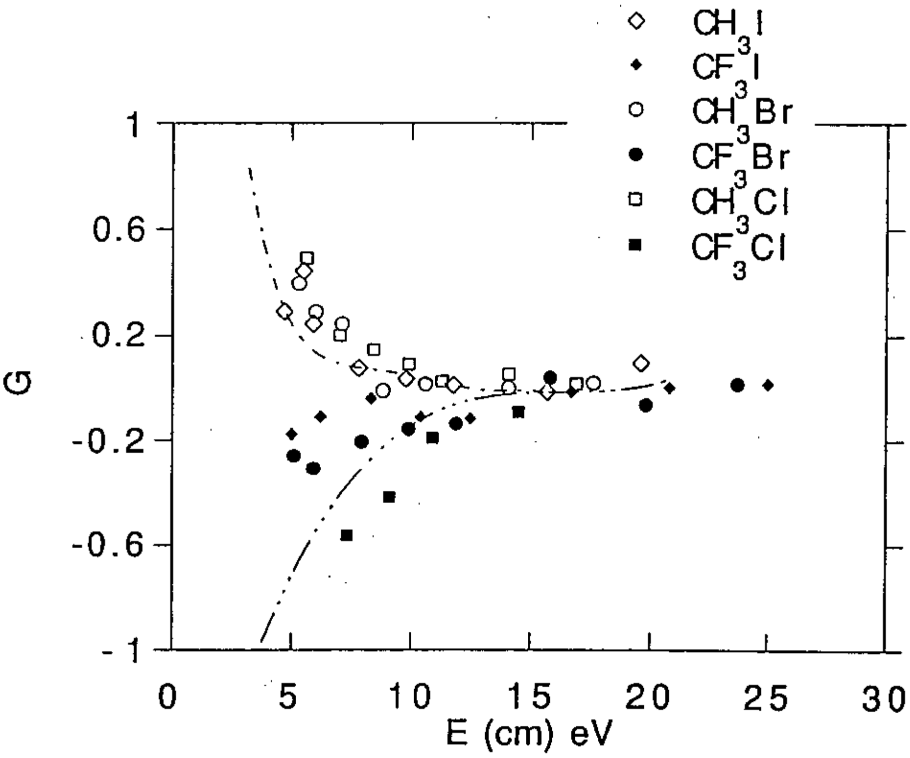

Figure 11

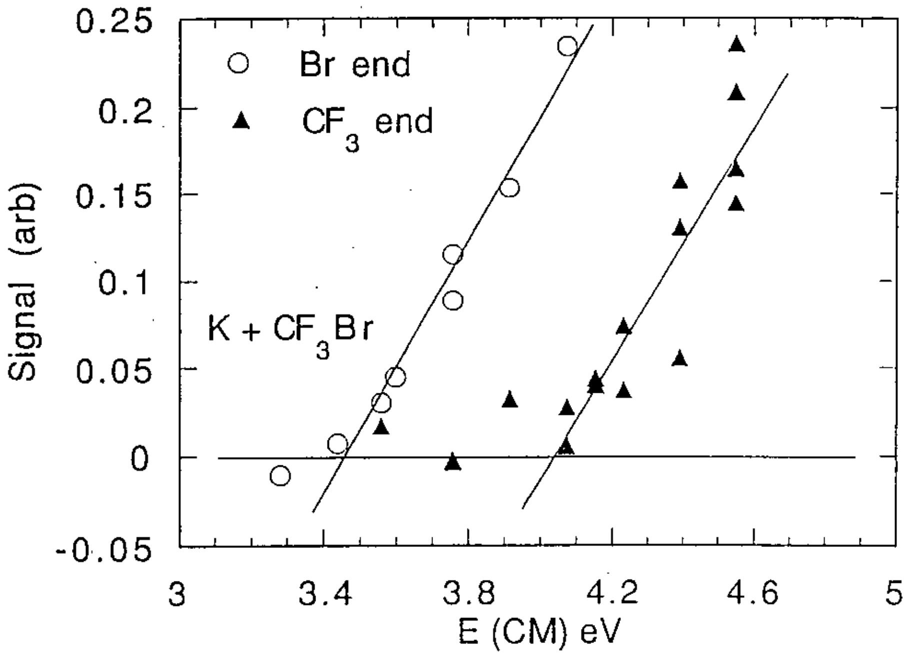

Figure 12

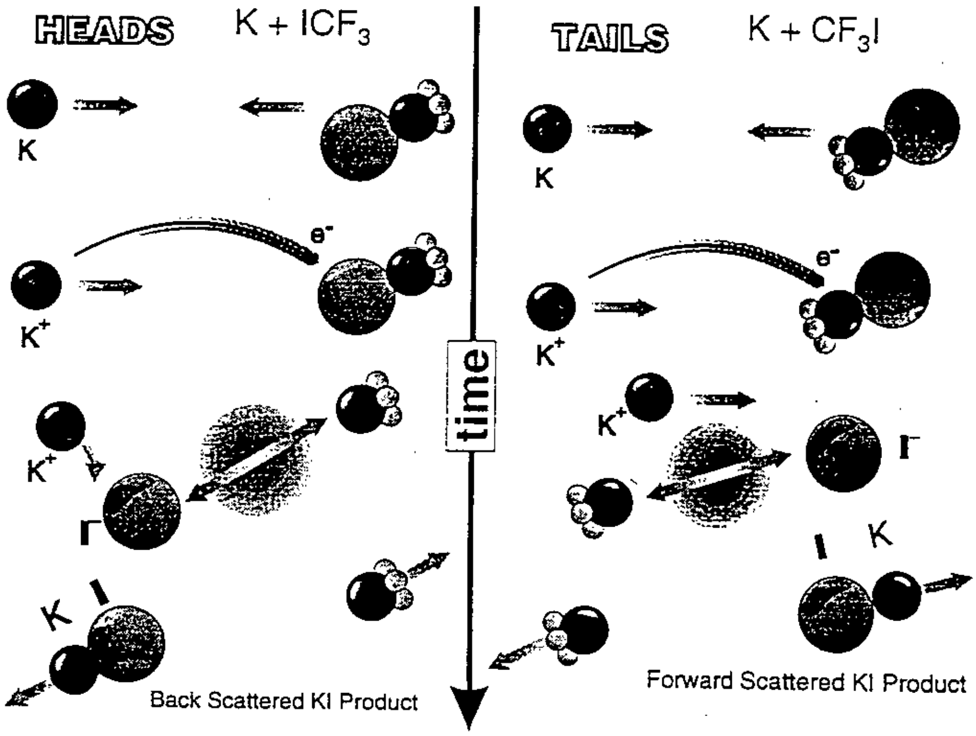

Figure 13

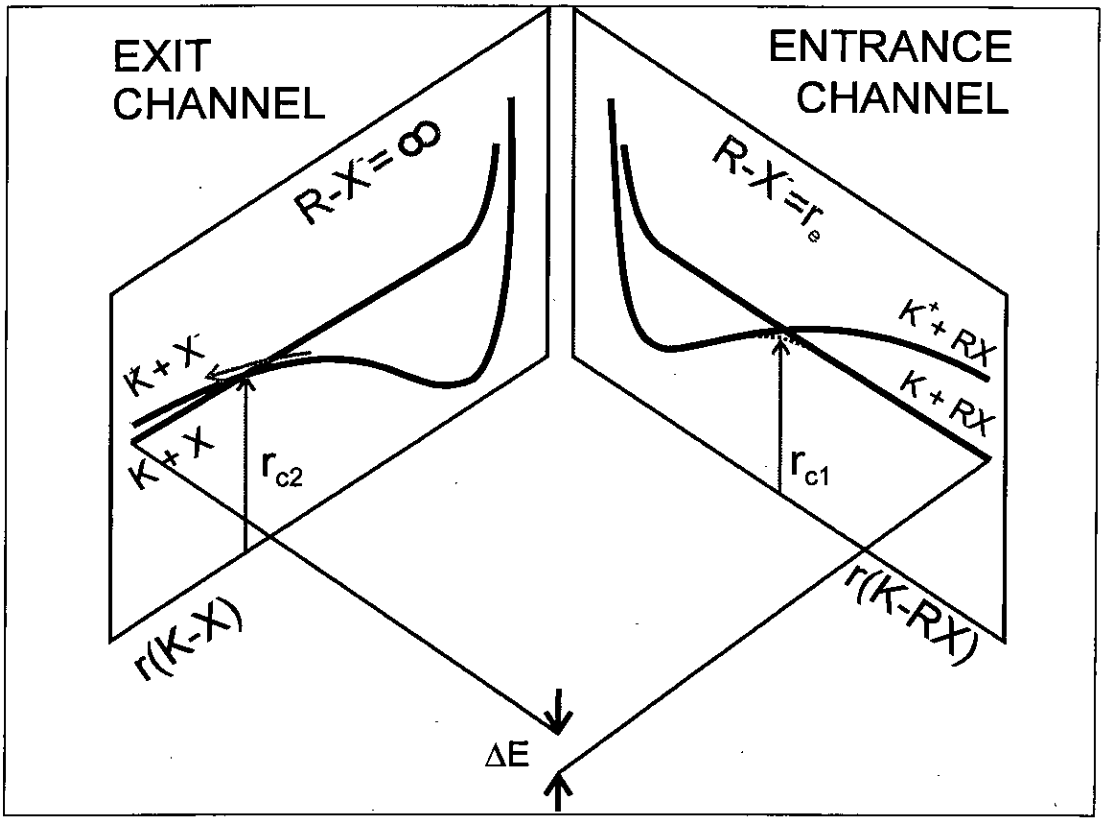

Figure 14

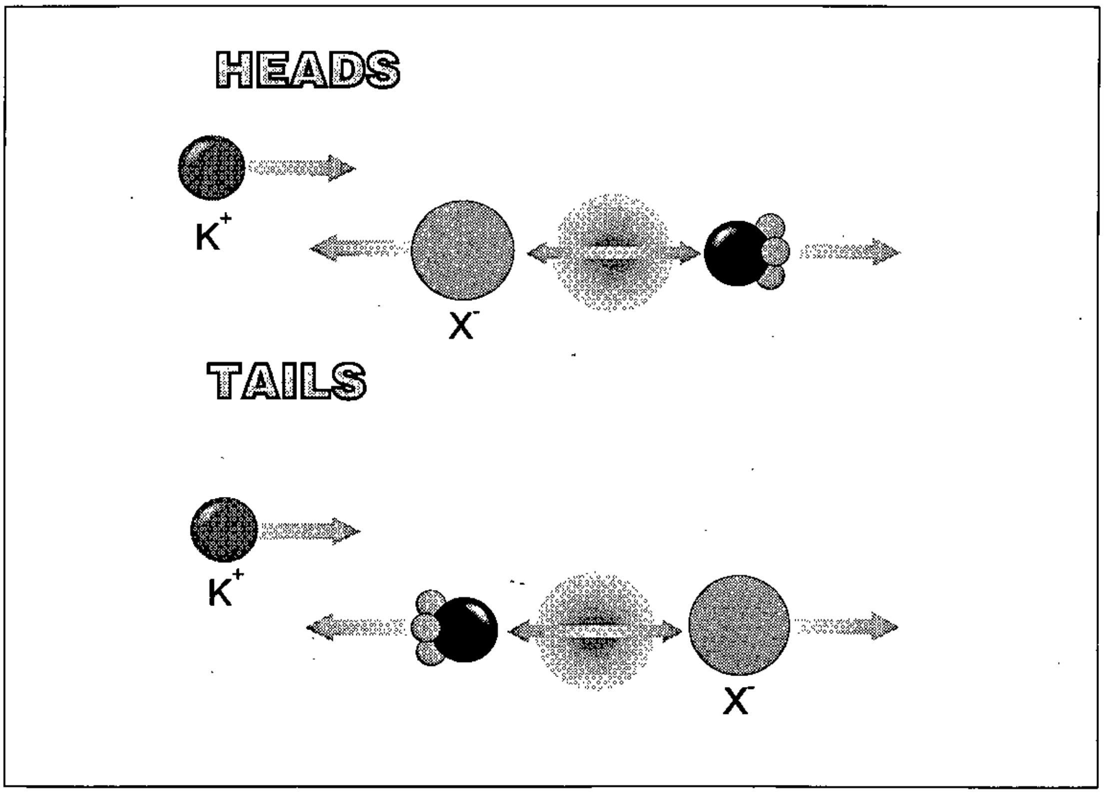

Figure 15

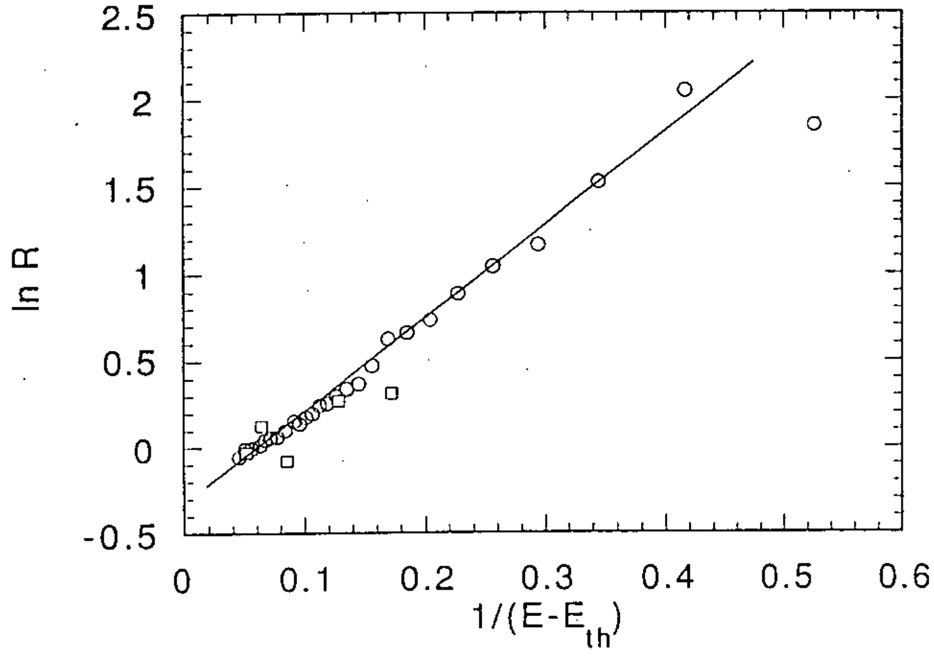

Figure 16

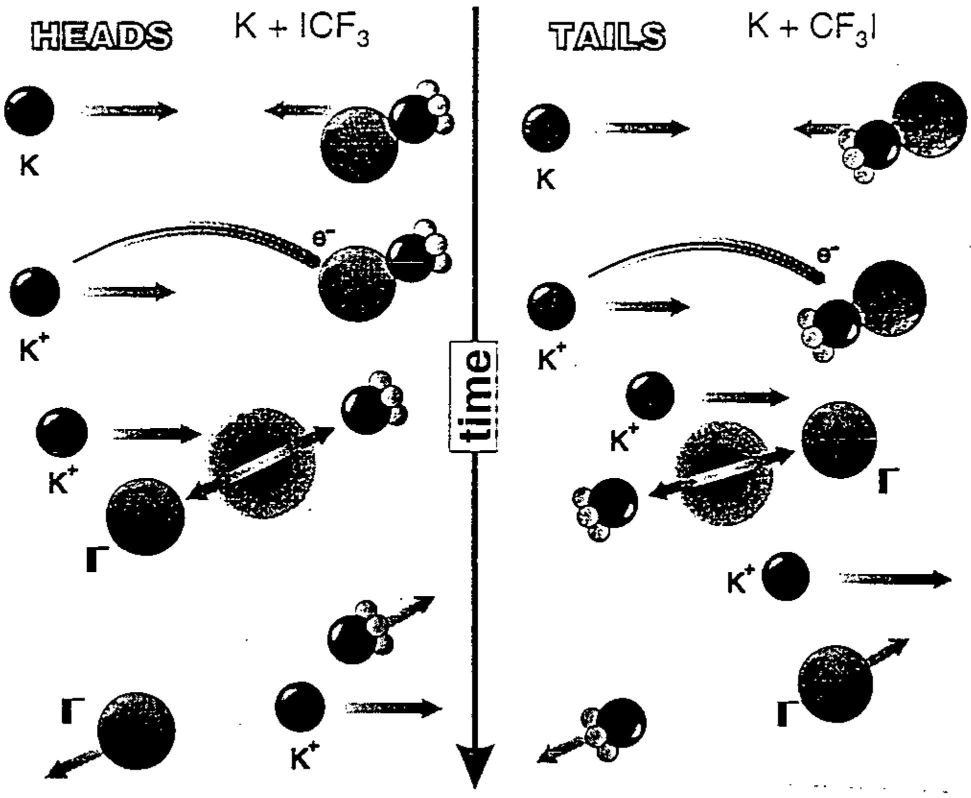

Figure 17

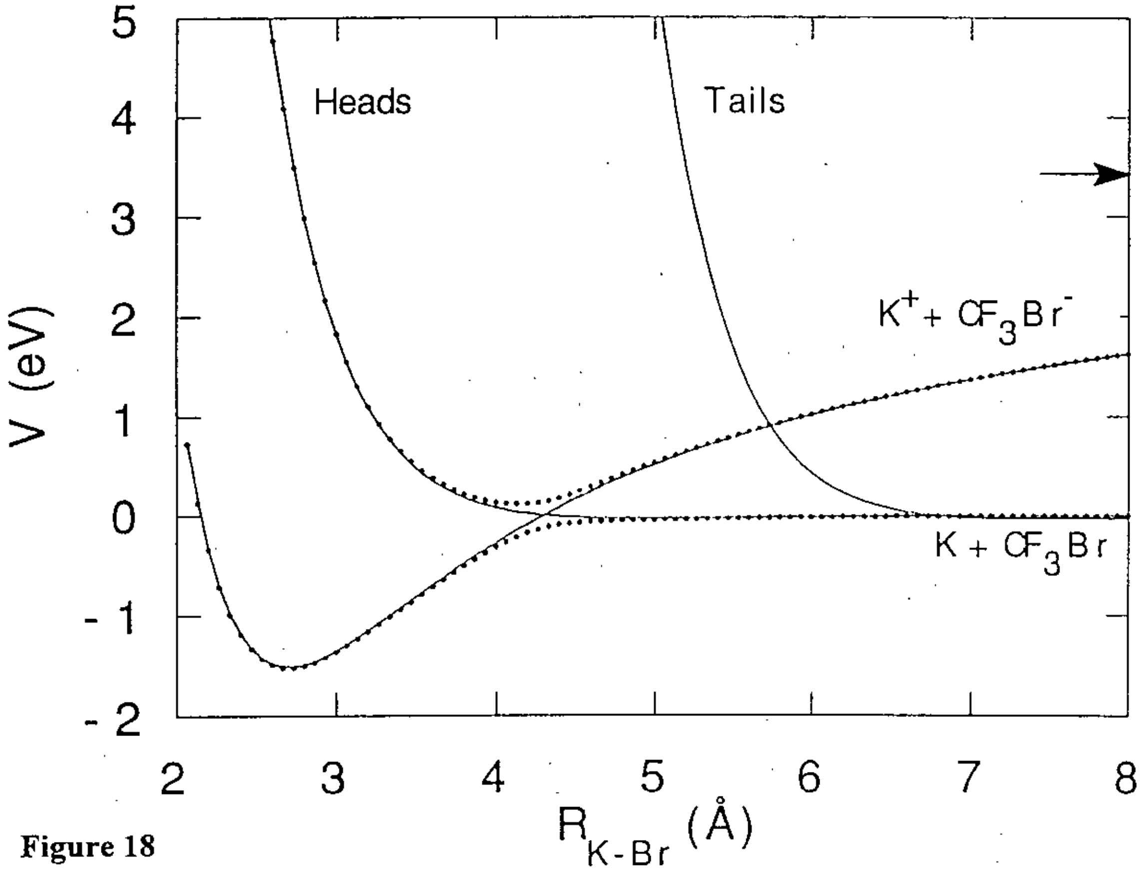

Figure 18

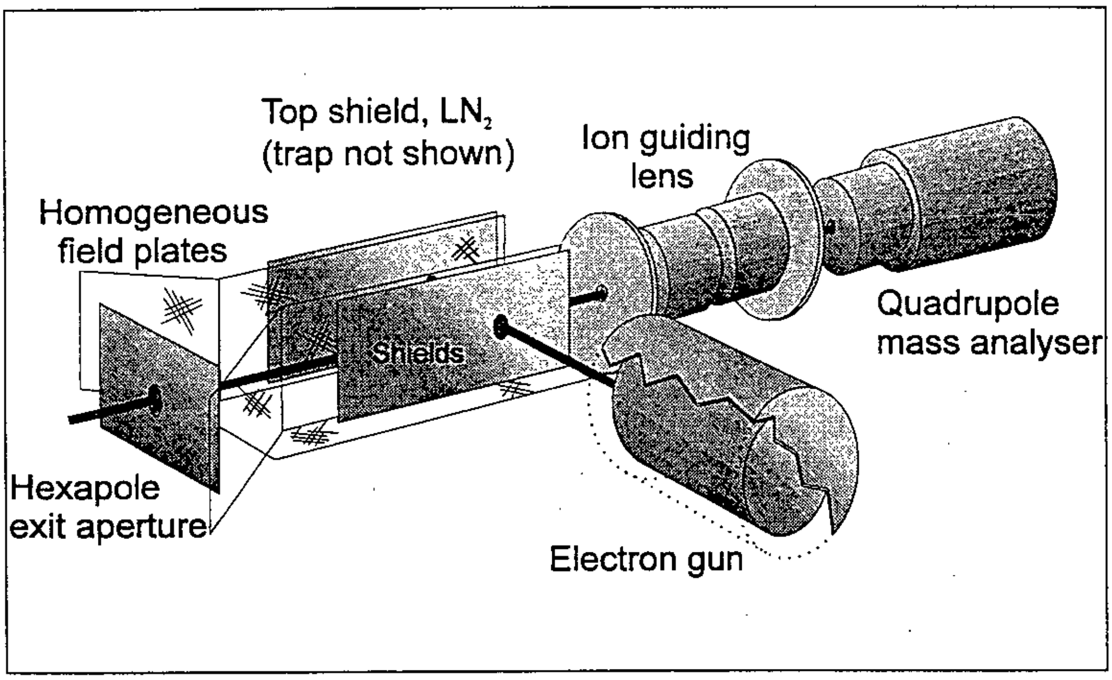

Figure 19

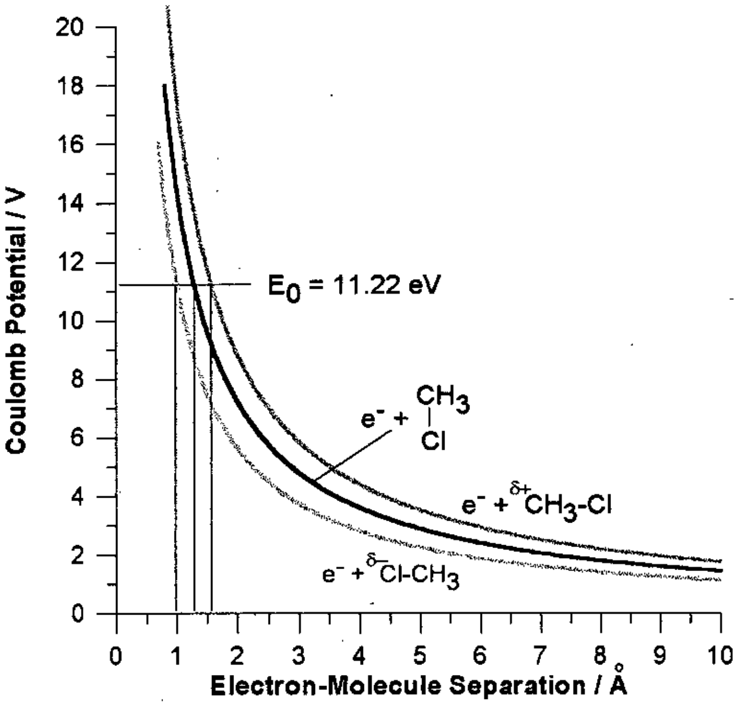

Figure 20

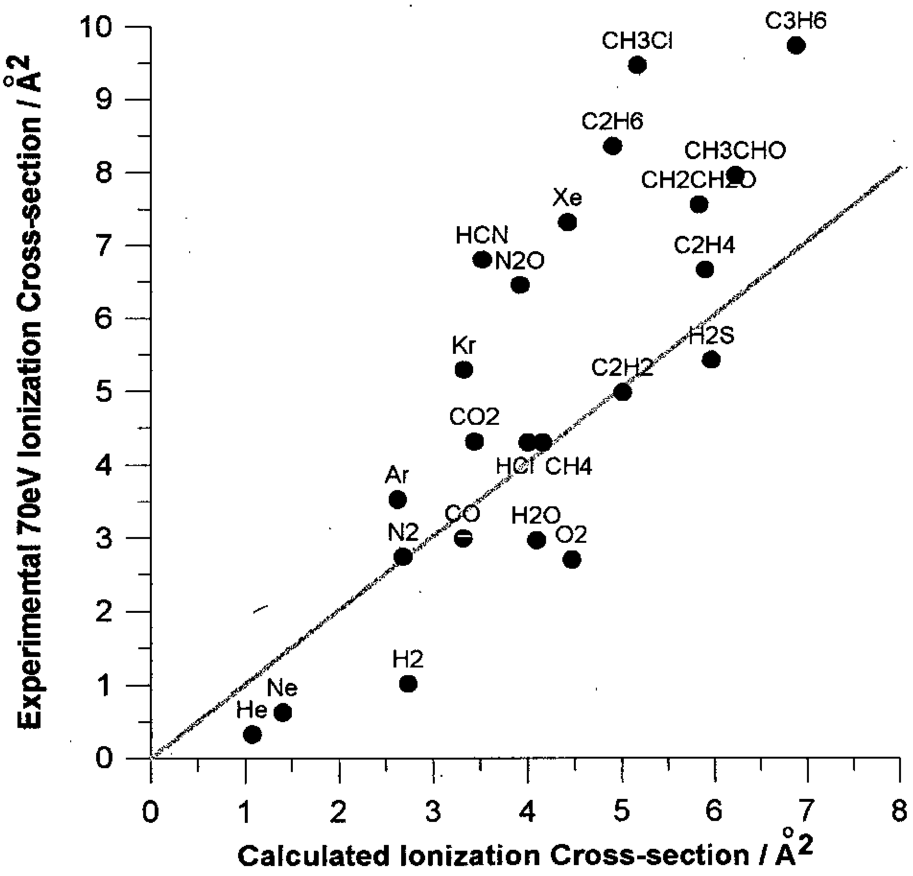

Figure 21

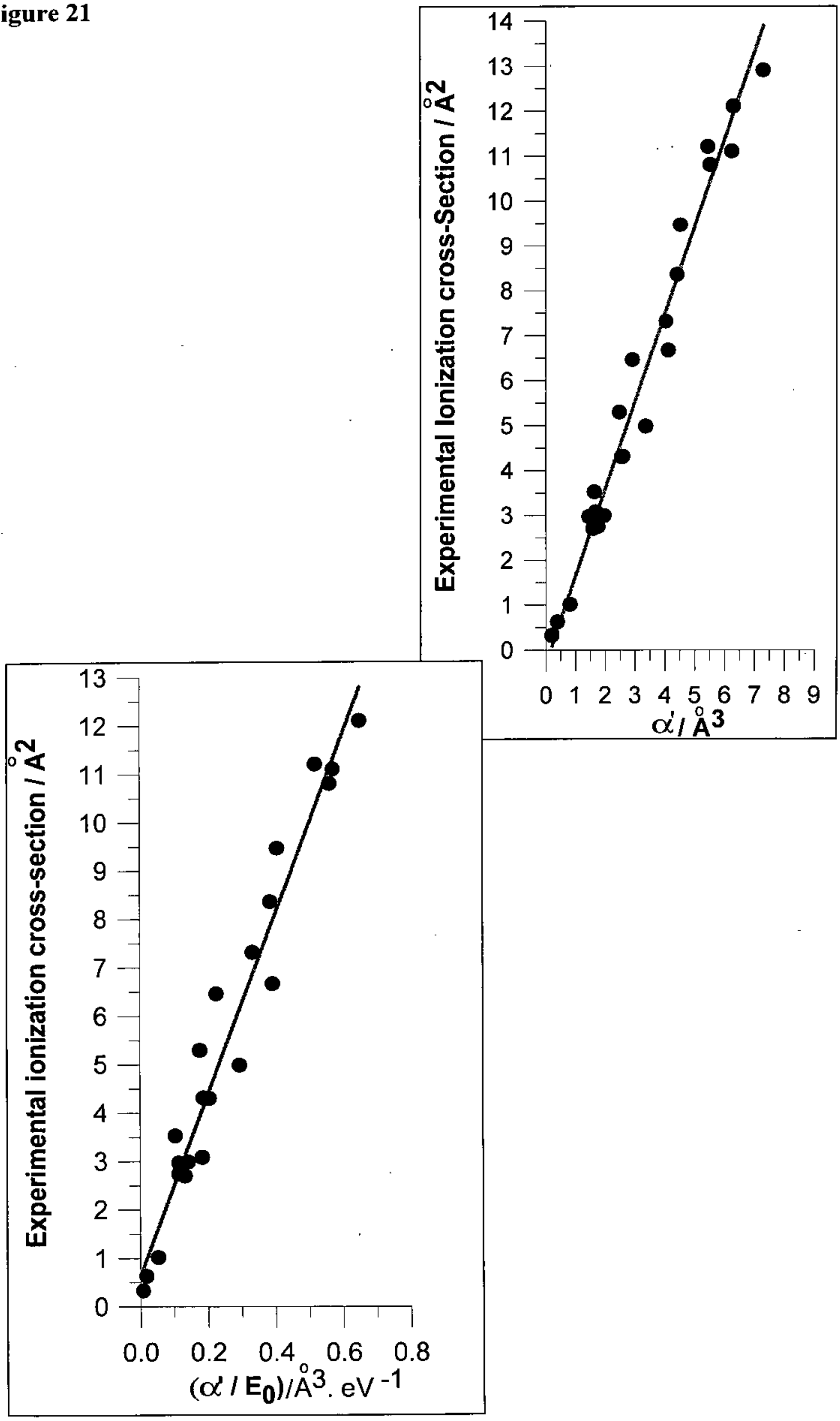
Experimental Ionization cross-Section / Å2
0
1
2
3
4
5
6
7
8
9
10
11
12
13
14
0 1 2 3 4 5 6 7 8 9
α' / Å3
Experimental ionization cross-section / Å2
0
1
2
3
4
5
6
7
8
9
10
11
12
13
0.0 0.2 0.4 0.6 0.8
(α' / E0)/Å3. eV -1